Fingerprints of order and disorder

The electronic structure and optical response of crystalline and amorphous materials

Marc Landmann

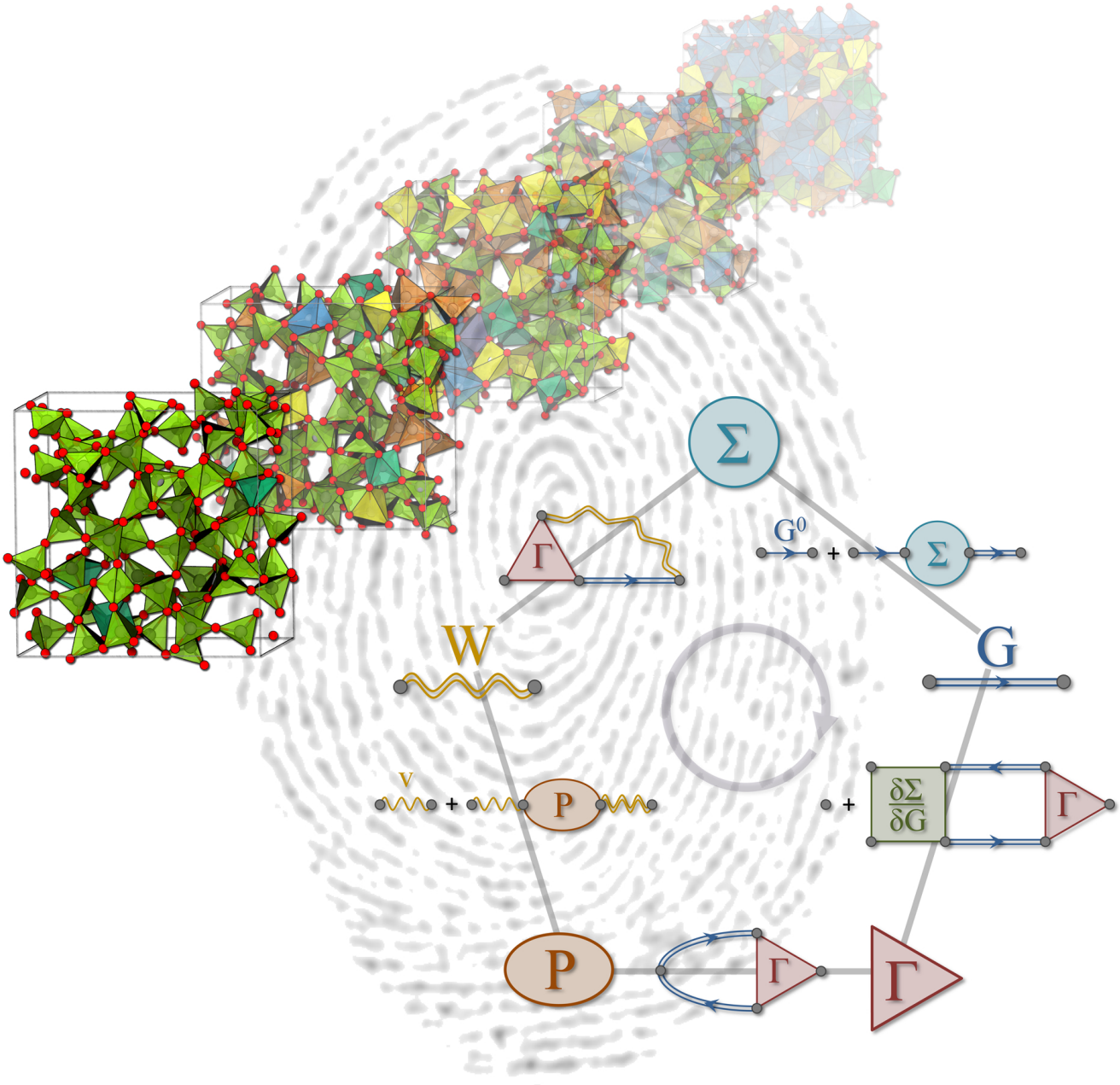

In Nature nothing is simple.

Stanisław Lem (1921–2006)

Fingerprints of order and disorder

The electronic structure and optical response
of crystalline and amorphous materials

Dissertation

zur Erlangung des akademischen Grades
Doktor der Naturwissenschaften (Dr. rer. nat.)

Vorgelegt dem
Fachbereich Physik der Fakultät für Naturwissenschaften
Universität Paderborn

Marc Landmann, M.Sc.

Paderborn, 2020

Eingereicht am: 12.05.2020
Tag der mündlichen Prüfung: 24.06.2020

Promotionskommission

Vorsitzender	Prof. Dr. Jörg Lindner [1]
Erstgutachter	Prof. Dr. Wolf Gero Schmidt [2]
Zweitgutachter	Prof. Dr. Thomas Kühne [3]
Vertreter des Mittelbaus:	Dr. Matthias Reichelt [4]

[1] Nanostrukturierung -Nanoanalytik - Photonische Materialien, Department Physik, Universität Paderborn
[2] Theoretische Materialphysik, Department Physik, Universität Paderborn
[3] Theoretische Chemie, Department Chemie, Universität Paderborn
[4] Theoretische Festkörperelektronik - Optoelektronik und - Photonik, Department Physik, Universität Paderborn

Abstract

The rapid technological progress in modern semiconductor industry, which is still widely driven by ongoing miniaturization processes enhancing the functional integration density of optoelectronic devices, progressively rises to challenge materials science to take control on fabrication processes of new functional (nano)materials on an atomic level. Suchlike, artificially designed material compounds allow for the purpose- and goal-oriented utilization of structural and functional synergies between diverse materials, different material modifications and chemical compositions, as well as size-related quantization effects modifying the structural and electronic material properties in the nano regime. Following from this, the central challenge directed to the theory-based branch of materials science is to find and illuminate structure-function correlations which, on the one hand, explain existing trends in experimental data on diverse materials and, on the other hand, promote the construction and refinement of basic scientific theories acting as the formal fundament for future experimental research as well as an orientation guide to further advancing materials design for technological and commercial applications.

A class of materials, whose characterization through materials science represents a severe experimental as well as theoretical challenge, are amorphous solids or, more generally speaking, any kind of structurally disordered (solid) material phase with atoms lacking the common long-range order characteristics of the crystalline state. The aim of the present thesis is to contribute to a mutual understanding between the electronic and optical material properties and the associated atomic structure features originating from preserved crystal-like short-range order and novel types of material specific medium-range order in disordered materials as well as functionalized nanostructures, in general. To this purpose, *density functional theory* (DFT) simulations for technologically relevant material groups as binary transition-metal (di)oxides (TiO_2, SiO_2), ternary amorphous $Ti_xSi_{1-x}O_2$ mixed oxides/hybrid oxides as well as crystalline binary (GaN, AlN) and ternary ($Al_xGa_{1-x}N$) group-III nitride semiconductors have been conducted within the present thesis.

Among the studied systems, the ternary amorphous $Ti_xSi_{1-x}O_2$ mixed oxides represent an extraordinary model system to study the systematic topological transformation of a ring-like medium-range ordered tetrahedral glass former into a short-range ordered amorphous solid with diverse coordination characteristics. The carried out simulations allow a detailed characterization of coordination characteristics and the network topology during the continuos structural disorder-disorder transition from prototypical glass-like order in SiO_2 to the diverse short-range order of amorphous TiO_2. The central characteristic of this transition is the occurrence of *non-crystalline*

fivefold coordination states for Si as well as Ti ions, which actually drive the conversion of the material's atomic order by acting as both network builders as well as network modifiers depending on concentration. The investigation of the structural order properties of the crystalline ternary $Al_xGa_{1-x}N$ alloys allows a detailed investigation of the variability of microscopic and macroscopic material characteristics depending on the compositional disorder in the cation sublattice. Complementary to bulk-phase order/disorder phenomena, the influence of point defects in GaN, the formation of nonpolar GaN surfaces, and nanostructuring in AlN/GaN quantum-well heterostructures on the electronic and optical material properties has been investigated. Not at least, these studies facilitate a systematic evaluation of the applicability and the reliability of the utilized numerical approaches for a broad range of structural and compositional problems.

A common limitation of numerical simulations based on *conventional* Kohn-Sham density-functional theory, running throughout this dissertation, is the systematic underestimation of electronic band gaps in semiconducting and insulating materials by common (semi)local exchange-correlation functionals. A more advanced description of the electronic structure improving the description of band gaps, defect levels, and band discontinuities is achieved by mixing a material specific fraction of non-local Fock exchange to commonly utilized density functionals within a generalized Kohn-Sham framework. The use of suchlike exact-exchange *adjusted* hybrid functionals allows for calculations that reach the accuracy of formally higher ranking theoretical approaches as the *GW* approximation to *many-body perturbation theory* (MBPT). It is further demonstrated how the independent-particle picture severely limits the predictive power of density-functional theory for optical material properties in various material modifications. The results obtained within the present thesis unambiguously demonstrate, that the inclusion of electron-hole interaction through solution of the Bethe-Salpeter equation for Coulomb-correlated electron-hole pairs is, despite its computational demands, indispensable for an accurate description, and therefore *parameter-free* prediction, of optical material parameters. This particularly includes structurally and compositionally complex systems including surfaces and disordered material phases.

Kurzzusammenfassung

Der rasante, gegenwärtig vorrangig durch Miniaturisierungsprozesse zur Erhöhung der funktionalen Integrationsdichte optoelektronischer Bauelemente getriebene, technologische Fortschritt der modernen Halbleiterindustrie stellt die Materialwissenschaften zunehmend vor die Herausforderung Herstellungsprozesse neuer funktionaler Nanomaterialien auf atomarer Ebene zu kontrollieren. Derartige, künstlich geschaffene, (Verbund-)Materialien erlauben die gezielte Ausnutzung von strukturellen und funktionalen Synergieeffekten zwischen verschiedenen Materialien, unterschiedlichen Materialmodifikationen und chemischen Zusammensetzungen sowie dimensionsbedingten Quantisierungseffekten in den strukturellen und elektronischen Materialeigenschaften innerhalb des Nanokosmoses. Die hieraus resultierende zentrale Herausforderung für die computergestützten Materialwissenschaften ist das Auffinden und Ergründen von Struktur-Funktions-Korrelationen, welche einerseits beobachtete Trends in experimentellen Daten zu erklären vermögen und andererseits die grundlegende wissenschaftliche Theoriebildung vorantreiben um weiterführender experimenteller Forschung, sowie zuklünftiger Technologie- und konsumorientierter Materialentwicklung, als Orientierungshilfe dienen.

Eine Materialklasse, deren materialwissenschaftliche Charakterisierung theoretisch, sowie experimentell, eine besondere Herausforderung darstellt sind die amorphen Festkörper oder, allgemeiner gefasst, jedwede Erscheinungsform strukturell ungeordneter (fester) Stoffe, deren Atomen die charakteristische langreichweitige Ordnung kristalliner Festkörper fehlt. Das Ziel der vorliegenden Dissertation ist der Beitrag zum grundlegenden gegenseitigen Verständnis zwischen elektronischen und optischen Materialeigenschaften und den, aus erhaltener kristallartiger kurzreichweitiger Ordnung und neuen mittelreichweitigen Ordnungstypen in ungeordneten Materialien resultierenden, atomaren Struktureigenschaften. Zu diesem Zweck wurden im Rahmen der vorliegenden Dissertation dichtefunktionaltheoretische Simulationen technologisch bedeutender Materialgruppen wie binären Übergangsmetalloxiden (TiO_2, SiO_2), ternären amorphen $Ti_xSi_{1-x}O_2$ Mischoxiden, sowie kristallinen binären (GaN, AlN) und ternären ($Al_xGa_{1-x}N$) Gruppe-III-Nitridhalbleitern durchgeführt.

Unter diesen Systemen stellen die ternären amorphen $Ti_xSi_{1-x}O_2$ Mischoxide ein ausgezeichnetes Modellsystem für die systematische Transformation eines mittelreichweitig ringartig geordneten tetraedrischen Glasformers in einen kurzreichweitig geordneten amorphen Festkörper mit variablen Koordinierungseigenschaften dar. Die vorliegenden Simulationen erlauben eine detaillierte Charakterisierung der Netzwerktopologie während des kontinuierlichen Unordnungs-Unordnungs-Überganges der prototypischen glassartigen Ordnung in SiO_2 hin zur vielschichti-

gen kurzreichweitigen Ordnung in amorphem TiO_2. Zentrales Charakteristikum dieses Überganges ist das Auftreten *nichtkristalliner* fünffacher Koordinationszustände von Si sowie Ti Ionen, welche in Abhängigkeit von ihrer Konzentration in Netzwerk-bildender sowie Netzwerkmodifizierender Funktion die Umformung der atomaren Materialordnung vorantreiben. Die Untersuchung der strukturellen Ordnungseigenschaften der kristallinen ternären, $Al_xGa_{1-x}N$ Mischnitride erlaubt insbesondere eine detaillierte Untersuchung der Veränderbarkeit mikroskopischer und makroskopischer Materialeigenschaften in Abhängigkeit von der chemischen Zusammensetzung des Kationen-Untergitters. Ergänzend zu strukturellen (Un-)ordnungsphänomenen in ausgedehnten volumenkristallartigen Materialien wurde der Einfluss von Punktdefekten in GaN, der Bildung von nichtpolaren GaN-Oberflächen sowie von Nanostrukturierung in AlN/GaN-Quantentrog-Heterostrukturen auf die elektronischen und optischen Materialeigenschaften untersucht, nicht zuletzt, um Anwendbarkeit und Zuverlässigkeit der verwendeten numerischen Ansätze für ein möglichst breites Problemspektrum zu evaluieren.

Eine, im Rahmen der Dissertation wiederkehrende, Problemstellung für numerische Materialsimulationen mittels *konventioneller* Kohn-Sham Dichtefunktionaltheorie ist die systematische Unterschätzung der elektronischen Bandlücke von halbleitenden und isolierenden Materialien durch gängige (semi)lokale Austausch-Korrelations-Funktionale. Eine verbesserte Beschreibung der elektronischen Struktur, einschließlich Bandlücken, Defektniveaus und Banddiskontinuitäten, läßt sich durch Beimischung eines materialspezifischen Anteils nicht-lokaler Fock-Austauschwechselwirkung zu prototypischen Dichtefunktionalen im Rahmen eines verallgemeinerten Kohn-Sham Ansatzes erzielen. Die Verwendung derartiger Austauschwechselwirkungs-*angepasster* Hybridfunktionale erreicht dabei die Genauigkeit formal höherrangiger theoretischer Zugänge im Rahmen der GW-Näherung der Vielteilchenstörungstheorie. Weiterhin wird am Beispiel verschiedener Materialmodifikationen aufgezeigt, wie die Verwendung des Einteilchenbildes die Vorhersagekraft optischer Materialeigenschaften erheblich einschränkt. Die im Rahmen der vorliegenden Arbeit erhaltenen Ergebnisse zeigen, dass die Einbeziehung der Elektron-Loch-Wechselwirkung durch Lösung der zugehörigen Bethe-Salpeter Gleichung für Coulomb korrelierte Elektron-Loch Paare trotz ihres erheblichen numerischen Aufwandes unabdingbar für die akkurate Beschreibung und damit *parameterfreien* Vorhersage optischer Materialcharakteristiken ist. Dies umfasst insbesondere strukturell und kompositionell komplexe Systeme wie Oberflächen und ungeordnete Materialmodifikationen.

Contents

Abstract v

Kurzzusammenfassung vii

Object of research and thesis outline xi

1 A bird's eye view on Oxides and Nitrides 1
- 1.1 Transition-metal dioxides . . . 2
- 1.2 Group-III nitrides . . . 11

2 Materials science: An atomistic perspective 19
- 2.1 The design of functionalized nanomaterials . . . 20
- 2.2 The versatile arrangement of atoms in solid matter . . . 24
  - 2.2.1 Order and disorder in natural and artificial materials . . . 24
  - 2.2.2 Classification of atomic order types . . . 32
- 2.3 Structure theory of glass . . . 38
  - 2.3.1 Classic theories on glass formation . . . 40

3 Electronic structure theory 49
- 3.1 The many-body problem . . . 51
  - 3.1.1 The Born-Oppenheimer approximation . . . 53
- 3.2 Density-functional theory . . . 56
  - 3.2.1 The Hohenberg-Kohn theorems . . . 57
  - 3.2.2 The Kohn-Sham approach . . . 59
- 3.3 Exchange-correlation functionals . . . 68
  - 3.3.1 Rung 1 – Local-density approximation . . . 69
  - 3.3.2 Rung 2 – Generalized gradient approximations . . . 71
  - 3.3.3 Rung 3 – Meta-generalized gradient approximations . . . 73
  - 3.3.4 Rung 4 – Hyper-generalized gradient approximations . . . 74
  - 3.3.5 Rung 5 – Complete-generalized gradient approximations . . . 78
  - 3.3.6 Scaling properties . . . 82
- 3.4 Many-body perturbation theory . . . 87
  - 3.4.1 Hedin's fundamental equations . . . 95

3.4.2 Hedin's *GW* approximation . . . 100
3.5 Optical response theory . . . 106
3.5.1 The Bethe-Salpeter equation . . . 107
3.5.2 The dielectric function . . . 111
3.5.3 Electron-hole pair excitations . . . 113

4 Research contributions **121**
4.1 Scientific publications . . . 122
4.1.1 List of contributing publications . . . 122
4.1.2 List of related publications . . . 123
4.1.3 Other publications . . . 124
4.1.4 Summaries of contributing publications . . . 126
4.1.5 Summaries of related publications . . . 139

5 Results and discussion **145**
5.1 A matter of methodology . . . 146
5.1.1 Density-functional theory . . . 146
5.1.2 Many-body perturbation theory . . . 161
5.2 Fingerprints of order and disorder . . . 166
5.2.1 Sort-range order . . . 167
5.2.2 Medium-range order . . . 172
5.2.3 Structure-function correlations in amorphous oxides . . . 173
5.2.4 Long-range order . . . 175
5.3 Future perspective . . . 180

Summary **183**

Bibliography **187**

Appendix **255**
Paper I . . . 255
Paper II . . . 267
Paper III . . . 275
Paper IV . . . 297
Paper V . . . 319
Paper VI . . . 367
Paper VII . . . 377
Paper VIII . . . 393
Paper IX . . . 399
Paper X . . . 409

Object of research and thesis outline

Density functional theory, introduced in its present, rather convenient, implementation by Walter Kohn and Lu J. Sham in 1964 [1, 2], has indisputably emerged into the working-horse of computational materials science. The unpretentious accessibility of modern density-functional theory codes set of a sheer unmanageable amount of scientific publications dealing with all types of physical problems in materials science, ranging from *trivial* lattice-parameter optimizations to highly non-trivial material properties, whose examination requires the most sophisticated computational methodologies, efficient algorithms, and an extensive high-performance computing infrastructure, all of them continuously pushing forward the frontiers of theoretical materials science. Recent examples for this progress include the search for (topological) two- as well as three-dimensional Dirac/Weyl semimetals [3–9], the physics of diverse two-dimensional/layered materials and their novel heterostructures [10–16], the fundamental understanding of molecular self-organisation processes [17, 18], the *ab initio* theory of superconductivity [19–21], or the pervasive strive for novel designs and materials in the ongoing optimization of visible-light absorbing materials for photoelectric or photo-chemical energy conversion. [22–24]

A common limitation of density-functional theory, spread as the *band-gap problem*, concerns the calculation of fundamental energy gaps in the electronic band structure of semiconducting and insulating materials. Ultimately, this limitation of density functional-theory arises from bypassing the actual problem of a lacking *proper* total-energy functional of the electron density, by introducing an *unknown*, but sound approximable, exchange-correlation energy functional within the framework of Kohn-Sham theory. Despite several known exact constraints and a number of widely used exchange-correlation functional approximations, no *exact* functional with universal applicability has been derived, so far. Notable progresses in the calculation of electronic band gaps has been made through the availability of non-local hybrid functionals for periodic density-functional theory calculations [25, 26], allowing more reliable atomic and electronic structure calculations for a broad spectrum of materials.

Kohn-Sham density-functional theory is essentially a ground-state theory working within a single-particle picture. Thus, a whole complex of problems arises from the computation of diverse fundamental (quasiparticle) excitations of the electron density, since an accurate functional dependence of excited states on the electron density is widely unknown. However, electronic excitations underlie the most relevant experimental approaches to probe material properties by response to electromagnetic radiation as direct and inverse photoemission, photoabsorption, or energy loss spectroscopy. Hence, an accurate treatment of electronic excitation is the essential prerequisite for

the theoretical simulation of photoexcitation properties of novel visible-light absorbing materials and the modeling of spectroscopic processes, in general. *Computational spectroscopy* from first principles aims at a comprehensive understanding and, in the best case, *parameter-free* prediction of fundamental radiation-matter interactions at the atomic level.

The necessary Green's function based theory for an accurate treatment of the quasiparticle nature of electronic excitations, known as *many-body perturbation theory*, has been formulated by Lars Hedin in 1965. [27, 28] Charged single-particle excitations are commonly calculated within the *GW* approximation to many-body perturbation theory for the single particle Green's function. Today, the treatment of single-particle excitations in the *GW* approximation tends to be the most promising, but system-size limited, ansatz for the systematic correction of the band-gap underestimation and a reliable, *virtually parameter-free*, simulation of electronic structures features. The calculation of optical material properties not only suffers from the underestimated band gap causing a rigid red-shift of the material's optical response but also from the single-particle nature of density-functional theory or *GW* quasiparticle theory. It has been demonstrated for many basic systems that the inclusion of excitonic contributions arising from the attractive Coulomb interaction between (quasi)electrons and (quasi)holes facilitates an effective *parameter-free* modeling of a material's optical response. The needed formalism to calculate the involved neutral two-particle excitations is derived within many-body perturbation theory for the two-particle Green's function leading to a Bethe-Salpeter equation for the four-point polarization function. [29, 30] Due to the outstanding demands on computational resources, that by default limit any universal applicability, the use of many-body perturbation theory based optical-response calculations for *extended* systems, as the *artificial* unit cells of amorphous solids or complex structure models of semiconductor surfaces, is just sporadically reported.

In the present thesis, the application of state-of-the-art *ab initio* simulation methods is extended to several complex systems as amorphous solids or the surfaces, alloys, and heterostructures of semiconductors that have not been treated by comparable high-level approaches in the past. Thus, new insights into the relevance of many-body effects in these systems are provided. Formulating a leading *physical* question, linking the various parts of this thesis, beyond a systematic evaluation of the relevance of many-body effects, one arrives at the search for *structure-function correlations between a material's microscopic/atomic structure and macroscopic material properties* as the response to electromagnetic radiation. Such structural fingerprints in the electronic structure and optical response become increasingly important with ongoing miniaturization of optical and electronic devices and nanostructuring to be taking place on an atomic length scale. Any precise knowledge on fundamental structure-function correlations will immediately apply towards the search for and practical development process of novel functional (nano)materials.

A particular challenge for materials science are the disordered structures of amorphous solids and glasses. In many cases, the microstructure of the disordered material phases is neither comprehensively characterized on a short-range order scale nor the structurally superordinate medium-range order features are entirely known. The simple assumption of common fundamental coordi-

nation complexes in amorphous and crystalline material phases might not be justified, in general, and the situation might become even more complicated for materials exhibiting an extended structure polymorphism and/or potential polyamorphism. The atomic structure of disordered material phases might either be determined by a competition between diverse network topologies interlinking the various crystalline coordination units or the rivalry of different, not necessarily crystal-like, fundamental building blocks. The former represents a dominant competition of medium-range order features while the later refers to a competition between basic coordination units determined by atomic short-range order. In both cases, the electronic structure and thus the character of electronic excitation, probed by spectroscopic approaches, should reflect key characteristics of the underlying atomic structure.

The content of this thesis roughly separates into three major parts:

PART I, consisting of the chapters one and two, serves two main purposes. On the one hand the present thesis is put into context and motivated in light of the most recent developments in materials science and the studied materials, namely transition-metal (di)oxides and group-III nitrides, are presented, in detail. On the other hand, the various classes of atomic order existing in crystalline and amorphous solids as well as the characteristic natural and artificial ordering-length scales of nanomaterials are introduced in chapter two and the functional interactions between chemical and structural order features are illustrated.

PART II, equivalent to chapter three, contains a detailed outline of the density-functional theory approach to electronic structure theory and a basic discussion on fundamental approximations to the exchange-correlation energy of Kohn-Sham theory. The theoretical framework of many-body perturbation theory, mandatory for making realistic *parameter-free* predictions of a semiconductor's optical response, is introduced, briefly.

PART III, containing the chapters four and five, deals with the actual scientific contributions made within the present thesis. Chapter four gives short summaries of the scientific publications contributing to this thesis (see appendices), while chapter five briefly discusses the scientific findings detached from the narrowed framing of the individual publications. The fundamental correlations between structural order on an atomic length scale and the resulting characteristic features in the electronic structure and optical response are highlighted.

1 A bird's eye view on Oxides and Nitrides

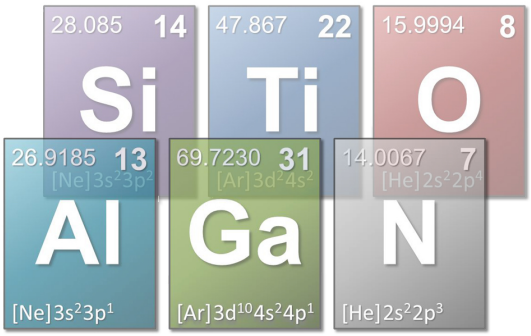

Faust

Geschrieben steht: "Im Anfang war das Wort"
Hier stock ich schon! Wer hilft mir weiter fort?
Ich kann das Wort so hoch unmöglich schätzen,
Ich muß es anders übersetzen,
Wenn ich vom Geiste recht erleuchtet bin.
Geschrieben steht: Im Anfang war der Sinn.
Bedenke wohl die erste Zeile,
Daß deine Feder sich nicht übereile!
Ist es der Sinn, der alles wirkt und schafft?
Es sollte stehn: Im Anfang war die Kraft!
Doch, auch indem ich dieses niederschreibe,
Schon warnt mich was, daß ich dabei nicht bleibe.
Mir hilft der Geist! Auf einmal seh ich Rat
Und schreibe getrost: Im Anfang war die Tat!

Johann W. von Goethe (1749-1832)

Contents

1.1 Transition-metal dioxides 2
1.2 Group-III nitrides 11

MATERIALS OF INTEREST – The catalytic and optical activity of solid-state materials correlates with diverse order features of the atomic structure, undissolvably. These are the crystal symmetry, the degree of structural disorder/amorphicity, as well as superordinate structural characteristics as grain size and pore size defining the effective surface area, and further (artificial) nanostructuring. Commonly, the physico-chemical properties of homogenous materials limit the tunability ranges of some of these properties, at least. In order to overcome these kinds of limitations, the industrial need for novel catalysts and phtotoabsorbers drives the engineering of new, partially nanostructured, multi-component hybrid materials. Thereby, the fabrication of mixed and nanostructured hybrid composites tries to meet two miscellaneous designing philosophies. On the one hand, systematic variation of the material composition as well as structure engeneering (e.g. quantum wells and superlattices) is used to benefit from synergies between the physical properties (e.g. refractive indices, band gaps, band offsets) of the individual constituents. On the other hand, the synthesization of new hybrid materials is often motivated by the pursuit of inducing new functional material characteristics (e.g. electronic states within the band gaps or new active lattice sites for catalyzing chemical reactions) that cannot be realized by any of the alloy components, individually.

Within the present thesis, two major material classes, both of tremendous importance for manifold technological and industrial applications, namely group-III nitride semiconductor alloys and transition-metal (di)oxides, have been selected to study the characteristic fingerprints of atomic order features in their electronic structure and optical response. [1]

1.1 Transition-metal dioxides

A class of materials, that stands for the manifold of oxide alloys that have attracted considerable attention over the last years, are mixed TiO_2/SiO_2 (titania-silica) hybrid oxides, also termed TiO_2/SiO_2 binary oxides as well as ternary $Ti_xSi_{1-x}O_2$ oxides in the case of atomically mixed alloys. Nowadays, transition-metal based compounds are a promising engineering platform for materials science with wide ranging applicability in chemical industry and optoelectronics by taking advantage of the catalytic properties of semiconducting TiO_2 and the high thermal stability and mechanical strength of SiO_2.

CRYSTALLINE TiO_2 – Titanium dioxide is a naturally occurring oxide mineral with traditional large-scale application as a whitening pigment in e.g. paint, sunscreen, tooth paste, and food [2] as well as industrial scale application as a photocatalyst [3]. [37–40] Crystalline TiO_2 shows an extended structure polymorphism, which is reflected in an extraordinary rich (high-

[1] Parts of the subsequent material characterization are taken and modified from Paper III (Ref. [31]) for TiO_2, from Paper V (Ref. [32]) for $Ti_xSi_{1-x}O_2$ and from Paper IV (Ref. [33]), Paper VI (Ref. [34]), and Paper VII (Ref. [35]) for the studied group-III nitrides.

[2] In the european union the food additive "E171" refers to TiO_2.

[3] The photocatalytic activity of TiO_2, has been investigated since the first half of the twentieth century. [36, 37] The interest in TiO_2 photocatalysis was most notably stimulated by the discovery of photoelctrolysis of water over TiO_2 rutile electrodes in 1967 by the japanese chemists Akira Fujishima and Kenichi Honda. [38]

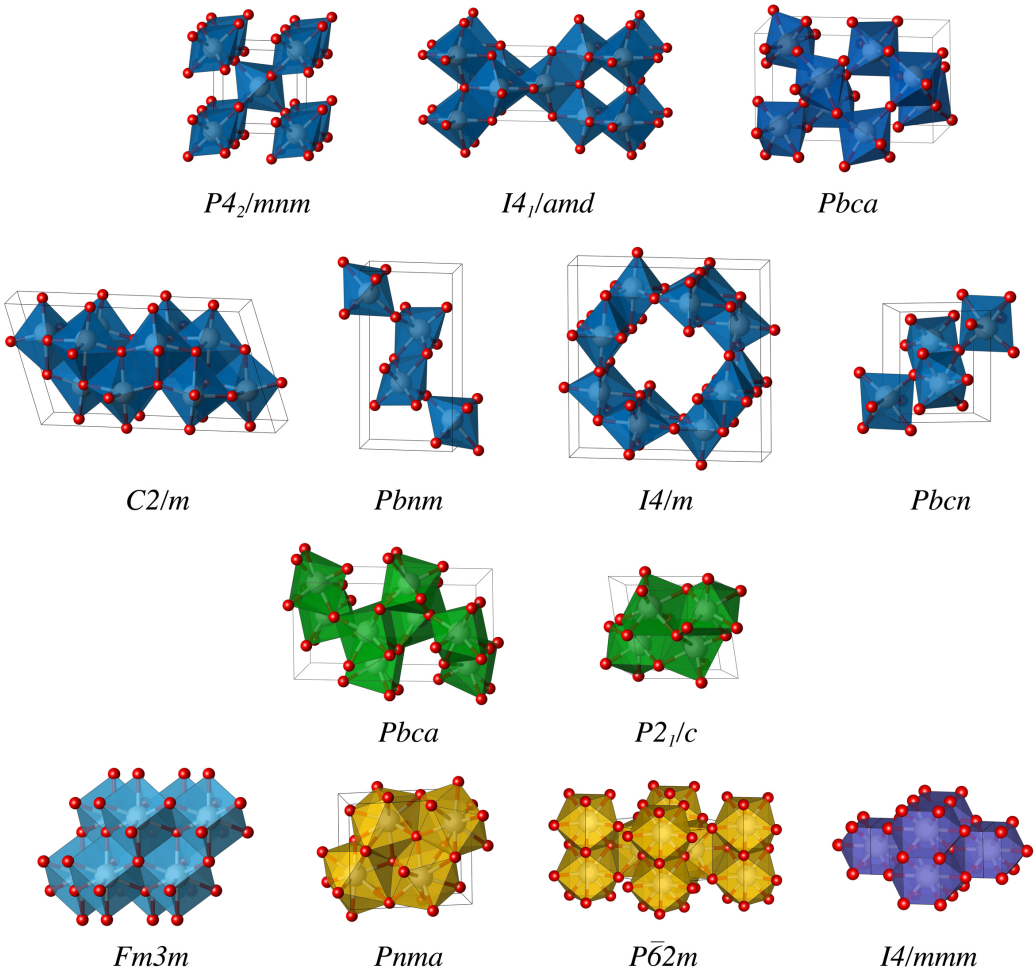

Figure 1.1: Overview of unit cells and space groups of crystalline TiO_2 polymorphs: rutile ($P4_2/mnm$, natural), anatase ($I4_1amd$, natural), brookite ($Pbca$, natural), TiO_2(B) ($C2/m$, bronze-type, natural), TiO_2(R) ($Pbnm$, ramsdellite-type, pressure-induced), TiO_2(H) ($I4/m$, hollandite-type, pressure-induced), TiO_2(II) ($Pbcn$, columbite-type, pressure-induced), TiO_2(OI) ($Pbca$, orthorhombic-type, high-pressure), TiO_2(MI) ($P2_1/c$, baddeleyite-type, high-pressue), cubic TiO_2 ($Fm\bar{3}m$, fluorite-type, high-pressue), TiO_2(OII) ($Pnma$, cotunnite-type, high-pressure), Fe_2P-type ($P\bar{6}2m$, post-cotunnite-type, high-pressure), $I4/mmm$ TiO_2 (post-Fe_2P-type, multi-megabar-pressure regime, theoretical). The TiO_n polyhedra are color-coded according to the titanium ion coordination state: blue $\leftrightarrow$ sixfold, green $\leftrightarrow$ sevenfold, light blue $\leftrightarrow$ eightfold, yellow $\leftrightarrow$ ninefold, and purple $\leftrightarrow$ tenfold.

pressure) phase diagram. The three crystalline polymorphs rutile {crystal system: tetragonal ($4/mmm$), space group: $P4_2/mnm-D_{4h}^{14}$}, anatase {tetragonal ($4/mmm$), $I4_1/amd-D_{4h}^{19}$}, and brookite {orthorhombic (mmm), $Pbca-D_{2h}^{15}$} are stable at atmospheric pressure and room temperature and commonly found in nature (see Fig. 1.1). Out of these three phases, rutile is the thermodynamically stable phase at all temperatures. [41] Anatase and brookite are considered as metastable phases [42–46], existing below $\sim 900\,^{\circ}C$. Anatase has also been discussed as a potentially stable nanophase. [47, 48] Among the natural polymorphs, only rutile and anatase play a significant role in industrial applications, e.g. the standard TiO_2 photocatalyst *Degussa*

P-25 consists of crystalline rutile and anatase particles in a ratio of 1 : 3 [49–52] and an small percentage of amorphous TiO_2 particles $\sim 1\,\%$. As a consequence, the available literature on TiO_2 brookite is much more limited, compared to rutile and anatase. A fourth naturally occurring phase TiO_2(B) [53, 54] {monoclinic, bronze-type, $C2/m - C_{2h}^3$} has been reported. Experiments have furthermore revealed the existence of the metastable oxide phases TiO_2(H) [55] {hollandite-type, $I4/m - C_{4h}^5$} and TiO_2(R) [56] {ramsdellite-type, $Pbnm - D_{2h}^{16}$}, as well as the TiO_2 high-pressure polymorphs TiO_2(II) [57–59] {columbite-type ($\alpha - PbO_2$ structure), $Pbcn - D_{2h}^{14}$}, TiO_2(MI) [58–60] {monoclinic, baddeleyite-type, $P2_1/c - C_{2h}^5$}, TiO_2(OI) [61] {orthohombic, *Pbca*}, and TiO_2(OII) [61, 62] {orthohombic, cotunnite-type, $Pnma - D_{2h}^{16}$}. The high-pressure formation of a cubic TiO_2 (c–TiO_2) [63, 64] {cubic, fluorite-type, $Fm\bar{3}m - O_h^5$} polymorph has been reported. However, the exact nature of the cubic phase is still debated, assuming fluorite ($Fm\bar{3}m - O_h^5$), pyrite ($Pa\bar{3} - T_h^6$), or $Pca21$–C_{2v}^5 symmetry-types. [65, 66] From combined experimental and theoretical studies the phase-transition path rutile $\rightarrow$ columbite-type (TiO_2(II)) $\rightarrow$ baddeleyite-type (TiO_2(MI)) $\rightarrow$ intermediate orthorhombic-type TiO_2(OI) $\rightarrow$ cotunnite-type TiO_2(OII) has been identified for compression at ambient temperature. [61, 67] A second ninefold coordinated polymorph of TiO_2, stabilizing at higher pressures, crystalizes in a hexagonal $Fe_2P - D_{3h}^3$-type structure. [68, 69] Most recently, a *final* transition to a tenfold coordinated metallic $I4/mmm - D_{4h}^{17}$ TiO_2 polymorph has been predicted theoretically. [70]

The atomic structures of the three most common phases rutile, anatase and brookite as well as the polymorphs TiO_2(B), TiO_2(R), TiO_2(H) and TiO_2(II) are well characterized by edge-sharing octahedron-chains build from distorted TiO_6 octahedra building blocks formed by a central titanium anion surrounded by six oxygen cations. [54, 63, 71–73] A complementary view of the electronic structure is given by crystal-lattice formation resting upon planar Ti_3O units. [74, 75] The coordination of the titanium ions and therefore the local atomic structure changes under pressure. TiO_2(MI) and TiO_2(OI) are characterized by a sevenfold coordination of titanium ions with oxygen ions. The Ti ions are eightfold coordinated in the cubic fluorite phase, which results in the formation of tetrahedrally coordinated oxygen ions. Titanium ions in the high pressure polymorphs TiO_2(OII) and the Fe_2P-polytype are ninefold coordinated by oxygen ions. Finally, a tenfold coordination is observed in the theoretically predicted $I4/mmm$ phase of TiO_2.

As a semiconductor material with long-term stability/corrosion resistance, non-toxic environmental acceptability, and low cost availability, TiO_2 has also taken into account for photovoltaic applications. However, due to optical energy gaps above or equal to $\sim 3\,\mathrm{eV}$ of the natural occurring phases (rutile: $3.0\,\mathrm{eV}$ [76, 77], anatase: $3.4\,\mathrm{eV}$ [78], and brookite: $3.27\,\mathrm{eV}$ [79]), TiO_2 is only photoactive in the ultraviolet-to-visible range of the electromagnetic spectrum and, thus, an inefficient *active* solar cell material. A notable reduced band-gap energy has been reported for the observed cubic phase of TiO_2. Theoretical calculations indicate a reduced fundamental (indirect) band gap of $\sim 2.3\,\mathrm{eV}$, hence, allowing absorption in the eligible visible spectral range. [80–82] However, the unlikely stabilization of high-pressure TiO_2 polymorphs under ambient conditions represents a major drawback, at least, for visible light absorption by a pure TiO_2 bulk semicon-

ductor. An alternative to metastable/unstable bulk phases might be given in form of thin-film and surface modifications of TiO_2 that could be stabilized at ambient conditions. Surface mediated visible-light photoactivity of bare TiO_2 has been reported by Ariga et al. [83] for the rutile(001) surface. Tao et al. [84] reported visible-light activity for a two-dimensional surface phase, formed on the rutile TiO_2(011) surface. A reduced band gap of $\sim 2.3\,\mathrm{eV}$ was observed for both nanostructured surfaces. However, the band-gap reduction for rutile TiO_2(001) has been attributed to the presence of four-fold coordinated titanium ions at the surface, which effectively reduce the band gap by formation of near-edge surface states [83, 85], while the band-gap reduction for rutile TiO_2(011) has been assigned to a two-dimensional surface phase showing resemblances to the cubic form of TiO_2.

Besides pure/homogenous phase modifications, also several attempts in form of material doping and molecular sensitizing have been made to reduce the electronic band gap in order to facilitate photovoltaic activity in the visible spectral range. In principle, the doping by (transition-)metal ions [86–89] and non-metal ions [86, 90–97] provides a promising approach for band-structure engineering aiming at visible light adsorption. However, such impurities commonly lead to dopant-induced defect states that act as charge-carrier traps for the generated electrons and holes as well as waste recombination sites that practically negate the higher photocatalytic activity due to the increased light-adsorption capabilities. [84, 98] Still, the material advantages of TiO_2 can be used indirectly in technologically and economically viable dye-sensitized solar cells [99–103], where it acts as an electron-transporting host-substrate for a chemisorbed photoactive molecular *dye*.

AMORPHOUS TiO_2 – Based on the extraordinary optical and catalytic properties known from the distinct crystalline phases of TiO_2 [37, 39], also amorphous TiO_2 (a-TiO_2) has received interest as a low-cost material modification for technological applications. Amorphous TiO_2 is a starting material (precursor) for the synthetization of various single-crystalline phases by hydrothermal treatment, in general. [73, 86, 104, 105] In practice a-TiO_2 is commonly produced in form of thin films prepared by various experimental methodologies as direct current (magnetron) sputtering [106–110], electron-beam evaporation [111, 112], cathodic vacuum arc deposition [113, 114], sol-gel deposition [115, 116], reactive sputtering, and arc ion plating. [117, 118] Also, dense or porous films of nanocrystal conglomerates are commonly prepared and referred to as amorphous films. However, depending on the intended usage this might be a significant difference. A fundamental property of the amorphous material is the absence of optical anisotropies that, for instance, occur in the uniaxial rutile and anatase phases or the biaxial brookite phase. In addition, a *truely* amorphous phase is not influenced by grain-boundary induced defects between the crystallites that modify the physical material properties. [119, 120] Closely related are size-effects that might favor various crystalline phases in nanoparticulated TiO_2. [105, 121–123] In practice, it has been shown that a-TiO_2 films are well suited for surface passivation in bioimplants due to their high stability and corrosion resistance *in vitro*. [124, 125]

While there is extended literature [67, 90, 126–143] on structural, elastic, thermodynamic, and optical/dielectric properties, obtained from numerical simulations of the three most common crys-

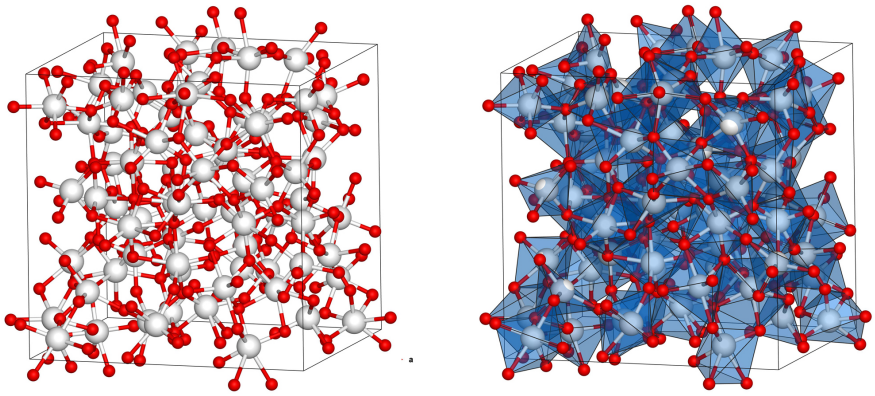

Figure 1.2: Ball-and-stick (left) and TiO_6 coordination-polyhedra representation (right) of a 216-atom unit-cell model of amorphous TiO_2 generated by density-functional–based tight-binding molecular dynamics simulations. (red: oxygen, white: titanium)

talline phases as well as their low index surfaces [144–151], computational data on a-TiO_2 is rather limited due to the necessity of using extended unit cells for an approximate numerical reproduction of the non-periodic disordered atomic structure of amorphous solids. So, in contrast to crystalline modifications, amorphous material phases stand out by their complete loss of translational symmetry/long-range order.

Reported experimental energy-gap data on variously prepared a-TiO_2 thin films covers an energy range from $\sim 3.2\,\text{eV}$ to $\sim 3.7\,\text{eV}$. [41, 106, 108, 109, 111–115, 117, 118] All these results were obtained from ultraviolet-visible spectroscopy followed by a direct or indirect Tauc analysis. [152, 153] Tauc plots are the most common approach to extract the optical energy gap from spectroscopic data on nanocrystalline (e.g. powder samples) and amorphous solids (e.g. glasses).

Crystalline and amorphous SiO_2 – Silicon dioxide is one of the most abundant minerals in the earth's crust. Traditionally, SiO_2 is used as the major ingredient of window glass and glassware for domestic and industrial usage. Since its utilization as the insulating gate dielectric in most transistors, used in modern CMOS technology, SiO_2 has become an integral component of today's integrated semiconductor electronics. [154, 155]

The structure polymorphism of crystalline SiO_2 tends to be even richer than observed for TiO_2. This stronger diversification of structural polytypes stabilizing in the low- and high-pressures regimes originates from stable tetravalent polymorphs at ambient conditions. Experimental studies as well as density-functional theory simulations on the structural properties of low-pressure silica revealed the crystalline polymorphs α-quartz ($P3_221 - D_3^6$), β-quartz ($P6_222 - D_6^4$), α-tridymite ($C222_1 - D_2^5$), β-tridymite ($P6_3/mmc - D_{6h}^4$), α-cristobalite ($P4_12_12 - D_4^4$), β-cristobalite ($Fd\bar{3}m - O_h^7$), moganite ($I2/a - C_{2h}^6$), keatite ($P4_32_12 - D_4^8$), and coesite ($C2/c - C_{2h}^6$). [156–162] Also, the existence of a low-framework-density polymorph, SiO_2 chabazite ($R\bar{3}m - D_{3d}^5$), has been reported. [163] A plethora of competing high-pressure phases with sixfold cation coordinations has been identified and/or predicted from numerous self-contained as well as combined

first principles simulations and compression experiments. These high-pressure phases include stishovite ($P4_2/mnm-D^6_{4h}$) [164–167], a Fe_2N-type ($P312-D^1_3$) [164, 168, 169], a $CaCl_2$-type ($Pnnm-D^{12}_{2h}$) [170–172], a monoclinic-type ($I2/a-C^6_{2h}$) [173, 174], an α-PbO_2-type ($Pnab-D^{14}_{2h}$) [171, 172, 175], a $P2_1/c-C^5_{2h}$-type [169], a fluorite-type $Pa\bar{3}-T^6_h$ [172], and a $Pnc2-C^6_{2v}$-type [175] polymorph. The origin of the *octahedral* high-pressure polymorphism of silica has been associated with the formation of a hexagonal close packing of oxygen atoms and silicon atoms occupying the octahedral and tetrahedral sites in various conformations. [169, 176] The study of the extended high pressure polymorphism is also essential for the understanding of the disordered atomic structure of densified amorphous SiO_2. [177–181]

Crystalline SiO_2 is an insulator with a large electronic/optical band gap around ~ 9 eV. From electron loss spectroscopy band gaps of 9.3 eV and 9.2 eV have been reported for α-quartz and coesite, while the band gap is notably reduced to 5.0 eV in stishovite. [182] The most accurate numerical band-gap data on SiO_2 α-quartz, based on self-consistent Green's function quasiparticle theory and the Bethe-Salpeter formalism for optical excitations, indicate a direct Γ-centered quasiparticle-band gap of 10.1 eV and a large binding energy of the lowest exciton in the range between 1.7 eV [183] and 1.2 eV. [184]

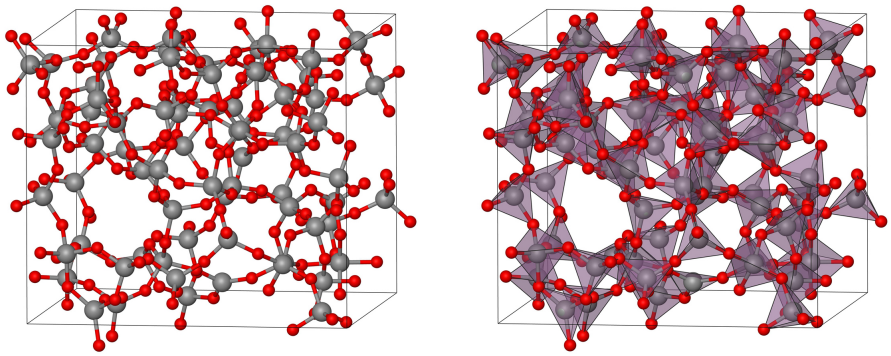

Figure 1.3: Ball-and-stick (left) and coordination-polyhedra representation (right) of the 216-atom unit cell model of amorphous SiO_2 generated by density-functional–based tight-binding molecular dynamics simulation. (red: oxygen, white: titanium)

Severe effort from experimental and theoretical sides has been devoted to the structure determination of amorphous SiO_2, silica glass respectively [185–192], as the prototypical inorganic glass former, as well as amorphous SiO_2 nanoparticles. [193–195] The reported energy gaps of amorphous SiO_2 / silica glass, are notably smaller than the band gaps of crystalline SiO_2. An absorption edge as low as 7.6 eV has been reported by Kaminow et al. [196] for silica glass indicating a reduced band gap in the amorphous state. In general, common interband-transition peak characteristics for crystalline and amorphous SiO_2 have been found by combined spectroscopic ellipsometry and vacuum ultraviolet spectroscopy. [197] Thereby, the spectral features are sharper accentuated in crystalline SiO_2. An a-SiO_2 band gap of 7.64 eV could be reproduced by Tan et al. [197] via direct energy-gap fitting of the fundamental absorption edge in the frequency range

between 2 cm^{-1} and 20 cm^{-1}, whereas a value of 9.56 eV is obtained from fitting the frequency range from 1×10^5 cm^{-1} to 1×10^6 cm^{-1}. The notable dependence of the optical energy gap on the spectral fitting range is significantly stronger in the amorphous phase. Fitting the optical response of SiO_2 α-quartz (Z-cut) in the frequency ranges 2 cm^{-1}–20 cm^{-1} and 1×10^5 cm^{-1}–1×10^6 cm^{-1} yielded band gaps of 8.29 eV and 9.55 eV, respectively. The similar energy gap for crystalline and disordered SiO_2, obtained by direct absorption edge fitting in the higher frequency range, hints on almost equally sized energy gaps of crystalline SiO_2 and the mobility gaps of amorphous SiO_2 which has been confirmed by calculated *GW* quasiparticle gaps of 9.4 eV for α-quartz and 9.3 eV for *a*-SiO_2. [198]

TERNARY $Ti_xSi_{1-x}O_2$ OXIDES – Many types of nano- and mesostructured TiO_2/SiO_2 mixed oxides have been synthesized by preparation techniques as electron-beam evaporation [199], vacuum deposition [200, 201], atomic layer deposition [202], liquid phase deposition [203], chemical vapour deposition [204–209], RF magnetron sputtering [210], ion-beam sputter deposition [211–213], plasma sputtering [214], and, prevalently, following sol-gel based preparation methods. [215–229] TiO_2/SiO_2 multilayer and thin films have been used in numerous coating applications like anti-reflective thin film coatings [199, 230], weather resistant thin film coatings [215], hydrophilic coatings [231], and implant coatings [227, 232]. Amorphous $Ti_xSi_{1-x}O_2$ thin films have also been deposited for the use as gate oxides in metal oxide semiconductor-field effect transistors [233]. Optical TiO_2/SiO_2 mixed oxide devices as active and passive planar optical waveguides [216, 219, 223, 234], channel waveguides [217, 235], tailored periodically or gradually modulated refractive index devices (e.g. rugate filters) [236–238], and dielectric mirrors [213] especially benefit from the large differences in the energy gaps and refractive indices (ranging from $\sim$ 1.5 to $\sim$ 2.5) of the SiO_2 and TiO_2 bulk oxides. [205, 207–209, 211, 239, 240]

Various studies have indicated that mixed TiO_2/SiO_2 binary oxides are more active catalysts than pure TiO_2 [225, 226] and a promising material for various catalytic applications. Comprehensive reviews on the structural as well as physico-chemical properties of mixed titania-silica oxide catalysts have been published by Davis and Liu [241] and Gao and Wachs. [242] In summary, the catalytic activity of TiO_2/SiO_2 compounds falls into three categories that reflect various characteristics of the utilized material. Photocatalytic properties are associated with band-structure features as well as quantum size-effects due to particle size and nanostructuring. Based on the photocatalytic activity, the potential use of crystalline and amorphous TiO_2/SiO_2 nanocomposites for photocatalytic purification of contaminated (waste-)water [243, 244], exhaust gas [245], and textiles [246] has been discussed. Acid-catalysis activity is generated by the character of newly formed acid sites in mixed and nanostructured TiO_2/SiO_2 oxides that are not present in the pure material phases. The acidity [202, 241, 242] of TiO_2/SiO_2 mixed oxides has been discussed in literature, controversially. [218, 241] The third category summarizes all material related properties of *supportive* nature that are indirectly related to the catalytic activity of a material as porosity or surface area of bulk and nanoparticle modifications as well as their thermal stability. Mixed amorphous and crystalline networks of micro- and mesoporous TiO_2/SiO_2 oxides are nowadays

widely used as catalysts in chemical industry. [221, 242, 247–260]

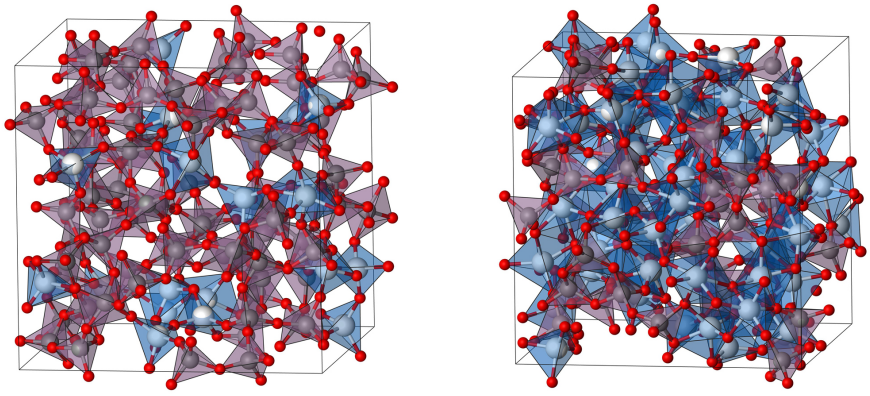

Figure 1.4: Coordination-polyhedra representation of 300-atom unit cell models of silicon-rich ($x = 20\,\%$, left) and titanium-rich ($x = 60\,\%$, right) amorphous $Ti_xSi_{1-x}O_2$ generated by density-functional–based tight-binding molecular dynamics simulation. (red: oxygen, white: titanium, blue: TiO_n polyhedra, violet: SiO_n polyhedra)

The atomic structure of amorphous TiO_2/SiO_2 oxides has been studied extensively over the last decades. Experimental studies [206] found no indication for substantial contributions from direct Si–Ti bonds in TiO_2/SiO_2 oxide films. Cross-linking between TiO_2 and SiO_2 domains in amorphous TiO_2/SiO_2 composites is rather found to be due to the formation of bridging O ions in Ti–O–Si bonds. [205–207, 209, 221, 229, 242, 242, 250, 261] Based on X-ray absorption spectroscopy (XAS) analysis of the electronic structure of the TiO_2/SiO_2 interface, Soriano et al. [262] proposed the formation of Ti-O-Si cross-linking oxygen bonds that connect Ti_{6c} ions in octahedral TiO_6 units and Si_{4c} ions in tetrahedral SiO_4 units. Similar conclusions have been drawn from extended X-ray absorption fine structure (EXAFS) and X-ray absorption near-edge spectroscopy (XANES) analysis in a proceeding study. [263] Experimental studies [205–209, 221, 222, 239, 242, 264–267], focusing on details of the local atomic structure, have further indicated that Ti ions in a-TiO_2/SiO_2 predominantly show a partially distorted tetrahedral coordination by oxygen ions at low titanium contents between ~ 0.05 and 9 weight percent (wt%). Increasing the amount of Ti ions in the amorphous TiO_2/SiO_2 matrix up to ~ 15 wt% of TiO_2 leads to an increasing amount of octahedrally coordinated Ti_{6c} ions. The segregation of TiO_2 as a second phase may occur above ~ 15 wt% TiO_2. Phase separation has also been reported for high TiO_2 concentrations of ~ 41 molecular percent (mol%) [222, 268]. Orignac [223] reported coexisting and continuously increasing hetero-condensation (formation of SiO_2 and TiO_2 domain-linking Ti–O–Si bonds) and homo-condensation (formation of Si–O–Si and Ti–O–Ti bonds) for an increasing amount of Ti with a maximum fraction of Ti–O–Si bonds (coexisting with a local minimum of Ti–O–Ti bonds) at a 20 mol% TiO_2 content.

Based on EXAFS and XANES analysis on TiO_2/SiO_2 mixed oxide glasses up to TiO_2 contents of 11.6 mol%, Henderson and Fleet [224] proposed the following scenario for the transition from

a homogeneously mixed oxide to a phase separated heterogeneous composite upon an increasing TiO_2 content: The onset of phase separation is not the distortion of the SiO_4 tetrahedron network but the formation of sixfold coordinated Ti_{6c} ions. At low TiO_2 content the fourfold coordination of the tetrahedron network remains undisturbed. However, the larger TiO_4 tetrahedron building blocks put volume constraints on the glassy network whose relatively incompressible Si–O bonds only show a limited ability to adjust to the volume increase. At some point it becomes more favorable for the strained TiO_2/SiO_2 framework to convert Ti_{4c} to Ti_{6c} rather than incorporating further fourfold coordinated Ti ions. Finally, the existence of crystal-like Ti_{6c} ions promotes the formation of a crystalline TiO_2 anatase phase. Very recent, the structure of low temperature (80 °C) prepared sol-gel TiO_2/SiO_2 composites has been extensively studied by X-ray total scattering techniques. [229] For all TiO_2/SiO_2 samples (titanium concentrations of 20, 35, and 50 mol%) large fractions of both nanocrystalline anatase and amorphous TiO_2 have been reported.

In contrast to the reported phase-separation tendency upon increasing TiO_2 content, it has been reported [209, 212, 213] that small amounts of SiO_2 enable TiO_2/SiO_2 mixed films to sustain higher annealing temperatures without TiO_2 phase transition from an amorphous state to polycrystalline anatase. Gracia et al. [207] reported the preparation of mixed TiO_2/SiO_2 optical thin films with silicon/titanium ratios covering the entire composition range from pure SiO_2 to pure TiO_2 by ion beam induced and plasma enhanced chemical vapor deposition (IBICVD and PECVD). The TiO_2/SiO_2 films have been characterized by Fourier transform IR (FT-IR) spectroscopy as homogenous a-$Ti_xSi_{1-x}O_2$ mixtures of the two binary oxides rather than a compound of separated SiO_2 and TiO_2 phases. From analysis of the crystal field splitting, the titanium ions at low concentrations (2 – 10 %) were attributed to TiO_4 building blocks. Upon TiO_2 content increase, the continuous increase in the crystal field splitting energies, towards the value representative for amorphous TiO_2, gives evidence for an increasing coordination number. Especially, the existence of an intermediate fivefold coordinated Ti ion species has been depicted as a likely coordination state at higher fractions of TiO_2 in a-$Ti_xSi_{1-x}O_2$ thin films. While titanium ions in the two most common crystalline coordination states of SiO_2 (fourfold) and TiO_2 (sixfold) are repeatedly reported, fivefold coordinated Ti_{5c} ions in hexahedral TiO_5 building blocks represent a less common coordination state that is only sporadically reported for pure TiO_2/SiO_2 mixed oxides. [202, 207, 224, 241] Apart from several known crystalline oxides as $K_2Ti_2O_5$ [269], the occurrence of TiO_5 units has been reported for ternary TiO_2/SiO_2 mixed oxides bearing fractions of alkali and alkaline-earth metal atoms that act as network modifiers (e.g. fresnoite ($Ba_2TiSi_2O_8$) [270] or Na_2TiSiO_5 [271]) [4]. [272–279]

A theoretical study on titanium-silicate glasses has been published by Rosenthal and Garofalini. [280] In their empirical potential molecular dynamics study, the structural properties of $Ti_xSi_{1-x}O_2$ compounds with TiO_2 contents ranging from 2 – 15 mol% have been simulated using 360 atom unit cells. The influence of slower molecular-dynamics cooling rates on the Ti coordi-

[4] Further details on the network-forming and network-modifying function of fivefold coordination units are discussed in Sec. 5.2.

nation state has been highlighted. While a fast quenching rate promotes significant fractions of fivefold coordinated Ti ions for all TiO_2 concentrations, a lower cooling rate strongly favors tetrahedrally coordinated Ti at low TiO_2 contents ($\lesssim$ 10 mol%). At higher TiO_2 content ($\sim$ 15 mol%), the slower quenching rate reduces the occurrence of TiO_4 building blocks in favor of fivefold (53 %) and sixfold (28 %) coordinated Ti ions, notably. More recently, Bernard et al. [281] studied the composition dependence of undoped and Er-doped TiO_2/SiO_2 mixed oxide glasses by large scale (5094 atom unit cells) empirical potential molecular dynamics simulations for Ti concentrations ranging from 7.8 mol% up to 50 mol%. In all undoped TiO_2/SiO_2 structure models, fourfold and fivefold coordinated Ti ions in TiO_4 and TiO_5 units represented the dominating structural building blocks. Already for the lowest simulated Ti concentration (7.8 mol% Ti), the formation of Ti_{4c} ions with 53 % was only slightly favored over Ti_{5c} ions with a fraction of 42 %. In the equimolar (50 mol% Ti) TiO_2/SiO_2 sample, Ti_{5c} ions were found to be the dominant coordination state with a 60 % fraction while Ti_{4c} ions were limited to 30 %. Higher Ti coordination states were limited to minor percentages with a maximum of 10 % for sixfold coordinated Ti_{6c} ions in the equimolar mixture. Based on a cluster analysis of Ti ions in the amorphous SiO_2 framework, the distribution of TiO_2 has been characterized to be neither homogeneous nor phase separated, but random like. Even in case of the equimolar TiO_2/SiO_2 structure model, no evidence for the formation of a separated TiO_2 phase was found. Nevertheless, a general tendency to higher Ti coordination states upon increasing TiO_2 contents was interpreted as a favorable factor for the formation of a crystalline TiO_2 phase.

1.2 Group-III nitrides

Throughout the last two decades, scientific breakthroughs in the field of the group-III nitride-semiconductor materials [282–285] gallium nitride (GaN), aluminum nitride (AlN), and indium nitride (InN) have always stimulated rapid technological progress in the manufacturing of electronic and optoelectronic devices. The importance of group-III nitride semiconductors has been underlined, by awarding the Nobel prize in physics 2014 [5] for the development of gallium nitride based blue light-emitting diodes whose fabrication has challenged materials science for more than three decades. Probably, the most appealing characteristic of the binary group-III nitrides and their multinary alloys is the extremely large range of accessible band-gap energies [6] and the *good* solubility of the binary nitrides among each other [7] into ternary [297–299] and quaternary [288, 300–

[5] The Nobel prize has been awarded in equal parts to Isamu Akasaki, Hiroshi Amano, and Shuji Nakamura "for the invention of efficient blue light-emitting diodes which has enabled bright and energy-saving white light sources".

[6] See discussion below.

[7] Under optimal growth conditions, the ternary, pseudobinary respectively, or multicomponent alloys of group-III nitrides exhibit a random distribution of group-III elements in the cation sublattice, while the overall chemical order between anions and cations is preserved. [286, 287] Consequently, also the tetrahedral structure is maintained and the effect of chemical sublattice disorder is reduced to weak random lattice distortions depending on the actual local composition. However, the relatively large lattice mismatch of roughly 14 % between the crystalline phases of AlN and InN represents a notable limitation to the formation of multi-component alloys and imposes temperature limits

302] compounds allowing an effective coverage of the entire ultraviolet-to-visible spectral range by nitride-based optoelectronic devices. The broard spectral working-range, combined with the excellent thermal and chemical stabilities [282], make the group-III nitrides, at this stage, the material of choice in the design and commercialization of optoelectronic devices. [285, 303, 304] Group-III nitride materials show excellent material properties for utilization in intersubband devices working at both the near-infrared telecommunication wavelength regime as well as the far-infrared THz wavelength edge by exploiting electronic transitions between nanostructure-confined electronic states in single or multiple quantum well or quantum-dot heterostructures. [305–308] Suchlike applications turn out to be feasible since the large range of accessible band-gap energies in group-III nitride heterostructures translates into a broad range of potential valence-band and conduction-band offsets in group-III nitride heterostructures. [8]

For a long time group-III nitride semiconductors have almost exclusively been grown along the polar (0001) c-direction of the hexagonal crystal. These hexagonal, or polar, group-III nitrides suffer from strong performance-limiting [310, 311] electric fields from piezoelectric and spontaneous polarization, since the barycenters of the opposite charges, carried by the group-III and the group-V ions, do not coincide along the c-axis. [312] The occurrence of polarization fields is a direct consequence of the lack of inversion symmetry in the hexagonal crystals, that naturally show both piezoelectric and spontaneous polarization parallel to the c-axis. [313] In recent years, the growth of nonpolar and semipolar nitrides has found increasing technological interest due to the possible avoidance of strong internal fields. [285, 314] In these nonpolar or semipolar nitrides, the c-axis is orthogonal or inclined to the growth direction, thus eliminating or mitigating the field effects in the growth direction. [315] However, the electrical, optical, and structural properties are still affected by notable lateral anisotropies. A way to fabricate group-III nitride based optoelectronic devices, fundamentally free of polarization fields [311], is the growth [316–322] of cubic nitride alloys and the fabrication of intrinsically nonpolar material compounds. [312, 321, 323–325]

Numerous structure-function engineered nanostructures as single-quantum well and multi-quantum well structures [310, 319, 321], superlattices [323, 326, 327], nanowires [328, 329] and quantum dots [330–333] have been prepared on basis of binary and multinary group-III nitride modifications in either hexagonal wurtzite phase or cubic zincblende phase [9].

THE CRYSTALLINE STATE – Group-III nitride semiconductors naturally crystallize in stable hexagonal lattices [283, 335] with wurtzite (*wz*) structure which is conform with the symmetry operations of space group $P6_3mc$ (C_{6v}^4). Artificially grown, group-III nitrides may also crystallize in a metastable cubic phase [322, 336–343] with a zincblende (*zb*) structure belonging to the space group $F\bar{4}3m$ (T_d^2). Both structure polymorphs are constructed from fully connected networks build from corner-linked tetrahedra (see Fig.1.5). A second cubic phase, crystallizing into

on the growth dynamics of multinary nitride alloys. These limits and related physical alloy properties have been addressed in various experimental [288, 289] and theoretical [290–296] studies.

[8] See Paper I (Ref. [309]) and Paper VI (Ref. [35]) for further details.

[9] Some additional details on nonpolar and semipolar surfaces as well as defects are provided in Paper VIII (Ref. [334]) and Paper VI (Ref. [34]).

a rocksalt (*rs*) structure, belonging to the space group $Fm\bar{3}m$ (O_h^5), might be prepared under high pressure conditions. [344–348] In contrast to the other two phases, the rocksalt phase is formed by sixfold coordinated octahedral units. The occurrence of a *rs*-GaN high pressure phase, coexisting with wurtzite and zincblende phases for pressures above 5 MPa has been reported. [346] A combination of wurtzite and zincblende conformations has been repeatedly observed under conventional normal-pressure growth conditions for various nitrides. [318, 337] Despite representing

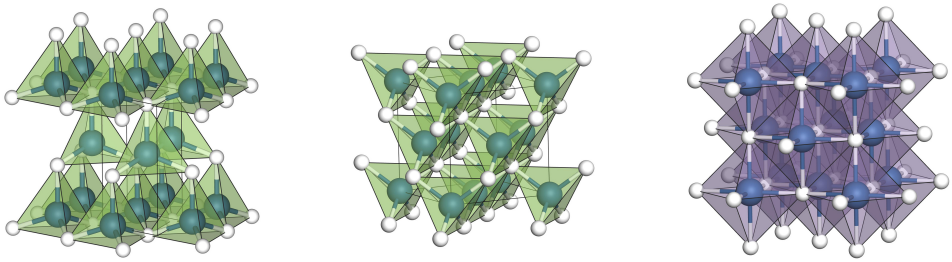

Figure 1.5: Overview of the conventional unit cells (coordination-polyhedra representation) and space groups of crystalline group-III nitride polymorphs: zincblende ($P6_3mc$, metastable), wurtzite ($F\bar{4}3m$, stable), and rocksalt ($Fm\bar{3}m$, high pressure). (blue: group-III element, white: nitrogen, green: wurtzite / zincblende cation-coordination tetrahedra, purple: rocksalt cation-coordination octahedra)

true high-pressure polymorphs, rocksalt-type AlN and GaN have been stabilized epitaxially as pseudomorphic layers grown on rocksalt-structured TiN(100) films. [349, 350] Epitaxial stabilization of *rs*-AlN has been observed in various multilayer structures and superlattices as AlN/VN, AlN/NbN, AlN/TiN, and AlN/CrN, likewise. [349, 351–353] The same stabilization mechanism is known for the cubic zincblende phases of group-III nitrides in e.g. AlN/W superlattices [354] and GaN/Mn multilayer [355] as well as for InN films on yttria-stabilized zirconia (YSZ) [356], on MgO [357], or on cubic GaN. [358] The growth of both *wz*-GaN as well as *zb*-GaN (with (111) orientation) might be selectively controlled by choosing proper deposition conditions of molecular-beam epitaxy. [359] Pure metastable *rs*-GaN has been stabilized in nanocrystalline form following chemically preparation via a benzene-thermal metathesis route [360] demonstrating the potential of phase stabilization of metastable semiconductor polymorphs through quantum-confinement constraints in various types of nanomaterials. [361–366] The rocksalt structure has also been predicted by first principles theory as the energetically favorable polytype for certain InN nanoparticles. [367] In addition to conventional three-dimensional bulk phases, the recent interest in two-dimensional materials also promoted substantial research on quasi two-dimensional ultra-thin film quantum structures of GaN [368] and led to quite recent preparation breakthroughs in the preparation of two-dimensional GaN via graphene encapsulation. [369] This recent progress promises the extension of low-dimensional group-III nitride-based optoelectronics, beyond two-dimensional BN [370]. Amorphous and nanocrystalline modifications of III-V nitrides, whose epitaxial growth is widely unaffected by deposition constraints due to interfacial lattice mismatch, have been considered as potential low cost alternatives to the crystalline phases. [371–376]

Focussing on the electronic material properties in detail, the hexagonal group-III nitrides InN, GaN, and AlN exhibit direct Brillouin-zone centered $\Gamma_v \rightarrow \Gamma_c$ band gaps of 0.68 eV in *wz*-InN [377, 378], ∼3.3 eV in *wz*-GaN [379, 380], and ∼6.0 eV in *wz*-AlN [381–383] at room temperature (300 K). The corresponding zero-temperature band gaps amount 0.69 eV for *wz*-InN [377], ∼3.5 eV for *wz*-GaN [379, 380], and ∼6.2 eV for *wz*-AlN. [381] The band gaps of the cubic analogues have been determined by room-temperature spectroscopic ellipsometry to 0.595 eV in *zb*-InN [384], 3.23 eV in *zb*-GaN [385], and 5.3 eV (indirect $\Gamma_v \rightarrow X_c$) [316, 386] and 5.93 eV (direct $\Gamma_v \rightarrow \Gamma_c$) in *zb*-AlN. [386] A low temperature *zb*-GaN band gap of 3.293 eV was reported [385], while the low temperature *zb*-AlN band gap has been estimated to 5.997 eV assuming similar low-to-room-temperature (direct) band-gap differences in the polar and nonpolar phases. [387]

NITRIDE ALLOYS – Devices based on multicomponent ternary and quaternary nitride compounds are fabricated from the stable polar wurtzite modifications, predominantly. Diverse optoelectronic devices as single-quantum well and multi-quantum well structured light emitting diodes working at characteristic blue and green wavelengths have been designed on the basis of InN containing III-V alloys. [388, 389] Light emission across the ultraviolet spectral range has been demonstrated for optical devises made from quaternary *wz*-AlInGaN/AlInGaN multiple-quantum well structures, e.g. working at wavelength bands of 280 nm [390], 340 nm [391, 392], and 352 nm [393]. In addition, multicomponent *wz*-(Al,Ga,In)N-based light emitting devices grown on nonpolar wurtzite lattice planes as $(1\bar{1}00)$ [394], $(20\bar{2}1)$ [395], $(10\bar{1}\bar{1})$ [396], $(10\bar{1}\bar{3})$ [397], or $(30\bar{3}\bar{1})$ [398] have demonstrated emission characteristics similar or superior to the common polar c-plane-grown samples. Beyond wurtzite structured nitrides, especially the photoluminescence characteristics of cubic double quantum well and quantum dot *zb*-InGaN/GaN heterostructures have been studied, in detail. [399–401] The potential of polarization-engineering in multicomponent III-V heterostructure devices has been discussed by Jena et al. . [402]

The optical properties of the binary wurtzite [403–406] and zincblende [385, 386, 403] phases have been comprehensively characterized by combinations of spectroscopic ellipsometry and first-principles electronic-structure and optical response calculations including the electron-hole interaction through solution of the Bethe-Salpeter equation. Spectroscopic ellipsometry was used to study the interband-transition energies in ternary *wz*-$Al_xGa_{1-x}N$ alloys. [407, 408] The fundamental electronic energy gap of the *wz*-$Al_xGa_{1-x}N$ alloys was found to depend nonlinear on the alloy composition parameter, x, with a moderate downward bowing between 0.9 eV and 1.6 eV. An even broader scattering of bowing parameters from -0.8 eV to 2.6 eV is obtained from numerical simulations on *wz*-$Al_xGa_{1-x}N$ alloys. [409, 410] The composition dependence of the dielectric function and transition energies of indium-rich *wz*-$In_xGa_{1-x}N$ alloys [378, 411] as well as *wz*-$In_xAl_{1-x}N$ [412] and Al-rich *wz*-$In_xAl_{1-x}N$ alloys [413, 414] has been investigated by spectroscopic ellipsometry indicating an In concentration-dependent non-linear bowing parameter for the variation of critical points in the band structures of the investigated samples.

Analog to the group-III arsenides, *zb*-AlN is the only binary compound with an non-direct fun-

damental band gap among the group-III nitride-semiconductors. Therefore, Al containing nitride alloys as *zb*-$Al_xGa_{1-x}N$ should exhibit a critical cation composition at which the alloy-conduction *band* edge changes from bulk-like Γ-point conduction-band states originating from *zb*-GaN to bulk-like conduction-band states originating from the global *X*-point conduction-band edge minimum in *zb*-AlN. The same effects should be visible in the band discontinuities between various non-polar group-III nitride heterostructures potentially also modifying the basic alignment character of nitride heterostructure. The preparation and optical characterization of cubic *zb*-$Al_xGa_{1-x}N$ alloys has first been reported by Baranov et al. [337] and an expectable increase of the alloy-band gap with Al content, the composition parameter x respectively, was observed for films with sufficient crystalline quality. Okumura et al. [415] investigated the optical properties of molecular beam epitaxy prepared *zb*-$Al_xGa_{1-x}N$ epilayers by cathodoluminesence and spectroscopic ellipsometry techniques. Their data indicate a direct nature of the fundamental band-edge transitions over the whole composition range, which characterized by a linear increase of the alloy-band gap with increasing Al content. Guerrero et al. [416] carried out room temperature reflectivity measurements on molecular beam epitaxy grown *zb*-$Al_xGa_{1-x}N$ epilayers and deduced a non-linear dependence of the lowest direct absorption edge on the Al concentration. Nakadaira and Tanaka [417] used near-bandedge photoluminescence spectroscopy at room temperature to investigate *zb*-Al_xGa_{1-x} alloys in the Ga-rich regime and reported a linear band-gap dependence on the alloy composition. In contrast, the majority of numerical studies predicts a direct-indirect band gap crossing, however, with substantial variations in the actual crossover concentration ranging from $x \approx 0.5$ to $x \approx 0.8$. [418–424]

THE AMORPHOUS STATE – GaN films have been prepared in amorphous and nanocrystalline phases [371, 372, 425–429] using ion-assisted deposition [427, 428], reactive sputtering [371, 425], and laser ablation. [372] The optical characterization yielded contradictory reports on the amorphous GaN (*a*-GaN) film photoluminescence properties at room temperature. Shim et al. [372] reported blue-light emission at ~ 2.8 eV while Trodahl et al. [427] found no "useful" luminescence in *a*-GaN. Band gaps ranging from 3.0 eV to 3.4 eV were reported by Kobayashi et al. [425] for nanocrystalline GaN (*nc*-GaN) thin films. Based on first-principles molecular dynamics simulations [430], the atomic structure of *a*-GaN was found to be composed predominantly from edge-sharing crystal-like tetrahedral units (~ 89 %) with a certain degree of disorder in the Ga-N-Ga bond-angle distribution. A minor contribution from threefold coordinated Ga (~ 10 %) and a sporadic occurrence of five-fold coordinated Ga (~ 1 %) was reported. The simulated amorphous networks have been found free of homopolar Ga-Ga bonds, while the formation of molecular N-N bonds seems possible, but rather exceptional. [430]

Amorphous AlN (*a*-AlN) films [374, 375, 431–435], have been prepared by reactive magnetron sputtering [374, 375, 431, 432, 434], plasma enhanced atomic layer deposition [435], and single ion beam sputtering. [433] An *a*-AlN thin film optical band gap of 5.84 ± 0.05 eV, close to the indirect band gap of *zb*-AlN has been reported by Khoshman and Kordesch. [374] In contrast, optical band gaps between 4.15 eV and 4.10 eV, decreasing with film-thickness augmentation, have

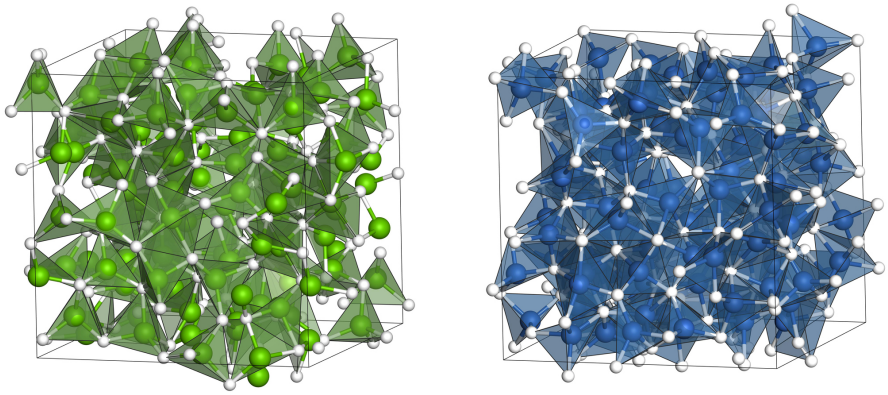

Figure 1.6: Cation-coordination polyhedra representation of 216-atom unit-cell models of amorphous GaN and AlN generated by density-functional theory molecular dynamics simulation. (green: gallium and GaN_n polyhedra, blue: aluminum and AlN_n polyhedra, white: nitrogen)

been reported. [433] Similar to *a*-GaN, ab initio molecular dynamics simulations [436] suggest a disordered structure of *a*-AlN consisting predominantly of tetrahedral coordination units ($\sim 92\,\%$) with minor contributions from threefold ($\gtrsim 4\,\%$) and fivefold coordinated ($\lesssim 4\,\%$) Al ions. In addition, the structure of *a*-AlN has been considered as chemically ordered, that is, an atomic framework free of homopolar Al-Al or N-N bonds. [436]

Chen et al. [437, 438] used an approximate self-consistent first principles multicenter tight-binding molecular-dynamics approach to study ternary amorphous $Al_xGa_{1-x}N$ (*a*-$Al_xGa_{1-x}N$) nitride alloys. The atomic structure in *a*-$Al_xGa_{1-x}N$ features a flexible mixture of threefold and fourfold coordinated cations and anions, sp^2-type and sp^3-type bonding environments respectively, with the number of threefold (fourfold) coordinated atoms in the alloys decreasing (increasing) with increasing Al content. Furthermore, no homonuclear bonds, leading to the formation of odd-numbered rings appeared in their studies. Despite the pronounced differences to the tetrahedral crystalline alloy phases, disorder in *a*-$Al_xGa_{1-x}N$ causes localized band-tail states instead of deep defects states. The calculated mobility gaps change between 4.62 eV and 7.24 eV for the end-point binary alloys *a*-GaN and *a*-AlN, respectively. [438] Kaufmann et al. [439] studied the electronic and topological properties of *a*-$Al_xGa_{1-x}N$ using density functional theory molecular dynamics. The reported extrapolated optical gaps vary between 3.65 eV for pure *a*-GaN to 5.06 eV for pure *a*-AlN, while the HOMO-LUMO-type band gap, affected from the localization of electronic states and band-tail formation in the density of states, changes from 3.25 eV to 4.66 eV with increasing Al content. [439]

Wagner

...
Es leuchtet! seht! - Nun läßt sich wirklich hoffen,
Daß, wenn wir aus viel hundert Stoffen
Durch Mischung - denn auf Mischung kommt es an -
Den Menschenstoff gemächlich komponieren,
In einen Kolben verlutieren
Und ihn gehörig kohobieren,
So ist das Werk im stillen abgetan.
Es wird! die Masse regt sich klarer!
Die Überzeugung wahrer, wahrer:
Was man an der Natur Geheimnisvolles pries,
Das wagen wir verständig zu probieren,
Und was sie sonst organisieren ließ,
Das lassen wir kristallisieren.

Mephistopheles

Wer lange lebt, hat viel erfahren,
Nichts Neues kann für ihn auf dieser Welt geschehn.
Ich habe schon in meinen Wanderjahren
Kristallisiertes Menschenvolk gesehn.

Johann W. von Goethe (1749-1832)

2 Materials science: An atomistic perspective

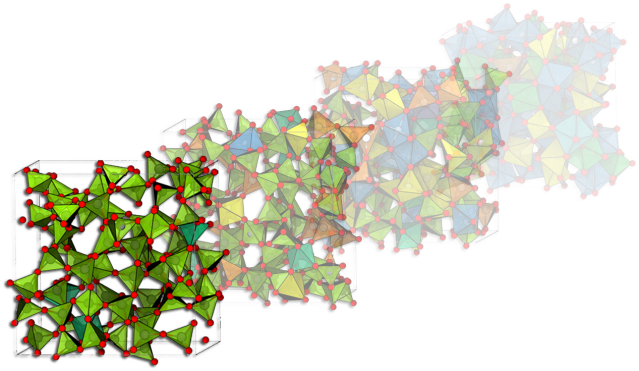

There is Plenty of Room at the Bottom – *When we get to the very, very small world ... we have a lot of new things that would happen that represent completely new opportunities for design. Atoms on a small scale behave like nothing on a large scale, for they satisfy the laws of quantum mechanics. ... At the atomic level, we have new kinds of forces and new kinds of possibilities, new kinds of effects. ... The principles of physics, as far as I can see, do not speak against the possibility of maneuvering things atom by atom.*

Richard P. Feynman (1918–1988)

Contents

2.1 The design of functionalized nanomaterials 20

2.2 The versatile arrangement of atoms in solid matter 24

2.2.1 Order and disorder in natural and artificial materials 24

2.2.2 Classification of atomic order types 32

2.3 Structure theory of glass 38

2.3.1 Classic theories on glass formation 40

2.1 The design of functionalized nanomaterials

THANKS FOR THE INSPIRTION, MR. FEYNMAN – Following Richard Feynman's visionary leitmotif for miniaturization, "There is Plenty of Room at the Bottom", the engineering of technological devices has led to an extensive exploration of the dimensions beyond humans' everyday perception and, quite often, even beyond the common worlds of human imagination. Guided by the spirit of Moore's law [1] [440], engineers in modern semiconductor industries have advanced rapidly towards the fundamental *atomic* ground of the formerly unknown open ranges of the nanoscopic world. [2] More and more, the shrinking of individual functional units starts to reach the flimsy size dimensions of just a few atomic layers. This trend finds its consequent culmination in the exploration and envisioned utilization of truly *atomistic* material modifications as a raw material for the manufacturing of new devices bearing never seen functional properties and efficiency.

IT'S ALL ABOUT CARBON, ... AGAIN! – For several decades, the undisputable star [3] in the ongoing search for the *ultimative* (electronic) material has always been pure carbon in its diverse "fascinating and aesthetically pleasing" [441] structural manifestations. The structure polymorphism, or, since considering a pure elemental solid material, allotropism, of carbon [441, 442] , covers the whole spectrum of well ordered material configurations from quasi-zero-dimensional fullerene-type clusters [443, 444], quasi-one-dimensional nanotubes [445], and nanorods [446] to virtually ideal two-dimensional graphene sheets [447–449], their stacked three-dimensional equivalent graphite and finally the ideal three-dimensional diamond structure [450] as well as diamond's *eclipsed* [4] hexagonal relative lonsdaleite [452]. The structure polymorphism of carbon [453], which further extends to exotic low-density nanofoams [454], various crystalline high-pressure phases [455], and diverse disordered amorphous/glassy forms of carbon [456, 457],

[1] Named after Gordon E. Moore, a co-founder of the Intel Corporation, Moore's law visualizes an empirical trend in the number of transistors assembled into a single integrated circuit. Thereby the number of transistors that are *crammed*, as formulated by Moore himself as early as 1965 [440], follows, with surprising accuracy, an exponential path of doubling every two years. In the most commonly quoted form Moore's law expresses the doubling of computer performance every one and a half year, which also considers the effects of *faster* transistors. Despite not being a physical nor a natural law, the validity of Moore's law has been proven for more than 40 years and, even if there are fundamental physical restrictions at some future point in time and space, Moore's law acts, ever since its emerging, as an indicator and even self-fulfilling target setting for the ongoing development of microelectronic technologies.

[2] While commonly utilized as a popular-science paraphrase for describing a size dimension beyond human cognitive abilities, a more sound standing definition of the intended meaning of the term *nano* [Etymology relates the prefix "nano" to the greek word νάνος (nanos) which translates into "dwarf".] should take into account not only the nanometre-size of a particular object. Rather, the appearance of fundamental correlations between the spatial size and shape and physical material properties should be emphasize as the main characteristic of the nanoscopic world. In a nanoscopic material phase or nano-structured solid, the size, more precisely the charge-carrier confinement within one or more spatial directions, modifies the basic material properties with respect to the well defined characteristics of the extended bulk-like material.

[3] In the last 20 years two Nobel prizes were directly awarded to outstanding breakthroughs in the fundamental research on carbon allotrops. In 1996 Robert F. Curl, Jr., Sir Harold W. Kroto, and Richard E. Smalley received the Nobel prize in chemistry "for their discovery of fullerenes". Andre Geim and Konstantin Novoselov were awarded by the Nobel prize in physics in 2010" for groundbreaking experiments regarding the two-dimensional material graphene".

[4] While diamond exhibits an staggered conformation of C_3C–C_3C bonds, lonsdalite shows an eclipsed conformation marking a distinct hexagonal crystal axis. [451]

as well as hypothetically envisioned classes of carbon allotropes as *schwarzites* [5] [453, 460–465], *graphyne* [6] [466–468], or *novamene* [7] [469] is an archetypical illustration of the complex competition between different fundamental bonding configurations, namely sp^2-hybridization, sp^3-hybridization [442, 457], and to some extend even sp^1-hybridization, in a single homogenous phase material [8].

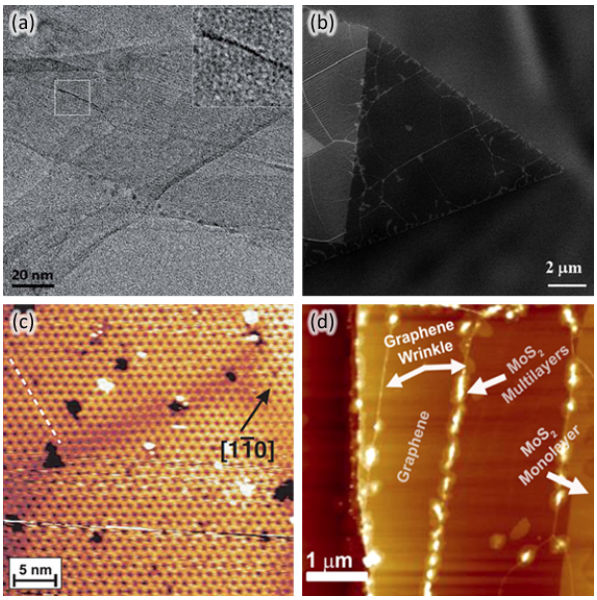

Figure 2.1: Atomic resolution images of various recently synthesized two-dimensional material phases. (a) Transition-electron microscopy image of a single-layered TiO_2 nanosheet, supposedly consisting of a single layer of corner-sharing TiO_6 units, taken from Ref. 458. (b) Scanning-electron microscopy image of triangle, graphene-like hexagonal BN sheets extracted from Ref. 12. (c) Scanning-tunneling microscopy mapping of an monoatomically thin Si layer, silicene respectively, supported onto an unreconstructed silver (111) surface from Ref. 15. (d) Atomic-force microscopy imaging of graphene supported MoS_2 mono-, bi-, and multilayer film growth taken from Ref. 459.

Despite its extraordinary physicochemical properties [448, 470, 471], as high mechanical strength, excellent electrical conductivity and extraordinary heat conductivity, elemental carbon might not be the *magic bullet* to take down all challenges of the post-silicon electronics era, may it be for still existing material limitations or for practical problems of the functionalization process into technological devices or demands of a cost-efficient mass-fabrication for future mainstream electronics. [461, 472, 473] In addition, even the Nobel prize awarded *heart* of todays carbon-materials science, is increasingly challenged by numerous layered material modifications, *discovered* in recent past. [9]

[5] Schwarzites, named after the german mathematician K. Hermann A. Schwarz (1843-1921), might be considered as the hyperbolic/negative-curvature analog of fullerenes. While the spherical structure of fullerenes necessitates the formation of carbon pentagons, the negative surface curvature of schwarzites is achieved by allowing carbon heptagons and/or octagons in addition to the conventional carbon hexagons. The high-strength and low density three-dimensional frameworks of schwarzites resemble the atomic structure of aluminosilicate zeolites.

[6] Graphyne represents an *extended* form of pure graphene constructed by linear C_2 units extending all or a part of the carbon-carbon bonds within a graphene sheet. The carbon bonding environment in graphyne sheets essentially represent a combination of the common sp^2-type and *non-graphene* sp^1-type hybrid orbitals. [466]

[7] The recently coined collective name *novamene* denominates a *novel* class of carbon allotropes constructed from combinations of sp^3-bonded lonsdaleite-type hexagonal diamond and sp^2-bonded graphene-type carbon rings. [469]

[8] The remarkably versatile bonding properties, that allow carbon to build complex molecular systems in one, two, and three dimensions by bonding to itself as well as the majority of elements in the periodic table, especially, other light *biologically relevant* atoms, can be seen as the *backbone* for the formation of biological active matter and therefore, as far as known to us, a prerequisite for life itself.

[9] The possible existence of (free-standing) two-dimensional sheets of atomic monolayer thickness has been envisioned by theoretical simulations for carbon's group IV elemental semiconductor analogues silicon and germanium even before the intended synthetization of graphene. [474, 475] Two-dimensional graphene-like silicon, named silicene (see Fig. 2.1 (c)), has been synthesized and subsequently characterized on silver (111) [459, 476–480] and iridium

A NEW KIND OF ARTIFICIAL SOLIDS – In general, a widespread class of layered materials might be comprehensively classified as van-der-Waals-stacked solids. [10–16] The basic *philosophy* behind van der Waals heterostructures has recently been illustrated by Geim and Grigorieva [493] using the striking analogy of atomic-scale lego blocks. In principle, various two-dimensional materials might be *stacked*, similar to differently colored lego bricks, in order to design new heterostructured materials, that might reveal unusual physical phenomena. Similar to graphite, these synthetically fabricated materials exhibit a stacked atomic structure of individual two-dimensional, not necessarily monoatomically thick, and covalently in-plane-bonded nanosheets, that stick together predominantly by relatively weak van der Waals forces. The most important and wide-ranging classes of such layered materials are two-dimensional transition-metal dichalcogenides [12, 13, 494–499] and (transition-)metal oxides. [12, 13, 500–502]

Probably, one of the greatest successes of graphene science is the massive resurgence of research interest into actually well-known *classic* two-dimensional materials as well as still to be discovered low-dimensional polymorphs and their potential for technological utilization. Reviewing the recent literature, this development is impressively demonstrated by several new arrivals on the candidate list of materials rivaling with graphene for the next two-dimensional "wonder material". [10,11] First complex van der Waals heterostructures, fabricated from monoatomically thin two-dimensional materials, e.g. combine several layers of BN, graphene, and various transition-metal dichalcogenides into single and multiple quantum wells for application as light-emitting diodes. [16] Apparently, these first complex prototypes, fabricated via mechanically stacking rather than epitaxial growing, are a foreshadowing of the tremendous technological potential that is inherent to this new class of materials.

(111) [481] surfaces as well as on zirconium diboride (ZrB_2) thin films. [482] The fabrication of a first silicene based field-effect transistor has been reported, recently. [483–485] In contrast to graphene, silicene seems to be much more suited for a direct integration into the existing technology of ubiquitous semiconductor devices. [483] The germanium analogue germanene, has most recently been grown on a gold (111) surface substrate. Besides, the pristine group IV modifications, especially atomically thin (*hexagonal*) boron-nitride (*h*-BN) [12, 486–490] (see Fig.2.1 (b)) as well as layered graphene–boron-nitride heterostructures [491, 492] have attracted recent interest as two-dimensional group III-V nanomaterials for electrical devices.

[10] Just recently, this list has been extended by the "rediscovery" [503–505] of puckered black phosphorus nanosheets with a few atomic layer thickness [506–508] as well as atomically thin arsenene and antimonene films predicted by *ab initio* theory simulations. [509] Also, a two-dimensional graphene-like pure-phase modification of tin, stanene, has been theoretically predicted [510, 511] and seems likely to be synthesized in nearby future.

[11] Planar pure-carbon allotropes, consisting of pentagons, conventional hexagons, and heptagons, have already been predicted by Crespi et al. . [512] This new class of carbon pentaheptites, showing potential planar, tubular, or spherical shapings, is closely related to Stone-Wales type defects [513] in carbon allotropes and was subsequently termed *Haeckelites* honoring the german zoologist Ernest H. P. A. Haeckel (1834-1919) and his artful, geometry inspired, drawings of radiolaria. [514, 515] Comparable haeckelite nanostructures have been proposed as potential structural candidates for low-dimensional nanostructures of hexagonal semiconductors as the group-III nitrides GaN or BN. [516, 517]

Latest, the possible existence of a new two-dimensional carbon allotrope, consisting entirely of five-membered carbon rings instead of the common six-membered graphene-like rings, named penta-graphene, has been theoretically predicted on the basis of first principles calculations. In contrast to graphene this new two-dimensional carbon phase exhibits a wide *quasi-direct* electronic band gap of 3.25 eV, close to the well-known band gaps of the important wide-gap semiconductors GaN and ZnO. [518]

FINDING MATERIALS SYNERGIES – Despite the tremendous advances in the fabrication of novel materials, every autochthonous material phase shows restrictions with respect to the accessible range of physical properties. A promising strategy to overcome the fundamental limitations of homogenous material phases, and a path to develop the true potential of artificial materials design, is the systematic utilization of synergetic effects associated with mixing various functional materials. Thereby, the excess value of combining materials might either come into effect by providing an essential material property as, e.g., visible-light photo-sensitivity to a mechanically or chemically stable and technologically well controllable wide-gap material or by creating new active sites for electrochemical catalysis within a new heterogenous hybrid material. Exemplarily, recent experimental studies on graphene wrapped/supported TiO_2 nanocomposites (see Fig.2.2 (d)) indicate enhanced lithium storage as well as electronic and ionic transport capabilities that are imperatively for future generations of high-power lithium-ion batteries. [523–528] Likewise, the fabrication of TiO_2-graphene hybrid materials (semiconductor-graphene nanocomposites in general, see Fig.2.2 (b)) for enhancing the photocatalytic material properties by *sensitizing* [12,13], i.e. generating a material response to visible-light illumination, is a highly appreciated results of designing heterostructured materials. [87, 520, 522, 527, 536, 537] Related materials as reduced graphene-oxide TiO_2 nanocomposites [538–541] (see Fig.2.2 (c)) facilitate the photocatalytic conversion of carbon dioxide into hydrocarbon fuels. A further step on the road towards enhanced visible-light absorption in wide-gap metal oxides has been done by hetero-structuring of TiO_2 and ZnO. Sev-

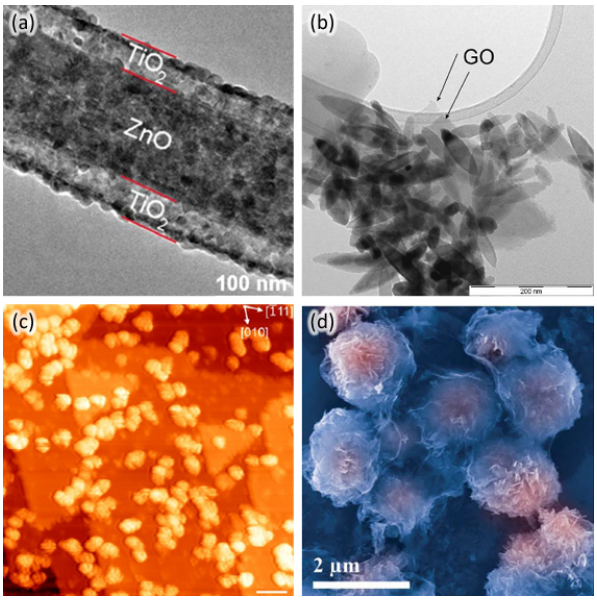

Figure 2.2: Atomic resolution images of various recently synthesized nanocomposite materials. (a) Transition-electron microscopy image of ZnO-TiO_2 core-shell heterojunction nanofibers extracted from Ref. 519. (b) Transition-electron microscopy imaging of a TiO_2-graphene nanocomposite taken from Ref. 520. (c) Scanning-tunneling microscopy image of a ruthenium based dye (N3) covered TiO_2 anatase (101) surface from Ref. 521. (d) Scanning-electron microscopy image of graphene-wrapped TiO_2 nanoflower composites from Ref. 522.

[12] The most common sensitizing strategy for wide gap (transition-)metal oxide semiconductors as TiO_2 is to attach molecular organic *dyes* to the surface of the host semiconductor in order to provide visible-light absorption capabilities that are a necessary prerequisite for potential solar-cell composite materials. [99, 102, 103, 529–532] In view of the requirements of cost-efficient solutions to the problem of renewable-energy generation, such dye-sensitized solar cells, commonly referred to as Grätzel cells according to their inventor Michael Grätzel [99, 102, 103], have received much attention as an entirely new design paradigm for the potential large-scale fabrication of solar cells. The pioneering work of Michael Grätzel was honored in 2010 by the Millennium Technology Grand Prize. [533]

[13] The general superiority of graphene based TiO_2 composites over other TiO_2-carbon composites has been discussed, controversially. [534, 535]

eral experimental studies [519, 542–545] recently indicated that nano-structured TiO_2/ZnO hybrid oxides (see Fig. 2.2 (a)) exhibit an enhanced photocatalytic activity under visible-light irradiation.

Aside from the inorganic and predominantly carbon based materials above, also organic molecules have emerged as an engineering platform for nanostructured and low-dimensional materials. While polymers naturally tend to form one-dimensional chainlike structures [14], recent advances in polymer synthesization indicate the existence and even selectively controllable preparation of extended free-standing two-dimensional molecular frameworks [548–555] as well as open porous or layered three-dimensional makromolecular complexes [550, 551, 554–557]. Besides *top-down*-like polymerization approaches in thermodynamically controlled chemical environments, biomolecular films of monoatomic thickness [558–563] or even one-dimensional chainlike topologies [564–566] might be obtained in a *bottom-up* fashion by taking advantage of well-defined surface-mediated and inter-molecular self-assembly effects on solid templates [567–569].

2.2 The versatile arrangement of atoms in solid matter

2.2.1 Order and disorder in natural and artificial materials

IF YOU WANT TO UNDERSTAND FUNCTION, STUDY STRUCTURE. [15] – Formulating the key-challenges of solid-state physics, one might come the the conclusion that the most relevant task of solid-state physicists is to find fundamental correlations between the atomic structure of a material and the associated microscopic and macroscopic material properties. Thus, from an atomistic point of view, which is more likely taken by a theoretician than an experimentalist, the first step in solid-state physics, or more generally materials science on the nanoscale, is to develop a basic understanding of the underlying characteristic arrangements of atoms in an investigated material(class) or a particular sample. In doing so, it becomes, at a certain point, inevitable to recognize that the typical length scales of nanostructuring (e.g. nanoparticle and quantum dot size) and heterostructring (e.g. quantum well sizes, superlattice periods) start to overlap with the atomic and chemical/compositional order characteristics of the examined materials. The atomic order of a material typically subsumes the spatial arrangement of atoms within a few next-neighbor distances as well as long-range order symmetry characteristics of the entire sample [see order type III in Fig. 2.3 (a)]. Typically, the first neighbor atoms, defining the first atomic coordination shell, represent a materials *short-range order* with characteristic correlation lengths/bonding distances of $\sim 2-3$ Å [see order type I in Fig. 2.3 (a),(b)]. Additional structural characteristics, sometimes referred to as a *hidden* order occurring predominantly, but not exclusively, in more or less disordered solids and extending over several next-neighbor distances, define *medium-range order* occurring on length scales of $\sim 5-20$ Å [see order types II in Fig. 2.3 (b)]. The medium range

[14] Certainly, the naturally occurring double-helical structure of nucleotide-biopolymers, Nobel prize worthy envisioned by Watson and Crick [546, 547], represents, despite its limited number of basic constituents, nature's most fundamental, complex, and elegant organic nanostructure.

[15] Quotation of the british molecular biologist and biophysicist Francis H. C. Crick (1916-2004).

order regime might further be subdivided into near-ranging, intermediate-ranging and far-ranging order regimes [16]. *Near medium-range order* ($\leq$5 Å) [order type IIa in Fig. 2.3 (b)] describes the connection of neighboring fundamental structural (coordination) units, frequently represented by tetrahedra or octahedra in three-dimensional oxide materials. *Intermediate medium-range order* [17]

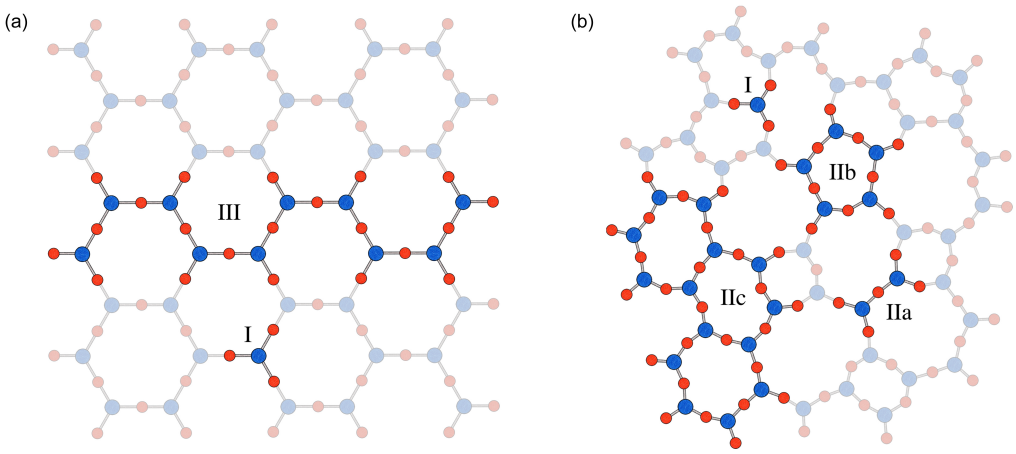

Figure 2.3: Schematic illustration of different ranges of structural order characteristics in (a) crystals and (b) a disordered material using the example of a two-dimensional binary network structure consisting of fundamental MX_3 coordination units. Illustrated are atomic short-range order (I), near medium-range order (IIa), intermediate medium-range order (IIb), and far medium-range order (IIc), as well as long-range order (III).

($\sim$ 5 – 8 Å) [see order type IIb in Fig. 2.3 (b)] occurs in form of more extended arrangements of fundamental coordination units in e.g. ring-like or cluster-type structures. *Far medium-range order* might occur, for instance, in form of ring clusters or extended chain-like order characteristics on a length scale between $\sim$ 8 – 20 Å [see order type IIc in Fig. 2.3 (b)]. Even above the far-medium-range order characteristics, structural correlation length > 20 Å might occur in case of very porous materials, that allow notable density fluctuations, sometimes, even up to the mesoscopic order regime.[18] The chemical (short-range) order characteristics of a composite material are particularly important in case of composite materials/solid solutions, as ternary or quaternary group-III semiconductor-solid solutions as AlGaAs, AlGaN or AlGaInN, where changes in the material composition strongly affect technological relevant optoelectronic properties (e.g. the electronic band gap, the onset of optical absorption). Chemical order on other length scales also occurs in heterogenous mixtures of nanoparticles with miscellaneous chemical characteristics. The chemical disorder is commonly accompanied by basic quantum-confinement effects due to the grain sizes, in the later case.

[16] The actual definition of correlation lengths for short-ranging, the various types of medium-ranging, and long-ranging order features of solids is, in general, not a fundamental separation, rather it depends on the specific network topology of the considered materials class. The definition given here is based on the classification given in Stephen R. Elliott's review on medium-range order in covalent amorphous solids. [570]

[17] Within this manuscript, *intermediate medium-range order* is abbreviated to *intermediate-range order* for simplicity.

[18] A wide class of oxide materials, showing these types of structural order, are zeolites. Zeolites are aluminosilicate minerals with predominantly well ordered and sometimes disordered microporous atomic structures.

PHYSICISTS DO PREFER SIMPLE THINGS [19] – Typically, the classification of atomic structure in solid-state physics starts by depicting a solid from an idealized crystallographic point of view. [20] A crystal is uniquely defined by an atomic basis, the body of chlemical elements forming the material respectively, and a set of symmetry-equivalent transformations mapping the crystal lattice onto itself. Thus, the whole of *three-dimensional* and *truely* crystalline solids is perfectly grouped into 32 crystallographic point groups, determining the occurrence of physical properties in a crystal class on a macroscopic scale [21] and, by inclusion of translational symmetry operations, 230 existing crystallographic space groups [22], defining the material properties on the microscopic level. The later classification contains complete information on the periodic spatial arrangement of atoms in a given *ideal* crystal with *proper* three-dimensional (triperiodic) order in all spatial directions. In case of layered three-dimensional materials with *proper* atomic ordering in two spatial directions and a stacking sequence in the third direction, as the van der Waals solids discussed above, the number of possible *diperiodic* space groups reduces to 80. Passing on to the two-dimensional space, this number is reduced to a subset of 17 distinct crystallographic plane groups (or wallpaper groups) [23]. Knowledge of the distinct crystalline symmetry allows to make qualitative a priori statements on the intrinsic microscopic (e.g. energy-level/crystal field splitting) and macroscopic [575, 576] (e.g. enatiomorphism, second-harmonic generation, piezoelectricity, pyroelectricity, and ferroelectricity for non-centrosymmetric point-group symmetries) physical properties of an investigated material. Therefore, precise information on the crystal inherent symmetry is on the one hand essential to interpret experimental data. On the other hand, symmetry considerations are not only *exploited* in experimental measurements but also in computational simulations of solid matter, where the computational cost for solving high-symmetry problems is drastically reduced by application of symmetry operations.

It is obvious that one cannot find something like an ideal, thus infinite, (bulk) crystal in nature. Rather, a natural solid is considered to be crystalline if he is *sufficiently* free of structural defects and, of prime importance, if perturbations through surface effects are negligible for a sample's

[19] The preceding statement [571] is just one way to paraphrase a plethora of common working practices in physics. In fact, the reduction to simplicity, finding a *simple* model or a comprehensible subsystem that still contains the the fundamental (physical) properties of interest, is one of the most essential scientific strategies. Choosing a well defined model system represents the scientific version of *devide et impera* or, as paraphrased by Einstein, "Everything should be made as simple as possible, but no simpler" to handle the vast number of degrees of freedom in complex lifelike systems.

[20] It might be surprising from today's perspective that the concept of a crystalline structure, introduced by X-ray crystallographers at the beginning of the twentieth century, had to face hard criticism from chemists and their paradigm of molecules being *the basis of the whole of chemistry* [572], including solids.

[21] This is the central consequence of Neumann's principle, stating that the macroscopic physical properties of a crystal, the associated tensors respectively, have at least the symmetry of the crystallographic point group.

[22] The 230 inequivalent space groups have been derived independently and almost contemporaneous by the german mathematician Arthur M. Schoenflies (1853-1928) and the russian crystallographer and mineralogist Evgraf S. Fedorov (1853-1919).

[23] Explicit inclusion of a discrete magnetic ordering in a crystal will increase the number of possible group-axiomatic configurations through inclusion of time/spin-reversal symmetry to 80 magnetic plane groups, 528 diperiodic magnetic space groups and 1651 triperiodic magnetic space groups. [573] Beyond, the general inclusion of non-collinear spin requires the generalization of magnetic groups towards so called spin groups. [574]

physical properties. Considering the vast number of atoms and the dominance of cubic volume over quadratic surface scaling, this condition in certainly meet for common every-day objects, the macrocosmos respectively. Certainly, this condition is also meet through the microcosmos and starts to soften in the sub-micrometer regime. Thus, aside from relying on a purely size-related definition, an alternative, supplementing respectively, and more physical definition of nanoscience might refer to material systems in which surface properties start to dominate bulk related material properties.

NOT YOUR AVERAGE ORDINARY CRYSTAL – Neglecting the existence of non-crystalline disordered matter yet another moment, the most severe cracks in the rigid fundament of traditional crystallography certainly originate from the paradigm shifting discovery of the existence of naturally occurring highly ordered but aperiodic, or more specific *quasiperiodic* [24], solids. That is saying, that it is possible to fabricate enigmatic objects that exhibit several features of a crystalline solid [25] but do not manifest those crystal-like physical properties in translational invariance in all spatial directions, which was believed to be a fundamental unalterable characteristic of a long-range ordered solid structure. Order in these *quasicyrstals* [577–598] has two fundamental facets. On the one hand, the entire solid is composed of a finite number of highly symmetric (short-range ordered) fundamental building blocks, representing the unit-cell analog of a crystal, roughly speaking. However, in contrast to a crystal, there are in principle no distinct restrictions for the allowed rotational symmetries of these fundamental objects. Arranging those fundamental units in space leads to an aperiodic quasicrystalline solid with perfect topological long-range order. Thus, the aperiodic long-range order of quasicrystals is subject to strictly deterministic rules of finite complexity [26]. The pure existence of quasicrystals has initially been refused to be accepted due to its pervasive consequences for the fundamentals of crystallography, classic lattice theory respectively. These fundamentals are concisely expressed in the classic *crystallographic restriction theorem* stating that point-group symmetries of two-dimensional and three-dimensional lattice groups are restricted to proper rotations by $(2\pi/n)^\circ$ with $n = 1, 2, 3, 4$, or 6. Ultimately, any possible symmetry operation is allowed in the world of quasicrystals, just with the restriction to one distinct *global* symmetry center within an entire *ideal* quasicrystal. So, *starting* from a fundamental building block with n-fold rotational symmetry or an n-fold symmetric *patch* of regular crystallographic objects, defines this building block or patch as the center for the n-fold rotational symmetry of the entire quasicrystal, while an ideal crystal exhibits an infinite number of symmetry centers. However, an infinite number of limited regions of crystallographically forbidden symmetry operations is allowed in a quasicrystal, locally. Most graphically, existing long-range order in a solid material, either crystalline or aperiodic, is represented by a (X-ray, electron, or neutron) diffraction pattern solely consisting of distinct Bragg peaks. However, no two-dimensional or

[24] This specification is necessary since quasicrystals only represent a subset of existing aperiodically ordered solids. Well known types of *aperiodic crystals* also originate from the formation of long-range ordered structures with a superimposed incommensurable chemical and/or structural ordering (cf. Fig. 2.5 (d)).

[25] A naked eye examination of a quasicrystal would not allow its differentiation from an crystalline material.

[26] "...the locations of the atoms can be obtained by a deterministic algorithm of finite complexity." [583]

three-dimensional crystal lattice allows the occurrence of Bragg peaks with fivefold or any other non-crystallographic rotational symmetry [27].

Ultimately, the discovery of quasicrystals with all its fundamental consequences for our understanding of solid-state materials, as the redefinition of a *crystal* by the International Union of Crystallographers [28] as well as the personal efforts in his fight against the prevailing scientific consensus have been acknowledged by awarding the 2011 Nobel prize in Chemistry to Daniel Shechtman (1941-) "for the discovery of quasicrystals". Since their discovery, laboratories around the world have successfully prepared numerous quasicrystalline material samples.[29] The development of a fundamental microscopic understanding for the macroscopic physical properties of quasicrystals is still an ongoing field of research with puzzling experimental observations and, due to the lack of periodicity, a very limited number of supporting theoretical studies on this matter. However, despite their brief history, quasicrystallography represents a vital field of research with tremendous significance for the understanding of the atomic structure of matter, in general.

IN MELANCHOLY SYMMETRY [30] – Sometimes exceptional examples exist that combine versatile ideas from various scientific disciplines in a rather unexpected way. A virus is a functional biological unit existing at the boarder between the microcosmos and the nanoscopic world, simply due to its extreme size. However, viruses raise various fundamental questions since they represent commuters across borders not only in a spatial dimension but also represent the edge between biologically active (living, animate) and unenlivened (inanimate) matter. Focussing on the nanoscopic structural characteristics, living organisms, represent some kind of disordered (soft matter and amorphous) conglomerates. Unenlivened matter can exist in ordered or disordered configurations,

[27] The difference between a crystal and a quasicrystal is expressed in the number D of linearly independent basis vectors needed to "index" the diffraction peaks. While any d-dimensional crystal, bound to the crystallographic restriction theorem, is completely indexable by a set of Miller indices referring to $D = d$ linear independent vectors, a quasicrystal's diffraction pattern requires $D > d$ linear independent vectors to index the occurring Bragg peaks. This is due to the fact that, according to the work of Bohr [599–601], any quasiperiodic function, or aperiodic function in general, can be considered as projection or irrational cut of a strictly periodic function in higher dimension.

[28] The definition of a *crystal* has been changed from laying the focus on periodicity to the quite open definition "by *crystal* we mean any solid having an essentially discrete diffraction diagram, and by *aperiodic crystal* we mean any crystal in which three-dimensional lattice periodicity can be considered to be absent." [602].

[29] The stable synthetic quasicrystals [589], existing so far, are predominantly ternary and sporadically binary and quaternary intermetallics covering a limited number of possible *forbidden* crystallographic symmetries as icosahedral [603–608], octagonal [609], decagonal [610–614], and dodecagonal [615]. Aside from metallic alloys, a dodecagonal three-dimensional quasicrystal phase has been observed for mesoporous silica (silicon dioxide) and a dodecagonal two-dimensional barium titanate ($BaTiO_3$) thin film, supported on platinum, has been reported implying possible quasicrystallinity in oxide materials. [616] Further examples, demonstrating (approximate) *quasicrystal*-like (self-assembled) oder characteristics in other material classes, such as soft matter, are enneagonal and dodecagonal symmetric organic colloidal quasicrystals [617], dodecagonal inorganic colloidal nanoparticle superlattices [618], and dodecagonal supramolecular dendritic liquid quasicrystals [619], as well as dodecagonal tilling patterns of extended quasicrystalline polymer arrangements [620]. The later examples clearly extend towards the mesoscopic ordering regime ($10-50$ nm), thus demonstrating quasicrystalline order on various length scales, as one might expect from a proper ordering state of matter. [616, 620]

[30] Occurring in the short story *The Queen of Spades'* of the russian author/poet Alexander S. Pushkin (1799-1837), describing the aged and faded furniture of an old lady. "Faded stuffed chairs and divans with soft cushions stood *in melancholy symmetry* around the room, the walls of which were hung with China silk." A more free, but in the present context slightly more fitting quotation is given as "In sad symmetry stood the furniture in the old lady's room". [621]

thereby crystalline order, at least in solid matter, is always related to an inanimate state, solidified in perfect symmetry. In a certain sense, the issue of biological activity reveals the deceiving site of crystalline symmetry that charms the observer with the gracefulness of a snowflake and fascinates by elegant mathematical/geometrical construction rules. The odd site of crystallinity has simply been put in a nutshell by the russian crystallographer and mineralogist Evgraf S. Fedorov (1853-1919) in the aphorism "Crystallization is death" [31,32]. [450]

As demonstrated by structural (molecular) biology, viruses posses a high degree of structural order and represent common examples for the natural occurrence of non-crystalline rotational symmetry in nature. About half of all (spherical) virus families, more precisely their *capsides*, the protein shells that enclose the genome of a virus, show a notable icosahedral symmetry. [623–626] Based on the repetitive occurrence of fivefold symmetry in primitive organisms as various echinoderms (including sea stars and sea urchins) it has been speculated[33] that non-crystalline rotational symmetry might represent an self-defense strategy against crystallization and, thus, ultimately death. This observation is even more fascinating in case of viruses, which might underline their exceptional position at the edge between dead crystallinity and enlivened amorphousness by adapting a non-crystalline symmetry.

MATERIALS OUT OF SHAPE – While crystalline objects dominate the curriculum of solid state physics, or materials science in general, a majority of solid everyday objects as wood [34] or cotton [35] contain large or dominating fractions of disordered atomic domains. Truly amorphous [36] materials are glass [37], plastic [38] and rubber [39] in all of their practical shapes. Amorphousness also occurs within some less obvious material classes. The atomic structure of ceramics covers the entire spectrum ranging from sintered crystalline ceramics, traditional fabricated in pottery and as building materials, to the amorphous structure of some modern heating-resistant glass-ceramics. Depending on their formation history and the actual definition, naturally occurring minerals and rocks might be found in a disordered structural state. Minerals are complexes with well defined

[31] The same quotation is also frequently attributed to the british physicist John D. Bernal (1901-1971).

[32] However, there is one important exception of the above rule in case of soft matter, namely "liquid crystals". Liquid crystals constitute a basic linkage between the realms of soft and hard matter carrying attributes of liquids and crystals at the same time. A liquid crystal possesses crystal like orientational order without the *solid crystal* inherent positional order of condensed matter. Since all animate matter obsessively necessitates the presence of water, *liquid-crystal order* is an essential state of living matter. [622]

[33] The idea that fivefold rotational symmetry might be a self-defense mechanism to prevent primitive organisms from crystallization is attributed to the russian crystallographer and mineralogist Nikolai W. Below (1891-1982) [627].

[34] From a materials-science point of view, wood represents a polymeric composite of mainly three organic polymers cellulose, hemicelluloses and lignin, which form complex cell walls that give wood its versatile viscoelastic properties on the macroscale. Whereby, the complex supermolecular cell-wall frameworks combine crystalline and amorphous oder. The amorphous matrix is build from the amorphous components lignin and hemicelluloses whereas cellulose consists of a major crystalline component in form of microfibrils and additional disordered domains. [628–630]

[35] Since cotton consists predominantly ($> 90\,\%$) of cellulose, it combines crystalline and amorphous order.

[36] Fitting the title of this subsection, the term amorphous goes back to the negating greek prefix "a" and the greek word $\mu o \rho \phi \grave{\eta}$ (morphè) which translate into "without shape".

[37] Glass (see below) represents the archetype of an amorphous/disordered solid, as discussed below.

[38] Plastics are complex synthetic conglomerates of organic molecules.

[39] From a materials science point of view rubber represents a polymeric elastomer with extraordinary viscoelastic properties.

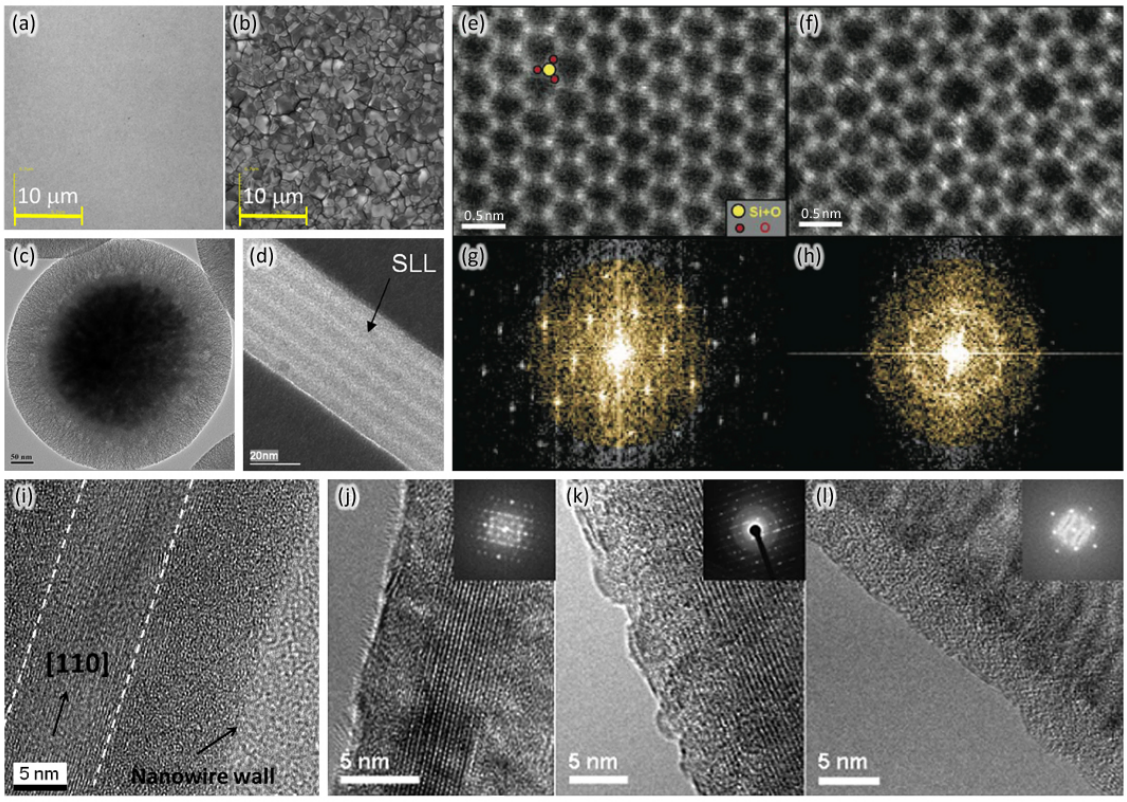

Figure 2.4: Illustration of different types of crystalline and amorphous order characteristics in solid nanostructures. (a)-(b) Confocal microscope image of the surface topographies of a smooth amorphous and a substantially corrugated nanocrystalline tantalum pentoxide (Ta_2O_5) surface extracted from Ref. [631]. (c) Transmission electron microscopy (TEM) image of a supermagnetic core-shell microsphere consisting of a Fe_3O_4 core surrounded by an inner nanocrystalline SiO_2 shell and an outer disordered mesoporous SiO_2 shell from Ref. [632]. (d) TEM photograph of a superlattice-like structure consisting of germanium tellurite (GeTe) and antimony tellurite (Sb_2Te_3) for application in phase change random access memory cells modified from Ref. [633]. (e)-(f) Dark-field scanning TEM (ADF-STEM) images of a two-dimensional SiO_2 crystal and a two-dimensional amorphous SiO_2 glass. (g)-(h) Fast Fourier transforms (FFTs) of the above STEM images of crystalline and amorphous two-dimensional SiO_2. The figures (e)-(h) are taken from Ref. [634]. (i) High resolution TEM micrograph of a silicon core-shell nanowire consisting of a highly crystalline core surrounded by an amorphous shell extracted from Ref. [635] (j)-(l) High resolution TEM images of crystalline ZnO nanowires coated with crystalline (left), nanocrystalline (middle), and amorphous (right) Al_2O_3 thin films extracted from Ref. [636]. The insets show the corresponding diffraction patterns.

chemical composition. Following the more general definition [40] given by H. Catherine W. Skinner (1941-), a mineral is any elemental or compound solid, amorphous or crystalline in atomic structure, that has formed through biogeochemical processes. [637] In contrast, rocks commonly represent chemically nonspecific disordered conglomerates of mineral components possibly containing fractions of solid amorphous inclusions depending on the formation history. Extrusive

[40] The mineral definition of "An element or compound, amorphous or crystalline, formed through biogeochemical processes"' of H. Catherine W. Skinner, given in Ref. [637], extends the more narrowed definition of Ernie Nickel of "A mineral is an element or chemical compound that is normally crystalline and formed as a result of geological processes." [638]

igneous rock might also solidify in an almost completely glassy state. Also, rocks of sedimentary origin might show notable disorder characteristics. However, they represent rather heterogenous mixtures of small /nano-sized crystalline grains. In general, such polycrystalline (nanocrystalline) conglomerates [639] are just disordered on the mesoscopic or macroscopic length scale but crystalline on the nanoscale, with possible amorphous domains at the (nano)grain boundaries. Due to their highly nondirectional metallic bonds, metals commonly solidify into densely packed crystalline lattices. Depending on the preparation conditions, it is also possible to fabricate amorphous metal alloys (metallic glasses) whose mechanical properties combine the yield strength of oxide glasses with the fracture toughness of steels or titan alloys. [640–645]

For several technical applications, the existence of structural phases with various order characteristics opens additional freedom in the functional utilization of a material. Thereby, the choice between a single crystal phase, produced at high price, or cost-efficient granular polycrystalline phases and universally disordered amorphous phases for technical application is commonly the result of intensive cost-and-use considerations. In recent past, the most prominent example of such cost-and-use considerations and competing material phases is the large-scale application of silicon in the photovoltaic industry. Similar to other semiconducting materials, used for *light harvesting* applications, polycrystallinity and amorphosness [41] reduce the efficiency of silicon-solar cells due to the presence of recombination centers at grain boundaries and structural defects. [649, 650, 659–664] A characteristic example for the preferential use of amorphous materials are several types of functional and protective thin film coatings. [631, 665–669] Amorphous thin films outperform their (nano)crystalline counterparts by allowing thinner uniform coatings that do not suffer from surface cracking (see Fig. 2.4 (b)). [631] The capacity of amorphous films to reduce the formation of grain boundaries, that act as crack-nucleation sites, allows for intergranular amorphous films providing higher ductility and fracture toughness to nanostructured materials. [670, 671] The formation of superhard nanocrystalline/amorphous composite materials, due to formation of a crack-formation hindering thin amorphous tissue between the crystallites, has been reported. [671–673] In addition, applications as chemical and biochemical sensors as well as electrodes in batteries benefit from the more open porous structure of amorphous thin films. [669, 674–676] To revisit the above idea of using materials synergies, the combined use of crystalline and amorphous material phases offers a new facet to material design, by combining different structural material phases in a homogenous chemical environment. Crystalline-amorphous *order-disorder homostructures* as well as heterostructures/heterojunctions increase the fabrication options of superlattices [42]/multilayer superstructures for technological ap-

[41] Commonly the phrase *amorphous solar cell* refers to amorphous hydrogenated silicon (*a*-Si:H) based solar cells rather than cells based on pure amorphous silicon. [646–651] The hydrogen saturates the structural defects, i.e. dangling bonds, and thus notably reduces the associated localized deep-gap states. A serious limitation of deposited *a*-Si:H films is the light-induced degradation of optoelectronic properties as photoconductivity and dark conductivity, known as the Staebler-Wronski effect.[652–658]

[42] The term superlattice refers to a periodic arrangement of chemically different materials in a single crystalline phase, in general. Thus, a periodic *superlattice-like heterostructure* arrangement of materials in different crystalline phases or different order states extends the original superlattice concept.

plications [633, 677–682]. As a direct application of an order-disorder transition, it has been demonstrated that a carefully designed superlattice-like heterostructure (see Fig. 2.4 (d)) enables promising device properties (phase change speed and phase stability) for phase-change random-access memory (PCRAM) [633, 678, 679, 682]. Today, phase-change materials [683–685], commonly made from binary and ternary compositions of germanium, antimony, and tellurium, represent a promising candidate for the next generation of nonvolatile memory devices[43]. Aside from data-storage applications, the thermo-physical properties of phase-change materials make them potential alternatives/supplements to conventional electrochemical batteries for large scale solar-energy storage in order to balance critical fluctuations in the generation infrastructure of sustainable energies [689–692, 692, 693]. The best characterized order-disorder heterojunction used for direct generation of photovoltaic energy is the *c*-Si/*a*-Si:H interface in silicon-based heterostructure-solar cells. [694–697] Aside from superlattice-like heterostructures representing layered crystalline-amorphous material compounds, bound order-disorder networks are formed in various types of core-shell nanomaterials[44]. One-dimensional core-shell nanoparticles (cf. Fig. 2.4 (i) -2.4 (i)) exhibit crystalline nanotube cores wrapped by a disordered surrounding material. [635, 702, 703] Equivalently, quantum-dot like zero-dimensional core-shell nanoparticles, as shown in Fig. 2.4 (c), are formed by a crystalline (spherical) core and an amorphous shell. [698–701] Each of these crystalline-amorphous nanomaterial modifications provides the potential for novel and unique ways to fabricate and control so far unreached and unexpected material characteristics. One outstanding example for unexpected material properties, originating from wrapping a material by a disordered shell, is *black* TiO_2. In contrast to various types of crystalline as well as amorphous TiO_2 modifications, black TiO_2 core shell nanoparticles facilitate absorption of visible and infrared light[45]. [704–709]

2.2.2 Classification of atomic order types

A JOURNEY FROM ORDER TO DISORDER – In light of the vast number of materials exhibiting either partial or complete disorder, it does not seem surprising that the term *amorphousness* merges a manifold of disorder characteristics, that influence the macroscopic material properties in different ways. Giving a strict definition of amorphousness, based on experimental characterization techniques, an amorphous solid might be, *for now*, defined as a material whose diffraction pattern resembles a series of *halos* with varying intensity (cf. Fig. 2.4 (g) and Fig. 2.4 (h) but is

[43] Phase change materials have already been used for data storage applications in the late 1990s in form of commercially marketed digital versatile disc random-access memory (DVD-RAM) based on $Ge_2Sb_2Te_5$. Interestingly, the true nature of the atomic structure changes around the crystallization-amorphization process haven not been understood during the time of use, in detail. [686–688]

[44] Here, the idea of a core-shell nanostructure is restricted to combinations of a crystalline core surrounded by an amorphous shell. A more comprehensive characterization of the manifold order types in this class of nanostructures, including entirely crystalline core-shell modifications, is given in Ref. [698–701].

[45] A detailed discussion of the optical properties of TiO_2 in various material phases is given in Sec. 5 .

free of sharp point-like (Bragg) diffraction peaks [46]. This definition naturally excludes any type of long-range ordered materials which denotes the totalities of proper translational invariant crystals as well as the aperiodically ordered quasi-crystals discussed above. However, this generic definition of amorphousness covers a manifold of different oder facets arising from two fundamentally different sources of (dis)order in solid materials. On the one hand, and this is the superficial impression of amorphousness, are translational invariances arising from structural distortions of the crystalline lattices (i.e. *structural disorder*). On the other hand, variations in the chemical composition (i.e. *chemical disorder*) are another fundamental source of atomic (dis)order.

An overview [47] of the most important order types, arising from structural and chemical order characteristics as well as their superpositions is illustrated in Fig. 2.5. Figure 2.5 (a) shows a perfectly ordered two-dimensional crystal arranged in an regular hexagonal lattice/network. In fact, this is an idealized monoatomic-sheet of an elemental two-dimensional crystal as graphene. In the same way, Fig. 2.5 (b) reflects a free standing binary two-dimensional crystal as *h*-BN. A first steps in structural disorder, illustrated in Fig. 2.5 (e), arises from allowing lattice *relaxations* in the perfectly long-range ordered crystalline lattice. In principle, such lattice relaxation might result in either a crystalline lattice with lower symmetry or, and this is the relaxation-type considered here, a randomly distorted atomic network, that preserves all connectivity properties of the crystal, its *network topology* respectively. The resulting disordered framework exhibits disorder in the bond-length distribution as well as in the orientation of bonds. Since the ring-like intermediate-range order characteristics remain unchanged with respect to the hexagonal network structure of the corresponding crystal-phase [48], this order type might also be named *cellular disorder*. *Bond disorder* and *orientational disorder* represent the weakest disorder types in amorphous solids and are, thus, necessarily present in every amorphous solids.

Besides, bond disorder and orientational disorder are intimately connected to each other and inseparable in a disordered solid material. The statistical analysis of the bond lengths and angels shows a sharp distribution around an average value. The original crystalline lattice remains clearly identifiable even to the naked eye. Fig. 2.5 (f) illustrates cellular disorder in an idealized binary

[46] An exception are dense conglomerates of nanoscopic crystallites which are not amorphous solids in the actual sense, even if their diffraction patterns might consist of massively broadened Bragg peaks due to the unfavorable grain-boundary–grain-size ratio. In many cases, the diffraction pattern of a nanocrystalline sample might actually look amorphous. Since the physical properties of nanocrystalline and amorphous materials might differ notably from each other, they should be distinguished from each other. However, with respect to the diffuse diffraction pattern, nanocrystalline solids are occasionally termed “X-ray amorphous”. [666, 710–712]

[47] For the sake of a clear qualitative representation of the different structural and chemical disorder-types, the network illustrations are restricted to the two-dimensional case. In principle all order types can be translated to a three-dimensional framework analog, straight forward. Only for a limited number of the disordered two-dimensional networks, presented in Fig. 2.5, *real world* equivalents are discussed, which is owned to the sparse number of known disordered two-dimensional materials. In contrast, all introduced order types, as well as their superpositions, exist in three-dimensional amorphous solids.

[48] In oder to reasonably compare a disordered material phase with a crystalline counterpart it is necessary to chose an appropriate reference phase. A reasonable choice would be the crystal in which the energy per functional unit is closest to value in the disordered material phase. Without *a priori* knowledge of formation energies, a comparable mass density of the crystalline and amorphous phases represents an adequate choice.

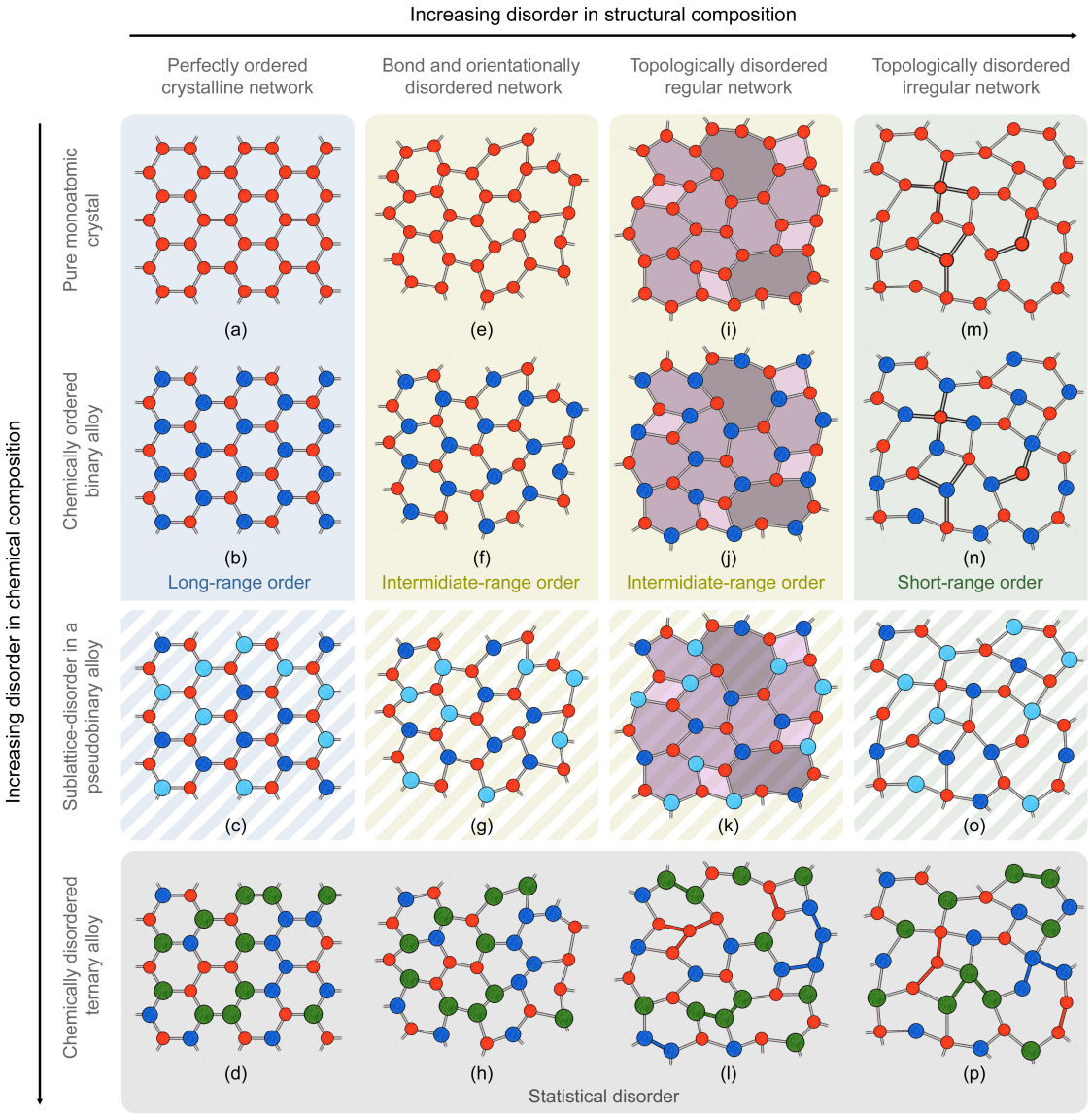

Figure 2.5: Types and combinations of structural and chemical atomic order in crystalline and amorphous solids. (a) A perfectly long-range ordered crystalline solid. (b) A long-range and chemically ordered binary (AB) crystal. (c) A structurally ordered pseudobinary (A/C)B alloy with random chemical order in one of two atomic sublattices. (d) A ternary (ABC) crystalline alloy with random/statistical disorder in its total chemical composition. (e) A monoatomic network with bond-length and orientational disorder. (f) A binary bond-length and orientational disordered network with global chemical ordering. (g) A pseudobinary bond-length and orientational disordered alloy with partial chemical order in (A/C)B(A/C)B...-type rings. (h) A bond-length and orientational disordered atomic ABC-type network with random chemical composition. (i) A regular monoatomic network with topological disorder and ring-like intermediate-range order characteristics. (j) A topologically disordered binary network with regular coordination and global chemical ordering in ABAB...-type rings. (k) A topologically disordered regular pseudobinary alloy with preserved chemical ordering in (A/C)B-type rings. (l) A regularly ordered ternary alloy with random chemical composition. (m) A monoatomic amorphous solid with topological disorder, including irregular coordination. (n) A irregular binary network with fixed AB-type short-range ordering and topological disorder. (o) A pseudobinary irregular amorphous (A/C)B alloy with partial CA and CB coordinations. (p) A completely randomly ordered network topology of an irregular ternary amorphous ABC network.

two-dimensional solid. Compared to the unary analog, it is evident that not only the ring-like features are preserved, but also the long-range chemical order is unaltered. *Real* structural disorder coming along with a notably higher degree of bond and orientational disorder is illustrated in Fig. 2.5 (i) and Fig. 2.5 (m) for a monoatomic network. This disorder type is termed *topological disorder* since fundamental order characteristics of the crystal lattice are changed in qualitative ways. In a topologically disordered lattice the original *cellular* structure of the crystal-network is partially *destroyed*. In Fig. 2.5 (i) the intermediate-range order variations in the size of *primitive*[49] rings are accentuated by a color cording, showing *n*-fold/*n*-membered rings with four, six, and eight atoms. Thereby, the majority of atomic-rings still shows the six-atom size of the ordered hexagonal network. The topological disorder in Fig. 2.5 (i) is classified as *regular* since the atomic (threefold) coordination of the individual chemical elements, the short-range order respectively, remains unaltered. A topologically disordered network in two as well as three dimensions, that *perfectly* preserves the short-range order in terms of coordination numbers as well as basic coordination-unit geometries, is historically known as *continuous random network*[50,51] and represents the archetypical structure model of amorphous oxides. [718–720] It has been demonstrated, in recent time, that graphene can be systematically transformed into a two-dimensional amorphous form, by electron irradiation. [721, 722] This topologically disordered modification of carbon shows all characteristics of a topologically disordered regular network modification, a two-dimensional elemental glass [722, 723] respectively. In contrast to the schematic illustration in Fig. 2.5 (i), amorphous graphene shows a distribution ranging from four-membered to eight-membered rings around the dominant crystalline six-membered ring-type. [722] A topologically disordered regular network has recently been used in computational simulations by Li and Drabold [724, 725] to study the localization of electronic eigenstates as well as vibrational modes within an amorphous graphene network. Aside from the global structural disorder types discussed here, structural defects might transform the lattice topology, locally. In case of a graphene-like sp^2-hybridized hexagonal lattice, as illustrated Fig. 2.5 (m), such local topology defects are known as Stone-Wales defects. [513, 721, 726–730] The simplest and energetically most favorable example of a Stone-Wales-type defect in graphene transforms four adjacent hexagons into two pentagons and two heptagons. [721] Obviously, the possible formation of odd-membered atomic rings is

[49] A primitive/irreducible ring within an amorphous framework is commonly defined by a *short-path* criterion, as the topologically shortest closed path starting from one particular atom and returning to that atom by stepwise, going from one adjacent/bonded atom to another. In case of a crystalline structure, an adjacent atom is simply defined as the nearest neighbor of a particular atom. For an amorphous solid adjacent atoms are defined by the cutoff spheres for each element (see discussion in Paper VII (Ref. [32])). The exact definition of a ring is not necessarily unique and different ring-formation criterions [713] have been defined among others by King [714] and Guttman. [715]

[50] The classification as *random* has been chosen quite unfortunately since the atomic structure in these kind of networks remains entirely ordered on the short-range scale and partially ordered on the intermediate-range scale.

[51] Since the atomic coordination, which is widely determined by chemical constraints, fixes the short-range order in the random network model, a *constructive* definition of the term "random" might relate to a truly random distribution of dihedral angles. [716] However, a random distribution of dihedral angles would exclude the presence of *substantial* medium-range order in form of *superstructural* units as rings or clusters that would give a certain preference to specific angular arrangements. [717]

essential to the carbon-structure polymorphism and the formation of a disordered carbon phase. The presence of odd-membered rings in topologically disordered two-dimensional network verifies that, in principle, structural units with non-crystallographic symmetries are allowed to form locally and might occur in an amorphous material, randomly.

Allowing coordination number changes results in the most comprehensive disorder type in solids, a topologically disordered network structure with an *irregular* interatomic connectivity. In Fig. 2.5 (m) coordination number changes between two and four in a topologically disordered network are illustrated. Again, the crystalline threefold coordination remains the dominant coordination type. Also, a notable degree of intermediate-range order is still present in the irregular network. To a certain degree, changes in the coordination number help to preserve order features, e.g. ring-like structures, of materials with a strong formation tendency for intermediate-range order. An irregular connectivity in disordered solids might not be expected a priori, since coordination-number changes at ambient conditions within a distinct chemical environment are commonly an energetically unfavorable process. Only a few elements, archetypically carbon, have proofed to be quite *tolerant* to different coordination states under ambient conditions, explaining its exceptional preference for phase diversity. Amorphous graphene, however, seems to be a counterexample for changes in the atomic short-range order, since under-coordinated carbon atoms are limited to isolated vacancy defects [729, 731] or extended holes within the graphene sheet[52]. [732, 733] Thus, amorphous graphene indeed represents a realization of a two-dimensional continuos network, a Zachariasen glass respectively (see below). In a disordered phase, such coordination number changes might either locally relax network strain or create defect-like local distortions in form of unsaturated (*dangling*) atomic bonds. As exemplified by (*a*-Si:H), the additional incorporation of e.g. hydrogen can be used to reduce this defect density and to enhance or strengthen the intermediate-range order features. [656, 734, 735] The development of a notable intermediate-range order in both topological disorder types, defined throughout the two right-hand colums of Fig. 2.5, shows a notable dependence on the particular chemical composition of a solid, in general.

Fig. 2.5 (j) and Fig. 2.5 (n) illustrate that chemical and structural order can exist independently. Even a topologically disordered solid with regular as well as irregular connectivity can possess a perfect chemical order throughout the entire material. Prominent examples of regular and irregular topological disorder are binary (transition)metal dioxides as diverse two- and three-dimensional modifications of SiO_2 and TiO_2 (see discussion below). As demonstrated throughout the figures 2.5 (c), 2.5 (g), 2.5 (k), and 2.5 (o), a certain long-range chemical ordering might also be preserved in ternary (or pseudobinary) and multicomponent alloys with independent substitutional disorder in the spatial distribution of one or more chemical species. Pseudobinarity implies the substitution of a chemical component of a binary mixture by a random distribution of two or more elements, all with similar chemical bonding characteristics. The formation of a pseudobi-

[52] Interestingly, structural holes in graphene show remarkable self-healing properties. Carbon atoms from edges and hydrocarbon contaminations are used to close existing structural holes with either regular hexagons or a random amorphous polygon network of five-, six- seven, and eight-membered carbon rings. [732]

nary compound occurs preferentially in case of strong directional bonds between qualitatively different, i.e. anions and cations, groups of chemical elements. The best known examples of pseudobinary compounds are certainly the multicomponent group III-V and II-VI semiconductor alloys. [297, 301, 736–739] Among these are, especially, technologically relevant group III-V multicomponent nitride semiconductors as AlGaN [297–299] and $Al_xGa_yIn_{1-x-y}N$ [288, 300–302] with varying fractions of aluminum, gallium, and indium in the cation-sublattice. Disorder might also occur in the anion sublattice as observed in $GaN_{1-x}As_x$ [739–742] and $GaN_{1-x}Sb_x$ semiconductor alloys. [743] The high lattice mismatch in these semiconductor alloys causes wide composition windows that lead to the formation of an amorphous material phase in which the optimal pseudobinary order might be slightly disturbed by the formation of small amounts of homopolar bonds. Further pseudobinary examples are multicomponent (transition)metal (di)oxides [744] and (transition)metal (di)chalcogenides. [745] Some recent accessions on the metal-oxide side are novel ternary wurtzite-derived I-III-O_2 oxides with technologically utilizable physical properties. Especially, the ultraviolet-to-visible direct band-gap material β-$CuGaO_2$ seems a promising candidate for light absorbing applications in solar cells. [746–750]

The *final* state of chemical disorder in a crystal, the random distribution of a mixture of two or more elements over all lattice sites, is illustrated in Fig. 2.5 (d). Even though the existence of a crystal with *universal* chemical disorder seems unlikely, its synthesization has been achieved in form of a ternary Si-Sn-Pb surface alloy on a silicon (111) substrate. [751] However, without the presence of a substrate that chemically binds, and thus fixes, the two-dimensional surface-alloy layer, the chemical disorder will inevitably cause a notable degree of cellular disorder (cf. Fig. 2.5 (h)). As a consequence, the character of any structural order characteristic is per definition *statistical* and, in contrast to the other structural order types, not necessarily limited to distinct distributions around well identifiable crystal-like equilibrium values. In general, multicomponent materials with random chemical composition are preferentially formed in materials with considerably non-directional bonds between atoms or functional units of similar chemical character. Since this situation is prototypically meet by the formation of metallic bonds, the topological disorder-types illustrated in Fig. 2.5 (l) and Fig. 2.5 (p) are characteristic to ternary or multinary amorphous metal alloys/intermetallic alloys and metallic glasses. [640–645, 752–754] In contrast to the prominent ring-like intermediate-range order of the chemically more ordered alloys, a chemically disordered material is less likely to manifest a distinct intermediate range order. Depending on the chemical elements, local arrangements of atoms might randomly form local cluster or filament-like conglomerates of a few atoms of a single species or different elements with a strong urge to form crystal grains, nanocrystals respectively. Ultimately, a strong tendency to cluster formation might result in the formation of a seperate nanophase and, thus, an alloy decomposition through phase separation. In many multi-component alloys atomic intermiscibility does not occur over the entire composition range, so that phase separation commonly depends on the actual composition parameters. [755, 756]

It is worth the effort to note that the presence of two-dimensional network structures is not

limited to either the atomic cosmos of materials science or abstract mathematics. This kind of networks seem to be a fundamental (dis)order principle in the organization of natural objects. Biological molecules are known to form randomly orientated two-dimensional molecular networks, *biological glasses* respectively. [757] For example, p-terphenyl-3,5,3',5'-tetracarboxylic acid adsorbed on graphite self-assembles into a rhombohedral two-dimensional random tiling. [758, 759] The surface polymerisation of the molecule 1,3,5-tris(4-bromophenyl)benzene on an Au(111) substrate forms extended two-dimensional nanoporous covalent networks consisting of polygons with four to eight edges. [760] Especially, on-surface self-assembled metal-organic thin films [563, 761, 762], self-assembled hydrogen-bonded networks [763] and liquid polymer systems [764] tend to form complex (*random*) molecular-network topologies. Further realizations, more precisely various types of *macroscopic* organization schemes, of two-dimensional continuous random networks with cellular as well as topological disorder exist in the real world. Certainly, the most eye-catching examples are geological network formations of basalt columns of *Fingal's Cave* and *Giant's Causeway*. [765] Topologically disordered networks are also formed by soap cells [765, 766], the cellular structure of dragonfly wings [767], the collagen network of lung tissue sheets [768], the head scales of snakes and crocodiles [769], the arrangement of plant cells in sectional images/the cross section through natural fibers [770], mud-crack patterns [771, 772] or the cellular structure in the administrative divisions of mainland France. [773] Similar to quasicrystalline tiling patterns, topological-network-type patterns are a frequently used design element of modern architecture. One of the most recent, and probably most impressive installations has been realized as a central wall-construction element in the design of Shanghai's new natural history museum to represent the organization of cells in living organisms.

2.3 Structure theory of glass

There are two main strategies to produce amorphous solids. Amorphous thin films are prepared by a number of preparation techniques based on vapor condensation from thermal evaporation [774], sputter deposition, or glow-discharge decomposition of gases. Further preparation procedures include electrolytic decomposition from solutions as well as high energy irradiation/particle bombardment of initially ordered materials samples. [722] Traditionally, an amorphous solid might be prepared from *quenching* (cooling) a melt to produce a disordered bulk phase. [775–778] As an important subclass among the non-crystalline materials, *glasses* raise some puzzling challenges to materials science, in general, as well as statistical thermodynamics on side of *solid-state* theory. Glasses represent a special class of *solids* that share similarities, as mechanical rigidity/strength, with crystalline solids and a disordered atomic structure similar to liquids. Actually non of these properties qualifies a glass to be different from other amorphous solids. Even though the identification of a glass seems to be intuitive and trivial from everyday's experience, a complete understanding of the glassy state, adopted by several non-crystalline materials and its relation to the amorphous state, is still open for debates.

THE VITREOUS STATE[53] – The existing conceptual difficulties are already evident in giving a definite definition of a *glass*. Thereby, the classification of non-crystalline solids as an amorphous or glassy solid is historically based on different phenomenological and physical concepts. Bulk glasses are, in general, prepared by (*super*)cooling a material in the liquid molten state sufficiently fast below the (crystal) melting (or freezing) temperature T_m to prevent crystallization. Upon decreasing temperature, the supercooled liquid solidifies into a disordered solid by *vitrification*[54] of the liquid at a *glass-transition* temperature T_g. In contrast to the first order *crystal-liquid transition* at T_m, T_g depends on a sample's history as details of the actual cooling or reheating rate and is not an as well defined phase transition temperature as T_m. [712, 780, 781] In fact, the exact nature of the glass transition, more precisely *liquid-glass transition*, exists as an abstract empirical concept and, most likely, does not represent a thermodynamic phase-transition at all. [782] It is still an unsolved question of glass science which fundamental physical changes in the structural and dynamic material properties underlie the glass-transition. Phenomenologically, the glass transition temperature marks the point below which the vitreous material gives the impression of being solid, has become too viscous to flow (*frozen*) on *reasonable* laboratory timescales, respectively. [782, 783] This reasonable time span is obviously an arbitrary function of an experimenters' patience, research time, lifetime, or whatsoever. Likewise, the time-scale, the computational time/cost respectively, of numerical simulations is crucial for theoretical materials scientists trying to get to the bottom of basic glass transition physics. With this limitation in mind, Berthier and Biroli [782] consider a material to be "glassy" when its typical relaxation-time scale becomes of the order of, and often much larger than, the typical duration of an experiment or a numerical simulation[55]. [781, 784–787] Obviously, this definition is quite comprehensive and a majority of disordered thin films as well as amorphous bulk samples might be considered as glasses. The advantage of this definition is its extendability towards *unorthodox* (non-structural) glass phases as spin glasses [788–792], electron glass [793–802], or molecular glasses [803–805]. This definition is basically what is intended by the most common definition of a glass as any disordered material exhibiting a glass transition when heated towards the liquid state. Thereby, the actual glass transition temperature T_g might be defined by an *arbitrary* limit of 10^{12} Pa·s for the shear viscosity. [783] Sometimes, the existence of a glass transition is used to divide disordered solids into disjunct sets of amorphous and glassy materials. [806] According to the classic phenomenological, and certainly *pragmatic* definition, among others, given by Mott and Davis in their book on "Electronic Processes in Non-Crystalline Materials" [807] every amorphous material that solidifies into an disordered solid phase by quenching from a melt is a glass[56]. Thus, per

[53] The main title of a textbook on the "Thermodynamics, Structure, Rheology, and Crystallization" of vitreous (glassy) materials by Gutzow and Schmelzer. [779]

[54] Commonly, the terms vitrified [derived from the latin word "vitreus", from "vitrum" ("glass"), based on the proto-italic word "wedro" ("glass"), from Proto-Indo-European "wed-ro" "water-like")] liquid and glass are used synonymously.

[55] An important consequence of the fact that glasses obviously exist in a non-equilibrium or quasi-equilibrium state is that its physical properties *suffer* from aging.

[56] Also see discussion in Ref [806].

definition every glass is necessarily an amorphous solid, while only a limited number of amorphous solids exist in the glassy state. All amorphous thin films as *a*-Si:H [774] which are for example prepared by plasma enhanced chemical vapor deposition [808] or glow-discharge decomposition [809, 810] are not glasses within the Mott-Davis definition. Also, many amorphous bulk semiconductors as silicon, silicon carbide (SiC), silicon nitride (SiN), or germanium carbide (GeC) cannot be obtained from quenching a melt and have to be prepared by suitable film deposition techniques. [811, 812] Further, even traditional oxide glasses as silica might be prepared by a sol-gel route yielding high surface area bulk glasses. [813–816]

It might be surprising to most people that natural inorganic glass is, in number, limited to a few examples formed under extreme conditions (volcanic activity (obsidian), meteorite impacts (tektites), lightning strikes (fulgurites)). Thus, the formation of natural glasses by non-biological processes is not necessarily less exotic than the formation of a natural quasicrystal. Both, glasses and quasicrystals represent material classes of predominantly synthetic solids. A notable exception are several primitive marine organisms as sponges and algae, whose skeletons are formed by glassy spicules consisting of a hydrated silica glass. [817–820] These natural glass fibers possess mechanical and optical properties that are quite similar to synthetic optical fibers of commercial glass. [817] However, returning to order characteristics in biological objects, its again the absence of crystalline symmetry that preserves biological activity. Similar to non-crystallographic symmetries, the formation of disordered biological glasses is an indispensable prerequisite for simple biological organisms to survive under extreme conditions. All desiccation-tolerant organisms form *glasses* upon drying, in which the cytoplasm transforms into a vitreous state. [821–825] These intracellular glasses allow plant constituents as seeds [823–825] and pollen [826] as well as resurrection plants [827] and bacteria [821, 822] to reduce damage upon complete dehydration by preventing phase separation and crystallization and provide long-term stability, which potentially allows long-time survival far beyond human lifespan. The storage stability of seeds and pollens is directly related to the molecular mobility and the packing density of the formed intracellular glasses. [823]

2.3.1 Classic theories on glass formation

Finding a comprehensive theory of glass formation, that predicts and explains the ability of a material to form a glass, the conditions necessary (structural as well as kinetical/thermodynamical) for glass formation in classic inorganic glass former, organic glass-forming systems as well as exotic glass-formation phenomena related to the solid state, and the atomistic structure of the glass phase, remains one of the greatest challenges in solid-state theory and has, over several decades, become an intransparent fractured field of competing ideas without universal applicability. In light of this thesis's subject and the considered materials, the subsequent *sparse* outline focusses, as far as possible, on the most relevant contributions to the field of oxide-glass formation and the

understanding of their atomic structure.[57]

RULES, CRITERIA AND HYPOTHESIS – The confusion that arises while trying to classify disordered materials as glasses, amorphous solids, or supercooled liquids brings to mind, that a long-term objective of condensed-matter theory has to be the identification of common structure characteristics and formation rules that determine the formation of disorder in all the extremely different material conglomerates solidifying into a vitreous state [58]. The first groundbreaking contributions to understand the constitution of glasses has been made by the baltic-german physical chemist Gustav H. J. A. Tammann (1861-1922) in his studies on the thermodynamic and kinetic properties of organic glass-forming substances. [844–846] For Tammann a glass basically represents a sufficiently fast cooled (supercooled) solidified/vitrified liquid. It was also Tammann who coined glass-related terms as *glass transition temperature* and noticed the process dependence of T_g. [844, 846] A first attempt to give a mandatory criterion for glass formation in inorganic substances, based on structural considerations, has been made by the norwegian mineralogist Victor M. Goldschmidt (1888-1947), one of the founding father of modern geochemistry and crystal chemistry. In crystal chemistry the atomic structure of a material is the consequence of a close packing of differently *sized* ions. Thereby, charge neutrality is ensured by formation of anion-cation *space groups* [59]. Only electropositive chemical species with a sufficiently small ionic radius and, thus, a high electrostatic charge are able to bind an adequate number of larger anions in order to form a close packed space-group building block. Taking the example of the Si ion as the prototypical glass former, the high oxidation state of the Si^{4+} ion allows it to bind four O^{2-} ions. Thereby, the ionic radii allows the Si^{4+}-cation to fit well in the tetrahedral hole between four O^{2-}-anions. In the formed SiO_4 tetrahedra, only one electron of each oxygen atom contributes to the ionic bond allowing adjacent tetrahedral units to share common oxygen atoms. This corner-linking mechanism allows the formation of extended chains, planar networks, or complex three-dimensional frameworks of *moderate* density. [847, 848] From observations of the correlations between a substance's ability to form a glass and its structure chemistry, Goldschmidt postulated an empirical criterion for glass-formation in binary ionic compounds (Goldschmidt's Rule). [779, 847, 848] According to Goldschmidt, the anionic (R_a) and cationic (R_c) radii of a good glass-former fulfill the inequality relation

$$0.2 < \frac{R_c}{R_a} < 0.4 \quad . \tag{2.1}$$

[57] Several comprehensive and worth reading review articles and monographs, each presenting their up-to-date state of knowledge, sometimes contradictory historical and scientific facts, as well as personal anecdotes are available to the reader holding any interest in the subtleties of glass-formation theory. [572, 828–830]

[58] An understanding of structural characteristics on the atomic scale is for example inevitable to understand structure phenomena as polyamorphism. Polyamorphism describes the occurrence of amorphous material phases with different, especially medium-range, order characteristics occurring by densification through external pressure. [831, 832] Such structural amorphous-amorphous high-pressure transitions are known in the atomic structure of vitreous silica [712, 833–840], amorphous silicon [841] and amorphous TiO_2 [842], as well as for metallic glasses [832] and amorphous water modifications. [843]

[59] Not to be mistaken with an actual crystallographic space group.

The majority of classical oxide glasses as SiO_2, P_2O_5 (diphosphor pentoxid), and GeO_2 as well as chalcogenide glasses as As_2S_3 (diarsen trisulfide) and $GeSe_2$ (germanium disulfide) fulfill Goldschmidt's criterion for glass formation. [60] Considering an anion-cation ratio of $R_c/R_a = 0.225$ of the ideal tetrahedral hole [61], it is not surprising that in the majority of classical glass formers the electropositive ion is tetrahedrally coordinated by electronegative ions. In contrast to prototypical tetrahedral oxids as SiO_2 and GeO_2, prominent octahedral oxides as TiO_2 and Al_2O_3 (dialuminium trioxide) are, despite repeated efforts, well known for not forming (bulk) glasses. [849, 850] This observation is again reasonably reflected by Goldschmidt's rule. An ideal square planar and, more relevant to solid state theory [62], ideal octahedral coordination implies an anion-cation ratio of 0.414. Thus, octahedral coordination lies outside the suggested glass formation range and, accordingly, an octahedral coordination state is only observed for e.g. color giving impurity ions as Cr3+, Mn3+, Fe2+, Ni2+, and Cu2+ in soda-lime-silica glasses. [854] However, it has been reported from experimental studies under high pressure, and optional high temperature conditions as well as numerical simulations, that densified prototypical tetrahedral (oxide) glasses might become real octahedral glasses. [177–181, 855–858] A transformation into an octahedral *glass* under high-pressure has been reported for SiO_2 at pressures above $\approx 40\,\mathrm{GPa}$. [177–181]. Also, GeO_2 completely transforms into a sixfold coordinated octahedral glass under pressure. Even larger ionic-radii ratios (0.732 for an ideal cubic arrangement of spheres) reflect dense, and almost certainly crystalline, structures. In addition, a ratio equal to one reflects a crystalline close-packed arrangement. Aside from tetrahedral coordination, also a threefold coordination is characteristic to some of the classical glass-forming chalcogenides as As_2S_3. [859–861] Thereby, the coordination units do not adopt trigonal planar building blocks, which could violate Goldschmidt's rule, sine the cation hole in an ideal trigonal configuration measures 0.155 times the ionic radii of the surrounding anions. Rather, a trigonal pyramidal structure is adopted.

A central point of criticism to Goldschmidt's theory on glass formation is that all classical glass-forming oxides are treated as purely ionic compounds. However, the bonding nature of classical oxides, and ionic bonds in general, always shows a certain accompanying contribution from covalent bonding [63] which limits the range of materials strictly covered by Goldschmidt's rule. A prominent example for the failure of Goldschmidt's rule is beryllium oxide (BeO) which exhibits an anion-cation ratio of $R_{Be^{2+}}/R_{O^{2-}} = 0.24$ but does not form glass. [718, 779, 862] Despite its limitations, Goldschmidt's rule applies well to classical glass-forming systems and allowed the identification of new glass-forming materials as beryllium fluorite (BeF_2, $R_{Be^{2+}}/R_{F^-} \mathrel{\widehat{=}} 0.34\,\text{Å}/1.36\,\text{Å} \approx 0.25$ [845, 848]) which even surpasses the glass

[60] SiO_2: $R_{Si^{4+}}/R_{O^{2-}} \mathrel{\widehat{=}} 0.39\,\text{Å}/1.4\,\text{Å} \approx 0.28$, P_2O_5: $R_{P^{5+}}/R_{O^{2-}} \mathrel{\widehat{=}} 0.34\,\text{Å}/1.4\,\text{Å} \approx 0.25$, GeO_2: $R_{Ge^{4+}}/R_{O^{2-}} \mathrel{\widehat{=}} 0.44\,\text{Å}/1.4\,\text{Å} \approx 0.31$, As_2S_3: $R_{As^{3+}}/R_{S^{2-}} \mathrel{\widehat{=}} 0.46\,\text{Å}/1.84\,\text{Å} \approx 0.25$, $GeSe_2$: $R_{Ge^{4+}}/R_{Se^{2-}} \mathrel{\widehat{=}} 0.44\,\text{Å}/1.98\,\text{Å} \approx 0.22$ [845, 848]

[61] The spherical hole formed within four mutually touching spheres of equal size.

[62] While a sixfold coordination state in an octahedral symmetry is among the most common coordination states in crystals and amorphous solids, the square planar coordination type is quite limited, with tenorite, a crystalline copper oxide (CuO) polymorph, being the most prominent example. [851–853]

[63] The covalent contribution to the Si-O bond in silicates is roughly 50 %. [779]

forming abilities of silica. [863] Most important, Goldschmidt's work laid the foundations for subsequent contributions to the structure theory of glasses.

W. H. ZACHARIASEN - THE MELODY LINGERS ON[64] – The single most recognized and still imagination shaping contribution to the structure theory of glasses has certainly been made by the norwegian physicist F. William H. Zachariasen (1906-1979). By refinement of Goldschmidt's structural theory of glass formation, Zachariasen established the foundations of the random-network theory of glass structure in his 1932 paper "The Atomic Arrangement in Glass". Assuming that the atom-linking forces in glasses, a periodicity lacking three-dimensional crystalline network, are essentially the same as in crystals and, thus, the energetics in both material modifications should be comparable[65] in a *good* glass forming material, Zachariasen formulated four rules for glass formation in (tetrahedrally) coordinated A_xO_y oxides. [718]

(I) An oxygen atom is linked to not more than two atoms A[66].
(II) The number of oxygen atoms surrounding atoms A must be small[67].
(III) The oxygen polyhedra share corners with each other, not edges or faces[68].
(IV) At least three corners in each oxygen polyhedron must be shared[69].

Even if Zachariasen's rules for glass formation have their roots in and essentially reflect the ideas of Goldschmidt theory, they comes with the additional benefit of making qualitative predictions on the actual character of the vitreous framework. Following Zachariasen, mono-component inorganic and tetrahedrally-coordinated oxide glasses, became the embodiment of glass structure. A central point of criticism to Zachariasen's theory, besides its general limitation to predominantly ionic materials, has been that, while indeed guaranteeing the *geometric freedom* for network formation[70], it does not per se predicts the glass formation ability. Any cation that allows the for-

[64] The title of a paper dedicated to W. H. Zachariasen and his ongoing influence on the understanding of the atomic arrangement in glasses. [864]

[65] On the one hand, both a glass and a crystal (e.g. silica) share common, comparable respectively, mechanical properties. On the other hand, a much higher energy state of atoms within glass would inevitably induce the formation of a crystalline phase.

[66] A small anion coordination number seems to be essential to permit the necessary bond-angle variations in a disordered glass-like network topology.

[67] The quite vague demand for a *small* coordination actually targets threefold triangular and fourfold tetrahedral coordinations. Similar to Goldschmidt, Zachariasen motivated this requirement by empirical reasoning, thus, rule (II) ultimately represents Zachariasen's version of Goldschmidt's rule.

[68] Rule (III) seems rather redundant, since it is essentially the direct consequence of the coordination constraints formulated by the rules (I) and (II). However, it emphasizes the importance of corner-sharing for network formation, while the formation of edge- and face-sharing oxygen polyhedra is expected to provoke the formation of more ordered three-dimenional structures and, ultimately, crystalline long-range order.

[69] This condition effectuate the dimensionality of the formed network. In case of only two corners shared between oxygen polyhedra, the resulting structure would most likely adopt a chain like configuration as observed in silicones or (single-)chain silicates as pyroxenes [865]. Zachariasen's rule (IV) was originally intended as an optional requirement for three-dimensional network formation. However, it actually ensures only a dimensionality of $n > 1$ as exemplified by the tetrahedra networks of two-dimensional silica glasses [634, 866].

[70] It has been demonstrated by Cooper, that Zachariasen's rules (1) and (2) are sufficient to ensure the formation of a glassy network. [864] Furthermore, Gupta and Cooper gave the intuitive and empirical Zachariasen theory a rigorous mathematical foundation by proving the existence of infinitely large, arbitrarily dimensional, and topologically disordered networks composed of rigid vertex/corner-sharing polytopes. [867]

mation of a vitreous network in accordance with Zachariasen's random network model might be considered as a *network-forming* ion [71].

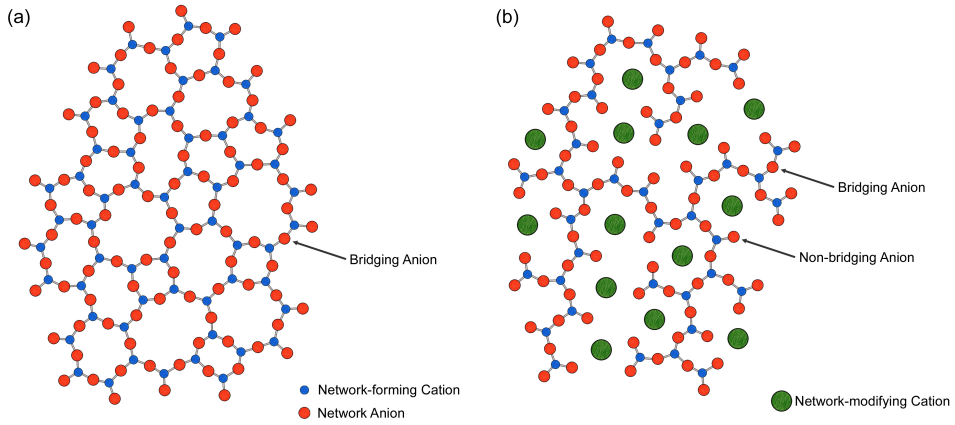

Figure 2.6: (a) A reproduction of Zachariasen continuos random network structure proposed in Ref. [718]. (b) A modified continuos random network, created following the ideas of Zachariansen-Warren structure theory for multicomponent oxides. [868]

Till this day, Zachariasen's four rules are the essential basis of the theory of *continuous random networks* [72] as the leading structure model for the atomic arrangement in, trigonal and tetrahedrally coordinated inorganic network-forming glasses. Strong evidence for the actual formation of random networks in the vitreous state has been given by the results of early X-ray diffraction studies of Warren and Co-workers as well as several other crystallographers on SiO_2 [719, 870–873], GeO_2 [870, 871], BeF_2 [872], and Na_2O-SiO_2 soda-silica glass. [868, 874, 875]

Just recently, breakthroughs in the direct observation of the atomic structure of two-dimensional *glasses*, have extended the existing knowledge on the *real* atomic structure of elemental as well as oxide glasses. A two-dimensional disordered phase of silica supported on graphene has *accidentally* been discovered by Huang et al. [634] and been characterized as a two-dimensional glass. [634, 866] The two-dimensional nature of the vitreous silica films enabled the direct transmission electron microscopy (TEM) imaging of the atomic network topology of a glass-forming material. In contrast to Zachariasen's two-dimensional drawing, the observed silica glass is formed by an out-of-plane bilayer stacking of corner-linked SiO_4 tetrahedra. However, the topological in-plane order, rendered in the TEM photographs, turns out to be virtually indistinguishable from Zachariasen's random network. As reported, large areas showed the random network topology, but also crystal-like in-plane ordered inclusions in the amorphous regions as well as polycrystalline regions were observed. The mixed occurrence of crystalline and amorphous domains has been attributed to growth kinetics of the glass film. Simultaneously, isostructural vitreous

[71] The most relevant glass-forming cations are B^{3+}, Si^{4+}, P^{3+}, As^{3+},As^{5+}, and Ge^{4+}. [718]

[72] It should be noted that the classification as *random* network is actually a misnomer since true randomness would require unrestricted accessibility to the entire configurational space of atoms or fundamental building blocks. [869] However, chemical constraints enforce a certain restriction on the parametrical space in order to develop energetically *resonable* short-range and medium-range orders.

silica films have been prepared on a ruthenium(0001) metal-support. [876–880] Again, the observed metal-supported silica films have been reported to be mixed crystalline-amorphous phases [877, 878, 880], while the crystalline bilayer domains form a perfect honeycomb lattice exclusively consisting of six-membered in-plane rings. Independent of the underlying support, the intermediate-range order in the vitreous bilayer films is characterized by a ring-size distribution ranging from four- to nine-membered silica rings. [634, 876, 878]

Since the recent discovery of the electron irradiation induced solid-state transformation of graphene into a layered vitreous carbon phase, amorphous graphene respectively, by Eder et al. [722], also a *truely* two-dimensional (monoatomic thickness) glass structure as well as atomic structure details of the actual order-disorder transition process are known. The transition starts by creation of localized point defects which merge into a vitreous framework separating crystalline regions. Upon increasing disorder, the vitreous framework growth on the expense of the nanocrystallites. At the final stage the disordered carbon network becomes indistinguishable from a two-dimensional random network.

EXTENSIONS, GENERALIZATIONS AND MODIFICATIONS – The mentioned example of soda-silica glass is an example for a multicomponent oxide glass, common to everyday experience. Domestic and industrial relevant glasses, e.g. window glass, typically contain more than two components and belong to the class as soda-lime(-silica) glass ($n_N Na_2O\, n_C CaO\, n_S SiO_2$) [73], enriched with smaller fractions of additional network-modifying cation species acting as *fluxes* [74] and *stabalizers* [75]. In light of complex multicomponent oxide glasses, containing non-glass forming ions, ions with a limited ability to be incorporated in the vitreous network structure, Zachariasen proposed a modified set of rules. [718]

(i) An oxide glass may be formed if the sample contains a high percentage of cations which are surrounded by oxygen tetrahedra or by oxygen triangles [76].
(ii) The tetrahedra or triangles share only corners with each other [77].
(iii) Some oxygen atoms are linked to only two such cations and do not form further bonds with any other cations [78].

Following Zachariasen's rules for *continuous disordered networks* (see Fig. 2.6) of multicomponent oxide glasses, it is obvious that only a limited number of non-network-forming cations, so called *network modifier*, occupying interstitial network sites, might be present in a multicom-

[73] The use of soda-lime-silica glassware on an *industrial* scale goes back to the ancient times of the roman empire.
[74] Fluxes as sodium carbonate lower the melting temperature of the network forming silica.
[75] Stabilizers as calcium carbonate increase the stability of silica network glasses by decreasing the viscosity at high temperatures and making it less prone to environmental damage.
[76] Recasting the rule (II) for mono-component oxide glasses, this condition states that a sufficient fraction of low-coordinated cation-oxygen polyhedra remains to ensure the formation of a *closed* network structure.
[77] Following condition (III) for mono-component oxides, this condition guarantees the necessary spatial freedom for network modification.
[78] This rule actually implies that a certain number of *bridging* anion (e.g. O^{2-}) bonds between two network-forming cations (not necessarily limited to the same chemical species) remains unaffected from the presence of non-network-forming cations, which again ensures at least partial network-formation.

ponent vitreous network. Common network modifier in silicate glasses are the oxides of the alkali and alkaline earth metal groups. The addition of network-modifying cations causes the formation of anion *bonds* between non-network-forming cations and network-forming ions. With regard to the network topology, these bonds are, from a chemical bond-formation perspective quite misleadingly, referred to as *non-bridging*. A sufficiently high content of network-modifying ions would ultimately prevent network formation and, thus, glass formation. In order to incorporate larger fractions of foreign oxides, numbers of cations respectively, network-forming ions of the dominant network-forming oxide, typically Si^{4+}, need to be replaced isomorphically, thus requiring cation species with an appreciable ability to form vitreous oxide networks with themselves and the main oxide component of the network. Cations without pronounced network-forming ability with themselves, but abundant glass-forming ability as a substitute in the random network structure of a glass-forming oxide, are labeled as *intermediate glass formers* or *conditional glass formers*. So, one of the most useful gains from early glass-formation theory is the classification of ions according to their glass forming ability into former, modifier, and intermediates, which has entered every academic textbook on glass science. One of the most prominent oxides with archetypical intermediate network-forming ability is TiO_2, which does not form glasses by itself. A network modifying role of TiO_2 has been reported for borate-glasses [881], phosphate glasses [882], and soda-lime borosilicate glasses. [883] From the observation of an increasing number of non-bridging oxygens with increasing TiO_2 concentration, Wren et al. [884] suggested that TiO_2 acts as a modifying oxide in SiO_2–ZnO–CaO–SrO glass. A change from a glass-network-forming to a glass-network-modifying role with increasing TiO_2 content has been reported for MgO–CaO–SiO_2–P_2O_5–F glasses. [885] Ti ions acting as a modifying species have been found in many-component oxide glasses as Na_2O–Al_2O_3–TiO_2–Nb_2O_5–P_2O_5 [886] and Na_2O–CaO–TiO_2–P_2O_5. [887] A network-forming function of TiO_2 has been reported for B_2O_3–CaO–ZnO–TiO_2 glasses with moderate molecular fractions (10–15 %) of TiO_2 [888]. Further technological relevant oxides with an intermediate glass forming ability, comparable to TiO_2, are ZnO and Al_2O_3. Both of them are, together with TiO_2, common aggregates of glass ceramics and show network-forming as well as network-modifying effects on the structure of silicate glasses. [884, 888–896] The apparently opposing functions of these intermediate oxide glasses are closely connected to the possible coordination states adopted by the (transition-)metal cations. In general, a silica like tetrahedral coordination state is expected to promote network-formation in accordance with Zachariasen's rules, while the octahedral crystalline coordination state is clearly expected to cause network-modifying behavior. The likely existence of fivefold coordinated Ti ions in silicate glasses [897] and TiO_2–SiO_2 sol-gel glasses [898, 899] hints on a combination of both effects within the vitreous network structure. Likewise, the presence of fivefold coordinated Zn ions in Na_2O-CaO-SrO-ZnO-SiO_2 glasses [895] and phosphosilicate glass compositions [900] as well as Al ions in aluminosilicate glasses [901–905] has been reported.

COMPETING IDEAS – Despite its obvious success story, Zachariasen's glass-structure theory is certainly not the fundamental, till today sought-after, universal theory on glass formation.

A vast number of competing or complementing structure theories of glass [79], assuming crystallite [906, 907], colloidal [908–910], random sphere packing [911], frozen liquid [912–924], network [718, 719], layer/sheet [925–927], pseudo-lattice/pseudo-Bragg plane [928–930], or microquasicrystalline [913, 931, 932] structures have been proposed and defended against each other since the early days of glass-formation theory [80].

[79] An excellent review article, magnificently loaded with wonderful quotations and filled with historical and scientific information as well as personal insights has recently been published by Wright. [869]

[80] More detailed reviews on the various glass-formation hypothesis, as well as further formation criteria or extensions to the theories presented above, are *more or less* comprehensively summarized in literature. [572, 830, 869, 933].

If, in some cataclysm, all of scientific knowledge were to be destroyed, and only one sentence passed on to the next generations of creatures, what statement would contain the most information in the fewest words? I believe it is the atomic hypothesis (or the atomic fact, or whatever you wish to call it) that all things are made of atoms–little particles that move around in perpetual motion, attracting each other when they are a little distance apart, but repelling upon being squeezed into one another. In that one sentence, you will see, there is an enormous amount of information about the world, if just a little imagination and thinking are applied ...

Richard P. Feynman (1918–1988)

3 Electronic structure theory

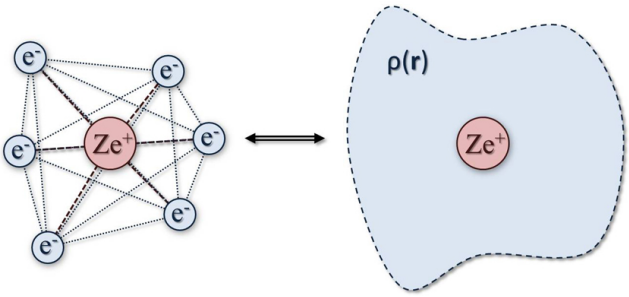

The underlying physical laws necessary for the mathematical theory of a large part of physics and the whole of chemistry are thus completely known, and the difficulty is only that the exact application of these laws leads to equations much too complicated to be soluble. It therefore becomes desirable that approximate practical methods of applying quantum mechanics should be developed, which can lead to an explanation of the main features of complex atomic systems without too much computation.

Paul A. M. Dirac (1902–1984)

Contents

3.1 The many-body problem 51
3.1.1 The Born-Oppenheimer approximation 53
3.2 Density-functional theory 56
3.2.1 The Hohenberg-Kohn theorems 57
3.2.2 The Kohn-Sham approach 59
3.3 Exchange-correlation functionals 68
3.3.1 Rung 1 – Local-density approximation 69
3.3.2 Rung 2 – Generalized gradient approximations 71
3.3.3 Rung 3 – Meta-generalized gradient approximations 73
3.3.4 Rung 4 – Hyper-generalized gradient approximations 74
3.3.5 Rung 5 – Complete-generalized gradient approximations 78
3.3.6 Scaling properties 82

3.4 Many-body perturbation theory 87
3.4.1 Hedin's fundamental equations 95
3.4.2 Hedin's *GW* approximation 100
3.5 Optical response theory 106
3.5.1 The Bethe-Salpeter equation 107
3.5.2 The dielectric function 111
3.5.3 Electron-hole pair excitations 113

3.1 The many-body problem

FUNDAMENTAL EQUATIONS – PART I – The two leading scientific theories of the twenties century, that entirely revolutionized humans *understanding* of the foundations of time and space as well as the *information* one might obtain from any microscopical physical systems, are Einstein's general theory of relativity and quantum mechanics. The first, a theory defining the fundamental nature of time and space itself, was ingeniously envisioned by a single human mind, while the later, reigning the quirky worlds of the nanocosmos, is strange enough to sophisticate the brilliant minds of *at least* a whole generation of theoretical physicists. Despite humans present inability to completely penetrate through every single filament, grain, or whatsoever [1] of quantum theory, it still lays the foundations that enables scientist to investigate materials' structures and physical properties on a microscopic level. Thereby, the deterministic articulateness of classical mechanics steps aside in favor of a probabilistic superpositioning nature of quantum physics. The fundamental complex [2] object, that permits the whole of information in the quantum world is called a "wave function". Since the wave function Ψ of a system of interest enables the calculation of exception values and, thus, *processable* information on the investigated quantum system, the efficient computation of Ψ is the fundamental challenge for materials science on the atomic scale.

On the *most* basic level, a *material* is nothing else than a conglomerate of atomic nuclei and a surrounding electron distribution, a many-body quantum system respectively, hold together by an all in all attractive interaction between the particles [3]. The corresponding many-body wave function depends on the positions of all nuclei and electrons in the system [4]. Thus, for a many-body system of M nuclei at positions $\mathbf{R}_I$ $(I = 1,2,\ldots,M)$ and N electrons at $\mathbf{r}_i$ $(i = 1,2,\ldots,N)$ ones seeks the many-body wave function $\Psi(\mathbf{r}_1,\mathbf{r}_2,\ldots,\mathbf{r}_N,\mathbf{R}_1,\mathbf{R}_2,\ldots,\mathbf{R}_M,t)$. The fundamental (non-relativistic) *wave equation* that determines the time development of the many-body wave function is the time-dependent Schrödinger equation,

$$i\hbar\frac{\partial}{\partial t}\Psi(\mathbf{r}_1,\mathbf{r}_2,\ldots,\mathbf{r}_N,\mathbf{R}_1,\mathbf{R}_2,\ldots,\mathbf{R}_M,t) = \hat{H}_{nuc,el}\Psi(\mathbf{r}_1,\mathbf{r}_2,\ldots,\mathbf{r}_N,\mathbf{R}_1,\mathbf{R}_2,\ldots,\mathbf{R}_M,t)\,. \tag{3.1}$$

Here, $\hat{H}_{nuc,el}$ denotes the total energy operator, Hamiltonian respectively, of the combined system of interacting nuclei and electrons. Several material properties are comprehensively described by a stationary state of the quantum system. This condition is certainly met for the (thermodynamic) ground state of a solid ($T \to 0\,\mathrm{K}$) where the potential energy environment of nuclei and electrons does not change with time. Thus, material properties as the equilibrium-lattice structure of a solid and the associated electronic structure might be obtained from finding the stationary wave function

[1] Whatever the fundamental nature of particles might turn out to consist of, ultimately.
[2] In a mathematical as well as conceptual sense.
[3] This is exactly what Feynman intended by highlighting the exceptional value of the atomic hypothesis that "... all things are made of atoms–little particles that move around in perpetual motion, attracting each other when they are a little distance apart, but repelling upon being squeezed into one another."
[4] The explicit wave-function dependence on spin is neglected throughout the subsequent considerations.

$\Psi_n(\mathbf{r}_1,\mathbf{r}_2,\ldots,\mathbf{r}_N,\mathbf{R}_1,\mathbf{R}_2,\ldots,\mathbf{R}_M)$ via solution of the time-independent Schrödinger equation,

$$\hat{H}_{nuc,el}\Psi_n(\mathbf{r}_1,\mathbf{r}_2,\ldots,\mathbf{r}_N,\mathbf{R}_1,\mathbf{R}_2,\ldots,\mathbf{R}_M) = E^n_{nuc,el}\Psi_n(\mathbf{r}_1,\mathbf{r}_2,\ldots,\mathbf{r}_N,\mathbf{R}_1,\mathbf{R}_2,\ldots,\mathbf{R}_M) \tag{3.2}$$

where $E^n_{nuc,el}$ denotes the energetic ground state of the many-body system in the quantum state $\Psi_n(\mathbf{r}_1,\mathbf{r}_2,\ldots,\mathbf{r}_N;\mathbf{R}_1,\mathbf{R}_2,\ldots,\mathbf{R}_M)$. The many-body Hamiltonian $\hat{H}_{nuc,el}$ follows from summing up all kinetic-energy contributions $\hat{T}_{particle}$ and the interaction contributions $\hat{V}_{particle,particle}$, of nuclei and electrons according to

$$\hat{H}_{nuc,el} = \hat{T}_{nuc} + \hat{T}_{el} + \hat{V}_{nuc,nuc} + \hat{V}_{nuc,el} + \hat{V}_{el,el}\,. \tag{3.3}$$

The kinetic energy operators of nuclei and electrons have the forms

$$\hat{T}_{nuc} = -\sum_{I=1}^{M}\frac{\hbar^2}{2M_I}\nabla^2_{\mathbf{R}_I} \tag{3.4}$$

and

$$\hat{T}_{el} = -\sum_{i=1}^{N}\frac{\hbar^2}{2m_m}\nabla^2_{\mathbf{r}_i}\,, \tag{3.5}$$

where M_I and m_e are the masses of nuclei and electrons, respectively, and $\nabla_{\mathbf{R}_I} = \frac{\partial}{\partial \mathbf{R}_I}$ and $\nabla_{\mathbf{r}_i} = \frac{\partial}{\partial \mathbf{r}_i}$ represent the partial derivatives with respect to the positions of nuclei and electrons. The interaction operators essentially sum up the individual Coulomb interactions between nuclei (atomic number Z_I with an integer multiple charge of $Z_I\,|e|$) and electrons as well as nuclei and electrons.

$$\hat{V}_{nuc,nuc} = \frac{1}{2}\sum_{I=1}^{M}\sum_{\substack{J=1\\J\neq I}}^{M}\frac{e^2}{4\pi\epsilon_0}\frac{Z_I Z_J}{|\mathbf{R}_I-\mathbf{R}_J|} \tag{3.6}$$

$$\hat{V}_{nuc,el} = \frac{1}{2}\sum_{I=1}^{M}\sum_{i=1}^{N}\frac{e^2}{4\pi\epsilon_0}\frac{Z_I}{|\mathbf{R}_I-\mathbf{r}_i|} \tag{3.7}$$

$$\hat{V}_{el,el} = \frac{1}{2}\sum_{i=1}^{N}\sum_{\substack{j=1\\j\neq i}}^{N}\frac{e^2}{4\pi\epsilon_0}\frac{1}{|\mathbf{r}_i-\mathbf{r}_j|} \tag{3.8}$$

The solution of the stationary and time-dependent many-body Schrödinger equation, Eq. (3.2), for the coupled nuclei-electron system is the fundamental challenge to materials science. Every formalism directly based on the fundamental many-body Hamiltonian, Eq. 3.3, might be classified as a *first principles* or *ab initio* approach. However, every practical solution scheme has to make several approximations. These approximations are owned to either the dimensionality of the mathematical problem (see below) or obligatory demands of the numerical implementation (e.g. discrete representations of continuos functions, finite basis sets, ...). Thus, *ab initio* does not imply a complete absence of approximations, rather, as emphasized by Engel and Dreizler [934]

the abstinence of *adjustable* parameters. Non–ab-inito approaches always rely on phenomenological models defining a parameter-dependent model Hamiltonian relying on parametric input from experimental measurements or *exact* ab initio simulations.

THE EXPONENTIAL WALL – In principle, finding of the lowest energy eigenstate E_0 (the ground state) of the many-body Schrödinger equation, Eq. (3.2), and the corresponding ground-state wave function $\Psi_0(\mathbf{r}_1, \mathbf{r}_2, \ldots, \mathbf{r}_N; \mathbf{R}_1, \mathbf{R}_2, \ldots, \mathbf{R}_M)$ provide all physical properties related to a material's groundstate as the equilibrium geometry, the associated electronic (band) structure, as well as its mechanical properties. Complete solution of the time-dependent many-body Schrödinger equation further provides all additional non–ground-state properties as the optical response, the electric conductivity, or thermal transport properties, which are related to the diverse flavors of fundamental *quasiparticle* excitations within a material. However, the many-body problem of quantum-mechanics could not be solved in the past and will withdraw itself from every direct future solution approach, even in case of supposedly *trivial* molecular systems. The reason for this fundamental limitation, known as the *exponential wall*, is the vast number of interdependent variables and, thus, the dimensionality of the mathematical problem. [5] While there is obviously no value in trying any direct solution to the many-body Schrödinger equation, Eq. (3.2), it is indispensable to find efficient procedures that allow a substantial downsizing of the dimensionality of the associated mathematical problem.

3.1.1 The Born-Oppenheimer approximation

DECOUPLING LIGHT AND HEAVY WEIGHTS – A fundamental approximation to reduce the dimensionality of the many-body problem originates from the mass difference between nuclei and electrons. Due to the at least three orders of magnitude mass difference [6], the dynamics of the nuclei and the electrons take place on notably different time scales. While frequencies of atomic vibrations are typically of the order 10^{13} Hz, electronic motion is associated with frequencies of 10^{15} Hz. Considering the time scale of nuclei movement, the electronic system will follow any position changes in a nearly instantaneous mode. The electrons are said to follow the nuclei motion adiabatically, while staying in the same stationary state of the electronic Hamiltonian

$$\hat{H}_{el} = \hat{T}_{el} + \hat{V}_{nuc,el} + \hat{V}_{el,el}\,. \tag{3.9}$$

[5] Paraphrasing two examples given by Blöchl [935] and Giustino. [936] one might consider the ordinary example of the wave function of a silicon crystal. Silicon crystallizes in a cubic diamond-type lattice which is represented by a primitive two-atom unit cell of volume $a^3/4$ with $a = 5.43$ Å being the lattice constant of silicon. A discretization grid with a point distance of $\Delta x \sim 0.1$ Å in the primitive unit cell contains roughly $N_{grid} \approx 40000$ points. Discretizing each variable in the system of $M = 2$ nuclei, considering only an explicit dependence on the $N_{val} = 8$ valence electrons, and (for completness) adding the corresponding 2^8 degrees of freedom to represent the electron spin, results in a total of $N_{grid}^{M+N_{val}} \cdot 2^{N_{val}}$ ($\sim 2 \cdot 10^{48}$) complex numbers needed to store the many-body wave function. Imagining significant advancement in data storage and a single reasonably sized data device, able of holding one exabyte(!) of data, one still needs the insane amount of roughly $4 \cdot 10^{31}$ devices. Assuming a small USB-stick sized volume of 1 cm^3 per data device leads to an estimated storage volume of $4 \cdot 10^{25}$ m^3, which represents a sphere of $\sim 4 \cdot 10^8$ m diameter, roughly the distance between earth and moon.

[6] The proton (neutron) is more massive than the electron by a factor of ∼1836 (∼1839).

On the contrary, the nuclei cannot adapt to the rapid position changes of the electronic system and will ultimately see a time-averaged version of the many-electron potential. Therefore the many-body wave function $\Psi(\mathbf{r}_1,\mathbf{r}_2,\ldots,\mathbf{r}_N,\mathbf{R}_1,\mathbf{R}_2,\ldots,\mathbf{R}_M,t)$ might be exactly expressed in products of a nuclear wave function, $\Theta_n(\mathbf{R}_1,\mathbf{R}_2,\ldots,\mathbf{R}_M,t)$, explicitly depending on the nuclei coordinates $\mathbf{R}_I$, and an electronic wave function, $\Phi_n(\mathbf{r}_1,\mathbf{r}_2,\ldots,\mathbf{r}_N;\{\mathbf{R}\})$, explicitly depending on the electron coordinates $\mathbf{r}_i$, but only depending parametrically on the current arrangement $\{\mathbf{R}\}$ of the nuclei.

$$\Psi(\mathbf{r}_1,\mathbf{r}_2,\ldots,\mathbf{r}_N,\mathbf{R}_1,\mathbf{R}_2,\ldots,\mathbf{R}_M,t)=\sum_n \Theta_n(\mathbf{R}_1,\mathbf{R}_2,\ldots,\mathbf{R}_M,t)\,\Phi_n(\mathbf{r}_1,\mathbf{r}_2,\ldots,\mathbf{r}_N;\{\mathbf{R}\}) \tag{3.10}$$

The wave functions, $\Phi_n(\mathbf{r}_1,\mathbf{r}_2,\ldots,\mathbf{r}_N;\{\mathbf{R}\})$ are solutions to the *many-electron problem*, the time-independent Schrödinger equation for the electronic Hamiltonian, $\hat{H}_{el}$, respectively.

$$\hat{H}_{el}\Phi_n(\mathbf{r}_1,\mathbf{r}_2,\ldots,\mathbf{r}_N;\{\mathbf{R}\})=E_n^{el}(\{\mathbf{R}\})\,\Phi_n(\mathbf{r}_1,\mathbf{r}_2,\ldots,\mathbf{r}_N;\{\mathbf{R}\}) \tag{3.11}$$

Thus, the study of electrons in a material, does not necessarily require the solution of the many-body Schrödinger equation for coupled nuclei and electrons. It is rather sufficient to solve the many-electron problem with the nuclei acting as a static *external potential* $\hat{V}_{ext}\equiv\hat{V}_{nuc,el}$ for the movement of electrons. Utilizing the ansatz Eq. (3.10) yields the time-dependent Schrödinger equation for nuclear motion

$$\begin{aligned}\left[i\frac{\partial}{\partial t}+\sum_{I=1}^{M}\frac{1}{2M_I}\nabla_{\mathbf{R}_I}^2-\hat{V}_{nuc,nuc}-E^{el}(\{\mathbf{R}\}_m)\right]\Theta_n(\mathbf{R}_1,\mathbf{R}_2,\ldots,\mathbf{R}_M,t)=\\ -2\sum_n\sum_{I=1}^{M}\frac{1}{2M_I}\nabla_{\mathbf{R}_I}\Theta_n(\mathbf{R}_1,\mathbf{R}_2,\ldots,\mathbf{R}_M,t)\,\langle\Phi_m|\nabla_{\mathbf{R}_I}|\Phi_n\rangle\\ -\sum_n\sum_{I=1}^{M}\frac{1}{2M_I}\langle\Phi_m|\nabla_{\mathbf{R}_I}^2|\Phi_n\rangle\,\Theta_n(\mathbf{R}_1,\mathbf{R}_2,\ldots,\mathbf{R}_M,t)\,,\end{aligned} \tag{3.12}$$

where the two terms on the right-hand side are the *non-adiabatic* coupling terms. Neglecting both terms yields the adiabatic or Born-Oppenheimer approximation [7] [937, 938] for nuclear motion.

$$i\hbar\frac{\partial}{\partial t}\Theta_n(\mathbf{R}_1,\mathbf{R}_2,\ldots,\mathbf{R}_M,t)=\left[-\sum_{I=1}^{M}\frac{1}{2M_I}\nabla_{\mathbf{R}_I}^2+\underbrace{\hat{V}_{nuc,nuc}+E_m^{el}(\{\mathbf{R}\})}_{:=E_n^{BO}(\{\mathbf{R}\})}\right]\Theta_n(\mathbf{R}_1,\mathbf{R}_2,\ldots,\mathbf{R}_M,t) \tag{3.13}$$

Inspecting the structure of the nuclear Born-Oppenheimer Hamiltonian illustrates that the solutions $E_m^{el}(\{\mathbf{R}\})$ of the many-electron system, Eq. (3.11), provide an additional potential-energy term. Together with the interaction potential $\hat{V}_{nuc,nuc}$ the solution of the electronic problem provides a potential-energy surface, the Born-Oppenheimer surface [8], for nuclear motion. In Born-

[7] Named after the Nobel prize awarded german mathematician and physicist Marx Born (1882–1970) and the US-american theoretical physicist J. Robert Oppenheimer (1904–1967).

[8] A $3N$-dimensional hypersurface in case of a N electron containing system.

Oppenheimer approximation the nuclei dynamics are, thus, constrained to a particular energy surface $E_n^{BO}(\{\mathbf{R}\})$, commonly, but not necessarily, the ground state $E_0^{BO}(\{\mathbf{R}\}_0)$ depending parametrically on the set of equilibrium lattice positions $\{\mathbf{R}\}_0$. Likewise, the nuclei dynamics might be restricted to any other potential-energy surface, eigenstate of the electronic system respectively. In both cases the system will strictly remain in its *enforced* electronic state. The Born-Oppenheimer approximation does not account for non-adiabatic transitions between different potential-energy surfaces.

The adiabatic Born-Oppenheimer approximation lies at the heart of the majority of all *ab initio* theory approaches determining the structure of molecules and solids. While a vast number on semiconducting and insulating materials has been studied successfully in the Born-Oppenheimer approximation [939–941], it is, despite successful application, partly questionable for metallic systems. [939, 942, 943] A failure of the adiabatic Born-Oppenheimer approximation has for example been reported for graphene [944] and carbon nanotubes. [945, 946] The accurate treatment of atomic systems without the Born-Oppenheimer approximation is a complex challenge for theoretical (and experimental) chemists and physicists and has been studied for the hydrogen molecular ion H_2^+ [947–949], for charge transfer processes [950], in vibronic spectroscopy [951, 952], or for the rotational spectra of SnSe and SnTe. [953]

CLASSICAL MOTION – Applying the Born-Oppenheimer approximation to a many-body system allows the effective description of the motion of the nuclei on a particular Born-Oppenheimer energy surface $E_n^{BO}(\{\mathbf{R}\})$. Optimization or dynamic treatment of the ionic subsystem is commonly done via neglect of nuclear quantum effects and classical treatment of their motion. Using the effective adiabatic form of the nuclear Hamiltonian of Eq. (3.13) yields the corresponding classical Hamilton function $H_n(\mathbf{P}_1,\mathbf{P}_2,\ldots,\mathbf{P}_M,\mathbf{R}_1,\mathbf{R}_2,\ldots,\mathbf{R}_M,t) \equiv H_n(\mathbf{P},\mathbf{R},t)$ for nuclear motion,

$$H_n(\mathbf{P}_1,\mathbf{P}_2,\ldots,\mathbf{P}_M,\mathbf{P}_1,\mathbf{R}_2,\ldots,\mathbf{R}_M,(t)) = \sum_{I=1}^{M}\frac{\mathbf{P}_I^2}{2M_I} + E_n^{BO}(\{\mathbf{R}\})\,. \tag{3.14}$$

Setting up the resulting Hamilton equations of motions leads to the conventional Newton's equation of motion,

$$M_I\frac{d^2\mathbf{R}_I}{dt^2} = -\nabla_{\mathbf{R}_I}E_n^{BO}(\{\mathbf{R}\})\,. \tag{3.15}$$

Due to the form of the Born-Oppenheimer Hamiltonian, the forces $\mathbf{F}_I \equiv -\nabla_{\mathbf{R}_I}E_n^{BO}(\{\mathbf{R}\})$ contain a term arising from the repulsive nuclear-nuclear interaction and a contribution from the derivative of the electronic eigenvalue $E_m^{el}(\{\mathbf{R}\})$. The second term is evaluated using the Hellmann-Feynman theorem [954–956], so that the forces are obtained from the exception value of the derivative of the electronic Hamiltonian with respect to the electronic wave function $\Phi_n(\mathbf{r}_1,\mathbf{r}_2,\ldots,\mathbf{r}_N;\{\mathbf{R}\})$ according to [9]

[9] The Hellmann-Feynman force theorem is only accurate in case of normalized wave functions Ψ_λ. However, in practical calculations the wave functions Ψ_λ need to be expressed by a complete (infinite) set of basis functions. While Eq. (3.16) applies to the plane wave case, localized basis function causes additional force terms, so called

$$-\nabla_{\mathbf{R}_I} E_n^{BO}(\{\mathbf{R}\}) = \left\langle \Phi_n(\mathbf{r}_1, \mathbf{r}_2, \ldots, \mathbf{r}_N; \{\mathbf{R}\}) \left| \frac{\partial \hat{H}_{BO}}{\partial \mathbf{R}_I} \right| \Phi_n(\mathbf{r}_1, \mathbf{r}_2, \ldots, \mathbf{r}_N; \{\mathbf{R}\}) \right\rangle . \tag{3.16}$$

Here, $\hat{H}_{BO}$ is the Born-Oppenheimer Hamiltonian, [10]

$$\hat{H}_{BO} = \hat{T}_{el} + \hat{V}_{nuc,nuc} + \hat{V}_{nuc,el} + \hat{V}_{el,el} . \tag{3.17}$$

Using the (classical) forces from the derivative of the Born-Oppenheimer energy surface is the common basis for structure optimizations [11] and molecular dynamics simulations. Thereby, the quantum-mechanical evaluation of $E_n^{BO}(\{\mathbf{R}\})$, e.g. using density-functional theory, classifies the molecular dynamics as an "*ab initio* " approach [12], while ordinary molecular dynamics approaches rely on some kind of approximative parametrization of the Born-Oppenheimer energy surface.

3.2 Density-functional theory

WAVE FUNCTION VS. ELECTRON DENSITY – Despite the separation of the nuclear degrees of freedom in the adiabatic Born-Oppenheimer approximation, the many-electron wave function still remains a complex $3N$ dimensional quantity [13] and the associated eigenvalue problem, the solution of the time-independent Schrödinger equation Eq. (3.11) respectively, remains extremely challenging.

Using the Hellmann-Feynman force theorem to calculate the forces acting on each ion via Eq. (3.16) results in forces

$$\mathbf{F}_I = -\int n_{\{\mathbf{R}\}}(\mathbf{r}) \frac{\partial \hat{V}_{ext}(\mathbf{r})}{\partial \mathbf{R}_I} d\mathbf{r} - \frac{\partial \hat{V}_{nuc,nuc}}{\partial \mathbf{R}_I} \tag{3.18}$$

where the definition of the electronic charge density

$$n_{\{\mathbf{R}\}}(\mathbf{r}) = N \int_{\mathbb{R}^3} \Phi_n^*(\mathbf{r}_1, \mathbf{r}_2, \ldots, \mathbf{r}_N; \{\mathbf{R}\}) \Phi_n(\mathbf{r}_1, \mathbf{r}_2, \ldots, \mathbf{r}_N; \{\mathbf{R}\}) \, \mathrm{d}^3\mathbf{r} \tag{3.19}$$

$$= N \int_{\mathbb{R}^3} |\Phi_n(\mathbf{r}_1, \mathbf{r}_2, \ldots, \mathbf{r}_N; \{\mathbf{R}\})|^2 \, \mathrm{d}^3\mathbf{r} \tag{3.20}$$

Pulay forces [957, 958], that needs to be considered in the calculation of forces and construction of optimized basis sets. [959–964]

[10] $\hat{H}_{BO}$ is equivalent to the many-body Hamiltonian $\hat{H}_{nuc,el}$, Eq. (3.3), without terms depending solely on the momenta of the nuclei, the kinetic energy of nuclei respectively.

[11] The calculated forces might be used for direct integration of the equations of motion for the nuclei in order to move the nuclear system towards it equilibrium structure. Alternatively, the equilibrium structure might be determined using various kinds of functional optimization techniques, such as quasi-Newton [965, 966] or conjugate gradient algorithms. [967–969]

[12] Instead of using "Born-Oppenheimer" molecular dynamics, alternative ab-inito approaches as extended Lagrangian methods (e.g. Car-Parrinello molecular dynamics) [970–974], Ehrenfest dynamics [975, 976], and surface hopping [975, 977] are known to propagate the nuclei. Whereby, the last two include non-adiabatic effects.

[13] Again, the inclusion of electron-spin degrees of freedom will further enhance the dimensionality of the problem.

for a particular nuclear configuration $\{\mathbf{R}\}$ has been used. Thus, the quantity needed for calculation of the forces acting on the nuclei is not the electronic wave function $\Phi_n(\mathbf{r}_1, \mathbf{r}_2, \ldots, \mathbf{r}_N; \{\mathbf{R}\})$ itself, but rather the electron-charge density $n_{\{\mathbf{R}\}}(\mathbf{r})$ for a given nuclear configuration. A similar conclusion might be drawn for the Hessian, the second partial derivatives with respect to the nuclei positions on the Born-Oppenheimer energy surface, which are needed for e.g. the evaluation of vibrational properties. [978] These simple considerations illustrate the tantalizing idea to replace the $3N$ dimensional electronic wave function by the three-dimensional electron density, which is essentially the fundamental idea behind every density-functional theory approach.

QUALITATIVE ARGUMENTATION – A qualitative justification for the use of the electron density as the fundamental quantity of electronic structure theory has been given by the theoretical spectroscopist Edgar B. Wilson, Jr. (1908–1992). [979] Knowing and inspecting an exact electron density $n_{\{\mathbf{R}\}}(\mathbf{r})$ would provide the nuclei positions $\{\mathbf{R}\}$ due to the characteristic cusps in $n_{\{\mathbf{R}\}}(\mathbf{r})$ [14]. Additionally, knowledge of the density gradient $\nabla n_{\{\mathbf{R}\}}(\mathbf{r})$ provides access to the nuclear charges. The number of electrons in any electron-charge density is generally given from the integral

$$N = \int_{\mathbb{R}^3} n_{\{\mathbf{R}\}}(\mathbf{r})\, \mathrm{d}^3\mathbf{r}\,. \tag{3.22}$$

Thus, the full Hamiltonian of the system might be constructed, reversely.

3.2.1 The Hohenberg-Kohn theorems

THE IMPOSSIBLE FUNCTIONAL – In order to justify the general use of the electron density to describe the nuclear dynamics of a quantum-mechanical many-body system, it is necessary to give a rigorous theoretical justification. This justification, the blueprint of existence theorems in density-functionals theory, in general, has been given by the french-american theoretical physicist Pierre C. Hohenberg (1934–2016) and the austrian-born US-american theoretical physicist Walter Kohn (1923–2017). [1] The basic statements of Hohenberg and Kohn are canonically expressed in form of two Theorems.

THEOREM I: *For non-degenerate ground states, the external potential $V_{ext}(\boldsymbol{r})$ of a system of interacting particles is uniquely determined, except an additive constant, by the (v-representable) ground-state electron density $n_0(\boldsymbol{r})$.*

THEOREM II: *There is a universal functional $F_{HK}[n(\boldsymbol{r})]$ of the electron density $n(\boldsymbol{r})$ which,*

[14] The connection between cusp's of a nucleus at R_I in the electron density and the corresponding nuclear charge has explicitly been made by Steiner [980], using Kato's theorem [981], in the form

$$\left.\frac{\partial \bar{n}_{\{\mathbf{R}\}}(r)}{\partial r}\right|_{r=0} = -2Z_I \bar{n}_{\{\mathbf{R}\}}(0)\,, \tag{3.21}$$

where $\bar{n}_{\{\mathbf{R}\}}(\mathbf{r})$ is the spherical average of $n_{\{\mathbf{R}\}}(\mathbf{r})$. [979] Cusp condition have also been derived for exited states [982, 983], thus, the electron density provides all necessary information on the associated many-body problem.

together with the external potential $V_{ext}(\mathbf{r})$, defines a density functional of the total energy. For every external potential $V_{ext}(\mathbf{r})$, the (non-degenerate) energetic ground state $E_{V_{ext}}$ is given by the global minimum of the energy functional $F_{HK}[n(\mathbf{r})]$, which is reached by varying the electron density towards the exact ground-state electron density $n_0(\mathbf{r})$ [15].

The second Hohenberg-Kohn theorem establishes the variational principle for the total energy functional $E_{V_{ext}}[n]$, essentially. Using the Rayleigh-Ritz variational principle and the basic statement of the first Hohenberg-Kohn theorem, asserting that a non-degenerate density $n(\mathbf{r})$ uniquely determines a corresponding external potential $V_{ext}(\mathbf{r})$, yields

$$\begin{aligned} \left\langle \Psi \left| \hat{H}_{el} \right| \Psi \right\rangle &= F_{HK}[n] + \int V_{ext}(\mathbf{r})\, n(\mathbf{r})\, \mathrm{d}^3\mathbf{r} \\ &= E_{V_{ext}}[n] > E_{V_{ext}}[n_0] = E_0 \,. \end{aligned} \tag{3.23}$$

with $F_{HK}[n]$ beeing the Hohenberg-Kohn energy functional

$$F_{HK}[n] := \left\langle \Psi_0[n] \left| \hat{T}_{el} + \hat{V}_{el,el} \right| \Psi_0[n] \right\rangle \tag{3.24}$$

encompassing, the kinetic energy of interacting electrons and the *full* electron-electron interaction including non-classical electron correlation. Thus, the basic statement of the second Hohenberg-Kohn theorem is that the total energy functional $E_{V_{ext}}[n]$ is minimized to the ground-state energy E_0 by variation of the electron density $n(\mathbf{r})$ towards the ground-state electron density $n_0(\mathbf{r})$

$$E_0 = \underbrace{\min}_{n \to n_0} E_{V_{ext}}[n] \,. \tag{3.25}$$

Assuming the differentiability of the total energy functional $E_{V_{ext}}[n]$, the variational principle (3.25) requires that the ground-state density satisfies the variational problem

$$\frac{\delta}{\delta n(\mathbf{r})} \left\{ E_{V_{ext}}[n(\mathbf{r})] - \mu \left[\int n(\mathbf{r})\, \mathrm{d}^3\mathbf{r} - N \right] \right\} \Bigg|_{n(\mathbf{r}) = n_0(\mathbf{r})} = 0 \tag{3.26}$$

under the constraint of particle conservation (cf. Eq. 3.22). Therefore, the fundamental equation of density-functional theory [16] is an Euler-Lagrange equation of the form

$$\mu = \frac{\delta E_{V_{ext}}[n(\mathbf{r})]}{\delta n(\mathbf{r})} = V_{ext}(\mathbf{r}) + \frac{\delta F_{HK}[n(\mathbf{r})]}{\delta n(\mathbf{r})} \,. \tag{3.27}$$

Several extensions [17], lifting limitations of the Hohenberg-Kohn theorems as V-representability

[15] See Ref. [1] as well as numerous textbooks on density-functional theory, e.g. Ref. [934, 984–987]. Especially the book of Parr and Yang, Ref. [984], is unsurpassed in its presentation of the basics of density-functional theory.

[16] More precisely orbital free density-functional theory, as discussed below.

[17] Hohenberg-Kohn theory has been extended towards non-degenerate ground states [934, 988–990], non-local external potentials [991], electron-spin and magnetization densities [2, 934, 987, 992, 993], current densities [934, 994, 995]

of densities or the non-degeneracy of the ground state as well as Hohenberg-Kohn-like theorems for more general density classes have been formulated underlining the claim for universal validness of the density-functional theory approach. In practical calculations, using some approximation to the true Hohenberg-Kohn energy functional, either the total energy functional might be minimized directly using numerical optimization techniques as steepest decent or conjugate gradient approximations [1003–1005] or transferred to a Schrödinger-like differential equation for a one-electron model that might be solved using the numerous numerical codes developed for (orbital dependent) density-functional theory. [1006] Both approaches allow linear scaling with system size, which underlines the theoretical potential of *pure* density-functional theory and justifies the search for an universal density functional.

3.2.2 The Kohn-Sham approach

CERTAINLY WELL HIDDEN, BUT NUMBERS MATTER – Despite the striking simplicity of the mathematical proof, given by Hohenberg and Kohn for the existence of an universal functional of the total energy, its analytic form is unknown [18] While the exact mathematical structure of the universal energy functional remains hidden [19] one might recognize that practical application of density-functional theory is less about understanding the fundamental physics of the universal density functional, but rather about calculation of explicit *numbers*, physical material properties respectively, that are, on the one hand, validated by experimental data and, on the other hand, predict material properties for future applications. To this purpose, an approximative treatment of the density functional might not only be thoroughly justified but also a common-sense imperative. In the best sense, Kohn [20] working together with the chinese theoretical physicist Lu J. Sham (1938–) ingeniously provided a formulation of density-functional theory, which avoids the paralyzing ballast of finding "the" universal functional and focusses on the feasibility of practical electronic structure calculations.

A FORMULA FOR SUCCESS – The key idea of the Kohn-Sham approach to the electronic-structure problem might be summarized as follows: "Calculate as much as possible of the fundamental energy contributions by means of well known and *understood* reference systems and

as well as temperature-dependence [996] and time-dependence (Runge-Gross theorems). [997–1002]

[18] Notwithstanding that, the universal energy functional itself is not unknown, in principle, as it is defined by explicit formal construction rules as Levi constrained search [988, 1007], Legendre-transformed representations of the total energy functional [1008, 1009], the local-scaling transformation version of density-functional theory [1010, 1011], or ground-state path-integral quantum Monte Carlo [1012]. Even, practical calculation schemes for the universal Levy-Lieb energy functional, developed on basis of the constraint search formalism, have been implemented. [1013–1015] However, all these approaches are either strictly imcomputable in any practical sense, or computationally simply less efficient than solution of the many-body Schödinger equation itself, which has been our problem from the beginning. [1016, 1017]. Actual determination of an, at least, *near-to-universal* functional would require solving the Schödinger equation many-times.

[19] It is even unclear if this analytic form, ones found, results in any numerically efficient computation scheme.

[20] For his fundamental contributions to the development of density-functional theory, Kohn was awarded by the Nobel prize in Chemistry in 1998. Kohn shared the Nobel prize on equal terms with the british mathematician and theoretical chemist John A. Polpe, who was awarded "for his development of computational methods in quantum chemistry".

introduce *working* approximations for the remaining energy contributions." In case of the interacting many-electron system, this well known and understood system is obviously a system of non-interacting electrons. For such a system of N non-interacting electrons, fermions respectively, the ground-state wave function $\Phi_0(\mathbf{r}_1, \mathbf{r}, \ldots, \mathbf{r}_N)$ has a single-determinantal form (Slater determinant), whose mathematical properties naturally met the asymmetry conditions demanded by the Pauli principle. The wave function is constructed from a set $\{\varphi_\lambda(\mathbf{r})\}$ of spatial orbitals [21] encompassing the N lowest energy eigenvalues of the Schrödinger equation

$$\hat{h}_s \varphi_\lambda(\mathbf{r}) = \varepsilon_\lambda \varphi_\lambda(\mathbf{r}) \tag{3.28}$$

for non-interacting electrons of the single-particle Hamiltonian

$$\hat{h}_S = -\frac{\hbar^2}{2m}\nabla^2 + V_s(\mathbf{r}) . \tag{3.29}$$

V_s is the potential energy of an electron in the non-interacting system. The ground-state electron density of the non-interacting system is defined through

$$n_S(\mathbf{r}) = \sum_\lambda n_\lambda |\varphi_\lambda(\mathbf{r})|^2 . \tag{3.30}$$

Here, the n_λ are the occupation numbers $n_\lambda = 0, 1$ normalized to the number

$$N = \sum_\lambda n_\lambda \tag{3.31}$$

of electrons. The kinetic energy of the non-interacting reference system, labeled by the superscript S, is exactly given by

$$T_S^{el}[n] = \sum_\lambda n_\lambda \left\langle \varphi_\lambda^* \left| -\frac{\hbar^2}{2m_e}\nabla^2 \right| \varphi_\lambda \right\rangle . \tag{3.32}$$

The total energy functional of the non-interacting reference system is defined through

$$E_S[n] = T_S^{el}[n] + \int n(\mathbf{r}) V_s(\mathbf{r}) \, \mathrm{d}^3\mathbf{r} . \tag{3.33}$$

Even though the kinetic energy, Eq. 3.32, of the non-interacting reference system is not the exact kinetic-energy functional of the interacting system, Kohn and Sham realized that the Hohenberg-Kohn energy functional might be rewritten by separating out $T_S^{el}[n]$ as the major kinetic-energy contribution. Using the definition of the Hohenberg-Kohn energy functional, Eq. 3.24 and re-

[21] The presented discussion of the Kohn-Sham formalism is restricted to the non–spin-polarized case; for a comprehensive discussion of the spin-polarized equations e.g. see Ref. [934, 987].

grouping of the various energy contributions yields

$$F_{HK}[n] = \left(T^{el}[n] - T_S^{el}[n]\right) + T_S^{el}[n] + (V_{el,el}[n] - V_H[n]) + V_H[n] \tag{3.34}$$

$$= T_S^{el}[n] + V_H[n] + \underbrace{\left(T^{el}[n] - T_S^{el}[n] + V_{el,el}[n] - V_H[n]\right)}_{:=E_{XC}[n]}$$

$$= T_S^{el}[n] + V_H[n] + E_{XC}[n]\,. \tag{3.35}$$

The last equality makes use of a newly introduced energy functional $E_{XC}[n]$, the so called exchange-correlation (density) functional of Kohn-Sham theory. While the kinetic energy term $T_S^{el}[n]$ and the Hartree term $V_H[n]$ are given exactly, all unknown energy contributions are subsumed in this new functional. $E_{XC}[n]$ contains a, presumably small, energy correction arising from the difference of the kinetic energy in the *true* interacting system and the fictitious reference system (at the same density), $\left(\left\langle \Phi_0[n] \middle| \hat{T}_{el} \middle| \Phi_0[n] \right\rangle - T_S^{el}[n]\right)$, and all non-classical contributions, $\left(\left\langle \Phi_0[n] \middle| \hat{V}_{el,el} \middle| \Phi_0[n] \right\rangle - V^H[n]\right)$, of the electron-electron interaction. The universal ground-state energy functional of Kohn and Sham, thus, reads

$$E_{V_{ext}}^{KS}[n(\mathbf{r})] = T_S^{el}[n] + \int V_{ext}(\mathbf{r})\, n(\mathbf{r})\, \mathrm{d}^3\mathbf{r} + V_H[n] + E_{XC}[n]\,. \tag{3.36}$$

The electron density is obtained from variational search for the minimum of the Kohn-Sham energy functional $E_{V_{ext}}^{KS}[n(\mathbf{r})] \equiv E_{V_{ext}}^{KS}[\{\varphi_\lambda(\mathbf{r})\}]$ within the Hilbert space of the single-particle wave functions $\left\{\varphi_\lambda^{KS}(\mathbf{r})\right\}$ under the orthonormalilty constraint

$$\int \varphi_\lambda^*(\mathbf{r})\, \varphi_{\lambda'}(\mathbf{r}) \mathrm{d}^3\mathbf{r} = \delta_{\lambda,\lambda'}\,, \tag{3.37}$$

which results in a variational problem with respect to the Kohn-Sham orbitals $\varphi_\lambda^{KS}(\mathbf{r})$ given by

$$\frac{\delta}{\delta \varphi_\lambda^{KS}(\mathbf{r})} \left\{ E_{V_{ext}}^{KS}\left[\left\{\varphi_\lambda^{KS}(\mathbf{r})\right\}\right] - \sum_{\lambda,\lambda'} \varepsilon_{\lambda\lambda'}^{KS} \left[\int \varphi_\lambda^{*KS}(\mathbf{r})\, \varphi_{\lambda'}^{KS}(\mathbf{r}) \mathrm{d}^3\mathbf{r} \right] \right\} = 0\,. \tag{3.38}$$

Unitary transformation to a standard eigenvalue problem yields the canonical *Kohn-Sham equations*

$$\hat{H}_{KS} \varphi_\lambda^{KS}(\mathbf{r}) = \left[-\frac{\hbar^2}{2m_e} \nabla^2 + V_{eff}(\mathbf{r}) \right] \varphi_\lambda^{KS}(\mathbf{r}) = \varepsilon_\lambda^{KS} \varphi_\lambda^{KS}(\mathbf{r}) \tag{3.39}$$

representing a set of integro-differential equations for electrons in the average effective potential

$$V_{eff}^{KS}(\mathbf{r}) = V_{ext}(\mathbf{r}) + V_H(\mathbf{r}) + V_{XC}(\mathbf{r}) \tag{3.40}$$

of the other electrons. Here, $V_{XC}(\mathbf{r})$ is the exchange-correlation potential obtained as the functional derivative

$$V_{XC}(\mathbf{r}) = \frac{\delta E_{XC}[n(\mathbf{r})]}{\delta n(\mathbf{r})}\,. \tag{3.41}$$

The Kohn-Sham approach belongs to the class of so called mean-field approaches, effectively mapping an interacting many-electron system onto a system of non-interacting electrons in an effective potential given by the potential of all other electrons [22]. The Kohn-Sham equations represent a system of coupled and highly non-linear eigenvalue equations which need to be solved numerically to find self-consistent solutions. The resulting ground state energy E_0^{KS} is ultimately given for the ground-state energy $n_0(\mathbf{r})$ constructed from the N lowest energy Kohn-Sham orbitals $\left\{\varphi_\lambda^{KS}(\mathbf{r})\right\}_N$,

$$E_0^{KS}[n_0(\mathbf{r})] = \sum_\lambda \varepsilon_\lambda^{KS} - V_H[n_0(\mathbf{r})] + E_{XC}[n_0(\mathbf{r})] - \int V_{XC}(\mathbf{r})\, n_0(\mathbf{r})\, \mathrm{d}^3\mathbf{r}. \tag{3.42}$$

Altogether, the Kohn-Sham approach provides a working scheme for *indirect* evaluation of the kinetic energy of a many-electron system to the price of replacing the single Euler-Lagrange equation of classical orbital-free density-functional theory with a system of N coupled single-particle equations by (re-)introducing orbitals into a theory initially intended to be orbital free. Thereby, the problem of finding an exact total energy functional is shifted towards the exchange-correlation functional, whose analytical form is unknown. Nevertheless, an actually substantial number of diverse approximations to the exchange-correlation functional of Kohn-Sham theory are known and compete among each other for high accuracy and predictive power, universal applicability, and, if nothing else, numerical efficiency.

No simple Meaning – A central question, arising within the practical use of Kohn-Sham theory, is the meaning of the single-particle eigenvalues and eigenstates of Kohn-Sham theory. Giving a straight forward answer would be "... one should expect no simple physical meaning for the Kohn-Sham orbital energies. There is none." [984, p. 149]. The Kohn-Sham orbitals are actually purely auxiliary mathematical constructions with the single purpose of adding up to the groundstate-electron density via Eq. 3.30. The corresponding Kohn-Sham orbital energies are *just* the Lagrange multipliers needed for incorporating the orthonormality constraint into the variational search for the ground-state energy. This limitation in meaning is formally expressed in the absence of a well defined Koopmans' theorem [23] analog in Kohn-Sham density-functional theory. Koopmans' theorem [1019] to Hartree-Fock theory states that, if no orbital relaxations are considered, the Hartree-Fock orbital energies $\varepsilon_\lambda^\varphi$ equal, approximately, the negative of the (vertical) single-particle excitation energies corresponding to the removal of one electron from the orbital

[22] Single-particle eigenvalue equations, similar to the Kohn-Sham-equation-type, Eq. 3.39, are known from the preceding Hartree and Hartree-Fock mean-field approaches. In contrast to these approaches, Kohn-Sham theory is, in principle, an exact theory that allows complete treatment of all exchange-correlation effects in the many-electron system through a universal and *local* effective potential. Thereby, the computational demands for solving the Hartree-Fock equations are highest due to the presence of a non-local exchange interaction. The extension of Hartree-Fock theory towards accurate and *systematic* inclusion of electron correlation led to the wave-function-based branches of ab initio approaches to the many-electron problem. A unmatched introduction into Hartree-Fock theory and wave-function-based (multi-determinant) electron-correlation methods is given by the standard work of Szabo and Ostlund. [1018]

[23] Named after the dutch american mathematician and Nobel prize awarded economist and physicist Tjalling C. Koopmans (1910–1985).

φ_λ. Thus, the highest occupied (HO) orbital energy equals the negative of the ionization energy $\varepsilon_\lambda^{HO} \simeq -I_\lambda$. As a generalization of Koopmans' theorem the lowest unoccupied (LO) orbital energy is commonly regarded as the negative of the electron affinity $\varepsilon_\lambda^{LO} \simeq -A_\lambda$. This identification is actually not well justified in the context of Hartree-Fock theory due to the necessity of empty states in order to ad an electron to the system. However, the empty states of Hartree-Fock theory are not self-interaction corrected. While the exchange term effectively lowers the energy of occupied states by canceling the self-interaction in the Hartree term, the exception value of the exchange operator vanishes for unoccupied states leading to a spurious repulsive self-interaction. Thus, empty states become unbound, which results not only in unreasonable electron affinities but also the commonly observed severe overestimation of electronic band gaps. [985–987]

Returning to Kohn-Sham theory, Koopmans' theorem does not apply to Kohn-Sham orbital energies, in general. In fact, Koopmans' theorem might be used to validate exchange-correlation approximations in density-functional theory. [1020, 1021] Kohn-Sham orbitals that, *approximatively*, satisfy Koopmans' theorem have been reported for various long-range corrected (nearly self-interaction free [24]) hybrid exchange-correlation functionals [1023] as the long-range corrected *w*PBE [1024], Mori-Sánchez-Cohen-Yang [1025], and Baer-Neuhauser-Livshits functionals. [1020, 1026] [25] Instead of Koopmans' theorem, the eigenvalues of Kohn-Sham density-functional theory obey a theorem formulated and proofed by Janak. [1035] Janak's theorem states that the derivative of the total energy of Kohn-Sham theory with respect to the occupation numbers n_λ equals the eigenvalue ε_λ^{KS},

$$\frac{\delta E^{KS}[n(\mathbf{r})]}{\delta n_\lambda} = \varepsilon_\lambda^{KS}. \tag{3.43}$$

In contrast to Koopmans' theorem Janak's theorem rather proofs a mathematical property of the eigenvalues within the Kohn-Sham framework than having an actual relevance for the description of physical properties of the many-electron system. Despite the harsh, but conceptually correct, view on Kohn-Sham eigenvalues as an unphysical quantity [1036], the whole of density-functional theory, and, at present, almost every relevant application of density-functional theory is synonymous to Kohn-Sham theory and lives from direct comparison to experimental data. From direct comparison to e.g. photoemission data, it has been found that the line shape of the wave-vector dispersion is mirrored qualitatively and with reasonable accuracy in the Kohn-Sham band structure. [987] In view of practical applications, the most important characteristic of a semiconductor material is the electronic band gap [26]. The electronic band gap of Kohn-Sham theory E_{gap}^{KS} of an N electron system is, straight forward, defined by the energy difference between the orbital energies

[24] See Ref. [1022] for an self-interaction classification of density functionals.

[25] There are, indeed, contrary views on this matter present in literature. [1026–1034]

[26] More general, one might speak of an energy gap, since an actual *band* gap is restricted to crystalline solids but energy gaps are present in disordered solids, molecules, or nano-clusters, which rather exhibit a well defined density of states but do not exhibit a well defined *band* structure.

of the highest occupied and the lowest unoccupied (also virtual) Kohn-Sham state. [27],

$$\begin{aligned} E_{gap}^{KS} &= \varepsilon_{N+1}^{KS}(N) - \varepsilon_{N}^{KS}(N) \\ &= \varepsilon_{LU}^{KS}(N) - \varepsilon_{HO}^{KS}(N) \,. \end{aligned} \tag{3.44}$$

The Kohn-Sham energy gap, E_{gap}^{KS}, is well known to substantially underestimate [28,29] [1036] the band gaps of many solids for conventional exchange-correlation functionals as the local density approximation (LDA) or the generalized gradient approximation (GGA) (see discussion below). This idiosyncrasy of Kohn-Sham theory has been epitomized as the *band-gap problem* of density-functional theory. [1041, 1042] Since the band-gap problem has deep roots in density-functional theory, it is essential to understand origin and meaning of the Kohn-Sham gap with respect to the *exact* fundamental energy gap, defined for a many-electron system in an external potential $V_{ext}(\mathbf{r})$, before going into detail with the manifold of existing exchange-correlation functionals.

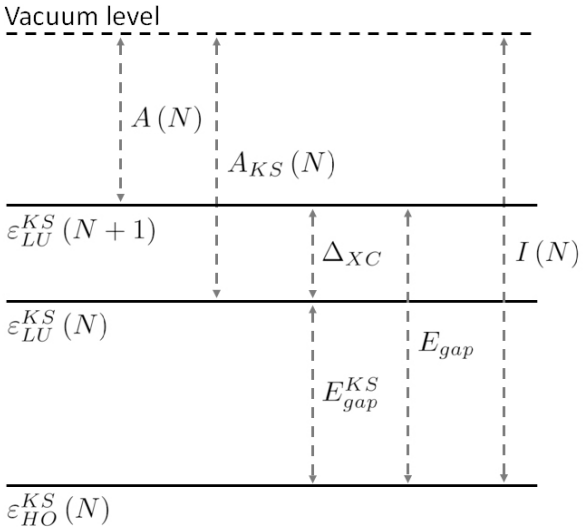

Figure 3.1: Schematic illustration (reproduced and modified from Ref. [1043]) of the energy levels defining the various types of energy gaps in Kohn-Sham density-functional theory.

MIND THE GAP – Conceptually, the exact (electronic) energy gap E_{gap} of a semiconducting or insulating N-electron system/material is exactly defined through the difference between the (vertical) ionization potential $I(N)$ and the electron affinity $A(N)$ (see Fig. 3.1) which are defined

[27] The conventional Kohn-Sham band gap is, thus, equivalent to the conventional definition of the HOMO-LUMO-type gap as the energy difference between the highest occupied molecule orbital (HOMO) and the lowest unoccupied molecule orbital (LUMO) in molecule-orbital theories.

[28] Roughly $\sim 40\,\%$ to call some approximative universal number.

[29] In some extreme cases, small-gap semiconductors as germanium, indium nitride, scandium nitride, or chalcopyrite compounds have even been unphysically characterized as metallic systems. [986, 1037–1040]

by the differences between the ground state energies of the $N-1$, N, and $N+1$ electron systems.

$$I(N) = E(N-1) - E(N) \tag{3.45}$$

$$A(N) = E(N) - E(N+1) \tag{3.46}$$

Unfortunately the calculation of electronic band gaps from energy differences between the Kohn-Sham groundstates $E^{KS}(N+1)$, $E^{KS}(N)$, and $E^{KS}(N-1)$ via

$$\begin{aligned} E_{gap} &= I(N) - A(N) \\ &= E(N+1) + E(N-1) - 2E(N) \end{aligned} \tag{3.47}$$

yields reasonable values for finite numbers of electron, only, e.g. atoms and molecules, but widely unsatisfactory results for extended systems exhibiting non-localized electrons as given in solid-state materials. [987, 1044]

The difference between the *exact* Kohn-Sham gap, given by Eq. (3.45), defined for the exact self-interaction-free exchange-correlation functional, and the *true* band gap, defined through Eq. (3.47), is given by the *derivative discontinuity* Δ_{XC} of the exchange-correlation functional $E_{XC}[n(\mathbf{r})]$ [1045–1048],

$$\Delta_{XC} = \lim_{\eta \to 0^+} \left\{ \left. \frac{\delta E_{XC}[n(\mathbf{r})]}{\delta n(\mathbf{r})} \right|_{N+\eta} - \left. \frac{\delta E_{XC}[n(\mathbf{r})]}{\delta n(\mathbf{r})} \right|_{N-\eta} \right\}. \tag{3.48}$$

Consequently, the exact energy gap E_{gap} is the sum of the exact Kohn-Sham gap and the exchange-correlation derivative discontinuity (cf. Fig. 3.1),

$$E_{gap} = E_{gap}^{KS} + \Delta_{XC}. \tag{3.49}$$

The presence of a derivative discontinuity in the total energy (see Fig. 3.2) and the exchange-correlation potential, respectively, has first been realized in the seminal Perdew-Parr-Levy-Balduz extension of density-functional theory towards non-integer particle numbers [1045] (also see Ref.[1036, 1049]). Instead of being a continuos function of the particle number N, the exchange-correlation potential *jumps* at integer electron numbers by a constant quantity, the derivative discontinuity, and the dependence of the total energy $E(n)$ on (fractional) electron numbers is characterized by a series of straight line segments ($\rightarrow$ piecewise linearity) [1045, 1050],

$$E_{N+\eta} = (1-\eta) E_N + \eta E_{N+1}. \tag{3.50}$$

The generalization towards fractional numbers of electrons further allows an alternative definition of the exact band gap E_{gap} by evaluation of total ground-state energy derivatives with respect to

the particle number. [1051, 1052] The *derivative gap* is defined through

$$E_{gap}^{der} = \lim_{\eta \to 0^+} \left\{ \left. \frac{\delta E_0 [n(\mathbf{r})]}{\delta n(\mathbf{r})} \right|_{N+\eta} - \left. \frac{\delta E_0 [n(\mathbf{r})]}{\delta n(\mathbf{r})} \right|_{N-\eta} \right\} + \Delta_{XC} \,. \tag{3.51}$$

In contrast to the Hartree and the external potential, which yield no derivative discontinuity, the kinetic-energy functional of non-interacting electrons shows a derivative discontinuity Δ_S [1053],

$$\Delta_S = \lim_{\eta \to 0^+} \left\{ \left. \frac{\delta T_S^{el} [n(\mathbf{r})]}{\delta n(\mathbf{r})} \right|_{N+\eta} - \left. \frac{\delta T_S^{el} [n(\mathbf{r})]}{\delta n(\mathbf{r})} \right|_{N-\eta} \right\} \equiv E_{gap}^{KS} \,. \tag{3.52}$$

Thus, the exact energy gap of the interacting system is given by the sum of the kinetic-energy functional derivative discontinuity, the Kohn-Sham gap respectively, and the exchange-correlation functional derivative discontinuity. [1043, 1051]

$$E_{gap} = \Delta_{KS} + \Delta_{XC} \equiv E_{gap}^{KS} + \Delta_{XC} \tag{3.53}$$

The functional form of standard exchange-correlation functionals (e.g. the local density approximation or semilocal generalized gradient approximations), defined through *simple* analytical expressions, do not allow the presence of any exchange-correlation derivative discontinuity (i.e. $\Delta_{XC} = 0$). Thus, conventional (semi)local exchange-correlation functionals yield a convex total-energy dependence on fractional occupation. In the previously mentioned Hartree-Fock theory, the presence of an exchange-correlation derivative $\Delta_{XC} < 0$ yields a concave dependence, while the exact total energy curve is linear with a positive derivative discontinuity $\Delta_{XC} > 0$. [1054] The incorrect convex dependence on fractional electron numbers is directly related to delocalization/localization errors of electronic charges observed in density-functional theory. [1055, 1056] Obviously, the underestimation of band gaps in Kohn-Sham theory has its origins in both, the approximative nature of commonly applied exchange-correlation functionals as well as the derivative discontinuity. An explicit example for the size of the derivative-discontinuity error of Kohn-Sham band gaps, Eq. 3.45, has been given by Godby et al. [1057]. The found band-gap underestimation for silicon in the local-density approximation to density-functional theory originates to $\sim 50\,\%$ from the derivative discontinuity. There are at least three major approaches to correct, more precisely circumvent, the problem of the missing derivative discontinuity. Namely, these are explicit self-interaction corrections (SICs) [1027, 1058–1061], the use of a generalized Kohn-Sham scheme [1062, 1063] whose *eigenvalue gap* naturally incorporates the exchange-correlation derivative discontinuity [30] and the application of, formally exact, many-body perturbation theory (see discussion below). Explicit, self-interaction corrections, namely the Hubbard-correction approach, known as (LDA)+U, [1060, 1061, 1064–1074] repre-

[30] The inclusion of the exchange-correlation derivative discontinuity is commonly neither universal nor complete within the generalized Kohn-Sham framework, but, at least, to a degree that substantially improves the description of electronic band gaps.

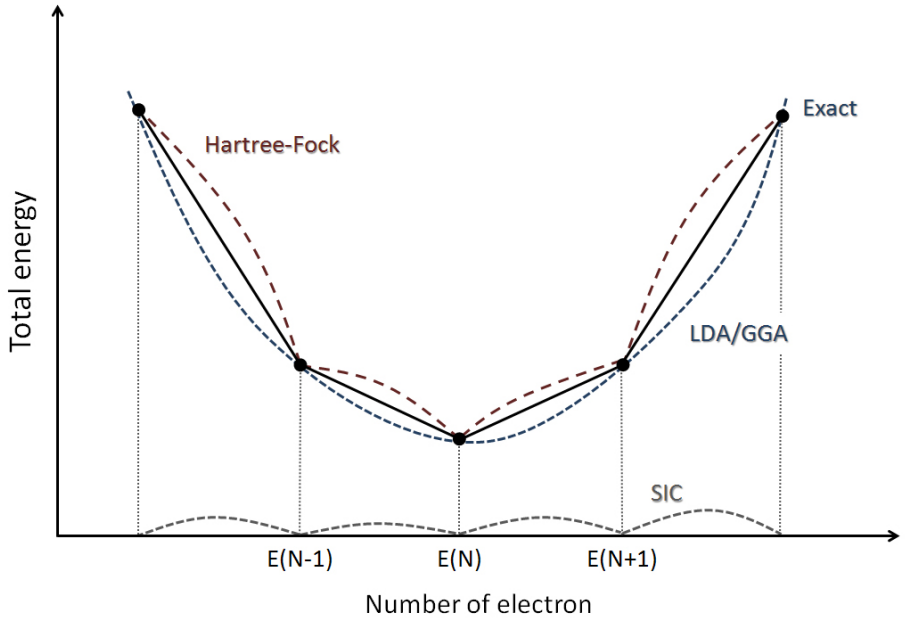

Figure 3.2: Illustration (reproduced and modified from Ref. [1064]) of the total energy dependence of the total Kohn-Sham groundstate energy on (fractional) electron numbers. Schematically shown are the convex, derivative-discontinuity-free Kohn-Sham total energy of conventional local density or generalized gradient approximations (LDA and GGA) [blue], the concave, derivative-discontinuous total energy of Hartree-Fock theory [red], the pairwise-linear exact total energy of the many-electron system [black], and a qualitative self-interaction correction (SIC) [gray]; .

sent pragmatical and phenomenological approaches to account for the unphysical delocalization of d and f-electrons [1052, 1075, 1076] as well as defect states [1052, 1077–1080] and for correcting the calculated Kohn-Sham orbital-energy differences. [1052, 1061, 1080–1082] The LDA+U approach found broad application due to its simple numerical implementation and *cheap* computation for solid-state systems. Alternative correction approaches are the well-known Perdew-Zunger self-energy correction [1027, 1083–1088], or the modified pseudopotential approach. [1089–1092] Interestingly, the connection [31] between self-interaction corrections and the derivative discontinuity is only made sporadically [32]. [1054, 1055, 1093, 1096] In the generalized Kohn-Sham (gKS) approach [1062, 1063, 1094] some contribution of Hartree-Fock-like exchange interaction (also labeled exact exchange) is incorporated into the exchange-correlation functional of Kohn-Sham theory defining the functional class of hybrid functionals. [25, 1097–1103] Incorporation of ex-

[31] The most apt quotation with respect to the connection between derivative discontinuity and the self-interaction correction approach has been given by Perdew. [1093] Actually, self-interaction corrections and the derivative discontinuity represent "doppelgänger" theories of each other, accounting for the same physical effects within different theoretical frameworks.

[32] The origin for this self-effacement might be that the idea of self-interaction is less obvious in a many-electron system than in an one-elctron system. In an one-electron system, the dependence of the Hartree term on the electron density generates an electron-electron repulsion, that is immediately recognized to be unphysical. In case of the H_2^+ molecule this leads to the well known delocalization error. [1055, 1056, 1094] In many-electron systems, self-energy contributions from the *density* of every electron will be present causing the convex dependence of the total energy on fractional electron charge (cf. Fig. 3.2). [1055, 1095]

act exchange introduces a notable correction of the exchange contribution to the derivative discontinuity or, in view of a self-interaction correction, leads to a more complete cancellation of self-interactions in the Hartree term. Since, the Hartree-Fock exchange is a non-local orbital-denendent functional rather than a local functional of electron density, the single-particle orbital energies of generalized Kohn-Sham theory already *carry* partial information on the derivative discontinuity [1063] allowing a more accurate approximation of electronic band gaps by a simple difference of generalized Kohn-Sham eigenvalues,

$$\varepsilon_{gap}^{gKS} = \varepsilon_{N+1}^{gKS}(N) - \varepsilon_{N}^{gKS}(N) \approx E_{gap}\,. \tag{3.54}$$

Obviously, the admixture of exact exchange does not represent a purely phenomenological correction, justified by contrariwise band-gap errors. In fact, the concave dependence on fractional electron numbers makes the exact-exchange interaction the natural ingredient to compensate for the convex total-energy dependence observed in conventional, self-interaction affected, density-functional theory. [1054] A formally accurate treatment of electronic band gaps, and band structures in general, can be achieved within the quasiparticle framework of many-body perturbation theory by thorough evaluation of the electron *self-energy*, which is free of spurious self-interactions[33] (see discussion below). [1104]

3.3 Exchange-correlation functionals

A Ladder to Heaven – The need for finding an approximation to the exchange-correlation functional has led to the development of a tremendous number of different exchange-correlation functionals. Inspired by the Jacob's-Ladder allegory of the old testament, Perdew and Schmidt [1105] proposed a ladder-like classification scheme for exchange-correlation functionals bridging the simplistic uncorrelated Hartree world [1106] towards the heavenly realm of fully-correlated chemical accuracy[34]. Perdew and Schmidt identified five rungs on the Jacob's-Ladder of density-functional theory, namely the *local* density approximation, the *semilocal* rungs of generalized gradient and meta-generalized gradient approximations, and the two *non-local* rungs of hyper- and complete-generalized gradient approximations[35] (cf. Fig. 3.3). As noted by the authors themselves, the five rung scheme is a simplified and not necessarily complete scheme that might be extended (e.g. see Ref. [1107]) to account explicitly for further (sub)classes of exchange-correlation functionals. [1108] Indeed, the given ladder classification is widely influenced by the

[33] The absence of self-interaction strictly applies only in case of the exact many-body self energy. The correlation part of the commonly utilized *GW* self-energy is not fundamentally free of spurious self-interactions.

[34] The definition of chemical accuracy is that energy errors do not exceed 1 kcal/mol $\widehat{=}$ 0.043363 eV, which is commonly viewed as the accuracy needed to predict the rate of chemical reactions. [1105]

[35] Whereas the term hyper-generalized gradient approximation has been used, explicitly, the name *complete* generalized-gradient approximation is a self-coined term in order to fit the rung nomenclature and to indicate that on the fifth rung information from all Kohn-Sham orbitals is explicitly used to evaluate a more *complete* correlation energy. Formally, all fundamental ingredients to an *exact* treatment of exchange-correlation are assembled.

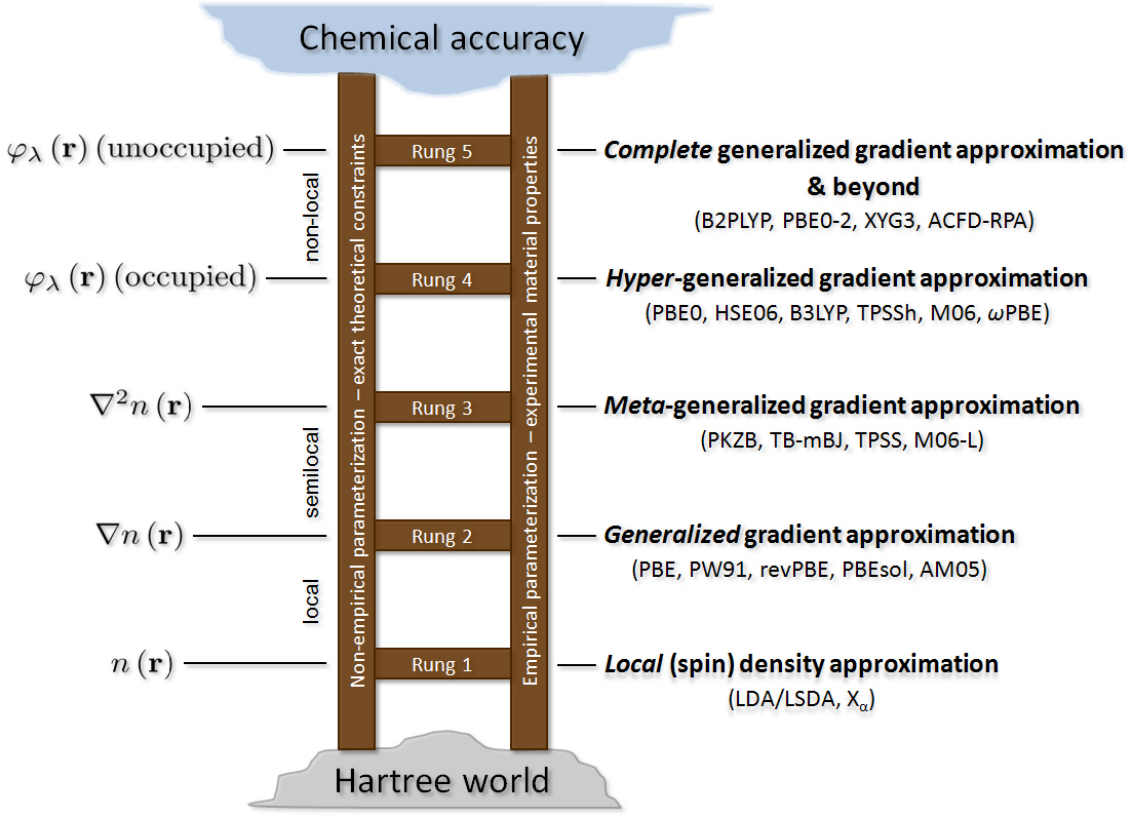

Figure 3.3: Schematic illustration of the Jacob's-Ladder allegory, following Perdew and Schmidt [1105], for the classification of exchange-correlation density functionals. The presented rung nomenclature is slightly modified with respect to the original definition in Ref. [1105].

authors' *reductionistic* and partially *idealistic* view on a systematic and constraints-driven construction of exchange-correlation functionals to (generalized) Kohn-Sham density-functional theory, which is expressed in several publications of Perdew and Coworkers. [1108–1118] Thereby, each rung is not only defined by its ingredients, but also by the exact constraints that can be fulfilled at a particular rung. Not all known exact constraints are intended to be satisfied at each rung of the ladder. *Climbing the ladder* has become a very common workflow outline of practical calculations on material properties (e.g. see Ref. [1119]). Thereby, the well known prospects and limitations of each rung allow some systematics in the study of material properties and an estimation of *missing physics* if higher rungs are locked by computational demands.

3.3.1 Rung 1 – Local-density approximation

LDA – Before climbing to precarious ladder heights, the first rung of exchange-correlation approximations is enviably simple. The single fundamental requirement to a first rung functional, the most basic density functional in general, is an accurate representation of the exchange-correlation energy of an uniform/homogenous electron gas (HEG), *jellium* respectively. [2, 1120] Considering

the inhomogenous electron system as a locally homogenous entity by assuming [1121]

$$\epsilon_{xc}^{LDA}\left(n\left(\mathbf{r}\right)\right) \approx \epsilon_{xc}^{HEG}\left(n\right)\big|_{n=n(\mathbf{r})}\,, \tag{3.55}$$

the corresponding exchange-correlation energy functional, in *local-density approximation*, is given by

$$E_{xc}^{LDA}\left[n\left(\mathbf{r}\right)\right] = \int n\left(\mathbf{r}\right)\epsilon_{xc}^{HEG}\left(n\left(\mathbf{r}\right)\right)\mathrm{d}^3\mathbf{r}\,. \tag{3.56}$$

Here, $\epsilon_{xc}^{HEG} = \epsilon_{x}^{HEG} + \epsilon_{c}^{HEG}$ is the exchange-correlation energie per electron of a uniform electron gas at the density $n\left(\mathbf{r}\right)$. In the absence of an external magnetic field, $E_{xc}^{LDA}\left[n\right]$ is a functional of the total electron density $n\left(\mathbf{r}\right)$. The exchange energy per electron in local-density approximation is given by Dirac's expression for exact exchange [1122] , the Hartree-Fock exchange energy of a homogenous non-spin-polarized electron gas [1123],

$$\epsilon_{x}^{LDA}\left(n\left(\mathbf{r}\right)\right) \equiv \epsilon_{x}^{HEG} = -\frac{3}{4}\frac{e^2}{4\pi\varepsilon_0}\left(\frac{3}{\pi}\right)^{\frac{2}{3}} n^{\frac{1}{3}}\left(\mathbf{r}\right)\,. \tag{3.57}$$

The correlation energy of the spin-polarized and non-spin-polarized homogenous electron gas has been determined by Perdew and Zunger [1027] through parametrization of quantum Monte Carlo simulation results by Ceperley and Alder [1124] for the ground-state correlation energy of the electron gas. Am alternative, and frequently used parametrization has been derived by Vosko, Wilk, and Nusair (VWN). [1125] The generalization towards spin-polarized densities is the subject of the local spin density approximation (LSDA). [993, 1121, 1126, 1127] Even so the jellium is "not a real system" [1120], it represents an excellent model density to approximate slowly varying electron densities of metals. Surprisingly, in many cases the local-density approximation also represents a reasonable approximation to bulk materials and surfaces of non-metallic systems. However, the trend to more uniform/homogenous electron densities leads to some well known side-effects in local-density approximation. Atoms and localized states are less accurately described due to incomplete self-interaction canceling, in general. [1128, 1129] For weakly bonded systems, the more homogenous electron distribution, the overbinding respectively, in local-density approximation partially improves [36] the description of cohesive energies and lattice constants of metallic systems, molecular crystals, and organic frameworks as well as physisorption on metallic substrates, compared to van-der-Waals-uncorrected second rung functionals [37]. In contrast, also a bond-strength overcompensation due to the local-density-approximation-inherent overbinding in observed for other weakly van-der-Waals- or hydrogen-bonded systems. [1134–1137] Sporadically, numerical studies on various systems indicate that the local-density approximation might compete with second rung functionals for description of vibrational or thermodynamical properties. [1138] As discussed repeatedly, the band gaps of the majority of semiconductors and insu-

[36] Probably "fortuitous error cancelation" [985, 1130] is an accurate description of the observed trends.

[37] See Ref. [1131] for graphene absorption on metal surfaces, Ref. [1132] for graphene, or Ref. [1133] for soft layered materials, exemplarily.

lators is dramatically underestimated, thus, the local-density approximation to density-functional theory is *useless* for an comprehensive quantitative evaluation of spectroscopic properties.

3.3.2 Rung 2 – Generalized gradient approximations

While the uniform electron gas represents a well defined model system leading to a single functional, the situation changes at the generalized gradient approximation (GGA) rung of exchange-correlation functionals. The totality of generalized gradient approximations to the exchange-correlation energy fragments into a manyfold of diverse functional types and forms with individual parametrizations in order to meet the requirements of different constraint subclasses. The feature, inherent to all second rung functionals, is the use of some kind of density gradients to evaluate the exchange-correlation energy. The gradient-corrected exchange-correlation functionals used today are widely based on the functional development that is associated with the work of John P. Perdew and several of his collaborators and coworkers. [1139–1147] The basic form of generalized gradient approximations to the exchange-correlation energy (e.g. see Ref. [1120]) is given by

$$\begin{aligned} E_{xc}^{GGA}[n(\mathbf{r})] &= \int n(\mathbf{r})\,\epsilon_x^{GGA}(n(\mathbf{r}),\nabla n(\mathbf{r}))\,\mathrm{d}^3\mathbf{r} \\ &= \int n(\mathbf{r})\,\epsilon_x^{HEG}(n(\mathbf{r}))\,F_{xc}^{GGA}(n(\mathbf{r}),s)\,\mathrm{d}^3\mathbf{r}, \end{aligned} \tag{3.58}$$

where

$$F_{xc}^{GGA}(n,s) = F_x^{GGA}(s) + F_c^{GGA}(n,s) \tag{3.59}$$

is an enhancement factor/function over the uniform electron-gas exchange due to electron correlation and s is the dimensionless reduced density gradient

$$s = \frac{|\nabla n|}{2(3\pi^2)^{1/3} n^{4/3}}\,. \tag{3.60}$$

The actual functional construction, thus, requires finding a suitable formal expressions for $F_{xc}^{GGA}(n,s)$ which is, as stated above, far from unique. Thereby, the set of fulfilled constraints defines the actual mathmatical form and parametrization, so to speak the *flavor*, of a particular generalized-gradient functional.

PBE – Probably the most relevant second rung functional, developed on basis of the PW91 exchange-correlation functional [1142, 1148, 1149], has been proposed by Perdew-Burke-Ernzerhof (PBE). [1146] PBE is essentially *free* of any empirical parameters, provides properties very similar to the preceding PW91, and forms a well defined basis for the construction of the higher rung functionals discussed below. The PBE enhancement function to the exchange contri-

bution depends only on the reduced density gradient s and is defined through

$$F_x^{PBE}(s) = 1 + \kappa - \frac{\kappa}{1 + \frac{\mu s^2}{\kappa}}, \tag{3.61}$$

with $\kappa = 0.804$ and $\mu = 0.235$. [1146] This form of $F_x(s)$ was originally introduced by Becke [1150] in his empirically parametrized B86 exchange functional [38]. The correlation contribution to the exchange-correlation energy in PBE follows the PW91 construction [39]. [987, 1146] According to other satisfied constraints, several modifications and reparametrizations of the PBE exchange-correlation functional as revised PBE (revPBE) [1155], an alternative version of revPBE (RPBE) [1156], modified PBE (mPBE) [1157], PBEα [1158], Wu-Cohen (WC) [1159], and a PBE-PBEsol interpolating functional (PBEint) [1160] have been developed over time. In general, the inclusion of gradient corrections allows all generalized-gradient functionals a more flexible and accurate representation of rapidly varying inhomogenities in the electron density than provided by the local-density approximation allowing a more accurate and universal description of structural properties [1158], atomization energies [1146], reaction barriers [1161], and chemisorption energies [1156] over a wide range of materials.

AM05 AND PBESOL – Notable improvements over typical generalized-gradient approximations (typically PBE or PW91 in solid state physics) in the structural characterization of various types of solids have been made by the two recently proposed functionals AM05 and PBEsol. While the construction of most density functionals basically references the homogenous electron gas only, the functional constructions of AM05 follows a subsystem division scheme accounting for the fact that real materials have *electronic edge regions*, where the character of the electronic wave functions change from oscillatory to exponentially decaying. The idea of subsystem division and an "edge electron gas" as a basis for the evaluation of the exchange-correlation energy has originally been introduced by Kohn and Mattsson [1162, 1163] in order to characterize systems consisting of more homogeneous interior/core regions and edge/surface regions. However, the subsystem approach might be extended to a general decomposition scheme into regions dominated by different density/interaction characteristics and application of local subsystem-specific approximations within these subspaces. [1164] The AM05 functional has been formalized by Armiento and Mattsson [1165] and is essentially an non-empirical generalized-gradient subsystem functional combining bulk-like local contributions, derived from the homogenous electron gas, and surface-like local contributions, derived from the Airy gas [1162, 1166] combined with

[38] The gradient-corrected B86 exchange functional was subsequently modified by Becke into the prominent B88 exchange functional. [1151, 1152] The B88 functional has become the leading exchange contribution to the BLYP/B3LYP [1103, 1153] branch of exchange-correlation functionals, where it is combined with the Lee-Yang-Parr (LYP) correlation energy. [1141, 1154] In practical calculations the B88 exchange functional was found to perform quite similar to the PW91 and the earlier PW86 [1140] exchange functionals. [1147]

[39] The correlation part of PW91 was derived as a complex, maximum number of constrains fulfilling, analytic refit [1148] of the numerical quantum Monte Carlo data of Ceperley and Alder [1124].

the jellium surface. [1167] The AM05 exchange-correlation density functional

$$\epsilon_{xc}^{AM05}(n,|\nabla n|) = \epsilon_c^{LAA}(n,|\nabla n|) + \epsilon_c^{LAA},|\nabla n| \tag{3.62}$$

contains the weighted contributions from bulk and surface electron-gas subsystems.

While AM05 was constructed from this subsystem approach, PBEsol is considered as "restoration of the first-principles gradient expansion for exchange". [1168] The AM05 functional provides tremendously accurate lattice parameters that even surpass several fourth's rung hybrid functionals to the computational cost of conventional semilocal density-functional theory. [1167] Interestingly, AM05 and PBEsol yield virtually "identical results for a wide range of solids" [1169] encompassing oxides, common III-V semiconductors, and transition metals [40]. [1170–1172] In general, PBEsol is repeatedly found to be similar but slightly more accurate than AM05. [1132, 1173–1175] Similar to AM05, also PBEsol is a generalized gradient-level functional constructed with the intend of an accurate description of the jellium surface. Despite the fundamental, but to a large degree non-systematic improvements over the local-density approximation, two basic limitations of exchange-correlation functionals are not *cured* by stepping onto the second ladder rung, irrespectively of the functional flavor of choice. On the one side, weak dispersion interactions, van der Waals forces respectively, are not represented accurately. Even though, dispersion corrections to generalized-gradient functionals are essential for an accurate modeling of, e.g., biological systems or layered materials. [1174, 1176] The other limitation is the persisting underestimation of electronic band gaps.

3.3.3 Rung 3 – Meta-generalized gradient approximations

The additionally added component to meta-generalized gradient functionals, that elevates a generalized gradient approximation to the third ladder rung, is the kinetic energy density [41]

$$\tau_{m_s}(\mathbf{r}) = \frac{1}{2}\sum_{\lambda} n_{\lambda,m_s} \left|\nabla\varphi_{\lambda,m_s}(\mathbf{r})\right|^2 . \tag{3.63}$$

Thus, a meta-generalized gradient (MGGA) functional is formally defined through

$$E_{xc}^{MGGA}[n(\mathbf{r})] = \int n(\mathbf{r})\,\epsilon_x^{MGGA}(n(\mathbf{r}),\nabla n(\mathbf{r}),\tau(\mathbf{r}))\,\mathrm{d}^3\mathbf{r}. \tag{3.64}$$

The semilocal meta-generalized gradient exchange-correlation functionals might be seen as the highest rung of sophistication before entering the computationally expensive field of nonlocality. [1105] Similar to the local-density and generalized-gradient approximations as well as the Dirac exchange, corrections based on the kinetic energy density find its roots in the Thomas-Fermi-Dirac-Weizsäcker theory, more precisely Weizsäcker's inhomogenity correction [1177, 1178] to

[40] Although, the reason for this similarity has been discussed controversially. [1168, 1169]
[41] And/or higher order density gradients, in general.

the kinetic energy in classical density-functional theory. [42] Early exchange-correlation functionals of the meta-generalizedgradient-type, historically preceding most of the prominent second rung generalized gradient functionals [1179], have been proposed in Ref. [1180, 1181].

PKZB, TPSS, AND CO. – Perdew, Kurth, Zupan, and Blaha (PKZB) [1179] constructed a meta-generalized gradient functional whose exchange component recovers the fourth-order gradient expansion. The PKZB exchange functional

$$E_x^{MGGA}[n(\mathbf{r})] = \int n(\mathbf{r})\,\epsilon_x^{HEG}(n(\mathbf{r}))\,F_x^{PKZB}(n(\mathbf{r}),\nabla n(\mathbf{r}),\tau(\mathbf{r}))\,\mathrm{d}^3\mathbf{r} \tag{3.65}$$

is defined through a fourth-order gradient expansion to the exchange-enhancement factor $F_x^{PKZB}(n,\nabla n,\tau)$ for slowly varying densities. [1182] The correlation energy is given as a fourth order self-interation-free functional.

Starting from the one-empirical parameter meta-generalized gradient functional PKZB, Tao, Perdew, Staroverov, and Scuseria [1183] constructed the non-empirical parameter free TPSS exchange-correlation functional. The TPSS exchange energy is taken in PKZB form featuring a modified PKZB exchange enhancement factor and a revised PKZB correlation energy. In addition, a revised form of TPSS, revTPSS, has been proposed recently [1184] showing an accuracy for lattice parameters on a par with the second rung functionals PBEsol and AM05. Several further meta-generalized gradient exchange-correlation functional forms (amongst others FT97 [1185],VS98 [1186], KCIS [1187], Bmτ1 [1187], M06-L [1188]) have been proposed in literature. A comparison of different meta-generalized gradient functionals for various material/system properties by Kurth at al. [1187] indicates that PKZB improves "rather consistently" over the second rung PBE functional. However, aside from constraint satisfactions, it seems difficult to categorize the general advancements and deficiencies of meta-generalized gradient approximations against second and fourth rung functionals, whose improvements over lower rung functionals in the description of real physical properties is much more emergent.

3.3.4 Rung 4 – Hyper-generalized gradient approximations

The essence of the fourth rung of exchange-correlation functionals is the introduction of nonlocality and orbital-dependence through the use of exact-exchange. As stated above, the resulting generalized Kohn-Sham framework [1062, 1189] is suited to correct basic shortcomings of conventional semilocal or even meta-generalized gradient exchange-correlation approximations arising from the self-interaction error, the missing derivative discontinuity respectively.

EXX – In general, the exchange-correlation energy in a global hybrid (gh) functional is composed according to

$$E_{xc}^{gh} = \alpha E_x^{EXX} + (1-\alpha)\,E_x^{(M)GGA} + E_c^{(M)GGA}\,. \tag{3.66}$$

[42] An excellent review on early density-functional theory is provide within the book of Parr and Yang on "Density-Functional Theory of Atoms and Molecules" (see Ref. [984]).

Here, E_x^{EXX} is the fraction of *added* Hartree-Fock-type exact-exchange interaction, while $E_x^{(M)GGA}$ and $E_c^{(M)GGA}$ represent the maintained exchange and correlation contributions from either second rung semilocal or third rung meta-generalized gradient exchange and correlation energies, respectively. The exact-exchange contribution is calculated according to

$$E_x^{EXX} = -\frac{e^2}{2}\sum_{\lambda,\lambda'} n_\lambda n_{\lambda'} \int\int \frac{\varphi_\lambda^*(\mathbf{r})\,\varphi_{\lambda'}^*(\mathbf{r}')\,\varphi_\lambda(\mathbf{r}')\,\varphi_{\lambda'}(\mathbf{r})}{|\mathbf{r}-\mathbf{r}'|} \mathrm{d}^3\mathbf{r}\,\mathrm{d}^3\mathbf{r}' \tag{3.67}$$

from the (occupied) Kohn-Sham orbitals $\{\varphi_\lambda(\mathbf{r})\}$.

B3LYP, PBE0 AND CO. – The idea of using exact-exchange in the construction of exchange-correlation functionals has first been introduced by Becke [1098] on basis of the adiabatic connection formula leading to Becke's *half-and-half* functional[43] and the denotation *hybrid* functional. Shortly after, the "formal structure" [1103] of global hybrid functionals, Eq. 3.66, was introduced in the construction of the B3PW91 functional[44]. [1097] Later on, Becke's B3PW91 exchange-correlation functional was modified into the prominent B3LYP functional[45] [1099], one of the most used exchange-correlation density functionals in molecular quantum chemistry. Despite its popularity for molecular systems the application to extended systems is quite limited[46]. [1103, 1192–1195] Both B3PW91 and B3LYP are constructed by combining diverse functional contributions in a semiempirical fashion.

The different philosophy of reductionism underlies the construction of the *parameter-free* global hybrid functional PBE0. [1109, 1196, 1197] PBE0, the prototypical global hybrid, *simply* combines a 25 % fraction of exact exchange (rationalized by theoretical considerations [1109]) with PBE quantities according to

$$E_{xc}^{PBE0} = 0.25E_x^{EXX} + 0.75E_x^{PBE} + E_c^{PBE}\,. \tag{3.68}$$

Overall the PBE0 exchange-correlation functional was found to be "slightly more reliable" than B3LYP for molecular systems. [1196] PBE0 also provides very accurate lattice constants and bulk moduli. [1198] A common limitation to the application of global exact-exchange functionals to

[43] Becke's half-and-half functional is essentially constructed as a "exact-exchange-plus-LSDA-correlation"-hybrid ($E_{xc}^{B_{h\&h}} = E_x^{EXX} + E_c^{LSDA}$). [1098]

[44] The B3PW91 exchange-correlation functional combines Becke's three parameter (B3) functional [1097] with Becke's B88 gradient correction to LSDA exchange [1151], and Perdew's and Wang's gradient correction to correlation via $E_{xc}^{B3PW91} = E_{xc}^{LSDA} + 0.20\left(E_x^{EXX} - E_x^{LSDA}\right) + 0.72\Delta E_x^{B_{88}} + 0.81\Delta E_c^{PW91}$. [1144]

[45] The B3LYP functional combines the B3 functional with the Lee-Yang-Parr (LYP) correlation functional [1141, 1154] according to $E_{xc}^{B3LYP} = E_{xc}^{LSDA} + 0.20\left(E_x^{EXX} - E_x^{LSDA}\right) + 0.72\Delta E_x^{B_{88}} + 0.19\Delta E_c^{VWN3} + 0.81\Delta E_c^{LYP}$. [1103, 1153] The Vosko, Wilk and Nusair (VWN) correlation [1125] is added to balance local and non-local correlation contributions due to the use of the LYP functional. Some inconsistencies in the reference to B3LYP and its practical implementation originate from different parametrizations of the VWN correlation energy (see Ref. [1153]).

[46] The quite recent implementation of the B3LYP functional for periodic plane-wave calculations into the VASP code [1190, 1191] has been systematically tested for applicability to solids. Since B3LYP has not been designed to provide an accurate description of the homogenous electron gas, the performance of B3LYP for atomization energies and other physical properties of metals has been characterized as "embarrassingly bad" and inferior to conceptually simpler generalized gradient approximations as PBE. [1103]

extended systems is the substantial increase in computational resources needed to evaluated the additional exact-exchange contributions for these systems. [47].

HSE – The recent success of hybrid-functional-based density-functional theory is widely due to the use of range-separated Heyd-Scuseria-Ernzerhof (HSE) hybrid functionals [25, 1100–1102], that restrict the inclusion of exact (Fock) exchange, E_X^{EXX}, to short-range contributions [48]. The long-range exchange interaction and the correlation energy E_c remain unchanged with respect to the PBE functional [49] (E_X^{PBE} and E_C^{PBE}), hence, a HSE-type functional exhibits the form

$$E_{XC}^{HSE} = \alpha E_X^{EXX,sr}(\mu) + (1-\alpha) E_X^{PBE,sr}(\mu) + E_X^{PBE,lr}(\mu) + E_C^{PBE}. \tag{3.69}$$

Thereby, the range separation into long-range (lr) and short-range (sr) parts of E_X^{EXX} is carried out by a decomposition of the Coulomb kernel according to

$$\frac{1}{r} = \underbrace{\frac{erfc(\mu r)}{r}}_{sr} + \underbrace{\frac{erf(\mu r)}{r}}_{lr}. \tag{3.70}$$

A 25 % fraction of exact exchange ($\alpha = 0.25$) and a screening parameter of μ =0.2 Å^{-1} define the HSE06 exchange-correlation functional [50]. [25, 1100, 1102, 1202] However, since a fixed amount of exact exchange and a non-variable screening limit the flexibility of the HSE06 functional, it is a common practice to sacrifice the essence of ab initio theory by searching material optimized parameter values instead of rationalizing them from theoretical considerations. Recently, Skone et al. [1203] proposed a self-consistent optimization scheme for determining the exact-exchange fractions in global hybrid functionals by setting the exact-exchange mixing parameter equal to the inverse macroscopic dielectric function and finding an optimal dielectric screening by iteration for self-consistency. A systematic investigation of the two-parameter space [51] (exchange fraction α and screening parameter μ) of HSE-type functionals has been published by Moussa et al. . [1204] Using various molecular and bulk-solid test sets, a "modest improvement" over HSE06 (labeled HSE12) has been found for the parameter set $\alpha = 0.313$ and μ =0.185 Å^{-1}. Also, the accuracy of HSE06 might be enhanced for an increased exact-exchange fraction ($\alpha = 0.425$) at reduced screening length (μ =0.408 Å^{-1}). The use of range-separated HSE-type hybrid function-

[47] The increase in computing time could be estimated to be roughly two orders of magnitude compared to semilocal density functionals. This massive increase is widely owned to the evaluation of a double-summation over **k**-points in the exact-exchange formula for periodic solid-state systems.

[48] First attempts in combining a non-local screened-exchange potential with conventional local density ingredients, known as sx-LDA [1062, 1199], has been proposed by Bylander and Kleinman. [1200]

[49] In order to improve the HSE06 performance for solids, also the PBE contributions in HSE06 have recently been replaced by the PBEsol functional. [1201] This new HSEsol functional provides an improved description of lattice constants and atomization energies of solids at the cost of a slightly worse accuracy for molecular systems.

[50] The use of a slightly different screening parameter in the *HSE03 functional* originates from an inaccurately quoted screening parameter in Ref. [1100]. [1102]

[51] An evaluation of the two-dimensional (μ,α)-parameter space of HSE functionals naturally encompasses the PBE and the PBE0 functionals, which are included as the limiting cases $\mu = \rightarrow \infty$ and $\mu = 0$, respectively.

als is commonly preferred over the global PBE0 hybrid functional[52]. The problem of finding an adequate range-separation is highly non-trivial in light of different requirements for molecular systems and solids. While long-range corrected hybrid functionals as LC-ωPBE [1024, 1205] provide a "remarkable" accuracy for diverse properties of molecular systems such as thermochemistry, barrier heights, and long-range charge transfer [1205], the short-range corrected HSE06 exchange-correlation functional accurately describes small-gap semiconductors and, partially, also metals[53]. [25] Therefore, a more elaborate range-separation scheme into short-, medium-, and long-range contributions and the exclusive use of medium-range exact-exchange contributions has been proposed in form of the Henderson-Izmaylov-Scuseria-Savin (HISS) functional. [1206–1208] A further generalization of the hybrid-functional approach might be given by *local* hybrid functionals, that effectively use different linear combinations of exact-exchange interaction and conventional semilocal generalized-gradient contributions at each point in space through a weighting function, e.g. determined from the ratio of the kinetic energy density of the real system and the uniform electron gas. [1108, 1209–1211] Also, the combination of exact-exchange with meta-generalized gradient functionals has generated a number of global as well as range separated hybrid-meta-generalized gradient functionals as several representatives of the Minnesota-functional family (M05, M05-2x, M06, M06-2x, M06-HF M08-HX, M11) [1212–1215] or the TPSS based hybrid functional TPSSh. [1216]

Despite the undeniable advances of fourth rung exchange-correlation functionals in the characterization of diverse material properties, most current hybrid functionals are "... unavoidably empirical" [1115], ultimately, even in consideration of a rationale for mixing a sizable exact-exchange interaction fraction of $\sim$25 % derived from Görling-Levy coupling-constant perturbation theory. [1109, 1217] While a 25 % or close fraction of exact-exchange might, in general, be obtained in empirical from by fitting to molecule-data sets, as done by Becke for B3LYP, several physical properties of solids require enhanced fractions of exact exchange to be adequately reproduced in numerical simulations. Especially, the application of screened hybrid functionals tends to underestimate band gaps of wide-gap semiconductors and insulators[54]. Nevertheless, the use of HSE-type hybrid functionals has shown significant improvements in the description of electronic band gaps and lattice parameters [75, 1101, 1198, 1218, 1219], band offsets [33, 309, 1220], defect levels [334, 1221–1223], and the prediction of accurate direct-indirect band-gap crossovers [33, 1220], in recent past. However, the accuracy gain in hybrid-functional-based density-functional theory increases the computational cost by roughly two orders of magnitude compared to conventional (semi)local density-functional theory (cf. Fig. 3.4).

[52] In plane-wave codes as VASP, the reduction of the screening length allows a more efficient numerical treatment due to a possible down-sampling of the **k**-point mesh for Brillouin-zone integration in the exact-exchange contribution. [1198, 1204]

[53] Hybrid functionals can not systematically improve the description of metallic systems compared to the most accurate semilocal functionals, in general. [1198]

[54] Adjusting the exact-exchange fraction to allow an accurate description of the electronic structure, in particular band gaps, of semiconductors is a problem occurring in the various publications contributing to the present thesis, repeatedly.

3.3.5 Rung 5 – Complete-generalized gradient approximations

At the fifth ladder rung exact (partial) correlation [55] joins the exact exchange of fourth rung hybrid functionals in form of a nonlocal functional of *all* [56] Kohn-Sham orbitals. [1105]

ADIABATIC CONNECTION – Using the adiabatic connection (or coupling constant integration) formula [1105, 1109, 1110, 1217, 1224, 1225], the exchange-correlation energy might be written as

$$E_{xc}[n] = \int_0^1 U_{xc}^{\lambda} \, \mathrm{d}\lambda \, . \tag{3.71}$$

The integrand $U_{xc,\lambda}$ is the exchange-correlation potential energy at intermediate coupling strength λ. [1098, 1105, 1110] The coupling constant λ represents a descriptor of the interelectronic interaction strength and connects the non-interacting ($\lambda = 0$) Kohn-Sham reference system with the *fully* interacting ($\lambda = 1$) many-electron system by continuously "switching on" the Coulomb repulsion between the electrons. [1098] At fixed density, the potential energy $U_{xc,\lambda}$ might be expanded in a perturbation series according to

$$\begin{aligned} U_{xc}^{\lambda} &= U_{xc}^{0} + \left.\frac{\partial U_{xc}^{\lambda}}{\partial \lambda}\right|_{\lambda=0} + \ldots \\ &= E_x^{EXX} + 2E_c^{GL2}\lambda + \ldots \, . \end{aligned} \tag{3.72}$$

U_{xc}^{0} of the non–interacting reference system obviously represents the antisymmetric exact-exchange energy [57]. E_c^{GL2} is the Görling-Levy second-order correlation energy, consisting of a double-excited second order perturbation theory contribution, E_c^{PT2}, and a non-vanishing contribution, $E_c^{\Delta HF}$, from single excitation integrals. [1226, 1227]

$$\begin{aligned} E_c^{GL2} &= E_c^{PT2} + E_c^{\Delta HF} \\ &= \frac{1}{4} \sum_{\lambda\lambda',\Lambda\Lambda'} \frac{|\langle \lambda\lambda' \| \Lambda\Lambda' \rangle|^2}{\varepsilon_\lambda + \varepsilon_{\lambda'} - \varepsilon_\Lambda - \varepsilon_{\Lambda'}} + \sum_{\lambda,\Lambda} \frac{\left|\left\langle \lambda \left| V_x^{KS} - V_x^{EXX} \right| \Lambda \right\rangle\right|^2}{\varepsilon_\lambda - \varepsilon_\Lambda} \, , \end{aligned} \tag{3.73}$$

where $\langle \lambda\lambda' \| \Lambda\Lambda' \rangle = \langle \lambda\lambda' | \Lambda\Lambda' \rangle - \langle \lambda\lambda' | \Lambda'\Lambda \rangle$ is an antisymmetrized two-electron integral (e.g. see Ref. [1018]). The regular two-electron integrals itself have the form

$$\left\langle \lambda\lambda' \mid \Lambda\Lambda' \right\rangle = \int\int \frac{\varphi_\lambda^*(\mathbf{r}) \, \varphi_{\lambda'}^*(\mathbf{r}') \, \varphi_\Lambda(\mathbf{r}') \, \varphi_{\Lambda'}(\mathbf{r})}{|\mathbf{r} - \mathbf{r}'|} \mathrm{d}^3\mathbf{r} \, \mathrm{d}^3\mathbf{r}' \, , \tag{3.74}$$

[55] More precisely, the essential new ingredient is the long-range part of exact correlation. Short-range correlation might actually approximated with sufficient accuracy using lower rung functionals.

[56] In fact, it can be shown that the formally complete methodological *gold standard* of quantum chemistry, full configuration interaction (CI) can be written as a functional of all, occupied as well as unoccupied/virtual, Kohn-Sham states. [1016]

[57] This is the exact-exchange contribution of fourth-rung hybrid functionals, the Hartree-Fock exchange calculated from the single-particle orbitals of the Kohn-Sham determinantal wave function, respectively.

where the indices λ and λ' refer to occupied Kohn-Sham states and Λ and Λ' to unoccupied virtual states. The single excitation integrals $E_c^{\Delta HF}$ are determined through the difference between the local multiplicative exchange potential, V_x^{KS}, of the Kohn-Sham hamiltonian and the non-local non-multiplicative exact-exchange-like (Hartree-Fock) potential, V_x^{EXX}. [934] E_c^{PT2} is essentially a second order Møller-Plesset (MP2) perturbation correction [1228] evaluated using *all* Kohn-Sham orbitals. In general, fifth rung partial correlation is defined by evaluating one or more of the non-local terms in Eq. (3.72), or an infinite sub-series of the expansion, exactly. [1105]

DOUBLE HYBRIDS – Incorporating a fraction of perturbative second-order correlation into an exchange-correlation functional, in the way done before for exact exchange, defines the class of fully non-local fifth rung *double-hybride* functionals. The common two-parameter double-hybrid form

$$E_{xc}^{dh,MP2} = \alpha_x E_x^{EXX} + (1-\alpha_x)\, E_x^{(m)GGA} + \alpha_c E_c^{MP2} + (1-\alpha_c)\, E_c^{(m)GGA}\,, \tag{3.75}$$

proposed by Grimme [58] [1226], allows a systematic, but empirical, weighting of the exact non-local contributions to exchange and correlation. Typically, all lower rung ingredients of a double hybrid are evaluated in the traditional self-consistent scheme, while the computationally very expensive second-order correlation is calculated non-self-consistently form the hybrid-functional orbitals of the generalized Kohn-Sham scheme. [1231] Several double-hybrid *flavors* have been proposed so far, most either based on the semiempirical LYP/B3LYP hybrid-functional branch (B2PLYP [1226], B2GP-PLYP [1232], and mPW2-PLYP [1233]) or derived from the *parameter-free* PBE/PBE0 branch of hybrid functionals (PBE0-DH[1234], PBE0-2 [1235], and xDH-PBE0 [1236]). Studies on the performance of various double-hybrid functionals for molecular systems are given in Ref. [1231, 1237, 1238]. Compared to conventional global and range-separated hybrid functionals, the exact-exchange fractions of double-hybrid functionals are much higher. Characteristic fractions of exact-exchange and exact-correlation are $a_x^{B2PLYP} = 0.53$ and $a_c^{B2PLYP} = 0.27$ in the B2PLYP double hybrid. [1226] A similar exact-exchange fraction of 0.5 has been derived for the PBE0-DH functional, while only one eights of non-local MP2 correlation was employed. [1234] In the three parameter double-hybrid functional XYG3 [1227] the exact-exchange contribution is increased to 80.33 % and 32.11 % of MP2 correlation are admixed. B2PLYP and mPW2-PLYP have been found to be robust improvements even over the best functional representatives of the lower rungs for diverse physicochemical properties of molecular systems. [1226, 1233] An quite impressive correspondence to coupled cluster reference data has been found for the XYG3 double-hybrid functional for thermochemistry and reaction barrier heights. [1227] One of the most severe limitations of the lower rungs is the missing description of weak long-range correlation, also dispersion or van der Waals interactions. Due to the relatively small fraction of exact correlation, double-hybrid functionals of the form Eq. (3.75) might not comprehensively benefit from the roughly 80 % to 90 % of exact (long-range) correlation con-

[58] Even though *double-hybrid* exchange-correlation is commonly associated with Grimme, the actual name has been coined before by Trular et al. [1229, 1230]

tained in Møller-Plesset second-order perturbation theory. Thus, also double-hybrids might still be corrected for dispersion interactions [59]. [1231, 1239–1241] Steinmetz and Grimme [1241] found that dispersion corrected hybrid functionals [60] outperform uncorrected double-hybrid functionals for transition-metal catalysts.

MP2 – As in case of hybrid functionals, the development of double-hybrids is extensively driven by molecular systems and corresponding test sets for evaluating the accuracy of newly developed exchange-correlation functionals. Møller-Plesset (MP2) perturbation theory has only been sporadically implemented for solids [1244–1252] and the application of range-separated double-hybrid density-functional theory to periodic systems has just been reported, recently. [1250, 1253] A plane-wave implementation of canonical second-order Møller-Plesset perturbation theory for periodic systems within the projector-augmented-wave method has been implemented [1245, 1247] in the VASP code, demonstrating an excellent description of lattice constants (typical deviations below 0.5 %). The addition of second-order Møller-Plesset correlation always results in a reduction of pure Hartree-Fock band gaps due to correlation screening of the Hartree-Fock exchange interaction. This reduction leads to dramatical underestimations or even negative band gaps in case of small-gap semiconductors as silicon or silicon carbide. [1247] In contrast, the pure second-order Møller-Plesset quasipartcle-band gaps of weakly-polarizable wide-gap materials as lithium fluoride (LiF) are reproduced, exactly. The MP2 quasipartcle-band gap error was found to increase rapidly with an increasing static dielectric constant. [1247] A severe limitation of correlation from second-order Møller-Plesset perturbation theory for the application to metals is the logarithmic divergence observed for the three-dimensional free-electron gas [1254], "presumably" [1105] existing for bulk metals, in general. [1105, 1247, 1255, 1256] This limitation can be cured by considering a non-local *random-phase* approximated version of electron correlation by formal consideration of an infinite sub-series of ring/bubble diagrams in the diagrammatic expansion of the exchange-correlation energy, which eliminates the divergence problem by staying finite for the three-dimensional electron gas. [1105, 1257]

RPA – The random-phase approximation (RPA) [1258], including additional *systematic* corrections [61] [1258], is seen by several authors [1264] as the most promising candidate for an universal parameter-free *post*-Kohn-Sham-correlation approach for reaching *chemical accuracy*. The appealing properties of random-phase correlation are its inherent compatibility to Hartree-Fock-type exact-exchange, both evaluated from a common set of Kohn-Sham orbitals, and the *seamless* inclusion of long-range dispersion interactions, van der Waals interactions respectively. [1265] For

[59] A comparative study on the performance of different van-der-Waals-correction approaches, including the random-phase approximation, is given in Ref. [1176]

[60] The best description was obtained for Grimme's D3 dispersion correction [1242, 1243] to the PBE0 hybride functional. [1241]

[61] Corrections to the random-phase approximation are necessary due to a poor description of short-range correlation and the presence of spurious one-electron self-interaction. [1259, 1260] The relevant correction terms to random-phase approximation are second-order screened exchange (SOSEX) [1258–1262], that removes the self-interaction error from random-phase correlation energy, renormalized single excitations (rSE) [1261, 1262], as well as higher order corrections. [1263]

solid-state total-energy calculations, the random-phase approximation is typically derived from the adiabatic-connection fluctuation-dissipation theorem. Using the adiabatic connection formula, Eq. (3.71), and the fluctuation-dissipation theorem [1266], the correlation energy in random-phase approximation [62] follows from [63]

$$E_c^{RPA} = \int_0^\infty \frac{1}{2\pi} \mathrm{Tr}\left\{\ln\left[1-\chi^0(i\omega)\,v\right] + \chi^0(i\omega)\,v\right\} \mathrm{d}\omega\,. \tag{3.76}$$

The required independent-particle approximation response function $\chi^0(\mathbf{q}, i\omega)$ in terms of Kohn-Sham states and eigenvalues is given by the Adler [1271] and Wiser [1272] expression

$$\chi^0_{\mathbf{G},\mathbf{G}'}(\mathbf{q}, i\omega) = \frac{1}{V} \sum_{\lambda,\lambda',\mathbf{k}} 2 g_{\mathbf{k}} \left(f_{\lambda',\mathbf{k}+\mathbf{q}} - f_{\lambda,\mathbf{k}}\right) \frac{\left\langle \phi_{\lambda',\mathbf{k}+\mathbf{q}} \left| e^{i(\mathbf{q}+\mathbf{G})\mathbf{r}} \right| \phi_{\lambda,\mathbf{k}} \right\rangle \left\langle \phi_{\lambda,\mathbf{k}} \left| e^{i(\mathbf{q}+\mathbf{G}')\mathbf{r}} \right| \phi_{\lambda',\mathbf{k}+\mathbf{q}} \right\rangle}{\varepsilon_{\lambda',\mathbf{k}+\mathbf{q}} - \varepsilon_{\lambda,\mathbf{k}} - i\omega}\,, \tag{3.77}$$

where $f_{\lambda,\mathbf{k}}$ is the occupation number of a Kohn-Sham state with band index λ at $\mathbf{k}$-point $\mathbf{k}$ and and $g_{\mathbf{q}}$ is a $\mathbf{k}$-point weighting factor.

The total energy functional in random-phase approximation-based Kohn-Sham theory is a non-local orbital-dependent functional given by

$$E_{xc}^{RPA}\left[n, \left\{\varphi_{\lambda,m_s}\right\}\right] = T_S^{el}[n] + V_{nuc,el}[n] + V_H[n] + E_x^{EXX}\left[\left\{\varphi_{\lambda,m_s}\right\}\right] + E_c^{RPA}\left[\left\{\varphi_{\lambda,m_s}\right\}\right]. \tag{3.78}$$

In principle, the self-consistent solution of the (generalized) Kohn-Sham equations for this energy functional provides accurate total energies as well as eigenvalues and eigenstates in adiabatic-connection dissipation-fluctuation theorem-derived random-phase approximation (ACFDT-RPA). Obviously, this self-consistent approach represents a substantial computational challenge through repeated evaluation of the correlation energy. Therefore, typical random-phase approximation calculations, especially for extended systems, are performed in a mixed self-consistent–non-self-consistent scheme by performing a self-consistent calculation for the fourth ladder rung hybrid-functional part and a subsequent *single-shot* evaluation of the random-phase approximation correlation energy [1259, 1273, 1274],

$$\begin{aligned} E_{tot}^{RPA}[n, \{\varphi_\lambda\}] = & \underbrace{E_{tot}^{DFT}[n, \{\varphi_\lambda\}] - E_{xc}^{DFT}[n, \{\varphi_\lambda\}] + E_x^{EXX}[\{\varphi_\lambda\}]}_{self-consistent} \\ & + \underbrace{E_c^{RPA}[\{\varphi_\lambda\}]}_{non-self-consistent}\,. \end{aligned} \tag{3.79}$$

Instead of completely replacing exchange and correlation contributions from (semi)local density functionals, also double-hybrid-like schemes, combining weighted full-range or long-range

[62] This expression actually represents Langreth's and Perdew's formula for random-phase correlation derived from the adiabatic-connection dissipation-fluctuation theorem. [1267]

[63] The subsequent plane-wave representation of the correlation energy in random-phase approximation follows Ref. [1268–1270].

corrected hybrid-functional exchange-correlation contributions with a partial input from random-phase correlation are a common strategy. For example, an effective double-hybrid-type random-phase correlation functional, $E_{xc}^{dh,RPA}$, constructed as a long-range correlation corrected hybrid functional according to

$$E_{xc}^{dh,RPA} = E_{xc}^{LDA,sr} + E_{x}^{EXX,lr} + c_{RPA} E_{c}^{RPA,lr} \tag{3.80}$$

has been proposed. [1259, 1274]

The general performance of the random-phase approximation within the framework of generalized Kohn-Sham density-functional theory [64] [1258, 1261, 1268, 1269, 1275–1278] has been examined for a wide range of materials. The random-phase approximation has successfully been applied to solve of the puzzling problem of carbon monoxide absorption on noble metal (111) surfaces [1273, 1279, 1280]. Further usage examples include strongly correlated f-electron systems [1281], van der Waals bonded molecular [1239, 1268] and layered [1276, 1282] systems, graphene adsorption on metal surfaces [1283] , themochemistry [1239], reaction barriers [1284], lattice parameters and general atomization energies of test sets of insulators, semiconductors, and metals. [1258, 1269, 1270] Random-phase approximation-based correlation approaches are generally found to be more accurate and universal, than second-order Møller-Plesset perturbation-theory-based correlation approaches. [1278] The actual computation cost of random-phase correlation is not much higher than the evaluation of Møller-Plesset second-order correlation, but still notably below accurate coupled-cluster reference calculations. One reason for the success of random-phase-approximation-based theories is the proof [1277] of a close analytic connection to coupled cluster theory [65]. [1261, 1277, 1285, 1286]

3.3.6 Scaling properties

Method of choice – Certainly, the broad success of density-functional theory is owned to some balance between computational cost, the scaling with system size respectively, and the amount of *exactly* contained physics. Considering the preceding discussion of available approximations to the exchange-correlation energy, it seems helpful to give a rough estimation of the scope of application for density-functional theory calculations. An overview on the characteristic scaling properties [66] of the most relevant numerical approaches is illustrated in Fig. 3.4.

Starting at the top of computational requiremets, configuration interaction (in the limit of a complete/infinite basis) provides an exact solutions to the non-relativistic many-electron Schrödinger

[64] Random-phase approximation routines for total energy calculations have been implemented in projector-augmented wave plane-wave density-functional theory within the VASP code. [1268–1270]

[65] More precisely, the random-phase approximation has been found to be identical to the *Coulomb-ring* approximation to coupled-cluster doubles (ring-CCD) theory [1261, 1277, 1285, 1286], thus, the random-phase approximation can be alternatively derived from coupled-cluster theory. [1277]

[66] The indicated scaling behavior refers to common implementations and eigenstate representations by N localized atomic basis functions. In principle, the plane-wave implementations' scaling should be of similar order, but with partially notable variations in the prefactors.

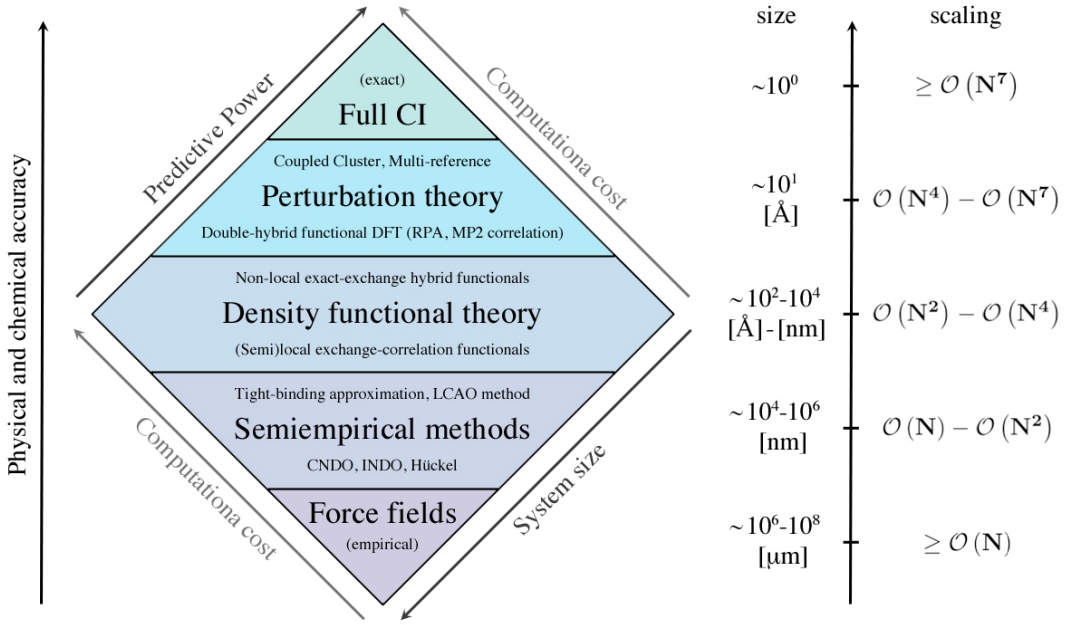

Figure 3.4: Schematic illustration of the system-size scaling behavior of various approaches to solve the electronic many-body problem. The largest accessible system size, length scale respectively, are roughly estimated.

equation. While full configuration interaction [1287] is, in any practical calculation, restricted to roughly one or two *light* atoms, a more realistic "gold standard" [1288] as reference for practical calculations is coupled-cluster theory using single, double and (perturbatively) triple excitations (CCSD(T)) [1287, 1289, 1290]. The tremendous price for an accurate chemical reference calculation is reflected in a seventh-order, or *worth*, numerical scaling. The use of fourth and fifth rung hybrid and double-hybrid functionals demonstrates that, in absence of a true universal density functional, orbital dependent non-local ingredients are essential to improve Kohn-Sham theory to become a *close-to-chemical-accuracy* method. Fifth rung exchange-correlation functionals almost enable modern density-functional theory to compete with the pure wave-function-based approaches of quantum chemistry bridging the long standing gap between density-functional and wave-function theories, formally. Nevertheless, the construction of exchange-correlation functionals and their ongoing improvement is always less systematic than the well defined trends of pure wave-function-based approaches. Obviously, double-hybrid functional calculations not only join the benefits of both worlds. Exemplarily, inclusion of exact correlation from second-order perturbation theory, evaluated for Kohn-Sham orbitals, actually elevates the density-functional theory scaling to fifth order[67], making double-hybrid implementations quite challenging for extended systems. Thus, much of the original benefits have inevitably been scarified to the accuracy gain during density-functionals theorie's *ascension*. Hybrid-functional calculations for solid-state systems show a scaling up to fourth order, which is inherent to the evaluation of the exact-exchange

[67] At least as long as the conventional form of canonical Møller-Plesset second-order perturbation theory is applied.

term [68]. In light of the sound and systematic improvement over semilocal density functionals, that is provided by hybrid functionals, this scaling seems to be an acceptable and feasible price to pay for future electronic-structure calculations of extended systems. Conventional density-functional theory calculations within the third-order scaling [1292] generalized as well as meta-generalized gradient approximations will remain the flayed *working horse* of solid-sate physics and materials science for quite some time. The increase in computational capabilities will provide access to successively larger system sizes, even above 10^4 atoms. Through this, especially long-ranging ordering effects and self-organization related trends, structure-function correlations, and material properties originating from complex nanostructuring in solids as well as functional biological complexes will be the future focus of *conventional* semilocal density-functional theory simulations, while resilient reference data will be generated by higher level functionals/approaches. The connection between density-functional theory and simplified semiempirical schemes is made by various tight-binding approaches. Tight-binding approaches can formally be derived as an approximative density-functional theory scheme. [1293–1295] Their scope of application covers large scale molecular-dynamics simulations and providing structurally optimized inputs for subsequent density-functional theory calculations. Several semiempirical quantum-chemistry techniques, developed in the past, represent simplified electronic-structure theory approaches obtained through specific approximations made in the evaluation of various integral-types. [1296] However, in light of accurate empirical force fields for very large systems ($\sim 10^6$–10^8 atoms) on the one side and effectively scaling density-functional-based electronic-structure simulation techniques, the future place for these simplified semiempirical techniques might be quite limited to the niche of estimating an approximative electronic structures for large scale systems. Empirical force fields allow a systematic parametrization of molecular interactions on the basis of experimental or accurate ab initio data. A comparison between various force-field methods, tested against highest-level ab initio calculations for a wide range of organic and biological molecules, is given in Ref. [1297], demonstrating that carefully parameterized force fields have the potential to compete with ab initio results for numerous materials. Empirical force fields, including pairwise dispersion interactions through the classical Lennard-Jones potential [1298]), allow large scale molecular-dynamics simulations of amorphous and porous systems (including their interaction with surrounding media) [1299–1301], polymer systems [1302–1304], or biological systems. [1305, 1306]

The scaling estimation provided in Fig. 3.4 refers to a conventional implementation of the standard/canonical formulas. Nevertheless, the computational cost of most of the standard implementations might be significantly reduced by one or two orders of magnitude, in the best case. Relevant examples of performance enhancement are resolution of identity approaches to evaluate correlation energies in Møller-Plesset perturbation theory or random phase approximation. [1307] Also, cubic scaling algorithms to the random phase approximation, including second-order screened exchange have been developed [1308] and linear scaling algorithms to conventional semilocal

[68] Hartree-Fock theory formally shows a fourth order scaling with the number of basis functions. [1291]

density-functional [1292] theory are a reoccurring *aim* in algorithm development. [1292, 1309–1311] In order to benefit from the combined capabilities of each level of theory and to bridge the *size-gap* between atomistic theories and *real-life* atomic (nano)structures, various multiscale-simulation techniques have been developed. Multiscale approaches divide a physical system of interest into various sub-systems, whose relevance for the total system determine the applied theoretical methodology. The basic challenge, arising in practical application of multiscale-simulation techniques, is the fulfillment of boundary conditions in order to provide *seamless* connections between the regions treated on different levels of sophistication. Multiscale modeling represents a promising approach to characterize functional units within large biological complexes. [1312–1314] The numerical treatment of dynamic properties of even larger systems is neither feasible nor constructive by maintaining an atomistic picture of materials. Thus, the investigation of macroscopic mechanical properties of materials rests on *continuum approaches* which might, however, use parametrical input from the various levels of atomistic theories. Prominent application examples are continuum-mechanics simulations of the material strength of concrete [1315, 1316], gas flow simulations [1317], or structure simulations for polymer systems. [1303, 1318]

UNEASY LIES THE HEAD THAT WEARS A CROWN[69] – Once having decided for density-functional theory as the method of choice, it remains a puzzling question which functional should be used in practical density-functional theory calculations in light of an efficient utilization of available hardware resources. Summing the above, one needs to admit that there is, at present, certainly no definite answer to the question which exchange-correlation functional is the *best*. Some functionals provide qualitative physics without accurate *numbers* and others correct experimental numbers without insights into the underlying physics. In practice, the choice of a specific exchange-correlation functional, or the decision for performing a density functional-calculation or applying a formally, more or less, accurate theoretical approach, always represents a compromise between desired accuracy and computational demands. On the one hand, calculation speed is worthless if missing accuracy does not provide a description of the relevant physical effects. On the other hand, accuracy kills applicability to *realistic* structure models. This is especially relevant for climbing the fourth and fifth rungs of the functional ladder which provide severe restrictions for extended systems. Ultimately, knowledge of functional capabilities and limitations, i.e. reading papers, experience in practical utilizaion and, above all, systematic testing cannot be replaced by straightforward *cooking recipes* pretending universal inerrant applicability[70]. Nonetheless, it is the diversity in exchange-correlation functionals that extends the applicability of density-functional theory to a wide range of physical effects and system sizes making density-functional theory the most universal atomistic theory, contemporaneously.

BREATHING LIFE INTO CATCHPHRASES – There is some indication that most recent technological developments foreshadow some fundamental breakovers in the way scientific theories

[69] From Shakespeare's Henry The Fourth, Part 2 Act 3, scene 1, line 31, 1597.

[70] Not to mention the manifold of numerical parameters, that need to be controlled in every existing implementation to reach *sufficiently* converged results.

are build. The current rapid progress in the development of artificial intelligence and the associated subfield of machine-learning technology, in general, as well as *deep learning* in the context of neuronal networks [1319] might provide the necessary instruments to advance fundamental frontiers in physics [71]. Thereby, machine learning in materials science offers a new approach facilitating high-throughput screening of the structural and compositional configuration space of functional materials in search for new structural polymorphs, unknown alloys, and their associated physico-chemical material properties. [1328, 1329] To this purpose automated *big data* algorithms are designed in order to process, categorize, and analyze the complex, little-structured, and partially volatile data streams provided by the vastly increasing computational output of today's high-performance computing facilities. Typically, machine-learning approaches aim at finding the nonlinear and nontrivial [72] statistical mappings between an atomic structure, the corresponding electron density and material parameters of interest on basis of machine-learning algorithms without explicitly *solving* the electronic structure problem in any *conventional* time-consuming way.

The existing data sets, generated by density-functional-based ab initio theory in recent years, represent a substantial and valuable feeding source for nowadays *smart* machine-learning algorithms allowing the possible identification of underlying exchange-correlation functional features as well as basic material trends, valuable to theoretical and practical materials' engineering, in general. Since the basic task of all machine learning approaches is the search for clandestine functional regularities and the development of associated *data functionals* from unstructured high-dimensional data sets, the utilization to the generation of exchange-correlation functionals, within the framework of Kohn-Sham theory, as well as *pure* orbital-free density-functional theory based on an universal density functional, seems tantalizing. Machine learning, on the long run, completely eliminates the need for human deductionism and might thus provide, potentially counter-intuitive ways to express functional dependencies in density-functional theory [73] and many-body physics, in general. However, it is not a priori self-reliant that the answers found by *artificial intelligences* provide new and *meaningful* insights into the underlying physics itself, since actual functional fits to the *machine-learned* mappings might become complex discontinuous functions of any order.

[71] Aside from the utilization in basic sciences, machine learning will have dramatic impact to pattern recognition [1320, 1321], e.g. facial-expression recognition [1322, 1323] or speech recognition [1324], and forecasting systems in finance, economy, and healthcare [1325–1327], which will clearly influence everyday's life by progressing medicine through machine-based diagnostics, communication through universal translation, or shipping and transport through self-driving vehicles, in near future.

[72] The actual representation of these maps might be given in huge number sequences (e.g. see Ref. [1330]) rather than any handy functional form accessible to human intuition. Hence, the actual connection and comparison to existing functional approximations is clearly not self-evident.

[73] Reported examples of machine learned functional contributions to density-functional theory are first approximate kinetic-energy density functionals for orbital free density-functional theory [1331] or density functionals of prototypical systems as noninteracting spinless fermions confined to a one-dimensional box. [1330] Machine learning is not necessarily restricted to functional design, it might actually be used for direct predictions of charge densities, total energies and potential-energy surfaces [1332–1334], electronic properties as the density of states [1335] and molecular atomization energies [1336], or density-functional theory hamiltonians. [1337]

3.4 Many-body perturbation theory

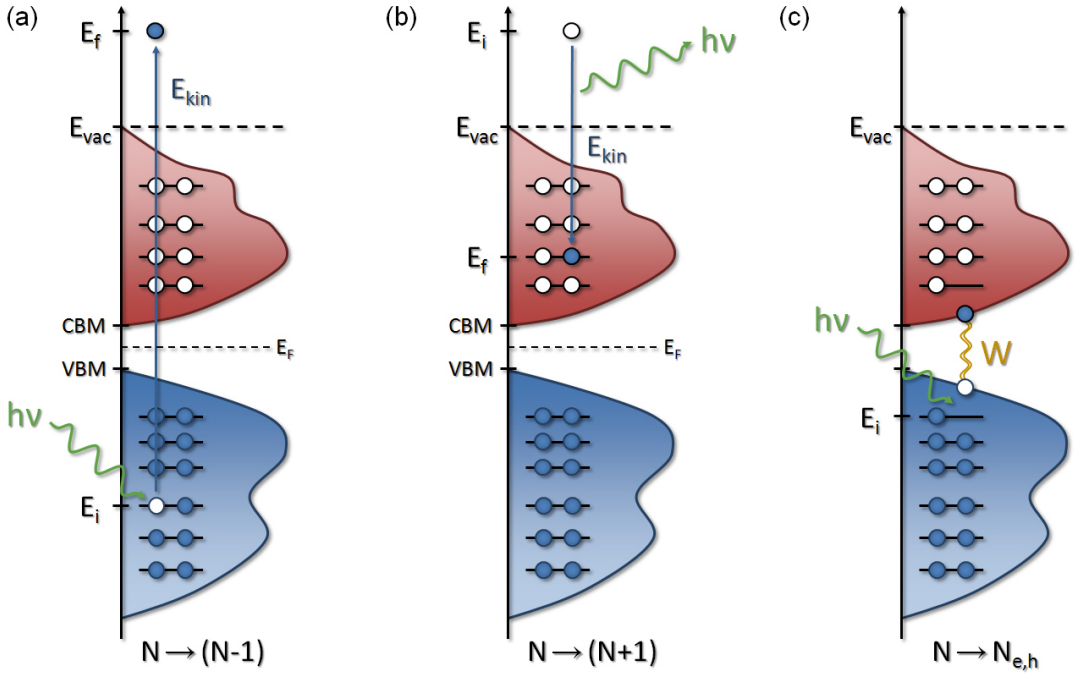

Figure 3.5: Schematic representation of optical excitation processes in semiconductor spectroscopy. Illustrated are direct photoelectron emission (a), indirect photoelectron emission (b), and photoabsorption.

EXCITING SPECTROSCOPY – Due to the relevance for technological applications, one of todays key challenges in computational materials science is the *parameter-free*, thus predictive, description of (optical) excitations in materials. Special interest is directed to the accurate simulation of electronic excitations, e.g. involved in direct and inverse photoemission processes (cf. Fig. 3.5 a and Fig. 3.5 b), which represent the experimental route towards direct examination of the electronic band structure by probing occupied or unoccupied electronic states, respectively.[74] In the conventional direct photoemission process (cf. Fig. 3.5 a) a single electron is removed by a photon of known energy $h\nu$ from the neutral N electron ground state. Energy conservation allows the determination of the initial electronic state of the removed electron by measurement of the kinetic energy according to

$$\begin{aligned} E(N) + h\nu &= E(N-1,i) + E_{kin} \\ E_i \equiv E(N) - E(N-1,i) &= E_{kin} - h\nu\,. \end{aligned} \tag{3.81}$$

In the inverse photoemission process (cf. Fig. 3.5 b) an additional electron, of kinetic energy E_{kin}, is added to a virtual electronic state of the N particle system and the excess energy of the

[74] Including information on momentum conservation, angle-resolved photoemission spectroscopy is the only experimental approach that allows a direct examination of band-structure features.

corresponding outgoing photon is measured. In this case energy conservation yields

$$E(N) + E_{kin} = E(N+1,i) + h\nu \qquad (3.82)$$
$$E_f \equiv E(N+1,i) - E(N) = E_{kin} - h\nu\,.$$

The conceptual difficulty, that arises within the interpretation/simulation of photoelectron spectroscopy data is how the single-particle picture of electronic excitations relates to the $N \pm 1$ initial and final states of the interacting many-electron system. An intuitive answer to this problem is provided by the quasiparticle concept.

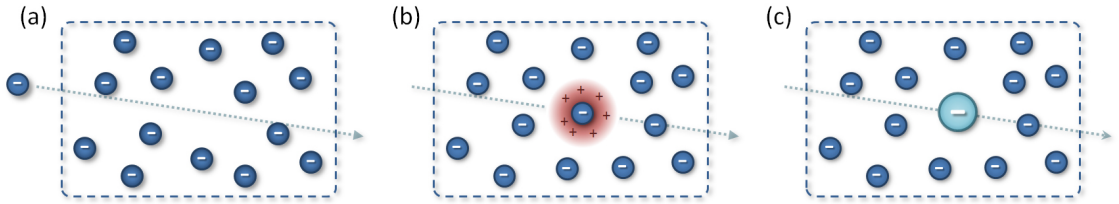

Figure 3.6: Schematic representation of the propagation of (a) an additional electron through a N-electron system, (b) the bare electron surrounded by its positively charged screening-cloud, and (c) the emergent renormalized quasiparticle state.

The propagation of the additional or *missing* photoelectron represents an elementary low-energy excitation of the N-particle system that falls well into the domain of the *quasiparticle picture*. An electronic quasiparticle, a *quasi-electron* for convenience, is a bare electron which is *dressed* (or renormalized) by a surrounding positively charged screening cloud caused by local electron repulsion in the direct vicinity of the electron, as schematically illustrated in Fig. 3.6. In the same way, we might consider a missing/removed electron as a negatively screened positive charge, a *quasi-hole* respectively.[75] The screening-cloud's repercussion on the bare electron is formally expressed in a (nonlocal) self-energy which can be related to the correlation energy per electron by use of Seitz's theorem. [1338, 1339] Even though quasiparticle formation is a true many-body effect, the appealing feature of this concept is that it allows to retain an effective single-particle picture, as far as possible, by replacing the propagating bare single-particle and its imminent interaction cloud with a renormalized quasiparticle state. If the renormalized quasiparticle states itself interact only weakly among each other, which might not necessarily be the case in the event of strongly correlated materials at all, and possess a *sufficiently* long life-time, they effectively carry on an independent-particle picture.[76] In this picture the added and removed electron of direct and inverse photoemission experiments provoke the formation of basic electron and hole related quasiparticle excitations, quasi-electrons and quasi-holes, respectively. The general validity of the quasiparticle picture requires the restriction to a small number of *weakly* interacting low-energy

[75] Clearly, quasiparticle formation represents an emergent phenomenon of the collectively interacting many-electron system, whose *existence* as a *real* physical entity might be debatable, but that allows for an interpretation of *measurable* physical properties showing a one-to-one correspondence to calculated quasiparticle states.

[76] This is essentially the idea of Landau's phenomenological Fermi liquid theory. [27, 1340, 1341]

quasiparticle excitations compared to the total number of interacting particles in the system. This limitation also illustrates the appealing character of the quasiparticle picture, instead of dealing with a vast number of mutual interacting electrons, the analysis of basic physics is essentially reduced to dealing with a *manageable* number of entities.

The theoretical formalism that naturally accounts for a seamless description of quasiparticle excitations is many-body Green's function theory [27, 28, 987, 1339, 1342–1348], while Kohn-Sham density-functional theory lacks a proper quasiparticle concept, at all. [1349] Within the framework of density-functional theory, the calculation of excited state properties is reserved for time-dependent density-functional theory. [77] The general extension of conventional density-functional theory towards exited states is non-trivial due to the complex and, again, unknown functional dependence on the electron density, which is not covered by the conventional existence theorems of densiy-functional theory. [78]

GREEN'S FUNCTION THEORY – The major part of computational spectroscopy simulations is currently performed within the Green's function based formalism of many-body perturbation theory. Many-body perturbation theory inherently facilitates the systematic treatment of many-body interactions within the many-electron system by going beyond the mean-field limits of conventional (semi)local density-functional theory. Thereby, knowledge of the single-particle Green's function allows straight forward evaluation of *any* exception value of one-particle related observables as the electron density, spin density, and total energy [79] as well as the quasiparticle excitation spectrum which, for instance, allows the description of the charged excitations involved in the direct and inverse photoemission processes (cf. Fig. 3.6 (a) and 3.6 (b)). [987, 1348] Material properties that are related to the two-particle Green's function, as the electrical conductivity, magnetic susceptibility, or optical response, as well as several non-equilibrium properties [1348] are

[77] Formally, time-dependent density-functional theory allows to expresses the full linear density-response function of the many-electron system, which exhibits poles at the exact excitation energies, in terms of the response function of the non-interacting Kohn-Sham system and a frequency-dependent exchange-correlation kernel [1350]. [997, 1351]

[78] Various approaches to excited-state density-functional theory have been proposed in recent past. [1352–1354]

[79] While density-functional theory has become the main vehicle to determine the ground-state energetics of molecular and solid-state systems, Green's function theory is currently primarily applied to correct the electronic structure features of semiconducting and insulating systems via perturbative or partially self-consistent simulation approaches. The application of the Green's function formalism to actually evaluate total energies [1355–1357] is rarely implemented in sate-of-the-art ab initio codes. Nevertheless, Green's function based energetics, within the framework of many-body perturbation theory, are of highest interest for the development of next-generation's solid-state-physics codes in order to enhance the numerical accuracy and predictive power of total energies by providing a more complete and, with respect to density-functional theory, a more systematic treatment of electron correlation. [1358] While different formal prescriptions of the total energy as the Galitskii-Migdal formula [1356, 1358, 1359] or the Luttinger and Ward [1360, 1361] or Klein energy functionals [1362–1364] are known within the Green's function formalism, the few reported practical implementations, e.g. Ref. [1355–1357], mostly rely on the formulation of Galitskii and Migdal. [1359] The Galitskii-Migdal total-energy formula reads

$$E = \frac{1}{2}\int \lim_{\mathbf{r}'\to\mathbf{r}} \lim_{t'\to t^+} \left[\frac{\partial}{\partial t} + i\left(\frac{\hbar^2}{2m_e}\nabla^2_{\mathbf{x}} - V_{ext}(\mathbf{x})\right)\right] G\left(\mathbf{x},t;\mathbf{x}',t'\right) \mathrm{d}\mathbf{x}. \tag{3.83}$$

With the availability of efficient total energy algorithms, Green's function theory or, synonymously, Hedin's formulation of many-body perturbation theory, offers a unified approach to the energetics as well as electronic properties of ground- and excited-state properties of many-electron systems.

treated within the same many-body perturbation-theory framework, elegantly. Albeit formally independent of density-functional theory, present implementations of many-body perturbation theory related approaches have been constructed reliant on *sound* input from the well established Kohn-Sham density-functional theory machinery instead of tending to replace it. [80]

THE SINGLE-PARTICLE GREEN'S FUNCTION – To begin with, the interacting single-particle time-ordered (zero-temperature) Green's function $G(\mathbf{r}_1, m_{s_1}, t_1; \mathbf{r}_2, m_{s_2}, t_2) \equiv G(\mathbf{x}, t; \mathbf{x}', t')$ is defined through

$$\begin{aligned} G\left(\mathbf{x},\mathbf{x}';t-t'\right) &= -\frac{i}{\hbar}\left\langle N,0\left|\hat{T}\left[\hat{\psi}\left(\mathbf{x},t\right)\hat{\psi}^{\dagger}\left(\mathbf{x}',t'\right)\right]\right|N,0\right\rangle \\ &= \underbrace{-\frac{i}{\hbar}\left\langle N,0\left|\left[\hat{\psi}\left(\mathbf{x},t\right)\hat{\psi}^{\dagger}\left(\mathbf{x}',t'\right)\right]\right|N,0\right\rangle\Theta\left(t-t'\right)}_{\text{electron propagator}} \\ &\quad \underbrace{+\frac{i}{\hbar}\left\langle N,0\left|\left[\hat{\psi}^{\dagger}\left(\mathbf{x}',t'\right)\hat{\psi}\left(\mathbf{x},t\right)\right]\right|N,\right\rangle\Theta\left(t'-t\right)}_{\text{hole propagator}}, \end{aligned} \tag{3.84}$$

where $|N,0\rangle$ is the N-electron ground-state wave function, $\hat{\psi}$ and $\hat{\psi}^{\dagger}$ are electron annihilation and creation field operators in the Heisenberg picture,

$$\hat{\psi}\left(\mathbf{x},t\right) = e^{(i/\hbar)\hat{H}t}\,\hat{\psi}\left(\mathbf{x}\right)e^{-(i/\hbar)\hat{H}t}, \tag{3.85}$$

$\hat{T}$ is Wick's time ordering operator yielding

$$\hat{T}\left[\hat{\psi}\left(\mathbf{x},t\right)\hat{\psi}^{\dagger}\left(\mathbf{x}',t'\right)\right] = \begin{cases} \hat{\psi}\left(\mathbf{x},t\right)\hat{\psi}^{\dagger}\left(\mathbf{x}',t'\right) & \text{if } t > t' \\ \hat{\psi}^{\dagger}\left(\mathbf{x}',t'\right)\hat{\psi}\left(\mathbf{x},t\right) & \text{if } t' > t \end{cases}, \tag{3.86}$$

and Θ represents the Heaviside function. For a time-independent Hamiltonian $\hat{H}$ the translational time invariance of the single particle Green's function $G(\mathbf{x},t;\mathbf{x}',t') \equiv G(\mathbf{x},\mathbf{x}';t-t')$ presupposes sole dependence on the relative time difference $t-t'$. For $t_1 > t_2$ the Green's function, Eq. 3.84, describes the propagation of an electron created at time t_2 and position $\mathbf{r}_2$ and annihilated at time t_1 and position $\mathbf{r}_1$. Analog, for $t_1 < t_2$ the propagation of a hole created at time t_1 and position $\mathbf{r}_1$ and annihilated at time t_2 and position $\mathbf{r}_2$ is described.

Introducing a complete set $\{|M,n\rangle\}$ of M-electron eigenstates [81] of the Hamiltonian $\hat{H}$,

$$\hat{H}\left|M,n\right\rangle = E_{M,n}\left|M,n\right\rangle \tag{3.87}$$

and Fourier transformation with respect to $t-t'$ yields the spectral representation (Lehmann rep-

[80] Therefore, this approach also carries on some of the quirkynesses of density-functional theory to many-body perturbation theory, which need to be considered carefully in case of *simple* perturbative treatment, but could be cured in case of a completely self-consistent many-body perturbation-theory treatment, comprehensively.

[81] Completeness implies validity of the closure relation $\sum_{M,n}|M,n\rangle\langle M,n| = 1$.

resentation) of the single-particle Green's function,

$$G\left(\mathbf{x},\mathbf{x}';\varepsilon\right) = \sum_n \frac{\langle N,0\,|\hat{\psi}\left(\mathbf{x}\right)|\,N+1,n\rangle\,\langle N+1,n\,|\hat{\psi}^\dagger\left(\mathbf{x}'\right)|\,N,0\rangle}{\varepsilon-\left(E_{N+1,n}-E_{N,0}\right)+i\delta} + \sum_n \frac{\langle N,0\,|\hat{\psi}^\dagger\left(\mathbf{x}\right)|\,N-1,n\rangle\,\langle N-1,n\,|\hat{\psi}\left(\mathbf{x}'\right)|\,N,0\rangle}{\varepsilon-\left(E_{N,0}-E_{N-1,0}\right)-i\delta}\,, \tag{3.88}$$

where δ is an infinitesimal positive shift ($\delta \to +0$). Through introduction of the *Lehmann amplitudes* $f_n\left(\mathbf{x}\right)$ and definition of the excitation energies $\varepsilon_n = \omega_n$ ($\hbar \equiv 1$) relative to the chemical potential μ according to

$$f_n\left(\mathbf{x}\right) = \begin{cases} \langle N,0\,|\hat{\psi}\left(\mathbf{x}\right)|\,N+1,n\rangle & \text{and} \quad \varepsilon_n = E_{N+1,n}-E_{N,0} \quad \text{if} \quad \varepsilon_n > \mu \\ \langle N+1,n\,|\hat{\psi}^\dagger\left(\mathbf{x}'\right)|\,N,0\rangle & \text{and} \quad \varepsilon_n = E_{N,0}-E_{N-1,0} \quad \text{if} \quad \varepsilon_n < \mu\,, \end{cases}$$

the Lehmann representation, Eq. 3.88, compactifies to

$$G\left(\mathbf{x},\mathbf{x}';\varepsilon\right) = \sum_n \frac{f_n\left(\mathbf{x}\right) f_n^*\left(\mathbf{x}'\right)}{\varepsilon-\varepsilon_n+i\delta\,\mathrm{sign}\left(\mu-\varepsilon_n\right)}\,. \tag{3.89}$$

The poles of the single-particle Green's function G provides the (charged) $N \to N \pm 1$ excitations of a N-electron system from its groundstate $|N,0\rangle$.

Introduction of the spectral (weight) function $A\left(\mathbf{x},\mathbf{x}';\varepsilon\right)$,

$$\begin{aligned} A\left(\mathbf{x},\mathbf{x}';\varepsilon\right) &= \sum_n \langle N,0\,|\hat{\psi}\left(\mathbf{x}\right)|\,N+1,n\rangle\,\langle N+1,n\,|\hat{\psi}^\dagger\left(\mathbf{x}'\right)|\,N,0\rangle \\ &\qquad \times\delta\left(\varepsilon-\left(E_{N+1,n}-E_{N,0}\right)\right) \\ &\quad + \sum_n \langle N,0\,|\hat{\psi}^\dagger\left(\mathbf{x}\right)|\,N-1,n\rangle\,\langle N-1,n\,|\hat{\psi}\left(\mathbf{x}'\right)|\,N,0\rangle \\ &\qquad \times\delta\left(\varepsilon-\left(E_{N-1,n}-E_{N,0}\right)\right) \end{aligned} \tag{3.90}$$

$$= \sum_n f_n\left(\mathbf{x}\right) f_n^*\left(\mathbf{x}'\right)\delta\left(\omega-\varepsilon_n\right)\,, \tag{3.91}$$

allows to rewrite Eq. 3.88 as the contour integral

$$G\left(\mathbf{x},\mathbf{x}';\varepsilon\right) = \int_{-\infty}^{\infty} \frac{A\left(\mathbf{x},\mathbf{x}';\varepsilon'\right)}{\omega-\omega'+i\eta}\,\mathrm{d}\omega'\,, \tag{3.92}$$

where the quantity $\eta = \pm\delta$ shifts the contour infinitesimally below or above the real axis. From the imaginary part of Eq. 3.88 it follows that the single-particle Green's function $G\left(\mathbf{x},\mathbf{x}';\omega\right)$ is directly proportional to the spectral function $A\left(\mathbf{x},\mathbf{x}';\varepsilon\right)$,

$$A\left(\mathbf{x},\mathbf{x}';\varepsilon\right) = \frac{1}{\pi}\left|\mathrm{Im}\,G\left(\mathbf{x},\mathbf{x}';\varepsilon\right)\right|\,. \tag{3.93}$$

Obviously, the spectral function $A(\mathbf{x},\mathbf{x}';\varepsilon)$ consists of a superposition of delta functions weighted by the Lehmann amplitudes $f_n(\mathbf{x})$ for each quasiparticle excitation of energy ε_n. [1343] Hence, the spectral function, Eq, 3.90, might be seen as a generalization of the density of states towards exited $N\pm1$ quasiparticle states. [1345] Given an appropriate single-electron state basis $\{\phi_i\}$, any *sufficiently* sharp peak in the matrix elements $A_{ij}(\omega) = \langle \phi_i | A(\mathbf{x},\mathbf{x}';\varepsilon) | \phi_j \rangle$ might be associated to a single-particle-like excitation of the many-electron system, initially. [1343, 1365] In contrast to a system of *truly* independent/non-interacting particles, not any excitation energy ε_n might be assigned to an individual *independent* single-particle like excitation. Not only the sharp independent-particle excitation peak is notably broadened [82] and shifted in energy in the fully interacting many-electron system, but also a fraction of the spectral weight might be transferred into what is called a *satellite state* or *sideband* [1347] of the quasiparticle excitation spectrum. [1343] The occurrence of satellite structures in the matrix elements of the spectral function are a feature of the interacting system and have no equivalent in the noninteracting system. The partial dominance of spectral side-features over sharp single-particle-like features is one basic signature of *strong correlation* in many-body systems. [1347]

QUASIPARTICLE EQUATION – Since experimental spectroscopy as direct or inverse photoemission spectroscopy is widely equivalent to probing the matrix elements $A_{ij}(\omega)$ of the spectral function, the basic challenge to theoretical spectroscopy is the determination of the single-particle Green's function G, it's poles respectively. The definition of the single particle Green's function through, e.g., Eq. 3.88 demands knowledge on the complete set, $\{|N\pm1,n\rangle\}$, of eigenstates of the singly charged $N\pm1$ electron system, a priori, making it intractable for practical calculations. As outlined below, the common approach to determine the single-particle Greens function of solid-state systems directly leads to the concept of a many-body *self energy*, which formally extends the Hartree-Fock treatment of exchange interaction by correlation effects.

Starting from Schrödinger's equation of motion for the field operators in the Heisenberg picture [83]

$$i\frac{\partial}{\partial t}\hat{\psi}(\mathbf{x},t) = \left[\hat{\psi}(\mathbf{x},t),\hat{H}\right] , \tag{3.94}$$

and using the definition of the Green's function, Eq. 3.84, in consideration of the anti-commutation relations of the field operators, leads to the equation of motion for the single-particle Green's function $G(\mathbf{x},\mathbf{x}';t-t')$,

$$\begin{aligned}\left\{i\frac{\partial}{\partial t} - h_0(\mathbf{x})\right\} G\left(\mathbf{x},t;\mathbf{x}'t'\right) &= \delta\left(\mathbf{x}-\mathbf{x}'\right)\delta\left(t-t'\right) \\ - i\int v\left(\mathbf{x},\mathbf{x}''\right) \left\langle N,0\left|\hat{T}\left[\hat{\psi}^{\dagger}\left(\mathbf{x}'',t\right)\hat{\psi}\left(\mathbf{x}'',t\right)\hat{\psi}(\mathbf{x},t)\,\hat{\psi}^{\dagger}\left(\mathbf{x}',t'\right)\right]\right|N,0\right\rangle \mathrm{d}^3\mathbf{x}'' .\end{aligned} \tag{3.95}$$

[82] The broadening is associated to the finite lifetime of the quasiparticle excitation which is not a *true* single-particle eigenstate of the excited many-electron system.

[83] At this point, the derivation of the quasipartcle equation as well as the formal introduction of the self energy and derivation of Hedin's equations widely follows the representation of Aryasetiawan in Ref. [1366]. Likewise, the common notation in atomic-units is adopted.

For conveniency the non-interacting contributions, namely the kinetic energy and the the external *static* potential of the ions, have been collected into the Hamiltonian $h_0(\mathbf{x}) \equiv -\frac{\nabla_{\mathbf{x}}^2}{2} + V_{ext}(\mathbf{x})$. $v(\mathbf{x},\mathbf{x}') = v(|\mathbf{r}-\mathbf{r}'|)\,\delta(t-t')$ is the bare Coulomb potential extended by a potential time-dependence, formally. The four-field-operator term $-i\left\langle N,0\left|\hat{T}\left[\hat{\psi}^\dagger(\mathbf{x}'',t)\,\hat{\psi}(\mathbf{x}'',t)\,\hat{\psi}(\mathbf{x},t)\,\hat{\psi}^\dagger(\mathbf{x}',t')\right]\right|N,0\right\rangle$ on the right hand side of Eq. 3.95 represents a special case of the general definition of a four-point propagator, a time-ordered two-particle[84] Green's function, respectively.

$$G_2(1,2,3,4) = (i)^2\left\langle N,0\left|\hat{T}\left[\hat{\psi}(1)\,\hat{\psi}(3)\,\hat{\psi}^\dagger(4)\,\hat{\psi}^\dagger(2)\right]\right|N,0\right\rangle . \tag{3.96}$$

Here, the common short hand notation $(1) \equiv (\mathbf{x}_1,t_1) \equiv (\mathbf{r}_1,m_{s_1},t_1)$ [27] is adopted. Depending on a proper time-ordering, the two-particle Green's function $G_2(1,2,3,4)$ actually describes the coupled propagation of two (quasi-)particles as two electrons, two holes, or an electron-hole pair, respectively. Equation 3.95 demonstrates that the single-particle Green's function directly depends on the two-particle Green's function. Further successive continuation reveals the hierarchical dependence of the single-particle Green's function on many-body Green's functions up to any order, in a similar vein. So, any practical use of many-body Green's functions in solid state physics necessitates a formal way to truncate this hierarchy of equations of motion.

An essential approach to decouple these increasingly complex order of equations, is the introduction of a many-body self energy, which allows the expression of the two-particle Green's function in terms of the single-particle Green's function. To this purpose, the *mass operator* $M(\mathbf{x},t;\mathbf{x}'t')$ is introduced according to

$$\begin{aligned}&\int M(\mathbf{x},t;\mathbf{x}''t'')\,G(\mathbf{x}'',t'';\mathbf{x}'t')\,\mathrm{d}^3\mathbf{x}''\,\mathrm{d}t'' \\ &= -i\int v(\mathbf{x},\mathbf{x}'')\left\langle N,0\left|\hat{T}\left[\hat{\psi}^\dagger(\mathbf{x}'',t)\,\hat{\psi}(\mathbf{x}'',t)\,\hat{\psi}(\mathbf{x},t)\,\hat{\psi}^\dagger(\mathbf{x}',t')\right]\right|N,0\right\rangle \mathrm{d}^3\mathbf{x}'' .\end{aligned} \tag{3.97}$$

Separation of the leading Hartree contribution [85]

$$\begin{aligned}V_H(\mathbf{x}) &= \int v(\mathbf{x},\mathbf{x}')\,n(\mathbf{x}')\,\mathrm{d}^3\mathbf{x}' \\ &= \int v(\mathbf{x},\mathbf{x}')\left\langle N,0\left|\hat{\psi}^\dagger(\mathbf{x}',t)\,\hat{\psi}(\mathbf{x}',t^+)\right|N,0\right\rangle \mathrm{d}^3\mathbf{x}'\end{aligned} \tag{3.98}$$

from the mass operator

$$M(\mathbf{x},t;\mathbf{x}'t') = V_H(\mathbf{x})\,\delta(\mathbf{x}-\mathbf{x}')\,\delta(t-t') + \Sigma(\mathbf{x},t;\mathbf{x}'t') \tag{3.99}$$

[84] It should be noted that the actual number of particles, propagated by higher order Green's functions depends on the actual time ordering. The $2n$-point quantity will describe the propagation of a maximum of n (quasi-)particles, since the corresponding n-th order Green's function refers to transitions between N, $N\pm1$, ... $N\pm n$-particle eigenstates. [1367]

[85] The subsequently introduced time variable superscript in $t^+ \equiv t+\eta$ indicates an infinitesimal positive time shift $\eta \to +0$ in order to provide a proper time-ordering of the field operators.

allows to rewrite the equation of motion, Eq.3.95, in the form

$$\left\{ i\frac{\partial}{\partial t} - h_0(\mathbf{x}) - V_H(\mathbf{x}) \right\} G(\mathbf{x},t;\mathbf{x}'t') = \delta(\mathbf{x}-\mathbf{x}')\,\delta(t-t') - i\int \Sigma(\mathbf{x},t;\mathbf{x}''t'')\,G(\mathbf{x}'',t'';\mathbf{x}'t')\,\mathrm{d}^3\mathbf{x}''\,\mathrm{d}t''\,. \tag{3.100}$$

Analog to the single-particle Green's function, Eq. 3.84, also the self-energy depends on the time difference $t-t'$, only, i.e. $\Sigma(\mathbf{x},t;\mathbf{x}'t') \equiv \Sigma(\mathbf{x},\mathbf{x}';t-t')$. Fourier transformation into the energy domain with respect to the time variable provides the equation of motion of the single particle Green's function [1344] according to

$$\{\varepsilon + i\eta - h_0(\mathbf{x}) - V_H(\mathbf{x})\}\,G(\mathbf{x},\mathbf{x}';\varepsilon) - \int \Sigma(\mathbf{x},\mathbf{x}'';\varepsilon)\,G(\mathbf{x}'',\mathbf{x}';\varepsilon)\,\mathrm{d}^3\mathbf{x}'' = \delta(\mathbf{x}-\mathbf{x}') \tag{3.101}$$

representing a non-Hermitian eigenvalue problem which describes the *dynamics* of single-quasiparticle excitations in a fully Coulomb correlated many-electron system.

MANY-BODY SELF-ENERGY – Addressing the nature of the self-energy, defined above, and the information encoded in it, an inspection of the structure of Eq. 3.100 indicates that all contributions arising from electron-electron exchange and correlation interactions are subsumed into the non-local and energy-dependent self-energy operator. According to this, setting the self-energy to zero defines the non-interacting (zeroth order) single-particle Green's function, $G_0(\mathbf{x},t;\mathbf{x}'t')$, via the equation of motion

$$\left\{ i\frac{\partial}{\partial t} - h_0(\mathbf{x}) - V_H(\mathbf{x}) \right\} G_0(\mathbf{x},t;\mathbf{x}'t') = \delta(\mathbf{x}-\mathbf{x}')\,\delta(t-t')\,. \tag{3.102}$$

Comparing the equations of motion of the interacting and non-interacting Green's functions, Eq. 3.100 and Eq. 3.102, illustrates that the self-energy connects both Green' functions via the Dyson equation

$$G(\mathbf{x},t;\mathbf{x}'t') = G_0(\mathbf{x},t;\mathbf{x}'t') - i\int G_0(\mathbf{x},t;\mathbf{x}''t'')\,\Sigma(\mathbf{x}'',t'';\mathbf{x}'''t''')\,G(\mathbf{x}''',t''';\mathbf{x}'t')\,\mathrm{d}^3\mathbf{x}''\mathrm{d}^3\mathbf{x}'''\,\mathrm{d}t''\mathrm{d}t'''\,. \tag{3.103}$$

Recalling that the quasiparticle concept is about replacing a bare entity as the electron by the practically observable complex of the particle and its *instantaneous* interaction cloud originating from local polarization of the many-electron system, the self-energy describes the *reciprocal* dynamical interaction of the particle and the *dressing* screening cloud. The self-energy $\Sigma(\mathbf{x},\mathbf{x}'';\varepsilon)$ formally allows a more *complete* and systematic treatment of exchange-correlation as provided by conventional density-functional theory approaches, in principal. If the self-energy is known or approximated *properly*, the quasiparticle equation, Eq. 3.101, could be solved self-consistenly for the interacting single-particle Green's function, giving access to the collective quasiparticle exci-

tation spectrum as well as all associated single-particle properties, exception values respectively. However, due to the complicated and self-referential functional dependence of the self-energy on the single-particle Green's function, $\Sigma \equiv \Sigma[G]$, a solution of Eq. 3.101 is far from trivial even in case of simple model systems. [1344]

A straightforward finite order expansion of the self-energy in powers of the bare Coulomb interaction $v(\mathbf{x},\mathbf{x}')$ results in the non-local exact-exchange interaction of Hartree-Fock therory (see Eq. 3.67), the (static) *self-energy of Hartree-Fock theory*, respectively. Though this lowest order expansion is well established, even in case of extended solid-state systems, the long-ranging nature of the bare Coulomb interaction provokes intractable or even diverging convergence in case of following the perturbation expansion to higher order. [27] There are two essential approaches that allow for a systematic and *meaningful*[86] evaluation of the self-energy. On the one hand, the self-energy is evaluated perturbatively through use of Wick's theorem.[87] [1372] On the other hand, Schwinger's approach of functional derivatives [1373, 1374], as adopted by Hedin to solid-state physics in order to generate an expansion of the self-energy in terms of a screened potential W [27, 28] (see discussion below), is widely adopted as the theoretical framework for numerical implementations of many-body perturbation theory.

3.4.1 Hedin's fundamental equations

Not much new in principle – In 1965 the swedish theoretical physicist Lars Hedin (1930–2002) published his seminal paper presenting a "New Method for Calculating the One-Particle Green's Function with Application to the Electron-Gas Problem". [27] Hedin himself labeled his work by the humble understatement "not much new in principle" referring to the fact that most results had been quite familiar to the Green's function community. [27] Nevertheless, Hedin's equations provide functional closure for the determination of the electronic self-energy and solution of the Dyson equation by starting from minimal prerequisites. Hedin's seminal scientific contributions had exceptional influence on the development of the theory of excited states and modern solid-state physics, in general.[88] Instead of an expansion of the self-energy in terms of the bare Coulomb interaction, Hedin established the self-energy expansion in terms of the more convenient dynamically screened Coulomb potential $W(\mathbf{x},\mathbf{x}';\omega)$,

$$W\left(\mathbf{x},\mathbf{x}';\omega\right) = \int \varepsilon^{-1}\left(\mathbf{x},\mathbf{x}'';\omega\right) v\left(\mathbf{x}''-\mathbf{x}'\right) \mathrm{d}^3\mathbf{x}'' \,. \tag{3.104}$$

[86] *Meaningful*, working in practice respectively, approximations to the self energy typically require summation of relevant diagrammatic classes of many-body interactions to infinite order. However, choosing proper classes of diagrams is subject to physical intuition rather than an object of *strict* formal justification. [1344, 1366] The most established summation in solid-state physics is the random phase approximation which can be derived from perturbation theory [1261, 1339, 1368] as well as the adiabatic-connection fluctuation-dissipation theorem [1261, 1267–1270].

[87] More precisely Wick's theorem in conjunction with Feynman's diagrammatic representation of perturbative quantum theory. [1369–1371]

[88] Lars Hedin's extensive contributions to the theory of excited states in solid-state physics have been reviewed by Rehr et al. [1375].

Here, $\varepsilon^{-1}(\mathbf{x},\mathbf{x}'';\omega)$ is the inverse of the non-local frequency-dependent (longitudinal) dielectric function. Adopting Hedins shorthand notation, Eq. 3.104 reads

$$W(1,2) = \int \varepsilon^{-1}(1,3)\, v(2,3)\, \mathrm{d}3\,. \tag{3.105}$$

$W(1,2)$ essentially represents the potential at point 1 due to the presence of a *test charge* at point 2, including local polarization effects of the many-electron system that effectively weaken the net electron-electron interaction by screening the bare Coulomb potential. [27]

Well known to the "Green's-function people" [89] – In his derivation of a fundamental system of equations that formally paraphrase the many-electron problem, Hedin adopted Schwinger's technique of functional derivatives (e.g. see Ref. [1366, 1376]) from quantum electrodynamics in order to generate an expansion of the self-energy in terms of a screened potential W. Following the roots of linear response theory, the response of the single-particle Green's function to an external perturbation, given by a time-dependent probing/perturbation field $\phi_{ext}(\mathbf{r},t)$, can be related to the two-particle Green's function according to

$$\frac{\delta G(1,2)}{\delta \phi_{ext}(3)} = G(1,2)\, G\left(3,3^{+}\right) - G_2\left(1,2,3,3^{+}\right). \tag{3.106}$$

Using this relation together with the definition of the mass-operator via Eq. 3.97 yields

$$\int M(1,3)\, G(3,2)\, \mathrm{d}3 = V_H(1)\, G(1,2) + i \int v(1,3)\, \frac{\delta G(1,2)}{\delta \phi_{ext}(3)} \mathrm{d}3\,. \tag{3.107}$$

Multiplication on both sides from the right by $G^{-1}(2,4)$ and integration over the space-time variable 2 defines the mass operator as

$$M(1,4) = V_H(1)\, \delta(1,4) + i \int v(1,3)\, \frac{\delta G(1,2)}{\delta \phi_{ext}(3)} G^{-1}(2,4)\, \mathrm{d}(3,2) \tag{3.108}$$

and, according to Eq. 3.99, the self energy as

$$\Sigma(1,2) = i \int v(1,3)\, \frac{\delta G(1,4)}{\delta \phi_{ext}(3)} G^{-1}(4,2)\, \mathrm{d}(3,4) \tag{3.109}$$

$$= -i \int v(1,3)\, G(1,4)\, \frac{\delta G^{-1}(4,2)}{\delta \phi_{ext}(3)} \mathrm{d}(3,4) \tag{3.110}$$

in terms of the single-particle Greens function as well as its functional derivative with respect to the probing field. Switching to the total (classical) potential $V_{tot} = V_H + \phi_{ext}$ and utilizing the chain rule on functional derivatives gives

$$\Sigma(1,2) = -i \int v(1,3)\, G(1,4)\, \frac{\delta G^{-1}(4,2)}{\delta V_{tot}(5)} \frac{\delta V_{tot}(5)}{\delta \phi_{ext}(3)} \mathrm{d}(3,4,5)\,, \tag{3.111}$$

[89] See Ref. [27].

which allows to discover the definition of the inverse (microscopic) dielectric function, that describes the variation of the total potential V_{tot} with respect to the external perturbation ϕ_{ext},

$$\varepsilon^{-1}(1,2) = \frac{\delta V_{tot}(1)}{\delta \phi_{ext}(2)}. \tag{3.112}$$

For later use it is convenient to express the inverse dielectric function through the (linear) *density-density response function*

$$\chi(1,2) = \frac{\delta n(1)}{\delta \phi_{ext}(2)}, \tag{3.113}$$

the reducible polarizability respectively,

$$\varepsilon^{-1}(1,2) = \delta(1,2) + \int v(1,3)\,\chi(3,2)\,\mathrm{d}3. \tag{3.114}$$

Finally, with introduction of the (irreducible [90]) three point *vertex function*,

$$\Gamma(4,2,5) = -\frac{\delta G^{-1}(4,2)}{\delta V_{tot}(5)}, \tag{3.115}$$

Eq. 3.111 turns into the commonly used expression for the self-energy,

$$\Sigma(1,2) = i\int W(5,1)\,G(1,4)\,\Gamma(4,2,5)\,\mathrm{d}(4,5). \tag{3.116}$$

The vertex function Γ could be expressed in the form

$$\Gamma(1,2,3) \equiv -\frac{\delta G^{-1}(1,2)}{\delta V_{tot}(3)} \tag{3.117}$$

$$= \delta(1,2)\,\delta(1,3) + \frac{\delta\Sigma(1,2)}{\delta V_{tot}(3)} \tag{3.118}$$

$$= \delta(1,2)\,\delta(1,3) + \int \frac{\delta\Sigma(1,2)}{\delta G(4,5)} G(4,6)\,G(7,5)\,\Gamma(6,7,3)\,\mathrm{d}(4,5,6,7). \tag{3.119}$$

According to its definition the vertex function can be viewed as the linear response of the self energy to changes of the total potential. [1378] The necessary integral equation to determine the screened Coulomb potential $W(1,2)$, Eq. 3.105, could be derived starting from Eq. 3.112. Considering $V_{tot}(1) = V_H(1) + \phi_{ext}(1)$ as well as the definition

$$V_H(1) = \int v(1,4)\,n(4)\,\mathrm{d}4 \tag{3.120}$$

$$\equiv -i\int v(1,4)\,G\left(4,4^+\right)\mathrm{d}4. \tag{3.121}$$

[90] According to its definition, the *irreducible* vertex function Γ contains the changes of the potentials with respect to changes of the total field V_{tot}. In contrast, the *reducible* vertex function $\widetilde{\Gamma}$ encompasses changes with respect to the time-varying perturbation potential ϕ_{ext}. Since the external perturbation potential provokes an counteracting induced potential, the changes in the *irreducible* vertex function Γ are expected to be smaller than in the *reducible* vertex function $\widetilde{\Gamma}$. [1377]

of the Hartree potential, one deduces

$$W(1,2) = v(1,2) + \int v(1,4)\,\frac{\delta n(4)}{\delta V_{tot}(5)}\,\frac{\delta V_{tot}(5)}{\delta \phi_{ext}(3)}\,v(3,2)\,\mathrm{d}(3,4,5) \tag{3.122}$$

$$= v(1,2) + \int v(1,4)\,\frac{\delta n(4)}{\delta V_{tot}(5)}\,W(5,2)\,\mathrm{d}(4,5)$$

$$\equiv v(1,2) + \int v(1,4)\,P(4,5)\,W(5,2)\,\mathrm{d}(4,5)\,. \tag{3.123}$$

The last step utilizes the definition of the (irreducible) *polarization function*

$$P(1,2) = \frac{\delta n(1)}{\delta V_{tot}(2)} \tag{3.124}$$

as the response function of the electron density with respect to the total potential V_{tot}. The polarization function can be expressed in term of the single-particle Green's function according to

$$P(1,2) = \frac{\delta n(1)}{\delta V_{tot}(2)} \equiv -i\frac{\delta G(1,1^+)}{\delta V_{tot}(2)} \tag{3.125}$$

$$= -i\int G(1,3)\,\Gamma(3,4,2)\,G\left(4,1^+\right)\mathrm{d}(3,4)\,.$$

The relation between irreducible polarization P and the density-density response function χ can be established using the chain rule of functional derivatives according to

$$\chi(1,2) = \int P(1,3)\,\varepsilon^{-1}(3,2)\,\mathrm{d}3\,, \tag{3.126}$$

which leads to the the Dyson equation

$$\chi(1,2) = P(1,2) + \int P(1,3)\,v(3,4)\,\chi(1,2)\,\mathrm{d}(4,2) \tag{3.127}$$

linking P and χ and a dielectric function given by

$$\varepsilon(1,2) = \delta(1,2) + \int v(1,3)\,P(3,2)\,\mathrm{d}3\,. \tag{3.128}$$

After some rearrangements one might write down a closed set of five fundamental coupled integro-differential equations, *Hedin's equations* [27, 28] [91,92], that represent the formal basis for

[91] Hedins equations have been derived for a Coulomb interacting many-electron system without taking into account explicit spin dependence.Therefore, Aryasetiawan and Biermann generalized Hedin's Equations for quantum many-body systems considering explicit spin-dependent interactions. [1379]

[92] Even though Hedin's equations, as well as the manifold of approximative solution schemes, form the basis of recent numerical implementations, alternative versions of fundamental equations have been considered. [1380, 1381] For example, Starke and Kresse [1380] derived a closed set of three equations from the equation of motion for the Green's function in combination with the Bethe-Salpeter equation for the scattering amplitude. Since these equations have been proven to be a formally exactly equivalent to Hedin's equations, they might be considered as a quasi-(re)derivation of Hedin's fundamental set of equations.

electronic-structure theory within the framework of many-body perturbation theory,

$$G(1,2) = G_0(1,2) + \int G_0(1,3)\,\Sigma(3,4)\,G(4,2)\,\mathrm{d}(3,4) \tag{3.129}$$

$$\Sigma(1,2) = i\int G(1,3)\,W\left(1^+,4\right)\Gamma(3,2;4)\,\mathrm{d}(3,4) \tag{3.130}$$

$$W(1,2) = v(1,2) + \int W(1,3)\,P(3,4)\,v(4,2)\,\mathrm{d}(3,4) \tag{3.131}$$

$$P(1,2) = -i\int G(2,3)\,G\left(4,2^+\right)\Gamma(3,4;1)\,\mathrm{d}(3,4) \tag{3.132}$$

$$\Gamma(1,2;3) = \delta(1,2)\,\delta(1,3) + \int \frac{\delta\Sigma(1,2)}{\delta G(4,5)}G(4,6)\,G(7,5)\,\Gamma(6,7;3)\,\mathrm{d}(4,5,6,7)\,. \tag{3.133}$$

Equation (3.129) is a Dyson equation relating non-interesting and interacting Green's functions through the self energy Σ (cf. Eq. 3.103). The self energy, Eq. 3.130, itself is a highly non-trivial functional of the Greens function $\Sigma = \Sigma[G]$ (cf. Eq. 3.116). A second Dyson-like equation, Eq. (3.131), defines the screened Coulomb interaction W in terms of the polarization propagator P (cf. Eq. 3.123). The irreducible polarization propagator (cf. Eq. 3.126) connects two separate interacting Green's functions through a vertex function Γ via equation Eq. (3.132). Finally, the irreducible vertex function, Eq. (3.133), is defined through a Bethe-Salpeter equation containing a non-trivial functional-derivative of the self-energy with respect to the Green's function as integral kernel (cf. Eq. 3.119). Starting from a given approximation to the self-energy, Hedin's equations provide a systematic framework for generation of higher order approximations [1366].

Strange Loops – A convenient way to represent many-body physics, and quantum-field theories in general, is provided by use of Feynman diagrams [93] originally introduced to tackle unmanageable calculations with infinite terms in quantum electrodynamics. [1369, 1383–1386] Feynman diagrams were later on utilized in various branches of theoretical physics including solid-state physics. [1339, 1342]

A diagrammatic representation of Hedin's equations (also see Ref. [1387]), which is formally analog to the system of equations (3.129) to (3.133) is given in Fig. 3.7. As illustrated in Fig. 3.8 Hedin's equations might, in principle, be solved self-consistently to find an exact solution to the many-electron problem. However, finding a converged *self-consistent* solution is probably intractable in the same manner as finding an exact solution to the many-electron Schrödinger equation itself; neither the absolute convergence of the iterative solution nor the numerical feasibility might be given. [987, 1379, 1388] The later is not only due to the necessary computational efforts but due to the non-trivial functional dependence of Σ on G through the functional derivative $\partial\Sigma/\partial G$ in the vertex function, Eq. (3.133), which prevents any straightforward numerical iteration. [1388, 1389] Practical *solutions* to Hedins equations are therefore restricted to a quite limited number of iterations, starting from sound density-functional theory input and effective truncation schemes to the full self-consistent cycle (cf. Fig. 3.9). Nevertheless, Hedin's equations still

[93] An historical review on Feynman diagrams is provided in Ref. [1382].

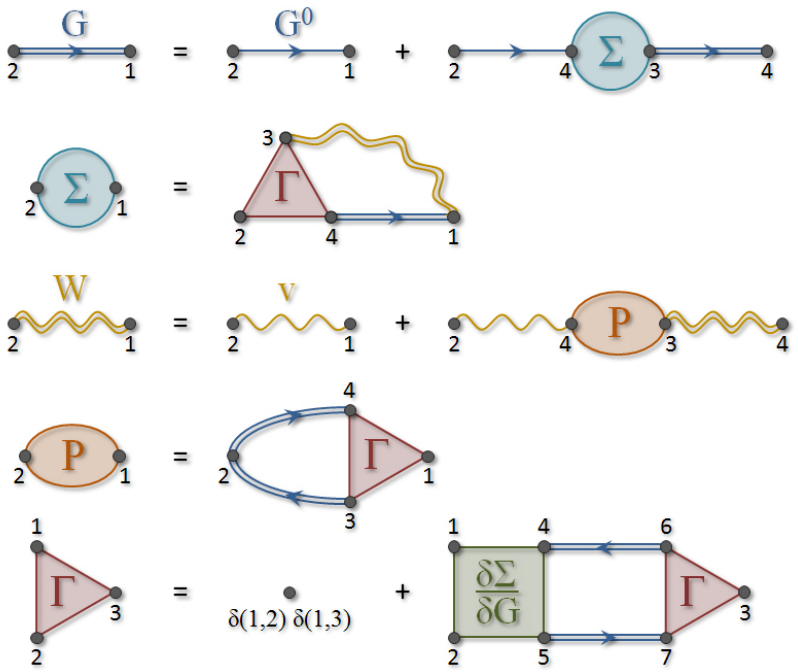

Figure 3.7: Diagrammatic representation of Hedin's equations.

provide a systematic scheme for evaluation of the electronic self-energy on different levels of approximation.

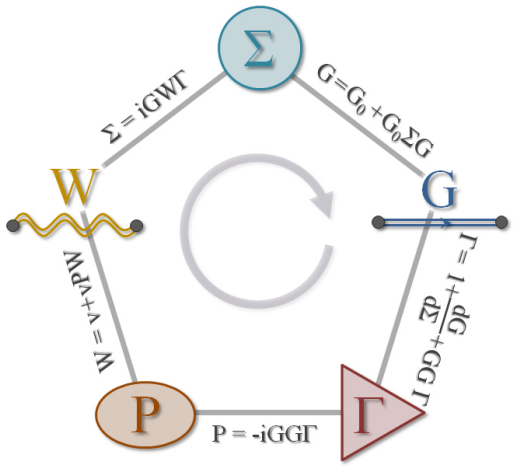

Figure 3.8: Pictorial illustration of the self-consistent solution cycle to Hedin's equations.

3.4.2 Hedin's *GW* approximation

Fifty Shades of Green – The most basic approximation to many-body perturbation theory is Hedin's *GW* approximation [28] which has been illustrated in Fig. 3.9. In this lowest order approximation, Hedin's equations are decoupled by narrowing the vertex corrections to

zeroth order, $\Gamma(1,2;3) = \delta(1,2)\,\delta(1,3)$ in all equations. On the one side, this yields the polarization propagator in random-phase approximation, $P_{RPA}(1,2) = -iG(1,2)\,G(2,1)$ which is formally exact in case of non-interacting (quasi)particles. The *GW* self-energy is defined through the name-giving product of single-particle Green's function and screened Coulomb interaction, $\Sigma_{GW}(1,2) = iG(1,2)\,W(1,2)$. In *GW* approximation Hedin's system of fundamental equations reduces to

$$G(1,2) = G_0(1,2) + \int G_0(1,3)\,\Sigma(3,4)\,G(4,2)\,\mathrm{d}(3,4) \tag{3.134}$$

$$\Sigma(1,2) = iG(1,2)\,W\left(1^+,2\right) \tag{3.135}$$

$$W(1,2) = v(1,2) + \int W(1,3)\,P(3,4)\,v(4,2)\,\mathrm{d}(3,4) \tag{3.136}$$

$$P(1,2) = -iG(1,2)\,G(2,1) \tag{3.137}$$

$$\Gamma(1,2;3) = \delta(1,2)\,\delta(1,3)\,. \tag{3.138}$$

Since the vertex function carries essential information on the exchange and correlation interactions between an electron and its screening cloud [1378], the neglect of vertex corrections in the polarization propagator especially involves the loss of information about quasiparticle interactions, more precisely, the quasielectron-quasihole interactions, which also give rise to excitonic contributions in the optical response. The *GW* self energy generalizes the non-local long-ranging Hartree-Fock exchange interaction $\Sigma_{HF}(1,2) = iG(1,2)\,v(1,2)$, by replacing the bare Coulomb potential $v(1,2)$ with the dynamically screened Coulomb interaction W. Hence, the *GW*-self energy $\Sigma_{GW}(1,2) = \Sigma_{HF}(1,2) + \Sigma_c(1,2)$ carries information on electron exchange as well as some correlation contributions Σ_c through polarization effects.

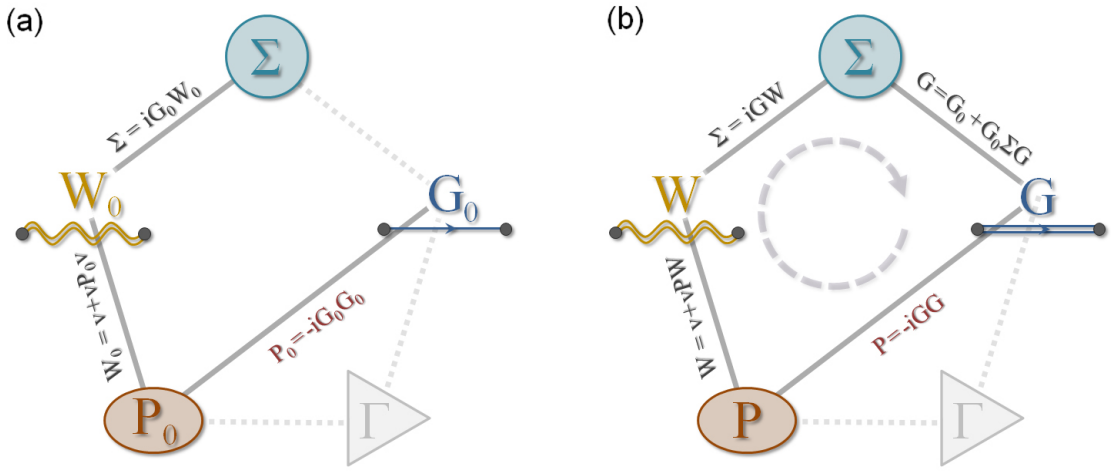

Figure 3.9: Schematic illustration of common solution strategies to evaluate *GW* quasiparticle corrections within the framework of many-body perturbation theory. Illustrated are the non-self-consistent G_0W_0 approach and a (partially) self-consistent *GW* scheme without vertex corrections.

Having set the formal basis of the *GW* formalism, it remains necessary to define a *reasonable*

starting point for a practical evaluation of the self-energy. In a straight forward approach one might start from setting the self-energy to zero, $\Sigma = 0$ and start from the independent-particle Green's function G_0 within the formal framework of Hartree theory. All effects of exchange and correlation are subsequently added through stepwise improvement of the *GW* self energy, Σ_{GW}, during a self-consistent solution of the *GW* equations (cf. Fig. 3.9 b), which also yields the interacting single-particle Green's function G. Even though the neglect of vertex corrections represents a substantial simplification of the many-body problem, reaching complete self-consistency is still considered a challenging task [94]. Obviously, the converged *GW* self-energy differs from the exact many-body self-energy due to the neglect of vertex corrections, the random-phase approximation to polarization, respectively. However, contemporarily available computational resources more and more allow the exact evaluation of the diagrammatic expansions of many-body interactions to higher orders, thereby shedding new light on the relevance of self-consistency in the *GW* formalism. [1393–1401]

Non-self-consistent *solution*/approximation schemes, in most cases even a reduction to a single evaluation loop, have become the widely-used modus operandi of practical *GW* calculations in view of computational demands. The typical *single shot* approximation, as illustrated in Fig. 3.9 a, is initialized via $\Sigma = 0$ and $G = G_0$. The polarization function in random-phase approximation [95], $P_0 = -iG_0G_0$, is used to construct the lowest order approximation of the screened Coulomb potential, W_0. Together, the product of the non-interacting Green's function G_0 and the screened Coulomb potential W_0 defines the G_0W_0 self-energy, $\Sigma_{GW} = iG_0W_0$. Obviously, the final nature of the G_0W_0 self-energy crucially depends on the numerical *input* used to construct the independent-particle Green's function G_0. In case of input from exchange-correlation-free Hartree theory the final result will be far-off from the actual many-body self-energy and even in case of correlation-free single-particle orbitals and energies from Hartree-Fock theory some discrepancies are inevitable. However, the G_0W_0 self-energy drastically improves upon constructing the non-interacting Green's function from ingredients provided by (generalized) Kohn-Sham theory, namely the single-particle orbitals/wave functions φ^{KS}, which provide a excellent approximation to the actual *GW* quasiparticle-wave functions, and the corresponding Kohn-Sham eigenvalues ε^{KS}. In a certain sense, this approach provides the *best* (*single-shot*) G_0 and, within a *generalized* random-phase approximation, the *best* approximation of the screened Coulomb potential W_0. The pursuit of using a *best G best W* approximation to evaluate the self energy has also motivated

[94] The substantial numerical cost involved in evaluation of the *GW* self-energy, even in its non-self-consistent version, also promoted more approximate self-energy treatments as the static Coulomb-hole screened-exchange (*COHSEX*) approximation. [27, 1390–1392] A comparative study on self-energy approximations of solids within different self-consistent approaches has been published by Bruneval et al. [1390], for instance.

[95] The term *random-phase approximation* actually refers to the actual non-interacting (Hartree) Green's function, a completely neglected exchange-correlation self energy (i.e. $\Sigma = 0$). However, it is a common practice to construct G_0 from, e.g., Kohn-Sham theory ingredients (see discussion above). Since the Kohn-Sham formalism explicitly accounts for exchange and correlation effects, the resulting Green's function G_0^{KS} and associated polarization function P_0^{KS} do not refer to the actual non-interacting system ($\Sigma = 0$). However, the use of Kohn-Sham single-particle orbitals and eigenvalues to evaluate the polarization in a *generalized* random-phase approximation has proven extremely favorable, with respect to accuracy as well as numerical cost, in non-self-consistent G_0W_0 approaches.

several partially self-consistent *GW* approaches, in which either the single-particle Green's function, GW_0, or the screened Coulomb potential, G_0W is evaluated repeatedly. [1396, 1402–1404] However, the practicality of non-selfconsistent and partially self-consistent *GW* schemes differs for various material classes and is subject to physical intuition and extensive operating experience on practical self-consistent and non-self-consistent *GW* calculations.

One general justification for this non-self-consistent treatment of the *GW* approximation has been the assumption that self-consistency effects and vertex corrections approximately cancel each other, at least in case of a sound density-functional theory input to evaluate the G_0W_0 self energy. [1395, 1405–1408] In order to cure some of the remaining drawbacks of non-self-consistent and self-consistent *GW* approximations, the increased performance of current high-performance facilities has allowed to illuminate the benefits from systematic inclusion of vertex corrections beyond the common random-phase polarization into fully self-consistent *GW* schemes. [1381, 1387, 1398, 1403, 1405, 1409–1418] Beyond the random-phase approximation, the polarization is determined from interacting electron-hole pairs. Thereby, the general inclusion of the attractive electron-hole interaction, through a more elaborate treatment of the vertex function within the self-consistent calculation of quasiparticle properties ($GW\Gamma$), tends to cure some of the still existing shortcomings of self-consistent *GW*. Especially, the observed (moderate) overestimation of electronic band gaps in fully self-consistent sc-*GW* is widely corrected towards the experimental value. [1398, 1413] Hence, converged sc-$GW\Gamma$ simulations clearly inhere the potential to provide parameter-free predictive numerical reference data for electronic band-structure features [96], but to the computational cost of an $\mathcal{O}(6)$ scaling that is on par with advanced wavefuntion-based methods. [1381]

How does it work in practice? The inhomogenous quasiparticle equation Eq. 3.101 represents an eigenvalue problem which is analog to the eigenvalue problem of generalized Kohn-Sham theory [1062, 1189], if the non-local self-energy operator $\Sigma(\mathbf{x},\mathbf{x}';\varepsilon)$ is replaced by the local Kohn-Sham exchange-correlation potential $V_{XC}(\mathbf{x})\,\delta(\mathbf{x}-\mathbf{x}')$. For obvious reason, this and the ubiquity of Kohn-Sham wave functions φ^{KS} in modern electronic-structure theory, suggests to represent basic quantities of quasiparticle theory as the Green's function $G(\mathbf{x},\mathbf{x}';\varepsilon)$ or the spectral function $A(\mathbf{x},\mathbf{x}';\varepsilon)$ in term of the complete set of Kohn-Sham eigenfunctions $\left\{\varphi^{KS}_{\lambda,\mathbf{k}}(\mathbf{x})\right\}$ [97]. [1344] Exemplarily, the single-particle Greens function is expressed in terms of the Kohn-Sham eigenfunctions according to

$$G\left(\mathbf{x},\mathbf{x}';\varepsilon\right) = \sum_{\lambda,\lambda'}\sum_{\mathbf{k}} G_{\lambda,\lambda'}(\mathbf{k},\varepsilon)\,\varphi^{KS}_{\lambda,\mathbf{k}}(\mathbf{x})\,\varphi^{*KS}_{\lambda,\mathbf{k}}(\mathbf{x})\,. \tag{3.139}$$

Thereby, the off-diagonal elements of $G_{\lambda,\lambda'}(\mathbf{k},\varepsilon)$ with respect to the band indices λ and λ' ac-

[96] In case of substantially strong correlated systems as some transition-metal oxides or f-electron systems with dominant contributions from local correlation, it becomes inevitable to join the qualities of the $GW(\Gamma)$ framework with the merits of dynamical mean-field theory [1419–1421] into a dynamical vertex approximation. [1387, 1422, 1423]

[97] Here, $\varphi^{KS}_{\lambda\mathbf{k}}(\mathbf{x})$ refers to the Bloch representation of the Kohn-Sham orbitals with the band index λ at the $\mathbf{k}$-point $\mathbf{k}$.

count for differences between the Kohn-Sham wave functions and the actual quasiparticle-wave functions. In case of the non-interacting zeroth order Green's function, the expansion coefficients $G^0_{\lambda,\lambda'}(\mathbf{k},\varepsilon)$ account for (unknown) quasiparticle-energy shifts $\Delta_{\lambda,\mathbf{k}}$ of the Kohn-Sham eigenvalues $\varepsilon^{KS}_{\lambda,\mathbf{k}}$ in the spectral function (cf. Eq. 3.91 and Eq. 3.92) according to

$$G^0_{\lambda,\lambda'}(\mathbf{k},\varepsilon) = \frac{1}{\varepsilon - \varepsilon^{QP}_{\lambda,\mathbf{k}} + i\eta_{\lambda,\mathbf{x}}}, \tag{3.140}$$

with $\varepsilon^{QP}_{\lambda,\mathbf{k}} = \varepsilon^{KS}_{\lambda,\mathbf{k}} + \Delta\varepsilon^{QP}_{\lambda,\mathbf{k}}$. Given the orbital representation of the single-particle Green's function, Eq. 3.139, and the self-energy $\Sigma_{\lambda,\lambda'}(\mathbf{k},\varepsilon)$, the Dyson-like quasiparticle equation Eq. 3.101 can be transformed into the matrix equation

$$G_{\lambda,\lambda'}(\mathbf{k},\varepsilon) = G^0_{\lambda,\lambda'}(\mathbf{k},\varepsilon)\left\{1 + \left[\delta\Sigma_{\lambda,\lambda'}(\mathbf{k},\varepsilon) - \Delta\varepsilon_{\lambda,\mathbf{k}}\right] G_{\lambda,\lambda'}(\mathbf{k},\varepsilon)\right\}, \tag{3.141}$$

where, $\delta\Sigma(\mathbf{x},\mathbf{x}';\varepsilon) = \Sigma(\mathbf{x},\mathbf{x}';\varepsilon) - V_{XC}(\mathbf{x})\,\delta(\mathbf{x}-\mathbf{x}')$ accounts for exchange-correlation effects in the *GW* self-energy that are not contained in the Kohn-Sham exchange-correlation potential. Assuming a small perturbation $\left[\mathrm{Re}\left\{\delta\Sigma^0_{\lambda,\lambda'}(\mathbf{k},\varepsilon) - \Delta\varepsilon_{\lambda,\mathbf{k}}\right\}\right]$ [98] against the actual quasiparticle energy shifts $\Delta^{QP}_{\lambda,\mathbf{k}}$ and restricting to the first non-vanishing order (e.g. see Ref. [987, 1344]) defines the quasiparticle-energy shifts, the *corrections* to the Kohn-Sham eigenvalues respectively, according to

$$\Delta\varepsilon^{QP}_{\lambda,\mathbf{k}} = \mathrm{Re}\left\{\delta\Sigma^0_{\lambda,\lambda'}\left(\mathbf{k},\varepsilon^{QP}_{\lambda,\mathbf{k}}\right)\right\}. \tag{3.143}$$

Hence, the *GW* quasiparticle shifts are defined in the spirit of a first order perturbation theory treatment with respect to the presumably *small* perturbation $\delta\Sigma(\mathbf{x},\mathbf{x}';\varepsilon)$. [99,100] Due to the dependence of the self-energy on the sought-after quasiparticle energies $\varepsilon^{QP}_{\lambda,\mathbf{k}}$, the quasiparticle shifts $\Delta\varepsilon^{QP}_{\lambda,\mathbf{k}}$ should be evaluated self-consistently through repeated iteration of Eq. 3.143. It is further common to assume a linear energy dependence of the self-energy difference $\delta\Sigma^0_{\lambda,\lambda'}(\mathbf{k},\varepsilon)$ around $\varepsilon = \varepsilon^{QP}_{\lambda,\mathbf{k}}$, which yields the renormalized quasiparticle shifts [987, 1189, 1344, 1365, 1424]

$$\Delta\varepsilon^{QP}_{\lambda,\mathbf{k}} = Z_{\lambda,\mathbf{k}}\mathrm{Re}\left\{\delta\Sigma^0_{\lambda,\lambda'}\left(\mathbf{k},\varepsilon_{\lambda,\mathbf{k}}\right)\right\} \tag{3.144}$$

[98] Here, $\Sigma^0_{\lambda,\lambda'}(\mathbf{k},\varepsilon)$ denotes the self-energy, in which the interacting Green's function $G(\mathbf{x},\mathbf{x}';\varepsilon)$, Eq. 3.139 in the *GW* self-energy Eq. 3.135, has been replaced by the non-interacting Kohn-Sham Green's function

$$G^{KS}_0(\mathbf{x},\mathbf{x}';\varepsilon) = \sum_{n\mathbf{k}} \frac{\varphi^{KS}_{\lambda,\mathbf{k}}(\mathbf{x})\,\varphi^{*KS}_{\lambda,\mathbf{k}}(\mathbf{x}')}{\varepsilon - \varepsilon^{QP}_{\lambda,\mathbf{k}} + i\eta_{\lambda,\mathbf{x}}}. \tag{3.142}$$

[99] A similar perturbative form of energy corrections has also been derived within the framework of generalized Kohn-Sham theory. [1062]

[100] The perturbative treatment of energy corrections in quasiparticle theory is commonly justified from the formal analogy of the (generalized) Kohn-Sham and quasiparticle eigenvalue problems Eq. 3.101 and Eq. 3.39.

with

$$Z_{\lambda,\mathbf{k}} = \left[1 - \frac{\partial \mathrm{Re}\left\{ \Sigma^0_{\lambda,\lambda'}(\mathbf{k},\varepsilon) \right\}}{\partial \varepsilon} \bigg|_{\varepsilon=\varepsilon_{\lambda,\mathbf{k}}} \right]^{-1} . \tag{3.145}$$

The singular (*single-shot*) evaluation of Eq. 3.146 yields G_0W_0 quasiparticle shifts exclusively depending on the Kohn-Sham reference system through the eigenvalues and single-particle wave functions $\varepsilon^{KS}_{\lambda,\mathbf{k}}$ and $\varphi^{KS}_{\lambda,\mathbf{k}}(\mathbf{x})$.

Partial *self-consistence* is introduced through repeated evaluation of the quasiparticle energies via

$$\varepsilon^{QP^{(N+1)}}_{\lambda,\mathbf{k}} = \varepsilon^{QP^{(N)}}_{\lambda,\mathbf{k}} + Z^{(N)}_{\lambda,\mathbf{k}} \mathrm{Re}\left\{ \delta\Sigma^0_{\lambda,\lambda'}\left(\mathbf{k}, \varepsilon^{(N)}_{\lambda,\mathbf{k}}\right) \right\} . \tag{3.146}$$

with

$$Z^{(N)}_{\lambda,\mathbf{k}} = \left[1 - \frac{\partial \mathrm{Re}\left\{ \Sigma^0_{\lambda,\lambda'}(\mathbf{k},\varepsilon) \right\}}{\partial \varepsilon} \bigg|_{\varepsilon=\varepsilon^{QP^{(N)}}_{\lambda,\mathbf{k}}} \right]^{-1} \quad \text{and} \quad \varepsilon^{QP^{(0)}}_{\lambda,\mathbf{k}} \equiv \varepsilon^{KS}_{\lambda,\mathbf{k}} \tag{3.147}$$

and repeated optimization of the self-energy through adjustment of the quasiparticle energies $\varepsilon^{QP^{(N)}}_{\lambda,\mathbf{k}}$ in the denominator of the single-particle Green's function Eq. 3.142 and, out of it, in the screened Coulomb potential. Commonly, the N-th iteration of quasiparticle energies is specified by G_NW_N, whereas one refers to the self-consistent solution as GW.[101] The screened Coulomb potential, calculated from the non-interacting Kohn-Sham Greens function $G^{KS}_0(\mathbf{x},\mathbf{x}';\varepsilon)$ (with $\varepsilon^{QP^{(N)}}_{\lambda,\mathbf{k}} \equiv \varepsilon^{KS^{(N)}}_{\lambda,\mathbf{k}}$), Eq. 3.142, represents an excellent approximation of the screened Coulomb potential for some material classes. In these cases, the energy dependence of the screened Coulomb potential might be fixed on the W_0 level throughout all iterations of the self-energy and the single particle Green's function is re-evaluated, only. The associated quasiparticle schemes are denoted as G_NW_0 and GW_0, respectively. While self-consistency in the actual GW scheme exclusively refers to the energy dependence, the poles of the single particle Green's function respectively, a complete self-consistent solution within the GW approximation also necessitates simultaneous optimization of the Kohn-Sham/quasiparticle orbitals. To this purpose the quasiparticle-wave functions $\varphi^{QP}_{\lambda,\mathbf{k}}(\mathbf{x})$ [102] might be expanded in a series of the orthonormal set $\left\{ \varphi^{KS}_{\lambda,\mathbf{k}}(\mathbf{x}) \right\}$ of Kohn-Sham orbitals according to

$$\varphi^{QP}_{\lambda,\mathbf{k}}(\mathbf{x}) = \sum_{\lambda'} c_{\lambda,\lambda'}(\mathbf{k})\, \varphi^{KS}_{\lambda',\mathbf{k}}(\mathbf{x}) , \tag{3.148}$$

which turns the quasiparticle equation, Eq. 3.101 [103], into a set of algebraic equations [987, 1426,

[101] Partially self-consistent GW schemes with updates of the quasiparticle energies in the Green's function and/or the screened Coulomb potential are also known as eigenvalue GW (EVGW).

[102] In view of the validity of the quasiparticle picture, the norm of the quasiparticle orbitals could be interpreted as a measure of how well the true many-body excitation can be described as a single-particle excitation. [1425]

[103] It is convenient to neglect the quasiparticle lifetime and restrict the explicit calculation to real eigenvalues $\varepsilon^{QP}_{\lambda,\mathbf{k}}$ by restriction to the hermitian part of the self-energy operator. [987]

1427]

$$\sum_{\lambda'}\left(\left[\varepsilon_{\lambda,\mathbf{k}}-\varepsilon^{QP}_{\lambda,\mathbf{k}}\right]\delta_{\lambda,\lambda'}+\mathrm{Re}\left\{\delta\Sigma^{0}_{\lambda,\lambda'}\left(\mathbf{k},\varepsilon^{QP}_{\lambda,\mathbf{k}}\right)\right\}\right)c_{\lambda,\lambda'}(\mathbf{k})=0\,, \tag{3.149}$$

that couple different eigenstates of the Kohn-Sham orbital basis through non-diagonal elements of the self-energy term. [987] *GW* schemes that include both updates of eigenvalues and wave functions are commonly signed with the self-evident label self-consistent *GW* (sc*GW*).[104,105] In case of successive iteration towards self-consistency, the fundamental dependence on the Kohn-Sham reference system persisting throughout all non-self-consistent or partially self-consistent *GW* schemes is lifted, completely. Obviously, the *quality* of the initial eigenvalues and single-particle wave functions is the key to limit the number of iterations towards a self-consistent solution. In contrast to non-self-consistent G_0W_0 theory, numerical artifact as erroneous hybridization or incorrect band ordering, that can be inherent to the underlying Kohn-Sham input, are thoroughly cured in a fully self-consistent sc*GW* framework.

There is a vast number of ab initio studies illustrating the substantially improved[106] *close-to-experiment* description of band-structure features within non-self-consistent *GW* quasiparticle schemes starting from diverse density-functional theory input. Just to mention a few examples, a wide range of bulk materials as simple group IV and group III-V semiconductors [1365, 1428–1431] and their surfaces [34, 1432–1434] or superlattices [309, 1435], (transition)metals [1396, 1436] and their oxides [75, 141, 143, 1437], two-dimensional materials [1438], and molecular systems [1439] have been studied despite the indispensable computational demands[107]. [1189, 1402] The accuracy of various *GW* self-consistency schemes [1357, 1400] has been tested for a wide range of materials as molecules [1357, 1358, 1440], semiconductors and insulators [1441, 1442], transition-metal semiconductors and metals [1396, 1443], and even more complex organic-anorganic hybrid systems [1444] or semiconductor surfaces. [1426]

3.5 Optical response theory

Neutral excitations – While the preceding section gives a comprehensive outline on the quasiparticle theory of charged single-particle excitations within the framework of Green's function theory, the comprehensive theoretical simulation of technologically relevant optical excitations still demands a many-body theory of *neutral excitation* emerging from the simultaneous creation of (quasi)electrons and (quasi)holes (see Fig. 3.5 c). As outlined below, the Bethe-Salpeter

[104] Fully self-consistent *GW* schemes with updates of quasiparticle energies as well as orbitals in the Green's function and/or the screened Coulomb potential are also known as quasiparticle *GW* (QP*GW*).

[105] Also, see the VASP manual as well as the associated publications Ref. [1189, 1402, 1413, 1424] for details on the recent state-of-the-art implementation of various *GW* schemes, which have been used in the present thesis.

[106] Compared to the description within Kohn-Sham density-functional theory using conventional local and semi-local exchange-correlation functionals.

[107] A sound rationale behind G_0W_0 quasiparticle-band gap calculations has been given by Niquet and Gonze demonstrating that the exact interacting band-gap energy $E_{gap}=E^{RPA(N+1)}+E^{RPA(N-1)}-2E^{RPA(N)}$ (cf. Eq. (3.47)) of a solid, calculated within the random-phase approximation to density-functional theory, differs from the Kohn-Sham band-gap energy by an unrenormalized G_0W_0 self-energy correction. [1408]

formalism [987, 1427, 1445–1447, 1447–1452] that determines the polarization function to the macroscopic dielectric function results in the derivation of an effective two-particle Schrödinger equation allowing the systematic treatment of interacting (quasi)electron-(quasi)hole pairs that manifest as *excitons* in optical spectroscopy. [108]

3.5.1 The Bethe-Salpeter equation

Even though Hedin's equation give access to the response functions $P(1,2)$ and $\chi(1,2)$ by transforming Hedin's three-point equation, Eq. 3.133, for the vertex function $\Gamma(1,2;3)$, to an integral equation determining a generalized three-point polarization function ${}^3P(1,2;3)$ [1451, 1452], it is common practice to calculate the response characteristics from a generalized four-point polarization function that follows from a Bethe-Salpeter equation for the two-particle density-density correlation function ${}^4L(1,2,3,4)$. In addition, switching towards a general four-point formalism allows for a seamless inclusion of (optical) local field effects arising from the microscopic nature of the density response.

FOUR-POINT FORMULATION – Within many-body perturbation theory, the fundamental quantity accounting for interaction processes of (quasi)particles as (quasi)electrons and (quasi)holes is the two-particle density-correlation function ${}^4L(1,2,3,4)$, which is formally defined as the variation of the single-particle Green's function with respect to a general nonlocal perturbation $\Phi_{ext}(12)$,

$$ {}^4L(1,2,3,4) = -i\frac{\delta G(1,2)}{\delta \Phi_{ext}(3,4)}. \tag{3.150} $$

Focusing on the formation of electron-hole pairs by simultaneous generation of an interacting (quasi)electron and (quasi)hole requires the study of the electron-hole correlation function ${}^4L(1,1^+;2,2^+)$. The two-point response functions $\chi(1,2)$ and $P(1,2)$ are related to the diagonal elements of ${}^4L(1,1^+;2,2^+)$ as well as to the electron-hole correlation function or irreducible polarization function ${}^4P(1,1^+;2,2^+)$ according to

$$ P(1,2) = {}^4P\left(1,1^+;2,2^+\right) \tag{3.151} $$

$$ \chi(1,2) = -i\,{}^4L\left(1,1^+;2,2^+\right). \tag{3.152} $$

The integral equation, a Dyson equation respectively, that determines the electron-hole correlation function ${}^4L(1,1';2,2')$ is the Bethe-Salpeter equation (BSE) [109]

$$ {}^4L\left(1,1';2,2'\right) = {}^4L_0\left(1,1';2,2'\right) + \int {}^4L_0\left(1,1';3,4\right)\widetilde{\Xi}(3,4;5,6)\,{}^4L\left(5,6;2,2'\right)\mathrm{d}(3,4,5,6) \tag{3.153} $$

[108] The subsequent section extensively follows the representation given by Bechstedt et al. [987, 1344, 1427].

[109] The Bethe-Salpeter equation for the four-point polarization function ${}^4L(1,1';2,2')$ can be obtained from combining Hedin's equation for the irreducible polarization function $P(1,2)$, Eq. 3.132, and the irreducible vertex function $\Gamma(1,2;3)$, Eq. 3.132, and generalization towards four-point quantities as well as from the equation of motion for the two-particle correlation function, directly.

with the integration kernel

$$\widetilde{\Xi}(3,4;5,6) = i\frac{\delta\widetilde{\Sigma}(4,3)}{\delta G(5,6)} \tag{3.154}$$

$$= i\frac{\delta\Sigma_H(4,3)}{\delta G(5,6)} + i\frac{\delta\Sigma(4,3)}{\delta G(5,6)} \tag{3.155}$$

$$\equiv i\frac{\delta\Sigma_H(4,3)}{\delta G(5,6)} + \Xi(3,4;5,6)\,. \tag{3.156}$$

Here, the total single particle self-energy $\widetilde{\Sigma}$ is the sum of the Hartree self-energy $\Sigma_H(1,2) = \delta(1,2)V_H(1)$ as well as the actual many-body self-energy Σ mediating the combined effects of exchange and correlation (cf. Eq. 3.99). The integral kernel $\widetilde{\Xi}(3,4;5,6)$ defines the effective two-particle interaction as functional derivative of the self-energy with respect to the single-particle Green's function.

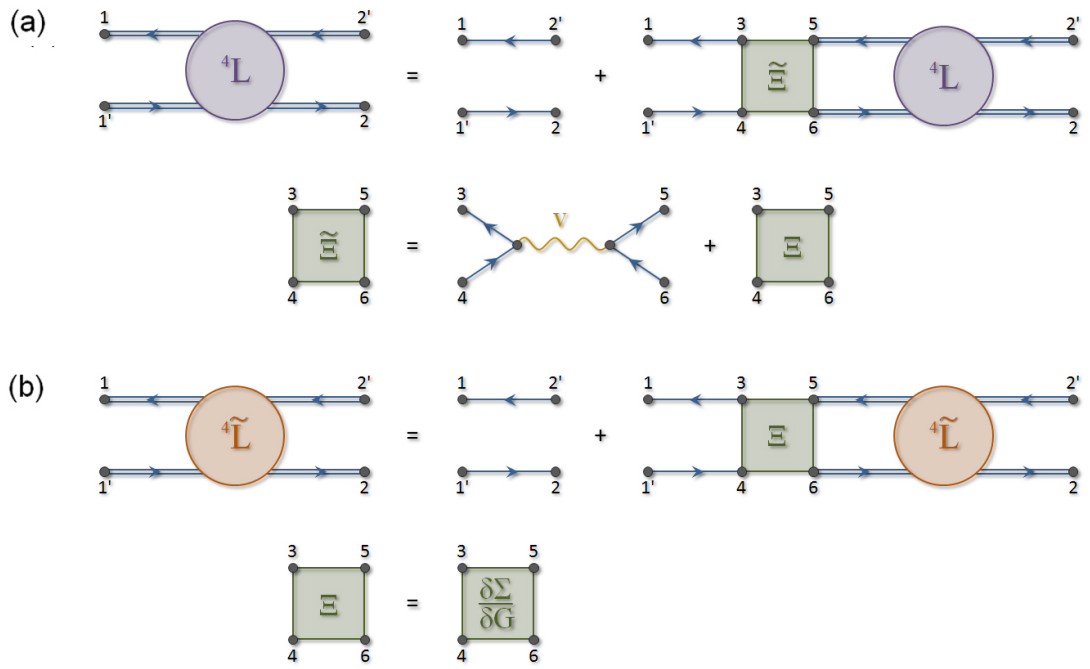

Figure 3.10: Schematic illustration of the two Bethe-Salpeter equations Eq. 3.153 and Eq. 3.157 defining the four-point electron-hole density-correlation function ${}^4L(1,1';2,2')$ and the four-point polarization function ${}^4L(1,1';2,2')$; adapted from Ref. [987].

A Dyson equation with additive contributions to the interaction kernel can be rewritten as a set of coupled Dyson equations. Hence, the introduction of the two-particle polarization function ${}^4P(1,1';2,2')$ allows to rewrite the Bethe-Salpeter equation for ${}^4L(1,1';2,2')$, Eq. 3.153, as a set of two coupled Bethe-Salpeter equations. The integral kernel $\Xi(3,4;5,6)$, defined in Eq. 3.156,

establishes the Bethe-Salpeter equation for the polarization function ${}^4P(1,1';2,2')$ according to

$$ {}^4P(1,1';2,2') = {}^4L_0(1,1';2,2') + \int {}^4L_0(1,1';3,4)\,\Xi(3,4;5,6)\,{}^4P(5,6;2,2')\,\mathrm{d}(3,4,5,6)\,. \tag{3.157} $$

Subsequently, ${}^4L(1,1';2,2')$ is evaluated from

$$ {}^4L(1,1';2,2') = {}^4P(1,1';2,2') + \int {}^4P(1,1';3,3)\,v(3,4)\,{}^4L(4,4^+;2,2')\,\mathrm{d}(3,4)\,. \tag{3.158} $$

BSE@RPA – Recapitulating Sec. 3.4.2, the most basic, or zeroth order, approximation to many-body perturbation theory is the random-phase approximation obtained by completely neglecting the exchange-correlation self energy, $\Sigma = 0$. Consequently, the only remaining ingredient to the interaction kernels is the variation of the Hartree potential with respect to the single-particle Green's function,

$$ \frac{\delta\Sigma_H(1,2)}{\delta G(3,4)} = -i\delta(1,2)\,\delta(3^+,4)\,v(1,3)\,, \tag{3.159} $$

and the two kernels Ξ and $\widetilde{\Xi}$ reduce to

$$ \Xi_{RPA}(3,4;5,6) \equiv 0 \tag{3.160} $$

$$ \widetilde{\Xi}_{RPA}(3,4;5,6) = \delta(3,4)\,\delta(5^+,6)\,v(3,5)\,. \tag{3.161} $$

Inserting Ξ_{RPA} into the Bethe-Salpeter equation, Eq. 3.157, returns the polarization function ${}^4P(1,1';2,2')$ in the common random-phase form of the *GW* approximation [110] (cf. Eq. 3.137),

$$ {}^4P(1,1';2,2') = {}^4L_0(1,1';2,2') \equiv -iG(1,2')\,G(2',1)\,. \tag{3.162} $$

Therefore, the two-particle density-correlation function ${}^4L(1,1';2,2')$, Eq. 3.158, becomes

$$ {}^4L(1,1';2,2') = {}^4L_0(1,1';2,2') + \int {}^4L_0(1,1';2,2')\,v(3,4)\,{}^4L(4,4^+;2,2')\,\mathrm{d}(3,4)\,. \tag{3.163} $$

It is important to note that the random-phase approximation only makes an approximation to the integral kernel Ξ of the polarization function ${}^4P(1,1';2,2')$. In contrast, the density response function is determined by microscopic fluctuations of the Hartree potential originating from fluctuations of the external potential and mediated by the Coulomb kernel v in the Bethe-Salpeter equation, Eq. 3.163, for ${}^4L(1,1';2,2')$. [987, 1347, 1453] Since long-range variations of the Hartree potential are contained in the Bethe-Salpeter equation for the density-response function ${}^4L(1,1';2,2')$, the random phase approximation is, in principle, suited to describe long-range charge oscillations, i.e. plasmons, reasonably. [1347] The microscopic components of the bare Coulomb interaction also account for so called (*crystal*) *local-field effects* that are relevant to the

[110] In case the single-particle Greens function of Eq. 3.162 is given by the Hartree-Green's function G_H, which represents the random-phase approximation in a narrower sense, the Hartree approximation is recovered. [987]

simulation of optical material properties. [987, 1271, 1272, 1347, 1445, 1446, 1454–1459]

INDEPENDENT PARTICLE APPROXIMATION – Making the additional approximation of completely neglecting microscopic variations in the evaluation of the two-particle density response by setting v to zero in the Bethe-Salpeter equation, Eq. 3.163 (i.e. $\widetilde{\Xi} \equiv 0$) reduces the two-particle density-correlation function to ${}^4L(1,1';2,2') \equiv {}^4L_0(1,1';2,2')$. The approximation of the density response function by ${}^4L_0(1,1';2,2')$ is called the *independent (quasi)particle approximation*, or *independent-particle random-phase approximation* for completeness, which has been a computationally cheap and frequently utilized procedure to simulate and analyze optical-response characteristics of materials of interest in computational materials science. However, due to the severe approximations in the independent-(quasi)particle picture the calculated optical spectra are highly defective and the savings in computational resources are dearly bought by a substantial loss of predictive power. [987, 1347, 1458, 1460–1462]

BSE@GW – Extensions beyond the *generalized* random-phase approximation require inclusion of the exchange-correlation self energy, which, in lowest order, is provided by the *GW* self energy $\Sigma_{GW}(1,2)$ (cf. Eq. 3.135). The associated integral kernel, Eq. 3.156, becomes

$$\Xi_{GW}(1,2;3,4) = i\,\delta(1,2)\,\delta(1',2')\,W(1^+,1') + i\,G(1,1')\,\frac{\delta W(1^+,1')}{\delta G(2,2')}\,. \tag{3.164}$$

While the first right-hand term is of first order in the screened Coulomb interaction W, the second term representing a more complex qunatity in second order of W (e.g. see Ref. [987]) is commonly neglected in practical calculations [111]. Hence, the *linearized GW* approximation to the integral kernel Ξ is determined by the screened Coulomb interaction, essentially. The kernel $\widetilde{\Xi}$, Eq. 3.154, only contains additional contribution from the bare Coulomb potential v (cf. Eq. 3.159). Relying on these approximations, the basic Bethe-Salpeter equations for the two-particle response functions, Eq. 3.157 and Eq. 3.153 become

$${}^4P(1,1';2,2') = {}^4L_0(1,1';2,2') - \int {}^4L_0(1,1';4^+,3)\,W(3,4)\,{}^4P(3,4^+;2,2')\,\mathrm{d}(3,4) \tag{3.165}$$

and

$$\begin{aligned} {}^4L(1,1';2,2') = {}^4L_0(1,1';2,2') & \\ - \int {}^4L_0(1,1';4^+,3)\,W(3,4)\,{}^4L(3,4^+;2,2')\,\mathrm{d}(3,4) & \\ + \int {}^4L_0(1,1';3,3^+)\,v(3,4)\,{}^4L(4,4^+;2,2')\,\mathrm{d}(3,4)\,. & \end{aligned} \tag{3.166}$$

The measurable optical properties of a material are the consequence of a material's response

[111] While this approximation becomes exact in the low electron-density limit, molecular systems respectively, it might have, despite it second order nature in the *GW* approximation, some relevance to the optical properties of solids due to screening of the electron-hole interaction. [987] An inclusion of higher order terms of the screened interaction W is, for instance, provided within the framework of the T-matrix approach. [987, 1347, 1463, 1464]

to the total macroscopic (classical) perturbation. [1347] Therefore, it can be useful to define a reduced density response function $\overline{\chi}$, which is determined by the short-range components of the bare Coulomb interaction

$$\overline{v}(|\mathbf{G}|) = \begin{cases} 0 & \text{for} \quad \mathbf{G} = 0 \\ v(|\mathbf{G}|) & \text{for} \quad \mathbf{G} \neq 0 \end{cases} , \tag{3.167}$$

only. The reduced density response function follows the Dyson equation

$$\overline{\chi}(1,2) = P(1,2) + \int P(1,3)\,\overline{v}(3,4)\,\overline{\chi}(1,2)\,\mathrm{d}(4,2) , \tag{3.168}$$

which is formally analog to Eq. 3.127 but excludes the long-range component of the Coulomb potential from self-consistent evaluation of the response functions. In the same way the density response function χ is determined from the two-particle density response function ${}^4L$ via Eq. 3.152, the reduced response function $\overline{\chi}$ could be calculated from $\overline{\chi}(1,2) = -i\,{}^4\overline{L}(1,1^+;2,2^+)$ using a modified two-particle density response function ${}^4\overline{L}$ responding to the Bethe-Salpeter equation

$${}^4\overline{L}(1,1';2,2') = {}^4P(1,1';2,2') + \int {}^4P(1,1';2,2')\,\overline{v}(3,4)\,{}^4\overline{L}(4,4^+;2,2')\,\mathrm{d}(3,4) , \tag{3.169}$$

which is formally identical to Eq. 3.158. The macroscopic dielectric function $\varepsilon^M(\mathbf{Q},\omega)$ could be calculated from the reduced density-response function for arbitrarily large wave vectors $\mathbf{Q}$, directly, [1347, 1465] via

$$\varepsilon^M(\mathbf{q},\omega) = 1 - v(\mathbf{q})\,\overline{\chi}(\mathbf{q},\omega) . \tag{3.170}$$

3.5.2 The dielectric function

Experimental setups in optical spectroscopy are commonly designed to probe fields of *macroscopic* electrodynamics. Relevant optical quantities as the absorption or reflection characteristics of a solid are linked to the associated macroscopic frequency-dependent dielectric function $\varepsilon^M(\mathbf{q},\omega) \equiv \varepsilon^M_{LL}(\mathbf{q},\omega)$ [112] (in the optical limit $\mathbf{q} \to 0$), whose wavelength is much greater than the sample's microscopic structure. In principle, all macroscopic fields of interest could be calculated from Maxwell's equations if the macroscopic dielectric tensor is known, completely. However, this macroscopic quantity is not directly accessible within atomistic theories as density-functional theory or many-body perturbation theory that give access to microscopic response functions. In

[112] Any vector field of macroscopic electrodynamics can be decomposed into longitudinal and transverse components. Depending on the crystal symmetry, the macroscopic dielectric tensor $\overline{\overline{\varepsilon}}(\mathbf{q},\omega)$ contains elements coupling the longitudinal and transverse components. For cubic materials the off-diagonal components of of the macroscopic dielectric tensor $\overline{\overline{\varepsilon}}(\mathbf{q},\omega)$ equal zero and, in the optical limit $\mathbf{q} \to 0$, the transverse-transverse dielectric function $\varepsilon^M_{TT}(\mathbf{q},\omega)$ equals the longitudinal-longitudinal component $\varepsilon^M_{LL}(\mathbf{q},\omega)$. [30, 1271, 1272, 1466] One can further show, see Ref. [30], that it is sufficient to narrow the discussion of the macroscopic dielectric response to the longitudinal-longitudinal tensor component $\varepsilon^M_{LL}(\mathbf{q},\omega)$ for arbitrary symmetries, since $\varepsilon^M_{LL}(\mathbf{q},\omega)$ preserves its *simple* expression through the density-density response function $\chi(\mathbf{q},\omega)$ (cf. Eq. 3.113) assuming a longitudinal nature of microscopic fields. [30]

other words, the variations of the macroscopic response function do not represent a spatial average of the associated microscopic quantities due to the induced microscopic contributions to polarization. [30]

MICROSCOPIC-TO-MACROSCOPIC CONNECTION – The differences between the microscopic and macroscopic quantities originates from the locally induced polarization fields, so called *local-field effects* [1271, 1272, 1445, 1454], that are induced in a material sample in response to the external (macroscopic) probe perturbation. This microscopic origin of a material's dielectric response is determined by its microscopic dielectric function $\varepsilon(\mathbf{q}+\mathbf{G},\mathbf{q}+\mathbf{G}',\omega)$, a second-rank tensor respectively, that effectively measures a samples screening characteristics by linking the (macroscopic) external and the effective total potentials to each other (cf. Eq. 3.112). The *microscopic-to-macroscopic connection* [1453] for the macroscopic dielectric function is given by inversion of the full dielectric matrix $\varepsilon(\mathbf{q}+\mathbf{G},\mathbf{q}+\mathbf{G}',\omega)$ and taking the *head*/macroscopic average $\varepsilon^{-1}(\mathbf{q}+\mathbf{G},\mathbf{q}+\mathbf{G}',\omega)\big|_{\mathbf{G}=\mathbf{G}'=0}$ according to

$$\varepsilon^M(\mathbf{q},\omega) = \frac{1}{\varepsilon^{-1}(\mathbf{q}+\mathbf{G},\mathbf{q}+\mathbf{G}',\omega)}\bigg|_{\mathbf{G}=\mathbf{G}'=0}. \tag{3.171}$$

Hence, all microscopic contributions of the dielectric response produce the macroscopic dielectric response, collectively. The difference between the macroscopic dielectric function $\varepsilon^M(\mathbf{q},\omega)$ and the head of the microscopic dielectric tensor $\varepsilon(\mathbf{q}+\mathbf{G},\mathbf{q}+\mathbf{G}',\omega)|_{\mathbf{G}=\mathbf{G}'=0} \equiv \varepsilon(\mathbf{q},\mathbf{q},\omega)$ formally encomprises the local-field effects. Physically, local-field effects originate from microscopic charge inhomogeneities, that are responsible for the substantial irregular variations of the induced part of the total potential on an interatomic-distance length scale.

A BETHE-SALPETER EQUATION FOR MACROSCOPIC POLARIZATION – Instead of calculating the totality of matrix elements $\varepsilon(\mathbf{q}+\mathbf{G},\mathbf{q}+\mathbf{G}',\omega)|_{\mathbf{G}=\mathbf{G}'}$ (including local-field effects as well as excitonic contributions) of the microscopic dielectric tensor, one can restate the macroscopic dielectric function [113] by introducing a modified *polarization function* $\overline{P}^M(\mathbf{q},\mathbf{q},\omega)$ of the macroscopic dielectric response [987, 1468], explicitly carrying local field as well as excitonic effects, according to

$$\varepsilon^M(\hat{\mathbf{q}};\omega) = 1 - \lim_{\mathbf{q}\to 0}\left[2\,v(|\mathbf{q}|)\,\overline{P}^M(\mathbf{q},\mathbf{q},\omega)\right]. \tag{3.173}$$

Here, the $\mathbf{q}\to 0$ limit needs to be considered to assure the correct analytical properties of the macroscopic dielectric function [987] due to the divergence of the coulomb potential. [1452] The additional factor of two accounts for the spin summed response function instead of the spin averaged case. The macroscopic polarization $\overline{P}^M$ is calculated from the Bethe-Salpeter equation

[113] Investigating atomic systems of arbitrary space-group symmetry, the (longitudinal) macroscopic dielectric function can be rewritten [987, 1467] as a second rank (cartesian) tensor according to

$$\varepsilon^M(\hat{\mathbf{q}};\omega) \equiv \hat{\mathbf{q}}\hat{\boldsymbol{\varepsilon}}^M(\omega)\hat{\mathbf{q}} = \sum_{i,j=1,2,3}\hat{q}_i\varepsilon^M_{ij}(\omega)\hat{q}_j, \tag{3.172}$$

with the three independent direction vectors $\hat{\mathbf{q}} = \mathbf{q}/|\mathbf{q}|$.

[987, 1427, 1445–1447, 1447–1451]

$$ {}^4\overline{P}^M\left(1,1';2,2'\right) = {}^4L_0\left(1,1';2,2'\right) + \int {}^4L_0\left(1,1';3,4\right)\Xi^M\left(3,4;5,6\right){}^4\overline{P}^M\left(5,6;2,2'\right)\mathrm{d}\left(3,4,5,6\right) \tag{3.174} $$

with the kernel [987, 1448] (cf. Eq. 3.156 and Eq.3.166)

$$ \Xi^M\left(3,4;5,6\right) = i\frac{\delta\Sigma\left(4,3\right)}{\delta G\left(5,6\right)} + i\frac{\delta\Sigma_H\left(4,3\right)}{\delta G\left(5,6\right)} \tag{3.175} $$

$$ \approx \delta\left(3,4\right)\delta\left(5^+,6\right)2\overline{v}\left(3,5\right) - \delta\left(4,5\right)\delta\left(3,6\right)W\left(4^+,3\right). \tag{3.176} $$

The Bethe-Salpeter equations for the two-particle density correlation function, Eq 3.166, and the macroscopic polarization function, Eq. 3.174, share a common functional structure. In both cases the integral kernel encompasses an attractive dynamically screened *direct* quasielectron-quasihole interaction ${}^4W\left(1,2;3,4\right) = \delta\left(1,3\right)\delta\left(2,4\right)W\left(1,2\right)$ accounting for bound two-particle states, i.e. *exciton* formation. The attractive kernel contribution originates from variation of the self-energy with respect to the single-particle Green's function (cf. Eq. 3.164), representing an exchange-like contribution in the one-(quasi)particle Hamiltonian, Eq. 3.100. [1451, 1452] The second terms within the integral kernels $\widetilde{\Xi}$, Eq. 3.154, and Ξ^M, Eq. 3.175, are related to the bare Coulomb interaction. The only difference, within these kernel contributions, is given by utilizing the long-range truncated Coulomb potential $\overline{v}$ in the interaction kernel Ξ^M for inclusion of (*optical*) *local-field effects* in the macroscopic polarization ${}^4\overline{P}^M$, while an unmodified bare Coulomb potential enters the integral kernel $\widetilde{\Xi}$ in the evaluation of the density correlation function ${}^4L$. In both cases the repulsive interaction arises from density variations with respect to variations of the Hartree potential causing an exchange-like interaction between electrons and holes; *electron-hole exchange* for short. [1445, 1451, 1452] The long-range contribution to the repulsive part of the interaction kernel might be safely omitted in, e.g. the calculation of the optical absorption spectrum. This is not the case for, e.g., the electron-energy loss function, that depends on the inverse of the dielectric function, explicitly. [1451, 1452] In this case, the inverse macroscopic dielectric response function can be obtained from the head $\chi\left(\mathbf{q}+\mathbf{G},\mathbf{q}+\mathbf{G}',\omega\right)|_{\mathbf{G}=\mathbf{G}'=0} \equiv \chi\left(\mathbf{q},\mathbf{q},\omega\right)$ of the microscopic density-response function $\chi\left(\mathbf{q}+\mathbf{G},\mathbf{q}+\mathbf{G}',\omega\right)$ via

$$ \varepsilon^{M^{-1}}\left(\hat{\mathbf{q}};\omega\right) = 1 + \lim_{\mathbf{q}\to 0}\left[2v\left(|\mathbf{q}|\right)\chi\left(\mathbf{q},\mathbf{q},\omega\right)\right], \tag{3.177} $$

using the unmodified bare Coulomb potential including its long-range tail. [1451, 1452]

3.5.3 Electron-hole pair excitations

Having formulated the Bethe-Salpeter equations that determine the four-point response functions, it is still necessary to transform these equations into a closed mathematical form that, on the one hand, allows an efficient numerical treatment and, on the other hand, highlights basic physics of the underlying two-particle processes.

NEGLECTING DYNAMICAL EFFECTS – The macroscopic dielectric function ε^M, relevant to characterize the optical properties, depends on a single frequency, only, implying that the corresponding macroscopic polarization function P^M should hold the same time dependence $\overline{P}^M \equiv \overline{P}^M(t_1 - t_2)$. Since the time-dependence of the integral kernel Ξ^M, Eq. 3.175, follows the time-dependence of the screened Coulomb potential $W(4^+,3) \approx W(t_4 - t_3)$, it is common to approximate $W(t_4 - t_3)$ by a static screening function [114,115] [987, 1347, 1451]

$$W(34) \approx W(\mathbf{x}_3, \mathbf{x}_4)\,\delta(t_3 - t_4)\,. \tag{3.178}$$

This approximation is commonly considered as (*linear response*) *time-dependent screened Hartree-Fock approximation*. [1347, 1451]

AN EFFECTIVE TWO-PARTICLE EIGENVALUE PROBLEM – Focusing on interacting electrons and holes in extended semiconducting or insulating materials with distinct translational symmetry [116], only fully occupied valence, $\lambda \to \{v\}$, and (virtual) conduction bands, $\lambda \to \{c\}$, are considered. In the long-wavelength limit of a vanishing wave vector $\mathbf{q} \to 0$, the optical response is characterized by *vertical* Brillouin zone transitions $|v,\mathbf{k}\rangle \to |c,\mathbf{k}\rangle$ between valence-band states $|v,\mathbf{k}\rangle$ and conduction-band states $|c,\mathbf{k}\rangle$. Within the context of semiconductors and insulators, intraband transitions are legitimately omitted due to the restriction to completely occupied bands. [117] Subject to these *limitations*, the Bethe-Salpeter equation, Eq. 3.174, can be transformed into a generalized non-hermitian eigenvalue problem for an effective two-particle (electron-hole pair) Hamiltonian $\mathscr{H}_{e-h}$ adopting the form of an inhomogeneous two-particle Schrödinger equation [987, 1344, 1457, 1471]

$$\sum_{\mathbf{k}''}\sum_{c'',v''} \mathscr{H}_{e-h}\left(c\mathbf{k}, v\mathbf{k}; c''\mathbf{k}'', v''\mathbf{k}''\right)\overline{P}^M\left(c''\mathbf{k}'', v''\mathbf{k}''; c'\mathbf{k}', v'\mathbf{k}'; \omega\right) = \tag{3.179}$$
$$-\delta_{cc'}\,\delta_{vv'}\,\delta_{\mathbf{k}\mathbf{k}'} + (\omega + i\eta)\,\overline{P}^M\left(c\mathbf{k}, v\mathbf{k}; c'\mathbf{k}', v'\mathbf{k}'; \omega\right)\,.$$

Here, the summation is running over all pairs of excited electrons in a conduction-band state $|c,\mathbf{k}\rangle$ and missing electrons, holes respectively, in a valence-band state $|v,\mathbf{k}\rangle$. The full electron-hole-pair Hamiltonian exhibits the characteristic block-matrix structure

$$\mathscr{H}_{e-h}\left(c\mathbf{k}, v\mathbf{k}; c'\mathbf{k}', v'\mathbf{k}'\right) = \begin{pmatrix} H_{e-h}^{res.}(c\mathbf{k}, v\mathbf{k}; c'\mathbf{k}', v'\mathbf{k}') & \Xi^M(v\mathbf{k}, c\mathbf{k}; c'\mathbf{k}', v'\mathbf{k}') \\ \Xi^M(c\mathbf{k}, v\mathbf{k}; v'\mathbf{k}', c'\mathbf{k}') & H_{e-h}^{antires.}(v\mathbf{k}, c\mathbf{k}; v'\mathbf{k}', c'\mathbf{k}') \end{pmatrix}, \tag{3.180}$$

[114] In addition to approximate W in its static limit $W \equiv W(\mathbf{x}, \mathbf{x}'; 0)$, cf. Eq. 3.104, W might be computed approximately using a simplified model-dielectric function as suggested by Bechstedt et al. [1469, 1470].

[115] A recent discussion of methodological approaches that allow for an inclusion of physical effects related to dynamic screening by going beyond the static-screening approximation is given by Bechstedt [987].

[116] The treatment of molecular systems and nanomaterials with reduced spatial dimensionality and/or arbitrary symmetry is formally identical within the commonly utilized supercell approach to restore an artificial three-dimensional translational symmetry for an efficient numerical treatment by plane-wave ab-initio codes.

[117] For metallic systems, transitions within a partially occupied band give rise to the so the called *Drude term* governing the screening properties in the long-wavelength limit (e.g. see Ref. [987, 1344]).

where the resonant and antiresonant electron-hole-pair Hamiltonians $H_{e-h}^{res.}(c\mathbf{k},v\mathbf{k};c'\mathbf{k}',v'\mathbf{k}')$ and $H_{e-h}^{antires.}(c\mathbf{k},v\mathbf{k};c'\mathbf{k}',v'\mathbf{k}')$ account for electron-hole pairs with positive or negative two-particle eigenvalues, respectively. [1449, 1472] The resonant part of the effective two-(quasi-)particle electron-hole pair Hamiltonian $H_{e-h}^{res.}(c\mathbf{k},v\mathbf{k};c'\mathbf{k}',v'\mathbf{k}')$ is defined through

$$\begin{aligned} H_{e-h}^{res.}\left(c\mathbf{k},v\mathbf{k};c'\mathbf{k}',v'\mathbf{k}'\right) &= \bar{v}\left(c\mathbf{k},v\mathbf{k};c'\mathbf{k}',v'\mathbf{k}'\right) - W\left(c\mathbf{k},v\mathbf{k};c'\mathbf{k}',v'\mathbf{k}'\right) \\ &\quad + \left[\varepsilon_c^{QP}(\mathbf{k}) - \varepsilon_v^{QP}(\mathbf{k})\right]\delta_{cc'}\,\delta_{vv'}\,\delta_{\mathbf{kk}'}\,, \end{aligned} \tag{3.181}$$

with

$$\bar{v}\left(c\mathbf{k},v\mathbf{k};c'\mathbf{k}',v'\mathbf{k}'\right) = \frac{1}{\Omega}\sum_{\mathbf{G}\neq 0} v\left(|\mathbf{G}|\right) B_{cv}^{\mathbf{kk}}(\mathbf{G})\left[B_{c'v'}^{\mathbf{k}'\mathbf{k}'}(\mathbf{G})\right]^* \tag{3.182}$$

and

$$\begin{aligned} W\left(c\mathbf{k},v\mathbf{k};c'\mathbf{k}',v'\mathbf{k}'\right) &= \frac{1}{\Omega}\sum_{\mathbf{q}}\sum_{\mathbf{G},\mathbf{G}'} \varepsilon^{-1}\left(\mathbf{q}+\mathbf{G},\mathbf{q}+\mathbf{G}',0\right) v\left(\left|\mathbf{q}+\mathbf{G}'\right|\right) \\ &\quad \times B_{cc'}^{\mathbf{kk}'}(\mathbf{q}+\mathbf{G})\left[B_{vv'}^{\mathbf{kk}'}\left(\mathbf{q}+\mathbf{G}'\right)\right]^* \end{aligned} \tag{3.183}$$

representing the matrix elements of the bare and screened Coulomb interactions in plane-wave representation, with $B_{\lambda\lambda'}^{\mathbf{kk}'}(\mathbf{q}+\mathbf{G})$ accounting for the Bloch integrals

$$B_{\lambda\lambda'}^{\mathbf{kk}'}(\mathbf{q}+\mathbf{G}) = \frac{1}{\Omega}\int \varphi_{\lambda\mathbf{k}}^*(\mathbf{x})\, e^{i(\mathbf{q}+\mathbf{G})\mathbf{x}} \varphi_{\lambda'\mathbf{k}'}(\mathbf{x})\,\mathrm{d}^3\mathbf{x}\,. \tag{3.184}$$

The off-diagonal coupling matrices, given by matrix elements of the integral kernel Ξ^M, Eq. 3.175, account for interactions between electron-hole-pairs with positive and negative pair energies. Following the Tamm-Dancoff approximation (TDA) [1473–1475], the coupling between electron-hole pairs and antipairs is frequently neglected due to their circumstantial nature compared to the exciton-binding energies. [987, 1476] Neglecting the coupling between resonant and antiresonant electron-hole pairs has shown little-to-no influence on the optical absorption properties of *simple* bulk materials as silicon [1449, 1477], but might have a more notable impact on energy-loss spectra [1478]. [987, 1476] A breakdown of the Tamm-Dancoff approximation has been reported for prototypical aromatic organic semiconductors as well as carbon nanotubes, exemplarily. [1479, 1480] Considering the block-diagonal electron-hole pair Hamiltonian in Tamm-Dancoff approximation,

$$\mathscr{H}_{TDA}^{e-h} = \begin{pmatrix} H_{e-h}^{res.} & 0 \\ 0 & H_{e-h}^{antires.} \end{pmatrix} \equiv \begin{pmatrix} H_{e-h} & 0 \\ 0 & -H_{e-h}^{+} \end{pmatrix}, \tag{3.185}$$

it becomes sufficient to study the eigenvalues of the resonant part $H_{e-h}^{res.} \equiv H_{e-h}$ of the electron-hole

Hamiltonian [118], which leads to the regular hermitian eigenvalue problem,

$$\sum_{c',v'}\sum_{\mathbf{k}'} H_{e-h}\left(c\mathbf{k},v\mathbf{k};c'\mathbf{k}',v'\mathbf{k}'\right)A_\Lambda\left(c'\mathbf{k}',v'\mathbf{k}'\right) = E_\Lambda A_\Lambda\left(c\mathbf{k},v\mathbf{k}\right). \tag{3.186}$$

The solution of this eigenvalue problem yields a spectral representation of the macroscopic polarization function $\overline{P}^M\left(c\mathbf{k},v\mathbf{k};c'\mathbf{k}',v'\mathbf{k}';\omega\right)$ according to

$$\overline{P}^M\left(c\mathbf{k},v\mathbf{k},c'\mathbf{k}',v'\mathbf{k}';\omega\right) = -\sum_\Lambda \frac{A_\Lambda\left(c\mathbf{k},v\mathbf{k}\right)A^*_\Lambda\left(c'\mathbf{k}',v'\mathbf{k}'\right)}{E_\Lambda-(\omega+i\eta)} \tag{3.187}$$

in terms of the two-particle eigenvalues E_Λ representing the pair-excitation energies and the two-particle pair states $A_\Lambda\left(c\mathbf{k},v\mathbf{k}\right)$. [987, 1344] The associated macroscopic dielectric function in Tamm-Dancoff approximation becomes

$$\varepsilon^M\left(\hat{\mathbf{q}};\omega\right) = 1+\frac{4\pi}{\Omega}\sum_\Lambda\left|\sum_{c,v}\sum_{\mathbf{k}}\left[M^{\mathbf{k},\mathbf{k}}_{c,v}\left(\hat{\mathbf{q}}\right)\right]^* A_\Lambda\left(c\mathbf{k},v\mathbf{k}\right)\right|^2 \sum_{\beta=\pm1}\left[\frac{1}{E_\Lambda-\beta\left(\omega+i\eta\right)}\right], \tag{3.188}$$

where $M^{\mathbf{k},\mathbf{k}}_{\lambda,\lambda'}\left(\hat{\mathbf{q}}\right)$ denotes the optical dipole-matrix element

$$M_{\lambda\lambda'}\left(\hat{\mathbf{q}}\right) = \lim_{\mathbf{q}\to0}\frac{1}{|\mathbf{q}|}B_{\lambda\lambda'}\left(\mathbf{q}\right). \tag{3.189}$$

In the limit of *infinite* lifetimes ($\eta\to0^+$) the macroscopic dielectric function $\varepsilon^M\left(\hat{\mathbf{q}};\omega\right)$ satisfies the Kramers-Kronig relations [119] connecting the real and imaginary parts of $\varepsilon^M\left(\hat{\mathbf{q}};\omega\right)$, which are effectively utilized in practical calculations.

A MATTER OF DIMENSION – In practice, the solution of the Bethe-Salpeter equation, the associated two-particle eigenvalue problem, Eq. 3.186, respectively, is limited by the high dimension of the electron-hole pair Hamiltonian $H_{e-h}\left(c\mathbf{k},v\mathbf{k};c'\mathbf{k}',v'\mathbf{k}'\right)$. The matrix rank N of the electron-hole pair eigenvalue problem is defined by the total number of electron-hole pair states, which is, as indicated by the summation, given as the product of the number of valence states N_v and conduction states N_c at $N_\mathbf{k}$ considered $\mathbf{k}$-points within the Brillouin zone, $N = N_v\times N_c\times N_\mathbf{k}$. [120] Even for conceptually simple bulk materials the size N of the pair-eigenvalue problem easily

[118] The eigenvectors $|A^*_\Lambda\rangle$ and eigenvalues $-E_\Lambda$ of the antiresonant Hamiltonian $H^{antires.}_{e-h}\equiv-H^+_{e-h}$ follow from their resonant complements, immediately. [987]

[119]
$$\mathrm{Re}\left\{\varepsilon^M\left(\hat{\mathbf{q}};\omega\right)\right\} = 1+\mathcal{P}\int_{-\infty}^{\infty}\frac{1}{\pi}\frac{1}{\omega'-\omega}\mathrm{Im}\left\{\varepsilon^M\left(\hat{\mathbf{q}};\omega'\right)\right\}\mathrm{d}\omega' \tag{3.190}$$

$$\mathrm{Im}\left\{\varepsilon^M\left(\hat{\mathbf{q}};\omega\right)\right\} = -\mathcal{P}\int_{-\infty}^{\infty}\frac{1}{\pi}\frac{1}{\omega'-\omega}\left(\mathrm{Re}\left\{\varepsilon^M\left(\hat{\mathbf{q}};\omega'\right)\right\}-1\right)\mathrm{d}\omega' \tag{3.191}$$

[120] The actual dimension, the number of electronic states as well as the number/density of *relevant* $\mathbf{k}$ points considered in the construction of the Hamiltonian $H_{e-h}\left(c\mathbf{k},v\mathbf{k};c'\mathbf{k}',v'\mathbf{k}'\right)$, is subject to rigorous testing for numerical convergence.

exceeds $\sim N^5$ and rapidly approaches dimensions of $\sim N^6$ for increasingly complex systems as surfaces or amorphous solids (e.g. see Ref. [31, 34, 1471, 1481, 1482]), which renders direct matrix diagonalization rather unfavorable, or even unfeasible, due to the inherent $\mathcal{O}\left(N^3\right)$ scaling. [121] Therefore, Schmidt et al. [1471] proposed an efficient $\mathcal{O}\left(N^2\right)$ scaling approach [122] to obtain the macroscopic polarization through a time-evolution algorithm. [987, 1457, 1471, 1486] Instead of a direct-diagonalization approach to solve the eigenvalue problem of the pair-Hamiltonian, Eq. 3.186, the calculation of the frequency-dependent macroscopic dielectric function, Eq. 3.188, is reformulated as an initial-value problem. Taking the example of the diagonal components $\varepsilon^M_{jj}(\omega) = 1 + 4\pi\alpha^M_{jj}(\omega)$ of the macroscopic dielectric tensor, Eq. 3.172, the macroscopic polarizability $\alpha^M_{jj}(\omega)$ can be expressed as (cf. Eq. 3.188)

$$\alpha^M_{jj}(\omega) = \frac{1}{\Omega}\sum_{\Lambda}\left|\langle M_j \mid A_\lambda\rangle\right|^2 \sum_{\beta=\pm 1}\left[\frac{1}{E_\Lambda - \beta(\omega + i\eta)}\right], \tag{3.192}$$

with

$$\langle M_j \mid A_\lambda\rangle = \sum_{c,v}\sum_{\mathbf{k}}\left(M^{\mathbf{k},\mathbf{k}}_{c,v}\right)^*_j A_\Lambda(c\mathbf{k}, v\mathbf{k}). \tag{3.193}$$

Here, $\left(M^{\mathbf{k},\mathbf{k}}_{c,v}\right)^*_j$ accounts for the jth cartesian component of the dipole operator $M^{\mathbf{k},\mathbf{k}}_{\lambda,\lambda'}(\hat{\mathbf{q}})$. Equation 3.192 is equivalent to the Fourier representation [987, 1471]

$$\alpha^M_{jj}(\omega) = \frac{i}{\Omega}\int_0^\infty \left\{\langle M_j \mid \xi_j(t)\rangle - \langle M_j \mid \xi_j(t)\rangle^*\right\} e^{i(\omega+i\eta)t}\mathrm{d}t\,, \tag{3.194}$$

where the time evolution of the vector $|\xi^j(t)\rangle$ is driven by the time-dependent Schrödinger equation

$$i\hbar\frac{d}{dt}|\xi^j(t)\rangle = \hat{H}\,|\xi^j(t)\rangle \tag{3.195}$$

for the electron-hole pair Hamiltonian $\hat{H} \equiv H^{res.}_{e-h}$, Eq. 3.181. The initial vector elements $|\xi(0)\rangle$ are given by the dipole matrix elements in the jth cartesian direction,

$$|\xi(0)\rangle = |M_j\rangle\,. \tag{3.196}$$

In practical calculations [123,124,125] the initial-value problem is solved applying a central-

[121] Even though, the actual construction of of the pair Hamiltonian within the framework of *GW* quasiparticle theory could be the computationally more expensive part in ab initio-optics simulations. [987]

[122] Another quadratic scaling alternative to the complete diagonalization of the electron-hole pair Hamiltonian, that gives access to excitonic features around the band edges, exciton binding energies respectively, is the iterative determination of the lowest eigenvalues within the Haydock recursion method. [1483–1485]

[123] This especially applies to recent implementations of numerical routines to solve the Bethe-Salpeter equation within the VASP code [1477, 1487] utilized throughout the present thesis.

[124] Likewise, the time-evolution approach has been implemented in the solution of the Bethe-Salpeter equation for the electron-hole two-particle Green's function within the WIEN2K code. [1480, 1488]

[125] Typically, the imaginary part of the dielectric function is calculated directly, while the real part is computed through the Kramers-Kronig relation, Eq. 3.190. [987]

differences (*leap-frog*) algorithm to calculate $|\xi(t_{i+2})\rangle$ from $|\xi(t_i)\rangle$ and $|\xi(t_{i+1})\rangle$ via

$$\hat{H}\,|\xi(t_{i+1})\rangle = i\frac{|\xi(t_{i+2})\rangle - |\xi(t_i)\rangle}{2\Delta t}\,. \tag{3.197}$$

The upper limit of the Fourier integral Eq. 3.194 can be truncated due to the exponential $e^{-\eta t}$. Therefore, the required number of time steps relates to the particular broadening parameter η and is nearly independent of the dimension of the system under consideration. [126] The initial-value/time-evolution approach provides the dielectric function (with a lifetime broadening η) at a significantly reduced computational cost due to the reduction of the actual matrix diagonalization to a highly efficiently parallizable matrix-vector multiplication per time step, only. The prize to pay for the reduced computational demands is the loos of explicit information on the eigenvectors, i.e. the exciton-wavefunction coefficients A_Λ, and the exciton-eigenvalues E_λ.

Despite the hard system-size limits, put into place by the vast computational demands to solve the Bethe-Salpeter equation for the Coulomb-correlated electron-hole pairs within any reasonably converged numerical approach, the resulting linear optical properties, commonly presented by means of the (complex) macroscopic dielectric function, represent the highest *rank* of accuracy in the ab initio theory of optical material properties allowing a thorough analysis and interpretation of basic physics underlying experimental findings as well as the virtually parameter-free prediction of optical material characteristics in novel materials and their diverse modifications. In this context, the ab initio theory of optical properties has been thoroughly extended to allow the study of many-body effects in the magneto-optical properties of spin-polarized systems. [987, 1481, 1489] While previous theoretical studies of many-body effects in the optical response by solution of the Bethe-Salpeter equation have primarily focused on prototypical bulk semiconductors as silicon [1449, 1471, 1488] and diverse nitrides [1485] and fluorides [1477, 1482, 1485, 1488] as well as simple models of semiconductor surfaces [1457, 1486], more recent studies increasingly focus on more complex materials as amorphous semiconductors [31], mixed semiconductor alloys [1490], two-dimensional materials [1489, 1491, 1492] or nanomodifications [1493], which are highly relevant for the design, refinement and fabrication of functional materials and optical devices.

[126] An order of 10^3 time steps has been reported in case of $\eta = 0.1\,\text{eV}$. [987, 1471]

I'm afraid everyone has heard of my game of Twenty Questions in its surprise version too often to want to hear it again, but let me only just recall – I come into the room, I say "Is it edible?" and my friend that I asked thinks, thinks, thinks, and says finally, "No". Then I asked the next person, "Is it mineral?" Thinks and thinks. "Yes." And so it goes. But before my twenty questions run out, I must arrive at some word. "Is it 'cloud'?" And the respondent that I ask this time thinks and thinks and thinks. I couldn't understand why the delay because supposedly the word already existed in the room, and all he'd have to do is give an answer "yes" or "no." But instead he thinks. Finally he says "yes" and everybody bursts out laughing. They explained to me that when I came in there was no word in the room, that everybody could answer my questions as he wished with one small proviso – that if I challenged, and he couldn't supply a word compatible with all the previous answers, he lost and I won. So it was just as difficult for them as it was for me. Thus the word was brought into being by the choice of questions asked and answers given. The game reminds us of how we find out about the electron, its position or its momentum. What we get depends partly on our choice of question asked. However, we don't have the whole voice in it. "Nature" has the rest of the answer.

John A. Wheeler (1911–2008)

4 Research contributions

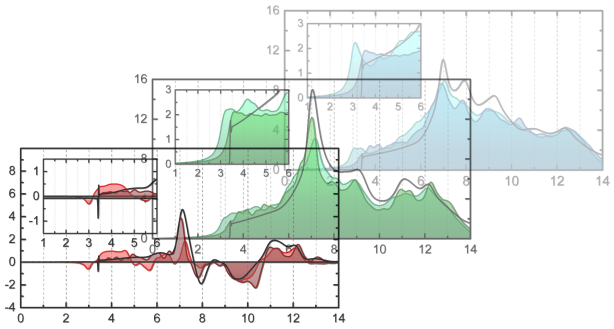

Most of the crackpot papers which are submitted to The Physical Review are rejected, not because it is impossible to understand them, but because it is possible. Those which are impossible to understand are usually published. When the great innovation appears, it will almost certainly be in a muddled, incomplete and confusing form. To the discoverer himself it will be only half-understood; to everybody else it will be a mystery. For any speculation which does not at first glance look crazy, there is no hope.

Freeman J. Dyson (1923 – 2020)

Contents

4.1 Scientific publications 122

4.1.1 List of contributing publications 122

4.1.2 List of related publications 123

4.1.3 Other publications 124

4.1.4 Summaries of contributing publications 126

4.1.5 Summaries of related publications 139

4.1 Scientific publications

4.1.1 List of contributing publications

The following enumeration contains a complete list of peer-reviewed scientific publications that directly contribute to the subject of the present thesis with major contributions of the thesis's author. The individual contributions to each publication are outlined in detail.

I . C. Mietze, M. Landmann, E. Rauls, H. Machhadani, S. Sakr, M. Tchernycheva, F. H. Julien, W. G. Schmidt, K. Lischka, and D. J. As: *Band offsets in cubic GaN/AlN superlattices*, PHYSICAL REVIEW B **83**, 195301, 10 pp. (2011) [309]

All ab initio calculations of this study, based on DFT as well as MBPT have been provided by the thesis's author. The major part of the manuscript, related to the realization and examination of the ab initio results against the effective mass model calculations have been written by the thesis's author.

II . M. Landmann, E. Rauls, and W. G. Schmidt: *The electronic structure and optical response of rutile, anatase and brookite TiO_2*, JOURNAL OF PHYSICS: CONDENSED MATTER **24**, 195503, 6 pp. (2012) – JPCM 2012 Highlight Paper [75]

The entire study, including the DFT and MBPT calculations as well as the manuscript preparation, has been realized by the thesis's author.

III . M. Landmann, T. Köhler, S. Köppen, E. Rauls, T. Frauenheim, and W. G. Schmidt: *Fingerprints of order and disorder in the electronic and optical properties of crystalline and amorphous TiO_2*, PHYSICAL REVIEW B **86**, 064201, 20 pp. (2012) [31]

With exception of the DFTB-MD amorphization simulations and the related methodology description, the entire manuscript was written by the thesis's author. All DFT based simulations of the various crystalline and amorphous TiO_2 modifications have been contributed.

IV . M. Landmann, M. Feneberg, M. Röppischer, T. Schupp, C. Cobet, E. Rauls, D. J. As, N. Esser, R. Goldhahn, and W. G. Schmidt: *Transition energies and direct-indirect band gap crossing in zinc-blende $Al_xGa_{1-x}N$*, PHYSICAL REVIEW B **87**, 195210, 21 pp. (2013) – Editors' Suggestion [33]

The thesis's author is responsible for all ab initio simulations in this study. The major part of this study, including the introduction, the examination of various numerical approaches to the electronic of structure group-III nitrides, as well as the joint analysis of experimental and theoretical data, has been written by the thesis's author.

V . M. Landmann, T. Köhler, E. Rauls, T. Frauenheim, and W. G. Schmidt: *The atomic structure of ternary amorphous $Ti_xSi_{1-x}O_2$ hybrid oxides*, JOURNAL OF PHYSICS: CONDENSED MATTER **26**, 253201, 46 pp. (2014) – Topical Review [32]

Aside from the initial preparation of the amorphous structures of TiO_2, SiO_2, as well as the ternary $Ti_xSi_{1-x}O_2$ hybrid oxides, by DFTB-MD, all calculation results presented in this study as well as the conception and writing of the manuscript were subject to the thesis's author's responsibility.

VI . M. Landmann, E. Rauls, W. G. Schmidt, M. D. Neumann, E. Speiser, and N. Esser: *GaN m-plane: Atomic structure, surface bands and optical response*, PHYSICAL REVIEW B **91**, 035302, 9 pp. (2015) [34]

All DFT and MBPT calculations have been conducted by the thesis's author. With exception of Fig. 9 all figures and tables as well as the description of the numerical methodology have been provided.

VII . M. Landmann, E. Rauls, and W. G. Schmidt: *Understanding band alignments in semiconductor heterostructures: Composition dependence and type-I-type-II transition of natural band offsets in nonpolar zinc-blende $Al_xGa_{1-x}N/Al_yGa_{1-y}N$ composites*, PHYSICAL REVIEW B **95**, 155310, 14 pp. (2017) [35]

The complete manuscript, including all DFT and hybrid functional calculations, has been prepared by the thesis's author.

4.1.2 List of related publications

The following enumeration contains a list of peer-reviewed scientific publications that are related to the subject of the present thesis with minor contributions of the thesis's author. For each paper the contributions of the thesis's author are outlined in detail.

VIII . J. von Bardeleben, J. L. Cantin, U. Gerstmann, A. Scholle, S. Greulich-Weber, E. Rauls, M. Landmann, W. G. Schmidt, A. Gentils, J. Botsoa, and M. F. Barthe: *Identification of the Nitrogen Split Interstitial $(N–N)_N$ in GaN*, PHYSICAL REVIEW LETTERS **109**, 206402, 5 pp. (2012) [334]

All HSE-type DFT hybrid-functional calculations providing the energy gap as well as the charge transition levels of the nitrogen $(N–N)_N$ split interstitial in GaN have been provided by the thesis's author.

IX . T. Köhler, M. Turowski, H. Ehlers, M. Landmann, D. Ristau, and T. Frauenheim: *Computational approach for structure design and prediction of optical properties in amorphous TiO_2 thin-film coatings*, JOURNAL OF PHYSICS D: APPLIED PHYSICS **46**, 325302, 9 pp. (2013) [1494]

The DFT-based structure relaxations of atomic structures, generated by various MD approaches, have been performed by the thesis's author. Also, the coordination-polyhedra representations of Fig. 1 as well as the summarized electronic-structure results for crystalline and amorphous TiO_2 modifications have been provided.

X . F. Schmidt, M. Landmann, E. Rauls, N. Argiolas, S. Sanna, W. G. Schmidt, and A. Schindlmayr: *Consistent Atomic Geometries and Electronic Structure of Five Phases of Potassium Niobate from Density-Functional Theory*, ADVANCES IN MATERIALS SCIENCE AND ENGINEERING, 3981317, 13 pp. (2017) [1495]

The HSE hybrid-functional DFT calculations have been conducted by the thesis's author. Likewise, Fig. 3 and Fig. 4 have been provided and notable parts of the manuscript were written by the thesis's author.

4.1.3 Other publications

XI . M. Landmann, E. Rauls, and W. G. Schmidt: *First-principles calculations of clean Au(110) surfaces and chemisorption of atomic oxygen*, PHYSICAL REVIEW B **79**, 045412, 10 pp. (2009) [1496]

XII . M. Landmann, E. Rauls, and W. G. Schmidt: *Chainlike Au-O Structures on Au(110)-(1×r) Surfaces Calculated from First Principles*, THE JOURNAL OF PHYSICAL CHEMISTRY C **113**, 5690, 9 pp. (2009) [1497]

XIII . A. Lücke, T. Biktagirov, A. Riefer, M. Landmann, M. Rohrmüller, C. Braun, S. Neufeld, U. Gerstmann, and W. G. Schmidt: *Photo-Excited Surface Dynamics from Massively Parallel Constrained-DFT Calculations*, HIGH PERFORMANCE COMPUTING IN SCIENCE AND ENGINEERING '17, Springer International Publishing AG, 157, 11 pp. (2018) [1498]

XIV . S. Sanna, C. Dues, U. Gerstmann, E. Rauls, D. Nozaki, A. Riefer, M. Landmann, M. Rohrmüller, N. J. Vollmers, R. Hölscher, A. Lücke, C. Braun, S. Neufeld, K. Holtgrewe, W. G. Schmidt: *Submonolayer Rare Earth Silicide Thin Films on the Si(111) Surface*, HIGH PERFORMANCE COMPUTING IN SCIENCE AND ENGINEERING '16, Springer International Publishing AG, 163, 12 pp. (2016) [1499]

XV . A. Lücke, U. Gerstmann, S. Sanna, M. Landmann, A. Riefer, M. Rohrmüller, N. J. Vollmers, M. Witte, E. Rauls, R. Hölscher, C. Braun, S. Neufeld, K. Holtgrewe, W. G. Schmidt: *Solving the Scattering Problem for the P3HT On-Chain Charge Transport*, HIGH PERFORMANCE COMPUTING IN SCIENCE AND ENGINEERING '15, Springer International Publishing Switzerland, 155, 15 pp. (2016) [1500]

XVI . S. Sanna, U. Gerstmann, E. Rauls, Y. Li, M. Landmann, A. Riefer, M. Rohrmüller, N. J. Vollmers, M. Witte, R. Hölscher, A. Lücke, C. Braun, S. Neufeld, K. Holtgrewe, W. G. Schmidt: *Surface Charge of Clean $LiNbO_3$ Z-Cut Surfaces*, HIGH PERFORMANCE COMPUTING IN SCIENCE AND ENGINEERING '14, Springer International Publishing Switzerland, 163, 15 pp. (2015) [1501]

XVII. S. Sanna, A. Riefer, M. Rohrmüller, M. Landmann, E. Rauls, N. J. Vollmers, R. Hölscher, M. Witte, Y. Li, U. Gerstmann, and W. G. Schmidt: *Polarization Dependent Water Adsorption on the Lithium Niobate Z-Cut Surfaces*, HIGH PERFORMANCE COMPUTING IN SCIENCE AND ENGINEERING '13, Springer International Publishing Switzerland, 155, 12 pp. (2013) [1502]

XVIII. A. Riefer, M. Rohrmüller, M. Landmann, S. Sanna, E. Rauls, N. J. Vollmers, R. Hölscher, M. Witte, Y. Li, U. Gerstmann, A. Schindlmayr, and W. G. Schmidt: *Lithium Niobate Dielectric Function and Second-Order Polarizability Tensor From Massively Parallel Ab Initio Calculations*, HIGH PERFORMANCE COMPUTING IN SCIENCE AND ENGINEERING '13, Springer International Publishing Switzerland, 93, 12 pp. (2013) [1503]

XIX. U. Gerstmann, M. Rohrmüller, N. J. Vollmers, A. Konopka, S. Greulich-Weber, E. Rauls, M. Landmann, S. Sanna, A. Riefer, and W. G. Schmidt: *Surface Magnetism: Relativistic Effects at Semiconductor Interfaces and Solar Cells*, HIGH PERFORMANCE COMPUTING IN SCIENCE AND ENGINEERING '12, Springer-Verlag, Berlin, 129, 15 pp. (2013) [1504]

XX. A. Riefer, M. Rohrmüller, M. Landmann, S. Sanna, E. Rauls, U. Gerstmann, and W. G. Schmidt: *Electronic and Optical Excitations of Aminopyrimidine Molecules from Many-Body Perturbation Theory*, HIGH PERFORMANCE COMPUTING IN SCIENCE AND ENGINEERING '12, Springer-Verlag, Berlin, 17, 12 pp. (2013) [1505]

XXI. W. G. Schmidt, E. Rauls, U. Gerstmann, S. Sanna, M. Landmann, M. Rohrmüller, A. Riefer, S. Wippermann, and S. Blankenburg: *Copper Substrate Catalyzes Tetraazaperopyrene Polymerization*, HIGH PERFORMANCE COMPUTING IN SCIENCE AND ENGINEERING '11, Springer-Verlag, Berlin, 47, 10 pp. (2012) [1506]

XXII. W. G. Schmidt, E. Rauls, U. Gerstmann, S. Sanna, M. Landmann, M. Rohrmüller, A. Riefer, and S. Wippermann: *Entropy and Metal-Insulator Transition in Atomic-Scale Wires: The Case of In-Si(111)(4×1)/(8×2)*, HIGH PERFORMANCE COMPUTING IN SCIENCE AND ENGINEERING '11, Springer-Verlag, Berlin, 131, 9 pp. (2012) [1507]

XXIII. W. G. Schmidt, S. Wippermann, E. Rauls, U. Gerstmann, S. Sanna, C. Thierfelder, M. Landmann, and L. S. dos Santos: *Si(111)-In Nanowire Optical Response from Large-scale Ab Initio Calculations*, HIGH PERFORMANCE COMPUTING IN SCIENCE AND ENGINEERING '10, Springer-Verlag, Berlin, 149, 10 pp. (2011) [1508]

XXIV. W. G. Schmidt, S. Blankenburg, E. Rauls, S. Wippermann, U. Gerstmann, S. Sanna, C. Thierfelder, N. Koch, and M. Landmann: *Understanding Long-range Indirect Interactions Between Surface Adsorbed Molecules*, HIGH PERFORMANCE COMPUTING IN SCIENCE AND ENGINEERING '09, Springer-Verlag, Berlin, 75, 10 pp. (2010) [1509]

4.1.4 Summaries of contributing publications

PAPER I [309]: *Band offsets in cubic GaN/AlN superlattices*

One of the most crucial parameters that determines the basic physical characteristics of semiconductor heterostructures and, therefore, provides the basis for the optimization and design of optoelectronic devices as (multi) quantum wells and superlattices is the alignment of electronic bands at the boundary of two interfacing semiconductors. These band offsets/discontinuities reflect how the band-gap difference of the involved semiconductor materials is portioned between the discontinuities of the highest occupied valence and lowest unoccupied conduction bands, the fundamental band edges respectively. While band offsets of group-III-nitride superlattices are well known for the naturally occurring hexagonal phases the band offsets in nonpolar cubic group-III-nitride heterostructures have rather been studied in theoretical simulations than in experimental approaches. This observation is certainly owned the fact that, on the one hand, the higher crystal symmetry simplifies and accelerates numerical simulations of the electronic structure. On the other hand, the preparation of defect free (cubic) single-crystal samples had not been achieved or even been a priority for experimenters during the heights of the silicon era. With increasing interest in optoelectronic devices based on group-III-nitride materials, the disadvantages of the wurtzite inherent strong internal piezoelectric and spontaneous polarization fields have been weight against the fabrication difficulties of semipolar and nonpolar material modifications. Currently, the potential replacement of wurtzite phase materials by cubic material modifications is investigated by fundamental researchers for a multitude of device applications in optoelectronics.

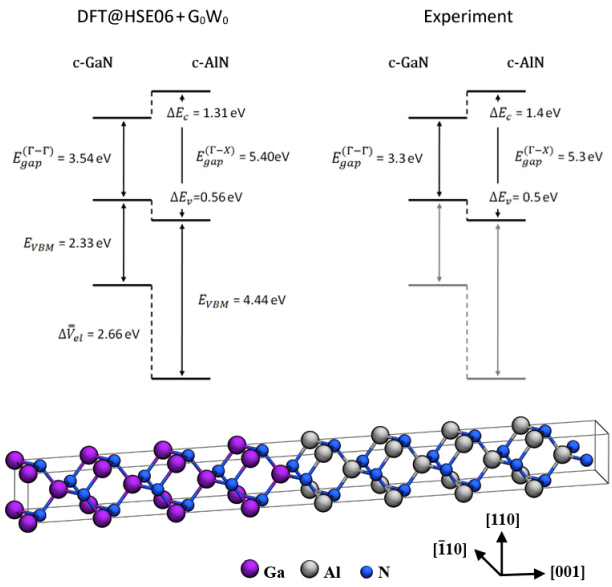

Figure 4.1: Schematic illustration of the calculated DFT@HSE06 + G_0W_0 and experimental band alignments (top) at the cubic GaN/AlN heterostructure interface with c-AlN pseudomorphically strained to c-GaN. (bottom)

Based on recent progress in the fabrication of cubic GaN/AlN superlattices by several of this paper's authors, the so far unknown band offsets in nonpolar cubic GaN/AlN superlattices are investigated by two different approaches, based on inter-sub-band and interband spectroscopy as well as state-of-the-art ab initio calculations. On one hand, the conduction-band offset is determined from the comparison of spectroscopically measured inter-sub-band and intraband transition energies with model calculations based on a single-band effective mass model with periodic

boundary conditions. From comparison of experimental transition energies with the model calculations, a conduction-band offset in the range of 1.4 ± 0.1 eV is determined reflecting 74 ± 5 % of the band-gap differences between cubic AlN and cubic GaN. On the other hand, the valence and conduction band offsets are accurately simulated from first principles by calculating many-body corrections within the *GW* approximation on top of hybrid-functional HSE-type density-functional theory simulations. The underestimated direct and indirect DFT-PBE band gaps of $E_{gap}^{GaN}(\Gamma-\Gamma) = 1.66\,\text{eV}$ and $E_{gap}^{AlN}(\Gamma-X) = 3.31\,\text{eV}$ of cubic GaN and AlN are improved to $E_{gap}^{GaN}(\Gamma-\Gamma) = 2.92\,\text{eV}$ and $E_{gap}^{AlN}(\Gamma-X) = 4.56\,\text{eV}$, respectively, by use of the HSE06 hybrid functional. The most promising results are obtained within non-selfconsistent *GW* energy corrections using the more accurate hybrid-functional single-particle wavefunctions and eigenvalues as a starting point. These calculated G_0W_0@HSE06 band gaps of $E_{gap}^{GaN}(\Gamma-\Gamma) = 3.54\,\text{eV}$ and $E_{gap}^{AlN}(\Gamma-X) = 5.40\,\text{eV}$ essentially demonstrate the gain from this conceptual and numerically rather simple *perturbative* approximation to MBPT and the necessity of highly accurate initial-state wavefunctions in this type of calculation. Using the calculated energy gaps above, the problem of the discontinuous band progression at a heterostructure interface is handled by aligning the fundamental energy gaps of the bulk materials according to the shift in the macroscopic average of the electrostatic potential across the interface of a the respective semiconductor heterostructure. The heterostructure itself is described within a supercell approach including lattice relaxations on the DFT-PBE level of theory and the potential shift is extracted either from (semi)local or hybrid functional DFT calculations. In this way, effects of strain due to the epitaxial growth on a substrate and electronic relaxations and/or redistributions at the heterostructure's interface are included and valence and conduction band offsets of $\Delta E_v = 0.56\,\text{eV}$ and $\Delta E_c = 1.31\,\text{eV}$ with a $70:30$ ratio of the band-gap difference are obtained.

In summary, the comprehensive analysis of experimental and ab initio simulation data gives strong evidence for valence-band and conduction-band discontinuities of pseudomorphically strained cubic GaN/AlN superlattices in the ranges of $\Delta E_v = 0.5 \pm 0.1$ eV and $\Delta E_c = 1.31 \pm 0.1$ eV (cf. figure 4.1). Although the local atomic structures and chemical bonding environments of wurtzite and zincblende materials are very similar for both systems, the cubic material value for the conduction-band offset differs significantly from the experimental value for the hexagonal system, where a conduction band offset of $(1.7 \pm 0.05)\,\text{eV}$ has been found. [1510] Hence, the results of this study not only quantify the band offsets in pseudomorphically grown cubic GaN/AlN superlattices but also demonstrate the importance of taking into account detailed atomic structure information in order to characterize new functional semiconductor heterostructures and nanostructured functional materials, in general.

PAPER II [75]: *The electronic structure and optical response of rutile, anatase and brookite TiO_2*

TiO_2 is a semiconductor with numerous favorable material characteristics as long-term stability, non-toxic environmental acceptability, broadly low-cost availability, and an excellent

photocatalytic potential. Due to the rich structure polymorphism of crystalline TiO_2, differences in the electronic and optical material properties between various TiO_2 modifications are of fundamental interest. Of the manifold of synthesizable crystalline TiO_2 polymorphs, mainly the three crystal types rutile {crystal system: tetragonal ($4/mmm$), space group: $P4_2/mnm$-D_{4h}^{14}}, anatase {tetragonal ($4/mmm$), $I4_1/amd$-D_{4h}^{19}}, and brookite {orthorhombic (mmm), $Pbca$-D_{2h}^{15}} are found in nature. While the first two play a significant role in industrial applications, experimental data on TiO_2 brookite is limited due to its rareness and the general difficulty of pure-phase preparation.

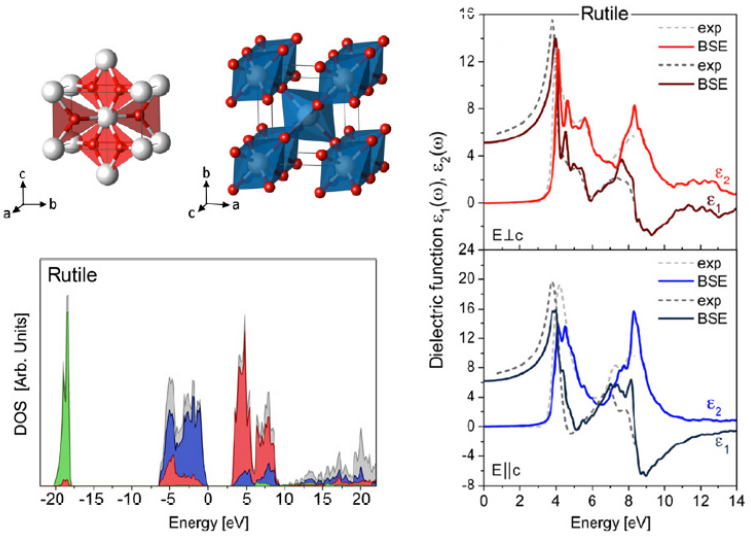

Figure 4.2: Planar OTi_3 building-block (top, left) and TiO_6 coordination polyhedra (top, middle) representation of the TiO_2 rutile phase. Total and angular momentum decomposed DFT-HSE06 densities of states. (bottom) Calculated direction/polarization dependent G_0W_0@PBE+BSE@PBE dielectric functions, of TiO_2 rutile. (right)

In the present manuscript the electronic properties of rutile, anatase, and brookite are investigated on the basis of HSE06 hybrid functional calculations and via inclusion of G_0W_0 quasiparticle corrections within the framework of MBPT. It is demonstrated that the electronic hybrid-functional band structure represents an accurate approximation of the G_0W_0@PBE quasiparticle-band structure within an energy range of a few eV around the band edges. Consequently, the electronic band gaps of 3.39 eV, 3.60 eV, and 3.30 eV from DFT-HSE06 and 3.46 eV, 3.73 eV, and 3.45 eV from G_0W_0@PBE calculations for rutile, anatase, and brookite are found to be quite similar in both numerical approaches.

The analysis of the band structures as well as densities of states indicates that all three material phases share common characteristics that are related to the octahedron-type short-range order in TiO_2 crystals. The crystal structure of all natural TiO_2 modifications consists of three-dimensional networks of edge- and/or corner-linked distorted TiO_6 octahedron building blocks with D_{2h}, D_{2d}, and C_1 symmetries in rutile, anatase, and brookite, respectively. In general, the valence-band edges are predominantly formed by O_{2p}-like states while the conduction band-edges are predominantly formed by Ti_{3d}-like states. As indicated in the densities of states, the broad Ti_{3d}-like conduction bands show a distinct separation into two sub-bands. This inner conduction-band structures are connected to the distorted-octahedron-type short-range order inherent crystal-field splitting of $3d$-electon transition-metal (di)oxide complexes. In an octahedral-type crystal field, the five unoccupied d-states of the central Ti ion split into the twofold-degenerate e_g-like states and the

energetically lower lying threefold-degenerate t_{2g}-like states.

Starting from the accurate G_0W_0@PBE quasiparticle-band structure, the optical response of the TiO_2 polymorphs is calculated by taking into account excitonic contributions and local field effects via solution of a BSE for Coulomb correlated (quasi-)electrons and (quasi-)holes. As a result of the common electronic structure, all three TiO_2 phases share a similar line shape of the dielectric function characterized by an absorption onset above 3 eV and two distinct broad absorption bands below and above $\sim 6.5\,\text{eV}$ (cf. figure 4.2). This characteristic spectral weight distribution is particularly observed for TiO_2 brookite, thus, indicating the defining influence of the common short-range order despite symmetry variations in the local atomic cation-coordination environment. The dielectric functions directly reflect the octahedron-like crystal-field splitting of the unoccupied Ti_{3d}-like states observed in the electronic structure. The first main peak can be identified with interband transitions from the O_{2p}-like valence band into the t_{2g}-like sub-band of Ti_{3d}-like states. The high-energy absorption feature arises from transitions into the e_g-like sub-band.

Not at least, the presented optical-response data indicate that the inclusion of electron-hole pair excitations on the BSE level of theory allows an accurate modeling of the polarization-dependent optical response of various naturally occurring TiO_2 polymorphs. As a final remark, previously reported discrepancies between BSE and measured dielectric functions for TiO_2 rutile have been traced back to the use of improper experimental reference data [1511] in preceding studies [141, 143] and the reliability of more recent experimental data [1512] has been proven.

PAPER III [31]: *Fingerprints of order and disorder in the electronic and optical properties of crystalline and amorphous TiO_2*

Titanium dioxide (TiO_2) shows an extended structure polymorphism, reflected in an extraordinary rich phase diagram even for the stoichiometric solid. Besides the manifold of ordered crystalline TiO_2 modifications that are characterized by well defined coordination numbers for every chemical element, also amorphous TiO_2 has received interest as a low-cost alternative for technical applications, assuming that at least fragments of the extraordinary optical and catalytic properties known from crystalline TiO_2 are retained in the disordered material phase. It is phenomenologically well known that the complete loss of long-range order in an amorphous solid modifies the electronic structure and optical response compared to the crystalline solid. Consequently, the theoretical tools developed mainly for the analysis of crystalline materials cannot be applied to amorphous materials, straightforwardly, in order to estimate their physical properties. An understanding of the formation of energy gaps and resulting optical properties in amorphous semiconductors is directly related to the question of whether the basic nature of electronic and optical properties depends on short-range order, i.e. localized electronic states, and/or long-range order, i.e. extended electronic states and well-defined energy bands. The general existence of diversely coordinated crystal phases as well as disordered material modification makes TiO_2 an

interesting test system to study the effects of long-range order loss and the fundamental correlations between the spatial and electronic structure and the associated optical properties, in detail.

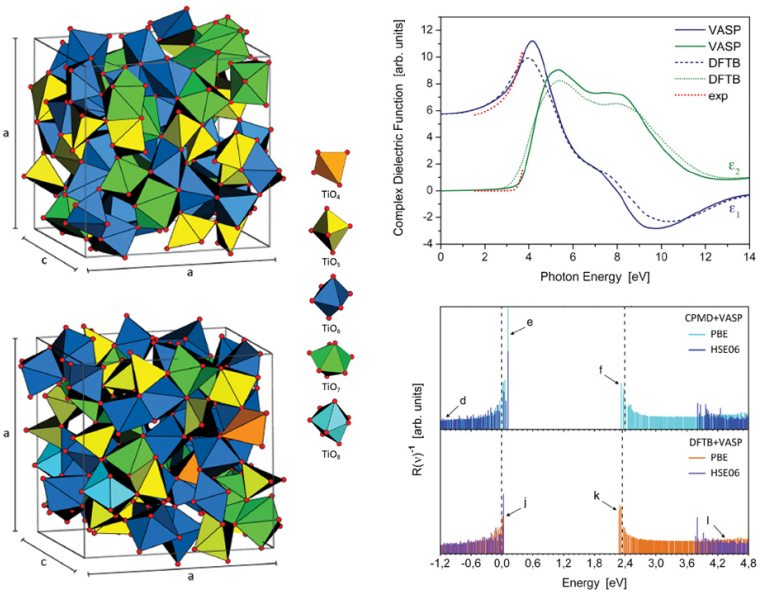

Figure 4.3: Polyhedra representation of TiO_x building blocks in two different 216-atom structure models of amorphous TiO_2 prepared my CPMD-MD (left, top) and DFTB-MD (left, bottom) as well as successive DFT structure relaxations. Calculated DFT-PBE complex dielectric functions in independent particle approximation (1.3 eV scissors shift) and DFT-PBE/HSE06 inverse participation ratios (right, bottom) corresponding to the atomic structure models on the left.

Within the present manuscript, the physical properties of amorphous TiO_2 are investigated within the framework of DFT and MBPT. Various atomic structure models are generated by numerically efficient DFTB-MD and CPMD-MD simulations and subsequently characterized by analysis of the structure factors, distribution functions, as well as total and partial coordination numbers and coordination-polyhedra statistics. In consideration of various types of experimental samples reported in literature, it is indicated that short-range order in disordered TiO_2 phases might be non-unique with notable variations in the local atomic coordination states. While the composition of the naturally occurring crystalline phases rutile, anatase, and brookite is well described by periodic arrangements of slightly distorted TiO_6 octahedra building blocks, the amorphous phase is always characterized by a partial loss of the octahedral coordination and the disorder-induced formation of under- and over-coordinated Ti ions. Only $50-60\,\%$ of the Ti ions still form, to some extend notably distorted, TiO_6 polyhedra-building blocks. The other Ti ions form substantial fractions of TiO_5 and TiO_7 building blocks, while the formation of TiO_4 and TiO_8 units depends strongly on the simulation approach (cf. figure 4.3). In general, the total *mean* coordination number of amorphous TiO_2 is found to be smaller than the sixfold coordination limit defined by crystalline TiO_2 of the same mass density.

Using both the semilocal PBE functional and the nonlocal HSE06 screened hybrid functional, the electronic energy gap of amorphous TiO_2 is found to be larger than in the crystalline TiO_2 phases rutile and brookite but close to the anatase band gap. The quasiparticle-energy gap of amorphous TiO_2 is determined to be 3.7 eV while the optical gap is estimated to 3.5 eV. The influence of band-tail states on the energy gap is found to be quite small (~ 0.1 eV) for the completely relaxed structure models, which formally represent the zero temperature limit. For this purpose,

the degree of (de)localization of electronic states due to disorder was estimated from the charge density distributions by means of the inverse participation ratio.

Similar to the three crystalline TiO_2 main phases, the valence and conduction *band* edges are formed by broad bands of occupied, predominantly O_{2p}-like, states and unoccupied Ti_{3d}-like states. The distinct splitting of the unoccupied Ti_{3d} states into e_g and t_{2g}-like sub-bands is almost absent and replaced by a single broad band of conduction states in amorphous TiO_2. The origin of this qualitative difference in the disordered material phase unambiguously traces back to the partial loss of octahedral coordination and the existence of under-coordinated and over-coordinated TiO_x complexes (cf. figure 4.3). The most important consequence of the loss of local symmetry and the variations in the Ti coordination number of amorphous TiO_2 is the modification of optical spectra in the energy region from 5 eV to 8 eV. More precisely, the two distinct spectral features below and above ~ 6.5 eV, observed in the TiO_2 rutile, anatase and brookite phases, are replaced by a broad spectral feature that shows only marginal indications of an octahedral-type crystal field and the related splitting in t_{2g}-like and e_g-like electronic states.

As final observation of this manuscript, a way to estimate the optical response characteristics of amorphous TiO_2 is proposed. Since an amorphous phase represents a metastable state, it is reasonable to assume that the versatile local atomic structure of the amorphous phase reflects a wide cross section of all possible binding situations appearing in the existing crystalline phases. This explicitly includes crystal phases that normally are unstable under ambient conditions. It is demonstrated that due to inclusion of TiO_2 high-pressure polymorphs, the averaging of dielectric functions from eleven crystalline TiO_2 phases allows the reproduction of all spectral features present in the dielectric function of the amorphous state.

PAPER IV [33]: *Transition energies and direct-indirect band gap crossing in zinc-blende $Al_xGa_{1-x}N$*

Throughout the last two decades, scientific breakthroughs in the field of group-III nitride semiconductor materials have always stimulated rapid technological progress in the manufacturing of optoelectronic and electronic devices. For a long time almost exclusively grown along the polar (0001) c-direction of the hexagonal crystal, group-III nitrides, and their multicomponent alloys exhibit strong internal piezoelectric and spontaneous polarization fields, which are undesirable for optoelectronic applications since they inherently limit the device performance. The growth of nonpolar and semipolar nitrides has found increasing technological interest over the past years to avoid these strong internal fields. Among all group-III nitride semiconductors, zb-AlN is the only binary semiconductor with a non-direct $(\Gamma_v \rightarrow X_c)$ fundamental bulk-band gap. Hence, an important alloy characteristic of the ternary zb-$Al_xGa_{1-x}N$ alloys is the critical concentration marking the transition of the fundamental alloy-band gap from involving either the bulk-like Γ_c conduction band states,

originating from the direct zb-GaN band gap, or the bulk-like X_c conduction band states of the indirect zb-AlN band gap.

The present manuscript represents a thorough investigation of this direct-indirect band-gap crossing by combining synchrotron-based ellipsometry measurements with state-of-the-art ab initio calculation data. The experimentally determined fundamental energy transitions originating from the Γ, X, and L points are identified by comparison to theoretical band-to-band transition energies. In order to determine the Al concentration at the direct-indirect crossing, the direct E_2 transition energies at the X point need to be aligned by the calculated relative difference of the highest X point valence states and the position of the highest Γ point valence state (cf. figure 4.5). For this purpose a variety of approaches, representing different approximation levels to either DFT or MBPT, is rigorously tested for their numerical accuracy and predictive power in the description of group-III nitride bulk and alloy semiconductors. In detail, DFT based approaches to the electronic structure, ranging from the standard (semi)local GGA, a self-energy corrected local density approximation (LDA-1/2), and a meta-GGA (TB-mBJLDA) to hybrid functional DFT and many-body perturbation theory in the GW approximation have been considered.

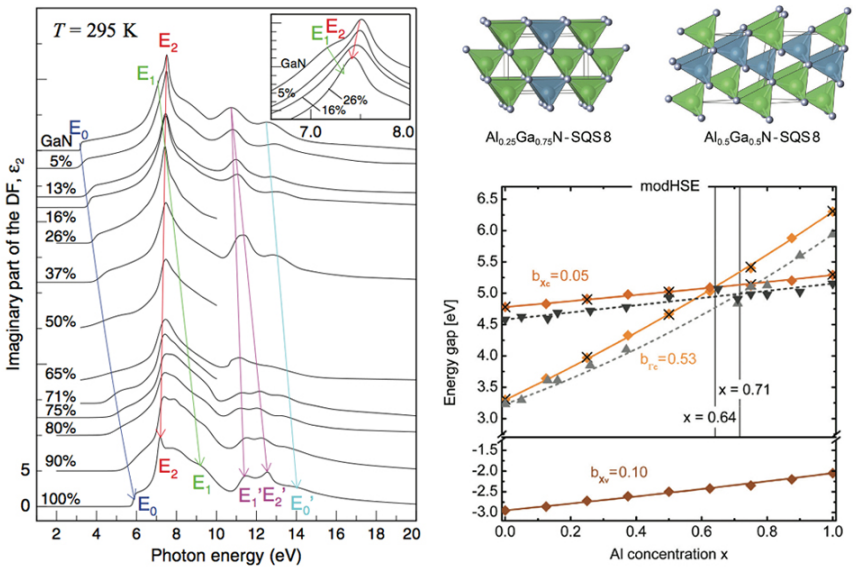

Figure 4.4: Imaginary parts (ε_2) of the complex dielectric functions of zb-$Al_xGa_{1-x}N$ samples at room temperature (295 K). (left) Tetrahedra representation of eight-atomic SQS unit cells for zb-$Al_xGa_{1-x}N$ alloys. (top, right) Fundamental alloyband gaps and position of the highest X point valence state of 64 (diamonds) and 216 (crosses) atom zb-$Al_xGa_{1-x}N$ unit cells calculated using an exact exchange adjusted HSE-type hybrid functional (modHSE). Bowing parameters and direct-indirect band-gap crossover concentrations are indicated. (bottom, right)

The substitutional disorder of the ternary semiconductor alloys is considered in 8 to 216 atom unit cells with randomly occupied cation sublattices as well as 8 to 32 atom special quasirandom structure (SQS) [1513, 1514] unit cells. As expected, the unit-cell representation of the zb-$Al_xGa_{1-x}N$ alloys suffers from notable periodicity errors for very small (eight atom) unit cells. This observation affects both unit-cell modeling approaches, even if the 8 atom SQS representation slightly reduces the periodicity errors. Compared to the largest 216 atom unit cells, the 32 atom SQS unit cells allow band-gap calculations with a significantly reduced number of atoms without any notable loss of accuracy. The direct-indirect band gap crossover concentration seems

to be quite insensitive to the specific unit-cell representation, since both the direct-type and the indirect-type alloy band gap are equally affected by the artificially introduced lattice periodicity. Even the critical Al concentrations at the direct-indirect crossing are found to be very reasonable for eight atom unit-cell calculations.

In summary, the direct-indirect band gap crossover in zb-$Al_xGa_{1-x}N$ as well as the band-gap bowing parameters have been determined on various levels of numerical accuracy in combination with the analysis of critical points in the dielectric functions obtained from ellipsometry measurements. A downward bowing of the direct $(\Gamma_v \rightarrow \Gamma_c)$-type alloy-band gap of $b_\Gamma = 0.85\,\text{eV}$ is obtained from the ellipsometry data. The indirect $(\Gamma_v \rightarrow X_c)$-type band gap shows a linear dependence on the Al concentration ($b_X = 0.01\,\text{eV}$). The direct-indirect band gap crossover in zb-$Al_xGa_{1-x}N$ is found at $x = 0.71$ after aligning the experimentally obtained E_2 transition energies according to the highest X point valence-state energies determined via hybrid-functional DFT. The TB-mBJLDA and LDA-1/2 approaches allow for a reasonable estimation of quasiparticle energies. Considering the moderate computational cost, which is comparable to (semi)local DFT calculations, both approaches allow an efficient approximation of the QP band structure, even for large scale unit cells. Nevertheless, while both approaches give highly accurate bulk-band gaps, they cannot compete with the overall hybrid-functional description of the electronic structure of zb-$Al_xGa_{1-x}N$ alloys. This is especially reflected in overestimated bowing parameters and a direct-indirect band-gap crossover at very high Al concentrations. Also, the position of valence bands, crucial to align the experimentally determined transition energies in order to determine the direct-indirect band gap crossing, is severely affected by the use of the more approximate QP approaches TB-mBJLDA and LDA-1/2. Basically, the observed properties of the TB-mBJLDA *potential-only* functional and to a lesser extend the results obtained via the LDA-1/2 technique reflect the limited adaptability of a local XC functional. Even the semi-local PBE functional might give better bowing characteristics and a significantly more accurate estimation of the direct-indirect band gap crossover point. Hybrid-functional DFT with an optimized exact-exchange fraction reproduces quasiparticle alloy-band gaps of GW@HSE06 calculations within 0.2 eV accuracy over the entire alloy composition range and the calculated direct-indirect band-gap crossover concentration is found in good agreement with the experimental findings.

PAPER V [32]: *The atomic structure of ternary amorphous $Ti_xSi_{1-x}O_2$ hybrid oxides*

The catalytic and optical activity of solid-state materials strongly depends on their diverse atomic structure characteristics. These are the crystal symmetry or, rather, the degree of structural order, superordinate structural characteristics as grain size and pore size, as well as further artificial nanostructuring of a particular material sample. Commonly, the homogenous material inherent physico-chemical properties limit the wide-range tunability of at least some of these material characteristics. In order to overcome these kinds of limitations, the industrial need for new catalysts and optical materials drives the engineering of

new, partially nanostructured, multicomponent hybrid materials.

A class of materials, that stands for the manifold of oxide alloys that have attracted considerable attention over the last years, are mixed TiO_2/SiO_2 (titania-silica) hybrid oxides, also termed TiO_2/SiO_2 binary oxides as well as ternary $Ti_xSi_{1-x}O_2$ oxides in the case of atomically mixed alloys. TiO_2/SiO_2 hybrid oxides take advantage of the catalytic properties of semiconducting TiO_2 and the high thermal stability and mechanical strength of SiO_2. TiO_2/SiO_2 based compounds nowadays offer a promising engineering platform for new materials with wide area applicability in chemical industry and optoelectronics.

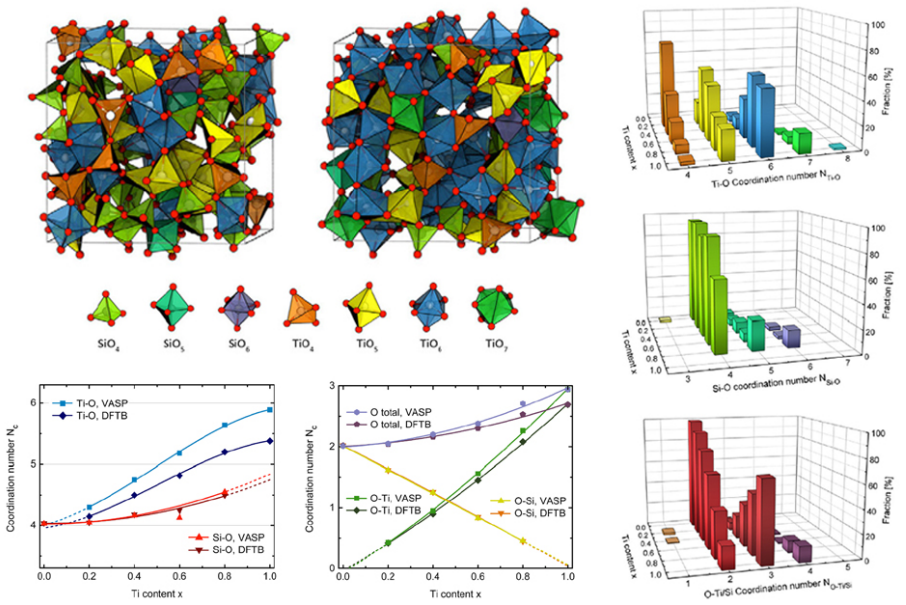

Figure 4.5: Coordination polyhedra representation of amorphous $Ti_{0.6}Si_{0.4}O_2$ (top, left) and $Ti_{0.6}Si_{0.4}O_2$ (top, middle) structure models. Conventional average coordination numbers of Ti and Si ions (bottom, left) as well as for O ions (bottom, middle) in $Ti_xSi_{1-x}O_2$ hybrid oxides. Distribution of local coordination states of Ti (top, right), Si (middle, right), and O (bottom, right) ions in $Ti_xSi_{1-x}O_2$.

In the present review, the analytic tools to classify various atomic length-scale order characteristics in an amorphous framework are presented and applied to the ternary $Ti_xSi_{1-x}O_2$ oxides. In detail, the conventional and effective coordination number concepts, distribution-function approaches and ring statistics are discussed comprehensively providing a fundamental understanding of the versatile atomic-structure characteristics. To this purpose, the structure formation of the amorphous oxides was simulated by performing combined self-consistent charge DFTB-MD [1293, 1515, 1516] stimulated annealing simulations and subsequent DFT structure relaxations. The stoichiometric structures, containing 216 atoms for the two binary oxides TiO_2 and SiO_2 and 300 atoms for the ternary $Ti_xSi_{1-x}O_2$ oxides (at compositions x = 0.2, 0.4, 0.6, and 0.8) have been initially prepared in a spatially and chemically randomized configuration and the mass densities were linearly interpolated between 4.20 g cm^{-3} for a-TiO_2 and 2.20 g cm^{-3} for a-SiO_2.

The combined effects of topological and chemical disorder in a-$Ti_xSi_{1-x}O_2$ alloys lead to a continuos increase in both the Si as well as the Ti coordination number with the chemical composition x. This fundamental-composition dependence of the cation-coordination numbers on the alloy compositions means that notable ion fractions experience a change in their local atomic coordina-

tion states with respect to their predominant coordination in crystalline binary (di)oxides. The average coordination number of pure a-TiO2 of 5.89 remains slightly below the crystal-coordination limit. However, an average Ti coordination number close to the sixfold crystalline coordination is by far no evidence for a disordered a-TiO2 network that is predominantly formed by (distorted) octahedron building blocks. Just slightly more than half of all Ti ions ($\sim 54\,\%$) preserve their crystalline coordination state. All other Ti coordination states are affected by *coordination defects* that increase or decrease the local atomic coordination number by ± 1 or ± 2 (cf. figure 4.7). Especially, the intermediate fivefold Ti coordination state contributes notably to the $Ti_xSi_{1-x}O_2$ coordination characteristics. In the a-$Ti_{0.6}Si_{0.4}O_2$ oxide alloy TiO_5 building blocks even become the predominant coordination-polyhedra type. With progressively decreasing Ti content, the Ti ions tend to adopt the dominating fourfold coordination state of Si ions in a-SiO_2. The average Si coordination number of 4.03 indicates a virtually perfect tetrahedral coordination in pure a-SiO_2. The local Si coordination numbers indicate that SiO_4 coordination polyhedra are very robust with respect to changes of the chemical composition parameter. The fractions of over-coordinated Si ions increase for a notable fraction of SiO_m coordination polyhedra only in the presence of a large number of higher coordinated Ti ions.

Aside from changes in the local coordination numbers and the ubiquitous distortions of the coordination polyhedra, also the basic coordination-polyhedra symmetry types change. Thus, amorphous alloys do not necessarily contain only weakly distorted versions of a single crystal-like coordination polyhedron, rather various deformed polyhedra types coexist side by side. While an in depth analysis of coordination-polyhedra geometry proofs to be an elaborate task and the conventional coordination numbers do not provide a measure for the degree of disorder within different coordination polyhedra, the effective coordination-number approach serves both purposes. Effective coordination numbers can be used as qualitative and, if compared to the conventional coordination numbers, quantitative measures for the degree of disorder within the first coordination shell around an atom. Thereby, the effective coordination numbers prove to be quite sensitive to symmetry reductions of the local cation coordination environment and thus, the particular shape and symmetry type of a coordination polyhedron.

Finally, a continuous decrease in ring size, the predominant mid-range scale ordering feature, with increasing Ti content reflects the progressive loss of mid-range order structure characteristics and the competing roles of network forming and network modifying SiO_m and TiO_n units in the mixed hybrid oxides.

PAPER VI [34]: *GaN m-plane: Atomic structure, surface bands and optical response*

Gallium nitride based heterostructures have been used, routinely, since the 1990s for electronic and optoelectronic applications that exploit its wide band gap of approximately 3.4 eV at room temperature. Typically these devices are based on heterostructures grown on c-plane substrates. This orientation, however, gives rise to strong electric fields that

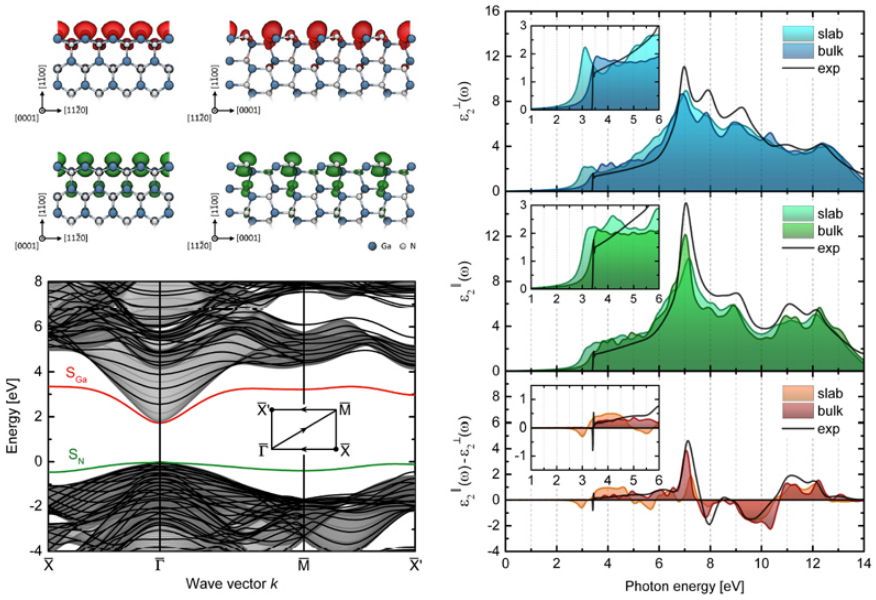

Figure 4.6: DFT-PBE band structure of a 16 layer GaN m-plane surface slab (bottom, left) and partial charge densities (isovalue: 0.01 e / Å^3) of the surface state S_{Ga} (top, left, red) and the surface-resonance state S_N. (top, left, green) Polarization dependent imaginary parts of the complex dielectric functions of the GaN m-plane surface slab and wz-GaN bulk material calculated on the BSE level of theory. (right)

are often disadvantageous for the performance of devices. It has been demonstrated, that the epitaxial growth along non-polar surface directions allows the fabrication of structures free of electrostatic fields due to an equal number of threefold-coordinated Ga and N atoms in the topmost atomic layer that allows charge neutrality without changes in stoichiometry or reconstruction.

In the present manuscript, density-functional theory calculations are combined with many-body perturbation theory in order to elucidate the geometry, electronic and optical properties of the wz-GaN($1\bar{1}00$) surface. The optical absorption related to electronic transitions between electronic surface states is identified by comparison with photoelectron spectroscopy data. The structural and electronic properties are described on the semilocal DFT-PBE level of theory. It is shown that the surface is characterized by a charge transfer from the surface Ga to the more electronegative surface N atom. This charge transfer results in a re-hybridization of the surface atoms that causes a buckling of about 8° of the surface atoms, where the Ga atoms move into the surface.

In order to approximate the QP surface band structure, a non-local HSE-type hybrid functional with an exact exchange fraction of 32 % is applied. Two bound surface states, one occupied, one unoccupied occur in the GaN band gap. The filled N-derived p-like surface state is resonant (energetically degenerate) with the bulk VBM at the origin of the Brillouin zone, but otherwise well separated from the continuum of bulk states. The empty Ga-derived p-like surface state, on the other hand, is well separated from the bulk CBM by at least 0.2 eV within the whole Brillouin zone and this gives rise to an intrinsic pinning of the Fermi level at the GaN m-plane.

The optical response of GaN bulk and surface models are accurately modeled by inclusion of two-particle electron-hole pair excitations within the BSE formalism. The optical responses, calculated via solution of the BSE, closely resemble experimental findings obtained by spectroscopic ellipsometry of GaN($1\bar{1}00$) wurtzite-film samples (cf. figure 4.8). It is found that the presence of

an intrinsic surface state substantially modifies the m-plane optical response with respect to the bulk material. The onset of optical absorption is redshifted with respect to the bulk data by about a few tenths of an eV and an enhanced optical anisotropy for low photon energies is observed. A narrow excitonic absorption in the calculated ordinary dielectric function occurs below the bulk-band gap and a broad optical absorption band for higher energies in the extraordinary dielectric function. This surface band related optical-absorption anisotropy is just as well observed in the RAS spectra obtained from photoelectron-spectroscopy data. For a quantitative comparison between the measured data and the calculated optical response, the optical anisotropy is modeled within a three-layer optical model that approximates the real system by a surface layer on top of the optically anisotropic GaN bulk material.

In summary, the contribution of the surface states to the optical anisotropy is very clearly visible both in experiment and simulation. The surface states gives rise to a narrow negative RAS feature below the band gap (due to the onset of the dielectric function in ordinary polarization) followed by a broad positive band above the fundamental band gap (due to the dielectric function in extraordinary polarization). It is clearly demonstrated that the onset of the optical absorption of the GaN m-plane is defined by surface excitons which intermix contributions of the two surface states and near-band-edge electronic bands of the bulk material.

PAPER VII [34]: *Understanding band alignments in semiconductor heterostructures: Composition dependence and type-I-type-II transition of natural band offsets in nonpolar zinc-blende $Al_xGa_{1-x}N/Al_yGa_{1-y}N$ composites*

In any semiconductor heterostructure the alignment of electronic bands at build-in heterojunctions, by means of valence-band edge and conduction-band edge offsets, is crucial for the electron-transport dynamics and charge carrier confinement. Thereby, the large range of accessible band-gap energies in *zb*-$Al_xGa_{1-x}N$ semiconductors translates into a broad range of valence-band offsets (VBO's) and conduction-band offsets (CBO's) that determine how the band-gap difference between the interfacing materials is distributed among valence and conduction-band states and, thus, the fundamental heterojunction type with electron and hole wave-function confinement in either a common spatial region (type I - *straddling gap*) or different spatial regions (type II - *staggered gap*). Consequentially, a transition from a type-I to a type-II alignment of electronic states substantially impacts the optoeletronic properties of heterostructure devices. Especially, the charge-carrier separation in type-II aligned heteromaterials represents an appealing characteristic for *light harvesting* in highly efficient photovoltaic devices.

In the present manuscript, the composition dependence of the natural band alignment at nonpolar $Al_xGa_{1-x}N/Al_yGa_{1-y}N$ heterojunctions is investigated via hybrid functional based density-functional theory with a composition depended exact-exchange contribution. Adjustment of the exact-exchange fraction represents an efficient approach to account for the band-gap

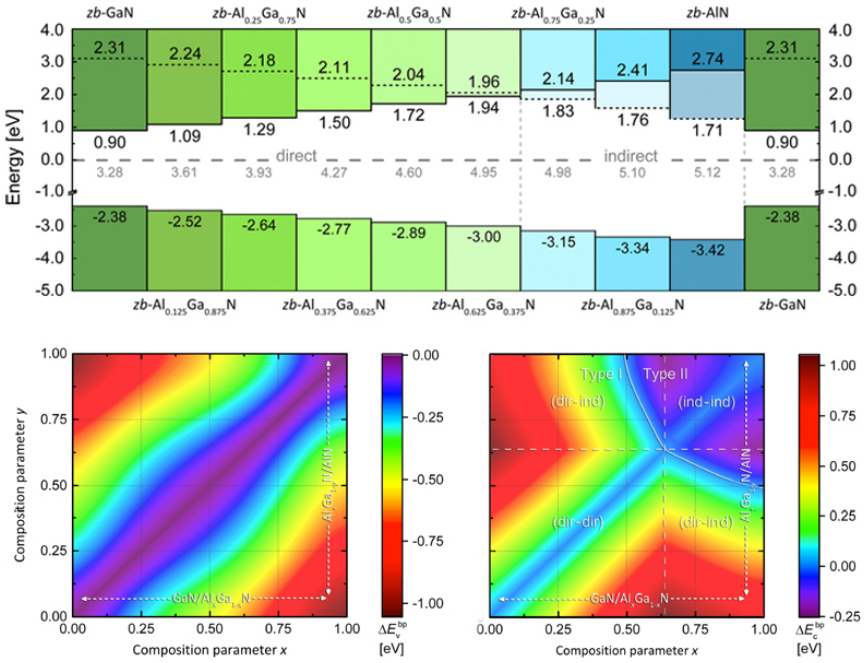

Figure 4.7: DFT-HSEmod valence and conduction-edge diagram of *zb*-$Al_xGa_{1-x}N$. The conduction states related to the lowest bulk-like Γ_c-type energy levels (solid lines) as well as the conduction states related to the lowest bulk-like X_c-type energy levels (dashed lines) are indicated. (top) Two-dimensional contour plots of the *zb*-$Al_xGa_{1-x}N/Al_yGa_{1-y}N$ valence band (bottom, left) and conduction band offset. (bottom, right) The boundary lines between the direct and indirect composition regimes (dashed white lines) and the type-I–type-II alignment crossover composition of the alloy heterostructures (solid white line) are highlighted.

underestimation of (semi)local density functional theory in order to provide reliable band offsets for all investigated alloys. The unstrained natural band alignment between zincblende (*zb*) $Al_xGa_{1-x}N$ semiconductor alloys is studied within the entire ternary composition range utilizing the branch-point technique to align the energy levels related to the bulk-like direct $\Gamma_v \rightarrow \Gamma_c$ and indirect, *pseudo-direct* respectively, $(\Gamma_v \rightarrow X_c)$-type transitions in *zb*-$Al_xGa_{1-x}N$.

The band edges in the binary/ternary *zb*-GaN/$Al_xGa_{1-x}N$ system show a type-I alignment, consistently. In addition, the presence of a direct-indirect band-gap transition in the investigated cubic *zb*-$Al_xGa_{1-x}N$ semiconductor alloys gives rise to a notable composition dependence of band discontinuities with weak nonlinear character in the predominantly Ga-rich direct-alloy regime below the critical direct-indirect Al/Ga-crossover concentration, $x_c = 0.63$, but substantial bowing characteristics in the Al-rich alloy regime. The relative position of fundamental band edges changes to a staggered type-II alignment in the Al-rich composition ranges of ternary/binary *zb*-$Al_xGa_{1-x}N$/AlN systems. The roughly linear composition dependence of the natural valance-band offsets, which originate from the alignment of Brillouin-zone center localized Γ_v-type alloy states at the top of the valence band, is observed throughout the entire two-dimensional composition range of nonpolar *zb*-$Al_xGa_{1-x}N/Al_yGa_{1-y}N$ composites. In contrast, a rather complex alignment of virtual energy states in *zb*-$Al_xGa_{1-x}N$ is indicated. The presence of a direct-indirect band-gap crossover gives rise to four distinct regions in the two-dimensional composition space of *zb*-$Al_xGa_{1-x}N/Al_yGa_{1-y}N$ heterostructures (cf. figure 4.7). Characteristic conduction-band alignment features can be observed in the pure direct regime (dir - dir)

for $(0 \leq x \leq 0.63) \wedge (0 \leq y \leq 0.63)$, two mixed direct-indirect composition regimes (dir - ind) for $(0 \leq x \leq 0.63) \wedge (0.63 \leq y \leq 1)$ and $(0.63 \leq x \leq 1) \wedge (0 \leq y \leq 0.63)$, and the pure indirect regime (ind - ind) for $(0.63 \leq x \leq 1) \wedge (0.63 \leq y \leq 1)$. The fundamental conduction-band offset changes roughly linear with (x,y)-composition in the predominantly Ga-rich direct alloy regime. The type-II alignment range includes the entire indirect-indirect composition regime, but also extends towards the mixed direct-indirect regime with the equimolar-ternary/binary system *zb*-$Al_{0.5}Ga_{0.5}N$/AlN roughly marking the lowest Al-content, hence smallest energy gap, type-II-alignment limit. The most pronounced type-II alignment character is formed between *zb*-Al and the ternary alloys close to the crossover composition. I detail, the valence and conduction band offsets between *zb*-$Al_{x_c}Ga_{1-x_c}N$ with $x_c = 0.63$ and *zb*-AlN amount $-0.41\,\text{eV}$ and $-0.24\,\text{eV}$, respectively. The promotion of charge separation via spatial localization of electrons and holes in type-II heterostructures is a committed alignment feature in the design of photovoltaic devices in order to prevent charge-carrier recombination. In the same way, the spatial separation of electron and hole wavefunctions within the type-II aligned heterostructures allows individual tuning of charge carrier confinement potentials through variations of the layer widths.

Despite being fundamentally unaffected by strain, present in any *real-world* device, the efficient calculation of natural band offsets via branch-point alignment allows the systematic study of composition dependent band-alignment trends, which are of vital interest for the design of optoelectronic devices. The natural band offsets itself can further be utilized alongside volume deformation potentials as input to effective-mass-theory-based simulation approaches (e.g. see Ref. [308, 309]) allowing the effective modeling of *realistic* nanometer sized semiconductor heterostructures.

In summary, the fundamental band edges in *zb*-$Al_xGa_{1-x}N$, aligned via the branch-point technique, show a rather complex composition dependence of fundamental band discontinuities in the *zb*-$Al_xGa_{1-x}N/Al_yGa_{1-y}N$ material system, which is characterized by the direct-indirect band-gap crossing of *zb*-$Al_xGa_{1-x}N$ alloys and a type-I-to-type-II band-alignment type transition in the Al-rich composition ranges of *zb*-$Al_xGa_{1-x}N$/AlN and *zb*-$Al_xGa_{1-x}N/Al_yGa_{1-y}N$.

4.1.5 Summaries of related publications

PAPER VIII [334]: *Identification of the Nitrogen Split Interstitial $(N–N)_N$ in GaN*

GaN is a wide-gap semiconductor with a broad range of applications in micro- and optoelectronics. Its high cohesive energy imposes particular growth conditions, and as-grown epitaxial film or bulk samples contain a high number of point and extended defects, which influence their electronic and optical properties. Contrary to the case of GaAs where most of the native intrinsic defects have been identified and characterized in detail, the nature of the intrinsic defects in GaN is not known with the exception of the Ga interstitial and the Ga monovacancy.

In the present work, an irradiation induced intrinsic defect is identified as a N interstitial in a split-interstitial configuration that pins the Fermi level at (1.0 ± 0.1) eV below the conduction band minimum. Its identification is based on electron paramagnetic resonance measurements (EPR)

and the theoretical prediction of the hyperfine structure and the g tensors of the main intrinsic defects in GaN that effectively rule out the V_{Ga} vacancy, the $V_{Ga}V_N$ divacancy, and also $V_{Ga}O_N$ pairs.

In order to further confirm the neutral charge state of the $(N\text{-}N)_N$ defect, the charge-transition energies are calculated using the concept of the Slater-Janak transition state theory. Similar to the band gap (PBE: 1.89 eV, HSE 3.55 eV), also the position of charge-transition levels is notably affected by the band-gap underestimation in (semi-)local DFT. While the semi-local PBE functional predicts charge transition levels of 1.50 eV ($^{2+/+}$), 0.72 eV ($^{+/0}$), and 0.35 eV ($^{0/-}$) below the conduction band, the use of a nonlocal HSE-type hybrid functional predicts transition energies of 2.56 eV ($^{2+/+}$), 1.45 eV ($^{+/0}$), and 1.01 eV ($^{0/-}$) below the conduction band. The significantly shifted charge-transition energy levels in hybrid-functional DFT show a nice agreement with the experimental finding for the ($^{0/-}$) transition energy.

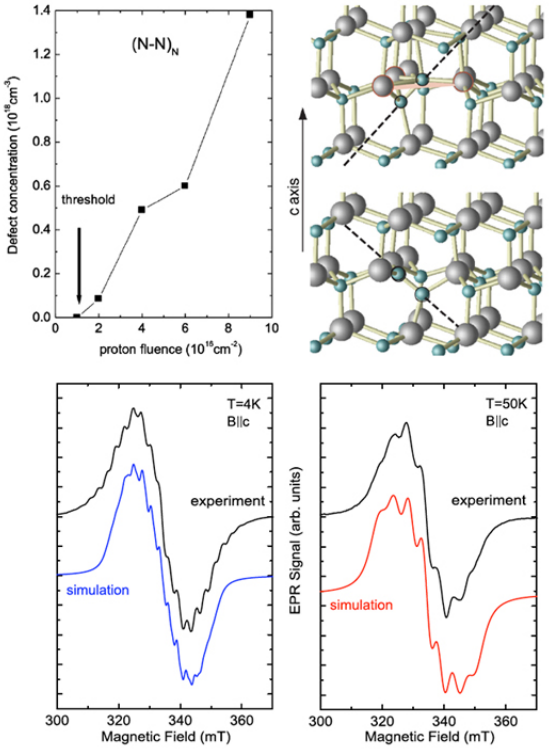

Figure 4.8: $(N\text{-}N)_N$ defect concentration as a function of $p+$ fluence. (left, top) Ground state (right, middle) and excited configuration (right, top) with one of the N-N dimer atoms moved through the plane of the three Ga ligands. Measured and simulated X-band EPR spectra of the $(N\text{-}N)_N$ center for B‖c at T =4 K (bottom, left) and 50 K (bottom, right).

In summary, a nitrogen sublattice defect in GaN, generated by room temperature particle irradiation ($e-$, $p+$, ions), was identified by EPR as $(N\text{-}N)_N$ split interstitial configuration. Whereas in previous studies the compensation between N vacancy donors, N interstitial acceptors, and Ga vacancy acceptors has been considered [1517, 1518], the results of the present study indicate that the N interstitial is ambipolar, i.e., a deep acceptor defect with an energy level 1.0 eV below the conduction band in n-type material and a deep donor state in p-type material.

PAPER IX [1494]: *Computational approach for structure design and prediction of optical properties in amorphous TiO_2 thin-film coatings*

The performance of optical components and, particularly, the quality of their surfaces are of critical importance for the success of optical technologies, in general. Since most of the presently used optical components feature a thin-film coating, improvements of the optical properties of the coating layer are crucial to obtain best device performance. In particular, ion coating methods tend to produce thin films which are amorphous and show

favorable coating characteristics such as low porosity, surface smoothness and high optical homogeneity. Experimentally, an improvement in optical layer quality is achieved empirically by comparing the properties of the optical coatings deposited under varying conditions. The present study demonstrates a more comprehensive approach to obtain a rather complete characterization and understanding of the correlations between deposition parameters and the optical properties as well as the structural quality of the deposited films which is based on atomistic modeling. Reliable numerical simulations of the film growth process would allow the prediction of the film structure and stoichiometry, obtained under certain deposition conditions, and provide a rather complete set of fundamental material properties utilizable in the conception of new materials for technological applications.

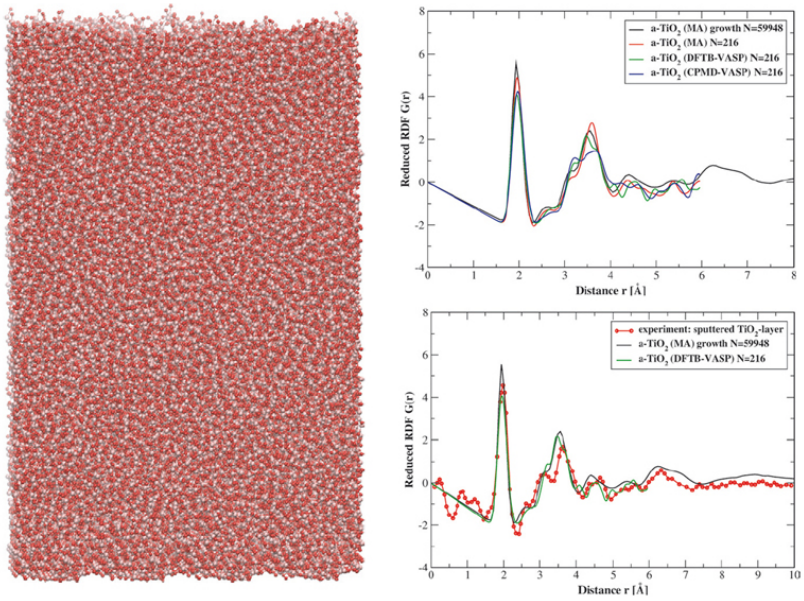

Figure 4.9: Structural snapshot of a 59948-atom a-TiO_2 structure model generated in classical molecular-dynamics growth simulations. (left) Reduced pair-distribution functions $G(r)$ of the classical grown a-TiO_2 model in comparison to ab initio simulation geometries of 216-atom super-cells. (top, right) Reduced pair-distribution function of classical MD as well as DFT super-cell calculations in comparison to those determined experimentally by electron diffraction for sputtered TiO_2 layers. (bottom, right)

A series of medium size (216 atom) stoichiometric a-TiO_2 structure models at various mass densities was generated on different levels of theory, including DFT geometry optimization, DFTB-MD, Car-Parrinello MD (CPMD) simulations, and classical MD using the empirical many-body potential proposed by Matsui and Akaogi (MA). [1519] In addition, a large-scale amorphous titania model was obtained by classical MD growth simulations using the empirical MA potential, containing 59948 atoms, in total.

The atomic structure correlations within the amorphous TiO_2 frameworks are characterized in terms of the reduced pair-correlation function and the reduced structure factor (cf. figure 4.6). It is found that the classically obtained models closely resemble the structure and coordination characteristics of the DFT post-relaxed atomic configurations. In general, the mean Ti–O coordination numbers of the structure models, generated by different simulation techniques, compare quite well to each other, approaching nearly the ideal coordination of TiO_2 bulk polymorphs at room temperature and atmospheric pressure. However, while the naturally occurring crystalline phases of TiO_2, rutile, anatase, and brookite, are well described by periodic arrangements of par-

tially distorted TiO_6 octahedral building blocks, the amorphous phase is clearly characterized by partial loss of this octahedral coordination and the disorder-induced formation of under- and over-coordinated Ti ions. The amorphous state represents an averaged picture of various local atomic coordination environments, including under-coordinated TiO_x building blocks ($x = 4, 5$) as well as over-coordinated TiO_x building blocks ($x = 7, 8$) that are characteristic for high-pressure polymorphs of crystalline TiO_2.

In summary, a deeper understanding of the fundamental processes during optical thin-film coating growth is obtained from an efficient classical potential MD simulation approach for a-TiO_2 under realistic growth conditions. The use of classical many-body potentials is validated through comparison to higher level DFT-based approaches to the atomic structure and electronic properties of small size super-cell models. The structural characterization of the large-scale a-TiO_2 model by pair-distribution functions and structure factors indicates that classical MD growth simulations, with well tailored empirical potentials, are able to reproduce the experimentally observed structural features of thin-oxide films with an accuracy comparable to numerically much more expensive DFT-MD simulations.

PAPER X [1495]: *Consistent Atomic Geometries and Electronic Structure of Five Phases of Potassium Niobate from Density-Functional Theory*

Among the macroscopically polarizable oxides, perovskite ferroelectrics stand out as object of modern-day research due to their potential relevance for technological integration into opto-electronic devices. The delicate balance between structural and charge distortions in ferroelectric perovskite materials promotes a distinct predisposition for structure polymorphism. Potassium niobate ($KNbO_3$) crystallizes in a paraelectric cubic phase (space group $Pm\bar{3}m$) at about 1325 K and undergoes successive phase transitions into distinct tetragonal ($P4mm$), orthorhombic ($Amm2$), and rhombohedral ($R3m$) ferroelectric phases, as well as a nanophase transition into a monoclinic (Pm) polytype.

In the present study, the structural and electronic properties of potassium niobate ($KNbO_3$) in its cubic, tetragonal, orthorhombic, monoclinic, and rhombohedral morphologies are studied based on density-functional theory. The influence of different parametrizations of the exchange-correlation functional on the investigated structural properties are analyzed in detail, and the results are compared to available experimental data. As the energetic separation and the structural differences between the individual structural polytypes are fairly small and thus potentially sensitive to details of the computational setup, special emphasis on the influence of different approximations for the exchange-correlation functional as well as convergence of numerical parameters is placed throughout the study. In detail, the functional performance of the local density approximation (LDA), the PBEsol and AM05 generalized gradient approximations, and the revised Tao-Perdew-Staroverov-Scuseria (RTPSS) meta-generalized gradient approximation is studied, thoroughly. Electronic structure calculations (band struc-

ture and density of states) are performed using the Heyd-Scuseria-Ernzerhof (HSE) screened-Coulomb-potential hybrid functional with an increased exact-exchange fraction of 30 % (HSE-30) to reproduce the experimentally observed band gap of the cubic $KNbO_3$ phase.

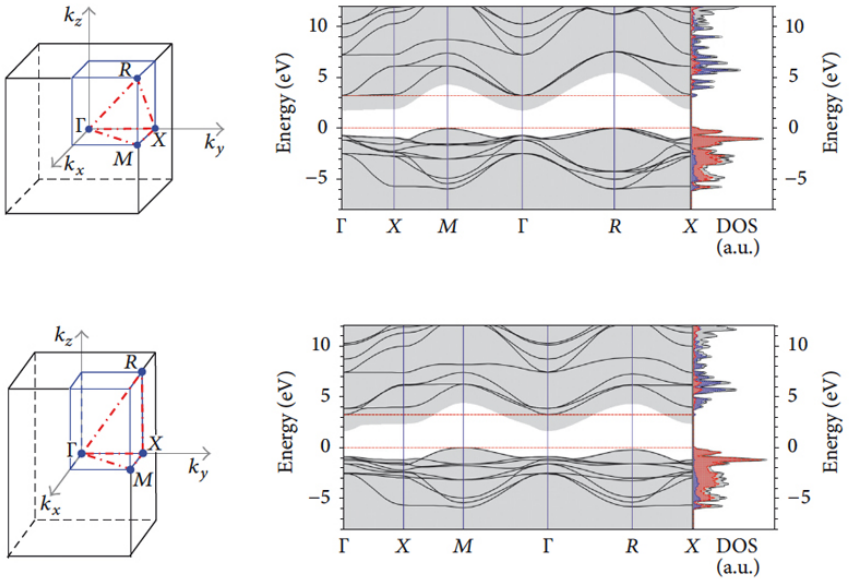

Figure 4.10: Electronic HSE-30 hybrid-functional band structure and density of states of the cubic (top) and tetragonal (bottom) $KNbO_3$ phases. The grey-shaded areas indicate the corresponding PBE band structures, and the dashed horizontal lines mark the valence-band maxima and conduction-band minima. The irreducible parts of the Brillouin zone as well as characteristic high-symmetry points are illustrated on the left-hand side.

Among the considered functionals, PBEsol as well as AM05 and RTPSS yield structural data in consistently good quantitative agreement with experimental measurements for all phases, while LDA and PBE systematically underestimate and overestimate the lattice parameters, respectively, and are also less accurate with respect to the atomic displacements inside the unit cell. It is found that all functionals predict the same energetic ordering of the phases, which, moreover, coincides with the order in which the phases become stable for increasing temperature. The performed band-structure calculations performed with the HSE-30 hybrid functional confirm the indirect fundamental band-gap nature for all phases (cf. figure 4.10). The variation in the size of the gap amounts to 0.66 eV through the successive phase transitions. In particular, in the room temperature orthorhombic phase, the band gap is found to be appreciably larger than in the tetragonal phase, which is often used as a structurally simpler substitute in the theoretical study of $KNbO_3$.

In summary, PBEsol and AM05, as well as RTPSS are reasonable starting points for elaborate ab initio investigations of the temperature dependence of the electronic and optical properties due to the electron-phonon coupling in $KNbO_3$ with higher-level perturbative methods that require highly accurate equilibrium geometries due to a high sensitivity to small changes in atomic spacings. The hybrid functional band-structure calculations also indicate significant near degeneracies of band-edge states in all phases which is expected to be highly relevant for the optical response of $KNbO_3$ in its diverse morphologies.

Science is a human activity, and the best way to understand it is to understand the individual human beings who practice it. Science is an art form and not a philosophical method. The great advances in science usually result from new tools rather than from new doctrines. If we try to squeeze science into a single philosophical viewpoint such as reductionism, we are like Procrustes chopping off the feet of his guests when they do not fit onto his bed. Science flourishes best when it uses freely all the tools at hand, unconstrained by preconceived notions of what science ought to be. Every time we introduce a new tool, it always leads to new and unexpected discoveries, because Nature's imagination is richer than ours.

Freeman J. Dyson (1923 – 2020)

5 Results and discussion

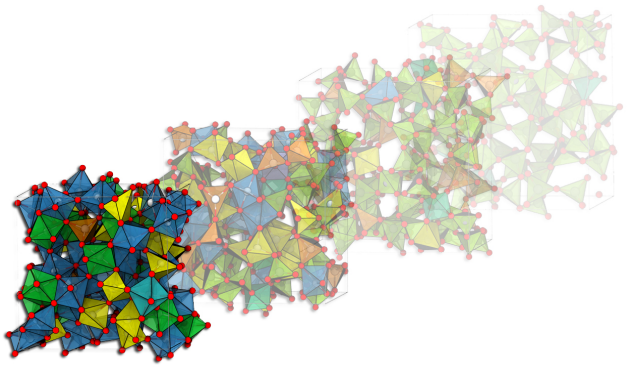

It is the function of science to discover the existence of a general reign of order in nature and to find the causes governing this order. And this refers in equal measure to the relations of man - social and political - and to the entire universe as a whole.

Dmitri I. Mendelejew (1834 – 1907)

Contents

5.1 A matter of methodology 146

5.1.1 Density-functional theory 146

5.1.2 Many-body perturbation theory 161

5.2 Fingerprints of order and disorder 166

5.2.1 Sort-range order 167

5.2.2 Medium-range order 172

5.2.3 Structure-function correlations in amorphous oxides 173

5.2.4 Long-range order 175

5.3 Future perspective 180

THE BEGINNING OF THE END – The final chapter gives a brief résumé of key ideas and results organized under the general heading of the present thesis. In doing so, the discussion recapitulates selected results, conclusions, and reasonings given within the publications summarized above. The focus, however, is directed to a more comprehensive discussion of basic structure-function correlations detached from the narrowing *ties* of an individual publication.

Two main ideas are examined in this context, which encompass central technical and physical aspects subject to each off the publications contributing to the thesis. [1] Within the first part, basic methodology questions concerning the accuracy of various approximations to the exchange-correlation energy of density-functional theory are discussed by means of different structural features and electronic structure characteristics. Especially, the necessity of many-body corrections as well as their approximate treatment within hybrid-functional–based density-functional theory is motivated. Beyond that, different numerical approaches to derive many-body corrections from Green's function-based many-body perturbation theory, systematically investigated throughout this thesis, are presented with a focus on the optical response properties of semiconducting materials. The second part recapitulates the fundamental correlations between atomic structure characteristics and the emerging electronic structure as well as their impact on the optical response. Here, atomic order phenomena are considered in the most comprehensive way allowing a unified discussion of structure-function correlations in crystalline and amorphous solids, nanostructures and surface systems. The origins of emerging electronic-structure features and optical response characteristics are traced back to common order facets on short-, medium-, and long-ranging length scales.

5.1 A matter of methodology

5.1.1 Density-functional theory

With its reputation as the *working horse* of computational materials science density-functional theory had and still has foremost impact on today's ab initio simulation and prediction of novel functional materials and their properties. However, with increasing computational resources, existing limitations in accuracy and predictiveness made their appearance necessitating an efficient bypassing or a systematic extension of conventional density-functional theory approaches to match essential modeling challenges redefining the foremost boundaries of computational materials science, progressively.

Within density-functional theory the major component in dealing with all issues related to numerical efficiency, accuracy and predictiveness is the exchange-correlation functional providing different approximation levels to non-classical electron interactions (see discussion in Sec. 3.2.2). As outlined in Sec. 3.3, the diverse functional *flavors* existing are subject to quiete diverse cata-

[1] Additional numerical results are sporadically included to corroborate and complement central findings and argumentations. In order to prevent unambiguities, the inclusion of additional results is restricted to footnote sections.

logues of requirements. The consideration of physical *ingredients*, numerical cost and the scope of application led to the superficial ladder classification of exchange-correlation functionals as illustrated in Fig. 3.3. The awareness of existing limitations on different levels/ranks of exchange-correlation treatment and the particular *philosophy* and parametrization of the functionals is essential to the interpretation and understanding of results from numerical simulations in the light of experimental findings.

Structural properties

Since the electronic structure and optical response characteristics are irresolvably tied to the atomic structure and chemical composition of a material, their reliable generation in numerical simulations is an inevitable prerequisite for the examination of any basic type of structure-function correlation between a spatial pattern of atoms and its inherent optoelectronic properties. For that matter, simulation results are routinely benchmarked against experimental findings. The crux with comparing findings from numerical simulations and experimental measurements is to ascertain the actual level of *meaning* and comparableness of *numbers* as well as their reproducibility on either side. In addition, materials showing various degrees of chemical and/or structural disorder (cf. Fig. 2.5) are subject to additional, to some extend non-trivial, *qualitative* measures.

CRYSTALLINE MATERIAL MODIFICATIONS – The determination of the equilibrium geometry of a crystals by means of unit-cell volumes and shapes, lattice parameters and basic symmetries, respectively, is certainly one of the most basic fields of application for density-functional theory simulations. The traditionally utilized local-density approximation or semilocal gradient-corrected functionals have proven to provide rather reliable lattice parameter within an error margin of roughly $\pm$ 1-3 % for a wide range of materials [2] (e.g. see Paper X [1495]). Hereby, the local density approximation shows excellent performance for several metallic systems (see Ref. [1132, 1496, 1521]), while common generalized gradient corrections, first of all the PBE

[2] Experimental and optimized theoretical lattice parameters of cubic group-III nitride phases. Percentage quotients $\left(\left(a^{eq} - a^{exp}\right) / a_{exp} \times 100\right)$, indicating deviations from recently reported experimental lattice parameters a_{exp}, are visualized in the diagrammatic insets.

	zb-AlN			*zb*-GaN			*zb*-InN		
	[Å]	[%]	[%]	[Å]	[%]	[%]	[Å]	[%]	[%]
Exp.	4.373[b]			4.503[c]			5.01[d]		
PBE	4.4003	0.62		4.5446	0.92		5.0512	0.82	
PBEsol	4.3766	0.08		4.4931	-0.22		4.9888	-0.42	
AM05	4.3764	0.08		4.4907	-0.27		4.9910	-0.38	
TPSS	4.3694	-0.08		4.5286	0.57		5.0375	0.56	
revTPSS	4.3682	-0.11		4.5311	0.62		5.0247	0.29	
HSE06	4.3643	-0.20		4.4934	-0.21		4.9877	-0.44	
HSEmod[e]	4.3643	-0.20		4.4847	-0.41		4.9855	-0.49	
HSEsol	4.3496	-0.54		4.4625	-0.90		4.9488	-1.22	

The lattice-parameters have been optimized using a 600 eV plane-wave energy cutoff and a Γ-centered $8 \times 8 \times 8$ **k**-point sampling of the primitive Brillouin zone. The exact-exchange fractions within the HSE-type hybrid functional were adjusted to 36 % for *zb*-AlN, 30 % for *zb*-GaN, and 26 % *zb*-InN. The experimental lattice parameter were taken from Ref. [322] for *zb*-AlN, Ref. [1520] for *zb*-GaN, and Ref. [384] for *zb*-InN.

functional, improve the functional performance for numerous bulk semiconductors (also see Ref. [1132]) as well as surfaces featuring a more inhomogenous electron density. [1167] Occasionally, meta-generalized gradient functionals have been considered as the *natural* solution to improve density-functional-theory–based predictions of structural features. [1171] Indeed, literature [1132, 1187] as well as own operating experience (e.g. see Footnote 2 and 7, as well as Paper X [1495]) indicate lattice parameters that are in agreement with experimental reference data within an error margin not substantially greater than 1 % for the meta-generalized gradient functionals TPSS [1183] and revTPSS [1184] over a wide range of materials. In addition, the non-empirical strongly constrained and appropriately normed (SCAN) meta-generalized gradient functional [1522, 1523] provides an excellent description of the lattice parameters of naturally occurring TiO_2 polymorphs (see Footnote 7). However, more recent functional parameterizations indicate that the same level of accuracy can be provided through novel generalized gradient functionals in equal measure. [1132, 1165, 1167, 1168, 1171] Here, especially PBEsol [1168] as well as AM05 [1165] stand out with a notable gain of accuracy in the calculation of lattice parameters and bonding geometries [3] for solid-state systems as outlined in Footnote 2 for the cubic group-III nitride family or indicated in Paper X [1495] and Footnote 7 for semiconducting bulk oxides.

In recent past the use of fourth rung hyper-generalized gradient functionals has shown substantial impact on the electronic structure theory of solid-sate materials (see discussion below). However, since the evaluation of the hybrid-functional-inherent exact-exchange contribution exhibits substantial demands on computational resources, it's use is frequently limited to the electronic structure rather than the atomic structure. Moreover, a key strategy to *improve*, or more precisely tune, the hybrid-functional performance towards a correspondence with numerical results, obtained by formally higher ranking theories based on Green's function theory, via increasing the amount of exact-exchange manually, might not necessarily improve the description of structural features on equal footing. This is exemplarily indicated in the lattice parameters obtained by a modified HSE functional (HSEmod) (see Footnote 2) where the accuracy of numerical results slightly declines for the cubic phase of the 3*d*-nitride GaN in case of an increased exact-exchange fraction. Taking into account the general dependence on the exact-exchange fraction as well as range-separation/screening parameters, the use of hybrid functionals for lattice-parameter optimization has limited appeal, only. Especially, the application to large-scale structure models can be restricted to generalized gradient and meta-generalized gradient approximations in good conscience. [4] Nevertheless, structural relaxation on the hybrid-functional level might become relevant in case of systems showing an artificial (meta-)generalized-gradient relaxation towards an inaccu-

[3] In contrast to the excellent performance of the PBEsol functional in the description of lattice parameters, energetics as the total energies of atoms, atomization energies of molecules, or the cohesive energies of solids have been reported to be less accurate compared to the conventional PBE parametrization. [1171]

[4] See Paper VI [34] for application of the PBE parametrization of the generalized gradient approximation to describe the structural relaxations in supercell models of the *m*-plane surface of wurtzite-type GaN or Paper I [309] and Paper IV [33] for (local) structural relaxations in super-cell models of cubic group-III nitride alloys and their heterostructures.

rate symmetry state or ground-state polymorph.

A key objective of numerical simulations in solid-state physics is to benchmark novel exchange-correlation functionals and parametrizations against experimental reference data. As long as characteristic differences between theoretically and experimentally determined lattice parameters were of the order of roughly 1-3 %, the use of the traditional numbers, ubiquitous in literature, did not represent a utterly severe problem, even in cases were the accuracy of the involved experimental setups or the sample quality itself were outdated or highly relevant conditions as the material temperature were not reported or cited, thoroughly. [5] With the notable increase in numerical accuracy for structural parameters, provided by novel exchange-correlation functionals, it becomes necessary to consider a shift of emphasis towards finding reliable reference data for a more profound evaluation of density-functional performances on the basis of a *comparison-to-experiment*. The equilibrium geometry obtained within a density-functional theory simulation, either through direct structure relaxations or the utilization of an equation-of-states, formally accounts for artificial ambient conditions as zero temperature and zero pressure. In contrast, numerous of the often-cited lattice parameters account for normal conditions. While the order of magnitude of lattice expansion from releasing the normal pressure towards the zero pressure limit is virtually negligible in light of common bulk moduli of solids, the thermal expansion between the *static* 0 K-limit and normal conditions might become relevant in the per-mill-regime of lattice-constant expansion. Hence, the thermal expansion coefficients of common semiconducting materials can be relevant for establishing a sound reference-data basis to benchmark simulation approaches and structural parameters should be extrapolated towards their 0 K-limit for making a direct comparison to density-functional-theory-derived quantities. Beyond this, the simulation-derived lattice parameters do not account for any contributions from zero-point vibrational energy contributions which modify the experimental lattice parameters. The modification of lattice parameters from the so called zero-point anharmonic expansion (ZPAE) [1132, 1201, 1524–1526] aries from anharmonic free-energy contributions to the equation of states, since the phonon frequencies itself depend on the unit-cell volume in an anharmonic way. A characteristic size of roughly one per-mill has been reported for the zero-point anharmonic expansion corrections to cubic group-III nitride semiconductors. [1201]

Additional difficulties arise for numerical simulations of metastable material phases whose stabilization is subject to artificial preparation conditions as high pressure or epitaxial stabilization. There is no *bulk* reference phase with a well defined one-to-one correspondence to the equilibrium-lattice parameters of density-functional theory simulations in these cases, and extrapolation towards a static limit might be non-trivial or even pointless. Even though the density-functional-theory-based optimization of structural parameters can reproduce experimentally observable trends in the stabilization of various bulk polymorphs as exemplarily outlined for potassium niobate ($KNbO_3$) polymorphs in Paper X [1495], highly artificial preparation or unconven-

[5] Similar considerations also affect the evaluation of the band-gap performance for the description of electronic structure features by different exchange-correlation functionals. See discussion below.

tional stabilization conditions should be considered in more detail throughout future studies.

In addition to the considerations above, the main emphasis towards lattice-constant reproduction limits the assessment of novel exchange-correlation functionals to the full extent. The *quality* of exchange-correlation functionals for structure modeling is expressed in its global quality rating of structural parameters including, aside from lattice constants, the lattice-constant ratios as well as all internal structural parameters [6], as demonstrated by the atomic displacement factors of NbO_6 coordination polyhedra in Paper X [1495]. A prototypical example of the relevance of an accurate modeling of lattice-constant ratios as well as the internal structural parameter describing the shift of anion and cation planes against each other are the wurtzite-type group-III nitride semiconductors. In the same way, also the lattice-constant ratios of prototypical oxide materials as TiO_2 anatase are affected by the structural performance of exchange-correlation functionals, crucially. [7]. In addition, the structure polymorphism of TiO_2 also allows, or rather demands, to study the significance of long-range dispersion interactions for the phase stability of existing bulk modifications (see discussion at the end of this subsection). Here, the inclusion van der Waals corrections on various levels of theoretical sophistication lead to a notable improvement in the lattice constant performance of standard semi-local exchange-correlation functionals (cf. Footnote 7).

CHEMICAL DISORDER - ALLOYS, SOLID SOLUTIONS, ETC. – Since the engineering of semiconductors with tailored material properties for diverse optoelectronic applications demands (crystalline) multicomponent alloys, a theoretical examination of this type of atomic disorder is highly relevant to computational materials science. The accurate representation of semiconductor alloys/solid solutions in numerical simulations calls for an *resonable* description of the respective chemical disorder by some sort of unit cell. Depending on the growth condition, the term *resonable* would imply either a stochastical distribution of chemical elements or a more ordered configura-

[6] While lattice constants and ratios relate to the actual (primitive) unit-cell representation, the internal structural parameters relate to the relaxation of secondary, unit-cell-internal entities that are related to a materials short-ranging atomic order. This accuracy for local relaxations and symmetries comes into play for the numerical modeling of structural defects, traditionally.

[7] Experimental and optimized theoretical lattice parameters of the three naturally occurring TiO_2 polymorphs. The values in the brackets indicate the percentaged deviations from reported experimental lattice parameters on TiO_2 (see Ref. [1527] for rutile, Ref. [1528] for anatase, and Ref. [1529] for brookite).

		exp.	PBE	PBEsol	PBE-D3	SCAN	SCAN+rVV10	RTPSS
rutile	a [Å]	4.5937	4.6349 (+0.90)	4.5840 (−0.21)	4.6002 (+0.14)	4.5799 (−0.30)	4.5635 (−0.66)	4.6064 (+0.28)
	c [Å]	2.9581	2.9365 (+0.10)	2.9365 (−0.73)	2.9513 (−0.23)	2.9470 (−0.37)	2.9436 (−0.49)	2.9578 (−0.01)
	c/a	0.6439	0.6389 (−0.79)	0.6406 (−0.52)	0.6416 (−0.37)	0.6435 (−0.08)	0.6450 (+0.17)	0.6421 (−0.01)
anatase	a [Å]	3.7842	3.7956 (+0.30)	3.7669 (−0.46)	3.7844 (+0.01)	3.7701 (−0.37)	3.7673 (−0.45)	3.7964 (+0.32)
	c [Å]	9.5146	9.6682 (+1.61)	9.5221 (+0.08)	9.5378 (+0.24)	9.5231 (+0.09)	9.4402 (−0.78)	9.5475 (+0.35)
	c/a	2.51	2.5472 (+1.31)	2.5278 (+0.54)	2.5203 (+0.24)	2.5260 (+0.46)	2.5058 (−0.34)	2.5149 (+0.02)
brookite	a [Å]	9.16	9.2433 (+0.91)	9.1553 (−0.05)	9.1889 (+0.14)	9.1555 (−0.05)	9.1292 (−0.34)	9.2116 (+0.56)
	b [Å]	5.43	5.4944 (+1.19)	5.4326 (+0.05)	5.4584 (−0.23)	5.4338 (+0.07)	5.4194 (−0.19)	5.4652 (+0.65)
	c [Å]	5.13	5.1616 (+0.62)	5.1106 (−0.38)	5.1301 (−0.23)	5.1213 (−0.17)	5.1052 (−0.48)	5.1373 (+0.14)
	c/a	0.56	0.5584 (−0.29)	0.5582 (−0.33)	0.5583 (−0.37)	0.5594 (−0.12)	0.5592 (−0.15)	0.5577 (−0.42)
	c/b	0.94	0.9394 (−0.56)	0.9407 (−0.43)	0.9399 (−0.37)	0.9425 (−0.24)	0.9420 (−0.29)	0.9400 (−0.50)

The lattice-parameters have been optimized using an 600 eV plane-wave energy cutoff and Γ-centered $12 \times 12 \times 16$, $14 \times 14 \times 10$, and $6 \times 10 \times 10$ **k**-point samplings of the primitive Brillouin zones of the rutile, anatase, and brookite phases of TiO_2 until reaching a force convergence criterion of 0.0001 eV/Å

tion of chemical conglomerates showing preferential formation constraints. While the later implies a highly nontrivial competition between the dominant binding forces at the given growth condition, a random distribution of chemical elements, in many cases within one well defined chemical subgroup, ion sublattice respectively, of a multicomponent alloy (cf. Fig. 2.5), is widely achieved in the molecular beam epitaxy of multicomponent semiconductor alloys. [736, 1530–1532] Due to the imposed periodic boundary conditions, some degree of artificial periodicity is inevitably *impressed* into all numerical models. Without careful estimation these (artificial) periodicity errors can severely affect the results of atomistic simulations for this class of random alloys. There are basically two approaches to deal with the occurrence of periodicity errors. Either, one can rely on statistics by calculating material properties from (weighted) ensemble averages of a *sufficiently* large test set of ordered atomic clusters that are fundamental to describe the disordered alloy [1533–1537] or one finds a single *best* unit-cell representation [8] of the particular random alloy.

Within the present thesis, the problem of finding an efficient representation of random chemical disorder within the atomic sublattice of one chemical ion species (cf. Fig. 2.5 (b)) has been systematically investigated for the group-III nitride family (cf. Paper IV [33] and Paper VII [34]) following two basic strategies. On the one hand, a random occupation of the lattice sites by various ion species could be achieved by a simple random-number generator [9]. On the other hand, the approach of special quasirandom structures (SQS) [1513, 1514] has been applied to generate a series of differently-sized unit cells [10,11]. Focussing on finding the *best* and simultaneously smallest unit cell that mimics the material properties of a bulk alloy/solid solution, a special quasirandom lattice is designed to mimic the structural correlations of a crystal with perfectly random ion order as closely as possible within the most relevant lowest order structure correlations. Thereby, the basic assumption of the special quasirandom-structure approach is that most physical properties show a hierarchical dependence on the interaction distance with clearly dominating short-range (pair) correlations and negligible pair and multisite correlations at larger distances. [1513, 1514, 1538] A comprehensive discussion of the accurate representation of sublattice-disorder and its fingerprints in the electronic material properties of cubic $Al_xGa_{1-x}N$ alloys by both utilized simulation approaches is given in Paper IV [33]. It is demonstrated that small unit-cells (eight atoms) suffer

[8] In the best case, the *quality* and accuracy of a single-unit cell, representing the random alloy, is always approximately estimated from a small statistical test set of several randomly generated unit-cell configurations with alternating chemical compositions.

[9] The random-unit cell approach has been applied in Paper VII [34] with a focus on the band alignment properties of cubic $Al_xGa_{1-x}N$ alloys.

[10] In detail, a random occupation of the cation-sublattice sites in 8, 64, and 216 atom unit cells of nonpolar $Al_xGa_{1-x}N$ alloys has been considered and special quasirandom structures with 8, 16, and 32 atoms have been generated (cf. Paper IV [33]).

[11] Since the lattice parameters of the investigated alloys can be determined from Vegard's law, accurately, it is sufficient to know the lattice parameters of the binary end compositions. Thus, the remaining local lattice relaxations, caused by the binary chemical randomization of the cation sublattice can be described by the universal PBE exchange-correlation functional, accurately, without focusing on tampering the alloy density by the common lattice-parameter overestimation inherent to this parametrization of the generalized-gradient approximation.

from notable periodicity errors for randomly occupied as well as special quasirandom structures, likewise. However, the description of random-alloy characteristics converges much more rapidly in the later case. A *resonable* quasirandom-structure allows electronic structure calculations that are on par with substantially larger unit cells constructed by random occupation without any notable loss of accuracy [12]. [33] In view of the computationally demanding simulations of electronic and optical properties within the framework of many-body perturbation theory, this potential reduction in unit-cell size proves to be extremely favorable facilitating significant and most advanced simulations on semiconductor alloys.

STRUCTURAL DISORDER - AMORPHOUS MATERIAL MODIFICATIONS – While the substitutional chemical disorder of semiconductor alloys discussed above might be seen as an ion-disorder *layer* put on top of the long-range ordered crystalline lattice leading to local and quiet moderate random displacements, a major part of solid matter exists in a spatially disordered amorphous state without any strict long-range order features. Without a well defined crystalline lattice, crystal symmetry respectively, underlying the *disorder* of an alloy, the problem of finding an accurate representation of structural features on an atomic-length scale raises additional challenges. Aiming at predicting the atomic structure of disordered materials *from scratch*, molecular-dynamics simulations [1539–1551] are an essential tool to provide fundamental insights into short-ranging structure-formation processes among individual atoms or the medium-ranging order features between basic functional units. In contrast, numerical approaches based on reverse engineering are tied to a material sample and experimental characterization technique acting as a target-setting for a successive refinement procedure [13] and do not hold the potential to provide reliable predictions of novel disordered material phases and/or modifications *ab initio*. Since the finite-size unit-cell representation of amorphous materials, combined with the utilized periodic-boundary conditions in common molecular-dynamics simulations, enforces identical atom position on opposing sides of the simulation cell not only the chemical ordering but also the spatial order is notably affected by periodicity errors in numerical simulations. The later tend to restrict potential lattice relaxations, hence, influencing or even preventing the formation of order features on an intermediate-to-far-ranging length scale. Common unit-cells in density-functional-theory–based molecular-dynamics simulations, which are also performed in order to study amorphous systems in the present thesis [14] , might contain up to a few hundred atoms. Alternatively, large scale simulations, e.g. based

[12] Within Paper IV [33] this behavior is highlighted for cubic $Al_xGa_{1-x}N$ alloys. Notable periodicity errors were observed for eight atom unit cells, in general. The simulation results of a 16 atom special quasirandom structure are already close to the vastly identical results of 32 atom quasirandom structures and 216 atom containing random unit cells.

[13] The reference *bond switching* algorithm for the construction of arbitrarily sized continuous random-network models has been developed by Wooten, Winer, and Weaire [1552, 1553] and used to study realistic random-network models with periodic-boundary conditions for amorphous elemental semiconductors as silicon and germanium. Later on, Wooten-Winer-Weaire-like algorithms have been widely applied to generate network models for disordered phases, e.g. carbon [1554] or silica [1555, 1556].

[14] In detail, 216 atom models of amorphous TiO_2 and a series of 300 atom containing unit cells covering the entire composition range of ternary amorphous $Ti_xSi_{1-x}O_2$ hybrid oxides have been generated in the present thesis. [31, 32]

on computationally efficient empirical potentials represent a viable alternative to the resource demanding ab initio molecular-dynamics simulations [15,16].

Within the present thesis unit-cell representations of oxide semiconductors have prevalently been prepared by a highly competitive approach well-balancing the counteracting demands on generating an highly accurate atomic structure from highly *predictive* algorithms and the associated demands on computational resources. The structure generation approach starts by a chemically and spatially completely random initialization of atoms within an unit cell whose size defines the material's mass density, simultaneously, followed by a short thermal equilibration phase. This random starting point guarantees that no spurious structural correlations, which might occur by starting from an crystalline state, for instance, are artificially transferred into the generated amorphous network. A density-functional-theory–based tight-binding molecular-dynamics simulation, following an exponential cooling path, relaxes the disordered material phase over several picoseconds towards its room-temperature equilibrium structure. Finally, the room temperature structure is relaxed to its 0 K ground-state morphology by using a density-functional-theory–based structure optimization utilizing the PBE exchange-correlation functional. A schematic illustration of this structure generation procedure is provided in Fig. 1 of Paper V [32]. The plausibility of this combined structure-generation approach has been verified for various atomistic models of amorphous TiO_2 in light of the reduced structure factors and radial pair-distribution functions of various types of differently prepared samples of amorphous TiO_2 (see Fig. 2 of Paper III [31]) demonstrating that all structure models are able to reproduce basic correlation features of the amorphous network. Differences due to the use of different simulation methods were found to be far smaller than the fluctuations observed in the pair distributions and structure factors of variously synthesized amorphous material samples. Also, a series of ternary amorphous $Ti_xSi_{1-x}O_2$ mixed oxides, combining chemical and spatial disorder (cf. Fig. 2.5 (o)), has been generated following the same pathway [17] (cf. Paper V [32]). Notable details of the comprehensive characterization of oder-features in all generated amorphous networks are highlighted throughout the consecutive section.

Electronic and optical properties

Beyond a reasonably optimized atomic structure, density-functional theory provides essential material parameters as the fundamental band gaps, the electronic band structure and density of states, or the band-alignment characteristics between two individual semiconductors that allow for a thor-

[15] A comparison between the generated 216 atom unit cells of amorphous TiO_2 and an equally sized as well as a 59948 atom containing large-scale model of amorphous TiO_2 is presented in Paper IX. [1494]

[16] Large scale atomic models not only allow an accurate mapping of realistically sized nanoclusters but can also more effectively deal with *finite-size-errors* arising from surface contributions, which alter the simulation results of the three-dimensional *bulk* structure of extended amorphous systems.

[17] Similar to the case of semiconductor alloys, the structure relaxations are conducted on the generalized gradient level using the PBE exchange-correlation functional. The *lattice parameter*, more precisely the mass density of the simulated amorphous oxides, is fixed according to experimental data or the mass density of crystalline phases in order to provide direct comparability between the short-ranging and medium-ranging order features of crystalline and amorphous materials.

ough estimation of a material's technological potential. Being aware of the the severe limitations of conventional (semi)local density-functional theory in making qualitative predictions on unoccupied electronic states (cf. Sec. 3.2.2) the use of hybrid functionals has become an appealing loophole, albeit vastly feasing on computational resources, in making accurate quantitative predictions on electronic structure features without extending the scope of electronic structure theory towards Green's function theory in the context of many-body perturbation theory. Nevertheless, the later provides the formal justification for making adjustments in the exact-exchange fractions of modern screened Coulomb potential hybrid functionals to evaluate the exchange-correlation energy. Since hybrid-functional calculations commonly emanate from a preparatory density-functional theory calculation to promote rapid convergence towards the electronic ground state using the already optimized Kohn-Sham single-particle orbitals as an input or even use direct lower-rung exchange-correlation contributions to construct the exchange-correlation energy (e.g. see Eq. 3.69), these results come without additional computational cost providing a basis of comparison at no additional cost.

ELECTRONIC STRUCTURE FROM HYBRID FUNCTIONALS ! – While the performance of lower rung exchange-correlation functionals has proofed sufficient predictive power for structural properties, their numerical forecasts might completely fail not only in a quantitative but, even worse, in a qualitative way for specific electronic structure features. Not only the electronic bands gaps [18] are dramatically underestimated up to the third rung meta-generalized gradient functionals (e.g. see Footnote 18 as well as documentation in scientific literature [1101, 1167, 1218, 1557]), also the fundamental material character might be biased by assigning a metal-like *zero-gap/negative-gap* band structure to some small gap semiconductors. Aside from the classically documented example Ge [1365, 1558, 1559], this shortcomming severely affects electronic-structure calculations of In

[18] Experimental and calculated electronic band gaps of cubic group-III nitride phases. The band gaps are reported either at the DFT optimized lattice parameters (cf. Footnote 2) or the experimentally reported lattice constants (bracketed values). The given percentage quotations $\left(\left(E_{gap}^{DFT} - E_{gap}^{exp}\right) / E_{gap}^{exp} \times 100\right)$, indicating deviations from recently reported experimental band gaps, are visualized in the diagrammatic insets. Upper (lower) bar lengths refer to band gaps at the optimized (experimental) lattice constants. For *zb*-AlN the brighter upper bars refer to the direct $(\Gamma_v \rightarrow \Gamma_c)$ band gap, while the lower bars depict the fundamental indirect $(\Gamma_v \rightarrow X_c)$ band gap.

	$E_{gap}^{zb\text{-AlN}}$			$E_{gap}^{zb\text{-GaN}}$		$E_{gap}^{zb\text{-InN}}$	
	$(\Gamma_v \rightarrow \Gamma_c)$ [eV]	$(\Gamma_v \rightarrow X_c)$ [eV]	[%]	$(\Gamma_v \rightarrow \Gamma_c)$ [eV]	[%]	$(\Gamma_v \rightarrow \Gamma_c)$ [eV]	[%]
Exp.	5.997[b]	5.3[c]		3.293[d]		0.595[e]	
PBE	4.002 (4.166)	3.306 (3.316)		1.573 (1.751)		0.000 (0.000)	
PBEsol	4.081 (4.103)	3.184 (3.186)		1.749 (1.707)		0.000 (0.000)	
AM05	4.135 (4.156)	3.193 (3.194)		1.850 (1.840)		0.000 (0.000)	
TPSS	4.317 (4.281)	3.375 (3.414)		1.552 (1.701)		0.000 (0.000)	
revTPSS	4.274 (4.177)	3.280 (3.310)		1.478 (1.633)		0.000 (0.000)	
HSE06	5.647 (5.589)	4.609 (4.603)		3.137 (3.090)		0.607 (0.557)	
HSEmod[f]	6.397 (6.236)	5.206 (5.187)		3.463 (3.419)		0.656 (0.600)	
HSEsol	5.710 (5.553)	4.537 (4.521)		3.247 (3.094)		0.636 (0.498)	

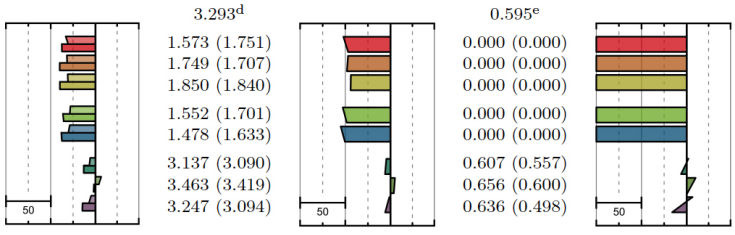

The electronic band gaps have been calculated using a 600 eV plane-wave energy cutoff and a Γ-centered $8 \times 8 \times 8$ **k**-point sampling of the primitive Brillouin zone. The exact-exchange fractions within the HSE-type hybrid functional were adjusted to 36 % for *zb*-AlN, 30 % for *zb*-GaN, and 26 % *zb*-InN. The experimental band gaps were taken from Ref. [386] for *zb*-AlN, Ref. [385] for *zb*-GaN, and Ref. [384] for *zb*-InN.

containing small-gap semiconductors as InAs, InSb, or CuInSe2. [1557, 1559, 1560] In fact, all tested exchange-correlation functionals up to the meta-generalized gradient-correction rung artificially predict the cubic zincblende phase of InN as a zero-gap material (cf. Footnote 18). While meta-generalized gradient approximations exhibit a lattice-parameter accuracy at least as high as the best representatives of the second rung generalized gradient approximations, this functional quality is not indicated in the band-gap data of the cubic group-III nitride semiconductors. [19] The historical success of the generalized gradient approximation also suggest some applicability to electronic structure theory. This is due to the fact that, despite the underestimated band gaps, the band dispersion of virtual electronic states close to the band edge could be reproduced by common generalized gradient approximations, quite reasonably. As highlighted in Paper VI [34], the results from generalized-gradient functional approximations still prove very useful to provide a qualitative analysis of layer resolved and atom decomposed densities of states in order to distinguish bulk-like electronic features from surface contributions of semiconducting materials. In the same way, it is possible to extract qualitative information on the localization of surface states [20]. Nevertheless, this correspondence is not a sufficient prerequisite for reliable predictions of electronic structure features throughout the catalog of known materials and especially for advanced computational screening campaigns to find *unknown* functional semiconducting materials or material modifications.

A major step in overcoming the limitations inherent to (semi-)local approximations of the Kohn-Sham exchange-correlation energy has been made by facilitating electronic structure simulations of continuous systems on basis of fourth rung hyper-generalized gradient approximations, also known as hybrid functionals, which mix a certain fraction of *exact* exchange energy with the common exchange and correlation contributions provided by (semi-)local functionals. Even though the idea of incorporating an analog [21] of the non-local exchange term of Hartree-Fock theory, if you want call it an *exact Kohn-Sham exchange energy* [1109], into a generalized Kohn-Sham density-functional theory framework could be rationalized from traditional Møller-Plesset perturbation theory [1109], thoroughly, error-compensation (cf. Fig. 3.2) between (semi-)local and nonlocal energy contributions is undeniable a major justification of this numerical practice. A clear indi-

[19] A formal exception to the band-gap problem of meta-generalized gradient functionals might be seen in the Tran-Blaha–modified Becke-Johnson (TB-mBJ) exchange potential [1561–1563] which provides significantly improved electronic band structures with an accuracy on par with fourth-rung hyper-generalized gradient approximations. However, despite its high numerical efficiency, this approximation of the exchange energy shows some limitations in universal validity. In addition, the *potential-only* nature of the TB-mBJ exchange functional prohibits force calculations and subsequent structure relaxations, which limits universal numerical application in computational solid-state theory. A comprehensive discussion of features and limitations of the TB-mBJ exchange potential has been provided as part of Paper IV [33] in the analysis of the direct-indirect band-gap crossing in zinc-blende $Al_xGa_{1-x}N$.

[20] The layer and atom resolved densities of states of Ga and N atoms in the topmost four layers of a semipolar GaN *m*-plane surface have been illustrated in Fig. 3 of Paper VI [34] alongside the bulk-like complement extracted from the center of the simulation slab. A visualization of surface states by means of an isosurface representation of partial charge densities is provided in Fig. 5 of the paper in question.

[21] This *exact* exchange term is easily constructed within the framework of Kohn-Sham theory since the solution of the Kohn-Sham equations provides not only an electronic ground-state density, but rather the necessary set of single-particle orbitals in the first place.

cation for the later more pragmatic justification for the use of hybrid functionals is given by the non-uniqueness and diversity of proposed hybrid-functional forms as well as the *(semi-)empirical* parameters contained in many cases. All hybrid-functional calculations conducted throughout the present thesis rely on the functional form, Eq. 3.69 of the range-separated (screened Coulomb-potential) hybrid functionals introduced by Heyd, Scuseria, and Ernzerhof [25, 1100–1102]. While the conventional 25 % exact-exchange parametrization of the original HSE06 functional provide excellent lattice parameters for a wide class of semiconductors (e.g. see Footnote 2 for the case of cubic group-III nitrides), the performance of the HSE06 hybrid functional for electronic structure calculations is slightly less universal and depends on the size of the electronic band gap as well as the material's screening characteristics. In order to estimate the reliability of approximations made by diverse hybrid functionals, their numerical results are commonly benchmarked against results from *GW* quasiparticle theory providing a formally more complete description of electron correlation through systematic evaluation of the many-body self energy of the interacting many-electron system as outlined throughout Sec. 3.4. The potential of hybrid functionals for providing a cheap approximation of quasiparticle properties has been outlined in Paper II [75] for the three natural polymorphs of TiO_2. The HSE06 hybrid functional has found to provide an excellent approximation to the quasiparticle-band structure around the valence-band and conduction-band edges, however, deep semicore states as well as unoccupied high-energy states from HSE06-based density-functional theory calculations show a progressive deviation from their quasiparticle counterparts with increasing distance from the band-edges (cf. Fig. 2 Paper II [75]). Similar observation can be made for the band gaps of group-III nitride semiconductors, in general. The conventional functional form of the HSE06 functional allows for a vast improvement in the band-gap performance over (semi)local density-functional theory [22], but still does not entirely reach the accuracy of quasiparticle-band gaps originating from the various non-self-consistent or self-consistent incarnations of *GW* theory. [23] This observation especially concerns semiconductors and insulators with large electronic band gaps. Among the investigated materials the calculated HSE06 band gaps of the wide-gap semiconductors *zb*-AlN show the most severe underestimation of reported experimental values [24]. A better performance of the HSE06 exchange-correlation functional is indicated for diverse modifications, crystalline (e.g. see Tab. 1 of Paper II [75] as well as amorphous (see Sec. III B of Paper III [31]), of the functional oxide TiO_2. As outlined in Paper VIII [334], the HSE06 hybrid functional was additionally found to be an excellent tool to determine the basic nature as well as the charge-transition levels of the nitrogen split-interstitial defect in GaN. Since the prediction performance the HSE06 functional for electronic structure features shows moderate but

[22] In the context of nonpolar group-III nitride physics, the correct prediction of *zb*-InN as a small-band-gap semiconductor (cf. Tab. 18) is one of the essential benefits from hybrid-functional-based density-functional theory simulations.

[23] This is exemplarily demonstrated by the calculated band gaps of the cubic group-III nitrides *zb*-GaN and *zb*-AlN in Tab. III of Paper I [309] or the band-gap data of *zb*-$Al_xGa_{1-x}N$ alloys presented in Fig. 7 of Paper IV [33].

[24] The direct HSE06 ($\Gamma_v \rightarrow \Gamma_c$) band gaps of *zb*-GaN and *zb*-AlN show a typical underestimation of ~ 0.3 eV; cf. Footnote 18 as well as Tab. III of Paper I [309] or Tab. III of Paper IV [33].

still prediction relevant variations for different classes of materials, the *optimal* [25] exact-exchange contribution can be material specific and does not necessarily represent an universal constant. [26] In order to manipulate the simulation results for characteristic band-structure features, it is possible to increase the exact-exchange fraction in hybrid functionals on an empirical basis. The actual size of this optimized fraction of exact-exchange energy could be obtained either from benchmarking the calculation results against experimental input or by aiming at reproducing results of formally higher ranking numerical approaches that include a more complete description of the underlying many-body interactions as provided by the fourth-rung hyper-generalized gradient-functional approximations, itself. This, however, affects multicomponent systems as mixed alloys or heterostructures, where the exact-exchange fraction should be adjusted to provide the most balanced description of electronic structure features in all functional material components. [27]

Within the present thesis HSE-type hybrid functionals with an increased exact-exchange fraction have been vastly used to *improve* the performance of hybrid-density functional simulations for group-III nitride semiconductors. In detail, exact-exchange fractions of 26 %, 30-32 %, and 36-39 % (see Paper I [309], Paper IV [33], and Paper VII [35]) have been found to match the experimental band gaps of the nonpolar zinc-blende modifications of InN, GaN and AlN. [28] These values also allow for an excellent approximation of the fundamental energy gaps of cubic $Al_xGa_{1-x}N$ alloys through the entire composition range (see Paper IV [33]). Some complication can arise for materials with an indirect fundamental band gap as the zincblende phase of AlN. The direct and indirect *zb*-AlN band gaps, obtained by an exact-exchange-modified HSE-type hybrid functional, show a disproportionate dependence on the exact-exchange fraction. [29] A notably larger exact-exchange fraction of 39 % is required to reproduce the indirect ($\Gamma_v \rightarrow X_c$) band gap of *zb*-AlN, numerically, while 32 % are sufficient to obtain the direct ($\Gamma_v \rightarrow \Gamma_c$) band gap. [30]

An immediate consequence of the severely improved performance in the calculation of semiconductor-band gaps is the potential to provide robust secondary information as the direct-indirect band-gap crossing composition in nonpolar *zb*-$Al_xGa_{1-x}N$ alloys, where the fundamental nature of the alloy-band gap originates from a composition-dependent competition between the direct and indirect conduction-band minima of the binary-end semiconductors *zb*-GaN and *zb*-AlN for the fundamental conduction-band minimum of the mixed ternary semiconductor. Likewise, the

[25] Optimal in the practical sense of being able to reproduce experimental data with highest accuracy.

[26] Even though the 25 % exact-exchange fraction of the HSE06 screened hybrid functional or the unscreened PBE0 global hybrid are rationalized [1109] but not *derived* from strict theoretical considerations.

[27] This limitation of global hybrid functionals could be overcome by transition towards local hybrid functionals that determine the *mixing parameter(s)* locally at each point in space. [1108, 1209–1211]

[28] The slight differences in the utilized exact-exchange fractions are owned to variations of the particular lattice parameters as well as the balance between an accurate description of direct and indirect band-structure features.

[29] While the fundamental direct HSE06 ($\Gamma_v \rightarrow \Gamma_c$) band gap of *zb*-AlN shows a typical underestimation of ~ 0.3 eV, the deviation from experimental data amounts up to ~ 0.7 eV for the indirect HSE06 ($\Gamma_v \rightarrow X_c$) band gap (cf. Footnote 18 as well as Tab. III of Paper I [309] or Tab. III of Paper IV [33].

[30] This illustrates that the unpretentious functional form of global hybrid functionals has limitations in providing an accurate many-body self energy and straightforward *empirical* refinement of mixing parameters should keep an eye on various material characteristics, at the same time.

compositional dependence (by means of bowing parameters) of electronic structure features as the fundamental alloy-band gap can be determined by hybrid-functional-based density-functional theory. As outlined in Paper IV [33], the use of HSE-type hybrid functionals with an adjusted amount of exact exchange allows the modeling of these secondary material features in close agreement with experimental data. Nevertheless, also the limitations of the fixed mathematical form of the HSE hybrid functional in providing all electronic structure features, simultaneously, has been addressed with regard to many-body perturbation theory-based quasiparticle theory (see discussion below). Similar, also the prediction accuracy for related material parameters as the band offset between two semiconducting materials benefits from application of hybrid functionals [31], notably, making them a method of choice for wide-ranging studies on band-alignment characteristics. A prototypical band-offset study on nonpolar *zb*-$Al_xGa_{1-x}N$ / $Al_yGa_{1-y}N$ composites highlighting alignment features as the composition dependence of the fundamental heterostructure character (type-I vs. type-II) throughout the entire composition range is provided by Paper VII. [35]

OPTICAL PROPERTIES FROM HYBRID FUNCTIONALS ? – Optical material properties of semiconducting materials are commonly expressed by means of the macroscopic dielectric function, which allows to access relevant optical functions as the refractive index, the reflectivity, the absorption coefficient, the extinction coefficient, as well as the electron-energy loss spectrum. [32] However, if compared to reference data obtained from optical spectroscopy, the dielectric functions calculated in Kohn-Sham density-functional theory utilizing (meta-)generalized gradient approximations to the exchange-correlation energy might fail to reproduce the correct absorption onset as well as the particular line shapes of optical functions, the spectral weight distributions respectively. Apparently, the generally observed red-shift of the absorption onset in the absorption coefficient or, homologous, the imaginary part of the complex dielectric function, directly follows the band-gap underestimation. The improved description of the electronic band structure, especially the comprehensively corrected size of semiconductor-band gaps, also suggest the use of hybrid functionals for optical response calculations by replacing the optical dipole-matrix elements and transition energies from generalized gradient approximations by their hybrid-functional analogous. In doing so, a notable blue shift of the absorption spectrum is observed, qualitatively, but the spectral weight distribution is widely unaffected. Due to the maintained single-particle picture in Kohn-Sham theory, the main effect of switching from (meta-)generalized gradient to hybrid functional ingredients is a rigid *quasiparticle-like* blue-shift (see discussion below) of the optical spectra coming along with a notable correction, in several cases even overcorrection, of the absorption onset. The sources of this overcorrection with respect to the experimentally observable absorption edge, as well as the still uncorrected spectral weight distribution, relates to the single-particle picture which does not account for the two-particle nature of the fundamental ex-

[31] The hybrid-functional band offsets in cubic GaN/AlN superlattices show an improvement over the results obtained by the PBE exchange-correlation functional. Thereby, the original functional form of the HSE06 screened hybrid functionals does not reach the accuracy of non-self-consistent G_0W_0 corrections (see Tab. V in Paper I [309]).

[32] The actual expressions of optical functions through the real and imaginary components of the complex dielectric function are provided in Sec. II C of Paper III [31].

citation process in optical spectroscopy. Their relevance will become more clear in the context of excitonic modifications to the optical response obtained from solution of the Bethe-Salpeter equation for the macroscopic polarization function (cf. Sec. 5.1.2). Nevertheless, a carefully adjusted hybrid-functional setup might still be very useful to provide a sound estimation of optical properties in case of a forbidden numerical cost for accurate quasiparticle-theory calculations on *large* structure models of, e.g., amorphous materials necessitating a unit-cell representation of several hundred atoms. [33]

Phase stability

In order give a brief example of the relevance of treating electron-electron interactions beyond the level of fourth rung hyper-generalized gradient approximations, one might have a look at the superficially straightforward example of structure polymorphism and the importance of being able to make reliable *predictions* on the energetic ordering of crystalline polymorphs under various ambient conditions. While common (semi)local exchange correlation functionals predict the correct energy ordering of crystalline phases of group-III nitrides by identifying the hexagonal wurtzite phase as the most stable crystalline bulk polymorph in the low temperature and pressure limit [34], the same task becomes vastly challenging when dealing with the structure polymorphism of crystalline TiO_2. Among the vast number of structural modification prepared by material scientists all around the world (see Sec. 1.1), TiO_2 is known to exist in three crystalline modifications (see Fig. 1 of Paper II [75]), naturally. While the brookite polytype is less common, both rutile and anatase are present in technologically relevant functional materials raising the question wether rutile or anatase represent the actual structural bulk and/or nanophase groundstate in the low temperature and pressure limit. Despite numerous density-functional theory studies on this matter, neither a conclusive nor a complete [35] view on TiO_2 phase stability has been provided in literature. Giving a résumé on partially contradictory reports from experimental studies, the rutile phase seems to be the thermodynamically stable TiO_2 bulk polymorph at all temperatures [41], while TiO_2 anatase is considered a metastable material phase [42–46] with the potential for representing the or a stable nanomodification of TiO_2. [47, 48]

A BRIEF PROSPECT ON RANDOM-PHASE CORRELATION – Addressing the problem of TiO_2 phase stability by density-functional theory inevitably leads to conflicting results finding that first to third rung exchange-correlation functionals predict anatase to be the stable TiO_2 bulk polymorph, consistently [36] (e.g. see Ref. [131, 1195, 1564–1568] as well as Footnote 36). Interestingly, this *problem* persist in the majority of all hybrid-functional studies on TiO_2 phase stability

[33] Numerical results following this leitmotif are provided in Footnote 58 for mixed ternary a-$Ti_xSi_{1-x}O_2$ oxides.

[34] Density-functional theory using the semilocal generalized gradient approximation in PBE parametrization provides a stabilization of the hexagonal wurtzite phase by 24 meV (1709 meV), 87 meV (391 meV), and 38 meV (606 meV) over the cubic zincblende (rocksalt) phase of GaN, AlN, and InN at the numerically optimized structure parameters.

[35] Both is not a concern of the present thesis, as well.

[36] Relative formation energies of the TiO_2 polymorphs anatase and brookite with respect TiO_2 rutile per formular TiO_2 unit. A positive/negative formation energy difference indicates a less/more stable polymorph.

(cf. Footnote 36). [37] [1568] Despite partially inconsistent experimental reports, the consistent predictions of anatase as the structural ground-state polymorph of TiO_2 can not necessarily be tagged a quality of these functionals. This fallacy becomes obvious if brookite, which is consistently found to be a metastable modification of TiO_2 in experimental studies, is included in the numerical picture of TiO_2 phase stability, consistently. Frequently, also a stabilization of the brookite polymorph over TiO_2 rutile is predicted by semilocal as well as hybrid exchange-correlation functionals (see Footnote 36). [1566, 1568]

The one ingredient all first-to-fourth rung exchange-correlation functionals miss, persistently, is an accurate treatment of dynamical long-range electron correlation, even though an explicit treatment of the associated non-covalent electron-dispersion forces, or van der Waals forces for short, is commonly neglected in the study of bulk semiconductors and their phase stability. Nevertheless, there are profound indications that electron-dispersion forces might also affect the cohesive energy of solids aside from prototypical application examples of dispersion-corrected density-functional theory as physisorption on (metal) surfaces or the layer interaction between stacked two-dimensional van der Waals solids. [38] In order to allow for a consistent and numerical effective supplement of common generalized-gradient approximations by dispersion interactions, several semiempirical approximation schemes have been developed (e.g. see Ref [1282, 1572, 1573]). Several of these semiempirical dispersion-correction approaches, traditional as Grimmes's DFT-D approaches [1242, 1243, 1574] or state-of-the art techniques as the recent pairwise Tkatchenko-Scheffler correction [1575, 1576] or a many-body dispersion scheme [1573, 1577], have been applied to study the phase stability of TiO_2 polymorphs indicating a general tendency to reduce the energy difference between the rutile and anatase polymorphs. However, a reversal in the stability ranking, intrinsic to semilocal density-functional approximations, is not indicated in general [82, 1565, 1578, 1579], as demonstrated by the relative rutile-anatase-formation energies listed in Footnote 36. An *elegant* approach to provide a numerical description of electron dispersive forces requires stepping up towards the final rung of Jacob's ladder (cf. Fig. 3.3) by calculat-

methodology		ΔE [eV]	
lattice	XC	rutile → anatase	rutile → brookite
exp.	DFT@PBE	-0.0952	0.1563
DFT@PBE+D3	DFT@PBE	-0.0970	-0.0536
DFT@PBE+D3	DFT@PBE+D3	-0.0274	-0.0304
DFT@PBE+D3	DFT@HSE06	-0.0866	0.1540
DFT@SCAN+rV10	DFT@PBE	-0.0967	-0.0538
DFT@SCAN+rV10	DFT@SCAN+rV10	-0.0815	-0.0174
DFT@SCAN+rV10	DFT@HSE06	-0.0845	-0.0423
exp.	RPA@PBE	0.0338	0.1983
DFT@PBE+D3	RPA@PBE	0.0338	-0.0148
DFT@SCAN+rV10	RPA@PBE	0.0287	-0.0159

The lattice-parameters used throughout the total energy calculations are identical to the values listed in Footnote 7. The total energies have been calculated using a 500 eV plane-wave energy cutoff and Γ-centered $7\times7\times11$, $9\times9\times3$, and $3\times5\times5$ **k**-point samplings of the primitive Brillouin zones of the rutile, anatase, and brookite phases of TiO_2.

[37] According to Curnan et al. [1568] a hybrid functional stabilization of TiO_2 rutile against TiO_2 anatase can only be achieved for *unphysically* high fractions of exact exchange spoiling an accurate simulation of the electronic structure, simultaneously.

[38] It has been estimated [1569] that van der Waals force induced non-covalent contributions amount up to 6 %, 14 %, and 17 % of the cohesive energies of the coinage metals Cu, Ag, and Au, respectively (also see Ref. [1570, 1571]).

ing the correlation energy in random-phase approximation (see Sec. 3.3.5), which allows for a *seamless* inclusion of long-range electron dispersion. In addition, the random-phase approximation has the appealing feature of being self-interaction free in its exchange contribution to the electron exchange-correlation energy, which severely reduces the self-interaction error of functional approximations inherent to lower ladder rungs.[39] The inclusion of correlation energy in random-phase approximation has the potential to stabilize TiO_2 rutile with respect to the anatase and brookite phases, consistently (see Ref. [1580, 1581] as well as Footnote 36). However, this stabilization tends to be very sensitive to the actual lattice parameter utilized to evaluate the random-phase correlation energy. As indicated by the data presented in Footnote 36, especially the brookite (de)stabilization depends critically on the underlying lattice parameters. This inconsistency originates from two essential limitations in the way the random-phase calculations are conducted. By virtue of computational demands, the structural optimization is limited to more feasible lower rung exchange-correlation functionals, in the first place.[40] Second, the random-phase correlation energy is commonly evaluated non–self-consistently using the Kohn-Sham single particle orbitals obtained by one of the lower rung exchange-correlation functionals, which also introduces some orbital-dependent uncertainty into the obtained correlation energy (e.g. see Ref. [1580, 1581]). Both, primarily numerical constrains, still add some degree of uncertainty to most of the present random-phase-approximation-based predictions on TiO_2 phase stability, which could only be eliminated by a full, self-consistent solution of the (generalized) Kohn-Sham equations for the random-phase total energy functional, Eq. 3.78. In addition, also a thorough inclusion of lattice dynamics, phonon contributions respectively, might be relevant to provide a *complete* picture of the thermodynamic phase stability of TiO_2 polymorphs. [1580, 1583]

5.1.2 Many-body perturbation theory

In review of the diversity and complexity and of the manifold of density-functional theory approximations to the exchange-correlation energy scrimmaging below the high grounds of a fully self-consistent random-phase-approximation-based density functional, one might be desirous of putting a more elaborate approach into place that allows for a systematic inclusion of many-body interactions of the many-electron system. The theoretical framework that, at least on paper, allows to bypass some of the idiosyncrasies and pitfalls of density-functional theory is provided in Green's function-based many-body perturbation theory which has been mentioned as a potential reference for approximative quasiparticle calculation via hybrid functionals, already. In many-body perturbation theory, formally expressed in Hedin's set of fundamental equations (cf. Eq. 3.134 to Eq. 3.138), the problem of finding an analytical expression for an unknown density functional is replaced by an elaborate hierarchy of approximations to the *electron-self energy* car-

[39] Nevertheless, the random-phase correlation energy itself is still subject to a spurious self-interaction. [1259, 1260]

[40] In case of low symmetry bulk systems it is possible to perform a series of fixed volume calculations to obtain lattice parameters in random-phase approximation by fitting an equation of states. [1580] Quiet recently, also the numerical framework for the calculation of interatomic forces in random-phase approximation has been framed. [1582]

rying the whole of exchange-correlation effects. As most of the post–density-functional theories, the various approximations derived from many-body perturbation theory face the problem of being severely demanding to any kind of computational resources making any large-scale application to more complex systems exceedingly challenging or, by the current status of computational high-performance capabilities and algorithm efficiencies, even prohibitive. However, already the lowest order solutions to Hedin's equations contain the ingredients essential to reproduce, analyze, and predict the outcome of experimental measurements and to highlight the underlying physics rendering their application to some prototypical material systems as well as diverse material modifications one of the centerpieces of this thesis.

Quasiparticle-band structure

The concept of quasiparticles, as outlined in Sec. 3.4, represent a key concept to interpret the results of spectroscopic measurements which, in contrast to optical absorption, probe the character of *single-particle-like* quasiparticle excitation of the many-electron system. Despite providing a *parameter-free* theoretical description of fundamental excitations of the many-electron system, formally, the underlying quasiparticle theory, required to calculate the electronic self-energy, comprehends numerous approximation levels that, on the on hand, can be capitalized to reduce the significant numerical cost but, on the other hand, add some degree of unintended empiricism to practical calculations. [41]

HEDIN'S *GW* APPROXIMATION & BEYOND – Taking into account the perturbation-theory character of *GW* quasiparticle theory, the most crucial component in practical calculation is the level of approximation underlying the preparative generation of single-particle states entering the actual evaluation of *GW* quasiparticle states and energies. The better, in the sense of being as close as possible to the actual quasiparticle orbitals, the starting single-particle wave functions are, the less steps are needed to converge the associated quasiparticle energies in case of (partial) self-consistency and so much better the quasiparticle energies from non–self-consistent G_0W_0 calculations will get. While the starting point of *GW* calculations is given by the *correlation-free* single-particle orbitals of Hartree-Fock theory, naturally, the use single-particle orbitals from correlation containing single-particle theories as density-functional theory can prove to be highly beneficial to evaluate the quasiparticle energies, albeit, the actually included many-body interactions become shrouded in non–self-consistent quasiparticle theory, in this way. With respect to Kohn-sham theory, the use of a proper hybrid functional is the most appealing functional choice to provide *GW* input in all cases, either reducing the number of steps to converge the quasiparticle

[41] Since many-body perturbation theory aims at finding an accurate description of the electronic self-energy, which allows an accurate description of electronic and optical features of semiconducting materials, but does not necessarily provide atomic forces in most numerical implementations, the use of experimental lattice parameters represents a well founded approach to exclude underlying imponderabilia of the structure-simulation process. This approach has for instance been adopted in Paper II [75] to model the electronic structure and optical response of naturally occurring TiO_2 polymorphs as well as in Paper VII [34] to estimate the band-alignment profiles between nonpolar $Al_xGa_{1-x}N/Al_yGa_{1-y}N$ heterostructures.

energies and orbitals or providing the best *single-shot* approximation to the *exact* quasiparticle state in case of a non–self-consistent perturbative treatment.

The performance of various levels of self-consistency has been outlined for the band-gaps of the cubic group-III nitride semiconductor family, exemplarily. As pointed out in Paper I [309] and Paper IV [33], the best band-gap performance has been found for a non-self-consistent G_0W_0 evaluation of quasiparticle-energy corrections on top of preceding HSE06 hybrid-functional density-functional theory calculations. In contrast, the inclusion of eigenvalue self-consistency (without consideration of vertex corrections) in the *GW* self-energy through the single-particle Green's function *G* and/or the screened Coulomb interaction *W* always increases the band-gap energies compared to the non-self-consistent evaluation leading to an increasing overestimation of experimentally reported band gaps (cf. Tab. III in Paper I [309] and Fig. 5 of Paper IV [33]). This overestimation tends to increase further if not only the eigenvalue convergence in the single-particle Green's function *G* and/or the screened Coulomb potential *W* is considered but also the quasiparticle orbitals are updated thoroughly during the evaluation of the *GW* self-energy. However, with respect to the band gap of *zb*-AlN, the final decision on the performance of the diverse levels of *GW* theory still demands for accurate photoemission data on direct and indirect band gaps complementing the reference data from optical measurements. Qualitatively similar observations have been made for perturbative electronic structure quasiparticle calculations of the three natural TiO_2 polymorphs rutile, anatase, and brookite as outlined in Paper II [75]. Here, the non–self-consistent quasiparticle corrections provide good approximations of photoemission data on the fundamental electronic band gaps. The quasiparticle-band structure calculations on TiO_2 also indicate that the major effect of quasiparticle-energy corrections to the Kohn-Sham eigenvalues persists in an almost rigid upward-shift of unoccupied electronic states throughout the entire Brillouin zone (cf. Fig. 2 of Paper II [75]) providing a sound justification for the application of the *scissor-shift* approximation. [1584] Due to the demands on computational resources, quasiparticle corrections might be bypassed by utilization of an adequate scissors shift in the evaluation of optical spectra. This rough approximation has proven to be very favorable for *large* atomic systems, where convergence of quasiparticle energies is hard to achieve or even prohibitive as demonstrated for the optical spectra of amorphous TiO_2 in Paper III [31], exemplarily. The degree of reliance in predicting quasiparticle-band gaps also allows for a more accurate estimation of secondary material parameters associated to their electronic structure. The most relevant parameter determining the electronic properties of a semiconductor heterostructure are the band offsets between the valence-band and conduction-band edges of two interfacing semiconducting materials. The combination of HSE-type hybrid-functional calculations with a non–self-consistent evaluation of G_0W_0 quasiparticle-energy corrections has been found to provide the band offsets in cubic group-III nitride heterostructures in close correspondence with experimental results (see Tab. V of Paper I [309]). [42]

[42] In detail, the G_0W_0@HSE06 quasiparticle-band offsets of 0.56 eV and 1.31 eV between valence and conduction band states and the associated offset ratio of 70:30 fall into the the error margin of the experimentally determined results

Aside from the manifold of promising results on electronic properties of prototypical oxide and nitride semiconductors, obtained form application of the *GW* approximation to many-body perturbation theory, there has been at least one partly *odd* result throughout the band-gap calculations in this thesis. Similar to hybrid functional calculations [43], non of the utilized *GW* approaches was able to provide the same accuracy for fundamental direct and indirect band-gap features in the investigated cubic group-III nitrides (cf. discussion in Paper I [309] as well as Paper IV [33]). [44] Finding an accurate description of the direct $(\Gamma_v \rightarrow \Gamma_c)$ band gap of *zb*-AlN by adjustment of the exact-exchange percentage in the exchange-correlation hybrid functional spoils the indirect $(\Gamma_v \rightarrow X_c)$ band gap of *zb*-AlN by increasing the deviation to the experimentally observed band gaps and vice vera. The results from non–self-consistent and self-consistent *GW* calculations show this problem in a similar way (cf. Fig. 5 in Paper IV [33])). The missing ingredient, next in line to refine the *GW* self-energy by a more complete treatment of many-body interactions, are the *vertex corrections* dropped in Hedin's *GW* approximation in order to facilitate the first generation of quasiparticle corrections to Hartree-Fock or Kohn-Sham eigenvalues. [45] As indicated in the band-gap data of Footnote 45 the inclusion of vertex corrections improves the correspondence of the converged quasiparticle-band gaps of fully self-consistent *GW* theory with band-gaps derived from optical spectroscopy. For convenience, the full self-consistence with respect to quasiparticle energies as well as quasiparticle orbitals completely removes any dependence on the input from various exchange-correlaion approximation levels in Kohn-Sham theory. The indicated overall

of 0.5 ± 0.1 eV and 1.4 ± 0.1 eV and a ratio of 74($\pm$5):26($\pm$5), exactly.

[43] Interestingly, the direct *zb*-AlN band-gap-optimized fraction of exact-exchange provides roughly the same degree of accuracy for the direct band gap of *zb*-GaN (cf. Tab. 3 in Paper IV [33])).

[44] In addition to the reasonable performance of hybrid functionals and quasiparticle theory, an excellent band-gap performance with respect to both direct as well as indirect electronic band gaps of cubic group-III nitride semiconductors (cf. Paper IV [33])) was observed within the LDA-1/2 half-occupation technique which was formally derived from Slater-Janak transition-state theory [1035, 1064, 1585] into an practical calculation scheme handling solid-state systems by Ferreira et al. [1586, 1587]. Within the LDA-1/2 technique, electrostatic *self-energy* potentials, derived from the Kohn-Sahm potential difference of an atom and its half-ion, are added to the atomic pseudopotentials in order to correct the numerical description of electronic band gaps in density-functional theory. Despite its successful use, the half-occupation technique for solids has its own imponderabilities and limitations [1587–1589] leading to a limited number of application examples, only. [1590–1594]

[45] Self-consistent *GW* quasiparticle band gaps with and without inclusion of vertex corrections.

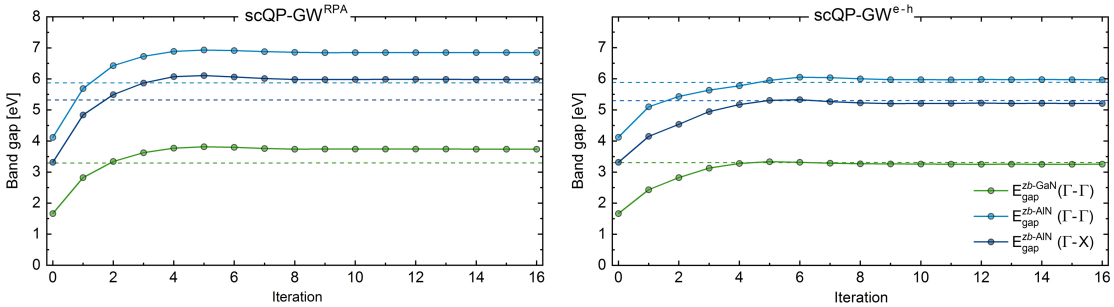

The quasiparticle band gaps have been calculated from vertex-corrected self-consistent *GW* theory using a 400 eV plane-wave energy cutoff, 256 electronic bands, and a Γ-centered $8 \times 8 \times 8$ **k**-point sampling of the primitive Brillouin zone. Vertex corrections have been included by means of a HSE-type screened Coulomb kernel in the vertex function with exact-exchange percentages of 32 % and 46 %. Experimental band gaps, taken from Ref. [386] and Ref. [385] for *zb*-AlN and *zb*-GaN, are indicated by dashed horizontal lines.

convergence of electronic band-gaps towards the experimental values makes the vertex-corrected $GW\Gamma$ scheme a high-priority goal for purely self-contained electronic structure simulations that are *completely* free of any adjustable parameter.

Optical response in many-body perturbation theory

The focus on optical material properties forces to open the single-quasiparticle picture maintained within the *GW* approach to account for the most relevant many-body effects underlying optical absorption processes. If an electron is optically excited from the valence band into an empty/virtual conduction-band state by absorption of a photon, the remaining hole and the excited electron attract each other by their Coulomb interaction (cf. Fig. 3.5). The Coulomb interaction itself is weekend by reaction of the surrounding electrons with an intensity determined by a system's dielectric screening properties. Together with an (unscreened) electron-hole exchange interaction (cf. Eq. 3.181) this screened Coulomb interaction defines the overall electron-hole pair coupling strength. Depending on the strength of the electron-hole pair interaction, unbound electrons and holes might form bound electron-hole states, itself representing self-contained quasiparticles. The excitation energy of bound exciton states is lower than the quasiparticle band gap by a material specific *exciton-binding energy*. Depending on screening characteristics and interaction strength, the newly formed exciton state might have the physical characteristics of a large-distance hydrogen-like entity showing large exciton radii delocalized over a few lattice constants in the *Wannier-Mott limit* [1595, 1596] or being of short-distance and strongly localized in the *Frenkel limit* [1597] (e.g. see Ref. [987]). The formation of excitons represents the leading many-body effect essential to interpret spectroscopic measurements.

THE BETHE-SALPETER EQUATION – Within the present thesis two-particle electron-hole excitations within the Bethe-Salpeter formalism have been treated for numerous TiO_2 bulk polymorphs in Paper II [75] and Paper III [31], amorphous TiO_2 in Paper III [31], and the nonpolar *m*-plane surface of hexagonal GaN in Paper VI [34]. Thereby, the dimensionality of the electron-hole pair Hamiltonian, Eq. 3.185 generally dictates the treatable system size as well as the accuracy, the convergence level of numerical results respectively. Especially, the numerical analysis of bound exciton states below the quasiparticle conduction-band edge requires an vastly accurate **k**-point sampling around critical points of the Brillouin zone. While the optical spectra of bulk semiconductors might be converged, in terms of two-particle states and **k** points, at a still manageable computational cost, comparable calculations are at the edge of todays high-performance computing infrastructure for more advanced structure models of, e.g., semiconductor surfaces (cf. Paper VI [34]) or amorphous oxides (cf. Paper III [31]).

The inclusion of electron-hole interaction in the Bethe-Salpeter formalism has two main effects on the simulated optical response. On the one hand, characteristic exciton states close to the quasiparticle-band edge missing in the independent-(quasi)particle approximations of density-functional theory or the *GW* formalism are now reproduced in close correspondence with exper-

imental observations. Correspondingly, the exciton formation causes a notable red-shift moving the absorption edge towards the experimentally measured optical energy gaps. On the other hand, various single-(quasi)particle transitions are mixed in the evaluation of the complex dielectric function, Eq. 3.188 weighted by the pair-states $A_\Lambda(c\mathbf{k}, v\mathbf{k})$ obtained from solution of the two-particle eigenvalue problem Eq. 3.186. In general, notable redistributions of spectral weights can appear throughout the entire absorption spectrum potentially modifying the spectral line shape also at higher absorption energies.

The excellent correspondence between the polarization-dependent dielectric functions of spectroscopic ellipsometry and the Bethe-Salpeter formalism in combination with G_0W_0 quasiparticle-energy shifts has been outlined for the two major natural TiO_2 polymorphs rutile and anatase in Paper II [75]. It is further highlighted that the accuracy of well converged optical response simulations allows to identify potential deficiencies in widely spread and frequently cited experimental reference data [46] (see discussion in Paper II [75]). In addition, the same numerical approach has been adopted to study the less common natural brookite polymorph (cf. Paper II [75]) as well as eight additional meta-stable and high-pressure polymorphs of TiO_2 (cf. Paper III [31]) illustrating how the particular short-range order of the TiO_2 crystals determines the optical response (see discussion below). As demonstrated in Paper III [31] the dielectric function of amorphous TiO_2 might be effectively approximated by an average over the dielectric functions of these numerous TiO_2 bulk polymorphs with high accuracy. The basic validity of this procedure renders *averaging* a potential approach to find reasonable numerical approximations to the optical response of disordered material phases, whose large atomic models prevent straightforward ab-initio-optics calculations, frequently.

5.2 Fingerprints of order and disorder

In many aspects, today's material science reverses the renowned design paradigm, *"Form follows function"*, by finding a materials microscopic structure at the center of its macroscopic properties and structure modification the most powerful instrument in the toolbox of material engineers. Here, we will consider the term *form* most widely as the entirety of atomic ordering characteristics encompassing both structural as well as chemical composition. The subsequent discussion of order features is roughly organized by their characteristic length scales with the exception of structure-function correlations in ternary amorphous oxides, which bring together essential facets of short-range oder as well as medium-range order depending on the actual alloy composition.

[46] While the existence of a second main peak above $\sim 6.5\,\mathrm{eV}$ is clearly observed in the dielectric function of TiO_2 rutile in ordinary as well as extraordinary polarization, a comparable absorption feature is not indicated in the most frequently cited experimental reference data of Cardona and Harbeke (1965) [1511]. However, the second spectral main feature is clearly indicated in the respective energy region in more recent, but substantially less-widely cited, absorption data of Tiwald and Schubert (2000) [1512].

5.2.1 Sort-range order

In a perfect crystalline environment short-range order and long-range order condition each other and cannot be viewed detached from each other; the actual space group of a crystal defines the order features on all length scales. For example, the atomic structure of the three natural crystalline TiO_2 polymorphs rutile, anatase and brookite consist of edge-linked and/or corner-linked TiO_6 building blocks in variously distorted octahedral conformations [47] and their spatial arrangements/interconnection actually defines the crystalline symmetry. However, even if a material looses its long-range order, the remaining order features on the atomic length scale still underly the macroscopic material properties, partially.

NON-DIVINE GEOMETRY – In principle, common well-established statistical instruments as radial distribution functions or structure factors allow for an comprehensive analysis of local coordination environments in form of bond-length and bond-angle statistics. [48] However, the averaged nature of these statistical functions implies a reduced sensitivity to geometrical/symmetry details of the local coordination environments of individual atoms, which complicates the establishment of general as well as material-specific trends in emerging structure-function correlations. While pure mathematical decomposition schemes as Voronoi tessellation [1598] or Delaunay triangulation [1599] do not necessarily provide intuitive and comprehensible insights into a material's microstructure, coordination polyhedra offer an convenient way to serve this purpose allowing to make reference to well established concepts of molecular physics, simultaneously. Starting from a preceding pair-correlation analysis to determine the cutoff radii for each pair of chemical species, a complete short-range order analysis of the atomic structure in terms of fundamental coordination polyhedra as well as their spatial arrangement on an intermediate-range scale provide rather complete information on atomic order in crystalline and non-crystalline materials (cf. Sec. 5.2.3). A main focus of the present thesis is the study and characterization of the local atomic order in the amorphous structure of functional oxides and the basic material properties emerging from this order regime. To this purpose, Paper III [31] essentially conceptualizes the approach of coordination-polyhedra analysis to provide a comprehensive microscopic description of a-TiO_2, while simultaneously establishing *meaningful* correlations to the macroscopic material characteristics. Following this route, Paper V [32] applies coordination-polyhedra analysis to various structure models of ternary a-$Ti_xSi_{1-x}O_2$ hybrid oxides in order to study the composition-dependent interaction and competition between the disordered framework morphologies of amorphous TiO_2 and SiO_2 glass.

The detailed study of the microstructure of various structure models to a-TiO_2 reveals that the

[47] In rutile, the O_h symmetry of an ideal octahedron is reduced to D_{2h} symmetry due to different in-plane (equatorial) and out-of-plane (axial) Ti-O bond lengths and two types of Ti-O-Ti in-plane bond angles deviating from 90 °. In the anatase phase, additional displacements of the O ions from the equatorial positions generate a local D_{2d} symmetry seen by the Ti ions. Due to stronger distortions in TiO_2 brookite, all bond lengths and bond angles slightly differ from each other, thus leading to C_1 symmetric TiO_6 units (cf. Fig. 1 in Paper II [75]).

[48] Examples for the application of pair-distribution function and structure-factor analysis are provided in Paper III [31] for a-TiO_2 (cf. Fig. 2) as well as in Paper V [32] for ternary a-$Ti_xSi_{1-x}O_2$ hybrid oxides (cf. Fig. 15 and Fig. 16).

amorphous state exhibits substantial modifications compared to the octahedral coordination environment of crystalline TiO_2. Even though the mean O coordination number of Ti ions changes only moderately from the sixfold crystalline state for properly relaxed structure models generated by ab-inito molecular dynamics, the actual local coordination states of roughly half of all Ti ions are modified towards higher or lower coordination (cf. Tab. 1 in Paper III [31]), which renders the short-range order of a-TiO_2 a versatile conglomerate of TiO_n coordination polyhedra with n ranging from four to eight (see Fig. 1 in Paper III [31] as well as Fig. 2 (b) of Paper V [32]). A slight prevalence for the lower fivefold coordination compared to the higher sevenfold coordination accounts for the reduced mean coordination of a-TiO_2. Beyond changes in the actual coordination state, also the local symmetry of the remaining half of sixfold coordinated Ti ions is subject to significant distortions, which change the fundamental polyhedra types for a substantial number of TiO_6 coordination units. Instead of the slightly wrapped TiO_6 coordination octahedra present in the crystalline state, several distorted polyhedra types, related to, e.g., a trigonal prism or truncated versions of the pentagonal bipyramid, can be identified in the amorphous state. Likewise, also higher and lower coordination states exhibit distorted versions of different basic coordination polyhedra, albeit, the highest number of basic coordination geometries has been identified for the still dominant sixfold coordination state. An overview of all basic symmetry types of TiO_n coordination polyhedra identified in a-TiO_2 is illustrated in Fig. 5 of Paper V [32].

Further facets of short-range order emerge in ternary a-$Ti_xSi_{1-x}O_2$ hybrid oxides. In the first place, the prototypical glass-forming material a-SiO_2 exhibits substantially less disorder in its short-range order. Over 90 % of all Si ions remain in the tetrahedral fourfold coordination state of crystalline silica phases at ambient conditions. Thereby, the SiO_4 coordination tetrahedra are only weakly distorted as indicated by their bond-lengths and bond-angle distributions (cf. Fig. 8 and Fig. 9 of Paper V [32]) as well as their *effective coordination numbers* (cf. Fig. 13 of Paper V [32]).[49] With increasing Ti content, the amorphous network of the a-$Ti_xSi_{1-x}O_2$ hybrid oxides starts to transform, progressively. At low concentration, Ti ions are predominantly embedded in tetrahedral network sites with marginal influence on the microstructure of SiO_2 glass. At intermediate Ti contents, the Ti ion is preferentially incorporated in an unconventional fivefold coordination state (cf. Fig. 7 of Paper V [32]). Here, Ti acts as a network forming species, that increases the network connectivity within the vitreous a-$Ti_xSi_{1-x}O_2$ frameworks without *destroying* the actual network topology as indicates by persisting ring-like medium-range order characteristics in this composition regime (see discussion below). With Ti ions becoming the major cation species in a-$Ti_xSi_{1-x}O_2$, the crystal-like sixfold coordination state is adopted, increasingly. At this point the microstructure of a-$Ti_xSi_{1-x}O_2$ starts to resemble more and more the amorphous framework of a-TiO_2 and even the coordination state for the wasting number of Si ions is partially

[49] The concept of effective coordination numbers, as introduced in Sec. 3.4 of Paper V [32], allows to incorporate some measure for *order* into the local coordination numbers. By introducing a bond-weight function (cf. Eq. 11 in Paper V [32]), effective coordination numbers are sensitive for radial variations in the bond distance providing an efficient indicator for the polyhedra symmetry/degree of order.

transformed from its persistent tetrahedral state towards higher coordinations. Hence, in its sixfold coordination state, Ti ions exhibit a more distinct network-modifying character and the transition between a predominant fivefold or sixfold Ti coordination might be seen as a key indicator for the transition from an actual vitreous oxide network to an amorphous oxide framework. The additional occurrence of higher Ti coordination states beyond the crystal-like sixfold coordination can be viewed as a general mechanism for relaxing the strain within the disordered oxide frameworks. The TiO_6 coordination polyhedra show their strongest distortions, by means of the average Ti-O bond length (cf. Fig. 10 (a) of Paper V [32]) or the related effective coordination numbers of Ti ions (cf. Fig. 14 (a) of Paper V [32]), just before the occurrence of sevenfold coordinated states and the simultaneous relaxation of TiO_6 coordination polyhedra. A similar observation can be made for the sporadic occurrence of TiO_8 coordination units at highest Ti contents, that allow for the relaxation of TiO_7 and TiO_6 coordination polyhedra. The successive transition towards higher coordination states resembles a bifurcation-like diversification (see Fig. 10 (a) of Paper V [32]) of the short-range order environments with increasing Ti content, or respectively the mass density acting as a critical parameter.

In sum, the atomic structure of amorphous oxide semiconductors is found to be highly versatile. A substantial fraction of ions exhibits non-crystalline coordination environments and/or notably distorted coordination geometries. Especially the, partially predominant, occurrence of TiO_5 coordination polyhedra in a-TiO_2 as well as a-$Ti_xSi_{1-x}O_2$ sheds new light on the fundamental role of intermediate coordination states, atypical to crystalline coordination environments, in the structure formation processes of Ti-rich oxide materials. Accordingly, the study of the microstructure of disordered materials and their materials properties should include an analysis on unconventional coordination states and distorted coordination environments, unconditionally, in order to explain differences in their material properties with respect to the crystalline state. In addition, the competition between the different order characteristics in amorphous and vitreous (oxide-)material modifications might be an essential paradigm in understanding basic structure-formation processes in disordered states of matter.

Localized states, band tails and the mobility gap – While the amorphous state misses a well defined electronic band structure due to the loss of long-range order, electronic structure concepts as the density of states still apply to the disordered solid as exemplified for various structure models of a-TiO_2 in Fig. 3 of Paper III [31]. Particularly with regard to semiconducting materials, the density of states exhibits valence and conduction band-domains well separated by an energy gap reminiscent of the band gap of crystalline semiconductors but less distinctive features of a basic crystal-field splitting. [50] Compared to the natural TiO_2 polymorphs, the quasiparticle-band gap of an amorphous TiO_2 phase exhibiting an atomic density close to the rutile phase shows a quasiparticle HOMO-LUMO–tpye energy gap around ~ 3.7 eV, which is larger than the quasiparticle-band gaps of rutile and brookite and close to the quasiparticle-energy gap of TiO_2

[50] Also see Fig. 3 of Paper III [31] for the (quasiparticle) eigenvalue spectrum of a-TiO_2.

anatase.[51] However, the HOMO-LUMO–tpye energy gap of a disordered material state is not the adequate analog of the actual band-gap of a crystal. The basic structure-function correlation effect coming into effect in the electronic structure of amorphous materials, exhibiting substantial amounts of over-coordinated and under-coordinated ions, is the formation of localized electronic states at the edges of the valence and conduction "bands".[52] In sum, several localized states add up to small *band tails* reaching into the forbidden energy region of the crystalline state. Due to the localized nature of charge carriers confined in the band tails, the HOMO-LUMO–tpye energy gap differs from the actual *mobility gap*, which represents the amorphous phase complement of the crystalline band gap defining the energy difference between non-localized occupied and unoccupied Bloch-type states. In order to estimate the size of the mobility gap within the conducted (hybrid) density-functional theory calculations it is necessary to measure the degree of localization for each Kohn-Sham state. To this end, information theory allows to derive entropy based measures as the *inverse participation ratio*[53] quantifying the degree of localization based on the partial charge density distributions[54] of each electronic state. The size of the band tails, illustrated in Fig. 5 of Paper III [31], shows a notable dependence on the actual structure model. While the molecular-dynamics–generated room-temperature structures show valence band tails of $\sim 0.4\,\mathrm{eV}$ and slightly smaller conduction band tails of $\sim 0.2\,\mathrm{eV}$. Structural relaxation to the 0 K ground state reduces the extent of the band tails to roughly $\sim 0.1\,\mathrm{eV}$, which puts the groundstate-mobility gap of a-TiO_2 to $\sim 3.8\,\mathrm{eV}$, hence, above the band-gap energies of natural TiO_2.

In order to classify the nature of the band-tail states, several electronic states of a-TiO_2, localized as well as extended, have been visualized by their electronic charge-density distributions in Fig. 5 of Paper III [31]. Despite their spatial localization, all band-tail states conserve the predominant O_{2p}-like valence-state and the Ti_{3d}-like conduction-state character observed for natural TiO_2 polymorphs (cf. Fig. 3 in Paper II [75]). The origin of the localized valence states can be assigned to two types of lattice sites, in general. On the one hand, the electronic states are localized at O ions in slightly distorted threefold coordination environments. On the other hand, we find significant contributions from under-coordinated O ions, bound to just two Ti ions. The localized conduction band-tail states, arise from electronic states located at over-coordinated Ti ions in TiO_7 building blocks as well as contributions from conventionally sixfold coordinated TiO_6 and, to a minor extent, from under-coordinated TiO_5 building blocks. Altogether, charge carrier localization in the amorphous state originates primarily from *coordination defects* as well as additional

[51] A comprehensive discussion comparing experimental and theoretical data on the fundamental band gaps of natural TiO_2 to the energy gap of a-TiO_2 is provided in Sec. III B of Paper III [31].

[52] Amorphous semiconductors actually show broad valence-state and conduction-state continua instead of a complex conglomerate of discrete energy bands.

[53] In detail, the exponentials of the two first order Rényi entropies, the Shannon and the extension entropy respectively, have been applied to the partial charge densities in order to measure the degree of localization for each Kohn-Sham state of a-TiO_2. Details on the determination of characteristic measures classifying the degree of localization of electronic states are provided in Sec. 3 D of Paper III [31]

[54] In terms of information theory, the partial charge densities simply represent discrete and non-negative N-point probability distributions.

contributions from structurally distorted coordination environments, which renders the amorphous phase of TiO_2 an ideal example of a topologically disordered irregular network structure following the order classification presented in Fig. 2.5. In several aspects, the amorphous phase is closely related to traditional defect physics of semiconducting materials. Viewing any deviation from the conventional crystalline coordination state/geometry of TiO_2 as a *defect*, one clearly recovers the characteristics of donor-like and acceptor-like states, immediately. The unpaired electrons of the under-coordinated O ions generate localized acceptor-like dangling-bond states at the valance-band edge. The local over-coordination of Ti ions, on the other hand, results in the presence of localized donor-like states at the conduction-band edge.

In sum, the electronic structure of amorphous semiconductors still carries notable imprints of short-range order features of the crystalline state determining the overall physical *character* of the material, while disorder not only *modulates* the crystal-like electronic structure, but also adds qualitatively new features as the formation of band tails, primarily due to the localization of electronic states.

MICROSCOPIC INSIGHTS FROM MACROSCOPIC RESPONSE – The coordination-polyhedra analysis of the amorphous frameworks of semiconducting oxides has illustrated a way to characterize a materials' microstructure in a comprehensive way. At the same time, the polyhedra view on short-range order allows to discuss and understand the emerging material properties on basis of common concepts of solid-state physics. In view of the practical measurement by optical spectroscopy, one might have an interest in turning the table on structure-function correlations by asking if one can gain notable insights on a materials microstructure from measuring the macroscopic optical response without performing additional diffraction measurements that directly focus on structural details and require a substantial body of distinct structure-function correlations, itself. To this purpose we consider the complex dielectric function of a-TiO_2 obtained from solution of the Bethe-Salpeter equation (cf. Fig. 9 (a) in Paper III [31]), which allows an accurate modeling of the absorption onset as well as the refractive index and the extinction coefficient in the visible-to-ultraviolet energy range (cf. Fig. 9 (b) in Paper III [31]). A straight forward attempt to model the optical absorption characteristics by averaging the dielectric functions of the three naturally occurring TiO_2 polymorphs rutile, anatase, and brookite fails to reproduce the dielectric function of a-TiO_2 with high accuracy (cf. Fig. 11 in Paper III [31]). The persisting differences are particularly related to the common octahedral coordination environments of crystalline TiO_2 phases and the related crystal-field splitting of the unoccupied Ti_{3d} states, which is deeply imprinted in the averaged dielectric function. In contrast, the inclusion of non-octahedrally coordinated TiO_2 polymorphs as the high-pressure polymorphs TiO_2(II), TiO_2(MI),TiO_2(OI), TiO_2(OII) (see Sec. 1.1 for details), which exhibit local metal-ion coordination environments with seven to nine O atoms (cf. Fig. 1.1), drastically improves the correspondence between the dielectric function of a-TiO_2 and it's averaged approximate (cf. Fig. 12 of Paper III [31]). Since one can exclude effects due to surfaces formation, grain boundaries, or particles size to be the origin due to the *layout* of the generated structure models, the improved correspondence clearly establishes the correlation be-

tween certain optical absorption features and *unconventional* [55] coordination states of the Ti ion in a-TiO_2. This observation illustrates that distinct features of the macroscopic optical response, by means of the imaginary part of the dielectric function, provide immediate insights into structure characteristics on an atomic length scale. Since the general existence of non-octahedral coordination states is a subject of debate in disordered phases and nanomodifications of TiO_2, experimental measurements on the dielectric function throughout the middle-to-far infrared regime, which encompasses the electronic transition related to the conduction states, splited by the octahedral-like coordination environments, offer a metodology to infer the presence of suchlike coordination states. Likewise, dielectric-response measurements beyond the optical energy range represent an efficient approach to analyze the degree of order/crystallization in TiO_2 samples. In order to extend and refine the understanding of microscopic-to-macroscopic structure-function correlations, also the study of potential metastable crystal phases might proof insightful.

In sum, the macroscopic material properties of disordered materials, as the studied optical response of amorphous functional oxides, is found to be a superposition of structure-function correlations imprinted into microscopic functional units determining the material properties of crystalline modifications, already. Consequentially, the numerical study of diverse crystalline polymorphs can provide potential insights into material properties of disordered phases as well as enable an approximate numerical investigation of complex material phases via first-principles simulations, that are otherwise untreatable on this level of theoretical sophistication.

5.2.2 Medium-range order

In contrast to short- and long-ranging order characteristics, medium-range order features are the hardest to classify and to discriminate against each other. Within the materials addressed in the present thesis, the most relevant case of medium-range order is the occurrence of distinct *ring-like* order features [56] in vitreous SiO_2 as well as low Ti-content a-$Ti_xSi_{1-x}O_2$ hybrid oxides (see Paper V [32] for details).

VITREOUS RING-LIKE ORDER – While distinct ring-like structures of high symmetry are a fundamental order characteristic present in the open low-pressure frameworks of prototypical tetrahedral oxides as SiO_2 [57], the amorphous structure of SiO_2 stands out by a broad $(SiO_4)_n$ ring-size distribution ranging from 4 to 24 atoms and moderately peaking at a crystal-untypical ring size of $n = 7$ (cf. Fig. 18 of Paper V [32]). Similar to the distribution of coordination-polyhedra in case of

[55] Based on the TiO_2 polymorphs included in the averaging procedure underlying Fig. 11 of Paper III [31] "unconventional" explicitly refers to higher TiO_n coordination states with $n \geq 6$ (cf. Fig. 11 of Paper III [31]).

[56] An atomic ring is defined as the topologically shortest closed path starting from one particular atom and returning to that atom by stepwise going from one adjacent/bonded atom to another. In case of a crystalline structure, an adjacent atom is simply defined as a nearest neighbor of a particular atom. For an amorphous solid, adjacent atoms are defined by cutoff spheres for each chemical element (cf. Sec. 2.2.2 and Paper V [32]).

[57] For example, the most common SiO_2 α-quartz phase is constructed from 12 atom and 16 atom wide $(SiO_4)_6$ and $(SiO_4)_8$ rings built from six and eight SiO_4 units, respectively. Additional n-membered $(SiO_4)_n$ ring configurations are present in the oxide frameworks of the various SiO_2 polymorphs in existence (see Paper V [32] for further details).

TiO_2 the disordered SiO_2 state is characterized not only by a broader distribution of order features compared to the crystalline state, but also by the presence, or even dominance, of non-crystalline variations of the dominant order feature. Almost, the entire variation and modification of order features in amorphous SiO_2 is carried in its medium-range order, while the coordination state of the Si ion, the short-range order of the crystalline state respectively, is virtually preserved for all Si ions with tetrahedral coordination units exhibiting minor distortions, only (see discussion above). Narrowing the examination to the two prototypical oxides SiO_2 and TiO_2, a fundamental distinction of the disordered frameworks of vitreous and non–glass-forming materials might be found in the *disorder-affected* order regime, the medium-range order in case of the vitreous tetrahedral insulator SiO_2 but the short-range order in case of the amorphous octahedral semiconductor TiO_2. Even though ring-like statistics are rarely applied to study the structure of more dense or higher coordinated oxide structures, the evaluation of ring-statistics is straightforward in case of amorphous TiO_2. Thereby, the higher coordination state of the Ti ion and the increased connectivity within the oxide network promote a more narrow distribution of shorter $(TiO_m)_n$ oxide rings ($n = 2 - 7$) build from different TiO_m coordination polyhedra instead of a single polyhedron type. Incorporation of lower amounts of the higher coordinated Ti ions into the vitreous network structure of SiO_2 increases the network connectivity and number of medium-size rings ($n = 5 - 7$), successively. Addition of Ti ions beyond $\sim 40\,\%$ starts to reduce the maximal size of rings in favor of shorter rings. Hence, Ti acts as an intermediate ion species showing a network forming and/or modifying character depending on the relative alloy composition (a comprehensive discussion of ring statistics is provided within Sec. 4.7 of Paper V [32]).

5.2.3 Structure-function correlations in amorphous oxides

The understanding of essential features of the optical response of the studied ternary amorphous hybrid oxides [58] is intimately tied to qualitative and quantitative characteristics/markers of both the short-range order by means of coordination-number/polyhedra statistics as well as the ring-like medium-range order present in the disordered oxide-glass frameworks. The optical properties of the studied mixed a-$Ti_xSi_{1-x}O_2$ oxides are presented in Footnote 58 indicating that the optical energy gaps derived from linear extrapolation of the absorption coefficient around the absorption onset show a nontrivial dependence on the composition parameter. In detail, the optical gap depends linear on the Ti content throughout the Ti-rich composition regime roughly above a composition parameter of $x \approx 0.4$. This linear dependence changes to an exponential dependence for smaller Ti contents in the Si-dominant alloy regime. Similar qualitative features are observed for important physical parameter as the onsets of optical absorption, the refractive index, the absorption coefficient or the dielectric constant, since all are derived from the complex dielectric function. The linear composition dependence of the optical alloy gap in the Ti-rich composition regime is

[58] Linear optical response properties of ternary a-$Ti_xSi_{1-x}O_2$ hybrid oxides. Displayed are (a) the real part and (b) the imaginary part of the complex dielectric function, (c) the refractive index, and (d) the absorption coefficients around the fundamental absorption edges, including the extrapolated energy gaps of the oxide alloys.

reflected not only in a breakdown of larger ring structures, but also the simultaneous change in the predominant oxygen coordination from Si to Ti ions (see Fig. 6 (c) and Fig. 6 (f), as well as Fig. 20 of Paper V [32]). This characteristic change in the chemical coordination environment of O ions is also marked by an inflection point in the O coordination number of Ti ions (cf. Fig. 6 (a) of Paper V [32]). The octahedral coordination geometries of Ti ions exhibit most characteristic distortions around a composition parameter of $x \approx 0.4$ (cf. Fig. 10 (a) and Fig. 10 (d) of Paper V [32]), which relax at higher Ti contents through formation of higher TiO_n, $n > 6$ coordination units corroborating the short-range order of basic coordination polyhedra as an essential indicator for the order features within the amorphous networks. In contrast, the coordination geometries of the Si ions exhibit only minor composition-dependent changes with respect to the average bond lengths and bond angles (see Fig. 10 (b) and Fig. 10 (e) of Paper V [32]), which indicates a more important role of medium-range order features in structure-formation processes in the Si-dominant composition regime. The differences in the underlying atomic structure render the profound change in the composition dependence of optical parameters an potential indicator for the transition towards a vitreous silica framework.

In sum, basic qualitative changes as well as quantitative classification numbers characterizing the microscopic order in the structure models of a-$Ti_xSi_{1-x}O_2$ unambiguously correlate with macroscopic material properties as the optical response providing potential insights into and indicators for fundamental structure-formation processes in the TiO_2-dominant amorphous oxide semiconductors as well as the disordered SiO_2-dominant frameworks of silica glasses.

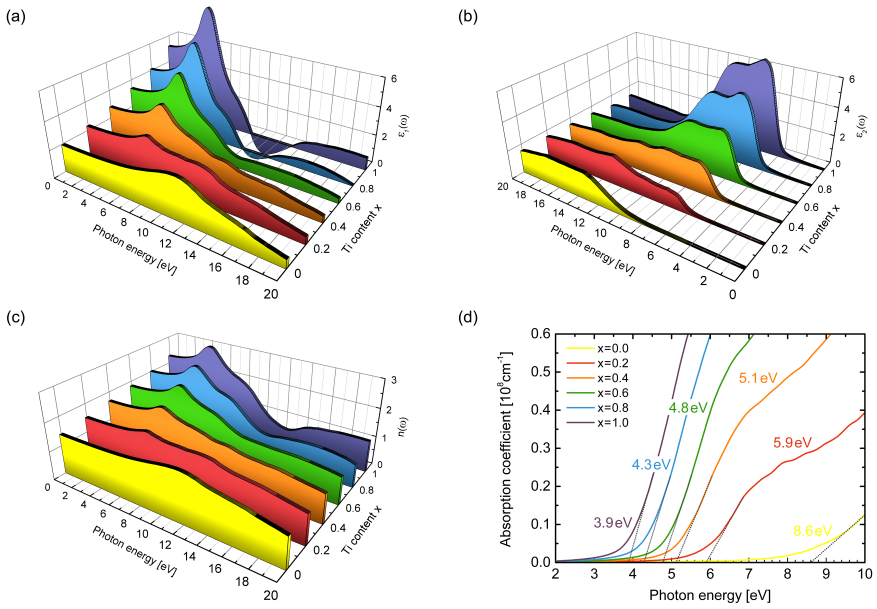

The optical spectra are calculated at the Γ point for 300 atom containing unit cells within the independent-particle approximation based on Kohn-Sham theory using modified HSE-type hybrid functionals with composition-dependent exact-exchange percentages linearly interpolated between 25 % for a-TiO_2 and 38 % for a-SiO_2.

5.2.4 Long-range order

The remaining order category is most familiar to solid-state physics. The macroscopic material properties of solid-state materials commonly emerge from the crystalline long-range order and manifesting itself in form of the fundamental symmetry type of a solid, which can be altered to modify its physical and chemical properties. The following section also encompasses structural phenomena related to formation of heterostructures, even though order features associated with heterostructuring are hardly classifiable. Within this thesis, the heterostructuring-effect of interest is the formation of semiconductor heterojunctions/superlattices. Depending on the superlattice periodicity, which could range from (mono-)atomically thin to a few hundred nanometers, a heterostructure might be classified as short-range or medium-range ordered. However, also the long-range order nature of heterostructures applies in case of an idealized view on heterojunctions as the interface between two *semi-infinite* materials. Likewise, the classification of order-scales in surface-formation processes is inconclusive. On one hand, surface formation represents an order formation process with a two-dimensionally long-range–ordered layer forming at the top of a semi-infinite material slab interfacing a vacuum. On the other hand, the arrangement of surface atoms during relaxation as well as reconstruction processes can occur on diverse locally competing short-range or medium-range length scales. In view of the idealized cases, heterostructuring as well as surface formation are included in the long-range order category, at this point. Furthermore, the formation of semiconductor alloys is assigned to the long-range order category, too. Even though alloying of two or more chemical species in a multicomponent semiconductor, or within a particular sublattice, takes place on a microscopic scale changing the short-range order of a material, actually, the perfect random semiconductor alloy with a macroscopically isotropic distribution of chemical elements, gives the effective impression of a homogenous semiconductor with novel macroscopic material properties.

BULK POLYMORPHISM – The general characteristic trait of crystalline materials to exist in different crystalline modifications, space groups respectively, stabilized under certain thermodynamical conditions, is known as *structure polymorphism*. Structure polymorphism represents an essential way to conduct basic solid-state engineering by changing a material's long-range order, e.g. by applying some kind of strain or pressure in order to modify its electronic structure and optical response as well as associated material properties.

The present thesis treats structure polymorphism by example of group-III nitride semiconductors (see Paper I [309], Paper IV [33], and Paper VII. [35]) as well as various (transition-)metal-oxide semiconductors (see Paper II [75]) [59], both representing simple long-range as well as chemically ordered crystalline network structures as pictured in Fig. 2.5 (b). The group-III nitrides crystallize in stable hexagonal lattices with a wurtzite-type ($P6_3mc$-C_{6v}^4) structure, naturally. Due to the lack of a proper inversion symmetry, the hexagonal nitride polymorphs give rise to strong

[59] In addition, the symmetry induced variations in the structural as well as electronic properties of five different potassium niobate ($KNbO_3$) polymorphs have been discussed in Paper VII. [35] (e.g. see Fig. 1 and Fig. 5 of Paper VII. [35])

strong internal piezo-electric and spontaneous polarization electric fields along the crystalline c-axis, which can be obstructive to the functionality of optoelectronic devices. In order to mitigate the strong internal fields, the growth of nonpolar and semipolar nitrides has found increasing technological interest over the past years. In nonpolar or semipolar hexagonal nitride semiconductors, the crystallographic c-axis is orthogonal or inclined to the growth direction, hence eliminating or at least reducing the field effects in the growth direction. However, the electrical, optical, and structural properties of semipolar semiconductors are still subject to notable lateral anisotropies. The electronic and optical properties of the wz-GaN$\left(1\bar{1}00\right)$ m-plane surface [60] have been studied within Paper VI [34], exemplarily (see discussion below). The transition towards the cubic zincblende ($F\bar{4}3m$-T_d^2) modification (see Fig. 1.5) of the group-III nitride semiconductors offers a way to fabricate nitride-based optoelectronic devices, fundamentally free of polarization fields, analog to the group-III arsenide family. Aside from their compatibility to alternative growth substrates and the general absence of strong polarization fields, the nonpolar group-III nitride semiconductors slightly extend the range of accessible electronic as well as optical band-gap energies (cf. Sec. 1.2). Thereby, zb-AlN is the only binary nitride semiconductor with a nondirect fundamental band gap exhibiting the conduction-band minimum at the X-point. This indirect band-gap nature becomes relevant in the physical properties of Al containing nonpolar group-III nitride semiconductor alloys and heterostructures as outlined below.

Titania and silica are prototypical oxide semiconductors exhibiting substantial polymorhisms of their bulk modifications as well their nanomodifications and amorphous structures. The later is known as *polyamorphism*. The present thesis especially covers the natural as well as artificial structure polymorphism of TiO_2 bulk modifications [61] (cf. Fig. 1.1) within the scope of Paper II [75] and Paper V [32]. Among the three natural TiO_2 bulk polymorphs rutile ($P4_2/mnm$-D_{4h}^{14}), anatase ($I4_1/amd$-D_{4h}^{19}), and brookite ($Pbca$-D_{2h}^{15}), the rutile and brookite polymorphs are direct Γ-point semiconductors with almost degenerate quasiparticle-band gaps of $\sim 3.7\,\mathrm{eV}$, whereas anatase is a nondirect semiconducting oxide with a slightly larger ($\approx 0.3\,\mathrm{eV}$) fundamental $(\Gamma \rightarrow M)_v \rightarrow \Gamma_c$ quasiparticle gap [62] (cf. Tab. 1 in Paper II [75]). Aside from the octahedral short-range order-related features in the optical response, the space-group variations between different polymorphs also determine the number of independent components of the dielectric tensor accounting for the characteristic anisotropies of the three natural polymorphs. [63] In addition to the natural structure polymorphism, additional eight metastable as well as high-pressure TiO_2

[60] An illustration of nonpolar surface planes in a hexagonal wurtzite-type crystal is provided in Fig. 1 of Paper VI [34] alongside atomistic details of the m-plane surface.

[61] The challenging task of providing an accurate numerical prediction of phase stability and energetic ordering of natural TiO_2 modifications is discussed in the context of calculating the correlation energy in random-phase approximation in Sec. 5.1.1.

[62] Referring to the conventional orthorhombic unit cell, the valence band maximum is located close to the M point along the Σ path connecting the high-symmetry points Γ and M (cf. Fig. 2 in Paper II [75]).

[63] The dielectric tensor of the two *uniaxial* tetragonal TiO_2 phases rutile and anatase contains two independent components, while three independent components are present for the *biaxial* orthorhombic brookite phase (cf. Fig. 4 of Paper II [75]).

polymorphs have been considered in the structure-function analysis of the optical response of a-TiO_2 rendering the short-range order, instead of the long-range order, the essential variable in understanding the microscopic structure and the optical response of disordered titania phases (see discussion above).

ALLOYING – Instead of focusing on localized defect states through incorporation or removal of a limited number *foreign* of atoms, alloying is commonly not achieved by *replacing* a substantial number of atoms within a material but by controlling the distribution of chemical species during the actual material-fabrication/growth process. Alloying preferentially relies on joining elements with quite similar chemical characteristics in order to allow for a rather homogenous mixture of atoms instead of a granular, more or less phase-separated compound with dominating interface effects. Despite missing translational symmetry on the microscopic length scale, an isotropic and random solid solution effectively shows macroscopic material characteristics of an isotropic material, that are different from its individual constituents. [64] A continuous transformation of physical material characteristics with changes in the alloy composition requires atomically mixed alloys without phase-separated domains, which is not given a priori for any material class. Assuming a smooth atomic miscibility over the entire composition range, the composition dependence of various alloy properties as the equilibrium lattice parameters, the fundamental band gaps, or the band offsets relative to a second material (see discussion below) typically deviates from a linear Vegard's-law–type dependence, which is indicated in the particular *bowing parameter*.

The present thesis addresses the effects of alloying for the metal-cation sublattice in ternary zb-$Al_xGa_{1-x}N$ semiconductors (see Paper IV [33]) [65]. The studied order type within the ternary group-III nitride semiconductors represents *substitutional sub-lattice disorder* [66] in an ordered network as illustrated in Fig. 2.5 (c). Aside from ubiquitous, but marginal, onsite lattice distortions, the investigated order type in the zb-$Al_xGa_{1-x}N$ semiconductors is a case of chemical disorder in a crystalline material. The random mixture of group-III metals in the cation sublattice of ternary and multi-component nitride semiconductors allows for a *continuous* modulation of the alloy characteristics between the known binary-end compositions of the constituent semiconductors, zb-GaN and zb-AlN. While zb-GaN is a direct semiconductor, analog to its hexagonal wurtzite-type counterpart zb-AlN is, similar to (cubic) AlAs within the group-III arsenides, the only binary semiconductor with an nondirect fundamental bulk-band gap exhibiting the conduction-band minimum at the X point. Both, the composition dependence of direct electronic transitions between Γ_v-type and Γ_c-type states and the indirect electronic transitions between Γ_v-type and X_c-type states can be extracted from the hybrid-density functional-theory calculations on zb-$Al_xGa_{1-x}N$ structure mod-

[64] This essentially justifies the use of phenomenological approaches on alloying as the *coherent potential* or *virtual crystal* approximations [986, 1600, 1601] treating the alloy by defining artificial composition-dependent potentials with restored translational symmetry in order to calculate an effective electronic structure mimicking the actual alloy properties and providing virtually identical macroscopic material properties.

[65] The results of Paper IV [33] have been resumed in Paper VII [35] to study the natural band alignment in group-III nitride heterostructures (see discussion below).

[66] Substitutional sublattice disorder (cf. Fig. 2.5 (o)) has also been studied in an irregular disordered network topology for ternary a-$Ti_xSi_{1-x}O_2$ hybrid oxides in Paper V [32] (see discussion in Sec. 5.2.1 as well as Sec. 5.2.2).

els [67] as well as linear optical response measurements by spectroscopic ellipsometry. [68] The bowing parameters found from the combined input of experimental and theoretical techniques indicate a characteristic downward bowing, $b_\Gamma = 0.85\,\text{eV}$, of the direct $(\Gamma_v \rightarrow \Gamma_c)$-type energy gap of the alloy, while an almost linear composition dependence of the $(\Gamma_v \rightarrow X_c)$-type alloy gap is indicated by a bowing parameter of $b_X = 0.01\,\text{eV}$. The contemporaneous occurrence of direct and indirect fundamental band-gap features in the binary representatives of the cubic group-III nitride family accounts for discontinuous transitions of the fundamental energy gap in the multinary nitride semiconductors. The critical crossover transition between *zb*-GaN and *zb*-AlN conduction-edge states determining the alloy-energy gap is found to occur at a composition parameter of $x = 0.71$ in ternary *zb*-$Al_xGa_{1-x}N$ alloys (cf. Fig. 10 of Paper IV [33]). Crossover concentrations represent an important characteristic number when dealing with the electronic and optical properties of multicomponent semiconductor alloys, e.g. by being essential to fully understand the band-alignment characteristics of their heterostructures. [69]

HETEROSTRUCTURES – The essential electronic structure feature of a semiconductor heterostructure is the discontinuous progression of the bulk valance-band and conduction-band edges across the interface of two adjacent materials. Thereby, the size of the intrinsic band offsets derives from the difference in the fundamental band gaps of the interfacing semiconductors. The band offsets of a semiconductor heterostructure are of utterly importance for the fabrication of optoelectronic devices by determining the fundamental characteristics of charge-carrier generation, localization and transport, as well as their effective recombination rates (also see Paper VII. [35]).

Within this thesis, the band offsets of various cubic group-III nitride heterostructures have been examined, in detail. The large range of accessible band offsets between group-III nitrides makes this semiconductor family quite appealing for technological applications. A comprehensive analysis of the strained band offsets in *zb*-GaN/AlN superlattices is provided in Paper I [309] based on theoretical as well as experimental considerations both indicating a type-I superlattice alignment characterized by a valence-to-conduction band-offset ration of $74\,(\pm5) : 26\,(\pm5)$. While the definition of strained band offsets is directly bound to the lattice parameters of a heterostructure, one can also think of the so called unstrained or *natural* band alignment representing a *bulk property* of the interfacing semiconductors that is independent of any structural details of the interface. Whereas the calculation of strained band offsets makes reference to an energy scale common to both of the interfacing materials, e.g. averages of local atomic potentials or core level energies on both sides of the interface, natural offsets are defined with respect to a *globally* defined reference as the vacuum level, or the branch-point energy (see Paper VII. [35] for additional details). Natural band offsets do not come into effect in the same way as strained band offsets by means of being measurable in a heterostructure device, directly. However, since the alignment of electronic

[67] See discussion above as well as Paper IV [33] for details.

[68] The experimentally measured imaginary parts of the complex dielectric function are provided in Fig. 1 of Paper IV [33] alongside details of the experimental setup in Sec. II A.

[69] A discussion of the band-alignment between *zb*-$Al_xGa_{1-x}N$ semiconductors is provided in the subsequent discussion of heterostructures.

states under particular strain conditions can be incorporated a posteriori in numerically efficient model theories via parametrical input in form of volume deformation potentials, the numerical study of natural band offsets has significant implications behind pure academical reasoning. The natural band offsets in ternary *zb*-$Al_xGa_{1-x}N$ / $Al_yGa_{1-y}N$ heterostructures are investigated in Paper VII [35] throughout the entire two-dimensional (x,y)-composition range. Investigating the properties of cubic group-III nitrides, more precisely the metastable zincblende phase, distinguishes from their thermodynamical stable hexagonal counterparts by the fundamental indirect band gap of *zb*-AlN, which leads to the presence of the direct-indirect band-gap crossover in ternary *zb*-$Al_xGa_{1-x}N$ semiconductors (cf. Paper IV [33])) and adds substantial complexity to the band alignment in *zb*-$Al_xGa_{1-x}N$ / $Al_yGa_{1-y}N$ heterostructures. The intermixed unoccupied Γ_c-type and X_c-type electronic states at the conduction band edge of mixed *zb*-$Al_xGa_{1-x}N$ semiconductors lead to four possible heterostructure alignments between occupied and unoccupied bands, four types of conduction-band offsets respectively. In detail, direct-direct ($\Gamma_c \rightarrow \Gamma_c$)-type, direct-indirect ($\Gamma_c \rightarrow X_c$)-type, indirect-direct ($X_c \rightarrow \Gamma_c$)-type, and indirect-indirect ($X_c \rightarrow X_c$)-type conduction band offsets will form depending on the alloy composition. The four different offset regimes are illustrated in Fig. 3 of Paper VII. [35]. The discrimination lines between the four basic alignment types are thoroughly defined by the critical alloy concentration x_c at the direct-indirect crossover of the *zb*-$Al_xGa_{1-x}N$ alloys; roughly 63 % Al content as predicted by exact-exchange–adjusted hybrid functionals (cf. Paper IV [33])). The direct-direct and indirect-indirect band-offset regimes are defined by both-sided *zb*-$Al_xGa_{1-x}N$ alloy compositions of $x \leq x_c$ and $x \geq x_c$. The presence of direct-indirect crossovers also accounts for differences in the bowing characteristics, a composition dependent bowing respectively, of the band offsets in the predominantly Ga rich and the Al-rich alloy composition regimes (e.g. see Fig. 2 of Paper VII. [35]). Two direct-indirect and indirect-direct regimes are determined by composition parameters of $x \leq x_c \wedge y \geq y_c$ and $x \geq x_c \wedge y \leq y_c$. Without inclusion of strain, which leads to a *forward-backward asymmetry* in the band alignment of two materials, the direct-indirect and indirect-direct band-offset regimes will be completely symmetric with indistinguishable offset values. This is essentially the commutativity, $\Delta E_{\mathrm{v/c}}(\mathrm{A/B}) = -\Delta \mathrm{E}_{\mathrm{v/c}}(\mathrm{B/A})$ of natural band offsets.Likewise, natural band offsets strictly follow the transitivity rule $\Delta E_{\mathrm{v/c}}(\mathrm{A/C}) = \Delta \mathrm{E}_{\mathrm{v/c}}(\mathrm{A/B}) + \Delta \mathrm{E}_{\mathrm{v/c}}(\mathrm{B/C})$. The calculated natural alignment of electronic states in *zb*-$Al_xGa_{1-x}N$ / $Al_yGa_{1-y}N$ heterostructures also indicates a potential switchover in the fundamental superlattice type. The entire indirect-indirect alignment regime exhibits a type-II alignment profile. Likewise, also small Al-rich regions in the the direct-indirect zones close to the crossover concentration lines belong to this alignment type (cf. Fig. 3 of Paper VII. [35]). In view of optical applications, the localization of charge carriers at distinct places in momentum space severely degrades e.g. electron-hole pair generation/recombination rates limiting the applicability of direct-indirect heteromaterials, in this case. In contrast, the staggered band alignment in type-II heterostructures confines charge carriers in different spatial regions promoting the separation of charge carriers, which is an appealing feature to, e.g., light harvesting devices. Again, the separation process will be more efficient in case of band extrema localized at

the same point in momentum space.

SURFACES – Surfaces formation can be understood as an order effect in the same way as heterostructure formation simply by removal of one material viewing the surface system as the interface between a semi-infinite crystal and the vacuum. In contrast to the formation of a heterostructure, the surface is not subject to comparable strain-induced structure modifications origination from the interfacing material's symmetry and lattice parameters. However, the non–structure-constraining vacuum side allows for atomic relaxations in the topmost surface layers and, in addition, for substantially long-ranging surface reconstructions that do not occur at semiconductor interfaces in the same way. The combined effects of surface relaxation and reconstruction determine the degree of modifications to the bulk-specific electronic structure conditioning novel material characteristics beneficial to their technological applicability.

In the present thesis, the electronic and optical properties of the nonpolar *wz*-GaN$\left(1\bar{1}00\right)$ *m*-plane surface have been investigated based on first-principles simulations within Paper VI [34]. The topmost surface layer of the structurally relaxed *wz*-GaN$\left(1\bar{1}00\right)$ surface exhibits a buckling angle of about 8° with respect to the bulk positions (cf. Fig. 2 in Paper VI [34]), which is caused by a charge transfer from the surface Ga to the more electronegative surface N atom and a rehybridization of the surface bonds. The presence of novel lattice sites calls for a modification of the electronic structure by formation of surface states. The *wz*-GaN$\left(1\bar{1}00\right)$ *m*-plane exhibits two distinct dangling-bond-type surface states that are predominantly localized at the under-coordinated ions within the first surface layer (cf. Fig. 5 in Paper VI [34]). In detail, these are an occupied N-derived surface-state, which is resonant with the bulk-valence band edge at the origin of the Brillouin zone, and an unoccupied Ga-derived surface state, well separated from the bulk conduction-band edge by at least 0.2 eV within the whole Brillouin zone (cf. Fig. 4 in Paper VI [34]). The existence of two surface-state bands modifies the optical response close to the bulk-absorption edge by shifting the surface-absorption edge towards lower energies due to surface excitons intermixing with near-band-edge electronic transitions of the bulk-like material. Thereby, the surface excitons accentuate the near-edge anisotropy of the surface's optical response.

5.3 Future perspective

THERE IS NO REAL ENDING. IT'S JUST WHERE YOU STOP THE STORY. [70] – The present thesis comprehensively compares and addresses various state-of-the-art density-functional theory related and many-body perturbation-theory-based approximations to calculate material properties of cubic group-III nitrides as well as prototypical transition-metal oxide semiconductors. Despite providing parameter-free predictiveness of the electronic structure and optical response, in theory, practical calculations almost exclusively rely on critical parametrical input at certain points of the numerical implementations. Clearly, one future challenge of electronic structure theory is to put

[70] Quotation of the US-american science-fiction and fantasy author Frank P. Herbert (1920-1986).

these partially *empirical* parameters on solid ground in order to *safe* and *restore* the essence of first-principles simulations. In the same breath, increasing computational efficiency of numerical algorithms, their optimization towards massively parallel hardware platforms, as well as improvement and availability of state-of-the-art high-performance computing infrastructure successively increases both the range of accessible systems as well as the calculation accuracy, the extend of *treatable* physical effects and material properties, respectively. The successive increase in system size also allows to investigate low-dimensional nanomaterials with increasingly complex topological properties or disordered network morphologies of soft matter and solid-state modifications. In light of modeling fundamental optical response properties, the thorough combination of lattice dynamics with many-body perturbation theory is essential to treat exciton-phonon interactions coupling the exciton dynamics to lattice distortions and allowing for a comprehensive prediction of nanomaterial properties at ambient conditions.

Following the track record of the publications constituting the present thesis, the modification of the atomic structure and chemical composition of semiconducting materials alters basic characteristics of the electronic structure and optical response in a complex but comprehendible as well as reproducible way. The analytic derivation of fundamental structure-function correlations from first-principles simulations proves to be a highly valuable tool to gain insights beyond pure experimental observation. On side of the semiconducting group-III nitrides, computationally demanding simulations of strained offsets, throughout the entire composition ranges of ternary and multi-component group-III nitrides are desirable to verify the presence as well as the conditions of type-I–type-II transitions in the strained band offsets of, e.g., *zb*-$Al_xGa_{1-x}N$ / $Al_yGa_{1-y}N$ heterostructures. Also the universal validity of the observed trends in structure-function correlations beyond prototypical oxide semiconductors still remains an open question. From the results above, the local coordination environment, the formation of a particular coordination polyhedra-type respectively, clearly seems to be the fundamental parameter determining a material's optical response for non-vitreous amorphous semiconductor as Ti_2O, while medium-range (dis)order adds some broadening and modulation. In contrast, the outstanding oxide-glass former Si_2O preserves its short-range order but contains extensive (dis)order features within its medium-range order. The systematic screening of major classes of disordered amorphous and glass-forming materials might form the basis to extend, refine and generalize observed trends in structure-function correlations, unmasking the fundamental roles of different order scales and their association with a materials glass-forming *ability*. Beyond the static view on structural properties, the inclusion of lattice dynamics will be essential to extend the discrete view on structure-function correlations towards a dynamic atomic structure theory of the thermodynamic properties of disordered materials in their amorphous states, in general, and the vitreous sate, in particular. Understanding the basic correlations between the inherent atomic structure of matter and emerging physical properties on various length scales exhibits a vast potential for both promoting the development of advanced functional (nano)materials with tailored physicochemical characteristics as well as throwing light on open fundamental questions of materials science.

Hofstadter's Law: It always takes longer than you expect,
even when you take into account Hofstadter's Law.
Douglas R. Hofstadter (1945 –)

Summary

The present thesis provides a broadly based outline of basic correlations between the microscopic atom structure and their emerging macroscopic electronic and optical properties in functional semiconducting materials as the group-III nitride family or binary and ternary mixed (transition-) metal oxides. The appealing quality of these material classes is their diverse structure polymorphism providing basic model systems to study the structure polymorphism of bulk modifications, the chemical disorder in mixed alloys, and structurally disordered amorphous networks, each showing unique examples of structure-function correlations. In addition, the effects of surface and interface formation have been treated on equal footing, numerically. A combination of the strengths of various methodologies by weighting their accuracies against their computational demands, is necessary to enable systematic numerical studies on correlations between material properties on the microscopic and macroscopic scale for diverse systems.

In recent past, density functional theory has become the method of choice to study fundamental material properties in computational solid-state physics. For density-functional theory being in a position to provide an accurate, still efficient, tool for providing diverse material characteristics of universal validity, the performance of the manifold approximations to the exchange-correlation energy of Kohn-Sham theory is essential. While modern (semi)local (meta-)generalized-gradient functionals, especially in case of modern parametrizations with a sound emphasize on solid-state properties as AM05 or PBEsol, may provide excellent structural data for fairly simple crystalline geometries as well as the disordered amorphous networks of multicomponent semiconductors, they are severely limited in their basic ability to provide an *exact* numerical description of the electronic structure. Focusing on a sustainable, still manageable, theoretical description of the quasiparticle-band structure, screened Coulomb-potential hybrid functionals are consistently found to provide a notably improved electronic structure and, if adjusted to contain a material specific exact-exchange contribution, to be sufficiently accurate to reach the accuracy of many-body perturbation theory-based quasiparticle theory at a reduced numerical cost still enabling the numerical treatment of amorphous mixed oxide semiconductors or crystalline group-III nitride alloys. Beyond Kohn-Sham theory, the *GW* approximation to many-body perturbation theory provides a computationally expensive still highly accurate approach to calculate an electronic quasiparticle-band structure that provides an excellent description of single-particle excitations in photoelectron spectroscopy. With its general accuracy, the quasiparticle eigenvalues and single-particle orbitals of *GW* theory represent a reference against which lower ranking approximations to the electronic-band structure are benchmarked and/or parametrized. The quasiparticle-band struc-

ture or its approximation by band-gap-understimation-corrected density-functional theory using hybrid functionals with a material specific exact-exchange fraction are an excellent foundation to provide electronic structure features associated with the formation of semiconductor alloys or interfaces as the presence of direct-indirect band-gap crossings or the discontinuities between valence and conduction-bands. Finally, the accurate modeling of a material's optical response proofs to be vastly challenging in terms of computational resources necessary to treat the underlying two-particle excitation processes, accurately, by solution of a Bethe-Salpeter equation for Coulomb-correlated (quasi)electron-(quasi)hole pairs. The inclusion of electron-hole interaction accounts for the gross of missing physics in the independent particle spectra of Kohn-Sham as well as *GW* theory. Thereby, the inclusion of excitonic contributions to the optical response originating from the pair interactions between electrons and holes strongly modifies the adsorption onset by (re)correcting the overcompensation of optical band-gaps underestimation in single-(quasi)particle theories. In the same way, the characteristic exciton peaks around the absorption onset as well as the spectral weight distributions across the energy spectrum are modeled in excellent agreement to experimental reference data as exemplified for diverse TiO_2 modifications. Likewise, the Bethe-Salpeter equation approach allows for a rigorous analysis of surface-state-induced contributions to the optical anisotropy spectra of semiconductor surfaces as imaged in reflection-anisotropy spectroscopy, experimentally.

The combined density-functional theory and many-body perturbation-theory study of the microscopic structure of diverse TiO_2 polymorphs allows to identify traces of the octahedral short-range order in their electronic structure and optical response. In contrast to the very few discrete coordination numbers in the crystalline state, the coordination number distribution of disordered material phases varies around the crystal-like coordination peaks. The basic functional structure units in the amorphous state are distorted versions of crystal-like high-symmetry clusters as well as minor contributions from *novel* coordination units and states atypical to thermodynamically stable bulk polymorphs but to some extend present in e.g. high-pressure modifications. The ubiquitous random distortions in the amorphous oxide phase provide basic broadening effects in the electronic density of states or optical response as well as the occurrence of characteristic band-tail states reaching into the forbidden-energy range of crystalline polymorphs and showing strong localization characteristics around the valence and conduction-band edges. Changes in the atomic coordination state as well as the formation of novel types of fundamental coordination geometries are identified as the origin of optical response contributions absent in the absorption spectra of naturally occurring bulk polymorphs. This highlights how the spectral distribution in the macroscopic optical response of amorphous TiO_2 phases allows to infer on fundamental atomic structure characteristics, directly, revealing the study of structure polymorphism in the crystalline state an essential prerequisite for an estimation of material characteristics in disordered material modifications at a favorable numerical cost by performing systematic averages and by identifying common and diverse short-range order characteristics. The ab initio study of mixed silica-titania alloys provides fundamental insides into the atomic structure of disordered materials highlighting

the formation of unconventional fivefold coordination-units in mixed tetrahedral-octahedral oxide complexes as an essential intermediate coordination state to understand the macroscopic alloy properties. These intermediate coordination states contemporaneously act as a network-forming as well as network-modifying species for the vitreous SiO_2-dominant low-coordination frameworks of a-$Ti_xSi_{1-x}O_2$ oxides and become a major component in the amorphous high-coordination state of TiO_2-rich a-$Ti_xSi_{1-x}O_2$ oxide alloys.

In sum, the state-of-the-art density-functional theory as well as many-body perturbation-theory studies contributing to the present thesis exemplarily illustrate how atomistic simulations on functional sub-units and model systems allow to gain fundamental insights into structure formation processes on atomic length scale and the emerging material properties of rather complex-material modifications advancing our current understanding of structure-function correlations in novel technological (nano)materials.

Bibliography

[1] HOHENBERG, P. ; KOHN, W.: Inhomogeneous Electron Gas. In: *Phys. Rev.* 136 (1964), S. B864–B871

[2] KOHN, W. ; SHAM, L. J.: Self-Consistent Equations Including Exchange and Correlation Effects. In: *Phys. Rev.* 140 (1965), S. A1133–A1138

[3] WAN, Xiangang ; TURNER, Ari M. ; VISHWANATH, Ashvin ; SAVRASOV, Sergey Y.: Topological semimetal and Fermi-arc surface states in the electronic structure of pyrochlore iridates. In: *Phys. Rev. B* 83 (2011), S. 205101

[4] HUANG, Shin-Ming ; XU, Su-Yang ; BELOPOLSKI, Ilya ; LEE, Chi-Cheng ; CHANG, Guoqing ; WANG, BaoKai ; ALIDOUST, Nasser ; BIAN, Guang ; NEUPANE, Madhab ; ZHANG, Chenglong ; JIA, Shuang ; BANSIL, Arun ; LIN, Hsin ; HASAN, M. Z.: A Weyl Fermion semimetal with surface Fermi arcs in the transition metal monopnictide TaAs class. In: *Nature Communications* 6 (2014), S. 7373

[5] YANG, Lexian ; LIU, Zhongkai ; SUN, Yan ; PENG, Han ; YANG, Haifeng ; ZHANG, Teng ; ZHOU, Bo ; ZHANG, Yi ; GUO, Yanfeng ; RAHN, Marein ; PRABHAKARAN, Dharmalingam ; HUSSAIN, Zahid ; MO, Sung-Kwan ; FELSER, Claudia ; YAN, Binghai ; CHEN, Yulin: Discovery of a Weyl Semimetal in non-Centrosymmetric Compound TaAs. In: *arXiv:1507.00521* (2015), S. 1–7

[6] XU, Su-Yang ; BELOPOLSKI, Ilya ; ALIDOUST, Nasser ; NEUPANE, Madhab ; BIAN, Guang ; ZHANGA, Chenglong ; SANKAR, Raman ; CHANG, Guoqing ; YUAN, Zhujun ; LEE, Chi-Cheng ; HUANG, Shin-Ming ; ZHENG, Hao ; MA, Jie ; SANCHEZ, Daniel S. ; BAOKAI WANG AND, Arun B. ; CHOU, Fangcheng ; SHIBAYEV, Pavel P. ; HSIN LIN AND, Shuang J. ; HASAN, M. Z.: Discovery of a Weyl fermion semimetal and topological Fermi arcs. In: *Science* 349 (2015), S. 613–617

[7] YANG, Shengyuan A.: Dirac and Weyl Materials: Fundamental Aspects and Some Spintronics Applications. In: *SPIN* 06 (2016), S. 1640003

[8] SHARMA, Girish ; GOSWAMI, Pallab ; TEWARI, Sumanta: Nernst and magnetothermal conductivity in a lattice model of Weyl fermions. In: *Phys. Rev. B* 93 (2016), S. 035116

[9] PARIARI, A. ; MANDAL, P: Coexistence of topological Dirac fermions on the surface and three-dimensional Dirac cone state in the bulk of $ZrTe_5$ single crystal. In: *Scientific Reports* 7 (2017), S. 40327

[10] OSADA, Minoru ; SASAKI, Takayoshi: Two-Dimensional Dielectric Nanosheets: Novel Nanoelectronics From Nanocrystal Building Blocks. In: *Advanced Materials* 24 (2012), S. 210–228

[11] GAO, Guanhui ; GAO, Wei ; CANNUCCIA, E. ; TAHA-TIJERINA, Jaime ; BALICAS, Luis ; MATHKAR, Akshay ; NARAYANAN, T. N. ; LIU, Zhen ; GUPTA, Bipin K. ; PENG, Juan ; YIN, Yansheng ; RUBIO, Angel ; AJAYAN, Pulickel M.: Artificially Stacked Atomic Layers: Toward New van der Waals Solids. In: *Nano Letters* 12 (2012), Nr. 7, S. 3518–3525

[12] XU, Mingsheng ; LIANG, Tao ; SHI, Minmin ; CHEN, Hongzheng: Graphene-Like Two-Dimensional Materials. In: *Chemical Reviews* 113 (2013), S. 3766–3798

[13] NICOLOSI, Valeria ; CHHOWALLA, Manish ; KANATZIDIS, Mercouri G. ; STRANO, Michael S. ; COLEMAN, Jonathan N.: Liquid Exfoliation of Layered Materials. In: *Science* 340 (2013), Nr. 6139

[14] ZHANG, Xiaodong ; XIE, Yi: Recent advances in free-standing two-dimensional crystals with atomic thickness: design, assembly and transfer strategies. In: *Chem. Soc. Rev.* 42 (2013), S. 8187–8199

[15] LIN, Yu-Chuan ; LU, Ning ; PEREA-LOPEZ, Nestor ; LI, Jie ; LIN, Zhong ; PENG, Xin ; LEE, Chia H. ; SUN, Ce ; CALDERIN, Lazaro ; BROWNING, Paul N. ; BRESNEHAN, Michael S. ; KIM, Moon J. ; MAYER, Theresa S. ; TERRONES, Mauricio ; ROBINSON, Joshua A.: Direct Synthesis of van der Waals Solids. In: *ACS Nano* 8 (2014), Nr. 4, S. 3715–3723

[16] WITHERS, F. ; DEL POZO-ZAMUDIO, O. ; MISHCHENKO, A. ; ROONEY, A. P. ; GHOLINIA, A. ; WATANABE, K. ; TANIGUCHI, T. ; HAIGH, S. J. ; GEIM, A. K. ; TARTAKOVSKII, A. I. ; NOVOSELOV, K. S.: Light-emitting diodes by band-structure engineering in van der Waals heterostructures. In: *Nature Materials* (doi:10.1038/nmat4205, 2015)

[17] BARLOW, S.M. ; RAVAL, R.: Complex organic molecules at metal surfaces: bonding, organisation and chirality. In: *Surface Science Reports* 50 (2003), S. 201 – 341

[18] HERMANN, B. A. ; ROHR, C. ; BALBÁS GAMBRA, M. ; MALECKI, A. ; MALAREK, M. S. ; FREY, E. ; FRANOSCH, T.: Molecular self-organization: Predicting the pattern diversity and lowest energy state of competing ordering motifs. In: *Phys. Rev. B* 82 (2010), S. 165451

[19] MISAWA, Takahiro ; IMADA, Masatoshi: Superconductivity and its mechanism in an ab initio model for electron-doped LaFeAsO. In: *Nature Communications* 5 (2014), S. 5738

[20] LINSCHEID, A. ; SANNA, A. ; ESSENBERGER, F. ; GROSS, E. K. U.: *Ab initio* theory of superconductivity in a magnetic field. I. Spin density functional theory for superconductors and Eliashberg equations. In: *Phys. Rev. B* 92 (2015), S. 024505

[21] LINSCHEID, A. ; SANNA, A. ; GROSS, E. K. U.: *Ab initio* theory of superconductivity in a magnetic field. II. Numerical solution. In: *Phys. Rev. B* 92 (2015), S. 024506

[22] ANGELIS, Filippo D. ; FANTACCI, Simona ; SELLONI, Annabella: Alignment of the dye's molecular levels with the TiO_2 band edges in dye-sensitized solar cells: a DFT–TDDFT study. In: *Nanotechnology* 19 (2008), S. 424002

[23] ASSMANN, Elias ; BLAHA, Peter ; LASKOWSKI, Robert ; HELD, Karsten ; OKAMOTO, Satoshi ; SANGIOVANNI, Giorgio: Oxide Heterostructures for Efficient Solar Cells. In: *Phys. Rev. Lett.* 110 (2013), S. 078701

[24] NASHED, Ramy ; ISMAIL, Yehea ; ALLAM, Nageh K.: Recent advances in the use of density functional theory to design efficient solar energy-based renewable systems. In: *Journal of Renewable and Sustainable Energy* 5 (2013), S. 022701

[25] HEYD, Jochen ; SCUSERIA, Gustavo E.: Efficient hybrid density functional calculations in solids: Assessment of the Heyd-Scuseria-Ernzerhof screened Coulomb hybrid functional. In: *The Journal of Chemical Physics* 121 (2004), S. 1187–1192

[26] HUMMER, Kerstin ; HARL, Judith ; KRESSE, Georg: Heyd-Scuseria-Ernzerhof hybrid functional for calculating the lattice dynamics of semiconductors. In: *Phys. Rev. B* 80 (2009), S. 115205

[27] HEDIN, Lars: New Method for Calculating the One-Particle Green's Function with Application to the Electron-Gas Problem. In: *Phys. Rev.* 139 (1965), S. A796–A823

[28] HEDIN, L. ; LUNDQVIST, S.: Effects of Electron-Electron and Electron-Phonon Interactions on the One-Electron States of Solids. In: SEITZ, F. (Hrsg.) ; TURNBULL, D. (Hrsg.) ; EHRENREICH, H. (Hrsg.): *Solid state physics* Bd. 23. Academic, New York, 1969, S. 1–181

[29] STOLZ, H.: *Einführung in die Vielteilchentheorie der Kristalle*. Academie-Verlag, Berlin, 1974

[30] DEL SOLE, R. ; FIORINO, E.: Macroscopic dielectric tensor at crystal surfaces. In: *Phys. Rev. B* 29 (1984), S. 4631–4645

[31] LANDMANN, M. ; KÖHLER, T. ; KÖPPEN, S. ; RAULS, E. ; FRAUENHEIM, T. ; SCHMIDT, W. G.: Fingerprints of order and disorder in the electronic and optical properties of crystalline and amorphous TiO_2. In: *Phys. Rev. B* 86 (2012), S. 064201

[32] LANDMANN, M ; KÖHLER, T ; RAULS, E ; FRAUENHEIM, T ; SCHMIDT, W G.: The atomic structure of ternary amorphous $Ti_xSi_{1-x}O_2$ hybrid oxides. In: *Journal of Physics: Condensed Matter* 26 (2014), Nr. 25, S. 253201

[33] LANDMANN, M. ; RAULS, E. ; SCHMIDT, W. G. ; RÖPPISCHER, Marcus ; COBET, Christoph ; ESSER, Norbert ; SCHUPP, Thorsten ; AS, Donat J. ; FENEBERG, Martin ; GOLDHAHN, Rüdiger: Transition energies and direct-indirect band gap crossing in zinc-blende $Al_xGa_{1-x}N$. In: *Phys. Rev. B* 87 (2013), S. 195210

[34] LANDMANN, M ; RAULS, E ; SCHMIDT, W G. ; NEUMANN, M D. ; SPEISER, E ; ESSER, N: GaN m-plane: Atomic structure, surface bands and optical response. In: *Phys. Rev. B* 91 (2015), S. 035302

[35] LANDMANN, M. ; RAULS, E. ; SCHMIDT, W. G.: Understanding band alignments in semiconductor heterostructures: Composition dependence and type-I–type-II transition of natural band offsets in nonpolar zinc-blende $Al_xGa_{1-x}N/Al_yGa_{1-y}N$ composites. In: *Phys. Rev. B* 95 (2017), S. 155310

[36] GOODEVE, C. F. ; KITCHENER, J. A.: The mechanism of photosensitisation by solids. In: *Trans. Faraday Soc.* 34 (1938), S. 902–908

[37] HASHIMOTO, Kazuhito ; IRIE, Hiroshi ; FUJISHIMA, Akira: TiO_2 Photocatalysis: A Historical Overview and Future Prospects. In: *Japanese Journal of Applied Physics* 44 (2005), S. 8269

[38] FUJISHIMA, Akira ; HANDA, Kenichi: Electrochemical Photolysis of Water at a Semiconductor Electrode. In: *Nature* 238 (1972), S. 37–38

[39] FUJISHIMA, Akira ; ZHANG, Xintong ; TRYK, Donald A.: TiO_2 photocatalysis and related surface phenomena. In: *Surface Science Reports* 63 (2008), S. 515 – 582

[40] SCHNEIDER, Jenny ; MATSUOKA, Masaya ; TAKEUCHI, Masato ; ZHANG, Jinlong ; HORIUCHI, Yu ; ANPO, Masakazu ; BAHNEMANN, Detlef W.: Understanding TiO_2 Photocatalysis: Mechanisms and Materials. In: *Chemical Reviews* 114 (2014), S. 9919–9986

[41] DELOACH, J. D. ; SCAREL, G. ; AITA, C. R.: Correlation between titania film structure and near ultraviolet optical absorption. In: *Journal of Applied Physics* 85 (1999), S. 2377–2384

[42] DACHILLE, Frank ; SIMONS, P. Y. ; ROY, Rustum: Pressure-temperature studies of anatase, brookite, rutile and TiO_2-II. In: *American Mineralogist* 53 (1968), S. 1929–1939

[43] ZHANG, Hengzhong ; BANFIELD, JillianF.: New kinetic model for the nanocrystalline anatase-to-rutile transformation revealing rate dependence on number of particles. In: *American Mineralogist* 84 (1999), S. 528–535

[44] ZHANG, Hengzhong ; BANFIELD, Jillian F.: Understanding Polymorphic Phase Transformation Behavior during Growth of Nanocrystalline Aggregates: Insights from TiO_2. In: *The Journal of Physical Chemistry B* 104 (2000), S. 3481–3487

[45] RANADE, M. R. ; NAVROTSKY, A. ; ZHANG, H. Z. ; BANFIELD, J. F. ; ELDER, S. H. ; ZABAN, A. ; BORSE, P. H. ; KULKARNI, S. K. ; DORAN, G. S. ; WHITFIELD, H. J.: Energetics of nanocrystalline TiO_2. 99 (2002), S. 6476–6481

[46] ZHANG, Hengzhong ; BANFIELD, Jillian F.: Polymorphic Transformations and Particle Coarsening in Nanocrystalline Titania Ceramic Powders and Membranes. In: *The Journal of Physical Chemistry C* 111 (2007), S. 6621–6629

[47] ZHANG, Hengzhong ; F. BANFIELD, Jillian: Thermodynamic analysis of phase stability of nanocrystalline titania. In: *J. Mater. Chem.* 8 (1998), S. 2073–2076

[48] ZHANG, Hengzhong ; ; BANFIELD, Jillian F.: Understanding Polymorphic Phase Transformation Behavior during Growth of Nanocrystalline Aggregates: Insights from TiO_2. In: *The Journal of Physical Chemistry B* 104 (2000), S. 3481–3487

[49] OHNO, Teruhisa ; SARUKAWA, Koji ; TOKIEDA, Kojiro ; MATSUMURA, Michio: Morphology of a TiO_2 Photocatalyst (Degussa, P-25) Consisting of Anatase and Rutile Crystalline Phases. In: *Journal of Catalysis* 203 (2001), S. 82 – 86

[50] HURUM, Deanna C. ; AGRIOS, Alexander G. ; GRAY, Kimberly A. ; RAJH, Tijana ; THURNAUER, Marion C.: Explaining the Enhanced Photocatalytic Activity of Degussa P25 Mixed-Phase TiO_2 Using EPR. In: *The Journal of Physical Chemistry B* 107 (2003), S. 4545–4549

[51] OHTANI, B. ; PRIETO-MAHANEY, O.O. ; LI, D. ; ABE, R.: What is Degussa (Evonik) P25? Crystalline composition analysis, reconstruction from isolated pure particles and photocatalytic activity test. In: *Journal of Photochemistry and Photobiology A: Chemistry* 216 (2010), S. 179 – 182

[52] SHIRAISHI, Yasuhiro ; HIRAKAWA, Hiroaki ; TOGAWA, Yoshiki ; SUGANO, Yoshitsune ; ICHIKAWA, Satoshi ; HIRAI, Takayuki: Rutile Crystallites Isolated from Degussa (Evonik) P25 TiO_2: Highly Efficient Photocatalyst for Chemoselective Hydrogenation of Nitroaromatics. In: *ACS Catalysis* 3 (2013), S. 2318–2326

[53] MARCHAND, René ; BROHAN, Luc ; TOURNOUX, Michel: TiO_2(B) a new form of titanium dioxide and the potassium octatitanate {K2Ti8O17}. In: *Materials Research Bulletin* 15 (1980), S. 1129 – 1133

[54] BANFIELD, Jillian F. ; VEBLEN, David R.: Conversion of perovskite to anatase and TiO_2(B): A TEM study and the use of fundamental building blocks for understanding relationships among the TiO_2 minerals. In: *American Mineralogist* 77 (1992), S. 545–557

[55] LATROCHE, M. ; BROHAN, L. ; MARCHAND, R. ; TOURNOUX, M.: New hollandite oxides: TiO_2(H) and $K_{0.06}TiO_2$. In: *Journal of Solid State Chemistry* 81 (1989), Nr. 1, S. 78 – 82

[56] AKIMOTO, J. ; GOTOH, Y. ; OOSAWA, Y. ; NONOSE, N. ; KUMAGAI, T. ; AOKI, K. ; TAKEI, H.: Topotactic Oxidation of Ramsdellite-Type $Li_{0.5}TiO_2$, a New Polymorph of Titanium Dioxide: TiO_2(R). In: *Journal of Solid State Chemistry* 113 (1994), S. 27 – 36

[57] SIMONS, P. Y. ; DACHILLE, F.: The structure of TiO_2II, a high-pressure phase of TiO_2. In: *Acta Crystallographica* 23 (1967), S. 334–336

[58] HAINES, Julian ; LÉGER, J.M.: X-ray diffraction study of TiO_2 up to 49 GPa. In: *Physica B: Condensed Matter* 192 (1993), S. 233 – 237

[59] LAGAREC, Ken ; DESGRENIERS, Serge: Raman study of single crystal anatase TiO_2 up to 70 {GPa}. In: *Solid State Communications* 94 (1995), S. 519 – 524

[60] SATO, H. ; ENDO, S. ; SUGIYAMA, M. ; KIKEGAWA, T. ; SHIMOMURA, O. ; KUSABA, K.: Baddeleyite-Type High-Pressure Phase of TiO_2. In: *Science* 251 (1991), S. 786–788

[61] DUBROVINSKAIA, Natalia A. ; DUBROVINSKY, Leonid S. ; AHUJA, Rajeev ; PROKOPENKO, Vitaly B. ; DMITRIEV, V. ; WEBER, H.-P. ; OSORIO-GUILLEN, J. M. ; JOHANSSON, Börje: Experimental and Theoretical Identification of a New High-Pressure TiO_2 Polymorph. In: *Phys. Rev. Lett.* 87 (2001), S. 275501

[62] DUBROVINSKY, L. S. ; DUBROVINSKAIA, N. A. ; SWAMY, V. ; MUSCAT, J. ; HARRISON, N. M. ; AHUJA, R. ; HOLM, B. ; JOHANSSON, B.: Materials science: The hardest known oxide. In: *Nature* 410 (2001), S. 653–654

[63] MATTESINI, M. ; ALMEIDA, J. S. ; DUBROVINSKY, L. ; DUBROVINSKAIA, N. ; JOHANSSON, B. ; AHUJA, R.: High-pressure and high-temperature synthesis of the cubic TiO_2 polymorph. In: *Phys. Rev. B* 70 (2004), S. 212101

[64] KIM, D. Y. ; ALMEIDA, J. S. ; KOČI, L. ; AHUJA, R.: Dynamical stability of the hardest known oxide and the cubic solar material: TiO_2. In: *Applied Physics Letters* 90 (2007), S. 171903

[65] ZHOU, Xiang-Feng ; DONG, Xiao ; QIAN, Guang-Rui ; ZHANG, Lixin ; TIAN, Yonjun ; WANG, Hui-Tian: Unusual compression behavior of TiO_2 polymorphs from first principles. In: *Phys. Rev. B* 82 (2010), S. 060102

[66] ABBASNEJAD, M. ; MOHAMMADIZADEH, M. R. ; MAEZONO, R.: Structural, electronic, and dynamical properties of Pca21-TiO_2 by first principles. In: *EPL (Europhysics Letters)* 97 (2012), S. 56003

[67] Wu, Xiang ; Holbig, Eva ; Steinle-Neumann, Gerd: Structural stability of TiO_2 at high pressure in density-functional theory based calculations. In: *Journal of Physics: Condensed Matter* 22 (2010), S. 295501

[68] Dekura, Haruhiko ; Tsuchiya, Taku ; Kuwayama, Yasuhiro ; Tsuchiya, Jun: Theoretical and Experimental Evidence for a New Post-Cotunnite Phase of Titanium Dioxide with Significant Optical Absorption. In: *Phys. Rev. Lett.* 107 (2011), S. 045701

[69] Ding, Yingchun ; Chen, Min ; Wu, Wenjuan: Mechanical properties, hardness and electronic structures of new post-cotunnite phase (Fe_2P-type) of TiO_2. In: *Physica B: Condensed Matter* 433 (2014), S. 48 – 54

[70] Lyle, M. J. ; Pickard, C. J. ; Needs, R. J.: Prediction of 10-fold coordinated TiO_2 and SiO_2 structures at multimegabar pressures. In: *Proceedings of the National Academy of Sciences of the United States of America* 112 (2015), S. 6898–6901

[71] Manzini, I ; Antonioli, G ; Bersani, D ; Lottici, P.P ; Gnappi, G ; Montenero, A: X-ray absorption spectroscopy study of crystallization processes in sol-gel-derived TiO_2. In: *Journal of Non-Crystalline Solids* 192–193 (1995), S. 519 – 523

[72] Petkov, V ; Holzhüter, G ; Tröge, U ; Gerber, Th ; Himmel, B: Atomic-scale structure of amorphous TiO_2 by electron, X-ray diffraction and reverse Monte Carlo simulations. In: *Journal of Non-Crystalline Solids* 231 (1998), S. 17 – 30

[73] Reyes-Coronado, D ; Rodríguez-Gattorno, G ; Espinosa-Pesqueira, M E. ; Cab, C ; Coss, R de ; Oskam, G: Phase-pure TiO_2 nanoparticles: anatase, brookite and rutile. In: *Nanotechnology* 19 (2008), S. 145605

[74] Verduzco, Jennifer M. ; Chung, Haemi ; Hu, Chunhua ; Choe, Wonyoung: Metal-Organic Framework Assembled from T-Shaped and Octahedral Nodes: A Mixed-Linker Strategy To Create a Rare Anatase TiO_2 Topology. In: *Inorganic Chemistry* 48 (2009), S. 9060–9062

[75] Landmann, M ; Rauls, E ; Schmidt, W G.: The electronic structure and optical response of rutile, anatase and brookite TiO_2. In: *Journal of Physics: Condensed Matter* 24 (2012), Nr. 19, S. 195503

[76] Amtout, A. ; Leonelli, R.: Optical properties of rutile near its fundamental band gap. In: *Phys. Rev. B* 51 (1995), S. 6842–6851

[77] Pascual, J. ; Camassel, J. ; Mathieu, H.: Fine structure in the intrinsic absorption edge of TiO_2. In: *Phys. Rev. B* 18 (1978), S. 5606–5614

[78] Tang, H. ; Lévy, F. ; Berger, H. ; Schmid, P. E.: Urbach tail of anatase TiO_2. In: *Phys. Rev. B* 52 (1995), S. 7771–7774

[79] Mattsson, A. ; Österlund, L.: Adsorption and Photoinduced Decomposition of Acetone and Acetic Acid on Anatase, Brookite, and Rutile TiO_2 Nanoparticles. In: *The Journal of Physical Chemistry C* 114 (2010), S. 14121–14132

[80] Kong, X. G. ; Yu, Y. ; Gao, T.: Electronic excitation energies in TiO_2 in the fluorite phase. In: *The European Physical Journal B* 76 (2010), S. 365–371. – ISSN 1434–6028

[81] Mattesini, M. ; Almeida, J. S. ; Dubrovinsky, L. ; Dubrovinskaia, N. ; Johansson, B. ; Ahuja, R.: Cubic TiO_2 as a potential light absorber in solar-energy conversion. In: *Phys. Rev. B* 70 (2004), S. 115101

[82] Zhu, Tong ; Gao, Shang-Peng: The Stability, Electronic Structure, and Optical Property of TiO_2 Polymorphs. In: *The Journal of Physical Chemistry C* 118 (2014), S. 11385–11396

[83] Ariga, Hiroko ; Taniike, Toshiaki ; Morikawa, Harumo ; Tada, Mizuki ; Min, Byoung K. ; Watanabe, Kazuya ; Matsumoto, Yoshiyasu ; Ikeda, Susumu ; Saiki, Koichiro ; Iwasawa, Yasuhiro: Surface-Mediated Visible-Light Photo-oxidation on Pure TiO_2(001). In: *Journal of the American Chemical Society* 131 (2009), S. 14670–14672

[84] Tao, Junguang ; Luttrell, Tim ; Batzill, Matthias: A two-dimensional phase of TiO_2 with a reduced bandgap. In: *Nature Chemistry* 3 (2010), S. 296–300

[85] Ariga, H. ; Taniike, T. ; Morikawa, H. ; Tero, R. ; Kondoh, H. ; Iwasawa, Y.: Lattice-work structure of a TiO_2(001) surface studied by STM, core-level spectroscopies and DFT calculations. In: *Chemical Physics Letters* 454 (2008), S. 350 – 354

[86] Chen, Xiaobo ; Mao, Samuel S.: Titanium Dioxide Nanomaterials: Synthesis, Properties, Modifications, and Applications. In: *Chemical Reviews* 107 (2007), S. 2891–2959

[87] Farhangi, Nasrin ; Chowdhury, Rajib R. ; Medina-Gonzalez, Yaocihuatl ; Ray, Madhumita B. ; Charpentier, Paul A.: Visible light active Fe doped TiO_2 nanowires grown on graphene using supercritical CO_2. In: *Applied Catalysis B: Environmental* 110 (2011), Nr. 0, S. 25 – 32. – ISSN 0926–3373

[88] Su, Ren ; Bechstein, Ralf ; Kibsgaard, Jakob ; Vang, Ronnie T. ; Besenbacher, Flemming: High-quality Fe-doped TiO_2 films with superior visible-light performance. In: *J. Mater. Chem.* 22 (2012), S. 23755–23758

[89] Sheppard, Leigh R. ; Hager, Simon ; Holik, John ; Liu, Rong ; Macartney, Sam ; Wuhrer, Richard: Tantalum Segregation in Ta-Doped TiO_2 and the Related Impact on Charge Separation during Illumination. In: *The Journal of Physical Chemistry C* 119 (2015), Nr. 1, S. 392–400

[90] ASAHI, R. ; TAGA, Y. ; MANNSTADT, W. ; FREEMAN, A. J.: Electronic and optical properties of anatase TiO_2. In: *Phys. Rev. B* 61 (2000), S. 7459–7465

[91] KHAN, Shahed U. M. ; AL-SHAHRY, Mofareh ; INGLER, William B.: Efficient Photochemical Water Splitting by a Chemically Modified n-TiO_2. In: *Science* 297 (2002), S. 2243–2245

[92] NIE, Xiliang ; ZHUO, Shuping ; MAENG, Gloria ; SOHLBERG, Karl: Doping of TiO_2 Polymorphs for Altered Optical and Photocatalytic Properties. In: *International Journal of Photoenergy* 2009 (2009), S. 294042

[93] WANG, Gongming ; WANG, Hanyu ; LING, Yichuan ; TANG, Yuechao ; YANG, Xunyu ; FITZMORRIS, Robert C. ; WANG, Changchun ; ZHANG, Jin Z. ; LI, Yat: Hydrogen-Treated TiO_2 Nanowire Arrays for Photoelectrochemical Water Splitting. In: *Nano Letters* 11 (2011), Nr. 7, S. 3026–3033

[94] XIA, Ting ; ZHANG, Chi ; OYLER, Nathan A. ; CHEN, Xiaobo: Hydrogenated TiO_2 Nanocrystals: A Novel Microwave Absorbing Material. In: *Advanced Materials* 25 (2013), Nr. 47, S. 6905–6910

[95] YAN, Hui ; WANG, Xudong ; YAO, Man ; YAO, Xiaojie: Band structure design of semiconductors for enhanced photocatalytic activity: The case of TiO_2. In: *Progress in Natural Science: Materials International* 23 (2013), Nr. 4, S. 402 – 407

[96] LU, Haiqiang ; ZHAO, Binbin ; PAN, Ruili ; YAO, Jianfeng ; QIU, Jianhao ; LUO, Li ; LIU, Yacong: Safe and facile hydrogenation of commercial Degussa P25 at room temperature with enhanced photocatalytic activity. In: *RSC Adv.* 4 (2014), S. 1128–1132

[97] DASHORA, Alpa ; PATEL, N. ; KOTHARI, D.C. ; AHUJA, B.L. ; MIOTELLO, A.: Formation of an intermediate band in the energy gap of TiO_2 by Cu–N-codoping: First principles study and experimental evidence. In: *Solar Energy Materials and Solar Cells* 125 (2014), S. 120 – 126

[98] CHOI, Wonyong ; TERMIN, Andreas ; HOFFMANN, Michael R.: The Role of Metal Ion Dopants in Quantum-Sized TiO_2: Correlation between Photoreactivity and Charge Carrier Recombination Dynamics. In: *The Journal of Physical Chemistry* 98 (1994), S. 13669–13679

[99] O'REGAN, Brian ; GRÄTZEL, Michael: A low-cost, high-efficiency solar cell based on dye-sensitized colloidal TiO_2 films. In: *Nature* 353 (1991), S. 737–740

[100] BACH, U. ; LUPO, D. ; COMTE, P. ; MOSER, J. E. ; WEISSÖRTEL, F. ; SALBECK, J. ; SPREITZER, H. ; GRÄTZEL, M.: Solid-state dye-sensitized mesoporous TiO_2 solar cells with high photon-to-electron conversion efficiencies. In: *Nature* 395 (1998), S. 583–585

[101] HAGFELDT, Anders ; GRÄTZEL, Michael: Molecular Photovoltaics. In: *Accounts of Chemical Research* 33 (2000), S. 269–277

[102] GRÄTZEL, Michael: Conversion of sunlight to electric power by nanocrystalline dye-sensitized solar cells. In: *Journal of Photochemistry and Photobiology A: Chemistry* 164 (2004), S. 3–14

[103] MATHEW, Simon ; YELLA, Aswani ; GAO, Peng ; HUMPHRY-BAKER, Robin ; E., CurchodBasile F. ; ASHARI-ASTANI, Negar ; TAVERNELLI, Ivano ; ROTHLISBERGER, Ursula ; NAZEERUDDIN ; KHAJA, Md. ; GRÄTZEL, Michael: Dye-sensitized solar cells with 13% efficiency achieved through the molecular engineering of porphyrin sensitizers. In: *Nature Chemistry* 6 (2014), S. 242–247

[104] HSU, L. S. ; RUJKORAKARN, R. ; SITES, J. R. ; SHE, C. Y.: Thermally induced crystallization of amorphous-titania films. In: *Journal of Applied Physics* 59 (1986), S. 3475–3480

[105] ZHANG, Hengzhong ; CHEN, Bin ; BANFIELD, Jillian F. ; WAYCHUNAS, Glenn A.: Atomic structure of nanometer-sized amorphous TiO_2. In: *Phys. Rev. B* 78 (2008), S. 214106

[106] AMOR, S.Ben ; BAUD, G ; BESSE, J.P ; JACQUET, M: Structural and optical properties of sputtered Titania films. In: *Materials Science and Engineering: B* 47 (1997), Nr. 2, S. 110 – 118

[107] DANNENBERG, Rand ; GREENE, Phil: Reactive sputter deposition of titanium dioxide. In: *Thin Solid Films* 360 (2000), S. 122 – 127

[108] AMOR, S.Ben ; GUEDRI, L ; BAUD, G ; JACQUET, M ; GHEDIRA, M: Influence of the temperature on the properties of sputtered titanium oxide films. In: *Materials Chemistry and Physics* 77 (2003), S. 903 – 911

[109] MARDARE, Diana ; RUSU, G.I.: The influence of heat treatment on the optical properties of titanium oxide thin films. In: *Materials Letters* 56 (2002), S. 210 – 214

[110] EUFINGER, K. ; POELMAN, D. ; POELMAN, H. ; GRYSE, R. D. ; MARIN, G.B.: Photocatalytic activity of dc magnetron sputter deposited amorphous TiO_2 thin films. In: *Applied Surface Science* 254 (2007), S. 148 – 152

[111] GOFUKU, E. ; TOYODA, Y. ; UEHARA, Y. ; KOHARA, M. ; NUNOSHITA, M.: Highly conductive TiO_2 thin films prepared by EB-modification. In: *Applied Surface Science* 48 (1991), S. 343 – 350

[112] KIM, S. Y.: Simultaneous determination of refractive index, extinction coefficient, and void distribution of titanium dioxide

thin film by optical methods. In: *Appl. Opt.* 35 (1996), S. 6703–6707

[113] TAKIKAWA, Hirofumi ; MATSUI, Takaaki ; SAKAKIBARA, Tateki ; BENDAVID, Avi ; MARTIN, Philip J.: Properties of titanium oxide film prepared by reactive cathodic vacuum arc deposition. In: *Thin Solid Films* 348 (1999), S. 145 – 151

[114] ZHAO, Z.W ; TAY, B.K ; LAU, S.P ; YU, G.Q: Optical properties of titania films prepared by off-plane filtered cathodic vacuum arc. In: *Journal of Crystal Growth* 268 (2004), S. 543 – 546

[115] LUCA, Vittorio ; DJAJANTI, Samitha ; HOWE, Russell F.: Structural and Electronic Properties of Sol-Gel Titanium Oxides Studied by X-ray Absorption Spectroscopy. In: *The Journal of Physical Chemistry B* 102 (1998), S. 10650–10657

[116] WANG, Zhongchun ; HELMERSSON, Ulf ; KÄLL, Per-Olov: Optical properties of anatase TiO_2 thin films prepared by aqueous sol-gel process at low temperature. In: *Thin Solid Films* 405 (2002), S. 50 – 54

[117] MARDARE, Diana ; HONES, Peter: Optical dispersion analysis of TiO_2 thin films based on variable-angle spectroscopic ellipsometry measurements. In: *Materials Science and Engineering: B* 68 (1999), Nr. 1, S. 42 – 47

[118] ZHANG, Min ; LIN, Guoqiang ; DONG, Chuang ; WEN, Lishi: Amorphous TiO_2 films with high refractive index deposited by pulsed bias arc ion plating. In: *Surface and Coatings Technology* 201 (2007), S. 7252 – 7258

[119] NOWOTNY, J. ; BAK, T. ; BURG, T. ; NOWOTNY, M. K. ; SHEPPARD, L. R.: Effect of Grain Boundaries on Semiconducting Properties of TiO_2 at Elevated Temperatures. In: *The Journal of Physical Chemistry C* 111 (2007), S. 9769–9778

[120] SARKAR, D. ; GHOSH, C.K. ; MAITI, U.N. ; CHATTOPADHYAY, K.K.: Effect of spin polarization on the optical properties of Co-doped TiO_2 thin films. In: *Physica B: Condensed Matter* 406 (2011), S. 1429 – 1435

[121] ZHANG, Hengzhong ; F. BANFIELD, Jillian: Thermodynamic analysis of phase stability of nanocrystalline titania. In: *J. Mater. Chem.* 8 (1998), S. 2073–2076

[122] FERNǴNDEZ-GARCÍA, Marcos ; BELVER, Carolina ; HANSON, Jonathan C. ; WANG, Xianqin ; RODRIGUEZ, José A.: Anatase-TiO_2 Nanomaterials: Analysis of Key Parameters Controlling Crystallization. In: *Journal of the American Chemical Society* 129 (2007), S. 13604–13612

[123] BAUER, Sebastian ; PITTROF, Andreas ; TSUCHIYA, Hiroaki ; SCHMUKI, Patrik: Size-effects in TiO_2 nanotubes: Diameter dependent anatase/rutile stabilization. In: *Electrochemistry Communications* 13 (2011), S. 538 – 541

[124] LEITÃO, E. ; SILVA, R.A. ; BARBOSA, M.A.: Electrochemical and surface modifications on N+-ION implanted $Ti_5Al_{2.5}Fe$ immersed in HBSS. In: *Corrosion Science* 39 (1997), Nr. 2, S. 377 – 383

[125] KARPAGAVALLI, Ramji ; ZHOU, Anhong ; CHELLAMUTHU, Prithiviraj ; NGUYEN, Kytai: Corrosion behavior and biocompatibility of nanostructured TiO_2 film on Ti_6Al_4V. In: *Journal of Biomedical Materials Research Part A* 83A (2007), S. 1087–1095

[126] GLASSFORD, Keith M. ; CHELIKOWSKY, James R.: Structural and electronic properties of titanium dioxide. In: *Phys. Rev. B* 46 (1992), S. 1284–1298

[127] HARDMAN, P. J. ; RAIKAR, G. N. ; MURYN, C. A. ; LAAN, G. van d. ; WINCOTT, P. L. ; THORNTON, G. ; BULLETT, D. W. ; DALE, P. A. D. M. A.: Valence-band structure of TiO_2 along the Γ-Δ- *X* and Γ-Σ- *M* directions. In: *Phys. Rev. B* 49 (1994), S. 7170–7177

[128] MO, Shang-Di ; CHING, W. Y.: Electronic and optical properties of three phases of titanium dioxide: Rutile, anatase, and brookite. In: *Phys. Rev. B* 51 (1995), S. 13023–13032

[129] MIKAMI, Masayoshi ; NAKAMURA, Shinichiro ; KITAO, Osamu ; ARAKAWA, Hironori ; GONZE, Xavier: First-Principles Study of Titanium Dioxide: Rutile and Anatase. In: *Japanese Journal of Applied Physics* 39 (2000), S. L847

[130] CALATAYUD, M. ; MORI-SÁNCHEZ, P. ; BELTRÁN, A. ; MARTÍN PENDÁS, A. ; FRANCISCO, E. ; ANDRÉS, J. ; RECIO, J. M.: Quantum-mechanical analysis of the equation of state of anatase TiO_2. In: *Phys. Rev. B* 64 (2001), S. 184113

[131] MUSCAT, Joseph ; SWAMY, Varghese ; HARRISON, Nicholas M.: First-principles calculations of the phase stability of TiO_2. In: *Phys. Rev. B* 65 (2002), S. 224112

[132] QIANG, Chen ; HONG-HONG, Cao: Ab initio calculations of electronic structure of anatase TiO_2. In: *Chinese Physics* 13 (2004), S. 2121

[133] JING-XIN, Yu ; MIN, Fu ; GUANG-FU, Ji ; XIANG-RONG, Chen: Phase transition and thermodynamic properties of TiO_2 from first-principles calculations. In: *Chinese Physics B* 18 (2009), S. 269

[134] HOSSAIN, Faruque M. ; SHEPPARD, Leigh ; NOWOTNY, Janusz ; MURCH, Graeme E.: Optical properties of anatase and rutile titanium dioxide: Ab initio calculations for pure and anion-doped material. In: *Journal of Physics and Chemistry of Solids* 69 (2008), S. 1820 – 1828

[135] SHOJAEE, E ; MOHAMMADIZADEH, M R.: First-principles elastic and thermal properties of TiO_2 : a phonon approach. In: *Journal of Physics: Condensed Matter* 22 (2010), S. 015401

[136] SILVA, A. Ferreira d. ; PEPE, I. ; SILVA BRASIL, C. S. ; DAVID, Denis G. F. ; SILVA, E. F. ; PERSSON, C. ; LINDGREN, T. ;

ALMEIDA, J. S. ; MOYSES ARAÚJO, C. ; AHUJA, R.: Electronic and optical properties of rutile titanium dioxide. In: *physica status solidi (c)* 1 (2004), S. S241–S244

[137] PERSSON, Clas ; SILVA, Antonio Ferreira d.: Strong polaronic effects on rutile TiO_2 electronic band edges. In: *Applied Physics Letters* 86 (2005), S. 231912

[138] THOMAZI, Fabiano ; ROMAN, Lucimara S. ; SILVA, Antonio Ferreira d. ; PERSSON, Clas: Optical absorption of rutile SnO_2 and TiO_2. In: *physica status solidi (c)* 6 (2009), S. 2740–2742

[139] DASH, L.K. ; BRUNEVAL, Fabien ; TRINITÉ, Virginie ; VAST, Nathalie ; REINING, Lucia: Electronic excitations: Ab initio calculations of electronic spectra and application to zirconia ZrO_2, titania TiO_2 and cuprous oxide Cu_2O. In: *Computational Materials Science* 38 (2007), Nr. 3, S. 482 – 493

[140] LAWLER, H. M. ; REHR, J. J. ; VILA, F. ; DALOSTO, S. D. ; SHIRLEY, E. L. ; LEVINE, Z. H.: Optical to UV spectra and birefringence of SiO_2 and TiO_2: First-principles calculations with excitonic effects. In: *Phys. Rev. B* 78 (2008), S. 205108

[141] CHIODO, L. ; GARCIA-LASTRA, A. J. M.and I. J. M.and Iacomino ; OSSICINI, S. ; ZHAO, J. ; PETEK, H. ; RUBIO, A.: Self-energy and excitonic effects in the electronic and optical properties of TiO_2 crystalline phases. In: *Phys. Rev. B* 82 (2010), S. 045207

[142] THILAGAM, A ; SIMPSON, D J. ; GERSON, A R.: A first-principles study of the dielectric properties of TiO_2 polymorphs. In: *Journal of Physics: Condensed Matter* 23 (2011), S. 025901

[143] KANG, W. ; HYBERTSEN, M. S.: Quasiparticle and optical properties of rutile and anatase TiO_2. In: *Phys. Rev. B* 82 (2010), S. 085203

[144] DIEBOLD, Ulrike: The surface science of titanium dioxide. In: *Surface Science Reports* 48 (2003), S. 53 – 229

[145] DIEBOLD, U. ; RUZYCKI, N. ; HERMAN, G.S. ; SELLONI, A.: One step towards bridging the materials gap: surface studies of TiO_2 anatase. In: *Catalysis Today* 85 (2003), S. 93 – 100

[146] RASMUSSEN, M. D. ; MOLINA, L. M. ; HAMMER, B.: Adsorption, diffusion, and dissociation of molecular oxygen at defected TiO_2(110): A density functional theory study. In: *The Journal of Chemical Physics* 120 (2004), S. 988–997

[147] WENDT, S. ; SCHAUB, R. ; MATTHIESEN, J. ; VESTERGAARD, E.K. ; WAHLSTRÖM, E. ; RASMUSSEN, M.D. ; THOSTRUP, P. ; MOLINA, L.M. ; LÆGSGAARD, E. ; STENSGAARD, I. ; HAMMER, B. ; BESENBACHER, F.: Oxygen vacancies on TiO_2(110) and their interaction with {H_2O} and O_2: A combined high-resolution {STM} and {DFT} study. In: *Surface Science* 598 (2005), S. 226 – 245

[148] GONG, Xue-Qing ; SELLONI, Annabella: First-principles study of the structures and energetics of stoichiometric brookite TiO_2 surfaces. In: *Phys. Rev. B* 76 (2007), S. 235307

[149] SELLONI, Annabella: Crystal growth: Anatase shows its reactive side. In: *Nature Materials* 7 (2008), S. 613–615

[150] GONG, Xue-Qing ; KHORSHIDI, Navid ; STIERLE, Andreas ; VONK, Vedran ; ELLINGER, Claus ; DOSCH, Helmut ; CHENG, Hongzhi ; SELLONI, Annabella ; HE, Yunbin ; DULUB, Olga ; DIEBOLD, Ulrike: The 2×1 reconstruction of the rutile TiO_2(011) surface: A combined density functional theory, X-ray diffraction, and scanning tunneling microscopy study. In: *Surface Science* 603 (2009), S. 138 – 144

[151] MARTINEZ, Umberto ; HAMMER, Björk: Adsorption properties versus oxidation states of rutile TiO_2(110). In: *The Journal of Chemical Physics* 134 (2011), S. 194703

[152] TAUC, J. ; GRIGOROVICI, R. ; VANCU, A.: Optical Properties and Electronic Structure of Amorphous Germanium. In: *physica status solidi (b)* 15 (1966), S. 627–637

[153] TAUC, J. ; MENTH, A. ; WOOD, D. L.: Optical and Magnetic Investigations of the Localized States in Semiconducting Glasses. In: *Phys. Rev. Lett.* 25 (1970), S. 749–752

[154] STATHIS, J.H.: Reliability limits for the gate insulator in CMOS technology. In: *IBM Journal of Research and Development* 46 (2002), March, S. 265–286

[155] BOOGAARD, A. ; KOVALGIN, A.Y. ; WOLTERS, R.A.M.: Net negative charge in low-temperature SiO_2 gate dielectric layers. In: *Microelectronic Engineering* 86 (2009), S. 1707 – 1710

[156] SHROPSHIRE, Joseph ; KEAT, Paul P. ; VAUGHAN, Philip A.: The crystal structure of keatite, a new form of silica. In: *Zeitschrift für Kristallographie - Crystalline Materials* 112 (1959), S. 409–413

[157] MAJ, Slawomir: On the relationship between refractive index and density for SiO_2 polymorphs. In: *Physics and Chemistry of Minerals* 10 (1984), S. 133–136. – ISSN 0342–1791

[158] VASHISHTA, P. ; KALIA, Rajiv K. ; RINO, José P. ; EBBSJÖ, Ingvar: Interaction potential for SiO_2: A molecular-dynamics study of structural correlations. In: *Phys. Rev. B* 41 (1990), S. 12197–12209

[159] LIU, Feng ; GAROFALINI, Stephen H. ; KING-SMITH, Dominic ; VANDERBILT, David: First-principles study of crystalline silica. In: *Phys. Rev. B* 49 (1994), S. 12528–12534

[160] DMITRIEV, V. ; TORGASHEV, V. ; TOLÉDANO, P. ; SALJE, E. K. H.: Theory of SiO_2 polymorphs. In: *EPL (Europhysics Letters)* 37 (1997), S. 553

[161] DEMUTH, Th ; JEANVOINE, Y ; HAFNER, J ; ÁNGYÁN, J G.: Polymorphism in silica studied in the local density and generalized-gradient approximations. In: *Journal of Physics: Condensed Matter* 11 (1999), S. 3833

[162] COH, Sinisa ; VANDERBILT, David: Structural stability and lattice dynamics of SiO_2 cristobalite. In: *Phys. Rev. B* 78 (2008), S. 054117

[163] DIAZ-CABANAS, Maria-Jose ; A. BARRETT, Philip: Synthesis and structure of pure SiO_2 chabazite: the SiO_2 polymorph with the lowest framework density. In: *Chem. Commun.* (1998), S. 1881–1882

[164] LIU, Lin-Gun ; BASSETT, William A. ; SHARRY, John: New high-pressure modifications of GeO_2 and SiO_2. In: *Journal of Geophysical Research: Solid Earth* 83 (1978), S. 2301–2305

[165] TSUCHIDA, Yoshihiko ; YAGI, Takehiko: New pressure-induced transformations of silica at room temperature. In: *Nature* 347 (1990), S. 267–269

[166] HAMANN, D. R.: Generalized Gradient Theory for Silica Phase Transitions. In: *Phys. Rev. Lett.* 76 (1996), S. 660–663

[167] YAMAKATA, Masaaki ; YAGI, Takehiko: New Stishovite-like Phase of Silica formed by Hydrostatic Compression of Cristobalite. In: *Proceedings of the Japan Academy, Series B* 73 (1997), S. 85–88

[168] SEKINE, Tosimori ; AKAISHI, Minoru ; SETAKA, Nobuo: Fe_2N-type SiO_2 from shocked quartz. In: *Geochimica et Cosmochimica Acta* 51 (1987), S. 379 – 381

[169] DUBROVINSKY, L.S ; DUBROVINSKAIA, N.A ; PRAKAPENKA, V ; SEIFERT, F ; LANGENHORST, F ; DMITRIEV, V ; WEBER, H.-P ; BIHAN, T L.: A class of new high-pressure silica polymorphs. In: *Physics of the Earth and Planetary Interiors* 143–144 (2004), S. 231 – 240

[170] KINGMA, KATHLEEN J. ; COHEN, RONALD E. ; HEMLEY, RUSSELL J. ; MAO, HO-KWANG: Transformation of stishovite to a denser phase at lower-mantle pressures. In: *Nature* 374 (1994), S. 243–245

[171] KARKI, B. B. ; WARREN, M. C. ; STIXRUDE, L. ; ACKLAND, G. J. ; CRAIN, J.: Ab initio studies of high-pressure structural transformations in silica. In: *Phys. Rev. B* 55 (1997), S. 3465–3471

[172] TETER, David M. ; HEMLEY, Russell J. ; KRESSE, Georg ; HAFNER, Jürgen: High Pressure Polymorphism in Silica. In: *Phys. Rev. Lett.* 80 (1998), S. 2145–2148

[173] TSE, John S. ; KLUG, Dennis D. ; LE PAGE, Yvon: Novel high pressure phase of silica. In: *Phys. Rev. Lett.* 69 (1992), S. 3647–3649

[174] TSE, John S. ; KLUG, Dennis D. ; ALLAN, Douglas C.: Structure and stability of several high-pressure crystalline polymorphs of silica. In: *Phys. Rev. B* 51 (1995), S. 16392–16395

[175] DUBROVINSKY, L. S. ; SAXENA, S. K. ; LAZOR, P. ; AHUJA, R. ; ERIKSSON, O. ; WILLS, J. M. ; JOHANSSON, B.: Experimental and theoretical identification of a new high-pressure phase of silica. In: *Nature* 388 (1997), S. 362–365

[176] DUBROVINSKY, L. S. ; DUBROVINSKAIA, N. A. ; PRAKAPENKA, V. ; SEIFERT, F. ; LANGENHORST, F. ; DMITRIEV, V. ; WEBER, H.-P. ; BIHAN, T. L.: High-pressure and high-temperature polymorphism in silica. In: *High Pressure Research* 23 (2003), S. 35–39

[177] MEADE, Charles ; HEMLEY, R. J. ; MAO, H. K.: High-pressure x-ray diffraction of SiO_2 glass. In: *Phys. Rev. Lett.* 69 (1992), S. 1387–1390

[178] SATO, Tomoko ; FUNAMORI, Nobumasa: Sixfold-Coordinated Amorphous Polymorph of SiO_2 under High Pressure. In: *Phys. Rev. Lett.* 101 (2008), S. 255502

[179] SATO, Tomoko ; FUNAMORI, Nobumasa: High-pressure structural transformation of SiO_2 glass up to 100 GPa. In: *Phys. Rev. B* 82 (2010), S. 184102

[180] ZEIDLERA, Anita ; SALMONA, Philip S. ; SKINNER, Lawrie B.: Packing and the structural transformations in liquid and amorphous oxides from ambient to extreme conditions. In: *Proceedings of the National Academy of Sciences* 111 (2014), S. 10045–10048

[181] ZEIDLER, Anita ; WEZKA, Kamil ; ROWLANDS, Ruth F. ; WHITTAKER, Dean A. J. ; SALMON, Philip S. ; POLIDORI, Annalisa ; DREWITT, James W. E. ; KLOTZ, Stefan ; FISCHER, Henry E. ; WILDING, Martin C. ; BULL, Craig L. ; TUCKER, Matthew G. ; WILSON, Mark: High-Pressure Transformation of SiO_2 Glass from a Tetrahedral to an Octahedral Network: A Joint Approach Using Neutron Diffraction and Molecular Dynamics. In: *Phys. Rev. Lett.* 113 (2014), S. 135501

[182] MCCOMB, D.W. ; HOWIE, A.: Valence loss spectra from SiO_2 polymorphs of different density. In: *Nuclear Instruments and Methods in Physics Research Section B: Beam Interactions with Materials and Atoms* 96 (1995), S. 569 – 574

[183] CHANG, Eric K. ; ROHLFING, Michael ; LOUIE, Steven G.: Excitons and Optical Properties of α-Quartz. In: *Phys. Rev. Lett.* 85 (2000), S. 2613–2616

[184] KRESSE, G. ; MARSMAN, M. ; HINTZSCHE, L. E. ; FLAGE-LARSEN, E.: Optical and electronic properties of Si_3N_4 and α-SiO_2. In: *Phys. Rev. B* 85 (2012), S. 045205

[185] KEEN, David A. ; DOVE, Martin T.: Local structures of amorphous and crystalline phases of silica, SiO_2, by neutron total scattering. In: *Journal of Physics: Condensed Matter* 11 (1999)

[186] CLARK, Ted M. ; GRANDINETTI, Philip J. ; FLORIAN, Pierre ; STEBBINS, Jonathan F.: Correlated structural distributions in silica glass. In: *Phys. Rev. B* 70 (2004), S. 064202

[187] VAN GINHOVEN, Renée M. ; JÓNSSON, Hannes ; CORRALES, L. R.: Silica glass structure generation for *ab initio* calculations using small samples of amorphous silica. In: *Phys. Rev. B* 71 (2005), S. 024208

[188] MARTÍNEZ, J.R. ; PALOMARES-SNCHEZ, S. ; ORTEGA-ZARZOSA, G. ; RUIZ, Facundo ; CHUMAKOV, Yurii: Rietveld refinement of amorphous SiO_2 prepared via sol-gel method. In: *Materials Letters* 60 (2006), S. 3526 – 3529

[189] NHAN, Nguyen T. ; HUNG, Pham K. ; NGHIEP, Do M. ; KIM, Hyoung S.: Molecular Dynamics Investigation on Microstructure and Void in Amorphous SiO_2. In: *Materials Transactions, JIM* 49 (2008), S. 1212–1218

[190] TAMURA, Tomoyuki ; ISHIBASHI, Shoji ; TANAKA, Shingo ; KOHYAMA, Masanori ; LEE, Ming-Hsien: First-principles analysis of the optical properties of structural disorder in SiO_2 glass. In: *Phys. Rev. B* 77 (2008), S. 085207

[191] MEI, Q. ; BENMORE, C. J. ; SEN, S. ; SHARMA, R. ; YARGER, J. L.: Intermediate range order in vitreous silica from a partial structure factor analysis. In: *Phys. Rev. B* 78 (2008), S. 144204

[192] LI, Neng ; SAKIDJA, Ridwan ; ARYAL, Sitaram ; CHING, Wai-Yim: Densification of a continuous random network model of amorphous SiO_2 glass. In: *Phys. Chem. Chem. Phys.* 16 (2014), S. 1500–1514

[193] HOANG, Vo V.: Molecular Dynamics Simulation of Amorphous SiO_2 Nanoparticles. In: *The Journal of Physical Chemistry B* 111 (2007), S. 12649–12656

[194] MUSI, S. ; FILIPOVI-VIINCEKOVI, N. ; SEKOVANI, L.: Precipitation of amorphous SiO_2 particles and their properties. In: *Brazilian Journal of Chemical Engineering* 28 (2011), S. 89–94

[195] VACCARO, G. ; AGNELLO, S. ; BUSCARINO, G. ; CANNAS, M. ; VACCARO, L.: Structural and luminescence properties of amorphous SiO_2 nanoparticles. In: *Journal of Non-Crystalline Solids* 357 (2011), S. 1941 – 1944

[196] KAMINOW, I. P. ; BAGLEY, B. G. ; OLSON, C. G.: Measurements of the absorption edge in fused silica. In: *Applied Physics Letters* 32 (1978), S. 98–99

[197] TAN, G. L. ; LEMON, M. F. ; JONES, D. J. ; FRENCH, R. H.: Optical properties and London dispersion interaction of amorphous and crystalline SiO_2 determined by vacuum ultraviolet spectroscopy and spectroscopic ellipsometry. In: *Phys. Rev. B* 72 (2005), S. 205117

[198] RICHARD, N ; MARTIN-SAMOS, L ; GIRARD, S ; RUINI, A ; BOUKENTER, A ; OUERDANE, Y ; MEUNIER, J-P: Oxygen deficient centers in silica: optical properties within many-body perturbation theory. In: *Journal of Physics: Condensed Matter* 25 (2013), S. 335502

[199] YU-ZHANG, K. ; BOISJOLLY, G. ; RIVORY, J. ; KILIAN, L. ; COLLIEX, C.: Characterization of TiO_2/SiO_2 multilayers by high resolution transmission electron microscopy and electron energy loss spectroscopy. In: *Thin Solid Films* 253 (1994), S. 299 – 302

[200] GALLAS, B. ; BRUNET-BRUNEAU, A. ; FISSON, S. ; VUYE, G. ; RIVORY, J.: SiO_2-TiO_2 interfaces studied by ellipsometry and x-ray photoemission spectroscopy. In: *Journal of Applied Physics* 92 (2002), S. 1922–1928

[201] MIYASHITA, K. ; KURODA, S. ; TAJIMA, S. ; TAKEHIRA, K. ; TOBITA, S. ; KUBOTA, H.: Photoluminescence study of electron-hole recombination dynamics in the vacuum-deposited SiO_2/TiO_2 multilayer film with photo-catalytic activity. In: *Chemical Physics Letters* 369 (2003), S. 225 – 231

[202] LU, Junling ; KOSUDA, Kathryn M. ; VAN DUYNE, Richard P. ; STAIR, Peter C.: Surface Acidity and Properties of TiO_2/SiO_2 Catalysts Prepared by Atomic Layer Deposition: UV-visible Diffuse Reflectance, DRIFTS, and Visible Raman Spectroscopy Studies. In: *The Journal of Physical Chemistry C* 113 (2009), S. 12412–12418

[203] LIU, C. ; FU, Q. ; WANG, J. B. ; ZHAO, W. K. ; FANG, Y. L. ; MIHARA, T. ; KIUCHI, M.: Structural Characterization of Nanocrystalline TiO_2 and TiO_2:SiO_2 Powders and Thin Films at 35°C. In: *Journal of the Korean Physical Society* 46 (2005), S. 104–108

[204] YOON, Jong G. ; OH, Hun K. ; KWAG, Young J.: Structural and Optical Properties of TiO_2-SiO_2 Composite Films Prepared by Aerosol-Assisted Chemical-Vapor Deposition. In: *Journal of the Korean Physical Society* 33 (1998), S. 699–704

[205] WANG, Z.M. ; FANG, Q. ; ZHANG, J.-Y. ; WU, J.X. ; DI, Y. ; CHEN, W. ; CHEN, M.L. ; BOYD, Ian W.: Growth of titanium silicate thin films by photo-induced chemical vapor deposition. In: *Thin Solid Films* 453-454 (2004), S. 167 – 171

[206] LAROUCHE, Stéphane ; SZYMANOWSKI, Hieronim ; KLEMBERG-SAPIEHA, Jolanta E. ; MARTINU, Ludvik ; GUJRATHI, Subhash C.: Microstructure of plasma-deposited SiO_2/TiO_2 optical films. In: *Journal of Vacuum Science & Technology A* 22

(2004), S. 1200–1207

[207] GRACIA, F. ; YUBERO, F. ; HOLGADO, J.P. ; ESPINOS, J.P. ; GONZALEZ-ELIPE, A.R. ; GIRARDEAU, T.: SiO_2/TiO_2 thin films with variable refractive index prepared by ion beam induced and plasma enhanced chemical vapor deposition. In: *Thin Solid Films* 500 (2006), S. 19 – 26

[208] GRACIA, F. ; YUBERO, F. ; ESPINOS, J. P. ; HOLGADO, J. P. ; GONZÁLEZ-ELIPE, A. R. ; GIRARDEAU, T.: Correlation between optical properties and electronic parameters for mixed oxide thin films. In: *Surface and Interface Analysis* 38 (2006), S. 752–756

[209] BUSANI, T. ; DEVINE, R. A. B. ; YU, Xiangkun ; SEO, Hye-Won: Electrical and physical properties of room temperature deposited, mixed TiO_2-SiO_2 oxidesa). In: *Journal of Vacuum Science & Technology A* 24 (2006), S. 369–374

[210] NAKAYAMA, Takahiro: Structure of TiO_2/SiO_2 Multilayer Films. 141 (1994), S. 237–241

[211] DEMIRYONT, Hulya: Optical properties of SiO_2–TiO_2 composite films. In: *Appl. Opt.* 24 (1985), S. 2647–2650

[212] CHAO, Shiuh ; WANG, Wen-Hsiang ; HSU, Min-Yu ; WANG, Liang-Chu: Characteristics of ion-beam-sputtered high-refractive-index TiO_2-SiO_2 mixed films. In: *J. Opt. Soc. Am. A* 16 (1999), S. 1477–1483

[213] CHAO, Shiuh ; WANG, Wen-Hsiang ; LEE, Cheng-Chung: Low-loss dielectric mirror with ion-beam-sputtered TiO_2–SiO_2 mixed films. In: *Appl. Opt.* 40 (2001), S. 2177–2182

[214] WANG, Xinrong ; MASUMOTO, Hiroshi ; SOMENO, Yoshihiro ; HIRAI, Toshio: Microstructure and optical properties of amorphous TiO_2-SiO_2 composite films synthesized by helicon plasma sputtering. In: *Thin Solid Films* 338 (1999), S. 105 – 109

[215] MATSUDA, Atsunori ; MATSUNO, Yoshihiro ; KATAYAMA, Shinya ; TSUNO, Toshio: Weathering resistance of glass plates coated with sol-gel derived $9TiO_2$-$91SiO_2$ films. In: *Journal of Materials Science Letters* 8 (1989), S. 902–904. – ISSN 0261–8028

[216] ESQUIVIAS, L ; BAHTAT, M. ; MUGNIER, J. ; BOVIER, C. ; ROUX, H. ; SERUGHETTI, J.: Advanced Materials from Gels Waveguide Raman spectroscopy of TiO_2:SiO_2 thin films. In: *Journal of Non-Crystalline Solids* 147 (1992), S. 123 – 126

[217] HOLMES, A. S. ; SYMS, R. R. A. ; LI, Ming ; GREEN, Mino: Fabrication of buried channel waveguides on silicon substrates using spin-on glass. In: *Appl. Opt.* 32 (1993), S. 4916–4921

[218] DOOLIN, P.K. ; ALERASOOL, S. ; ZALEWSKI, D.J. ; HOFFMAN, J.F.: Acidity studies of titania-silica mixed oxides. In: *Catalysis Letters* 25 (1994), S. 209–223

[219] ALMEIDA, R.M. ; ORIGNAC, X. ; BARBIER, D.: Silica-based sol-gel films doped with active elements. In: *Journal of Sol-Gel Science and Technology* 2 (1994), S. 465–467. – ISSN 0928–0707

[220] LIU, Zhufang ; DAVIS, Robert J.: Investigation of the Structure of Microporous Ti-Si Mixed Oxides by X-ray, UV Reflectance, FT-Raman, and FT-IR Spectroscopies. In: *The Journal of Physical Chemistry* 98 (1994), S. 1253–1261

[221] KESHAVARAJA, A. ; RAMASWAMY, V. ; SONI, H.S. ; RAMASWAMY, A.V. ; RATNASAMY, P.: Synthesis, Characterization, and Catalytic Properties of Micro-Mesoporous, Amorphous Titanosilicate Catalysts. In: *Journal of Catalysis* 157 (1995), S. 501 – 511

[222] RIGDEN, J. S. ; NEWPORT, R.J. ; SMITH, M.E. ; DIRKEN, P.J.: X-Ray Diffraction Studies of Silica: Titania Sol-Gel Glasses. In: *Materials Science Forum* 228-231 (1996), S. 519–524

[223] ORIGNAC, Xavier ; VASCONCELOS, H.C. ; DU, X.M. ; ALMEIDA, R.M.: Influence of solvent concentration on the microstructure of SiO_2-TiO_2 sol-gel films. In: *Journal of Sol-Gel Science and Technology* 8 (1997), S. 243–248

[224] HENDERSON, G.S. ; FLEET, M.E.: The structure of titanium silicate glasses investigated by Si K-edge X-ray absorption spectroscopy. In: *Journal of Non-Crystalline Solids* 211 (1997), S. 214 – 221

[225] GRIEKEN, R V. ; SOTELO, J.L ; MARTOS, C ; FIERRO, J.L.G ; LÓPEZ-GRANADOS, M ; MARISCAL, R: Surface modified amorphous titanosilicate catalysts for liquid phase epoxidation. In: *Catalysis Today* 61 (2000), S. 49 – 54

[226] JUNG, Kyeong Y. ; PARK, Seung B.: Photoactivity of SiO_2/TiO_2 and ZrO_2/TiOv mixed oxides prepared by sol-gel method. In: *Materials Letters* 58 (2004), S. 2897 – 2900

[227] ÄÄRITALO, Virpi ; AREVA, Sami ; JOKINEN, Mika ; LINDÉN, Mika ; PELTOLA, Timo: Sol-gel-derived TiO_2-SiO_2 implant coatings for direct tissue attachment. Part I: design, preparation and characterization. In: *Journal of Materials Science: Materials in Medicine* 18 (2007), S. 1863–1873. – ISSN 0957–4530

[228] INDREA, Emil ; PETER, Anca ; SILIPAS, Danut T. ; DREVE, Simina ; SUCIU, Ramona-Crina ; ROSU, Marcela C. ; DANCIU, Virginia ; COSOVEANU, Veronica: Structural characterisation of binary SiO_2/TiO_2 nanoparticle aerogels by X-ray scattering. In: *Journal of Physics: Conference Series* 182 (2009), S. 012066

[229] CERNUTO, Giuseppe ; GALLI, Simona ; TRUDU, Federica ; COLONNA, Gian M. ; MASCIOCCHI, Norberto ; CERVELLINO, Antonio ; GUAGLIARDI, Antonietta: Investigating the Amorphous-Crystalline Interplay in SiO_2/TiO_2 Nanocomposites by

Total Scattering Methods. In: *Angewandte Chemie International Edition* 50 (2011), S. 10828–10833

[230] BRUN, NATHALIE ; COLLIEX, CHRISTIAN ; RIVORY, JOSETTE ; KUI, YU-ZHANG: Spatially Resolved EELS Fine Structures at a SiO_2/TiO_2 Interface. In: *Microsc. Microanal. Microstruct.* 7 (1996), S. 161–174

[231] NAKAMURA, M. ; KOBAYASHI, M. ; KUZUYA, N. ; KOMATSU, T. ; MOCHIZUKA, T.: Hydrophilic property of SiO_2/TiO_2 double layer films. In: *Thin Solid Films* 502 (2006), S. 121 – 124

[232] AREVA, Sami ; ÄÄRITALO, Virpi ; TUUSA, Sari ; JOKINEN, Mika ; LINDÉN, Mika ; PELTOLA, Timo: Sol-Gel-derived TiO_2-SiO_2 implant coatings for direct tissue attachment. Part II: Evaluation of cell response. In: *Journal of Materials Science: Materials in Medicine* 18 (2007), S. 1633–1642

[233] MASUDA, Yoshitake ; JINBO, Yasuhiro ; KOUMOTO, Kunihito: Room Temperature CVD of TiO_2 Thin Films and Their Electronic Properties. In: *Science of Advanced Materials* 1 (2009), S. 138–143

[234] SOREK, Y. ; REISFELD, R. ; FINKELSTEIN, I. ; RUSCHIN, S.: Sol-gel glass waveguides prepared at low temperature. In: *Applied Physics Letters* 63 (1993), S. 3256–3258

[235] SYMS, R.R.A. ; HOLMES, A.S.: Reflow and burial of channel waveguides formed in sol-gel glass on Si substrates. In: *Photonics Technology Letters, IEEE* 5 (1993), S. 1077–1079

[236] BOVARD, Bertrand G.: Rugate filter theory: an overview. In: *Appl. Opt.* 32 (1993), S. 5427–5442

[237] POITRAS, Daniel ; LAROUCHE, Stéphane ; MARTINU, Ludvik: Design and plasma deposition of dispersion-corrected multiband rugate filters. In: *Appl. Opt.* 41 (2002), S. 5249–5255

[238] LORENZO, E. ; OTON, C. J. ; CAPUJ, N. E. ; GHULINYAN, M. ; NAVARRO-URRIOS, D. ; GABURRO, Z. ; PAVESI, L.: Fabrication and optimization of rugate filters based on porous silicon. In: *physica status solidi (c)* 2 (2005), S. 3227–3231

[239] NETTERFIELD, R. P. ; MARTIN, P. J. ; PACEY, C. G. ; SAINTY, W. G. ; MCKENZIE, D. R. ; AUCHTERLONIE, G.: Ion-assisted deposition of mixed TiO_2-SiO_2 films. In: *Journal of Applied Physics* 66 (1989), S. 1805–1809

[240] WANG, X. ; MASUMOTO, H. ; SOMENO, Y. ; HIRAI, T.: Optical properties of titania/silica multilayer filters prepared by helicon plasma sputtering. In: *Journal of Vacuum Science & Technology A* 16 (1998), S. 2926–2930

[241] DAVIS, Robert J. ; LIU, Zhufang: Titania-Silica: A Model Binary Oxide Catalyst System. In: *Chemistry of Materials* 9 (1997), S. 2311–2324

[242] GAO, Xingtao ; WACHS, Israel E.: Titania-silica as catalysts: molecular structural characteristics and physico-chemical properties. In: *Catalysis Today* 51 (1999), S. 233 – 254

[243] DAGAN, Geula ; SAMPATH, Srinivasan ; LEV, Ovadia: Preparation and Utilization of Organically Modified Silica-Titania Photocatalysts for Decontamination of Aquatic Environments. In: *Chemistry of Materials* 7 (1995), S. 446–453

[244] JUNG, Kyeong Y. ; PARK, Seung B.: Enhanced photoactivity of silica-embedded titania particles prepared by sol-gel process for the decomposition of trichloroethylene. In: *Applied Catalysis B: Environmental* 25 (2000), S. 249 – 256

[245] PITONIAK, Erik ; WU, Chang-Yu ; MAZYCK, David W. ; POWERS, Kevin W. ; SIGMUND, Wolfgang: Adsorption Enhancement Mechanisms of Silica-Titania Nanocomposites for Elemental Mercury Vapor Removal. In: *Environmental Science & Technology* 39 (2005), S. 1269–1274

[246] QI, Kaihong ; CHEN, Xianqiong ; LIU, Yuyang ; XIN, John H. ; MAK, C. L. ; DAOUD, Walid A.: Facile preparation of anatase/SiO_2 spherical nanocomposites and their application in self-cleaning textiles. In: *J. Mater. Chem.* 17 (2007), S. 3504–3508

[247] THANGARAJ, A. ; SIVASANKER, S. ; RATNASAMY, P.: Catalytic properties of crystalline titanium silicalites III. Ammoximation of cyclohexanone. In: *Journal of Catalysis* 131 (1991), S. 394 – 400

[248] PEI, S. ; ZAJAC, G.W. ; KADUK, J.A. ; FABER, J. ; BOYANOV, B.I. ; DUCK, D. ; FAZZINI, D. ; MORRISON, T.I. ; YANG, D.S.: Re-investigation of titanium silicalite by X-ray absorption spectroscopy: Are the novel titanium sites real? In: *Catalysis Letters* 21 (1993), S. 333–344

[249] ANDERSON, M. W. ; TERASAKI, O. ; T. OHSUNA A. PLIPPOU, S. P. M. ; FERREIRA, A. ; ROCHA, J. ; LIDIN, S.: Structure of the microporous titanosilicate ETS-10. In: *Nature* 367 (1994), S. 347–351

[250] UGUINA, M.A. ; SERRANO, D.P. ; OVEJERO, G. ; GRIEKEN, R. V. ; CAMACHO, M.: Preparation of TS-1 by wetness impregnation of amorphous SiO_2–TiO_2 solids: influence of the synthesis variables. In: *Applied Catalysis A: General* 124 (1995), S. 391 – 408

[251] LIU, Z. ; CRUMBAUGH, G. M. ; DAVIS, R. J.: Effect of Structure and Composition on Epoxidation of HexeneCatalyzed by Microporous and Mesoporous Ti-Si Mixed Oxides. In: *Journal of Catalysis* 159 (1996), S. 83 – 89

[252] ROBERTS, M. A. ; SANKAR, G. ; THOMAS, J. M. ; JONES, R. H. ; DU, H. ; CHEN, J. ; PANG, W. ; XU, R.: Synthesis and structure of a layered titanosilicate catalyst with five-coordinate titanium. In: *Nature* 381 (1996), S. 347–351

[253] SERRANO, D.P. ; UGUINA, M.A. ; OVEJERO, G. ; GRIEKEN, R. V. ; CAMACHO, M.: Evidence of solid-solid transformations

during the TS-1 crystallization from amorphous wetness impregnated SiO_2-TiO_2 xerogels. In: *Microporous Materials* 7 (1996), S. 309 – 321

[254] BORELLO, Enzo ; LAMBERTI, Carlo ; BORDIGA, Silvia ; ZECCHINA, Adriano ; AREÁN, Carlos O.: Quantum-size effects in the titanosilicate molecular sieve. In: *Applied Physics Letters* 71 (1997), S. 2319–2321

[255] KO, YongSig ; AHN, WhaSeung: Characterization and catalytic properties of titanium silicalite-1 catalyst. In: *Korean Journal of Chemical Engineering* 15 (1998), S. 182–191

[256] KUZNICKI, Steven M. ; BELL, Valerie A. ; NAIR, Sankar ; HILLHOUSE, Hugh W. ; JACUBINAS, Richard M. ; BRAUNBARTH, Carola M. ; TOBY, Brian H. ; TSAPATSIS, Michael: A titanosilicate molecular sieve with adjustable pores for size-selective adsorption of molecules. In: *Nature* 412 (2001), S. 720–724

[257] MÉNDEZ-VIVAR, J. ; MENDOZA-SERNA, R.: SiO_2-TiO_2 membranes by the sol-gel process. In: *Silicon Chemistry* 3 (2006), S. 59–64

[258] CAO, Shengli ; YAO, Nan ; YEUNG, KingLun: Synthesis of freestanding silica and titania-silica aerogels with ordered and disordered mesopores. In: *Journal of Sol-Gel Science and Technology* 46 (2008), S. 323–333

[259] GAMBA, Aldo ; TABACCHI, Gloria ; FOIS, Ettore: TS-1 from First Principles. In: *The Journal of Physical Chemistry A* 113 (2009), S. 15006–15015

[260] FAUSTINI, Marco ; VAYER, Marylene ; MARMIROLI, Benedetta ; HILLMYER, Marc ; AMENITSCH, Heinz ; SINTUREL, Christophe ; GROSSO, David: Bottom-up Approach toward Titanosilicate Mesoporous Pillared Planar Nanochannels for Nanofluidic Applications. In: *Chemistry of Materials* 22 (2010), S. 5687–5694

[261] BEST, M.F. ; CONDRATE, Sr R.A.: A raman study of TiO_2-SiO_2 glasses prepared by sol-gel processes. In: *Journal of Materials Science Letters* 4 (1985), S. 994–998. – ISSN 0261–8028

[262] SORIANO, L. ; FUENTES, G. G. ; QUIRÓS, C. ; TRIGO, J. F. ; SANZ, J. M. ; BRESSLER, P. R. ; GONZÁLEZ-ELIPE, A. R.: Crystal-Field Effects at the TiO_2-SiO_2 Interface As Observed by X-ray Absorption Spectroscopy. In: *Langmuir* 16 (2000), S. 7066–7069

[263] ESPINÓS, J. P. ; LASSALETTA, G. ; CABALLERO, A. ; FERNÁNDEZ, A. ; GONZÁLEZ-ELIPE, A. R. ; STAMPFL, A. ; MORANT, C. ; SANZ, J. M.: Synchrotron Photoemission Characterization of TiO_2 Supported on SiO_2. In: *Langmuir* 14 (1998), S. 4908–4914

[264] SANDSTROM, Donald R. ; LYTLE, Farrel W. ; WEI, P.S.P. ; GREEGOR, Robert B. ; WONG, Joe ; SCHULTZ, Peter: Coordination of Ti in TiO_2-SiO_2 glass by X-ray absorption spectroscopy. In: *Journal of Non-Crystalline Solids* 41 (1980), S. 201 – 207

[265] GREEGOR, Robert B. ; LYTLE, Farrel W. ; SANDSTROM, Donald R. ; WONG, Joe ; SCHULTZ, Peter: Investigation of TiO_2-SiO_2 glasses by X-ray absorption spectroscopy. In: *Journal of Non-Crystalline Solids* 55 (1983), S. 27 – 43

[266] SMITH, D. Y. ; BLACK, C. E. ; HOMES, C. C. ; SHILES, E.: Optical properties of TiO_2-SiO_2 glass over a wide spectral range. In: *physica status solidi (c)* 4 (2007), S. 838–842

[267] CHENG, S.C.: Coordination and optical attenuation of TiO_2-SiO_2 glass by electron energy loss spectroscopy. In: *Journal of Non-Crystalline Solids* 354 (2008), Nr. 31, S. 3735 – 3741

[268] RIGDEN, J S. ; WALTERS, J K. ; DIRKEN, P J. ; SMITH, M E. ; BUSHNELL-WYE, G ; HOWELLS, W S. ; NEWPORT, R J.: The role of titanium in mixed sol-gels: an x-ray and neutron diffraction study. In: *Journal of Physics: Condensed Matter* 9 (1997), S. 4001

[269] ANDERSON, Sten ; WADSLEY, A. D.: The Crystal Structure of $K_2Ti_2O_5$. In: *Acta Chemica Scandinavica* 15 (1961), S. 663–669

[270] MARKGRAF, S. A. ; HALLIYAL, A. ; BHALLA, A. S. ; NEWNHAM, R. E. ; PREWITT, C. T.: X-ray structure refinement and pyroelectric investigation of fresnoite, $Ba_2TiSi_2O_8$. In: *Ferroelectrics* 62 (1985), S. 17–26

[271] NYMAN, H. ; O'KEEFFE, M. ; BOVIN, J.-O.: Sodium titanium silicate, Na_2TiSiO_5. In: *Acta Crystallographica Section B* 34 (1978), S. 905–906

[272] YARKER, Colin A. ; JOHNSON, Peter A. ; WRIGHT, Adrian C. ; WONG, Joe ; GREEGOR, Robert B. ; LYTLE, Farrel W. ; SINCLAIR, Roger N.: Neutron diffraction and EXAFS evidence for TiO_2 units in vitreous KO_2-TiO_2-$2SiO_2$. In: *Journal of Non-Crystalline Solids* 79 (1986), Nr. 1, S. 117 – 136

[273] DINGWELL, D.B. ; PARIS, E. ; SEIFERT, F. ; MOTTANA, A. ; ROMANO, C.: X-ray absorption study of Ti-bearing silicate glasses. In: *Physics and Chemistry of Minerals* 21 (1994), S. 501–509. – ISSN 0342–1791

[274] HENDERSON, Grant S.: The structure of silicate melts: A glass perspective. In: *The Canadian Mineralogist* 43 (2005), S. 1921

[275] FARGES, Franćois ; JR., Gordon E. B. ; REHR, John J.: Coordination chemistry of Ti(IV) in silicate glasses and melts: I.

{XAFS} study of titanium coordination in oxide model compounds. In: *Geochimica et Cosmochimica Acta* 60 (1996), S. 3023 – 3038

[276] FARGES, Franćois ; JR., Gordon E. B. ; NAVROTSKY, Alexandra ; GAN, Hao ; REHR, John J.: Coordination chemistry of Ti(IV) in silicate glasses and melts: II. Glasses at ambient temperature and pressure. In: *Geochimica et Cosmochimica Acta* 60 (1996), S. 3039 – 3053

[277] FARGES, Franćois ; JR., Gordon E. B. ; NAVROTSKY, Alexandra ; GAN, Hao ; REHR, John R.: Coordination chemistry of Ti(IV) in silicate glasses and melts: III. Glasses and melts from ambient to high temperatures. In: *Geochimica et Cosmochimica Acta* 60 (1996), S. 3055 – 3065

[278] FARGES, FranÃ§ois ; JR., Gordon E. B.: Coordination chemistry of titanium (IV) in silicate glasses and melts: IV. {XANES} studies of synthetic and natural volcanic glasses and tektites at ambient temperature and pressure. In: *Geochimica et Cosmochimica Acta* 61 (1997), S. 1863 – 1870

[279] OSIPOV, A.A. ; KORINEVSKAYA, G.G. ; OSIPOVA, L.M. ; MUFTAKHOV, V.A.: Titanium coordination in TiO_2-Na_2O-SiOv glasses of x(TiO_2)·(100-x)[2Na_2O·3SiO_2] ($0 \leq x \leq 30$) composition based on Raman spectroscopy. In: *Glass Physics and Chemistry* 38 (2012), S. 357–360. – ISSN 1087–6596

[280] ROSENTHAL, Allan B. ; GAROFALINI, Stephen H.: Molecular dynamics study of amorphous titanium silicate. In: *Journal of Non-Crystalline Solids* 107 (1988), S. 65 – 72

[281] BERNARD, C. ; CHAUSSEDENT, S. ; MONTEIL, A. ; MONTAGNA, M. ; ZAMPEDRI, L. ; FERRARI, M.: Simulation by Molecular Dynamics of Erbium-Activated Silica-Titania Glasses. In: *Journal of Sol-Gel Science and Technology* 26 (2003), S. 925–929. – ISSN 0928–0707

[282] AMBACHER, O. ; BRANDT, M. S. ; DIMITROV, R. ; METZGER, T. ; STUTZMANN, M. ; FISCHER, R. A. ; MIEHR, A. ; BERGMAIER, A. ; DOLLINGER, G.: Thermal stability and desorption of Group III nitrides prepared by metal organic chemical vapor deposition. In: *Journal of Vacuum Science & Technology B* 14 (1996), S. 3532–3542

[283] VURGAFTMAN, I. ; MEYER, J. R.: Band parameters for nitrogen-containing semiconductors. In: *Journal of Applied Physics* 94 (2003), S. 3675–3696

[284] WU, Junqiao: When group-III nitrides go infrared: New properties and perspectives. In: *Journal of Applied Physics* 106 (2009), S. 011101

[285] HARDY, Matthew T. ; FEEZELL, Daniel F. ; DENBAARS, Steven P. ; NAKAMURA, Shuji: Group III-nitride lasers: a materials perspective. In: *Materials Today* 14 (2011), S. 408 – 415

[286] MARCINKEVIČIUS, S. ; JAIN, R. ; SHATALOV, M. ; YANG, J. ; SHUR, M. ; GASKA, R.: High spectral uniformity of AlGaN with a high Al content evidenced by scanning near-field photoluminescence spectroscopy. In: *Applied Physics Letters* 105 (2014), S. 241108

[287] KRAUSE, Florian F. ; AHL, Jan-Philipp ; TYTKO, Darius ; CHOI, Pyuck-Pa ; EGOAVIL, Ricardo ; SCHOWALTER, Marco ; MEHRTENS, Thorsten ; MÜLLER-CASPARY, Knut ; VERBEECK, Johan ; RAABE, Dierk ; HERTKORN, Joachim ; ENGL, Karl ; ROSENAUER, Andreas: Homogeneity and composition of AlInGaN: A multiprobe nanostructure study. In: *Ultramicroscopy* 156 (2015), S. 29 – 36

[288] MATSUOKA, T. ; YOSHIMOTO, N. ; SASAKI, T. ; KATSUI, A.: Wide-gap semiconductor InGaN and InGaAln grown by MOVPE. In: *Journal of Electronic Materials* 21 (1992), S. 157–163

[289] O'DONNELL, K. P. ; MARTIN, R. W. ; MIDDLETON, P. G.: Origin of Luminescence from InGaN Diodes. In: *Phys. Rev. Lett.* 82 (1999), S. 237–240

[290] HO, I hsiu ; STRINGFELLOW, G. B.: Solid phase immiscibility in GaInN. In: *Applied Physics Letters* 69 (1996), S. 2701–2703

[291] TAKAYAMA, Toru ; YURI, Masaaki ; ITOH, Kunio ; JR., James S. H.: Theoretical predictions of unstable two-phase regions in wurtzite group-III-nitride-based ternary and quaternary material systems using modified valence force field model. In: *Journal of Applied Physics* 90 (2001), S. 2358–2369

[292] TAKAYAMA, T. ; YURI, M. ; ITOH, K. ; BABA, T. ; JR, J.S. H.: Analysis of phase-separation region in wurtzite group {III} nitride quaternary material system using modified valence force field model. In: *Journal of Crystal Growth* 222 (2001), S. 29 – 37

[293] TELES, L. K. ; MARQUES, M. ; SCOLFARO, L. M. R. ; LEITE, J. R. ; FERREIRA, L. G.: Phase separation and ordering in group-III nitride alloys. In: *Brazilian Journal of Physics* 34 (2004), S. 593 – 597

[294] ADHIKARI, Jhumpa ; KOFKE, David A.: Molecular simulation study of miscibility in $In_xGa_{1-x}N$ ternary alloys. In: *Journal of Applied Physics* 95 (2004), S. 4500–4502

[295] KARPOV, Sergey Y. ; PODOLSKAYA, Natalya I. ; ZHMAKIN, Igor A. ; ZHMAKIN, Alexander I.: Statistical model of ternary group-III nitrides. In: *Phys. Rev. B* 70 (2004), S. 235203

[296] ZHAO, Guijuan ; XU, Xiaoqing ; LI, Huijie ; WEI, Hongyuan ; HAN, Dongyue ; JI, Zesheng ; MENG, Yulin ; WANG, Lianshan ; YANG, Shaoyan: The immiscibility of InAlN ternary alloy. In: *Scientific Reports* 6 (2016), S. 26600

[297] KHAN, M. A. ; SHATALOV, M. ; MARUSKA, H. P. ; WANG, H. M. ; KUOKSTIS, E.: III-Nitride UV Devices. In: *Japanese Journal of Applied Physics* 44 (2005), S. 7191

[298] JAYASAKTHI, M. ; RAMESH, R. ; ARIVAZHAGAN, P. ; LOGANATHAN, R. ; PRABAKARAN, K. ; BALAJI, M. ; BASKAR, K.: Structural and optical characterization of AlGaN/GaN layers. In: *Journal of Crystal Growth* 401 (2014), S. 527 – 531

[299] SHATALOV, Max ; SUN, Wenhong ; JAIN, Rakesh ; LUNEV, Alex ; HU, Xuhong ; DOBRINSKY, Alex ; BILENKO, Yuri ; YANG, Jinwei ; GARRETT, Gregory A. ; RODAK, Lee E. ; WRABACK, Michael ; SHUR, Michael ; GASKA, Remis: High power AlGaN ultraviolet light emitters. In: *Semiconductor Science and Technology* 29 (2014), S. 084007

[300] MATSUOKA, Takashi: InGaAlN and II-VI Systems for Blue-Green Light-Emitting Devices. In: *Advanced Materials* 8 (1996), S. 469–479

[301] AS, D. J. ; SCHNIETZ, M. ; SCHÖRMANN, J. ; POTTHAST, S. ; GERLACH, J. W. ; VOGT, J. ; LISCHKA, K.: MBE growth of cubic $Al_xIn_{1-x}N$ and $Al_xGa_yIn_{1-x-y}N$ lattice matched to GaN. In: *physica status solidi (c)* 4 (2007), S. 2318–2321

[302] JEON, Seong-Ran ; SON, Sung-Jin ; PARK, Si-Hyun: Growth and characterization of quaternary AlGaInN layers and performance of AlGaInN-based ultraviolet light-emitting diodes. In: *Journal of the Korean Physical Society* 63 (2013), S. 2204–2208. – ISSN 0374–4884

[303] MOHAMMAD, S.N. ; SALVADOR, A.A. ; MORKOC, Hadis: Emerging gallium nitride based devices. In: *Proceedings of the IEEE* 83 (1995), S. 1306–1355

[304] NAKAMURA, Shuji: Blue light emitting laser diodes. In: *Thin Solid Films* 343–344 (1999), S. 345 – 349

[305] BEELER, M ; TRICHAS, E ; MONROY, E: III-nitride semiconductors for intersubband optoelectronics: a review. In: *Semiconductor Science and Technology* 28 (2013), S. 074022

[306] AS, Donat J. ; MIETZE, Christian: MBE growth and applications of cubic AlN/GaN quantum wells. In: *physica status solidi (a)* 210 (2013), S. 474–479

[307] BEELER, Mark ; BOUGEROL, Catherine ; BELLET-AMALARIC, Edith ; MONROY, Eva: THz intersubband transitions in AlGaN/GaN multi-quantum-wells. In: *physica status solidi (a)* 211 (2014), S. 761–764

[308] WECKER, Tobias ; CALLSEN, Gordon ; HOFFMANN, Axel ; REUTER, Dirk ; AS, Donat J.: Photoluminescence excitation spectroscopy of excited states of an asymmetric cubic $GaN/Al_{0.25}Ga_{0.75}N$ double quantum well grown by molecular beam epitaxy. In: *Japanese Journal of Applied Physics* 55 (2016), S. 05FG01

[309] MIETZE, C. ; LANDMANN, M. ; RAULS, E. ; MACHHADANI, H. ; SAKR, S. ; TCHERNYCHEVA, M. ; JULIEN, F. H. ; SCHMIDT, W. G. ; LISCHKA, K. ; AS, D. J.: Band offsets in cubic GaN/AlN superlattices. In: *Phys. Rev. B* 83 (2011), S. 195301

[310] SEO IM, Jin ; KOLLMER, H. ; OFF, J. ; SOHMER, A. ; SCHOLZ, F. ; HANGLEITER, A.: Reduction of oscillator strength due to piezoelectric fields in $GaN/Al_xGa_{1-x}N$ quantum wells. In: *Phys. Rev. B* 57 (1998), S. R9435–R9438

[311] PARK, Seoung-Hwan ; CHUANG, Shun-Lien: Comparison of zinc-blende and wurtzite GaN semiconductors with spontaneous polarization and piezoelectric field effects. In: *Journal of Applied Physics* 87 (2000), S. 353–364

[312] MACHHADANI, H ; KANDASWAMY, P ; SAKR, S ; VARDI, A ; WIRTMÃ $\frac{1}{4}$LLER, A ; NEVOU, L ; GUILLOT, F ; POZZOVIVO, G ; TCHERNYCHEVA, M ; LUPU, A ; VIVIEN, L ; CROZAT, P ; WARDE, E ; BOUGEROL, C ; SCHACHAM, S ; STRASSER, G ; BAHIR, G ; MONROY, E ; JULIEN, F H.: GaN/AlGaN intersubband optoelectronic devices. In: *New Journal of Physics* 11 (2009), S. 125023

[313] BERNARDINI, Fabio ; FIORENTINI, Vincenzo ; VANDERBILT, David: Spontaneous polarization and piezoelectric constants of III-V nitrides. In: *Phys. Rev. B* 56 (1997), S. R10024–R10027

[314] ADACHI, Masahiro: InGaN based green laser diodes on semipolar GaN substrate. In: *Japanese Journal of Applied Physics* 53 (2014), S. 100207

[315] WALTEREIT, P. ; BRANDT, O. ; TRAMPERT, A. ; GRAHN, H. T. ; MENNIGER, J. ; RAMSTEINER, M. ; REICHE, M. ; PLOOG, K. H.: Nitride semiconductors free of electrostatic fields for efficient white light-emitting diodes. In: *Nature* 406 (2000), S. 865–868

[316] THOMPSON, Margarita P. ; AUNER, Gregory W. ; ZHELEVA, Tsvetanka S. ; JONES, Kenneth A. ; SIMKO, Steven J. ; HILFIKER, James N.: Deposition factors and band gap of zinc-blende AlN. In: *Journal of Applied Physics* 89 (2001), S. 3331–3336

[317] RAMÍREZ-FLORES, G. ; NAVARRO-CONTRERAS, H. ; LASTRAS-MARTÍNEZ, A. ; POWELL, R. C. ; GREENE, J. E.: Temperature-dependent optical band gap of the metastable zinc-blende structure β-GaN. In: *Phys. Rev. B* 50 (1994), S. 8433–8438

[318] DAUDIN, B. ; FEUILLET, G. ; HÜBNER, J. ; SAMSON, Y. ; WIDMANN, F. ; PHILIPPE, A. ; BRU-CHEVALLIER, C. ; GUILLOT, G. ; BUSTARRET, E. ; BENTOUMI, G. ; DENEUVILLE, A.: How to grow cubic GaN with low hexagonal phase content on (001) SiC by molecular beam epitaxy. In: *Journal of Applied Physics* 84 (1998), S. 2295–2300

[319] SCHÖRMANN, J. ; POTTHAST, S. ; AS, D. J. ; LISCHKA, K.: Near ultraviolet emission from nonpolar cubic $Al_xGa_{1-x}N$–GaN quantum wells. In: *Applied Physics Letters* 89 (2006), S. 131910

[320] NOVIKOV, S. V. ; FOXON, C. T. ; KENT, A. J.: Growth and characterization of free-standing zinc-blende GaN layers and substrates. In: *physica status solidi (a)* 207 (2010), S. 1277–1282

[321] AS, D.J.: Cubic group-III nitride-based nanostructures–basics and applications in optoelectronics. In: *Microelectronics Journal* 40 (2009), S. 204 – 209

[322] SCHUPP, T. ; LISCHKA, K. ; AS, D.J.: MBE growth of atomically smooth non-polar cubic AlN. In: *Journal of Crystal Growth* 312 (2010), Nr. 9, S. 1500 – 1504

[323] DECUIR, E. A. ; FRED, E. ; MANASREH, M. O. ; SCHÖRMANN, J. ; AS, D. J. ; LISCHKA, K.: Near-infrared intersubband absorption in nonpolar cubic GaN-AlN superlattices. In: *Applied Physics Letters* 91 (2007), S. 041911

[324] TSCHUMAK, E. ; GRANZNER, R. ; LINDNER, J. K. N. ; SCHWIERZ, F. ; LISCHKA, K. ; NAGASAWA, H. ; ABE, M. ; AS, D. J.: Nonpolar cubic AlGaN/GaN heterojunction field-effect transistor on Ar+ implanted 3C-SiC (001). In: *Applied Physics Letters* 96 (2010), S. 253501

[325] ZAINAL, N. ; NOVIKOV, S. V. ; MELLOR, C. J. ; FOXON, C. T. ; KENT, A. J.: Current-voltage characteristics of zinc-blende (cubic) $Al_{0.3}Ga_{0.7}N$/GaN double barrier resonant tunneling diodes. In: *Applied Physics Letters* 97 (2010), S. 112102

[326] SCHUBERT, M ; KASIC, A ; ŠIK, J ; EINFELDT, S ; HOMMEL, D ; HÄRLE, V ; OFF, J ; SCHOLZ, F: Phonons and free carriers in strained hexagonal GaN/AlGaN superlattices measured by infrared ellipsometry and Raman spectroscopy. In: *Materials Science and Engineering: B* 82 (2001), Nr. 1–3, S. 178 – 181

[327] MIETZE, C. ; DECUIR, E. A. ; MANASREH, M. O. ; LISCHKA, K. ; AS, D. J.: Inter- and intrasubband spectroscopy of cubic AlN/GaN superlattices grown by molecular beam epitaxy on 3C-SiC. In: *physica status solidi (c)* 7 (2010), S. 64–67

[328] MASTRO, Michael A. ; JR, Jaime A F. ; GLEMBOCKI, Orest ; JR, Charles R E. ; HOLM, R T. ; HENRY, Rich L. ; CALDWELL, Josh ; RENDELL, Ronald W. ; KUB, Fritz ; KIM, J: Plasmonically enhanced emission from a group-III nitride nanowire emitter. In: *Nanotechnology* 18 (2007), S. 265401

[329] DONG, Yajie ; TIAN, Bozhi ; KEMPA, Thomas J. ; LIEBER, Charles M.: Coaxial Group III-Nitride Nanowire Photovoltaics. In: *Nano Letters* 9 (2009), S. 2183–2187

[330] MARTINEZ-GUERRERO, E. ; ADELMANN, C. ; CHABUEL, F. ; SIMON, J. ; PELEKANOS, N. T. ; MULA, Guido ; DAUDIN, B. ; FEUILLET, G. ; MARIETTE, H.: Self-assembled zinc blende GaN quantum dots grown by molecular-beam epitaxy. In: *Applied Physics Letters* 77 (2000), S. 809–811

[331] CHO, Yong-Hoon ; KWON, B. J. ; BARJON, J. ; BRAULT, J. ; DAUDIN, B. ; MARIETTE, H. ; DANG, Le S.: Optical characteristics of hexagonal GaN self-assembled quantum dots: Strong influence of built-in electric field and carrier localization. In: *Applied Physics Letters* 81 (2002), S. 4934–4936

[332] GOGNEAU, N. ; FOSSARD, F. ; MONROY, E. ; MONNOYE, S. ; MANK, H. ; DAUDIN, B.: Effects of stacking on the structural and optical properties of self-organized GaN/AlN quantum dots. In: *Applied Physics Letters* 84 (2004), S. 4224–4226

[333] SERGENT, S. ; KAKO, S. ; BÃ$\frac{1}{4}$RGER, M. ; AS, D. J. ; ARAKAWA, Y.: Narrow spectral linewidth of single zinc-blende GaN/AlN self-assembled quantum dots. In: *Applied Physics Letters* 103 (2013), S. 151109

[334] BARDELEBEN, H. J. ; CANTIN, J. L. ; GERSTMANN, U. ; SCHOLLE, A. ; GREULICH-WEBER, S. ; RAULS, E. ; LANDMANN, M. ; SCHMIDT, W. G. ; GENTILS, A. ; BOTSOA, J. ; BARTHE, M. F.: Identification of the Nitrogen Split Interstitial $(\mathbf{N}\text{-}\mathbf{N})_\mathbf{N}$ in GaN. In: *Phys. Rev. Lett.* 109 (2012), S. 206402

[335] AMBACHER, O.: Growth and applications of Group III-nitrides. In: *Journal of Physics D: Applied Physics* 31 (1998), S. 2653

[336] SEIFERT, W. ; TEMPEL, A.: Zur Epitaxie von Galliumnitrid auf Korund im System GaCl/NH3/Ar. In: *Kristall und Technik* 9 (1974), S. 1213–1221

[337] BARANOV, B. ; DÄWERITZ, L. ; GUTAN, V. B. ; JUNGK, G. ; NEUMANN, H. ; RAIDT, H.: Growth and properties of $Al_xGa_{1-x}N$ epitaxial layers. In: *physica status solidi (a)* 49 (1978), S. 629–636

[338] MIZUTA, Masashi ; FUJIEDA, Shinji ; MATSUMOTO, Yoshishige ; KAWAMURA, Tsutomu: Low Temperature Growth of GaN and AlN on GaAs Utilizing Metalorganics and Hydrazine. In: *Japanese Journal of Applied Physics* 25 (1986), S. L945

[339] PAISLEY, M. J. ; SITAR, Z. ; POSTHILL, J. B. ; DAVIS, R. F.: Growth of cubic phase gallium nitride by modified molecular-beam epitaxy. In: *Journal of Vacuum Science & Technology A* 7 (1989), S. 701–705

[340] PETROV, I. ; MOJAB, E. ; POWELL, R. C. ; GREENE, J. E. ; HULTMAN, L. ; SUNDGREN, J.-E.: Synthesis of metastable

epitaxial zincblende structure AlN by solid-state reaction. In: *Applied Physics Letters* 60 (1992), S. 2491–2493

[341] ABERNATHY, C. R. ; MACKENZIE, J. D. ; BHARATAN, S. R. ; JONES, K. S. ; PEARTON, S. J.: Electrical and structural properties of $In_xGa_{1-x}N$ on GaAs. In: *Applied Physics Letters* 66 (1995), S. 1632–1634

[342] LIN, Wen-Tai ; MENG, Ling-Cheng ; CHEN, Guo-Ju ; LIU, Hok-Shin: Epitaxial growth of cubic AlN films on (100) and (111) silicon by pulsed laser ablation. In: *Applied Physics Letters* 66 (1995), S. 2066–2068

[343] KEMPER, R.M. ; HILLER, L. ; STAUDEN, T. ; PEZOLDT, J. ; DUSCHIK, K. ; NIENDORF, T. ; MAIER, H.J. ; MEERTENS, D. ; TILLMANN, K. ; AS, D.J. ; LINDNER, J.K.N.: Growth of cubic GaN on 3C-SiC/Si (001) nanostructures. In: *Journal of Crystal Growth* 378 (2013), S. 291 – 294

[344] UENO, Masaki ; YOSHIDA, Minoru ; ONODERA, Akifumi ; SHIMOMURA, Osamu ; TAKEMURA, Kenichi: Stability of the wurtzite-type structure under high pressure: GaN and InN. In: *Phys. Rev. B* 49 (1994), S. 14–21

[345] UENO, Masaki ; YOSHIDA, Minoru ; ONODERA, Akifumi ; SHIMOMURA, Osamu ; TAKEMURA, Kenichi: Stability of the wurtzite-type structure under high pressure: GaN and InN. In: *Phys. Rev. B* 49 (1994), S. 14–21

[346] XIE, Yi ; QIAN, Yitai ; ZHANG, Shuyuan ; WANG, Wenzhong ; LIU, Xianming ; ZHANG, Yuheng: Coexistence of wurtzite GaN with zinc blende and rocksalt studied by x-ray power diffraction and high-resolution transmission electron microscopy. In: *Applied Physics Letters* 69 (1996), S. 334–336

[347] LIMPIJUMNONG, Sukit ; LAMBRECHT, Walter R. L.: Theoretical study of the relative stability of wurtzite and rocksalt phases in MgO and GaN. In: *Phys. Rev. B* 63 (2001), S. 104103

[348] HALSALL, M. P. ; HARMER, P. ; PARBROOK, P. J. ; HENLEY, S. J.: Raman scattering and absorption study of the high-pressure wurtzite to rocksalt phase transition of GaN. In: *Phys. Rev. B* 69 (2004), S. 235207

[349] MADAN, A. ; KIM, I. W. ; CHENG, S. C. ; YASHAR, P. ; DRAVID, V. P. ; BARNETT, S. A.: Stabilization of Cubic AlN in Epitaxial AlN/TiN Superlattices. In: *Phys. Rev. Lett.* 78 (1997), S. 1743–1746

[350] RAWAT, Vijay ; ZAKHAROV, Dmitri N. ; STACH, Eric A. ; SANDS, Timothy D.: Pseudomorphic stabilization of rocksalt GaN in TiN/GaN multilayers and superlattices. In: *Phys. Rev. B* 80 (2009), S. 024114

[351] LI, Quan ; KIM, I. W. ; BARNETT, S. A. ; MARKS, L. D.: Structures of AlN/VN Superlattices with Different AlN Layer Thicknesses. In: *JMR Journal of Materials Research* 17 (2002), S. 1224–1231

[352] BARNETT, Scott A. ; MADAN, Anita ; KIM, Ilwon ; MARTIN, Keith: Stability of Nanometer-Thick Layers in Hard Coatings. In: *JMR Journal of Materials Research* 28 (2003), S. 169–172

[353] BARTOSIK, M. ; TODT, M. ; HOLEC, D. ; TODT, J. ; ZHOU, L. ; RIEDL, H. ; BÃ¶HM, H. J. ; RAMMERSTORFER, F. G. ; MAYRHOFER, P. H.: Thermal expansion of rock-salt cubic AlN. In: *Applied Physics Letters* 107 (2015), S. 071602

[354] KIM, I. W. ; MADAN, A. ; GURUZ, M. W. ; DRAVID, V. P. ; BARNETT, S. A.: Stabilization of zinc-blende cubic AlN in AlN/W superlattices. In: *Journal of Vacuum Science & Technology A: Vacuum, Surfaces, and Films* 19 (2001), S. 2069–2073

[355] CUI, Y. ; LAZOROV, V. K. ; GOETZ, M. M. ; LIU, H. ; ROBERTSON, D. P. ; GAJDARDZISKA-JOSIFOVSKA, M. ; LI, L.: Cubic GaN formation in Mn/GaN multilayer films grown on 6H-SiC(0001). In: *Applied Physics Letters* 82 (2003), S. 4666–4668

[356] NAKAMURA, T. ; TOKUMOTO, Y. ; KATAYAMA, R. ; YAMAMOTO, T. ; ONABE, K.: RF-MBE growth and structural characterization of cubic InN films on yttria-stabilized zirconia (001) substrates. In: *Journal of Crystal Growth* 301-302 (2007), S. 508 – 512

[357] IWAHASHI, Y. ; YAGUCHI, H. ; NISHIMOTO, A. ; ORIHARA, M. ; HIJIKATA, Y. ; YOSHIDA, S.: RF-MBE growth of cubic InN films on MgO (001) substrates. In: *physica status solidi (c)* 3 (2006), S. 1515–1518

[358] NISHIDA, K. ; KITAMURA, Y. ; HIJIKATA, Y. ; YAGUCHI, H. ; YOSHIDA, S.: Epitaxial growth of hexagonal and cubic InN films. In: *physica status solidi (b)* 241 (2004), S. 2839–2842

[359] SHI, B. M. ; XIE, M. H. ; WU, H. S. ; WANG, N. ; TONG, S. Y.: Transition between wurtzite and zinc-blende GaN: An effect of deposition condition of molecular-beam epitaxy. In: *Applied Physics Letters* 89 (2006), S. 151921

[360] XU, Fen ; XIE, Yi ; ZHANG, Xu ; ZHANG, Shuyuan ; SHI, Lei: A benzene-thermal metathesis route to pure metastable rocksalt GaN. In: *New J. Chem.* 27 (2003), S. 565–567

[361] GAO, Shanmin ; ZHU, Liying ; XIE, Yi ; QIAN, Xiaobo: Formation of Cubic GaN Nanocrystals: A Study of the Thermal Stability of GaP Nanocrystals under Nitrogen. In: *European Journal of Inorganic Chemistry* 2004 (2004), S. 557–561

[362] SARDAR, Kripasindhu ; DAN, Meenakshi ; SCHWENZER, Birgit ; RAO, C. N. R.: A simple single-source precursor route to the nanostructures of AlN, GaN and InN. In: *J. Mater. Chem.* 15 (2005), S. 2175–2177

[363] MAZUMDER, Baishakhi ; HECTOR, Andrew L.: Synthesis and applications of nanocrystalline nitride materials. In: *J. Mater. Chem.* 19 (2009), S. 4673–4686

[364] YANG, Yefeng ; JIN, Yizheng ; HE, Haiping ; WANG, Qingling ; TU, Yao ; LU, Huanming ; YE, Zhizhen: Dopant-Induced Shape Evolution of Colloidal Nanocrystals: The Case of Zinc Oxide. In: *Journal of the American Chemical Society* 132

(2010), S. 13381–13394

[365] CHEN, Zhuo ; LI, Yanan ; CAO, Chuanbao ; ZHAO, Songrui ; FATHOLOLOUMI, Saeed ; MI, Zetian ; XU, Xingyan: Large-Scale Cubic InN Nanocrystals by a Combined Solution- and Vapor-Phase Method under Silica Confinement. In: *Journal of the American Chemical Society* 134 (2012), S. 780–783

[366] SHAHIEN, Mohammed ; YAMADA, Motohiro ; YASUI, Toshiaki ; FUKUMOTO, Masahiro: Synthesis of Cubic Aluminum Nitride Coating from Al_2O_3 Powder in Reactive Plasma Spray Process. In: *MATERIALS TRANSACTIONS* 54 (2013), S. 207–214

[367] KAUR, Prabhsharan ; SEKHON, S. S. ; KUMAR, Vijay: Prediction of rock salt structure of $(InN)_{32}$ nanoparticles from first principles calculations. In: *The Journal of Chemical Physics* 138 (2013), S. 114310

[368] RONG, Xin ; WANG, Xinqiang ; IVANOV, Sergey V. ; JIANG, Xinhe ; CHEN, Guang ; WANG, Ping ; WANG, Weiying ; HE, Chenguang ; WANG, Tao ; SCHULZ, Tobias ; ALBRECHT, Martin ; JMERIK, Valentin N. ; TOROPOV, Alexey A. ; RATNIKOV, Viacheslav V. ; KOZLOVSKY, Vladimir I. ; MARTOVITSKY, Victor P. ; JIN, Peng ; XU, Fujun ; YANG, Xuelin ; QIN, Zhixin ; GE, Weikun ; SHI, Junjie ; SHEN, Bo: High-Output-Power Ultraviolet Light Source from Quasi-2D GaN Quantum Structure. In: *Advanced Materials* 28 (2016), S. 7978–7983

[369] AL BALUSHI, Zakaria ; WANG, Y. K. ; GHOSH, Ram K. ; VILÁ, Rafael A. ; EICHFELD, Sarah M. ; CALDWELL, Joshua D. ; QIN, Xiaoye ; LIN, Yu-Chuan ; DESARIO, Paul A. ; STONE, Greg ; SUBRAMANIAN, Shruti ; PAUL, Dennis F. ; WALLACE, Robert M. ; DATTA, Suman ; REDWING, Joan M. ; ROBINSON, Joshua A.: Two-dimensional gallium nitride realized via graphene encapsulation. In: *Nature Materials* 15 (2016), S. 1166–1171

[370] CASSABOIS, G. ; VALVIN, P. ; GIL, B.: Hexagonal boron nitride is an indirect bandgap semiconductor. In: *Nature Photonics* 10 (2016), S. 262–266

[371] KOBAYASHI, Satoshi ; NONOMURA, Shuichi ; OHMORI, Takashi ; ABE, Koichi ; HIRATA, Satoshi ; UNO, Takahito ; GOTOH, Tamihiro ; NITTA, Shoji ; KOBAYASHI, Satoshi: Optical and electrical properties of amorphous and microcrystalline GaN films and their application to transparent {TFT}. In: *Applied Surface Science* 113–114 (1997), S. 480 – 484

[372] SHIM, Seung H. ; SHIM, Kwang B. ; YOON, Jong W. ; SHIMIZU, Yoshiki ; SASAKI, Takeshi ; KOSHIZAKI, Naoto: Blue luminescence from amorphous GaN films deposited by pulsed-laser ablation at room temperature. In: *Thin Solid Films* 472 (2005), Nr. 1–2, S. 11 – 15

[373] YOON, Jong-Won ; SHIM, Seung H. ; SHIM, Kwang B. ; KOSHIZAKI, Naoto ; KWON, Young-Soo: Quantum Confinement Effect of Amorphous GaN Quantum Dots Prepared by Pulsed-Laser Ablation. In: *Japanese Journal of Applied Physics* 44 (2005), S. 788

[374] KHOSHMAN, Jebreel M. ; KORDESCH, Martin E.: Optical characterization of sputtered amorphous aluminum nitride thin films by spectroscopic ellipsometry. In: *Journal of Non-Crystalline Solids* 351 (2005), Nr. 40–42, S. 3334 – 3340

[375] LI, Guanqun ; LI, Yuge ; LI, Geyang: Crystallization of amorphous AlN and superhardness effect in VC/AlN nanomultilayers. In: *Thin Solid Films* 520 (2012), S. 2032 – 2035

[376] SUZUKI, Toshimasa ; HIBINO, Shun ; KATAYAMA, Ruichi ; KATO, Yoshinori ; OHASHI, Fumitaka ; ITOH, Takashi ; NONOMURA, Shuichi: Effects of Substrate Temperature on Properties of Amorphous $In_xGa_{1-x}N$ Films Deposited by Reactive Radio Frequency Sputtering. In: *Japanese Journal of Applied Physics* 52 (2013), S. 11NG05

[377] WALUKIEWICZ, W ; III, J W A. ; YU, K M. ; LILIENTAL-WEBER, Z ; WU, J ; LI, S X. ; JONES, R E. ; DENLINGER, J D.: Structure and electronic properties of InN and In-rich group III-nitride alloys. In: *Journal of Physics D: Applied Physics* 39 (2006), S. R83

[378] SCHLEY, P. ; GOLDHAHN, R. ; WINZER, A. T. ; GOBSCH, G. ; CIMALLA, V. ; AMBACHER, O. ; LU, H. ; SCHAFF, W. J. ; KUROUCHI, M. ; NANISHI, Y. ; RAKEL, M. ; COBET, C. ; ESSER, N.: Dielectric function and Van Hove singularities for In-rich $In_xGa_{1-x}N$ alloys: Comparison of N- and metal-face materials. In: *Phys. Rev. B* 75 (2007), S. 205204

[379] KORONA, K. P. ; WYSMOŁEK, A. ; PAKUŁA, K. ; STĘPNIEWSKI, R. ; BARANOWSKI, J. M. ; GRZEGORY, I. ; ŁUCZNIK, B. ; WRÓBLEWSKI, M. ; POROWSKI, S.: Exciton region reflectance of homoepitaxial GaN layers. In: *Applied Physics Letters* 69 (1996), S. 788–790

[380] OH, Eunsoon ; LEE, S. K. ; PARK, S. S. ; LEE, K. Y. ; SONG, I. J. ; HAN, J. Y.: Optical properties of GaN grown by hydride vapor-phase epitaxy. In: *Applied Physics Letters* 78 (2001), S. 273–275

[381] GUO, Qixin ; YOSHIDA, Akira: Temperature Dependence of Band Gap Change in InN and AlN. In: *Japanese Journal of Applied Physics* 33 (1994), S. 2453

[382] LI, J. ; NAM, K. B. ; NAKARMI, M. L. ; LIN, J. Y. ; JIANG, H. X. ; CARRIER, Pierre ; WEI, Su-Huai: Band structure and fundamental optical transitions in wurtzite AlN. In: *Applied Physics Letters* 83 (2003), S. 5163–5165

[383] SILVEIRA, E. ; FREITAS, J. A. ; KNEISSL, M. ; TREAT, D. W. ; JOHNSON, N. M. ; SLACK, G. A. ; SCHOWALTER, L. J.:

Near-bandedge cathodoluminescence of an AlN homoepitaxial film. In: *Applied Physics Letters* 84 (2004), S. 3501–3503

[384] SCHLEY, P ; GOLDHAHN, R ; NAPIERALA, C ; GOBSCH, G ; SCHÖRMANN, J ; AS, D J. ; LISCHKA, K ; FENEBERG, M ; THONKE, K: Dielectric function of cubic InN from the mid-infrared to the visible spectral range. In: *Semiconductor Science and Technology* 23 (2008), S. 055001

[385] FENEBERG, Martin ; RÖPPISCHER, Marcus ; COBET, Christoph ; ESSER, Norbert ; SCHÖRMANN, Jörg ; SCHUPP, Thorsten ; AS, Donat J. ; HÖRICH, Florian ; BLÄSING, Jürgen ; KROST, Alois ; GOLDHAHN, Rüdiger: Optical properties of cubic GaN from 1 to 20 eV. In: *Phys. Rev. B* 85 (2012), S. 155207

[386] RÖPPISCHER, M. ; GOLDHAHN, R. ; ROSSBACH, G. ; SCHLEY, P. ; COBET, C. ; ESSER, N. ; SCHUPP, T. ; LISCHKA, K. ; AS, D. J.: Dielectric function of zinc-blende AlN from 1 to 20 eV: Band gap and van Hove singularities. In: *Journal of Applied Physics* 106 (2009), S. 076104

[387] FENEBERG, Martin ; ROMERO, María F. ; RÖPPISCHER, Marcus ; COBET, Christoph ; ESSER, Norbert ; NEUSCHL, Benjamin ; THONKE, Klaus ; BICKERMANN, Matthias ; GOLDHAHN, Rüdiger: Anisotropic absorption and emission of bulk $(1\bar{1}00)$ AlN. In: *Phys. Rev. B* 87 (2013), S. 235209

[388] CHICHIBU, S. ; AZUHATA, T. ; SOTA, T. ; NAKAMURA, S.: Spontaneous emission of localized excitons in InGaN single and multiquantum well structures. In: *Applied Physics Letters* 69 (1996), S. 4188–4190

[389] NAGAHAMA, Shin ichi ; YANAMOTO, Tomoya ; SANO, Masahiko ; MUKAI, Takashi: Wavelength Dependence of InGaN Laser Diode Characteristics. In: *Japanese Journal of Applied Physics* 40 (2001), S. 3075

[390] YASAN, A. ; MCCLINTOCK, R. ; MAYES, K. ; DARVISH, S. R. ; KUNG, P. ; RAZEGHI, M.: Top-emission ultraviolet light-emitting diodes with peak emission at 280 nm. In: *Applied Physics Letters* 81 (2002), Nr. 5, S. 801–802

[391] ADIVARAHAN, V. ; CHITNIS, A. ; ZHANG, J. P. ; SHATALOV, M. ; YANG, J. W. ; SIMIN, G. ; KHAN, M. A. ; GASKA, R. ; SHUR, M. S.: Ultraviolet light-emitting diodes at 340 nm using quaternary AlInGaN multiple quantum wells. In: *Applied Physics Letters* 79 (2001), S. 4240–4242

[392] FUJIKAWA, Sachie ; TAKANO, Takayoshi ; KONDO, Yukihiro ; HIRAYAMA, Hideki: Realization of 340-nm-Band High-Output-Power (>7 mW) InAlGaN Quantum Well Ultraviolet Light-Emitting Diode with p-Type InAlGaN. In: *Japanese Journal of Applied Physics* 47 (2008), S. 2941

[393] HIRAYAMA, Hideki ; AKITA, Katsushi ; KYONO, Takashi ; NAKAMURA, Takao ; ISHIBASHI, Koji: High-Efficiency 352 nm Quaternary InAlGaN-Based Ultraviolet Light-Emitting Diodes Grown on GaN Substrates. In: *Japanese Journal of Applied Physics* 43 (2004), S. L1241

[394] SCHMIDT, Mathew C. ; KIM, Kwang-Choong ; SATO, Hitoshi ; FELLOWS, Natalie ; MASUI, Hisashi ; NAKAMURA, Shuji ; DENBAARS, Steven P. ; SPECK, James S.: High Power and High External Efficiency m -Plane InGaN Light Emitting Diodes. In: *Japanese Journal of Applied Physics* 46 (2007), S. L126

[395] YAMAMOTO, Shuichiro ; ZHAO, Yuji ; PAN, Chih-Chien ; CHUNG, Roy B. ; FUJITO, Kenji ; SONODA, Junichi ; DENBAARS, Steven P. ; NAKAMURA, Shuji: High-Efficiency Single-Quantum-Well Green and Yellow-Green Light-Emitting Diodes on Semipolar (2021) GaN Substrates. In: *Applied Physics Express* 3 (2010), S. 122102

[396] ZHAO, Yuji ; SONODA, Junichi ; PAN, Chih-Chien ; BRINKLEY, Stuart ; KOSLOW, Ingrid ; FUJITO, Kenji ; OHTA, Hiroaki ; DENBAARS, Steven P. ; NAKAMURA, Shuji: 30-mW-Class High-Power and High-Efficiency Blue Semipolar (1011) InGaN/GaN Light-Emitting Diodes Obtained by Backside Roughening Technique. In: *Applied Physics Express* 3 (2010), S. 102101

[397] SHARMA, R. ; PATTISON, P. M. ; MASUI, H. ; FARRELL, R. M. ; BAKER, T. J. ; HASKELL, B. A. ; WU, F. ; DENBAARS, S. P. ; SPECK, J. S. ; NAKAMURA, S.: Demonstration of a semipolar $(10\bar{1}3)$ InGaN-GaN green light emitting diode. In: *Applied Physics Letters* 87 (2005), S. 231110

[398] KOSLOW, Ingrid L. ; SONODA, Junichi ; CHUNG, Roy B. ; PAN, Chih-Chien ; BRINKLEY, Stuart ; OHTA, Hiroaki ; NAKAMURA, Shuji ; DENBAARS, Steven P.: High Power and High Efficiency Blue InGaN Light Emitting Diodes on Free-Standing Semipolar (3031) Bulk GaN Substrate. In: *Japanese Journal of Applied Physics* 49 (2010), S. 080203

[399] HUSBERG, O ; KHARTCHENKO, A ; VOGELSANG, H ; AS, D.J ; LISCHKA, K ; NORIEGA, O.C ; TABATA, A ; SCOLFARO, L.M.R ; LEITE, J.R: Photoluminescence associated with quantum dots in cubic GaN/InGaN/GaN double heterostructures. In: *Physica E: Low-dimensional Systems and Nanostructures* 13 (2002), S. 1090 – 1093

[400] HUSBERG, O. ; KHARTCHENKO, A. ; AS, D.J. ; LISCHKA, K. ; SILVEIRA, E. ; NORIEGA, O.C. ; FERNANDEZ, J.R.L. ; LEITE, J.R.: Thermal Annealing of Cubic-InGaN/GaN Double Heterostructures. In: *physica status solidi (c)* 0 (2003), S. 293–297

[401] XIA, Congxin ; JIANG, Fengchn ; WEI, Shuyi: Exciton states in zinc-blende InGaN/GaN quantum dot. In: *Current Applied Physics* 8 (2008), S. 153 – 158

[402] JENA, Debdeep ; SIMON, John ; WANG, Albert (. ; CAO, Yu ; GOODMAN, Kevin ; VERMA, Jai ; GANGULY, Satyaki ; LI, Guowang ; KARDA, Kamal ; PROTASENKO, Vladimir ; LIAN, Chuanxin ; KOSEL, Thomas ; FAY, Patrick ; XING, Huili: Polarization-engineering in group III-nitride heterostructures: New opportunities for device design. In: *physica status solidi (a)* 208 (2011), S. 1511–1516

[403] BROCKT, G ; LAKNER, H: Probing the local dielectric/optical properties of group III-Nitrides by spatially resolved {EELS} on the nanometer scale. In: *Materials Science and Engineering: B* 59 (1999), Nr. 1–3, S. 155 – 158

[404] EDWARDS, N.V. ; BREMSER, M.D. ; BATCHELOR, A.D. ; BUYANOVA, I.A. ; MADSEN, L.D. ; YOO, S.D. ; WETHKAMP, T. ; WILMERS, K. ; COBET, C. ; ESSER, N. ; DAVIS, R.F. ; ASPNES, D.E. ; MONEMAR, B.: Optical characterization of wide bandgap semiconductors. In: *Thin Solid Films* 364 (2000), Nr. 1–2, S. 98 – 106

[405] PERSSON, C. ; AHUJA, R. ; SILVA, A. F. ; JOHANSSON, B.: First-principle calculations of optical properties of wurtzite AlN and GaN. In: *Journal of Crystal Growth* 231 (2001), S. 407 – 414

[406] FURTHMÜLLER, J. ; HAHN, P. H. ; FUCHS, F. ; BECHSTEDT, F.: Band structures and optical spectra of InN polymorphs: Influence of quasiparticle and excitonic effects. In: *Phys. Rev. B* 72 (2005), S. 205106

[407] WETHKAMP, T. ; WILMERS, K. ; ESSER, N. ; RICHTER, W. ; AMBACHER, O. ; ANGERER, H. ; JUNGK, G. ; JOHNSON, R.L. ; CARDONA, M.: Spectroscopic ellipsometry measurements of $Al_xGa_{1-x}N$ in the energy range 3-25 eV. In: *Thin Solid Films* 313–314 (1998), S. 745 – 750

[408] BUCHHEIM, C. ; GOLDHAHN, R. ; RAKEL, M. ; COBET, C. ; ESSER, N. ; ROSSOW, U. ; FUHRMANN, D. ; HANGLEITER, A.: Dielectric function and critical points of the band structure for AlGaN alloys. In: *physica status solidi (b)* 242 (2005), S. 2610–2616

[409] LEE, S. R. ; WRIGHT, A. F. ; CRAWFORD, M. H. ; PETERSEN, G. A. ; HAN, J. ; BIEFELD, R. M.: The band-gap bowing of $Al_xGa_{1-x}N$ alloys. In: *Applied Physics Letters* 74 (1999), S. 3344–3346

[410] DRIDI, Z. ; BOUHAFS, B. ; RUTERANA, P.: First-Principles Calculation of Structural and Electronic Properties of Wurtzite $Al_xGa_{1-x}N$, $In_xGa_{1-x}N$, and $In_xAl_{1-x}N$ Random Alloys. In: *physica status solidi (c)* 0 (2003), S. 315–319

[411] SCHLEY, P. ; GOLDHAHN, R. ; WINZER, A. T. ; GOBSCH, G. ; CIMALLA, V. ; AMBACHER, O. ; RAKEL, M. ; COBET, C. ; ESSER, N. ; LU, H. ; SCHAFF, W. J.: Transition energies and Stokes shift analysis for In-rich InGaN alloys. In: *physica status solidi (b)* 243 (2006), S. 1572–1576

[412] GOLDHAHN, R. ; SCHLEY, P. ; WINZER, A. T. ; GOBSCH, G. ; CIMALLA, V. ; AMBACHER, O. ; RAKEL, M. ; COBET, C. ; ESSER, N. ; LU, H. ; SCHAFF, W. J.: Detailed analysis of the dielectric function for wurtzite InN and In-rich InAlN alloys. In: *physica status solidi (a)* 203 (2006), S. 42–49

[413] SAKALAUSKAS, E ; BEHMENBURG, H ; HUMS, C ; SCHLEY, P ; ROSSBACH, G ; GIESEN, C ; HEUKEN, M ; KALISCH, H ; JANSEN, R H. ; BLÄSING, J ; DADGAR, A ; KROST, A ; GOLDHAHN, R: Dielectric function and optical properties of Al-rich AlInN alloys pseudomorphically grown on GaN. In: *Journal of Physics D: Applied Physics* 43 (2010), S. 365102

[414] SAKALAUSKAS, E. ; BEHMENBURG, H. ; SCHLEY, P. ; GOBSCH, G. ; GIESEN, C. ; KALISCH, H. ; JANSEN, R. H. ; HEUKEN, M. ; GOLDHAHN, R.: Dielectric function of Al-rich AlInN in the range 1-18 eV. In: *physica status solidi (a)* 208 (2011), S. 1517–1519

[415] OKUMURA, H. ; KOIZUMI, T. ; ISHIDA, Y. ; YAGUCHI, H. ; YOSHIDA, S.: Optical Characterization of Cubic AlGaN Epilayers by Cathodoluminescence and Spectroscopic Ellipsometry. In: *physica status solidi (b)* 216 (1999), S. 211–214

[416] MARTINEZ-GUERRERO, E. ; ENJALBERT, F. ; BARJON, J. ; BELLET-ALMARIC, E. ; DAUDIN, B. ; FERRO, G. ; JALABERT, D. ; SI DANG, Le ; MARIETTE, H. ; MONTEIL, Y. ; MULA, G.: Optical Characterization of MBE Grown Zinc-Blende AlGaN. In: *physica status solidi (a)* 188 (2001), S. 695–698

[417] NAKADAIRA, Atsushi ; TANAKA, Hidenao: Metalorganic vapor-phase epitaxy of cubic $Al_xGa_{1-x}N$ alloy on a GaAs (100) substrate. In: *Applied Physics Letters* 70 (1997), S. 2720–2722

[418] FAN, W. J. ; LI, M. F. ; CHONG, T. C. ; XIA, J. B.: Electronic properties of zincblende GaN, AlN, and their alloys $Ga_{1-x}Al_xN$. In: *Journal of Applied Physics* 79 (1996), S. 188–194

[419] FAN, W.J. ; LI, M.F. ; CHONG, T.C. ; XIA, J.B.: Band structure parameters of zinc-blende GaN, AlN and their alloys $Ga_{1-x}Al_xN$. In: *Solid State Communications* 97 (1996), S. 381 – 384

[420] ALBANESI, E. A. ; LAMBRECHT, W. R. L. ; SEGALL, B.: Electronic structure and equilibrium properties of $Ga_xAl_{1-x}N$ alloys. In: *Phys. Rev. B* 48 (1993), S. 17841–17847

[421] SÖKELAND, F. ; ROHLFING, M. ; KRÜGER, P. ; POLLMANN, J.: Density functional and quasiparticle band-structure calculations for $Ga_xAl_{1-x}N$ and $Ga_xIn_{1-x}N$ alloys. In: *Phys. Rev. B* 68 (2003), S. 075203

[422] KANOUN, M. B. ; GOUMRI-SAID, S. ; MERAD, A. E. ; MARIETTE, H.: Ab initio study of structural parameters and gap bowing in zinc-blende $Al_xGa_{1-x}N$ and $Al_xIn_{1-x}N$ alloys. In: *Journal of Applied Physics* 98 (2005), S. 063710

[423] LEE, Byounghak ; WANG, Lin-Wang: Electronic structure of zinc-blende $Al_xGa_{1-x}N$: Screened-exchange study. In: *Phys. Rev. B* 73 (2006), S. 153309

[424] LIOU, B.-T.: Electronic and structural properties of zincblende $Al_xGa_{1-x}N$. In: *Applied Physics A* 86 (2007), S. 539–543

[425] KOBAYASHI, S. ; NONOMURA, S. ; ABE, K. ; USHIKOSHI, K. ; NITTA, S.: Preparation of field effect transistor using nano-crystalline GaN. In: *Journal of Non-Crystalline Solids* 227–230, Part 2 (1998), S. 1245 – 1249

[426] HONDA, T. ; INAO, Y. ; KONNO, K. ; MINEO, K. ; KUMABE, S. ; KAWANISHI, H.: Amorphous GaN-Based Electroluminescent Devices Operating in UV Spectral Region. In: *physica status solidi (c)* 0 (2003), S. 29–33

[427] TRODAHL, H.J. ; RUCK, B.J. ; KOO, A. ; LANKE, U.D. ; BITTAR, A.: Amorphous GaN: Optoelectronic properties and device potential. In: *Transparent Optical Networks, 2003. Proceedings of 2003 5th International Conference on* Bd. 1, 2003, S. 198–200 vol.1

[428] METSON, J.B. ; RUCK, B.J. ; BUDDE, F. ; TRODAHL, H.J. ; BITTAR, A. ; PRINCE, K.E.: Characterisation of amorphous GaN films. In: *Applied Surface Science* 244 (2005), Nr. 1–4, S. 264 – 268

[429] AL-ZOUHBI, Abla ; AL-DIN, NasserSaad: Structural and optoelectronic properties of amorphous GaN thin films. In: *Optical Review* 15 (2008), S. 251–254. – ISSN 1340–6000

[430] CAI, B. ; DRABOLD, D. A.: Properties of amorphous GaN from first-principles simulations. In: *Phys. Rev. B* 84 (2011), S. 075216

[431] KHOSHMAN, Jebreel M. ; KORDESCH, Martin E.: Spectroscopic ellipsometry characterization of amorphous aluminum nitride and indium nitride thin films. In: *physica status solidi (c)* 2 (2005), S. 2821–2827

[432] DENIZ, D. ; KARABACAK, T. ; HARPER, J. M. E.: Competitive growth mechanisms of aluminum nitride thin films deposited by off-normal reactive magnetron sputtering. In: *Journal of Applied Physics* 103 (2008), S. 083553

[433] HAJAKBARI, Fatemeh ; LARIJANI, Majid M. ; GHORANNEVISS, Mahmood ; ASLANINEJAD, Morteza ; HOJABRI, Alireza: Optical Properties of Amorphous AlN Thin Films on Glass and Silicon Substrates Grown by Single Ion Beam Sputtering. In: *Japanese Journal of Applied Physics* 49 (2010), S. 095802

[434] JOSE, Feby ; RAMASESHAN, R ; DASH, S ; BERA, S ; TYAGI, A K. ; RAJ, Baldev: Response of magnetron sputtered AlN films to controlled atmosphere annealing. In: *Journal of Physics D: Applied Physics* 43 (2010), S. 075304

[435] BOSUND, Markus ; SAJAVAARA, Timo ; LAITINEN, Mikko ; HUHTIO, Teppo ; PUTKONEN, Matti ; AIRAKSINEN, Veli-Matti ; LIPSANEN, Harri: Properties of AlN grown by plasma enhanced atomic layer deposition. In: *Applied Surface Science* 257 (2011), S. 7827 – 7830

[436] DURANDURDU, Murat: Uncovering Nanoclusters in Amorphous AlN: An Ab Initio Study. In: *Journal of the American Ceramic Society* 98 (2015), S. 1095–1098

[437] CHEN, Hong ; CHEN, Kuiying ; DRABOLD, D. A. ; KORDESCH, M. E.: Band gap engineering in amorphous $Al_xGa_{1-x}N$: Experiment and ab initio calculations. In: *Applied Physics Letters* 77 (2000), S. 1117–1119

[438] CHEN, Kuiying ; DRABOLD, David A.: First principles molecular dynamics study of amorphous $Al_xGa_{1-x}N$ alloys. In: *Journal of Applied Physics* 91 (2002), S. 9743–9751

[439] TAMARIZ-KAUFMANN, Sebastian P. ; VALLADARES, Ariel A. ; VALLADARES, Alexander ; VALLADARES, R.M.: First-principles calculation of the electronic and topological properties of crystalline and amorphous $Al_xGa_{1-x}N$. In: *Journal of Non-Crystalline Solids* 420 (2015), S. 7 – 11

[440] MOORE, G. E.: Cramming More Components onto Integrated Circuits. In: *Electronics* (1965), S. 114–117

[441] HIRSCH, Andreas: The era of carbon allotropes. In: *Nature Materials* 9 (2010), S. 868–871

[442] DIEDERICH, François ; RUBIN, Yves: Synthetic Approaches toward Molecular and Polymeric Carbon Allotropes. In: *Angewandte Chemie International Edition in English* 31 (1992), Nr. 9. – ISSN 1521–3773

[443] KROTO, H. W. ; HEATH, J. R. ; O'BRIEN, S. C. ; CURL, R. F. ; SMALLEY, R. E.: C_{60}: Buckminsterfullerene. In: *Nature* 318 (1985), S. 162–163

[444] KRÄTSCHMER, W. ; LAMB, Lowell D. ; FOSTIROPOULOS, K. ; HUFFMAN, Donald R.: Solid C60: a new form of carbon. In: *Nature* 347 (1990), S. 354–358

[445] IIJIMA, Sumio: Helical microtubules of graphitic carbon. In: *Nature* 354 (1991), S. 56–58

[446] APPELL, David: Nanotechnology: Wired for success. In: *Nature* 419 (2002), S. 553–555

[447] NOVOSELOV, K. S. ; GEIM, A. K. ; MOROZOV, S. V. ; JIANG, D. ; ZHANG, Y. ; DUBONOS, S. V. ; GRIGORIEVA, I. V. ; FIRSOV, A. A.: Electric Field Effect in Atomically Thin Carbon Films. 306 (2004), Nr. 5696, S. 666–669

[448] GEIM, A. K.: Graphene: Status and Prospects. In: *Science* 324 (2009), Nr. 5934, S. 1530–1534

[449] HUANG, Xiao ; YIN, Zongyou ; WU, Shixin ; QI, Xiaoying ; HE, Qiyuan ; ZHANG, Qichun ; YAN, Qingyu ; BOEY, Freddy

; ZHANG, Hua: Graphene-Based Materials: Synthesis, Characterization, Properties, and Applications. In: *Small* 7 (2011), S. 1876–1902

[450] MACKAY, A. L. ; H., Terrones: Diamond from graphite. In: *Nature* 352 (1991), S. 762

[451] SPEAR, Karl E. ; FRENKLACH, Michael ; SPEAR, Karl E. (Hrsg.) ; DISMUKES, John P. (Hrsg.): *Mechanisms for CVD Diamond Growth*. 1st. John Wiley & Sons, 1994. – ISBN 978–0471535898

[452] FRONDEL, Clifford ; MARVIN, Ursula B.: Lonsdaleite, a Hexagonal Polymorph of Diamond. In: *Nature* 214 (1967), S. 587–589

[453] TERRONES, Humberto ; TERRONES, Mauricio: Curved nanostructured materials. In: *New Journal of Physics* 5 (2003), S. 126

[454] RODE, A.V. ; HYDE, S.T. ; GAMALY, E.G. ; ELLIMAN, R.G. ; MCKENZIE, D.R. ; BULCOCK, S.: Structural analysis of a carbon foam formed by high pulse-rate laser ablation. In: *Applied Physics A* 69 (1999), Nr. 1, S. S755–S758. – ISSN 0947–8396

[455] FERROIR, Tristan ; DUBROVINSKY, Leonid ; GORESY, Ahmed E. ; SIMIONOVICI, Alexandre ; NAKAMURA, Tomoki ; GILLET, Philippe: Carbon polymorphism in shocked meteorites: Evidence for new natural ultrahard phases. In: *Earth and Planetary Science Letters* 290 (2010), Nr. 1-2, S. 150–154

[456] ROBERTSON, J.: Amorphous carbon. In: *Advances in Physics* 35 (1986), Nr. 4, S. 317–374

[457] ROBERTSON, J.: Diamond-like amorphous carbon. In: *Materials Science and Engineering: R: Reports* 37 (2002), Nr. 4-6, S. 129–281

[458] LENG, Mei ; CHEN, Yu ; XUE, Junmin: Synthesis of TiO_2 nanosheets via an exfoliation route assisted by a surfactant. In: *Nanoscale* 6 (2014), S. 8531–8534

[459] VOGT, Patrick ; DE PADOVA, Paola ; QUARESIMA, Claudio ; AVILA, Jose ; FRANTZESKAKIS, Emmanouil ; ASENSIO, Maria C. ; RESTA, Andrea ; EALET, Bénédicte ; LE LAY, Guy: Silicene: Compelling Experimental Evidence for Graphene-like Two-Dimensional Silicon. In: *Phys. Rev. Lett.* 108 (2012), S. 155501

[460] PHILLIPS, Rob ; DRABOLD, David A. ; LENOSKY, Thomas ; ADAMS, Gary B. ; SANKEY, Otto F.: Electronic structure of schwarzite. In: *Phys. Rev. B* 46 (1992), S. 1941–1943

[461] SPADONI, S. ; COLOMBO, L. ; MILANI, P. ; BENEDEK, G.: Routes to carbon schwarzites from fullerene fragments. In: *Europhys. Lett.* 39 (1997), S. 269–274

[462] BENEDEK, G. ; COLOMBO, L. ; SPADONI, S. ; GAITO, S. ; MILANI, P.: Carbon Schwarzites: Properties and Growth Simulation from Fullerene Fragments. In: *MRS Proceedings* 491 (1997), S. 529

[463] ROSATO, Vittorio ; CELINO, Massimo ; GAITO, Sabrina ; BENEDEK, Giorgio: Thermodynamic behavior of a carbon schwarzite. In: *Computational Materials Science* 20 (2001), S. 387–393

[464] PARK, Sora ; KITTIMANAPUN, Kritsada ; AHN, Jeung S. ; KWON, Young-Kyun ; TOMÁNEK, David: Designing rigid carbon foams. In: *Journal of Physics: Condensed Matter* 22 (2010), S. 334220

[465] LHERBIER, Aurélien ; TERRONES, Humberto ; CHARLIER, Jean-Christophe: Three-dimensional massless Dirac fermions in carbon schwarzites. In: *Phys. Rev. B* 90 (2014), S. 125434

[466] LI, Zhihai ; SMEU, Manuel ; RIVES, Arnaud ; MARAVAL, Valérie ; CHAUVIN, Remi ; RATNER, Mark A. ; BORGUET, Eric: Towards graphyne molecular electronics. In: *Nature Communications* 6 (2014), S. 6321

[467] PENG, Qing ; DEARDEN, Albert K. ; CREAN, Jared ; HAN, Liang ; LIU, Sheng ; WEN, Xiaodong ; DE, Suvranu: New materials graphyne, graphdiyne, graphone, and graphane: review of properties, synthesis, and application in nanotechnology. In: *Science and Applications* 7 (2014), S. 1–29

[468] HAN, Nannan ; LIU, Hongsheng ; ZHOU, Si ; ZHAO, Jijun: Possible Formation of Graphyne on Transition Metal Surfaces: A Competition with Graphene from the Chemical Potential Point of View. In: *The Journal of Physical Chemistry C* 120 (2016), S. 14699–14705

[469] BURCHFIELD, Larry A. ; FAHIM, Mohamed A. ; WITTMAN, Richard S. ; DELODOVICI, Francesco ; MANINI, Nicola: Novamene: A new class of carbon allotropes. In: *Heliyon* 3 (2017), S. e00242

[470] BALANDIN, Alexander A. ; GHOSH, Suchismita ; BAO, Wenzhong ; CALIZO, Irene ; TEWELDEBRHAN, Desalegne ; MIAO, Feng ; LAU, Chun N.: Superior Thermal Conductivity of Single-Layer Graphene. In: *Nano Letters* 8 (2008), Nr. 3, S. 902–907

[471] CASTRO NETO, A. H. ; GUINEA, F. ; PERES, N. M. R. ; NOVOSELOV, K. S. ; GEIM, A. K.: The electronic properties of graphene. In: *Rev. Mod. Phys.* 81 (2009), S. 109–162

[472] LIU, Guanxiong ; AHSAN, Sonia ; KHITUN, Alexander G. ; LAKE, Roger K. ; BALANDIN, Alexander A.: Graphene-based non-Boolean logic circuits. In: *Journal of Applied Physics* 114 (2013), S. 154310

[473] SCHWIRTZ, Frank: Graphene Transistors: Status, Prospects, and Problems. In: *Proceedings of the IEEE* 101 (2013), S. 1567–1584

[474] TAKEDA, Kyozaburo ; SHIRAISHI, Kenji: Theoretical possibility of stage corrugation in Si and Ge analogs of graphite. In: *Phys. Rev. B* 50 (1994), S. 14916–14922

[475] GUZMÁN-VERRI, Gian G. ; LEW YAN VOON, L. C.: Electronic structure of silicon-based nanostructures. In: *Phys. Rev. B* 76 (2007), S. 075131

[476] LAY, G. L. ; PADOVA, P. D. ; RESTA, A. ; BRUHN, T. ; VOGT, P.: Epitaxial silicene: can it be strongly strained? In: *Journal of Physics D: Appl. Phys.* 45 (2012), S. 392001

[477] CHEN, Lan ; LIU, Cheng-Cheng ; FENG, Baojie ; HE, Xiaoyue ; CHENG, Peng ; DING, Zijing ; MENG, Sheng ; YAO, Yugui ; WU, Kehui: Evidence for Dirac Fermions in a Honeycomb Lattice Based on Silicon. In: *Phys. Rev. Lett.* 109 (2012), S. 056804

[478] FENG, Baojie ; DING, Zijing ; MENG, Sheng ; YAO, Yugui ; HE, Xiaoyue ; CHENG, Peng ; CHEN, Lan ; WU, Kehui: Evidence of Silicene in Honeycomb Structures of Silicon on Ag(111). In: *Nano Letters* 12 (2012), Nr. 7, S. 3507–3511

[479] GORI, Paola ; PULCI, Olivia ; RONCI, Fabio ; COLONNA, Stefano ; BECHSTEDT, Friedhelm: Origin of Dirac-cone-like features in silicon structures on Ag(111) and Ag(110). In: *Journal of Applied Physics* 114 (2013), S. 113710

[480] KAWAHARA, K. ; SHIRASAWA, T. ; ARAFUNE, R. ; LIN, C.-L. ; TAKAHASHI, T. ; KAWAI, M. ; TAKAGI, N.: Determination of atomic positions in silicene on Ag(111) by low-energy electron diffraction. In: *Surface Science* 623 (2014), Nr. 0, S. 25–28

[481] MENG, Lei ; WANG, Yeliang ; ZHANG, Lizhi ; DU, Shixuan ; WU, Rongting ; LI, Linfei ; ZHANG, Yi ; LI, Geng ; ZHOU, Haitao ; HOFER, Werner A. ; GAO, Hong-Jun: Buckled Silicene Formation on Ir(111). In: *Nano Letters* 13 (2013), S. 685–690

[482] FLEURENCE, Antoine ; FRIEDLEIN, Rainer ; OZAKI, Taisuke ; KAWAI, Hiroyuki ; WANG, Ying ; YAMADA-TAKAMURA, Yukiko: Experimental Evidence for Epitaxial Silicene on Diboride Thin Films. In: *Phys. Rev. Lett.* 108 (2012), S. 245501

[483] TAO, Li ; CINQUANTA, Eugenio ; CHIAPPE, Daniele ; GRAZIANETTI, Carlo ; FANCIULLI, Marco ; DUBEY, Madan ; MOLLE, Alessandro ; AKINWANDE, Deji: Silicene field-effect transistors operating at room temperature. In: *Nature Nanotechnology* (doi:10.1038/nnano.2014.325, 2015)

[484] LE LAY, Guy: 2D materials: Silicene transistors. In: *Nature Nanotechnology* (doi:10.1038/nnano.2015.10, 2015)

[485] PEPLOW, Mark: GrapheneÕs cousin silicene makes transistor debut. In: *Nature* 518 (2015), S. 17–18

[486] PACILÉ, D. ; MEYER, J. C. ; GIRIT, Č. Ö. ; ZETTL, A.: The two-dimensional phase of boron nitride: Few-atomic-layer sheets and suspended membranes. In: *Applied Physics Letters* 92 (2008), Nr. 13, S. 133107

[487] ALEM, Nasim ; ERNI, Rolf ; KISIELOWSKI, Christian ; ROSSELL, Marta D. ; GANNETT, Will ; ZETTL, A.: Atomically thin hexagonal boron nitride probed by ultrahigh-resolution transmission electron microscopy. In: *Phys. Rev. B* 80 (2009), S. 155425

[488] LIU, Lei ; PARK, Jewook ; SIEGEL, David A. ; MCCARTY, Kevin F. ; CLARK, Kendal W. ; DENG, Wan ; BASILE, Leonardo ; IDROBO, Juan C. ; LI, An-Ping ; GU, Gong: Heteroepitaxial Growth of Two-Dimensional Hexagonal Boron Nitride Templated by Graphene Edges. In: *Science* 343 (2014), Nr. 6167, S. 163–167

[489] TAY, Roland Y. ; GRIEP, Mark H. ; MALLICK, Govind ; TSANG, Siu H. ; SINGH, Ram S. ; TUMLIN, Travis ; TEO, Edwin Hang T. ; KARNA, Shashi P.: Growth of Large Single-Crystalline Two-Dimensional Boron Nitride Hexagons on Electropolished Copper. In: *Nano Letters* 14 (2014), Nr. 2, S. 839–846

[490] ZHONG, Xiaoliang ; AMORIM, Rodrigo G. ; ROCHA, Alexandre R. ; PANDEY, Ravindra: Hybridization effects on the out-of-plane electron tunneling properties of monolayers: is h-BN more conductive than graphene? In: *Nanotechnology* 25 (2014), Nr. 34, S. 345703

[491] YANKOWITZ, Matthew ; XUE, Jiamin ; LEROY, B J.: Graphene on hexagonal boron nitride. In: *Journal of Physics: Condensed Matter* 26 (2014), Nr. 30, S. 303201

[492] KVASHNIN, D. G. ; BELLUCCI, S. ; CHERNOZATONSKII, L. A.: Sharp variations in the electronic properties of graphene deposited on the h-BN layer. In: *Phys. Chem. Chem. Phys.* 17 (2015), S. 4354

[493] GEIM, A. K. ; V., Grigorieva I.: Van der Waals heterostructures. In: *Nature* 499 (2013), S. 419–425

[494] WILSON, J.A. ; YOFFE, A.D.: The transition metal dichalcogenides discussion and interpretation of the observed optical, electrical and structural properties. In: *Advances in Physics* 18 (1969), Nr. 73, S. 193–335

[495] BENAMEUR, M M. ; RADISAVLJEVIC, B ; HÉRON, J S. ; SAHOO, S ; BERGER, H ; KIS, A: Visibility of dichalcogenide nanolayers. In: *Nanotechnology* 22 (2011), Nr. 12, S. 125706

[496] COLEMAN, Jonathan N. ; LOTYA, Mustafa ; OÕNEILL, Arlene ; BERGIN, Shane D. ; KING, Paul J. ; KHAN, Umar ; YOUNG, Karen ; GAUCHER, Alexandre ; DE, Sukanta ; SMITH, Ronan J. ; SHVETS, Igor V. ; ARORA, Sunil K. ; STANTON, George

; KIM, Hye-Young ; LEE, Kangho ; KIM, Gyu T. ; DUESBERG, Georg S. ; HALLAM, Toby ; BOLAND, John J. ; WANG, Jing J. ; DONEGAN, John F. ; GRUNLAN, Jaime C. ; MORIARTY, Gregory ; SHMELIOV, Aleksey ; NICHOLLS, Rebecca J. ; PERKINS, James M. ; GRIEVESON, Eleanor M. ; THEUWISSEN, Koenraad ; MCCOMB, David W. ; NELLIST, Peter D. ; NICOLOSI, Valeria: Two-Dimensional Nanosheets Produced by Liquid Exfoliation of Layered Materials. In: *Science* 331 (2011), Nr. 6017, S. 568–571

[497] FENG, Jun ; PENG, Lele ; WU, Changzheng ; SUN, Xu ; HU, Shuanglin ; LIN, Chenwen ; DAI, Jun ; YANG, Jinlong ; XIE, Yi: Giant Moisture Responsiveness of VS_2 Ultrathin Nanosheets for Novel Touchless Positioning Interface. In: *Advanced Materials* 24 (2012), Nr. 15, S. 1969–1974

[498] WANG, Qing H. ; KALANTAR-ZADEH, Kourosh ; KIS, Andras K. ; COLEMAN, Jonathan N. ; STRANO, Michael S.: Electronics and optoelectronics of two-dimensional transition metal dichalcogenides. In: *Nano Nanotechnology* 7 (2012), S. 699–712

[499] QIAN, Xiaofeng ; LIU, Junwei ; FU, Liang ; LI, Ju: Quantum spin Hall effect in two-dimensional transition metal dichalcogenides. In: *Science* 346 (2014), S. 1344–1347

[500] TARANCÓN, Albert ; BURRIEL, Mónica ; SANTISO, José ; SKINNER, Stephen J. ; KILNER, John A.: Advances in layered oxide cathodes for intermediate temperature solid oxide fuel cells. In: *J. Mater. Chem.* 20 (2010), S. 3799–3813

[501] MA, Renzhi ; SASAKI, Takayoshi: Nanosheets of Oxides and Hydroxides: Ultimate 2D Charge-Bearing Functional Crystallites. In: *Advanced Materials* 22 (2010), Nr. 45, S. 5082–5104

[502] PACCHIONI, Gianfranco: Two-Dimensional Oxides: Multifunctional Materials for Advanced Technologies. In: *Chemistry, A European Journal* 18 (2012), Nr. 33, S. 10144–10158

[503] KEYES, Robert W.: The Electrical Properties of Black Phosphorus. In: *Phys. Rev.* 92 (1953), S. 580–584

[504] MORITA, A.: Semiconducting black phosphorus. In: *Applied Physics A* 39 (1986), Nr. 4, S. 227–242. – ISSN 0947–8396

[505] CHANG, K. J. ; COHEN, Marvin L.: Structural stability of phases of black phosphorus. In: *Phys. Rev. B* 33 (1986), S. 6177–6186

[506] LI, Likai ; YU, Yijun ; YE, Guo J. ; GE, Qingqin ; OU, Xuedong ; WU, Hua ; FENG, Donglai ; CHEN, Xian H. ; ZHANG, Yuanbo: Black phosphorus field-effect transistors. In: *Nature Nanotechnology* 9 (2014), S. 372–377

[507] TRAN, Vy ; SOKLASKI, Ryan ; LIANG, Yufeng ; YANG, Li: Layer-controlled band gap and anisotropic excitons in few-layer black phosphorus. In: *Phys. Rev. B* 89 (2014), S. 235319

[508] LOW, Tony ; RODIN, A. S. ; CARVALHO, A. ; JIANG, Yongjin ; WANG, Han ; XIA, Fengnian ; CASTRO NETO, A. H.: Tunable optical properties of multilayer black phosphorus thin films. In: *Phys. Rev. B* 90 (2014), S. 075434

[509] ZHANG, Shengli ; YAN, Zhong ; LI, Yafei ; CHEN, Zhongfang ; ZENG, Haibo: Atomically Thin Arsenene and Antimonene: Semimetal–Semiconductor and Indirect–Direct Band-Gap Transitions. In: *Angewandte Chemie International Edition* 54 (2015), S. 1–5

[510] XU, Yong ; YAN, Binghai ; ZHANG, Hai-Jun ; WANG, Jing ; XU, Gang ; TANG, Peizhe ; DUAN, Wenhui ; ZHANG, Shou-Cheng: Large-Gap Quantum Spin Hall Insulators in Tin Films. In: *Phys. Rev. Lett.* 111 (2013), S. 136804

[511] BROEK, B van d. ; HOUSSA, M ; SCALISE, E ; POURTOIS, G ; ÄÒEV, V V A. ; STESMANS, A: Two-dimensional hexagonal tin: ab initio geometry, stability, electronic structure and functionalization. In: *2D Materials* 1 (2014), Nr. 2, S. 021004

[512] CRESPI, Vincent H. ; BENEDICT, Lorin X. ; COHEN, Marvin L. ; LOUIE, Steven G.: Prediction of a pure-carbon planar covalent metal. In: *Phys. Rev. B* 53 (1996), S. R13303–R13305

[513] STONE, A.J. ; WALES, D.J.: Theoretical studies of icosahedral C_{60} and some related species. In: *Chemical Physics Letters* 128 (1986), Nr. 5-6, S. 501 – 503

[514] TERRONES, H. ; TERRONES, M. ; HERNÁNDEZ, E. ; GROBERT, N. ; CHARLIER, J-C. ; AJAYAN, P. M.: New Metallic Allotropes of Planar and Tubular Carbon. In: *Phys. Rev. Lett.* 84 (2000), S. 1716–1719

[515] MPOURMPAKIS, Giannis ; FROUDAKIS, George E. ; TYLIANAKIS, Emmanuel: Haeckelites: A promising anode material for lithium batteries application. An ab initio and molecular dynamics theoretical study. In: *Applied Physics Letters* 89 (2006), S. 233125

[516] LISENKOV, S. V. ; VINOGRADOV, G. A. ; ASTAKHOVA, T. Y. ; LEBEDEV, N. G.: Geometric structure and electronic properties of planar and nanotubular BN structures of the Haeckelite type. In: *Physics of the Solid State* 48 (2006), S. 192–198

[517] CAMACHO-MOJICA, Dulce C. ; LÓPEZ-URÍAS, Florentino: GaN Haeckelite Single-Layered Nanostructures: Monolayer and Nanotubes. In: *Sci. Rep.* 5 (2015), S. 17902

[518] ZHANG, Shunhong ; ZHOU, Jian ; WANG, Qian ; CHEN, Xiaoshuang ; KAWAZOE, Yoshiyuki ; JENA, Puru: Penta-graphene: A new carbon allotrope. In: *Proceedings of the National Academy of Sciences* 112 (2015), S. 2372–2377

[519] KAYACI, Fatma ; VEMPATI, Sesha ; OZGIT-AKGUN, Cagla ; DONMEZ, Inci ; BIYIKLI, Necmi ; UYAR, Tamer: Selective isolation of the electron or hole in photocatalysis: ZnO-TiO_2 and TiO_2-ZnO core-shell structured heterojunction nanofibers via electrospinning and atomic layer deposition. In: *Nanoscale* 6 (2014), S. 5735–5745

[520] ŠTENGL, Vaclav ; BAKARDJIEVA, Snejana ; GRYGAR, Tomáš M. ; BLUDSKÁ, Jana ; KORMUNDA, Martin: TiO_2-graphene oxide nanocomposite as advanced photocatalytic materials. In: *Chemistry Central Journal* 7 (2013), Nr. 1, S. 41

[521] KLEY, Christopher S. ; DETTE, Christian ; RINKE, Gordon ; PATRICK, Christopher E. ; ČECHAL, Jan ; JUNG, Soon J. ; BAUR, Markus ; DÜRR, Michael ; RAUSCHENBACH, Stephan ; GIUSTINO, Feliciano ; STEPANOW, Sebastian ; KERN, Klaus: Atomic-Scale Observation of Multiconformational Binding and Energy Level Alignment of Ruthenium-Based Photosensitizers on TiO_2 Anatase. In: *Nano Letters* 14 (2014), Nr. 2, S. 563–569

[522] LUI, Gregory ; LIAO, Jin-Yun ; DUAN, Aoshu ; ZHANG, Zisheng ; FOWLER, Michael ; YU, Aiping: Graphene-wrapped hierarchical TiO_2 nanoflower composites with enhanced photocatalytic performance. In: *J. Mater. Chem. A* 1 (2013), S. 12255–12262

[523] SHEN, Laifa ; ZHANG, Xiaogang ; LI, Hongsen ; YUAN, Changzhou ; CAO, Guozhong: Design and Tailoring of a Three-Dimensional TiO_2-Graphene-Carbon Nanotube Nanocomposite for Fast Lithium Storage. In: *The Journal of Physical Chemistry Letters* 2 (2011), Nr. 24, S. 3096–3101

[524] CHEN, Jun S. ; WANG, Zhiyu ; DONG, Xiao C. ; CHEN, Peng ; LOU, Xiong Wen D.: Graphene-wrapped TiO_2 hollow structures with enhanced lithium storage capabilities. In: *Nanoscale* 3 (2011), S. 2158–2161

[525] LI, Wei ; WANG, Fei ; FENG, Shanshan ; WANG, Jinxiu ; SUN, Zhenkun ; LI, Bin ; LI, Yuhui ; YANG, Jianping ; ELZATAHRY, Ahmed A. ; XIA, Yongyao ; ZHAO, Dongyuan: Sol-Gel Design Strategy for Ultradispersed TiO_2 Nanoparticles on Graphene for High-Performance Lithium Ion Batteries. In: *Journal of the American Chemical Society* 135 (2013), Nr. 49, S. 18300–18303

[526] SHEN, Yaodong ; CHEN, JunSong ; ZHU, Jixin ; YAN, Qingyu ; HU, Xiao: Growth of two-dimensional ultrathin anatase TiO_2 nanoplatelets on graphene for high-performance lithium-ion battery. In: *Journal of Nanoparticle Research* 15 (2013), Nr. 10, S. 1913. – ISSN 1388–0764

[527] DAHL, Michael ; LIU, Yiding ; YIN, Yadong: Composite Titanium Dioxide Nanomaterials. In: *Chemical Reviews* (2014)

[528] LIU, Yingliang ; WANG, Shengping ; XU, Shengang ; CAO, Shaokui: Evident improvement of nitrogen-doped graphene on visible light photocatalytic activity of N-TiO_2/N-graphene nanocomposites. In: *Materials Research Bulletin* 65 (2015), Nr. 0, S. 27 – 35

[529] OGURA, Reiko Y. ; NAKANE, Shigeru ; MOROOKA, Masahiro ; ORIHASHI, Masaki ; SUZUKI, Yusuke ; NODA, Kazuhiro: High-performance dye-sensitized solar cell with a multiple dye system. In: *Applied Physics Letters* 94 (2009), Nr. 7, S. 073308

[530] NATTESTAD, A. ; MOZER, A. J. ; FISCHER, M. K. R. ; CHENG, Y.-B. ; MISHRA, A. ; BAUERLE, P. ; BACH, U.: Highly efficient photocathodes for dye-sensitized tandem solar cells. In: *Nature Materials* 9 (2010), S. 31–35

[531] PETER, Laurence M.: The Grätzel Cell: Where Next? In: *The Journal of Physical Chemistry Letters* 2 (2011), Nr. 15, S. 1861–1867

[532] HARDIN, Brian E. ; SNAITH, Henry J. ; MCGEHEE, Michael D.: The renaissance of dye-sensitized solar cells. In: *Nature Photonics* 6 (2012), S. 162–169

[533] MEYER, Gerald J.: The 2010 Millennium Technology Grand Prize: Dye-Sensitized Solar Cells. In: *ACS Nano* 4 (2010), Nr. 8, S. 4337–4343

[534] ZHANG, Yanhui ; TANG, Zi-Rong ; FU, Xianzhi ; XU, Yi-Jun: TiO_2-Graphene Nanocomposites for Gas-Phase Photocatalytic Degradation of Volatile Aromatic Pollutant: Is TiO_2-Graphene Truly Different from Other TiO_2-Carbon Composite Materials? In: *ACS Nano* 4 (2010), Nr. 12, S. 7303–7314

[535] ZHANG, Hao ; LV, Xiaojun ; LI, Yueming ; WANG, Ying ; LI, Jinghong: P25-Graphene Composite as a High Performance Photocatalyst. In: *ACS Nano* 4 (2010), Nr. 1, S. 380–386

[536] HUANG, Qingwu ; TIAN, Shouqin ; ZENG, Dawen ; WANG, Xiaoxia ; SONG, Wulin ; LI, Yingying ; XIAO, Wei ; XIE, Changsheng: Enhanced Photocatalytic Activity of Chemically Bonded TiO_2/Graphene Composites Based on the Effective Interfacial Charge Transfer through the C-Ti Bond. In: *ACS Catalysis* 3 (2013), Nr. 7, S. 1477–1485

[537] YANG, Min-Quan ; ZHANG, Nan ; PAGLIARO, Mario ; XU, Yi-Jun: Artificial photosynthesis over graphene-semiconductor composites. Are we getting better? In: *Chem. Soc. Rev.* 43 (2014), S. 8240–8254

[538] LIU, Jincheng ; LIU, Lei ; BAI, Hongwei ; WANG, Yinjie ; SUN, Darren D.: Gram-scale production of graphene oxide–TiO_2 nanorod composites: Towards high-activity photocatalytic materials. In: *Applied Catalysis B: Environmental* 106 (2011), Nr. 1–2, S. 76 – 82

[539] KIM, Suenne ; ZHOU, Si ; HU, Yike ; ACIK, Muge ; CHABAL, Yves J. ; BERGER, Claire ; HEER, Walt d. ; BONGIORNO, Angelo ; RIEDO, Elisa: Room-temperature metastability of multilayer graphene oxide films. In: *Nature Materials* (2012), S. 544–549

[540] TAN, Lling-Lling ; ONG, Wee-Jun ; CHAI, Siang-Piao ; MOHAMED, AbdulRahman: Reduced graphene oxide-TiO_2 nanocomposite as a promising visible-light-active photocatalyst for the conversion of carbon dioxide. In: *Nanoscale Research Letters* 8 (2013), Nr. 1, S. 465. – ISSN 1931–7573

[541] HOW, Gregory Thien S. ; PANDIKUMAR, Alagarsamy ; MING, Huang N. ; NGEE, Lim H.: Highly exposed 001 facets of titanium dioxide modified with reduced graphene oxide for dopamine sensing. In: *Scientific Reports* 4 (2014), S. 5044

[542] ZHAO, Lei ; XIA, Maosheng ; LIU, Yuhua ; ZHENG, Biju ; JIANG, Qing ; LIAN, Jianshe: Structure and Photocatalysis of TiO_2/ZnO Double-Layer Film Prepared by Pulsed Laser Deposition. In: *Materials Transactions* 53 (2012), S. 463–468

[543] YAN, Xiaodong ; ZOU, Chongwen ; GAO, Xiangdong ; GAO, Wei: ZnO/TiO_2 core-brush nanostructure: processing, microstructure and enhanced photocatalytic activity. In: *J. Mater. Chem.* 22 (2012), S. 5629–5640

[544] GU, Yu-Zhu ; LU, Hong-Liang ; GENG, Yang ; YE, Zhi-Yuan ; ZHANG, Yuan ; SUN, Qing-Qing ; DING, Shi-Jin ; ZHANG, David W.: Optical and microstructural properties of ZnO/TiO_2 nanolaminates prepared by atomic layer deposition. In: *Nanoscale Research Letters* 8 (2013), S. 107

[545] CHENG, Chun ; AMINI, Abbas ; ZHU, Chao ; XU, Zuli ; SONG, Haisheng ; WANG, Ning: Enhanced photocatalytic performance of TiO_2-ZnO hybrid nanostructures. In: *Scientific Reports* 4 (2014), S. 4181

[546] WATSON, J. D. ; CRICK, F. H. C.: Molecular Structure of Nucleic Acids: A Structure for Deoxyribose Nucleic Acid. In: *Nature* 171 (1953), S. 737–738

[547] CRICK, F. H. C.: THE COMPLEMENTARY STRUCTURE OF DNA. In: *Proc. Nat. Acad. Sci. U.S.A.* 40 (1954), Nr. 8, S. 756–758

[548] SAKAMOTO, Junji ; HEIJST, Jeroen van ; LUKIN, Oleg ; SCHL|ÜTER, A. D.: Two-Dimensional Polymers: Just a Dream of Synthetic Chemists? In: *Angewandte Chemie International Edition* 48 (2009), Nr. 6, S. 1030–1069

[549] SPITLER, Eriv L. ; DICHTEL, William R.: Lewis acid-catalysed formation of two-dimensional phthalocyanine covalent organic frameworks. In: *Nature Chemistry* 2 (2010), S. 672–677

[550] URIBE-ROMO, Fernando J. ; DICHTEL, William R.: Two-dimensional materials: Polymers stripped down. In: *Nature Chemistry* 4 (2012), S. 244–245

[551] COLSON, John W. ; DICHTEL, William R.: Rationally synthesized two-dimensional polymers. In: *Nature Chemistry* 5 (2013), S. 453–465

[552] ZHANG, Liang ; ZHOU, Tian-You ; TIAN, Jia ; WANG, Hui ; ZHANG, Dan-Wei ; ZHAO, Xin ; LIU, Yi ; LI, Zhan-Ting: A two-dimensional single-layer supramolecular organic framework that is driven by viologen radical cation dimerization and further promoted by cucurbit[8]uril. In: *Polym. Chem.* 5 (2014), S. 4715–4721

[553] CHAMPNESS, Neil R.: Two-dimensional materials: Crystallized creations in 2D. In: *Nature Chemistry* 6 (2014), S. 757–759

[554] KISSEL, Patrick ; MURRAY, Daniel J. ; WULFTANGE, William J. ; CATALANO, Vincent J. ; KING, Benjamin T.: A nanoporous two-dimensional polymer by single-crystal-to-single-crystal photopolymerization. In: *Nature Chemistry* 6 (2014), S. 774–778

[555] KORY, Max J. ; WÖRLE, Michael ; WEBER, Thomas ; PAYAMYAR, Payam ; POLL, Stan W. d. ; DSHEMUCHADSE, Julia ; TRAPP, Nils ; SCHLÜTER, A. D.: Gram-scale synthesis of two-dimensional polymer crystals and their structure analysis by X-ray diffraction. In: *Nature Chemistry* 6 (2014), S. 779–784

[556] LI, Gao ; ZHU, Chengfeng ; XI, Xiaobing ; CUI, Yong: Selective binding and removal of organic molecules in a flexible polymeric material with stretchable metallosalen chains. In: *Chem. Commun.* (2009), S. 2118–2120

[557] DAWSON, Robert ; COOPER, Andrew I. ; ADAMS, Dave J.: Nanoporous organic polymer networks. In: *Progress in Polymer Science* 37 (2012), Nr. 4, S. 530 – 563

[558] BARTH, J. V. ; COSTANTINI, G. ; KERN, K.: Engineering atomic and molecular nanostructures at surfaces. In: *Nature* 437 (2005), S. 671–679

[559] BETTI, Maria G. ; GARGIANI, Pierluigi ; MARIANI, Carlo ; BIAGI, Roberto ; FUJII, Jun ; ROSSI, Giorgio ; RESTA, Andrea ; FABRIS, Stefano ; FORTUNA, Sara ; TORRELLES, Xavier ; KUMAR, Manvendra ; PEDIO, Maddalena: Structural Phases of Ordered FePc-Nanochains Self-Assembled on Au(110). In: *Langmuir* 28 (2012), Nr. 37, S. 13232–13240

[560] FORTUNA, Sara ; GARGIANI, Pierluigi ; BETTI, Maria G. ; MARIANI, Carlo ; CALZOLARI, Arrigo ; MODESTI, Silvio ; FABRIS, Stefano: Molecule-Driven Substrate Reconstruction in the Two-Dimensional Self-Organization of Fe-Phthalocyanines on Au(110). In: *The Journal of Physical Chemistry C* 116 (2012), Nr. 10, S. 6251–6258

[561] ZALAKE, Pratap ; THOMAS, K. G.: Role of Hydrogen Bonding on the Self-Organization of Phenyleneethynylenes on

Surfaces. In: *Langmuir* 29 (2013), Nr. 7, S. 2242–2249

[562] STÖCKL, Quirin ; BANDERA, Davide ; KAPLAN, Craig S. ; ERNST, Karl-Heinz ; SIEGEL, Jay S.: Gear-Meshed Tiling of Surfaces with Molecular Pentagonal Stars. In: *Journal of the American Chemical Society* 136 (2014), S. 606–609

[563] URGEL, José I. ; ECIJA, David ; AUWÄRTER, Willi ; PAPAGEORGIOU, Anthoula C. ; SEITSONEN, Ari P. ; VIJAYARAGHAVAN, Saranyan ; JOSHI, Sushobhan ; FISCHER, Sybille ; REICHERT, Joachim ; BARTH, Johannes V.: Five-Vertex Lanthanide Coordination on Surfaces: A Route to Sophisticated Nanoarchitectures and Tessellations. In: *The Journal of Physical Chemistry C* 118 (2014), S. 12908–12915

[564] LAFFERENTZ, Leif ; AMPLE, Francisco ; YU, Hao ; HECHT, Stefan ; JOACHIM, Christian ; GRILL, Leonhard: Conductance of a Single Conjugated Polymer as a Continuous Function of Its Length. In: *Science* 323 (2009), Nr. 5918, S. 1193–1197

[565] OUCHI, Makoto ; BADI, Nezha ; LUTZ, Jean-François ; SAWAMOTO, Mitsuo: Single-chain technology using discrete synthetic macromolecules. In: *Nature Chemistry* 3 (2011), S. 917–924

[566] KAWAI, Shigeki ; KOCH, Matthias ; GNECCO, Enrico ; SADEGHI, Ali ; PAWLAK, Rémy ; GLATZEL, Thilo ; SCHWARZ, Jutta ; GOEDECKER, Stefan ; HECHT, Stefan ; BARATOFF, Alexis ; GRILL, Leonhard ; MEYER, Ernst: Quantifying the atomic-level mechanics of single long physisorbed molecular chains. In: *Proceedings of the National Academy of Sciences* 111 (2014), Nr. 11, S. 3968–3972

[567] WHITESIDES, George M. ; BONCHEVA, Mila: Beyond molecules: Self-assembly of mesoscopic and macroscopic components. In: *Proc. Nat. Acad. Sci. U.S.A.* 99 (2002), Nr. 8, S. 4769–4774

[568] WHITESIDES, George M. ; GRZYBOWSKI, Bartosz: Self-Assembly at All Scales. In: *Science* 295 (2002), Nr. 5564, S. 2418–2421

[569] BLANKENBURG, S. ; SCHMIDT, W. G.: Long-Range Chiral Recognition due to Substrate Locking and Substrate-Adsorbate Charge Transfer. In: *Phys. Rev. Lett.* 99 (2007), S. 196107

[570] ELLIOTT, S. R.: Medium-range structural order in covalent amorphous solids. In: *Nature* 354 (1991), S. 445–452

[571] JANOT, C.: *Quasicrystals – A Primer*. Oxford University Press, 2012. – ISBN 978–0–19–965740–7

[572] WRIGHT, Adrian C.: The Great Crystallite Versus Random Network Controversy: A Personal Perspective. In: *International Journal of Applied Glass Science* 5 (2014), S. 31–56

[573] LITVIN, D. B.: Tables of crystallographic properties of magnetic space groups. In: *Acta Crystallographica Section A* 64 (2008), S. 419–424

[574] LITVIN, D. B.: Spin translation groups and neutron diffraction analysis. In: *Acta Crystallographica Section A* 29 (1973), S. 651–660

[575] HALASYAMANI, P. S. ; POEPPELMEIER, Kenneth R.: Noncentrosymmetric Oxides. In: *Chemistry of Materials* 10 (1998), S. 2753–2769

[576] OK, Kang M. ; CHI, Eun O. ; HALASYAMANI, P. S.: Bulk characterization methods for non-centrosymmetric materials: second-harmonic generation, piezoelectricity, pyroelectricity, and ferroelectricity. In: *Royal Society of Chemistry* 35 (2006), S. 710–717

[577] SHECHTMAN, D. ; BLECH, I. ; GRATIAS, D. ; CAHN, J. W.: Metallic Phase with Long-Range Orientational Order and No Translational Symmetry. In: *Phys. Rev. Lett.* 53 (1984), S. 1951–1953

[578] LEVINE, Dov ; STEINHARDT, Paul J.: Quasicrystals: A New Class of Ordered Structures. In: *Phys. Rev. Lett.* 53 (1984), S. 2477–2480

[579] SOCOLAR, Joshua E. S. ; STEINHARDT, Paul J. ; LEVINE, Dov: Quasicrystals with arbitrary orientational symmetry. In: *Phys. Rev. B* 32 (1985), S. 5547–5550

[580] LEVINE, Dov ; STEINHARDT, Paul J.: Quasicrystals. I. Definition and structure. In: *Phys. Rev. B* 34 (1986), S. 596–616

[581] SOCOLAR, Joshua E. S. ; STEINHARDT, Paul J.: Quasicrystals. II. Unit-cell configurations. In: *Phys. Rev. B* 34 (1986), S. 617–647

[582] ONODA, George Y. ; STEINHARDT, Paul J. ; DIVINCENZO, David P. ; SOCOLAR, Joshua E. S.: Growing Perfect Quasicrystals. In: *Phys. Rev. Lett.* 60 (1988), S. 2653–2656

[583] GRATIAS, D: Quasicrystals: A New Kind of Ordered Solids. In: *Physica Scripta* 1989 (1989), S. 38

[584] STEINHARDT, Paul J. ; JEONG, H.-C. ; SAITOH, K. ; TANAKA3, M. ; ABE, E. ; TSAI, A. P.: Experimental verification of the quasi-unit-cell model of quasicrystal structure. In: *Nature* 396 (1998), S. 55–57

[585] JANOT, C. ; PATERA, J.: Simple physical generation of quasicrystals. In: *Physics Letters A* 233 (1997), Nr. 1-2, S. 110 – 114

[586] STEINHARDT, Paul J.: Penrose tilings, cluster models and the quasi-unit cell picture. In: *Materials Science and Engineering: A* 294-296 (2000), S. 205 – 210

[587] LU, Peter J. ; DEFFEYES, Kenneth ; STEINHARDT, Paul J. ; YAO, Nan: Identifying and Indexing Icosahedral Quasicrystals from Powder Diffraction Patterns. In: *Phys. Rev. Lett.* 87 (2001), S. 275507

[588] GÄHLER, Franz ; REICHERT, Michael: Cluster models of decagonal tilings and quasicrystals. In: *Journal of Alloys and Compounds* 342 (2002), S. 180–185

[589] STEURER, Walter: Twenty years of structure research on quasicrystals. Part I. Pentagonal, octagonal, decagonal and dodecagonal quasicrystals. In: *Zeitschrift für Kristallographie* 219 (2004), S. 391–446

[590] DUBOIS, Jean-Marie: New prospects from potential applications of quasicrystalline materials. In: *Materials Science and Engineering: A* 294-296 (2000), S. 4 – 9

[591] BINDI, Luca ; STEINHARDT, Paul J. ; YAO, Nan ; LU, Peter J.: Natural Quasicrystals. In: *Science* 324 (2009), S. 1306–1309

[592] BINDI, Luca ; STEINHARDT, PauL J. ; YAO, Nan ; LU, Peter J.: IIcosahedrite, $Al_{63}Cu_{24}Fe_{13}$, the first natural quasicrystal. In: *American Mineralogist* 96 (2011), S. 928

[593] BINDI, Luca ; EILER, John M. ; GUAN, Yunbin ; HOLLISTER, Lincoln S. ; MACPHERSON, Glenn ; STEINHARDT, Paul J. ; YAO, Nan: Evidence for the extraterrestrial origin of a natural quasicrystal. In: *Proceedings of the National Academy of Sciences* 109 (2012), S. 1396–1401

[594] STEINHARDT, Paul J. ; BINDI, Luca: In search of natural quasicrystals. In: *Reports on Progress in Physics* 75 (2012), S. 092601

[595] STEINHARDT, Paul J.: Quasicrystals: a brief history of the impossible. In: *Rendiconti Lincei* 24 (2013), S. 85–91

[596] AU-YANG, Helen ; PERK, Jacques H.: Quasicrystalsâ – The impact of N.G. de Bruijn. In: *Indagationes Mathematicae* 24 (2013), S. 996 – 1017

[597] SHECHTMAN, Daniel: Quasi-Periodic Crystals–The Long Road from Discovery to Acceptance. In: *Rambam Maimonides Medical Journal* 4 (2013), S. e0002

[598] GROSSMAN, Lisa: Rock from a hard place. In: *New Scientist* 223 (2014), S. 38 – 41

[599] BOHR, Harald: Zur Theorie der fastperiodischen Funktionen. In: *Acta Mathematica* 45 (1925), S. 29

[600] BOHR, Harald: Zur Theorie der fastperiodischen Funktionen. In: *Acta Mathematica* 46 (1925), S. 101–214

[601] BOHR, Harald: Zur Theorie der fastperiodischen Funktionen. In: *Acta Mathematica* 47 (1926), S. 237

[602] Report of the Executive Committee for 1991. In: *Acta Crystallographica Section A* 48 (1992), S. 922–946

[603] EBERT, Ph. ; FEUERBACHER, M. ; TAMURA, N. ; WOLLGARTEN, M. ; URBAN, K.: Evidence for a Cluster-Based Structure of AlPdMn Single Quasicrystals. In: *Phys. Rev. Lett.* 77 (1996), S. 3827–3830

[604] TSAI1, A. P. ; GUO, J. Q. ; ABE, E. ; TAKAKURA1, H. ; SATO, T. J.: Alloys: A stable binary quasicrystal. In: *Nature* 408 (2000), S. 537–538

[605] HENNIG, R. G. ; MAJZOUB, E. H. ; CARLSSON, A. E. ; KELTON, K. F. ; HENLEY, C. L. ; YELON, W. B. ; MISTURE, S.: Structural modelling of the Ti-Zr-Ni quasicrystal. In: *Materials Science and Engineering* 294-296 (2000), S. 361–365

[606] ZIJLSTRA, E. S. ; BOSE, S. K. ; DOLINŠEK, J.: Structural model and electronic structure of the icosahedral $Al-Ga-Pd-Mn$ quasicrystal. In: *Phys. Rev. B* 72 (2005), S. 092203

[607] YADAV, T.P. ; SINGH, Devinder ; SHAHI, Rohit R. ; SHAZ, M.A. ; TIWARI, R.S. ; SRIVASTAVA, O.N.: Synthesis of quasicrystalline film of Al–Ga-Pd–Mn alloy. In: *Thin Solid Films* 534 (2013), S. 265 – 269

[608] STAGNO, Vincenzo ; BINDI, Luca ; SHIBAZAKI, Yuki ; TANGE, Yoshinori ; HIGO, Yuji ; MAO, H.-K. ; STEINHARDT, Paul J. ; FEI, Yingwei: Icosahedral AlCuFe quasicrystal at high pressure and temperature and its implications for the stability of icosahedrite. In: *Scientific Reports* 4 (2014), S. 5869

[609] WANG, N. ; CHEN, H. ; KUO, K. H.: Two-dimensional quasicrystal with eightfold rotational symmetry. In: *Phys. Rev. Lett.* 59 (1987), S. 1010–1013

[610] BURKOV, S. E.: Structure model of the Al-Cu-Co decagonal quasicrystal. In: *Phys. Rev. Lett.* 67 (1991), S. 614–617

[611] ABE, Eiji ; SAITOH, Koh ; TAKAKURA, H. ; TSAI, A. P. ; STEINHARDT, P. J. ; JEONG, H.-C.: Quasi-Unit-Cell Model for an Al-Ni-Co Ideal Quasicrystal based on Clusters with Broken Tenfold Symmetry. In: *Phys. Rev. Lett.* 84 (2000), S. 4609–4612

[612] MIYAZAKI, Yoshinobu ; OKADA, Junpei ; ABE, Eiji ; YOKOYAMA, Yoshihiko ; KIMURA, Kaoru: Quasicrystalline Tenfold Symmetry Order in Boron Compounds. In: *Journal of the Physical Society of Japan* 79 (2010), S. 073601

[613] YAMAMOTO, Akiji: Short-range-order diffuse scattering in decagonal Ni-rich Al-Ni-Co quasicrystals. In: *Phys. Rev. B* 83 (2011), S. 184203

[614] ORS, Taylan ; TAKAKURA, Hiroyuki ; ABE, Eiji ; STEURER, Walter: The quasiperiodic average structure of highly disordered decagonal Zn–Mg–Dy and its temperature dependence. In: *Acta Crystallographica Section B* 70 (2014), S. 315–330

[615] IGA, Hayato ; MIHALKOVIČ, Marek ; ISHIMASA, Tsutomu: Approximant of dodecagonal quasicrystal formed in Mn–Si–V

alloy. In: *Philosophical Magazine* 91 (2011), S. 2624–2633

[616] XIAO, Changhong ; FUJITA, Nobuhisa ; MIYASAKA, Keiichi ; SAKAMOTO, Yasuhiro ; TERASAKI, Osamu: Dodecagonal tiling in mesoporous silica. In: *Nature* 487 (2012), S. 349–353

[617] FISCHERA, Steffen ; EXNERA, Alexander ; ZIELSKEA, Kathrin ; PERLICHB, Jan ; DELOUDIC, Sofia ; STEURERC, Walter ; LINDNERD, Peter ; FÖRSTERE, Stephan: Colloidal quasicrystals with 12-fold and 18-fold diffraction symmetry. In: *Proceedings of the National Academy of Sciences of the United* 108 (2011), S. 1810–1814

[618] TALAPIN, Dmitri V. ; SHEVCHENKO, Elena V. ; BODNARCHUK, Maryna I. ; YE, Xingchen ; CHEN, Jun ; MURRAY, Christopher B.: Quasicrystalline order in self-assembled binary nanoparticle superlattices. In: *Nature* 461 (2009), S. 964–967

[619] ZENG, Xiangbing ; UNGAR, Goran ; LIU, Yongsong ; PERCEC, Virgil ; DULCEY, Andrés E. ; HOBBS, Jamie K.: Supramolecular dendritic liquid quasicrystals. In: *Nature* 428 (2004), S. 157–160

[620] HAYASHIDA, Kenichi ; DOTERA, Tomonari ; TAKANO, Atsushi ; MATSUSHITA, Yushu: Polymeric Quasicrystal: Mesoscopic Quasicrystalline Tiling in *ABC* Star Polymers. In: *Phys. Rev. Lett.* 98 (2007), S. 195502

[621] HARGITTAI, Istvan ; HARGITTAI, Magdolna: *In Our Own Image: Personal Symmetry in Discovery*. Springer, 2000. – ISBN 978–0306460913

[622] HYDE, Stephen T.: Crystals: animal, vegetable or mineral? In: *Interface Focus* 5 (2015), S. 20150027

[623] ZLOTNICK, Adam: Viruses and the physics of soft condensed matter. In: *Proceedings of the National Academy of Sciences of the United States of America* 101 (2004), S. 15549–15550

[624] ZANDI, Roya ; REGUERA, David ; BRUINSMA, Robijn F. ; GELBART, William M. ; RUDNICK, Joseph: Origin of icosahedral symmetry in viruses. In: *Proceedings of the National Academy of Sciences of the United States of America* 101 (2004), S. 15556–15560

[625] YAN, Xiaodong ; CHIPMAN, Paul R. ; CASTBERG, Tonje ; BRATBAK, Gunnar ; BAKER, Timothy S.: The Marine Algal Virus PpV01 Has an Icosahedral Capsid with T=219 Quasisymmetry. In: *Journal of Virology* 79 (2005), S. 9236–9243

[626] CHERRIER, Mickaël V. ; KOSTYUCHENKO, Victor A. ; XIAO, Chuan ; BOWMAN, Valorie D. ; BATTISTI, Anthony J. ; YAN, Xiaodong ; CHIPMAN, Paul R. ; BAKER, Timothy S. ; VAN ETTEN, James L. ; ROSSMANN, Michael G.: An icosahedral algal virus has a complex unique vertex decorated by a spike. In: *Proceedings of the National Academy of Sciences* 106 (2009), S. 11085–11089

[627] HARGITTAI, István: Limits of perfection. In: *Computers and Mathematics with Applications* 12 (1986), Nr. 1-2, Part B, S. 1 – 17

[628] KELLEY, Stephen S. ; RIALS, Timothy G. ; GLASSER, Wolfgang G.: Relaxation behaviour of the amorphous components of wood. In: *Journal of Materials Science* 22 (1987), S. 617–624

[629] DEGUCHI, Shigeru ; TSUJII, Kaoru ; HORIKOSHI, Koki: Crystalline-to-amorphous transformation of cellulose in hot and compressed water and its implications for hydrothermal conversion. In: *Green Chem.* 10 (2008), S. 191–196

[630] RUEL, Katia ; NISHIYAMA, Yoshiharu ; JOSELEAU, Jean-Paul: Crystalline and amorphous cellulose in the secondary walls of Arabidopsis. In: *Plant Science* 193-194 (2012), S. 48 – 61

[631] BRIGHT, T. J. ; WATJEN, J. I. ; ZHANG, Z. M. ; MURATORE, C. ; VOEVODIN, A. A. ; KOUKIS, D. I. ; TANNER, D. B. ; ARENAS, D. J.: Infrared optical properties of amorphous and nanocrystalline Ta_2O_5 thin films. In: *Journal of Applied Physics* 114 (2013), S. 083515

[632] DENG, Yonghui ; QI, Dawei ; DENG, Chunhui ; ZHANG, Xiangmin ; ZHAO, Dongyuan: Superparamagnetic High-Magnetization Microspheres with an Fe_3O_4@SiO_2 Core and Perpendicularly Aligned Mesoporous SiO_2 Shell for Removal of Microcystins. In: *Journal of the American Chemical Society* 130 (2008), S. 28–29

[633] CHONG, T. C. ; SHI, L. P. ; ZHAO, R. ; TAN, P. K. ; LI, J. M. ; LEE, H. K. ; MIAO, X. S. ; DU, A. Y. ; TUNG, C. H.: Phase change random access memory cell with superlattice-like structure. In: *Applied Physics Letters* 88 (2006), S. 122114

[634] HUANG, Pinshane Y. ; KURASCH, Simon ; SRIVASTAVA, Anchal ; SKAKALOVA, Viera ; KOTAKOSKI, Jani ; KRASHENINNIKOV, Arkady V. ; HOVDEN, Robert ; MAO, Qingyun ; MEYER, Jannik C. ; SMET, Jurgen ; MULLER, David A. ; KAISER, Ute: Direct Imaging of a Two-Dimensional Silica Glass on Graphene. In: *Nano Letters* 12 (2012), Nr. 2, S. 1081–1086

[635] ADACHI, M. M. ; ANANTRAM, M. P. ; KARIM, K. S.: Optical Properties of Crystalline-Amorphous Core-Shell Silicon Nanowires. In: *Nano Letters* 10 (2010), S. 4093–4098

[636] PROKES, S. M. ; KATZ, M. B. ; TWIGG, M. E.: Growth of crystalline Al_2O_3 via thermal atomic layer deposition: Nanomaterial phase stabilization. In: *APL Materials* 2 (2014), S. 032105

[637] SKINNER, H. C. W.: Biominerals. In: *Mineralogical Magazine* 69 (2005), S. 621–641

[638] NICKEL, Ernest H.: The definition of a mineral. In: *The Canadian Mineralogist* 33 (1995), S. 689–690

[639] SURYANARAYANA, C. ; KOCH, C.C.: Nanocrystalline materials, Current research and future directions. In: *Hyperfine*

Interactions 130 (2000), S. 5–44. – ISSN 0304–3843

[640] LU, Z. P. ; LIU, C. T. ; THOMPSON, J. R. ; PORTER, W. D.: Structural Amorphous Steels. In: *Phys. Rev. Lett.* 92 (2004), S. 245503

[641] XU, Donghua ; DUAN, Gang ; JOHNSON, William L.: Unusual Glass-Forming Ability of Bulk Amorphous Alloys Based on Ordinary Metal Copper. In: *Phys. Rev. Lett.* 92 (2004), S. 245504

[642] SCHROERS, Jan ; JOHNSON, William L.: Ductile Bulk Metallic Glass. In: *Phys. Rev. Lett.* 93 (2004), S. 255506

[643] KAZIMIROV, V. Y. ; LOUCA, Despina ; WIDOM, M. ; GU, X.-J. ; POON, S. J. ; SHIFLET, G. J.: Local organization and atomic clustering in multicomponent amorphous steels. In: *Phys. Rev. B* 78 (2008), S. 054112

[644] DEMETRIOU, Marios D. ; LAUNEY, Maximilien E. ; GARRETT, Glenn ; SCHRAMM, Joseph P. ; HOFMANN, Douglas C. ; JOHNSON, William L. ; RITCHIE, Robert O.: A damage-tolerant glass. In: *Nature Materials* 10 (2011), S. 123–128

[645] CHU, Jinn P. ; JANG, J.S.C. ; HUANG, J.C. ; CHOU, H.S. ; YANG, Y. ; YE, J.C. ; WANG, Y.C. ; LEE, J.W. ; LIU, F.X. ; LIAW, P.K. ; CHEN, Y.C. ; LEE, C.M. ; LI, C.L. ; RULLYANI, Cut: Thin film metallic glasses: Unique properties and potential applications. In: *Thin Solid Films* 520 (2012), S. 5097 – 5122

[646] STREET, R. A.: *Hydrogenated amorphous silicon*. Camebridge University Press, 1988. – ISBN 978–0521371568

[647] WINER, K.: Defects in hydrogenated amorphous silicon. In: *Annual Review of Materials Science* 21 (1991), S. 1 – 21

[648] RECH, B. ; WAGNER, H.: Potential of amorphous silicon for solar cells. In: *Applied Physics A* 69 (1999), S. 155–167. – ISSN 0947–8396

[649] BEAUCARNE, Guy: Silicon Thin-Film Solar Cells. In: *Advances in OptoElectronics* 2007 (2007), S. 36970

[650] ABERLE, Armin G.: Thin-film solar cells. In: *Thin Solid Films* 517 (2009), S. 4706 – 4710

[651] GE, J. ; LING, Z.P. ; WONG, J. ; MUELLER, T. ; ABERLE, A.G.: Optimisation of Intrinsic a-Si:H Passivation Layers in Crystalline-amorphous Silicon Heterojunction Solar Cells. In: *Energy Procedia* 15 (2012), S. 107 – 117

[652] STAEBLER, D. L. ; WRONSKI, C. R.: Reversible conductivity changes in discharge–produced amorphous Si. In: *Applied Physics Letters* 31 (1977), S. 292–294

[653] STAEBLER, D. L. ; WRONSKI, C. R.: Optically induced conductivity changes in discharge-produced hydrogenated amorphous silicon. In: *Journal of Applied Physics* 51 (1980), S. 3262–3268

[654] STUTZMANN, M. ; JACKSON, W. B. ; TSAI, C. C.: Light-induced metastable defects in hydrogenated amorphous silicon: A systematic study. In: *Phys. Rev. B* 32 (1985), S. 23–47

[655] PRASAD, Rajendra ; SHENOY, Subodh R.: Staebler-Wronski effect in hydrogenated amorphous silicon. In: *Physics Letters A* 218 (1996), Nr. 1-2, S. 85 – 90

[656] KOŁODZIEJ: Staebler-Wronski effect in amorphous silicon and its alloys. In: *Opto-Electronics Review* 12 (2004), S. 21–32

[657] SHIMIZU, Tatsuo: Staebler-Wronski Effect in Hydrogenated Amorphous Silicon and Related Alloy Films. In: *Japanese Journal of Applied Physics* 43 (2004), S. 3257

[658] KÖHLER, F. ; ZIMMERMANN, T. ; MUTHMANN, S. ; GORDIJN, A. ; CARIUS, R.: Structural Order and Staebler Wronski Effect in Hydrogenated Amorphous Silicon Films and Solar Cells. In: *Photovoltaics, IEEE Journal of* 4 (2014), S. 4–9

[659] BERGMANN, R.B.: Crystalline Si thin-film solar cells: a review. In: *Applied Physics A* 69 (1999), S. 187–194. – ISSN 0947–8396

[660] BURGELMAN, M ; NOLLET, P ; DEGRAVE, S: Modelling polycrystalline semiconductor solar cells. In: *Thin Solid Films* 361-362 (2000), S. 527 – 532

[661] WERNER, J.H. ; DASSOW, R. ; RINKE, T.J. ; KÖHLER, J.R. ; BERGMANN, R.B.: From polycrystalline to single crystalline silicon on glass. In: *Thin Solid Films* 383 (2001), Nr. 1-2, S. 95 – 100

[662] MATSUI, Takuya ; TSUKIJI, Masaharu ; SAIKA, Hiroyuki ; TOYAMA, Toshihiko ; OKAMOTO, Hiroaki: Correlation between Microstructure and Photovoltaic Performance of Polycrystalline Silicon Thin Film Solar Cells. In: *Japanese Journal of Applied Physics* 41 (2002), S. 20

[663] FUHS, W. ; GALL, S. ; RAU, B. ; SCHMIDT, M. ; SCHNEIDER, J.: A novel route to a polycrystalline silicon thin-film solar cell. In: *Solar Energy* 77 (2004), S. 961 – 968

[664] GLUNZ, S. W.: High-Efficiency Crystalline Silicon Solar Cells. In: *Advances in OptoElectronics* 2007 (2007), S. 97370

[665] VOEVODIN, A.A ; ZABINSKI, J.S: Supertough wear-resistant coatings with chameleon surface adaptation. In: *Thin Solid Films* 370 (2000), Nr. 1-2, S. 223 – 231

[666] MUSIL, J.: Hard and superhard nanocomposite coatings. In: *Surface and Coatings Technology* 125 (2000), S. 322 – 330

[667] ZHANG, Sam ; SUN, Deen ; FU, Yongqing ; DU, Hejun: Recent advances of superhard nanocomposite coatings: a review. In: *Surface and Coatings Technology* 167 (2003), S. 113 – 119

[668] MAHÉ, Marie ; HEINTZ, Jean-Marc ; RÖDEL, Jürgen ; REYNDERS, Peter: Cracking of titania nanocrystalline coatings. In: *Journal of the European Ceramic Society* 28 (2008), S. 2003–2010

[669] THANAWALA, Sachin S. ; BAIRD, Ronald J. ; GEORGIEV, Daniel G. ; AUNER, Gregory W.: Amorphous and crystalline IrO_2 thin films as potential stimulation electrode coatings. In: *Applied Surface Science* 254 (2008), S. 5164 – 5169

[670] PAN, Zhiliang ; RUPERT, Timothy J.: Amorphous intergranular films as toughening structural features. In: *Acta Materialia* 89 (2015), S. 205 – 214

[671] VEPŘEK, S. ; HAUSSMANN, M. ; REIPRICH, S.: Superhard nanocrystalline W_2N/amorphous Si_3N_4 composite materials. In: *Journal of Vacuum Science & Technology A* 14 (1996), S. 46–51

[672] VEPŘEK, S. ; REIPRICH, S. ; SHIZHI, Li: Superhard nanocrystalline composite materials: The TiN/Si_3N_4 system. In: *Applied Physics Letters* 66 (1995), S. 2640–2642

[673] NESLÁDEK, P. ; VEPŘEK, S.: Superhard Nanocrystalline Composites with Hardness of Diamond. In: *physica status solidi (a)* 177 (2000), S. 53–62

[674] COLLINO, R. ; THERASSE, J. ; BINDER, P. ; CHAPUT, F. ; BOILOT, J.-P. ; LEVY, Y.: Thin films of functionalized amorphous silica for immunosensors application. In: *Journal of Sol-Gel Science and Technology* 2 (1994), S. 823–826. – ISSN 0928–0707

[675] DUTTA, Prabir K. ; FRANK, Marla ; HUNTER, Gary W. ; GEORGE, Michael: Reactively sputtered titania films as high temperature carbon monoxide sensors. In: *Sensors and Actuators B: Chemical* 106 (2005), S. 810 – 815

[676] ROMANO, L. ; IMPELLIZZERI, G. ; BOSCO, L. ; RUFFINO, F. ; MIRITELLO, M. ; GRIMALDI, M. G.: Nanoporosity induced by ion implantation in deposited amorphous Ge thin films. In: *Journal of Applied Physics* 111 (2012), S. 113515

[677] ABELES, B. ; TIEDJE, T.: Amorphous Semiconductor Superlattices. In: *Phys. Rev. Lett.* 51 (1983), S. 2003–2006

[678] SIMPSON, R. E. ; FONS, P. ; KOLOBOV, A. V. ; FUKAYA, T. ; KRBAL, M. ; YAGI, T. ; TOMINAGA, J.: Interfacial phase-change memory. In: *Nature Nanotechnology* 6 (2011), S. 501 – 505

[679] LU, Yegang ; SONG, Sannian ; SONG, Zhitang ; WU, Liangcai ; HE, Aodong ; GONG, Yuefeng ; RAO, Feng ; LIU, Bo: Superlattice-like electrode for low-power phase-change random access memory. In: *Applied Physics Letters* 101 (2012), Nr. 11, S. 113104

[680] HUANG, H.S. ; PEI, H.J. ; CHANG, Y.C. ; LEE, C.J. ; HUANG, J.C.: Tensile behaviors of amorphous-ZrCu/nanocrystalline-Cu multilayered thin film on polyimide substrate. In: *Thin Solid Films* 529 (2013), S. 177 – 180

[681] FRANCE-LANORD, Arthur ; MERABIA, Samy ; ALBARET, Tristan ; LACROIX, David ; TERMENTZIDIS, Konstantinos: Thermal properties of amorphous/crystalline silicon superlattices. In: *Journal of Physics: Condensed Matter* 26 (2014), S. 355801

[682] YANG, Hongxin ; SHI, Luping ; ZHAO, Rong ; LEE, Hock K. ; LI, Jianming ; LIM, Kian G. ; NG, Lung T. ; CHONG, Tow C.: Growth-Dominant Superlattice-Like Medium and Its Application in Phase Change Memory. In: *ECS Journal of Solid State Science and Technology* 4 (2015), S. N13–N17

[683] OVSHINSKY, Stanford R.: Reversible Electrical Switching Phenomena in Disordered Structures. In: *Phys. Rev. Lett.* 21 (1968), S. 1450–1453

[684] WUTTIG, Matthias ; YAMADA, Noboru: Phase-change materials for rewriteable data storage. In: *Nature Materials* 6 (2007), S. 824–832

[685] XU, Cheng ; SONG, Zhitang ; LIU, Bo ; FENG, Songlin ; CHEN, Bomy: Lower current operation of phase change memory cell with a thin TiO_2 layer. In: *Applied Physics Letters* 92 (2008), Nr. 6, S. 062103

[686] KOLOBOV, Alexander V. ; FONS, Paul ; FRENKEL, Anatoly ; ANKUDINOV, Alexei ; TOMINAGA, Junji ; URUGA, Tomoya: Understanding the phase-change mechanism of rewritable optical media. In: *Nature Materials* 3 (2004), S. 703–708

[687] HEGEDÜS, J. ; ELLIOTT, S. R.: Microscopic origin of the fast crystallization ability of Ge-Sb-Te phase-change memory materials. In: *Nature Materials* 7 (2008), S. 399–405

[688] CAI, B. ; DRABOLD, D. A. ; ELLIOTT, S. R.: Structural fingerprints of electronic change in the phase-change-material: Ge2Sb2Te5. In: *Applied Physics Letters* 97 (2010), S. 191908

[689] KENISARIN, Murat ; MAHKAMOV, Khamid: Solar energy storage using phase change materials. In: *Renewable and Sustainable Energy Reviews* 11 (2007), Nr. 9, S. 1913 – 1965

[690] SHARMA, Atul ; TYAGI, V.V. ; CHEN, C.R. ; BUDDHI, D.: Review on thermal energy storage with phase change materials and applications. In: *Renewable and Sustainable Energy Reviews* 13 (2009), S. 318 – 345

[691] YE, Shibing ; ZHANG, Qinglong ; HU, Dingding ; FENG, Jiachun: Core-shell-like structured graphene aerogel encapsulating paraffin: shape-stable phase change material for thermal energy storage. In: *J. Mater. Chem. A* 3 (2015), S. 4018–4025

[692] CABEZA, Luisa F. ; GUTIERREZ, Andrea ; BARRENECHE, Camila ; USHAK, Svetlana ; FERNÁNDEZ, Angel G. ; FERNÁDEZ,

A. I. ; GRÁGEDA, Mario: Lithium in thermal energy storage: A state-of-the-art review. In: *Renewable and Sustainable Energy Reviews* 42 (2015), Nr. 0, S. 1106 – 1112

[693] SHIN, Donghyun ; BANERJEE, Debjyoti: Enhanced thermal properties of SiO_2 nanocomposite for solar thermal energy storage applications. In: *International Journal of Heat and Mass Transfer* 84 (2015), S. 898 – 902

[694] JENSEN, N. ; HAUSNER, R. M. ; BERGMANN, R. B. ; WERNER, J. H. ; RAU, U.: Optimization and characterization of amorphous/crystalline silicon heterojunction solar cells. In: *Progress in Photovoltaics: Research and Applications* 10 (2002), S. 1–13

[695] FUHS, W. ; KORTE, L. ; SCHMIDT, M.: Heterojunctions of hydrogenated amorphous silicon and monocrystalline silicon. In: *Progress in Photovoltaics: Research and Applications* 8 (2006), S. 1989–11995

[696] KLEIDER, Jean-Paul: Band Lineup Theories and the Determination of Band Offsets from Electrical Measurements. In: SARK, WilfriedG.J.H.M. van (Hrsg.) ; KORTE, Lars (Hrsg.) ; ROCA, Francesco (Hrsg.): *Physics and Technology of Amorphous-Crystalline Heterostructure Silicon Solar Cells* Bd. 0. Springer Berlin Heidelberg, 2012. – ISBN 978–3–642–22274–0, S. 405–444

[697] COURTOIS, GUILLAUME ; CHATTERJEE, PARSATHI ; SUENDO, VEINARDI ; SALOMON, ANTOINE ; ROCA I CABARROCAS, PERE: Investigation of silicon heterojunction solar cells by photoluminescence under DC-bias. In: *EPJ Photovolt.* 4 (2013), S. 45106

[698] REISS, Peter ; PROTIÈRE, Myriam ; LI, Liang: Core/Shell Semiconductor Nanocrystals. In: *Small* 5 (2009), S. 154–168

[699] WEI, Suying ; WANG, Qiang ; ZHU, Jiahua ; SUN, Luyi ; LIN, Hongfei ; GUO, Zhanhu: Multifunctional composite core-shell nanoparticles. In: *Nanoscale* 3 (2011), S. 4474–4502

[700] GHOSH CHAUDHURI, Rajib ; PARIA, Santanu: Core/Shell Nanoparticles: Classes, Properties, Synthesis Mechanisms, Characterization, and Applications. In: *Chemical Reviews* 112 (2012), S. 2373–2433

[701] HAYES, Richard ; AHMED, Adham ; EDGE, Tony ; ZHANG, Haifei: Core-shell particles: Preparation, fundamentals and applications in high performance liquid chromatography. In: *Journal of Chromatography A* 1357 (2014), S. 36 – 52. – Advanced Materials for Separation Science

[702] HER, Yung-Chiun ; CHANG, Chia-Chun: Facile synthesis of one-dimensional crystalline/amorphous tungsten oxide core/shell heterostructures with balanced electrochromic properties. In: *CrystEngComm* 16 (2014), S. 5379–5386

[703] ZHONG, Bo ; TANG, Xiaohui ; HUANG, Xiaoxiao ; XIA, Long ; ZHANG, Xiaodong ; WEN, Guangwu ; CHEN, Zi: Metal-semiconductor Zn/ZnO core-shell nanocables: facile and large-scale fabrication, growth mechanism, oxidation behavior, and microwave absorption performance. In: *CrystEngComm* 17 (2015), S. 2806

[704] HU, Yun H.: A Highly Efficient PhotocatalystÑHydrogenated Black TiO_2 for the Photocatalytic Splitting of Water. In: *Angewandte Chemie International Edition* 51 (2012), S. 12410–12412

[705] YANG, Chongyin ; WANG, Zhou ; LIN, Tianquan ; YIN, Hao ; LÜ, Xujie ; WAN, Dongyun ; XU, Tao ; ZHENG, Chong ; LIN, Jianhua ; HUANG, Fuqiang ; XIE, Xiaoming ; JIANG, Mianheng: Core-Shell Nanostructured "Black" Rutile Titania as Excellent Catalyst for Hydrogen Production Enhanced by Sulfur Doping. In: *Journal of the American Chemical Society* 135 (2013), S. 17831–17838

[706] XIA, Ting ; CHEN, Xiaobo: Revealing the structural properties of hydrogenated black TiO_2 nanocrystals. In: *J. Mater. Chem. A* 1 (2013), S. 2983–2989

[707] CHEN, Xiaobo ; LIU, Lei ; LIU, Zhi ; MARCUS, Matthew A. ; WANG, Wei-Cheng ; OYLER, Nathan A. ; GRASS, Michael E. ; MAO, Baohua ; GLANS, Per-Anders ; YU, Peter Y. ; GUO, Jinghua ; MAO, Samuel S.: Properties of Disorder-Engineered Black Titanium Dioxide Nanoparticles through Hydrogenation. In: *Nature* 3 (2013), S. 1510

[708] WANG, Haonan ; LIN, Tianquan ; ZHU, Guilian ; YIN, Hao ; LÜ, Xujie ; LI, Yanting ; HUANG, Fuqiang: Colored titania nanocrystals and excellent photocatalysis for water cleaning. In: *Catalysis Communications* 60 (2015), S. 55 – 59

[709] CHEN, Xiaobo ; LIU, Lei ; HUANG, Fuqiang: Black titanium dioxide (TiO_2) nanomaterials. In: *Chem. Soc. Rev.* 44 (2015), S. 1861

[710] HWANG, Seong-Ju ; CHOY, Jin-Ho: Local Atomic Arrangement and Electronic Structure of Nanocrystalline Transition Metal Oxides Determined by X-ray Absorption Spectroscopy. In: *The Journal of Physical Chemistry B* 107 (2003), S. 5791–5796

[711] BATES, Simon ; ZOGRAFI, George ; ENGERS, David ; MORRIS, Kenneth ; CROWLEY, Kieran ; NEWMAN, Ann: Analysis of Amorphous and Nanocrystalline Solids from Their X-Ray Diffraction Patterns. In: *Pharmaceutical Research* 23 (2006), S. 2333–2349

[712] LOERTING, Thomas ; BRAZHKIN, Vadim V. ; MORISHITA, Tetsuya: *Multiple Amorphous-Amorphous Transitions*. John Wiley & Sons, Inc., 2009. – 29–82 S. – ISBN 9780470508602

[713] ROUX, Sébastien L. ; JUND, Philippe: Ring statistics analysis of topological networks: New approach and application to

amorphous GeS_2 and SiO_2 systems. In: *Computational Materials Science* 49 (2010), S. 70 – 83

[714] KING, Shirley V.: Ring Configurations in a Random Network Model of Vitreous Silica. In: *Nature* 213 (1967), S. 1112–1113

[715] GUTTMAN, Lester: Ring structure of the crystalline and amorphous forms of silicon dioxide. In: *Journal of Non-Crystalline Solids* 116 (1990), S. 145 – 147

[716] ELLIOTT, S.R.: Medium-range order in amorphous materials: documented cases. In: *Journal of Non-Crystalline Solids* 97–98, Part 1 (1987), S. 159 – 162

[717] ELLIOTT, S. R.: Origin of the first sharp diffraction peak in the structure factor of covalent glasses. In: *Phys. Rev. Lett.* 67 (1991), S. 711–714

[718] ZACHARIASEN, W. H.: The Atomic Arrangement in Glass. In: *Journal of the American Chemical Society* 54 (1932), S. 3841–3851

[719] WARREN, B. E.: X-Ray Diffraction of Vitreous Silica. In: *Zeitschrift fü Kristallographie - Crystalline Materials* 86 (2002), S. 349–358

[720] MOUSSEAU, Normand ; BARKEMA, G. T. ; NAKHMANSON, S. M.: Recent developments in the study of continuous random networks. In: *Philosophical Magazine Part B* 82 (2002), S. 171–183

[721] KOTAKOSKI, J. ; KRASHENINNIKOV, A. V. ; KAISER, U. ; MEYER, J. C.: From Point Defects in Graphene to Two-Dimensional Amorphous Carbon. In: *Phys. Rev. Lett.* 106 (2011), S. 105505

[722] EDER, Franz R. ; KOTAKOSKI, Jani ; KAISER, Ute ; C. MEYER, Jannik: A journey from order to disorder – Atom by atom transformation from graphene to a 2D carbon glass. In: *Scientific Reports* 4 (2014), S. 4060

[723] KUMAR, Avishek ; WILSON, Mark ; THORPE, M F.: Amorphous graphene: a realization of Zachariasen's glass. In: *Journal of Physics: Condensed Matter* 24 (2012), S. 485003

[724] LI, Y. ; DRABOLD, D. A.: Symmetry breaking and low energy conformational fluctuations in amorphous graphene. In: *physica status solidi (b)* 250 (2013), S. 1012–1019

[725] LI, Yuting ; DRABOLD, David A.: Electronic signatures of topological disorder in amorphous graphene. In: *IET Circuits, Devices & Systems* 9 (2015), S. 13–18(5)

[726] MA, Jie ; ALFÈ, Dario ; MICHAELIDES, Angelos ; WANG, Enge: Stone-Wales defects in graphene and other planar sp^2-bonded materials. In: *Phys. Rev. B* 80 (2009), S. 033407

[727] MEYER, Jannik C. ; KISIELOWSKI, C. ; ERNI, R. ; ROSSELL, Marta D. ; CROMMIE, M. F. ; ZETTL, A.: Direct Imaging of Lattice Atoms and Topological Defects in Graphene Membranes. In: *Nano Letters* 8 (2008), S. 3582–3586

[728] LUSK, Mark T. ; CARR, L. D.: Nanoengineering Defect Structures on Graphene. In: *Phys. Rev. Lett.* 100 (2008), S. 175503

[729] BANHART, Florian ; KOTAKOSKI, Jani ; KRASHENINNIKOV, Arkady V.: Structural Defects in Graphene. In: *ACS Nano* 5 (2011), S. 26–41

[730] KOTAKOSKI, J. ; MEYER, J. C. ; KURASCH, S. ; SANTOS-COTTIN, D. ; KAISER, U. ; KRASHENINNIKOV, A. V.: Stone-Wales-type transformations in carbon nanostructures driven by electron irradiation. In: *Phys. Rev. B* 83 (2011), S. 245420

[731] MEYER, Jannik C. ; KISIELOWSKI, C. ; ERNI, R. ; ROSSELL, Marta D. ; CROMMIE, M. F. ; ZETTL, A.: Direct Imaging of Lattice Atoms and Topological Defects in Graphene Membranes. In: *Nano Letters* 8 (2008), S. 3582–3586

[732] ZAN, Recep ; RAMASSE, Quentin M. ; BANGERT, Ursel ; NOVOSELOV, Konstantin S.: Graphene Reknits Its Holes. In: *Nano Letters* 12 (2012), S. 3936–3940

[733] O'HERN, Sean C. ; BOUTILIER, Michael S. H. ; IDROBO, Juan-Carlos ; SONG, Yi ; KONG, Jing ; LAOUI, Tahar ; ATIEH, Muataz ; KARNIK, Rohit: Selective Ionic Transport through Tunable Subnanometer Pores in Single-Layer Graphene Membranes. In: *Nano Letters* 14 (2014), S. 1234–1241

[734] ROBERTSON, J.: Amorphous carbon. In: *Advances in Physics* 35 (1986), S. 317–374

[735] GUHA, S. ; YANG, J. ; WILLIAMSON, D. L. ; LUBIANIKER, Y. ; COHEN, J. D. ; MAHAN, A. H.: Structural, defect, and device behavior of hydrogenated amorphous Si near and above the onset of microcrystallinity. In: *Applied Physics Letters* 74 (1999), S. 1860–1862

[736] VURGAFTMAN, I. ; MEYER, J. R. ; RAM-MOHAN, L. R.: Band parameters for III-V compound semiconductors and their alloys. In: *Journal of Applied Physics* 89 (2001), S. 5815–5875

[737] ADACHI, Sadao: III-V Ternary and Quaternary Compounds. In: KASAP, Safa (Hrsg.) ; CAPPER, Peter (Hrsg.): *Springer Handbook of Electronic and Photonic Materials*. Springer US, 2007. – ISBN 978–0–387–26059–4, S. 735–752

[738] TRIVEDI, Sudhir B. ; WANG, Chen-Chia ; KUTCHER, Susan ; HOMMERICH, Uwe ; PALOSZ, Witold: Crystal growth technology of binary and ternary II-VI semiconductors for photonic applications. In: *Journal of Crystal Growth* 310 (2008), S. 1099 – 1106

[739] YU, K. M. ; NOVIKOV, S. V. ; BROESLER, R. ; LEVANDER, A. X. ; LILIENTAL-WEBER, Z. ; LUCKERT, F. ; MARTIN, R. W. ; DUBON, O. ; WU, J. ; WALUKIEWICZ, W. ; FOXON, C. T.: GaNAs alloys over the whole composition range grown on crystalline and amorphous substrates. In: *physica status solidi (c)* 8 (2011), S. 2503–2505

[740] TAN, Chee-Keong ; ZHANG, Jing ; LI, Xiao-Hang ; LIU, Guangyu ; TAYO, Benjamin O. ; TANSU, Nelson: First-Principle Electronic Properties of Dilute-As GaNAs Alloy for Visible Light Emitters. In: *J. Display Technol.* 9 (2013), S. 272–279

[741] KANDEMIR, E. B. ; GÖNÜL, B. ; BARKEMA, G.T. ; YU, K.M. ; WALUKIEWICZ, W. ; WANG, L.W.: Modeling of the atomic structure and electronic properties of amorphous $GaN_{1-x}As_x$. In: *Computational Materials Science* 82 (2014), S. 100 – 106

[742] TAN, Chee-Keong ; TANSU, Nelson: First-principle natural band alignment of GaN / dilute-As GaNAs alloy. In: *AIP Advances* 5 (2015), S. 017129

[743] SARNEY, W.L. ; SVENSSON, S.P. ; NOVIKOV, S.V. ; YU, K.M. ; WALUKIEWICZ, W. ; FOXON, C.T.: $GaN_{1-x}Sb_x$ highly mismatched alloys grown by low temperature molecular beam epitaxy under Ga-rich conditions. In: *Journal of Crystal Growth* 383 (2013), Nr. 0, S. 95 – 99

[744] YUAN, Changzhou ; WU, Hao B. ; XIE, Yi ; LOU, Xiong Wen D.: Mixed Transition-Metal Oxides: Design, Synthesis, and Energy-Related Applications. In: *Angewandte Chemie International Edition* 53 (2014), S. 1488–1504

[745] ALDAKOV, Dmitry ; LEFRANCOIS, Aurelie ; REISS, Peter: Ternary and quaternary metal chalcogenide nanocrystals: synthesis, properties and applications. In: *J. Mater. Chem. C* 1 (2013), S. 3756–3776

[746] OMATA, Takahisa ; NAGATANI, Hiraku ; SUZUKI, Issei ; KITA, Masao ; YANAGI, Hiroshi ; OHASHI, Naoki: Wurtzite $CuGaO_2$: A New Direct and Narrow Band Gap Oxide Semiconductor Applicable as a Solar Cell Absorber. In: *Journal of the American Chemical Society* 136 (2014), Nr. 9, S. 3378–3381

[747] OMATA, Takahisa ; NAGATANI, Hiraku ; SUZUKI, Issei ; KITA, Masao: Wurtzite-derived ternary I-III-O 2 semiconductors. In: *Science and Technology of Advanced Materials* 16 (2015), Nr. 2, S. 024902

[748] NAGATANI, Hiraku ; SUZUKI, Issei ; KITA, Masao ; TANAKA, Masahiko ; KATSUYA, Yoshio ; SAKATA, Osami ; MIYOSHI, Shogo ; YAMAGUCHI, Shu ; OMATA, Takahisa: Structural and Thermal Properties of Ternary Narrow-Gap Oxide Semiconductor; Wurtzite-Derived β-$CuGaO_2$. In: *Inorganic Chemistry* 54 (2015), Nr. 4, S. 1698–1704

[749] NAGATANI, Hiraku ; SUZUKI, Issei ; KITA, Masao ; TANAKA, Masahiko ; KATSUYA, Yoshio ; SAKATA, Osami ; OMATA, Takahisa: Structure of β-$AgGaO_2$; ternary I-III-VI2 oxide semiconductor with a wurtzite-derived structure. In: *Journal of Solid State Chemistry* 222 (2015), S. 66 – 70

[750] OMATA, T.: Ternary and quaternary wurtzite-type oxide semiconductors: new materials and their properties. In: *Proc. SPIE* 9364 (2015), S. 93641L–93641L

[751] SUGIMOTO, Yoshiaki ; POU, Pablo ; ABE, Masayuki ; JELINEK, Pavel ; PÉREZ, Rubén ; MORITA, Seizo ; CUSTANCE, Óscar: Chemical identification of individual surface atoms by atomic force microscopy. In: *Nature* 446 (2007), S. 64–67

[752] E., Ma.: Amorphization and metastable polymorphs of ordered intermetallics Zr_3Al and Ni_3AI. In: *Journal of Materials Research* 9 (1994), S. 592–597

[753] SI, Pengchao ; BIAN, Xiufang ; LI, Wang ; ZHANG, Junyan ; YANG, Zhongxi: Relationship between intermetallic compound formation and glass forming ability of Al-Ni-La alloy. In: *Physics Letters A* 319 (2003), S. 424 – 428

[754] LIN, S.L. ; CHEN, S.F. ; CHEN, J.K. ; LIN, Y.L.: Formation and magnetic properties of Fe-Si-B-Dy amorphous alloy. In: *Intermetallics* 18 (2010), S. 1826 – 1828

[755] CAI, Liuchun ; BOOLCHAND, P.: Nanoscale phase separation of GeS_2 glass. In: *Philosophical Magazine Part B* 82 (2002), S. 1649–1657

[756] KOZICKI, M.N ; MITKOVA, M ; ZHU, J ; PARK, M: Nanoscale phase separation in Ag-Ge-Se glasses. In: *Microelectronic Engineering* 63 (2002), S. 155 – 159

[757] SHEN, Yongtao ; DENG, Ke ; YANG, Songlin ; QIN, Bo ; CHENG, Shiyu ; ZHU, Ningbo ; DING, Jiejin ; ZHAO, Dahui ; LIU, Ji ; ZENG, Qingdao ; WANG, Chen: Triangular-shaped molecular random tiling and molecular rotation in two-dimensional glassy networks. In: *Nanoscale* 6 (2014), S. 7221–7225

[758] BLUNT, Matthew O. ; RUSSELL, James C. ; GIMÉNEZ-LÓPEZ, María del Carmen ; GARRAHAN, Juan P. ; LIN, Xiang ; SCHRÖDER, Martin ; CHAMPNESS, Neil R. ; BETON, Peter H.: Random Tiling and Topological Defects in a Two-Dimensional Molecular Network. In: *Science* 322 (2008), S. 1077–1081

[759] GARRAHAN, Juan P. ; STANNARD, Andrew ; BLUNT, Matthew O. ; BETON, Peter H.: Molecular random tilings as glasses. In: *Proceedings of the National Academy of Sciences* 106 (2009), S. 15209–15213

[760] BLUNT, Matthew O. ; RUSSELL, James C. ; CHAMPNESS, Neil R. ; BETON, Peter H.: Templating molecular adsorption using a covalent organic framework. In: *Chem. Commun.* 46 (2010), S. 7157–7159

[761] ÉCIJA, David ; URGEL, José I. ; PAPAGEORGIOU, Anthoula C. ; JOSHI, Sushobhan ; AUWÄRTER, Willi ; SEITSONEN, Ari P. ;

KLYATSKAYA, Svetlana ; RUBEN, Mario ; FISCHER, Sybille ; VIJAYARAGHAVAN, Saranyan ; REICHERT, Joachim ; BARTH, Johannes V.: Five-vertex Archimedean surface tessellation by lanthanide-directed molecular self-assembly. In: *Proceedings of the National Academy of Sciences* 110 (2013), S. 6678–6681

[762] NIECKARZ, Damian ; SZABELSKI, Pawel: Understanding Pattern Formation in 2D Metal-Organic Coordination Systems on Solid Surfaces. In: *The Journal of Physical Chemistry C* 117 (2013), S. 11229–11241

[763] PALMA, Carlos-Andres ; SAMOR, Paolo ; CECCHINI, Marco: Atomistic Simulations of 2D Bicomponent Self-Assembly: From Molecular Recognition to Self-Healing. In: *Journal of the American Chemical Society* 132 (2010), S. 17880–17885

[764] TSCHIERSKE, Carsten: Entwicklung struktureller Komplexität durch Selbstorganisation in flüssigkristallinen Systemen. In: *Angewandte Chemie* 125 (2013), S. 8992–9047

[765] WEAIRE, D. ; RIVIER, N.: Soap, cells and statistics - random patterns in two dimensions. In: *Contemporary Physics* 25 (1984), S. 59–99

[766] ABOAV, D.A.: The arrangement of cells in a net. In: *Metallography* 13 (1980), S. 43 – 58

[767] JONGERIUS, S.R. ; LENTINK, D.: Structural Analysis eof a Dragonfly Wing. In: *Experimental Mechanics* 50 (2010), S. 1323–1334

[768] CAVALCANTE, Francisco S. A. ; ITO, Satoru ; BREWER, Kelly ; SAKAI, Hiroaki ; ALENCAR, Adriano M. ; ALMEIDA, Murilo P. ; ANDRADE, José S. ; MAJUMDAR, Arnab ; INGENITO, Edward P. ; SUKI, Béla: Mechanical interactions between collagen and proteoglycans: implications for the stability of lung tissue. In: *Journal of Applied Physiology* 98 (2005), Nr. 2, S. 672–679

[769] MILINKOVITCH, Michel C. ; MANUKYAN, Liana ; DEBRY, Adrien ; DI-POÏ, Nicolas ; MARTIN, Samuel ; SINGH, Daljit ; LAMBERT, Dominique ; ZWICKER, Matthias: Crocodile Head Scales Are Not Developmental Units But Emerge from Physical Cracking. In: *Science* 339 (2013), S. 78–81

[770] FIDELIS, Maria Ernestina A. ; PEREIRA, Thatiana Vitorino C. ; GOMES, Otávio da Fonseca M. ; SILVAA, Flávio de A. ; FILHOA, Romildo Dias T.: The effect of fiber morphology on the tensile strength of natural fibers. In: *Journal of Materials Research and Technology* 2 (2013), S. 149–157

[771] GOEHRING, Lucas ; CONROY, Rebecca ; AKHTER, Asad ; CLEGG, William J. ; ROUTH, Alexander F.: Evolution of mud-crack patterns during repeated drying cycles. In: *Soft Matter* 6 (2010), S. 3562–3567

[772] GOEHRING, Lucas: Evolving fracture patterns: columnar joints, mud cracks and polygonal terrain. In: *Philosophical Transactions of the Royal Society of London A: Mathematical, Physical and Engineering Sciences* 371 (2013), Nr. 2004

[773] CAËR, G. L. ; DELANNAY, R.: The administrative divisions of mainland France as 2D random cellular structures. In: *J. Phys. I France* 3 (1993), S. 1777–1800

[774] PATHAK, M.J.M. ; PEARCE, J.M. ; HARRISON, S.J.: Effects on amorphous silicon photovoltaic performance from high-temperature annealing pulses in photovoltaic thermal hybrid devices. In: *Solar Energy Materials and Solar Cells* 100 (2012), S. 199 – 203

[775] BRESSER, W. J. ; BOOLCHAND, P. ; SURANYI, P. ; NEUFVILLE, J. P.: Direct Evidence for Intrinsically Broken Chemical Ordering in Melt-Quenched Glasses. In: *Phys. Rev. Lett.* 46 (1981), S. 1689–1692

[776] STILLINGER, Frank H.: A Topographic View of Supercooled Liquids and Glass Formation. In: *Science* 267 (1995), Nr. 5206, S. 1935–1939

[777] HAYASHI, Akitoshi ; YAMASHITA, Hideki ; TATSUMISAGO, Masahiro ; MINAMI, Tsutomu: Characterization of Li_2S-SiS_2-Li_xMO_y (M=Si, P, Ge) amorphous solid electrolytes prepared by melt-quenching and mechanical milling. In: *Solid State Ionics* 148 (2002), S. 381 – 389

[778] LEE, Joo W. ; THOMAS, Leonard C. ; SCHMIDT, Shelly J.: Effects of Heating Conditions on the Glass Transition Parameters of Amorphous Sucrose Produced by Melt-Quenching. In: *Journal of Agricultural and Food Chemistry* 59 (2011), S. 3311–3319

[779] GUTZOW, Ivan S. ; SCHMELZER, Jürn W. P.: *The Vitreous State; Thermodynamics, Structure, Rheology, and Crystallization*. Springer-Verlag Berlin Heidelberg, 2013. – ISBN 978–3642346323

[780] KAUZMANN, Walter.: The Nature of the Glassy State and the Behavior of Liquids at Low Temperatures. In: *Chemical Reviews* 43 (1948), S. 219–256

[781] ANGELL, C. A. ; NGAI, K. L. ; MCKENNA, G. B. ; MCMILLAN, P. F. ; MARTIN, S. W.: Relaxation in glassforming liquids and amorphous solids. In: *Journal of Applied Physics* 88 (2000), S. 3113–3157

[782] BERTHIER, Ludovic ; BIROLI, Giulio: Theoretical perspective on the glass transition and amorphous materials. In: *Rev. Mod. Phys.* 83 (2011), S. 587–645

[783] DEBENEDETTI, Pablo G. ; STILLINGER, Frank H.: Supercooled liquids and the glass transition. In: *Nature* 410 (2001), S.

259–267

[784] LUDWIG, S. ; OSHEROFF, D. D.: Field-Induced Structural Aging in Glasses at Ultralow Temperatures. In: *Phys. Rev. Lett.* 91 (2003), S. 105501

[785] BORINI, Stefano ; BOARINO, Luca ; AMATO, Giampiero: Slow conductivity relaxation and simple aging in nanostructured mesoporous silicon at room temperature. In: *Phys. Rev. B* 75 (2007), S. 165205

[786] AMIR, Ariel ; BORINI, Stefano ; OREG, Yuval ; IMRY, Yoseph: Huge (but Finite) Time Scales in Slow Relaxations: Beyond Simple Aging. In: *Phys. Rev. Lett.* 107 (2011), S. 186407

[787] AMIR, Ariel ; OREG, Yuval ; IMRY, Yoseph: On relaxations and aging of various glasses. In: *Proceedings of the National Academy of Sciences* 109 (2012), S. 1850–1855

[788] CANNELLA, V. ; MYDOSH, J. A.: Magnetic Ordering in Gold-Iron Alloys. In: *Phys. Rev. B* 6 (1972), S. 4220–4237

[789] BINDER, K. ; YOUNG, A. P.: Spin glasses: Experimental facts, theoretical concepts, and open questions. In: *Rev. Mod. Phys.* 58 (1986), S. 801–976

[790] GUERRA, Francesco ; TONINELLI, Fabio L.: The Thermodynamic Limit in Mean Field Spin Glass Models. In: *Communications in Mathematical Physics* 230 (2002). – ISSN 0010–3616

[791] STEIN, D. L.: Spin Glasses: Still Complex After All These Years? In: *arXiv:cond-mat/0301104* (2003), S. 1–12

[792] DOMINICS, Cirano D. ; GIARDINA, Irene: *Random Fields and Spin Glasses*. Cambridge University Press, 2006. – ISBN 978–1441995094

[793] DAVIES, J. H. ; LEE, P. A. ; RICE, T. M.: Electron Glass. In: *Phys. Rev. Lett.* 49 (1982), S. 758–761

[794] GRÜNEWALD, M ; POHLMANN, B ; SCHWEITZER, L ; WÜRTZ, D: Mean field approach to the electron glass. In: *Journal of Physics C: Solid State Physics* (1982), Nr. 32

[795] PÉREZ-GARRIDO, A. ; ORTUÑO, M. ; DÍAZ-SÁNCHEZ, A. ; CUEVAS, E.: Numerical study of relaxation in electron glasses. In: *Phys. Rev. B* 59 (1999), S. 5328–5332

[796] EFROS, A. L. ; TSIGANKOV, D. N. ; PAZY, E. ; LAIKHTMAN, B. D.: Long-time relaxation of conductivity in hopping regime. In: *physica status solidi (b)* 241 (2004), S. 20–25

[797] KOLTON, Alejandro B. ; GREMPEL, D. R. ; DOMÍNGUEZ, Daniel: Heterogeneous dynamics of the three-dimensional Coulomb glass out of equilibrium. In: *Phys. Rev. B* 71 (2005), S. 024206

[798] LEE, M ; OIKONOMOU, P ; SEGALOVA, P ; ROSENBAUM, T F. ; HOEKSTRA, A F T. ; LITTLEWOOD, P B.: The electron glass in a switchable mirror: relaxation, ageing and universality. In: *Journal of Physics: Condensed Matter* 17 (2005), S. L439

[799] AMIR, Ariel ; OREG, Yuval ; IMRY, Yoseph: Mean-field model for electron-glass dynamics. In: *Phys. Rev. B* 77 (2008), S. 165207

[800] AMIR, Ariel ; OREG, Yuval ; IMRY, Yoseph: Electron Glass Dynamics. In: *Annual Review of Condensed Matter Physics* 2 (2011), S. 235–262

[801] OVADYAHU, Z.: Intrinsic electron-glass effects in strongly localized Tl_2O_{3-x} films. In: *Phys. Rev. B* 88 (2013), S. 085106

[802] OVADYAHU, Z.: Electron glass in a three-dimensional system. In: *Phys. Rev. B* 90 (2014), S. 054204

[803] DAI, Junyan ; CHANG, Seung W. ; HAMAD, Alyssandrea ; YANG, Da ; FELIX, Nelson ; OBER, Christopher K.: Molecular Glass Resists for High-Resolution Patterning. In: *Chemistry of Materials* 18 (2006), S. 3404–3411

[804] YANG, Da ; CHANG, Seung W. ; OBER, Christopher K.: Molecular glass photoresists for advanced lithography. In: *J. Mater. Chem.* 16 (2006), S. 1693–1696

[805] PLANTE, André ; PALATO, Samuel ; LEBEL, Olivier ; SOLDERA, Armand: Functionalization of molecular glasses: effect on the glass transition temperature. In: *J. Mater. Chem. C* 1 (2013), S. 1037–1042

[806] TANAKA, Keiji ; SHIMAKAWA, Koichi: *Amorphous Chalcogenide Semiconductors and Related Materials*. Springer NewYork Dordrecht Heidelberg London, 2011. – ISBN 978–1441995094

[807] MOTT, N. F. ; DAVIS, E. A.: *Electronic Processes in Non-Crystalline Materials, Second Edition*. Oxford University Press, USA, 2012. – ISBN 978–0199645336

[808] SCOTT, B. A. ; REIMER, J. A. ; PLECENIK, R. M. ; SIMONYI, E. E. ; REUTER, W.: Low defect density amorphous hydrogenated silicon prepared by homogeneous chemical vapor deposition. In: *Applied Physics Letters* 40 (1982), S. 973–975

[809] BRODSKY, M. H. ; CARDONA, Manuel ; CUOMO, J. J.: Infrared and Raman spectra of the silicon-hydrogen bonds in amorphous silicon prepared by glow discharge and sputtering. In: *Phys. Rev. B* 16 (1977), S. 3556–3571

[810] ROEDERN, B. von ; LEY, L. ; CARDONA, M. ; SMITH, F. W.: Photoemission studies on in situ prepared hydrogenated

amorphous silicon films. In: *Philosophical Magazine Part B* 40 (1979), S. 433–450

[811] CHITTICK, R. C. ; ALEXANDER, J. H. ; STERLING, H. F.: The Preparation and Properties of Amorphous Silicon. In: *Journal of The Electrochemical Society* 116 (1969), S. 77–81

[812] ANDERSON, D. A. ; SPEAR, W. E.: Electrical and optical properties of amorphous silicon carbide, silicon nitride and germanium carbide prepared by the glow discharge technique. In: *Philosophical Magazine* 35 (1977), S. 1–16

[813] DING, J.Y. ; DAY, D.E.: Preparation of silica glass microspheres by sol-gel processing. In: *Journal of Materials Research* 6 (1991), S. 168–174

[814] MCDONAGH, C. ; SHERIDAN, F. ; BUTLER, T. ; MACCRAITH, B.D.: Characterisation of sol-gel-derived silica films. In: *Journal of Non-Crystalline Solids* 194 (1996), Nr. 1-2, S. 72 – 77

[815] FARDAD, M.A.: Catalysts and the structure of SiO_2 sol-gel films. In: *Journal of Materials Science* 35 (2000), S. 1835–1841

[816] HOBBS, L. W. ; JESURUM, C. E. ; BERGER, B. ; DEVINE, R. A. B. (Hrsg.) ; DURAUD, J.-P. (Hrsg.) ; DOORYHÉE, E. (Hrsg.): *The Topology of Silica Networks*. John Wiley & Sons, LTD, 2000. – 1–47 S. – ISBN 978–0471975366

[817] SARIKAYA, M. ; FONG, H. ; SUNDERLAND, N. ; FLINN, B. D. ; MAYER, G. ; MESCHER, A. ; GAINO, E.: Biomimetic model of a sponge-spicular optical fiber-mechanical properties and structure. In: *Journal of Materials Research* 16 (2001), S. 1420–1428

[818] EHRLICH, Hermann ; JANUSSEN, Dorte ; SIMON, Paul ; BAZHENOV, Vasily V. ; SHAPKIN, Nikolay P. ; ERLER, Christiane ; MERTIG, Michael ; BORN, René ; HEINEMANN, Sascha ; HANKE, Thomas ; WORCH, Hartmut ; ; VOURNAKIS, John N.: Nanostructural Organization of Naturally Occurring CompositesÑPart II: Silica-Chitin-Based Biocomposites. In: *Journal of Nanomaterials* (2008), S. 670235

[819] EHRLICH, Hermann ; WORCH, Hartmut: *Collagen: A Huge Matrix in Glass Sponge Flexible Spicules of the Meter-Long Hyalonema sieboldi*. Wiley-VCH Verlag GmbH, 2008. – 22–41 S. – ISBN 9783527619443

[820] BRÜMMER, Franz ; PFANNKUCHEN, Martin ; BALTZ, Alexander ; HAUSER, Thomas ; THIEL, Vera: Light inside sponges. In: *Journal of Experimental Marine Biology and Ecology* 367 (2008), S. 61 – 64

[821] POTTS, S.: Desiccation tolerance of prokaryotes. In: *Microbiological Reviews* 58 (1994), S. 755–805

[822] SUN, Wendell Q.: Glassy State and Seed Storage Stability: The WLF Kinetics of Seed Viability Loss at $T > T_g$ and the Plasticization Effect of Water on Storage Stability. In: *Annals of Botany* 79 (1997), S. 291–297

[823] BUITINK, Julia ; LEPRINCE, Olivier: Glass formation in plant anhydrobiotes: survival in the dry state. In: *Cryobiology* 48 (2004), S. 215 – 228

[824] BALLESTEROS, Daniel ; WALTERS, Christina: Detailed characterization of mechanical properties and molecular mobility within dry seed glasses: relevance to the physiology of dry biological systems. In: *The Plant Journal* 68 (2011), S. 607–619

[825] TANNE, C. ; GOLOVINA, E.A. ; HOEKSTRA, F.A. ; MEFFERT, A. ; GALINSKI, E.A.: Glass-forming property of hydroxyectoine is the cause of its superior function as a desiccation protectant. In: *Frontiers in Microbiology* 5 (2014)

[826] BUITINK, Julia ; WALTERS-VERTUCCI, Christina ; HOEKSTRA, Folkert A. ; LEPRINCE, Olivier: Calorimetric Properties of Dehydrating Pollen - Analysis of a Desiccation-Tolerant and an lntolerant Species. In: *Plant Physiology* 111 (1996), S. 235–242

[827] WOLKERS, Willem F. ; OLDENHOF, Harriëtte ; ALBERDA, Mark ; HOEKSTRA, Folkert A.: A Fourier transform infrared microspectroscopy study of sugar glasses: application to anhydrobiotic higher plant cells. In: *Biochimica et Biophysica Acta (BBA) - General Subjects* 1379 (1998), S. 83 – 96

[828] GALEENER, F.L. ; WRIGHT, A.C.: The J.C. Phillips model for vitreous SiO_2: A critical appraisal. In: *Solid State Communications* 57 (1986), S. 677 – 682

[829] GUTZOW, I. ; AVRAMOV, I. ; KÄSTNER, K.: Glass formation and crystallization. In: *Journal of Non-Crystalline Solids* 123 (1990), S. 97 – 113

[830] WRIGHT, A. C. ; THORPE, M. F.: Eighty years of random networks. In: *physica status solidi (b)* 250 (2013), S. 931–936

[831] YAVARI, Alain R.: Metallic glasses: The changing faces of disorder. In: *Nature Materials* 6 (2007), S. 181–182

[832] SHENG, H. W. ; LIU, H. Z. ; CHENG, Y. Q. ; WEN, J. ; LEE, P. L. ; LUO, W. K. ; SHASTRI, S. D. ; MA, E.: Polyamorphism in a metallic glass. In: *Nature Materials* 6 (2007), S. 192–197

[833] GRIMSDITCH, M.: Polymorphism in Amorphous SiO_2. In: *Phys. Rev. Lett.* 52 (1984), S. 2379–2381

[834] MCMILLAN, Paul ; PIRIOU, Bernard ; COUTY, René: A Raman study of pressure-densified vitreous silica. In: *The Journal of Chemical Physics* 81 (1984), S. 4234–4236

[835] HEMLEY, R. J. ; MAO, H. K. ; BELL, P. M. ; MYSEN, B. O.: Raman Spectroscopy of SiO_2 Glass at High Pressure. In: *Phys. Rev. Lett.* 57 (1986), S. 747–750

[836] INAMURA, Y. ; ARAI, M. ; KITAMURA, N. ; BENNINGTON, S.M. ; HANNON, A.C.: Intermediate-range structure and low-energy dynamics of densified SiO_2 glass. In: *Physica B: Condensed Matter* 241-243 (1997), S. 903 – 905

[837] LACKS, Daniel J.: First-Order Amorphous-Amorphous Transformation in Silica. In: *Phys. Rev. Lett.* 84 (2000), S. 4629–4632

[838] INAMURA, Y. ; ARAI, M. ; NAKAMURA, M. ; OTOMO, T. ; KITAMURA, N. ; BENNINGTON, S.M. ; HANNON, A.C. ; BUCHENAU, U.: Intermediate range structure and low-energy dynamics of densified vitreous silica. In: *Journal of Non-Crystalline Solids* 293-295 (2001), S. 389 – 393

[839] TRACHENKO, Kostya ; DOVE, Martin T.: Compressibility, kinetics, and phase transition in pressurized amorphous silica. In: *Phys. Rev. B* 67 (2003), S. 064107

[840] INAMURA, Y. ; KATAYAMA, Y. ; UTSUMI, W.: Transformation in intermediate-range structure of vitreous silica under high pressure and temperature. In: *Journal of Physics: Condensed Matter* 19 (2007), S. 415104

[841] MCMILLAN, Paul F. ; WILSON, Mark ; DAISENBERGER, Dominik ; MACHON, Denis: A density-driven phase transition between semiconducting and metallic polyamorphs of silicon. In: *Nature Materials* 4 (2005), S. 680–684

[842] MACHON, Denis ; DANIEL, Marlène ; PISCHEDDA, Vittoria ; DANIELE, Stéphane ; BOUVIER, Pierre ; LEFLOCH, Sylvie: Pressure-induced polyamorphism in TiO_2 nanoparticles. In: *Phys. Rev. B* 82 (2010), S. 140102

[843] NELMES, Richard J. ; LOVEDAY, John S. ; STRÄSSLE, Thierry ; GUTHRIE, Craig L. Bulland M. ; HAMEL, Gérard ; KLOTZ, Stefan: Annealed high-density amorphous ice under pressure. In: *Nature Physics* 2 (2006), S. 414–418

[844] TAMMANN, Gustav: *Der Glaszustand*. Leopold Voss, 1933. – ISBN 978–3642927140

[845] VOGEL, Werner: Classical Theories of Glass Structure. In: VOGEL, Werner (Hrsg.): *Glass Chemistry*. Springer Berlin Heidelberg, 1994. – ISBN 978–3–642–78725–6, S. 41–56

[846] GUTZOW, Ivan S. ; MAZURIN, Oleg V. ; SCHMELZER, Jurn W. P. ; TODOROVA, Snejana V. ; PETROFF, Boris B. ; PRIVEN, Alexander I.: *Glasses and the Glass Transition*. Wiley-VCH Verlag GmbH & KGaA, Weinheim, 2011. – ISBN 978–3527409686

[847] GOLDSCHMIDT, V. M.: Crystal structure and chemical constitution. In: *Trans. Faraday Soc.* 25 (1929), S. 253–283

[848] SALMANG, H.: *Die Glasfabrikation-Physikalische und chemische Grundlagen*. Springer-Verlag OHG., Berlin/Göttingen/Heidelberg, 1957. – ISBN 978–3642927140

[849] EL-MALLAWANY, Raouf A.: *Tellurite Glasses Handbook: Physical Properties and Data*. Taylor&Francis Group, LLC, 2001. – ISBN 978–1420042085

[850] RAO, K. J.: *Structural Chemistry of Glasses*. Elsevier Science Ltd., Oxford, 2002. – ISBN 978–0080439586

[851] GHIJSEN, J. ; TJENG, L. H. ; ELP, J. van ; ESKES, H. ; WESTERINK, J. ; SAWATZKY, G. A. ; CZYZYK, M. T.: Electronic structure of Cu_2O and CuO. In: *Phys. Rev. B* 38 (1988), S. 11322–11330

[852] MEYER, B. K. ; POLITY, A. ; REPPIN, D. ; BECKER, M. ; HERING, P. ; KLAR, P. J. ; SANDER, Th. ; REINDL, C. ; BENZ, J. ; EICKHOFF, M. ; HEILIGER, C. ; HEINEMANN, M. ; BLÄSING, J. ; KROST, A. ; SHOKOVETS, S. ; MÜLLER, C. ; RONNING, C.: Binary copper oxide semiconductors: From materials towards devices. In: *physica status solidi (b)* 249 (2012), S. 1487–1509

[853] HEINEMANN, Markus ; EIFERT, Bianca ; HEILIGER, Christian: Band structure and phase stability of the copper oxides Cu_2O, CuO, and Cu_4O_3. In: *Phys. Rev. B* 87 (2013), S. 115111

[854] JANSSENS, Koen H. A.: *Modern Methods for Analysing Archaeological and Historical Glass*. John Wiley & Sons, Ltd., 2013. – ISBN 978–0470516140

[855] GUTHRIE, M. ; TULK, C. A. ; BENMORE, C. J. ; XU, J. ; YARGER, J. L. ; KLUG, D. D. ; TSE, J. S. ; MAO, H-k. ; HEMLEY, R. J.: Formation and Structure of a Dense Octahedral Glass. In: *Phys. Rev. Lett.* 93 (2004), S. 115502

[856] SHEN, Guoyin ; LIERMANN, Hanns-Peter ; SINOGEIKIN, Stanislav ; YANG, Wenge ; HONG, Xinguo ; YOO, Choong-Shik ; CYNN, Hyunchae: Distinct thermal behavior of GeO_2 glass in tetrahedral, intermediate, and octahedral forms. In: *Proceedings of the National Academy of Sciences* 104 (2007), S. 14576–14579

[857] SALMON, Philip S. ; DREWITT, James W E. ; WHITTAKER, Dean A J. ; ZEIDLER, Anita ; WEZKA, Kamil ; BULL, Craig L. ; TUCKER, Matthew G. ; WILDING, Martin C. ; GUTHRIE, Malcolm ; MARROCCHELLI, Dario: Density-driven structural transformations in network forming glasses: a high-pressure neutron diffraction study of GeO_2 glass up to 17.5 GPa. In: *Journal of Physics: Condensed Matter* 24 (2012), S. 415102

[858] HONG, Xinguo ; NEWVILLE, Matthew ; DUFFY, Thomas S. ; SUTTON, Stephen R. ; RIVERS, Mark L.: X-ray absorption spectroscopy of GeO_2 glass to 64 GPa. In: *Journal of Physics: Condensed Matter* 26 (2014), S. 035104

[859] BORISOVA, Z. U. ; SIROTA, N. N. (Hrsg.): *Influence of the nature of the chemical bond on the physicochemical properties of glassy semiconductors*. Springer, 1972. – ISBN 978–0306171543

[860] BORISOVA, Z.: *Glassy Semiconductors*. Springer Science+Buisiness Media New York, 1981. – ISBN 978–1475708530

[861] UCHINO, T. ; ELLIOTT, S. R.: Electronic excitation and transient defects in As_2S_3 glass. In: *Phys. Rev. B* 67 (2003), S. 174201

[862] PAUL, A.: *Chemistry of Glasses*. Springer, 1982. – ISBN 978–9400959200

[863] VOGEL, Werner: *Structure & Crystalization of Glasses*. Pergamon, 1971. – ISBN 978–1483168524

[864] JR., Alfred R C.: W.H. Zachariasen - the melody lingers on. In: *Journal of Non-Crystalline Solids* 49 (1982), S. 1 – 17

[865] VEBLEN, David R. ; BUSECK, Peter R. ; BURNHAM, Charles W.: AsbestiformChainSilicates: New Minerals and Structural Groups. In: *Science* 198 (1977), S. 359–365

[866] HUANG, Pinshane Y. ; KURASCH, Simon ; ALDEN, Jonathan S. ; SHEKHAWAT, Ashivni ; ALEMI, Alexander A. ; MCEUEN, Paul L. ; SETHNA, James P. ; KAISER, Ute ; MULLER, David A.: Imaging Atomic Rearrangements in Two-Dimensional Silica Glass: Watching Silica's Dance. In: *Science* 342 (2013), S. 224–227

[867] GUPTA, P.K. ; COOPER, A.R.: Topologically disordered networks of rigid polytopes. In: *Journal of Non-Crystalline Solids* 123 (1990), S. 14 – 21

[868] WARREN, B. E.: Summary of Work on Atomic Arrangement in Glass. In: *Journal of The American Ceramic Society* 24 (1941), S. 256–261

[869] WRIGHT, Adrian C.: Crystalline-like ordering in melt-quenched network glasses? In: *Journal of Non-Crystalline Solids* 401 (2014), S. 4 – 26

[870] WARREN, B. E.: X-RAY DETERMINATION OF THE STRUCTURE OF GLASS. In: *Journal of the American Ceramic Society* 17 (1934), S. 249–254

[871] WARREN, B. E.: The Diffraction of X-Rays in Glass. In: *Phys. Rev.* 45 (1934), S. 657–661

[872] WARREN, B. E. ; HILL, C. F.: The Structure of Vitreous BeF_2. In: *Zeitschrift für Kristallographie - Crystalline Materials* 89 (1934), S. 481–486

[873] WARREN, B. E.: X-ray Diffraction Study of the Structure of Glass. In: *Chemical Reviews* 26 (1940), S. 237–255

[874] WARREN, B. E. ; BISCCE, J.: THE STRUCTURE OF SILICA GLASS BY X-RAY DIFFRACTION STUDIES. In: *Journal of the American Ceramic Society* 21 (1938), S. 49–54

[875] BISCOE, J.: X-RAY STUDY OF SODA-LIME-SILICA GLASS. In: *Journal of the American Ceramic Society* 24 (1941), S. 262–264

[876] LICHTENSTEIN, Leonid ; HEYDE, Markus ; FREUND, Hans-Joachim: Crystalline-Vitreous Interface in Two Dimensional Silica. In: *Phys. Rev. Lett.* 109 (2012), S. 106101

[877] LICHTENSTEIN, Leonid ; HEYDE, Markus ; FREUND, Hans-Joachim: Atomic Arrangement in Two-Dimensional Silica: From Crystalline to Vitreous Structures. In: *The Journal of Physical Chemistry C* 116 (2012), Nr. 38, S. 20426–20432

[878] LICHTENSTEIN, Leonid ; BÜCHNER, Christin ; YANG, Bing ; SHAIKHUTDINOV, Shamil ; HEYDE, Markus ; SIERKA, Marek ; WŁODARCZYK, Radosław ; SAUER, Joachim ; FREUND, Hans-Joachim: The Atomic Structure of a Metal-Supported Vitreous Thin Silica Film. In: *Angewandte Chemie International Edition* 51 (2012), Nr. 2, S. 404–407

[879] BEN ROMDHANE, Ferdaous ; BJÖRKMAN, Torbjörn ; RODRÍGUEZ-MANZO, Julio A. ; CRETU, Ovidiu ; KRASHENINNIKOV, Arkady V. ; BANHART, Florian: In Situ Growth of Cellular Two-Dimensional Silicon Oxide on Metal Substrates. In: *ACS Nano* 7 (2013), S. 5175–5180

[880] BÜCHNER, Christin ; LICHTENSTEIN, Leonid ; STUCKENHOLZ, Stefanie ; HEYDE, Markus ; RINGLEB, Franziska ; STERRER, Martin ; KADEN, William E. ; GIORDANO, Livia ; PACCHIONI, Gianfranco ; FREUND, Hans-Joachim: Adsorption of Au and Pd on Ruthenium-Supported Bilayer Silica. In: *The Journal of Physical Chemistry C* 118 (2014), S. 20959–20969

[881] SOUSA, N.C.A. de ; ARAUJO, M.T. de ; JACINTO, C. ; VERMELHO, M.V.D. ; DANTAS, N.O. ; SANTOS, C.C. ; GUEDES, I.: The role of TiO_2 in the B_2O_3–Na_2O-PbO–Al_2O_3 glass system. In: *Journal of Solid State Chemistry* 184 (2011), S. 3062 – 3065

[882] BRAUER, Delia S. ; KARPUKHINA, Natalia ; LAW, Robert V. ; HILL, Robert G.: Effect of TiO_2 addition on structure, solubility and crystallisation of phosphate invert glasses for biomedical applications. In: *Journal of Non-Crystalline Solids* 356 (2010), S. 2626 – 2633

[883] RUENGSRI, S. ; KAEWKHAO, J. ; LIMSUWAN, P.: Optical Characterization of Soda Lime Borosilicate Glass Doped with TiO_2. In: *Procedia Engineering* 32 (2012), S. 772 – 779

[884] WREN, A.W. ; LAFFIR, F.R. ; KIDARI, A. ; TOWLER, M.R.: The structural role of titanium in Ca–Sr–Zn–Si/Ti glasses for medical applications. In: *Journal of Non-Crystalline Solids* 357 (2011), S. 1021 – 1026

[885] PARK, Jongee ; OZTURK, Abdullah: Effect of TiO_2 addition on the crystallization and tribological properties of MgO–CaO–SiO_2–P_2O_5–F glasses. In: *Thermochimica Acta* 470 (2008), S. 60 – 66

[886] TEIXEIRA, Zaine ; ALVES, Oswaldo L. ; MAZALI, Italo O.: Structure, Thermal Behavior, Chemical Durability, and Optical

Properties of the Na_2O–Al_2O_3–TiO_2–Nb_2O_5–P_2O_5 Glass System. In: *Journal of the American Ceramic Society* 90 (2007), S. 256–263

[887] NEEL, Ensanya Ali A. ; O'DELL, Luke A. ; CHRZANOWSKI, Wojciech ; SMITH, Mark E. ; KNOWLES, Jonathan C.: Control of surface free energy in titanium doped phosphate based glasses by co-doping with zinc. In: *Journal of Biomedical Materials Research Part B: Applied Biomaterials* 89B (2009), S. 392–407

[888] GABR, Mohamed ; ALI, Abdel-Ati ; MOSTAFA, Ahmed Gamal El-Din: Infrared Analysis and Physical Properties Studies of B_2O_3–CaO–ZnO–TiO_2 Glass System. In: *Turkish Journal of Physics* 31 (2007), S. 31–39

[889] MASAI, Hirokazu ; TODA, Tatsuya ; UENO, Takahiro ; TAKAHASHI, Yoshihiro ; FUJIWARA, Takumi: ZnO glass-ceramics: An alternative way to produce semiconductor materials. In: *Applied Physics Letters* 94 (2009), Nr. 15, S. 151908

[890] ZHANG, X.F. ; KEHOE, S. ; ADHI, S.K. ; AJITHKUMAR, T.G. ; MOANE, S. ; O'SHEA, H. ; BOYD, D.: Composition-structure-property (Zn^{2+} and Ca^{2+} ion release) evaluation of Si-Na-Ca-Zn-Ce glasses: Potential components for nerve guidance conduits. In: *Materials Science and Engineering: C* 31 (2011), S. 669 – 676

[891] STAVROU, Elissaios ; KRIPOTOU, Sotiria ; RAPTIS, Constantine ; TURRELL, Sylvia ; SYASSEN, Karl: Raman and DSC studies of fragility in tellurium-zinc oxide glass formers. In: *physica status solidi (c)* 8 (2011), S. 3039–3042

[892] MOHD ZAID, Mohd H. ; MATORI, Khamirul A. ; ABDUL AZIZ, Sidek H. ; ZAKARIA, Azmi ; MOHD GHAZALI, Mohd S.: Effect of ZnO on the Physical Properties and Optical Band Gap of Soda Lime Silicate Glass. In: *International Journal of Molecular Sciences* 13 (2012), S. 7550

[893] SMITH, Charmayne E. ; BROW, Richard K. ; MONTAGNE, Lionel ; REVEL, Bertrand: The structure and properties of zinc aluminophosphate glasses. In: *Journal of Non-Crystalline Solids* 386 (2014), S. 105 – 114

[894] CHEN, X. ; BRAUER, D.S. ; KARPUKHINA, N. ; WAITE, R.D. ; BARRY, M. ; MCKAY, I.J. ; HILL, R.G.: Šmartácid-degradable zinc-releasing silicate glasses. In: *Materials Letters* 126 (2014), S. 278 – 280

[895] BACHAR, Ahmed ; MERCIER, Cyrille ; TRICOTEAUX, Arnaud ; HORNEZ, Jean-Christophe ; LERICHE, Anne ; FOLLET, Claudine ; REVEL, Bertrand ; HAMPSHIRE, Stuart ; TOWLER, Mark R.: Effect of Nitrogen on Properties of Na_2O–CaO–SrO–ZnO–SiO_2 Glasses. In: *Journal of the American Ceramic Society* 98 (2015), S. 748–757

[896] IORDANOVA, R. ; ATAALLA, M. ; MILANOVA, M. ; ALEKSANDROV, L. ; STANEVA, A. ; DIMITRIEV, Y.: Glass formation and structure of glasses in the WO_3–ZnO–Nd_2O_3–Al_2O_3 system. In: *Journal of Non-Crystalline Solids* 414 (2015), S. 42 – 50

[897] CORMIER, L. ; GASKELL, P. H. ; CALAS, G. ; SOPER, A. K.: Medium-range order around titanium in a silicate glass studied by neutron diffraction with isotopic substitution. In: *Phys. Rev. B* 58 (1998), S. 11322–11330

[898] PICKUP, David M. ; SOWREY, Frank E. ; NEWPORT, Robert J. ; GUNAWIDJAJA, Philips N. ; DRAKE, Kieran O. ; SMITH, Mark E.: The Structure of TiO_2–SiO_2 Sol–Gel Glasses from Neutron Diffraction with Isotopic Substitution of Titanium and ^{17}O and ^{49}Ti Solid-State NMR with Isotopic Enrichment. In: *The Journal of Physical Chemistry B* 108 (2004), S. 10872–10880

[899] WALLIDGE, G.W. ; ANDERSON, R. ; MOUNTJOY, G. ; PICKUP, D.M. ; GUNAWIDJAJA, P. ; NEWPORT, R.J. ; SMITH, M.E.: Advanced physical characterisation of the structural evolution of amorphous $(TiO_2)_x(SiO_2)_{1-x}$ sol-gel materials. In: *Journal of Materials Science* 39 (2004), S. 6743–6755. – ISSN 0022–2461

[900] KAPOOR, Saurabh ; GOEL, Ashutosh ; TILOCCA, Antonio ; DHUNA, Vikram ; BHATIA, Gaurav ; DHUNA, Kshitija ; FERREIRA, José M.: Role of glass structure in defining the chemical dissolution behavior, bioactivity and antioxidant properties of zinc and strontium co-doped alkali-free phosphosilicate glasses. In: *Acta Biomaterialia* 10 (2014), S. 3264 – 3278

[901] ONORATO, Paulette I. K. ; ALEXANDER, Michael N. ; STRUCK, Charles W. ; TASKER, G. W. ; UHLMANN, D. R.: Bridging and Nonbridging Oxygen Atoms in Alkali Aluminosilicate Glasses. In: *Journal of the American Ceramic Society* 68 (1985), S. C–148–C–150

[902] TOPLIS, Michael J. ; KOHN, Simon C. ; SMITH, Mark E. ; POPLETT, Iain J. F.: Fivefold-coordinated aluminum in tectosilicate glasses observed by triple quantum MAS NMR. In: *American Mineralogist* 85 (2000), S. 1556–1560

[903] THOMPSON, Linda M. ; STEBBINS, Jonathan F.: Non-stoichiometric non-bridging oxygens and five-coordinated aluminum in alkaline earth aluminosilicate glasses: Effect of modifier cation size. In: *Journal of Non-Crystalline Solids* 358 (2012), S. 1783 – 1789

[904] STEBBINS, Jonathan F. ; WU, Jingshi ; THOMPSON, Linda M.: Interactions between network cation coordination and non-bridging oxygen abundance in oxide glasses and melts: Insights from {NMR} spectroscopy. In: *Chemical Geology* 346 (2013), S. 34 – 46

[905] SMEDSKJAER, Morten M. ; YOUNGMAN, Randall E. ; MAURO, John C.: Impact of ZnO on the structure and properties of sodium aluminosilicate glasses: Comparison with alkaline earth oxides. In: *Journal of Non-Crystalline Solids* 381 (2013), S.

58 – 64

[906] FANKENHEIM, M. C.: *Die Lehre von der Kohäsion: umfassend die Elastizität der Gase, die Elastizität und Kohärenz der flüssigen und festen Körper und die Kristallkunde*. 1835

[907] ROSENHAIN, W.: The Structure and Constitution of Glass. In: *J. Soc. Glass Technol. Trans.* 11 (1927), S. 77–97

[908] WEIMARN, P.P. von: Zur Lehre von den kolloiden, amorphen und kristallinischen Zuständen. In: *Zeitschrift für Chemie und Industrie der Kolloide* 2 (1907), S. 76–83. – ISSN 0368–6590

[909] WEIMARN, P.P. von: Zur Lehre von den Zuständen der Materie. In: *Zeitschrift für Chemie und Industrie der Kolloide* 4 (1909), S. 123–139. – ISSN 0368–6590

[910] WEIMARN, P.P. von: Zur Lehre von den Zuständen der Materie. In: *Zeitschrift für Chemie und Industrie der Kolloide* 3 (1908), S. 282–304. – ISSN 0368–6590

[911] WHITTAKER, E.J.W.: Factors affecting element ratios in the crystallization of minerals. In: *Geochimica et Cosmochimica Acta* 31 (1967), S. 2275 – 2288

[912] SACHDEV, Subir ; NELSON, David R.: Order in metallic glasses and icosahedral crystals. In: *Phys. Rev. B* 32 (1985)

[913] ROBERTSON, J. L. ; MOSS, S. C. ; KREIDER, K. G.: Comparison of Amorphous and Quasicrystalline Films of Sputtered $Al_{0.72}Mn_{0.22}Si_{0.06}$. In: *Phys. Rev. Lett.* 60 (1988), S. 2062–2065

[914] KUIYING, Chen ; HONGBO, Liu ; XIAOPING, Li ; QIYONG, Han ; ZHUANGQI, Hu: Molecular dynamics simulation of local structure of aluminium and copper in supercooled liquid and solid state by using EAM. In: *Journal of Physics: Condensed Matter* 7 (1995), S. 2379

[915] XING, L.Q. ; OCHIN, P. ; HARMELIN, M. ; FAUDOT, F. ; BIGOT, J.: Alloys of high glass-forming ability. In: *Journal of Non-Crystalline Solids* 205—207, Part 2 (1996), S. 597 – 601

[916] KÖSTER, U. ; MEINHARDT, J. ; ROOS, S. ; BUSCH, R.: Formation of quasicrystals in bulk glass forming Zr–Cu–Ni–Al alloys. In: *Materials Science and Engineering: A* 226–228 (1997), S. 995 – 998

[917] CHEN, M. W. ; ZHANG, T. ; INOUE, A. ; SAKAI, A. ; SAKURAI, T.: Quasicrystals in a partially devitrified Zr65Al7.5Ni10Cu12.5Ag5 bulk metallic glass. In: *Applied Physics Letters* 75 (1999), S. 1697–1699

[918] JAKSE, Noël ; PASTUREL, Alain: Local Order of Liquid and Supercooled Zirconium by Ab Initio Molecular Dynamics. In: *Phys. Rev. Lett.* 91 (2003), S. 195501

[919] SHENG, H. W. ; LUO, W. K. ; ALAMGIR, F. M. ; BAI, J. M. ; MA, E.: Atomic packing and short-to-medium-range order in metallic glasses. In: *Nature* 439 (2006), S. 419–425

[920] GANESH, P. ; WIDOM, M.: Signature of nearly icosahedral structures in liquid and supercooled liquid copper. In: *Phys. Rev. B* 74 (2006), S. 134205

[921] HUI, Li ; PEDERIVA, F.: Structural study of local order in quenched lead under high pressures. In: *Chemical Physics* 304 (2004), S. 261–271

[922] CELINO, M.: Molecular dynamics characterization of icosahedral short range order in undercooled copper. In: *The European Physical Journal Special Topics* 196 (2011), S. 35–43

[923] GUAN, P. F. ; FUJITA, T. ; HIRATA, A. ; LIU, Y. H. ; CHEN, M. W.: Structural Origins of the Excellent Glass Forming Ability of $Pd_{40}Ni_{40}P_{20}$. In: *Phys. Rev. Lett.* 108 (2012), S. 175501

[924] SHIMONO, Masato ; ONODERA, Hidehiro: Dynamics and Geometry of Icosahedral Order in Liquid and Glassy Phases of Metallic Glasses. In: *Metals* 5 (2015), S. 1163–1187

[925] WRIGHT, Adrian C. ; SINCLAIR, Roger N. ; LEADBETTER, Alan J.: Effect of preparation method on the structure of amorphous solids in the system As–S. In: *Journal of Non-Crystalline Solids* 71 (1985), S. 295 – 302

[926] WRIGHT, A. C. ; D. L. PRICE, A. G. C. ; ETHERINGTON, G. ; SINCLAIR, R.: Diffraction by Glasses With a Layer Structure. In: *Defect and Diffusion Forum* 53–54 (1987), S. 255–264

[927] AMATO, IVAN: A New Order in Glass. In: *Science* 252 (1991), S. 1377–1378

[928] GASKELL, P.H.: The structure of simple glasses: Randomness or pattern - The debate goes on. In: *Glass Physics and Chemistry* 24 (1998), S. 180–188

[929] UCHINO, T. ; HARROP, J. D. ; TARASKIN, S. N. ; ELLIOTT, S. R.: Real and reciprocal space structural correlations contributing to the first sharp diffraction peak in silica glass. In: *Phys. Rev. B* 71 (2005), S. 014202

[930] TARASKIN, S N.: Connection between structural characteristics of glasses and their crystalline counterparts. In: *Journal of Physics: Condensed Matter* 19 (2007), S. 455215

[931] C., Chen L. ; F., Spaepen: Calorimetric evidence for the micro-quasicrystalline structure of 'amorphous' Al/transition metal alloys. In: *Nature* 336 (1988), S. 366–368

[932] CHEN, L. C. ; SPAEPEN, F.: Analysis of calorimetric measurements of grain growth. In: *Journal of Applied Physics* 69 (1991), S. 679–688

[933] VARSHNEYA, A.: *Fundamentals of Inorganic Glasses*. Academic Press, 1993. – ISBN 978–0127149707

[934] ENGEL, Eberhard ; DREIZLER, Reiner M.: *Density Functional Theory–An Advanced Course*. Springer-Verlag, Berlin Heidelberg, 2011. – ISBN 978–3642140891

[935] BLÖCHL, Peter: *Advanced Topics of Theoretical Physcs I - The electronic structure of matter*. http://orion.pt.tu-clausthal.de/atp/phisx.html, 2015

[936] GIUSTINO, Feliciano: *Materials Modelling using Density Functional Theory*. Oxford University Press, 2014. – ISBN 978–0199662449

[937] BORN, M. ; OPPENHEIMER, R.: Zur Quantentheorie der Molekeln. In: *Annalen der Physik* 389 (1927), S. 457–484

[938] BORN, Max ; HUANG, Kun: *Dynamical Theory of Crystal Lattices (Oxford Classic Texts in the Physical Sciences)*. Oxford University Press, USA, 1954. – ISBN 978–0198503699

[939] CHESTER, G.V.: The theory of the interaction of electrons with lattice vibrations in metals. In: *Advances in Physics* 10 (1961), S. 357–400

[940] KROES, Geert-Jan ; GROSS, Axel ; BAERENDS, Evert-Jan ; SCHEFFLER, Matthias ; MCCORMACK, Drew A.: Quantum Theory of Dissociative Chemisorption on Metal Surfaces. In: *Accounts of Chemical Research* 35 (2002), S. 193–200

[941] WALKER, B G. ; MOLTENI, C ; MARZARI, N: Ab initio molecular dynamics of metal surfaces. In: *Journal of Physics: Condensed Matter* 16 (2004), S. S2575

[942] BROVMAN, E G. ; KAGAN, Yurii M.: Phonons in nontransition metals. In: *Soviet Physics Uspekhi* 17 (1974), S. 125

[943] WHITE, Jason D. ; CHEN, Jun ; MATSIEV, Daniel ; AUERBACH, Daniel J. ; WODTKE, Alec M.: Conversion of large-amplitude vibration to electron excitation at a metal surface. In: *Nature* 433 (2005), S. 503–505

[944] PISANA, Simone ; LAZZERI, Michele ; CASIRAGHI, Cinzia ; NOVOSELOV, Kostya S. ; GEIM, A. K. ; FERRARI, Andrea C. ; MAURI, Francesco: Breakdown of the adiabatic Born-Oppenheimer approximation in graphene. In: *Nature Materials* 6 (2007), S. 198–201

[945] PISCANEC, Stefano ; LAZZERI, Michele ; ROBERTSON, J. ; FERRARI, Andrea C. ; MAURI, Francesco: Optical phonons in carbon nanotubes: Kohn anomalies, Peierls distortions, and dynamic effects. In: *Phys. Rev. B* 75 (2007), S. 035427

[946] BUSHMAKER, Adam W. ; DESHPANDE, Vikram V. ; HSIEH, Scott ; BOCKRATH, Marc W. ; CRONIN, Stephen B.: Direct Observation of Born-Oppenheimer Approximation Breakdown in Carbon Nanotubes. In: *Nano Letters* 9 (2009), S. 607–611

[947] BISHOP, David M. ; SOLUNAC, Sasha A.: Breakdown of the Born-Oppenheimer Approximation in the Calculation of Electric Hyperpolarizabilities. In: *Phys. Rev. Lett.* 55 (1985), S. 1986–1988

[948] HUGHES, Sharon M. ; HAGEDORN, George A.: Diatomic molecules with large angular momentum in the Born-Oppenheimer approximation. In: *Journal of Physics A: Mathematical and Theoretical* 42 (2009), S. 035305

[949] ISHIKAWA, Atsushi ; NAKASHIMA, Hiroyuki ; NAKATSUJI, Hiroshi: Accurate solutions of the Schrödinger and Dirac equations of , HD+, and HT+: With and without Born-Oppenheimer approximation and under magnetic field. In: *Chemical Physics* 401 (2012), S. 62 – 72

[950] KUZNETSOV, Alexander M. ; MEDVEDEV, Igor G.: Does really Born-Oppenheimer approximation break down in charge transfer processes? An exactly solvable model. In: *Chemical Physics* 324 (2006), S. 148 – 159

[951] BURLAND, D. M. ; ROBINSON, G. W.: Is the Breakdown of the Born-Oppenheimer Approximation Responsible for Internal Conversion in Large Molecules. In: *Proceedings of the National Academy of Sciences* 66 (1970), S. 257–264

[952] STRICKLER, S. J.: Spectroscopic effects of a breakdown of the Born-Oppenheimer approximation. In: *The Journal of Physical Chemistry* 80 (1976), S. 2149–2154

[953] BIZZOCCHI, Luca ; GIULIANO, Barbara M. ; HESS, Mareike ; GRABOW, Jens-Uwe: The rotational spectra, potential function, Born-Oppenheimer breakdown, and magnetic shielding of SnSe and SnTe. In: *The Journal of Chemical Physics* 126 (2007), S. 114305

[954] FEYNMAN, R. P.: Forces in Molecules. In: *Phys. Rev.* 56 (1939), S. 340–343

[955] DI VENTRA, Massimiliano ; PANTELIDES, Sokrates T.: Hellmann-Feynman theorem and the definition of forces in quantum time-dependent and transport problems. In: *Phys. Rev. B* 61 (2000), S. 16207–16212

[956] HELLMANN, Hans ; ANDRAE, Dirk (Hrsg.): *Hans Hellmann: Einführung in die Quantenchemie*. Springer-Verlag, Berlin Heidelberg, 2015. – ISBN 978–3662459669

[957] PULAY, P.: Ab initio calculation of force constants and equilibrium geometries in polyatomic molecules. In: *Molecular Physics* 17 (1969), S. 197–204

[958] LIN, Zijing: Pulay forces in density functional theory for periodic and molecular systems. In: *Physics Letters A* 299 (2002), S. 413 – 417

[959] JACKSON, Koblar ; PEDERSON, Mark R.: Accurate forces in a local-orbital approach to the local-density approximation. In: *Phys. Rev. B* 42 (1990), S. 3276–3281

[960] FRANCIS, G P. ; PAYNE, M C.: Finite basis set corrections to total energy pseudopotential calculations. In: *Journal of Physics: Condensed Matter* 2 (1990), S. 4395

[961] YU, Rici ; SINGH, D. ; KRAKAUER, H.: All-electron and pseudopotential force calculations using the linearized-augmented-plane-wave method. In: *Phys. Rev. B* 43 (1991), S. 6411–6422

[962] METHFESSEL, M. ; SCHILFGAARDE, M. van: Derivation of force theorems in density-functional theory: Application to the full-potential LMTO method. In: *Phys. Rev. B* 48 (1993), S. 4937–4940

[963] JAFFE, John E. ; HESS, Anthony C.: Gaussian basis density functional theory for systems periodic in two or three dimensions: Energy and forces. In: *The Journal of Chemical Physics* 105 (1996), S. 10983

[964] LIN, Lin ; LU, Jianfeng ; YING, Lexing ; E, Weinan: Optimized local basis set for Kohn-Sham density functional theory. In: *Journal of Computational Physics* 231 (2012), S. 4515 – 4529

[965] PULAY, Péter: Convergence acceleration of iterative sequences. the case of scf iteration. In: *Chemical Physics Letters* 73 (1980), S. 393 – 398

[966] FLETCHER, R.: *Newton-Like Methods*. John Wiley & Sons, Ltd, 2000. – 44–79 S. – ISBN 9781118723203

[967] SCHMIT, Lucien A. ; LAI, Ye-Chen: Structural optimization based on preconditioned conjugate gradient analysis methods. In: *International Journal for Numerical Methods in Engineering* 37 (1994), S. 943–964

[968] FLETCHER, R.: *Conjugate Direction Methods*. John Wiley & Sons, Ltd, 2000. – 80–94 S. – ISBN 9781118723203

[969] SCHLEGEL, H. B.: *Optimization of Equilibrium Geometries and Transition Structures*. John Wiley & Sons, Inc., 2007. – 249–286 S. – ISBN 9780470142936

[970] CAR, R. ; PARRINELLO, M.: Unified Approach for Molecular Dynamics and Density-Functional Theory. In: *Phys. Rev. Lett.* 55 (1985), S. 2471–2474

[971] PAYNE, M. C. ; TETER, M. P. ; ALLAN, D. C. ; ARIAS, T. A. ; JOANNOPOULOS, J. D.: Iterative minimization techniques for *ab initio* total-energy calculations: molecular dynamics and conjugate gradients. In: *Rev. Mod. Phys.* 64 (1992), S. 1045–1097

[972] LAASONEN, Kari ; PASQUARELLO, Alfredo ; CAR, Roberto ; LEE, Changyol ; VANDERBILT, David: Car-Parrinello molecular dynamics with Vanderbilt ultrasoft pseudopotentials. In: *Phys. Rev. B* 47 (1993), S. 10142–10153

[973] HUTTER, Jürg: Car-Parrinello molecular dynamics. In: *WIREs Computational Molecular Science* 2 (2012), S. 604–612

[974] NIKLASSON, Anders M. N. ; CAWKWELL, Marc J.: Generalized extended Lagrangian Born-Oppenheimer molecular dynamics. In: *The Journal of Chemical Physics* 141 (2014), S. 164123

[975] PARANDEKAR, Priya V. ; TULLY, John C.: Mixed quantum-classical equilibrium. In: *The Journal of Chemical Physics* 122 (2005), S. 094102

[976] LI, Xiaosong ; TULLY, John C. ; SCHLEGEL, H. B. ; FRISCH, Michael J.: Ab initio Ehrenfest dynamics. In: *The Journal of Chemical Physics* 123 (2005), S. 084106

[977] SCHMIDT, J. R. ; PARANDEKAR, Priya V. ; TULLY, John C.: Mixed quantum-classical equilibrium: Surface hopping. In: *The Journal of Chemical Physics* 129 (2008), S. 044104

[978] BARONI, Stefano ; GIRONCOLI, Stefano de ; DAL CORSO, Andrea ; GIANNOZZI, Paolo: Phonons and related crystal properties from density-functional perturbation theory. In: *Rev. Mod. Phys.* 73 (2001), S. 515–562

[979] HANDY, N. C. ; BICOUT, Dominique (Hrsg.) ; FIELD, Martin (Hrsg.): *Density Functional Theory*. Springer Verlag, Berlin Heidelberg, 1995. – 1–27 S. – ISBN 978–3540608691

[980] STEINER, Erich: Charge Densities in Atoms. In: *The Journal of Chemical Physics* 39 (1963), S. 2365

[981] KATO, Tosio: On the eigenfunctions of many-particle systems in quantum mechanics. In: *Communications on Pure and Applied Mathematics* 10 (1957), S. 151–177

[982] NAGY, Á. ; SEN, K D.: Higher-order cusp of the density in certain highly excited states of atoms and molecules. In: *Journal of Physics B: Atomic, Molecular and Optical Physics* 33 (2000), S. 1745

[983] NAGY, Á. ; SEN, K. D.: Ground- and excited-state cusp conditions for the electron density. In: *The Journal of Chemical Physics* 115 (2001), S. 6300–6308

[984] PARR, Robert G. ; YANG, Weitao: *Density-Functional Theory of Atoms and Molecules*. Oxford University Press, New York, 1989. – ISBN 0195092767

[985] KOHANOFF, Jorge: *Electronic Structure Calculations for Solids and Molecules: Theory and Computational Methods*. Cam-

bridge University Press, 2006. – ISBN 9780521815918

[986] MARTIN, Richard M.: *Electronic Structure: Basic Theory and Practical Methods*. Cambridge University Press, 2008. – ISBN 9780521534406

[987] BECHSTEDT, Friedhelm: *Many-Body Approach to Electronic Excitations: Concepts and Applications (Springer Series in Solid-State Sciences)*. Springer-Verlag, Berlin Heidelberg, 2015. – ISBN 9783662445921

[988] LEVY, Mel: Universal variational functionals of electron densities, first-order density matrices, and natural spin-orbitals and solution of the v-representability problem. In: *Proceedings of the National Academy of Sciences* 76 (1979), S. 6062–6065

[989] LEVY, Mel: Electron densities in search of Hamiltonians. In: *Phys. Rev. A* 26 (1982), S. 1200–1208

[990] LIEB, Elliott H.: Density functionals for coulomb systems. In: *International Journal of Quantum Chemistry* 24 (1983), S. 243–277

[991] GILBERT, T. L.: Hohenberg-Kohn theorem for nonlocal external potentials. In: *Phys. Rev. B* 12 (1975), S. 2111–2120

[992] RAJAGOPAL, A. K. ; CALLAWAY, J.: Inhomogeneous Electron Gas. In: *Phys. Rev. B* 7 (1973), S. 1912–1919

[993] GUNNARSSON, O. ; LUNDQVIST, B. I.: Exchange and correlation in atoms, molecules, and solids by the spin-density-functional formalism. In: *Phys. Rev. B* 13 (1976), S. 4274–4298

[994] LIEB, Elliott H. ; SCHRADER, Robert: Current densities in density-functional theory. In: *Phys. Rev. A* 88 (2013), S. 032516

[995] LAESTADIUS, Andre ; BENEDICKS, Michael: Nonexistence of a Hohenberg-Kohn variational principle in total current-density-functional theory. In: *Phys. Rev. A* 91 (2015), S. 032508

[996] PRIBRAM-JONES, Aurora ; PITTALIS, Stefano ; GROSS, E.K.U. ; BURKE, Kieron: Thermal Density Functional Theory in Context. In: GRAZIANI, Frank (Hrsg.) ; DESJARLAIS, Michael P. (Hrsg.) ; REDMER, Ronald (Hrsg.) ; TRICKEY, Samuel B. (Hrsg.): *Frontiers and Challenges in Warm Dense Matter* Bd. 96. Springer International Publishing, 2014. – ISBN 978–3–319–04911–3, S. 25–60

[997] RUNGE, Erich ; GROSS, E. K. U.: Density-Functional Theory for Time-Dependent Systems. In: *Phys. Rev. Lett.* 52 (1984), S. 997–1000

[998] LI, Tie-cheng ; TONG, Pei-qing: Hohenberg-Kohn theorem for time-dependent ensembles. In: *Phys. Rev. A* 31 (1985), S. 1950–1951

[999] DHARA, Asish K. ; GHOSH, Swapan K.: Density-functional theory for time-dependent systems. In: *Phys. Rev. A* 35 (1987), S. 442–444

[1000] AYERS, Paul W. ; LEVY, Mel: Time-independent (static) density-functional theories for pure excited states: Extensions and unification. In: *Phys. Rev. A* 80 (2009), S. 012508

[1001] AYERS, Paul W. ; LEVY, Mel ; NAGY, Agnes: Time-independent density-functional theory for excited states of Coulomb systems. In: *Phys. Rev. A* 85 (2012), S. 042518

[1002] EVANGELISTA, Francesco A. ; SHUSHKOV, Philip ; TULLY, John C.: Orthogonality Constrained Density Functional Theory for Electronic Excited States. In: *The Journal of Physical Chemistry A* 117 (2013), S. 7378–7392

[1003] LARSEN, Helena ; OLSEN, Jeppe ; JØRGENSEN, Poul ; HELGAKER, Trygve: Direct optimization of the atomic-orbital density matrix using the conjugate-gradient method with a multilevel preconditioner. In: *The Journal of Chemical Physics* 115 (2001), S. 9685–9697

[1004] JIANG, Hong ; YANG, Weitao: Conjugate-gradient optimization method for orbital-free density functional calculations. In: *The Journal of Chemical Physics* 121 (2004), S. 2030–2036

[1005] HO, Gregory S. ; LIGNÉRES, Vincent L. ; CARTER, Emily A.: Introducing PROFESS: A new program for orbital-free density functional theory calculations. In: *Computer Physics Communications* 179 (2008), S. 839 – 854

[1006] LEHTOMÄKI, Jouko ; MAKKONEN, Ilja ; CARO, Miguel A. ; HARJU, Ari ; LOPEZ-ACEVEDO, Olga: Orbital-free density functional theory implementation with the projector augmented-wave method. In: *The Journal of Chemical Physics* 141 (2014), S. 234102

[1007] LEVY, Mel ; PERDEW, John P.: The Constrained Search Formulation of Density Functional Theory. In: DREIZLER, Reiner M. (Hrsg.) ; PROVIDÄNCIA, Joêo da (Hrsg.): *Density Functional Methods In Physics* Bd. 123. 1985, S. 11–30

[1008] NALEWAJSKI, Roman F. ; PARR, Robert G.: Legendre transforms and Maxwell relations in density functional theory. In: *The Journal of Chemical Physics* 77 (1982), S. 399–407

[1009] COLONNA, François ; SAVIN, Andreas: Correlation energies for some two- and four-electron systems along the adiabatic connection in density functional theory. In: *The Journal of Chemical Physics* 110 (1999), S. 2828–2835

[1010] KRYACHKO, Eugene S. ; LUDEA, Eduardo V.: Formulation of N - and v -representable density-functional theory. I. Ground states. In: *Phys. Rev. A* 43 (1991), S. 2179–2193

[1011] LUDEÑA, Eduardo V. ; LÓPEZ-BOADA, Roberto ; MALDONADO, Jorge E. ; VALDERRAMA, Elmer ; KRYACHKO, Eugene S. ; KOGA, Toshikatsu ; HINZE, Juergen: Local-scaling transformation version of density functional theory. In: *International Journal of Quantum Chemistry* 56 (1995), S. 285–301

[1012] DELLE SITE, Luigi ; GHIRINGHELLI, Luca M. ; CEPERLEY, David M.: Electronic energy functionals: Levy-Lieb principle within the ground state path integral quantum Monte Carlo. In: *International Journal of Quantum Chemistry* 113 (2013), S. 155–160

[1013] CIOSLOWSKI, J.: Density Functionals for the Energy of Electronic Systems: Explicit Variational Construction. In: *Phys. Rev. Lett.* 60 (1988), S. 2141–2143

[1014] TEALE, A. M. ; CORIANI, S. ; HELGAKER, T.: The calculation of adiabatic-connection curves from full configuration-interaction densities: Two-electron systems. In: *The Journal of Chemical Physics* 130 (2009), S. 104111

[1015] TEALE, A. M. ; CORIANI, S. ; HELGAKER, T.: Accurate calculation and modeling of the adiabatic connection in density functional theory. In: *The Journal of Chemical Physics* 132 (2010), S. 164115

[1016] AYERS, Paul W. ; PARR, Robert G.: Is it impossible to find the universal density functional? Or is it just well-hidden? In: *Indian Journal of Chemistry* 53A (2014), S. 929–931

[1017] WAGNER, Lucas O. ; BAKER, Thomas E. ; STOUDENMIRE, E. M. ; BURKE, Kieron ; WHITE, Steven R.: Kohn-Sham calculations with the exact functional. In: *Phys. Rev. B* 90 (2014), S. 045109

[1018] SZABO, Attila ; OSTLUND, Neil S.: *Modern Quantum Chemistry - Introduction to Advanced Electronic structure theory*. Dover Publications, 1996. – ISBN 048669186

[1019] KOOPMANS, T: Über die Zuordnung von Wellenfunktionen und Eigenwerten zu den Einzelnen Elektronen Eines Atoms. In: *Physica* 1 (1934), S. 104 – 113

[1020] STEIN, Tamar ; EISENBERG, Helen ; KRONIK, Leeor ; BAER, Roi: Fundamental Gaps in Finite Systems from Eigenvalues of a Generalized Kohn-Sham Method. In: *Phys. Rev. Lett.* 105 (2010), S. 266802

[1021] STEIN, Tamar ; AUTSCHBACH, Jochen ; GOVIND, Niranjan ; KRONIK, Leeor ; BAER, Roi: Curvature and Frontier Orbital Energies in Density Functional Theory. In: *The Journal of Physical Chemistry Letters* 3 (2012), S. 3740–3744

[1022] MORI-SÁNCHEZ, Paula ; COHEN, Aron J. ; YANG, Weitao: Many-electron self-interaction error in approximate density functionals. In: *The Journal of Chemical Physics* 125 (2006), S. 201102

[1023] TSUNEDA, Takao ; SONG, Jong-Won ; SUZUKI, Satoshi ; HIRAO, Kimihiko: On Koopmans' theorem in density functional theory. In: *The Journal of Chemical Physics* 133 (2010), S. 174101

[1024] VYDROV, Oleg A. ; SCUSERIA, Gustavo E. ; PERDEW, John P.: Tests of functionals for systems with fractional electron number. In: *The Journal of Chemical Physics* 126 (2007), Nr. 15, S. 154109

[1025] COHEN, Aron J. ; MORI-SÁNCHEZ, Paula ; YANG, Weitao: Fractional charge perspective on the band gap in density-functional theory. In: *Phys. Rev. B* 77 (2008), S. 115123

[1026] SALZNER, Ulrike ; BAER, Roi: Koopmans' springs to life. In: *The Journal of Chemical Physics* 131 (2009), S. 231101

[1027] PERDEW, J. P. ; ZUNGER, Alex: Self-interaction correction to density-functional approximations for many-electron systems. In: *Phys. Rev. B* 23 (1981), S. 5048–5079

[1028] PERDEW, John P. ; NORMAN, Michael R.: Electron removal energies in Kohn-Sham density-functional theory. In: *Phys. Rev. B* 26 (1982), S. 5445–5450

[1029] PERDEW, John P. ; LEVY, Mel: Physical Content of the Exact Kohn-Sham Orbital Energies: Band Gaps and Derivative Discontinuities. In: *Phys. Rev. Lett.* 51 (1983), S. 1884–1887

[1030] STOWASSER, Ralf ; ; HOFFMANN, Roald: What Do the Kohn-Sham Orbitals and Eigenvalues Mean? In: *Journal of the American Chemical Society* 121 (1999), S. 3414–3420

[1031] CHONG, D. P. ; GRITSENKO, O. V. ; BAERENDS, E. J.: Interpretation of the Kohn-Sham orbital energies as approximate vertical ionization potentials. In: *The Journal of Chemical Physics* 116 (2002), Nr. 5, S. 1760–1772

[1032] GRITSENKO, O. V. ; BAERENDS, E. J.: The analog of Koopmans' theorem in spin-density functional theory. In: *The Journal of Chemical Physics* 117 (2002), Nr. 20, S. 9154–9159

[1033] GRITSENKO, O. V. ; BRAÏDA, B. ; BAERENDS, E. J.: Physical interpretation and evaluation of the Kohn-Sham and Dyson components of the ε-I relations between the Kohn-Sham orbital energies and the ionization potentials. In: *The Journal of Chemical Physics* 119 (2003), S. 1937–1950

[1034] PUEYO BELLAFONT, Noelia ; ILLAS, Francesc ; BAGUS, Paul S.: Validation of Koopmans' theorem for density functional theory binding energies. In: *Phys. Chem. Chem. Phys.* 17 (2015), S. 4015–4019

[1035] JANAK, J. F.: Proof that $\frac{\partial E}{\partial n_i} = \epsilon$ in density-functional theory. In: *Phys. Rev. B* 18 (1978), S. 7165–7168

[1036] PERDEW, John P. ; LEVY, Mel: Physical Content of the Exact Kohn-Sham Orbital Energies: Band Gaps and Derivative

Discontinuities. In: *Phys. Rev. Lett.* 51 (1983), S. 1884–1887

[1037] STÄDELE, M. ; MOUKARA, M. ; MAJEWSKI, J. A. ; VOGL, P. ; GÖRLING, A.: Exact exchange Kohn-Sham formalism applied to semiconductors. In: *Phys. Rev. B* 59 (1999), S. 10031–10043

[1038] QTEISH, Abdallah ; RINKE, Patrick ; SCHEFFLER, Matthias ; NEUGEBAUER, Jörg: Exact-exchange-based quasiparticle energy calculations for the band gap, effective masses, and deformation potentials of ScN. In: *Phys. Rev. B* 74 (2006), S. 245208

[1039] PERSSON, Clas ; MIRBT, Susanne: Improved electronic structure and optical properties of sp-hybridized semiconductors using LDA+USIC. In: *Brazilian Journal of Physics* 36 (2006), S. 286 – 290

[1040] XIAO, Hai ; TAHIR-KHELI, Jamil ; WILLIAM A. GODDARD, III: Accurate Band Gaps for Semiconductors from Density Functional Theory. In: *The Journal of Physical Chemistry Letters* 2 (2011), S. 212–217

[1041] PERDEW, John P. ; LEVY, Mel: Density Functional Theory and the Band Gap Problem. In: *International Journal of Quantum Chemistry Quantum Chemistry Symposium* 19 (1986), S. 497–523

[1042] SEIDL, A. ; GÖRLING, A. ; VOGL, P. ; MAJEWSKI, J. A. ; LEVY, M.: Generalized Kohn-Sham schemes and the band-gap problem. In: *Phys. Rev. B* 53 (1996), S. 3764–3774

[1043] CAPELLE, Klaus: A bird's-eye view of density-functional theory. In: *Brazilian Journal of Physics* 36 (2006), S. 1318 – 1343

[1044] JAIN, Manish ; CHELIKOWSKY, James R. ; LOUIE, Steven G.: Reliability of Hybrid Functionals in Predicting Band Gaps. In: *Phys. Rev. Lett.* 107 (2011), S. 216806

[1045] PERDEW, John P. ; PARR, Robert G. ; LEVY, Mel ; BALDUZ, Jose L.: Density-Functional Theory for Fractional Particle Number: Derivative Discontinuities of the Energy. In: *Phys. Rev. Lett.* 49 (1982), S. 1691–1694

[1046] JONES, R. O. ; GUNNARSSON, O.: The density functional formalism, its applications and prospects. In: *Rev. Mod. Phys.* 61 (1989), S. 689–746

[1047] CHAI, Jeng-Da ; CHEN, Po-Ta: Restoration of the Derivative Discontinuity in Kohn-Sham Density Functional Theory: An Efficient Scheme for Energy Gap Correction. In: *Phys. Rev. Lett.* 110 (2013), S. 033002

[1048] MORI-S'ANCHEZ, Paula ; COHEN, Aron J.: The derivative discontinuity of the exchange-correlation functional. In: *Phys. Chem. Chem. Phys.* 16 (2014), S. 14378–14387

[1049] SHAM, L. J. ; SCHLÜTER, M.: Density-Functional Theory of the Energy Gap. In: *Phys. Rev. Lett.* 51 (1983), S. 1888–1891

[1050] KRAISLER, Eli ; KRONIK, Leeor: Piecewise Linearity of Approximate Density Functionals Revisited: Implications for Frontier Orbital Energies. In: *Phys. Rev. Lett.* 110 (2013), S. 126403

[1051] MORI-SÁNCHEZ, Paula ; COHEN, Aron J. ; YANG, Weitao: Localization and Delocalization Errors in Density Functional Theory and Implications for Band-Gap Prediction. In: *Phys. Rev. Lett.* 100 (2008), S. 146401

[1052] FREYSOLDT, Christoph ; GRABOWSKI, Blazej ; HICKEL, Tilmann ; NEUGEBAUER, Jörg ; KRESSE, Georg ; JANOTTI, Anderson ; WALLE, Chris G. d.: First-principles calculations for point defects in solids. In: *Rev. Mod. Phys.* 86 (2014), S. 253–305

[1053] GIULIANI, Gabriele ; VIGNALE, Giovanni: *Quantum Theory of the Electron Liquid*. Cambridge University Press, 2005

[1054] PERDEW, John P. ; RUZSINSZKY, Adrienn ; CSONKA, Gábor I. ; VYDROV, Oleg A. ; SCUSERIA, Gustavo E. ; STAROVEROV, Viktor N. ; TAO, Jianmin: Exchange and correlation in open systems of fluctuating electron number. In: *Phys. Rev. A* 76 (2007), S. 040501

[1055] COHEN, Aron J. ; MORI-SÁNCHEZ, Paula ; YANG, Weitao: Insights into Current Limitations of Density Functional Theory. In: *Science* 321 (2008), S. 792–794

[1056] AUTSCHBACH, Jochen ; SREBRO, Monika: Delocalization Error and "Functional Tuning" in Kohn-Sham Calculations of Molecular Properties. In: *Accounts of Chemical Research* 47 (2014), S. 2592–2602

[1057] GODBY, R. W. ; SCHLÜTER, M. ; SHAM, L. J.: Accurate Exchange-Correlation Potential for Silicon and Its Discontinuity on Addition of an Electron. In: *Phys. Rev. Lett.* 56 (1986), S. 2415–2418

[1058] ZHANG, Yingkai ; YANG, Weitao: A challenge for density functionals: Self-interaction error increases for systems with a noninteger number of electrons. In: *The Journal of Chemical Physics* 109 (1998), S. 2604–2608

[1059] POLO, VICTOR ; KRAKA, ELFI ; CREMER, DIETER: Electron correlation and the self-interaction error of density functional theory. In: *Molecular Physics* 100 (2002), S. 1771–1790

[1060] COCOCCIONI, Matteo ; GIRONCOLI, Stefano de: Linear response approach to the calculation of the effective interaction parameters in the LDA + U method. In: *Phys. Rev. B* 71 (2005), S. 035105

[1061] COCOCCIONI, Matteo: The LDA+U Approach: A Simple Hubbard Correction for Correlated Ground States. In: PAVARINI, E. (Hrsg.) ; KOCH, E. (Hrsg.) ; ANDERS, F. (Hrsg.) ; JARRELL, M. (Hrsg.): *Correlated Electrons: From Models to Materials* Bd. 2. Forschungszentrum Jülich, 2012. – ISBN 978–3893367962, S. 1–40

[1062] SEIDL, A. ; GÖRLING, A. ; VOGL, P. ; MAJEWSKI, J. A. ; LEVY, M.: Generalized Kohn-Sham schemes and the band-gap problem. In: *Phys. Rev. B* 53 (1996), S. 3764–3774

[1063] EISENBERG, Helen R. ; BAER, Roi: A new generalized Kohn-Sham method for fundamental band-gaps in solids. In: *Phys. Chem. Chem. Phys.* 11 (2009), S. 4674–4680

[1064] SANNA, Simone ; FRAUENHEIM, Th. ; GERSTMANN, U.: Validity of the Slater-Janak transition-state model within the LDA + U approach. In: *Phys. Rev. B* 78 (2008), S. 085201

[1065] HUBBARD, J.: Electron Correlations in Narrow Energy Bands. In: *Proceedings of the Royal Society of London A: Mathematical, Physical and Engineering Sciences* 276 (1963), S. 238–257

[1066] HUBBARD, J.: Electron Correlations in Narrow Energy Bands. II. The Degenerate Band Case. In: *Proceedings of the Royal Society of London A: Mathematical, Physical and Engineering Sciences* 277 (1964), S. 237–259

[1067] HUBBARD, J.: Electron Correlations in Narrow Energy Bands. III. An Improved Solution. In: *Proceedings of the Royal Society of London A: Mathematical, Physical and Engineering Sciences* 281 (1964), S. 401–419

[1068] HUBBARD, J.: Electron Correlations in Narrow Energy Bands. IV. The Atomic Representation. In: *Proceedings of the Royal Society of London A: Mathematical, Physical and Engineering Sciences* 285 (1965), S. 542–560

[1069] LIECHTENSTEIN, A. I. ; ANISIMOV, V. I. ; ZAANEN, J.: Density-functional theory and strong interactions: Orbital ordering in Mott-Hubbard insulators. In: *Phys. Rev. B* 52 (1995), S. R5467–R5470

[1070] LICHTENSTEIN, A. I. ; KATSNELSON, M. I.: ***Ab initio*** calculations of quasiparticle band structure in correlated systems: LDA++ approach. In: *Phys. Rev. B* 57 (1998), S. 6884–6895

[1071] ANISIMOV, Vladimir I. ; ZAANEN, Jan ; ANDERSEN, Ole K.: Band theory and Mott insulators: Hubbard U instead of Stoner I. In: *Phys. Rev. B* 44 (1991), S. 943–954

[1072] ANISIMOV, Vladimir I. ; ARYASETIAWAN, F ; LICHTENSTEIN, A I.: First-principles calculations of the electronic structure and spectra of strongly correlated systems: the LDA + U method. In: *Journal of Physics: Condensed Matter* 9 (1997), S. 767

[1073] PICKETT, W. E. ; ERWIN, S. C. ; ETHRIDGE, E. C.: Reformulation of the LDA + U method for a local-orbital basis. In: *Phys. Rev. B* 58 (1998), S. 1201–1209

[1074] HIMMETOGLU, Burak ; FLORIS, Andrea ; GIRONCOLI, Stefano de ; COCOCCIONI, Matteo: Hubbard-corrected DFT energy functionals: The LDA+U description of correlated systems. In: *International Journal of Quantum Chemistry* 114 (2014), S. 14–49

[1075] JIANG, Hong ; GOMEZ-ABAL, Ricardo I. ; RINKE, Patrick ; SCHEFFLER, Matthias: Localized and Itinerant States in Lanthanide Oxides United by GW @ LDA + U. In: *Phys. Rev. Lett.* 102 (2009), S. 126403

[1076] JIANG, Hong ; GOMEZ-ABAL, Ricardo I. ; RINKE, Patrick ; SCHEFFLER, Matthias: First-principles modeling of localized d states with the GW@LDA + U approach. In: *Phys. Rev. B* 82 (2010), S. 045108

[1077] ERHART, Paul ; ALBE, Karsten ; KLEIN, Andreas: First-principles study of intrinsic point defects in ZnO: Role of band structure, volume relaxation, and finite-size effects. In: *Phys. Rev. B* 73 (2006), S. 205203

[1078] PAUDEL, Tula R. ; LAMBRECHT, Walter R. L.: First-principles calculation of the O vacancy in ZnO: A self-consistent gap-corrected approach. In: *Phys. Rev. B* 77 (2008), S. 205202

[1079] SINGH, Abhishek K. ; JANOTTI, Anderson ; SCHEFFLER, Matthias ; WALLE, Chris G. d.: Sources of Electrical Conductivity in SnO_2. In: *Phys. Rev. Lett.* 101 (2008), S. 055502

[1080] JANOTTI, Anderson ; WALLE, Chris G. d.: LDA+U and hybrid functional calculations for defects in ZnO, SnO_2, and TiO_2. In: *physica status solidi (b)* 248 (2011), S. 799–804

[1081] PERSSON, Clas ; MIRBT, Susanne: Improved electronic structure and optical properties of sp-hybridized semiconductors using LDA+U^{SIC}. In: *Brazilian Journal of Physics* 36 (2006), S. 286–290

[1082] DOMPABLO, M. E. ; MORALES-GARCÍA, A. ; TARAVILLO, M.: DFT+U calculations of crystal lattice, electronic structure, and phase stability under pressure of TiO_2 polymorphs. In: *The Journal of Chemical Physics* 135 (2011), S. 054503

[1083] VYDROV, Oleg A. ; SCUSERIA, Gustavo E.: Effect of the Perdew–Zunger self-interaction correction on the thermochemical performance of approximate density functionals. In: *The Journal of Chemical Physics* 121 (2004), S. 8187–8193

[1084] VYDROV, Oleg A. ; SCUSERIA, Gustavo E.: Ionization potentials and electron affinities in the Perdew-Zunger self-interaction corrected density-functional theory. In: *The Journal of Chemical Physics* 122 (2005), S. 184107

[1085] VYDROV, Oleg A. ; SCUSERIA, Gustavo E. ; PERDEW, John P. ; RUZSINSZKY, Adrienn ; CSONKA, Gábor I.: Scaling down the Perdew-Zunger self-interaction correction in many-electron regions. In: *The Journal of Chemical Physics* 124 (2006), S. 094108

[1086] GUDMUNDSDÓTTIR, Hildur ; ZHANG, Yao ; WEBER, Peter M. ; JÓNSSON, Hannes: Self-interaction corrected density functional calculations of molecular Rydberg states. In: *The Journal of Chemical Physics* 139 (2013), S. 194102

[1087] LEHTOLA, Susi ; JÓNSSON, Hannes: Variational, Self-Consistent Implementation of the Perdew-Zunger Self-Interaction Correction with Complex Optimal Orbitals. In: *Journal of Chemical Theory and Computation* 10 (2014), S. 5324–5337

[1088] JÓNSSON, Susi L.: Correction to Variational, Self-Consistent Implementation of the Perdew-Zunger Self-Interaction Correction with Complex Optimal Orbitals. In: *Journal of Chemical Theory and Computation* 0 (0)

[1089] SEGEV, David ; JANOTTI, Anderson ; WALLE, Chris G. d.: Self-consistent band-gap corrections in density functional theory using modified pseudopotentials. In: *Phys. Rev. B* 75 (2007), S. 035201

[1090] WANG, Lin-Wang: Large-scale local-density-approximation band gap-corrected GaAsN calculations. In: *Applied Physics Letters* 78 (2001), S. 1565–1567

[1091] LI, Jingbo ; WANG, Lin-Wang: Band-structure-corrected local density approximation study of semiconductor quantum dots and wires. In: *Phys. Rev. B* 72 (2005), S. 125325

[1092] LI, Jingbo ; WEI, Su-Huai: Alignment of isovalent impurity levels: Oxygen impurity in II-VI semiconductors. In: *Phys. Rev. B* 73 (2006), S. 041201

[1093] PERDEW, John P.: Size-Consistency, Self-Interaction Correction, and Derivative Discontinuity in Density Functional Theory. In: LÖWDIN, Per-Olov (Hrsg.): *Density Functional Theory of Many-Fermion Systems* Bd. 21. Academic Press, 1990, S. 113 – 134

[1094] COHEN, Aron J. ; MORI-SÁNCHEZ, Paula ; YANG, Weitao: Challenges for Density Functional Theory. In: *Chemical Reviews* 112 (2012), S. 289–320

[1095] JENSEN, Frank: *Introduction to Computational Chemistry*. Wiley-VCH Verlag GmbH, 2007. – ISBN 978–0470011874

[1096] KÜMMEL, Stephan ; KRONIK, Leeor: Orbital-dependent density functionals: Theory and applications. In: *Rev. Mod. Phys.* 80 (2008), S. 3–60

[1097] BECKE, Axel D.: Density-functional thermochemistry. III. The role of exact exchange. In: *The Journal of Chemical Physics* 98 (1993), S. 5648–5652

[1098] BECKE, Axel D.: A new mixing of Hartree-Fock and local density-functional theories. In: *The Journal of Chemical Physics* 98 (1993), Nr. 2, S. 1372–1377

[1099] STEPHENS, P. J. ; DEVLIN, F. J. ; CHABALOWSKI, C. F. ; FRISCH, M. J.: Ab Initio Calculation of Vibrational Absorption and Circular Dichroism Spectra Using Density Functional Force Fields. In: *The Journal of Physical Chemistry* 98 (1994), S. 11623–11627

[1100] HEYD, Jochen ; SCUSERIA, Gustavo E. ; ERNZERHOF, Matthias: Hybrid functionals based on a screened Coulomb potential. In: *The Journal of Chemical Physics* 118 (2003), S. 8207–8215

[1101] HEYD, Jochen ; PERALTA, Juan E. ; SCUSERIA, Gustavo E. ; MARTIN, Richard L.: Energy band gaps and lattice parameters evaluated with the Heyd-Scuseria-Ernzerhof screened hybrid functional. In: *The Journal of Chemical Physics* 123 (2005), S. 174101

[1102] HEYD, Jochen ; SCUSERIA, Gustavo E. ; ERNZERHOF, Matthias: Erratum “Hybrid functionals based on a screened Coulomb potential” [J. Chem. Phys.118, 8207 (2003)]. In: *The Journal of Chemical Physics* 124 (2006), S. 219906

[1103] PAIER, Joachim ; MARSMAN, Martijn ; KRESSE, Georg: Why does the B3LYP hybrid functional fail for metals? In: *The Journal of Chemical Physics* 127 (2007), S. 024103

[1104] NELSON, W. ; BOKES, P. ; RINKE, Patrick ; GODBY, R. W.: Self-interaction in Green’s-function theory of the hydrogen atom. In: *Phys. Rev. A* 75 (2007), S. 032505

[1105] PERDEW, John P. ; SCHMIDT, Karla: Jacob’s ladder of density functional approximations for the exchange-correlation energy. In: *AIP Conference Proceedings* 577 (2001), S. 1–20

[1106] KURTH, Stefan ; PERDEW, John P.: Role of the exchange-correlation energy: Nature’s glue. In: *International Journal of Quantum Chemistry* 77 (2000), S. 814–818

[1107] JANESKO, Benjamin G.: Rung 3.5 density functionals: Another step on Jacob’s ladder. In: *International Journal of Quantum Chemistry* 113 (2013), S. 83–88

[1108] PERDEW, John P. ; STAROVEROV, Viktor N. ; TAO, Jianmin ; SCUSERIA, Gustavo E.: Density functional with full exact exchange, balanced nonlocality of correlation, and constraint satisfaction. In: *Phys. Rev. A* 78 (2008), S. 052513

[1109] PERDEW, John P. ; ERNZERHOF, Matthias ; BURKE, Kieron: Rationale for mixing exact exchange with density functional approximations. In: *The Journal of Chemical Physics* 105 (1996), S. 9982–9985

[1110] PERDEW, John P. ; RUZSINSZKY, Adrienn ; TAO, Jianmin ; STAROVEROV, Viktor N. ; SCUSERIA, Gustavo E. ; CSONKA, Gábor I.: Prescription for the design and selection of density functional approximations: More constraint satisfaction with fewer fits. In: *The Journal of Chemical Physics* 123 (2005), S. 062201

[1111] SAGVOLDEN, Espen ; PERDEW, John P.: Discontinuity of the exchange-correlation potential: Support for assumptions used

to find it. In: *Phys. Rev. A* 77 (2008), S. 012517

[1112] JIMÉNEZ-HOYOS, Carlos A. ; JANESKO, Benjamin G. ; SCUSERIA, Gustavo E. ; STAROVEROV, Viktor N. ; PERDEW, John P.: Assessment of a density functional with full exact exchange and balanced non-locality of correlation. In: *Molecular Physics* 107 (2009), S. 1077–1088

[1113] SUN, Jianwei ; PERDEW, John P. ; SEIDL, Michael: Correlation energy of the uniform electron gas from an interpolation between high- and low-density limits. In: *Phys. Rev. B* 81 (2010), S. 085123

[1114] CSONKA, Gábor I. ; PERDEW, John P. ; RUZSINSZKY, Adrienn: Global Hybrid Functionals: A Look at the Engine under the Hood. In: *Journal of Chemical Theory and Computation* 6 (2010), S. 3688–3703

[1115] RUZSINSZKY, Adrienn ; PERDEW, John P.: Twelve outstanding problems in ground-state density functional theory: A bouquet of puzzles. In: *Computational and Theoretical Chemistry* 963 (2011), S. 2 – 6

[1116] HAUNSCHILD, Robin ; ODASHIMA, Mariana M. ; SCUSERIA, Gustavo E. ; PERDEW, John P. ; CAPELLE, K.: Hyper-generalized-gradient functionals constructed from the Lieb-Oxford bound: Implementation via local hybrids and thermochemical assessment. In: *The Journal of Chemical Physics* 136 (2012), S. 184102

[1117] SUN, Jianwei ; RUZSINSZKY, Adrienn ; PERDEW, John P.: Strongly Constrained and Appropriately Normed Semilocal Density Functional. In: *Phys. Rev. Lett.* 115 (2015), S. 036402

[1118] SUN, Jianwei ; PERDEW, John P. ; RUZSINSZKY, Adrienn: Semilocal density functional obeying a strongly tightened bound for exchange. In: *Proceedings of the National Academy of Sciences* 112 (2015), S. 685–689

[1119] XIAO, Bing ; SUN, Jianwei ; RUZSINSZKY, Adrienn ; PERDEW, John P.: Testing the Jacob's ladder of density functionals for electronic structure and magnetism of rutile VO_2. In: *Phys. Rev. B* 90 (2014), S. 085134

[1120] PERDEW, John P. ; RUZSINSZKY, Adrienn ; SUN, Jianwei ; BURKE, Kieron: Gedanken densities and exact constraints in density functional theory. In: *The Journal of Chemical Physics* 140 (2014), S. 18A533

[1121] KARASIEV, Valentin V. ; SJOSTROM, Travis ; DUFTY, James ; TRICKEY, S. B.: Accurate Homogeneous Electron Gas Exchange-Correlation Free Energy for Local Spin-Density Calculations. In: *Phys. Rev. Lett.* 112 (2014), S. 076403

[1122] DIRAC, P. A. M.: Note on Exchange Phenomena in the Thomas Atom. In: *Mathematical Proceedings of the Cambridge Philosophical Society* 26 (1930), S. 376–385

[1123] GHOSH, Sankha ; GILL, Peter M. W.: Finite jellium models. I. Restricted Hartree-Fock calculations. In: *The Journal of Chemical Physics* 122 (2005), S. 154108

[1124] CEPERLEY, D. M. ; ALDER, B. J.: Ground State of the Electron Gas by a Stochastic Method. In: *Phys. Rev. Lett.* 45 (1980), S. 566–569

[1125] VOSKO, S. H. ; WILK, L. ; NUSAIR, M.: Accurate spin-dependent electron liquid correlation energies for local spin density calculations: a critical analysis. In: *Canadian Journal of Physics* 58 (1980), S. 1200–1211

[1126] OLIVER, G. L. ; PERDEW, J. P.: Spin-density gradient expansion for the kinetic energy. In: *Phys. Rev. A* 20 (1979), S. 397–403

[1127] BECKE, A.D. ; SAVIN, A. ; STOLL, H.: Extension of the local-spin-density exchange-correlation approximation to multiplet states. In: *Theoretica chimica acta* 91 (1995), S. 147–156. – ISSN 0040–5744

[1128] SZOTEK, Z. ; TEMMERMAN, W.M. ; SVANE, A. ; WINTER, H. ; BEIDEN, S.V. ; GEHRING, G.A. ; DUDAREV, S.L. ; SUTTON, A.P.: Applications of Self-Interaction Correction to Localized States in Solids. In: ALLAN, R.J. (Hrsg.) ; GUEST, M.F. (Hrsg.) ; SIMPSON, A.D. (Hrsg.) ; HENTY, D.S. (Hrsg.) ; NICOLE, D.A. (Hrsg.): *High-Performance Computing*. 1999. – ISBN 978–1–4613–7211–0, S. 207–212

[1129] PERSSON, Clas ; MIRBT, Susanne: Improved electronic structure and optical properties of sp-hybridized semiconductors using LDA+USIC. In: *Brazilian Journal of Physics* 36 (2006), S. 286 – 290

[1130] HARRIS, J.: Simplified method for calculating the energy of weakly interacting fragments. In: *Phys. Rev. B* 31 (1985), S. 1770–1779

[1131] VANIN, M. ; MORTENSEN, J. J. ; KELKKANEN, A. K. ; GARCIA-LASTRA, J. M. ; THYGESEN, K. S. ; JACOBSEN, K. W.: Graphene on metals: A van der Waals density functional study. In: *Phys. Rev. B* 81 (2010), S. 081408

[1132] HAAS, Philipp ; TRAN, Fabien ; BLAHA, Peter: Calculation of the lattice constant of solids with semilocal functionals. In: *Phys. Rev. B* 79 (2009), S. 085104

[1133] GRAZIANO, Gabriella ; KLIMEʻS, Jiří ; FERNANDEZ-ALONSO, Felix ; MICHAELIDES, Angelos: Improved description of soft layered materials with van der Waals density functional theory. In: *Journal of Physics: Condensed Matter* 24 (2012), S. 424216

[1134] SIM, Fiona ; AMANT, Alain S. ; PAPAI, Imre ; SALAHUB, Dennis R.: Gaussian density functional calculations on hydrogen-bonded systems. In: *Journal of the American Chemical Society* 114 (1992), S. 4391–4400

[1135] KASCHNER, R. ; SEIFERT, G.: Investigations of hydrogen-bonded systems: Local density approximation and gradient corrections. In: *International Journal of Quantum Chemistry* 52 (1994), S. 957–961

[1136] TKATCHENKO, Alexandre ; LILIENFELD, O. A.: Popular Kohn-Sham density functionals strongly overestimate many-body interactions in van der Waals systems. In: *Phys. Rev. B* 78 (2008), S. 045116

[1137] LIU, Chun-Sheng ; PILANIA, Ghanshyam ; WANG, Chenchen ; RAMPRASAD, Ramamurthy: How Critical Are the van der Waals Interactions in Polymer Crystals? In: *The Journal of Physical Chemistry A* 116 (2012), S. 9347–9352

[1138] HE, Lianhua ; LIU, Fang ; HAUTIER, Geoffroy ; OLIVEIRA, Micael J. T. ; MARQUES, Miguel A. L. ; VILA, Fernando D. ; REHR, J. J. ; RIGNANESE, G.-M. ; ZHOU, Aihui: Accuracy of generalized gradient approximation functionals for density-functional perturbation theory calculations. In: *Phys. Rev. B* 89 (2014), S. 064305

[1139] LANGRETH, David C. ; MEHL, M. J.: Beyond the local-density approximation in calculations of ground-state electronic properties. In: *Phys. Rev. B* 28 (1983), S. 1809–1834

[1140] PERDEW, John P. ; YUE, Wang: Accurate and simple density functional for the electronic exchange energy: Generalized gradient approximation. In: *Phys. Rev. B* 33 (1986), S. 8800–8802

[1141] LEE, Chengteh ; YANG, Weitao ; PARR, Robert G.: Development of the Colle-Salvetti correlation-energy formula into a functional of the electron density. In: *Phys. Rev. B* 37 (1988), S. 785–789

[1142] PERDEW, J. P.: Unified Theory of Exchange and Correlation Beyond the Local Density Approximation. In: ZIESCHE, P. (Hrsg.) ; ESCHRIG, H. (Hrsg.): *In Electronic Structure of Solids '91*. Akademie Verlag, Berlin, 1991, S. 11–20

[1143] PERDEW, John P.: Generalized gradient approximations for exchange and correlation: A look backward and forward. In: *Physica B: Condensed Matter* 172 (1991), S. 1 – 6

[1144] PERDEW, John P. ; CHEVARY, J. A. ; VOSKO, S. H. ; JACKSON, Koblar A. ; PEDERSON, Mark R. ; SINGH, D. J. ; FIOLHAIS, Carlos: Atoms, molecules, solids, and surfaces: Applications of the generalized gradient approximation for exchange and correlation. In: *Phys. Rev. B* 46 (1992), S. 6671–6687

[1145] LEVY, Mel ; PERDEW, John P.: Tight bound and convexity constraint on the exchange-correlation-energy functional in the low-density limit, and other formal tests of generalized-gradient approximations. In: *Phys. Rev. B* 48 (1993), S. 11638–11645

[1146] PERDEW, John P. ; BURKE, Kieron ; ERNZERHOF, Matthias: Generalized Gradient Approximation Made Simple. In: *Phys. Rev. Lett.* 77 (1996), S. 3865–3868

[1147] PERDEW, John P. ; BURKE, Kieron: Comparison shopping for a gradient-corrected density functional. In: *International Journal of Quantum Chemistry* 57 (1996), S. 309–319

[1148] PERDEW, John P. ; WANG, Yue: Accurate and simple analytic representation of the electron-gas correlation energy. In: *Phys. Rev. B* 45 (1992), S. 13244–13249

[1149] BURKE, Kieron ; PERDEW, JohnP. ; WANG, Yue: Derivation of a Generalized Gradient Approximation: The PW91 Density Functional. In: DOBSON, JohnF. (Hrsg.) ; VIGNALE, Giovanni (Hrsg.) ; DAS, Mukunda P. (Hrsg.): *Electronic Density Functional Theory*. Springer US, 1998. – ISBN 978–1–4899–0318–1, S. 81–111

[1150] BECKE, A. D.: Density functional calculations of molecular bond energies. In: *The Journal of Chemical Physics* 84 (1986), S. 4524–4529

[1151] BECKE, A. D.: Density-functional exchange-energy approximation with correct asymptotic behavior. In: *Phys. Rev. A* 38 (1988), S. 3098–3100

[1152] PETER ELLIOTT, Kieron B.: Non-empirical 'derivation' of B88 exchange functional. In: *arXiv:0902.1491* (2009), S. 1–8

[1153] HERTWIG, Roland H. ; KOCH, Wolfram: On the parameterization of the local correlation functional. What is Becke-3-LYP? In: *Chemical Physics Letters* 268 (1997), S. 345 – 351

[1154] MIEHLICH, Burkhard ; SAVIN, Andreas ; STOLL, Hermann ; PREUSS, Heinzwerner: Results obtained with the correlation energy density functionals of Becke and Lee, Yang and Parr. In: *Chemical Physics Letters* 157 (1989), S. 200 – 206

[1155] ZHANG, Yingkai ; YANG, Weitao: Comment on "Generalized Gradient Approximation Made Simple". In: *Phys. Rev. Lett.* 80 (1998), S. 890–890

[1156] HAMMER, B. ; HANSEN, L. B. ; NØRSKOV, J. K.: Improved adsorption energetics within density-functional theory using revised Perdew-Burke-Ernzerhof functionals. In: *Phys. Rev. B* 59 (1999), S. 7413–7421

[1157] ADAMO, Carlo ; BARONE, Vincenzo: Physically motivated density functionals with improved performances: The modified Perdew-Burke-Ernzerhof model. In: *The Journal of Chemical Physics* 116 (2002), S. 5933–5940

[1158] MADSEN, Georg K. H.: Functional form of the generalized gradient approximation for exchange: The PBEα functional. In: *Phys. Rev. B* 75 (2007), S. 195108

[1159] WU, Zhigang ; COHEN, R. E.: More accurate generalized gradient approximation for solids. In: *Phys. Rev. B* 73 (2006), S. 235116

[1160] FABIANO, Eduardo ; CONSTANTIN, Lucian A. ; DELLA SALA, Fabio: Generalized gradient approximation bridging the rapidly and slowly varying density regimes: A PBE-like functional for hybrid interfaces. In: *Phys. Rev. B* 82 (2010), S. 113104

[1161] KANAI, Yosuke ; WANG, Xiaofei ; SELLONI, Annabella ; CAR, Roberto: Testing the TPSS meta-generalized-gradient-approximation exchange-correlation functional in calculations of transition states and reaction barriers. In: *The Journal of Chemical Physics* 125 (2006), S. 234104

[1162] KOHN, Walter ; MATTSSON, Ann E.: Edge Electron Gas. In: *Phys. Rev. Lett.* 81 (1998), S. 3487–3490

[1163] MATTSSON, Ann E. ; KOHN, Walter: An energy functional for surfaces. In: *The Journal of Chemical Physics* 115 (2001), S. 3441–3443

[1164] ARMIENTO, R. ; MATTSSON, A. E.: Subsystem functionals in density-functional theory: Investigating the exchange energy per particle. In: *Phys. Rev. B* 66 (2002), S. 165117

[1165] ARMIENTO, R. ; MATTSSON, A. E.: Functional designed to include surface effects in self-consistent density functional theory. In: *Phys. Rev. B* 72 (2005), S. 085108

[1166] CONSTANTIN, Lucian A. ; RUZSINSZKY, Adrienn ; PERDEW, John P.: Exchange-correlation energy functional based on the Airy-gas reference system. In: *Phys. Rev. B* 80 (2009), S. 035125

[1167] MATTSSON, Ann E. ; ARMIENTO, Rickard ; PAIER, Joachim ; KRESSE, Georg ; WILLS, John M. ; MATTSSON, Thomas R.: The AM05 density functional applied to solids. In: *The Journal of Chemical Physics* 128 (2008), S. 084714

[1168] PERDEW, John P. ; RUZSINSZKY, Adrienn ; CSONKA, Gábor I. ; VYDROV, Oleg A. ; SCUSERIA, Gustavo E. ; CONSTANTIN, Lucian A. ; ZHOU, Xiaolan ; BURKE, Kieron: Restoring the Density-Gradient Expansion for Exchange in Solids and Surfaces. In: *Phys. Rev. Lett.* 100 (2008), S. 136406

[1169] MATTSSON, Ann E. ; ARMIENTO, Rickard ; MATTSSON, Thomas R.: Comment on "Restoring the Density-Gradient Expansion for Exchange in Solids and Surfaces". In: *Phys. Rev. Lett.* 101 (2008), S. 239701

[1170] ROPO, M. ; KOKKO, K. ; VITOS, L.: Assessing the Perdew-Burke-Ernzerhof exchange-correlation density functional revised for metallic bulk and surface systems. In: *Phys. Rev. B* 77 (2008), S. 195445

[1171] CSONKA, Gábor I. ; PERDEW, John P. ; RUZSINSZKY, Adrienn ; PHILIPSEN, Pier H. T. ; LEBÈGUE, Sébastien ; PAIER, Joachim ; VYDROV, Oleg A. ; ÁNGYÁN, János G.: Assessing the performance of recent density functionals for bulk solids. In: *Phys. Rev. B* 79 (2009), S. 155107

[1172] PIOTROWSKI, Maurício J. ; PIQUINI, Paulo ; ODASHIMA, Mariana M. ; DA SILVA, Juarez L. F.: Transition-metal 13-atom clusters assessed with solid and surface-biased functionals. In: *The Journal of Chemical Physics* 134 (2011), S. 134105

[1173] DELCZEG, L ; DELCZEG-CZIRJAK, E K. ; JOHANSSON, B ; VITOS, L: Density functional study of vacancies and surfaces in metals. In: *Journal of Physics: Condensed Matter* 23 (2011), S. 045006

[1174] TUNEGA, Daniel ; BUČKO, Tomáš ; ZAOUI, Ali: Assessment of ten DFT methods in predicting structures of sheet silicates: Importance of dispersion corrections. In: *The Journal of Chemical Physics* 137 (2012), S. 114105

[1175] FRIEDRICH, Michael ; RIEFER, Arthur ; SANNA, Simone ; SCHMIDT, W G. ; SCHINDLMAYR, Arno: Phonon dispersion and zero-point renormalization of $LiNbO_3$ from density-functional perturbation theory. In: *Journal of Physics: Condensed Matter* 27 (2015), S. 385402

[1176] BJÖRKMAN, T. ; GULANS, A. ; KRASHENINNIKOV, A. V. ; NIEMINEN, R. M.: van der Waals Bonding in Layered Compounds from Advanced Density-Functional First-Principles Calculations. In: *Phys. Rev. Lett.* 108 (2012), S. 235502

[1177] YANG, Weitao: Gradient correction in Thomas-Fermi theory. In: *Phys. Rev. A* 34 (1986), S. 4575–4585

[1178] YIN, Wan-Jian ; GONG, Xin-Gao: Hybridized kinetic energy functional for orbital-free density functional method. In: *Physics Letters A* 373 (2009), S. 480 – 483

[1179] PERDEW, John P. ; KURTH, Stefan ; ZUPAN, Aleš ; BLAHA, Peter: Accurate Density Functional with Correct Formal Properties: A Step Beyond the Generalized Gradient Approximation. In: *Phys. Rev. Lett.* 82 (1999), S. 2544–2547

[1180] PERDEW, John P.: Accurate Density Functional for the Energy: Real-Space Cutoff of the Gradient Expansion for the Exchange Hole. In: *Phys. Rev. Lett.* 55 (1985), S. 1665–1668

[1181] GHOSH, Swapan K. ; PARR, Robert G.: Phase-space approach to the exchange-energy functional of density-functional theory. In: *Phys. Rev. A* 34 (1986), S. 785–791

[1182] SVENDSEN, P. S. ; BARTH, U. von: Gradient expansion of the exchange energy from second-order density response theory. In: *Phys. Rev. B* 54 (1996), S. 17402–17413

[1183] PERDEW, John P. ; TAO, Jianmin ; STAROVEROV, Viktor N. ; SCUSERIA, Gustavo E.: Meta-generalized gradient approximation: Explanation of a realistic nonempirical density functional. In: *The Journal of Chemical Physics* 120 (2004), S. 6898–6911

[1184] SUN, Jianwei ; MARSMAN, Martijn ; CSONKA, Gábor I. ; RUZSINSZKY, Adrienn ; HAO, Pan ; KIM, Yoon-Suk ; KRESSE, Georg ; PERDEW, John P.: Self-consistent meta-generalized gradient approximation within the projector-augmented-wave method. In: *Phys. Rev. B* 84 (2011), S. 035117

[1185] FILATOV, Michael ; THIEL, Walter: Exchange-correlation density functional beyond the gradient approximation. In: *Phys. Rev. A* 57 (1998), S. 189–199

[1186] VAN VOORHIS, Troy ; SCUSERIA, Gustavo E.: A novel form for the exchange-correlation energy functional. In: *The Journal of Chemical Physics* 109 (1998), S. 400–410

[1187] KURTH, Stefan ; PERDEW, John P. ; BLAHA, Peter: Molecular and solid-state tests of density functional approximations: LSD, GGAs, and meta-GGAs. In: *International Journal of Quantum Chemistry* 75 (1999), S. 889–909

[1188] ZHAO, Yan ; TRUHLAR, Donald G.: A new local density functional for main-group thermochemistry, transition metal bonding, thermochemical kinetics, and noncovalent interactions. In: *The Journal of Chemical Physics* 125 (2006), S. 194101

[1189] FUCHS, F. ; FURTHMÜLLER, J. ; BECHSTEDT, F. ; SHISHKIN, M. ; KRESSE, G.: Quasiparticle band structure based on a generalized Kohn-Sham scheme. In: *Phys. Rev. B* 76 (2007), S. 115109

[1190] KRESSE, G. ; HAFNER, J.: *Ab initio* molecular dynamics for open-shell transition metals. In: *Phys. Rev. B* 48 (1993), S. 13115–13118

[1191] KRESSE, G. ; FURTHMÜLLER, J.: Efficiency of ab-initio total energy calculations for metals and semiconductors using a plane-wave basis set. In: *Computational Materials Science* 6 (1996), S. 15 – 50

[1192] BREDOW, Thomas ; GERSON, Andrea R.: Effect of exchange and correlation on bulk properties of MgO, NiO, and CoO. In: *Phys. Rev. B* 61 (2000), S. 5194–5201

[1193] FENG, Xiaobing: Electronic structure of MnO and CoO from the B3LYP hybrid density functional method. In: *Phys. Rev. B* 69 (2004), S. 155107

[1194] TODOROVA, Teodora ; SEITSONEN, Ari P. ; HUTTER, Jürg ; KUO, I-Feng W. ; MUNDY, Christopher J.: Molecular Dynamics Simulation of Liquid Water: Hybrid Density Functionals. In: *The Journal of Physical Chemistry B* 110 (2006), S. 3685–3691

[1195] LABAT, Fr(́e)d(́e)ric ; BARANEK, Philippe ; DOMAIN, Christophe ; MINOT, Christian ; ADAMO, Carlo: Density functional theory analysis of the structural and electronic properties of TiO_2 rutile and anatase polytypes: Performances of different exchange-correlation functionals. In: *The Journal of Chemical Physics* 126 (2007), S. 154703

[1196] ADAMO, Carlo ; BARONE, Vincenzo: Toward reliable density functional methods without adjustable parameters: The PBE0 model. In: *The Journal of Chemical Physics* 110 (1999), S. 6158–6170

[1197] ERNZERHOF, Matthias ; SCUSERIA, Gustavo E.: Assessment of the Perdew-Burke-Ernzerhof exchange-correlation functional. In: *The Journal of Chemical Physics* 110 (1999), S. 5029–5036

[1198] PAIER, J. ; MARSMAN, M. ; HUMMER, K. ; KRESSE, G. ; GERBER, I. C. ; ÁNGYÁN, J. G.: Screened hybrid density functionals applied to solids. In: *The Journal of Chemical Physics* 124 (2006), S. 154709

[1199] RHIM, S. H. ; KIM, Miyoung ; FREEMAN, A. J. ; ASAHI, Ryoji: Fully first-principles screened-exchange LDA calculations of excited states and optical properties of III-V semiconductors. In: *Phys. Rev. B* 71 (2005), S. 045202

[1200] BYLANDER, D. M. ; KLEINMAN, Leonard: Good semiconductor band gaps with a modified local-density approximation. In: *Phys. Rev. B* 41 (1990), S. 7868–7871

[1201] SCHIMKA, Laurids ; HARL, Judith ; KRESSE, Georg: Improved hybrid functional for solids: The HSEsol functional. In: *The Journal of Chemical Physics* 134 (2011), S. 024116

[1202] V., Krukau A. ; A., Vydrov O. ; F., Izmaylov A. ; E., Scuseria G.: Influence of the exchange screening parameter on the performance of screened hybrid functionals. In: *J. Chem. Phys.* 125 (2006), S. 224106

[1203] SKONE, Jonathan H. ; GOVONI, Marco ; GALLI, Giulia: Self-consistent hybrid functional for condensed systems. In: *Phys. Rev. B* 89 (2014), S. 195112

[1204] MOUSSA, Jonathan E. ; SCHULTZ, Peter A. ; CHELIKOWSKY, James R.: Analysis of the Heyd-Scuseria-Ernzerhof density functional parameter space. In: *The Journal of Chemical Physics* 136 (2012), S. 204117

[1205] VYDROV, Oleg A. ; SCUSERIA, Gustavo E.: Assessment of a long-range corrected hybrid functional. In: *The Journal of Chemical Physics* 125 (2006), S. 234109

[1206] HENDERSON, Thomas M. ; IZMAYLOV, Artur F. ; SCUSERIA, Gustavo E. ; SAVIN, Andreas: The importance of middle-range Hartree-Fock-type exchange for hybrid density functionals. In: *The Journal of Chemical Physics* 127 (2007), S. 221103

[1207] HENDERSON, Thomas M. ; IZMAYLOV, Artur F. ; SCUSERIA, Gustavo E. ; SAVIN, Andreas: Assessment of a Middle-Range Hybrid Functional. In: *Journal of Chemical Theory and Computation* 4 (2008), S. 1254–1262

[1208] LUCERO, M J. ; HENDERSON, T M. ; SCUSERIA, G E.: Improved semiconductor lattice parameters and band gaps from a middle-range screened hybrid exchange functional. In: *Journal of Physics: Condensed Matter* 24 (2012), S. 145504

[1209] JANESKO, Benjamin G. ; SCUSERIA, Gustavo E.: Local hybrid functionals based on density matrix products. In: *The Journal of Chemical Physics* 127 (2007), S. 164117

[1210] JANESKO, Benjamin G. ; SCUSERIA, Gustavo E.: Parameterized local hybrid functionals from density-matrix similarity metrics. In: *The Journal of Chemical Physics* 128 (2008), S. 084111

[1211] JOHNSON, Erin R.: Local-hybrid functional based on the correlation length. In: *The Journal of Chemical Physics* 141 (2014), S. 124120

[1212] ZHAO, Yan ; SCHULTZ, Nathan E. ; TRUHLAR, D. G.: Exchange-correlation functional with broad accuracy for metallic and nonmetallic compounds, kinetics, and noncovalent interactions. In: *The Journal of Chemical Physics* 123 (2005), S. 161103

[1213] ZHAO, Yan ; TRUHLAR, DonaldG.: The M06 suite of density functionals for main group thermochemistry, thermochemical kinetics, noncovalent interactions, excited states, and transition elements: two new functionals and systematic testing of four M06-class functionals and 12 other functionals. In: *Theoretical Chemistry Accounts* 120 (2008), S. 215–241

[1214] ZHAO, Yan ; TRUHLAR, Donald G.: Exploring the Limit of Accuracy of the Global Hybrid Meta Density Functional for Main-Group Thermochemistry, Kinetics, and Noncovalent Interactions. In: *Journal of Chemical Theory and Computation* 4 (2008), S. 1849–1868

[1215] PEVERATI, Roberto ; TRUHLAR, Donald G.: Improving the Accuracy of Hybrid Meta-GGA Density Functionals by Range Separation. In: *The Journal of Physical Chemistry Letters* 2 (2011), S. 2810–2817

[1216] STAROVEROV, Viktor N. ; SCUSERIA, Gustavo E. ; TAO, Jianmin ; PERDEW, John P.: Comparative assessment of a new nonempirical density functional: Molecules and hydrogen-bonded complexes. In: *The Journal of Chemical Physics* 119 (2003), S. 12129–12137

[1217] ERNZERHOF, Matthias: Construction of the adiabatic connection. In: *Chemical Physics Letters* 263 (1996), S. 499 – 506

[1218] MARSMAN, M ; PAIER, J ; STROPPA, A ; KRESSE, G: Hybrid functionals applied to extended systems. In: *Journal of Physics: Condensed Matter* 20 (2008), S. 064201

[1219] HENDERSON, Thomas M. ; PAIER, Joachim ; SCUSERIA, Gustavo E.: Accurate treatment of solids with the HSE screened hybrid. In: *physica status solidi (b)* 248 (2011), S. 767–774

[1220] NICKLAS, Jeremy W. ; WILKINS, John W.: Accurate ab initio predictions of III-V direct-indirect band gap crossovers. In: *Applied Physics Letters* 97 (2010), S. 091902

[1221] KOMSA, Hannu-Pekka ; BROQVIST, Peter ; PASQUARELLO, Alfredo: Alignment of defect levels and band edges through hybrid functionals: Effect of screening in the exchange term. In: *Phys. Rev. B* 81 (2010), S. 205118

[1222] CHEN, Wei ; TEGENKAMP, Christoph ; PFNÜR, Herbert ; BREDOW, Thomas: Color centers in NaCl by hybrid functionals. In: *Phys. Rev. B* 82 (2010), S. 104106

[1223] ŚPIEWAK, P. ; VANHELLEMONT, J. ; KURZYDLOWSKI, K. J.: Improved calculation of vacancy properties in Ge using the Heyd-Scuseria-Ernzerhof range-separated hybrid functional. In: *Journal of Applied Physics* 110 (2011), S. 063534

[1224] GÖRLING, Andreas ; LEVY, Mel: Correlation-energy functional and its high-density limit obtained from a coupling-constant perturbation expansion. In: *Phys. Rev. B* 47 (1993), S. 13105–13113

[1225] LANGRETH, D.C. ; PERDEW, J.P.: The exchange-correlation energy of a metallic surface. In: *Solid State Communications* 17 (1975), S. 1425 – 1429

[1226] GRIMME, Stefan: Semiempirical hybrid density functional with perturbative second-order correlation. In: *The Journal of Chemical Physics* 124 (2006), S. 034108

[1227] ZHANG, Ying ; XU, Xin ; GODDARD, William A.: Doubly hybrid density functional for accurate descriptions of nonbond interactions, thermochemistry, and thermochemical kinetics. In: *Proceedings of the National Academy of Sciences* 106 (2009), S. 4963–4968

[1228] MØLLER, Chr. ; PLESSET, M. S.: Note on an Approximation Treatment for Many-Electron Systems. In: *Phys. Rev.* 46 (1934), S. 618–622

[1229] ZHAO, Yan ; LYNCH, Benjamin J. ; ; TRUHLAR, Donald G.: Doubly Hybrid Meta DFT: New Multi-Coefficient Correlation and Density Functional Methods for Thermochemistry and Thermochemical Kinetics. In: *The Journal of Physical Chemistry A* 108 (2004), S. 4786–4791

[1230] ZHAO, Yan ; LYNCH, Benjamin J. ; TRUHLAR, Donald G.: Multi-coefficient extrapolated density functional theory for thermochemistry and thermochemical kinetics. In: *Phys. Chem. Chem. Phys.* 7 (2005), S. 43–52

[1231] SCHWABE, Tobias ; GRIMME, Stefan: Double-hybrid density functionals with long-range dispersion corrections: higher accuracy and extended applicability. In: *Phys. Chem. Chem. Phys.* 9 (2007), S. 3397–3406

[1232] KARTON, Amir ; TARNOPOLSKY, Alex ; LAMERE, Jean-Francois ; SCHATZ, George C. ; MARTIN, Jan M. L.: Highly Accurate First-Principles Benchmark Data Sets for the Parametrization and Validation of Density Functional and Other Ap-

proximate Methods. Derivation of a Robust, Generally Applicable, Double-Hybrid Functional for Thermochemistry and Thermochemical Kinetics. In: *The Journal of Physical Chemistry A* 112 (2008), S. 12868–12886

[1233] SCHWABE, Tobias ; GRIMME, Stefan: Towards chemical accuracy for the thermodynamics of large molecules: new hybrid density functionals including non-local correlation effects. In: *Phys. Chem. Chem. Phys.* 8 (2006), S. 4398–4401

[1234] BRÉMOND, Eric ; ADAMO, Carlo: Seeking for parameter-free double-hybrid functionals: The PBE0-DH model. In: *The Journal of Chemical Physics* 135 (2011), S. 024106

[1235] CHAI, Jeng-Da ; MAO, Shan-Ping: Seeking for reliable double-hybrid density functionals without fitting parameters: The PBE0-2 functional. In: *Chemical Physics Letters* 538 (2012), S. 121 – 125

[1236] SU, Neil Q. ; ADAMO, Carlo ; XU, Xin: A comparison of geometric parameters from PBE-based doubly hybrid density functionals PBE0-DH, PBE0-2, and xDH-PBE0. In: *The Journal of Chemical Physics* 139 (2013), S. 174106

[1237] SHARKAS, Kamal ; TOULOUSE, Julien ; SAVIN, Andreas: Double-hybrid density-functional theory made rigorous. In: *The Journal of Chemical Physics* 134 (2011), S. 064113

[1238] GOERIGK, Lars ; GRIMME, Stefan: Efficient and Accurate Double-Hybrid-Meta-GGA Density Functionals-Evaluation with the Extended GMTKN30 Database for General Main Group Thermochemistry, Kinetics, and Noncovalent Interactions. In: *Journal of Chemical Theory and Computation* 7 (2011), S. 291–309

[1239] ESHUIS, Henk ; FURCHE, Filipp: A Parameter-Free Density Functional That Works for Noncovalent Interactions. In: *The Journal of Physical Chemistry Letters* 2 (2011), S. 983–989

[1240] SANCHO-GARCÍA, J.C.: Extending the applicability of the PBE0-DH double-hybrid model to weak interactions. In: *Chemical Physics Letters* 535 (2012), S. 136 – 139

[1241] STEINMETZ, Marc ; GRIMME, Stefan: Benchmark Study of the Performance of Density Functional Theory for Bond Activations with (Ni,Pd)-Based Transition-Metal Catalysts. In: *ChemistryOpen* 2 (2013), S. 115–124

[1242] GRIMME, Stefan ; ANTONY, Jens ; EHRLICH, Stephan ; KRIEG, Helge: A consistent and accurate ab initio parametrization of density functional dispersion correction (DFT-D) for the 94 elements H-Pu. In: *The Journal of Chemical Physics* 132 (2010), S. 154104

[1243] GRIMME, Stefan ; EHRLICH, Stephan ; GOERIGK, Lars: Effect of the damping function in dispersion corrected density functional theory. In: *Journal of Computational Chemistry* 32 (2011), S. 1456–1465

[1244] PISANI, Cesare ; MASCHIO, Lorenzo ; CASASSA, Silvia ; HALO, Migen ; SCHÜTZ, Martin ; USVYAT, Denis: Periodic local MP2 method for the study of electronic correlation in crystals: Theory and preliminary applications. In: *Journal of Computational Chemistry* 29 (2008), S. 2113–2124

[1245] MARSMAN, M. ; GRÜNEIS, A. ; PAIER, J. ; KRESSE, G.: Second-order Møller-Plesset perturbation theory applied to extended systems. I. Within the projector-augmented-wave formalism using a plane wave basis set. In: *The Journal of Chemical Physics* 130 (2009), S. 184103

[1246] USVYAT, Denis ; MASCHIO, Lorenzo ; PISANI, Cesare ; SCHÜTZ, Martin: Second Order Local Møller-Plesset Perturbation Theory for Periodic Systems: the CRYSCOR Code. In: *Zeitschrift für Physikalische Chemie International journal of research in physical chemistry and chemical physics* 224 (2010), S. 441–454

[1247] GRÜNEIS, Andreas ; MARSMAN, Martijn ; KRESSE, Georg: Second-order Møller-Plesset perturbation theory applied to extended systems. II. Structural and energetic properties. In: *The Journal of Chemical Physics* 133 (2010), S. 074107

[1248] GRÜNEIS, Andreas ; BOOTH, George H. ; MARSMAN, Martijn ; SPENCER, James ; ALAVI, Ali ; KRESSE, Georg: Natural Orbitals for Wave Function Based Correlated Calculations Using a Plane Wave Basis Set. In: *Journal of Chemical Theory and Computation* 7 (2011), S. 2780–2785

[1249] PISANI, Cesare ; SCHUTZ, Martin ; CASASSA, Silvia ; USVYAT, Denis ; MASCHIO, Lorenzo ; LORENZ, Marco ; ERBA, Alessandro: Cryscor: a program for the post-Hartree-Fock treatment of periodic systems. In: *Phys. Chem. Chem. Phys.* 14 (2012), S. 7615–7628

[1250] BEN, Mauro D. ; HUTTER, Jörg ; VANDEVONDELE, Joost: Second-Order Möller-Plesset Perturbation Theory in the Condensed Phase: An Efficient and Massively Parallel Gaussian and Plane Waves Approach. In: *Journal of Chemical Theory and Computation* 8 (2012), S. 4177–4188

[1251] USVYAT, Denis: Linear-scaling explicitly correlated treatment of solids: Periodic local MP2-F12 method. In: *The Journal of Chemical Physics* 139 (2013), S. 194101

[1252] GRÜNEIS, Andreas ; SHEPHERD, James J. ; ALAVI, Ali ; TEW, David P. ; BOOTH, George H.: Explicitly correlated plane waves: Accelerating convergence in periodic wavefunction expansions. In: *The Journal of Chemical Physics* 139 (2013), S. 084112

[1253] SANSONE, Giuseppe ; CIVALLERI, Bartolomeo ; USVYAT, Denis ; TOULOUSE, Julien ; SHARKAS, Kamal ; MASCHIO,

Lorenzo: Range-separated double-hybrid density-functional theory applied to periodic systems. In: *The Journal of Chemical Physics* 143 (2015), S. 102811

[1254] GELL-MANN, Murray ; BRUECKNER, Keith A.: Correlation Energy of an Electron Gas at High Density. In: *Phys. Rev.* 106 (1957), S. 364–368

[1255] SHEPHERD, James J. ; GRÜNEIS, Andreas: Correlation Energy Divergences in Metallic Systems. In: *arXiv:1208.6103* (2012), S. 1–6

[1256] SHEPHERD, James J. ; GRÜNEIS, Andreas: Many-Body Quantum Chemistry for the Electron Gas: Convergent Perturbative Theories. In: *Phys. Rev. Lett.* 110 (2013), S. 226401

[1257] LANGRETH, David C. ; PERDEW, John P.: Theory of nonuniform electronic systems. I. Analysis of the gradient approximation and a generalization that works. In: *Phys. Rev. B* 21 (1980), S. 5469–5493

[1258] ESHUIS, Henk ; BATES, JeffersonE. ; FURCHE, Filipp: Electron correlation methods based on the random phase approximation. In: *Theoretical Chemistry Accounts* 131 (2012), S. 1084

[1259] PAIER, Joachim ; JANESKO, Benjamin G. ; HENDERSON, Thomas M. ; SCUSERIA, Gustavo E. ; GRÜNEIS, Andreas ; KRESSE, Georg: Hybrid functionals including random phase approximation correlation and second-order screened exchange. In: *The Journal of Chemical Physics* 132 (2010), S. 094103

[1260] HENDERSON, Thomas M. ; SCUSERIA, Gustavo E.: The connection between self-interaction and static correlation: a random phase approximation perspective. In: *Molecular Physics* 108 (2010), S. 2511–2517

[1261] PAIER, Joachim ; REN, Xinguo ; RINKE, Patrick ; SCUSERIA, Gustavo E. ; GRÃ$\frac{1}{4}$NEIS, Andreas ; KRESSE, Georg ; SCHEFFLER, Matthias: Assessment of correlation energies based on the random-phase approximation. In: *New Journal of Physics* 14 (2012), S. 043002

[1262] REN, Xinguo ; RINKE, Patrick ; SCUSERIA, Gustavo E. ; SCHEFFLER, Matthias: Renormalized second-order perturbation theory for the electron correlation energy: Concept, implementation, and benchmarks. In: *Phys. Rev. B* 88 (2013), S. 035120

[1263] HESSELMANN, Andreas: Third-order corrections to random-phase approximation correlation energies. In: *The Journal of Chemical Physics* 134 (2011), S. 204107

[1264] FURCHE, Filipp: Developing the random phase approximation into a practical post-Kohn-Sham correlation model. In: *The Journal of Chemical Physics* 129 (2008), S. 114105

[1265] DOBSON, John F. ; WANG, Jun: Successful Test of a Seamless van der Waals Density Functional. In: *Phys. Rev. Lett.* 82 (1999), S. 2123–2126

[1266] CALLEN, Herbert B. ; WELTON, Theodore A.: Irreversibility and Generalized Noise. In: *Phys. Rev.* 83 (1951), S. 34–40

[1267] LANGRETH, David C. ; PERDEW, John P.: Exchange-correlation energy of a metallic surface: Wave-vector analysis. In: *Phys. Rev. B* 15 (1977), S. 2884–2901

[1268] HARL, Judith ; KRESSE, Georg: Cohesive energy curves for noble gas solids calculated by adiabatic connection fluctuation-dissipation theory. In: *Phys. Rev. B* 77 (2008), S. 045136

[1269] HARL, Judith ; KRESSE, Georg: Accurate Bulk Properties from Approximate Many-Body Techniques. In: *Phys. Rev. Lett.* 103 (2009), S. 056401

[1270] HARL, Judith ; SCHIMKA, Laurids ; KRESSE, Georg: Assessing the quality of the random phase approximation for lattice constants and atomization energies of solids. In: *Phys. Rev. B* 81 (2010), S. 115126

[1271] ADLER, Stephen L.: Quantum Theory of the Dielectric Constant in Real Solids. In: *Phys. Rev.* 126 (1962), S. 413–420

[1272] WISER, Nathan: Dielectric Constant with Local Field Effects Included. In: *Phys. Rev.* 129 (1963), S. 62–69

[1273] REN, Xinguo ; RINKE, Patrick ; SCHEFFLER, Matthias: Exploring the random phase approximation: Application to CO adsorbed on Cu(111). In: *Phys. Rev. B* 80 (2009), S. 045402

[1274] JANESKO, Benjamin G. ; HENDERSON, Thomas M. ; SCUSERIA, Gustavo E.: Long-range-corrected hybrids including random phase approximation correlation. In: *The Journal of Chemical Physics* 130 (2009), S. 081105

[1275] MIYAKE, T. ; ARYASETIAWAN, F. ; KOTANI, T. ; SCHILFGAARDE, M. van ; USUDA, M. ; TERAKURA, K.: Total energy of solids: An exchange and random-phase approximation correlation study. In: *Phys. Rev. B* 66 (2002), S. 245103

[1276] MARINI, Andrea ; GARCÍA-GONZÁLEZ, P. ; RUBIO, Angel: First-Principles Description of Correlation Effects in Layered Materials. In: *Phys. Rev. Lett.* 96 (2006), S. 136404

[1277] SCUSERIA, Gustavo E. ; HENDERSON, Thomas M. ; SORENSEN, Danny C.: The ground state correlation energy of the random phase approximation from a ring coupled cluster doubles approach. In: *The Journal of Chemical Physics* 129 (2008), S. 231101

[1278] BLEIZIFFER, Patrick ; HESSELMANN, Andreas ; GÖRLING, Andreas: Resolution of identity approach for the Kohn-Sham correlation energy within the exact-exchange random-phase approximation. In: *The Journal of Chemical Physics* 136 (2012),

S. 134102

[1279] FEIBELMAN, Peter J. ; HAMMER, B. ; NØRSKOV, J. K. ; WAGNER, F. ; SCHEFFLER, M. ; STUMPF, R. ; WATWE, R. ; DUMESIC, J.: The CO/Pt(111) Puzzle. In: *The Journal of Physical Chemistry B* 105 (2001), S. 4018–4025

[1280] SCHIMKA, L. ; HARL, J. ; STROPPA, A. ; GRÜNEIS, A. ; MARSMAN1, M. ; MITTENDORFER, F. ; KRESSE, G.: Accurate surface and adsorption energies from many-body perturbation theory. In: *Nature Materials* 9 (2010), S. 741–744

[1281] CASADEI, Marco ; REN, Xinguo ; RINKE, Patrick ; RUBIO, Angel ; SCHEFFLER, Matthias: Density-Functional Theory for f-Electron Systems: The α-γ Phase Transition in Cerium. In: *Phys. Rev. Lett.* 109 (2012), S. 146402

[1282] BJÖRKMAN, T ; GULANS, A ; KRASHENINNIKOV, A V. ; NIEMINEN, R M.: Are we van der Waals ready? In: *Journal of Physics: Condensed Matter* 24 (2012), S. 424218

[1283] OLSEN, Thomas ; THYGESEN, Kristian S.: Random phase approximation applied to solids, molecules, and graphene-metal interfaces: From van der Waals to covalent bonding. In: *Phys. Rev. B* 87 (2013), S. 075111

[1284] HESSELMANN, A. ; GÖRLING, A.: Random-phase approximation correlation methods for molecules and solids. In: *Molecular Physics* 109 (2011), S. 2473–2500

[1285] JANSEN, Georg ; LIU, Ru-Fen ; ÁNGYÁN, János G.: On the equivalence of ring-coupled cluster and adiabatic connection fluctuation-dissipation theorem random phase approximation correlation energy expressions. In: *The Journal of Chemical Physics* 133 (2010), S. 154106

[1286] VERMA, Prakash ; BARTLETT, Rodney J.: Increasing the applicability of density functional theory. II. Correlation potentials from the random phase approximation and beyond. In: *The Journal of Chemical Physics* (2012), S. 044105

[1287] PALDUS, J. ; ČÍŽEK, J. ; SHAVITT, I.: Correlation Problems in Atomic and Molecular Systems. IV. Extended Coupled-Pair Many-Electron Theory and Its Application to the BH_3 Molecule. In: *Phys. Rev. A* 5 (1972), S. 50–67

[1288] BOOTH, George H. ; GRÜNEIS, Andreas ; KRESSE, Georg ; ALAVI, Ali: Towards an exact description of electronic wavefunctions in real solids. In: *Nature* 493 (2013), S. 365–370

[1289] BISHOP, R. F. ; LÜHRMANN, K. H.: Electron correlations: I. Ground-state results in the high-density regime. In: *Phys. Rev. B* 17 (1978), S. 3757–3780

[1290] BARTLETT, Rodney J. ; MUSIAŁ, Monika: Coupled-cluster theory in quantum chemistry. In: *Rev. Mod. Phys.* 79 (2007), S. 291–352

[1291] STROUT, Douglas L. ; SCUSERIA, Gustavo E.: A quantitative study of the scaling properties of the Hartree-Fock method. In: *J. Chem. Phys.* 102 (1995), S. 8448–8452

[1292] MOHR, Stephan ; RATCLIFF, Laura E. ; GENOVESE, Luigi ; CALISTE, Damien ; BOULANGER, Paul ; GOEDECKER, Stefan ; DEUTSCH, Thierry: Accurate and efficient linear scaling DFT calculations with universal applicability. In: *Phys. Chem. Chem. Phys.* 17 (2015), S. 31360–31370

[1293] POREZAG, D. ; FRAUENHEIM, Th. ; KÖHLER, Th. ; SEIFERT, G. ; KASCHNER, R.: Construction of tight-binding-like potentials on the basis of density-functional theory: Application to carbon. In: *Phys. Rev. B* 51 (1995), S. 12947–12957

[1294] ELSTNER, M. ; FRAUENHEIM, Th. ; KAXIRAS, E. ; SEIFERT, G. ; SUHAI, S.: A Self-Consistent Charge Density-Functional Based Tight-Binding Scheme for Large Biomolecules. In: *physica status solidi (b)* 217 (2000), S. 357–376

[1295] KOSKINEN, Pekka ; MÄKINEN, Ville: Density-functional tight-binding for beginners. In: *Computational Materials Science* 47 (2009), S. 237 – 253

[1296] POPLE, John A.: *Approximate Molecular Orbital Theory*. McGraw Hill Higher Education, 1970. – ISBN 978–0070505124

[1297] WANG, Junmei ; CIEPLAK, Piotr ; KOLLMAN, Peter A.: How well does a restrained electrostatic potential (RESP) model perform in calculating conformational energies of organic and biological molecules? In: *Journal of Computational Chemistry* 21 (2000), S. 1049–1074

[1298] JONES, J. E.: On the Determination of Molecular Fields. II. From the Equation of State of a Gas. In: *Proceedings of the Royal Society of London A: Mathematical, Physical and Engineering Sciences* 106 (1924), S. 463–477

[1299] HARTKAMP, R.M. ; LUDING, S.: A continuum approach applied to a strongly confined Lennard-Jones fluid. In: GUMBSCH, Peter (Hrsg.) ; GIESSEN, Erik van d. (Hrsg.): *Proceedings of the Fifth International Conference Multiscale Materials Modeling*. Freiburg im Breisgau, Germany : Fraunhofer Verlag, 2010

[1300] CAZADE, Pierre-Andre ; HARTKAMP, Remco ; COASNE, Benoit: Structure and Dynamics of an Electrolyte Confined in Charged Nanopores. In: *The Journal of Physical Chemistry C* 118 (2014), S. 5061–5072

[1301] HARTKAMP, Remco ; SIBOULET, Bertrand ; DUFRECHE, Jean-Francois ; COASNE, Benoit: Ion-specific adsorption and electroosmosis in charged amorphous porous silica. In: *Phys. Chem. Chem. Phys.* 17 (2015), S. 24683–24695

[1302] FOO, Grace M. ; PANDEY, R. B.: Discrete-to-continuum simulation approach to polymer chain systems: Subdiffusion, segregation, and chain folding. In: *Phys. Rev. E* 57 (1998), S. 5802–5810

[1303] SHENOGIN, Sergei ; OZISIK, Rahmi: Simulation of plastic deformation in glassy polymers: Atomistic and mesoscale approaches. In: *Journal of Polymer Science Part B: Polymer Physics* 43 (2005), S. 994–1004

[1304] MAUREL, G. ; GOUJON, F. ; SCHNELL, B. ; MALFREYT, P.: Multiscale Modeling of the Polymer-Silica Surface Interaction: From Atomistic to Mesoscopic Simulations. In: *The Journal of Physical Chemistry C* 119 (2015), S. 4817–4826

[1305] MACKERELL, Alexander D.: Empirical force fields for biological macromolecules: Overview and issues. In: *Journal of Computational Chemistry* 25 (2004), S. 1584–1604

[1306] VANOMMESLAEGHE, K. ; HATCHER, E. ; ACHARYA, C. ; KUNDU, S. ; ZHONG, S. ; SHIM, J. ; DARIAN, E. ; GUVENCH, O. ; LOPES, P. ; VOROBYOV, I. ; MACKERELL, A. D.: CHARMM general force field: A force field for drug-like molecules compatible with the CHARMM all-atom additive biological force fields. In: *Journal of Computational Chemistry* 31 (2010), S. 671–690

[1307] BEN, Mauro D. ; HUTTER, Jörg ; VANDEVONDELE, Joost: Electron Correlation in the Condensed Phase from a Resolution of Identity Approach Based on the Gaussian and Plane Waves Scheme. In: *Journal of Chemical Theory and Computation* 9 (2013), S. 2654–2671

[1308] MOUSSA, Jonathan E.: Cubic-scaling algorithm and self-consistent field for the random-phase approximation with second-order screened exchange. In: *The Journal of Chemical Physics* 140 (2014), S. 014107

[1309] SCUSERIA, Gustavo E.: Linear Scaling Density Functional Calculations with Gaussian Orbitals. In: *The Journal of Physical Chemistry A* 103 (1999), S. 4782–4790

[1310] SKYLARIS, Chris-Kriton ; HAYNES, Peter D.: Achieving plane wave accuracy in linear-scaling density functional theory applied to periodic systems: A case study on crystalline silicon. In: *The Journal of Chemical Physics* 127 (2007), S. 164712

[1311] KHALIULLIN, Rustam Z. ; VANDEVONDELE, Joost ; HUTTER, Jörg: Efficient Linear-Scaling Density Functional Theory for Molecular Systems. In: *Journal of Chemical Theory and Computation* 9 (2013), S. 4421–4427

[1312] ZENG, Q.H. ; YU, A.B. ; LU, G.Q.: Multiscale modeling and simulation of polymer nanocomposites. In: *Progress in Polymer Science* 33 (2008), S. 191 – 269

[1313] LYUBARTSEV, Alexander ; TU, Yaoquan ; LAAKSONEN, Aatto: Hierarchical Multiscale Modelling Scheme from First Principles to Mesoscale. In: *Journal of Computational and Theoretical Nanoscience* 6 (2009), S. 951–959

[1314] MORALES MEDINA, Giovanni ; MARTÍNEZ REY, Ramiro: MOLECULAR AND MULTISCALE MODELING: REVIEW ON THE THEORIES AND APPLICATIONS IN CHEMICAL ENGINEERING. In: *CT&F - Ciencia, Tecnología y Futuro* (2009), S. 205 – 224. – ISSN 0122–5383

[1315] OLIVER, J. ; HUESPE, A. E. ; SAMANIEGO, E. ; CHAVES, E. W. V.: Continuum approach to the numerical simulation of material failure in concrete. In: *Int. J. Numer. Anal. Meth. Geomech.* 28 (2004), S. 609–632

[1316] OLIVER, J. ; HUESPE, A.E. ; BLANCO, S. ; LINERO, D.L.: Evolving Material Discontinuities: Numerical Modeling by the Continuum Strong Discontinuity Approach (CSDA). In: COMBESCURE, Alain (Hrsg.) ; DE BORST, René (Hrsg.) ; BELYTSCHKO, Ted (Hrsg.): *IUTAM Symposium on Discretization Methods for Evolving Discontinuities* Bd. 5. 2007. – ISBN 978–1–4020–6529–3, S. 123–138

[1317] SUN, Quanhua ; BOYD, Iain D. ; CANDLER, Graham V.: A hybrid continuum/particle approach for modeling subsonic, rarefied gas flows. In: *Journal of Computational Physics* 194 (2004), S. 256 – 277

[1318] GREST, GaryS. ; LACASSE, Martin-D. ; MURAT, Michael: Polymer Surfaces and Interfaces: A Continuum Simulation Approach. In: LANDAU, DavidP. (Hrsg.) ; MON, K.K. (Hrsg.) ; SCHÜTTLER, Heinz-Bernd (Hrsg.): *Computer Simulation Studies in Condensed-Matter Physics X* Bd. 83. 1998. – ISBN 978–3–642–46853–7, S. 23–36

[1319] LECUN, Yann ; BENGIO, Yoshua ; HINTON, Geoffrey: Deep learning. In: *Nature* 521 (2015), S. 436–444

[1320] KOWALSKI, B. R. ; BENDER, C. F.: Journal of the American Chemical Society. In: *Pattern Recognition. A Powerful Approach to Interpreting Chemical Data* 94 (1972), S. 5632–5639

[1321] NANDHAKUMAR, N. ; AGGARWAL, J. K.: The artificial intelligence approach to pattern recognition – A perspective and an overview. In: *Pattern Recognition* 18 (1985), S. 383–389

[1322] PERVEEN, Nazia ; AHMAD, Nazir ; KHAN, M. Abdul Qadoos B. ; KHALID, Rizwan ; QADRI, Salman: Facial Expression Recognition Through Machine Learning. In: *International Journal of Scientific & Technology Research* 5 (2016), S. 91–97

[1323] LOPES, André T. ; AGUIAR, Edilson de ; SOUZA, Alberto F. D. ; OLIVEIRA-SANTOS, Thiago: Facial expression recognition with Convolutional Neural Networks: Coping with few data and the training sample order. In: *Pattern Recognition* 61 (2017), S. 610–628

[1324] HINTON, Geoffrey ; DENG, Li ; YU, Dong ; DAHL, George ; MOHAMED, Abdel rahman ; JAITLY, Navdeep ; SENIOR, Andrew ; VANHOUCKE, Vincent ; NGUYEN, Patrick ; SAINATH, Tara ; KINGSBURY brian: Deep Neural Networks for Acoustic Modeling in Speech Recognition. In: *IEEE SIGNAL PROCESSING MAGAZINE* 2 (2012), S. 1053

[1325] LUXHØJ, James T. ; RIIS, Jens O. ; STENSBALLE, Brian: A hybrid econometric–neural network modeling approach for sales forecasting. In: *International Journal of Production Economics* 2 (1996), S. 175–192

[1326] KAASTRA, Iebeling ; BOYD, Milton: Designing a neural network for forecasting financial and economic time series. In: *Neurocomputing* 10 (1996), S. 215–236

[1327] KUO, R. J.: A sales forecasting system based on fuzzy neural network with initial weights generated by genetic algorithm. In: *European Journal of Operational Research* 129 (2001), S. 496–517

[1328] MEREDIG, B. ; AGRAWAL, A. ; KIRKLIN, S. ; SAAL, J. E. ; DOAK, J. W. ; THOMPSON, A. ; ZHANG, K. ; CHOUDHARY, A. ; WOLVERTON, C.: Combinatorial screening for new materials in unconstrained composition space with machine learning. In: *Phys. Rev. B* 89 (2014), S. 094104

[1329] MOUNET, N. ; GIBERTINI, M. ; SCHWALLER, P. ; CAMPI, D. ; MERKYS, A. ; MARRAZZO, A. ; SOHIER, T. ; ELIGIO CASTELLI, I. ; CEPELLOTTI, A. ; PIZZI, G. ; MARZARI, N.: Two-dimensional materials from high-throughput computational exfoliation of experimentally known compounds. In: *Nature Nanotechnology* 13 (2018), S. 246–252

[1330] SNYDER, John C. ; RUPP, Matthias ; HANSEN, Katja ; MÜLLER, Klaus-Robert ; BURKE, Kieron: Finding Density Functionals with Machine Learning. In: *Phys. Rev. Lett.* 108 (2012), S. 253002

[1331] LI, Li ; SNYDER, John C. ; PELASCHIER, Isabelle M. ; HUANG, Jessica ; NIRANJAN, Uma-Naresh ; DUNCAN, Paul ; RUPP, Matthias ; MÜLLER, Klaus-Robert ; BURKE, Kieron: Understanding machine-learned density functionals. In: *International Journal of Quantum Chemistry* 116 (2016), S. 819–833

[1332] GHASEMI, S. A. ; HOFSTETTER, Albert ; SAHA, Santanu ; GOEDECKER, Stefan: Interatomic potentials for ionic systems with density functional accuracy based on charge densities obtained by a neural network. In: *Phys. Rev. B* 92 (2015), S. 045131

[1333] BROCKHERDE, Felix ; VOGT, Leslie ; LI, Li ; TUCKERMAN, Mark E. ; BURKE, Kieron ; MÜLLER, Klaus-Robert: Bypassing the Kohn-Sham equations with machine learning. In: *Nature Communications* 8 (2017), S. 872

[1334] BEHLER, Jörg ; PARRINELLO, Michele: Generalized Neural-Network Representation of High-Dimensional Potential-Energy Surfaces. In: *Phys. Rev. Lett.* 98 (2007), S. 146401

[1335] SCHÜTT, K. T. ; GLAWE, H. ; BROCKHERDE, F. ; SANNA, A. ; MÜLLER, K. R. ; GROSS, E. K. U.: How to represent crystal structures for machine learning: Towards fast prediction of electronic properties. In: *Phys. Rev. B* 89 (2014), S. 205118

[1336] RUPP, Matthias ; TKATCHENKO, Alexandre ; MÜLLER, Klaus-Robert ; LILIENFELD, O. A.: Fast and Accurate Modeling of Molecular Atomization Energies with Machine Learning. In: *Phys. Rev. Lett.* 108 (2012), S. 058301

[1337] HEGDE, Ganesh ; BOWEN, R. C.: Machine-learned approximations to Density Functional Theory Hamiltonians. In: *Scientific Reports* 17 (2017), S. 42669

[1338] QUINN, John J. ; FERRELL, Richard A.: Electron Self-Energy Approach to Correlation in a Degenerate Electron Gas. In: *Phys. Rev.* 112 (1958), S. 812–827

[1339] MAHAN, Gerald D.: *Many-Particle Physics, Third Edition*. Springer Science+Business Media New York, 2000 (Pysics of Solids and Liquids). – ISBN 9781441933393

[1340] LANDAU, L. D.: The Theory of a Fermi Liquid. In: *Soviet Physics JETP* 3 (1956), S. 1058–1064

[1341] LANDAU, L. D.: Oscillations in a Fermi Liquid. In: *Soviet Physics JETP* 32 (1956), S. 59–66

[1342] MATTUCK, Richard D.: *A Guide to Feynman Diagrams in the Many-Body Problem: Second Edition*. Dover Publications, 1992. – ISBN 978–0486670478

[1343] GODBY, Rex W. ; GARCÍA-GONZÁLEZ, Pablo ; C.FIOLHAIS (Hrsg.) ; F.NOGUEIRA (Hrsg.) ; M.MARQUES (Hrsg.): *Density Functional Theories and Self-energy Approaches*. Springer-Verlag Berlin Heidelberg, 2003. – 185–217 S.

[1344] BECHSTEDT, F.: *Principles of Surface Science*. Springer-Verlag Berlin Heidelberg, 2007. – ISBN 9783642802836

[1345] CINI, Michele: *Topics and Methods in Condensed Matter Theory: From Basic Quantum Mechanics to the Frontiers of Research*. Springer; 2007 edition, 2007. – ISBN 9783540707264

[1346] ZAGOSKIN, Alexandre: *Quantum Theory of Many-Body Systems: Techniques and Applications*. Springer; Auflage: 2nd ed., 2014. – ISBN 9783319070483

[1347] MARTIN, Richard M. ; REINING, Lucia ; CEPERLEY, David M.: *Interacting Electrons: Theory and Computational Approaches*. Cambridge University Press, 2016. – ISBN 9780521871501

[1348] COHEN, Marvin L. ; LOUIE, Steven G.: *Fundamentals of Condensed Matter Physics*. Cambridge University Press, 2016. – ISBN 9780521513319

[1349] ASGARI, R. ; DAVOUDI, B. ; POLINI, M. ; GIULIANI, Gabriele F. ; TOSI, M. P. ; VIGNALE, G.: Quasiparticle self-energy and many-body effective mass enhancement in a two-dimensional electron liquid. In: *Phys. Rev. B* 71 (2005), S. 045323

[1350] PETERSILKA, M. ; GOSSMANN, U. J. ; GROSS, E. K. U.: Excitation Energies from Time-Dependent Density-Functional

Theory. In: *Phys. Rev. Lett.* 76 (1996), S. 1212–1215

[1351] ELLIOTT, Peter ; FURCHE, Filipp ; BURKE, Kieron: *Excited States from Time-Dependent Density Functional Theory*. John Wiley & Sons, Inc., 2009. – 91–165 S. – ISBN 9780470399545

[1352] HARBOLA, Manoj K. ; HEMANADHAN, M ; SHAMIM, Md ; SAMAL, P: Excited-state density functional theory. In: *Journal of Physics: Conference Series* 388 (2012), S. 012011

[1353] EVANGELISTA, Francesco A. ; SHUSHKOV, Philip ; TULLY, John C.: Orthogonality Constrained Density Functional Theory for Electronic Excited States. In: *The Journal of Physical Chemistry A* 117 (2013), S. 7378–7392

[1354] HANSON-HEINE, Magnus W. D. ; GEORGE, Michael W. ; BESLEY, Nicholas A.: Calculating excited state properties using Kohn-Sham density functional theory. In: *The Journal of Chemical Physics* 138 (2013), S. 064101

[1355] HOLM, Bengt: Total Energies from *GW* Calculations. In: *Phys. Rev. Lett.* 83 (1999), S. 788–791

[1356] HOLM, B. ; ARYASETIAWAN, F.: Total energy from the Galitskii-Migdal formula using realistic spectral functions. In: *Phys. Rev. B* 62 (2000), S. 4858–4865

[1357] CARUSO, F. ; RINKE, P. ; REN, X. ; SCHEFFLER, M. ; RUBIO, A.: Unified description of ground and excited states of finite systems: The self-consistent *GW* approach. In: *Phys. Rev. B* 86 (2012), S. 081102

[1358] CARUSO, Fabio ; ROHR, Daniel R. ; HELLGREN, Maria ; REN, Xinguo ; RINKE, Patrick ; RUBIO, Angel ; SCHEFFLER, Matthias: Bond Breaking and Bond Formation: How Electron Correlation is Captured in Many-Body Perturbation Theory and Density-Functional Theory. In: *Phys. Rev. Lett.* 110 (2013), S. 146403

[1359] GALITSKII, V. M. ; MIGDAL, A. B.: Application of quantum field theory methods to the many body problem. In: *Soviet Physics JETP* 34 (1958), S. 96–105

[1360] KOHN, W. ; LUTTINGER, J. M.: Ground-State Energy of a Many-Fermion System. In: *Phys. Rev.* 118 (1960), S. 41–45

[1361] LUTTINGER, J. M. ; WARD, J. C.: Ground-State Energy of a Many-Fermion System. II. In: *Phys. Rev.* 118 (1960), S. 1417–1427

[1362] KLEIN, Abraham ; PRANGE, Richard: Perturbation Theory for an Infinite Medium of Fermions. In: *Phys. Rev.* 112 (1958), S. 994–1007

[1363] KLEIN, Abraham: Perturbation Theory for an Infinite Medium of Fermions. II. In: *Phys. Rev.* 121 (1961), S. 950–956

[1364] KLEIN, Abraham: Perturbation Theory for an Infinite Medium of Fermions. III. Derivation of the Landau Theory of Fermi Liquids. In: *Phys. Rev.* 121 (1961), S. 957–961

[1365] HYBERTSEN, Mark S. ; LOUIE, Steven G.: Electron correlation in semiconductors and insulators: Band gaps and quasiparticle energies. In: *Phys. Rev. B* 34 (1986), S. 5390–5413

[1366] ARYASETIAWAN, F. ; ANISIMOV, V. (Hrsg.): *The GW Approximation and Vertex Corrections*. Springer-Verlag Berlin Heidelberg, 2003. – 1–87 S.

[1367] BARBIERI, Carlo: Notes on Green's Functions Theory for Quantum Many-Body Systems. In: *Theoretical Nuclear Physics Laboratory Nishina Center for Accelerator-Based Science, RIKEN* (2009)

[1368] BARTH, U von ; HEDIN, L: A local exchange-correlation potential for the spin polarized case. i. In: *Journal of Physics C: Solid State Physics* 5 (1972), S. 1629

[1369] FEYNMAN, R. P.: Space-Time Approach to Quantum Electrodynamics. In: *Phys. Rev.* 76 (1949), S. 769–789

[1370] WICK, G. C.: The Evaluation of the Collision Matrix. In: *Phys. Rev.* 80 (1950), S. 268–272

[1371] MOLINARI, Luca G.: Notes on Wick's theorem in many-body theory. In: *arXiv:1710.09248* (2011)

[1372] LEEUWEN, R. van ; STEFANUCCI, G.: Wick theorem for general initial states. In: *Phys. Rev. B* 85 (2012), S. 115119

[1373] SCHWINGER, Julian: The Theory of Quantized Fields. I. In: *Phys. Rev.* 82 (1951), S. 914–927

[1374] MARTIN, Paul C. ; SCHWINGER, Julian: Theory of Many-Particle Systems. I. In: *Phys. Rev.* 115 (1959), S. 1342–1373

[1375] REHR, J J.: Lars Hedin and the quest for a theory of excited states. In: *Physica Scripta* 2005 (2005), S. 19

[1376] ARYASETIAWAN, F.: Functional derivative technique (Lecture Notes).

[1377] GATTI, Matteo: Ab-Initio Calculations of Many body effects in electronic spectre. In: *Optics* Ecole Polytechnique X (2007)

[1378] MARINI, A. ; SOLE, R. D. ; RUBIO, A. ; MARQUES, Miguel A. (Hrsg.) ; ULLRICH, Carsten A. (Hrsg.) ; NOGUEIRA, Fernando (Hrsg.) ; RUBIO, Angel (Hrsg.) ; BURKE, Kieron (Hrsg.) ; GROSS, Eberhard K. U. (Hrsg.): *Approximate Functionals from Many-Body Perturbation Theory*. Springer-Verlag Berlin Heidelberg New York, 2010. – 161–180 S.

[1379] ARYASETIAWAN, F. ; BIERMANN, S.: Generalized Hedin's Equations for Quantum Many-Body Systems with Spin-Dependent Interactions. In: *Phys. Rev. Lett.* 100 (2008), S. 116402

[1380] STARKE, Ronald ; KRESSE, Georg: Self-consistent Green function equations and the hierarchy of approximations for the four-point propagator. In: *Phys. Rev. B* 85 (2012), S. 075119

[1381] MAGGIO, Emanuele ; KRESSE, Georg: GW Vertex Corrected Calculations for Molecular Systems. In: *Journal of Chemical Theory and Computation* 13 (2017), S. 4765–4778

[1382] KAISER, David: Physics and Feynman's Diagrams. In: *American Scientist* 93 (2005), S. 156–165

[1383] DYSON, F. J.: The Radiation Theories of Tomonaga, Schwinger, and Feynman. In: *Phys. Rev.* 75 (1949), S. 486–502

[1384] DYSON, F. J.: The *S* Matrix in Quantum Electrodynamics. In: *Phys. Rev.* 75 (1949), S. 1736–1755

[1385] FRANK, R. M.: The Fourth-Order Contribution to the Self-Energy of the Electron. In: *Phys. Rev.* 83 (1951), S. 1189–1193

[1386] GELL-MANN, Murray ; LOW, Francis: Bound States in Quantum Field Theory. In: *Phys. Rev.* 84 (1951), S. 350–354

[1387] HELD, K. ; TARANTO, C. ; ROHRINGER, G. ; TOSCHI, A.: *Hedin Equations, GW, GW+DMFT, and All That*. 2011. – 1–17 S.

[1388] SCHINDLMAYR, Arno ; GODBY, R. W.: Systematic Vertex Corrections through Iterative Solution of Hedin's Equations Beyond the *GW* Approximation. In: *Phys. Rev. Lett.* 80 (1998), S. 1702–1705

[1389] SCHINDLMAYR, Arno: *Self-consistency and vertex corrections beyond the GW approximation*. 2002. – 1–10 S.

[1390] BRUNEVAL, Fabien ; VAST, Nathalie ; REINING, Lucia: Effect of self-consistency on quasiparticles in solids. In: *Phys. Rev. B* 74 (2006), S. 045102

[1391] KANG, Wei ; HYBERTSEN, Mark S.: Enhanced static approximation to the electron self-energy operator for efficient calculation of quasiparticle energies. In: *Phys. Rev. B* 82 (2010), S. 195108

[1392] JAIN, Manish ; DESLIPPE, Jack ; SAMSONIDZE, Georgy ; COHEN, Marvin L. ; CHELIKOWSKY, James R. ; LOUIE, Steven G.: Improved quasiparticle wave functions and mean field for G_0W_0 calculations: Initialization with the COHSEX operator. In: *Phys. Rev. B* 90 (2014), S. 115148

[1393] SHIRLEY, Eric L. ; MARTIN, Richard M.: GW quasiparticle calculations in atoms. In: *Phys. Rev. B* 47 (1993), S. 15404–15412

[1394] SHIRLEY, Eric L.: Self-consistent *GW* and higher-order calculations of electron states in metals. In: *Phys. Rev. B* 54 (1996), S. 7758–7764

[1395] ARYASETIAWAN, F. ; GUNNARSSON, O.: The GW method. In: *Reports on Progress in Physics* 61 (1998), S. 237

[1396] BARTH, Ulf von ; HOLM, Bengt: Self-consistent GW_0 results for the electron gas: Fixed screened potential W_0 within the random-phase approximation. In: *Phys. Rev. B* 54 (1996), S. 8411–8419

[1397] STEFANUCCI, G. ; PAVLYUKH, Y. ; UIMONEN, A.-M. ; LEEUWEN, R. van: Diagrammatic expansion for positive spectral functions beyond *GW*: Application to vertex corrections in the electron gas. In: *Phys. Rev. B* 90 (2014), S. 115134

[1398] GRÜNEIS, Andreas ; KRESSE, Georg ; HINUMA, Yoyo ; OBA, Fumiyasu: Ionization Potentials of Solids: The Importance of Vertex Corrections. In: *Phys. Rev. Lett.* 112 (2014), S. 096401

[1399] REN, Xinguo ; RINKE, Patrick ; SCUSERIA, Gustavo E. ; SCHEFFLER, Matthias: Renormalized second-order perturbation theory for the electron correlation energy: Concept, implementation, and benchmarks. In: *Phys. Rev. B* 88 (2013), S. 035120

[1400] KUTEPOV, A L.: Full self-consistency versus quasiparticle self-consistency in diagrammatic approaches: exactly solvable two-site Hubbard model. In: *Journal of Physics: Condensed Matter* 27 (2015), S. 315603

[1401] REN, Xinguo ; MAROM, Noa ; CARUSO, Fabio ; SCHEFFLER, Matthias ; RINKE, Patrick: Beyond the *GW* approximation: A second-order screened exchange correction. In: *Phys. Rev. B* 92 (2015), S. 081104

[1402] SHISHKIN, M. ; KRESSE, G.: Self-consistent *GW* calculations for semiconductors and insulators. In: *Phys. Rev. B* 75 (2007), S. 235102

[1403] STAN, Adrian ; DAHLEN, Nils E. ; LEEUWEN, Robert van: Levels of self-consistency in the GW approximation. In: *Journal of Chemical Physics* 130 (2009), S. 114105

[1404] KANG, Gijae ; KANG, Youngho ; HAN, Seungwu: Influence of wave-function updates in *GW* calculations on titanates. In: *Phys. Rev. B* 91 (2015), S. 155141

[1405] BOBBERT, P. A. ; HAERINGEN, W. van: Lowest-order vertex-correction contribution to the direct gap of silicon. In: *Phys. Rev. B* 49 (1994), S. 10326–10331

[1406] GROOT, H. J. ; UMMELS, R. T. M. ; BOBBERT, P. A. ; HAERINGEN, W. v.: Lowest-order corrections to the RPA polarizability and *GW* self-energy of a semiconducting wire. In: *Phys. Rev. B* 54 (1996), S. 2374–2380

[1407] UMMELS, R. T. M. ; BOBBERT, P. A. ; HAERINGEN, W. van: First-order corrections to random-phase approximation GW calculations in silicon and diamond. In: *Phys. Rev. B* 57 (1998), S. 11962–11973

[1408] NIQUET, Y. M. ; GONZE, X.: Band-gap energy in the random-phase approximation to density-functional theory. In: *Phys. Rev. B* 70 (2004), S. 245115

[1409] DEL SOLE, R. ; REINING, Lucia ; GODBY, R. W.: GWΓ approximation for electron self-energies in semiconductors and

insulators. In: *Phys. Rev. B* 49 (1994), S. 8024–8028

[1410] BRUNEVAL, Fabien ; SOTTILE, Francesco ; OLEVANO, Valerio ; DEL SOLE, Rodolfo ; REINING, Lucia: Many-Body Perturbation Theory Using the Density-Functional Concept: Beyond the *GW* Approximation. In: *Phys. Rev. Lett.* 94 (2005), S. 186402

[1411] SCHILFGAARDE, M. van ; KOTANI, Takao ; FALEEV, S.: Quasiparticle Self-Consistent *GW* Theory. In: *Phys. Rev. Lett.* 96 (2006), S. 226402

[1412] MORRIS, Andrew J. ; STANKOVSKI, Martin ; DELANEY, Kris T. ; RINKE, Patrick ; GARCÍA-GONZÁLEZ, P. ; GODBY, R. W.: Vertex corrections in localized and extended systems. In: *Phys. Rev. B* 76 (2007), S. 155106

[1413] SHISHKIN, M. ; MARSMAN, M. ; KRESSE, G.: Accurate Quasiparticle Spectra from Self-Consistent *GW* Calculations with Vertex Corrections. In: *Phys. Rev. Lett.* 99 (2007), S. 246403

[1414] PAIER, Joachim ; MARSMAN, Martijn ; KRESSE, Georg: Dielectric properties and excitons for extended systems from hybrid functionals. In: *Phys. Rev. B* 78 (2008), S. 121201

[1415] KUWAHARA, Riichi ; NOGUCHI, Yoshifumi ; OHNO, Kaoru: GWΓ + Bethe-Salpeter equation approach for photoabsorption spectra: Importance of self-consistent GWΓ calculations in small atomic systems. In: *Phys. Rev. B* 94 (2016), S. 121116

[1416] KUTEPOV, Andrey L.: Self-consistent solution of Hedin's equations: Semiconductors and insulators. In: *Phys. Rev. B* 95 (2017), S. 195120

[1417] KUTEPOV, A. L. ; KOTLIAR, G.: One-electron spectra and susceptibilities of the three-dimensional electron gas from self-consistent solutions of Hedin's equations. In: *Phys. Rev. B* 96 (2017), S. 035108

[1418] SCHMIDT, Per S. ; PATRICK, Christopher E. ; THYGESEN, Kristian S.: Simple vertex correction improves *GW* band energies of bulk and two-dimensional crystals. In: *Phys. Rev. B* 96 (2017), S. 205206

[1419] GEORGES, Antoine ; KOTLIAR, Gabriel ; KRAUTH, Werner ; ROZENBERG, Marcelo J.: Dynamical mean-field theory of strongly correlated fermion systems and the limit of infinite dimensions. In: *Rev. Mod. Phys.* 68 (1996), S. 13–125

[1420] LICHTENSTEIN, A. I. ; KATSNELSON, M. I. ; KOTLIAR, G.: Finite-Temperature Magnetism of Transition Metals: An ab initio Dynamical Mean-Field Theory. In: *Phys. Rev. Lett.* 87 (2001), S. 067205

[1421] BIERMANN, S. ; ARYASETIAWAN, F. ; GEORGES, A.: First-Principles Approach to the Electronic Structure of Strongly Correlated Systems: Combining the *GW* Approximation and Dynamical Mean-Field Theory. In: *Phys. Rev. Lett.* 90 (2003), S. 086402

[1422] TOSCHI, A. ; KATANIN, A. A. ; HELD, K.: Dynamical vertex approximation: A step beyond dynamical mean-field theory. In: *Phys. Rev. B* 75 (2007), S. 045118

[1423] GALLER, Anna ; THUNSTRÖM, Patrik ; GUNACKER, Patrik ; TOMCZAK, Jan M. ; HELD, Karsten: Ab initio dynamical vertex approximation. In: *Phys. Rev. B* 95 (2017), S. 115107

[1424] SHISHKIN, M. ; KRESSE, G.: Implementation and performance of the frequency-dependent *GW* method within the PAW framework. In: *Phys. Rev. B* 74 (2006), S. 035101

[1425] HÜSER, Falco ; OLSEN, Thomas ; THYGESEN, Kristian S.: Quasiparticle GW calculations for solids, molecules, and two-dimensional materials. In: *Phys. Rev. B* 87 (2013), S. 235132

[1426] PULCI, Olivia ; BECHSTEDT, Friedhelm ; ONIDA, Giovanni ; DEL SOLE, Rodolfo ; REINING, Lucia: State mixing for quasiparticles at surfaces: Nonperturbative GW approximation. In: *Phys. Rev. B* 60 (1999), S. 16758–16761

[1427] HAHN, P. H. ; SCHMIDT, W. G. ; BECHSTEDT, F.: Molecular electronic excitations calculated from a solid-state approach: Methodology and numerics. In: *Phys. Rev. B* 72 (2005), S. 245425

[1428] GODBY, R. W. ; SCHLÜTER, M. ; SHAM, L. J.: Self-energy operators and exchange-correlation potentials in semiconductors. In: *Phys. Rev. B* 37 (1988), S. 10159–10175

[1429] WENZIEN, B. ; CAPPELLINI, G. ; BECHSTEDT, F.: Efficient quasiparticle band-structure calculations for cubic and noncubic crystals. In: *Phys. Rev. B* 51 (1995), S. 14701–14704

[1430] SCHÖNE, Wolf-Dieter ; EGUILUZ, Adolfo G.: Self-Consistent Calculations of Quasiparticle States in Metals and Semiconductors. In: *Phys. Rev. Lett.* 81 (1998), S. 1662–1665

[1431] BECHSTEDT, F. ; FURTHMÜLLER, J.: Do we know the fundamental energy gap of InN? In: *Journal of Crystal Growth* 246 (2002), S. 315 – 319

[1432] KRESS, C. ; FIEDLER, M. ; SCHMIDT, W. G. ; BECHSTEDT, F.: Geometrical and electronic structure of the reconstructed diamond (100) surface. In: *Phys. Rev. B* 50 (1994), S. 17697–17700

[1433] ROHLFING, Michael ; KRÜGER, Peter ; POLLMANN, Johannes: Efficient scheme for GW quasiparticle band-structure calculations with applications to bulk Si and to the Si(001)-(2×1) surface. In: *Phys. Rev. B* 52 (1995), S. 1905–1917

[1434] ROHLFING, Michael ; KRÜGER, Peter ; POLLMANN, Johannes: Quasiparticle band structures of clean, hydrogen-, and

sulfur-terminated Ge(001) surfaces. In: *Phys. Rev. B* 54 (1996), S. 13759–13766

[1435] TAGHIPOUR, Zahra ; SHOJAEE, Ezad ; KRISHNA, Sanjay: Many-body perturbation theory study of type-II InAs/GaSb superlattices within the GW approximation. In: *Journal of Physics: Condensed Matter* 30 (2018), S. 325701

[1436] ARYASETIAWAN, F ; BARTH, U von: Dielectric response and quasiparticle energies in nickel. In: *Physica Scripta* 1992 (1992), S. 270

[1437] ARYASETIAWAN, F. ; GUNNARSSON, O.: Electronic Structure of NiO in the *GW* Approximation. In: *Phys. Rev. Lett.* 74 (1995), S. 3221–3224

[1438] RASMUSSEN, Filip A. ; SCHMIDT, Per S. ; WINTHER, Kirsten T. ; THYGESEN, Kristian S.: Efficient many-body calculations for two-dimensional materials using exact limits for the screened potential: Band gaps of MoS_2, *h*-BN, and phosphorene. In: *Phys. Rev. B* 94 (2016), S. 155406

[1439] BLASE, X. ; ATTACCALITE, C. ; OLEVANO, V.: First-principles *GW* calculations for fullerenes, porphyrins, phtalocyanine, and other molecules of interest for organic photovoltaic applications. In: *Phys. Rev. B* 83 (2011), S. 115103

[1440] CARUSO, Fabio ; RINKE, Patrick ; REN, Xinguo ; RUBIO, Angel ; SCHEFFLER, Matthias: Self-consistent *GW*: All-electron implementation with localized basis functions. In: *Phys. Rev. B* 88 (2013), S. 075105

[1441] ROHLFING, Michael ; KRÜGER, Peter ; POLLMANN, Johannes: Quasiparticle band-structure calculations for C, Si, Ge, GaAs, and SiC using Gaussian-orbital basis sets. In: *Phys. Rev. B* 48 (1993), S. 17791–17805

[1442] SCHMIDT, Per S. ; PATRICK, Christopher E. ; THYGESEN, Kristian S.: Simple vertex correction improves *GW* band energies of bulk and two-dimensional crystals. In: *Phys. Rev. B* 96 (2017), S. 205206

[1443] NORTHRUP, John E. ; HYBERTSEN, Mark S. ; LOUIE, Steven G.: Theory of quasiparticle energies in alkali metals. In: *Phys. Rev. Lett.* 59 (1987), S. 819–822

[1444] STRANGE, Mikkel ; THYGESEN, Kristian S.: Towards quantitative accuracy in first-principles transport calculations: The GW method applied to alkane/gold junctions. In: *Journal of Nanotechnology* 2 (2011), S. 746–754

[1445] SHAM, L. J. ; RICE, T. M.: Many-Particle Derivation of the Effective-Mass Equation for the Wannier Exciton. In: *Phys. Rev.* 144 (1966), S. 708–714

[1446] HANKE, W. ; SHAM, L. J.: Local-field and excitonic effects in the optical spectrum of a covalent crystal. In: *Phys. Rev. B* 12 (1975), S. 4501–4511

[1447] HANKE, W. ; SHAM, L. J.: Many-Particle Effects in the Optical Excitations of a Semiconductor. In: *Phys. Rev. Lett.* 43 (1979), S. 387–390

[1448] STRINATI, G.: Effects of dynamical screening on resonances at inner-shell thresholds in semiconductors. In: *Phys. Rev. B* 29 (1984), S. 5718–5726

[1449] ALBRECHT, Stefan ; REINING, Lucia ; DEL SOLE, Rodolfo ; ONIDA, Giovanni: *Ab Initio* Calculation of Excitonic Effects in the Optical Spectra of Semiconductors. In: *Phys. Rev. Lett.* 80 (1998), S. 4510–4513

[1450] ROHLFING, Michael ; LOUIE, Steven G.: Electron-hole excitations and optical spectra from first principles. In: *Phys. Rev. B* 62 (2000), S. 4927–4944

[1451] ONIDA, Giovanni ; REINING, Lucia ; RUBIO, Angel: Electronic excitations: density-functional versus many-body Green's-function approaches. In: *Rev. Mod. Phys.* 74 (2002), S. 601–659

[1452] BUSSI, Giovanni: Effects of the Electron-Hole Interaction on the Optical Properties of Materials: the Bethe-Salpeter Equation. In: *Physica Scripta* 2004 (2004), S. 141

[1453] HYBERTSEN, Mark S. ; LOUIE, Steven G.: Ab initio static dielectric matrices from the density-functional approach. I. Formulation and application to semiconductors and insulators. In: *Phys. Rev. B* 35 (1987), S. 5585–5601

[1454] LOUIE, Steven G. ; CHELIKOWSKY, James R. ; COHEN, Marvin L.: Local-Field Effects in the Optical Spectrum of Silicon. In: *Phys. Rev. Lett.* 34 (1975), S. 155–158

[1455] MOCHÁN, W. L. ; BARRERA, Rubén G.: Intrinsic Surface-Induced Optical Anisotropies of Cubic Crystals: Local-Field Effect. In: *Phys. Rev. Lett.* 55 (1985), S. 1192–1195

[1456] KRASOVSKII, E. E. ; SCHATTKE, W.: Local field effects in optical excitations of semicore electrons. In: *Phys. Rev. B* 60 (1999), S. R16251–R16254

[1457] W.G., Schmidt ; P.H., Hahn ; F., Bechstedt ; KRAUSE, E. (Hrsg.) ; JÄGER, W. (Hrsg.): *Excitonic and Local-Field Effects in Optical Spectra from Real-Space Time-Domain Calculations*. Springer, Berlin, Heidelberg, 2003. – 133 S.

[1458] CARAMELLA, L. ; ONIDA, G. ; FINOCCHI, F. ; REINING, L. ; SOTTILE, F.: Optical properties of real surfaces: Local-field effects at oxidized $Si(100)(2\times1)$ computed with an efficient numerical scheme. In: *Phys. Rev. B* 75 (2007), S. 205405

[1459] DAMEWOOD, L. ; FONG, C. Y.: Local field effects in half-metals: A *GW* study of zincblende CrAs, MnAs, and MnC. In: *Phys. Rev. B* 83 (2011), S. 113102

[1460] SIPE, J. E. ; GHAHRAMANI, Ed: Nonlinear optical response of semiconductors in the independent-particle approximation. In: *Phys. Rev. B* 48 (1993), S. 11705–11722

[1461] HANSEN, D. L. ; HEMMERS, O. ; WANG, H. ; LINDLE, D. W. ; FOCKE, P. ; SELLIN, I. A. ; HESKE, C. ; CHAKRABORTY, H. S. ; DESHMUKH, P. C. ; MANSON, S. T.: Validity of the independent-particle approximation in x-ray photoemission: The exception, not the rule. In: *Phys. Rev. A* 60 (1999), S. R2641–R2644

[1462] KOTANI, Takao ; SCHILFGAARDE, Mark van ; FALEEV, Sergey V.: Quasiparticle self-consistent *GW* method: A basis for the independent-particle approximation. In: *Phys. Rev. B* 76 (2007), S. 165106

[1463] BAYM, Gordon ; KADANOFF, Leo P.: Conservation Laws and Correlation Functions. In: *Phys. Rev.* 124 (1961), S. 287–299

[1464] ROMANIELLO, Pina ; BECHSTEDT, Friedhelm ; REINING, Lucia: Beyond the *GW* approximation: Combining correlation channels. In: *Phys. Rev. B* 85 (2012), S. 155131

[1465] CUDAZZO, Pierluigi ; GATTI, Matteo ; RUBIO, Angel: Local-field effects on the plasmon dispersion of two-dimensional transition metal dichalcogenides. In: *New Journal of Physics* 15 (2013), S. 125005

[1466] JOHNSON, David L.: Local field effects and the dielectric response matrix of insulators: A model. In: *Phys. Rev. B* 9 (1974), S. 4475–4484

[1467] PICK, Robert M. ; COHEN, Morrel H. ; MARTIN, Richard M.: Microscopic Theory of Force Constants in the Adiabatic Approximation. In: *Phys. Rev. B* 1 (1970), S. 910–920

[1468] RÖDL, Claudia: Elektronische und exzitonische Anregungen in magnetischen Isolatoren. In: *Dissertation, Friedrich-Schiller-Universität Jena* (2009)

[1469] BECHSTEDT, F. ; SOLE, R. D. ; CAPPELLINI, G. ; REINING, Lucia: An efficient method for calculating quasiparticle energies in semiconductors. In: *Solid State Communications* 84 (1992), S. 765 – 770

[1470] CAPPELLINI, G. ; DEL SOLE, R. ; REINING, Lucia ; BECHSTEDT, F.: Model dielectric function for semiconductors. In: *Phys. Rev. B* 47 (1993), S. 9892–9895

[1471] SCHMIDT, W. G. ; GLUTSCH, S. ; HAHN, P. H. ; BECHSTEDT, F.: Efficient $\mathcal{O}(N^2)$ method to solve the Bethe-Salpeter equation. In: *Phys. Rev. B* 67 (2003), S. 085307

[1472] EKARDT, W. ; PACHECO, J. M.: Effective particle-hole interaction and the optical response of simple-metal clusters. In: *Phys. Rev. B* 52 (1995), S. 16864–16868

[1473] FETTER, A. L. ; WALECKA, J. D.: *Quantum Theory of Many-Particle Systems*. Dover Publications, 2012

[1474] TAMM, I. J.: Relativistic interaction of elementary particles. In: *J.Phys.(USSR)* 9 (1945), S. 449

[1475] DANCOFF, S. M.: Nonadiabatic meson theory of nuclear forces. In: *Phys. Rev.* 78 (1950), S. 382–385

[1476] REINING, L. ; PAVARINI, E. (Hrsg.) ; KOCH, E. (Hrsg.) ; BRINK, J. van d. (Hrsg.) ; SAWATZKY, G. (Hrsg.): *Linear Response and More: the Bethe-Salpeter Equation*. Forschungszentrum Jülich, Modeling and Simulation Vol. 6, 2016. – 10.1–10.24 S.

[1477] SANDER, Tobias ; MAGGIO, Emanuele ; KRESSE, Georg: Beyond the Tamm-Dancoff approximation for extended systems using exact diagonalization. In: *Phys. Rev. B* 92 (2015), S. 045209

[1478] OLEVANO, Valerio ; REINING, Lucia: Excitonic Effects on the Silicon Plasmon Resonance. In: *Phys. Rev. Lett.* 86 (2001), S. 5962–5965

[1479] GRÜNING, M. ; MARINI, A. ; GONZE, X.: Exciton-Plasmon States in Nanoscale Materials: Breakdown of the Tamm-Dancoff Aproximation. In: *Nano Letters* 9 (2009), S. 2820–2824

[1480] PUSCHNIG, P. ; MEISENBICHLER, C. ; DRAXL, C.: Excited State Properties of Organic Semiconductors: Breakdown of the Tamm-Dancoff Approximation. In: *arXiv:1306.3790v2* (2013)

[1481] RÖDL, C. ; FUCHS, F. ; FURTHMÜLLER, J. ; BECHSTEDT, F.: Ab initio theory of excitons and optical properties for spin-polarized systems: Application to antiferromagnetic MnO. In: *Phys. Rev. B* 77 (2008), S. 184408

[1482] CAPPELLINI, Giancarlo ; FURTHMÜLLER, Jürgen ; CADELANO, Emiliano ; BECHSTEDT, Friedhelm: Electronic and optical properties of cadmium fluoride: The role of many-body effects. In: *Phys. Rev. B* 87 (2013), S. 075203

[1483] HAYDOCK, Roger: The recursive solution of the Schrödinger equation. In: *Computer Physics Communications* 20 (1980), S. 11 – 16

[1484] BENEDICT, Lorin X. ; SHIRLEY, Eric L. ; BOHN, Robert B.: Optical Absorption of Insulators and the Electron-Hole Interaction: An *Ab Initio* Calculation. In: *Phys. Rev. Lett.* 80 (1998), S. 4514–4517

[1485] BENEDICT, Lorin X. ; SHIRLEY, Eric L.: Ab initio calculation of $\epsilon_2(\omega)$ including the electron-hole interaction: Application to GaN and CaF_2. In: *Phys. Rev. B* 59 (1999), S. 5441–5451

[1486] HAHN, P. H. ; SCHMIDT, W. G. ; BECHSTEDT, F.: Bulk Excitonic Effects in Surface Optical Spectra. In: *Phys. Rev. Lett.* 88 (2001), S. 016402

[1487] FUCHS, F. ; RÖDL, C. ; SCHLEIFE, A. ; BECHSTEDT, F.: Efficient $\mathcal{O}(N^2)$ approach to solve the Bethe-Salpeter equation for excitonic bound states. In: *Phys. Rev. B* 78 (2008), S. 085103

[1488] PUSCHNIG, Peter ; AMBROSCH-DRAXL, Claudia: Optical absorption spectra of semiconductors and insulators including electron-hole correlations: An ab initio study within the LAPW method. In: *Phys. Rev. B* 66 (2002), S. 165105

[1489] M. WU AND, Z. L. ; CAO, T. ; LOUIE, S. G.: Physical origin of giant excitonic and magneto-optical responses in two-dimensional ferromagnetic insulators. In: *Nature Communications* 10 (2019), S. 2371

[1490] CARVALHO, Luiz C. ; SCHLEIFE, André ; FURTHMÜLLER, Jürgen ; BECHSTEDT, Friedhelm: Ab initio calculation of optical properties with excitonic effects in wurtzite $In_xGa_{1-x}N$ and $In_xAl_{1-x}N$ alloys. In: *Phys. Rev. B* 87 (2013), S. 195211

[1491] GIORGI, Giacomo ; PALUMMO, Maurizia ; CHIODO, Letizia ; YAMASHITA, Koichi: Excitons at the (001) surface of anatase: Spatial behavior and optical signatures. In: *Phys. Rev. B* 84 (2011), S. 073404

[1492] HAASTRUP, Sten ; STRANGE, Mikkel ; PANDEY, Mohnish ; DEILMANN, Thorsten ; SCHMIDT, Per S. ; HINSCHE, Nicki F. ; GJERDING, Morten N. ; TORELLI, Daniele ; LARSEN, Peter M. ; RIIS-JENSEN, Anders C. ; GATH, Jakob ; JACOBSEN, Karsten W. ; MORTENSEN, Jens J. ; OLSEN, Thomas ; THYGESEN, Kristian S.: The Computational 2D Materials Database: high-throughput modeling and discovery of atomically thin crystals. In: *2D Materials* 5 (2018), S. 042002

[1493] CHIODO, L. ; IACOMINO, A. ; PALUMMO, M. ; RUBIO, A.: *Titania nanostructures electronic and optical response by high-level ab-initio computational approaches*. Nova Science Publishers, Ltd., 2014

[1494] KÖHLER, Thomas ; TUROWSKI, Marcus ; EHLERS, Henrik ; LANDMANN, Marc ; RISTAU, Detlev ; FRAUENHEIM, Thomas: Computational approach for structure design and prediction of optical properties in amorphous TiO_2 thin-film coatings. In: *Journal of Physics D: Applied Physics* 46 (2013), Nr. 32, S. 325302

[1495] SCHMIDT, Falko ; LANDMANN, Marc ; RAULS, Eva ; ARGIOLAS, Nicola ; SANNA, Simone ; SCHMIDT, W. G. ; SCHINDLMAYR, Arno: Consistent Atomic Geometries and Electronic Structure of Five Phases of Potassium Niobate from Density-Functional Theory. In: *Advances in Materials Science and Engineering* (2017), S. 3981317

[1496] LANDMANN, M. ; RAULS, E. ; SCHMIDT, W. G.: First-principles calculations of clean Au(110) surfaces and chemisorption of atomic oxygen. In: *Phys. Rev. B* 79 (2009), Jan, S. 045412

[1497] LANDMANN, M. ; RAULS, E. ; SCHMIDT, W. G.: Chainlike Au-O Structures on Au(110)-(1×r) Surfaces Calculated from First Principles. In: *The Journal of Physical Chemistry C* 113 (2009), S. 5690–5699

[1498] LÜCKE, A. ; BIKTAGIROV, T. ; RIEFER, A. ; LANDMANN, M. ; ROHRMÜLLER, M. ; BRAUN, C. ; NEUFELD, S. ; GERSTMANN, U. ; SCHMIDT, W. G.: Photo-Excited Surface Dynamics from Massively Parallel Constrained-DFT Calculations. In: NAGEL, Wolfgang E. (Hrsg.) ; KRÖNER, Dietmar H. (Hrsg.) ; RESCH, Michael M. (Hrsg.): *High Performance Computing in Science and Engineering ' 17*, Springer International Publishing, 2018, S. 157–168

[1499] SANNA, S. ; DUES, C. ; GERSTMANN, U. ; RAULS, E. ; NOZAKI, D. ; RIEFER, A. ; LANDMANN, M. ; ROHRMÜLLER, M. ; VOLLMERS, N. J. ; HÖLSCHER, R. ; LÜCKE, A. ; BRAUN, C. ; NEUFELD, S. ; HOLTGREWE, K. ; SCHMIDT, W. G.: Submonolayer Rare Earth Silicide Thin Films on the Si(111) Surface. In: *High Performance Computing in Science and Engineering '16* (2016), S. 163

[1500] LÜCKE, A. ; GERSTMANN, U. ; SANNA, S. ; LANDMANN, M. ; RIEFER, A. ; ROHRMÜLLER, M. ; VOLLMERS, N. J. ; RAULS, M. Wittev E. ; HÖLSCHER, R. ; BRAUN, C. ; NEUFELD, S. ; HOLTGREWE, K. ; SCHMIDT, W. G.: Solving the Scattering Problem for the P3HT On-Chain Charge Transport. In: *High Performance Computing in Science and Engineering '15* (2016), S. 155

[1501] SANNA, S. ; GERSTMANN, U. ; RAULS, E. ; LI, Y. ; LANDMANN, M. ; RIEFER, A. ; ROHRMÜLLER, M. ; VOLLMERS, N. J. ; WITTE, M. ; HÖLSCHER, R. ; LÜCKE, A. ; BRAUN, C. ; NEUFELD, S. ; HOLTGREWE, K. ; SCHMIDT, W. G.: Surface Charge of Clean $LiNbO_3$ Z-Cut Surfaces. In: *High Performance Computing in Science and Engineering '14* (2015), S. 163

[1502] SANNA, S. ; RIEFER, A. ; ROHRMÜLLER, M. ; LANDMANN, M. ; RAULS, E. ; VOLLMERS, N. J. ; HÖLSCHER, R. ; WITTE, M. ; LI, Y. ; GERSTMANN, U. ; SCHMIDT, W. G.: Polarization Dependent Water Adsorption on the Lithium Niobate Z-Cut Surfaces. In: *High Performance Computing in Science and Engineering '13* (2013), S. 155

[1503] RIEFER, A. ; ROHRMÜLLER, M. ; LANDMANN, M. ; SANNA, S. ; RAULS, E. ; VOLLMERS, N. J. ; HÖLSCHER, R. ; WITTE, M. ; LI, Y. ; GERSTMANN, U. ; SCHINDLMAYR, A. ; SCHMIDT, W. G.: Lithium Niobate Dielectric Function and Second-Order Polarizability Tensor From Massively Parallel Ab Initio Calculations. In: *High Performance Computing in Science and Engineering '13* (2013), S. 93

[1504] GERSTMANN, U. ; ROHRMÜLLER, M. ; VOLLMERS, N. J. ; KONOPKA, A. ; GREULICH-WEBER, S. ; RAULS, E. ; LANDMANN, M. ; SANNA, S. ; RIEFER, A. ; SCHMIDT, W. G.: Surface Magnetism: Relativistic Effects at Semiconductor Interfaces and Solar Cells. In: *High Performance Computing in Science and Engineering '12* (2013), S. 129

[1505] RIEFER, A. ; ROHRMÜLLER, M. ; LANDMANN, M. ; SANNA, S. ; RAULS, E. ; GERSTMANN, U. ; SCHMIDT, W. G.: Electronic and Optical Excitations of Aminopyrimidine Molecules from Many-Body Perturbation Theory. In: *High Performance*

Computing in Science and Engineering '12 (2013), S. 17

[1506] SCHMIDT, W. G. ; RAULS, E. ; GERSTMANN, U. ; SANNA, S. ; LANDMANN, M. ; ROHRMÜLLER, M. ; RIEFER, A. ; WIPPERMANN, S. ; BLANKENBURG, S.: Copper Substrate Catalyzes Tetraazaperopyrene Polymerization. In: *High Performance Computing in Science and Engineering '11* (2012), S. 47

[1507] SCHMIDT, W. G. ; RAULS, E. ; GERSTMANN, U. ; SANNA, S. ; LANDMANN, M. ; ROHRMÜLLER, M. ; RIEFER, A. ; WIPPERMANN, S.: Entropy and Metal-Insulator Transition in Atomic-Scale Wires: The Case of In-Si(111)(4×1)/(8×2). In: *High Performance Computing in Science and Engineering '11* (2012), S. 131

[1508] SCHMIDT, W. G. ; WIPPERMANN, S. ; RAULS, E. ; GERSTMANN, U. ; SANNA, S. ; THIERFELDER, C. ; LANDMANN, M. ; SANTOS, L. S.: Si(111)-In Nanowire Optical Response from Large-scale Ab Initio Calculations. In: *High Performance Computing in Science and Engineering '10* (2011), S. 149

[1509] SCHMIDT, W. G. ; BLANKENBURG, S. ; RAULS, E. ; WIPPERMANN, S. ; GERSTMANN, U. ; SANNA, S. ; THIERFELDER, C. ; KOCH, N. ; LANDMANN, M.: Understanding Long-range Indirect Interactions Between Surface Adsorbed Molecules. In: *High Performance Computing in Science and Engineering '09* (2010), S. 75

[1510] TCHERNYCHEVA, M. ; NEVOU, L. ; DOYENNETTE, L. ; JULIEN, F. H. ; WARDE, E. ; GUILLOT, F. ; MONROY, E. ; BELLET-AMALRIC, E. ; REMMELE, T. ; ALBRECHT, M.: Systematic experimental and theoretical investigation of intersubband absorption in GaNAlN quantum wells. In: *Phys. Rev. B* 73 (2006), S. 125347

[1511] CARDONA, M. ; HARBEKE, G.: Optical Properties and Band Structure of Wurtzite-Type Crystals and Rutile. In: *Phys. Rev.* 137 (1965), S. A1467–A1476

[1512] TIWALD, T. E. ; SCHUBERT, M.: Measurement of rutile TiO_2 dielectric tensor from 0.148 to 33 μm using generalized ellipsometry. In: *Proc. SPIE* 4103 (2000), S. 19–29

[1513] WEI, S.-H. ; FERREIRA, L. G. ; BERNARD, James E. ; ZUNGER, Alex: Electronic properties of random alloys: Special quasirandom structures. In: *Phys. Rev. B* 42 (1990), S. 9622–9649

[1514] ZUNGER, Alex ; WEI, S.-H. ; FERREIRA, L. G. ; BERNARD, James E.: Special quasirandom structures. In: *Phys. Rev. Lett.* 65 (1990), S. 353–356

[1515] ELSTNER, M. ; POREZAG, D. ; JUNGNICKEL, G. ; ELSNER, J. ; HAUGK, M. ; FRAUENHEIM, Th. ; SUHAI, S. ; SEIFERT, G.: Self-consistent-charge density-functional tight-binding method for simulations of complex materials properties. In: *Phys. Rev. B* 58 (1998), S. 7260–7268

[1516] FRAUENHEIM, T. ; SEIFERT, G. ; ELSTERNER, M. ; HAJNAL, Z. ; JUNGNICKEL, G. ; POREZAG, D. ; SUHAI, S. ; SCHOLZ, R.: A Self-Consistent Charge Density-Functional Based Tight-Binding Method for Predictive Materials Simulations in Physics, Chemistry and Biology. In: *Phys. Status Solidi B* 217 (2000), S. 41–62

[1517] LOOK, D. C. ; REYNOLDS, D. C. ; HEMSKY, J. W. ; SIZELOVE, J. R. ; JONES, R. L. ; MOLNAR, R. J.: Defect Donor and Acceptor in GaN. In: *Phys. Rev. Lett.* 79 (1997), S. 2273–2276

[1518] LOOK, D. C. ; FARLOW, G. C. ; DREVINSKY, P. J. ; BLISS, D. F. ; SIZELOVE, J. R.: On the nitrogen vacancy in GaN. In: *Applied Physics Letters* 83 (2003), Nr. 17, S. 3525–3527

[1519] MATSUI, Masanori ; AKAOGI, Masaki: Molecular Dynamics Simulation of the Structural and Physical Properties of the Four Polymorphs of TiO_2. In: *Molecular Simulation* 6 (1991), Nr. 4-6, S. 239–244

[1520] SCHUPP, T.: In: *unpublished*

[1521] PATRA, Abhirup ; BATES, Jefferson E. ; SUN, Jianwei ; PERDEW, John P.: Properties of real metallic surfaces: Effects of density functional semilocality and van der Waals nonlocality. In: *Proceedings of the National Academy of Sciences* 114 (2017), S. E9188–E9196

[1522] SUN, Jianwei ; RUZSINSZKY, Adrienn ; PERDEW, John P.: Strongly Constrained and Appropriately Normed Semilocal Density Functional. In: *Phys. Rev. Lett.* 115 (2015), S. 036402

[1523] SUN, Jianwei ; REMSING, Richard C. ; ZHANG, Yubo ; SUN, Zhaoru ; RUZSINSZKY, Adrienn ; PENG, Haowei ; YANG, Zenghui ; PAUL, Arpita ; WAGHMARE, Umesh ; WU, Xifan ; KLEIN, Michael L. ; PERDEW, John P.: Accurate first-principles structures and energies of diversely bonded systems from an efficient density functional. In: *Nature Chemistry* 8 (2016), S. 831

[1524] STAROVEROV, Viktor N. ; SCUSERIA, Gustavo E. ; TAO, Jianmin ; PERDEW, John P.: Tests of a ladder of density functionals for bulk solids and surfaces. In: *Phys. Rev. B* 69 (2004), S. 075102

[1525] GRABOWSKI, Blazej ; HICKEL, Tilmann ; NEUGEBAUER, Jörg: Ab initio. In: *Phys. Rev. B* 76 (2007), S. 024309

[1526] HAO, Pan ; FANG, Yuan ; SUN, Jianwei ; CSONKA, Gábor I. ; PHILIPSEN, Pier H. T. ; PERDEW, John P.: Lattice constants from semilocal density functionals with zero-point phonon correction. In: *Phys. Rev. B* 85 (2012), S. 014111

[1527] G., Wyckoff R. W.: Crystal Structures. In: *NewYork: Wiley* 1 (1963)

[1528] HORN, M. ; SCHWERDTFEGER, C. ; MEAGHER, E.: Refinement of the structure of anatase at several temperatures. In: *Zeitschrift für Kristallographie* 136 (1963), S. 273–281

[1529] C., Hermann ; O., Lohrmann ; H., Philipp: Strukturbericht Band II 1928?1932. In: *Leipzig: Akademische Verlagsgesellschaft MBH* (1937)

[1530] LORDI, Vincenzo ; GAMBIN, Vincent ; FRIEDRICH, Stephan ; FUNK, Tobias ; TAKIZAWA, Toshiyuki ; UNO, Kazuyuki ; HARRIS, James S.: Nearest-Neighbor Configuration in (GaIn)(NAs) Probed by X-Ray Absorption Spectroscopy. In: *Phys. Rev. Lett.* 90 (2003), S. 145505

[1531] CHRISTEN, J. ; RIEMANN, T. ; BERTRAM, F. ; RUDLOFF, D. ; FISCHER, P. ; KASCHNER, A. ; HABOECK, U. ; HOFFMANN, A. ; THOMSEN, C.: Optical micro-characterization of group-III-nitrides: correlation of structural, electronic and optical properties. In: *physica status solidi (c)* 0 (2003), S. 1795–1815

[1532] CRAMER, Richard C. ; BONEF, Bastien ; ENGLISH, John ; DREYER, Cyrus E. ; WALLE, Chris G. d. ; SPECK, James S.: Growth of coherent BGaN films using BBr_3 gas as a boron source in plasma assisted molecular beam epitaxy. In: *Journal of Vacuum Science & Technology A* 35 (2017), S. 041509

[1533] CONNOLLY, J. W. D. ; WILLIAMS, A. R.: Density-functional theory applied to phase transformations in transition-metal alloys. In: *Phys. Rev. B* 27 (1983), S. 5169–5172

[1534] SHER, A. ; SCHILFGAARDE, Mark van ; CHEN, An-Ban ; CHEN, William: Quasichemical approximation in binary alloys. In: *Phys. Rev. B* 36 (1987), S. 4279–4295

[1535] TELES, L. K. ; FURTHMÜLLER, J. ; SCOLFARO, L. M. R. ; LEITE, J. R. ; BECHSTEDT, F.: First-principles calculations of the thermodynamic and structural properties of strained $In_xGa_{1-x}N$ and $Al_xGa_{1-x}N$ alloys. In: *Phys. Rev. B* 62 (2000), S. 2475–2485

[1536] CAETANO, C. ; TELES, L. K. ; MARQUES, M. ; DAL PINO, A. ; FERREIRA, L. G.: Phase stability, chemical bonds, and gap bowing of $In_xGa_{1-x}N$ alloys: Comparison between cubic and wurtzite structures. In: *Phys. Rev. B* 74 (2006), S. 045215

[1537] SCHLEIFE, A. ; EISENACHER, M. ; RÖDL, C. ; FUCHS, F. ; FURTHMÜLLER, J. ; BECHSTEDT, F.: Ab initio description of heterostructural alloys: Thermodynamic and structural properties of $Mg_xZn_{1-x}O$ and $Cd_xZn_{1-x}O$. In: *Phys. Rev. B* 81 (2010), S. 245210

[1538] RUBAN, A V. ; ABRIKOSOV, I A.: Configurational thermodynamics of alloys from first principles: effective cluster interactions. In: *Reports on Progress in Physics* 71 (2008), S. 046501

[1539] WOODCOCK, L. V. ; ANGELL, C. A. ; CHEESEMAN, P.: Molecular dynamics studies of the vitreous state: Simple ionic systems and silica. In: *The Journal of Chemical Physics* 65 (1976), S. 1565–1577

[1540] STILLINGER, Frank H. ; WEBER, Thomas A.: Computer simulation of local order in condensed phases of silicon. In: *Phys. Rev. B* 31 (1985), S. 5262–5271

[1541] BISWAS, R. ; HAMANN, D. R.: Interatomic Potentials for Silicon Structural Energies. In: *Phys. Rev. Lett.* 55 (1985), S. 2001–2004

[1542] DING, Kejian ; ANDERSEN, Hans C.: Molecular-dynamics simulation of amorphous germanium. In: *Phys. Rev. B* 34 (1986), S. 6987–6991

[1543] TERSOFF, J.: New empirical approach for the structure and energy of covalent systems. In: *Phys. Rev. B* 37 (1988), S. 6991–7000

[1544] CAR, R. ; PARRINELLO, M.: Structural, Dymanical, and Electronic Properties of Amorphous Silicon: An *ab initio* Molecular-Dynamics Study. In: *Phys. Rev. Lett.* 60 (1988), S. 204–207

[1545] TSUNEYUKI, S. ; TSUKADA, M. ; AOKI, H. ; MATSUI, Y.: First-Principles Interatomic Potential of Silica Applied to Molecular Dynamics. In: *Phys. Rev. Lett.* 61 (1988), S. 869–872

[1546] HOLENDER, J M. ; MORGAN, G J.: Generation of a large structure (10 5 atoms) of amorphous Si using molecular dynamics. In: *Journal of Physics: Condensed Matter* 3 (1991), S. 7241

[1547] COOK, Stephen J. ; CLANCY, Paulette: Comparison of semi-empirical potential functions for silicon and germanium. In: *Phys. Rev. B* 47 (1993), S. 7686–7699

[1548] NAKANO, Aiichiro ; BI, Lingsong ; KALIA, Rajiv K. ; VASHISHTA, Priya: Molecular-dynamics study of the structural correlation of porous silica with use of a parallel computer. In: *Phys. Rev. B* 49 (1994), S. 9441–9452

[1549] SHIMOJO, Fuyuki ; EBBSJÖ, Ingvar ; KALIA, Rajiv K. ; NAKANO, Aiichiro ; RINO, Jose P. ; VASHISHTA, Priya: Molecular Dynamics Simulation of Structural Transformation in Silicon Carbide under Pressure. In: *Phys. Rev. Lett.* 84 (2000), S. 3338–3341

[1550] EBBSJO, Ingvar ; KALIA, Rajiv K. ; NAKANO, Aiichiro ; RINO, Jose P. ; VASHISHTA, Priya: Topology of amorphous gallium arsenide on intermediate length scales: A molecular dynamics study. In: *Journal of Applied Physics* 87 (2000), S. 7708–7711

[1551] DURANDURDU, M. ; DRABOLD, D. A. ; MOUSSEAU, N.: Approximate *ab initio* calculations of electronic structure of amorphous silicon. In: *Phys. Rev. B* 62 (2000), S. 15307–15310

[1552] WOOTEN, F. ; WINER, K. ; WEAIRE, D.: Computer Generation of Structural Models of Amorphous Si and Ge. In: *Phys. Rev. Lett.* 54 (1985), S. 1392–1395

[1553] WOOTEN, F. ; WEAIRE, D.: Modeling Tetrahedrally Bonded Random Networks by Computer. Academic Press, 1987, S. 1 – 42

[1554] DJORDJEVIĆ, B. R. ; THORPE, M. F. ; WOOTEN, F.: Computer model of tetrahedral amorphous diamond. In: *Phys. Rev. B* 52 (1995), S. 5685–5689

[1555] TRACHENKO, Kostya ; DOVE, Martin T.: Densification of silica glass under pressure. In: *Journal of Physics: Condensed Matter* 14 (2002), S. 7449

[1556] CABRIOLU, R. ; DEL POPOLO, M. G. ; BALLONE, P.: Melting of a tetrahedral network model of silica. In: *Phys. Chem. Chem. Phys.* 11 (2009), S. 10820–10823

[1557] ZHAO, Yan ; TRUHLAR, Donald G.: Calculation of semiconductor band gaps with the M06-L density functional. In: *The Journal of Chemical Physics* 130 (2009), S. 074103

[1558] JOHNSON, Kurt A. ; ASHCROFT, N. W.: Corrections to density-functional theory band gaps. In: *Phys. Rev. B* 58 (1998), S. 15548–15556

[1559] REMEDIAKIS, I. N. ; KAXIRAS, Efthimios: Band-structure calculations for semiconductors within generalized-density-functional theory. In: *Phys. Rev. B* 59 (1999), S. 5536–5543

[1560] KIM, Yoon-Suk ; HUMMER, Kerstin ; KRESSE, Georg: Accurate band structures and effective masses for InP, InAs, and InSb using hybrid functionals. In: *Phys. Rev. B* 80 (2009), S. 035203

[1561] BECKE, Axel D. ; JOHNSON, Erin R.: A simple effective potential for exchange. In: *The Journal of Chemical Physics* 124 (2006), S. 221101

[1562] TRAN, Fabien ; BLAHA, Peter ; SCHWARZ, Karlheinz: Band gap calculations with Becke-Johnson exchange potential. In: *Journal of Physics: Condensed Matter* 19 (2007), S. 196208

[1563] TRAN, Fabien ; BLAHA, Peter: Accurate Band Gaps of Semiconductors and Insulators with a Semilocal Exchange-Correlation Potential. In: *Phys. Rev. Lett.* 102 (2009), S. 226401

[1564] MA, X. G. ; LIANG, P. ; MIAO, L. ; BIE, S. W. ; ZHANG, C. K. ; XU, L. ; JIANG, J. J.: Pressure-induced phase transition and elastic properties of TiO_2 polymorphs. In: *physica status solidi (b)* 246 (2009), S. 2132–2139

[1565] CONESA, José C.: The Relevance of Dispersion Interactions for the Stability of Oxide Phases. In: *The Journal of Physical Chemistry C* 114 (2010), S. 22718–22726

[1566] MEHTA, Prateek ; SALVADOR, Paul A. ; KITCHIN, John R.: Identifying Potential BO_2 Oxide Polymorphs for Epitaxial Growth Candidates. In: *ACS Applied Materials & Interfaces* 6 (2014), S. 1944–8244

[1567] MEI, Zhi-Gang ; WANG, Yi ; SHANG, Shunli ; LIU, Zi-Kui: First-principles study of the mechanical properties and phase stability of TiO_2. In: *Computational Materials Science* 83 (2014), S. 114 – 119

[1568] CURNAN, Matthew T. ; KITCHIN, John R.: Investigating the Energetic Ordering of Stable and Metastable TiO_2 Polymorphs Using DFT+U and Hybrid Functionals. In: *The Journal of Physical Chemistry C* 119 (2015), S. 21060–21071

[1569] REHR, J. J. ; ZAREMBA, E. ; KOHN, W.: van der Waals forces in the noble metals. In: *Phys. Rev. B* 12 (1975), S. 2062–2066

[1570] LEE, Ji-Hwan ; PARK, Jong-Hun ; SOON, Aloysius: Assessing the influence of van der Waals corrected exchange-correlation functionals on the anisotropic mechanical properties of coinage metals. In: *Phys. Rev. B* 94 (2016), S. 024108

[1571] AMBROSETTI, Alberto ; SILVESTRELLI, Pier L.: Cohesive properties of noble metals by van der Waals–corrected density functional theory: Au, Ag, and Cu as case studies. In: *Phys. Rev. B* 94 (2016), S. 045124

[1572] KLIMES, Jiri ; MICHAELIDES, Angelos: Perspective: Advances and challenges in treating van der Waals dispersion forces in density functional theory. In: *The Journal of Chemical Physics* 137 (2012), S. 120901

[1573] TKATCHENKO, Alexandre: Current Understanding of Van der Waals Effects in Realistic Materials. In: *Advanced Functional Materials* 25 (2015), S. 2054–2061

[1574] GRIMME, Stefan ; HUJO, Waldemar ; KIRCHNER, Barbara: Performance of dispersion-corrected density functional theory for the interactions in ionic liquids. In: *Phys. Chem. Chem. Phys.* 14 (2012), S. 4875–4883

[1575] TKATCHENKO, Alexandre ; SCHEFFLER, Matthias: Accurate Molecular Van Der Waals Interactions from Ground-State Electron Density and Free-Atom Reference Data. In: *Phys. Rev. Lett.* 102 (2009), S. 073005

[1576] KRONIK, Leeor ; TKATCHENKO, Alexandre: Understanding Molecular Crystals with Dispersion-Inclusive Density Functional Theory: Pairwise Corrections and Beyond. In: *Accounts of Chemical Research* 47 (2014), S. 3208–3216

[1577] JR, Robert A D. ; GOBRE, Vivekanand V. ; TKATCHENKO, Alexandre: Many-body van der Waals interactions in molecules and condensed matter. In: *Journal of Physics: Condensed Matter* 26 (2014), S. 213202

[1578] MOELLMANN, Jonas ; EHRLICH, Stephan ; TONNER, Ralf ; GRIMME, Stefan: A DFT-D study of structural and energetic properties of TiO_2 modifications. In: *Journal of Physics: Condensed Matter* 24 (2012), S. 424206

[1579] DERINGER, Volker L. ; CSANYI, Gabor: Many-Body Dispersion Correction Effects on Bulk and Surface Properties of Rutile and Anatase TiO_2. In: *The Journal of Physical Chemistry C* 120 (2016), S. 21552–21560

[1580] CUI, Zhi-Hao ; WU, Feng ; JIANG, Hong: First-principles study of relative stability of rutile and anatase TiO_2 using the random phase approximation. In: *Phys. Chem. Chem. Phys.* 18 (2016), S. 29914–29922

[1581] PATRICK, Christopher E. ; THYGESEN, Kristian S.: Hubbard-*U* corrected Hamiltonians for non-self-consistent random-phase approximation total-energy calculations: A study of ZnS, TiO_2, and NiO. In: *Phys. Rev. B* 93 (2016), S. 035133

[1582] RAMBERGER, Benjamin ; SCHÄFER, Tobias ; KRESSE, Georg: Analytic Interatomic Forces in the Random Phase Approximation. In: *Phys. Rev. Lett.* 118 (2017), S. 106403

[1583] ZHANG, Yubo ; FURNESS, James W. ; XIAO, Bing ; SUN, Jianwei: Subtlety of TiO_2 phase stability: Reliability of the density functional theory predictions and persistence of the self-interaction error. In: *The Journal of Chemical Physics* 150 (2019), S. 014105

[1584] ADOLPH, B. ; GAVRILENKO, V. I. ; TENELSEN, K. ; BECHSTEDT, F. ; DEL SOLE, R.: Nonlocality and many-body effects in the optical properties of semiconductors. In: *Phys. Rev. B* 53 (1996), S. 9797–9808

[1585] SLATER, J. C. ; JOHNSON, K. H.: Self-Consistent-Field X_α Cluster Method for Polyatomic Molecules and Solids. In: *Phys. Rev. B* 5 (1972), S. 844–853

[1586] FERREIRA, Luiz G. ; MARQUES, Marcelo ; TELES, Lara K.: Approximation to density functional theory for the calculation of band gaps of semiconductors. In: *Phys. Rev. B* 78 (2008), S. 125116

[1587] FERREIRA, Luiz G. ; MARQUES, Marcelo ; TELES, Lara K.: Slater half-occupation technique revisited: the LDA-1/2 and GGA-1/2 approaches for atomic ionization energies and band gaps in semiconductors. In: *AIP Advances* 1 (2011), S. 032119

[1588] YUAN, Jun-Hui ; CHEN, Qi ; FONSECA, Leonardo R C. ; XU, Ming ; XUE, Kan-Hao ; MIAO, Xiang-Shui: GGA-1/2 self-energy correction for accurate band structure calculations: the case of resistive switching oxides. In: *Journal of Physics Communications* 2 (2018), S. 105005

[1589] XUE, Kan-Hao ; YUAN, Jun-Hui ; FONSECA, Leonardo R. ; MIAO, Xiang-Shui: Improved LDA-1/2 method for band structure calculations in covalent semiconductors. In: *Computational Materials Science* 153 (2018), S. 493 – 505

[1590] BELABBES, A. ; FURTHMÜLLER, J. ; BECHSTEDT, F.: Electronic properties of polar and nonpolar InN surfaces: A quasiparticle picture. In: *Phys. Rev. B* 84 (2011), S. 205304

[1591] BELABBES, Abderrezak ; PANSE, Christian ; FURTHMÜLLER, Jürgen ; BECHSTEDT, Friedhelm: Electronic bands of III-V semiconductor polytypes and their alignment. In: *Phys. Rev. B* 86 (2012), S. 075208

[1592] PELA, R. R. ; CAETANO, C. ; MARQUES, M. ; FERREIRA, L. G. ; FURTHMÜLLER, J. ; TELES, L. K.: Accurate band gaps of AlGaN, InGaN, and AlInN alloys calculations based on LDA-1/2 approach. In: *Applied Physics Letters* 98 (2011), S. 151907

[1593] RIBEIRO, M. ; FONSECA, L. R. C. ; FERREIRA, L. G.: First-principles calculation of the AlAs/GaAs interface band structure using a self-energy–corrected local density approximation. In: *EPL (Europhysics Letters)* 94 (2011), S. 27001

[1594] KÜFNER, Sebastian ; SCHLEIFE, André ; HÖFFLING, Benjamin ; BECHSTEDT, Friedhelm: Energetics and approximate quasiparticle electronic structure of low-index surfaces of SnO_2. In: *Phys. Rev. B* 86 (2012), S. 075320

[1595] WANNIER, G. H.: On the Transformation of Light into Heat in Solids. II. In: *Phys. Rev.* 52 (1937), S. 191–197

[1596] MOTT, N. F.: Conduction in polar crystals. II. The conduction band and ultra-violet absorption of alkali-halide crystals. In: *Trans. Faraday Soc.* 34 (1938), S. 500–506

[1597] FRENKEL, J.: On the Transformation of Light into Heat in Solids. II. In: *Phys. Rev.* 37 (1931), S. 1276–1294

[1598] VORONOI, Georges: Nouvelles applications des paramètres continus à la théorie des formes quadratiques. Deuxième mémoire. Recherches sur les parallélloèdres primitifs. In: *Journal für die reine und angewandte Mathematik* 134 (1908), S. 198–287

[1599] DELAUNAY, Boris: Nouvelles applications des paramètres continus à la théorie des formes quadratiques. Deuxième mémoire. Recherches sur les parallélloèdres primitifs. In: *Bulletin of the Academy of Science of the USSR, Clase des Sciences Mathématiques et Naturelles* 7 (1934), S. 793–800

[1600] HOSHEN, Joseph ; JORTNER, Joshua: Application of the Coherent Potential Approximation to the Excited Electronic States of Substitutionally Disordered Molecular Crystals. In: *The Journal of Chemical Physics* 56 (1972), S. 5550–5575

[1601] COHEN, Marvin L. ; LOUIE, Steven G.: *Models of Itinerant Ordering in Crystals, CHAPTER 9 - Alloys, Disordered Systems*. Elsevier Science Ltd, Oxford, 2007

Appendix

Paper I

Band offsets in cubic GaN/AlN superlattices

C. Mietze, M. Landmann, E. Rauls, H. Machhadani, S. Sakr, M. Tchernycheva, F. H. Julien, W. G. Schmidt, K. Lischka, and D. J. As, PHYSICAL REVIEW B **83**, 195301, 10 pp. (2011)

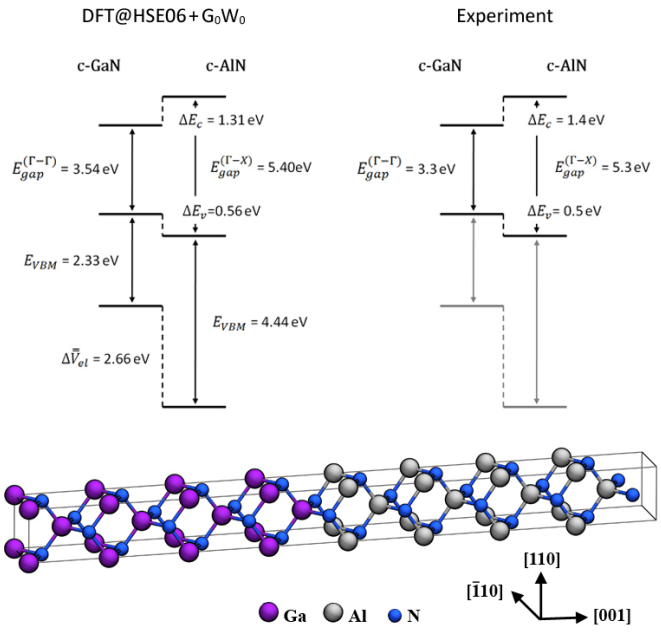

PHYSICAL REVIEW B **83**, 195301 (2011)

Band offsets in cubic GaN/AlN superlattices

C. Mietze,[1] M. Landmann,[2] E. Rauls,[2] H. Machhadani,[3] S. Sakr,[3] M. Tchernycheva,[3]
F. H. Julien,[3] W. G. Schmidt,[2] K. Lischka,[1] and D. J. As[1]
[1]*Experimentalphysik, Universität Paderborn, Warburger Strasse 100, D-33098, Germany*
[2]*Lehrstuhl für Theoretische Physik, Universität Paderborn, Warburger Strasse 100, D-33098, Germany*
[3]*Institut d'Electronique Fondamentale, UMR 8622 CNRS, University Paris-Sud 11, F-91405 Orsay, France*
(Received 30 November 2010; revised manuscript received 17 March 2011; published 4 May 2011)

The presently unknown band offset in nonpolar cubic GaN/AlN superlattices is investigated by inter-sub-band and interband spectroscopies as well as *ab initio* calculations. On one hand, the conduction-band offset (CBO) has been determined from the comparison of the measured transition energies with model calculations within the effective mass approximation. On the other hand, the valence-band offset (VBO) and the CBO are accurately simulated by calculating many-body corrections within the GW approximation on top of hybrid-functional density functional theory calculations. Thus, a CBO of (1.4 ± 0.1) eV and a VBO of (0.5 ± 0.1) eV is obtained as a result of both approaches.

DOI: 10.1103/PhysRevB.83.195301 PACS number(s): 78.67.Pt, 73.21.Cd, 81.15.Hi, 71.15.Mb

I. INTRODUCTION

One of the most crucial parameters that determines the physics in heterostructures and for the optimization and design of optoelectronic devices, based on, e.g., quantum wells (QWs), is the electronic band alignment at the interface between two semiconductors. More precisely, one is interested in the valence-band offset (VBO) and the conduction-band offset (CBO), which reflect how the band-gap difference of the involved semiconductor materials is portioned between the discontinuities of the occupied and unoccupied energy bands. Due to their technological importance, the band offsets between various semiconductor alloys have been subjected to extensive experimental and computational studies. Today, group-III nitrides are the materials of choice for manifold device applications, such as light-emitting diodes (LEDs), laser diodes, or field-effect transistors. Based on the large band discontinuity between AlN, GaN, and InN, novel nitride devices based on inter-sub-band transitions (ISBTs), such as quantum well infrared photodetectors (QWIPs) or quantum cascade lasers operating at telecommunication wavelengths are proposed.[1]

State-of-the-art group-III nitrides crystallize in the stable wurtzite structure. This hexagonal phase is characterized by strong internal piezoelectric and pyroelectric fields along the c axis, which are undesirable for many optoelectronic applications. In multi-QWs or superlattices (SLs), these internal fields complicate the design and limit the tunability of ISBT energies. In polar group-III nitride QWs, the transition energy is observed to be almost independent of the well width for thick wells due to the confinement of carriers in a triangular potential caused by the internal field. The growth of nonpolar and semipolar nitrides has found increasing interest in the past years to avoid these strong internal fields. In these nonpolar (semipolar) nitrides, the c axis is orthogonal (inclined) to the growth direction, eliminating the field effects in the growth direction. The absence of these internal fields leads to an increased transition probability and, therefore, to enhanced luminescence intensity and reduced shift in emission wavelength in LEDs. However, the electrical, optical, and structural properties show strong lateral anisotropy since the polarization field is now in the plane of growth. Furthermore, due to the large anisotropic biaxial stress, relaxation and cracking of AlGaN in one direction are observed.

An alternative way to fabricate group-III nitrides without spontaneous polarization fields is the growth of metastable nonpolar cubic (c) group-III nitrides.[2] Zinc-blende GaN, InN, and AlN epilayers and just recently, free-standing GaN substrates have been successfully synthesized using plasma-assisted molecular-beam epitaxy (PA-MBE).[2,3] Especially, the determination of optimal growth conditions for nonpolar c-GaN (Ref. 4) and c-AlN (Ref. 5) has pushed the development of electronic and optoelectronic devices, such as heterojunction field-effect transistors,[6] resonant tunneling diodes,[7] and QWIPs[8] based on zinc-blende group-III nitrides. Furthermore, the tunability of ISBTs from mid- to far-infrared regions in cubic GaN/AlN SLs has been shown.[9]

ISBTs give direct access to the CBO. The ISBT energy for a fixed QW structure depends only on the barrier height or the CBO between well and barrier material. Hence, the CBO can be used as a fitting parameter in model calculations of ISBT energies based on an effective mass model.

The *ab initio* access to the band alignment at heterostructure interfaces is directly related to referring the calculated energy levels in an extended solid to a well-defined energy reference. The average electrostatic potential of an infinite bulk crystal is an ill-defined constant,[10,11] but it is a well-defined quantity for the interface of two semi-infinite solids. This property was used by Baldereschi *et al.*[10] to split the VBO $\Delta E_v^{(A,B)}$ of two semiconductors A and B into two terms according to

$$\Delta E_v^{(A,B)} = \Delta \overline{\overline{V}}_{el}^{(A/B)} + \Delta E_{vbm}^{(A,B)}. \quad (1)$$

Here, $\Delta \overline{\overline{V}}_{el}^{(A/B)}$ is the shift in the macroscopic average of the electrostatic potential across the interface of a semiconductor-alloy heterostructure. Usually, it is obtained from *ab initio* calculations of periodic SLs within the supercell approach. Thus, all effects of strain due to the epitaxial growth on a substrate and electronic relaxations and/or redistributions at the heterostructure's interface are included in the first term. The second contribution, $\Delta E_{vbm}^{(A,B)}$, is the difference between

 ©2011 American Physical Society

the valence-band maxima of the bulk materials calculated separately for both semiconductors A and B. Based on Eq. (1), the CBO $\Delta E_c^{(A,B)}$ may be obtained by adding the difference $\Delta E_g^{(A,B)}$ of the fundamental bulk band gaps of the semiconductor materials A and B,

$$\Delta E_c^{(A,B)} = -\Delta E_v^{(A,B)} + \Delta E_g^{(A,B)}. \quad (2)$$

In this paper, we report on the optical characterization of nonpolar c-GaN/AlN SL structures by inter-sub-band absorption and photoluminescence (PL) measurements. *Ab initio* calculations are performed to accurately determine the VBO. Combining the results of the *ab initio* calculations with the experimental data of the ISBT and interband transition, a CBO-to-VBO ratio of 74(±5):26(±5) is obtained.

This paper is organized as follows: Sec. II describes the methodological approaches of the underlying experimental and computational frameworks. In Sec. III, we present and discuss the results of the particular methods. Finally, Sec. IV is used for a summary and a comparative discussion of experimental and theoretical results.

II. METHODOLOGY

A. Experiment and model calculations

Our samples were grown by PA-MBE on 10-μm-thick 3C-SiC substrates on top of Si (100) (NovaSiC). Two series of samples were fabricated. Samples of series A consist of a 100-nm c-GaN buffer followed by a 20-period GaN/AlN SL. The active region is capped by a 100-nm GaN layer. The AlN thickness varied between 1.3 and 1.7 nm, and the GaN QW thickness varied between 2.0 and 2.5 nm. In the second series of samples (series B), the number of SL periods was extended to 40. The AlN barrier thickness was 3.0 nm, and GaN QW thickness was varied from 1.8 to 5.0 nm. The cap layer was 7-nm thick. Growth rates of the different layers were observed *in situ* by reflection high-energy electron diffraction intensity oscillations. The strain of the samples was determined using high-resolution x-ray diffraction (HRXRD). A modification of the band gap due to strain can be calculated using Eqs. (3) and (4),

$$E_{\text{gap,strained}} = E_{\text{gap},0} + 2a_c\left(1 - \frac{c_{12}}{c_{11}}\right)\epsilon_{xx}, \quad (3)$$

$$\epsilon_{xx} = \frac{a_{\text{GaN}}}{a_{\text{AlN}}} - 1. \quad (4)$$

Here, $E_{\text{gap,strained}}$ is the band-gap energy of the strained layer, $E_{\text{gap},0}$ is the band-gap energy of the bulk material, a_c is the deformation potential, and c_{11} and c_{12} are the elastic constants. ϵ_{xx} is the misfit between GaN and AlN with the lattice parameters a_{AlN} and a_{GaN}. The thicknesses of the single layers were verified by simulations of HRXRD data based on dynamical scattering theory.[12]

Inter-sub-band spectroscopy is performed with a Fourier transform infrared spectrometer. Two opposite facets of the samples were optically polished at an angle of 30° in order to allow multiple passes in the active layers when irradiating the input facet at normal incidence. Interband spectroscopy is performed using a HeCd laser (325 nm) as the excitation source. A Spex 270M monochromator combined with a GaAs photomultiplier and a Hamamatsu C3866 photon counter were used to detect emitted light from the SL samples.

TABLE I. Parameters used for transition energy calculations.

Parameter	c-AlN	c-GaN
$E_{\text{gap},300\text{ K}}$ (eV)	5.3[a]	3.2[b]
a (Å)	4.38[c]	4.52[c]
m^*_{hh}/m_0	1.2[d]	0.8[d]
m^*_{lh}/m_0	0.33[d]	0.18[d]
m_e/m_0	0.19[d]	0.13[d]
a_c (eV)	−6.8[e]	−2.77[e]
c_{11} (GPa)	304[e]	296[e]
c_{12} (GPa)	152[e]	156[e]
E_p (eV)	23.84[f]	16.86[f]
F		0.6
Δ (eV)		0.017[g]

[a]Reference 19.
[b]Reference 20.
[c]References 21 and 22.
[d]References 23 and 24.
[e]References 25 and 26.
[f]Reference 27.
[g]Reference 28.

Model calculations based on a single-band effective mass model with periodic boundary conditions using nextnano^3 (Ref. 13) are performed to obtain theoretical ISBT energies. More detailed information on nextnano^3 can be found in Refs. 14 and 15. For all QW samples, an enhancement of effective masses due to nonparabolicity effects is also taken into account. In thin GaAs/AlAs QWs, it has been shown that the effective electron masses increase with decreasing well width.[16] For all samples, the energy dependency of the effective electron mass is calculated using a modified Kane formula,[17,18]

$$\frac{m_0}{m^*(\epsilon)} = 1 + 2F + \frac{E_p}{3}\left(\frac{2}{E_g + \epsilon} + \frac{1}{E_g + \Delta + \epsilon}\right). \quad (5)$$

Here, ϵ is the confinement energy of the lowest sub-band, E_p is the interband matrix element, F accounts for coupling to remote bands, and Δ is the spin-orbit splitting of the valence band. The value of F was assumed to be 0.6 so that the effective mass for zero confinement energy results in the bulk value. The parameters of c-GaN and c-AlN used for these calculations are given in Table I. Then, the CBO is used as a fitting parameter to achieve optimal agreement between calculated and measured ISBT energies.

B. *Ab initio* calculations

We have performed density functional theory (DFT) calculations[29,30] using the projector-augmented wave (PAW) method[31,32] as implemented in the Vienna *Ab initio* Simulation Package (VASP).[33] An energy cutoff of 400 eV was used throughout this paper to expand the Kohn-Sham orbitals into plane-wave basis sets. Within the DFT approach, the electronic band structure of semiconductors, and, therefore, the band gap, depends on the choice of the exchange correlation (XC) functional. Therefore, we applied both the local-density

approximation (LDA) [34,35] and the nonlocal screened Coulomb potential hybrid density functionals [Heyd-Scuseria-Ernzerhof (HSE)].[36–39] The LDA functional is well known to significantly underestimate semiconductor band gaps or even to predict zero band gaps for small-gap semiconductors in some cases.[38,40] This is among other reasons due to a missing derivative discontinuity[41,42] and an incomplete self-interaction cancellation[35,43] in the LDA XC potential.

The mixing of a notable amount of nonlocal Hartree-Fock (HF) exchange interaction in so-called hybrid functionals [e.g., PBE0 (Refs. 44–47)] has proven to improve the description of the electronic structure (i.e., band gaps). Most of the computational difficulties of this approach arise from the evaluation of the slowly decaying Fock exchange E_X^{HF} (also called exact exchange) with distance, which is why the use of traditional hybrid functionals is avoided for large systems.[36,37] In consideration of this problem, Heyd *et al.*[36] proposed a more tractable hybrid-functional scheme for extended systems.

In general, the HSE-type functional exhibits the form

$$E_{\mathrm{XC}}^{\mathrm{HSE}} = \alpha E_X^{\mathrm{HF,SR}}(\mu) + (1-\alpha)E_X^{\mathrm{PBE,SR}}(\mu) + E_X^{\mathrm{PBE,LR}}(\mu) + E_C^{\mathrm{PBE}}. \tag{6}$$

Here, α defines the percentage of Fock exchange included, and μ is the actual controlling parameter for the range separation of the exchange interaction into short-range (SR) and long-range (LR) components. The correlation energy E_c remains unchanged with respect to the Perdew-Burke-Ernzerhof (PBE)[48] functional. In agreement with the original definitions,[36,37,39,49] we refer to the parameter values $\alpha = 0.25$, $\mu = 0.3$ Å^{-1} as HSE03 and to $\alpha = 0.25$, $\mu = 0.2$ Å^{-1} as HSE06, respectively. In some calculations, we changed the amount of exact exchange in Eq. (6) from its standard value $\alpha = 0.25$. In these cases, the applied functional is labeled by mod (α)HSE03/06. So far, DFT HSE-functional calculations with similar settings have been successfully applied to molecules,[36] extended crystals,[50,51] and defect levels.[52]

Besides the hybrid-functional approach, which basically developed from the observation of reverse errors in the electronic structure in classic DFT and HF calculations,[53] many-body perturbation theory (MBPT) offers a way to include many particle interactions beyond the single-particle mean-field theories. A successful approximation within MBPT[54,55] is Hedin's GW approximation[56,57] for independent quasiparticles (QPs). Within the GW approximation,[58] QP energies $E_{n\mathbf{k}}^{\mathrm{QP}}$, as measured in photoabsorption and photoemission spectroscopies, are solutions to a set of nonlinear equations containing the nonlocal energy-dependent self-energy operator $\Sigma(r,r',E_{n\mathbf{k}}^{\mathrm{QP}})$ instead of the Kohn-Sham XC functional,

$$\left(T + V_{\mathrm{ext}} + V_H - E_{n\mathbf{k}}^{\mathrm{QP}}\right)\Psi_{n\mathbf{k}}(\mathbf{r}) + \int d^3\mathbf{r}'\,\Sigma\left(r,r',E_{n\mathbf{k}}^{\mathrm{QP}}\right)\Psi_{n\mathbf{k}}(\mathbf{r}') = 0. \tag{7}$$

The self-energy is obtained as a convolution of the single-particle Green's function G and the dynamically screened Coulomb interaction W, which is constructed from the polarization propagator in random-phase approximation,[55]

$$\Sigma(r,r',\omega) = \frac{i}{4\pi}\int_{-\infty}^{\infty} d\omega'\, e^{i\omega'\delta} G(\mathbf{r},\mathbf{r}',\omega+\omega')W(\mathbf{r},\mathbf{r}',\omega'). \tag{8}$$

In principle, these QP equations should be solved self-consistently by updating QP wave functions and QP energies.

In practice, the lowest-order non-self-consistent GW results are obtained from application of first-order perturbation theory to the results of computationally less demanding DFT calculations. The first-order energy corrections (so-called QP shifts) $\Delta E_{n\mathbf{k}}^{\mathrm{QP}}$ are given by

$$\Delta E_{n\mathbf{k}}^{\mathrm{QP}} = \langle n\mathbf{k}|\Sigma - V_{xc}^{\mathrm{DFT}}|n\mathbf{k}\rangle, \tag{9}$$

where the perturbation is given by the difference between the self-energy and the DFT XC functional.

Generally, this single shot GW strategy is known as the G_0W_0 approach. G_0W_0 systematically improves band gaps with a remaining underestimation tendency of experimental values.[59] Besides non-self-consistent G_0W_0 calculations, partially self-consistent schemes for G or W and fully self-consistent schemes for G and W have been applied to selected problems.[60,63] However, especially for the full update of G and W, a significant overestimation of electronic band gaps is observed for some materials (e.g., GaAs, GaN).[60] We calculated QP corrections for the bulk materials by various frequency-dependent GW schemes on top of LDA and HSE calculations.

The GW calculations for primitive bulk unit cells were carried out with 240 electronic bands, 200 frequency grid points for sampling the dielectric function, and a regular Γ-centered $8 \times 8 \times 8$ k-point mesh. The Brillouin-zone integration of heterostructure-unit cells was performed using a $12 \times 12 \times 2$ Monkhorst-Pack k-point sampling[64] in LDA-PBE calculations and a regular Γ-centered $8 \times 8 \times 2$ k-point mesh in HSE calculations. The k-point grid was down-sampled by a factor of 2 to evaluate the Fock exchange in the HSE heterostructure calculation.

All calculations treated the $3d$ electrons of Ga as valence states within the PAW potentials.

The heterostructure-unit cell (cf. Fig. 1) represents a periodic array of 1.8-nm (eight layers) c-GaN and 1.6-nm (eight layers) c-AlN slabs. In detail, the unit cell has been constructed to match the experimental structure of the pseudomorphically grown SL with a strained c-AlN lattice matched to the c-GaN substrate system. Therefore, the experimental value $a_{exp}^{\mathrm{GaN}} = 4.52$ Å (Ref. 22) has been chosen for the in-plane and out-of-plane lattice constants of the GaN part as well as for the in-plane lattice constant of AlN. The out-of-plane lattice constant of the AlN slab $a_{z,\mathrm{GaN}} = 4.12$ Å has been determined with respect to volume conservation of the strained material. A structural relaxation of the AlN out-of-plane lattice constant on the LDA level results in exactly the same value. Additionally, we performed calculations with a fully optimized out-of-plane lattice constant in the whole unit cell and in-plane lattice constants fixed to the optimized DFT (LDA, PBE) lattice constants of GaN and AlN ($a_{\mathrm{GaN}}^{\mathrm{LDA}} = 4.46$ Å, $a_{\mathrm{GaN}}^{\mathrm{PBE}} = 4.54$ Å, $a_{\mathrm{AlN}}^{\mathrm{LDA}} = 4.35$ Å, $a_{\mathrm{AlN}}^{\mathrm{PBE}} = 4.40$ Å) to estimate the influence of

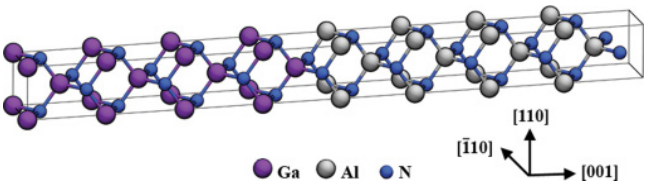

FIG. 1. (Color online) Unit cell of the pseudomorphically strained $(GaN)_8(AlN)_8(001)$ heterostructure.

lattice relaxations on the potential steps and band offsets (cf. Table IV). For the bulk-unit cells, the experimental lattice constants $a_{GaN} = 4.52$ Å and $a_{AlN} = 4.38$ Å were used.[22,65,66]

The potential shifts $\Delta\overline{\overline{V}}_{el}(z)$ across the growth direction z of the SL have been estimated by performing a two-step averaging procedure on the local electrostatic potential. First, a microscopic planar average over the lattice periodic directions x and y (i.e., [110], [$\bar{1}$10], cf. Fig. 1) has been calculated according to

$$\overline{V}_{el}(z) = \frac{1}{A_{cell}} \int dx\, dy\, V_{el}(x,y,z). \tag{10}$$

In a second step, the remaining rapid bulklike oscillations (cf. Fig. 2) have been averaged out by

$$\overline{\overline{V}}_{el}(z) = \int dz'\, dz''\, \omega_{GaN}(z - z') \times \omega_{AlN}(z - z') V_{el}(x,y,z''), \tag{11}$$

with

$$\omega_{GaN,AlN}(z) = \frac{1}{2d_{GaN,AlN}} \Theta(d_{GaN,AlN} - |z|). \tag{12}$$

Here, $d_{GaN,AlN}$ are the growth-direction interlayer distances of the c-GaN and strained c-AlN bulk materials, and Θ is the Heaviside function.

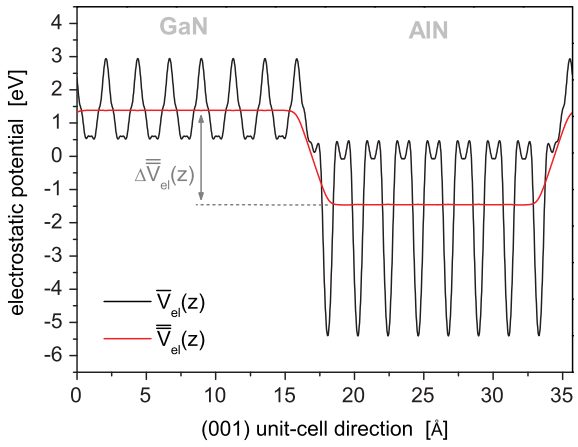

FIG. 2. (Color online) Microscopic planar average $\overline{V}_{el}(z)$ and macroscopic average $\overline{\overline{V}}_{el}(z)$ of the local electrostatic potential of the pseudomorphic GaN/AlN heterostructure. The local electrostatic potential was determined from a DFT-LDA calculation with PAW pseudopotentials and Ga d electrons treated as valence states.

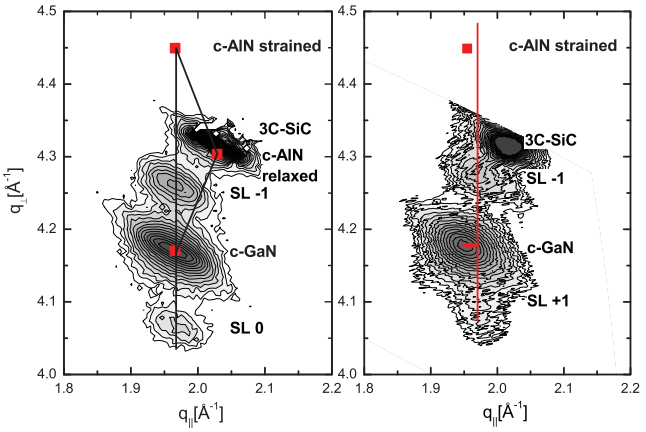

FIG. 3. (Color online) RSMs of samples A3 (left) and B2 (right) revealing strain in the SL structures. The SL in sample A3 is pseudomorphically strained to the GaN buffer while sample B2 shows partial relaxation.

III. RESULTS AND DISCUSSION

A. Experiment and model calculations

In the following paragraphs, the results of structural and optical characterizations and model calculations are summarized. The structural properties are characterized in Sec. III A 1. In Sec. III A 2, the results of inter-sub-band and interband spectroscopies are depicted. A detailed description of the model calculation results is given in Sec. III A 3.

1. Structural properties

The HRXRD reciprocal space maps (RSMs) of the asymmetric (113) reflection of samples A3 (left) and B2 (right) are shown in Fig. 3.

Both RSMs reveal two SL satellites, the reflexes of the substrate and the buffer and cap layers. As can be seen in the left-side diagram, the SL satellites have the same $q_\parallel$ like the c-GaN. We conclude that the SLs are pseudomorphically grown on the c-GaN buffer for series A, resulting in strained AlN barriers. The AlN layers are tensile strained to the GaN buffer due to the smaller lattice parameter of AlN with respect to GaN. As a result of the tensile strain, we find a reduction of the band-gap energy of the AlN of about 0.2–5.1 eV [see Eq. (3)]. The right diagram shows that the SL satellites do not have the same $q_\parallel$ as the c-GaN. Thus, we conclude that the SL is partially relaxed (maximum 30%) due to the higher total volume of AlN for series B. This partial relaxation results in an additional modification of the band gaps of well and barrier. The modified band gaps are 3.23 eV for GaN and 5.15 eV for AlN. These small modifications result in a change in ISBT energy, for example, less than 10 meV for sample B3 and, therefore, are neglected for further considerations. The structural properties of the samples are summarized in Table II.

2. Optical properties

Figure 4 shows normalized inter-sub-band absorption spectra of all samples under TM-polarized light.The spectra are fitted by Gaussian functions. The absorption spectra for series

TABLE II. Structural properties of the SLs obtained from HRXRD measurements and simulations.

Sample	d_{GaN} [nm]	d_{AlN} [nm]
A1	2.0	1.3
A2	2.2	1.3
A3	2.5	1.7
B1	5.0	3.0
B2	3.0	3.0
B3	1.8	3.0

A are taken from Ref. 67. Most of the spectra show oscillations from Fabry-Pérot interferences in the 10-μm-thick 3C-SiC layer. The absence of these oscillations for samples A1 and A3 is explained by larger interface roughnesses between 3C-SiC and Si. As shown in Fig. 4, all samples exhibit inter-sub-band absorption with a peak energy in the range of 0.3–0.9 eV. Furthermore, the absorption spectra of series B show a smaller full width at half maximum (FWHM) than series A. This may be explained by the thicker AlN barriers. AlN shows a tendency to smaller roughness and smooth interfaces.[5]

The measured PL spectra of our samples are plotted in Fig. 5.

From these, spectra transition energies of interband transitions from the lowest conduction-band level to the highest valence-band level are obtained. The FWHM of the PL lines is increasing with increasing PL transition energy, since the effect of monolayer (ML) thickness fluctuations is increasing with decreasing well width.

3. *Model calculations*

The ISBT and interband transition energies in our SLs are calculated with an effective mass model using nextnano.[3] From Eq. (5), we obtain a maximum effective electron mass of 0.15 m_0 for the largest confinement energy.

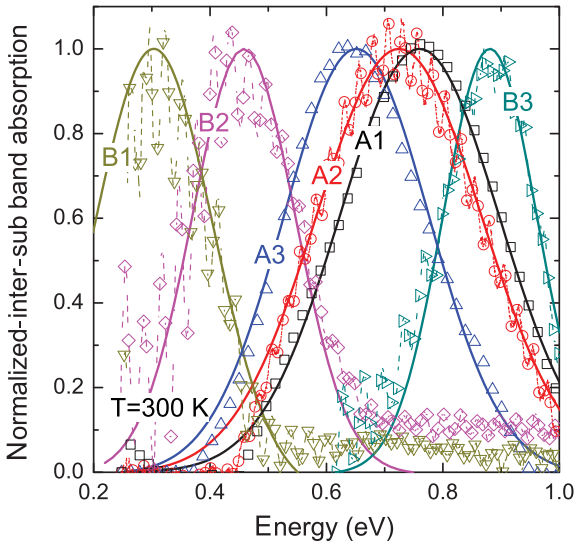

FIG. 4. (Color online) Normalized room-temperature inter-sub-band absorption spectra (symbols) fitted with Gaussian functions (lines).

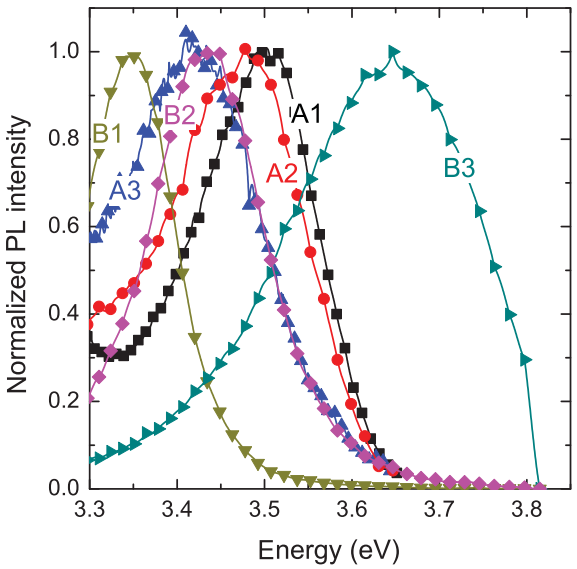

FIG. 5. (Color online) Normalized room-temperature PL spectra.

Figure 6 shows a comparison between measured and calculated ISBT energies.The symbols represent the experimental data. For fixed well and barrier widths, the CBO is one parameter that influences the ISBT energy. For our samples, we varied the CBO between 1.0 and 1.7 eV, which corresponds to a ratio of ΔE_c:ΔE_v between 50:50 and 90:10, respectively. The curves in Fig. 6 are calculated ISBT energies and are plotted versus the CBO. First, we see that the transition energy dependency on the CBO is increasing with decreasing well width and higher confinement energies consequently. Therefore, the samples with higher ISBT energies provide higher reliability of the determined CBO. We find good agreement for all samples assuming a CBO of 1.4 ± 0.1 eV

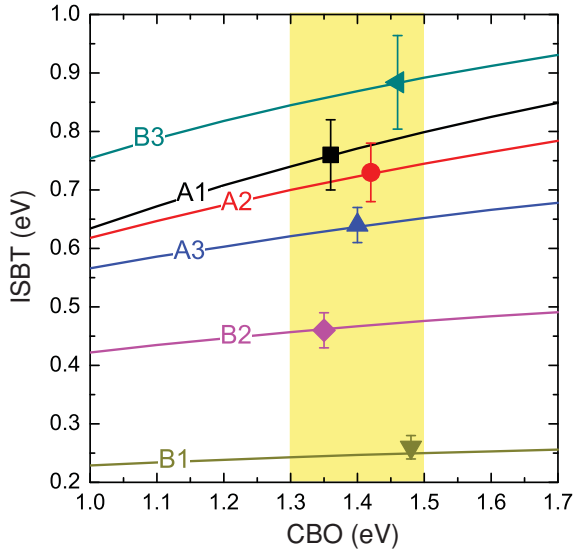

FIG. 6. (Color online) Calculated ISBT energy for different CBOs (lines) in comparison to experimental values (symbols). The bars indicate the calculated variation of the transition energy for a variation of the well width of ±1 ML.

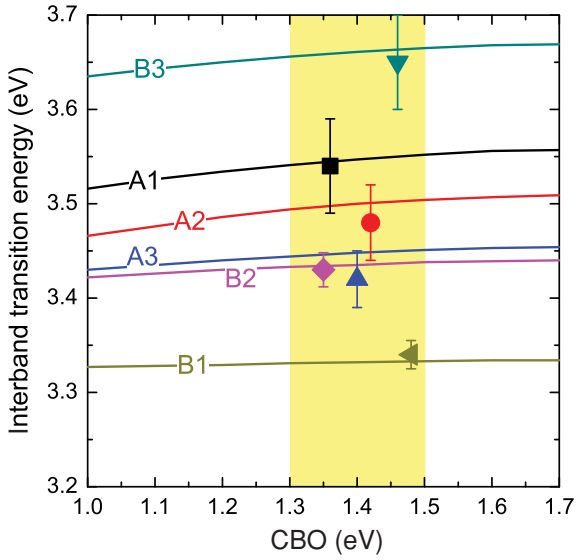

FIG. 7. (Color online) Calculated interband transition energy for different CBOs (lines) in comparison to experimental values (symbols). The bars indicate the calculated variation of the transition energy for a variation of the well width of ±1 ML.

resulting in $(74 \pm 5)\%$ of the band-gap differences ΔE_{gap} between GaN and AlN.

In Fig. 7, we compare calculated and measured interband transition energies.These studies verify the results of the ISBT investigations. All samples show good agreement within the uncertainty resulting from a variation of the calculated transition energy for a variation of the well width of ±1 ML. The band-offset dependency of the interband transition energy is larger for thinner QWs, e.g., samples A1, A2, A3, and B3. This results in smaller slopes of the calculated curves for thick QWs (B1, B2) than in thin QWs. Furthermore, we find that a 1-ML fluctuation in QW thickness results in a larger change of transition energy for thinner QWs. All experimental data show good agreement with our calculations based on the preliminarily determined band offsets and effective masses from inter-sub-band spectroscopy. In addition, a fluctuation in layer thickness of more than 1 ML cannot be excluded for larger well widths.

In summary, comparison of experimental ISBT and interband transition energies with model calculations gives evidence for a CBO in the range of 1.4 ± 0.1 eV. This value differs from experimental values for the hexagonal system where a CBO of 1.7 eV is found.[68] Although the local structure and bonding are very similar for both systems, there are significant differences. In contrast to our indirect c-AlN, the wurtzite AlN is a direct semiconductor with a 0.7-eV larger band gap.[69] Furthermore, the band gap of c-GaN is 0.19-eV smaller than in hexagonal GaN.[20] This may explain the differences in band offsets, although the local structure is very similar.

B. *Ab initio* calculations

In this section, we report and discuss the results of our *ab initio* calculations with the focus on band gaps, potential shifts, and band offsets.

TABLE III. Calculated band gaps of c-GaN and c-AlN. Approximations for the XC functional in the DFT calculation and the used GW methods are given in the first and second columns. For c-AlN, the direct and indirect band gaps are listed. Reported experimental values are $E_{\text{gap}}^{\text{GaN}}(\Gamma-\Gamma) = 3.3$ eV, $E_{\text{gap}}^{\text{AlN}}(\Gamma-\Gamma) = 5.9$ eV, and $E_{\text{gap}}^{\text{AlN}}(\Gamma-X) = 5.3$ eV.

Method		GaN	AlN	
XC	GW	$(\Gamma-\Gamma)$	$(\Gamma-\Gamma)$	$(\Gamma-X)$
LDA		1.67	4.15	3.22
LDA	G_0W_0	2.95	5.71	4.83
LDA	GW_0	3.13	6.00	5.13
LDA	GW	3.46	6.48	5.61
PBE		1.66	4.12	3.31
HSE03		2.70	5.25	4.32
HSE03	G_0W_0	3.45	6.28	5.31
HSE03	GW_0	3.55	6.44	5.47
HSE03	GW	3.73	6.70	5.73
HSE06		2.92	5.50	4.56
HSE06	G_0W_0	3.54	6.37	5.40
mod (30)HSE06	-	3.19	5.78	4.82
mod (30)HSE06	G_0W_0	3.65	6.50	5.52

1. *Band gaps*

The results of our band-gap calculations for c-GaN and c-AlN bulk materials carried out on the different levels of theory are summarized in Table III. Reported experimental reference values are $E_{\text{gap}}^{\text{GaN}}(\Gamma-\Gamma) = 3.3$ eV (Ref. 66), $E_{\text{gap}}^{\text{AlN}}(\Gamma-\Gamma) = 5.9$ eV (Ref. 19), and $E_{\text{gap}}^{\text{AlN}}(\Gamma-X) = 5.3$ eV (Ref. 19). The (semi)local XC functionals, LDA and PBE, perform equally bad and underestimate the band gaps of GaN by almost a factor of 2 and the indirect gap of AlN by 2 eV. We should note that the similarity of LDA and PBE values is due to the usage of experimental lattice constants in the bulk calculations. Differences in other calculations[70,71] are mainly due to different equilibrium lattice constants, obtained from an optimization of the supercell volume using LDA or PBE functionals. A significant improvement of band gaps on the DFT level is obtained by inclusion of exact exchange in the form of HSE-type functionals for both materials. For HSE03/HSE06, the GaN-gap underestimation is reduced to 0.6 eV/0.38 eV, and in the case of a modified exact-exchange percentage of 30% [cf. Eq. (6)], the underestimation of the experimental value is minimized to 0.11 eV. For AlN, the HSE functionals still underestimate the indirect band gap significantly. The best value for the indirect gap of 4.82 eV again, is obtained for an increased amount of Fock exchange but is still approximately half an eV too small. This behavior of HSE-type functionals exemplarily demonstrates the characteristics of this approach. Medium-sized band-gap materials (such as GaN) are reasonably described in HSE03 and HSE06. Especially, the band gap may be tuned to match the experiment by slight modifications of the exact-exchange fraction. In addition, the HSE06 functional tends to describe the midgap semiconductors slightly better than HSE03. In contrast to medium band-gap materials, band gaps of wide-gap semiconductors (such as AlN) cannot be described accurately by HSE-type functionals using a reasonable (i.e., universally

applicable) amount of exact exchange. The description of wide-gap materials should rather tend to the HF limit instead of showing significant screening properties that are described by HSE. Accordingly, a general HSE-DFT problem arises if, as in this study, midgap and wide-gap semiconductor-material properties are mixed up in a single system. In this case, the constant amount of Fock exchange cannot be changed in a way that both subsystems are described equally well.

The band-gap results for the various GW approaches exhibit a rather heterogeneous picture. Starting from DFT-LDA wave functions, the midgap material GaN is best described in a partially (LDA + GW_0) or fully (LDA + GW) self-consistent GW approach. In LDA + GW_0, W is fixed to its initial DFT value W_0, and G is repeatedly iterated a fixed number of steps or until self-consistency. In this paper, G is iterated four times with respect to the QP eigenvalues, which has proven to produce reliable QP energies.[72,73] The LDA + GW_0 band gap of 3.13 eV underestimates the measured value by 0.17 eV, which is comparable to the mod (30)HSE06 result without QP corrections. In LDA + GW calculations, W is iterated in the same way as G (i.e., four times). Since the iteration of G and W increases the band gap, the GaN band-gap underestimation is turned into almost the same overestimation of 0.16 eV. A single shot G_0W_0 correction to the LDA eigenvalues still suffers from an significant band-gap underestimation by 0.35 eV. These trends change by going to the HSE functional. Starting from HSE03 wave functions, an almost identical to LDA + GW GaN band gap is obtained in HSE03 + G_0W_0. HSE06 + G_0W_0 and mod (30)HSE06 + G_0W_0 tend to increase this overestimation. The GW_0 and GW calculations on top of the HSE03 calculation lead to an even stronger overestimation of the band gap by 0.25 and 0.43 eV.

For the wide-gap semiconductor AlN, the HSE + G_0W_0 approach gives reliable indirect band gaps that are within ± 0.2 eV of the experimental value. In HSE03 + G_0W_0, the calculated band gap of 5.31 eV is almost identical to the experimental value. On the LDA + G_0W_0 level, the DFT underestimation is not completely compensated by G_0W_0 QP shifts. In the partially self-consistent GW_0 scheme, the LDA result is significantly improved. The HSE03 GW_0 result shows a slight band-gap overestimation that becomes significantly worse in the self-consistent GW procedure with updated G and W. This self-consistency problem has been traced back to be mainly due to the neglect of vertex corrections[60] (i.e., electron-hole interaction) in the self-consistent independent QP (GW) approaches.

In conclusion, the best description of the common GaN/AlN system may be obtained by performing single shot G_0W_0 calculations on top of a HSE-type calculation obtained with a screening parameter and an exact-exchange percentage that represent the best compromise for describing both materials. In general, one could expect that the original HSE03/HSE06 parameters are the best choice in preparation of a G_0W_0 calculation. The conceptual and pragmatical advantages of this approach are that the best DFT wave functions (i.e., the wave functions closest to the QP wave functions) are used in a traditional first-order perturbation theory approach, thereby avoiding the necessity to think about corrections to the self-consistent GW cycle. Nevertheless, if self-consistency is desirable (as for QP corrections to LDA results), the combination of an iterated G and screening on the DFT level via W_0 leads to quite accurate results. This is due to a surprisingly good description of screening properties on the DFT level. Finally, we have to note that there is a significant overestimation of the reported experimental value for the direct AlN ($\Gamma - \Gamma$) gap, despite the accurate description of the indirect ($\Gamma - X$) gap.

TABLE IV. Calculated shifts of the macroscopically averaged electrostatic potential $\overline{\overline{V}}_{el}(z)$ [cf. Eq. (11)] of pseudomorphically strained and various DFT-optimized $(GaN)_8(AlN)_8(001)$ heterostructure-unit cells (cf. Fig. 1).

In-plane lattice constant	Electrostatic potential $\overline{\overline{V}}_{el}(z)$ [eV]		
	$a_{\text{exp}}^{\text{GaN}}$	$a_{\text{DFT}}^{\text{GaN}}$	$a_{\text{DFT}}^{\text{AlN}}$
LDA	3.12	2.82	2.84
PBE	2.71	2.81	2.83
HSE03	2.69		
HSE06	2.66		

2. Potential shifts

In Table IV, the shifts in the macroscopically averaged electrostatic potential across the heterostructure interface $\overline{\overline{V}}_{el}(z)$, as defined in Eq. (11), are summarized. Obviously, the potential shifts across the pseudomorphic $(GaN)_8(AlN)_8(001)$ unit cells are very similar for PBE- and HSE-type functionals. The actual difference between the PBE and the HSE potential shifts is <0.1 eV. These results indicate a similar description of structural properties of the c-group-III nitrides by PBE and HSE (i.e., the PBE equilibrium lattice constant is $a_{\text{GaN}}^{\text{PBE}} = 4.54$ Å and the HSE value is $a_{\text{GaN}}^{\text{HSE}} = 4.52$ Å as reported in Ref. 38). Since HSE-type calculations on the extended heterostructure-unit cells are computationally extremely demanding, therefore, it is a well-justified practice to use the DFT-PBE result to align the energy levels of the separate bulk calculations. Moreover, the self-consistent computation of the local electrostatic potential on the HSE level demonstrates one eminent advantage of the HSE approach. The HSE functionals allow a self-consistent calculation of the electronic structure in contrast to the perturbative GW implementations. Relaxing the heterostructure-unit cells in the growth direction yields a potential shift of 2.82 ± 0.02 eV. This potential shift is almost independent of the XC functional (LDA or PBE) and the particular supercell's in-plane lattice constant. The typical potential-step differences between growth-direction-optimized and pseudomorphic unit cells are about 0.2 eV with the exception of the LDA result. The larger deviation of the LDA value is due to the fact that the experimental lattice constant $a_{\text{GaN}} = 4.52$ Å , used to construct the pseudomorphic unit cell, leads to an atomic structure that is closer to the PBE energy minimum than to the LDA minimum ($a_{\text{GaN}}^{\text{LDA}} = 4.46$ Å).

3. Band offsets

Our QP VBOs and QP CBOs calculated from the fundamental band gaps in Table III, the potential shifts in

TABLE V. DFT and QP VBOs [Eq. (1)] and CBOs of the pseudomorphic $(GaN)_8(AlN)_8(001)$ heterostructure (cf. Fig. 1). The last column lists the ΔE_c:ΔE_v ratios.

		Band offsets [eV]		
XC functional	GW method	ΔE_v	ΔE_c	Ratio
LDA		0.73	0.82	53:47
LDA	G_0W_0	0.91	0.98	52:48
PBE		0.37	1.28	78:22
PBE	G_0W_0	0.54	1.32	71:29
HSE03		0.43	1.20	74:26
HSE03	G_0W_0	0.58	1.29	69:31
HSE06		0.42	1.22	74:26
HSE06	G_0W_0	0.56	1.31	70:30
Experimental[a]		0.5 ± 0.1	1.4 ± 0.1	74(±5):26(±5)

[a]This paper.

Table IV, and the corresponding valence-band maxima are listed in Table V. As discussed for the band gaps, we focus on the G_0W_0 approach to QP energies. The QP-band alignment, on the LDA + G_0W_0, HSE06, and HSE06 + G_0W_0 levels of theory, is additionally depicted in Fig. 8. All our calculations unambiguously predict, in agreement with the experiment, a type-I SL-band alignment between the c phases of the III-V semiconductor materials GaN and AlN. Most obviously, the obtained HSE and HSE + G_0W_0 VBOs are significantly smaller than the LDA values. The main reason for this difference is, as described in Sec. III B 2, the larger potential shift at the interface in LDA calculations, which is mainly due to the pseudomorphically strained SL unit used in our calculations. Taking a fully structural relaxation of the GaN/AlN SL into account, with an in-plane lattice constant fixed to the optimized LDA lattice constant of GaN (see Table IV), the resulting VBO/CBO is 0.43 eV/1.12 eV and 0.61 eV/1.28 eV by inclusion of G_0W_0 QP corrections. By doing the same for the PBE functional, we obtain a VBO/CBO of 0.47 eV/1.18 eV and 0.64 eV/1.22 eV with QP corrections. Therefore, the LDA and PBE functionals lead to very similar results for SLs that are not artificially strained. In the same way, these values are closer to the HSE results. Analyzing the G_0W_0 results, a general trend for calculated QP energies is observable. Besides the band gaps, the single shot G_0W_0 QP shifts also affect the valence-band maxima of GaN and AlN differently. In agreement with previous studies,[74] this leads to a slight increase ($\leqslant 0.2$ eV) of the VBOs. For LDA, the VBO increases by 0.18 eV, for HSE functionals, the VBOs increase by about 0.15 eV.

We note that our LDA and LDA + G_0W_0 band offsets of the pseudomorphic structure are comparable to other reported values by various authors for zinc-blende GaN/AlN SLs. Albanesi *et al.*[75] obtained a VBO of 0.85 eV using a linear muffin-tin orbital method. Wei and Zunger[76] obtained a similar value of 0.84 eV using a DFT-LDA method. A larger DFT-LDA result of 0.98 eV has been reported by Binggeli *et al.*[77] for a GaN/AlN SL pseudomorphically strained to the AlN lattice constant. Cociorva *et al.*[74] calculated G_0W_0 corrections on top of a DFT-LDA approach and obtained a VBO/CBO of 0.76 eV/0.78 eV for an optimized SL unit cell with a GaN in-plane lattice constant. Altogether, the LDA-based results are, compared to our experimental results, clearly inferior to the HSE-based calculations with and without many-body corrections. Besides the VBOs, the remarkable quality of the HSE-functional calculations is evident by looking at the band-offset ratio ΔE_c:ΔE_v. The experimental band-offset ratio of 74(±5):26(±5) is well reproduced by the HSE-type XC functionals. Moreover, calculated QP-band offsets tend to predict a very similar 70:30 ratio. The most accurate VBO and CBO ($\Delta E_v = 0.56$ eV and $\Delta E_c = 1.31$ eV) are obtained by HSE06 + G_0W_0 calculations.

One concluding comment on CBOs and the predictive capability of *ab initio* band-offset calculations: Calculated by DFT-related methods, the CBOs always reflect the methods ability to describe unoccupied electronic states. Therefore, results on the LDA/PBE-DFT level, suffering from the serious band-gap underestimation, are not reliable for predicting CBOs. For the considered material system, our hybrid-functional DFT calculations, especially with the inclusion of many-body corrections, allow the calculation of CBOs, with relevant predictive power (i.e., within a relative error of ~ 0.1 eV for the band offsets and an absolute error of ~ 0.2 eV for the band gaps). The present calculations further indicate that standard DFT results using the LDA or PBE functionals are less reliable for predicting VBOs than hybrid functionals. Nevertheless, to establish general trends in the description of semiconductor band offsets by hybrid functionals with

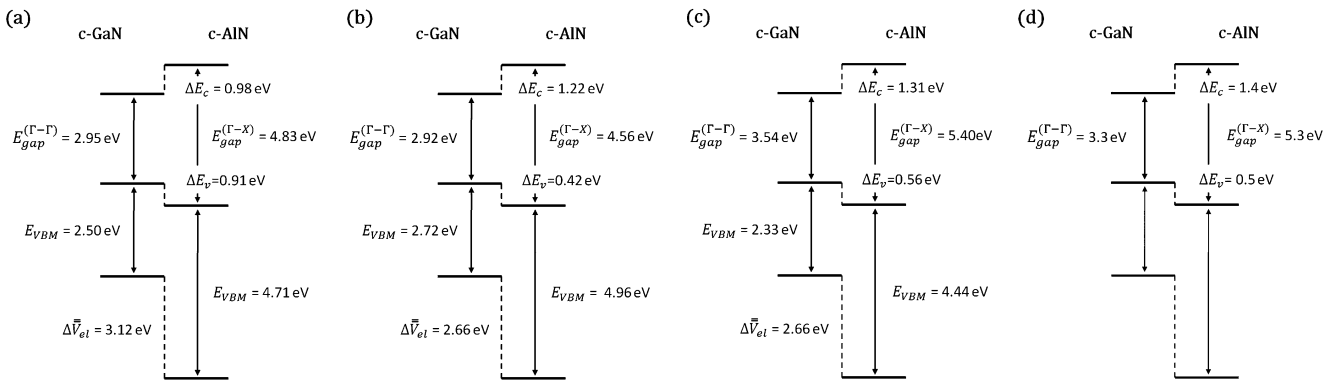

FIG. 8. Schematic of the calculated type-I QP-band alignment for (a) LDA + G_0W_0, (b) HSE06, (c) HSE06 + G_0W_0, and (d) experimental results.

and without QP corrections within the GW approach, a further analysis of band offsets in heterostructures composed of different technologically relevant semiconductor materials remains necessary.

IV. SUMMARY

High-quality c-GaN/AlN SLs were fabricated using PA-MBE. We determined the ratio of CBO to VBO between c-GaN and c-AlN in our structures by the analysis of ISBT and interband transition energies. For the calculation of ISBT and interband transition energies, the CBO was varied using the structural properties known from HRXRD. Optimal agreement between calculated and experimental data was achieved for a CBO-to-VBO ratio of (74:26)% within an accuracy of ±5% of the band-gap difference ΔE_{gap}.

For all QWs, an energy dependency of effective masses was taken into account to fit the experimental values. These values were verified by the analysis of interband transition energies of our samples in comparison to calculated values using the CBO obtained from inter-sub-band spectroscopy and model calculations.

Furthermore, we have demonstrated that state-of-the-art hybrid-functional DFT calculations and the inclusion of many-body corrections on the G_0W_0 level are able to reproduce the experimental VBO and CBO within 0.1-eV accuracy.

Finally, we conclude that our comprehensive experimental and theoretical results give strong evidence for a CBO of (1.4 ± 0.1) eV and a VBO of (0.5 ± 0.1) eV in c-GaN/AlN SL structures.

ACKNOWLEDGMENTS

This work was financially supported by the Deutsche Forschungsgemeinschaft (Projects No. As 107/4-1 and No. SCHM 1361/11-1). The financial support by the EC FET-OPEN program Unitride under Grant No. ga#233950 and the French National Research Agency Project Cosni Grant No. ANR-08-BLAN-0298-01 is acknowledged. The calculations were performed using grants of computer time from the Paderborn Center for Parallel Computing (PC2) and the High Performance Computing Center Stuttgart (HLRS).

[1] H. Machhadani, P. Kandaswamy, S. Sakr, A. Vardi, A. Wirtmüller, L. Nevou, F. Guillot, G. Pozzovivo, M. Tchernycheva, A. Lupu, L. Vivien, P. Crozat, E. Warde, C. Bougerol, S. Schacham, G. Strasser, G. Bahir, E. Monroy, and F. H. Julien, New J. Phys. **11**, 125023 (2009).

[2] D. As, Microelectron. J. **40**, 204 (2009).

[3] S. V. Novikov, C. T. Foxon, and A. J. Kent, Phys. Status Solidi A **207**, 1277 (2010).

[4] J. Schörmann, S. Potthast, D. J. As, and K. Lischka, Appl. Phys. Lett. **89**, 131910 (2006).

[5] T. Schupp, K. Lischka, and D. J. As, J. Cryst. Growth **312**, 1500 (2010).

[6] E. Tschumak, R. Granzner, J. K. N. Lindner, F. Schwierz, K. Lischka, H. Nagasawa, M. Abe, and D. J. As, Appl. Phys. Lett. **96**, 253501 (2010).

[7] N. Zainal, S. V. Novikov, C. J. Mellor, C. T. Foxon, and A. J. Kent, Appl. Phys. Lett. **97**, 112102 (2010).

[8] J. E. A. DeCuir, E. Fred, M. O. Manasreh, J. Schörmann, D. J. As, and K. Lischka, Appl. Phys. Lett. **91**, 041911 (2007).

[9] H. Machhadani, M. Tchernycheva, S. Sakr, L. Rigutti, R. Colombelli, E. Warde, C. Mietze, D. J. As, and F. H. Julien, Phys. Rev. B **83**, 075313 (2011).

[10] A. Baldereschi, S. Baroni, and R. Resta, Phys. Rev. Lett. **61**, 734 (1988).

[11] L. Kleinman, Phys. Rev. B **24**, 7412 (1981).

[12] O. Brandt, P. Waltereit, and K. H. Ploog, J. Phys. D **35**, 577 (2002).

[13] nextnano^3 device simulator: The program is available at [www.wsi.tum.de/nextnano3 and www.nextnano.de].

[14] A. Trellakis, T. Zibold, T. Andlauer, S. Birner, R. K. Smith, R. Morschl, and P. Vogl, J. Comp. Elec. **5**, 285 (2006).

[15] S. Birner, S. Hackenbuchner, M. Sabathil, G. Zandler, J. A. Majewski, T. Andlauer, T. Zibold, R. Morschl, A. Trellakis, and P. Vogl, Acta Phys. Pol. A **110**, 111 (2006).

[16] M. Städele and K. Hess, J. Appl. Phys. **88**, 6945 (2000).

[17] E. O. Kane, J. Phys. Chem. Solids **1**, 249 (1957).

[18] C. Wetzel, R. Winkler, M. Drechsler, B. K. Meyer, U. Rössler, J. Scriba, J. P. Kotthaus, V. Härle, and F. Scholz, Phys. Rev. B **53**, 1038 (1996).

[19] M. Röppischer, R. Goldhahn, G. Rossbach, P. Schley, C. Cobet, N. Esser, T. Schupp, K. Lischka, and D. J. As, J. Appl. Phys. **106**, 076104 (2009).

[20] V. Bougrov, M. Levinshtein, S. Rumyantsev, and A. Zubrilov, *Properties of Advanced Semiconductor Materials GaN, AlN, InN, BN, SiC, SiGe* (Wiley, New York, 2001).

[21] I. Petrov, E. Mojab, R. C. Powell, J. E. Greene, L. Hultman, and J.-E. Sundgren, Appl. Phys. Lett. **60**, 2491 (1992).

[22] M. Mizuta, S. Fujieda, Y. Matsumoto, and T. Kawamura, Jpn. J. Appl. Phys., Part 2 **25**, L945 (1986).

[23] S. K. Pugh, D. J. Dugdale, S. Brand, and R. A. Abram, Semicond. Sci. Technol. **14**, 23 (1999).

[24] W. J. Fan, M. F. Li, T. C. Chong, and J. B. Xia, J. Appl. Phys. **79**, 188 (1996).

[25] C. G. V. de Walle and J. Neugebauer, Appl. Phys. Lett. **70**, 2577 (1997).

[26] K. Kim, W. R. L. Lambrecht, and B. Segall, Phys. Rev. B **53**, 16310 (1996).

[27] P. Rinke, M. Winkelnkemper, A. Qteish, D. Bimberg, J. Neugebauer, and M. Scheffler, Phys. Rev. B **77**, 075202 (2008).

[28] J. W. Orton, Semicond. Sci. Technol. **12**, 64 (1997).

[29] P. Hohenberg and W. Kohn, Phys. Rev. **136**, B864 (1964).

[30] W. Kohn and L. J. Sham, Phys. Rev. **140**, A1133 (1965).

[31] P. E. Blöchl, Phys. Rev. B **50**, 17953 (1994).

[32] G. Kresse and D. Joubert, Phys. Rev. B **59**, 1758 (1999).

[33] G. Kresse and J. Furthmller, Comput. Mater. Sci. **6**, 15 (1996).

[34] D. M. Ceperley and B. J. Alder, Phys. Rev. Lett. **45**, 566 (1980).

[35] J. P. Perdew and A. Zunger, Phys. Rev. B **23**, 5048 (1981).

[36]J. Heyd, G. E. Scuseria, and M. Ernzerhof, J. Chem. Phys. **118**, 8207 (2003).
[37]J. Heyd and G. E. Scuseria, J. Chem. Phys. **121**, 1187 (2004).
[38]J. Heyd, J. E. Peralta, G. E. Scuseria, and R. L. Martin, J. Chem. Phys. **123**, 174101 (2005).
[39]J. Heyd, G. E. Scuseria, and M. Ernzerhof, J. Chem. Phys. **124**, 219906 (2006).
[40]J. P. Perdew, Int. J. Quantum Chem. **28**, 497 (1985).
[41]J. P. Perdew and M. Levy, Phys. Rev. Lett. **51**, 1884 (1983).
[42]L. J. Sham and M. Schlüter, Phys. Rev. Lett. **51**, 1888 (1983).
[43]O. A. Vydrov and G. E. Scuseria, J. Chem. Phys. **121**, 8187 (2004).
[44]J. P. Perdew, M. Ernzerhof, and K. Burke, J. Chem. Phys. **105**, 9982 (1996).
[45]M. Ernzerhof, J. P. Perdew, and K. Burke, Int. J. Quantum Chem. **64**, 285 (1997).
[46]C. Adamo and V. Barone, J. Chem. Phys. **110**, 6158 (1999).
[47]M. Ernzerhof and G. E. Scuseria, J. Chem. Phys. **110**, 5029 (1999).
[48]J. P. Perdew, K. Burke, and M. Ernzerhof, Phys. Rev. Lett. **77**, 3865 (1996).
[49]A. V. Krukau, O. A. Vydrov, A. F. Izmaylov, and G. E. Scuseria, J. Chem. Phys. **125**, 224106 (2006).
[50]T. M. Henderson, J. Paier, and G. E. Scuseria, Phys. Status Solidi B **248**, 767 (2011).
[51]J. W. Nicklas and J. W. Wilkins, Appl. Phys. Lett. **97**, 091902 (2010).
[52]H.-P. Komsa, P. Broqvist, and A. Pasquarello, Phys. Rev. B **81**, 205118 (2010).
[53]However, the admixing of $\frac{1}{4}$ exact exchange has been rationalized by perturbation theory.[44]
[54]L. Hedin, Phys. Rev. **139**, A796 (1965).
[55]L. Hedin and S. Lundqvist, in *Solid State Physics*, edited by F. Seitz, D. Turnbull, and H. Ehrenreich (Academic, New York, 1965), Vol. 23.
[56]M. S. Hybertsen and S. G. Louie, Phys. Rev. B **32**, 7005 (1985).
[57]M. S. Hybertsen and S. G. Louie, Phys. Rev. B **34**, 5390 (1986).
[58]Details of VASP implementation are given in Refs. 59– 62.
[59]M. Shishkin and G. Kresse, Phys. Rev. B **75**, 235102 (2007).
[60]M. Shishkin, M. Marsman, and G. Kresse, Phys. Rev. Lett. **99**, 246403 (2007).
[61]M. Shishkin and G. Kresse, Phys. Rev. B **74**, 035101 (2006).
[62]F. Fuchs, J. Furthmüller, F. Bechstedt, M. Shishkin, and G. Kresse, Phys. Rev. B **76**, 115109 (2007).
[63]J. Paier, M. Marsman, and G. Kresse, Phys. Rev. B **78**, 121201 (2008).
[64]H. J. Monkhorst and J. D. Pack, Phys. Rev. B **13**, 5188 (1976).
[65]T. Lei, T. D. Moustakas, R. J. Graham, Y. He, and S. J. Berkowitz, J. Appl. Phys. **71**, 4933 (1992).
[66]I. Vurgaftman, J. R. Meyer, and L. R. Ram-Mohan, J. Appl. Phys. **89**, 5815 (2001).
[67]C. Mietze, E. A. DeCuir, M. O. Manasreh, K. Lischka, and D. J. As, Phys. Status Solidi C **7**, 1610 (2010).
[68]M. Tchernycheva, L. Nevou, L. Doyennette, F. H. Julien, E. Warde, F. Guillot, E. Monroy, E. Bellet-Amalric, T. Remmele, and M. Albrecht, Phys. Rev. B **73**, 125347 (2006).
[69]Q. Guo, A. Yoshida, Jpn. J. Appl. Phys., Part 1 **33**, 2453 (1994).
[70]A. F. Wright and J. S. Nelson, Phys. Rev. B **51**, 7866 (1995).
[71]C. Stampfl and C. G. Van de Walle, Phys. Rev. B **59**, 5521 (1999).
[72]T. Kotani, M. van Schilfgaarde, and S. V. Faleev, Phys. Rev. B **76**, 165106 (2007).
[73]S. Lany and A. Zunger, Phys. Rev. B **81**, 113201 (2010).
[74]D. Cociorva, W. G. Aulbur, and J. W. Wilkins, Solid State Commun. **124**, 63 (2002).
[75]E. A. Albanesi, W. R. L. Lambrecht, and B. Segall, J. Vac. Sci. Technol. B **12**, 2470 (1994).
[76]S.-H. Wei and A. Zunger, Appl. Phys. Lett. **72**, 2011 (1998).
[77]N. Binggeli, P. Ferrara, and A. Baldereschi, Phys. Rev. B **63**, 245306 (2001).

Paper II

The electronic structure and optical response of rutile, anatase and brookite TiO_2

M. Landmann, E. Rauls, and W. G. Schmidt, JOURNAL OF PHYSICS: CONDENSED MATTER **24**, 195503, 6 pp. (2012) – JPCM 2012 Highlight Paper

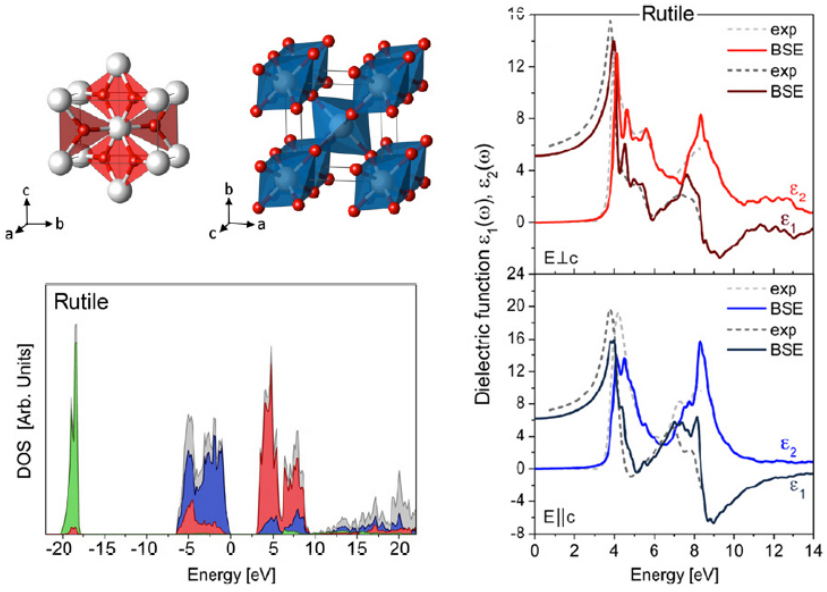

J. Phys.: Condens. Matter **24** (2012) 195503 (6pp) doi:10.1088/0953-8984/24/19/195503

The electronic structure and optical response of rutile, anatase and brookite TiO_2

M Landmann, E Rauls and W G Schmidt

Lehrstuhl für Theoretische Physik, Universität Paderborn, D-33095 Paderborn, Germany

E-mail: landmann@mail.upb.de

Received 4 January 2012, in final form 21 March 2012
Published 19 April 2012
Online at stacks.iop.org/JPhysCM/24/195503

Abstract

In this study, we present a combined density functional theory and many-body perturbation theory study on the electronic and optical properties of TiO_2 brookite as well as the tetragonal phases rutile and anatase. The electronic structure and linear optical response have been calculated from the Kohn–Sham band structure applying (semi)local as well as nonlocal screened hybrid exchange–correlation density functionals. Single-particle excitations are treated within the GW approximation for independent quasiparticles. For optical response calculations, two-particle excitations have been included by solving the Bethe–Salpeter equation for Coulomb correlated electron–hole pairs. On this methodological basis, gap data and optical spectra for the three major phases of TiO_2 are provided. The common characteristics of brookite with the rutile and anatase phases, which have been discussed more comprehensively in the literature, are highlighted. Furthermore, the comparison of the present calculations with measured optical response data of rutile indicate that discrepancies discussed in numerous earlier studies are due to the measurements rather than related to an insufficient theoretical description.

(Some figures may appear in colour only in the online journal)

1. Introduction

Of the manifold of synthesizable crystalline TiO_2 polymorphs, mainly the three crystal types rutile {crystal system: tetragonal ($4/mmm$), space group: $P4_2/mnm$–D_{4h}^{14}}, anatase {tetragonal ($4/mmm$), $I4_1/amd$–D_{4h}^{19}} and brookite {orthorhombic (mmm), $Pbca$–D_{2h}^{15}} are found in nature. Only the first two play a significant role in industrial applications. Experimental data on TiO_2 brookite is limited due to its rareness and difficult preparation [1].

As a semiconductor material with long-term stability, non-toxic environmental acceptability and broadly low cost availability TiO_2 has also been taken into account for photovoltaic applications. However, due to optical gaps slightly above 3 eV (rutile: ∼3.0 eV [3, 4], anatase: ∼3.4 eV [5] and brookite: ∼3.3 eV [6]), natural TiO_2 is only photoactive in the UV region of the electromagnetic spectrum and an inefficient active solar cell material. Still, the material advantages of TiO_2 can be used indirectly in technically and economically viable dye-sensitized solar cells [7–9] where it acts as an electron-transporting substrate for a chemisorbed photoactive dye.

The structure of the three main phases is well characterized by the two complementary Ti_xO_y building-block representations pictured in figure 1. The most common representation is the view of the crystal structures as networks of edge- and/or corner-linked distorted TiO_6 octahedron building blocks. Rutile and brookite exhibit corner—as well as edge-sharing TiO_6 units. In rutile, the O_h symmetry of an ideal octahedron is reduced to D_{2h} symmetry due to different in-plane (equatorial) and out-of-plane (axial) Ti–O bond lengths and two types of Ti–O–Ti in-plane bond angles deviating from 90°. In the anatase phase, additional displacements of the O ions from the equatorial positions generate a local D_{2h} symmetry seen by the Ti ions. Due to stronger distortions in TiO_2 brookite, all bond lengths and

 © 2012 IOP Publishing Ltd Printed in the UK & the USA

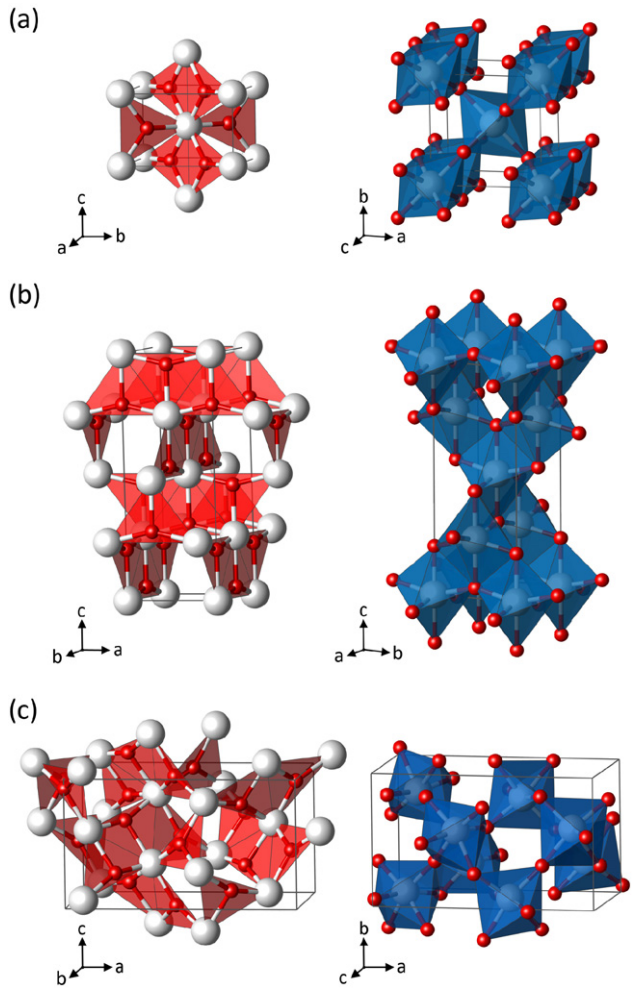

Figure 1. Planar Ti_3O building-block representation (left) and TiO_6 polyhedra (right) for the TiO_2 phases rutile (a), anatase (b) and brookite (c) (Ti (white); O (red)). The experimental lattice parameters $a = b = 4.5937$ Å, $c = 2.9581$ Å for rutile [10], $a = b = 3.7842$ Å, $c = 9.5146$ Å for anatase [11] and $a = 9.16$ Å, $b = 5.43$ Å, $c = 5.13$ Å for brookite [12] have been used throughout this work.

bond angles slightly differ from each other, thus leading to the formal loss of local symmetry and C_1 symmetric TiO_6 units.

A complementary view of the crystal structure is given by the threefold coordination of O ions in trigonal-planar-type Ti_3O building blocks. While the Ti_3O units exhibit a Y-shaped conformation in rutile, the anatase units are closer to a T-shape. In brookite, both T- and Y-shaped Ti_3O units are present.

The linear optical absorption properties of rutile have been investigated, among other studies, in reflection measurements by Cardona and Harbeke [13] and in a more recent reflection-generalized ellipsometry study by Tiwald and Schubert [14]. Their results have demonstrated the characteristic anisotropy in the optical absorption for $E \parallel c$ (extraordinary polarization) and $E \perp c$ (ordinary polarization). However, the reported dielectric functions show significant deviations. In the Cardona–Harbeke data the spectral weight on the first main peak at ∼4 eV is much more pronounced for $E \parallel c$ than for $E \perp c$. In contrast, more recently published data by Tiwald and Schubert indicate a less intense peak for $E \parallel c$ at ∼4 eV. Also, the existence of distinct second main peaks above 6.5 eV in both polarizations, observed in the newer data, is not resolved in the Cardona–Harbeke data either. The anisotropies in the optical functions of anatase for $E \parallel c$ and $E \perp c$ have been characterized, among others, by Hosaka *et al* [15]. The optical properties of brookite TiO_2 have been investigated in the last few years by several experimental studies [17–21, 6], predominantly focusing on the absorption edge.

Several density functional theory (DFT)-based studies on various TiO_2 phases (mainly rutile and anatase) have been published so far [22–31]. The improved description of the electronic structure by hybrid-functional schemes has been discussed in the literature [32–37]. Recently, some studies have investigated many-body effects (self-energy corrections and excitonic effects) on the optical absorption [38–40] of rutile and anatase. Lawler *et al* investigated the birefringence of the oxides TiO_2 including excitonic effects from the solution of the Bethe–Salpeter equation (BSE). Kang and Hybertson [40] as well as Chiodo *et al* [39] both applied many-body perturbation theory (MBPT) methods (i.e. GW approximation and BSE) to calculate optical properties. Their results have clearly demonstrated the necessity of quasiparticle corrections to reproduce experimental photoemission bandgap data as well as the importance of including electron–hole interaction in the simulation of the optical response of the two tetragonal polytypes rutile and anatase. So far, a similar investigation for the more complex brookite phase, whose symmetry-reduced structure might indicate how optical characteristics in TiO_2 are affected by increasing disorder, is still missing.

Several authors [39, 40] have attributed the observed differences between the theoretical dielectric function and the experimental data of Cardona and Harbeke [13], among other reasonings, to possible deficiencies of the BSE formalism in describing all spectral features of the TiO_2 rutile phase. However, as we will demonstrate in light of our numerical results and the comparison with the data published by Tiwald and Schubert [14], there is strong evidence for an insufficient description of the optical properties of rutile by the Cardona–Harbeke data.

2. Methodology

We have performed DFT calculations [41, 42] using the projector-augmented wave (PAW) method [43, 44] as implemented in the Vienna *ab initio* simulation package (VASP) [45]. An energy cutoff of 400 eV was used to expand the Kohn–Sham orbitals into plane wave basis sets. In addition to the 3d and 4s valence states, the 3s and 3p semicore states of Ti have been explicitly treated as valence states throughout this work. We applied both the standard generalized gradient approximation (GGA) exchange–correlation (XC) functional according to Perdew–Burke–Ernzerhof (PBE) [46] as well as a modern nonlocal, range-separated, screened Coulomb potential hybrid density functional proposed by Heyd,

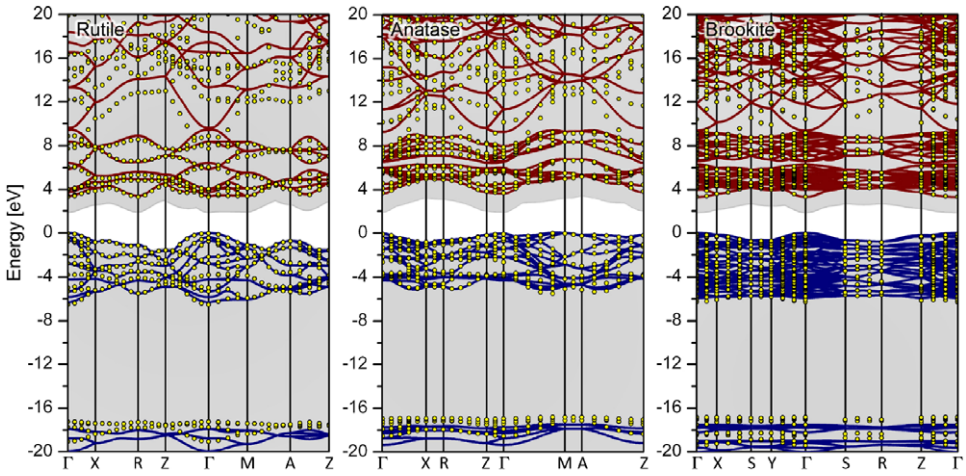

Figure 2. TiO_2 band structures for the rutile (left), anatase (middle) and brookite (right) polymorphs. Pictured are the DFT–HSE06 band structure as well as QP energies (dots) obtained from PBE–G_0W_0 calculations. The gray shaded areas correspond to energies below the highest valence band and above the lowest conduction band from DFT–PBE calculations. For PBE and HSE06 eigenvalues the valence band maximum has been chosen as the zero point of the energy scale. G_0W_0 QP energies are given with respect to DFT–PBE energy scale. The HSE06 calculations have been carried out with regular $7 \times 7 \times 11$, $9 \times 9 \times 3$ and $3 \times 5 \times 5$ Γ-centered *k*-point meshes for rutile anatase and brookite. The various high symmetry lines were additionally sampled by 40 *k*-points to obtain the HSE06 band structure. For rutile, anatase and brookite, the GW calculations were carried out on top of DFT–PBE calculations with 192, 384 and 768 electronic bands, regular $8 \times 8 \times 12$, $10 \times 10 \times 4$ and $4 \times 6 \times 6$ Γ-centered *k*-point meshes, and 192 frequency points for sampling the dielectric function. These numerical parameters provide bandgaps converged within about 0.02 eV accuracy, as tested for the case of rutile.

Scuseria and Ernzerhof (HSE06) [47–50] that corrects, to a large part, the bandgap underestimation in standard DFT.

Quasiparticle (QP) corrections due to self-energy effects within the GW approximation have been included perturbatively in a full-frequency-dependent G_0W_0 scheme (for details on VASP implementation see [51–54]) on top of DFT–PBE and DFT–HSE06 calculations.

In order to account for excitonic contributions and local field effects, the Coulomb correlation of (quasi-)electrons and (quasi-)holes is included by solution of the Bethe–Salpeter equation [55–60] in the Tamm–Dancoff approximation. Instead of an unfavorable $\mathcal{O}\left(N^3\right)$ scaling diagonalization of the electron–hole pair Hamiltonian, the calculation of the frequency-dependent dielectric function is performed by an $\mathcal{O}\left(N^2\right)$ scaling time-evolution scheme proposed by Schmidt *et al* [61].

3. Results and discussion

3.1. Electronic properties

The electronic band structures of the three TiO_2 modifications rutile, anatase and brookite are shown in figure 2. Besides HSE06 and G_0W_0 results, the DFT–PBE band edge positions are included to demonstrate the DFT–PBE underestimation of the electronic bandgap. The fundamental bandgaps have been summarized in table 1. The rutile and brookite PBE gaps of 1.88 and 1.86 eV are direct (d) at Γ. However, the Γ-point conduction band minimum in rutile is almost degenerate with the local R and minima M (0.03 and 0.05 eV higher in energy). For anatase, an indirect (id) energy gap of 1.94 eV is observed between the conduction band minimum at Γ and the valence band maximum along the Σ path ($0.88\Gamma \rightarrow$ M), that is marginally smaller than the direct Γ-point gap of 2.07 eV. Using the HSE06 hybrid functional, the bandgaps of rutile, anatase and brookite are increased to 3.39 eV (d), 3.60 eV (id) and 3.30 eV (d), which follows the trends in previous hybrid-functional studies [27, 32, 33, 35, 37].

Table 1. Calculated fundamental bandgaps (given in eV) of the TiO_2 main phases.

	Fundamental bandgaps		
Method	Rutile	Anatase	Brookite
DFT–PBE	1.88 (Γ → Γ)	1.94 ($0.88\Sigma \rightarrow \Gamma$)	1.86 (Γ → Γ)
DFT–HSE06	3.39 (Γ → Γ)	3.60 ($0.89\Sigma \rightarrow \Gamma$)	3.30 (Γ → Γ)
PBE–G_0W_0	3.46 (Γ → Γ)	3.73 (Σ → Γ)	3.45 (Γ → Γ)
HSE06–G_0W_0	3.73 (Γ → Γ)	4.05 (Σ → Γ)	3.68 (Γ → Γ)

Our full-frequency-dependent G_0W_0 calculations predict QP gaps of 3.46 eV (d) for rutile, 3.73 eV (id) for anatase and 3.45 eV (d) for brookite. These results are slightly (0.1–0.15 eV) above the HSE06 values, thus demonstrating that the QP characteristics of TiO_2 are well approximated by the HSE06 functional. The rutile and anatase bandgaps are comparable to the G_0W_0 QP gaps of 3.34 eV (Γ → R)/3.38 eV (Γ → Γ) and 3.56 eV (id) recently reported by Kang and Hybertson [40] as well as close to the 3.59 eV (d) and 3.83 eV (id) reported by Chiodo *et al* [39].

The HSE06 functional reproduces the G_0W_0 QP bands close to the band edges with high accuracy (cf figure 2). This conformity becomes significantly worse further away from the band edges as demonstrated by HSE06 O_{2s} states ∼0.7 eV below the G_0W_0 QP energies.

We also tested the influence of different initial wavefunctions by calculating G_0W_0 QP shifts for HSE06 wavefunctions which increases the QP gaps by 0.40 ± 0.05 eV

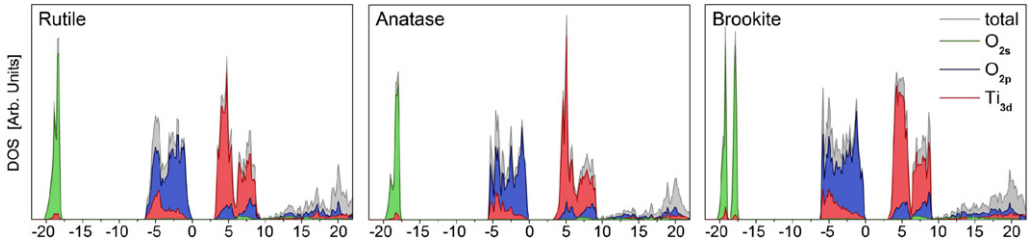

Figure 3. Total and angular momentum decomposed densities of states for the three TiO_2 crystal polymorphs rutile, anatase and brookite calculated with the HSE06 XC functional. Shown are the Ti_{3d}, O_{2s} and O_{2p} contributions to the local densities of states.

(cf table 1). Similar to the HSE06–G_0W_0 value of 3.73 eV, a bandgap of 3.67 eV is obtained for TiO_2 rutile if partial self-consistency in the Green's function G is included by updating the eigenvalues four times.

Experimentally, QP properties are probed by direct and inverse photoemission spectroscopy (IPS). For rutile, Tezuka *et al* [62] reported a bandgap of 3.3 ± 0.5 eV (d) from combined photoemission and bremsstrahlung isochromat spectroscopy. In a combined ultraviolet photoemission spectroscopy (UPS) and IPS study [63], a bandgap of 3.6 eV (d) has been determined. This means that the HSE06 and PBE–G_0W_0 rutile bandgaps of 3.39 and 3.46 eV agree very well with the experimental data range. By taking into account a bandgap of ∼4 eV from angle-resolved photoemission spectroscopy [23], the HSE06–G_0W_0 bandgap of 3.73 is also a reasonable result. Due to missing photoemission data, QP gaps of ∼3.7 eV for anatase and ∼3.5 eV for brookite could only be estimated from the smaller optical gaps by assuming similar trends as obtained for rutile. Consequently, the HSE06 and PBE–G_0W_0 calculations provide reliable bandgap data on crystalline TiO_2.

An analysis of the density of states (DOS), depicted in figure 3, shows predominantly O_{2p}-like valence band states and Ti_{3d}-like conduction band states around the band edges for all three major phases. As indicated in the DOS and band structures, the broad Ti_{3d}-like bands show a distinct separation into two sub-bands. This inner conduction band structure is connected to the distorted-octahedron-type short-range order described in the introductory section and descriptively derivable from the crystal-field theory of transition-metal (di)oxide complexes [64]. In an octahedral-type crystal field, the five unoccupied d-states of the central Ti ion are split into the twofold-degenerate e_g-like states with $d_{x^2-y^2}$ and d_{z^2} character and the energetically lower lying threefold-degenerate t_{2g}-like d_{xy}, d_{yz} and d_{xz} type states.

In the O_{2p}-like valence band, a weak two-peak separation is recognizable for rutile and much less prominent for anatase and brookite. The O_{2p} band splitting in rutile results from the sp^2-like hybridization in the planar (Y-shaped) OTi_3 building blocks. The p_x and p_y states of the O ion form bonding σ-hybrid states with the central Ti ion. These σ states form the lower edge of the O_{2p}-like valence band and extend almost through the whole band. The uppermost valence band edge consists of p_z-type states which form the lone pair (out-of-plane) π states that are higher in energy than the sp^2-like hybrid states. The slightly different characteristics in anatase are due to the more T-like shape of the OTi_3 building blocks that lead to stronger deviations from the ideal sp^2 hybrid states than in rutile. In brookite, both rutile-like (Y-shape) and anatase-like (T-shape) OTi_3 building blocks are present, which is why the O_{2p} valence band shows characteristics from both tetragonal phases.

3.2. Optical properties

In figure 4, the dielectric functions including electron–hole interaction from solution of the BSE are shown for all three major phases in ordinary and extraordinary polarization. The overall line shape of the dielectric functions is characterized by an absorption onset above 3 eV and two distinct broad peaks below and above ∼6.5 eV. This characteristic spectral weight distribution directly reflects the octahedron-type crystal-field splitting of the Ti_{3d}-like valence states. The first main peak can be identified with interband transitions from the O_{2p}-like valence band into the t_{2g}-like sub-band. The high-energy main peak arises from transitions into the e_g-like sub-band. Even for the symmetry-reduced TiO_6 units of brookite, the formal sixfold coordination leads to identical qualitative properties.

For rutile, the imaginary part of $\varepsilon(\omega)$ shows a sharp excitonic feature for $E \perp c$ (cf figure 4(a)) at the adsorption onset, which is missing in the independent (quasi-)particle spectra on the PBE and G_0W_0 levels of theory. This first main peak is in excellent agreement with the experimental data of Tiwald and Schubert [14]. Also for $E \parallel c$, the position of the first main peak agrees with the experiment. Nevertheless, the peak height is underestimated in our calculation and the predicted doublet structure of this peak is not resolved in the experiment. The second major spectral features present above 6.5 eV in the calculated spectra for both polarizations are clearly resolved in the Tiwald–Schubert data. Even the single-peak characteristic for $E \perp c$ and the double-peak characteristic for $E \parallel c$ is seen experimentally. Further evidence for notable spectral features above 6.5 eV is also given by electron energy loss spectroscopy measurements of Rocquefelte *et al* [65].

In light of the newer experimental data and our calculated spectra, it appears reasonable to argue that the experimental data of Cardona and Harbeke [13], commonly used as experimental reference on TiO_2 rutile but not indicating a second main peak neither for $E \perp c$ nor for $E \parallel c$, do not properly reflect the absorption characteristics.

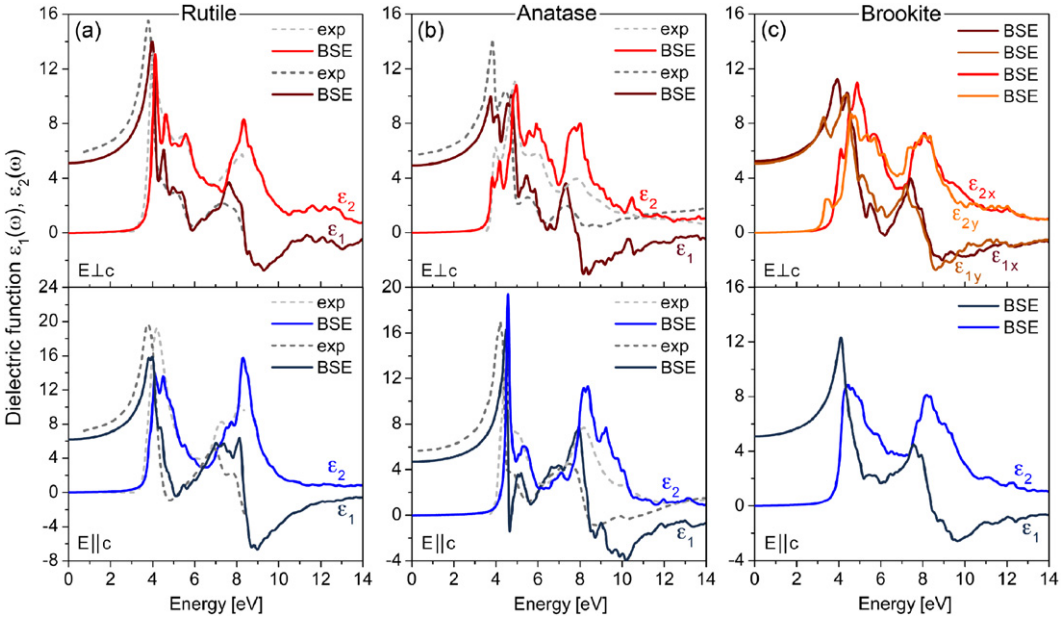

Figure 4. Polarization-dependent real ($\varepsilon_1(\omega)$) and imaginary ($\varepsilon_2(\omega)$) parts of the complex dielectric function for TiO_2 rutile (a), anatase (b) and brookite (c). The dielectric functions have been calculated on the BSE level of theory using 72, 144 and 288 electronic bands, 539, 243 and 75 regularly distributed irreducible k-points, and QP energies obtained from G_0W_0 calculations. The included experimental reference data were extracted from [14] for rutile and from [15] for anatase.

For TiO_2 anatase (cf figure 4(b)) the calculated line shape of the G_0W_0–BSE dielectric function is in good agreement with the experimental data published by Hosaka *et al* [15] for both polarizations. The perhaps most characteristic difference from rutile is the low-energy shoulder at ∼4 eV and the resulting main peak triplet structure in $\varepsilon_2(\omega)$ for $E \perp c$. It should be noted that this triplet structure exists already in the PBE and G_0W_0 spectra. For $E \parallel c$ no low-energy shoulder is observable. The lowest energy feature is a very sharp exciton peak at ∼4.5 eV which is slightly blueshifted and slightly overestimated compared to position and intensity in the experiment. Since the absorption onset for $E \parallel c$ is found at significantly higher energies, our results indicate a more pronounced optical dichroism for anatase than for rutile.

In contrast to the dielectric tensor of the uniaxial materials rutile and anatase, the orthorhombic brookite phase is a biaxial material with three independent components. Similar to anatase, the absorption edge of brookite is found to be dichroic due to low-energy features in the two in-plane components $\varepsilon_{2x}(\omega)$ and $\varepsilon_{2y}(\omega)$ (cf figure 4(c)). In contrast to $\varepsilon_{2x}(\omega)$, the low-energy feature in $\varepsilon_{2y}(\omega)$ exists already in the independent-particle spectra at the PBE and G_0W_0 levels of theory, whereas this feature in $\varepsilon_{2x}(\omega)$ arises from excitonic contributions. As observed for anatase, the first main peak exhibits a triplet structure. In contrast, the first peak for $E \parallel c$ is almost structureless, more similar to rutile. The overall influence of electron–hole interaction on the spectral weight distribution is less pronounced in brookite than in the tetragonal phases. This suggests that less local symmetry, which corresponds to smaller spatial anisotropies, diminishes the formation of sharp exciton features.

Since it is difficult to extract the adsorption onset from the dielectric functions in figure 4, we have determined the lowest eigenvalues of the electron–hole pair Hamiltonian for the three TiO_2 materials by a recursive approach [67, 68, 66]. For TiO_2 rutile, the lowest G_0W_0–BSE pair-excitation energy is 3.28 eV. This value is larger than the fundamental optical bandgap of 3.03 eV determined in absorption/photoluminescence spectroscopy measurements [2–5]. A similar result is obtained for TiO_2 anatase. While photoluminescence spectroscopy yields a fundamental gap of 3.2 eV, the lowest calculated pair-excitation energy in the G_0W_0–BSE approach is 3.57 eV. Our calculated pair-excitation energies of rutile and anatase agree well with the bandgaps of 3.37 and 3.53 eV that were reported by Coronado *et al* [20] from direct Tauc analysis of UV–visible reflectance spectra. However, the lowest pair-excitation energy of 3.56 eV for brookite in the just mentioned study is found to be larger than the calculated lowest pair-excitation energy of 3.13 eV.

4. Concluding remarks

In this study, we have investigated the electronic and optical properties of the three naturally occurring TiO_2 polymorphs rutile, anatase and brookite. The more complex orthorhombic brookite phase has, for the first time, been treated systematically with the same accuracy as the two tetragonal phases. Thus, this work provides TiO_2 brookite HSE06 hybrid functional and G_0W_0 QP reference data for further studies as well as optical spectra from solution of the BSE. Our results indicate that the inclusion of electron–hole pair excitations on the BSE level of theory allows an accurate modeling of the polarization-dependent optical properties. This is especially true for TiO_2 rutile, where, in light of the more recent data of Tiwald and Schubert [14], the

reported discrepancies between the calculated and measured dielectric functions seem to be primarily caused by improper experimental reference data used in the preceding studies.

Acknowledgments

The calculations were done using grants of computer time from the Regionales Rechenzentrum of the Universität zu Köln (RRZK), the Paderborn Center for Parallel Computing (PC2) and the Höchstleistungs-Rechenzentrum Stuttgart. The Deutsche Forschungsgemeinschaft is acknowledged for financial support.

References

[1] Dambournet D, Belharouak I and Amine K 2010 *Chem. Mater.* **22** 1173
[2] Pascual J, Camassel J and Mathieu H 1977 *Phys. Rev. Lett.* **39** 1490
[3] Pascual J, Camassel J and Mathieu H 1978 *Phys. Rev.* B **18** 6842
[4] Amtout A and Leonelli R 1995 *Phys. Rev.* B **51** 6842
[5] Tang H, Lévy F, Berger H and Schmid P E 1995 *Phys. Rev.* B **52** 7771
[6] Mattsson A and Österlund L 2010 *J. Phys. Chem.* C **114**
[7] Bach U, Lupo D, Comte P, Moser J E, Weissörtel F, Salbeck J, Spreitzer H and Grätzel M 1998 *Nature* **395** 583
[8] Grätzel M 2005 *MRS Bull.* **30** 23
[9] Hagfeldt A, Boschloo G, Sun L, Kloo L and Pettersson H 2010 *Chem. Rev.* **110** 6595
[10] Wyckoff R W G 1963 *Crystal Structures* vol 1 (New York: Wiley)
[11] Horn M, Schwerdtfeger C F and Meagher E P 1972 *Z. Kristallogr.* **136** 273–81
[12] Hermann C, Lohrmann O and Philipp H 1937 *Strukturbericht Band II 1928–1932* (Leipzig: Akademische Verlagsgesellschaft MBH)
[13] Cardona M and Harbeke G 1965 *Phys. Rev.* **137** 1467
[14] Tiwald T E and Schubert M 2000 *Proc. SPIE* **4103** 19
[15] Hosaka N, Sekiya T, Satoko C and Kurita S 1997 *J. Phys. Soc. Japan* **66** 877
[16] Sekiya T, Igarashi M, Kurita S, Takekawa S and Fujisawa M 1998 *J. Electron Spectrosc. Relat. Phenom.* **92** 247
[17] Koelsch M, Cassaignon S, Guillemoles J F and Jolivet J P 2002 *Thin Solid Films* **403–404** 312
[18] Zallen R and Moret M P 2006 *Solid State Commun.* **137** 154
[19] Li J-G, Ishigaki T and Sun X 2007 *J. Phys. Chem.* C **111** 4969
[20] Reyes-Coronado D, Rodríguez-Gattorno G, Espinosa-Pesqueira M E, Cab C, de Coss R and Oskam G 2008 *Nanotechnology* **19** 145605
[21] Wanbiao H, Liping L, Guangshe L, Ghanglin T and Lang S 2009 *Cryst. Growth Des.* **9** 3676
[22] Glassford K M and Chelikowsky J R 1992 *Phys. Rev.* B **46** 1284
[23] Hardman P J, Raikar G N, Muryn C A, van der Laan G, Wincott P L, Thornton G, Bullett D W and Dale P A D M A 1994 *Phys. Rev.* B **49** 7170
[24] Mo S-D and Ching W Y 1995 *Phys. Rev.* B **51** 13023
[25] Mikami M, Nakamura S, Kitao O, Arakawa H and Gonze X 2000 *Japan. J. Appl. Phys.* **39** L847
[26] Asahi R, Taga Y, Mannstadt W and Freeman A J 2000 *Phys. Rev.* B **61** 7459
[27] Calatayud M, Mori-Sánchez P, Beltrán A, Pendás A M, Francisco E, Andrés J and Recio J M 2001 *Phys. Rev.* B **64** 184113
[28] Muscat J, Swamy V and Harrison N M 2002 *Phys. Rev.* B **65** 224112
[29] Hossain F M, Sheppard L, Nowotny J and Murch G E 2008 *J. Phys. Chem. Solids* **69** 1820
[30] Wu X, Holbig E and Steinle-Neumann G 2010 *J. Phys.: Condens. Matter* **22** 295501
[31] Shojaee E and Mohammadizadeh M R 2010 *J. Phys.: Condens. Matter* **22** 015401
[32] Zhang Y, Lin W, Li Y, Ding K and Li J 2005 *J. Phys. Chem.* B **109** 19270
[33] Beltrán A, Gracia L and Andrés J 2006 *J. Phys. Chem.* B **110** 23417
[34] Lee B, Lee C, Hwang C S and Han S 2011 *Curr. Appl. Phys.* **11** S293
[35] Janotti A, Varley J B, Rinke P, Umezawa N, Kresse G and Van de Walle C G 2010 *Phys. Rev.* B **81** 085212
[36] Deák P, Aradi B and Frauenheim T 2011 *Phys. Rev.* B **83** 155207
[37] Deák P, Aradi B and Frauenheim T 2011 *J. Phys. Chem.* C **115** 3443
[38] Lawler H M, Rehr J J, Vila F, Dalosto S D, Shirley E L and Levine Z H 2008 *Phys. Rev.* B **78** 205108
[39] Chiodo L, Garcia-Lastra J M, Iacomino A, Ossicini S, Zhao J, Petek H and Rubio A 2010 *Phys. Rev.* B **82** 045207
[40] Kang W and Hybertsen M S 2010 *Phys. Rev.* B **82** 085203
[41] Hohenberg P and Kohn W 1964 *Phys. Rev.* B **136** 864
[42] Kohn W and Sham L J 1965 *Phys. Rev.* A **140** 1133
[43] Blöchl P E 1994 *Phys. Rev.* B **50** 17953
[44] Kresse G and Joubert D 1999 *Phys. Rev.* B **59** 1758
[45] Kresse G and Furthmüller J 1996 *Comput. Mater. Sci.* **6** 15
[46] Perdew J P, Burke K and Ernzerhof M 1996 *Phys. Rev. Lett.* **77** 3865
[47] Heyd J, Scuseria G E and Ernzerhof M 2003 *J. Chem. Phys.* **118** 8207
[48] Heyd J and Scuseria G E 2004 *J. Chem. Phys.* **121** 1187
[49] Heyd J, Peralta J E, Scuseria G E and Martin R L 2005 *J. Chem. Phys.* **123** 174101
[50] Heyd J, Scuseria G E and Ernzerhof M 2006 *J. Chem. Phys.* **124** 219906
[51] Shishkin M and Kresse G 2006 *Phys. Rev.* B **74** 035101
[52] Shishkin M and Kresse G 2007 *Phys. Rev.* B **75** 235102
[53] Fuchs F, Furthmüller J, Bechstedt F, Shishkin M and Kresse G 2007 *Phys. Rev.* B **76** 115109
[54] Shishkin M, Marsman M and Kresse G 2007 *Phys. Rev. Lett.* **99** 246403
[55] Sham L J and Rice T M 1966 *Phys. Rev.* **144** 708
[56] Hanke W and Sham L J 1975 *Phys. Rev.* B **12** 4501
[57] Hanke W and Sham L J 1980 *Phys. Rev.* B **21** 4656
[58] Albrecht S, Reining L, Del Sole R and Onida G 1998 *Phys. Rev. Lett.* **80** 4510
[59] Rohlfing M and Louie S G 2000 *Phys. Rev.* B **62** 4927
[60] Puschnig P and Ambrosch-Draxl C 2002 *Phys. Rev.* B **66** 165105
[61] Schmidt W G, Glutsch S, Hahn P H and Bechstedt F 2003 *Phys. Rev.* B **67** 085307
[62] Tezuka Y, Shin S, Ishii T, Ejima T, Suzuki S and Sato S 1994 *J. Phys. Soc. Japan* **63** 347
[63] Rangan S, Katalinic S, Thorpe R, Bartynski R A, Rochford J and Galoppini E 2010 *J. Phys. Chem.* C **114** 1139
[64] Lucovsky G 2001 *J. Optoelectron. Adv. Mater.* **3** 155
[65] Rocquefelte X, Goubin F, Montardi Y, Viadere N, Demourgues A, Tressaud A, Whangbo M and Jobic S 2005 *Inorg. Chem.* **44** 3589
[66] Fuchs F, Rödl C, Schleife A and Bechstedt F 2008 *Phys. Rev.* B **78** 085103
[67] Haydock R 1980 *Comput. Phys. Commun.* **20** 11
[68] Benedict L X, Shirley E L and Bohn R B 1998 *Phys. Rev. Lett.* **80** 4514

Paper III

Fingerprints of order and disorder in the electronic and optical properties of crystalline and amorphous TiO_2

M. Landmann, T. Köhler, S. Köppen, E. Rauls, T. Frauenheim, and W. G. Schmidt

PHYSICAL REVIEW B **86**, 064201, 20 pp. (2012)

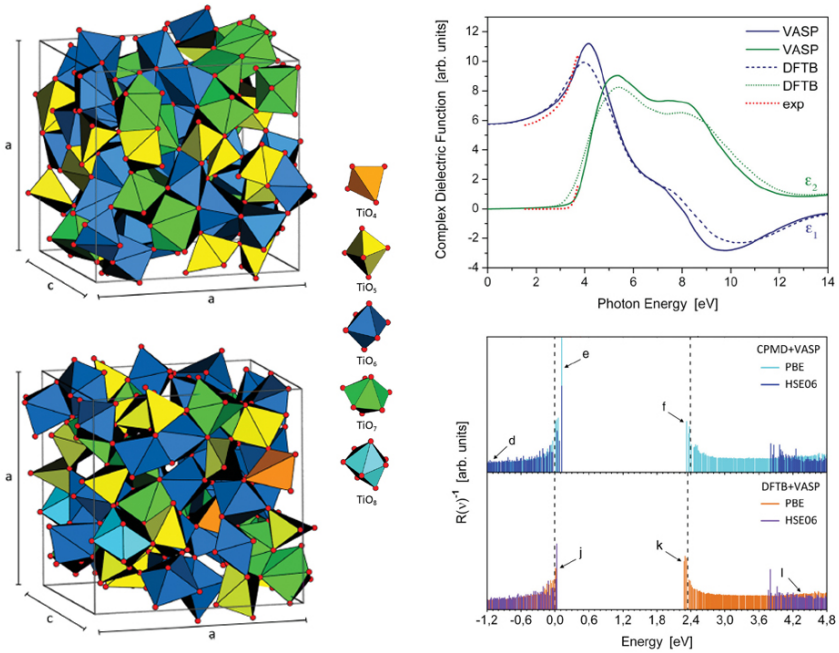

Fingerprints of order and disorder in the electronic and optical properties of crystalline and amorphous TiO_2

M. Landmann,[1] T. Köhler,[2] S. Köppen,[2] E. Rauls,[1] T. Frauenheim,[2] and W. G. Schmidt[1]
[1]*Lehrstuhl für Theoretische Physik, Universität Paderborn, 33095 Paderborn, Germany*
[2]*Bremen Center for Computational Materials Science, Universität Bremen, 28359 Bremen, Germany*
(Received 5 April 2012; published 6 August 2012)

We have investigated the structural and electronic properties as well as the linear optical response of amorphous TiO_2 within density functional theory and a numerically efficient density functional based tight-binding approach as well as many-body perturbation theory. The disordered TiO_2 phase is modeled by molecular dynamics. The equivalence to experimentally characterized amorphous phases is demonstrated by atomic structure factors and radial pair-distribution functions. By density functional theory calculations, using both the semilocal Perdew-Burke-Ernzerhof functional and the nonlocal Heyd-Scuseria-Ernzerhof screened hybrid functional, the electronic energy gap is found to be larger than in the crystalline TiO_2 phases rutile and brookite but close to the anatase band gap. The quasiparticle energy gap of amorphous TiO_2 is determined to be $\gtrsim$3.7 eV, while the optical gap is estimated to $\lesssim$3.5 eV. The disorder-induced formation of localized electronic states has been analyzed by the information entropy of the charge density distributions. The frequency-dependent optical constants, calculated from the complex dielectric function, have been determined in independent particle approximation. Besides similar absorption characteristics between the most common crystalline phases and amorphous TiO_2, we find distinct differences in the optical spectra in the energy region between 5 eV and 8 eV. These differences can be assigned to the loss of symmetry in the local atomic structure of the disordered material. While the composition of the crystalline phases rutile, anatase, and brookite is well described by periodic arrangements of distorted TiO_6 octahedra building blocks, the amorphous phase is characterized by partial loss of this octahedral coordination and the disorder-induced formation of under- and over-coordinated Ti ions. This leads to the absence of the characteristic crystal-field splitting of unoccupied Ti_{3d} states into e_g and t_{2g} like subbands. The optical characteristics of the amorphous phase are interpreted as a superposition of optical transitions that reflect the various local symmetries of the manifold of synthesizable crystalline TiO_2 phases. The linear optical properties, calculated within the independent-particle approximation, are found to be in good agreement with the available experimental data.

DOI: 10.1103/PhysRevB.86.064201 PACS number(s): 81.05.Gc, 71.23.Cq, 71.23.An

I. INTRODUCTION

TiO_2 shows an extended structure polymorphism, reflected in an extraordinary rich phase diagram. The three crystal types rutile [crystal system: tetragonal ($4/mmm$), space group: $P4_2/mnm$-D_{4h}^{14}], anatase [tetragonal ($4/mmm$), $I4_1/amd$-D_{4h}^{19}], and brookite [orthorhombic (mmm), $Pbca$-D_{2h}^{15}] are stable at atmospheric pressure and room temperature and commonly found in nature. A fourth naturally occurring phase TiO_2(B)[1,2] (monoclinic, bronze-type, $C2/m$) has been reported. Experiments have furthermore revealed the existence of the metastable oxides TiO_2(H)[3] (hollandite type, $I4/m$) and TiO_2(R)[4] (ramsdellite type, $Pbnm$), as well as the TiO_2 high-pressure polymorphs TiO_2(II)[5–7] [columbite type (α-PbO_2 structure), $Pbcn$], TiO_2(MI)[6–8] (monoclinic, baddeleyite type, $P2_1/c$), TiO_2(OI)[9] (orthohombic, $Pbca$), TiO_2(OII)[9,10] (orthohombic, cotunnite type, $Pnma$), and c-TiO_2[11,12] (cubic, fluorite type, $Fm3m$). From combined experimental and theoretical studies the phase-transition path rutile → columbite type [TiO_2(II)] → baddeleyite type [TiO_2(MI)] → intermediate orthorhombic type [TiO_2(OI)] → cotunnite type [TiO_2(OII)] has been identified for compression at ambient temperature.[9,13]

The structure of the three most common phases rutile, anatase, and brookite as well as the polymorphs TiO_2(B), TiO_2(R), TiO_2(H), and TiO_2(II) is well characterized in an edge-sharing octahedron-chain picture with single distorted TiO_6 octahedron building blocks formed by a central Ti ion surrounded by six O ions.[2,11,14–16] A complementary view of the electronic structure is given by crystal-lattice formation resting upon planar Ti_3O units.[17,18] Under pressure the coordination of the Ti ions and therefore the local atomic structure changes. TiO_2(MI) and TiO_2(OI) are characterized by a sevenfold coordination of Ti ions with O ions. In the cubic fluorite phase the Ti ions are eightfold coordinated, which results in the formation of tetrahedrally coordinated O ions. Finally, Ti ions in the high-pressure polymorph TiO_2(OII) are ninefold coordinated by O ions.

Besides this manifold of well-ordered TiO_2 modifications that are characterized by their ion's constant coordination number, also amorphous TiO_2 (a-TiO_2) has received interest as a low-cost material for technical applications, based on the extraordinary optical and catalytic properties known from the crystalline phases.[19,20] A graphical representation of a-TiO_2 is given in Fig. 1 using polyhedra to identify the TiO_x building blocks. a-TiO_2 is a general starting material (precursor) for the synthesis of various single-crystalline phases by hydrothermal treatment.[16,21–23] In practice a-TiO_2 is commonly produced in the form of thin films prepared by various experimental strategies as direct current (magnetron) sputtering,[24–28] electron-beam evaporation,[29,30] cathodic vacuum arc deposition,[31,32] sol-gel deposition,[33,34] reactive sputtering, and arc ion plating.[35,36] Also dense or porous disordered films of nanocrystallites are commonly

 ©2012 American Physical Society

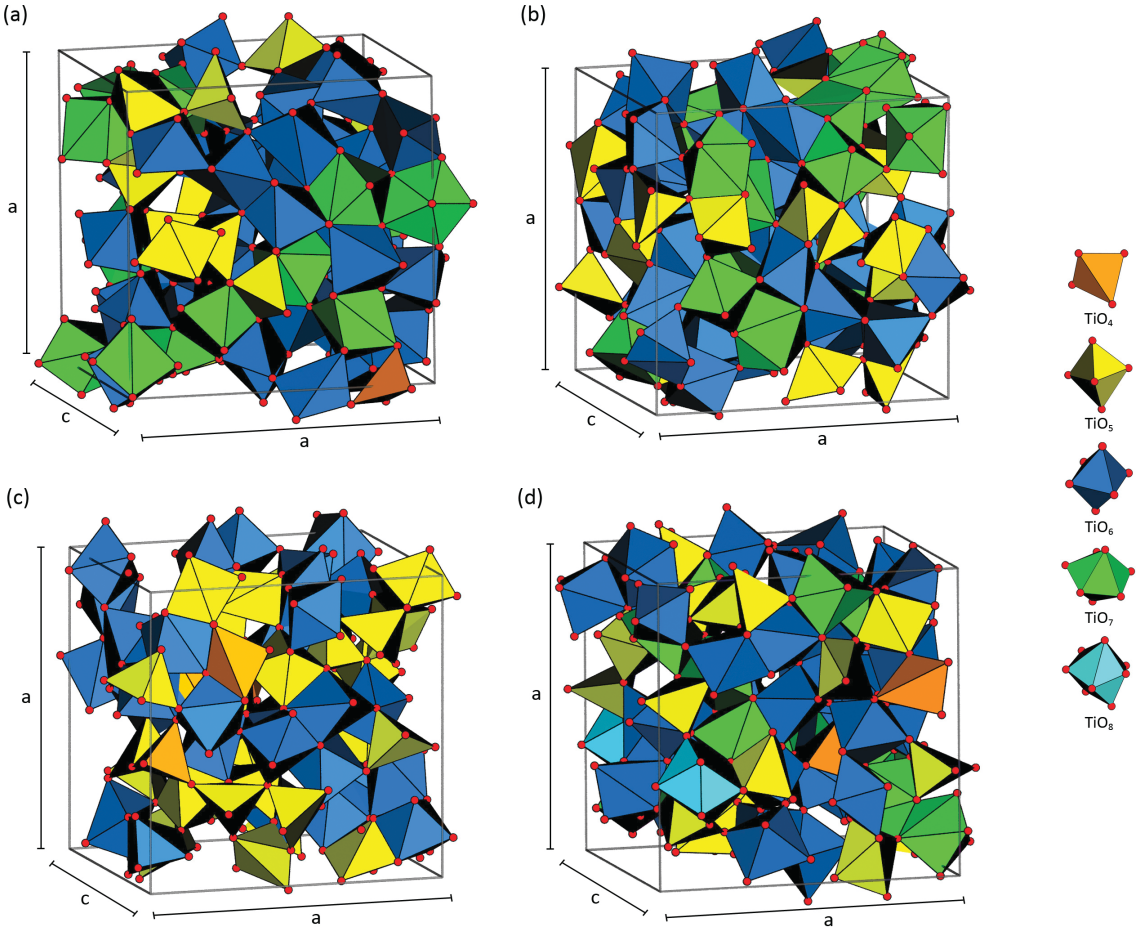

FIG. 1. (Color online) Polyhedra representation (2.5 Å Ti-O bond-length cutoff) of the TiO_x building blocks for the 216-atom rectangular cuboidal unit cells ($a = 13.80$ Å, $a = 11.93$ Å) of amorphous TiO_2 with a mass density of 4.20 g/cm^3. The structures on the left-hand side are room-temperature (300 K) structures generated by (a) CPMD and (c) DFTB based MD. On the right-hand side the geometry after structural relaxation with VASP is shown [(b) CPMD + VASP, (d) DFTB + VASP].

produced and referred to as amorphous films. Depending on the intended usage this might be a significant difference. A fundamental property of the amorphous material is the absence of optical anisotropies that, for instance, occur in the uniaxial rutile and anatase phases or the biaxial brookite phase. In addition, a pure amorphous phase is not influenced by grain boundary induced defects between the crystallites that modify the physical properties.[37,38] Closely related are size effects that might favor various crystalline phases in nanoparticulated TiO_2.[23,39–41] Also, it had been shown that a-TiO_2 films are well suited for surface passivation in bioimplant applications due to their high stability and corrosion resistance *in vitro*.[42,43]

While there is extended literature[13,44–62] on structural, elastic, thermodynamic, and optical/dielectric properties obtained from numerical simulations of the three most common crystalline phases as well as their low index surfaces,[63–70] computational data on a-TiO_2 are rather limited due to the necessity of using extended unit cells for an approximate numerical reproduction of amorphicity. In contrast to crystalline modifications, amorphous material phases stand out by their loss of translational symmetry/long-range order. Consequently, the theoretical tools developed mainly for crystalline materials cannot straightforwardly be applied to amorphous materials and their physical properties. An understanding of the formation of energy gaps and resulting optical properties in amorphous semiconductors is directly related to the question of whether the basic nature of electronic and optical properties depends on short-range order, i.e., localized electronic states, and/or long-range order, i.e., extended electronic states and well-defined energy bands.

Due to the early works of Anderson,[71,72] Cohen,[73] and Mott[74] on the electronic structure of disordered materials, a fundamental structural disorder induced localization of electronic states was realized. In contrast to the crystal, structural disorder induces under- and over-coordinated ions in the amorphous material phase. Such variations in the atomic and electronic structure are expected to cause localized states near the energy-gap edges, forming tails of occupied and unoccupied localized states that range into the forbidden energy region of the pure crystal phase. These tails (and the loss of momentum conservation) induce a HOMO-LUMO-type energy gap that deviates from the band gap defined for the crystal. The amorphous phase complement of the crystalline band gap, defined between valence and conduction band states, is called the "mobility gap" and defined as the energy difference between filled and empty nonlocalized extended

Bloch-type states. The mobility gap is always larger than the HOMO-LUMO-type gap and an important quantity with respect to the electrical properties, like the electron mobility and transport characteristics in amorphous solids in general.

To the best of our knowledge, no theoretical studies on the optical properties, in particular based on *ab initio* calculations, have been published for a-TiO_2 so far. A first density functional theory (DFT) study on the electronic structure of a-TiO_2 has been published recently.[75] The atomic structure of amorphous samples has been characterized in terms of distribution functions and structure factors by model calculations.[15,23,75,76] Petkov *et al.*[15] published a combined experimental and theoretical work on the structure of amorphous TiO_2. On the one hand, they fabricated thin films and bulk powder samples of a-TiO_2 that have been characterized by electron and x-ray diffraction. On the other hand, the experimental distribution functions have been compared to results of a reversed Monte Carlo (RMC) approach that optimizes a starting configuration to match the experimentally derived structure data. As a key result they reported a considerable resemblance of the atomic arrangement in their amorphous sample to the crystalline brookite phase. This observation has also been confirmed by molecular-dynamics (MD) simulations of Hoang[76] using empirical pair-interaction potentials. Therefore, it has been stated that there is a close relation between brookite and the amorphous phase of TiO_2. In addition, experimental results suggest brookite growth directly out of an amorphous phase. This has been demonstrated by brookite nanoparticles surrounded by an amorphous-like shell.[16] In contrast, predominantly phase transitions upon heating from a-TiO_2 films to anatase and partially to rutile are reported.[27,29,31,34–36] The difference in crystallization behavior of a-TiO_2 has been attributed to a strong dependence on the sample history as precursor chemistry, preparation method, and heat treatment.[16,77] Theoretically, the ratio of edge to vertex linked TiO_6 octahedral building blocks[15,76] has been found to play a major role in the crystallization behavior of a-TiO_2.

In this paper we will investigate the relevance of long-range order or rather its loss, thus extending our preceding study on crystalline TiO_2 polymorphs[17] to the structural, electronic, and optical properties to the amorphous phase of TiO_2. The paper is organized as follows: Section II describes the underlying theoretical molecular-dynamics (MD) frameworks needed to generate the amorphous material unit cells as well as the used numerical parameters to obtain the optical spectra within the DFT approach. Also, the information theory related concepts necessary to measure the degree of localization of electronic states are introduced. Section III is used for characterization of the amorphous structure and presenting the calculated electronic structure and optical spectra, which are discussed alongside existing experimental data. Finally, Sec. IV summarizes the relevant results and gives concluding comments and reasonings.

II. METHODOLOGY AND NUMERICAL DETAILS

DFT calculations[78,79] have been performed using the projector-augmented wave (PAW) method[80,81] as implemented in the Vienna *Ab initio* Simulation Package (VASP).[82] Both the generalized gradient approximation (GGA) according to Perdew-Burke-Ernzerhof (PBE)[83] as well as the nonlocal, range-separated, screened Coulomb potential hybrid density functional proposed by Heyd, Scuseria, and Ernzerhof (HSE06)[84–87] have been applied. Within the framework of many-body perturbation theory (MBPT),[88,89] quasiparticle (QP) corrections due to self-energy effects within the GW approximation have been included perturbatively in a full-frequency-dependent G_0W_0 scheme[90–93] (see also discussion in Ref. 94). Two-particle excitations are taken into account by solution of the Bethe-Salpeter equation (BSE) for Coulomb correlated (quasi)electrons and (quasi)holes.[95–98] To avoid the $O(N^3)$ scaling diagonalization of the electron-hole pair Hamiltonian, the calculation of the frequency-dependent dielectric function is performed by an $O(N^2)$ scaling time-evolution scheme.[99] A similar numerical setup has been applied to crystalline TiO_2 (see Ref. 17).

We additionally utilized the self-consistent charge density functional tight-binding (SCC-DFTB)[100–102] approach to the electronic structure of large-scale systems with the objective of generating and characterizing amorphous TiO_2 polymorphs by molecular dynamics. SCC-DFTB offers a good compromise between accuracy and computational efficiency and successfully addressed a wide range of material properties. We refer the reader to recent studies on diamond nucleation in amorphous carbon systems[103] or the discussion of the properties of exofluorinated carbon nanotubes,[104] as examples for either extended or low-dimensional systems of interest.

A. Modeling of amorphous materials

To model the structure formation in stoichiometric amorphous TiO_2 thin films, we performed MD simulated annealing (SA) calculations. On the one hand the SCC-DFTB scheme and on the other hand the *ab initio* Car-Parrinello molecular-dynamics (CPMD) method[105] were used. For the MD simulations we prepared initial structures containing 216 atoms, spatially and chemically randomly distributed, like a gas of hard spheres. The atoms are placed in a fixed-volume rectangular cuboidal supercell arrangement of a size matching the microscopic mass density of 4.20 g/cm^3 and the ideal 1:2 stoichiometry. For the present DFTB calculations we used the Ti-O interaction parametrization of Ref. 106. The dynamical quenching path for relaxation started from a partly equilibrated liquid state of the model structure at 5000 K and followed a path of exponentially decreasing temperature towards room temperature at 300 K. The total duration of the cooling procedure amounts 23 ps. The Newton's equations of motion are solved using the Verlet algorithm. The coupling to a heat bath, according to the canonical (*NVT*) ensemble, was realized by an Anderson thermostat.

The CPMD calculation was done under usage of norm-conserving pseudopotentials of Troullier-Martins type, proposed for Ti and O by Glassford *et al.*,[107,108] and application of the Becke88 exchange functional.[109] The total simulation time of 8.6 ps was discretized by 51 000 steps to ensure energy convergence. At the beginning and the end of the cooling process we performed thermal equilibration phases of 4000 steps at 5000 K and 5000 steps at room temperature 300 K,

respectively, and in between we followed an exponential like path approximated by a suitable stepwise function. Here the Nosé-Hoover thermostat ensures the conditions of a canonical ensemble and the volume was kept constant, too.

We additionally performed structural relaxations for both the DFTB and the CPMD room temperature structure using the the Vienna *Ab initio* Simulation Package (VASP).[82] The atomic positions have been relaxed using the PBE[83] (Perdew-Burke-Ernzerhof) functional, a $2 \times 2 \times 2$ Monkhorst-Pack k-point sampling, and a force convergence criterion of 0.01 eV/Å.

B. Characterization of amorphous materials

The characteristics of the remaining short-range order of amorphous materials can be characterized by a detailed analysis of the mean local bonding environment, describable in bond lengths and angle statistics as well as mean coordination numbers. All of that is typically expressed in terms of atomic structure factors and radial pair distribution functions (RDFs). If the total reduced atomic distribution function $G(r)$, directly accessible through numerical simulations, is defined through

$$G(r) = 4\pi r[\varrho(r) - \varrho_0] \tag{1}$$

with $\varrho(r)$ and ϱ_0 being the averaged atomic densities, both quantities are connected by a Fourier representation of the structure factor $S(q)$, respectively the reduced quantity $F(q) = q[S(q) - 1]$, according to

$$G(r) = \frac{2}{\pi}\int_0^\infty F(q)\sin(qr)dq, \tag{2}$$

where q is the the magnitude of the wave vector of the scattered photons/particles. The function $F(q)$ is also known as total reduced interference function.[110,111] The static atomic structure factor $S(q)$ is experimentally accessible by various diffraction techniques (electron, x ray, or neutron diffraction, depending on the type of the manufactured sample).

C. Numerical details

An energy cutoff of 400 eV was used and the $3s$ and $3p$ semicore states of Ti have been treated as valence states within the PAW potentials throughout this work. In agreement with the original definitions,[87,112] an exact exchange fraction of $\alpha = 0.25$ and a screening parameter of $\mu = 0.2$ Å^{-1} have been used in the HSE06 screened hybrid functional. The energy-loss function $L(\omega)$, the reflectivity $R(\omega)$, the refraction index $n(\omega)$, the extinction coefficient $\kappa(\omega)$, and the absorption coefficient $\alpha(\omega)$ have been calculated via

$$L(\omega) = \frac{\varepsilon_2(\omega)}{\varepsilon_1(\omega)^2 + \varepsilon_2(\omega)^2}, \tag{3}$$

$$R(\omega) = \left|\frac{\sqrt{\varepsilon_1(\omega) + i\varepsilon_2(\omega)} - 1}{\sqrt{\varepsilon_1(\omega) + i\varepsilon_2(\omega)} + 1}\right|^2, \tag{4}$$

$$n(\omega) = \frac{1}{\sqrt{2}}\sqrt{\varepsilon_1(\omega) + \sqrt{\varepsilon_1(\omega)^2 + \varepsilon_2(\omega)^2}}, \tag{5}$$

$$\kappa(\omega) = \frac{1}{\sqrt{2}}\sqrt{-\varepsilon_1(\omega) + \sqrt{\varepsilon_1(\omega)^2 + \varepsilon_2(\omega)^2}}, \tag{6}$$

$$\alpha(\omega) = \frac{\sqrt{2}\omega}{c}\sqrt{-\varepsilon_1(\omega) + \sqrt{\varepsilon_1(\omega)^2 + \varepsilon_2(\omega)^2}}, \tag{7}$$

from the frequency-dependent complex dielectric function $\varepsilon(\omega) = \varepsilon_1(\omega) + i\varepsilon_2(\omega)$ which is determined in independent particle approximation (IPA) [also termed random phase approximation (RPA)] by the Ehrenreich-Cohen formula[113] in the optical limit of vanishing wave vectors. The DFT energy gap underestimation has been corrected by a scissors shift approximation. The reliability and value of the applied scissors shift for the unoccupied energy bands in crystalline TiO_2 is discussed in Ref. 17. In the case of calculations for crystalline TiO_2 atomic positions and unit cells have been relaxed on the DFT-PBE level. Dielectric functions, the eigenvalue spectrum, and densities of states have been calculated for the relaxed unit cells using 28 electronic bands per formal TiO_2 unit. A $12 \times 12 \times 16$ Monkhorst-Pack k-point set for relaxation and 768 irreducible k points for determination of the dielectric properties have been applied for the rutile phase. For all other TiO_2 phases the k-point mesh has been adapted to reproduce a comparable point density in k space. DFT-PBE optical spectra of a-TiO_2 have been obtained for stoichiometric 216-atom orthorhombic unit cells ($a = 13.8046$ Å and $c = 11.9321$ Å; cf. Fig. 1) using 1920 electronic bands, a scissors shift of 1.3 eV, and a Γ-centered $3 \times 3 \times 3$ Monkhorst-Pack k-point mesh. The optical properties of four a-TiO_2 structure models, generated by DFTB and CPMD MD as well as additional structural relaxations by VASP, have been investigated on the DFT-IPA level of theory. Further numerical details and convergence considerations concerning the HSE06, G_0W_0, and BSE calculations are discussed in the text.

D. Analysis of electronic-state localization

The analysis of the disorder-induced localization of quantum states requires a measure to quantify the degree of localization. Information theory that unifies concepts from probability theory and statistics offers the necessary theoretical tools to determine this degree of localization, respectively the deviation from randomness. As expressed in the existence theorems of DFT, the information on the spatial extent of the individual electronic-state wave functions is bidirectionally unique contained in the corresponding charge density distributions. In the language of information theory, these electronic densities represent discrete, nonnegative N-point probability distributions that are in some way normalized to the number of electrons found in each electronic state and the number of sites used to represent the electron density.

In this study, we have investigated two measures to determine the degree of (de)localization of electronic states from their charge density distributions. Both measures are based on the generalized entropy concept of information theory. More precisely, both quantities are derived from the one-parametric continuous family of information entropies introduced by Alfréd Rényi.[114] For a finite discrete N-point probability distribution $\mathcal{P} = \{p_1, p_2 \ldots p_N\}$ with $\sum_{\nu=1}^{N} p_\nu = 1$, the Rényi entropy $H[\mathcal{P}] = H(p_1, p_2 \ldots p_N)$ of order α is

defined through

$$H_\alpha[\mathcal{P}] = \frac{1}{1-\alpha} \ln\left[\sum_{\nu=1}^{N} p_\nu^\alpha\right] \tag{8}$$

with $\alpha \geqslant 0$ and $\alpha \neq 1$. In the limit $\alpha \to 1$ this entropy definition tends to

$$H_1[\mathcal{P}] = \lim_{\alpha\to 1} H_\alpha[\mathcal{P}] = -\sum_{\nu=1}^{N} p_\nu \ln p_\nu. \tag{9}$$

Thus, the order-one Rényi entropy is identified as the information entropy introduced by Shannon.[114–117] The Rényi entropy of order two

$$H_2[\mathcal{P}] = -\ln\left[\sum_{\nu=1}^{N} p_\nu^2\right] \tag{10}$$

is known as extension entropy.[115] Both information and extension entropy provide a measures for the amount of uncertainty concerning the outcome of an *experiment* whose individual results are described by the probability distribution $\mathcal{P}$. In the same way, the entropies provide the amount of information that is obtained by carrying out the *experiment*. In analogy to the partition function of statistical thermodynamics and its relation to the entropy by the Boltzmann formula, the exponentiations $W[\mathcal{P}] = \exp\{H_1[\mathcal{P}]\}$ (Ref. 118) and $R[\mathcal{P}] = \exp\{H_2[\mathcal{P}]\}$ give the effective numbers of different outcomes, respectively the sum of accessible microstates in thermodynamic ensembles. The quantity $R[\mathcal{P}]$ is known as participation ratio (PR). Here, we will use the inverse quantities

$$W^{-1}[\mathcal{P}] = \exp\left\{\sum_{\nu=1}^{N} p_\nu \ln p_\nu\right\} \tag{11}$$

and

$$R^{-1}[\mathcal{P}] = \sum_{\nu=1}^{N} p_\nu^2 \tag{12}$$

to determine the degree of localization of electronic states in real space. $R^{-1}[\mathcal{P}]$ is commonly called the inverse participation ratio (IPR).[115,121–123]

Applied to the (partial) charge density distribution $\varrho_\nu(\mathbf{r})$ corresponding to a particular electronic state (respectively energy) ν, we obtain the degree of localization by

$$W^{-1}(\nu) = \exp\left\{\sum_{\mu=1}^{N} \varrho_\mu(\nu) \ln \varrho_\mu(\nu)\right\} \tag{13}$$

and

$$R^{-1}(\nu) = \sum_{\mu=1}^{N} [\varrho_\mu(\nu)]^2. \tag{14}$$

Here, μ describes the real-space grid points used to represent the charge density in the case of a plane wave representation of the Kohn-Sham eigenstate or the μ atom sites in the case of maximal localized basis states (i.e., Mulliken charge representation). According to the definitions above, higher values of $W^{-1}[\nu]$ and $R^{-1}[\nu]$ indicate stronger localization of the considered electronic state.

III. RESULTS AND DISCUSSION

A. Characterization of amorphous structures

We have analyzed the structural order in a-TiO_2 in terms of the reduced structure factor $F(q) = q[S(q) - 1]$ and its Fourier-transformed analogon, the reduced atomic pair-distribution function $G(r)$. From comparison to available experimental data[15] on structure factors and distribution functions, a mass density of 4.20 g/m^3, which is comparable to the density of the rutile phase, matches the reported experimental data[15] best and has, therefore, been chosen for further analysis. Choosing the same density as one of the crystal phases also allows the direct comparison of the electronic energy gap which commonly depends on the density. However, in consideration of the general dependence of electronic properties and optical transitions on the mass density, we will discuss the influence of density fluctuations exemplarily for the dielectric function at the end of this section.

In Fig. 2 the calculated reduced structure factor and reduced RDF [cf. Eq. (2)] for four amorphous unit cells are shown. As described in the methodology section, the position of the atoms in the unit cells have been optimized by MD approaches using DFTB and CPMD and structure relaxation via VASP.

The overall line shape of the structure factors is characterized by strong oscillations at smaller wave vectors with the most pronounced interference peak around a scattering vector magnitude of $\sim$4 Å^{-1} and slightly decreasing amplitudes at higher magnitudes of the wave vector. The qualitative agreement in shape, peak positions, and amplitudes of the calculated and experimental data is particularly evident for the experimental x-ray diffraction (XRD) data on bulk TiO_2 powders. Moreover, the structure factor derived from electron diffraction measurements on radio frequency (RF) sputtered TiO_2 films deviates from the bulk powder result mainly in from of peak heights variations. Even the electron diffraction data on the sol-gel dip-coated TiO_2 films show a comprehensive agreement in peak positions, whereas the amplitudes for smaller magnitudes of the wave vector show substantial deviations. In general, experimentally observed differences in variously prepared amorphous TiO_2 samples may suggest that the short-range order is not uniquely determined by the particular chemical elements, but rather depends on the preparation route (cf. discussion by Petkov *et al.*[15]). However, the qualitative correspondences between experimental results and the simulated data indicate the unit cells' general ability to reproduce an adequate representation of the amorphous-phase structure in reciprocal and real space. From Fig. 2(a) also the DFTB approach's suitability to model a-TiO_2 is apparent. In general, the deviations between the variously simulated a-TiO_2 structures are less pronounced than differences between various experimental samples. Qualitatively similar conclusions can be drawn from an analysis of the RDF.

The RDFs, shown in Fig. 2(b), are characterized by a single sharp main peak slightly below 2 Å ($\sim$1.95 Å). This peak clearly arises from the first-neighbor, more precisely the first O ion shell, Ti-O correlations and agrees well with the Ti-O bond lengths between 1.8 Å and 2.1 Å found in the three main crystal phases of TiO_2. First-order O-O correlations are weakly indicated around 2.6 Å. The second main feature between 2.8 Å and 4.0 Å belongs to Ti-Ti pair correlations. The observed

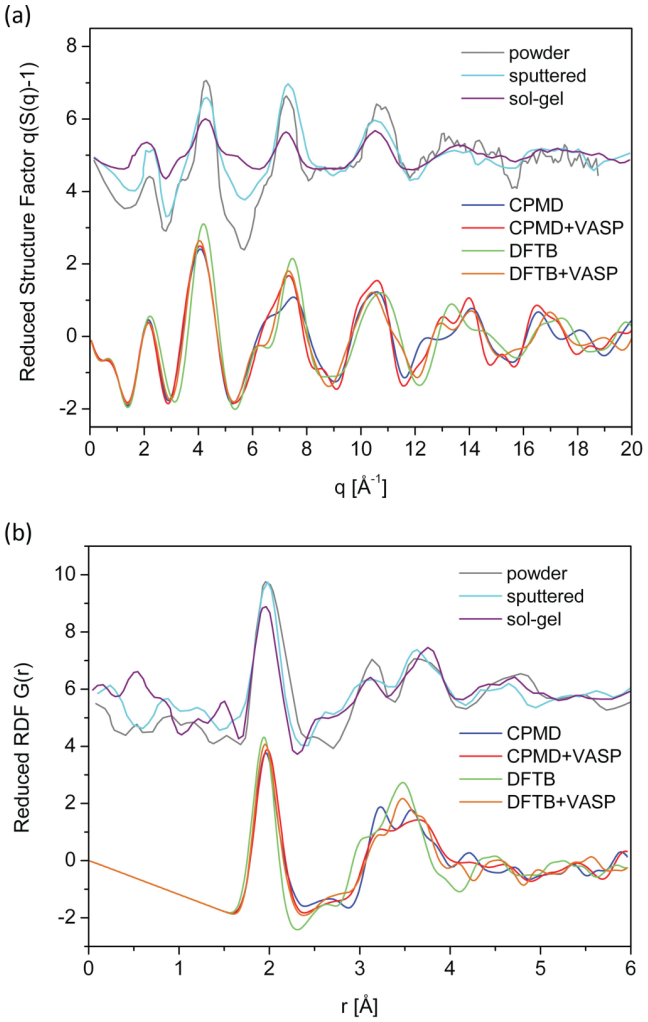

FIG. 2. (Color online) (a) Reduced static structure factors and (b) reduced atomic RDFs of DFTB, CPMD, and VASP optimized 4.20 g/m^3, 216-atom unit cells. Also displayed are the experimental results (extracted from Ref. 15) of diffraction experiments on sol-gel prepared and sputtered TiO_2 layers as well as TiO_2 powders.

two-peak characteristic reflects local symmetries characterized by edge-linked TiO_x building blocks with Ti-Ti distances around 3.2 Å and corner-linked TiO_x building blocks with Ti-Ti distances around 3.6 Å. The further curve progression shows exponentially decaying oscillations that arise from higher order pair correlations. The decay of long-range correlation further indicates the loss of long-range order in the amorphous material. However, the description of long-range contributions is limited by the confined unit cell volume. From comparison of the theoretical data curves with each other, quantitative differences in the first O coordination shell of Ti ions are small. Slightly more pronounced differences occur for Ti-Ti pair correlations. In general, a slight tendency of the main peaks towards lower distances is indicated in the DFTB data.

We have further analyzed the small differences between the MD results at room temperature (300 K) and the relaxed VASP structures, which formally represent the $T = 0$ K case, by a detailed investigation of the local atomic structure. In contrast to all non-high-pressure TiO_2 crystal phases, the local atomic environment in a-TiO_2 is not only characterized by sixfold coordinated Ti ions. In Fig. 1 we have used a polyhedra representation of TiO_x-polyhedron building blocks to identify differently coordinated Ti ions in the four investigated structure models of a-TiO_2. Based on the RDF's first main peaks, assigned to first-order Ti-O correlations, and the subsequent RDF's minima close to ∼2.3 Å, a 2.5 Å Ti-O bond-length cutoff was chosen for the polyhedron representation. The polyhedra representation immediately allows us to distinguish various types of short-range order.

In the case of the VASP relaxed CPMD configuration [see Fig. 1(b)], the amorphous unit cell contains 50% of TiO_6 building blocks and TiO_5 and TiO_7 units each with a fraction of 25%. Therefore, only half the Ti ions remain sixfold coordinated, while the other Ti ions gain or loose one O ion. As a consequence, the mean coordination number $Z_{\mathrm{Ti-O}} = 6$ of Ti ions in (crystalline) octahedral-networks may be preserved in the disordered phase. This finding agrees with MD results published by Hoang[76] ($Z_{\mathrm{Ti-O}} \approx 6$) and is in the error margin of $Z_{\mathrm{Ti-O}} = 5.6 \pm 0.4$ reported by Petkov[15] for amorphous bulk powder samples.

The CPMD structure itself, which to some extent carries temperature influences on the atomic structure due to MD annealing to 300 K and a subsequent equilibration phase at 300 K, possesses a mean coordination number of Ti ions of $Z_{\mathrm{Ti-O}} = 5.97$. The marginally smaller mean coordination is due to a 1.4% fraction of fourfold coordinated Ti ions. Nevertheless, despite the very similar coordination numbers, there are noticeable differences. TiO_6-polyhedron building blocks occur with an even higher fraction of 62%, while fivefold and sevenfold coordinated units occur with a ratio of 18.3% both.

As indicated by the RDF, the local atomic environment in the DFTB structure [see Fig. 1(a)] is slightly different from the structures generated by the other approaches. The DFTB structure exhibits a larger fraction of lower coordinated TiO_x-polyhedron building blocks. TiO_6, TiO_5, and tetrahedrally coordinated TiO_4 units occur with a ratio of 48% : 43% : 9%. As a consequence the mean coordination number is reduced to $Z_{\mathrm{Ti-O}} = 5.4$ which agrees very well with the mean coordination number of $Z_{\mathrm{Ti-O}} = 5.4 \pm 0.4$ found in Petkov's study for sputtered TiO_2 films[15] and is still in the error margin of the mean coordination number of the bulk powder samples. In the same study an even lower mean coordination number of $Z_{\mathrm{Ti-O}} = 4.5 \pm 0.4$ was obtained for sol-gel prepared films. This low coordination reduces the amplitude of the reduced structure factor [cf. Fig 1(a)].

Finally the VASP relaxation of the DFTB geometry significantly increases the mean coordination number to $Z_{\mathrm{Ti-O}} = 5.82$. In contrast to the other configurations, the remaining fraction of 2.7% fourfold coordinated Ti ions is mainly compensated by the occurrence of eightfold coordinated Ti ions. While TiO_5, TiO_6, and TiO_7 units occur with a ratio of 27.4% : 47.9% : 19.2%. We have summarized the TiO_x compositions and the mean coordination numbers of the four unit cells in Table I.

In summary, our simulation results indicate that short-range order in disordered material phases is nonunique. Nevertheless, the differences due to the use of different simulation methods are far smaller than the fluctuations

TABLE I. TiO_x polyhedron statistic (2.5 Å Ti-O bond-length cutoff) for the four 216-atom TiO_2 unit cells generated by CPMD, DFTB, and successive VASP relaxation.

Simulation approach	TiO_x building block fraction (%)					Mean coord. number
	TiO_4	TiO_5	TiO_6	TiO_7	TiO_8	
CPMD	1.4	18.3	62	18.3		5.96
CPMD + VASP		25	50	25		6.00
DFTB	9	43	48			5.40
DFTB + VASP	2.7	27.4	47.9	19.2	2.7	5.82

observed in the RDFs and structure factors of variously synthesized amorphous material samples. In detail, the atomic structure generated by DFTB MD is a good model for the sputtered TiO_2 films. On the other hand, the CPMD and VASP relaxed structures are closest to the bulk powder samples, characterized by mean coordination numbers close to the crystalline material. Furthermore, neither the DFTB nor the DFT structures seem to reproduce the very weak short-range order characteristics of the sol-gel prepared TiO_2 samples. This suggests a distinct local atomic environment in amorphous TiO_2 films prepared by the sol-gel technique and therefore a preparation specific short-range order in amorphous materials. Besides the significant disturbances in the local atomic structure by variations in the local and mean coordination numbers, also a notable fraction of the remaining TiO_6-polyhedron blocks in a-TiO_2 is significantly stronger distorted than in the brookite phase, which shows the lowest TiO_6 polyhedron symmetry among the main crystal phases. Hence, a central question in the further discussion will be how the physical properties in a-TiO_2 are modified as a consequence of these structural changes in local atomic order.

B. Electronic properties of amorphous TiO_2

After verifying the feasibility of describing the disordered material phase by our unit cells, we have investigated the local angular-momentum quantum number (l) decomposed density of states (DOS). According to Fig. 3 all four structure models are characterized by energy gaps that essentially do not contain defect states. Thereby, both VASP relaxed geometries show a comparable energy gap while the room-temperature structures show a significant energy gap reduction. Similar to the three crystalline main phases, the broad bands of occupied and unoccupied energy states show predominantly O_{2p}-like valence state and Ti_{3d}-like conduction state character. To some extent a hybridization between both types of electronic states is observed for occupied and unoccupied states. As a main characteristic of the crystalline material, the octahedral symmetry leads to a splitting of the unoccupied Ti_{3d} states into e_g and t_{2g} like subbands.[17,46,49,125,126] This distinct splitting is almost absent in the broad band of conduction states in a-TiO_2. Further analysis of the DOS, by decomposition of the l-decomposed DOS according to the magnetic quantum number m, also reveals a missing separation of the Ti_{3d}-like states into distinct energy-dependent d_{z^2}-, d_{xy}-, d_{yz}-, d_{xz}-, and $d_{x^2-z^2}$-like contributions. Again, this is in contrast to a well-defined separation in crystalline TiO_2.

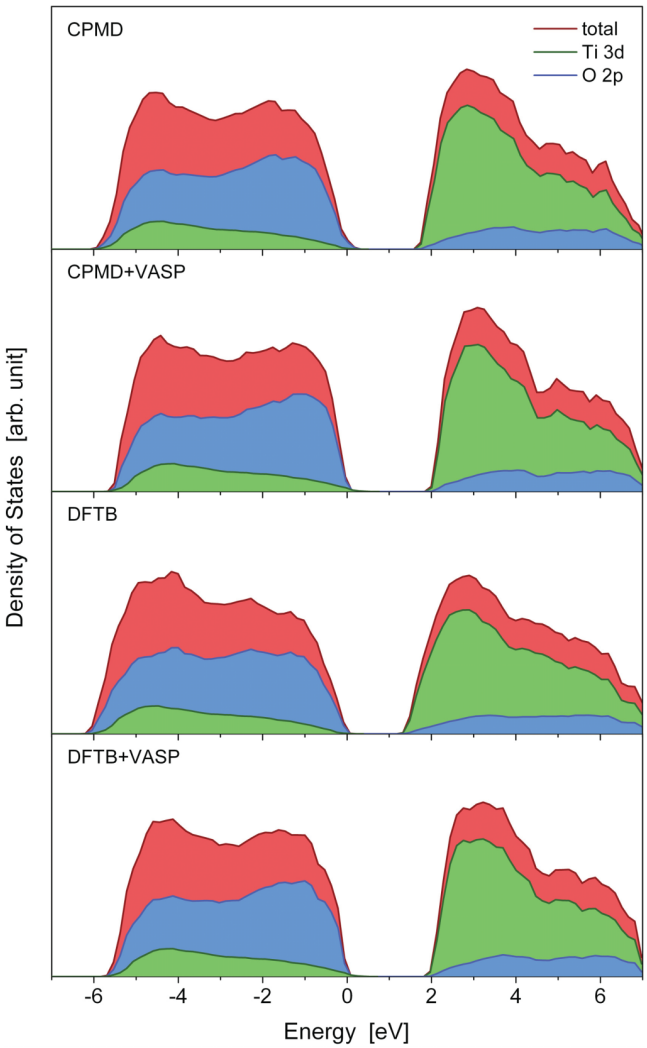

FIG. 3. (Color online) Total density of occupied and unoccupied states calculated from the DFT-PBE eigenvalues and local l-decomposed components for $3d$ states of Ti and $2p$ states of O.

From the representation of the DOS in Fig. 3, it is difficult to estimate the extent of valence and conduction band tails that are expected to form in a disordered material phase. A weak indication of band tails is given by the valence *band* edge in the DOS of the CPMD configuration. Also the significant energy gap reduction for the DFTB structure indicates the possible influence of band-tail states. In general, weakly pronounced band-tail features, depending on a small fraction of the electronic states of the complete system, are just weakly indicated in the electronic DOS due to its state counting nature and the numerically enforced broadening.

We used the VASP relaxed CPMD geometry to investigate the numerical description of the electronic structure of a-TiO_2 on different levels of theory in more detail. Figure 4 shows the eigenvalue spectrum obtained for Γ-point-only calculations using the PBE and HSE06 functionals. Due to the absence of periodicity and therefore a well-defined k vector, the electronic energy gap is simply given by the Kohn-Sham eigenvalue difference between the highest occupied and lowest unoccupied state. This definition is equivalent to the definition

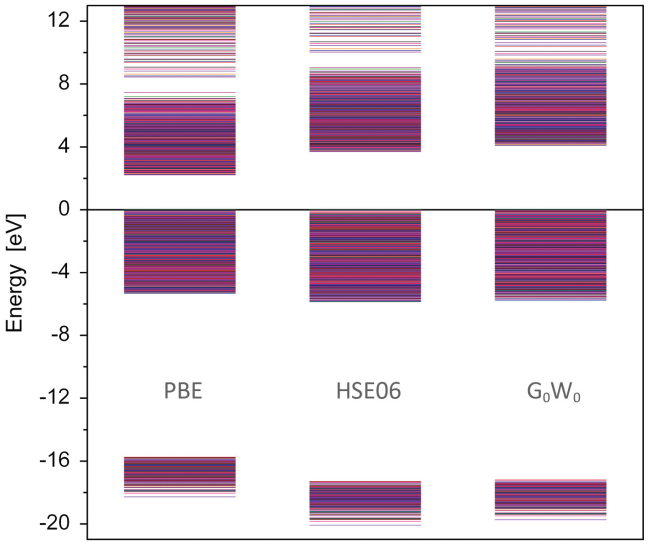

FIG. 4. (Color online) Kohn-Sham eigenvalues of the VASP relaxed CPMD structure calculated at the Γ point using the PBE and the HSE06 functional. Also shown are the QP energies obtained by G_0W_0 QP corrections on top of the PBE calculation. For details on the numerical convergence of the G_0W_0 results see discussion in the text.

of the HOMO-LUMO gap in molecular systems. The PBE energy gap of 2.21 eV is larger than the fundamental PBE gaps of the crystalline phases rutile (1.88 eV, direct), anatase (1.94 eV, indirect), and brookite (1.86 eV, direct). Using the HSE06 hybrid functional, the gap is widened to 3.69 eV which is close to the direct/indirect HSE06 anatase energy gap of 3.71 eV/3.60 eV. As demonstrated in our study on crystalline TiO_2,[17] the HSE06 eigenvalues represent a very accurate approximation of the QP energies, obtained from G_0W_0 calculations, as long as we consider energy states within ∼5 eV from the band edges. With this, the QP gap of the amorphous phase falls into the range of an anatase QP band gap of 3.7 eV to 3.9 eV estimated from the measured optical gap.

Also the G_0W_0 QP eigenvalue spectrum is presented in Fig. 4(c) and shows a large energy gap of 4.08 eV. However, this requires some comment concerning the numerical convergence of this value. Due to the large system size our G_0W_0 calculation was constrained to a set of minimal numerical parameters, mainly regarding the number of frequency grid points and the GW energy cutoff used to evaluate the response function. Aiming on a rough estimation of the associated error in the calculated energy gap, we applied a similar set of minimal parameters to the rutile bulk material. Similar to the enlarged energy gap of a-TiO_2, the obtained direct rutile band gap was 3.78 eV which is 0.46 eV larger than the converged result of 3.32 eV. Therefore, we expect that the G_0W_0 value of 4.08 eV overestimates the converged QP gap by ∼0.4 eV. Furthermore, the analysis of the rutile G_0W_0 QP gap convergence with the number of unoccupied bands (here: 2048, ∼28 per stoichiometric TiO_2 unit in a-TiO_2) further influences the result by at least 100–200 meV. The only approximation made in the HSE06 calculation was the reduction of the fast Fourier transformation grid in the exact exchange routines which significantly accelerates Hartree-Fock-type calculations. This typically adds an uncertainty not larger than a few hundred meV to the obtained band gaps. Compared to a calculation of the rutile phase using this limitation, the obtained HSE06 band gap is converged within ∼0.01 eV. The restriction to only the Γ point on the other hand does not influence the band gap notably. In fact the Γ point is even sufficient to obtain all characteristics of optical spectra.

From all these considerations, we expect the HSE06 energy gap of 3.69 eV to be a very reliable value for the QP gap of a-TiO_2.

Reported experimental energy gap data on variously prepared a-TiO_2 thin films cover an energy range from 3.2 eV to 3.7 eV.[24,26–33,35,36,127] All these results were obtained from UV-VIS spectroscopy followed by direct or indirect Tauc analysis/plots[128–130] to extract the optical gap. This means $(\alpha E)^{1/2}$ or $(\alpha E)^2$, with α being the absorption coefficient, is plotted versus the photon energy and the linear part of the curves is extrapolated towards the energy scale to define the optical gap. Besides UV-VIS spectroscopy data, we are not aware of any photoemission-spectroscopy data on a-TiO_2 that allow a direct verification of the calculated QP result. Therefore an experimental QP gap could only be estimated to be larger than the measured optical gap. A more accurate data examination shows a cumulatively reported optical gap between 3.2–3.5 eV,[26,29,31,32,36] obtained from indirect Tauc analysis $(\alpha E)^{1/2}$, and an energy gap >3.6 eV,[33] determined by direct Tauc analysis $(\alpha E)^2$ of the Kubelka-Munk function[131,132] that is proportional to the absorption coefficient.

Besides the exact energy gap value, general tendencies within the existing TiO_2 modifications are of interest in order to identify materials best suited for an intended usage and to understand underlying physical principles in general. While there is clear experimental evidence for an amorphous phase energy gap that is larger than the band gap in TiO_2 rutile, the relation $E_{\mathrm{gap}}^{\mathrm{am}} \gtrless E_{\mathrm{gap}}^{\mathrm{an}}$ between amorphous and anatase TiO_2 is unclear. Even the relation $E_{\mathrm{gap}}^{\mathrm{an}} \gtrless E_{\mathrm{gap}}^{\mathrm{br}}$ between the band gaps of crystalline anatase and brookite seems not completely unambiguously decided by experimental literature data. Since experimental data on TiO_2 brookite is limited and theoretical calculations[17] favor $E_{\mathrm{gap}}^{\mathrm{an}} > E_{\mathrm{gap}}^{\mathrm{br}}$, we will focus on the energy gaps of anatase and a-TiO_2. On the one hand, Amor *et al.*[24] demonstrated a sharp rise of the energy gap from 3.46 eV to 3.54 eV at the anatase crystallization temperature (350 °C) during annealing of a-TiO_2 films. Mardare *et al.*[35] estimated the optical gap of a-TiO_2 films to 3.25 eV and to 3.4 eV in crystalline anatase films. Also, a large band gap value of 3.8 eV for direct optical absorption in anatase TiO_2 films was obtained by Wang *et al.*[34] In addition Gofuku *et al.*[29] obtained identical energy gaps (3.4 eV) for both amorphous and anatase films. On the other hand, direct optical gaps of ∼3.4 eV for anatase and 3.66 eV for amorphous TiO_2 have been published by Luca *et al.*[33] Mardare *et al.*[27] observed an energy gap decreasing from 3.37 eV to 3.01 eV with increasing annealing temperature causing anatase formation. However, the behavior in the last study seems to be caused by the notable and, at higher temperature, even major coexisting fraction of the rutile TiO_2 phase. Within our theoretical description the

HSE06 calculations had shown almost identical energy gaps of 3.69 eV and 3.71 eV for a-TiO_2 and anatase. The assumption of similar electronic energy gaps in anatase and amorphous TiO_2 is further supported by results for mixed anatase-amorphous phases. DeLoach *et al.*[127] reported an indirect band gap of 3.41 eV for thin TiO_2 films build up by coexisting anatase and amorphous phases and a small volume fraction (0.02–0.017) of rutile.

We conclude that the pure stoichiometric amorphous phase of TiO_2, with an atomic density close to the rutile phase, shows a QP gap $\gtrsim$3.7 eV that is larger than the experimental and theoretical values reported for rutile and brookite, and that is comparable to the theoretically determined anatase QP band gap, as well as to the reported direct optical gaps of anatase thin films. So far we have restricted the discussion to the HOMO-LUMO-type energy gap, which, as we will see in the following section, was the main reason for choosing one of the VASP relaxed configurations due to the reduced influence of band-tail state localization.

C. Localization of band-tail states

In order to characterize the band-tail states, that were only weakly indicated in the electronic densities of states, we have calculated the information entropy based quantities $W^{-1}(\nu)$ and $R^{-1}(\nu)$ [cf. Eqs. (13), (14), Sec. II D] for the four structure models investigated here. Both representations give qualitatively similar information on the degree of electronic localization. Due to the difficulty to clearly distinguish between the localized and extended states, the determination of the mobility gap remains uncertain to some extent. Nevertheless, both the $W^{-1}(\nu)$ and $R^{-1}(\nu)$ representation allow a qualitative analysis of electronic state localization and the estimation of the mobility edge within a few tenths of an eV. In Fig. 5, the estimated separation between localized and extended states is indicated by vertical dashed lines, whose positions were chosen from the distinct quantitative differences in $W^{-1}(\nu)$ and $R^{-1}(\nu)$ values for the two VASP relaxed configurations. As a general limitation we have to keep in mind that the sizes of our unit cells represent a severe limitation to the accurate

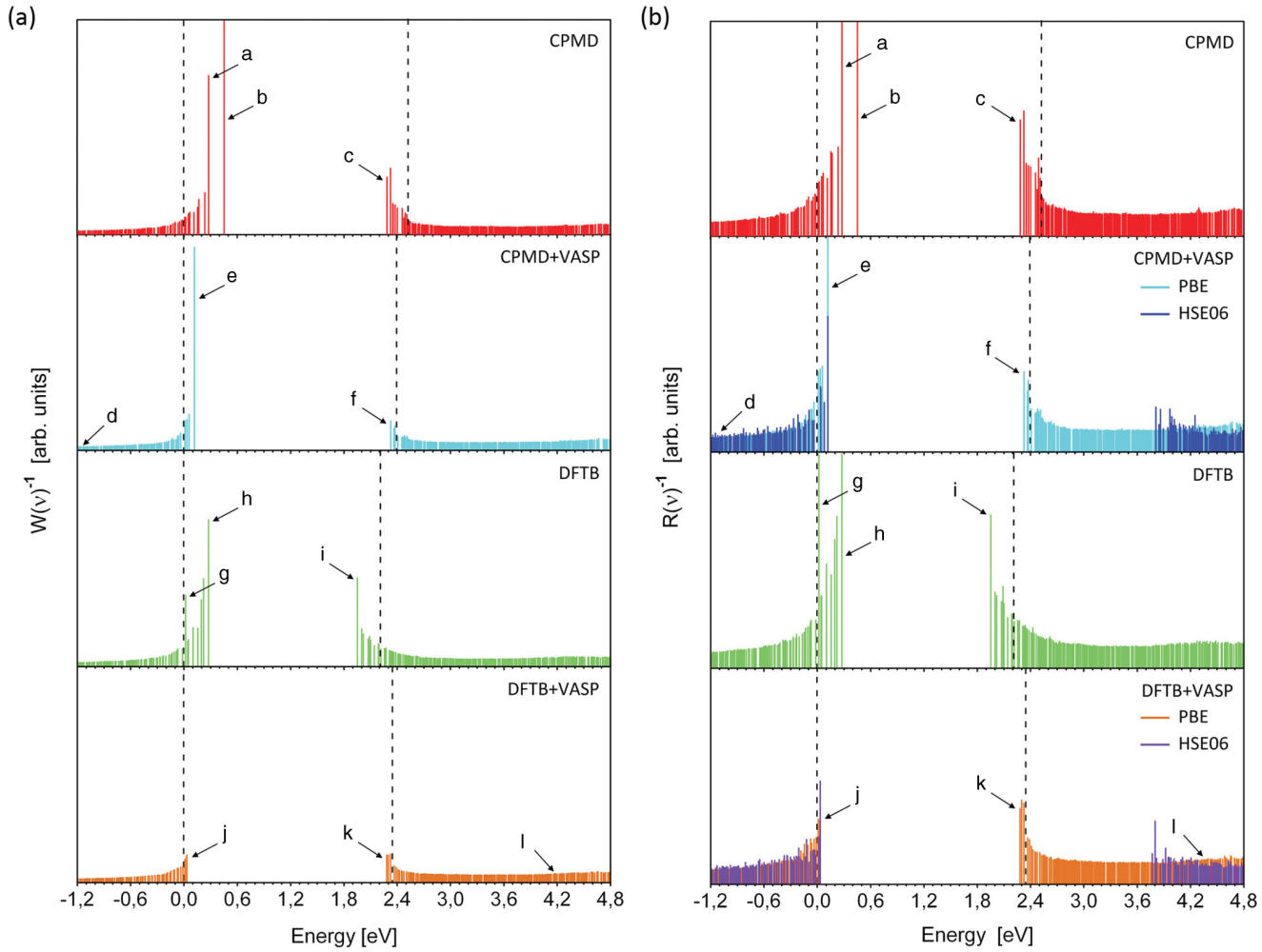

FIG. 5. (Color online) Information entropy based measures of state localization $W^{-1}(\nu)$ and $R^{-1}(\nu)$ for the CPMD MD and DFTB MD generated as well as VASP relaxed models of 4.20 g/cm^3 a-TiO_2 (cf. Fig. 1). Based on the definitions in Sec. II D, a higher value corresponds to stronger localization for both quantities. For the two VASP optimized structures, the IPRs based on the HSE06 electron densities have been included. The DFT-PBE electron densities for marked electronic states are visualized in Fig. 6. Also indicated are the estimated positions of the mobility edges that separate the strongly localized states from the delocalized Bloch-type states. The estimated position of the valence states mobility edge has been chosen as the zero point of the energy scale (x axis).

modeling of localized states and the transition to extended states in an amorphous material phase.

In Fig. 5, we clearly observe extended valence and conduction band tails for the two room-temperature structures generated by CPMD and DFTB MD. These band tails are responsible for the smaller HOMO-LUMO-type energy gaps at room temperature structures. We find the weakest formation of band-tail states for the VASP relaxed DFTB geometry. However, the VASP relaxation of the CDMD generated structure shows equally weak pronounced band-edge tails with exception of the highest distinctly localized valence state. These observations, in general, demonstrate a significant influence of temperature-induced disorder on the localization of electronic states. Interestingly, the formation of band-tail states does not directly seem to be correlated to the mean coordination number. While the mean coordination number decreases significantly for the DFTB geometry, no significant difference to the crystalline mean coordination was found in the CPMD geometry as already discussed above.

In detail the estimated mobility gaps of the VASP relaxed CPMD and DFTB structures are 2.39 eV and 2.35 eV which is only slightly larger than the energy differences of 2.21 eV and 2.25 eV of the lowest occupied and the highest unoccupied state, respectively the HOMO-LUMO-type gap. Compared to the DFT-PBE band gaps of the crystalline TiO_2 phases (rutile: 1.88 eV, anatase: 1.94 eV, and brookite: 1.83 eV), the gap energies increase about $\sim$0.4 eV due to structural disorder. The mobility gaps of the two room-temperature MD configurations show no clear tendency in the development of the mobility edge due to temperature-induced disorder. On the one hand, the band-tail states' adjusted gap of the CPMD structure increases to 2.52 eV. On the other hand, the same quantity is reduced to 2.21 eV in the case of the DFTB structure.

Figure 5 also displays the IPR based on the electron densities from HSE06 calculations for the two VASP optimized structure models. In both cases the HSE06 data show quite similar localization characteristics. Similar to the PBE data, the valance tail shows a slightly more distinct localization of band-tail states. Based on the HSE06 calculation, we obtain an estimated mobility gap of $\sim$3.8 eV for both a-TiO_2 structure models. Similar to the PBE data these gaps are only slightly ($\sim$0.1 eV) larger than the HOMO-LUMO-type energy gaps of 3.69 eV and 3.73 eV for the CPMD + VASP and the DFTB + VASP structures.

In order to classify the nature of the localized band-tail states, we have selected characteristic examples of localized electronic states and visualized the electronic charge-density distributions in Fig. 6. Despite their spatial localization, we find that all band-tail states conserve the O_{2p}-like valence state and the Ti_{3d}-like conduction state character. The electronic states labeled by a and b for the CPMD structure as well as e and h for the CPMD + VASP and DFTB structures represent the strongest localized states found in our models. The nature of these localized valence states can be assigned to two types of lattice sites. On the one hand, we find *p*-type charge density contributions from threefold coordinated O ions that are slightly displaced from the plane of the three Ti ions in Ti_3O units. On the other hand, we find significant contributions from under-coordinated O ions, bound to just two Ti ions. Also the less confined electronic state visualized in Fig. 6(j), that forms the highest valence state in the VASP relaxed DFTB configuration, belongs to this type of localized states. The localized conduction band-tail states, in all configurations, arise from charge densities located at over-coordinated Ti ions in TiO_7 building blocks as well as contribution from formally sixfold coordinated TiO_6 and, to a minor extent, from under-coordinated TiO_5 building blocks.

We have also included examples of completely delocalized Bloch-type states. Figure 6(d) exemplarily represents states out of the continuum of delocalized O_{2p}-like states in a-TiO_2. The charge density distribution in Fig. 6(l) belongs to the class of delocalized Ti_{3d}-like states in a-TiO_2. Similar to crystalline TiO_2 the optical characteristics of a-TiO_2 are thus expected to be significantly characterized by optical transitions between these two continua of Bloch-type states.

A more detailed representation of the dependence of the local coordination number and the character of associated electronic states is given in Fig. 7. Here, the local/site-decomposed densities of states are displayed for the various coordinations of O and Ti ions found in the CPMD + VASP configuration [cf. Fig. 1(b)]. In agreement with the charge densities of the different localized valence-tail states pictured in Fig. 6, the topmost valence states show a characteristic predominance of under-coordinated oxygen ions in Ti_2O filaments. Energetically slightly lower lying states show the common threefold coordination of the most common crystalline phases (cf. Ref. 17). As mentioned above, the corresponding Ti_3O units show structural distortions from the planar-trigonal crystal-type building blocks. Hence, the valence band tail arises primarily from localized states due to variations of the local oxygen coordination number and additional contributions from state localization due to structural disorder in deformed Ti_3O building blocks. The DOS contributions of over-coordinated, distorted-tetrahedron-type Ti_4O building blocks show a clear separation from the contributions of lower coordinated O ions and a dominant contribution at the bottom of the first valence *band*. The DOS differences in the lower half of Fig. 7(a) indicate that the amounts of lower coordinated and higher coordinated DOS contributions show an approximately antiproportional distribution over the whole energy range.

While the observable energetic separation of differently coordinated ions in the local DOS gives rise to the slightly more pronounced valence tails of a-TiO_2 indicated by the IPR in Fig. 5, the conduction band edge shows a stronger superposition of states originating from differently coordinated ions. Over-coordinated TiO_7, normal-coordinated TiO_6, and under-coordinated TiO_5 building-block states occur directly at the conduction band-tail edge. In general, a slight preference for higher coordination is still notable at the bottom of the conduction *band*, whereas, at higher energies, the superposition of DOS contributions from different coordinations is less structured.

Bridging the gap to language and concepts bound to a common view of deviations from a normal crystal-type atomic coordination as defects, we may also recover the characteristics of donor- and acceptor-like states. The unpaired electrons of the under-coordinated O ions generate localized acceptor-like dangling bond states at the valance band-tail edge. The local over-coordination of Ti ions on the other hand results in the presence of localized donor-like electronic states at

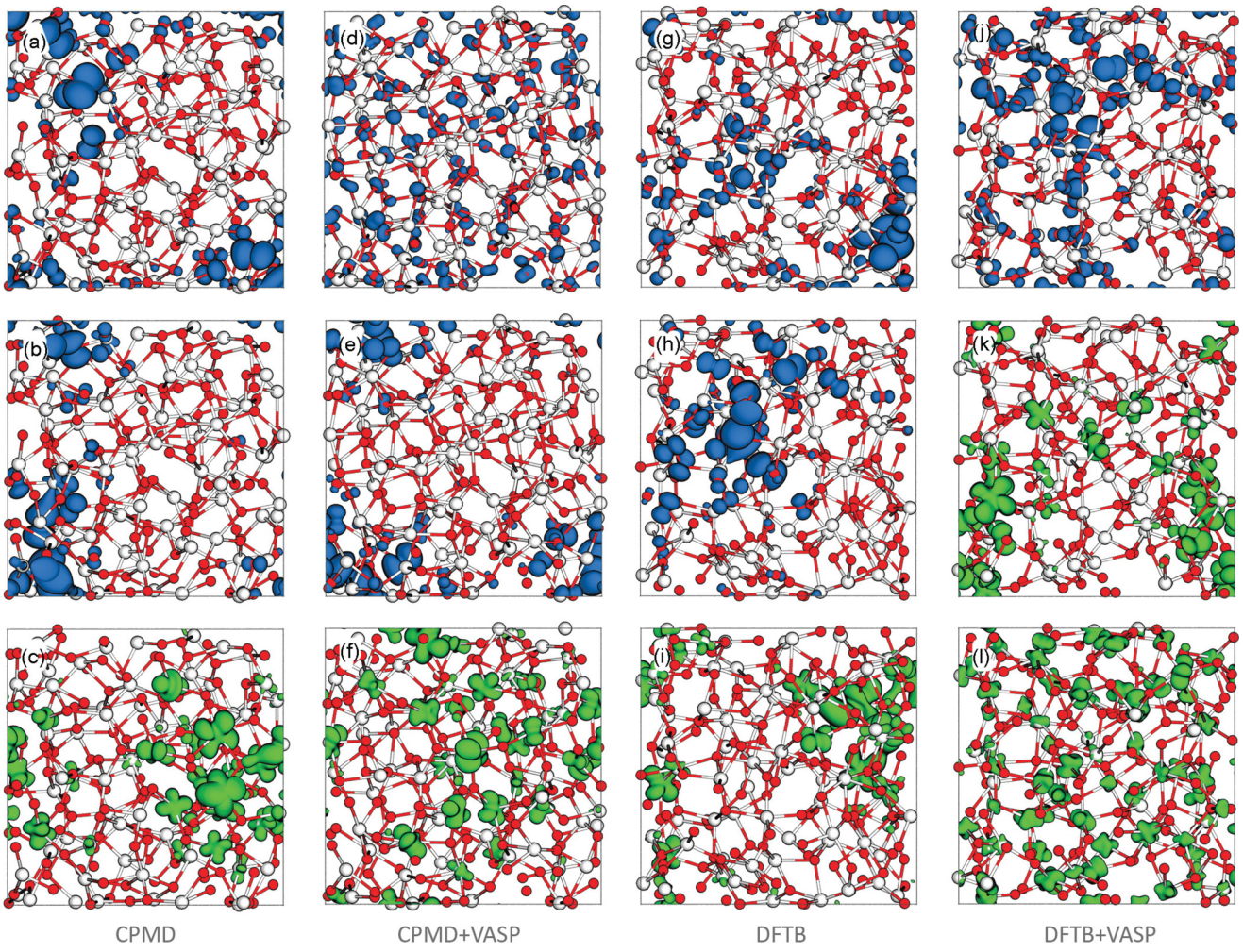

FIG. 6. (Color online) Isosurfaces of various electronic states in a-TiO_2. The states are labeled corresponding to the energy levels in Fig. 5. The states represent different degrees of localization for occupied and unoccupied states. The subfigures d and l are examples for completely delocalized Bloch-type states.

the conduction band-tail edge. Similar to the well-defined separation of bonding and antibonding states discussed above and the resulting crystal-like electronic structure, the formation of crystal-type defect states due to over- and under-coordinated ions demonstrates the strong influence of short-range order on the formation of the electronic structure in disordered semiconductors.

D. Optical properties of amorphous TiO_2

To obtain more insight into the optical characteristics of a-TiO_2 we investigated the dielectric function and related frequency-dependent optical constants of our structure models over an extended energy range. In Fig. 8, the real and imaginary parts of the calculated IPA dielectric functions are shown for all four unit cells. As already indicated by the structural characteristics in Sec. III A and the electronic properties described in Sec. III B, the CPMD, CPMD + VASP, and DFTB + VASP configurations show almost identical dielectric properties. Also the DFTB MD generated structure shows very similar spectral features with some variations in peak heights. Thus, in the following discussion, we will focus on the VASP relaxed CPMD configuration and compare the results obtained for the DFTB structure at the end of this section. For simplicity we will refer to the CPMD + VASP structure just as the VASP configuration. Considered together, these two structures allow us to estimate the variations in the optical properties originating, on the one hand, from the room-temperature influences on electronic structure, and on the other hand from different types of local symmetries, generated by various numerical approaches.

The optical frequency-dependent constants of a-TiO_2, defined through Eqs. (3)–(7), are displayed in Fig. 9. More precisely the plotted curves correspond to the isotropic optical functions obtained by averaging the nonvanishing components of the dielectric tensor [i.e., $(\varepsilon_{xx} + \varepsilon_{yy} + \varepsilon_{zz})/3$]. Without these averaging procedures, the obtained dielectric functions still show some weak anisotropies due to the limited super cell size while the qualitative distribution of oscillator strength is identical. Instead of using the insufficiently converged G_0W_0 results to derive QP shifts, we applied the scissors-shift approximation to shift the unoccupied DFT-PBE Kohn-Sham

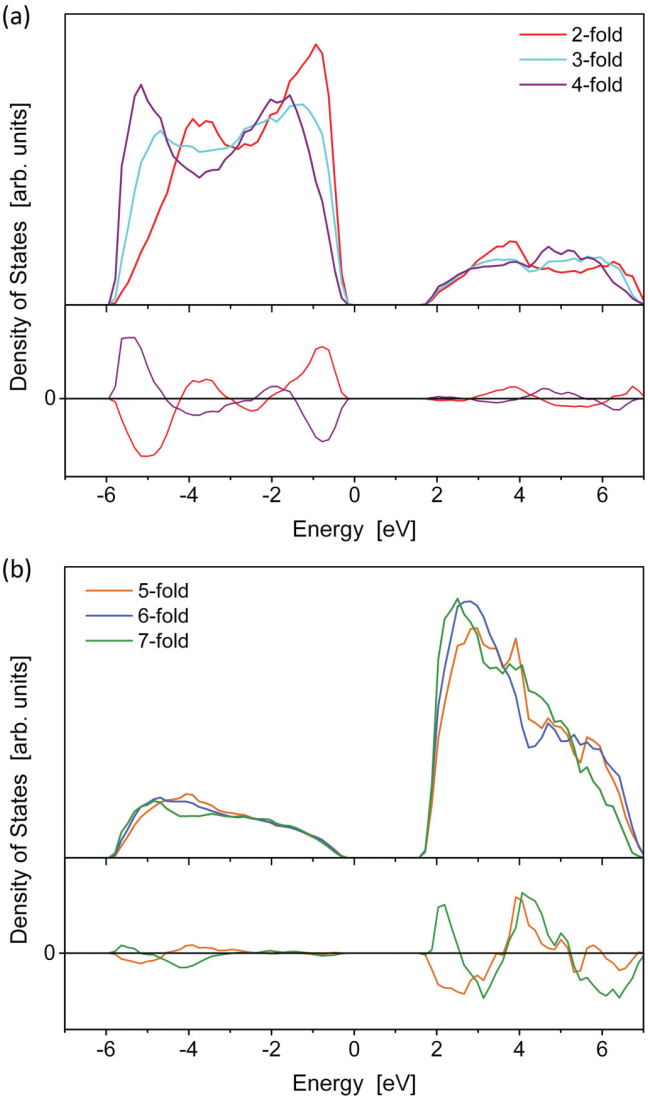

FIG. 7. (Color online) Local densities of states for the various coordination numbers occurring in the CPMD + VASP model. The total site-projected densities of states have been averaged over all O ions (a) and Ti ions (b) showing the particular coordination. The lower graphs show the differences between the normal coordinated ions (threefold in the case of O ions and sixfold for Ti ions) and the over- and under-coordinated ions.

states in energy while keeping the PBE wave functions to calculate matrix elements. Motivated by scissors shifts of 1.2 eV, 1.3 eV, and 1.3 eV for the crystalline phases rutile, anatase, and brookite [chosen to match direct optical band gaps of rutile and anatase (cf. Ref. 17)], we applied a scissors shift of 1.3 eV for our a-TiO_2 models. In contrast to the DFT-PBE eigenvalue spectrum in Fig. 4, the optical spectra were calculated using a regular $3 \times 3 \times 3$ k-point mesh. However, the restriction to one k-point only results in oscillations of the oscillator strength in the dielectric function's main peaks that are small if compared to the results obtained by the coarser k-point grid.

Figure 9(a) shows the real and imaginary parts of the dielectric function calculated using 1920 electronic bands and

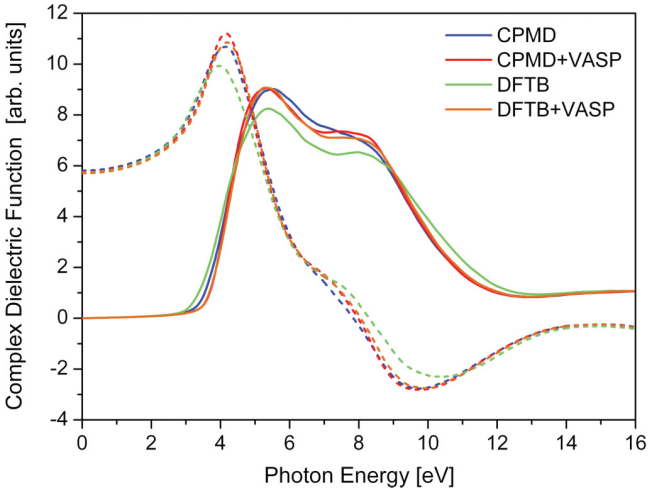

FIG. 8. (Color online) Real (dashed line) and imaginary (solid lines) parts of the isotropic complex dielectric functions $\varepsilon(\omega)$ of the four a-TiO_2 models (cf. Fig. 1).

a Γ-centered $3 \times 3 \times 3$ k-point mesh. By extrapolating the linear low-energy flank of the imaginary part of the dielectric function towards the energy axis, the absorption onset around ∼3.65 eV is found to be close to the minimal estimated value for the QP gap. This tendency is quite similar to the difference in QP band gaps and extrapolated optical band gaps of the crystalline phases obtained from solving the BSE for Coulomb correlated QP.[17]

Compared to very recent data for ion-beam sputtered films [see red dotted curves in Fig. 9(a)] that indicate the absorption onset around 3.6 eV, our calculated dielectric function is found to be in good agreement with the experiment. Also, the real part of the dielectric function demonstrates a fairly reasonable agreement between theory and experiment on the dielectric constants in the visible range of the spectrum. Comparing the dielectric constants at 2 eV (i.e., a wavelength of 620 nm), we find an agreement between the experimental value of $\varepsilon(620\ \text{nm}) = 5.93$ and the theoretical result $\varepsilon(620\ \text{nm}) = 6.37$ within ∼7%. Unfortunately the measured dielectric function data are limited to a small energy region around the absorption onset, and we cannot compare spectral features at higher energies. An extended spectroscopic ellipsometry data set for the complex refractive index of electron-beam evaporation prepared TiO_2 thin films is found in the literature,[30] spanning an energy interval from 1.5 eV to 5.5 eV. These results are included in Fig. 9(b). The experimentally observed peak at 4 eV in the real part of the complex refractive index $\tilde{n}$, respectively the refractive index n, is qualitatively resolved in our data, while the peak height is noticeably underestimated and the peak position is slightly overestimated by ∼0.2 eV. However, the refractive index in the visible range around 2 eV [$n(620\ \text{nm}) = 2.52$] agrees perfectly with the experimentally derived data. Additionally we have summarized the further available data on the refractive index $n(\lambda)$ and the extinction coefficient $\kappa(\lambda)$ (mainly given for 500–600 nm green light) in Table II.

These collected experimental dielectric constants give further evidence for a reasonable description of optical constants by our data, even though the calculated values tend to

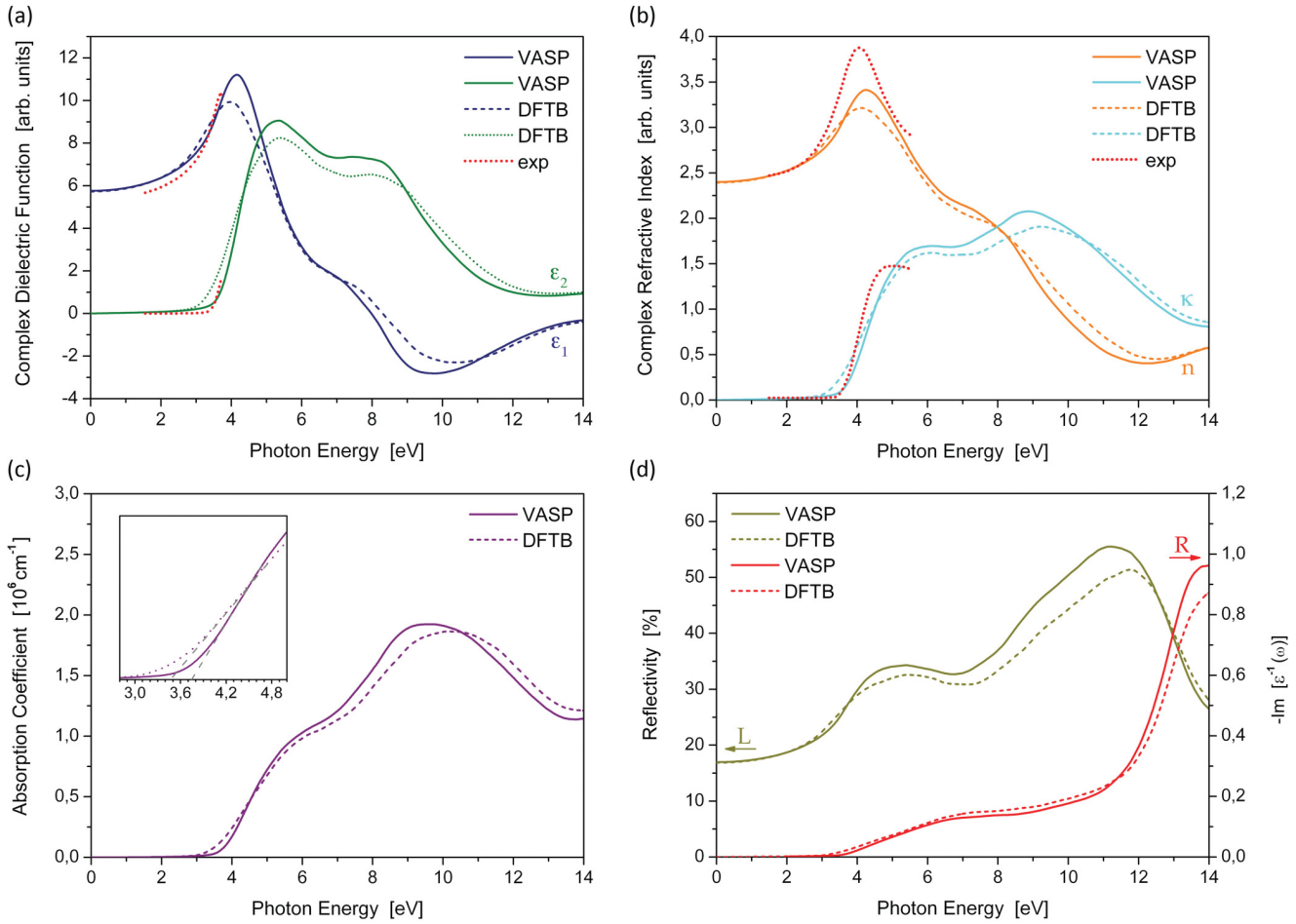

FIG. 9. (Color online) (a) Real part $\varepsilon_1(\omega)$ and imaginary part $\varepsilon_2(\omega)$ of the complex dielectric function $\varepsilon(\omega) = \varepsilon_1(\omega) + i\varepsilon_2(\omega)$, (b) real part $n(\omega)$ and imaginary part $\kappa(\omega)$ of the complex refractive index $\tilde{n} = n + i\kappa$, (c) absorption coefficient $\alpha(\omega)$, and (d) reflectivity $R(\omega)$ (left axis) and energy loss spectrum $R(\omega)$ (right axis). The optical spectra are calculated from the DFT-PBE eigenvalues (CPMD + VASP or DFTB structure, 1920 electronic bands, $3 \times 3 \times 3$ k points) applying a scissors shift of 1.3 eV to the unoccupied states. For comparison, experimental data for the dielectric function from Ref. 133 and refractive data from Ref. 30 have been included.

overestimate the measured ones up to 20%. Generally, one should keep in mind that the reported data are significantly influenced by temperature[135] and density fluctuations of the films.[134] A comparison of the calculated imaginary part of the complex refractive index, i.e., the extinction coefficient κ, to plotted experimental result in Fig. 9(b) shows a deviation in peak height and position but still comparable curve characteristics. The calculated extinction coefficients in the visible wavelength regime (see Table II) are significantly overestimated. However, the description of such small absolute values is beyond the accuracy of the applied theoretical framework. Errors of this size are already caused by the choice of the broadening parameter for evaluating the dielectric function.

TABLE II. Experimentally determined refractive indices $n(\lambda)$ and extinction coefficients $\kappa(\lambda)$ in the visible range measured for variously prepared (predominantly) amorphous TiO_2 thin films. To preserve clearness, only the values for experimental conditions closest to the theoretical calculation (0 K and 4.20 g/cm^3) are included.

Wavelength (nm)	n	κ	Film preparation	Ref.
500	2.51	3×10^{-3}	ion-beam evaporation	134
550	2.51		bias arc ion plating	36
550	2.40		DC sputtering	25
550	2.57	$\sim 10^{-4}$	vacuum arc deposition	32
552	2.21	0.8×10^{-3}	DC sputtering	27
600	2.24	2.6×10^{-3}	magnetron sputtering	135
600	2.12	1.8×10^{-3}	magnetron sputtering	26
500	2.61	23×10^{-3}	this work	
550	2.56	19×10^{-3}	this work	
600	2.53	16×10^{-3}	this work	

In Fig. 9(c) the absorption coefficient for the amorphous material is given. The inset gives a detailed view of the absorption coefficient around the adsorption onset. From the linear rise of the absorption coefficient and linear extrapolation to the energy axis, the energy gap has been estimated to 3.74 eV, which is in the region of the (estimated) QP gap. At this point an additional comment on the determination of energy gaps from experimental data seems appropriate. Basically, all the discussed experimental data on TiO_2 thin

films (crystalline, nano/micro-crystalline, or amorphous) rely on the, strictly speaking empirical, fitting of an exponential law to the measured absorption data. Thereby, the actual value of the exponent is related to the assumption of direct or indirect optical transitions. To demonstrate the ambiguity of the various optical-gap extrapolation methods, we obtain an energy gap of 3.34 eV from analyzing $(\alpha h\nu)^{1/2}$, 4.5 eV from $(\alpha h\nu)^2$, and 3.74 eV in the case of analyzing α itself. Moreover, the differentiation into "direct" and "indirect" transitions or the denotation "band" gaps is misleading in the case of an amorphous phase, since these are concepts of crystalline materials with a well-defined k vector and cannot be applied to amorphous solids. However, the 3.34 eV gap energy, obtained from analyzing $(\alpha h\nu)^{1/2}$ for our calculated absorption coefficient, agrees with the reported thin film values of 3.2–3.5 eV obtained from indirect Tauc analysis. In this way our results support the empirically motivated fitting procedure to derive energy gaps from amorphous samples by using the extrapolation of the linear progression in $(\alpha h\nu)^{1/2}$ to define the optical band gap. For the sake of completeness, the energy-dependent reflectivity and the (low) energy loss spectrum have been calculated from the dielectric function; see Fig. 9(d).

Throughout all optical spectra, the frequency-dependent optical constants calculated for the 300 K DFTB-MD geometry show qualitatively identical spectral features. However, the slightly different type of short-range order, which is for example indicated by the lower mean coordination number of Ti ions, seems to result in some spectral weight relocation away from the center of the main peaks in the imaginary part of dielectric function towards the low- and high-frequency flanks. This also reflects the reduced energy gap obtained for the DFTB geometry. The differences in the imaginary part of the dielectric function also affect the peak heights in the real part. Nevertheless, the spectrum in the visible range coincides with the VASP structure data curve in that region. From extrapolating the linear parts in the imaginary part of the dielectric function and the absorption coefficient, energy gaps of ∼3.35 eV and ∼3.49 eV are obtained. These values are 0.25 eV and 0.3 eV below the corresponding quantity calculated from the VASP optimized structure.

Altogether, the structure provided by the numerical efficient DFTB-MD simulation allows a cost-efficient generation of amorphous structures with optical properties that are very close to the properties of CPMD-MD results. After additional (zero temperature) DFT structure relaxations of the DFTB-MD and CPMD-MD configurations, no significant differences in the dielectric functions (cf. Fig. 8) remain.

E. Many-body contributions to the optical response of amorphous TiO_2

The preceding discussion of optical properties was strictly based on a pure DFT-PBE single-particle picture for the dielectric function (i.e., IPA). In order to estimate the influence of many-particle interactions on the optical response of the many-electron system, we have treated one- and two-particle excitation within the framework of many-body perturbation theory in the commonly applied two-step procedure.

In a first step we consider QP self-energy corrections to the eigenvalue spectrum by the first-order perturbative G_0W_0 approach. The resulting QP energies determine the dielectric function in independent QP approximation (IQPA). Compared to the IPA dielectric function (without taking into account a scissor shift correction), the IQPA dielectric function (see Fig. 10) shows a strong blueshift of the absorption edge of ∼1.85 eV but almost identical spectral features. As discussed in the context of electronic energy gaps, this strong blueshift might suffer from an overestimation of QP shifts by ∼0.4 eV that is owned to the indispensable reduction of numerical parameters in our G_0W_0 calculation. As shown elsewhere (see Ref. 17), the use of the HSE06 hybrid functional allows an accurate approximation of TiO_2 QP properties. Thus, we expect the the HSE06 energy shifts/the HSE06-IPA dielectric function to be more reliable. In analogy to the energy gap, the blueshift (∼1.5 eV) of the absorption edge is less pronounced by using the hybrid functional data.

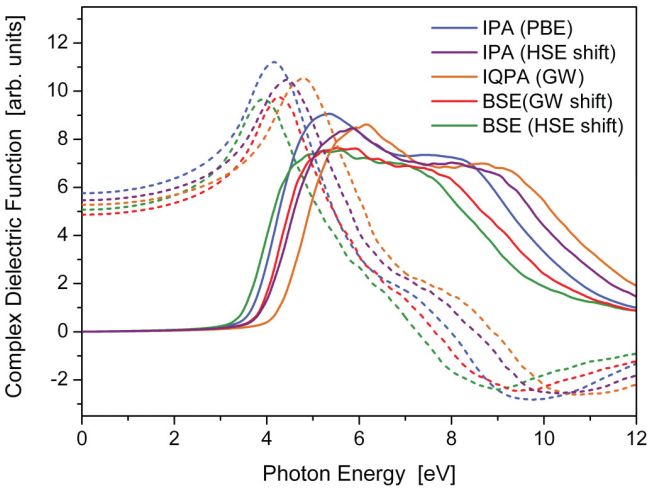

FIG. 10. (Color online) Real (dashed line) and imaginary (solid lines) parts of the isotropic complex dielectric function $\varepsilon(\omega)$ calculated for the CPMD + VASP structure model on different levels of theory.

The second step of many-particle effect-inclusion accounts for two-particle electron-hole pair excitations (i.e., excitonic effects) and necessitates the computational demanding solution of a Bethe-Salpeter equation for Coulomb correlated (quasi)particles. For the most common crystalline phases distinct modifications of the optical response have been observed[17,59,60,62] by inclusion of the two-particle excitations. On the one hand the absorption onset is redshifted compared to the IQPA data. On the other hand electron-hole pair interactions add and modify spectral features in the optical response functions. In particular, characteristic excitonic feature are found in the dielectric function of rutile and anatase close to the adsorption onset. For the symmetry-reduced TiO_2 brookite phase these excitonic features are found to be less pronounced.[17] Obviously these trends hold for a-TiO_2. The BSE dielectric functions show an absorption edge redshift of ∼0.5 eV compared to the IQPA-G_0W_0 respectively the IPA-HSE06 dielectric function.

Apart from the redshift, no distinct excitonic modifications of the BSE dielectric function are found. In summary, the main effect of many-body contributions to the linear optical response is a pronounced energy shift while the spectral

weight distribution is widely preserved. All together, these observations provide a sufficient justification for the computationally efficient use of the well-converged IPA dielectric function in combination with a simple scissors shift approximation. Some of the differences between the scissor shifted IPA and the BSE dielectric function may also be related to the numerical setup used to solve the BSE. Especially, the reduction of the energy cutoff for pairs of Kohn-Sham eigenvalues that enter the constructing of the electron-hole pair Hamiltonian, the restriction to only the Γ point, and the energy cutoff for evaluating of the Kohn-Sham-Bloch matrix elements add some uncertainty to the BSE dielectric function.

F. Order and disorder in optical spectra

In this subsection we will address the question of how the optical properties of the crystal are modified by its loss of long-range order in the context of a further analysis of the complex dielectric function. In order to single out the differences between the amorphous and crystalline phases, the isotropic real and imaginary parts of the IPA dielectric functions of rutile, anatase, and brookite are plotted in Fig. 11 alongside the result for the amorphous material (CPMD + VASP structure). In contrast to the most common crystalline phases, the imaginary part of the dielectric function of a-TiO_2 indicates stronger absorption in the energy range between 5 eV to 8 eV by an enhanced oscillator strength in this energy region. Nevertheless, the two main-peak characteristic observed in the spectra of crystalline TiO_2 remains identifiable. Similar to anatase, the center of the first main peak is slightly shifted to higher energies (∼5.3 eV) compared to rutile.

The comparison of the isotropic dielectric functions again prove the common optical characteristics of rutile, anatase, and brookite. However, despite the suggested close relation of a-TiO_2 to brookite or anatase, pronounced differences are obvious. Even the equally weighted average over the three crystalline main phases does not show any more resemblance to a-TiO_2. The reason for the differences can be traced to the differences in the local atomic structure already emphasized in the discussion of structural properties in Sec. III A. For the crystalline phases rutile and anatase the existence of the two peaks has been assigned to the crystal-field spitting[17,48,49,125,126,136] of the unoccupied broad Ti_{3d} energy band into e_g and t_{2g} like subbands. This splitting is directly connected to the local octahedral coordination of a Ti ion by six O ions, which even holds for the stronger distorted octahedra in the symmetry-reduced brookite phase. Since the octahedral-like local symmetry is partially lifted in the amorphous phase due to strong distortion in the TiO_6 building blocks and the formation of TiO_x units with $x = 4, 5, 7, 8$, this characterization cannot be applied to the entire amorphous material complex. Due to the missing distinct separation of Ti $3d$ states into e_g and t_{2g} like states, optical excitations take place between two broad energy continua of electronic states whose types are exemplarily visualized in Fig. 6(d) and Fig. 6(l). These are on the one hand the occupied $2p$-like states of oxygen, covering the energy range from −5.3 eV to 0 eV, and on the other hand the unoccupied $3d$-like states in the energy region from 3.5 eV to 8.8 eV. Here, the energy of the highest occupied Kohn-Sham state has been chosen as the zero point of the energy scale and, in contrast to the l-DOS reported in Fig. 3, a scissors shift of 1.3 eV has been taken into account. From these broad energy bands, electronic transitions in the energy range from 3.5 eV to 14 eV are possible without significant forbidden energy ranges. As a key result, this demonstrates that the amorphous phase of TiO_2 obeys peculiar optical features that are commonly not observed in the long-range ordered crystalline TiO_2 main phases rutile, anatase, and brookite.

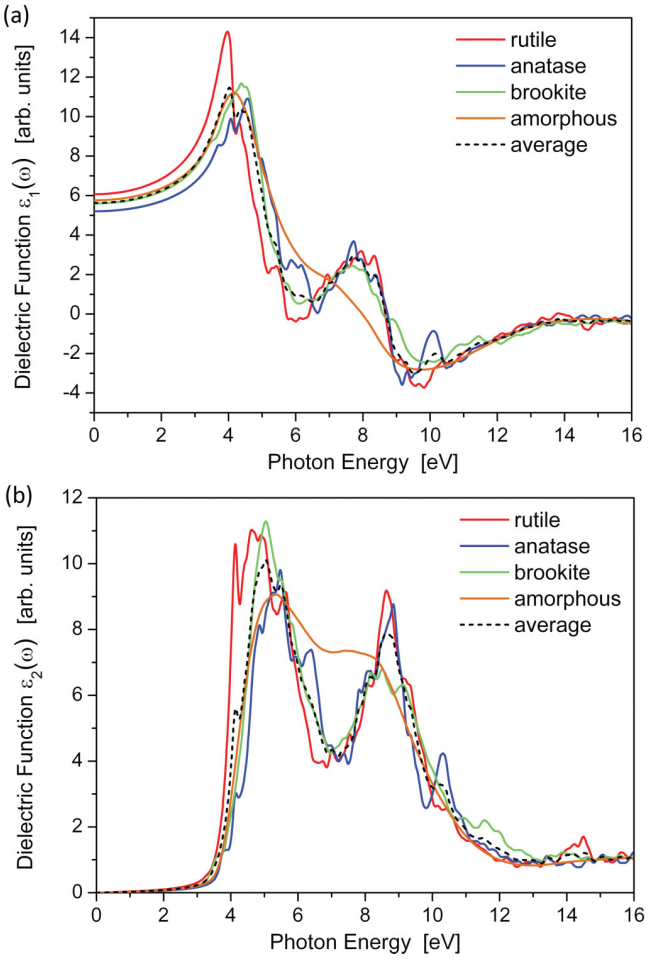

FIG. 11. (Color online) Comparison of the real part $\varepsilon_1(\omega)$ and imaginary part $\varepsilon_2(\omega)$ of the isotropic dielectric function of the crystalline TiO_2 phases rutile, anatase, and brookite and the disordered phase (CPMD + VASP structure) of TiO_2. Also plotted is the equally weighted average of the three crystalline phases.

One interesting observation is related to the phase-averaged dielectric function shown in Fig. 8. Instead of resembling the spectra of a-TiO_2 it is quite close to the brookite phase itself. This indicates a certain similarity between the local atomic environment of orthorhombic brookite and both higher symmetry phases rutile and anatase (see Ref. 17).

G. Optical properties of TiO_2 crystals

So far, we have compared the optical adsorption in a-TiO_2 to the three crystalline main phases rutile, anatase, and brookite. However, most of the existing/fabricable TiO_2 modifications, identified in the extraordinarily rich phase diagram of TiO_2,

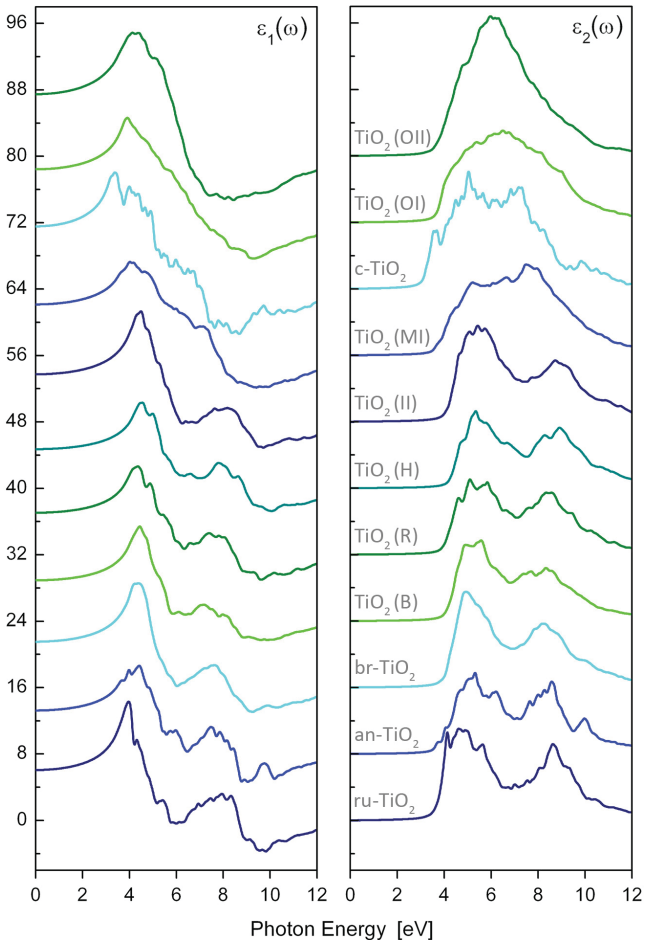

FIG. 12. (Color online) Real and imaginary part of the isotropic dielectric functions of (in ascending order) the crystalline TiO_2 phases rutile (ru-TiO_2), anatase (an-TiO_2), brookite (br-TiO_2), TiO_2(B), TiO_2(R), TiO_2(H), TiO_2(II), TiO_2(MI), c-TiO_2, TiO_2(OI), and TiO_2(OII).

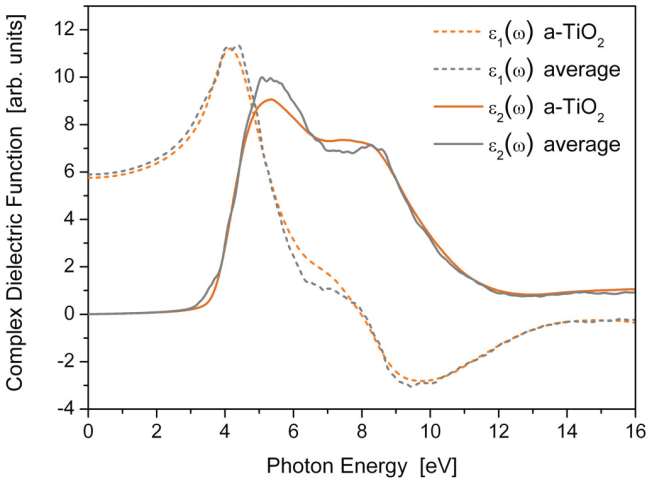

FIG. 13. (Color online) Real and imaginary part of the isotropic dielectric function of a-TiO_2 and the equally weighted averages of the eleven crystalline phases listed in Fig. 12.

have been ignored so far. In order to identify the additional contributions in the optical spectra of a-TiO_2 it seems natural to extend the investigation to the existing metastable and high-pressure phases. In detail, we have investigated the metastable phases TiO_2(B), TiO_2(R), and TiO_2(H) and the high-pressure phases TiO_2-OI, TiO_2-OII, TiO_2-MI, TiO_2 II, and c-TiO_2. In Fig. 12, the calculated isotropic dielectric functions in IPA are depicted. With exception of 1.2 eV for rutile, a scissors shift of 1.3 eV was applied to all crystalline phases in order to preserve comparability and due to missing experimental band-gap reference data for most phases. From the dielectric functions, it is obvious that all crystalline TiO_2 phases, whose structure is composed from TiO_6 octahedron building bocks, show common optical properties. Especially the characteristic two-peak shape of the imaginary part of the IPA dielectric function, connected to the octahedral-like crystal-field splitting of the unoccupied Ti_{3d} states into e_g and t_{2g} like states, is obvious. Consequently, a change in the local atomic structure, i.e., a Ti ion coordinated by more than 6 O ions, results in a single broad peak in the dielectric function due to the lifting of the octahedral-like symmetry and a continuous first broad conduction band in the electronic DOS. This is comparable to the observed continua of electronic states and optical transition energies in the DOS and dielectric function of the amorphous phase. The non-sixfold-coordinated TiO_2 modifications are the four high-pressure phases TiO_2-OI, TiO_2-OII, TiO_2-MI, and c-TiO_2. Out of these, Ti ions are sevenfold coordinated in TiO_2-OI and TiO_2-MI, eightfold coordinated in c-TiO_2, and ninefold coordinated in TiO_2-OII by O ions. As a side note, the reduced band gap of the cubic fluorite phase, reported by various authors,[11,12,137] is reproduced in our data.

In Fig. 13, we have compared the equally weighted average of the dielectric functions of all investigated eleven crystalline phases. Thereby, we assume that the versatile local structure of the amorphous phase reflects a wide cross section of all possible binding situations appearing in the crystalline phases. The obtained crystal-phase average basically reproduces all features of the amorphous phase. The height of the first main peak around 5 eV in the imaginary part is slightly overestimated. However, this discrepancy could probably be further reduced by inclusion of excitonic effects that can have significant influence on the energy region close to the absorption onset, as demonstrated for rutile and anatase. Hence, we emphasize that the amorphous phase of TiO_2 can be understood as a superposition of the diversified local atomic environments (i.e., different types of short-range order) existing in crystalline TiO_2 modofications.

H. Density dependence of the optical response in amorphous TiO_2

In general, electronic properties as the electronic *band* gap and related quantities as the dielectric function should be compared for amorphous and crystalline material phases that approximately share the same mass density. In doing so, the basic influence of density variations does not superimpose the effects of structural disorder. However, an amorphous material modification is not necessarily a disordered phase with a homogeneous mass distribution on an atomic length scale. Commonly, nano- and microstructural inhomogeneities occur in form of voids and formation of grainlike crystallized

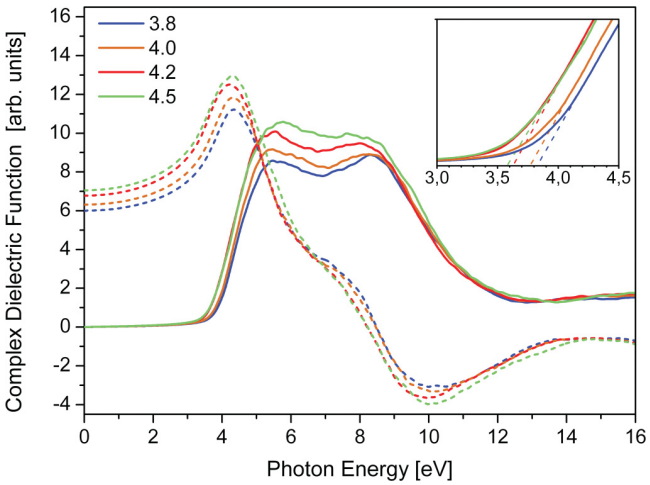

FIG. 14. (Color online) Real (dashed line) and imaginary (solid lines) parts of the isotropic dielectric function $\varepsilon(\omega)$ for a-TiO_2 structure models with mass densities of 3.8, 4.0, 4.2, and 4.5 g/cm^3 obtained using 1632 electronic bands, the Γ points only, and a 1.3 eV scissors shift in all calculations. The inset on the upper right gives a detailed view on the imaginary part of the dielectric function close to the absorption edge.

domains in amorphous samples and have to be considered as sources of local density fluctuations. In order to estimate the extend of linear-response modifications due to variations of the material density, we have generated a series of structure models with different mass densities. All structures were generated by DFTB-MD and successive structural relaxation using VASP.

Figure 14 shows the real and imaginary components of the complex dielectric function for the four mass densities 3.8, 4.0, 4.2, and 4.5 g/cm^3. As a major observation, all four structure models exhibit the same spectral characteristics consisting of the broad absorption band in the energy region from 4 eV to 11 eV. Similar to the structure models investigated up to now, this absorption band still allows the identification of a two-peak substructure which is reminiscent of the e_g and t_{2g} like subband structure of Ti_{3d} conduction states in crystalline TiO_2. With decreasing density, the second subpeak above 7 eV becomes marginally more pronounced than the first subpeak.

From linear extrapolation of the dielectric function (cf. inset in Fig. 14), the energy gap of a-TiO_2 is found to decrease with increasing density. Thereby, the energy gap changes from ∼3.8 to ∼3.6 eV when going from 3.8 to 4.5 g/cm^3. Accordingly, the calculated DFT-PBE HOMO-LUMO-type energy gaps show a decrease from 2.3 eV to 2.06 eV. A band gap decrease with increasing density is also indicted for crystalline TiO_2 by DFT-PBE band gaps of 1.94 eV for anatase (3.8 g/cm^3) and 1.88 eV for rutile (4.2 g/cm^3). The band gap decrease with increasing density is reflected in the real part of the dielectric function by an increase in the dielectric constants in the static limit and across the visible spectral energy range.

In contrast to the differences in the dielectric functions depicted in Fig. 8 that are related to temperature effects and different simulation techniques, changes in the mass density influence the qualitative characteristics of the optical response of a-TiO_2. Especially, the slight change in the spectral-weight distribution of the dielectric function from one subpeak to the other seems to be characteristic to density fluctuations. With increasing density the first subpeak becomes marginally more pronounced than the second. Moreover, the changes in the static dielectric constant are a clear indication for mass-density variations. Neither the numerical simulation technique nor the influence of temperature show a comparable influence on the static and visible-range optical constants.

IV. SUMMARY AND CONCLUSION

From analysis of the static structure factor and the atomic RDFs, we have demonstrated the feasibility of the DFTB and CPMD approach to generate amorphous TiO_2 structures.

The calculated a-TiO_2 (HOMO-LUMO-type) QP gap of ∼3.7 eV for the completely relaxed 4.2 g/cm^3 atomic structures is found to be larger than the QP band gap in rutile and brookite but comparable to anatase. Like for the crystalline phases, the energy states in a-TiO_2 around the fundamental energy gap are formed by occupied $2p$-like states of oxygen and unoccupied $3d$-like states of Ti. The band-tail states that form due to the structural disorder and variations in the local coordination numbers also show the $2p$- and $3d$-like distributions of the electronic charge density. Thereby, states of the more extended valence band tail are located at under-coordinated O ions in Ti_2O building blocks and O ions residing in structural distorted Ti_3O building blocks. The conduction band-tail states represent a superposition of electronic states located at variously coordinated Ti ions in TiO_7, TiO_6, and TiO_5 building blocks. In contrast to octahedrally coordinated TiO_2 crystal phases, neither the density of states nor the dielectric function indicates a distinct crystal field induced splitting of the unoccupied $3d$ states into e_g and t_{2g} like subbands. These differences in the electronic structure occur due to the differences in the local atomic structure. Only ∼50–60 % of the Ti ions still form, partially strongly distorted, TiO_6 polyhedron building blocks. The most important consequence of the loss of local symmetry in a-TiO_2 is the characteristic modification of optical spectra in the energy region from 5 eV to 8 eV.

The DFT-PBE mobility gaps, estimated from an analysis of the localization of electronic states by information entropy based quantities, are at least ∼0.4 eV larger than the DFT-PBE band gaps of the crystalline TiO_2 main phases. The overall size of band tails for occupied and unoccupied states is strongly modified by temperature influences on the atomic structure. While extended band tails result in a significantly reduced HOMO-LUMO-type energy gap for a-TiO_2 structures equilibrated at room temperature, additional structure relaxation increases the energy gap above the calculated band gaps of crystalline TiO_2 polymorphs. Thereby, only a few electronic states within ∼0.1 eV around the band edges show a notable degree of localization for the 0 K equilibrium structure.

In summary, the electronic structure of a-TiO_2 can be characterized as follows: Despite the formal nonvalidity of Bloch's theorem in amorphous solids, the remaining short-range order causes a well-defined separation of bonding and antibonding states separated by an energy gap. Similar to a crystal the small energy differences between various electronic states promote the formation of *band*-type characteristics in the electronic DOS that are comparable to the DOS in TiO_2 crystals. Electronic states close to the *band* edges show

distinct localization characteristics and range into the energy region of the crystal band gap. The tail states emerge from distortions in the local atomic environment of the majority of Ti and accordingly O ions and changes in the local atomic coordination numbers. Similar to defects in crystals, under-coordinated O ions are represented by acceptor like states in the valence tail and over-coordinated Ti ions form donor-like conduction-tail states.

The calculated complex dielectric functions and complex refractive indices of a-TiO_2 are close to the data obtained from various experiments and indicate an optical gap $\lesssim$3.5 eV. Compared to the dielectric function obtained from solution of the BSE, the IPA dielectric functions provide a reasonable basis for analyzing the optical response of a-TiO_2. The inclusion of two-particle excitations mainly accounts for a redshift, while the overall curve characteristics remain qualitatively unchanged. Unfortunately, experimental data on a-TiO_2 are missing in the higher energy range (5–8 eV) that is characterized by stronger absorption/higher oscillator strength as observed for rutile, anatase, and brookite.

The optical-response characteristics are found to be very similar over the whole energy range when changing the mass density from 3.8 to 4.5 g/cm^3, although the energy gap of a-TiO_2 decreases with increasing density.

Since an amorphous TiO_2 phase represents a metastable state, it is reasonable to interpret it as a superposition of the manifold of local atomic configurations that occur in existing crystalline material phases. This explicitly includes crystal phases that normally are unstable under the ambient conditions. Due to inclusion of TiO_2 high-pressure polytypes, the average over eleven crystalline phases allows the reproduction of all spectral features of the a-TiO_2 dielectric function. Such a superposition of crystalline phases could possibly also offer a way for approximately accounting for electron-hole interaction in a-TiO_2 by solving the BSE only for the small unit cells of the various single crystal modifications and avoiding the use of the large unit cells necessary to simulate the disordered material phase.

ACKNOWLEDGMENTS

We thank the Laser Zentrum Hannover e.V. (LZH) for providing us the dielectric function data on ion-beam-sputtered a-TiO_2 films. The calculations were done using grants of computer time from the Regionales Rechenzentrum of the Universität zu Köln (RRZK), the Paderborn Center for Parallel Computing (PC2), and the Höchstleistungs-Rechenzentrum Stuttgart. The Deutsche Forschungsgemeinschaft is acknowledged for financial support. The authors are also grateful to the BMBF, Germany, for financial support in terms of the PluTO-grant to promote modern optical technologies.

[1] R. Marchand, L. Brohan, and M. Tournoux, Mater. Res. Bull. **15**, 1129 (1980).
[2] J. F. Banfield and D. R. Veblen, Am. Mineral. **77**, 545 (1992).
[3] M. Latroche, L. Brohan, R. Marchand, and M. Tournoux, J. Solid State Chem. **81**, 78 (1989).
[4] J. Akimoto, Y. Gotoh, Y. Oosawa, N. Nonose, T. Kumagai, K. Aoki, and H. Takei, J. Solid State Chem. **113**, 27 (1994).
[5] P. Y. Simons and F. Dachille, Acta Cryst. **23**, 334 (1967).
[6] J. Haines and J. M. Léger, Physica B **192**, 233 (1993).
[7] K. Lagarec and S. Desgreniers, Solid State Commun. **94**, 519 (1995).
[8] H. Sato, S. Endo, M. Sugiyama, T. Kikegawa, O. Shimomura, and K. Kusaba, Science **251**, 786 (1991).
[9] N. A. Dubrovinskaia, L. S. Dubrovinsky, R. Ahuja, V. B. Prokopenko, V. Dmitriev, H. P. Weber, J. M. Osorio-Guillen, and B. Johansson, Phys. Rev. Lett. **87**, 275501 (2001).
[10] L. S. Dubrovinsky, N. A. Dubrovinskaia, V. Swamy, J. Muscat, N. M. Harrison, R. Ahuja, B. Holm, and B. Johansso, Nature (London) **410**, 653 (2001).
[11] M. Mattesini, J. S. de Almeida, L. Dubrovinsky, N. Dubrovinskaia, B. Johansson, and R. Ahuja, Phys. Rev. B **70**, 212101 (2004).
[12] D. Y. Kim, J. S. de Almeida, L. Koči, and R. Ahuja, Appl. Phys. Lett. **90**, 171903 (2007).
[13] X. Wu, E. Holbig, and G. Steinle-Neumann, J. Phys.: Condens. Matter **22**, 295501 (2010).
[14] I. Manzini, G. Antonioli, D. Bersani, P. P. Lottici, G. Gnappi, and A. Montenero, J. Non. Cryst. Sol., **192** 519 (1995); **193** 519 (1995).
[15] V. Petkov, G. Holzhüter, U. Tröge, Th. Gerber, and B. Himmel, J. Non-Crystal. Sol. **231**, 17 (1998).
[16] D. Reyes-Coronado, G. Rodríguez-Gattorno, M. E. Espinosa-Pesqueira, C. Cab, R. de Coss, and G. Oskam, Nanotechnology **19**, 145605 (2008).
[17] M. Landmann, E. Rauls, and W. G. Schmidt, J. Phys.: Condens. Matter **24**, 195503 (2012).
[18] J. M. Verduzco, H. Chung, C. Hu, and W. Choe, Inorg. Chem. **48**, 9060 (2009).
[19] K. Hashimoto, H. Irie, and A. Fujishima, AAPPS Bulletin **17**, 12 (2007).
[20] A. Fujishima, X. Zhang, and D. A. Tryk, Surf. Sci. Rep. **63**, 515 (2008).
[21] L. S. Hsu, R. Rujkorakarn, J. R. Sites, and C. Y. She, J. Appl. Phys. **59**, 3475 (1986).
[22] X. Chen and S. S. Mao, Chem. Rev. **107**, 2891 (2007).
[23] H. Zhang, B. Chen, J. F. Banfield, and G. A. Waychunas, Phys. Rev. B **78**, 214106 (2008).
[24] S. B. Amor, G. Baud, J. P. Besse, and M. Jacquet, Mater. Sci. Eng. B **47**, 110 (1997).
[25] R. Dannenberg and P. Greene, Thin Sol. Films **360**, 122 (2000).
[26] S. B. Amor, L. Guedri, G. Baud, M. Jacquet, and M. Ghedira, Mat. Chem. Phys. **77**, 903 (2002).
[27] D. Mardare and G. I. Rusu, Mat. Lett. **56**, 210 (2002).
[28] K. Eufinger, D. Poelman, H. Poelman, R. De Gryse, and G. B. Marin, Appl. Surf. Sci. **254**, 148 (2007).
[29] E. Gofuku, Y. Toyoda, Y. Uehara, M. Kohara, and M. Nunoshita, Appl. Surf. Sci. **48**, 343 (1991); **49**, 343 (1991).

[30] S. Y. Kim, Appl. Optics **35**, 6703 (1996).
[31] H. Takikawa, T. Matsui, T. Sakakibara, A. Bendavid, and P. J. Martin, Thin Sol. Films **348**, 145 (1999).
[32] Z. W. Zhao, B. K. Tay, S. P. Lau, and G. Q. Yu, J. Cryst. Growth **268**, 543 (2004).
[33] V. Luca, S. Djajanti, and R. F. Howe, J. Phys. Chem. B **102**, 10650 (1998).
[34] Z. Wang, U. Helmersson, and P.-O. Käll, Thin Sol. Films **405**, 50 (2002).
[35] D. Mardare and P. Hones, Mater. Sci. Eng. B **68**, 42 (1999).
[36] M. Zhang, G. Lin, C. Dong, and L. Wen, Surf. & Coat. Technol. **201**, 7252 (2007).
[37] J. Nowotny, T. Bak, T. Burg, M. K. Nowotny, and L. R. Sheppard, J. Phys. Chem. C **111**, 9769 (2007).
[38] D. Sarkar, C. K. Ghosh, U. N. Maiti, and K. K. Chattopadhyay, Physica B **406**, 1429 (2011).
[39] H. Zhang, J. F. Banfield, and L. Wen, J. Mater. Chem. **8**, 2073 (1998).
[40] M. Fernández-García, C. Belver, Jonathan C. Hanson, Xianqin Wang, and J. A. Rodriguez, J. Am. Chem. Soc. **129**, 13604 (2007).
[41] S. Bauer, A. Pittrof, H. Tsuchiya, and P. Schmuki, Electrochem. Commun. **13**, 538 (2011).
[42] E. Leitão, R. A. Silva, and M. A. Barbosa, Corros. Sci. **39**, 377 (1996).
[43] R. Karpagavalli, A. Zhou, P. Chellamuthu, and K. Nguyen, J. Biomed. Mater. Res. Part A **83**, 1087 (2007).
[44] K. M. Glassford and J. R. Chelikowsky, Phys. Rev. B **46**, 1284 (1992).
[45] P. J. Hardman, G. N. Raikar, C. A. Muryn, G. van der Laan, P. L. Wincott, G. Thornton, D. W. Bullett, and P. A. D. M. A. Dale, Phys. Rev. B **49**, 7170 (1994).
[46] S.-D. Mo and W. Y. Ching, Phys. Rev. B **51**, 13023 (1995).
[47] M. Mikami, S. Nakamura, O. Kitao, H. Arakawa, and X. Gonze, Jpn. J. Appl. Phys. **39**, L847 (2000).
[48] R. Asahi, Y. Taga, W. Mannstadt, and A. J. Freeman, Phys. Rev. B **61**, 7459 (2000).
[49] M. Calatayud, P. Mori-Sánchez, A. Beltrán, A. M. Pendás, E. Francisco, J. Andrés, and J. M. Recio, Phys. Rev. B **64**, 184113 (2001).
[50] J. Muscat, V. Swamy, and N. M. Harrison, Phys. Rev. B **65**, 224112 (2002).
[51] C. Qiang and C. Hong-Hong, Chin. Phys. **13**, 2121 (2004).
[52] Y. Jing-Xin, F. Min, J. Guang-Fu, and C. Xiang-Rong, Chin. Phys. B **18**, 269 (2009).
[53] F. M. Hossain, L. Sheppard, J. Nowotny, and G. E. Murch, J. Phys. Chem. Sol. **69**, 1820 (2008).
[54] E. Shojaee and M. R. Mohammadizadeh, J. Phys.: Condens. Matter **22**, 015401 (2010).
[55] A. F. da Silva, I. Pepe, C. S. S. Brasil, D. G. F. David, E. F. da Silva Jr., C. Persson, T. Lindgren, J. S. de Almeida, C. M. Araújo, and R. Ahuja, Phys. Status Solidi C **1**, S241 (2004).
[56] C. Persson and A. F. da Silva, Appl. Phys. Lett. **86**, 231912 (2005).
[57] F. Thomazi, L. S. Roman, A. F. da Silva, and C. Persson, Phys. Status Solidi C **6**, 2740 (2009).
[58] L. K. Dash, F. Bruneval, V. Trinité, N. Vast, and L. Reining, Comput. Mater. Sci. **38**, 482 (2007).
[59] H. M. Lawler, J. J. Rehr, F. Vila, S. D. Dalosto, E. L. Shirley, and Z. H. Levine, Phys. Rev. B **78**, 205108 (2008).
[60] L. Chiodo, J. M. García-Lastra, A. Iacomino, S. Ossicini, J. Zhao, H. Petek, and A. Rubio, Phys. Rev. B **82**, 045207 (2010).
[61] A. Thilagam, D. J. Siompson, and A. R. Gerson, J. Phys.: Condens. Matter **23**, 025901 (2011).
[62] W. Kang and M. S. Hybertsen, Phys. Rev. B **82**, 085203 (2010).
[63] U. Diebold, Surf. Sci. Rep. **48**, 53 (2003).
[64] U. Diebold, N. Ruzycki, G. S. Herman, and A. Selloni, Catalysis Today **85**, 93 (2003).
[65] X.-Q. Gong and A. Selloni, Phys. Rev. B **76**, 235307 (2007).
[66] A. Selloni, Nat. Mater. **7**, 613 (2008).
[67] X.-Q. Gong, N. Khorshidi, A. Stierle, V. Vonk, C. Ellinger, H. Dosch, H. Cheng, A. Selloni, Y. He, O. Dulub, and U. Diebold, Surf. Sci. **603**, 138 (2009).
[68] M. D. Rasmussen, L. M. Molina, and B. Hammer, J. Chem. Phys. **120**, 988 (2004).
[69] S. Wendt, R. Schaub, J. Matthiesen, E. K. Vestergaard, E. Wahlström, M. D. Rasmussen, P. Thostrup, L. M. Molina, E. Lægsgaard, I. Stensgaard, B. Hammer, and F. Besenbacher, Surf. Sci. **598**, 226 (2005).
[70] U. Martinez and B. Hammer, J. Chem. Phys. **134**, 194703 (2011).
[71] P. W. Anderson, Phys. Rev. **109**, 1492 (1958).
[72] P. W. Anderson, Phys. Rev. Lett. **34**, 953 (1975).
[73] M. H. Cohen, H. Fritzsche, and S. R. Ovshinsky, Phys. Rev. Lett. **22**, 1065 (1969).
[74] Sir N. Mott, Rev. Mod. Phys. **50**, 203 (1978).
[75] B. Prasai, B. Cai, D. A. Drabold, M. K. Underwood, and J. P. Lewis, *MS&T-11 Conf. Proceedings* (Curran Associates, Inc., New York, 2011).
[76] V. van Hoang, Phys. Status Solidi B **244**, 1280 (2007).
[77] Bokhimi, A. Morales, O. Novaro, T. López, E. Sánchez, and R. Gómez, J. Mater. Res. **10**, 2788 (1995).
[78] P. Hohenberg and W. Kohn, Phys. Rev. **136**, B864 (1964).
[79] W. Kohn and L. J. Sham, Phys. Rev. **140**, A1133 (1965).
[80] P. E. Blöchl, Phys. Rev. B **50**, 17953 (1994).
[81] G. Kresse and D. Joubert, Phys. Rev. B **59**, 1758 (1999).
[82] G. Kresse and J. Furthmüller, Comput. Mater. Sci. **6**, 15 (1996).
[83] J. P. Perdew and K. Burke and M. Ernzerhof, Phys. Rev. Lett. **77**, 3865 (1996).
[84] J. Heyd, G. E. Scuseria, and M. Ernzerhof, J. Chem. Phys. **118**, 8207 (2003).
[85] J. Heyd and G. E. Scuseria, J. Chem. Phys. **121**, 1187 (2004).
[86] J. Heyd, J. E. Peralta, G. E. Scuseria, and R. L. Martin, J. Chem. Phys. **123**, 174101 (2005).
[87] J. Heyd, G. E. Scuseria, and M. Ernzerhof, J. Chem. Phys. **124**, 219906 (2006).
[88] L. Hedin, Phys. Rev. **139**, A796 (1965).
[89] L. Hedin and S. Lundqvist, in *Solid State Physics*, edited by F. Seitz, D. Turnbull, and H. Ehrenreich (Academic Press, New York, 1970), Vol. 23, p. 1.
[90] M. Shishkin and G. Kresse, Phys. Rev. B **74**, 035101 (2006).
[91] M. Shishkin and G. Kresse, Phys. Rev. B **75**, 235102 (2007).
[92] F. Fuchs, J. Furthmüller, F. Bechstedt, M. Shishkin, and G. Kresse, Phys. Rev. B **76**, 115109 (2007).
[93] M. Shishkin, M. Marsman, and G. Kresse, Phys. Rev. Lett. **99**, 246403 (2007).
[94] C. Mietze, M. Landmann, E. Rauls, H. Machhadani, S. Sakr, M. Tchernycheva, F. H. Julien, W. G. Schmidt, K. Lischka, and D. J. As, Phys. Rev. B **83**, 195301 (2011).

[95]L. J. Sham and T. M. Rice, Phys. Rev. **144**, 708 (1966).
[96]W. Hanke and L. J. Sham, Phys. Rev. B **12**, 4501 (1975).
[97]W. Hanke and L. J. Sham, Phys. Rev. B **21**, 4656 (1980).
[98]S. Albrecht, L. Reining, R. Del Sole, and G. Onida, Phys. Rev. Lett. **80**, 4510 (1998).
[99]W. G. Schmidt, S. Glutsch, P. H. Hahn, and F. Bechstedt, Phys. Rev. B **67**, 085307 (2003).
[100]M. Elstner, D. Porezag, G. Jungnickel, J. Elsner, M. Haugk, T. Frauenheim, S. Suhai, and G. Seifert, Phys. Rev. B **58**, 7260 (1998).
[101]D. Porezag, T. Frauenheim, T. Köhler, G. Seifert, and R. Kaschner, Phys. Rev. B **51**, 12947 (1995).
[102]Th. Frauenheim, G. Seifert, M. Elstner, Z. Haynal, G. Jungnickel, S. Suhai, and R. Scholz, Phys. Status Solidi B **227**, 41 (2000).
[103]Y. Lifshitz, Th. Köhler, Th. Frauenheim, I. Guzmann, A. Hoffman, R. Q. Zhang, X. T. Zhou, and S. T. Lee, Science **297**, 1531 (2002).
[104]G. Seifert, Th. Köhler, and Th. Frauenheim, Appl. Phys. Lett. **77**, 1313 (2000).
[105]R. Car and M. Parrinello, Phys. Rev. Lett. **55**, 2471 (1985).
[106]G. Dolgonos, B. Aradi, N. H. Moreira, and Th. Frauenheim, J. Chem. Theory Comput. **6**, 266 (2010).
[107]K. M. Glassford, N. Troullier, José Luis Martins, and J. R. Chelikowsky, Solid State Commun. **76**, 653 (1990).
[108]S. Langel, W. Surf. Sci **496**, 141 (2002).
[109]A. D. Becke, Phys. Rev. A **38**, 3098 (1988).
[110]C. N. J. Wagner, J. Non.-Cryst. Sol. **31**, 1 (1978).
[111]K. S. Vahvaselkä, Phys. Status Solidi A **72**, 261 (1982).
[112]A. V. Krukau, O. A. Vydrov, A. F. Izmaylov, and G. E. Scuseria, J. Chem. Phys. **125**, 224106 (2006).
[113]H. Ehrenreich and M. H. Cohen, Phys. Rev. **115**, 786 (1959).
[114]A. Rényi, in *Proceedings of the Fourth Berkeley Symposium on Mathematical Statistics and Probability*, edited by J. Neyman (University of California Press, Berkeley, 1961), Vol. 1, p. 547.
[115]K. Życzkowski, Open Sys. Information Dyn. **10**, 297 (2003).
[116]C. E. Shannon, Bell Syst. Tech. J. **27**, 379 (1948).
[117]C. E. Shannon, Bell Syst. Tech. J. **30**, 50 (1951).
[118]The information entropy based quantity $W(\lambda)$ was applied by Lewis *et al.* (Refs. 119 and 120) to investigate the localization of electronic states in a DNA double-helix model.
[119]J. P. Lewis, J. Pikus, T. E. Cheatham, III, E. B. Starikov, H. Wang, J. Tomfohr, and O. F. Sankey, Phys. Status Solidi B **233**, 90 (2002).
[120]J. P. Lewis, T. E. Cheatham, III, E. B. Starikov, H. Wang, and O. F. Sankey, J. Phys. Chem. B **107**, 2581 (2003).
[121]B. Mirbach and H. J. Korsch, Ann. Phys. **265**, 80 (1998).
[122]R. Atta-Fynn, P. Biswas, P. Ordejón, and D. A. Drabold, Phys. Rev. B **69**, 085207 (2004).
[123]The IPR was used by Atta-Fynn *et al.* (Ref. 122) to investigate electronic localization in amorphous hydrogenated Si (a-Si:H). Recently Cai *et al.* (Ref. 124) investigated localized states in the electronic structure of amorphous GaN.
[124]B. Cai and D. A. Drabold, Phys. Rev. B **84**, 075216 (2011).
[125]P. Sorantin and K. Schwarz, Inorg. Chem. **31**, 567 (1992).
[126]B. Jiang, J. M. Zuo, N. Jiang, M. O'Keeffe, and J. C. H. Spence, Acta Cryst. Mater. A **59**, 341 (2003).
[127]J. D. DeLoach, G. Scarel, and C. R. Aita, J. Appl. Phys. **85**, 2377 (1999).
[128]J. Tauc, R. Grigorovici, and A. Vancu, Phys. Status Solidi **15**, 627 (1966).
[129]J. Tauc, A. Menth, and D. L. Wood, Phys. Rev. Lett. **25**, 749 (1970).
[130]J. Tauc (ed.), *Amorphous and Liquid Semiconductors* (Plenum Press, London, 1974).
[131]P. Kubelka and F. Munk, Zeitschrift für technische Physik **12**, 593 (1931).
[132]P. Kubelka, J. Opt. Soc. Am. **38**, 448 (1948).
[133]M. Turowski, H. Ehlers, and D. Ristau, Laser Zentrum Hannover e.V. (LZH) (unpublished).
[134]Y. Yamada, H. Uyama, T. Murata, and H. Nozoye, J. Vac. Sci. Technol. A **19**, 2479 (2001).
[135]M. H. Suhail, G. M. Rao, and S. Mohan, J. Appl. Phys. **71**, 1421 (1992).
[136]G. Lucovsky, J. Optoelectron. Adv. Mater. **3**, 155 (2001).
[137]X. G. Kong, Y. Yu, and T. Gao, Euro Phys. J. B **76**, 365 (2010).

Paper IV

Transition energies and direct-indirect band gap crossing in zinc-blende $Al_xGa_{1-x}N$

M. Landmann, M. Feneberg, M. Röppischer, T. Schupp, C. Cobet, E. Rauls,
D. J. As, N. Esser, R. Goldhahn, and W. G. Schmidt

PHYSICAL REVIEW B **87**, 195210, 21 pp. (2013) – Editors' Suggestion

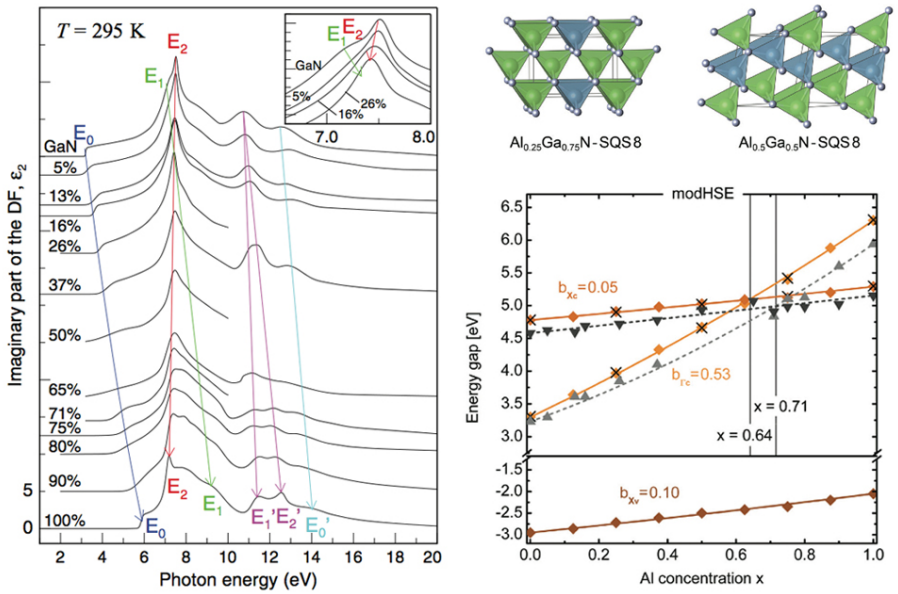

PHYSICAL REVIEW B **87**, 195210 (2013)

Transition energies and direct-indirect band gap crossing in zinc-blende $Al_xGa_{1-x}N$

M. Landmann,* E. Rauls, and W. G. Schmidt
Lehrstuhl für Theoretische Physik, Universität Paderborn, 33095 Paderborn, Germany

Marcus Röppischer, Christoph Cobet, and Norbert Esser
Leibniz-Institut für Analytische Wissenschaften - ISAS - e.V., Albert-Einstein-Str. 9, 12489 Berlin, Germany

Thorsten Schupp and Donat J. As
Experimentalphysik, University of Paderborn, Warburger Str. 100, 33098 Paderborn, Germany

Martin Feneberg and Rüdiger Goldhahn
Institut für Experimentelle Physik, Otto-von-Guericke-Universität Magdeburg, Universitätsplatz 2, 39106 Magdeburg, Germany
(Received 2 March 2013; published 29 May 2013)

The electronic and optical properties of zinc-blende (zb) $Al_xGa_{1-x}N$ over the whole alloy composition range are presented in a joint theoretical and experimental study. Because zb-GaN is a direct ($\Gamma_v \rightarrow \Gamma_c$) semiconductor and zb-AlN shows an indirect ($\Gamma_v \rightarrow X_c$) fundamental band gap, the ternary alloy exhibits a concentration-dependent direct-indirect band gap crossing point the position of which is highly controversial. The dielectric functions of zb-$Al_xGa_{1-x}N$ alloys are measured employing synchrotron-based ellipsometry in an energy range between 1 and 20 eV. The experimentally determined fundamental energy transitions originating from the Γ, X, and L points are identified by comparison to theoretical band-to-band transition energies. In order to determine the direct-indirect band gap crossing point, the measured transition energies at the X point have to be aligned by the calculated position of the highest valence state. Thereby density-functional theory (DFT) based approaches to the electronic structure, ranging from the standard (semi)local generalized gradient approximation (GGA), self-energy corrected local density approximation (LDA-1/2), and meta-GGA DFT (TB-mBJLDA) to hybrid functional DFT and many-body perturbation theory in the GW approximation, are applied to random and special quasirandom structure models of zb-$Al_xGa_{1-x}N$. This study provides interesting insights into the accuracy of the various numerical approaches and contains reliable *ab initio* data on the electronic structure and fundamental alloy band gaps of zb-$Al_xGa_{1-x}N$. Nonlocal Heyd-Scuseria-Ernzerhof-type hybrid-functional DFT calculations or, alternatively, GW quasiparticle calculations are required to reproduce prominent features of the electronic structure. The direct-indirect band gap crossing point of zb-$Al_xGa_{1-x}N$ is found in the Al rich composition range at an Al content between $x = 0.64$ and 0.69 in hybrid functional DFT, which is in good agreement with $x = 0.71$ determined from the aligned experimental transition energies. Thus our study solves the long-standing debate on the nature of the fundamental zb-$Al_xGa_{1-x}N$ alloy band gap.

DOI: 10.1103/PhysRevB.87.195210 PACS number(s): 71.15.Mb, 78.20.−e, 81.05.Ea

I. INTRODUCTION

Throughout the last two decades, scientific breakthroughs on the field of group-III nitride semiconductor materials have always stimulated rapid technological progress in the manufacturing of optoelectronic and electronic devices. Group-III nitrides naturally crystallize in stable hexagonal lattices with wurtzite (wz) structure (space group: $P6_3mc - C_{6v}^4$). Artificially grown, group-III nitrides may adopt a metastable cubic phase with a zinc-blende (zb) structure (space group: $F\bar{4}3m - T_d^2$). Probably the most appealing characteristic of binary group-III nitrides and their multicomponent alloys is the extremely large accessible range of band gap energies, i.e., from ∼0.7 eV (wz-InN)[1] to ∼6.0 eV (wz-AlN)[2,3] for the hexagonal compounds and from ∼0.6 eV (zb-InN)[4] to ∼5.3 eV (zb-AlN)[5] for the cubic ones.

For a long time almost exclusively grown along the polar (0001) c direction of the hexagonal crystal, group-III nitrides, and their multicomponent alloys exhibit strong internal piezoelectric and spontaneous polarization electric fields, which are undesirable for optoelectronic applications since they inherently limit the device performance.[6,7] The occurrence of such polarization fields is a direct consequence of the lack of inversion symmetry in the hexagonal crystal that naturally show both piezoelectric and spontaneous polarization parallel to the c axis.[8] The growth of nonpolar and semipolar nitrides has found increasing technological interest over the past years to avoid these strong internal fields. In these nonpolar or semipolar nitrides, the c axis is orthogonal or inclined to the growth direction, thus eliminating or limiting the field effects in the growth direction.[9] However, the electrical, optical, and structural properties are affected by strong lateral anisotropies. A way to fabricate group-III nitride based optoelectronic devices, fundamentally free of polarization fields,[7] is the growth[5,10–14] of cubic nitride alloys with (001) orientation and the engineering of nanostructured material compounds (e.g., quantum wells and superlattices).[15–20]

Among all group-III nitride semiconductors, zb-AlN is the only binary semiconductor with an nondirect $\Gamma_v \rightarrow X_c$ fundamental bulk band gap.[5] In the ternary (also *pseudobinary*) zb-$Al_xGa_{1-x}N$ alloys, the electronic states, responsible for the band gaps in the pure bulk phases, intermix with respect to the relative concentration of each material component. Thus there

 ©2013 American Physical Society

is a critical cation concentration that marks the transition of the fundamental alloy band gap from involving either the bulklike Γ_c conduction band states originating from the direct zb-GaN band gap or the bulklike X_c conduction band states of the indirect zb-AlN band gap. This direct-indirect band gap crossing is a common alloy characteristic of the cubic group-III nitrides and the group-III arsenides. Analogously to zb-AlN, AlAs, which naturally crystallizes in a stable zinc-blende structure, is the only indirect semiconductor among the group-III arsenides. The critical Al concentration for the direct-indirect band gap crossing in $Al_xGa_{1-x}As$ has experimentally been found at $\sim$0.4.[21] A detailed knowledge of the direct-indirect band gap crossing points and accurate band gap data over the whole composition range of multicomponent semiconductor alloys is of fundamental interest for the engineering of optoelectronic and electronic devices.

The experimental band gaps of the binary bulk semiconductors zb-AlN and zb-GaN have been reported consistently in several experimental studies. The absorption/ellipsometry/reflectivity investigations of zb-AlN at room temperature (RT) yielded for the indirect $\Gamma_v \rightarrow X_c$ band gap values of 5.34 eV (see Ref. 5) and 5.3 eV (see Ref. 22) as well as of 5.93 eV (see Ref. 22) and 6.05 eV (see Ref. 23) for the direct $\Gamma_v \rightarrow \Gamma_c$ band gap. The direct $\Gamma_v \rightarrow \Gamma_c$ band gap of zb-GaN at RT was determined with 3.231 eV (see Ref. 10), 3.2 eV (see Ref. 24), 3.25 eV (see Ref. 23), and 3.232 eV (see Ref. 25), while values of 3.302 eV (see Ref. 10) and 3.295 eV (see Ref. 25) have been reported for $T = 10$ K.

For zb-$Al_xGa_{1-x}N$ alloys, the experimental data on the direct-indirect band gap crossover are limited and partially completely inconsistent with theoretical data. Okumura *et al.*[24] investigated the optical properties of molecular beam epitaxy (MBE) zb-$Al_xGa_{1-x}N$ epilayers by cathodoluminesence and spectroscopic ellipsometry techniques. Their data indicate a direct nature of the fundamental band-edge transitions over the whole composition range that is characterized by a linear increase of the alloy band gap [$E_{\rm gap}^{\text{zb-Al}_x\text{Ga}_{1-x}\text{N}}(x) = 1.6\,x + 3.2$ eV] with increasing Al content. Guerrero *et al.*[23] carried out room temperature reflectivity measurements on MBE grown zb-$Al_xGa_{1-x}N$ epilayers and deduced a nonlinear functional dependence [$E_{\rm gap}^{\text{zb-Al}_x\text{Ga}_{1-x}\text{N}}(x) = 6.05\,x + 3.25(1-x) - 1.4\,x(1-x)$ eV] of the lowest direct absorption edge on the Al concentration. Nakadaira and Tanaka[26] used near-band-edge photoluminescence spectroscopy at room temperature to investigate the zb-$Al_xGa_{1-x}N$ alloy in the Ga-rich region for $0 \leqslant x \leqslant 0.23$ and reported a linear band gap dependence [$E_{\rm gap}^{\text{zb-Al}_x\text{Ga}_{1-x}\text{N}}(x) = 1.85\,x + 3.2$ eV] on the Al content. All three experimental studies on zb-$Al_xGa_{1-x}N$ predict similar direct band gap transitions below $x \leqslant 0.5$. However, only the data of Guerrero *et al.* are consistent with the measured direct band gap of zb-AlN, while the data of Okumura *et al.* are neither in agreement with the direct nor the indirect band gap of zb-AlN. Guerrero *et al.* explicitly stated that there is no experimental indication for a direct fundamental absorption edge of zb-$Al_xGa_{1-x}N$ alloys. To the best of our knowledge, no experimental study has published a definitive value for the direct-indirect band gap crossing point in zb-$Al_xGa_{1-x}N$ alloys so far.

An analysis of reported theoretical data reveals inconsistencies in the numerical description of the composition dependence of the fundamental zb-$Al_xGa_{1-x}N$ band gaps as well. Recently, Amin *et al.*[27] employed the Wu-Cohen generalized gradient approximation (GGA) within a full-potential linearized augmented plane wave approach (FLAPW) to calculate the zb-$Al_xGa_{1-x}N$ band gaps over the entire composition range. Consistent with the band gap data of Okumura *et al.*, the alloy band gap was found to be direct for the entire composition range, increasing linearly from a direct band gap of 3.00 eV in zb-GaN to a direct band gap of 5.50 eV in zb-AlN. However, this result stands in disagreement with the majority of theoretical studies. Early effective pseudopotential method (EPM) studies of Fan *et al.*[28,29] reported a direct-indirect band gap crossover in zb-$Al_xGa_{1-x}N$ at $x = 0.52$. Albanesi *et al.*[30] reported a similar crossing point of $x = 0.57$ from band structure calculations applying a linear-muffin-tin-orbital (LMTO) implementation of density functional theory (DFT) in local density approximation (LDA). In this study, a cluster expansion approach (CEA)[31–33] was used to treat the problem of the stochastically occupied semiconductor alloys. Sökeland *et al.*[34] published the first *GW* quasiparticle (QP) theory data on zb-$Al_xGa_{1-x}N$ alloys. Their data indicate an increase of the critical Al content from $x = 0.54$ in DFT-LDA to $x = 0.63$ in the *GW* approximation (*GW*A). In both cases, the virtual crystal approximation (VCA)[33] was applied to model the semiconductor alloys. A DFT-LDA band gap crossing point of $\sim$0.6 has been confirmed in further studies.[35,36] Using the screened-exchange LDA method[37–39] within DFT and special quasirandom structures (SQS's),[33,40] Lee and Wang[41] predicted the direct-indirect band gap crossing point at $x = 0.85$. Very recently, Mourad and Czycholl[42] employed an empirical tight-binding model (ETBM) to calculate the electronic structure of substitutionally disordered alloys. Besides large unit-cell (2000–4000 atoms) calculations, the disordered systems were treated within the coherent potential approximation (CPA)[43–45] and the VCA. The crossover point in zb-$Al_xGa_{1-x}N$ was found to fall into the concentration range from $x = 0.7$ to $x = 0.8$. A short summary of various theoretical studies, including the computational method and the modeling approach to treat the substitutional disorder in the Al-Ga cation sublattice is given in Table I. In light of the partially contradictory results, a

TABLE I. Theoretical data on the direct-indirect band gap crossover in zb-$Al_xGa_{1-x}N$ alloys. Listed are the approaches to describe the electronic structure and the substitutionally disordered alloy as well as the Al concentration x at the crossing point. The entries are ordered according to their time of publication.

Simulation method		Crossing	
Electronic structure	Random alloy	x	Ref.
LMTO-LDA	CEA	0.52	30
EPM	VCA	0.57	28, 29
DFT-LDA	VCA	0.54	34
GWA	VCA	0.63	34
DFT-LDA	8 atom unit cells	0.6	35
DFT-LDA	8/16 atom SQS's	0.61	41
DFT-(sX-LDA)	8/16 atom SQS's	0.85	41
DFT-LDA	8 atom unit cells	0.69	36
ETBM	CPA, VCA	0.7–0.8	42

rigorous numerical study as well as a careful investigation of zb-$Al_xGa_{1-x}N$ alloys by experimental techniques is needed to verify the true nature of the fundamental alloy band gap. This study serves both aspects by presenting state-of-the-art *ab initio* calculations and latest synchrotron based ellipsometry data on zb-$Al_xGa_{1-x}N$ over the entire concentration range.

The paper is organized as follows. Section II contains the details of the experimental setup as well as a discussion of critical points in the measured dielectric functions (DFs). In Sec. III, the key ideas of the numerical approaches, needed to calculate accurate band gaps and to model the infinite randomly occupied semiconductor alloys, are summarized. Furthermore, the application to the binary bulk materials is discussed in detail. Section IV is used for the presentation and discussion of the theoretical and experimental transition energies, while Sec. V summarizes the relevant results of this study and gives concluding comments and reasonings.

II. EXPERIMENT

A. Experimental details

For this study, epitaxial zb-$Al_xGa_{1-x}N$ layers spanning the full composition range were grown by plasma assisted molecular beam epitaxy. The two binary samples, zb-GaN and zb-AlN, were taken from earlier studies. Detailed reports about their optical properties and sample structures can be found elsewhere.[22,25] The zb-$Al_xGa_{1-x}N$ layers were grown on 3C-SiC(001)/Si substrates. The thickness of the sample layers ranges between 50 and 380 nm. Lattice parameters and Al concentration were determined by high-resolution x-ray diffraction (HRXRD). The amount of hexagonal group III-nitride inclusions have also been checked by performing reciprocal space maps (RSM) around the symmetric GaN (002) or AlN (002) reflex. From the intensity ratio of the cubic (002) reflex to the hexagonal ($10\bar{1}1$) reflex, we estimate about 99% cubic phase in both GaN and AlN samples. Further details on the structural properties are given in Refs. 46 and 13.

The linear optical response of all samples was measured by spectroscopic ellipsometry (SE) using two different setups at room temperature. In the energy range between 1 and 6.4 eV, a variable angle ellipsometer (J.A. Woollam) was used at the incidence angles of 60°, 67°, and 74°. Data up to 20 eV were recorded employing the dedicated rotating analyzer ellipsometer attached to the Berlin electron storage ring for synchrotron radiation (BESSY II). Here, the angle of incidence is fixed to 67.5° up to 10 eV and to 45° between 10 and 20 eV. Low-temperature experiments at 10 K are only possible in the range between 5 and 10 eV due to limitations of the setup. More details about the synchrotron-ellipsometer setup are published elsewhere.[47]

The ellipsometric parameters Ψ and Δ from both setups and all angles of incidence were merged and fitted by taking into account the layer structure, surface and interface roughnesses of the respective sample yielding the complex DF $\bar{\varepsilon}(\hbar\omega) = \varepsilon_1(\hbar\omega) + j\varepsilon_2(\hbar\omega)$. As ε_1 and ε_2 are related by the Kramers-Kronig relations, it is sufficient to present either one. Here, we show the imaginary part of the DFs, ε_2.

B. Experimental results

The imaginary parts of the DFs at room temperature are presented in Fig. 1. Note that for three of our samples ($x = 0.26$, 0.50, and 0.71), only data up to 10 eV are available. At the low-energy side, each sample shows an absorption onset, i.e., a steplike behavior of ε_2 marking the energy position of the direct band gap. While the steps are relatively sharp for the two binary compounds, the ternary alloy films show larger broadenings of the onset. This behavior is expected already from statistical disorder in the randomly distributed cation matrix containing Al and Ga atoms in a certain fraction but with locally different concentrations. The large broadening and the low layer thicknesses do not allow to determine the indirect band gaps in this composition range. However, as demonstrated previously for zb-AlN[22] and zb-GaN,[25] accurate values for the $\Gamma_v \rightarrow \Gamma_c$ spacing (band gap E_0) can be determined from the analysis of the ε_2 data by taking the excitonic effects around the absorption edge into account yielding for the two binaries 5.93 and 3.232 eV, respectively. The obtained E_0 values of all samples are summarized in Fig. 2.

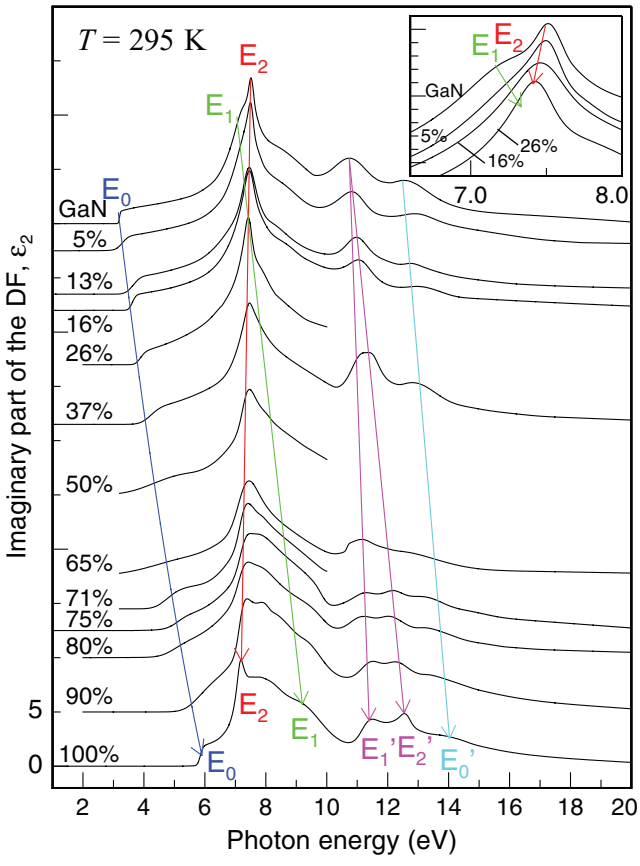

FIG. 1. (Color online) Imaginary parts (ε_2) of the complex dielectric function of the zb-$Al_xGa_{1-x}N$ samples up to 20 eV measured at room temperature (295 K). The spectra are shifted vertically for clarity proportional to their gallium content [$\times 50(1-x)$]. The connecting continuous curves are guidelines for the eye and mark absorption transitions occurring at the same point in the Brillouin zone. The inset presents details around the E_2 contribution for low aluminum content samples. It can be clearly seen that E_2 shifts to lower energy for increasing Al concentration.

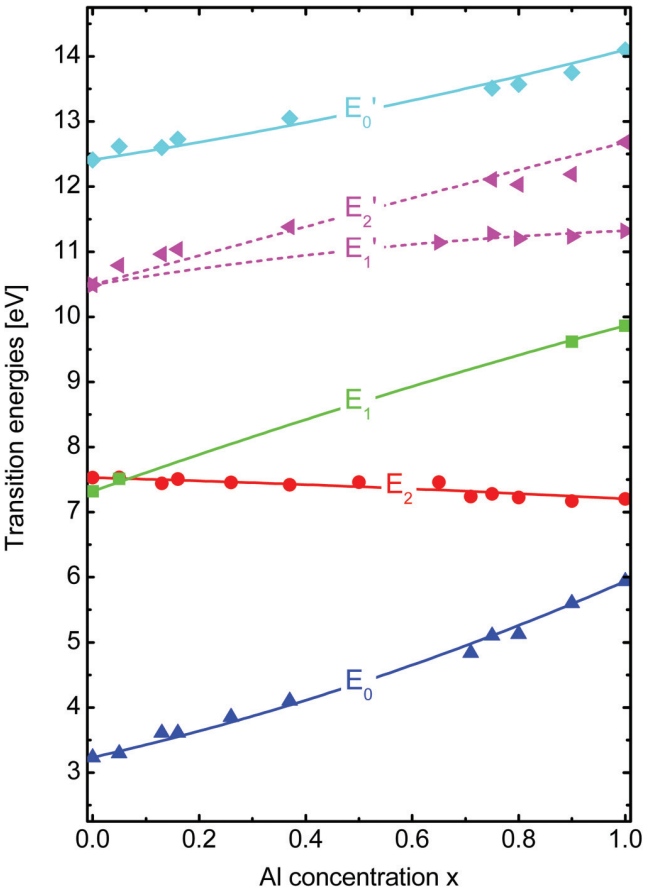

FIG. 2. (Color online) Characteristic transition energies as obtained from analysis of critical points in the measured dielectric functions of zb-$Al_xGa_{1-x}N$ at room temperature (295 K) as a function of the aluminum concentration x.

A couple of characteristic high-energy features are found in all spectra, their dependence on the alloy content are indicated by continuous lines in Fig. 1. Except for E_2, all characteristic transitions shift to higher energies for increasing Al concentration. This behavior is analogous to that of wz-$Al_xGa_{1-x}N$ alloys[48] where also only one feature is shifting to smaller energy for an increasing Al content. The most prominent feature in ε_2 is visible at around 7.5 eV for all samples. This sharp peak (E_2) has already been successfully identified with the interband absorption at the X point of the Brillouin zone in zb-AlN[22] and zb-GaN.[25] A more detailed analysis of this peak reveals that it shifts from 7.51 eV for zb-GaN to 7.204 eV for zb-AlN. The inset in Fig. 1 displays a closer look of the behavior of E_2 for the low Al content samples. In the direct vicinity of E_2 in the spectra we find a feature labeled E_1, which is below the E_2 contribution for zb-GaN (at 7.23 eV) but above E_2 for zb-AlN (at 9.8 5eV). We identify this band by interband absorption at the Λ line between the L and Γ points of the zinc-blende Brillouin zone in agreement with earlier studies.[25,49] At even higher energies we find two separate contributions for zb-GaN at 10.72 and 12.87 eV, while in zb-AlN these contributions are split into three peaks at 11.32, 12.68, and 14.1 eV. We label them E_1', E_2', and E_0', respectively. The prime marks interband transitions into higher conduction bands at the same point in the Brillouin zone.

In order to allow a comparison of these experimental transition energies with the results of the band structure calculations, the influence of electron-hole interaction (excitonic effects) on the shape of ε_2 in the vicinity of high-energy critical points has to be considered. A detailed discussion for zb-AlN has been published recently where the shape of the independent-quasiparticle DF (disregarding electron-hole many-body interaction) and the excitonic DF as obtained by solving the Bethe-Salpeter equation was analyzed.[49] In particular, a pronounced feature related to E_2 becomes only visible by the inclusion of excitons (inset of Fig. 6 in Ref. 49). It peaks at 7 eV, while the corresponding quasiparticle gap amounts to 7.22 eV. Conversely, by adding the 220 meV difference to the experimental E_2 value reported above one obtains 7.424 eV for the quasiparticle gap at the X point. The size of the shift has not been calculated yet for the alloys, i.e., we cannot correct the whole curve in Fig. 2. However, a pronounced change of the correction value is unlikely because the transition energy undergoes only a 300 meV upshift with decreasing Al content. Correspondingly, the excitonic-induced downshift for E_2' amounts to 300 meV, while other transitions cannot be unambiguously identified in the calculated DF.[49]

In order to quantify the nonlinear deviations of the alloy band gaps, the bowing parameters $b_{\mathbf{k}}$ were determined according to

$$E_{\mathrm{gap},\mathbf{k}}^{\mathrm{Al}_x\mathrm{Ga}_{1-x}\mathrm{N}} = E_{\mathrm{gap},\mathbf{k}}^{\mathrm{AlN}}\, x + E_{\mathrm{gap},\mathbf{k}}^{\mathrm{GaN}}(1-x) - b_{\mathbf{k}}\, x(1-x). \qquad (1)$$

The k-point index indicates that the electronic states of the alloy are labeled by the symmetry of their equivalents in the individual bulk materials. Positive and negative bowing parameters indicate a downward and upward bowing, respectively, with respect to a linear dependence on the alloy composition. The fundamental direct band gap (E_0) can be described by a nonlinear interpolation including a notable downward bowing characterized by a bowing factor of $b_\Gamma = 0.85$ eV. In general, other high-energy critical-point energies also show a nonlinear dependence on the Al concentration as discussed below. Theoretical first-principles calculations as presented below are usually performed for zero temperature. It is thus appropriate to consider the influence of sample temperatures on the energy positions of the features in the DFs. Therefore we have performed low-temperature (10 K) synchrotron spectroscopic ellipsometry experiments for the binary components zb-GaN and zb-AlN. While the data for zb-GaN were already published earlier,[25] these for zb-AlN are presented in Fig. 3. For 10 K, we find decreasing broadening and increasing amplitude of high-energy features in the DF. Furthermore, the whole DF is shifted to higher energy values due to reduced electron-phonon interaction. E_2 is located at 7.271 eV for 10 K, which resembles an upshift of 67 meV. The shift of E_0 is found to be similar. The corresponding shifts were found to be 63 meV (E_0) and 110 meV (E_2) for zb-GaN (see Ref. 25). It is therefore reasonable to estimate the temperature shift from 295 to 10 K for all features in ε_2 to about 100 meV for the whole alloy system. When comparing calculated quasiparticle band energies to experimentally obtained transitions as done below, this shift should be kept in mind.

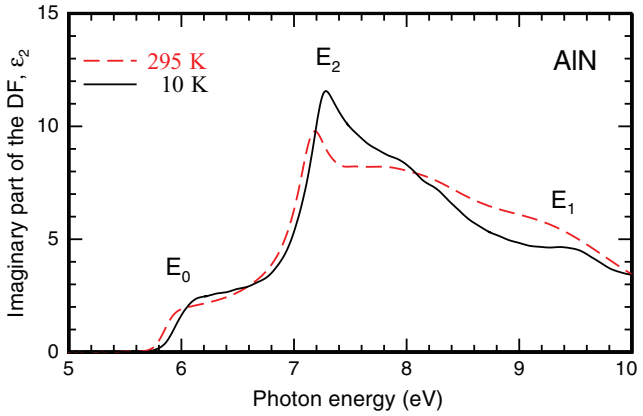

FIG. 3. (Color online) Imaginary parts of the dielectric functions (ε_2) of the zb-AlN samples up to 10 eV at 295 and 10 K.

In order to determine the Al concentration at the direct-indirect crossing the direct E_2 transition energies at the X point need to be aligned by the relative difference of the highest X point valence states and the position of the highest Γ point valence state (zero point of the energy scale). Since the accurate calculation of the valence band position is crucial to obtain the band gap crossing concentration, we will first discuss the suitability of various numerical approaches to simulate the electronic structure of nitride semiconductors before returning to the direct-indirect band gap crossing in Sec. IV.

III. THEORY

A. *Ab initio* calculations

The theoretical determination of the direct-indirect band gap crossing necessitates both a highly precise description of all extremal points of the band structure and an accurate reproduction of the infinite randomly occupied semiconductor alloy over the entire composition range.

Nowadays, the Kohn-Sham formulation[50] of DFT[51] is practically established as a standard for atomistic calculations in the solid-state community. The interpretation of energy differences between Kohn-Sham ground-state eigenvalues,[52] obtained using either the LDA[53–55] or the GGA[56–59] to approximate the exchange-correlation (XC) potentials and energies, as excitation energies have resulted in severely underestimated, unsatisfying band gap energies for a vast majority of semiconductors and insulators or even absent band gaps for small-gap systems (e.g., Ge, GaSb, and InAs, see Ref. 60). This so-called *band gap problem* is commonly portrayed as the most prominent unsolved problem of DFT and handicaps the communication of numerical results to nonspecialist readers less familiar with the theoretical foundations of DFT. The origin of the band gap underestimation can be traced back to self-interaction errors as well as the lack of a derivative discontinuity at integer electron number in approximated XC functionals.[52,60–65] The accuracy of conventional (semi)local DFT is often still sufficient to provide a sound basis for qualitative and quantitative interpretation of experimental data and, beyond that, it even shows some degree of inherent predictive power. Nevertheless, much methodological work in electronic structure theory has been devoted to the band gap problem in DFT. From a theoretical point of view, the focus of this study is to go beyond conventional DFT and apply various electronic structure methods, including many-body perturbation theory (MBPT),[66,67] that can be expected to give more accurate band gap values.

(1) TB-mBJLDA: Recently, Tran and Blaha[68] proposed an in-real-space multiplicative Kohn-Sham-like potential by modifying the Becke-Johnson (BJ) exchange potential[69,70]

$$v_{x,\sigma}^{\text{TB-mBJ}}(\mathbf{r}) = c\, v_{x,\sigma}^{\text{BR}}(\mathbf{r}) + (3c-2)\,\frac{1}{\pi}\sqrt{\frac{5}{12}}\sqrt{\frac{2t_\sigma(\mathbf{r})}{\rho_\sigma(\mathbf{r})}}, \quad (2)$$

where

$$v_{x,\sigma}^{\text{BR}}(\mathbf{r}) = -\frac{1}{b_\sigma(\mathbf{r})}\left[1 - e^{-x_\sigma(\mathbf{r})} - \frac{1}{2}x_\sigma(\mathbf{r})\, e^{-x_\sigma(\mathbf{r})}\right] \quad (3)$$

is the Becke-Roussel exchange potential[71] as proposed earlier to model the Coulomb potential created by the exchange hole. Here, $\rho_\sigma = \sum_{i=1}^{N_\sigma} |\psi_{i,\sigma}|^2$ and $t_\sigma = (1/2)\sum_{i=1}^{N_\sigma}(\nabla\psi_{i,\sigma}^* \cdot \nabla\psi_{i,\sigma})$ are the electron and kinetic-energy densities, x_σ is determined from a nonlinear equation containing t_σ as well as the density gradients ρ_σ,$\nabla\rho_\sigma$, and $\nabla^2\rho_\sigma$ and b_σ are calculated according to $b_\sigma = [x_\sigma^3\, e^{-x_\sigma}/(8\pi\rho_\sigma)]^{1/3}$. Equation (2) ensures that for any value of c the LDA exchange potential is approximately recovered for a constant electron density. For $c = 1$ the original BJ potential is recovered. The actual value of the c parameter in Eq. (2) is calculated from the cell average of the quantity $|\nabla\rho/\rho|$ via

$$c = \alpha + \beta\left[\frac{1}{V_{\text{cell}}}\int_{\text{cell}}\frac{|\nabla\rho(\mathbf{r}')|}{\rho(\mathbf{r}')}d^3r'\right]^{1/2}, \quad (4)$$

where V_{cell} is the unit-cell volume and α and β are two free parameters, whose values ($\alpha = -0.012$, $\beta = 1.023$ bohr$^{1/2}$) are determined to minimize the mean absolute relative error of the band gap for a representative set of solids (see Ref. 68). Due to their dependence on the kinetic energy density t_σ, the exchange potentials above can be classified as meta-GGA's. In practical calculations, the TB-mBJ exchange potential is used in combination with an LDA correlation potential[55] (TB-mBJLDA). Since the TB-mBJ exchange potential cannot be obtained as a functional derivative ($\delta E_{\text{xc}}[\rho]/\delta\rho$) of the total energy,[72] it is not possible to use the TB-mBJLDA potential for force calculations. Thus structure relaxations have to be done using alternative XC functionals.

The TB-mBJLDA potential has been shown to reproduce experimental band gaps with an error margin of the same order as hybrid functional or GW approaches (see Ref. 68), thereby preserving the moderate computational cost of conventional DFT. In principle, the TB-mBJLDA method can be seen as a parameter-free approach, since the c parameter can be calculated self-consistently according to Eq. (4). However, using the self-consistently estimated values of c electronic band gaps in semiconductors and insulators tend to be underestimated.[73–75] Since band gaps typically show a monotone increase with increasing c,[68] c can be adjusted manually to match the experimental band gaps. In a study on band structure topologies of III-V semiconductors, Kim *et al.*[73] reported an excellent TB-mBJLDA description of band gaps at high-symmetry points, although a general overestimation of effective masses by 20–30% was reported.

Recently, Kresse *et al.*[75] demonstrated that fundamental band gap energies obtained with the TB-mBJLDA potential and a properly adjusted c parameter can even compete with the most sophisticated self-consistent GW schemes. However, a significant tendency toward to narrow bandwidth and consequentially a nonadequate representation of the optical response was reported by using TB-mBJLDA orbitals to solve the Bethe-Salpeter equation.

(2) LDA-1/2: Another approach to improve the description of band gaps by approximately taking into account self-energy corrections within the framework of conventional Kohn-Sham DFT in LDA is the LDA-1/2 half-occupation technique. LDA-1/2 has been derived in the spirit of Slater-Janack transition-state theory[76–78] and was recently developed by Ferreira *et al.*[79,80] into a practical scheme for band gap calculations of semiconductors. While the half-occupation scheme provides accurate atomic ionization potentials,[79] it cannot be directly applied to extended crystalline systems. In the LDA-1/2 approach the orbital-dependent self-energy

$$S_\alpha = \int n_\alpha(\mathbf{r})\, V_S(\mathbf{r})\, d^3r \tag{5}$$

of a Kohn-Sham state α with electron density $n_\alpha(\mathbf{r})$ is subtracted from the Kohn-Sham eigenvalue at full occupation. Therefore the self-energy potential V_S, is approximately given as the difference

$$V_S \approx -V(-1/2,r) + V(0,r) \tag{6}$$

between the all-electron potentials of an atom and its half-ion. V_S has been interpreted as the work required to transform the charge of a Bloch function into a localized hole state.[81] In crystals, the self-energy correction is added to the atomic (pseudo)potentials of all atoms, thus calculating the properties of a "filled hole band" instead of individual localized hole states. To avoid the penetration of the self-energy Coulomb tails into neighboring atom sites, the self-energy potentials are trimmed according to $V_S' = \theta(r) V_S$ by a cutoff function $\theta(r)$:

$$\theta(r) = \begin{cases} \left[1 - \left(\frac{r}{\mathrm{CUT}}\right)^{n=8}\right]^3 & r \leqslant \mathrm{CUT}, \\ 0 & r > \mathrm{CUT}. \end{cases} \tag{7}$$

Ideally, LDA-1/2 can be considered to be fully *ab initio*, since the value of the CUT parameter is determined in a variational way to make the band gaps extremal without falling back to empirical parameters. If not stated otherwise, the LDA-1/2 results, presented throughout this study, are obtained by adding self-energy correction potentials with a cutoff of CUT = 2.90 a.u. to the N_{2p} states in zb-AlN and zb-GaN. For zb-GaN, additional self-energy corrections with a cutoff of CUT = 1.15 a.u. have been included for the Ga_{3d} states.

LDA-1/2 has led to very impressive band gap results[79] for a large number of materials ranging from small-gap semiconductors to wide-gap semiconductors and insulators. Thereby, LDA-1/2 even surpasses non-self-consistent GWA approaches[82,83] and partially or fully self-consistent GW approaches that neglect the influence of electron-hole vertex corrections (cf. Ref. 84). The LDA-1/2 approach was recently used by Pelá *et al.*[85] to model the band gaps of the ternary group-III nitride alloys wz-$Al_xGa_{1-x}N$, wz-$In_xGa_{1-x}N$, and wz-$Al_xIn_{1-x}N$. The LDA-1/2 band gaps were found to fit remarkably well with the experimental results for all studied alloys. Using the example of polar and nonpolar InN surfaces Belabbes *et al.*[86] demonstrated that the LDA-1/2 method allows an approximate computation of accurate QP excitations, that are on the same level as combined hybrid functional and GW results, even for extended surface systems. Further examples of LDA-1/2 studies include the electronic bands and their alignment in various III-V semiconductors and their polytypes,[87] the energetics of SnO_2 surfaces,[88] and the band offsets at AlAs/GaAs and $Al_xGa_{1-x}As$/GaAs interfaces[89] as well as Si/SiO_2 interfaces.[81] In a nutshell, the LDA-1/2 method provides a promising approach for an approximate description of QP characteristics of the electronic-structure of large scale semiconductor and insulator structure models at the computational cost of conventional (semi)local DFT.

(3) HSE: An alternative approach to an accurate, DFT-based band-structure description is the use of nonlocal, nonmultiplicative XC potentials to solve a generalized eigenvalue problem that formally lies outside the KS framework.[37,38] Especially nonlocal hybrid functionals, which replace some fraction of (semi)local DFT exchange by (Hartree-)Fock (also exact) exchange energy (e.g., PBE0[59,63,90,91]), have been applied quite successfully in solid state theory. Thereby the inclusion of an exact-exchange interaction fraction (∼25%) is not only motivated by the observation of reverse band gap errors in (semi)local DFT and Hartree-Fock (HF) theory, but also rationalized by theoretical considerations.[92] A class of modern, extensively applied, hybrid functionals are HSE (Heyd-Scuseria-Ernzerhof) functionals[60,93–95] that restrict the inclusion of exact Fock exchange E_X^{HF} to short-range contributions. In general, the long-range (LR) exchange interaction and the correlation energy E_c remain unchanged with respect to the PBE functional (E_X^{PBE} and E_C^{PBE}), therefore, a HSE-type functional exhibits the form

$$\begin{aligned} E_{\mathrm{XC}}^{\mathrm{HSE}} = {} & \alpha E_X^{\mathrm{HF,SR}}(\mu) + (1-\alpha) E_X^{\mathrm{PBE,SR}}(\mu) \\ & + E_X^{\mathrm{PBE,LR}}(\mu) + E_C^{\mathrm{PBE}}. \end{aligned} \tag{8}$$

Thereby the range separation into LR and short-range (SR) parts of E_X^{HF} is carried out by a decomposition of the Coulomb kernel according to

$$\frac{1}{r} = \underbrace{\frac{erfc(\mu r)}{r}}_{\mathrm{SR}} + \underbrace{\frac{erf(\mu r)}{r}}_{\mathrm{LR}}. \tag{9}$$

The parameter α defines the percentage of exact Fock exchange. In agreement with the original definitions,[93–96] we refer to the parameter values $\alpha = 0.25$, $\mu = 0.2$ Å^{-1} as HSE06. The screening parameter μ is not changed throughout this work. However, since a fixed amount of exact exchange and a nonvariable screening limit the flexibility of the HSE06 functional, it is a common practice (especially for wide-gap materials[20]) to sacrifice the essence of *ab initio* theory by searching material optimized values for α and μ.

In general, the use of HSE-type hybrid functionals has shown significant improvements in the description of electronic band gaps,[60,97–100] band offsets,[20,101] defect levels,[102–104] and the prediction of accurate direct-indirect band gap crossovers.[101] Nevertheless the gain of accuracy increases the

computational cost by two orders of magnitude compared to conventional (semi)local DFT.

(4) GW: The final approach applied in this study to include many-particle interactions beyond Kohn-Sham-like single-particle mean-field theories is based on MBPT, as formulated by Hedin.[66,67] MBPT formally recast the solution of the *electronic-structure problem* into a closed fundamental system of five coupled integral equations for the Greens function G, the screened Coulomb interaction W, the self-energy Σ, the polarization propagator P, and a vertex function Γ. Due to the complicated nature of the functional dependence of $\Sigma = \Sigma[G]$ on G, Hedin's equations have to be solved self-consistently. In practice, these equations are decoupled by narrowing the vertex corrections to zeroth order as originally proposed by Hedin[67] (i.e., GWA). Within GWA, the energies $E_{n\mathbf{k}}^{\mathrm{QP}}$ of single excited (quasi)electrons and (quasi)holes, as experimentally accessible in direct and inverse photoemission spectroscopy experiments, are obtained as solutions to a set of nonlinear differential equations,[67,105] that are found to be similar to the Kohn-Sham equations:

$$\left(T + V_{\mathrm{ext}} + V_H - \varepsilon_{n\mathbf{k}}^{\mathrm{QP}}\right)\Psi_{n\mathbf{k}}(\mathbf{r}) + \int d^3\mathbf{r}'\,\Sigma\left(r,r',\varepsilon_{n\mathbf{k}}^{\mathrm{QP}}\right)\Psi_{n\mathbf{k}}(\mathbf{r}') = 0. \tag{10}$$

Here, the Kohn-Sham XC functional $V_{xc}^{\mathrm{KS}}(r)$ is replaced by the nonlocal energy-dependent self-energy operator $\Sigma(r,r',\varepsilon_{n\mathbf{k}}^{\mathrm{QP}})$ that carries the information of the many-body interactions. The GWA self-energy, given to first order in W, is evaluated as a convolution integral of the single-particle Greens function G and the dynamically screened Coulomb interaction W,

$$\Sigma(r,r',\omega) = \frac{i}{4\pi}\int_{-\infty}^{\infty} d\omega' e^{i\omega'\delta} G(\mathbf{r},\mathbf{r}',\omega+\omega')W(\mathbf{r},\mathbf{r}',\omega'). \tag{11}$$

Here, δ is a infinitesimal positive number. In the most common GWA calculations, DFT eigenvalues and wave functions are used as input for the calculation of QP energy correction within a first-order perturbation theory approach (i.e., G_0W_0). The first-order energy corrections (so-called QP shifts) $\Delta\varepsilon_{n\mathbf{k}}^{\mathrm{QP}}$ are given by

$$\Delta\varepsilon_{n\mathbf{k}}^{\mathrm{QP}} = Z_{n\mathbf{k}}\,\mathrm{Re}\left\langle\Psi_{n\mathbf{k}}^{\mathrm{KS}}\middle|\Sigma\left(\varepsilon_{n\mathbf{k}}^{\mathrm{KS}}\right) - V_{xc}^{\mathrm{KS}}\middle|\Psi_{n\mathbf{k}}^{\mathrm{KS}}\right\rangle, \tag{12}$$

where the perturbation is given by the difference between the self-energy and the DFT XC functional and $Z_{n\mathbf{k}}$ represents a renormalization factor.[38,105–107] G_0W_0 calculations systematically improve the DFT band gaps.[83,108,109] However, this perturbative approach shows a strong dependence on the choice of the initial wave functions that can be taken from (semi)local DFT, hybrid functional DFT or other approaches.[20,38,110] Effects of self-consistency within the GW approach are considered partially by repeated calculation of QP corrections with updated QP eigenvalues in G or both G and W.[38,107] The according approaches are known as, GW_0 and GW. For numerous semiconductors, GW_0 QP energies are very close to experimental results.[83,107] Nevertheless, QP corrections in the various self-consistent approaches do not necessarily improve the band gap description over the computationally less demanding non-self-consistent G_0W_0 approaches. Especially the fully self-consistent GW QP energies tend to overestimate the experimental values for electronic band gaps.[38,83] Aside from self-consistency with respect to QP energies, also the one-electron orbitals, initialized by various choices of Kohn-Sham DFT orbitals, may be updated self-consistenly.[82,84,111] Again, updated QP energies and one-electron orbitals may be considered in the Green function G only (i.e., scGW_0) or in G and the screened Coulomb potential W (i.e., scGW). Since improvement over *single shot* G_0W_0 with carefully selected initial DFT one-electron orbitals are sparse in the self-consistency schemes above, it has been stated that the inclusion of an attractive electron-hole interaction (i.e., vertex corrections) might be the next systematic improvement over the various GW schemes applied hitherto.[75,84,112] In practice, even non-self-consistent G_0W_0 calculations show a prohibitive computational cost for larger unit cells of, e.g., surfaces or alloys by even surpassing the computational demands of hybrid-functional approaches.

Obviously, a detailed knowledge of the performance of the approaches above with respect to various material characteristics is of fundamental interest. In particular, given that the computational expense of these approaches increases from standard (semi)local DFT equivalent cost by two to three orders of magnitude in case of hybrid-functional DFT or the even more sophisticated GW QP theories.

B. Alloy modeling

In order to simulate the substitutional disorder of the ternary semiconductor compounds, we adopted two different strategies both aiming at an adequate *single* unit-cell representation of the alloys. On the one hand, we generated cubic 8, 64, and 216 atom unit cells (labeled by RAND) with randomly occupied cation sublattices to study the influence of the artificially introduced system size dependent periodicity errors. We compare these arbitrary representations of the random alloys to special quasirandom structures (SQSs) constructed according to Zunger (see Refs. 33 and 40). A SQS is designed to mimic the structural correlations of the perfectly random alloy as closely as possible within the most relevant lowest order structure correlations. Thereby the basic assumption of the SQS approach is that most physical properties show a hierarchical dependence on the interaction distance with clearly dominating short-range (pair) correlations and negligible pair and multisite correlations at larger distances. For details on the generation of SQSs, we refer the reader to the numerous literature.[33,40,45] SQSs, with just a few atoms per unit cell, promise to keep the required resources of the more elaborate computational schemes within reasonable limits and to circumvent the problem of scanning a large number of different lattice configurations to utilize statistical approaches. Nevertheless, it is worth to note that alloys are best described by statistical averages on sufficiently extended unit cells. Ultimately, an answer to the basic question if a single unit-cell-based approach can be sufficient to characterize stochastic substitutional disorder in an semiconductor alloy will be closely connected to its chemical composition. In particular, the extend of the lattice mismatch between the individual material components and the degree of local atomic relaxations, will be significant. So far, SQSs have been successfully applied to calculate the spatial and electronic structures

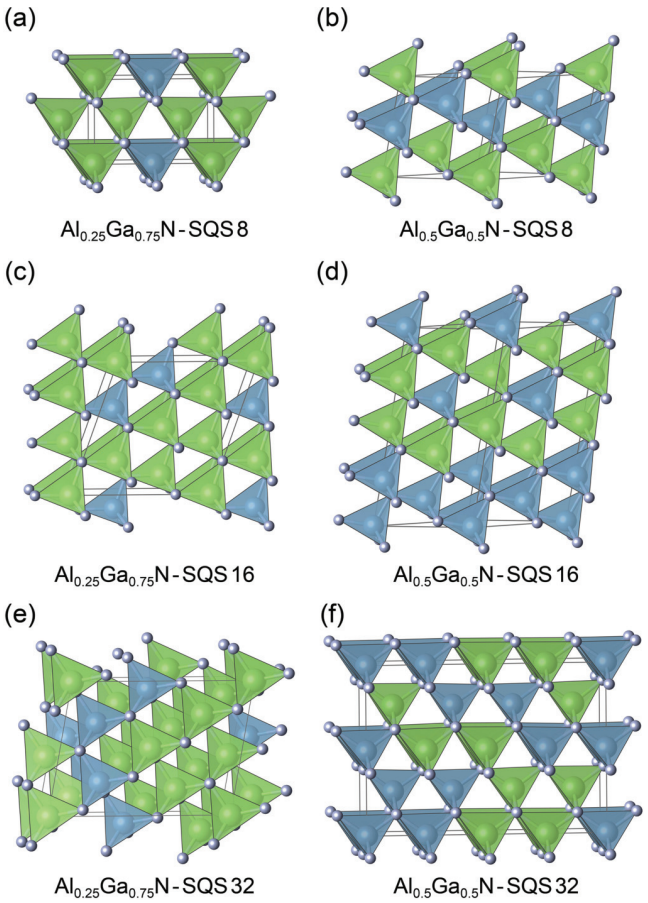

FIG. 4. (Color online) Polyhedra representation of 8, 16, and 32 atom SQS's unit cell for ternary zb-$Al_xGa_{1-x}N$ alloys. Tetrahedral AlN_4 units are displayed in blue and GaN_4 units in green. For zb-$Al_{0.75}Ga_{0.25}N$, the chemical elements of the zb-$Al_{0.25}Ga_{0.75}N$ cation sublattice are interchanged. For each SQS, the particular unit cell is draw as grey lines. The illustrations have been done using VESTA.[113]

of various binary and multicomponent alloys.[38,114–119] An automated SQSs generation tool is provided by the alloy theoretic automated toolkit (ATAT).[120]

Our generated SQSs with 8, 16, and 32 atoms for Al concentrations of $x = 0.25$ and 0.5 are displayed in Fig. 4. The SQSs for $x = 0.75$ are obtained by interchanging the chemical elements of the zb-$Al_{0.25}Ga_{0.75}N$ SQS's cation sublattices. Details on the SQS unit cells are given in Table II. For all

TABLE II. Details on the basic shape of the generated zb-$Al_xGa_{1-x}N$ SQS unit cells. The lattice vectors are given in units of $a_{\text{zb-}Al_xGa_{1-x}N}/2$ with linearly interpolated alloy lattice constant according to Eq. (13).

Model	x	Lattice vectors		
SQS 8	0.25/0.75	(0, −1, −1)	(−2,0,0)	(0,2, −2)
SQS 8	0.5	(−2, −1, −1)	(−1, −1, −2)	(1, −2,1)
SQS 16	0.25/0.75	(−2,2, −2)	(2,2,2)	(1,0, −1)
SQS 16	0.5	(2,1, −1)	(1,1, −2)	(−2,4,2)
SQS 32	0.25/0.75	(1,1, −2)	(0, −3, −1)	(−4,1, −1)
SQS 32	0.5	(0, −1, −1)	(−4,0,0)	(0,4, −4)

composition ratios the local atomic relaxations are considered by separate relaxations of the atomic structure.

To ensure consistency throughout the different numerical approaches, all bulk calculations are performed at the experimental zb lattice constants[121,122] ($a_{\text{zb-AlN}} = 4.38$ Å, $a_{\text{zb-GaN}} = 4.52$ Å). In view of the small lattice mismatch (∼3%) of the zb-AlN and zb-GaN bulk, the zb-$Al_xGa_{1-x}N$ alloys are constructed assuming a linear Al concentration dependent lattice constant $a(x) = x\,4.52 + (1-x)4.38$ Å following Vegard's law,

$$a_{\text{zb-}Al_xGa_{1-x}N} = x\,a_{\text{zb-AlN}} + (1-x)a_{\text{zb-GaN}}. \qquad (13)$$

The validity of Vegard's law for group-III nitride alloys has been confirmed experimentally[123] for wz-$Al_xGa_{1-x}N$ and in several theoretical studies on zb-$Al_xGa_{1-x}N$.[35,36,124] In all structure models, local atomic relaxations were considered at the DFT-GGA level applying the Perdew-Becke-Ernzerhof (PBE)[59] XC functional and a force convergence criterion of 0.005 eV/Å.

C. Numerical details

The DFT and *GW* calculations of this study were performed using the Vienna *ab initio* simulation package (VASP) implementations.[38,83,84,107,125] An energy cutoff of 400 eV was used throughout this work to expand the Kohn-Sham orbitals into plane wave basis sets. The electron-ion interaction was described by the projector-augmented wave (PAW) method.[126,127] Throughout this work the Ga_{3d} semicore states were treated as valence states in the PAW potentials. The *GW* calculations for primitive bulk unit cells of zb-AlN and zb-GaN were carried out with 256 electronic bands and 160 frequency grid points for sampling the dielectric function. In all partially or fully self-consistent *GW* calculations, the one-electron energies and optionally the one-electron orbitals have been updated eight times to reach QP band gaps that are converged within an accuracy of 0.01 eV. If not stated otherwise, the Brillouin zone integration of primitive unit cells was performed using regular Γ-centered $8 \times 8 \times 8$ k-point meshes. This again guarantees the convergence of bulk QP band gaps within 0.01 eV. In all electronic band-structure calculations the high-symmetry lines were sampled by 100 k points. Further details on the parameters used in TB-mBJLDA und HSE calculations as well as further details on the LDA-1/2 scheme as well as the *GW* approaches are given below. The Brillouin zone integration for zb-$Al_xGa_{1-x}N$ alloys was performed by regular Γ-centered $8 \times 8 \times 8$ and $3 \times 3 \times 3$ k-point sets for cubic 8 and 64 atom unit cells. For cubic 216 atom unit cell, the calculations were restricted to the Γ point only. For the more complicated SQS unit cells the k-point mesh was chosen to match a comparable point density in the reciprocal space.

All numerical simulations of this study do not include effects of spin polarization. Without saying, the experimental transition energies reflect the splitting due to spin-orbit interaction that is neglected in our calculations. Therefore we will not make use of explicit electronic state symmetry labels in the discussion of theoretical and experimental results. For a detailed discussion of the valence-band splitting due to spin-orbit coupling in binary group-III bulk nitrides see Refs. 128 and 129.

TABLE III. Calculated band gaps of zb-GaN and zb-AlN. Experimental data are taken from Ref. 22 for the direct and indirect band gaps of zb-AlN and from Ref. 25 for the direct band gap of zb-GaN. TB-mBJLDA results are given for two optimized c-parameter values. TB-mBJLDA* and TB-mBJLDA** refer to c parameters of $c = 1.45$ and 1.55. For modified HSE calculations, the fraction (α) of exact exchange is given. In partially and fully self-consistent GW calculations, the QP eigenvalues have been updated eight times. In the scGW_0 and scGW schemes, also updates of the one-electron orbitals have been included in the self-consistency cycle. The relative errors of the calculated band gaps with respect to the experimental values are visualized in Fig. 5. All band gap values are given in eV.

	zb-AlN		zb-GaN
Method	$(\Gamma_v \rightarrow X_c)$	$(\Gamma_v \rightarrow \Gamma_c)$	$(\Gamma_v \rightarrow \Gamma_c)$
LDA	3.22	4.15	1.68
PBE	3.31	4.12	1.66
TB-mBJLDA* ($c = 1.45$)	5.40	5.78	2.99
TB-mBJLDA** ($c = 1.55$)	5.79	6.09	3.29
LDA-1/2	5.34	5.87	3.31
HSE06	4.56	5.50	2.92
mod(32)HSE ($\alpha = 0.32$)	4.92	5.90	3.30
mod(39)HSE ($\alpha = 0.39$)	5.29	6.30	3.69
G_0W_0@PBE	4.59	5.64	2.92
G_0W_0@HSE06	5.16	6.25	3.47
GW_0@PBE	5.09	6.04	3.03
GW@PBE	5.57	6.53	3.37
scGW_0@PBE	5.47	6.25	3.34
scGW@PBE	5.42	6.30	3.71
exp	5.3 (295 K)	5.9 (295 K)	3.3 (10 K)

D. Band gaps of zb-AlN and zb-GaN

In order to find an accurate description of the zb-$Al_xGa_{1-x}N$ alloys, we start our discussion of the numerical approaches by a comparison of the zb-AlN and zb-GaN bulk-band structure characteristics. In Table III, the absolute values of the fundamental direct and indirect energy transitions are summerized for both materials. Additionally, Fig. 5 visualizes the relative percentaged band gap errors $(E_{\text{gap}}^{\text{calc}} - E_{\text{gap}}^{\text{exp}})/E_{\text{gap}}^{\text{exp}} \times 100$ for all approaches.

The use of the LDA and the semilocal PBE functional yields quite similar band gaps. For both semiconductors, the calculated (semi)local band gaps show the expected characteristic underestimation. In case of zb-AlN, the direct band gap is underestimated by ∼39% and the indirect band gap by ∼30%. For zb-GaN, this underestimation actually increases to almost 50%. Larger differences between DFT-LDA and DFT-PBE results, occasionally reported, might arise from the differences in the equilibrium lattice constants of zb-AlN and zb-GaN.

The use of the TB-mBJLDA potential to calculate band gap energies drastically increases the BGs towards their experimental size. However, self-consistently determined c parameters (not listed in Table III) of $c_{\text{zb-AlN}} = 1.29$ and $c_{\text{zb-GaN}} = 1.33$ still show notably underestimated band gaps of $E_{\text{gap}}^{\text{zb-AlN}}(\Gamma_v \rightarrow X_c) = 4.81$ eV, $E_{\text{gap}}^{\text{zb-AlN}}(\Gamma_v \rightarrow \Gamma_c) = 5.25$ eV, and $E_{\text{gap}}^{\text{zb-GaN}}(\Gamma_v \rightarrow \Gamma_c) = 2.66$ eV. This tendency has already been reported earlier.[73,75] The TB-mBJLDA band gap increases monotonically with increasing the c parameter, and c can thus be adjusted separately for each material. The optimal choice of c for zb-GaN is $c \approx 1.55$ (labeled as TB-mBJLDA**) to reproduce the experimental band gap. For the same value of c the zb-AlN band gaps are overestimated by ∼9% and ∼3% for the indirect and direct band gaps. In case of zb-AlN we searched for a c parameter that equally improves the indirect and direct band gap. For $c \approx 1.45$ (labeled as TB-mBJLDA*), we obtain band gaps of $E_{\text{gap}}^{\text{zb-AlN}}(\Gamma_v \rightarrow X_c) = 5.40$ eV and $E_{\text{gap}}^{\text{zb-AlN}}(\Gamma_v \rightarrow \Gamma_c) = 5.78$ eV. The error for both zb-AlN band gaps is below ∼2%. Nevertheless, the reverse sign of the errors shows that this is the best simultaneous description of the indirect and direct band gaps. The c parameter optimized for zb-AlN leads to a band gap underestimated of ∼9% for zb-GaN. One interesting property of the TB-mBJLDA potential is that the increase of the c parameter systematically reduces the difference between the indirect and direct band gaps of zb-AlN. For $c = 1$, we obtain a ratio of $E_{\text{gap}}^{\text{zb-AlN}}(\Gamma_v \rightarrow X_c)/E_{\text{gap}}^{\text{zb-AlN}}(\Gamma_v \rightarrow \Gamma_c) = 0.84$ for $c = 1.6$ this value increases to $E_{\text{gap}}^{\text{zb-AlN}}(\Gamma_v \rightarrow X_c)/E_{\text{gap}}^{\text{zb-AlN}}(\Gamma_v \rightarrow \Gamma_c) = 0.96$.

The calculated LDA-1/2 band gaps of $E_{\text{gap}}^{\text{zb-AlN}}(\Gamma_v \rightarrow X_c) = 5.34$ eV, $E_{\text{gap}}^{\text{zb-AlN}}(\Gamma_v \rightarrow \Gamma_c) = 5.87$ eV, and $E_{\text{gap}}^{\text{zb-GaN}}(\Gamma_v \rightarrow \Gamma_c) = 3.31$ eV are an astonishing result. The relative error is significantly below 1% for all band gaps. Therefore also the ratio between the direct and the indirect band gap of zb-AlN is accurately reproduced. This feature singles out the LDA-1/2 approach from all other numerical approaches applied in this study, especially since these at least need separately adjusted parameters for both binary materials to reach the same accuracy. As stated above, these results were obtained by adding self-energy correction potentials to the N_{2p}

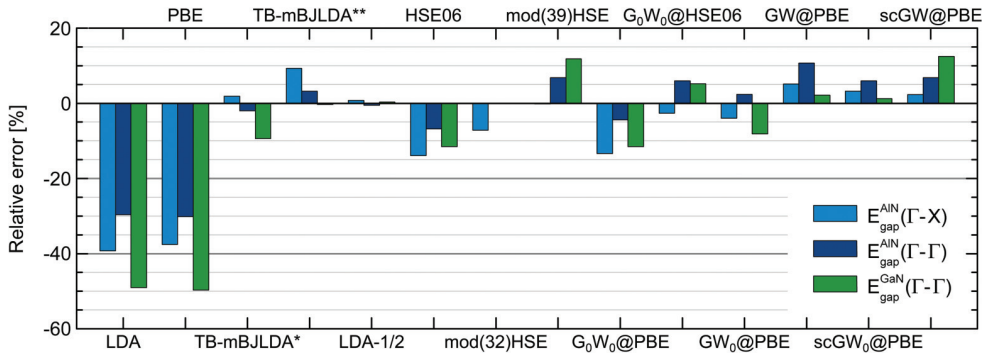

FIG. 5. (Color online) Relative percentaged errors $(E_{\rm gap}^{\rm calc} - E_{\rm gap}^{\rm exp})/E_{\rm gap}^{\rm exp}\,100$ of the calculated direct $\Gamma_v \to \Gamma_c$ and indirect $\Gamma_v \to X_c$ band gaps of zb-AlN and the direct zb-GaN band gap. TB-mBJLDA* and TB-mBJLDA** refer to c parameters of $c = 1.45$ and 1.55. For HSE-type calculations, the used fraction of exact exchange is indicated in brackets. In partially and fully self-consistent GW calculations, the QP eigenvalues have been updated eight times to reach self-consistency. In the scGW_0 and scGW schemes, also updates of the one-electron orbitals have been considered. The absolute band gap values corresponding to this diagrammatic representation are summarized in Table III.

states for zb-AlN and to the N_{2p} and Ga_{3d} states for zb-GaN. The LDA-1/2 band gaps are predominantly influenced by self-energy corrections to the N_{2p} states. Considering only the N_{2p} state self-energy corrections for calculations on zb-GaN results in a slightly smaller band gap of $E_{\rm gap}^{\text{zb-GaN}}(\Gamma_v \to \Gamma_c) = 3.15$ eV. Additional Al_{2p} self-energy corrections increase the zb-AlN band gaps to $E_{\rm gap}^{\text{zb-AlN}}(\Gamma_v \to X_c) = 5.42$ eV and $E_{\rm gap}^{\text{zb-AlN}}(\Gamma_v \to \Gamma_c) = 6.05$ eV.

Next, we consider the band gap description in hybrid-functional DFT. Starting from the original HSE06 parameters, we find that a 25% exact SR exchange contribution, underestimates the band gaps between ∼7% and ∼14%. This is consistent with preceding studies that reported the best HSE performance for small and midgap semiconductors and a band gap underestimation for wide-gap semiconductors and insulators.[60,97,98] We systematically increased the exact exchange fraction α [cf. Eq. (8)] in our modified HSE-type hybrid functional calculations to determine the value for α best suited to reproduce the experimental data. 32% exact exchange [mod(32)HSE] exactly reproduces the direct band gaps of both bulk material. Simultaneously, the indirect zb-AlN band gap of $E_{\rm gap}^{\text{zb-AlN}}(\Gamma_v \to X_c) = 4.92$ eV shows an ∼7% underestimation of the reported experimental value. The indirect band gap of zb-AlN is not reproduced until a Fock exchange fraction of ∼39% [mod(39)HSE] is used. The difference of the indirect and direct zb-AlN band gaps is close to 1 eV independently of the exact-exchange fraction thus above the 0.6 eV difference between the experimental values. Based on these observations it seems reasonable to introduce a composition-dependent exact exchange fraction in the HSE hybrid-functional description of the ternary zb-$Al_xGa_{1-x}N$ alloys.

Finally, we address the manifold of GWA based QP theory approaches starting with the non-self-consistent G_0W_0 results obtained in first order perturbation theory according to Eq. (12). G_0W_0 QP corrections, obtained from DFT-PBE one-electron orbitals (i.e., G_0W_0@PBE), increase the DFT band gaps to values very similar to the HSE06 results. A G_0W_0@PBE band gap underestimation between ∼4% and ∼13% is observed. Since the results of the non-self-consistent GWA critically depend on the initial wavefunctions, one-electron orbitals from HSE hybrid-functional calculations are a significantly improved basis to evaluate the QP shifts. Consequently, the G_0W_0@HSE06 QP band gaps of $E_{\rm gap}^{\text{zb-AlN}}(\Gamma_v \to X_c) = 5.16$ eV, $E_{\rm gap}^{\text{zb-AlN}}(\Gamma_v \to \Gamma_c) = 6.25$ eV, and $E_{\rm gap}^{\text{zb-GaN}}(\Gamma_v \to \Gamma_c) = 3.47$ eV are significantly closer to the fundamental experimental band gaps within an error range from ∼−3% to ∼6%. Thereby, the direct $\Gamma_v \to \Gamma_c$ band gaps are overestimated while the indirect zb-AlN band gap is still underestimated. With 1.09 eV the difference of indirect and direct zb-AlN band gap energies is close to the results of hybrid-functional DFT. Notably, the direct G_0W_0@HSE06 QP band gap exactly corresponds to the fundamental (direct) band gap of wz-AlN.[130] The results of the various self-consistent GW schemes are quite inconclusive with relative band gap errors between ∼−8% and ∼12%. No systematic trend in the QP band gaps is found. The partial inclusion of self-consistency in the scGW$_0$@PBE scheme is the only scheme that generates improved band gap data for the two materials considered in this study. The calculated band gaps of $E_{\rm gap}^{\text{zb-AlN}}(\Gamma_v \to X_c) = 5.47$ eV, $E_{\rm gap}^{\text{zb-AlN}}(\Gamma_v \to \Gamma_c) = 6.25$ eV, and $E_{\rm gap}^{\text{zb-GaN}}(\Gamma_v \to \Gamma_c) = 3.34$ eV overestimate the experimental gaps by ∼1% to ∼6%. Another important observation is the relative close agreement (< 0.13 eV) between the mod(39)HSE result and the QP band gaps obtained by fully self-consistent scGW@PBE calculations. This accordance implies two things. On the one hand, HSE-type hybrid functionals can be adjusted to reach even the QP band gap accuracy of sophisticated GW schemes. On the other hand, the mod(39)HSE wave functions are expected to be very close to the true QP wave functions. Summarizing, the results from the self-consistent GW approaches, even the best results represent only marginal improvements over the G_0W_0@HSE06 results. Further improvements most likely require the inclusion of additional vertex corrections to include the electron-hole interaction, that is neglected in all GWA schemes, into the self-consistency cycle.[75,84,112] Considering the lower computational cost, non-self-consistent G_0W_0 corrections obtained from high-quality (hybrid-functional DFT) one-electron orbitals, that follow the

originally intended idea of a perturbative approach, probably still represent a very meaningful approach to obtain reliable QP energies.

E. Band structure of zb-AlN and zb-GaN

In order to compare the electronic structure beyond the fundamental direct and indirect band gap transitions, we have visualized the TB-mBJLDA, LDA-1/2, modHSE, and G_0W_0@HSE06 band structures in Fig. 6. For the TB-mBJLDA and modHSE band structures the fundamental band gap optimized c parameters and exact exchange fractions were used. The G_0W_0@HSE06 QP band structure (see gray dots) is taken as reference for QP energies. Ignoring the strongly bound energy states that originate from the Ga_{3d} semicore and N_{2s} states for a moment, our modified HSE-type hybrid-functional calculations show an excellent agreement with the G_0W_0@HSE06 band structures for valence and conduction band states in both materials. This result again justifies the adjustment of the exact-exchange fraction in HSE-type hybrid-functional calculations to reproduce the GW QP band structure. As already indicted by the fundamental band gaps, the TB-mBJLDA and LDA-1/2 approaches both provide reasonable approximations to the QP band structure. Differences between TB-mBJLDA as well as LDA-1/2 energy bands and the G_0W_0@HSE06 band structures increase significantly with the excitation energy as well as the reciprocal lattice vector. This affects band-structure characteristics such as the effective masses. These deviations also affect the size and relative differences of energy transitions, as indicated by the lowest valence-to-conduction band transitions at the Γ, X, and L points sketched in Fig. 6. Differences are in particular obvious with respect to the modHSE band structures.

Compared to the G_0W_0@HSE06 QP energies, dramatic deviations are found for the low lying, stronger localized energy states. The N_{2s} valence-band states in zb-AlN are located between −13.3 and −16.1 eV in G_0W_0@HSE06. TB-mBJLDA surprisingly well reproduces the QP N_{2s} band with maximal differences of ∼0.7 eV (at the Γ point). Comparing the band energies at the Γ point, the LDA-1/2 calculation overestimates the position of the N_{2s} band energy by ∼1.7 eV. Equivalently, the mod(39)HSE band structure shows an N_{2s} band underestimation of ∼1.1 eV. From G_0W_0@HSE06 calculations the position of the Ga_{3d} bands in zb-GaN is found between ∼−17 and ∼−18 eV. The N_{2s} band is located at ∼−18 eV at the Γ point and thus partially hybridized with the Ga_{3d} states around the Γ point. The N_{2s} states at −13.7 eV are well separated from the Ga_{3d} states around the W point. In general, the character of the s-d coupling of N_{2s} and Ga_{3d} semicore states depends critical on the energy differences between both states. Ding *et al.*[131] used angle-resolved photoelectron spectroscopy to study the valence band structure of zb-GaN. In the high binding-energy region, a sharp peak at 17.7 eV has been assigned to the Ga_{3d} states, while a second less intense peak at 14.2 eV binding energy belongs to the N_{2s} states. The photoemission data further indicate a very clear separation of Ga_{3d} and N_{2s} states by 3.5 eV and a N_{2s} band width of 0.65 eV. Considering these experimental findings, our G_0W_0@HSE06 QP energies are in good agreement with the experiment except for the hybridization around the Γ point that might be an artifact from the initial HSE06 hybrid-functional DFT wave functions.

The mod(39)HSE calculations approximately place the Ga_{3d} semicore and N_{2s} energy states in the same energy region (−13.3 to −17.8 eV) as obtained from G_0W_0@HSE06. In LDA-1/2, the occupied Ga_{3d} and N_{2s} states show the same qualitative result, but shifted to higher energies. Even the TB-mBJLDA energy bands show roughly the same band characteristics. All these calculations are affected by a hybridization of the electronic states that is even stronger than the hybridization found in the G_0W_0@HSE06 data. Generally, in all our calculations the Ga_{3d} and N_{2s} states occupy the same energy region. Compared to the undisturbed N_{2s} band in zb-AlN, the Ga_{3d} semicore states in a certain sense *cut* the s band of N into two branches that hybridize with the d sates. Thus one band with partial N_{2s} character is found below and one above the d-like energy bands. To single out the effects from using different numerical approaches, we should predominantly compare the position of the *inert* Ga_{3d} energy bands that are not notably affected by hybridization and that show the expected low-energy dispersion of a localized d band. The XC functional effect on the N_{2s} states could be estimated from the energy states at the W point. The mod(39)HSE QP calculation places the (inert) d bands at ∼ −16.0 eV, almost 2 eV above the G_0W_0@HSE06 d bands. For the N_{2s} states at −13.3 eV, the upward shift with respect to the G_0W_0@HSE06 position is about 0.5 eV. In LDA-1/2, the Ga_{3d} semicore states are shifted by >4 eV to ∼ −13.7 eV and the anion N_{2s} states by ∼ 2 eV to −11.3 eV. The TB-mBJLDA calculation finds the N_{2s} states at the same energy as in LDA-1/2. The Ga_{3d} states experience an additional shift of ∼1 eV to ∼−12.6 eV.

Summarizing, our band structure calculations clearly demonstrate that calculations based on the TB-mBJLDA potential with a properly adjusted c parameter as well as the self-energy corrected LDA-1/2 approach allow the approximate description of QP band gap energies. The overall band topologies are in reasonable qualitative agreement close to the band edges. However, the relative differences in the transition energies at high-symmetry points might be critical for the description of the direct-indirect band gap crossover. Furthermore, important band-structure characteristics as the effective masses might deviate significantly from the QP result, as reported by other authors.[73] The position of the strongly localized low lying energy states are severely affected by an artificial hybridization in all applied approaches that is not seen in the experiment. Even the G_0W_0@HSE06 QP bands are still hybridized around the Γ point. HSE-type calculations reproduce the entire G_0W_0@HSE06 QP band structure over a wide-energy range with high accuracy. Table IV summarizes the lowest band-to-band transition energies of zb-AlN and zb-GaN at the Γ, X, and L points that are relevant for the interpretation of experimental data in the following section.

IV. BAND GAPS, TRANSITION ENERGIES, AND DIRECT-INDIRECT CROSSOVER

In order to discuss the band gaps of zb-$Al_xGa_{1-x}N$ we have to be able to identify and label the electronic states of the alloy consistently, which is not per se a trivial task. To begin

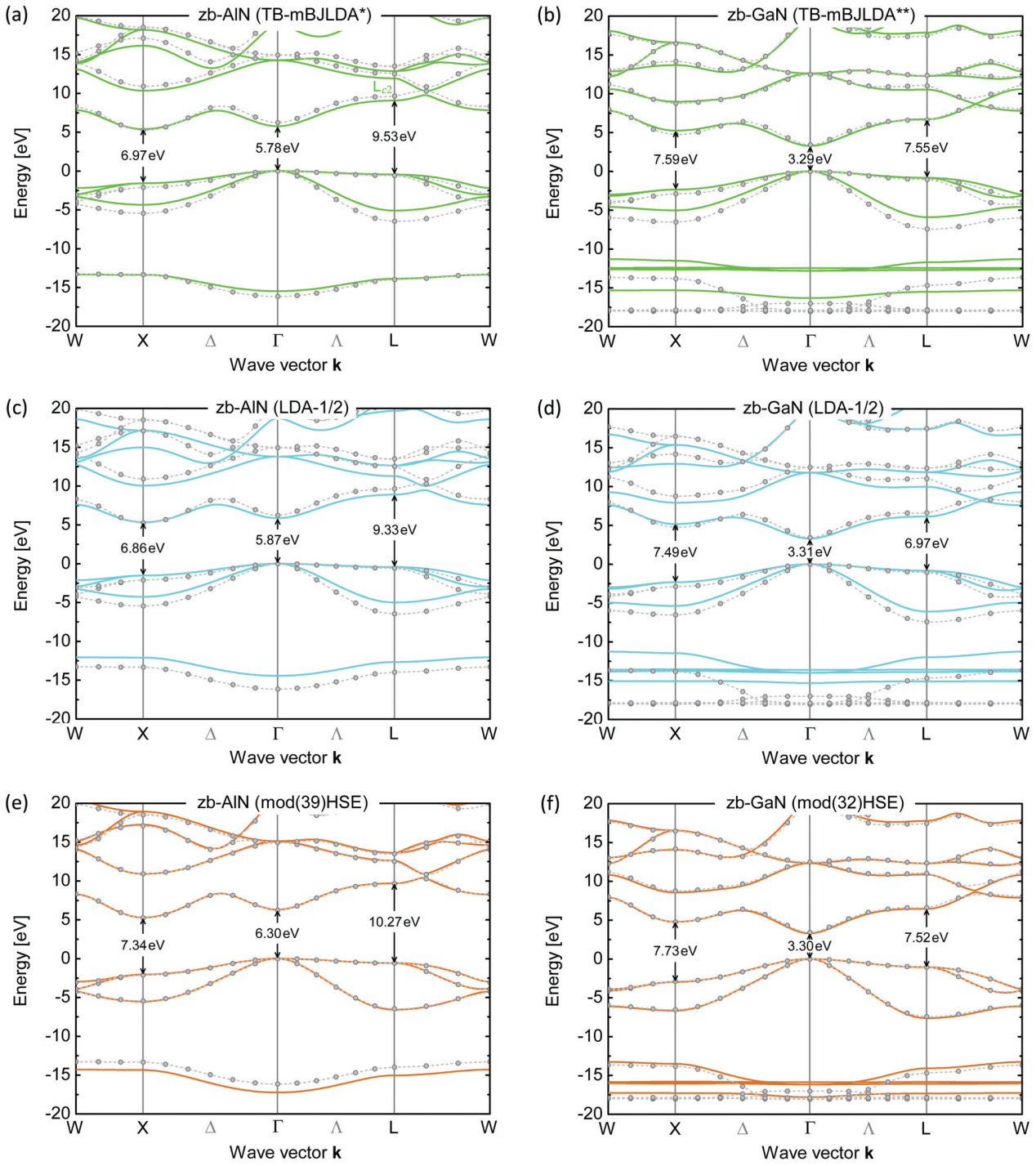

FIG. 6. (Color online) Band structure of zb-AlN and zb-GaN calculated by the TB-MBJLDA meta-GGA potential, the LDA-1/2 technique, and HSE-type hybrid functionals. TB-mBJLDA* and TB-mBJLDA** refer to optimized c parameters of $c = 1.45$ and 1.55. For HSE-type calculations, the used fraction of exact exchange is indicated in brackets. The direct band gaps at the Γ, L, and X points are indicated. The gray dots represent G_0W_0@HSE06 QP energies. The gray dashed lines are guidelines to the eyes.

with, the electronic states of the bulk materials are completely characterized by a band index, labeling the corresponding valence as well as conduction band, and a k-point index, labeling the position of the electronic state in the irreducible part of the Brillouin zone. Additionally, we have information about the symmetry of the corresponding one-electron orbitals and thus the degeneracy of the corresponding eigenvalues. Type (direct/indirect) and size of the fundamental band gap are commonly determined by band structure calculations on a primitive unit cell of the periodic crystal lattice. Generally, the use of nonprimitive unit cells in the numerical description of the binary bulk materials gives rise to zone folding effects

TABLE IV. Summary of the two lowest valence-to-conduction band transitions at the Γ, X, and L high-symmetry points corresponding to the band gap data visualized in Fig. 6. Also the indirect $\Gamma_v \rightarrow X_c$ and $\Gamma_v \rightarrow L_c$ band gaps are included. TB-mBJLDA* and TB-mBJLDA** refer to optimized c parameters of $c = 1.45$ and 1.55. For HSE-type calculations the fraction of exact exchange is indicated in brackets. All transition energies are given in eV.

	TB-mBJLDA*	TB-mBJLDA**	LDA-1/2		mod(39)HSE	mod(32)HSE	G_0W_0@HSE06	
Band transition	zb-AlN	zb-GaN	zb-AlN	zb-GaN	zb-AlN	zb-GaN	zb-AlN	zb-GaN
$\Gamma_v \rightarrow \Gamma_c$	5.78	3.29	5.87	3.31	6.30	3.30	6.25	3.47
$\Gamma_v \rightarrow \Gamma_{c2}$	14.27	12.62	13.80	11.78	15.12	12.34	14.95	12.49
$X_v \rightarrow X_c$	6.97	7.59	6.86	7.49	7.34	7.73	7.36	7.65
$X_v \rightarrow X_{c2}$	11.92	11.31	11.58	10.24	12.97	11.52	13.04	11.65
$L_v \rightarrow L_c$	9.53	7.55	9.33	6.97	10.27	7.52	10.21	7.65
$L_v \rightarrow L_{c2}$	12.36	11.36	11.72	10.81	13.19	11.94	13.08	12.05
$\Gamma_v \rightarrow X_c$	5.40	5.25	5.34	5.17	5.29	4.78	5.16	4.77
$\Gamma_v \rightarrow L_c$	9.08	6.72	8.90	6.13	9.70	6.47	9.64	6.61

that map one or more irreducible k points onto k points in the new Brillouin zone. For instance, the threefold degenerate X_c states of zb-AlN in the primitive zinc-blende Brillouin zone are mapped onto the Γ point in a cubic unit-cell representation, but this is a pure zone-folding effect, the optical dipole-matrix elements remain unchanged and there is no influence on the fundamental direct/indirect nature of the electronic band gap. In contrast, the substitutional disorder, and to a very small extend the topological disorder due to local atomic relaxations, in a multicomponent semiconductor alloy lift the strict long-range order of the bulk material. Thus the Bloch theorem is not strictly valid, k is *not* a *good* quantum number anymore and the band gaps of the semiconductor alloy will, strictly speaking, become always direct. However, in contrast to a truly amorphous material, the one-electron orbitals in the substitutionally disordered crystal will remain similar to the states in the bulk material even close to the band edges. Therefore the nature of the alloy band gap will be different if the electronic states at the band edges are similar to electronic states forming a direct or an indirect bulk band gap. For zb-$Al_xGa_{1-x}N$ alloys in the Al-rich concentration range, the conduction band edge (at the Γ point) is formed by electronic states similar to the X_c states of zb-AlN. This band gap is only *pseudodirect*, since the dipole-matrix elements of such a band gap will always be similar to the indirect bulk transitions and thus smaller than those of a truly direct transition. It is common to reduce the terminology to describe the alloy completely to that of the bulk semiconductors, as already done in the introductory section. In the ternary zb-$Al_xGa_{1-x}N$ alloys, the electronic states, responsible for the band gaps in the pure bulk phases, intermix with respect to the relative Ga : Al concentration. It is possible to trace the bulklike electronic states throughout the whole composition range of the ternary alloy. In general, the critical point of the cation concentration that marks the transition of the fundamental alloy band gap from involving either the bulklike Γ_c conduction band states originating from zb-GaN or the bulklike X_c conduction band states of zb-AlN is called a direct-indirect band gap crossing/crossover instead of the more precise term *direct-to-pseudodirect* transition. The influence of alloy disorder is ultimately reflected in a lifted degeneracy of electronic states that are degenerate in zb-AlN and zb-GaN. In a unit-cell approach, the degree of disorder and thus the degeneracy of the electronic states is directly related to a particular lattice configuration (i.e., local atomic structure) in a specific unit cell. To minimize the artificial *periodicity errors*, we take the average of the originally degenerate bulk-energy levels to extract the alloy band gaps.

In Fig. 7, the calculated zb-$Al_xGa_{1-x}N$ band gaps for eight atom unit cells (i.e., RAND 8) are plotted for various numerical approaches. The visualized band gap data especially confirm the relative close agreement between band gaps from non-self-consistent GW and HSE-type hybrid-functional DFT calculations over the entire composition range of zb-$Al_xGa_{1-x}N$. In detail, the band gaps obtained from the unmodified HSE06 hybrid functional agree very well with G_0W_0@PBE QP band gaps. G_0W_0@HSE06 QP gaps are found to be in excellent agreement with the band gaps obtained from our modified HSE-type calculations. In the modHSE approach, the exact-exchange fraction α in the alloy is linearly

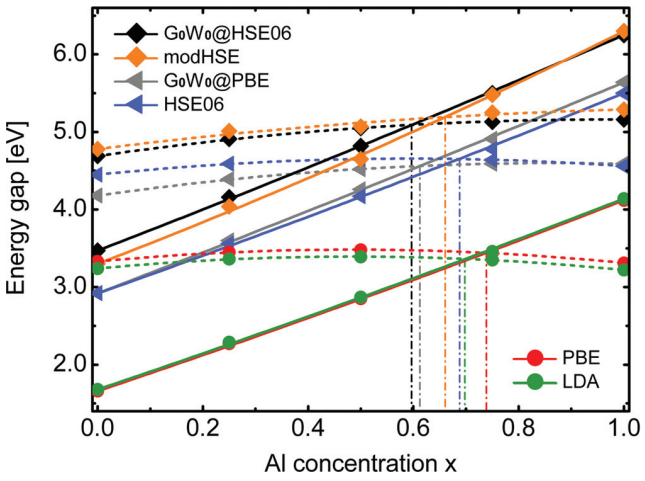

FIG. 7. (Color online) Fundamental alloy band gaps of zb-$Al_xGa_{1-x}N$ for cubic eigth atom unit cells (RAND 8). Symbols represent calculated values. Solid and dotted lines represent nonlinear fits according to Eq. (1) for the direct $\Gamma_v \rightarrow \Gamma_c$ type and indirect $\Gamma_v \rightarrow X_c$ type alloy band gaps. In modHSE calculations, the exact exchange fraction was linearly interpolated between $\alpha_{AlN} = 0.39$ and $\alpha_{GaN} = 0.32$.

TABLE V. Bowing parameters (in eV) of the direct $\Gamma_v \rightarrow \Gamma_c$ type and indirect $\Gamma_v \rightarrow X_c$ type zb-$Al_xGa_{1-x}N$ alloy band gaps [calculated via Eq. (1)] as well as critical Al concentration at the direct-indirect band gap crossover point.

Simulation method		Bowing parameter (eV)		Crossing
Method	Unit cell	b_Γ	b_X	x
PBE	RAND 8	0.17	−0.65	0.74
	RAND 64	0.50	−0.06	0.72
	RAND 216	0.56	−0.02	0.72
	SQS 8	0.15	−0.65	0.74
	SQS 16	0.50	−0.06	0.72
	SQS 32	0.55	−0.03	0.72
TB-mBJLDA	RAND 8	0.69	−0.21	0.88
	RAND 64	1.12	0.29	0.87
	RAND 216	1.17	0.30	0.88
LDA-1/2	RAND 8	0.60	−0.30	0.83
	RAND 64	0.86	0.08	0.82
	RAND 216	0.93	0.07	0.83
HSE06	RAND 8	0.22	−0.58	0.69
	RAND 64	0.53	−0.01	0.67
	RAND 216	0.59	0.01	0.69
	SQS 8	0.30	−0.35	0.68
	SQS 16	0.47	−0.08	0.67
	SQS 32	0.59	0.02	0.69
mod(32)HSE	RAND 8	0.21	−0.55	0.67
	RAND 64	0.54	0.00	0.65
	RAND 216	0.60	0.04	0.65
modHSE	RAND 8	0.40	−0.33	0.66
	RAND 64	0.53	0.05	0.64
	RAND 216	0.59	0.09	0.64
G_0W_0@PBE	RAND 8	0.11	−0.55	0.61
G_0W_0@HSE06	RAND 8	0.16	−0.50	0.60
G_0W_0@HSE06	SQS 8	0.11	−0.64	0.61
exp		0.85	0.01	0.71

interpolated between the optimized values of $\alpha_{\mathrm{AlN}} = 0.39$ for zb-AlN and $\alpha_{\mathrm{GaN}} = 0.32$ for zb-GaN. Thus a properly adjusted HSE-type functional allows us to calculate accurate QP band gaps even for the large unit-cell alloys that are computationally beyond the scope of even non-self-consistent GW calculations.

Subsequently, we discuss the Al-dependent bowing characteristics of the energy transitions in zb-$Al_xGa_{1-x}N$ alloys according to Eq. (1). All calculated bowing parameters, as well as the direct-indirect transition points are summarized in Table V. From the experimental transition energies (cf. Fig. 2), a bowing parameter of $b_\Gamma = 0.85$ eV for the direct $\Gamma_v \rightarrow \Gamma_c$ type band gap is obtained. In addition, no significant bowing is indicated in the $X_v \rightarrow X_c$ transition energies. In anticipation of the alignment of the E_2 transition energies discussed below, the indirect $\Gamma_v \rightarrow X_c$ type alloy band gap will preserve this characteristic, almost linear, dependence on the alloy composition.

Independent of the numerical methodology, the alloy band gaps of all eight atom unit-cell calculations visualized in Fig. 7 share common bowing characteristics. The direct $\Gamma_v \rightarrow \Gamma_c$ type band gaps in the zb-$Al_xGa_{1-x}N$ alloys show an increase with Al content that only weakly differs from a linear dependence as indicated by bowing parameters b_Γ between 0.11 and 0.22 eV, which significantly underestimate the experimental value. Only in the modHSE calculations a notable downward bowing of 0.40 eV is indicated. The indirect $\Gamma_v \rightarrow X_c$ type band gap is characterized by a notable upward bowing with a b_X parameter between −0.50 and −0.65 eV, which is in disagreement with the linear dependence observed in the experimental data. Again a slightly improved value of $b_X = -0.33$ eV is obtained by modHSE calculations. As we will see in a moment, these bowing parameters are affected by the poor alloy description through cubic eight atom unit cells that are affected by spurious symmetry. The nonlinear curve fits in Fig. 7 further illustrate that an increased exact exchange fraction, changes the distinct downward bending at higher Al content in LDA/GGA DFT to a more constant progression in hybrid-functional DFT and G_0W_0 calculations. This directly influences the direct-indirect band gap transition that occurs in the high Al concentration range. In LDA and PBE DFT the transition concentration is $x = 0.70$ and 0.74, respectively. In HSE hybrid-functional DFT the critical Al content is found to decrease for a higher exact exchange fraction from $x = 0.69$ in conventional HSE06 to $x = 0.66$ in modHSE. The G_0W_0 QP results provide an even lower transition concentration of ∼0.6. From the bowing parameters listed in Table V it is further obvious that both the TB-mBJLDA functional and the LDA-1/2 technique lead to significantly larger (more positive, less negative) bowing parameters that are closer to the experimental observations. Aside from the

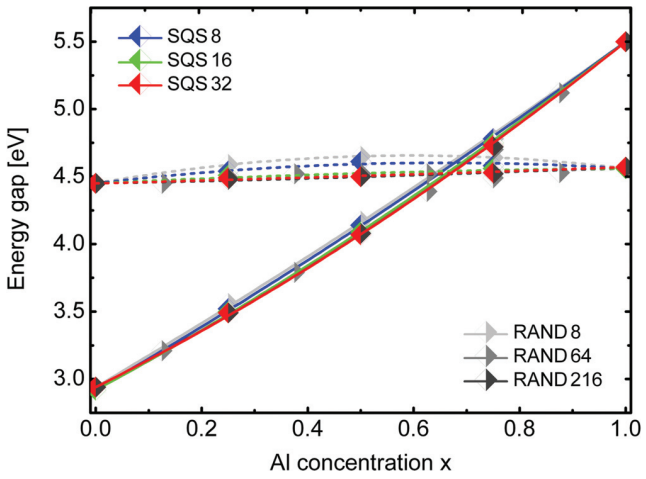

FIG. 8. (Color online) Calculated DFT-HSE06 alloy band gaps of zb-$Al_xGa_{1-x}N$ for various SQS and randomly occupied cubic unit-cell structure models (RAND). The symbols represent calculated values. Solid and dotted lines represent trend lines of the direct $\Gamma_v \rightarrow \Gamma_c$ type and indirect $\Gamma_v \rightarrow X_c$ type band gaps.

modHSE results, the bowing parameters increase by roughly 0.4 eV in TB-mBJLDA as well as LDA-1/2. As argued below, this assumed improvement rather represents a fortuitous than a systematic improvement by partially canceling the small unit-cell-induced periodicity errors with an overestimation of the bowing parameters.

In order to identify the artificial periodicity errors introduced by the small unit-cell representation of the zb-$Al_xGa_{1-x}N$ alloys, the HSE06 band gaps for all different structure models are displayed in Fig. 8. It is obvious that the Al-content dependent bowing characteristics of the alloy band gaps are significantly influenced by the unit-cell representation. Especially the indirect alloy band gap, obtained from the X_c-type energy states, is affected by such unit-cell periodicity errors. At $x = 0.5$, the difference between eight atom unit-cell calculations and calculations on the RAND 216 and SQS 32 alloy unit cells is largest ($\sim$0.15 eV). This behavior directly reflects the artificial alloy symmetry, which is necessarily largest for a 50:50 cation ratio due to the formation of a superlattice-type zb-AlN/GaN alloy. The periodicity error is slightly reduced by the SQS 8 structure that can be characterized as a staggered superlattice-type alloy [see Fig. 4(b)]. The SQS 16 alloy band gaps show just marginal deviations from the RAND 216 and SQS 32 alloy unit-cell results. The RAND 216, and SQS 32 unit-cell representations of the zb-$Al_xGa_{1-x}N$ alloy basically show identical band gap energies and fitting-curve characteristics. For both structure models, a notable bowing of the direct $\Gamma_v \rightarrow \Gamma_c$ type alloy band gap of $b_\Gamma = 0.59$ eV is obtained. The direct $\Gamma_v \rightarrow X_c$ type band gap shows a nearly linear increase over the complete composition range. This linear dependence nicely matches the linear dependence indicated in the experimental data. For both alloy representations (RAND and SQS), the direct-indirect band gap crossover is found at $x = 0.69$. The RAND 64 unit-cell calculations show band gap deviations $\leqslant 0.02$ eV from the RAND 216 and SQS 32 results and the nonlinear fitted band gap curves are almost identical to the results of RAND 216 and SQS 32 unit cells. Also the Al content at the direct-indirect band gap crossover of $x = 0.67$ is only marginally affected.

In summary, the unit-cell representation of the randomly occupied zb-$Al_xGa_{1-x}N$ alloy suffers from notable periodicity errors for very small (eight atom) unit cells. This observation affects both unit-cell modeling approaches, even if the SQS 8 representation slightly reduces the periodicity errors. Compared to the largest 216 atom unit cells, the 32 atom SQS unit cells allow band gap calculations with a significantly reduced number of atoms without any notable loss of accuracy. The modeling of the zb-$Al_xGa_{1-x}N$ alloy seems to benefit significantly from the similar lattice characteristics of zb-AlN and zb-GaN. The direct-indirect band gap crossover concentration seems to be quite insensitive to the specific unit-cell representation, since both the direct-type and the indirect-type alloy band gap are equally affected by the artificially introduced lattice periodicity. In fact, the differences in the direct-indirect band gap crossing point between eight atom unit cells and the 32 atom SQSs as well as the RAND 216 unit cells never exceeds 0.02 (cf. Table V) for the various numerical approaches. Thus even the critical Al concentrations for the direct-indirect crossing from eight atom unit cells are very reasonable.

While the direct-indirect band gap crossing is weakly affected by the unit-cell representation, the bowing parameters show a significant dependence on the alloy modeling. The unit-cell representation related trends in the bowing parameters, discussed above for the conventional HSE06 hybrid functional, are found to be qualitatively very similar in the other numerical approaches. The more accurate (i.e., less symmetric and *more random*) alloy representation always increases the downward bowing b_Γ of the direct $\Gamma_v \rightarrow \Gamma_c$ type alloy band gap. The smallest increase (0.19 eV) is found in the modHSE approach. However, modHSE already predicted a notable bowing for eight atom unit cells. For the other XC functionals b_Γ increases between 0.29 eV (HSE06, SQS unit cells) and 0.48 eV (TB-mBJLDA, RAND unit cells). For LDA-1/2 and TB-mBJLDA, the increase of the bowing parameter even results in an overestimation of the experimental bowing parameter of $b_\Gamma = 0.85$ eV by 0.08 eV in LDA-1/2 and 0.32 eV in TB-mBJLDA. Alongside the observed increase of the $\Gamma_v \rightarrow \Gamma_c$ type gap for all XC functionals, the indirect $\Gamma_v \rightarrow X_c$ type alloy band gap shows an even stronger increase (between 0.37 eV in HSE06 and 0.63 eV in PBE) of the bowing parameter b_X. While the results of eight atom unit-cell calculations indicate a notable upward bowing by negative values of b_X for all numerical approaches, the larger alloy unit cells reproduce the expected linear dependence on x very well. With exception of $b_X = 0.30$ eV in TB-mBJLDA, all numerical approaches yield bowing parameters b_X between -0.03 eV (PBE, RAND unit cells) and 0.09 eV (modHSE, RAND unit cells).

Surprisingly, the comparison of bowing parameters and direct-indirect crossing points shows that, despite the severe band gap underestimation, the results of calculations using the conventional semilocal PBE functional are very close to the HSE-type hybrid functional data. This indicates that the fundamental direct and indirect zb-$Al_xGa_{1-x}N$ alloy band gaps are rigidly narrowed in the DFT-PBE approach over the entire composition range. In contrast, the LDA-1/2 and

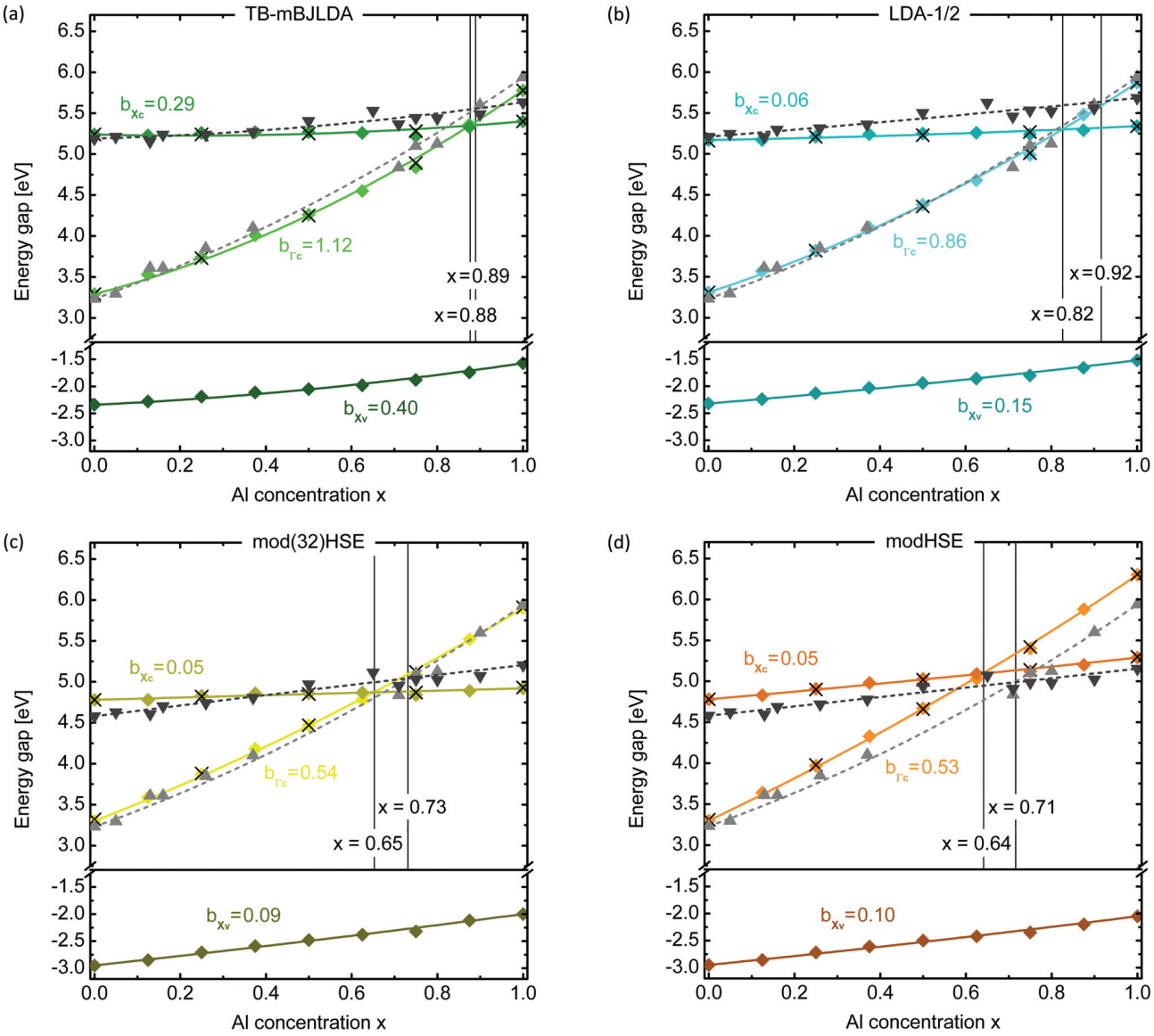

FIG. 9. (Color online) Fundamental alloy band gaps (upper panels) and position of the highest X point valence state (lower panel) of zb-$Al_xGa_{1-x}N$ calculated using (a) the TB-mBJLDA (c parameter linear interpolated between $c_{AlN} = 1.45$ and $c_{GaN} = 1.55$), (b) LDA-1/2 (self-energy corrections to N_{2p} and Ga_{3d} states), (c) mod(32)HSE (exact exchange fraction of $\alpha = 0.32$ for all Al concentrations), and (d) modHSE (exact exchange fraction linear interpolated between $\alpha_{AlN} = 0.39$ and $\alpha_{GaN} = 0.32$) approaches. Diamonds represent the calculated band gaps for randomly occupied 64 atom unit cells. Crosses indicate the corresponding band gaps from 216 atom unit cells. Solid and dotted lines represent nonlinear band gap fits according to Eq. (1). b_{Γ_c} and b_{X_c} are the bowing parameters of the direct $\Gamma_v \rightarrow \Gamma_c$ type and indirect $\Gamma_v \rightarrow X_c$ type alloy band gaps. b_{X_v} is the bowing parameter of the highest valence state at the X point. The position of the direct-indirect band gap crossover is indicated. Also included (light and dark gray symbols and lines) are the experimental transition energies (aligned according to the position of the X point valence states visualized in the lower panel) and nonlinear band gap fits.

TB-mBJLDA bowing parameters and the particular direct-indirect band gap crossing points show significantly larger deviations from the hybrid functional DFT results than the DFT-PBE results. Both LDA-1/2 and TB-mBJLDA predict very high Al concentrations ($x = 0.83$ in LDA-1/2 and $x = 0.88$ in TB-mBJLDA) at the direct-indirect band gap crossing. While LDA-1/2 calculations result in a slight overestimation of bowing parameters, TB-mBJLDA severely overestimates the bowing.

In Fig. 9, the $\Gamma_v \rightarrow \Gamma_c$ and $\Gamma_v \rightarrow X_c$ type alloy band gaps of zb-$Al_xGa_{1-x}N$ are plotted for the TB-mBJLDA and LDA-1/2 methods as well as for two HSE-type hybrid functional approaches. Besides the modHSE approach, a HSE-type hybrid functional with an exact-exchange fraction of 32% [mod(32)HSE] was used over the entire alloy composition range. The mod(32)HSE approach allows the simultaneous exact reproduction of the direct experimental $\Gamma_v \rightarrow \Gamma_c$ band gaps of zb-AlN and zb-GaN (cf. Table III). The modHSE approach accurately reproduces the experimental values of the direct $\Gamma_v \rightarrow \Gamma_c$ band gap of zb-GaN and the indirect $\Gamma_v \rightarrow X_c$ band gap of zb-AlN. The TB-mBJLDA and LDA-1/2 techniques have already proven to allow the

approximate calculation of bulk-QP band gaps with high accuracy.

Figure 9 also contains the position and the corresponding bowing parameter b_{X_v} of the highest valence state at the X point (lower panels) over the entire composition range. For each numerical approach considered in Fig. 9, the X point valence states have been used to align the measured direct $X_v \rightarrow X_c$ type transition energies (cf. E_2 transition energies in Fig. 2) in order to extract the position of the *experimental* direct-indirect band gap crossing point.

(1) TB-mBJLDA: The direct-type zb-$Al_xGa_{1-x}N$ alloy band gaps from TB-mBJLDA calculations agree reasonably with the experiment, even if the calculated bowing parameter $b_\Gamma = 1.12$ eV significantly exceeds the experimental bowing of $b_\Gamma = 0.85$ eV. The indirect-type alloy band gap is characterized by a downward bowing of $b_X = 0.29$ eV. Compared to the other simulation approaches, the distinct bowing characteristics seem to be related to the TB-mBJLDA valence band structure. Also, the highest X point valence state of zb-$Al_xGa_{1-x}N$ shows a notable bowing of 0.4 eV throughout the alloy [cf. Fig. 9(a)] that is not reproduced in any other approach. Already in the TB-mBJLDA band structure calculations for the binary zinc-blende semiconductors [cf. Figs. 6(a) and 6(b)] a strong upward shift of the highest valence band around the X point with respect to the G_0W_0@HSE06 QP band structure was indicated. Hence the position of the indirect type alloy band gap seems to be overestimated over the entire composition range and the direct-indirect crossover point ($x = 0.89$) is shifted to far into the Al rich regime. The TB-mBJLDA alignment of the experimental transition energies leads to a very similar crossover point of $x = 0.88$. Although, the calculated TB-mBJLDA transition energies are fortuitously close to the experimental ones, the alignment by TB-mBJLDA valence states seems to be an improper choice for obtaining the accurate position of the direct-indirect band gap grossing point.

(2) LDA-1/2: LDA-1/2 reproduces the experimentally observed $\Gamma_v \rightarrow \Gamma_c$ type alloy band gaps very well. The calculated bowing of $b_\Gamma = 0.86$ eV almost perfectly reproduces the experimental bowing. The bowing parameter $b_X = 0.06$ eV indicates an almost linear dependence of the indirect $\Gamma_v \rightarrow X_c$ type alloy band gap on the Al content in LDA-1/2 calculations. Similar to TB-mBJLDA, the direct-indirect band gap crossover Al concentration is found at $x = 0.82$ well in the Al rich regime. The LDA-1/2 alignment of the experimental transition energies shifts the crossover point to an even higher Al concentration of $x = 0.92$. Analog to TB-mBJLDA the high Al crossover concentration seems to be the consequence of artificially high lying X point type valence states, that is as well indicated in the LDA-1/2 band structure of the binary semiconductors [cf. Figs. 6(c) and 6(d)]. In fact, the energy differences between the highest X point type valence band states are $\leqslant$0.15 eV between TB-mBJLDA and LDA-1/2 calculations. Obviously, the inaccurate reproduction of QP valence band features in TB-mBJLDA as well as LDA-1/2, especially the relative energy difference between the highest Γ and X point type valence states, seems to fudge the direct-indirect band gap crossing point. The limitations of TB-mBJLDA and LDA-1/2 are best illustrated by comparison to the HSE-type hybrid functional data.

(3) mod(32)HSE: The mod(32)HSE alloy band gaps are found to be a good approximation of the measured $\Gamma_v \rightarrow \Gamma_c$ type direct alloy band gaps. However, the calculated bowing parameter of $b_\Gamma = 0.54$ eV underestimates the experimental bowing parameter notably. The indirect $\Gamma_v \rightarrow X_c$ type band gaps of zb-$Al_xGa_{1-x}N$ show a close to linear dependence ($b_X = 0.05$ eV) on the Al concentration and the direct-indirect band gap crossing is found at an Al:Ga ratio of 1.54 ($x = 0.65$). This value is significantly smaller than the crossover concentrations in TB-mBJLDA and LDA-1/2. Compared to TB-mBJLDA and LDA-1/2 the X point energies, necessary for the transition energy alignment, are reduced by roughly 0.5 eV and the bowing of 0.09 eV indicates an almost linear dependence of the valence states on the alloy composition. Consequently, the mod(32)HSE alignment of the experimental transition energies predicts a lower direct-indirect band gap crossing point of $x = 0.73$ than obtained for the TB-mBJLDA and LDA-1/2 alignments. In addition, an almost linear trend in the indirect $\Gamma_v \rightarrow X_c$ type alloy band gap is indicated after the alignment. In the middle of the composition range, the indirect $\Gamma_v \rightarrow X_c$ band gaps from the mod(32)HSE approach and the aligned experimental transition energies agree very well. However, through a slight mod(32)HSE overestimation of the indirect type gap, in the Ga-rich composition range and an underestimation at Al-rich conditions, the slope of the indirect $\Gamma_v \rightarrow X_c$ type alloy band gap with Al content x differs. mod(32)HSE predicts a much weaker slope than the one actually found for the aligned experimental transition energies.

(4) modHSE: In modHSE the overall agreement between the pure theoretical description and the modHSE aligned experimental data is very reasonable with respect to the qualitative features, while an overall overestimation of the experimental data is obvious. Compared to mod(32)HSE, the indirect $\Gamma_v \rightarrow X_c$ type alloy band gap increases almost linear as well, as indicated by an identical bowing parameter of $b_X = 0.05$ eV. However, the slope in modHSE is much closer to the aligned experimental data. Similar to mod(32)HSE, the direct-indirect band gap crossing is found at $x = 0.64$ in the modHSE calculations and at $x = 0.71$ from the aligned experimental transition energies. The common features between both hybrid functional approaches are also related to the quite similar description of the valence band structure. The position of the highest X point valence states is almost identical in the mod(32)HSE and the mod HSE approaches. The largest differences occur at Al-rich conditions and shift the X point valence states in modHSE by $\leqslant -0.05$ eV with respect to the mod(32)HSE energies. Even if there is a systematic overestimation of all experimentally determined energy gaps, we expect the modHSE results to be a very accurate and the most reasonable approximation to the true QP band structure of zb-$Al_xGa_{1-x}N$ alloys. This statement is based on two observation. On the one hand, we know that the modHSE calculations reproduce all G0W0@HSE06 QP alloy gaps within deviations $\leqslant$0.2 eV [cf. Fig. 7 for the alloys and Figs. 6(e) and 6(f) for the binary semiconductors]. On the other hand, the modHSE approach reproduces all experimentally observed features of the alloy band gap dependence on the Al concentration with an nearly constant offset $<$200 meV. This offset is explainable by the difference between calculated QP

band gaps and experimental band gaps obtained by optical measurements (→ optical gaps) at room temperature. As already discussed in the experimental section, temperature effects, mediated by the electron-phonon coupling, seem to be responsible for an downward shift of the absorption edge in zb-$Al_xGa_{1-x}N$ alloys of approximately 100 meV as indicated in Fig. 3 for zb-AlN. To a small extend, also, the neglected spin-orbit interaction might be responsible for the observed difference between the experimental and theoretical data. Finally, the general influence of excitonic contributions through electron-hole interaction has already been discussed above in Sec. II.

In summary, TB-mBJLDA and LDA-1/2 allow a rough estimation of bowing parameters and the band gap crossover point. Considering the electronic structure characteristics, both approaches certainly fall into the same accuracy class. In consideration of the very moderate computational cost, our results support the use of both approaches to approximate the QP band structure for large unit cells of alloys, surfaces, and other nanostructured systems. Choosing between the two approaches, LDA-1/2 seems to be a slightly more reliable choice for approximate QP calculations. However, apart from the compensation of the band gap underestimation, even conventional semilocal DFT approaches (here, the PBE XC functional) might outperform the TB-mBJLDA and LDA-1/2 approaches in predicting electronic structure parameters as the band gap crossover points in semiconductor alloys. If reliable QP properties are desired, hybrid-functional approaches seem to be the best choice to obtain QP band gaps, band structures, and further characteristics of the electronic structure, at least if an accurate treatment of self-energy corrections within MBPT is computationally off-limits. Using an Al-concentration dependent exact-exchange parameter in HSE hybrid-functional calculations, the direct $\Gamma_v \rightarrow \Gamma_c$ type and indirect $\Gamma_v \rightarrow X_c$ type zb-$Al_xGa_{1-x}N$ alloy band gaps are given by $E_{\mathrm{gap},\Gamma}^{\text{zb-}Al_xGa_{1-x}N}(x) = 6.30x + 3.30(1-x) - 0.53x(1-x)$ eV and $E_{\mathrm{gap},X}^{\text{zb-}Al_xGa_{1-x}N}(x) = 5.29x + 4.78(1-x) - 0.05x(1-x)$ eV, respectively.

In Fig. 10, the measured energy transitions of Fig. 2 are aligned according to the energy positions of the highest L_v and X_v valence states (relative to the Γ point valence band maximum) taken from modHSE calculations on 64 atom unit cells. As stated above, also the high-energy optical transitions show a nonlinear dependence on the Al concentration. The E_1 transition energies, originating from fundamental $L_v \rightarrow L_c$ transitions, are in good agreement with the modHSE data. However, the corresponding bowing parameters are inconsistent. The experimental data indicate an pronounced upward bowing of $b_L = -0.59$ eV while the hybrid-functional data show a strong downward bowing characterized by a bowing parameter of $b_L = 1.05$ eV. Also, for E_0' transitions from the Γ_v valence band edge to the second conduction band Γ_{c2}, a reasonable agreement of theoretical and experimental transition energies is found while the bowing parameters differ. Bowing parameters of $b_{E_0'} = 0.42$ eV and $b_{E_0'} = -0.10$ eV are obtained from analyzing the experimental and modHSE data, respectively. For the E_1' and E_2' transition energies, it is not possible to prove the assumed correspondence to the high-energy $L_v \rightarrow L_{c2}$ and $X_v \rightarrow X_{c2}$ type energy transitions

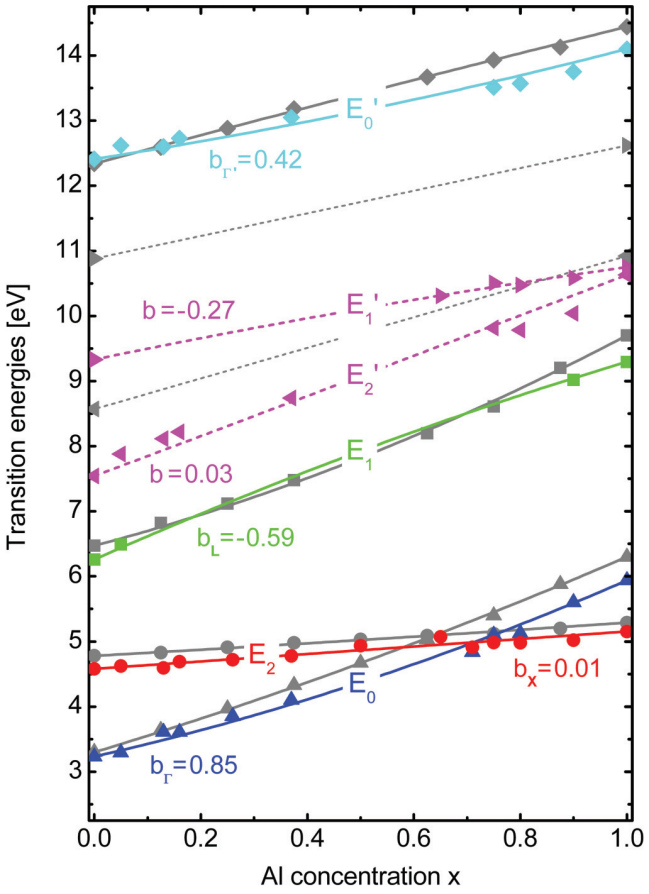

FIG. 10. (Color online) Analysis of Γ, L, and X point type fundamental (E_0, E_1, E_2) and high energy transitions (E_0', E_1', E_2') in zb-$Al_xGa_{1-x}N$ as a function of the Al content. Symbols indicate measured transition energies (cf. Fig. 2) aligned according to the energy positions of the highest L_v and X_v valence states (relative to the Γ point valence band maximum) taken from modHSE calculations on 64 atom unit cells. Lines represent nonlinear fits according to Eq. (1). Also included (gray symbols and lines) are the corresponding modHSE band gap energies and nonlinear curve fits.

(plotted in Fig. 10 as dotted gray lines form modHSE bulk data). This indicates that these optical transitions do not directly originate from transitions between high-symmetry point type electronic states.

We conclude our study by a comparison of our current experimental data to experimental data on zb-$Al_xGa_{1-x}N$ alloys reported in literature so far. While deviations of earlier cathodoluminescence measurements to the present data[24] are obvious from Fig. 11, the reflectivity measurement band gap data of Guerrero *et al.*[23] agree rather well with our measured alloy band gaps. However, a nonlinear band gap fit of the Guerrero *et al.* data gives a notable downward bowing of $b_\Gamma = 1.18$ eV larger than the bowing parameter of $b_\Gamma = 0.85$ eV from the present ellipsometry data. In consideration of the photoluminescence data of Nakadaira and Tanaka[26] that show a linear increase of the fundamental alloy band gaps in the Ga-rich composition region, we have additionally calculated separate nonlinear modHSE band gap fits for the direct alloy band gap below and above the direct-indirect band gap crossover. The band gap up to the band gap crossover

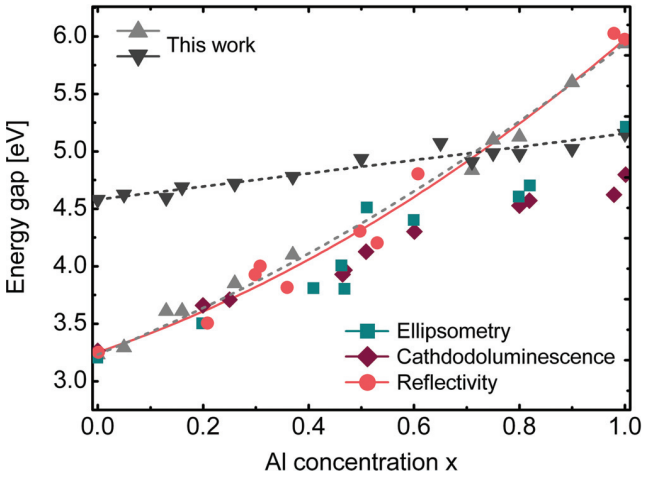

FIG. 11. (Color online) Experimental alloy band gaps of zb-$Al_xGa_{1-x}N$. Black and gray triangles represent alloy band gaps determined from the ellipsometry data of this study. Solid and dotted lines represent nonlinear fits according to Eq. (1) for the direct $\Gamma_v \rightarrow \Gamma_c$ type and indirect $\Gamma_v \rightarrow X_c$ type band gaps. Reflectivity data (dots) are reproduced from Ref. 23 and cathodoluminescence (diamonds) and ellipsometry (squares) data from Ref. 24.

point is approximately linear, as indicated by a bowing of $b_\Gamma^{\text{Ga-rich}} = 0.06$ eV. In the Al-rich composition range above the direct-indirect crossover point, the separately calculated bowing parameter of $b_\Gamma^{\text{Al-rich}} = 0.11$ eV also indicates a weak downward bowing. Obviously, the nature of the direct zb-$Al_xGa_{1-x}N$ alloy bowing parameter appears significantly different, if only the Ga-rich or Al-rich regimes are considered.

V. SUMMARY

In this study, we have investigated the nature of the fundamental zb-$Al_xGa_{1-x}N$ alloy band gap. The existence and value of the critical direct-indirect band gap crossover as well as band gap bowing parameters have been determined by a series of calculations of various levels of sophistication and from the interpretation of critical points in the dielectric functions obtained from ellipsometry measurements. Our results show the interpretation of the measured data depends critically on the quality of the underlying electronic structure calculation.

The ellipsometry data indicate an downward bowing of the direct $\Gamma_v \rightarrow \Gamma_c$ type alloy band gap of $b_\Gamma = 0.85$ eV. The indirect $\Gamma_v \rightarrow X_c$ type band gap shows a linear dependence on the Al concentration ($b_X = 0.01$ eV). The direct-indirect band gap crossover in zb-$Al_xGa_{1-x}N$ is found at $x = 0.71$ after aligning the experimentally obtained E_2 transition energies according to the highest X point valence-state energies in hybrid-functional DFT.

We have extensively tested the adaptability of the TB-mBJLDA and LDA-1/2 approaches to calculate approximate QP energies. Considering the computational cost which is comparable to (semi)local DFT calculations, both approaches allow an efficient description of QP band-structure characteristics. Both approaches give highly accurate bulk-band gaps for zb-AlN and zb-GaN. Nevertheless, they cannot compete with the HSE-type hybrid-functional description of the electronic structure of the zb-$Al_xGa_{1-x}N$ alloys. This is especially reflected in overestimated bowing parameters and a too high Al concentration at the direct-indirect band gap crossover. Also, the position of valence bands, crucial to align the experimentally determined transition energies in order to determine the direct-indirect band gap crossing, is severely affected by the use of the more *approximate* QP approaches TB-mBJLDA and LDA-1/2. Basically, the observed properties of the TB-mBJLDA functional and to a lesser extend the results obtained via the LDA-1/2 technique reflect the limited adaptability of a purely local XC functional. Even the semilocal PBE functional might give better bowing characteristics and a significantly more accurate estimation of the direct-indirect band gap crossover point. Hybrid functional DFT with an optimized exact exchange fraction reproduces QP alloy band gaps from G_0W_0@HSE06 calculations within 0.2 eV over the entire alloy composition range. The calculated direct-indirect band gap crossover between $x = 0.64$ and 0.69 in hybrid functional DFT is found in good agreement with our experimental findings.

ACKNOWLEDGMENTS

The calculations were done using grants of computer time from the Regionales Rechenzentrum of the Universität zu Köln (RRZK). Part of this work was funded by the Deutsche Forschungsgemeinschaft DFG in the framework of Major Research Instrumentation Program No. INST 272/205-1 and was supported by the DFG graduate program GRK 1464 Micro- and Nanostructures in Optoelectronics and Photonics. Furthermore, we gratefully acknowledge support by the synchrotron radiation sources BESSY II of the Helmholtz-Zentrum Berlin (HZB).

*Corresponding author: landmann@mail.upb.de

[1] V. Yu. Davydov, A. A. Klochikhin, R. P. Seisyan, V. V. Emtsev, S. V. Ivanov, F. Bechstedt, J. Furthmüller, H. Harima, A. V. Mudryi, J. Aderhold, O. Semchinova, and J. Graul, Phys. Status Solidi B **229**, R1 (2002).

[2] J. Li, K. B. Nam, M. L. Nakarmi, J. Y. Lin, H. X. Jiang, P. Carrier, and S.-H. Wei, Appl. Phys. Lett. **83**, 5163 (2003).

[3] E. Silveira, J. A. Freitas, Jr., M. Kneissl, D. W. Treat, N. M. Johnson, G. A. Slack, and L. J. Schowalter, Appl. Phys. Lett. **84**, 3501 (2004).

[4] P. Schley, R. Goldhahn, C. Napierala, G. Gobsch, J. Schörmann, D. J. As, K. Lischka, M. Feneberg, and K. Thonke, Semicond. Sci. Technol. **23**, 055001 (2008).

[5] M. P. Thompson, G. W. Auner, T. S. Zheleva, K. A. Jones, S. J. Simko, and J. N. Hilfiker, J. Appl. Phys. **89**, 3331 (2001).

[6] J. S. Im, H. Kollmer, J. Off, A. Sohmer, F. Scholz, and A. Hangleiter, Phys. Rev. B **57**, R9435 (1998).

[7] S.-H. Park and S.-L. Chuang, J. Appl. Phys. **87**, 353 (2000).

[8] F. Bernardini, V. Fiorentini, and D. Vanderbilt, Phys. Rev. B **56**, R10024 (1997).

[9]P. Waltereit, O. Brandt, A. Trampert, H. T. Grahn, J. Menninger, M. Ramsteiner, M. Reiche, and K. H. Ploog, Nature **406**, 865 (2000).
[10]G. Ramìrez-Flores, H. Navarro-Contreras, A. Lastras-Martìnez, R. C. Powell, and J. E. Greene, Phys. Rev. B **50**, 8433 (1994).
[11]B. Daudin, G. Feuillet, J. Hübner, Y. Samson, F. Widmann, A. Philippe, C. Bru-Chevallier, G. Guillot, E. Bustarret, G. Bentoumi, and A. Deneuville, J. Appl. Phys. **84**, 2295 (1998).
[12]J. Schörmann, S. Potthast, D. J. As, and K. Lischka, Appl. Phys. Lett. **89**, 131910 (2006).
[13]T. Schupp, K. Lischka, and D. J. As, J. Cryst. Growth **312**, 1500 (2010).
[14]S. V. Novikov, C. T. Foxon, and A. J. Kent, Phys. Status Solidi A **207**, 1277 (2010).
[15]E. A. DeCuir, Jr., E. Fred, M. O. Manasreh, J. Schörmann, D. J. As, and K. Lischka, Appl. Phys. Lett. **91**, 041911 (2007).
[16]D. J. As, Microelectron. J. **40**, 204 (2009).
[17]H. Machhadani, P. Kandaswamy, S. Sakr, A. Vardi, A. Wirtmüller, L. Nevou, F. Guillot, G. Pozzovivo, M. Tchernycheva, A. Lupu, L. Vivien, P. Crozat, E. Warde, C. Bougerol, S. Schacham, G. Strasser, G. Bahir, E. Monroy, and F. H. Julien, New J. Phys. **11**, 125023 (2009).
[18]E. Tschumak, R. Granzner, J. K. N. Lindner, F. Schwierz, K. Lischka, H. Nagasawa, M. Abe, and D. J. As, Appl. Phys. Lett. **96**, 253501 (2010).
[19]N. Zainal, S. V. Novikov, C. J. Mellor, C. T. Foxon, and A. J. Kent, Appl. Phys. Lett. **97**, 112102 (2010).
[20]C. Mietze, M. Landmann, E. Rauls, H. Machhadani, S. Sakr, M. Tchernycheva, F. H. Julien, W. G. Schmidt, K. Lischka, and D. J. As, Phys. Rev. B **83**, 195301 (2011).
[21]W. Yi, V. Narayanamurti, H. Lu, M. A. Scarpulla, A. C. Gossard, Y. Huang, J.-H. Ryou, and Russell D. Dupuis, Appl. Phys. Lett. **95**, 112102 (2009).
[22]M. Röppischer, R. Goldhahn, G. Rossbach, P. Schley, C. Cobet, N. Esser, T. Schupp, K. Lischka, and D. J. As, J. Appl. Phys. **106**, 076104 (2009).
[23]E. Martinez-Guerrero, F. Enjalbert, J. Barjon, E. Bellet-Almaric, B. Daudin, G. Ferro, D. Jalabert, L. S. Dang, H. Mariette, Y. Monteil, and G. Mula, Phys. Status Solidi A **188**, 695 (2001).
[24]H. Okumura, T. Koizumi, Y. Ishida, H. Yaguchi, and S. Yoshida, Phys. Status Solidi B **216**, 211 (1999).
[25]M. Feneberg, M. Röppischer, C. Cobet, N. Esser, J. Schörmann, T. Schupp, D. J. As, F. Hörich, J. Bläsing, A. Krost, and R. Goldhahn, Phys. Rev. B **85**, 155207 (2012).
[26]A. Nakadaira and H. Tanaka, Appl. Phys. Lett. **70**, 2720 (1997).
[27]B. Amin, I. Ahmad, M. Maqbool, S. Goumri-Said, and R. Ahmad, J. Appl. Phys. **109**, 023109 (2011).
[28]W. J. Fan, M. F. Li, T. C. Chong, and J. B. Xia, J. Appl. Phys. **79**, 188 (1996).
[29]W. J. Fan, M. F. Li, T. C. Chong, and J. B. Xia, Solid State Commun. **97**, 381 (1996).
[30]E. A. Albanesi, W. R. L. Lambrecht, and B. Segall, Phys. Rev. B **48**, 17841 (1993).
[31]J. W. D. Connolly and A. R. Williams, Phys. Rev. B **27**, 5169 (1983).
[32]S.-H. Wei, L. G. Ferreira, and A. Zunger, Phys. Rev. B **41**, 8240 (1990).
[33]S.-H. Wei, L. G. Ferreira, J. E. Bernard, and A. Zunger, Phys. Rev. B **42**, 9622 (1990).
[34]F. Sökeland, M. Rohlfing, P. Krüger, and J. Pollmann, Phys. Rev. B **68**, 075203 (2003).
[35]M. B. Kanoun, S. Goumri-Said, A. E. Merad, and H. Mariette, J. Appl. Phys. **98**, 063710 (2005).
[36]B.-T. Liou, Appl. Phys. A **86**, 539 (2007).
[37]A. Seidl, A. Görling, P. Vogl, J. A. Majewski, and M. Levy, Phys. Rev. B **53**, 3764 (1996).
[38]F. Fuchs, J. Furthmüller, F. Bechstedt, M. Shishkin, and G. Kresse, Phys. Rev. B **76**, 115109 (2007).
[39]C. B. Geller, W. Wolf, S. Picozzi, A. Continenza, R. Asahi, W. Mannstadt, A. J. Freeman, and E. Wimmer, Appl. Phys. Lett. **79**, 368 (2001).
[40]A. Zunger, S.-H. Wei, L. G. Ferreira, and J. E. Bernard, Phys. Rev. Lett. **65**, 353 (1990).
[41]B. Lee and L.-W. Wang, Phys. Rev. B **73**, 153309 (2006).
[42]D. Mourad and G. Czycholl, Eur. Phys. J. B **85**, 153 (2012).
[43]P. Soven, Phys. Rev. **156**, 809 (1967).
[44]B. Velický, S. Kirkpatrick, and H. Ehrenreich, Phys. Rev. **175**, 747 (1968).
[45]A. V. Ruban and I. A. Abrikosov, Rep. Prog. Phys. **71**, 046501 (2008).
[46]D. J. As and K. Lischka, in *Molecular Beam Epitaxy: From Quantum Wells to Quantum Dots; From Research to Mass Production*, edited by M. Henini (Elsevier, Amsterdam, 2013), Chap. 11, p. 203.
[47]C. Cobet, R. Goldhahn, W. Richter, and N. Esser, Phys. Status Solidi B **246**, 1440 (2009).
[48]C. Buchheim, R. Goldhahn, M. Rakel, C. Cobet, N. Esser, U. Rossow, D. Fuhrmann, and A. Hangleiter, Phys. Status Solidi B **242**, 2610 (2005).
[49]A. Riefer, F. Fuchs, C. Rödl, A. Schleife, F. Bechstedt, and R. Goldhahn, Phys. Rev. B **84**, 075218 (2011).
[50]W. Kohn and L. J. Sham, Phys. Rev. **140**, A1133 (1965).
[51]P. Hohenberg and W. Kohn, Phys. Rev. **136**, B864 (1964).
[52]J. P. Perdew and M. Levy, Phys. Rev. Lett. **51**, 1884 (1983).
[53]D. M. Ceperley and B. J. Alder, Phys. Rev. Lett. **45**, 566 (1980).
[54]J. P. Perdew and A. Zunger, Phys. Rev. B **23**, 5048 (1981).
[55]J. P. Perdew and Y. Wang, Phys. Rev. B **45**, 13244 (1992).
[56]J. P. Perdew, D. C. Langreth, and V. Sahni, Phys. Rev. Lett. **38**, 1030 (1977).
[57]D. C. Langreth and J. P. Perdew, Phys. Rev. B **21**, 5469 (1980).
[58]J. P. Perdew, K. Burke, and M. Ernzerhof, Phys. Rev. Lett. **77**, 3865 (1996).
[59]J. P. Perdew, K. Burke, and Y. Wang, Phys. Rev. B **54**, 16533 (1996).
[60]J. Heyd, J. E. Peralta, G. E. Scuseria, and R. L. Martin, J. Chem. Phys. **123**, 174101 (2005).
[61]J. P. Perdew, R. G. Parr, M. Levy, and J. L. Balduz, Jr., Phys. Rev. Lett. **49**, 1691 (1982).
[62]L. J. Sham and M. Schlüter, Phys. Rev. Lett. **51**, 1888 (1983).
[63]J. P. Perdew and M. Levy, Phys. Rev. B **56**, 16021 (1997).
[64]Y. Zhang and W. Yang, J. Chem. Phys. **109**, 2604 (1998).
[65]W. Yang, A. J. Cohen, and P. Mori-Sànchez, J. Chem. Phys. **136**, 204111 (2012).
[66]L. Hedin, Phys. Rev. **139**, A796 (1965).
[67]L. Hedin and S. Lundqvist, in *Solid State Physics*, edited by F. Seitz, D. Turnbull, and H. Ehrenreich, Vol. 23 (Academic Press, New York, 1965).
[68]F. Tran and P. Blaha, Phys. Rev. Lett. **102**, 226401 (2009).

[69] A. D. Becke and E. R. Johnson, J. Chem. Phys. **124**, 221101 (2006).
[70] F. Tran, P. Blaha, and K. Schwarz, J. Phys.: Condens. Matter **19**, 196208 (2007).
[71] A. D. Becke and M. R. Roussel, Phys. Rev. A **39**, 3761 (1989).
[72] A. P. Gaiduk and V. N. Staroverov, J. Chem. Phys. **131**, 044107 (2009).
[73] Y.-S. Kim, M. Marsman, G. Kresse, F. Tran, and P. Blaha, Phys. Rev. B **82**, 205212 (2010).
[74] D. Koller, F. Tran, and P. Blaha, Phys. Rev. B **83**, 195134 (2011).
[75] G. Kresse, M. Marsman, L. E. Hintzsche, and E. Flage-Larsen, Phys. Rev. B **85**, 045205 (2012).
[76] J. C. Slater and K. H. Johnson, Phys. Rev. B **5**, 844 (1972).
[77] J. F. Janak, Phys. Rev. B **18**, 7165 (1978).
[78] S. Sanna, Th. Frauenheim, and U. Gerstmann, Phys. Rev. B **78**, 085201 (2008).
[79] L. G. Ferreira, M. Marques, and L. K. Teles, AIP Adv. **1**, 032119 (2011).
[80] L. G. Ferreira, M. Marques, and L. K. Teles, Phys. Rev. B **78**, 125116 (2008).
[81] M. Ribeiro, Jr., L. R. C. Fonseca, and L. G. Ferreira, Phys. Rev. B **79**, 241312(R) (2009).
[82] M. van Schilfgaarde, T. Kotani, and S. Faleev, Phys. Rev. Lett. **96**, 226402 (2006).
[83] M. Shishkin and G. Kresse, Phys. Rev. B **75**, 235102 (2007).
[84] M. Shishkin, M. Marsman, and G. Kresse, Phys. Rev. Lett. **99**, 246403 (2007).
[85] R. R. Pelá, C. Caetano, M. Marques, L. G. Ferreira, J. Furthmüller, and L. K. Teles, Appl. Phys. Lett. **98**, 151907 (2011).
[86] A. Belabbes, J. Furthmüller, and F. Bechstedt, Phys. Rev. B **84**, 205304 (2011).
[87] A. Belabbes, C. Panse, J. Furthmüller, and F. Bechstedt, Phys. Rev. B **86**, 075208 (2012).
[88] S. Küfner, A. Schleife, B. Höffling, and F. Bechstedt, Phys. Rev. B **86**, 075320 (2012).
[89] M. Ribeiro, Jr., L. R. C. Fonseca, and L. G. Ferreira, Eur. Phys. Lett. **94**, 27001 (2011).
[90] C. Adamo and V. Barone, J. Chem. Phys. **110**, 6158 (1999).
[91] M. Ernzerhof and G. E. Scuseria, J. Chem. Phys. **110**, 5029 (1999).
[92] J. P. Perdew, M. Ernzerhof, and K. Burke, J. Chem. Phys. **105**, 9982 (1996).
[93] J. Heyd, G. E. Scuseria, and M. Ernzerhof, J. Chem. Phys. **118**, 8207 (2003).
[94] J. Heyd and G. E. Scuseria, J. Chem. Phys. **121**, 1187 (2004).
[95] J. Heyd, G. E. Scuseria, and M. Ernzerhof, J. Chem. Phys. **124**, 219906 (2006).
[96] A. V. Krukau, O. A. Vydrov, A. F. Izmaylov, and G. E. Scuseria, J. Chem. Phys. **125**, 224106 (2006).
[97] J. Paier, M. Marsman, K. Hummer, G. Kresse, C. Gerber, and J. G. Ángyán, J. Chem. Phys. **124**, 154709 (2006).
[98] M. Marsman, J. Paier, A. Stroppa, and G. Kresse, J. Phys.: Condens. Matter **20**, 064201 (2008).
[99] T. M. Henderson, J. Paier, and G. E. Scuseria, Phys. Status Solidi B **248**, 767 (2011).
[100] M. Landmann, E. Rauls, and W. G. Schmidt, J. Phys.: Condens. Matter **24**, 195503 (2012).
[101] J. W. Nicklas and J. W. Wilkins, Appl. Phys. Lett. **97**, 091902 (2010).
[102] H. P. Komsa, P. Broqvist, and A. Pasquarello, Phys. Rev. B **81**, 205118 (2010).
[103] W. Chen, C. Tegenkamp, H. Pfnür, and T. Bredow, Phys. Rev. B **82**, 104106 (2010).
[104] H. J. von Bardeleben, J. L. Cantin, U. Gerstmann, A. Scholle, S. Greulich-Weber, E. Rauls, M. Landmann, W. G. Schmidt, A. Gentils, J. Botsoa, and M. F. Barthe, Phys. Rev. Lett. **109**, 206402 (2012).
[105] M. S. Hybertsen and S. G. Louie, Phys. Rev. B **34**, 5390 (1986).
[106] M. Rohlfing and S. G. Louie, Phys. Rev. B **62**, 4927 (2000).
[107] M. Shishkin and G. Kresse, Phys. Rev. B **74**, 035101 (2006).
[108] M. Rohlfing, P. Krüger, and J. Pollmann, Phys. Rev. B **48**, 17791 (1993).
[109] M. Rohlfing, P. Krüger, and J. Pollmann, Phys. Rev. B **56**, R7065 (1997).
[110] F. Caruso, P. Rinke, X. Ren, M. Scheffler, and A. Rubio, Phys. Rev. B **86**, 081102(R) (2012).
[111] T. Kotani, M. van Schilfgaarde, and S. V. Faleev, Phys. Rev. B **76**, 165106 (2007).
[112] P. Romaniello, S. Guyot, and L. Reining, J. Chem. Phys. **131**, 154111 (2009).
[113] K. Momma and F. Izumi, J. Appl. Crystallogr. **44**, 1272 (2011).
[114] K. C. Hass, L. C. Davis, and A. Zunger, Phys. Rev. B **42**, 3757 (1990).
[115] C. Jiang, C. Wolverton, J. Sofo, L.-Q. Chen, and Z.-K. Liu, Phys. Rev. B **69**, 214202 (2004).
[116] C. K. Gan, Y. P. Feng, and D. J. Srolovitz, Phys. Rev. B **73**, 235214 (2006).
[117] D. Shin, R. Arròyave, Z.-K. Liu, and A. Van de Walle, Phys. Rev. B **74**, 024204 (2006).
[118] F. Wang, S.-S. Li, J.-B. Xia, H. X. Jiang, J. Y. Lin, J. Li, and S.-H. Wei, Appl. Phys. Lett. **91**, 061125 (2007).
[119] J. von Pezold, A. Dick, M. Friák, and J. Neugebauer, Phys. Rev. B **81**, 094203 (2010).
[120] A. Van de Walle, M. Asta, and G. Ceder, Calphad: Comput. Coupling of Phase Diagrams and Thermochem. **26**, 539 (2002).
[121] I. Petrov, E. Mojab, R. C. Powell, J. E. Greene, L. Hultman, and J.-E. Sundgren, Appl. Phys. Lett. **60**, 2491 (1992).
[122] M. Mizuta, S. Fujieda, Y. Matsumoto, and T. Kawamura, Jpn. J. Soc. Appl. Phys. **25**, L945 (1986).
[123] Y. Koide, H. Itoh, N. Sawaki, I. Akasaki, and M. Hashimoto, J. Electrochem. Soc. **133**, 1956 (1986).
[124] L. K. Teles, J. Furthmüller, L. M. R. Scolfaro, J. R. Leite, and F. Bechstedt, Phys. Rev. B **62**, 2475 (2000).
[125] G. Kresse and J. Furthmüller, Comput. Mater. Sci. **6**, 15 (1996).
[126] P. E. Blöchl, Phys. Rev. B **50**, 17953 (1994).
[127] G. Kresse and D. Joubert, Phys. Rev. B **59**, 1758 (1999).
[128] L. C. de Carvalho, A. Schleife, F. Fuchs, and F. Bechstedt, Appl. Phys. Lett. **97**, 232101 (2010).
[129] L. C. de Carvalho, A. Schleife, and F. Bechstedt, Phys. Rev. B **84**, 195105 (2011).
[130] M. Feneberg, M. F. Romero, B. Neuschl, K. Thonke, M. Röppischer, C. Cobet, N. Esser, M. Bickermann, and R. Goldhahn, Appl. Phys. Lett. **102**, 052112 (2013).
[131] S. A. Ding, G. Neuhold, J. H. Weaver, P. Häberle, and K. Horn, J. Vac. Sci. Technol. A **14**, 819 (1996).

Paper V

The atomic structure of ternary amorphous $Ti_xSi_{1-x}O_2$ hybrid oxides

M. Landmann, T. Köhler, E. Rauls, T. Frauenheim, and W. G. Schmidt,

JOURNAL OF PHYSICS: CONDENSED MATTER **26**, 253201, 46 pp. (2014) – Topical Review

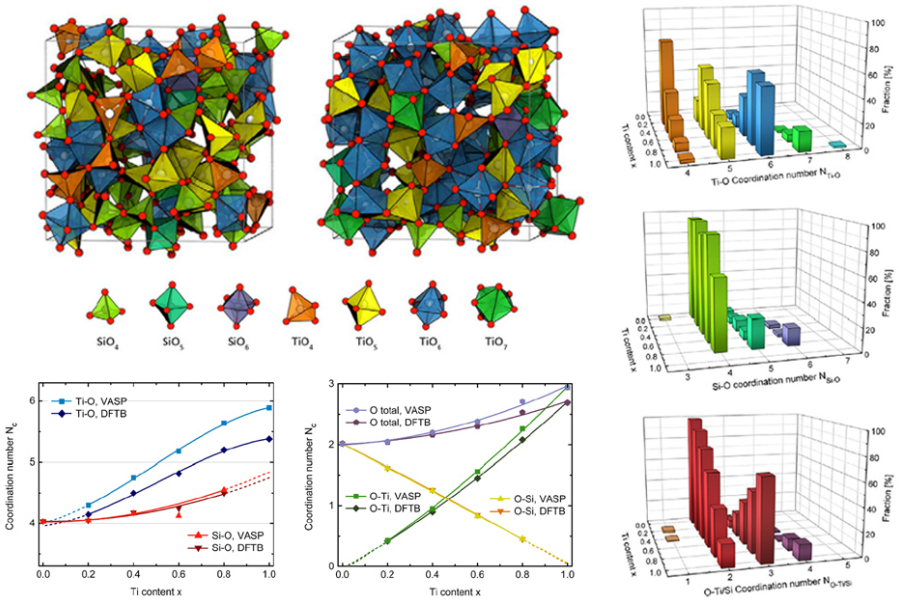

IOP Publishing Journal of Physics: Condensed Matter

J. Phys.: Condens. Matter **26** (2014) 253201 (46pp) doi:10.1088/0953-8984/26/25/253201

Topical Review

The atomic structure of ternary amorphous $Ti_xSi_{1-x}O_2$ hybrid oxides

M Landmann[1], T Köhler[2], E Rauls[1], T Frauenheim[2] and W G Schmidt[1]

[1] Lehrstuhl für Theoretische Physik, Universität Paderborn, 33095 Paderborn, Germany
[2] Bremen Center for Computational Materials Science, Universität Bremen, 28359 Bremen, Germany

E-mail: landmann@mail.uni-paderborn.de

Received 13 February 2014
Accepted for publication 7 April 2014
Published 22 May 2014

Abstract

Atomic length-scale order characteristics of binary and ternary amorphous oxides are presented within the framework of *ab initio* theory. A combined numerically efficient density functional based tight-binding molecular dynamics and density functional theory approach is applied to model the amorphous (a) phases of SiO_2 and TiO_2 as well as the amorphous phase of atomically mixed $Ti_xSi_{1-x}O_2$ hybrid-oxide alloys over the entire composition range. Short and mid-range order in the disordered material phases are characterized by bond length and bond-angle statistics, pair distribution function analysis, coordination number and coordination polyhedra statistics, as well as ring statistics. The present study provides fundamental insights into the order characteristics of the amorphous hybrid-oxide frameworks formed by versatile types of TiO_n and SiO_m coordination polyhedra. In a-SiO_2 the fourfold crystal coordination of Si ions is almost completely preserved and the atomic structure is widely dominated by ring-like mid-range order characteristics. In contrast, the structural disorder of a-TiO_2 arises from short-range disorder in the local coordination environment of the Ti ion. The coordination number analysis indicates a large amount of over and under-coordinated Ti ions (coordination defects) in a-TiO_2. Aside from the ubiquitous distortions of the crystal-like coordinated polyhedra, even the basic coordination-polyhedra geometry type changes for a significant fraction of TiO_6 units (geometry defects). The combined effects of topological and chemical disorder in a-$Ti_xSi_{1-x}O_2$ alloys lead to a continuos increase in both the Si as well as the Ti coordination number with the chemical composition x. The important roles of intermediate fivefold coordination states of Ti and Si cations are highlighted for ternary a-$Ti_xSi_{1-x}O_2$ as well as for binary a-TiO_2. The continuous decrease in ring size with increasing Ti content reflects the progressive loss of mid-range order structure characteristics and the competing roles of network forming and network modifying SiO_m and TiO_n units in the mixed hybrid oxides.

Keywords: a-TiO_2, a-SiO_2, a-$Ti_xSi_{1-x}O_2$, ternary amorphous oxides, DFT, molecular dynamics, coordination polyhedra

(Some figures may appear in colour only in the online journal)

1. Introduction

The catalytic and optical activity of solid-state materials strongly depends on diverse characteristics of the atomic structure. These are the crystal symmetry or rather the degree of structural disorder/amorphicity, as well as superordinate structural characteristics as grain size and pore size a.k.a. the effective surface area, and further (artificial) nanostructuring of a particular sample. Commonly, the physico-chemical properties of pure materials limit the tunability of at least some of these properties. In order to overcome these kinds of limitations, the industrial need for new catalysts and optical materials drives the engineering of new, partially nanostructured, multi-component hybrid materials. Thereby, the fabrication of mixed and nanostructured

 © 2014 IOP Publishing Ltd Printed in the UK

hybrid composites tries to meet two miscellaneous designing philosophies. On the one hand, systematic variation of the material composition as well as spatial structuring (e.g. quantum wells and superlattices) is used to benefit from synergetic effects between the physical properties (e.g. refractive indices, band gaps, band offsets) of the individual constituents. On the other hand, the synthesization of new hybrid materials is often motivated by the pursuit of novel physical material properties (e.g. electronic states within the band gaps or new active lattice sites for catalyzing chemical reactions) that cannot be realized by any of the alloy components.

One class of materials, that stands for the manifold of oxide alloys that have attracted considerable attention over the last years, are mixed TiO_2/SiO_2 (titania-silica) hybrid oxides, also termed TiO_2/SiO_2 binary oxides as well as ternary $Ti_xSi_{1-x}O_2$ oxides in the case of atomically mixed alloys. TiO_2/SiO_2 hybrid oxides take advantage of the catalytic properties of semiconducting TiO_2 and the high thermal stability and mechanical strength of SiO_2. TiO_2/SiO_2 based compounds nowadays offer a promising engineering platform for new materials with wide area applicability in chemical industry and optoelectronics.

Many types of thin film, layered, and supported as well as nano- and mesostructured TiO_2/SiO_2 mixed oxides have been synthesized by electron-beam evaporation [1], vacuum deposition [2, 3], atomic layer deposition [4], liquid phase deposition [5], chemical vapour deposition [6–11], RF magnetron sputtering [14], ion-beam sputter deposition [15–17], plasma sputtering [18], and prevalently following sol-gel based preparation methods [19–29, 30, 32–34]. TiO_2/SiO_2 multilayer and thin films have been used in numerous coating applications like anti-reflective thin film coatings [1, 35], weather resistant thin film coatings [19], hydrophilic coatings [36], and implant coatings [32, 37]. Amorphous $Ti_xSi_{1-x}O_2$ thin films have also been deposited for the use as gate oxides in metal oxide semiconductor-field effect transistors [38]. Various optical devices as active and passive planar optical waveguides [20, 23, 27, 39], channel waveguides [21, 40], tailored periodically or gradually modulated refractive index devices (e.g. rugate filters) [41–43], and dielectric mirrors [17] especially benefit from the large differences in the refractive indices ($\sim$ 1.5 and $\sim$2.5 for the bulk oxides of SiO_2 and TiO_2 [7, 9–11, 15, 44, 45]) and band gap energies ($\sim$ 8.5 and $\sim$3.2 for the SiO_2 and TiO_2 bulk oxides [9, 15]) of TiO_2/SiO_2 hybrid materials.

Various studies have indicated that mixed TiO_2/SiO_2 binary oxides are more active catalysts than pure TiO_2 [29, 30] and a promising material for various catalytic applications. Comprehensive reviews on the structural as well as physicochemical properties of mixed titania-silica oxide catalysts have been published by Davis and Liu [31] and Gao and Wachs [46]. In summary, the catalytic activity of TiO_2/SiO_2 compounds falls into three categories that reflect various characteristics of the utilized material. Photocatalytic properties are associated with band structure features as well as quantum size-effects due to particle size and nanostructuring. Based on the photocatalytic activity, the potential use of crystalline and amorphous TiO_2/SiO_2 nanocomposites for photocatalytic purification of contaminated (waste-) water [47, 48], exhaust gas [49], and textiles [50] has been discussed. Acid catalysis activity is generated by the character of newly formed acid sites in mixed and nanostructured TiO_2/SiO_2 oxides that are not present in the pure material phases. The acidity [4, 31, 46] of TiO_2/SiO_2 mixed oxides has been discussed controversely in literature [22, 31]. The third category summarizes material related to supporting properties as porosity, surface area as well as thermal stability that are indirectly related to the catalytic activity of a material. Mixed amorphous and crystalline networks of micro- and mesoporous TiO_2/SiO_2 oxides are nowadays widely used as catalysts in chemical industry [25, 46, 51–64].

One prominent representative of the crystalline $Ti_xSi_{1-x}O_2$ structure family is the molecular sieve-type titanium-silicalite TS-1. TS-1 catalyzes several chemical reactions as phenol hydroxylation, cyclohexanone ammoximation, or propylene epoxidation at different stages of industrial application. In general, isolated fourfold coordinated Ti ions (Ti_{4c}) substituting Si_{4c} ions in the zeolite structure have been identified as the active sites in the mixed crystalline framework [51, 52, 54, 58, 65, 66]. TS-1 has been found to be a more active catalyst as amorphous TiO_2/SiO_2 itself. Hence, different species of Ti^{4+}ions in the crystalline TS-1 framework and in amorphous TiO_2/SiO_2 catalysts have been assumed [51].

The atomic structure of amorphous TiO_2/SiO_2 oxides has been investigated extensively over the last decades. Experimental studies [8] found no indication for substantial contributions from direct Si–Ti bonds in TiO_2/SiO_2 oxide films. Cross-linking between TiO_2 and SiO_2 domains in amorphous TiO_2/SiO_2 composites is rather found to be connected to the formation of bridging O ions in Ti–O–Si cross-linking bonds. The most common way to prove presence and amount of Ti–O–Si linkages is the identification by the intensity of an infrared (IR) absorption band between 900 and 965 cm^{-1} in IR spectroscopy [7–9, 11, 25, 34, 46, 54]. This absorption band has been associated with the motion of a bridging O ion in Ti–O–Si bonds, a Si–O vibrational mode disturbed by the presence of Ti ions, respectively. Further evidence on the formation of Ti–O–Si bonds in TiO_2/SiO_2 mixed oxides is given by Raman spectroscopy and the assignment of two frequency bands at 960 cm^{-1} and 1100 cm^{-1} to vibrational modes in Ti–O–Si linkages [46, 67]. Based on x-ray absorption spectroscopy (XAS) analysis of the electronic structure of the TiO_2/SiO_2 interface, Soriano *et al* [68] proposed the formation of Ti–O–Si cross-linking oxygen bonds that connect Ti_{6c} ions in octahedral TiO_6 units and Si_{4c} ions in SiO_4 tetrahedral units. Similar conclusions have been drawn from extended x-ray absorption fine structure (EXAFS) and x-ray absorption near-edge spectroscopy (XANES) analysis in a preceding study [69].

Experimental studies [7–13, 25, 26, 44, 46, 70, 71], focusing on details of the local atomic structure, have further indicated that Ti ions in a-TiO_2/SiO_2 show predominantly a partially distorted tetrahedral coordination of Ti ions by O ions at low Ti concentration between $\sim$0.05 and 9 weight percent (wt%). Increasing the amount of Ti ions in the amorphous TiO_2/SiO_2 matrix up to $\sim$15 wt% of TiO_2 leads to an increasing amount of octahedrally coordinated Ti_{6c} ions. Above $\sim$15 wt% TiO_2 the segregation of TiO_2 as a second phase may occur. Phase separation has also been reported for high TiO_2 concentrations of $\sim$41 molecular percent (mol%) [26, 72]. Orignac [73] reported coexisting and continuously increasing hetero-condensation (formation of SiO_2 and TiO_2 domain linking Ti–O–Si

bonds) and homo-condensation (formation of Si–O–Si and Ti–O–Ti bonds) for an increasing amount of Ti with a maximum fraction of Ti–O–Si bonds (coexisting with a local minimum of Ti–O–Ti bonds) at 20 mol% TiO_2 content. Based on EXAFS and XANES on TiO_2/SiO_2 mixed oxide glasses up to TiO_2 contents of 11.6 mol%, Henderson and Fleet [28] proposed the following scenario for the transition from a homogeneous mixed oxide to a phase separated heterogeneous composite upon an increasing TiO_2 content: The onset of phase separation is not the distortion of the SiO_4 tetrahedron network but the formation of sixfold coordinated Ti_{6c} ions. At low TiO_2 content the fourfold coordination of the tetrahedron network remains undisturbed. However, these larger TiO_4 tetrahedron building blocks put volume constraints on the glassy network whose relatively incompressible Si–O bonds only show a limited ability to adjust to the volume increase. From XAS studies [28, 74–76], also, the formation of larger TiO_4 tetrahedron building-block clusters seems highly unlikely. At some point it becomes more favorable for the strained TiO_2/SiO_2 framework to convert Ti_{4c} to Ti_{6c} rather than incorporating further fourfold coordinated Ti ions. Finally, the existence of crystal-like Ti_{6c} ions promotes the formation of a crystalline TiO_2 anatase phase.

Surprisingly, Greegor *et al* [71] reported the existence of Ti_{6c} ions at very low TiO_2 concentrations below ~0.05 wt% . However, such observations seem inconsistent with various other studies and have not been confirmed experimentally or theoretically.

Very recently, the structure of low temperature (80 °C) prepared sol-gel TiO_2/SiO_2 composites has been extensively investigated by x-ray total scattering techniques [34]. For all TiO_2/SiO_2 samples (Ti concentrations of 20, 35, and 50 mol%) large fractions of both nanocrystalline anatase and amorphous TiO_2 have been reported.

In contrast to the reported phase-separation tendency upon increasing TiO_2 content, it has been reported [16, 17] that small amounts of SiO_2 enable TiO_2/SiO_2 mixed films to sustain higher annealing temperatures without TiO_2 phase transition from an amorphous state to polycrystalline anatase. While pure TiO_2 films exhibit a crystallization temperature of ~200 °C, the admixture of 5% SiO_2 increases the onset of crystallization to ~250 °C, the admixture of 9 % SiO_2 to ~300 °C, and the admixture of 17 % SiO_2 beyond 400 °C. Similarly, solid phase precipitation of crystalline TiO_2 has been found by Busani *et al* [11] in pure amorphous TiO_2 upon annealing to 400 °C while no phase segregation occurred for $Ti_xSi_{1-x}O_2$ oxide films even for TiO_2 fractions as high as 75% . Due to the nonfulfillment of the Bruggeman effective medium approximation for separated material phases of measured TiO_2/SiO_2 coating refractive indices, Larouche *et al* [8] excluded the formation of a heterogeneous mixture of SiO_2 and TiO_2 phases. Annealing to 400 °C induced TiO_2 crystallization in the high refractive index (TiO_2 rich) films while no crystal formation occurred in low refractive index (TiO_2 poor) mixtures. Therefrom, the necessity of TiO_2-rich regions as a seed for TiO_2 crystal growth has been deduced.

Gallas *et al* [2] studied the interface between SiO_2 and TiO_2. It has been shown that the growth of TiO_2 on SiO_2 begins with an amorphous interface layer even when the growth occurs at temperatures as high as 400 °C. Evidence for TiO_2–SiO_2 bonding by Ti–O–Si cross-linkages was given by x-ray photoemission spectroscopy (XPS) measurements. The possible fabrication of well defined multilayer structures from amorphous SiO_2 and TiO_2 films has been demonstrated by Wang *et al* [45].

Gracia *et al* [9] reported the preparation of mixed TiO_2/SiO_2 optical thin films with Si/Ti ratios covering the total composition range from pure SiO_2 to pure TiO_2 by ion beam induced and plasma enhanced chemical vapor deposition (IBICVD and PECVD). By Fourier transform IR (FT-IR) spectroscopy the TiO_2/SiO_2 films have been characterized as homogenous a-$Ti_xSi_{1-x}O_2$ mixtures of the two binary oxides rather than a compound of separated SiO_2 and TiO_2 phases. From analysis of the crystal field splitting, Ti ions at low concentrations (2–10%) were attributed to TiO_4 building blocks. Upon TiO_2 content increase, the continuous increase in the crystal field splitting energies towards the value, representative for amorphous TiO_2, gives evidence for an increasing coordination number. Especially, the existence of an intermediate fivefold coordinated Ti species has been depicted as a likely coordination state at higher fractions of TiO_2 in a-$Ti_xSi_{1-x}O_2$ thin films.

While Ti ions in the two most common crystalline coordination states of SiO_2 (fourfold) and TiO_2 (sixfold) are repeatedly reported, fivefold coordinated Ti_{5c} ions in hexahedral TiO_5 building blocks represent a rarer coordination state that is only sporadically reported for pure TiO_2/SiO_2 mixed oxides [4, 9, 28, 31]. Besides, in several known crystalline oxides as $K_2Ti_2O_5$ [77] and silicates as fresnoite ($Ba_2TiSi_2O_8$) [78] or Na_2TiSiO_5 [79] the occurrence of TiO_5 units has been reported for ternary TiO_2/SiO_2 mixed oxides bearing fractions of alkali and alkaline-earth metal atoms that act as network modifiers [74–76, 80–83, 120].

In summary, the detailed analysis of existing literature shows that most experimental techniques have difficulties identifying fundamental correlations of material specific short-range order characteristics on the atomic level (within the first coordination shell) and the resulting trends in physical material properties on a mesoscopic or macroscopic length scale. Especially, the identification of possibly existing Ti_{5c} ions in a fivefold coordinated TiO_5 bonding environment and the differentiation of these ions from a superposition of Ti_{4c} ions in tetrahedral and Ti_{6c} ions in octahedral bonding environments demands a high accuracy of experimental techniques. Thus, finding fundamental structure-function relationships, that may support the engineering of advanced functional materials, can substantially benefit from modern high-performance computer simulations on the atomic structure of disordered solids. Recently, the structure and stability as well as the vibrational and excitation properties of numerous pure $(SiO_2)_n$ and $(TiO_2)_n$ as well as mixed $Ti_mSi_{n-m}O_{2n}$ clusters with n between 2 and 5 and m between 1 and (n-1) have been investigated by Bandyopadhyay and Aikens in a combined density functional theory (DFT), time-dependent DFT, and coupled-cluster study. [84] Their results demonstrate that pure $(SiO_2)_n$ favors linear chain-like structures with tetravalent states and $(TiO_2)_n$ prefers compact three-dimensional configurations with hexavalent states. The structure of mixed $Ti_mSi_{n-m}O_{2n}$ clusters shows a dependence on the compound stoichiometry with a stabilization of three-dimensional structures by incorporation of even small percentages of Ti. A theoretical study on larger scale models of titanium silicate glasses has been published by Rosenthal and Garofalini [85]. In their empirical potential MD study the structural properties of $Ti_xSi_{1-x}O_2$ compounds with

TiO_2 contents ranging from 2–15 mol% have been simulated using 360 atom unit cells. The influence of slower MD cooling rates on the Ti coordination state has been outlined. While a fast quenching rate promotes significant fractions of fivefold coordinated Ti ions for all TiO_2 concentrations, a lower cooling rate strongly favors tetrahedrally coordinated Ti at low TiO_2 contents ($\lesssim$10 mol%). At higher TiO_2 content ($\sim$ 15 mol%), the slower quenching rate drastically reduces the occurrence of TiO_4 building blocks in favor of fivefold (53 %) and sixfold (28 %) coordinated Ti ions. In consideration of the strong dependence of the Ti coordination state on the cooling rate, the existence of TiO_5 building blocks in a-$Ti_xSi_{1-x}O_2$ mixed oxides remained still uncertain.

More recently, Bernard *et al* [121] studied the composition influence of undoped and Er doped TiO_2/SiO_2 mixed oxide glasses by large scale (5094 atom unit cells) empirical potential MD simulations for Ti concentrations ranging from 7.8 mol% up to 50 mol% . In all (pure) TiO_2/SiO_2 structure models, fourfold and fivefold coordinated Ti ions in TiO_4 and TiO_5 units represented the dominating structural building blocks. Already for the lowest simulated Ti concentration (7.8 mol% Ti), the formation of Ti_{4c} ions with 53% was only slightly favored over Ti_{5c} ions with a fraction of 42% . In the equimolar (50 mol% Ti) TiO_2/SiO_2 sample Ti_{5c} ions were found to be the dominant coordination state with a 60 % fraction while Ti_{4c} ions were limited to 30 % . Higher Ti coordination states were limited to minor percentages with a maximum of 10% of sixfold coordinated Ti_{6c} ions for the equimolar mixture. Based on a cluster analysis of Ti ions in the amorphous SiO_2 framework, the distribution of TiO_2 has been characterized to be neither homogeneous nor phase separated but rather random like. Even in the case of the equimolar TiO_2/SiO_2 structure model no evidence for the formation of a separated TiO_2 phase was found. Nevertheless, a general tendency to higher Ti coordination states upon increasing TiO_2 contents was interpreted as a favorable factor for the formation of a crystalline TiO_2 phase. Similar to the preceding work of Rosenthal and Garofalini [85] the quenching rate used in the MD simulations has been identified as the most crucial numerical parameter. In general, the time scales of the MD simulations might not have been sufficient to observe the possible occurrence of crystallization processes.

Aside from small cluster model *ab inito* calculations and the mentioned empirical potential MD studies, comprehensive numerical investigations of TiO_2/SiO_2 hybrid oxides are missing. The purpose of this study is to give new insights into the structural short-range and mid-range order characteristics of the pure binary phases of a-SiO_2 and a-TiO_2 as well as atomically mixed ternary a-$Ti_xSi_{1-x}O_2$ oxides over the entire composition range.

The paper is organized as follows: section 2 summarizes the underlying numerical framework for the MD simulations needed to generate the amorphous structure models. The basic ideas of structure analysis by (effective) coordination number analysis as well as coordination polyhedra and ring statistics are introduced in section 3. Section 4 provides presentation and discussion of physical trends in the structural material characteristics. Finally, section 5 summarizes the results and gives concluding comments and reasonings.

2. Methodology and numerical details

The structure formation of the amorphous oxides was simulated by performing combined self-consistent charge (SCC) density functional theory tight binding (DFTB) [86–88] MD simulated annealing (SA) and DFT [89, 90] calculations. SCC-DFTB based MD offers a good compromise between accuracy and computational efficiency for large-scale unit-cell simulations of the atomic and electronic structure of amorphous oxides [98, 99]. In the DFTB simulations, the Ti–O interaction parametrization of [93] was used. Within the MD-SA simulations, the Newton's equations of motion were solved using the Verlet-algorithm and the coupling to a heat-bath, according to a canonical (NVT) ensemble, was realized by an Anderson thermostat. The DFT structure relaxations and groundstate calculations have been performed using the projector-augmented wave (PAW) method [94, 95] as implemented in the Vienna *ab initio* simulation package (VASP) [96]. The generalized gradient approximation (GGA) according to Perdew, Burke, and Ernzerhof (PBE) [97] was applied to describe the exchange-correlation (XC) energy. In the DFT calculations, an energy cutoff of 400 eV was used to expand the wavefunctions into plane-wave basis sets. The *k*-point sampling was restricted to the Γ point and the DFTB optimized structure models were relaxed until a force convergence criterion of 0.001 eV $Å^{-1}$ was reached.

Initial structures, containing 216 atoms for the two binary oxides TiO_2 and SiO_2 and 300 atoms for the ternary $Ti_xSi_{1-x}O_2$ oxides (at composition parameters of x = 0.2, 0.4, 0.6, and 0.8) in a spatially and chemically randomized configuration, have been prepared as the starting point for the MD simulations. More abstractly speaking, the initial configurations have been prepared assuming the model of a hard sphere gas. All structure models considered in this study are strictly stoichiometric. The atoms are placed in fixed-volume rectangular cuboidal supercell arrangements of a size matching the microscopic mass densities of 4.20 g cm^{-3} for a-TiO_2 and 2.20 g cm^{-3} for a-SiO_2. Since experimental data on the mass densities of ternary a-$Ti_xSi_{1-x}O_2$ oxides over the entire composition range are limited and large variations in the atomic mass densities upon the sample preparation routes are reported in literature, we assume a mass-density dependence on the composition parameter following Vegrad's law [91, 92]. Thus, the unit mass-density of the ternary oxides was linearly interpolated between the binary oxide mass densities.

As illustrated in figure 1, the amorphization starts with a short (500 time steps) equilibration phase at 5000 K that is followed by an exponential 23 000 time step cooling towards room temperature (300 K). The total duration of the cooling procedure amounts 23 ps. In general, For most structural features we report the structure statistics for both, the last DFTB-MD generated configuration (DFTB geometry) and the DFT post-relaxed VASP geometry. Detailed visualizations of the atomic structures of all VASP geometries are given in the figures 2, 3 and 4 as well as in figure 19.

The structure characterization in terms of coordination statistics, distribution function analysis and ring statistics has partially been done by the use of the structure analysis tools provided within the RINGS [100] and ISAACS [101] codes.

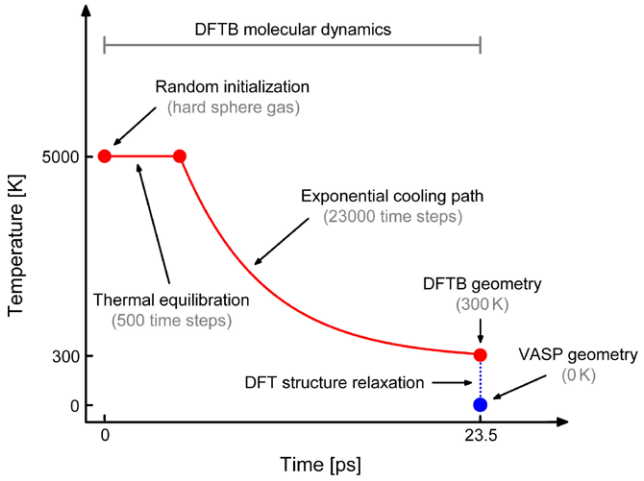

Figure 1. Schematic representation of the combined DFTB-MD and DFT amorphization approach applied for generating a-$Ti_xSi_{1-x}O_2$ structure models (see text for details).

3. Characterization of structural material properties

Crystalline materials are completely determined by their symmetry and chemical composition. A direct consequence of the lattice symmetry and translational invariance are long-range order attributes of the electronic wave function that are formally expressed in the validity of Bloch's theorem. In an amorphous solid the crystalline long-range order is completely lost due to random distortions in the atomic network. However, on a small length scale the atomic order in an amorphous solid partially commemorates the crystalline order characteristics. The existence of such short-range and in some cases also mid-range order characteristics is a material property that fundamentally distinguishes the class of amorphous solids from liquids. This paper especially focuses on the identification of the fundamental order characteristics of amorphous solids on an atomic length scale. While *nearest neighbor* bond lengths, bond angles and coordination characteristics are subsumed under the general term short-range order, mid-range order subsumes topological properties of the amorphous network. Characteristic examples of mid-range order are filament-like or ring-like structure elements. The type of order that is found in an amorphous solid strongly depends on the mass density, more precisely the density dependent ion-coordination states, of the considered material as exemplified by a-TiO_2 and a-SiO_2. Amorphous TiO_2 is known to be dominated by short-range order coordination characteristics [98], while the amorphous framework of a-SiO_2 predominantly shows ring-type mid-range order characteristics [100, 102–106]. Below, we will summarize the key concepts of the most important structure-analysis approaches that are required for an in-depth analysis of the mean local bonding environment and the topological network structure of the binary and multi-component amorphous oxides.

3.1. Short-range to mid-range order: pair distribution function analysis

Short-range as well as mid-range order characteristics of amorphous solids can be analyzed by interatomic correlation functions [107–109]. The (partial) distribution $g_{\alpha\beta}(r)$ of interatomic distances between atom pairs of the chemical types α and β is given as a one-dimensional radial function quantifying the probability of finding an atom off atomic type β within a radius r around an atom of type α at the origin:

$$g_{\alpha\beta}(r) = \frac{1}{4\pi r^2 \rho(r)} \frac{N}{N_\alpha N_\beta} \sum_{i=1}^{N_\alpha} \sum_{j=1}^{N_\beta} \delta(r - |\mathbf{r}_{ij}|). \quad (1)$$

Here, $\rho(r)$ is the real-space pair density function of the N atom containing system and N_α and N_β are the numbers of atoms of the chemical species α and β respectively. $|\mathbf{r}_{ij}|$ is the absolute value of the distance vector between an atom i of the chemical type α and an atom j of the chemical type β. The weighted sum of the partial pair distribution functions $g_{\alpha\beta}(r)$ with respect to the number concentrations $c_\alpha = N_\alpha/N$ and $c_\beta = N_\beta/N$ of chemical elements α and β gives the total (radial) pair distribution function $g(r)$.

$$g(r) = \sum_{\alpha,\beta} c_\alpha c_\beta g_{\alpha\beta}(r) \quad (2)$$

$$= \frac{1}{4\pi N \rho_0 r^2} \sum_{i=1}^{N} \sum_{j=1, j\neq i}^{N} \delta(r - |\mathbf{r}_{ij}|) \quad (3)$$

Instead of $g(r)$ and $g_{\alpha\beta}(r)$ themselves, we will make use of the reduced pair correlation functions

$$G_{\alpha\beta}(r) = 4\pi\rho_0 r(g_{\alpha\beta}(r) - 1) \quad (4)$$

and

$$G(r) = 4\pi\rho_0 r[g(r) - 1] \quad (5)$$

$$= 4\pi r[\rho(r) - \rho_0] \quad (6)$$

throughout this study.

Here, $\rho_0 = N/V$ is the average number density of N atoms in the unit cell of volume V and in the second step of equation (5) the relation $\rho(r) = \rho_0 g(r)$ between pair density function $\rho(r)$ and pair distribution function $g(r)$ has been used. In numerical simulations, the correlation functions $g(r)$ and $g_{\alpha\beta}(r)$ as well as the related reduced quantities $G(r)$ and $G_{\alpha\beta}(r)$ are directly accessible through real-space analysis of the generated atomic structure models. The total and partial pair distribution functions also give access to the total and partial coordination numbers and provide reasonable cutoff lengths for the coordination polyhedra analysis discussed below.

3.2. Short-range order: coordination number analysis

The most important short-range order information is given by the atomic coordination numbers, the mean atomic coordination numbers, respectively. For a monoatomic solid, the total (first) coordination number of an atom is defined as the average number of atoms within the first coordination spheres of radius $r_{\min}$

$$N_C = 4\pi \int_0^{r_{\min}} \rho(r)\, r^2 \mathrm{d}r = 4\pi\rho_0 \int_0^{r_{\min}} g(r)\, r^2 \mathrm{d}r. \quad (7)$$

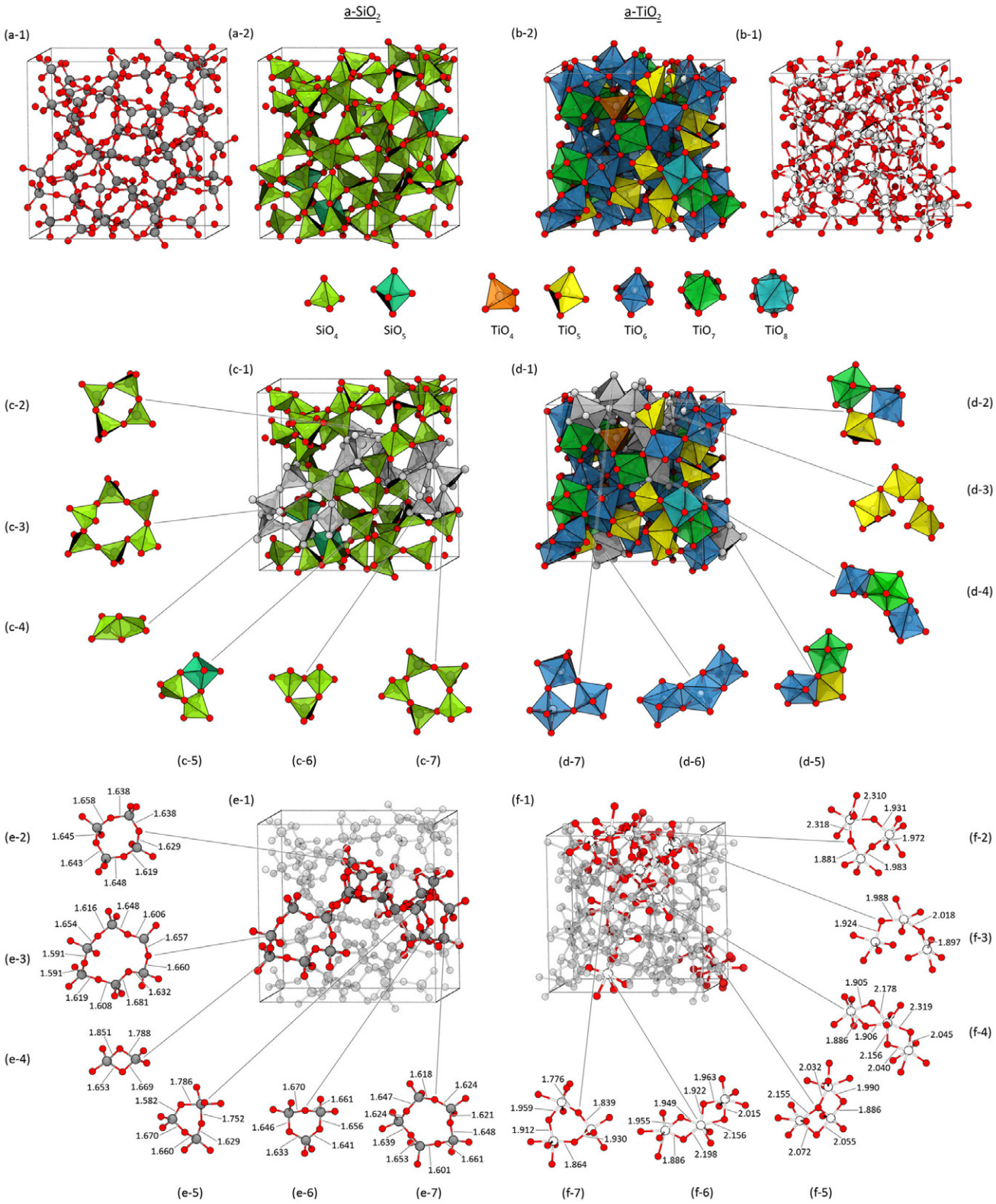

Figure 2. Ball and stick as well as coordination polyhedra representation for the a-SiO_2 (left) and a-TiO_2 (right) VASP geometries. Characteristic structure elements are visualized in the lower panels. The color coding indicates the local coordination states of the Ti and Si cations in TiO_n, $n = 4 \ldots 8$ and SiO_m, $m = 4 \ldots 5$ building blocks.

Hence, $r_{\min}$ acts as a *static* cutoff parameter that determines the coordination number. A reasonable choice for $r_{\min}$ is given by the first minimum of the pair distribution function. Coordination numbers of higher coordination shells can be obtained by integrating the atomic density within spherical shells whose limits are determined by higher local minima of the pair distribution function. Going to a multi-component system, the coordination number of an atom of chemical

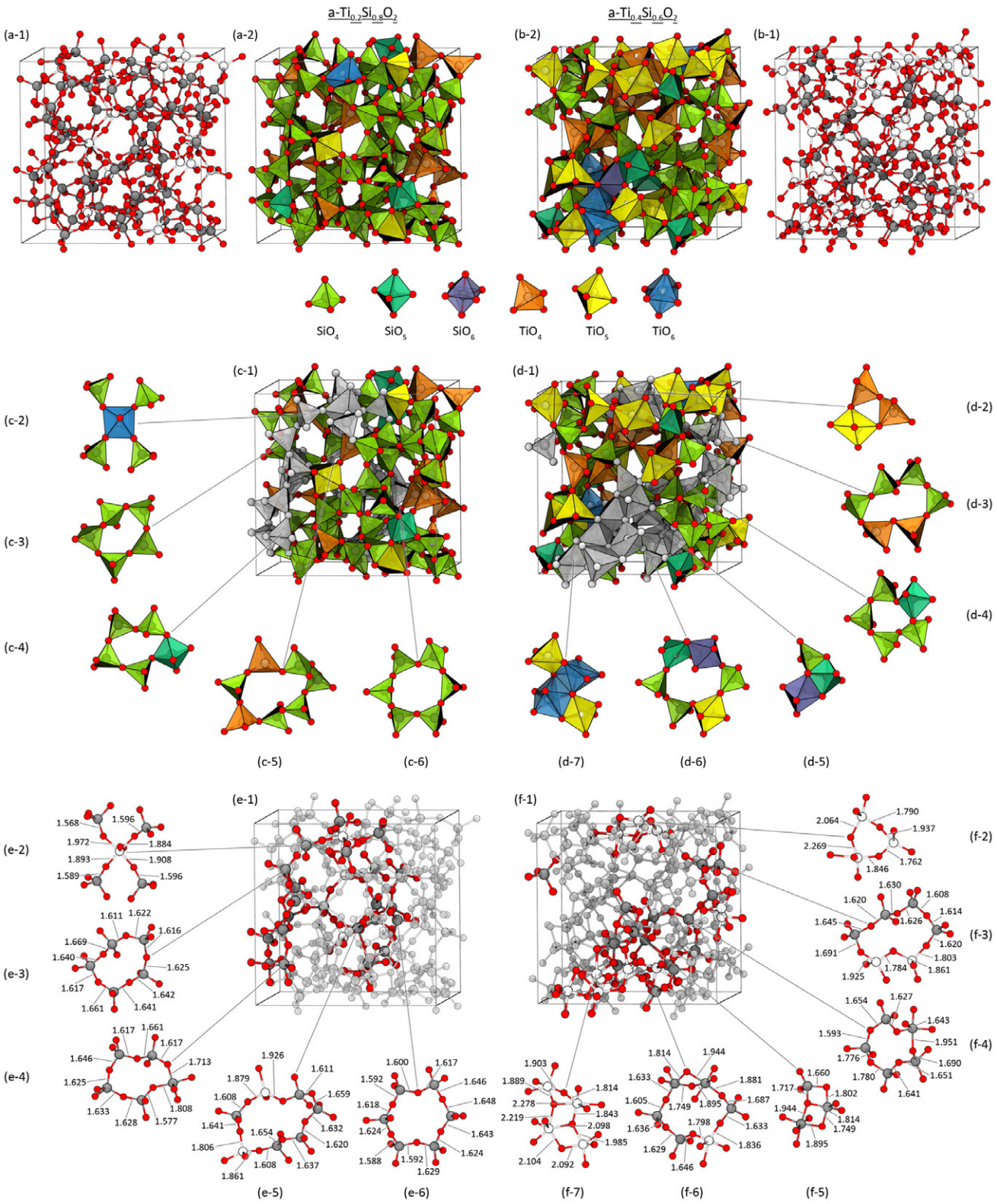

Figure 3. Ball and stick as well as coordination polyhedra representation for the a-$Ti_{0.2}Si_{0.8}O_2$ (left) and a-$Ti_{0.4}Si_{0.6}O_2$ (right) VASP geometries. Characteristic structure elements are visualized in the lower panels. The color coding indicates the local coordination states of the Ti and Si cations in TiO_n, $n = 4 \ldots 6$ and SiO_m, $m = 4 \ldots 6$ building blocks.

species α can also be decomposed into partial contributions $N_{\alpha\beta}$ from individual atom types β. $N_{\alpha\beta}$ is defined as the average number of atoms of type β within a spherical shell around an atom of type α

$$N_{C_{\alpha\beta}} = 4\pi \int_0^{r_{\min}} \rho_{\alpha\beta}(r)\, r^2 \mathrm{d}r = 4\pi\rho_0 c_\beta \int_0^{r_{\min}} g_{\alpha\beta}(r)\, r^2 \mathrm{d}r \tag{8}$$

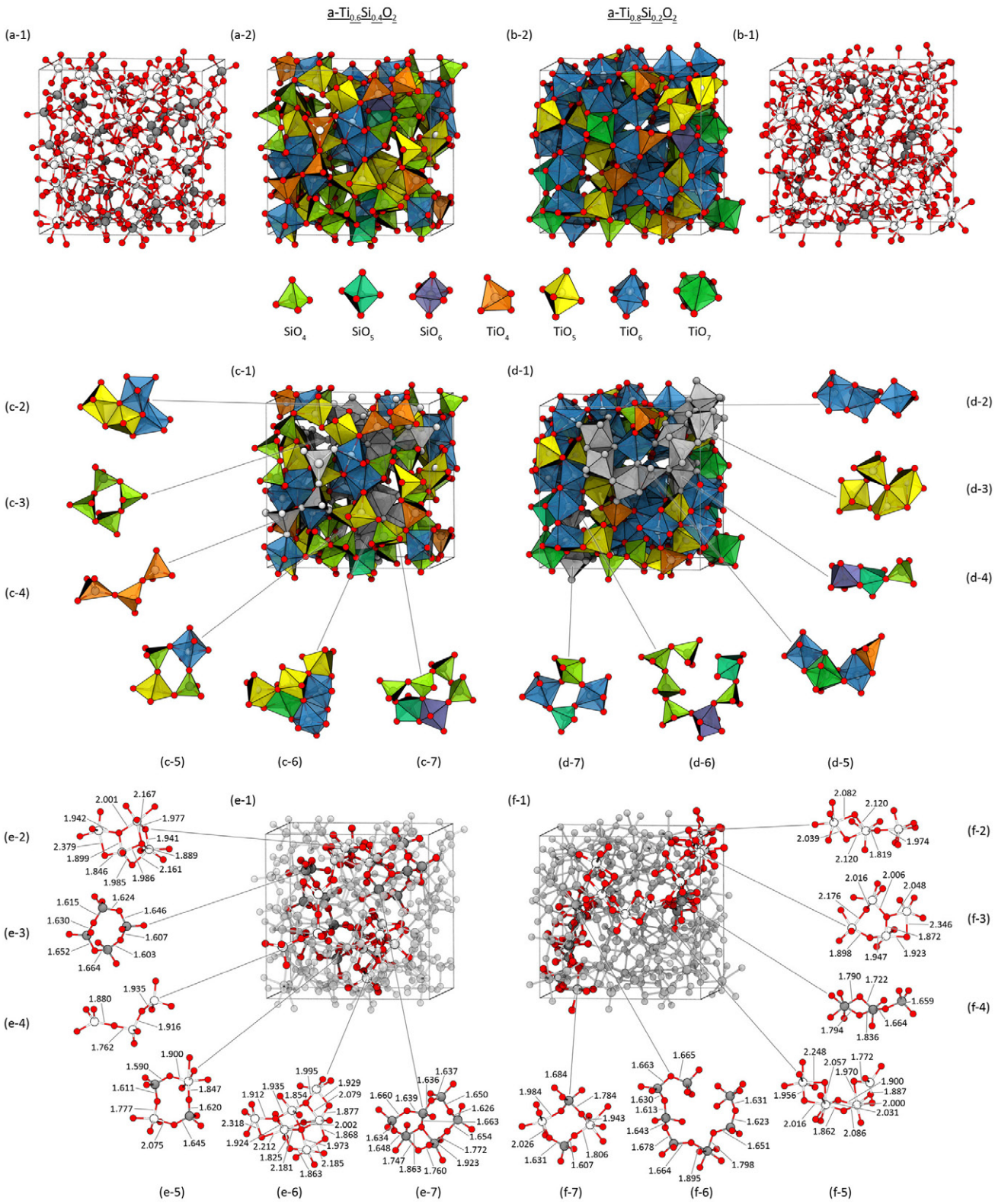

Figure 4. Ball and stick as well as coordination polyhedra representation for the a-$Ti_{0.6}Si_{0.4}O_2$ (left) and a-$Ti_{0.8}Si_{0.2}O_2$ (right) VASP geometries. Characteristic structure elements are visualized in the lower panels. The color coding indicates the local coordination states of the Ti and Si cations in TiO_n, $n = 4 \ldots 7$ and SiO_m, $m = 4 \ldots 6$ building blocks.

Necessarily, summation over all atomic species β provides the total coordination number of atom α by arbitrary atoms

$$N_{C_\alpha} = \sum_\beta N_{\alpha\beta}. \tag{9}$$

A general shortcoming of this *conventional* approach to determine the (average) coordination state of an atom is a pronounced dependence on the choice of the cutoff parameters.

3.3. Short-range order: coordination polyhedra statistics

While the pair-distribution analysis is a powerful technique to analyze and compare averaged topological features on a short-range and the mid-range length-scale, it does not necessarily allow us to identify distinct characteristics of the short-range order within the first coordination shell. This shortcoming especially arises in amorphous structures due to the superposition of pair correlations from atoms in various coordination environments and through ubiquitous lattice distortions. In order to gain fundamental insights into the atomic structure within the first coordination shell, it is necessary to analyze the structural properties on the atomic level by splitting the solid into a set of simple geometric units that map the atomic structure characteristics of the solid and that appear repeatedly throughout the crystal. Besides strict mathematical decomposition schemes based on Voronoi tessellation and, complementary, Delaunay triangulation, one of the most useful and illustrative decomposition schemes is the description of the disordered atomic structure by coordination polyhedra as fundamental building blocks. These are constructed by considering the bonded atoms, the nearest neighbor atoms or ligands, respectively, within some specific cutoff range defining the actual coordination sphere, as the vertices of a geometrical object, more precisely an irregular polyhedron composed from differently shaped polygons. Such coordination polyhedra inherently combine the coordination number as a quantitative measure for the atomic environment with the topological information contained in the shape of a particular coordination polyhedron. In general, a coordination polyhedra will reflect a particular hybrid-orbital-type whose shape will be specified by a linear combination of the involved atomic orbitals. Hence, the diversity of coordination polyhedra is associated with the valence-orbital type of the involved chemical elements. In $Ti_xSi_{1-x}O_2$ compounds especially, the d electrons of Ti will increase the number of occurring coordination polyhedron-types.

Even if there are, strictly speaking, not two identical coordination polyhedra in an amorphous solid, it should be possible to assign the distorted polyhedra to a discrete number of fundamental *high symmetry* coordination polyhedra. Most likely, these fundamental structural units correspond to or at least include distorted elementary building blocks of crystalline material modifications with a comparable chemical composition and mass density. Many elements of coordination polyhedra statistics are also contained in the ideas of crystal field and ligand field theory that connect the local coordination geometry of molecules and solids to characteristic features, in particular the energy level splitting, of the electronic structure. The basic ideas of the coordination-polyhedra analysis, as well as the concept of coordination numbers itself, were brought up by Alfred Werner as early as 1893 [122] in the characterization of inorganic metal salts. Ever since, coordination number and polyhedra statistics have been proven to be important concepts to understand the atomic structure of crystalline solids [124]. Most notably, the topology of tetrahedrally [100, 106, 113] and octahedrally [98, 106] coordinated materials have been investigated. Both, SiO_2 and TiO_2 might be seen as the archetypes of fourfold tetrahedral coordination (SiO_2) and sixfold octahedral coordination (TiO_2). The coordination polyhedra analysis especially illustrates the common short-range order features between crystalline modifications and amorphous phases of these oxides [98].

Idealized coordination polyhedra in a mathematical sense, exist in crystalline solids, but can not be found in an amorphous solid. In fact, an amorphous solid is formed by any number of randomly distorted polyhedron building blocks. Hence, we will label and subsume the distorted coordination polyhedra according to their basic high-symmetry structure types. In particular cases, prevalent at high coordination numbers, disorder induced distortions can severely handicap the assignment of a specific structure type to a particular coordination polyhedra. Also, the shape of coordination polyhedra can change continuously between various basic types. Nevertheless, in most cases the conserved short-range order allows the identification of various fundamental polyhedron-building block configurations for a given coordination number.

In order to unify the discussion, we will refer to all considered atomic building blocks as coordination polyhedra, including fundamental building blocks that are not a polyhedron in a mathematical sence or a polyhedron at all (i.e. simple polygons). Strictly speaking, there are only five regular polyhedra, the tetrahedron ($N_c = 4$), the octahedron ($N_c = 6$), the cube ($N_c = 8$), the dodecahedron ($N_c = 12$) and the icosahedron ($N_c = 20$), the Platonic solids. There are thirteen additional semi-regular polyhedra of the Archimedean solid family with $N_c > 12$ vertices. With respect to the coordination numbers, only the tetrahedron and the octahedron are found among the fundamental a-$Ti_xSi_{1-x}O_2$ building blocks. Single coordination polyhedra shapes can also be assigned to the infinite familiy of prisms. Further polyhedra types belong to the 92 membered family of Johnson solids [126], formed by non-uniform polyhedra ($N_c > 5$)) constructed from regular polygons.

In order to define reasonable *convex* coordination polyhedra it is necessary to limit the radius of the coordination spheres around each atom. This is done by using the first minimum of the partial reduced pair distribution functions $G_{ij}(r)$ for each pair of chemical elements as cutoff radii. The applied cutoff radii for coordination-polyhedra statistics are 2.4 Å for Ti–O and 2.1 Å for Si–O pair correlations. The coordination polyhedra, that have been identified as structural building blocks of a-$Ti_xSi_{1-x}O_2$ mixed oxides, are discussed below and visualized in figure 5.

3.3.1. Threefold coordination ($N_c = 3$). Threefold coordinated AX_3 units, trigons respectively, occur in two basic configurations. In the trigonal pyramidal coordination type ([TPY-3]) the central atom is displaced along the surface normal from the ligand plane. The prototypical example for this coordination type is the C_{3v} symmetric NH_3 molecule. In the planar type the central atom is coplanar with its three ligands. The planar coordination type, splits into two subtypes, a regular trigonal plane type ([TP-3]) and a T-shaped ([TS-3]) configuration. Characteristic examples for threefold coordinated complexes are trifluoride molecules, with BF_3 showing a D_{3h}

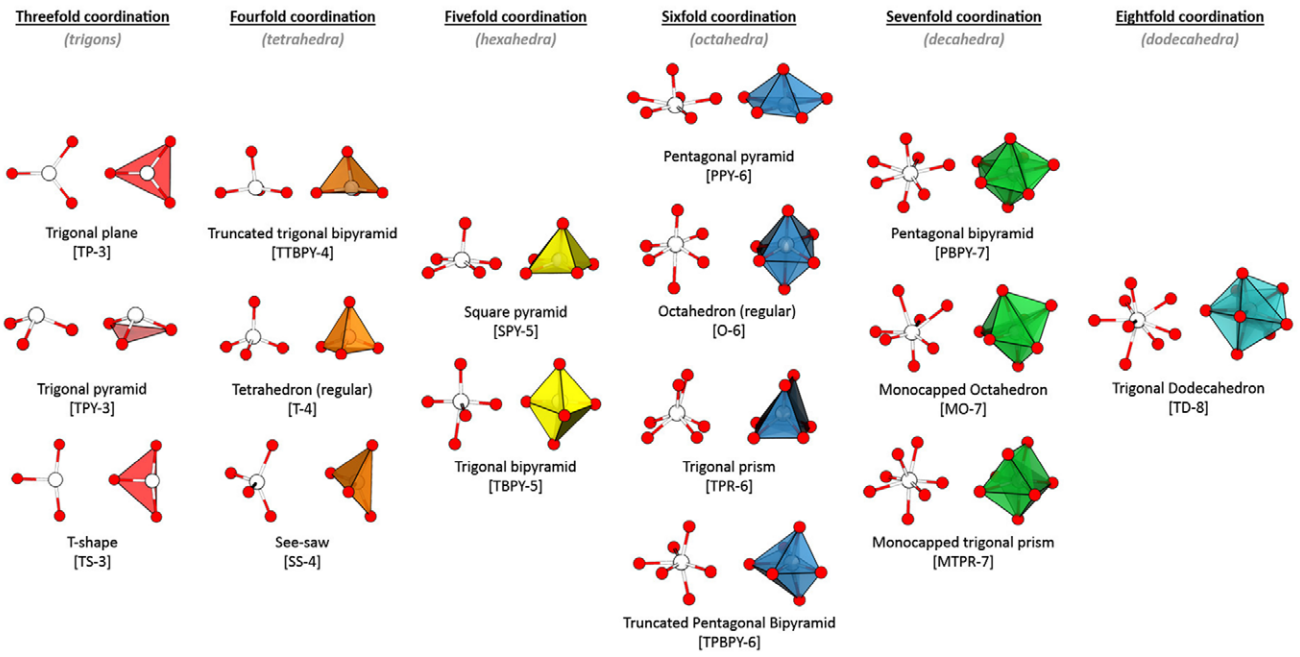

Figure 5. Coordination polyhedra for coordination numbers between three and eight. Characteristic examples are visualized of weakly distorted coordination polyhedra that can be found in the ternary a-$Ti_xSi_{1-x}O_2$ alloys. The polyhedra are labeled according to their corresponding high symmetry basic types, largely following the IUPAC recommended nomenclature [123].

symmetric [TP-3]-type structure and ClF_3 showing a C_{2v} symmetric [TS-3]-type structure.

A threefold planar coordination is the conventional coordination type of O ions in natural c-TiO_2 modification. Thereby, the OTi_3 units of rutile adopt a [TP-3]-shape and a [TS-3]-shape in anatase (see reference [125]). The more complex brookite phase combines [TP-3]-like and [TS-3]-like OTi_3 units. Consequently, both plane types also occur in the amorphous solid. Thereby, the disorder of the amorphous solid is reflected in an almost continuous variation of OTi_3 topologies between the [TP-3] and [TS-3] border cases. There are no pyramidal OTi_3 units in the three natural occurring TiO_2 polytypes rutile, anatase, and brookite. However, O ions in the metastable TiO_2 polymorphs hollandite and ramsdellite partially show a [TPY-3]-type coordination. Also, the threefold coordinated O_{3c} ions in the high pressure TiO_2 polytypes baddeleyite (TiO_2(MI)), columbite (TiO_2(II)) and the orthohombic-type I (TiO_2(OI)) show a weak displacement from the Ti ion plane. Ti ions are never found in a threefold coordination state, neither in crystalline nor in amorphous TiO_2 phases.

In SiO_2 threefold coordinated ions only occur in exceptional cases. The very dense SiO_2 polymorphs stishovite (rutile-like) and seifertite show fundamental [TP-3]-like OSi_3 building blocks. Also, a-SiO_2 threefold coordinated ions represent a very exceptional coordination state that can occur for both chemical elements in a very limited number of OSi_3 and O_3Si units.

3.3.2. Fourfold coordination (N_c = 4). There are four basic types of AX_4 coordination polyhedra, the square plane, the square pyramid, the tetrahedron and the see-saw type. Out of the four basic structure types, the square plane-type with the central atom coplanar with all four ligands and the pyramidal-type with the central element A displaced from the ligand plane (i.e. square pyramid) is not found in the investigated a-$Ti_xSi_{1-x}O_2$ alloys or the pure crystalline phases of TiO_2 or SiO_2. The regular [T-4] structure type with T_d symmetry is known among others from the CH_4 molecule and several tetrachlorides. The C_{2v} symmetric see-saw structure ([SS-4]) is a common geometry for tetrafluorides as SF_4.

No O ion, neither in crystalline nor amorphous SiO_2, shows a fourfold coordinated state. In contrast, a certain amount of O ions in a-TiO_2 forms [T-4]-type and [SS-4]-type coordination polyhedra. OTi_4 building blocks are also common for a fraction of O ions in crystalline bronze-type TiO_2(B) as well as for the crystalline TiO_2 high-pressure polytypes baddeleyite, orthohombic-type I, fluorite (cubic TiO_2), and cotunnite (TiO_2(OII)). Thereby, the OTi_4 units adopt a [SS-4]-type geometry in TiO_2(B), TiO_2(OI) and TiO_2(OII) and a [T-4]-type geometry in cubic TiO_2.

The fourfold coordination state is by far the most common coordination of Si in SiO_2 and silicates in general. With exception of the extremely dense SiO_2 polytypes stishovite and seifertite, all SiO_2 crystal phases (α-quartz, β-quartz, α-tridymite, β-tridymite, α-cristobalite, β-cristobalite, keatite, moganite, and coesite) form more or less complex three-dimensional networks of corner connected [T-4]-type SiO_4 units.

The fourfold coordination state of Ti ions is rarely found in pure a-TiO_2, never found in pure crystalline TiO_2, and sporadically found in the surface layers of low-index TiO_2 surfaces. Such surfaces are the rutile(0 0 1) surface [130], the anatase(1 1 0) surface and one coordination of the anatase(1 0 3) surface [131], as well as the brookite(0 1 0) surface [132]. In these surfaces the AX_4 coordination polyhedra adopt a [SS-4]-type geometry and form corner-linked rows. TiO_4 units are also repeatedly found in a-$Ti_xSi_{1-x}O_2$ alloys with low Ti

content and for Ti ions in titanium silicalites [51, 52, 54, 58, 65, 66]. A further fourfold coordination geometry, best characterized as a truncated trigonal bipyramid ([TTBPY-4]), can sometimes be found (mainly) for Ti ions. These coordination polyhedra may also be seen as a distorted regular polyhedron type in which the central atom is shifted into one of the faces, thus becoming the [TP-3]-type basis of a trigonal pyramid. Through atomic disorder in the amorphous alloys, the coordination geometry can change continuously between the [T-4] and the [TTBPY-4]-type.

3.3.3. Fivefold coordination (N_c = 5). The basic types of AX_5 coordination polyhedra are the square pyramid ([SPY-5]) and the trigonal bipyramid ([TBPY-5]), that represent the two five-vertex Johnson solids J_1 and J_{12}. Both structures are closely connected since the [TBPY-5]-type can be seen as an intermediate polyhedron occurring in the Berry pseudorotation-type interconversion [133, 134] (exchange of apical and equatorial ligands) between different [TBPY-5]-type isomers. Molecular examples for the basic C_{4v} and D_{3h} symmetries of [SPY-5]-type and [TBPY-5]-type coordination polyhedra are the pentafluorides ClF_5 and $BrFl_5$ as well as the pentachlorides PCl_5 and $AsCl_5$. No pentagonal planar configuration was found in the a-$Ti_xSi_{1-x}O_2$ mixed-oxide alloys.

With the exception of the ultra-dense cotunnite polytype, no fivefold coordinated O ions are found in the pure and mixed ordered and disordered phases of TiO_2 and SiO_2.

Si_{5c} ions in [SPY-5] and [TBPY-5]-type coordination polyhedra occur extremely rare in our structure models of pure a-SiO_2, but repeatedly in the ternary a-$Ti_xSi_{1-x}O_2$ mixed oxides. The occurrence of SiO_5 units under high pressure conditions has been reported experimentally in silicate liquids and glasses [127–129].

The possible occurrence of fivefold coordinated Ti_{5c} ions in hexahedral building blocks has already been discussed in the introductory section. In summary, a fivefold coordination seems to be a likely intermediate Ti coordination state especially in a-$Ti_xSi_{1-x}O_2$ thin-film alloys. Fivefold coordinated Ti_{5c} ions are also a common coordination state in low-index TiO_2 surface layers. Among these surfaces are the TiO_2 rutile surfaces (1 1 0), (1 0 0), and (1 0 1) [130], the TiO_2 anatase surfaces (1 0 1), (1 0 0), (0 0 1), and one of two possible coordinations of (103) [131], as well as the TiO_2 brookite surfaces (1 0 0) and (1 1 0) [132]. The fivefold coordinated Ti_{5c} surface ions show a characteristic alignment of edge-linked [SPY-5]-type coordination polyhedra in row-like structures with the square face oriented towards the vacuum.

3.3.4. Sixfold coordination (N_c = 6). There are three basic types of AX_6 coordination polyhedra. The regular O_h symmetric octahedron ([O-6]) that, together with the tetrahedron, is one of the occurring Platonic solid type polyhedra. Regular octahedral geometries are known in molecular form from hexachlorines (e.g. WCl_6) as well as hexafluorides (e.g. SF_6). The pentagonal pyramid type ([PPY6]) as well as the trigonal prism type ([TPR-6]) represent less common representatives of AX_6 coordination polyhedra. The pentagonal pyramid is yet another example of a Johnson-type (J_2) coordination polyhedron. Both the trigonal prism and the pentagonal pyramid in general are not octahedral solid figures. In fact, the D_{3h} symmetric regular trigonal prism is a pentahedron and the C_{5v} symmetric pentagonal pyramid is a hexahedron. However, both become octahedra in their distorted geometries. In some cases, molecular compounds as sixfold coordinated methyl complexes $[(CH_3)_nMX_{6-n}]$ tend to adopt a trigonal prismatic instead of an octahedral geometry [135]. A pentagonal pyramidal structure for instance occurs in the form of anionic $XeOF_5^-$ complexes [136]. A fourth structure type repeatedly found for sixfold coordinated Ti ions in a-$Ti_xSi_{1-x}O_2$ alloys can be described as a truncated pentagonal bipyramid ([TPBPY-6]) obtained through removal of one equatorial vertex. The [TPBPY-6]-type coordination state might also be considered a bicapped tetrahedron or even more obvious as a skewed trapezoidal bipyramid. In addition, [TPBPY-6]-like coordination polyhedra are characteristic intermediate states in the interconvesion between octahedron and trigonal prism by a Bailar twist [138–141].

A sixfold coordination of Si ions occurs rarely in a-$Ti_xSi_{1-x}O_2$ alloy phases due to locally high coordinated ions in the vicinity of the Si ion. There is no indication of a Si coordination state with $N_c \geqslant 5$ in pure SiO_2, although [O-6]-type Si_{6c} ions are known from the high density SiO_2 modifications stishovite and seifertite.

In contrast to the coordination states of the Si ion, a sixfold coordinated state represents the dominant coordination type of Ti ions in crystalline and amorphous TiO_2. Besides the naturally occurring polytypes rutile, anatase, and brookite, also the metastable TiO_2 polymorphs TiO_2(H), TiO_2(R) and TiO_2(II) belong to the class of octahedra network forming oxides. Also, pure a-TiO_2 shows Ti_{6c} ions as the dominant Ti coordination state.

The sixfold coordination of Ti ions in various c-TiO_2 modifications (with the exception of TiO_2(B)) commonly implies a threefold coordination of O ions. Thus, network forming TiO_6 as well as OTi_3 building blocks can be seen as complementary representations of the crystal structure of low-pressure c-TiO_2 polymorphs (see reference [125]).

3.3.5. Sevenfold coordination (N_c = 7). Sevenfold coordinated AX_7 geometries occur in three basic geometries. Among these polyhedra types the undistorted pentagonal bipyramidal geometry-type ([PBPY-7]) with D_{5h} symmetry shows the highest symmetry. The further sevenfold coordinated geometry types are monocapped versions of octahedral coordination polyhedra. They are monocapped, more precisely the square face is monocapped, trigonal prism ([MTPR-7]) with idealized C_{2v} symmetry and the monocapped octrahedron ([MO-7]) with idealized C_{3v} symmetry. Both, the [PBPY-7] and the [MTPR-7] geometries belong to the Johnson type solids (J_{13} and J_{49}). A sevenfold coordination state represents a less common molecular coordination state. Nevertheless, there are experimentally verified molecular examples for all structure types. The [PBPY-7]-type coordination geometriy is archetypically exemplified in iodine heptafluoride (IF_7) [142, 143]. Also, the simplest examples of monocapped trigonal prismatic type molecules are heptafluoride complexes as $[NbF_7]^{2-}$ and

$[TaF_7]^{2-}$ [144]. A capped octahedral geometry has been reported for the chloride complex $TaCl_4(PMe_3)_3$ [145].

In a-$Ti_xSi_{1-x}O_2$ the sevenfold coordination state is reserved to a small number of Ti ions in the Ti-rich composition region and pure a-TiO_2. Thereby, the [PBPY-7]-type coordination polyhedra represent the most common coordination geometry. Also, the crystalline TiO_2 high pressure modifications TiO_2(MI) and TiO_2(OI) consist of fundamental [MO-7]-type TiO_7 building blocks.

3.3.6. Eightfold coordination (N_c = 8). There are several basic geometries of AX_8 complexes. The most important eightfold coordinated polyhedra are the trigonal irregular dodecahedron or snub disphenoid (Johnson solid J_{84}, D_{2d} symmetry), the cube (O_h), the square antiprism (D_{4d}), the hexagonal bipyramid (D_{6h}) as well as some capped octahedron and prism geometries. Eightfold coordinated ions are commonly found in cubic (ionic) binary solids and even the crystalline cubic fluorite-type high-pressure phase of TiO_2. Only the trigonal dodecahedral structure type [TD-8] is found as an extremely rare coordination state in the investigated a-$Ti_xSi_{1-x}O_2$ alloys, more precisely in pure a-TiO_2. An example of the rare case of [TD-8]-type molecular coordination geometry is the Na ion in the molecular Schiff base compound [(NiL)Na(NiL)]ClO_4 [146].

3.3.7. Further coordination states (N_c = 1, 2). Onefold coordinated or single bonded ([SB-1]) atoms, with the exception of the H atom, are typically found in small molecules, trivially in diatomic complexes. A onefold coordination in solids is typically connected to the formation of dangling-bond-type states at surfaces, around crystal defects and in amorphous solids and their saturation by a single bonded atom. To a large extent, a-$Ti_xSi_{1-x}O_2$ forms *well* connected network structures free of structural *defects*. However, sometimes a onefold coordination state is observed for O ions in the ternary a-$Ti_xSi_{1-x}O_2$ oxides. A prominent example for the fundamental importance of onefold coordinated states is hydrogenated amorphous silicon a-Si:H. In a-Si:H the hydrogen atoms occupy onefold coordinated sites in order to saturate dangling-bond type sites of under-coordinated Si ions. As a consequence, the high structural-defect density of pure a-Si is drastically reduced [147, 148].

Twofold coordinated atoms occur in a large number of molecular complexes. The two possible AX_2 type coordination geometries are a bend/angular configuration ([A-2]) and a linear alignment ([L-2]). There are two configurations for each geometry type, a homonuclear (XAX) and a heteronuclear (XAY) twofold coordination state. Examples for twofold coordinated atoms in linear molecules are the $D_{\infty h}$ symmetric CO_2 molecule for the homonuclear [L-2]-type ([HOL-2]) and the $C_{\infty h}$ symmetric HCN molecule for the heteronuclear [L-2]-type ([HEL-2]). The most prominent example of a homonuclear [A-2]-type coordination ([HOA-2]) is the C_{2v} symmetric H_2O molecule. A heteronuclear [A-2]-type complex ([HEA-2]) is exemplified in the C_s symmetric NOCl molecule.

In fact, a strictly linear coordination geometry does not occur in the amorphous solids. However, some configurations are very close to the linear alignment and we will consider twofold coordinated complexes with an bonding angle $\geqslant 177°$ as a distorted linear geometry of the [HOL-2] or [HEL-2]-tpye. In $Ti_xSi_{1-x}O_2$ only the O ion exists in a twofold coordinated state. In pure a-TiO_2 a notable fraction of [A-2]-type coordinated O ions exists next to an equal fraction of fourfold coordinated O ions and the dominant threefold coordination types. Besides sporadic examples of threefold coordinated O ions, the dominant fraction of O ions in pure a-SiO_2 shows a [A-2]-type coordination geometry and a very small fraction is found in an almost linear [L-2]-type coordination environment. Amorphous $Ti_xSi_{1-x}O_2$ alloys show, depending on the composition, all four possible twofold coordination types of the O ion by Si and Ti ions.

In all tetrahedrally coordinated crystalline SiO_2 modifications of the O ions show a twofold coordination by Si ions. Interestingly, also TiO_2(B), one of the lowest density polymorphs of crystalline TiO_2, contains some twofold coordinated O ions that interconnect more densely packed layers formed by threefold and fourfold coordinated O ions.

3.4. Short-range order: effective coordination numbers

One shortcoming of the conventional coordination-number analysis, introduced above, is the use of static cutoff parameters $r_{cut} \equiv r_{min}$. In general, the result of a coordination number as well as coordination polyhedra analysis will show a strong dependence on the choice of the cutoff parameter for disordered systems. Additionally, all bonded atoms are considered to contribute equally to the coordination of an atom. This approach corresponds to the use of equal bond-weighting functions, i.e. weights of $\omega_{ij} = 1$, for all atomic bonds between a central atom i and its surrounding neighbors j. While an equal weight of all interatomic bonds might be adequate for regular coordination polyhedra in crystalline systems with constant nearest neighbor distances, amorphous solids show a notable bond length disorder that is not reflected by the equal weights of the conventional coordination numbers analysis. In fact, an atom j with a larger bond-length distance d_{ij} from the considered atom i will show weaker bonding characteristics than an alternative atom j with smaller distance from atom i. In contrast, detailed information on bond length and bond angle disorder is contained in the geometrical shape of a particular coordination polyhedra, respectively its shape deviation from the idealized high-symmetry polyhedra geometry. Despite the comprehensive analysis of the local coordination environment by polyhedra building blocks, a complete coordination polyhedra analysis is an elaborate task resulting in a complex amount of data. A more straight forward way to consider the influence of short-range disorder in amorphous solids is given by the idea of using coordination numbers that rest upon the use of some kind of bond-weight function, i.e. weights of $\omega_{ij} \neq 1$, to account for different bonding distances between pairs ij of atoms. Such coordination numbers are called *weighted* or *effective* coordination numbers. In fact, all surrounding atoms j are considered with a fractional weight to calculate the effective coordination number of an atom i, thus eliminating the necessity of an initial bond-length cutoff parameter. The actual determination of appropriate bond

weights has a long standing history in coordination chemistry and various weighting concepts have been proposed (e.g. see reference [124] and references therein).

The concept of effective coordination numbers considered in this study is based on the concepts introduced by Hoppe *et al* in inorganic chemistry [149–151]. The effective coordination number η_c^i of an atom i is defined as a sum over bond-weight functions ω_{ij} for surrounding atoms j

$$\eta_c^i = \sum_j \omega_{ij}. \tag{10}$$

Commonly, an exponential bond-weight function is chosen in which the ratio of the actual pair distance d_{ij} and the average weighted bond length δ_{av}^i enters to the power of six.

$$\omega_{ij} = \exp\left[1 - \left(\frac{d_{ij}}{\delta_i^{av}}\right)^6\right]. \tag{11}$$

In that way, the effective coordination numbers are actually parameter free. However, the result depends on a reasonable choice for the analytic form of the bond-weight function and a reasonable weighting function should recover the conventional coordination numbers of high-symmetry coordination polyhedra in crystals. The average weighted pair distance δ_{av}^i is defined individually for each atom i by

$$\delta_i^{av} = \frac{\sum_j d_{ij}\exp\left[1 - \left(\frac{d_{ij}}{\delta_i^{av}}\right)^6\right]}{\sum_j \exp\left[1 - \left(\frac{d_{ij}}{\delta_i^{av}}\right)^6\right]}. \tag{12}$$

Originally, the minimal bond distance d_i^{min} between atoms i and j instead of δ_i^{av} itself has been considered in the definition of δ_i^{av}. Due to the both-sided dependence, d_{av}^i needs to be calculated self-consistently for every atom. Following references [152–154] the δ_i^{av} self-consistency cycle is initialized to be the minimal bond distance d_i^{min} and iterated until self-consistency within an stoping condition of $|(\delta_i^{av}[n+1] - \delta_i^{av}[n])| \leq 0.0001$ is reached. In practice δ_i^{av} converges rapidly within a few iteration steps. Effective coordination numbers defined in that way have recently been applied in the analysis of transparent conducting oxides [152], metal clusters [153, 154] and ternary telluride compounds [155]. In contrast to the conventional local coordination numbers n_c, the effective coordination numbers are, with exception of high symmetry polyhedra in crystalline systems, in general non-integer valued. The average weighted bond distances $\delta_{c_{(\alpha)}}$ and effective coordination $\eta_{c_{(\alpha)}}$ of a set of $N_{(\alpha)}$ atoms (of chemical species α) are given by

$$\delta_{c_{(\alpha)}} = \frac{1}{N_{(\alpha)}} \sum_i \delta_i^{av} \tag{13}$$

and

$$\eta_{c_{(\alpha)}} = \frac{1}{N_{(\alpha)}} \sum_i \eta_c^i. \tag{14}$$

Since the effective coordination numbers η_c^i and $\eta_{c_{(\alpha)}}$ take into account deviations from an average bonding distance, they include effects of *radial disorder* that essentially reduce the value of the effective coordination numbers with respect to the conventional local and total equal weight coordination numbers n_c and N_c. Consequently, the differences $n_c - \eta_c^i$ and $N_{c_{(\alpha)}} - \eta_{c_{(\alpha)}}$ are simple measures for the extent of short-range disorder of particular coordination polyhedra or ions of a chemical component in total, respectively.

3.5. Mid-range order: ring statistics

Even though some fundamental characteristics of the interconnectivity of coordination polyhedra are already contained in the pair distribution functions, the average radial character of the pair distribution functions is not sufficient to describe the distinct mid-range order features found in some amorphous oxides. The formation of extended ring-like structures throughout an amorphous solid is a distinct feature of low-density amorphous solids and has been discussed in literature predominantly for tetrahedrally coordinated materials as a-SiO_2 [100, 102–106]. Other amorphous materials whose atomic structures have been recently characterized by ring statistics are the amorphous binary antimonides GaSb [110] and InSb [111] as well as binary amorphous GeTe [113] and ternary amorphous GeSbTe alloys [112, 114].

In order to characterize the amorphous network, we define a ring as the *topologically shortest* closed path starting from one particular atom and returning to that atom by stepwise, going from one adjacent/bonded atom to another. In case of a crystalline structure, an adjacent atom is simply defined as a nearest neighbor of a particular atom. For an amorphous solid adjacent atoms are defined by the cutoff spheres for each element. Analog to the coordination polyhedra the cutoff parameters can be obtained from the RDFs. An *n*-fold ring represents a closed *n* step path within a crystal lattice or the disordered network of an amorphous solid. If the focus is directed mainly to the topological properties, it is common practice to use the terms vertices instead of atoms, and edges instead of bonds to characterize disordered network structure. In general there is no size limit for an n-fold ring. However, the requirement of a topological shortest path or *smallest* ring ensures that only rings are considered that cannot be decomposed into a *sum* of shorter closed paths by considering the path between any two atoms of the ring. Rings that fulfill the above requirements are called to be *primitive* or *irreducible* [100, 115–117]. By definition a primitive ring cannot be decomposed into smaller rings.

Besides the irreducibility criterion for primitive rings, different *shortest path* definitions for topological rings have been proposed in literature (see reference [100]). The most common definitions have been given by King [118] and Guttman [119]. In general, the characteristics of the ring size distribution in an amorphous solid will depend on the applied definition of topological rings and should be compared to ring distributions, obtained from differing definitions, with caution.

4. Results and discussion

4.1. Coordination numbers

The *average* coordination numbers of the investigated VASP as well as DFTB a-$Ti_xSi_{1-x}O_2$ structure models are visualized

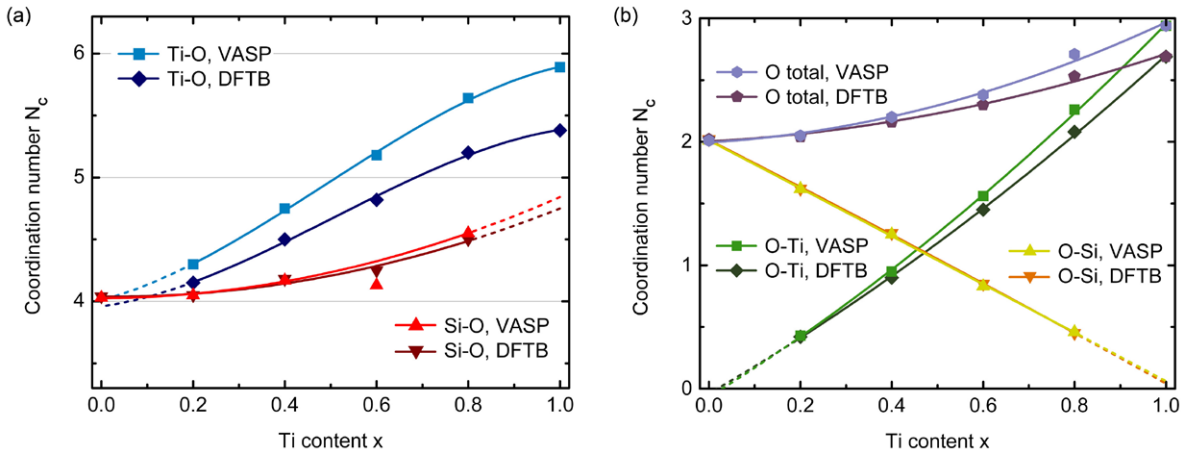

Figure 6. Conventional total and partial coordination numbers of Ti, Si, and O ions in a-$Ti_xSi_{1-x}O_2$ hybrid oxides (VASP and DFTB geometries). The trend lines were fitted by a third order polynomial for the Ti ion coordination by oxygen and by second order polynomials for all other coordinations. Dotted lines indicate extrapolations of the fitted trend lines.

in figure 6. Since all atomic bonds in the amorphous networks show an oxide-type cation-anion bonding behavior, i.e. the absence of cation-cation and anion-anion bonds, the total Ti and Si coordination numbers are given by their particular O coordination. The cutoff parameters of r_{cut}[Ti] = 2.4 Å for Ti–O bonds and r_{cut}[Si] = 2.1 Å for Si–O bonds, considered in the coordination number analysis, have been chosen based on the minima of the partial pair distribution functions discussed below. For the oxygen ions both the total as well as the partial coordinations by Ti and Si have been considered.

To begin with, we examine the coordination properties of the a-$Ti_xSi_{1-x}O_2$ VASP structure models. In pure a-SiO_2 the total Si coordination number of $N_{C_{Si}} = 4.03$ indicates a virtually perfect tetrahedral coordination. At low Ti content ($\leqslant$20%) the average coordination number of the Si ions increases marginally. The Si coordination number increases nonlinear with the Ti content. In order to estimate the the dependence of the coordination number on the composition parameter, we have fitted the Si coordination number by a second order polynomial. However, since the Si coordination number of the a-$Ti_{0.6}Si_{0.4}O_2$ VASP structure model seems to be artificially low ($N_{C_{Si}}[0.6] = 4.13$) and no other anomalies with respect to the fitted trend lines has been observed, we have excluded this point from the data fitting. The data fitting results in a coordination number of $N_{C_{Si}}[0.6] = 4.32$. The estimated coordination for an equimolar Ti/Si composition is $N_{C_{Si}}[0.5] = 4.24$. For the highest calculated Ti content of $x = 0.8$ the Si coordination increases to 4.55 and the extrapolation towards a very dilute Si dispersion indicates a coordination number around ~4.8 at very high Ti content. However, it is not possible to estimate weather the higher coordination state of the Si ion is the result of a large fraction of locally fivefold coordinated Si ions or the results of averaging the coordination states of the tetrahedrally coordinated Si_{4c} ions and a small fraction of c-TiO_2 like sixfold coordinated Si_{6c} ions.

The Ti coordination in the a-$Ti_xSi_{1-x}O_2$ VASP structure models shows a qualitatively different trend than the Si coordination number. The overall dependence on the composition parameter x is nonlinear but rather cubic than quadratic. At the lowest calculated Ti content the Ti coordination number is $N_{C_{Ti}}[0.2] = 4.30$. The extrapolation towards very dilute Ti concentrations indicate that a single Ti ion inserted into an a-SiO_2 matrix might preferably adopt a fourfold coordination state. For an equimolar composition the estimated coordination number of $N_{C_{Ti}}[0.5] = 4.97$ reflects almost the average of the tetrahedral and octahedral coordinations of crystalline TiO_2 and SiO_2. However, similar to the Si ions, it is not clear to what extend this number represents a superposition of TiO_4 and TiO_6 building blocks or the formation of fivefold coordinated TiO_5 units. At very high Ti content, the coordination of the Ti ion tends to saturate below the crystalline sixfold coordination. The calculated coordination number of pure a-TiO_2 is $N_{C_{Ti}}[1.0] = 5.89$. Thus, the Ti coordination number almost covers the entire coordination range between the two crystalline coordination limits. The averaged coordination numbers clearly illustrate the existence of under-coordinated Ti ions even in pure a-TiO_2. Thereby, it is not indicated wether the lower coordination numbers are related to four- or fivefold coordinated Ti_{4c} or Ti_{5c} ions in general. Only for dilute Ti ion concentrations, the occurrence of fourfold coordinated Ti_{4c} ions has been confirmed without doubt by the analysis of the average coordination numbers.

The fact that Ti might reach a fourfold coordination state but not the sixfold coordination of the crystalline TiO_2 rutile phase, that exhibits the same mass density, points towards the qualitative different types of atomic order characteristics in TiO_2 and SiO_2. The tetrahedral SiO_4 units in a-SiO_2 are sufficiently *stiff* to prevent a predominant fraction of Si ions from changing their coordination state by the influence of topological disorder. Therefore, in low Ti content a-$Ti_xSi_{1-x}O_2$ the Ti ion is preferably incorporated in form of TiO_4 units that, despite their larger size, can be incorporated into the relatively open-porous amorphous framework of the dominating SiO_2 component without the need for large readjustments of the amorphous network due to an increased connectivity of a higher coordinated cation. In the case of high Ti content a-$Ti_xSi_{1-x}O_2$ and pure a-TiO_2, that represent rather dense solid material phases, the topological disorder of the amorphous

network is predominantly mediated by changes in the local atomic coordination environment of the Ti ions, especially the occurrence of under-coordinated Ti ions, which basically prevents the reaching of a crystal-like coordination.

The total coordination number of oxygen changes nonlinear from an almost perfect ($N_{Co}[0.0] = 2.01$) twofold Si_{2c} crystal type coordination state in pure a-SiO_2 to $N_{Co}[1.0] = 2.94$ which is close to the O coordination in crystalline TiO_2. However, equivalent to the Ti ions, the crystal-coordination state is not entirely reached. For a composition parameter of $x = 0.5$ the decomposition into partial contributions from Ti and Si ions indicates that this nonlinear behavior is due to changes in the partial coordination by Ti ions, while the O–Si coordination decreases linearly with the Ti content from $N_{Co-Si}[0.0] = 2.01$ to $N_{Co-Si}[0.8] = 0.46$ which practically extrapolates linearly to zero. An equal coordination of O ions by Ti and Si ions is observed slightly below an equimolar composition at $x = 0.46$. The nonlinear increase in the O coordination number might also be seen as a first fingerprint of edge-linked coordination-polyhedra building blocks that are formed progressively with increasing mass density between higher coordinated cations.

Qualitatively, the DFTB geometries show practically identical trends in the coordination numbers of a-$Ti_xSi_{1-x}O_2$. Nevertheless, looking at the Ti–O coordination, the O-Ti coordination respectively, it is obvious that the DFTB structure models show substantial differences to the VASP post relaxed geometries. The DFTB coordination number of $N_{Ti}[1.0] = 5.38$ indicates half an electron less within the fixed cutoff radius around the Ti ions in pure a-TiO_2. This difference reduces to ∼0.15 at a Ti content of 20 mol% . Extrapolation further indicates a DFTB Ti–O coordination slightly below fourfold for a very dilute TiO_2 component. As a consequence of the reduced Ti–O coordination in the DFTB structure models, also, the O–Ti coordination is reduced compared to the VASP geometries. This reduction becomes observable around a Ti content of ∼30 mol% and increases to 0.25 Ti ions in the first O coordination sphere in pure a-TiO_2. In contrast to the Ti–O and the O–Ti coordination numbers, the Si ion related coordination numbers nearly agree for both numerical approaches. While the O–Si coordination is identical in both simulation approaches, the O–Si coordination tends to marginally lower values in the high Ti content regime. In turn, this effect seems to be related to the lower connectivity of the lower coordinated Ti ions in the DFTB geometries. The calculated difference between the VASP and DFTB geometries is 0.05 at a composition parameter of $x = 0.8$. The extrapolation towards pure a-TiO_2 indicates a maximum Si coordination around ∼4.7, which is only ∼0.1 below the value estimated for the VASP post-relaxed model.

The differences between then VASP and DFTB structure models may have different origins. On the one hand, the DFTB structure models of a-$Ti_xSi_{1-x}O_2$ represent room temperature (300 K) geometries while the VASP post-relaxed structures formally represent the 0 K limit. Thus, the DFTB geometries are influenced by thermally induced fluctuations of the amorphous network, the local coordination state of Ti ions respectively. On the other hand, the structural properties are subject to the different numerical description within the VASP-DFT and DFTB schemes. Differences in the DFTB approach most likely represent influences from the parametrization of interatomic pair interactions within Slater-Koster integral tables [93]. Since both, DFTB and VASP seem to describe different Ti coordination environments the question arises which unit-cell representations better reproduces the structural characteristics of a-$Ti_xSi_{1-x}O_2$ hybrid oxides. To answer this question, we have analyzed the coordination statistics of an a-TiO_2 structure model, that has been generated by DFT Car-Parrinello molecular dynamics (CPMD) under conditions similar to the DFTB molecular dynamics of this study. [3]

The properties of this CPMD structure model have been discussed in detail elsewhere. [98, 99] Adopting the same cutoff parameters used above, the coordination numbers of Ti and O ions in the CPMD structure model are 5.94 and 2.97 which is in excellent agreement to the respective VASP geometry coordination numbers of 5.89 and 2.94. Hence, it seems unlikely that the coordination number differences between the VASP and DFTB generated a-TiO_2 models are primarily related to temperature induced changes in the amorphous framework.

We further have to compare the generated structure models to published experimental data on a-TiO_2. Published experimental coordination numbers depict a quite inconclusive picture on the a-TiO_2 coordination properties. Petkov *et al* [159] reported coordination numbers of sputtered a-TiO_2 layers as well as a-TiO_2 bulk powder samples. The Ti–O coordination number of amorphous bulk TiO_2 powders of 5.6 ± 0.4 is found to be in reasonable agreement with the calculated Ti–O coordination number of 5.89 for the VASP geometry. In contrast, the coordination number of 5.4 ± 0.4 for sputtered a-TiO_2 layers is in excellent agreement to the calculated DFTB geometry Ti–O coordination of 5.38. Thus, there is no distinct answer to the above question which approach is more suited to model the amorphous phases. In addition, some uncertainty remains due to missing information on the mass density of the prepared amorphous samples. Since the amorphous state of a solid is not defined by a specific atomic configuration, rather, from an experimental point of view, as the result of a samples preparation history, the direct comparison between experiment and theory might be seen as an ambiguous task, as long as preparation and simulation conditions do not match in detail. In fact, both simulation approaches seem to represent diverse facets of short-range disorder in the a-TiO_2 and in the same way the a-$Ti_xSi_{1-x}O_2$ networks.

The close agreement in Si–O and O–Si coordination numbers of VASP and DFTB geometries in low Ti content a-$Ti_xSi_{1-x}O_2$ clearly originates from the stiffness of the tetrahedral SiO_4 units that seem to be insensitive with respect to the applied simulation approach.

[3] The CPMD calculations were performed using norm-conserving pseudopotentials of the Troullier-Martins type [156, 157] and the Becke88 exchange functional [158]. The total simulation time of 8.6 ps was discretized by 51 000 steps to ensure energy convergence. At the beginning and the end of the cooling thermal equilibration phases of 4000 steps at 5000 K and 5000 steps at a room temperature of 300 K have been performed. In between an exponential-like cooling path, approximation by a suitable stepwise function was applied. A Nóse–Hoover thermostat ensured the conditions of a canonical ensemble and the volume was kept constant.

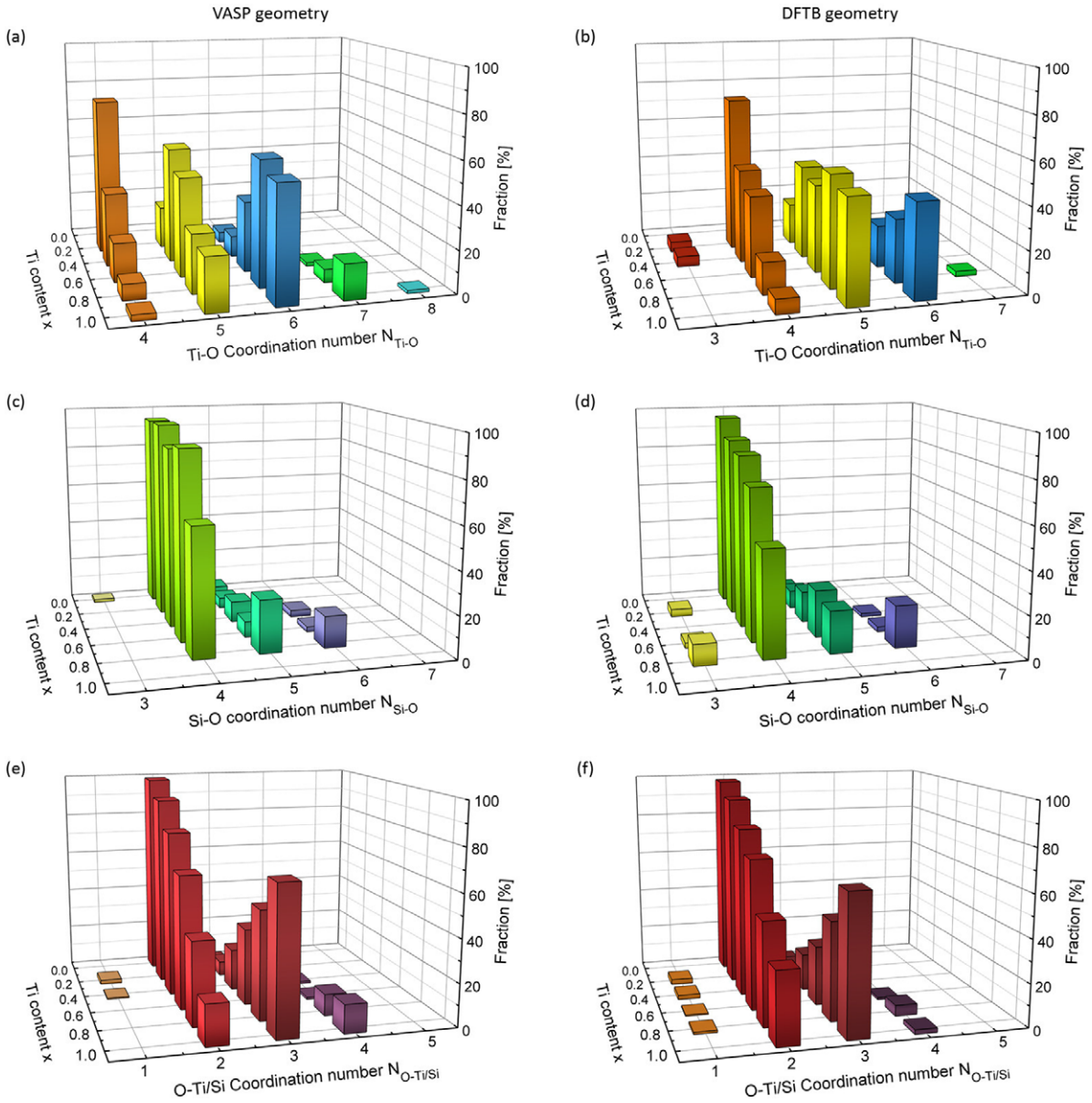

Figure 7. Bar diagram of the distribution of local coordination states in the a-$Ti_xSi_{1-x}O_2$ VASP (left) and the DFTB (right) geometries. See table 1 as well as figures 2, 3, and 4 for additional data.

In summary, the overall increase in the cation coordination-numbers, observed in both the VASP and the DFTB geometries, means that some of the Ti and Si ions experience a change in the local atomic O ion coordination state. This observation has led to the question; if the increase of the coordination numbers is the result of Ti in tetrahedral and Si in octahedral lattice sites or if considerable amounts of intermediate fivefold coordination states are formed in the disordered frameworks of a-$Ti_xSi_{1-x}O_2$ hybrid oxides. Since this information is not contained in the average coordination numbers, we have used the coordination polyhedra analysis to study the character of the local atomic coordination state in more detail.

4.2. Local coordination numbers

The fractional distributions of the local ion-coordination states in the a-$Ti_xSi_{1-x}O_2$ VASP and DFTB geometries are illustrated in figure 7. Additionally, detailed coordination-polyhedra illustrations of the a-$Ti_xSi_{1-x}O_2$ VASP geometries are given in figures 2, 3, and 4. In contrast to the coordination number statistics above, the detailed analysis of the local atomic coordination states reveals short-range order features within the amorphous network that are commonly hidden by the averaging procedure.

Starting with the Ti–O coordination in the VASP geometry of pure a-TiO_2, the local coordination numbers indicate a much more diverse short-range order than might be expected from the Ti–O coordination number of ($N_{C_{Ti}}[1.0] = 5.89$). In fact, only slightly more than half of all Ti ions ($\sim$ 54%) preserve their crystalline coordination state. All other Ti coordination states arise from *coordination defects* that increase or decrease the local atomic coordination by ±1 or ±2. Significant fractions of Ti ions are found in a fivefold (25%) and a sevenfold ($\sim$ 17%) coordination environment. Even $\sim$3% and $\sim$1%

of the Ti ions respectively reside in TiO_4 and TiO_8 units. In sum, the slight prevalence for under-coordinated structural building blocks in the disordered polyhedra network results in the reduced coordination number of a-TiO_2 compared to TiO_2 in low-pressure crystal phases.

A similar distribution of local TiO_n coordination polyhedra in a-TiO_2 has been reported by Van Hoang [163, 164] on the basis of MD simulations using the Matsui and Akaogi (MA) force field [165] to simulate the structural properties of liquid and amorphous TiO_2. At 4.20 g cm^{-3} (3000 atom unit cell, 350 K) TiO_5, TiO_6 and TiO_7 fractions of 11%, 75%, and 14% have been observed. Even some minor contribution from TiO_8 units (<1%) has been reported. Tetrahedral TiO_4 building blocks were only reported at a lower mass density of 3.80 g cm^{-3} with a fraction <1% . In accordance with the higher fraction of sixfold coordinated units, the reported average Ti–O coordination number of 6.03 slightly overestimates the octahedral crystal limit and our value of 5.89.[4]

The a-$Ti_{0.8}Si_{0.2}O_2$ hybrid oxide structure model is characterized by a decrease of over-coordinated TiO_n structural units in favor of an increasing fraction of tetrahedrally coordinated Ti ions. However, the basic coordination-polyhedra distribution still resembles the distribution in pure a-TiO_2. The minor fraction of TiO_8 building blocks vanishes completely and the fraction of the TiO_7 unit decreases from ∼17% to ∼6% . The TiO_4 building block fraction is found to increase to ∼8% . For the two main-coordination states, sixfold and fivefold, a slight increase compared to pure a-TiO_2 is observed. The fraction of crystal-like coordinated Ti_{6c} ions increases to ∼59% and the fraction of intermediate coordinated Ti_{5c} ions to ∼28% . First qualitative differences in the distribution of TiO_n coordination polyhedra occur in the a-$Ti_{0.6}Si_{0.4}O_2$ oxide alloy. At this composition the ∼47% fraction of TiO_5 building blocks becomes the predominant coordination state. Only one third of all structural units shows the sixfold coordination of TiO_2 crystals. TiO_7 building blocks are just found sporadically (∼ 2%). The fraction of tetrahedrally coordinated structure units is more than doubled to ∼18% . For a composition parameter of $x = 0.4$, the fivefold coordination reaches its maximum. 55% of all Ti ions show the intermediate coordination state. The fraction of TiO_4 building blocks increases to 35% while the sixfold coordinated crystal-type building blocks reduce to 10% . Finally, the 20 mol% Ti containing oxide alloy is dominated by the fourfold coordination state with a predominant fraction of 75% . The number of Ti ions in an intermediate fivefold coordination state collapses. Only 20% are incorporated into TiO_5 building blocks. The sixfold crystal coordination state becomes quite exceptional with a minor fraction of 5 % .

Compared to empirical potential MD results of Bernard *et al* [120] for titania-silica glasses, the Ti coordination environment in our structure models stronger favors the fourfold coordination state at low Ti content (20 mol%). The reported fractions of 42%, 54%, and 4% for locally fourfold, fivefold, and sixfold coordinated Ti ions indicate a slight preference for the formation of TiO_5 units over the tetrahedral coordination in TiO_4 building blocks while our data indicate TiO_4, TiO_5, and TiO_6 fractions of 75%, 25%, and 5% . This difference, in particular is, remarkable since the optimized density of the 20% Ti oxide alloy of 2.29 g cm^{-3} is notably smaller than our simulation density of 2.60 g cm^{-3}. Consequently, the average Ti coordination by O ions of 4.61 exceeds our calculated value of 4.3 significantly. A dominance of fourfold coordinated Ti_{4c} ions was observed for Ti concentrations as low as 7.8 mol% . An even more pronounced dominance of fivefold coordinated Ti_{5c} ions with a fraction of 60% over Ti_{4c} and Ti_{6c} ions with percentages of 30% and 10%, respectively, was observed at an equimolar Ti/Si alloy composition at a mass density of 2.50 g cm^{-3}. This distribution of local Ti coordination states closely resembles the coordination polyhedra distribution observed in the a-$Ti_{0.4}Si_{0.6}O_2$ VASP geometry. A general tendency towards the predominant formation of TiO_5 units (53%) at a composition close to $x = 0.2$ has also been reported in a preceding empirical potential MD study by Rosenthal and Garofalini for structure models generated with a low cooling rate [85]. At a higher cooling rate, a fourfold local coordination environment has been found to be the prevalent coordination state of Ti ions with a fraction of 55% .

In summary, the overall distribution of coordination polyhedra indicates a *richer*, more flexible Ti ion coordination environment in Ti-rich a-$Ti_xSi_{1-x}O_2$ hybrid oxides. With decreasing Ti content, the Ti ions progressively adapt the dominant fourfold coordination state of the amorphous matrix of the SiO_2 *host* material. In addition, an average Ti coordination number close to the sixfold crystalline coordination is by far no evidence for an amorphous network that is predominantly formed by (distorted) octahedron building blocks.

As already indicated in the average coordination number for pure a-SiO_2, the predominant fraction of Si ions is fourfold coordinated. The dominant fraction of SiO_4 building blocks (∼ 94%) is attended by minor fractions of under-coordinated Si_{3c} and over-coordinated Si_{5c} ions in SiO_3 (∼ 1%) and SiO_5 (∼ 4%) building blocks. Due to the small preference of over-coordinated Si_{5c} ions against under-coordinated Si_{3c} ions, the mean Si coordination exceeds the common fourfold crystal coordination marginally. Similar to the high Ti content ternary oxides, the high Si content a-$Ti_xSi_{1-x}O_2$ hybrid oxides ($x \leqslant 0.2$) show a coordination-polahedra distribution similar to the pure amorphous phase. The crystal-type fourfold coordination remains almost constant at 95% . All remaining Si ions show the intermediate fivefold coordination state. For lower Si contents of 60%($x = 0.4$) and 40%($x = 0.6$) the fraction of SiO_4 building blocks decreases slightly, but not continuously, to ∼87%($x = 0.4$) and 90%($x = 0.6$), respectively. Simultaneously, larger fractions of SiO_5 units (10% for $x = 0.4$ and ∼8% for $x = 0.6$) are found. Furthermore, the incorporation of 40% and 60% Si ions, respectively, promotes the formation of a new highly coordinated Ti-like coordination state for Si ions. Approximately ∼3% of the Si ions form octahedrally coordinated SiO_6 units. The lowest Si content a-$Ti_{0.8}Si_{0.2}O_2$ structure model is the only ternary oxide whose

[4] The difference in the average coordination number is partially related to the applied cutoff parameter. In contrast to our study, a marginally larger Ti–O correlation cutoff was applied. Compared to our value of 5.89 reported above, a slightly larger coordination number of 5.96 is obtained using the same cutoff parameter of 2.5 Å to estimate the average Ti–O coordination state.

local coordination characteristics show notable differences in the Si coordination-polyhedra distribution. The crystal-type fourfold coordination is reduced abruptly from the ∼90–95% in the Si richer ternary oxides to *only* 60% . In addition, the fractions of over-coordinated Si ions in SiO_5 and SiO_6 building blocks increase to 25% and 15%, respectively.

Altogether, the local Si coordination numbers indicate that tetrahedrally coordinated Si_{4c} ions are very robust with respect to changes in the chemical composition of SiO_2/TiO_2 hybrid oxides. Only in the presence of a large number of higher coordinated Ti ions and a significantly increased mass density of the hybrid-oxide alloy, the fractions of over-coordinated Si ions in an intermediate fivefold coordination state as well as a c-TiO_2 type sixfold coordination state increase notably. Up to now, preceding numerical studies on Ti containing SiO_2 glasses have paid less attention to the possible changes in the Si coordination environment that possibly might occur in Si rich a-$Ti_xSi_{1-x}O_2$ hybrid oxides.

The local coordination environment of O ions in the a-$Ti_xSi_{1-x}O_2$ VASP geometries shows a continuos transition of the predominant coordination state from a c-SiO_2 type twofold coordination to a c-TiO_2 type threefold coordination. In pure SiO_2, ∼99% of the O anions are twofold coordinated as expected from the fourfold coordination of the Si cations. The fraction of twofold coordinated O ions decreases nonlinearly to ∼19% in a-TiO_2. Simultaneously, the fraction of threefold coordinated O ions increases from ∼1% in pure a-SiO_2 to ∼68% in pure a-TiO_2. The crossing point of nonlinear (second order polynomial) fits for the fractions of two- and threefold coordinated O ions indicates equal contributions from $O(Ti,Si)_2$ and $O(Ti,Si)_3$ building blocks in the Ti rich regime around $x = 0.76$. While onefold coordination states of O ions are generally not observed in the two binary oxides, they occur in the lower Ti content VASP geometries. In the a-$Ti_{0.2}Si_{0.8}O_2$ hybrid oxide 2% of all oxygen atoms are onefold coordinated by a Ti ion. For a composition parameter of $x = 0.4$ this fraction reduces to <1%. In addition, the a-$Ti_{0.4}Si_{0.6}O_2$ alloy is the first structure that indicates the existence of a fourfold O ion coordination state with a fraction of 1%. The fraction of $O(Ti,Si)_4$ building blocks remains constant for 60 mol% of Ti ions, rises abruptly to 10% for an Ti content of 80 mol% and reaches ∼13% in pure a-TiO_2.

In general, the local coordination of O ions gives a complementary view on the local coordination characteristics. Again, the fact that ∼32% of O ions in a-TiO_2 differ from the threefold coordination state but only ∼1% of O ions in a-SiO_2 deviates from a twofold coordination state implies a more flexible bonding environment in the denser and higher coordinated framework of a-TiO_2. The general occurrence of onefold Ti coordinated O states (O_{1c}) in the ternary oxides demonstrates that the disordered hybrid-oxide frameworks are locally limited in their ability to adapt completely to the higher connectivity of the Ti ion. Thus, a non-bridging O ion in the disordered hybrid-oxide network might be accepted, even if energetically unfavorable, in favor of the network connectivity and to sustain the mid-range order within the amorphous solids.

The coordination numbers of the a-$Ti_xSi_{1-x}O_2$ DFTB geometries indicated a substantially reduced average coordination number for the Ti ion. Indeed, the local coordination environment of the Ti ion (see figure 7(*b*)) is the only element that shows pronounced coordination state changes in the DFTB structure models with respect to the VASP geometries.

While the main coordination type changes from fivefold to sixfold as a result of the increasing Ti content in the VASP geometries, all Ti containing DFTB structure models predict TiO_5 structure-building blocks as the largest coordination-polyhedra fraction. Even in pure a-TiO_2 a slight preference for fivefold coordinated TiO_5 units (∼ 49%) over TiO_6 units (∼ 44%) is observed. With decreasing Ti content the fraction of octahedrally coordinated Ti ions decrease almost linearly to 5% in a-$Ti_{0.4}Si_{0.6}O_2$. For a composition parameter of $x = 0.2$ no TiO_6 structure units are found. The fraction of intermediate fivefold coordinated states represents not only the largest structural building block in all ternary oxides but also remains roughly constant over a wide composition range with percentages of ∼53% for $x = 0.8$, ∼42% for $x = 0.6$, and 45% for $x = 0.4$. Between a Ti content of 40 and 20 mol% the fraction of intermediate coordinated Ti ions drops abruptly to 20% . This sharp drop in the fivefold coordination of Ti ions is connected to a simultaneous increase of tetrahedrally coordinated Ti_{4c} ions (75%), similar to the observations for the VASP geometries. In addition, pronounced differences between both approaches are found for the over and under-coordinated extreme coordination states, namely threefold, sevenfold and eightfold coordinated Ti ions and threefold and sixfold coordinated Si ions. The DFTB structure models indicate the possible occurrence of strongly under-coordinated Ti ions in TiO_3 building blocks at low Ti contents ($x = 0.2$ and $x = 0.4$) that could not be observed in the VASP geometries. Equally, characteristic differences occur for structurally highly coordinated Ti ions. Not only the exceptional eightfold coordination is absent also the sevenfold coordinated Ti_{7c} ions have almost completely vanished. Only the DFTB structure model of a-$Ti_{0.8}Si_{0.2}O_2$ contains a minor fraction of <3% of TiO_7 building blocks. The decrease of tetrahedrally coordinated Si ions with increasing Ti content is more continuous in the DFTB geometries. In addition, the percentage of SiO_4 building blocks in the Ti rich ternary oxides is stronger reduced. For $x = 0.8$ the fraction of SiO_4 units reduces to 50% . A stronger DFTB geometry preference for fivefold coordinated SiO_5 building blocks is indicated in the mean composition range with a maximum of ∼23% SiO_5 units in a-$Ti_{0.6}Si_{0.4}O_2$. The distribution of c-TiO_2 like coordinated Si_{6c} ions is very similar in both numerical approaches. Only for a very high Ti content ($x = 0.8$) an slight increase of SiO_6 units to 20% is observed. Under-coordinated SiO_3 building blocks are not any longer limited to pure a-SiO_2. Threefold coordinated Si ions are contained in the DFTB geometries with a fraction of ∼4% for $x = 0.2$ and ∼3% for $x = 0.6$. In case of a-$Ti_{0.8}Si_{0.2}O_2$ an unexpected large fraction of 10% SiO_3 units is found. In sum, both the occurrence of threefold coordinated Si_{3c} ions at high Ti content and the larger percentage of octahedrally coordinated Si_{6c} give the picture of a more versatile Si coordination environment in the DFTB optimized geometries. The differences in the local coordination state occur despite the quite similar average coordination numbers (see figure 6).

Qualitatively similar to the VASP geometries, the fraction on twofold coordinated O_{2c} ions decreases nonlinearly from ∼98% in pure a-SiO_2 to ∼33% in pure a-TiO_2 and the percentage of threefold coordinated O_{3c} ions increases (nonlinear) from ∼2% in pure a-SiO_2 to ∼65% in pure a-TiO_2. The transition point from a prevalently twofold coordination state to a prevalently threefold coordination state of O ions is estimated at a composition parameter of $x = 0.84$. Compared to the VASP geometries, the fraction of twofold coordinated O_{2c} ions is less strongly reduced in the DFTB geometries at high Ti content. In view of similar fractions of O_{3c} ions for both structure-model types, this difference is mainly due to the preference for twofold coordinated structural units against fourfold coordinated O_{4c} ions. The percentage of tetrahedrally coordinated O_{4c} ions is notably reduced in the DFTB structure models for high Ti contents. In pure a-TiO_2 only ∼2% of the O ions show a fourfold coordination state compared to ∼13% in the VASP structure. In contrast to the VASP geometries, all ternary oxide structure models show minor contributions from onefold coordinated (predominantly by Ti ions) O_{1c} ions. Thus, the existence of a onefold coordination state of the O anion is not necessarily limited to the low Ti content composition regime of a-$Ti_xSi_{1-x}O_2$ hybrid oxides.

As stated above, we expect that the VASP and DFTB structure models represent slightly different types of topological disorder in the a-$Ti_xSi_{1-x}O_2$ oxide alloys. In sum, both simulation approaches indicate a diverse coordination environment within the investigated binary and ternary oxides that is characterized by composition dependent variations of the local atomic coordination-defect states. Significant contributions from single and multiple over- and under-coordinated ions are found in all hybrid oxides. Even the binary amorphous oxides show large fractions of non-crystal-type coordination states. This is especially true for a-TiO_2 where the local coordination of roughly 50% of all ions shows an over- or under-coordinated state. In addition, the intermediate fivefold coordination state of Ti seems to be found as likely as a fourfold or sixfold Ti coordination state. Considering the entire composition range, Ti ions are found in a manifold of coordination states with local coordination numbers n_c ranging from 3 to 8. Less degrees of freedom are observed for the Si ions with coordination numbers of $n_c = 3 \ldots 6$ and the local coordination numbers of O ions with $n_c = 1 \ldots 4$. While the total *mean* coordination numbers vary continuously with the composition parameter, changes in the local coordination environment can be much more pronounced and volatile. It is not possible to deduce details of the local coordination environment and thus the atomic structure of the amorphous framework from a simple analysis of conventional averaged coordination numbers. The general existence of over and under-coordinated coordination-defect states indicates that the local coordination environment of a particular chemical component not only depends on the favorable crystal-type coordination number but also on the local availability of binding sites within the disordered atomic network. Especially in the presence of distinct mid-range order characteristics, the formation of a favorable local coordination state competes with the involved distortions of the amorphous framework.

4.3. Coordination polyhedra

The (local) coordination number statistics revealed that the crystalline coordination states (tetrahedrally for SiO_2 and octahedrally for TiO_2, respectively) in amorphous a-$Ti_xSi_{1-x}O_2$ hybrid oxides represent the main coordination states only for the pure binary oxides as well as for the limits of very dilute ion distributions in the disordered framework of the host oxide (Si ions in TiO_2 and Ti ions in SiO_2, respectively). In addition to a pure coordination number based analysis of the local coordination environment, the classification of coordination polyhedra according to their basic *symmetry* types provides additional structural information in order to characterize the oxide-network topology. The occurrence of alternative symmetry types for a given coordination number might be seen as a direct consequence of the competing short-range and mid-range order. Thereby, the existence of various polyhedra types allows local coordination units to adapt to the distorted atomic framework in a more efficient way, without changing their preferential coordination state. Changes of the basic symmetry types of a coordination polyhedra are of particular interest in order to discover basic correlations between the atomic structure of amorphous solids and the electronic and optical material properties as well as their fundamental deviations from crystalline material phases.

In table 1 the fractions of particular geometry types (see figure 5) of coordination polyhedra for the a-$Ti_xSi_{1-x}O_2$ VASP geometries are listed. Among the various chemical species, the Si ions show less distinct variations in the coordination-polyhedra geometry types. In agreement with the fundamental SiO_4 coordination-polyhedron type in SiO_2 crystals, fourfold coordinated Si_{4c} ions in the a-$Ti_xSi_{1-x}O_2$ oxides show an extreme preference for tetrahedral [T-4]-type coordination polyhedra (see figures 3(*c*-6), 3(*d*-4)). In addition, [SS-4]-type coordination polyhedra represent an geometry type occurring sporadically (<2%) in pure a-SiO_2 and frequently (∼ 17%) for a dilute distribution of SiO_4 units in an a-TiO_2 matrix at a composition of $x = 0.8$ (see figure 4(*d*-6)). In the Ti-rich alloys, the distortions of [T-4]-type coordination polyhedra into a [SS-4]-type geometry allow a better adaptation of SiO_4 building blocks to the, in general, larger TiO_n coordination polyhedra. With exception of a-$Ti_{0.2}Si_{0.8}O_2$, the coordination polyhedra of fivefold coordinated Si_{5c} ions show an approximate 1 : 2 partitioning between a [SPY-5]-type and [TBPY-5]-type polyhedron shape (see figures 3(*d*-4) and (*d*-5)). Due to the minor dependence of this partitioning ratio on the actual polyhedra fraction, both symmetry types need to be considered as fundamental units for highly coordinated Si ions in general. The SiO_6 building blocks exclusively belong to the class of octahedron type [O-6] polyhedra (see figures 4(*c*-7) and (*d*-6)). Thus, the sixfold coordination environment of Si ions is identical in a-$Ti_xSi_{1-x}O_2$ alloys and the ultra dense SiO_2 crystal phases stishovite and seifertite.

Considering the fourfold coordination state of the Ti ion, it is obvious that in the case of larger fractions of fourfold coordinated Ti ions (>18%, $x \geqslant 0.4$) the main coordination-polyhedron type is the tetrahedron type [T-4] (see figures 3(*c*-5) and (*d*-3)). However, compared to Si_{4c} ions this preference

Table 1. Fractions of coordination polyhedra occurring in the a-$Ti_xSi_{1-x}O_2$ VASP geometries. Listed are the ion fractions that show a particular local coordination state of $n_c = 1 \ldots 8$ (see figure 7). The fractions of a particular geometry type (see figure 5) are given with respect to the total number of n_c-fold coordinated ions.

			Polyhedron fraction (%)					
Coordination	Ion	Polyhedron	$x = 0.0$	$x = 0.2$	$x = 0.4$	$x = 0.6$	$x = 0.8$	$x = 1.0$
$n_c = 1$	**O**			2.0	0.5			
		[SB-1]-[Ti]		100	100			
$n_c = 2$	**O**		98.6	91.0	78.5	63.0	39.0	18.8
		[HOA-2]-[Ti]		5.0	22.3	30.2	62.8	100
		[HOL-2]-[Ti]				0.8		
		[HOA-2]-[Si]	97.9	67.6	43.3	31.0	11.5	
		[HOL-2]-[Si]	2.1	0.5				
		[HEA-2]		26.4	34.4	37.3	25.7	
		[HEL-2]		0.5				
$n_c = 3$	**Si**		1.4					
		[TP-3]	100					
	O		1.4	7.0	19.5	36.0	51.0	68.1
		[TP-3]	100	28.6	27.5	22.2	19.6	19.4
		[TPY-3]		71.4	70.0	69.5	77.5	76.5
		[TS-3]			2.5	8.3	2.9	4.1
$n_c = 4$	**Ti**			75.0	35.0	18.3	7.5	2.8
		[TTBPY-4]		6.7	14.3			50.0
		[T-4]		73.3	57.1	81.8	33.3	50.0
		[SS-4]		20.0	28.6	18.2	66.7	
	Si		94.4	95.0	86.7	90.0	60.0	
		[TTBPY-4]	1.5					
		[T-4]	97.0	100	100	100	83.3	
		[SS-4]	1.5				16.7	
	O				1.0	1.0	10.0	13.2
		[T-4]					60.0	57.9
		[SS-4]			100	100	40.0	42.1
$n_c = 5$	**Ti**			20.0	55.0	46.7	27.5	25.0
		[SPY-5]		50.0	45.4	35.7	50.0	61.1
		[TBPY-5]		50.0	54.5	64.3	50.0	38.9
	Si		4.2	5.0	10.0	7.5	25.0	
		[SPY-5]	33.3	75.0	33.3	33.3	40.0	
		[TBPY-5]	66.7	25.0	66.7	66.7	60.0	
$n_c = 6$	**Ti**			5.0	10.0	33.3	58.8	54.2
		[PPY-6]						2.6
		[O-6]		100	25.0	75.0	76.6	56.4
		[TPR-6]			50.0	15.0	17.0	25.6
		[TPBPY-6]			25.0	10.0	6.4	15.4
	Si				3.3	2.5	15.0	
		[O-6]			100	100	100	
$n_c = 7$	**Ti**					1.7	6.3	16.7
		[PBPY-7]					100	83.3
		[MO-7]						16.7
		[MTPR]				100		
$n_c = 8$	**Ti**							1.4
		[TD-8]						100

for [T-4]-type coordination polyhedra is much less pronounced. The ternary oxides exhibit notable polyhedra fractions of $\gtrsim 20\%$ of [SS-4]-type units in all oxide alloys (see figures 3(*b*-2) and 4(*c*-4)) that are less common for Si_{4c} ions. In addition, [SS-4]-type polyhedra actually represent the dominating Ti_{4c} coordination-polyhedron type in the Ti rich alloys ($x = 0.8$) with a fraction of $\sim 67\%$ (see figure 4(*d*-5)). Thereby, the function of the [SS-4]-type coordination polyhedra in the hybrid oxides of higher density ($\geqslant 3.80$ g cm^{-3}) is basically the same for Si_{4c} and Ti_{4c} ions. In both cases the stronger geometry distortions of low coordinated polyhedra-building blocks are necessary in order to adapt to the surrounding larger polyhedra units of higher-coordinated ions. The [TTBPY-4]-type coordination state seems to be a sporadically occurring extreme distortion of the tetrahedral Ti coordination environment in the mixed alloys at lower mass density ($\leqslant 3.00$ g cm^{-3}). The coordination-polyhedra shapes of fivefold coordinated Ti_{5c} ions are roughly equally separated into [SPY-5]-type and [TBPY-5]-type coordination polyhedra. A slight prevalence for the trigonal bipyramidal [TBPY-5]-type is observed for a-$Ti_{0.6}Si_{0.4}O_2$ (see figure 4(*c*-6)) and for the truncated octahedron like [SPY-5]-type in pure a-TiO_2. The most common coordination type of Ti_{6c} ions is the crystal type [O-6] coordination polyhedron with a fraction of $\sim 56\%$ in pure a-TiO_2 (see figure 2(*d*-7)). In the low Si content a-$Ti_xSi_{1-x}O_2$ hybrid oxides ($x = 0.6, 0.8$) the fraction of [O-6]-type coordination polyhedra is usually even higher with a fraction of $\sim 75\%$. Sixfold coordinated Ti_{6c} ions at low Ti content always exhibit an octahedral crystal-like [O-6]-type coordination environment. With exception of a very dilute Ti distribution, also the distortion of TiO_6 building blocks into a trigonal prismatic geometry ([TPR-6]-type)

seems to be a fundamental but less frequently occurring (∼ 26% in pure a-TiO_2) structure characteristic of TiO_6 units (see figure 2(*d*-6)). Out of the two truncated pentagonal bipyramidal types [PPY-6] and [TPBPY-6] only the less symmetric second type (see figure 4(*d*-2)) occurs repeatedly for $x \geqslant 0.4$ with roughly half the frequency (∼ 15% in pure a-TiO_2) of [TPR-6]-type coordination polyhedra. [PPY-6]-type coordination polyhedra seem to be a rather exceptional structural unit that is only observed in the VASP optimized structure model of pure a-TiO_2. Altogether, sixfold coordinated Ti_{6c} ions show the most versatile coordination environments in a-$Ti_xSi_{1-x}O_2$ alloys and pure a-TiO_2. Sevenfold coordinated Ti_{7c} ions are predominantly found within [PBPY-7]-type geometrical units (100% in a-$Ti_{0.8}Si_{0.2}O_2$ and ∼83% in pure a-TiO_2) (see figures 2(*d*-4) and (*d*-5)). The monocapped versions of the octahedron ([MO-7]-type) as well as the trigonal prism ([MTPR-7]-type) are significantly less frequently observed (see figure 4(*d*-5)) . In pure a-TiO_2 the ratio of [PBPY-7]-type to [MO-7]-type coordination polyhedra is approximately 5 : 1. Only mono-capped prismatic [MTPR-7]-type coordination polyhedra are rather coincidentally observed for the 60 mol% Ti containing alloy. At all, only one (i.e. 1.4%) TiO_8 coordination-polyhedron building block, adopting a trigonal dodecahedron shape ([TD-8]-type), is observed for pure a-TiO_2.

The majority of twofold coordinated O_{2c} ions is arranged in homopolar angular [HOA-2] configurations. The sum of [HOA-2]-[Ti] and [HOA-2]-[Si] units is always ≳60%. Depending on the composition, notable fractions (between ∼ 26% and ∼37%) of O_{2c} ions in the ternary oxides show a heteropolar twofold coordination environment. O_{2c} ions in more linear homopolar and heteropolar configurations (bonding angles >177°) are extremely rare structure elements within the disordered oxide framework. In case of threefold coordinated O_{3c} ions $O(Ti,Si)_3$ units typically show a ≳70% fraction of pyramidal [TPY-3]-type coordination polyhedra. The corresponding close-to-planar structure type [TP-3] contributes with ∼20 to ∼29% to the TiO_3 coordination polyhedra, whereas the lower percentages are found in the Ti rich composition range. Also, some [TS-3]-type coordination polyhedra (one bonding angle >150°) are found at higher Ti content. The rarer $O(Ti,Si)_4$ coordination polyhedra exist in two configurations, the [T-4]-type and the [SS-4]-type. In the mid composition range ($x = 0.4$ and $x = 0.6$) the $O(Ti,Si)_4$ coordination polyhedra prefer the less symmetric [SS-4]-type shape. A percentage of 60% and ∼58% [T-4]-type coordination polyhedra is characteristic for fourfold coordinated O_{4c} ions in the denser high Ti content ($x = 0.8$) ternary oxides and pure a-TiO_2, respectively. In general, the formation of [T-4]-type $O(Ti,Si)_{4c}$ units necessitates a higher mass density than necessary for the formation [SS-4]-type $O(Ti,Si)_{4c}$ coordination polyhedra. The existence of O_{4c} ions is an indication for the formation of local cluster-like entities governed by edge-linked coordination polyhedra. These structure units are almost exclusively formed by TiO_n coordination polyhedra. An characteristic example of such a TiO_2 cluster is visualized in figure 4(*c*-6).

In summary, the detailed analysis of the individual coordination polyhedra demonstrates that disorder in binary and ternary a-$Ti_xSi_{1-x}O_2$ is not only related to changes in the local coordination numbers but also to variations in the basic coordination-polyhedron symmetry types for a given local coordination state. Thus, the shape information contained in the polyhedra geometries points towards an additional facet of topological disorder in amorphous oxides. Amorphous alloys do not necessarily contain only weakly distorted versions of a single crystal-like coordination polyhedron, rather various deformed polyhedra types coexist side by side. With respect to the well defined high-symmetry coordination polyhedra of the fourfold and sixfold coordinated cations in c-SiO_2 and c-TiO_2 these new polyhedra types might be characterized as *defective* coordination-polyhedra geometries. Thus, on an atomic level the topological disorder of an amorphous solid is not only visible as moderately distorted coordination polyhedra but also as a manyfold of coordination and geometry defects as well as their hybrid forms. This observation indicates a rich structure polymorphism of coordination polyhedra even aside from coordination number changes that is of fundamental importance for the physical properties of materials.

Taking the example of TiO_2, the polyhedra geometry in c-TiO_2 leads to distinct crystal-field splitting related variations in the electronic density of states and the optical response [98, 125, 160, 161]. This is especially true for the TiO_6 coordination polyhedra in the natural occurring c-TiO_2 phases rutile, anatase, and brookite, whose TiO_6 units represent D_{2h}, D_{2d}, and even C_1 distorted versions of an idealized O_h symmetric TiO_6 octahedron (see TiO_2 coordination polyhedra in figure 11). These octahedral units typically show a splitting of electronic states into t_{2g} and e_g like states that are well separated in energy and reflected in the optical response [125, 137]. In amorphous solids the electronic structure reflects a superposition of the energy-level alignments in the diverse local coordination units. In general, the existence of alternative coordination-polyhedra geometry types will lead to distinct differences in the local electronic structure and the optical response. Especially the notable amount of trigonal prismatic D_{3h} like coordination units, whose energy level alignments substantially deviate from the octahedral type crystal-field splitting in O_h like coordination units [138], will change the electronic structure and optical functions of the amorphous phase from their characteristic form in the crystal phases. In contrast to a-TiO_2, a-SiO_2 is not only insignificantly affected by the formation of notable amounts of coordination defects, but also only weakly affected by coordination-polyhedra polytypism since the topological disorder is preferentially mediated through the amorphous framework itself. In ternary hybrid oxides as a-$Ti_xSi_{1-x}O_2$, the mixture of the different atomic-order types of the individual binary oxides results in a coordination-number and coordination-polyhedra distribution with features qualitatively different from the binary phases due to the formation and alignment of new fundamental structure-building blocks.

4.4. Bond length and bond angle distribution

We have analyzed the composition and coordination dependent distribution of bond lengths and bond angles in the VASP

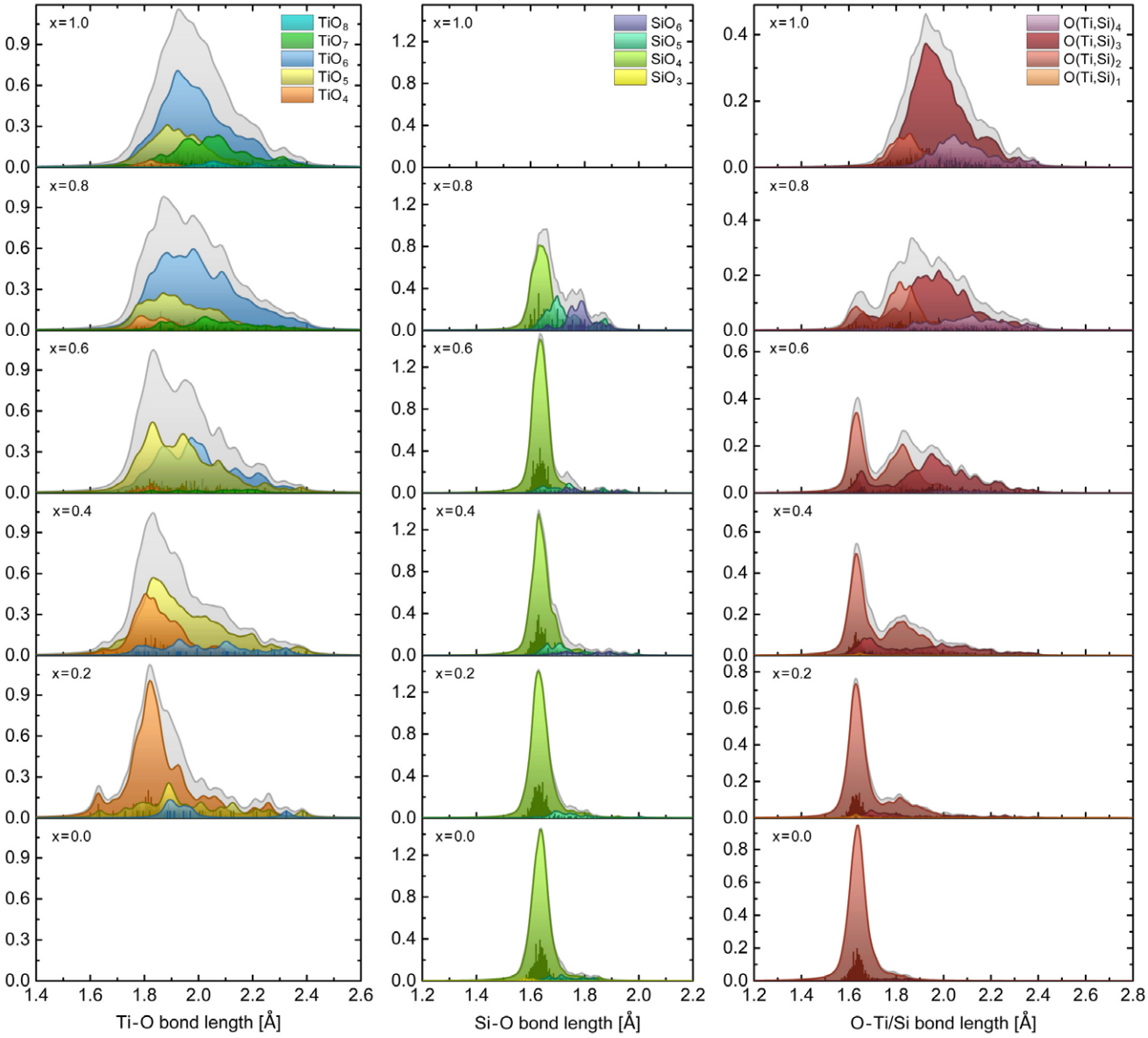

Figure 8. Total and local-coordination state decomposed Ti–O, Si–O and O-Ti/Si bond-lengths distributions in the a-$Ti_xSi_{1-x}O_2$ VASP geometries. The discrete line spectra are visualized as well as a continuos spectrum obtained by a Gaussian type line broadening.

relaxed structure models of a-$Ti_xSi_{1-x}O_2$, in more detail, in order to discuss the various types of coordination polyhedra, quantitatively. The figures 8 and 9 show discrete line spectra and broadened spectra of the distribution of bond lengths and bond angles for all existing local coordination states. The average bond lengths and bond angles are visualized in figure 10 and tabulated in tables 2–4 for Si, Ti, and O ions. In addition, tables 2–4 list the minimal and maximal values of bond lengths and bond angles.

The extraordinary stability of the tetrahedral SiO_4 units is reflected in the extremely sharp distribution of Si–O bond lengths and bond angles over a wide alloy-composition range. Despite the occurrence of higher Si coordination states and some disorder induced broadening effects on the SiO_4 bond length and angle distributions, the position of the central peaks does not change notably up to the the Ti richest alloy ($x = 0.8$). The average Si–O bond lengths of 1.639 ± 0.002 Å and the average O–Si–O bond angles of 108.9° ± 0.3° remain nearly constant over the entire composition range (see figures 10(*b*) and (*e*)). A similar independence on the Ti content, the alloy-mass density, is not observed for any other coordination state. It's interesting to note that the disorder induced distortions of tetrahedral SiO_4 units still increase the average Si–O bond length compared to the (average) Si–O bond length of 1.628 Å and 1.615 Å in the crystalline SiO_2 polytypes α-quartz and β-cristobalite (see figure 11). Nevertheless, individual Si–O bonds in the amorphous oxides can be significantly smaller than their crystal counterparts, as indicated by the minimal Si–O bond lengths of SiO_4 coordination polyhedra listed in table 2. In addition, the average SiO_3 unit bond length of 1.586 Å in pure a-SiO_2 is clearly smaller than the average bond length in any ordered or disordered fourfold coordinated polyhedron-building block. The average Si–O bond lengths of higher coordinated Si ions show a tendency to

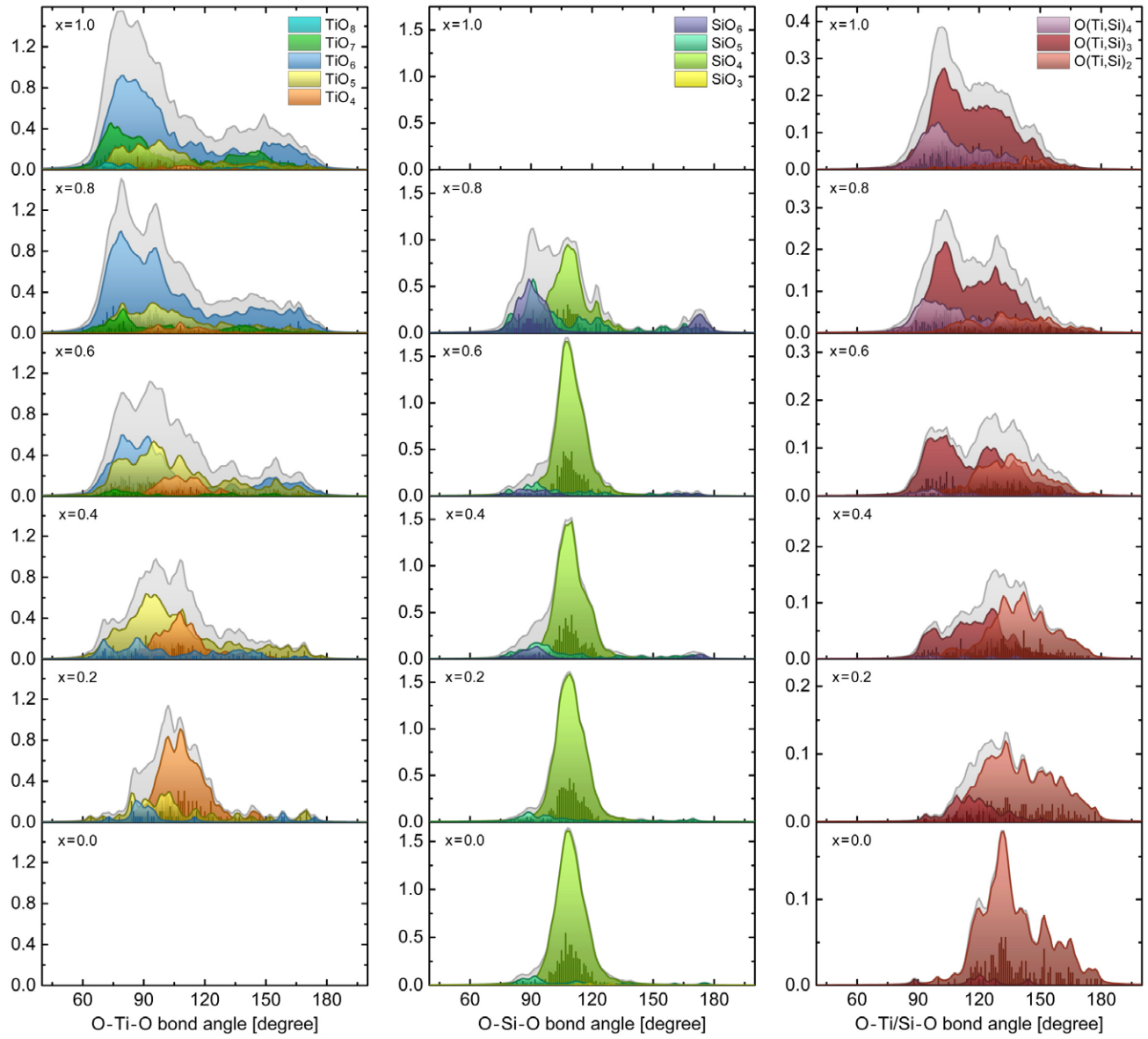

Figure 9. Total and local-coordination state decomposed O–Ti–O, O–Si–O and O-Ti/Si-O bond-angles distributions in the a-$Ti_xSi_{1-x}O_2$ VASP geometries. The discrete line spectra are visualized as well as a continuos spectrum obtained by a Gaussian type line broadening.

larger bond distances with both an increasing local coordination number and an increasing Si content. The average Si–O bond length in SiO_5 coordination polyhedra decreases from 1.737 Å in pure a-SiO_2 to 1.729 Å in a-$Ti_{0.8}Si_{0.2}O_2$ with a local maximum of 1.741 Å at a composition parameter of $x = 0.2$. For SiO_6 coordination polyhedra, the average Si–O bond length decreases almost linearly from 1.809 Å to 1.784 Å with increasing alloy-mass density. Altogether, the average bond lengths of Si–O bond pairs clearly separate the various local coordination states from each other (see figures 10(*b*)). In addition, this separation is nicely illustrated in figure 8 by the coordination dependent shift of the Si–O bond-length distribution peaks at a composition parameter of $x = 0.8$. The O–Si–O bond-angle distributions of high coordinated Si_{5c} and Si_{6c} ions, illustrated in figure 9, indicate that it might be quite difficult to separate angle contributions from fivefold coordinated units and a superposition of bond angles in tetrahedral and octahedral building blocks. Compared to SiO_4 units, the most notable difference of the bond-angles distributions of SiO_5 and SiO_6 units is the presence of O–Si–O bond angles around 90°. Right angles are characteristic to the bond angles between an apical O ion, the central Si ion, and an O ion from the equatorial planes in [TBPY-5]-type SiO_5 and [O-6]-type SiO_6 coordination polyhedra. The average bond angles in SiO_5 building blocks show a slight continuos decrease from 107.3° to 106.7° with increasing alloy density up to a composition parameter of $x = 0.6$. At higher Ti content ($x = 0.8$), the average bond angle increases slightly to 107.0°. No definite trend is observed in SiO_6 units average O–Si–O bond angles between 106.4° and 105.3°. This might be due to the relatively small number of SiO_6 coordination polyhedra in the oxide alloys. Nevertheless, the minimal average bond angle is found for the a-$Ti_{0.6}Si_{0.4}O_2$ alloy for both fivefold coordinated Si_{5c} ions and sixfold coordinated Si_{6c} ions.

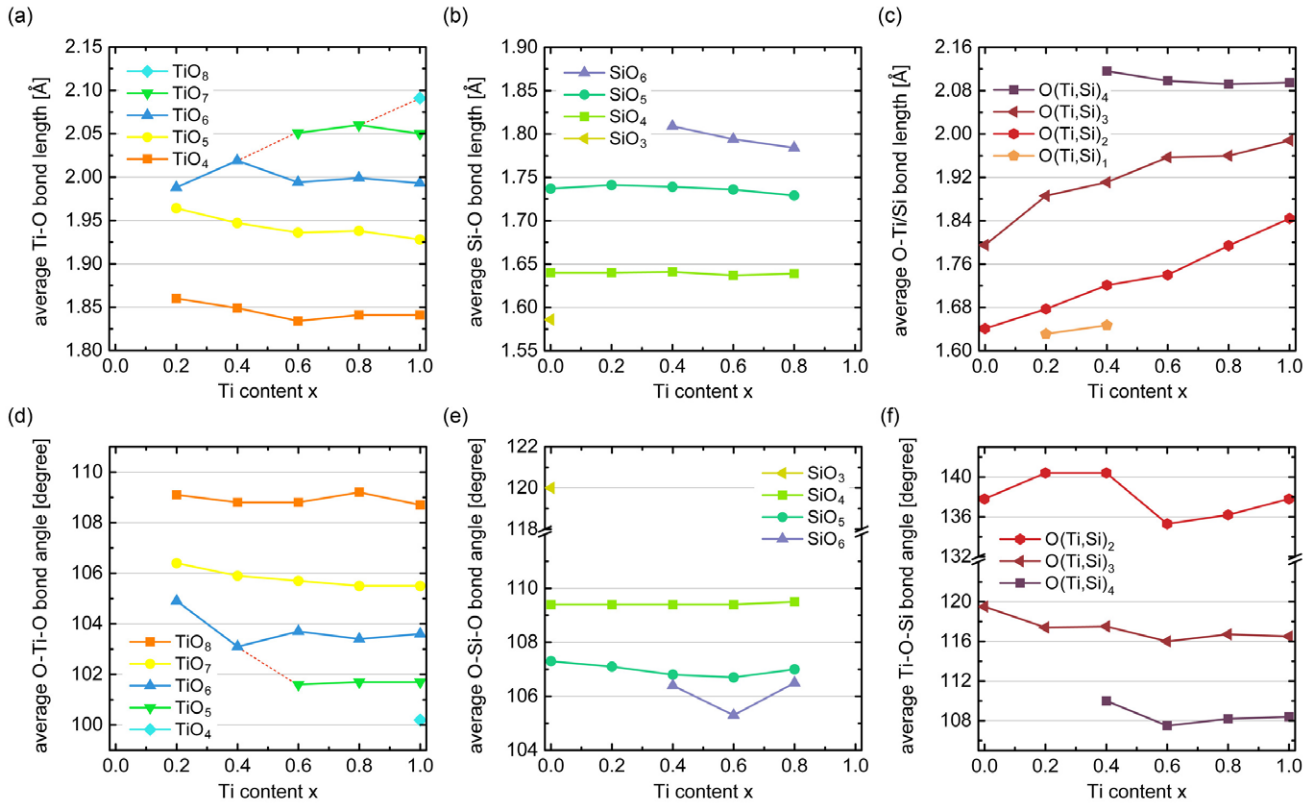

Figure 10. Average coordination polyhedra bond lengths (upper panels) and bond angles (lower panels) of the a-$Ti_xSi_{1-x}O_2$ VASP geometries. The dashed red lines in figures (*a*) and (*d*) are used to represent trends in the Ti–O bond length and O–Ti–O bond angles.

Table 2. Average Si–O bond lengths d_{ij}^{av} and O–Si–O bond angles φ_{ij}^{av} for the various coordination states of Si ions in the a-$Ti_xSi_{1-x}O_2$ VASP geometries. Values in brackets represent the corresponding minimal and maximal bond lengths and bond angles (d_{ij}^{min} / d_{ij}^{max}), (φ_{ij}^{min} / φ_{ij}^{max}), respectively.

	Bond lengths d_{ij} (Å) and bond angles φ_{ij} (degree)					
Ion	$x = 0.0$	$x = 0.2$	$x = 0.4$	$x = 0.6$	$x = 0.8$	$x = 1.0$
Si3c	1.586Å (1.572Å/1.607Å) 120.0° (112.8°/128.8°)					
Si4c	1.640Å (1.572Å/1.855Å) 109.4° (83.3°/138.6°)	1.640Å (1.568Å/1.923Å) 109.4° (92.5°/135.2°)	1.641Å (1.582Å/1.792Å) 109.4° (85.5°/129.3°)	1.637Å (1.586Å/1.731Å) 109.4° (92.6°/128.9°)	1.639Å (1.581Å/1.718Å) 109.5° (94.5°/133.2°)	
Si5c	1.737Å (1.651Å/1.837Å) 107.3° (82.7°/176.3°)	1.741Å (1.624Å/2.007Å) 107.1° (79.7°/170.1°)	1.739Å (1.633Å/1.993Å) 106.8° (76.2°/169.9°)	1.736Å (1.622Å/1.948Å) 106.7° (78.3°/171.3°)	1.729Å (1.631Å/1.879Å) 107.0° (78.7°/175.1°)	
Si6c			1.809Å (1.681Å/1.944Å) 106.4° (76.3°/174.9°)	1.794Å (1.731Å/1.923Å) 105.3° (76.4°/172.2°)	1.784Å (1.663Å/1.895Å) 106.5° (78.4°/177.5°)	

In summary, the SiO_m coordination polyhedra seem to participate rather passively in the formation of the amorphous frameworks of a-$Ti_xSi_{1-x}O_2$ hybrid oxides. The individual coordination units do not absorb significant fractions of atomic short-range disorder by strong distortions into the direct coordination environment of Si ions and the generation of new coordination-polyhedra geometry types. However, under extreme conditions the Si ions will actually respond to the increased network connectivity by increasing their coordination state in order to allow structure modifications of the amorphous framework on a mid-range order scale that affects the arrangement of coordination polyhedra over a few neighbor units.

Next, we consider the broader and substantially more complex distributions of Ti–O bond lengths and O–Ti–O bond angles (see figures 8 and 9). In general, the total distributions of Ti–O bond lengths and O–Ti–O bond angles closely follow the distributions of the dominant coordination

Table 3. Average Ti–O bond lengths d_{ij}^{av} and O–Ti–O bond angles φ_{ij}^{av} for the various coordination states of Ti ions in the a-$Ti_xSi_{1-x}O_2$ VASP geometries. Values in brackets represent the corresponding minimal and maximal bond lengths and bond angles (d_{ij}^{min} / d_{ij}^{max}), (φ_{ij}^{min} / φ_{ij}^{max}), respectively.

	Bond lengths d_{ij} (Å) and bond angles φ_{ij} (degree)					
Ion	$x = 0.0$	$x = 0.2$	$x = 0.4$	$x = 0.6$	$x = 0.8$	$x = 1.0$
Ti4c		1.860Å (1.627Å/2.260Å) 109.1° (86.4°/146.6°)	1.849Å (1.651Å/2.082Å) 108.8° (87.9°/152.1°)	1.834Å (1.747Å/1.945Å) 108.8° (84.3°/132.4°)	1.841Å (1.767Å/1.978Å) 109.2° (91.1°/147.0°)	1.841Å (1.774Å/1.917Å) 108.7° (88.5°/135.0°)
Ti5c		1.964Å (1.635Å/2.384Å) 106.4° (63.7°/170.0°)	1.947Å (1.643Å/2.393Å) 105.9° (62.8°/177.3°)	1.936Å (1.703Å/2.379Å) 105.7° (67.1°/172.1°)	1.938Å (1.732Å/2.383Å) 105.5° (67.0°/175.9°)	1.928Å (1.725Å/2.374Å) 105.5° (67.5°/177.6°)
Ti6c		1.988Å (1.884Å/2.325Å) 104.9° (72.7°/173.9°)	2.019Å (1.770Å/2.327Å) 103.1° (66.9°/169.5°)	1.994Å (1.728Å/2.344Å) 103.7° (64.9°/177.1°)	1.999Å (1.740Å/2.400Å) 103.4° (61.1°/178.5°)	1.993Å (1.759Å/2.388Å) 103.6° (64.7°/177.8°)
Ti7c				2.051Å (1.825Å/2.212Å) 101.6° (71.1°/155.3°)	2.060Å (1.858Å/2.355Å) 101.7° (61.5°/177.9°)	2.050Å (1.726Å/2.378Å) 101.7° (61.1°/175.2°)
Ti8c						2.091Å (1.985Å/2.219Å) 100.2° (67.2°/149.1°)

Table 4. Average O–Ti/Si bond lengths d_{ij}^{av} and Ti/Si–O–Ti/Si bond angles φ_{ij}^{av} for the various coordination states of O ions a-$Ti_xSi_{1-x}O_2$ VASP geometries. Values in brackets represent the corresponding minimal and maximal bond lengths and bond angles (d_{ij}^{min} / d_{ij}^{max}), (φ_{ij}^{min} / φ_{ij}^{max}), respectively.

	Bond lengths d_{ij} (Å) and bond angles φ_{ij} (degree)					
Ion	$x = 0.0$	$x = 0.2$	$x = 0.4$	$x = 0.6$	$x = 0.8$	$x = 1.0$
O1c		1.631Å (1.627Å/1.635Å)	1.647Å (1.643Å/1.651Å)			
O2c	1.641Å (1.572Å/1.837Å) 137.8° (99.5°/177.8°)	1.677Å (1.568Å/2.325Å) 140.4° (111.2°/177.2°)	1.721Å (1.582Å/2.119Å) 140.4° (98.4°/173.9°)	1.740Å (1.586Å/2.083Å) 135.3° (96.3°/176.0°)	1.794Å (1.581Å/2.065Å) 136.2° (99.2°/175.4°)	1.844Å (1.725Å/2.070Å) 137.8° (104.3°/161.6°)
O3c	1.795Å (1.722Å/1.855Å) 119.5° (88.3°/144.2°)	1.886Å (1.625Å/2.384Å) 117.4° (93.2°/150.7°)	1.911Å (1.619Å/2.393Å) 117.5° (91.1°/156.2°)	1.957Å (1.605Å/2.379Å) 116.0° (86.4°/160.6°)	1.960Å (1.604Å/2.400Å) 116.7° (82.4°/165.4°)	1.988Å (1.776Å/2.339Å) 116.5° (81.1°/167.0°)
O4c			2.116Å (1.889Å/2.278Å) 110.0° (89.0°/138.1°)	2.098Å (1.973Å/2.251Å) 107.5° (85.2°/162.9°)	2.092Å (1.646Å/2.397Å) 108.2° (78.3°/149.2°)	2.095Å (1.881Å/2.388Å) 108.4° (82.3°/150.4°)

state(s). Therefore, it might be rather difficult to identify contributions from non-dominant coordination states in experimental approaches. For example, the Ti–O bond length and O–Ti–O bond angles of under-coordinated Ti_{5c} ions and over-coordinated Ti_{7c} ions are completely enclosed by larger contributions from TiO_6 coordination polyhedra in pure a-TiO_2 and Ti rich a-$Ti_xSi_{1-x}O_2$ alloys ($x \geqslant 0.8$). It seems natural to assume that due to the similar coordination-environment characteristics to a superposition of under- and over-coordinated Ti ions, a-TiO_2 might have been sporadically misinterpreted as a purely octahedrally coordinated material. In the mid-composition range, comparable contributions to the bond lengths as well as bond-angles arise from differently coordinated Ti ions. At a composition parameter of $x = 0.4$ these are Ti ions located in TiO_4 as well as TiO_5 coordination polyhedra and for $x = 0.6$ Ti ions in TiO_5 as well as TiO_6 coordination units. The main peaks of the total Ti–O bond length distributions show small variations in the Si rich regime ($x < 0.6$) but shift to higher bond length in the Ti rich hybrid oxides and pure a-TiO_2. The bond lengths as well as bond-angles distributions demonstrate that the individual TiO_n coordination states show slightly different distribution characteristics at various composition parameters. For example, the Ti–O bond length distribution of TiO_6 coordination polyhedra shows a two peak characteristic at a composition parameter of $x = 0.6$, a broadened multi-peak distribution at $x = 0.8$ and single broad main peak in pure TiO_2. Similarly, the O–Ti–O bond-angle distribution shows a two-peak characteristic between ∼70° and ∼100° at composition parameters of $x = 0.6$ and $x = 0.8$, while the bond-angle distribution of pure a-TiO_2 shows a broad single peak in this angle-size range. Qualitative differences are also observed for the distribution of bond lengths and bond angles of TiO_5 coordination polyhedra for Ti fractions of 40 and 60 mol%.

The qualitative differences in the distribution of bond lengths and bond angels clearly indicate that the TiO_n coordination polyhedra, all possibly occurring associated geometry types respectively, cannot be seen as rigid building blocks that assemble the amorphous solid. Rather, the TiO_n coordination units in a-$Ti_xSi_{1-x}O_2$ hybride oxides show density dependent distortions for each alloy composition. It is particularly noteworthy that the average Ti–O bond lengths, and to a comparable extent the average O–Ti–O bond angles, presented in the figures 10(*a*) and (*d*), actually give some insights into the short-range order formation processes and the origin of higher coordinated TiO_n coordination polyhedra in a-TiO_2 and its amorphous alloys. The actual formation trends are most clearly observed for the octahedrally coordinated TiO_6 building blocks. The TiO_6 coordination polyhedra show an average Ti–O bond length of 1.988 Å at low Ti content ($x = 0.2$) and moderate alloy-mass density of 2.60 g cm^{-3}. This value is extremely close to the average Ti–O bond length of 1.981 Å in the C_1 symmetric TiO_6 octahedrons of crystalline TiO_2 in the brookite phase. With increasing mass density (3.00 g cm^{-3}) of the oxide alloys, a maximal average Ti–O bond length of 2.019 Å is reached for a composition parameter of $x = 0.4$. This point actually represents an extremum of absorbed short-range disorder through distortions of the TiO_6 building blocks. The extremal behavior is also reflected in the formation of alternative symmetry types for the TiO_6 coordination polyhedra (see table 1). While the TiO_6 coordination polyhedra exclusively show an [O-6]-type geometry at $x = 0.2$, only 25.0% of the TiO_6 coordination polyhedra can be attributed to this geometry type at the critical composition parameter of $x = 0.4$. 50.0% of TiO_6 coordination polyhedra are distorted to a [TPR-6]-type geometry. The remaining 25.0% are best characterized as a [TPBPY-6]-type coordination state. Thus, the increase in the average bond lengths is also related to massive changes in the geometry types of TiO_6 octahedrons, with which the local Ti ion coordination units try to diminish the tension within the amorphous framework. If the Ti content and for this reason the mass density is increased beyond 3.00 g cm^{-3}, $x = 0.4$ respectively, the individual TiO_6 building blocks cannot absorb anymore atomic disorder from the increasingly denser amorphous framework. Ultimately, at some point the system will spontaneously start to form sevenfold coordinated TiO_7 building blocks to increase the connectivity of the coordination polyhedra and to allow local relaxations of the distorted amorphous framework. The average bond length of 2.019 Å of maximal distorted TiO_6 coordination-polyhedra bonds is quite close to the average Ti–O bond length of 2.051 Å in the newly formed TiO_7 units, which actually facilitates the transition from a lower to a higher coordination state. The formation of the higher coordination complexes for the Ti ion actually takes away constrains of the amorphous framework onto the highest coordinated and likewise most flexible coordination unit that is present in the system at that time. After the formation of higher coordinated units the average bond length in TiO_6 building blocks relaxes to a value of 1.994 Å which is similar to the average Ti–O bond length at low alloy density. Subsequently, the average TiO_6 coordination-polyhedra bond lengths remain roughly constant at high Ti contents and even in pure a-TiO_2. Also, the number of crystal-like [O-6]-type coordination polyhedra increases abruptly and becomes the clearly dominant coordination-geometry state with fractions of 75.0% and 76.6% at compositions of $x = 0.6$ and $x = 0.8$. In complete analogy to the TiO_6 units, also the TiO_7 coordination polyhedra show a maximal average bond length of 2.060 Å at a composition parameter of $x = 0.8$ just before TiO_8 units are formed at even higher alloy density or in pure a-TiO_2 and the average Ti–O bond length of TiO_7 building blocks relaxes back to 2.050 Å. Similar transitions to higher coordinated units could not be observed for lower coordinated units in our data since TiO_4 and TiO_5 coordination polyhedra are present in any Ti containing a-$Ti_xSi_{1-x}O_2$ hybrid oxide. However, the trends in the average Ti–O bond length indicate that a transition from fivefold coordinated Ti_{5c} ions to sixfold coordinated Ti_{6c} ions as the highest coordination state might occur in a-$Ti_xSi_{1-x}O_2$ hybrid oxides for a composition parameter of $x \ll 0.2$. In addition, the average bond lengths within the TiO_5 building blocks show the strongest dependence on the Ti content. The average bond length decreases almost continuously from 1.964 Å in a-$Ti_xSi_{1-x}O_2$ to 1.928 Å in pure a-TiO_2. The notable dependence of the TiO_5 polyhedra volume on the mass density hints to the role of TiO_5 units as some kind of transition state that mediate the transformation from fourfold coordinated Ti ions to a sixfold coordination state of Ti ions. TiO_5 coordination polyhedra show the distinct ability to adapt very flexible to the surrounding coordination polyhedra in size and shape alongside the density variations of the amorphous oxide alloy. Similar to the SiO_4 units, the TiO_4 coordination polyhedra units seem to be the most rigid coordination environment for Ti ions with variations in the average bond length between 1.860 Å in a-$Ti_{0.2}Si_{0.8}O_2$ and 1.834 Å in the a-$Ti_{0.6}Si_{0.4}O_2$ alloy. Especially at high Ti content, the average TiO_4 coordination bond length shows a constant value of 1.841 Å. The separation between the average Ti–O bond lengths of TiO_4 and TiO_5 coordination polyhedra of ∼0.1 Å is quite large and remains constant for the largest part of the alloy composition range. Therefore, it seems unlikely that even for an ultra-low density oxide, that contains some amount of low coordinated TiO_n building blocks, a generation mechanism, similar to the the high coordination states might be observable. In light of existing TiO_9 coordination polyhedra in the ultra-dense cotunnite polytype of c-TiO_2, higher TiO_n coordination states seem to be likely in amorphous oxides of high mass density or under significant pressure. However, since highly coordinated TiO_n units are formed locally, primarily due to disorder effects of the amorphous framework, and might be compensated by lower coordinated surrounding TiO_n coordination polyhedra (see figure 4(*c*-6)), there is a significantly higher probability of finding high Ti coordination states in an amorphous oxide phases than in a crystalline oxide phase under similar thermodynamical conditions.

The whole argumentation on the formation mechanism of higher coordination states might for the largest part be equivalently given in terms of the average O–Ti–O bond angles

(see figure 10(*d*)). However, instead of repeating the discussion itself, we will just shortly summarize the key data subsequently. The average O–Ti–O bond angle of TiO_6 coordination polyhedra exhibits a minimal value of 103.7° at a composition parameter of $x = 0.4$ and relaxes back to an average bond angle between 103.4° and 103.7° in the high Ti content alloys. With the increase of the coordination state, the average bond angle reduces successively to 101.7°±0.1° in the TiO_7 coordination polyhedra and to 100.2° for the TiO_8 building blocks in pure a-TiO_2. In case of fivefold coordinated Ti_{5c} ion, the average O–Ti–O coordination-polyhedra bond angle decreases continuously over the entire composition range from 106.4° at a composition parameter of $x = 0.2$ to 105.5° in pure a-TiO_2. The tetrahedral TiO_4 coordination units are characterized by tetrahedron type average O–Ti–O bond angles of 109.0°± 0.3°.

In summary, the formation of new high coordination states in a-$Ti_xSi_{1-x}O_2$ hybrid oxides shows a critical dependence on the Ti content, and therefore the mass density of the mixed oxides. As indicated by the average Ti–O bond lengths and O–Ti–O bond angles and their trends indicated in figures 10(*a*) and (*b*), the changes in the network topology due to the formation of new TiO_n coordination polyhedra closely resemble bifurcation-like changes of states in complex systems. Ultimately, the mass density acts as the critical system parameter for the spontaneous formation of new coordination units that itself is triggered by strong deformations in the direct coordination environment of existing coordination-polyhedra building blocks. It is obvious that all these complex trends seem to be restricted to the Ti coordination environment. Therefore, it seems reasonable to assume that disorder effects within the first Ti–O coordination shell play a fundamental and active role in the structure formation processes and, upon heat treatment, the crystallization dynamics in a-$Ti_xSi_{1-x}O_2$ hybrid oxides.

The distributions of the average O–Ti/Si bond lengths in figure 8(*c*) basically reflect the continuos transition from pure a-SiO_2 to pure a-TiO_2. In pure a-SiO_2, almost the entire amorphous network is connected by corner-linking Si–O–Si bonds between tetrahedral SiO_4 units with an O–Si average bond length of 1.641 Å. In pure a-TiO_2, in contrast, only a small number of O ions is actually twofold coordinated by Ti ions. The corresponding average O–Ti bond length is 1.844 Å. With increasing Ti content, the bond length distribution of twofold coordinated O_{2c} ions in the oxide alloys shows a continuos transition between OSi_2-like and OTi_2-like coordination units and thus a two-peak characteristic (see figure 8). These two subpeaks at ∼1.64 Å and ∼1.84 Å do not show a notable dependence on the Ti concentration in the alloy. However, the peak heights change with the ratio of Ti and Si ions. Up to a composition parameter of $x = 0.4$, the total bond-length distribution closely follows the bond distribution of twofold coordinated O_{2c} ions. At composition parameters of $x = 0.6$ and $x = 0.8$ the total bond-length distribution is a superposition of contributions from $O(Ti,Si)_2$ and $O(Ti,Si)_3$ coordination units. In pure a-TiO_2 the total bond-length distribution is predominantly determined by contributions from threefold coordinated O_{3c} ions round an average O–Ti bond length of 1.988 Å. Due to the various possible combinations of O–Ti and O–Si bonds, a significant broadening, compared to the $O(Ti,Si)_2$ units, of the O–$(Ti,Si)_3$ bond-lengths distributions is observed. In the composition range between $x = 0.4$ and $x = 0.8$ a bond-length feature from short O–Si bonds remains identifiable. Higher bond length features originate from a mixture of elongated O–Si bonds and, prevalently, from the various types of O–Ti bonds. The new long-distance bond-length peak of threefold coordinated O_{3c} ions, located around ∼1.95 Å, indicates substantially longer O–Ti bonds in $O(Ti,Si)_3$ complexes and, thus, different average O–Ti bond lengths in $O(Ti,Si)_2$ and $O(Ti,Si)_3$ coordination units. An even larger average bond length is indicated for tetrahedral $O(Ti,Si)_4$ coordination units in the Ti rich oxide alloys. In general, the average O–Ti/Si bond lengths (see figure 10) increase continuously from 1.641 Å to 1.844 Å for twofold coordinated O_{2c} and from 1.795 Å to 1.988 Å for threefold coordinated O_{3c} ions. Extremely short average O–Ti bond lengths of 1.631 Å and 1.647 Å are observed for onefold coordinated O_{1c} ions in the a-$Ti_{0.2}Si_{0.8}O_2$ and a-$Ti_{0.4}Si_{0.6}O_2$ alloys. In contrast, tetrahedral $O(Ti,Si)_4$ coordination polyhedra occur for the first time at a Ti content of 40 mol% with an extremely high average bond lengths of 2.116 Å. The average O–(Ti-Si) bond length for fourfold coordinated O_{4c} ions is reduced to 2.092 Å in Ti rich mixed oxides ($x = 0.8$), which is almost identical to the value of 2.095 Å in pure a-TiO_2. As might be expected from the large average bond length, the $O(Ti,Si)_4$ coordination polyhedra show a [SS-4]-type geometry at composition parameters of $x = 0.4$ and $x = 0.6$. In turn, the reduction of the average bond length for high Ti content alloys and pure a-TiO_2 is caused by the formation of an ∼60% fraction of [T-4]-type $O(Ti,Si)_4$ coordination polyhedra.

The average O–Ti/Si–O bond angles of $O(Ti,Si)_2$ coordination units displayed in figure 10(*f*) indicate a rather complex dependence on the alloy composition. An identical average O–Si–O and accordingly O–Ti–O bond angle of 137.8° is observed for the two binary oxides. In the Si rich hybrid oxides the average O–Ti/Si–O bond angle increases to 140.4°. With Ti ions becoming the major cation type ($x > 0.5$), the O–Ti/Si–O angle drops considerably to 135.3° in a-$Ti_{0.6}Si_{0.4}O_2$ and increases slightly to 136.2° in a-$Ti_{0.8}Si_{0.2}O_2$. The average O–Ti/Si–O bond angle of O $(Ti, Si)_3$ units in pure a-SiO_2 decreases stepwise from 119.5°, indicating almost perfectly planar OTi,Si_3 units, to 116.5° in a-TiO_2, indicating a predominance of pyramidal distorted $O(Ti,Si)_3$ coordination polyhedra.

It is interesting to note that, compared to the higher coordination states, small coordination numbers (⩽3) tend to result in a reversed density dependence of the bond lengths. This trend seems to reflect that the average bond length in $O(Ti,Si)_2$ and $O(Ti,Si)_3$ coordination units is actually the result of randomly arranged TiO_n and SiO_m coordination polyhedra of different size, of different coordination states n and m respectively, within the amorphous framework of the hybrid oxides. More or less, the continuos increase in the average bond length of both $O(Ti,Si)_2$ and $O(Ti,Si)_3$ coordination polyhedra is a first hint on the atomically mixed nature of the generated a-$Ti_xSi_{1-x}O_2$ structure models. In a phase separated oxide alloy, coordination units of O_{2c} and O_{3c} ions would reflect the bond

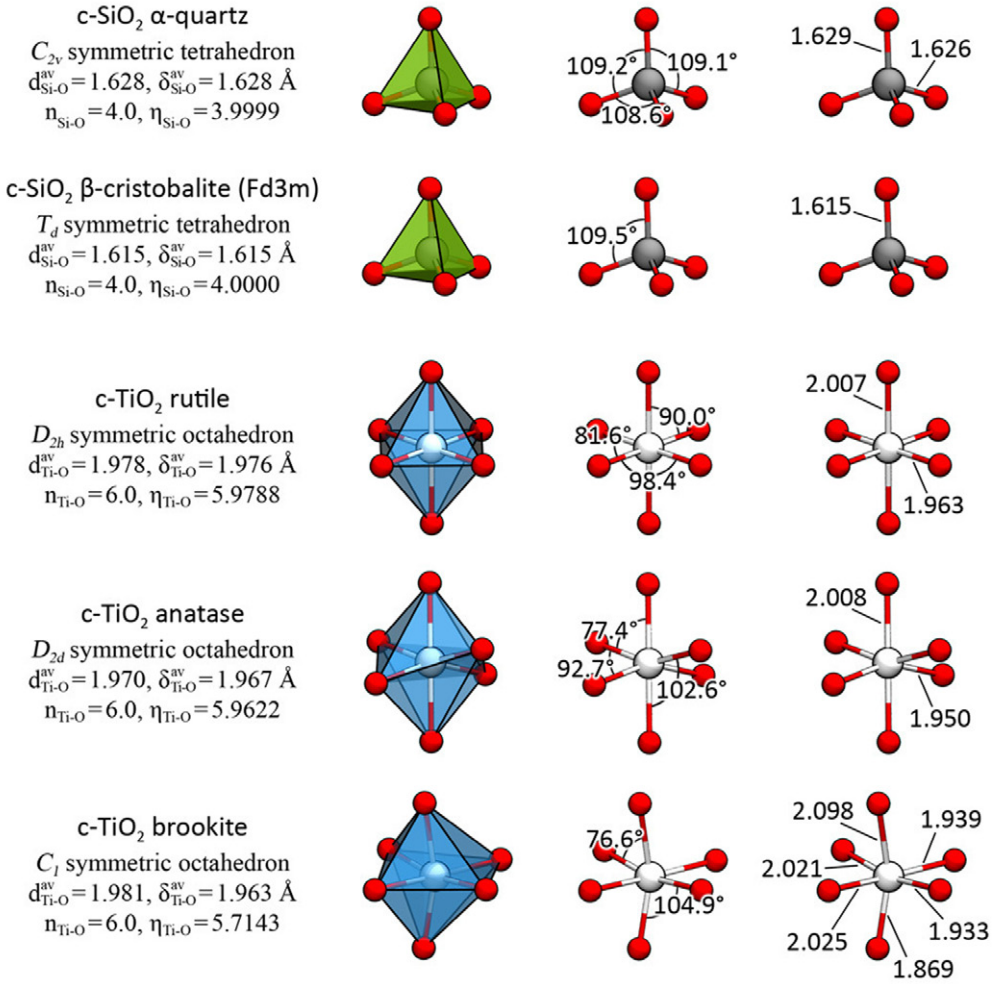

Figure 11. Overview on structural characteristics of the fundamental coordination polyhedra in crystalline TiO_2 and SiO_2 phases. Listed are the conventional and effective coordination numbers n_{Ti-O} and η_{Ti-O}, as well as the average and weighted average coordination-polyhedra bond lengths d^{av} and δ^{av}. With the exception of the TiO_2 brookite phase, all different O–Ti–O bond angles and Ti–O bond lengths are given for the DFT-PBE optimized crystal structures. For brookite, only the minimal and the maximal O–Ti–O bond angles are documented.

length distribution in the binary-oxide domains of a-SiO_2 and a-TiO_2, respectively. In that case the average bond length of $O(Ti,Si)_2$ and $O(Ti,Si)_3$ coordination polyhedra should neither show a similar mass-density dependence nor a continuously increasing value over the entire composition range. However, the analysis of the average O–Ti/Si–O bond angles, and their less significant composition dependence, indicate that it might be difficult to deduce specific mid-range order characteristics solely from the analysis of the atomic structure within first cation-coordination shell of O ions.

4.5. Effective coordination numbers

In order to demonstrate the differences between the conventional coordination-number analysis and the effective coordination-number concept, we have calculated [5] the Ti–O and Si–O coordination numbers of some crystalline TiO_2 as well as SiO_2 polymorphs (see figure 11). In the case of c-SiO_2, the crystalline phases α-quartz and β-cristobalite have been investigated. In detail, we have chosen the highest-symmetry *Fd3m*-type polymorph from the theoretically proposed β-cristobalite structure models [162]. As characteristic for all c-SiO_2 low-pressure phases, α-quartz and β-cristobalite are composed of corner-sharing tetrahedral SiO_4 building blocks that form some kind of a regular three-dimensional network. For c-TiO_2 we have considered the three most common, naturally occurring, crystalline phases rutile, anatase, and brookite. These low-pressure polymorphs of c-TiO_2 are characterized by three-dimensional networks of edge as well as corner sharing TiO_6 octahedron building blocks [125].

The SiO_4 units in Fd3m β-cristobalite exhibit an idealized T_d symmetric tetrahedron shape that are characterized by idealized O–Si–O bond angles of ∼109.5° and equal Si–O bond

[5] The reported results refer to fully optimized DFT-PBE unit cells. In detail, a kinetic-energy plane-wave cutoff of 550 eV and k point samplings of 12 × 12 × 16, 14 × 14 × 6, and 6 × 10 × 10 have been applied to the rutile, anatase, and brookite phases of c-TiO_2. In the case of the c-SiO_2 phases α-quartz and β-cristobalite, a k point mesh of 7 × 7 × 7 has been used. The atomic position and unit cell volumes were relaxed until a force convergence criterion of 0.001 eV $Å^{-1}$ was reached.

lengths of 1.615 Å. As expected for a high symmetry coordination state, both conventional and effective coordination numbers result in a coordination number of 4.0. In the most common c-SiO_2 polytype α-quartz, the tetrahedron symmetry of SiO_4 units is reduced to a C_{2v} symmetry due to two bond lengths pairs of 1.629 Å and 1.626 Å each and three slightly different O–Si–O bond angles between 108.6° and 109.2°. Since the SiO_4 tetrahedra turn out to be rather stiff and the bond-lengths variations are quite small, the α-quartz effective Si coordination number of $\eta_{Si-O} = 3.9999$ shows only marginal deviations from the conventional local coordination number of $n_{Si-O} = 4.0$. Also, differences between the average and the average weighted bond length are negligible (see figure 11).

In contrast to c-SiO_2, the effective coordination number differences of Ti ions in various TiO_2 crystal phases are much more obvious. In the c-TiO_2 rutile phase the TiO_6 octahedra-building blocks are slightly distorted with respect to the O_h symmetry of an ideal octahedron. The symmetry reduced octahedra are characterized by different in-plane (equatorial) and out-of-plane (apical) Ti–O bond lengths of 2.007 Å and 1.963 Å and two deformed O–Ti–O in-plane bond angles of 84.6° and 98.4°. The deviations from an ideal octahedron reduce the effective coordination number to $\eta_{Ti-O} = 5.9788$. In the c-TiO_2 anatase phase the O ions are displaced alternating below and above the equatorial octahedron plane, thus decreasing and increasing the ideal 90.0° out-of-plane O–Ti–O bond angles by 12.6°. The deformed in-plane bond angle is 92.7°. With respect to the rutile phase, the effective coordination numbers of the D_{2d} symmetric anatase TiO_6 coordination polyhedra are slightly reduced to $\eta_{Ti-O} = 5.9622$. Notable deviations from an idealized octahedral coordination are found for the TiO_6 building blocks of the c-TiO_2 brookite phase. In fact, the local coordination environment of brookite shows a complete loss of symmetry. The O–Ti–O bond angles of these C_1 symmetric coordination polyhedra vary between 76.6° and 104.9°. The Ti–O bond lengths of c-TiO_2 brookite span the range from 1.869 Å to 2.098 Å. In contrast to rutile and anatase, the notable distortions of the brookite coordination polyhedra lead to a much greater reduction of the effective coordination number to $\eta_{Ti-O} = 5.7143$. The calculated c-TiO_2 brookite average weighted bond length of 1.963 Å falls below the average bond length of 1.981 Å by ~1% . For rutile and anatase this differences is of the order of 1-2 per mill.

In sum, the effective coordination numbers prove to be quite sensitive to symmetry reductions of the local cation coordination environment and thus the particular shape and symmetry type of various coordination polyhedra. Thus, we expect the effective coordination numbers to be qualitative and, if compared to the conventional coordination numbers, quantitative measures for the degree of disorder within the first coordination shell around an atom. Notable deviations (≳5%) from the conventional local coordination numbers, as observed for c-TiO_2 brookite, are a definite indicator for strongly distorted, non-crystalline coordination polyhedra, whose occurrence is characteristic to a-TiO_2 as indicated by the coordination polyhedra analysis above.

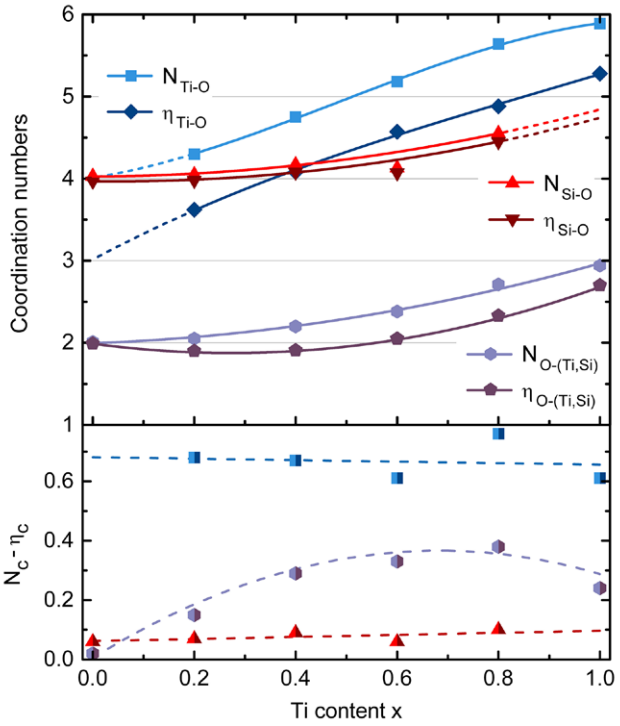

Figure 12. Upper panel: conventional (see figure 6) and effective coordination numbers N_c and η_c for the a-$Ti_xSi_{1-x}O_2$ VASP geometries. Solid lines refer to polynomial data fits (third order for Ti–O and second order for Si–O as well as O–Ti/Si coordination numbers). Dashed lines indicate data extrapolation towards the binary oxide limits. Lower panel: difference N_{Ti-O}–η_{Ti-O} between the conventional and local coordination numbers. Dashed lines represent linear (Ti–O and Si–O coordination) and second order polynomial (O–Ti/Si coordination) fits.

The differences between the conventional and effective coordination numbers of each chemical component of the a-$Ti_xSi_{1-x}O_2$ hybrid oxides (VASP geometries) are illustrated in figure 12 over the entire composition range. Obviously, all chemical components show notable deviations from the conventional coordination numbers. The smallest coordination number differences are observed for the Si ion. The difference of N_{Si-O}–η_{Si-O} between conventional and effective coordination numbers remains nearly constant over the entire composition range with variations between 0.06 and 0.1 (see lower panel of figure 12). In consideration of the rather stiff SiO_4 building blocks this is a notable change that reflects distortions of the Si coordination tetrahedra. Also in the case of the Ti ions, the difference between both coordination numbers remains almost constant over the entire composition range. Nevertheless, the degree of disorder in the O coordination environment of the Ti ion is much stronger as observed for the Si ion with difference variations between 0.61 and 0.76. Considering a difference of N_{Ti-O}–$\eta_{Ti-O} = 0.29$ in c-TiO_2 brookite, these values indicate substantial deviations from crystalline order in the binary and ternary amorphous oxides. This larger degree of disorder in the Ti coordination environment is in agreement with the larger number of possible coordination-polyhedra shapes that was observed above. While the effective coordination number of Ti as well as Si ions shows almost constant deviations from

the conventional coordination numbers, the coordination-number difference shows a more complex dependence on the alloy composition for O ions. The value of $N_{O-(Ti,Si)}-\eta_{O-(Ti,Si)}$ increases up to a composition parameter of $x = 0.8$ but with different slopes below $x = 0.4$ and between $x = 0.4$ and $x = 0.8$. For pure a-TiO_2 the data indicate a decrease of the coordination number difference compared to the Ti rich alloys. In general, the non-linear difference between conventional and effective coordination numbers arise from the mixing of short Si–O and long Ti–O bonds within particular coordination units. The coexistence of Si–O and Ti–O bonds necessarily increase the bond length deviations from the average coordination-polyhedron bond length. Considering the fact that the local coordination environment of the O ions reflects the linking between the various coordination polyhedra, the degree of disorder of the O ion coordination environment additionally represents *partial* information on the degree of disorder in the amorphous network while in the case of the Ti and Si ions the disorder *within* a particular coordination polyhedron is reflected. In fact, the information on the disorder is only given partially since a large part of the information on the network topology is contained in the bond angles of bridging O ions, Ti/Si–O–Ti/Si bond angles, respectively, rather than in the bond lengths variations. Nevertheless, some qualitative structure-formation trends are observable. While the effective coordination numbers show a constant degree of disorder within the cation-coordination polyhedra, smaller fractions of Ti ions act as a network modifying species. The differences in the coordination numbers indicate a notable influence of Ti ions on the mid-range ordered network topology of Si rich alloys up to a Ti concentrations of ∼40 mol% . In the mid and high Ti content alloy-composition range between $x = 0.4$ and $x = 0.8$, the amorphous network shows smaller adaptations to a larger content of TiO_2 units indicating the successive transition towards a short-range ordered alloy. Finally, the formation of a pure a-TiO_2 phase slightly reduces the amount of disorder in the amorphous framework due to the absence of contributions from compositional disorder.

To put it in different words, the disorder of the amorphous network increases with increasing Ti content. A dominant but almost constant fraction of disorder is carried by the local Ti ion coordination environments and to a much smaller extend by the local Si ion coordination environments. Further disorder effects are projected onto the spatial arrangement of the coordination polyhedra, a.k.a. the amorphous network itself.

Further details on the effective coordination numbers are provided by the effective coordination-number distributions of the a-$Ti_xSi_{1-x}O_2$ VASP geometries illustrated in figure 13. The effective Ti ion coordination numbers indicate a complex spectrum of coordination states with several major and secondary features. Nevertheless, the basic characteristics of the distributions of conventional coordination numbers (see figure 7) are maintained. At low Ti content, large part of the Ti ions reside in distorted tetrahedral units. However, the broadening of this peak indicates notable disorder in the fourfold coordinated Ti units. The most notable differences to the conventional coordination numbers, that indicate TiO_4 units as the lowest coordination state, are effective coordination numbers between 2.0 and 3.0. Obviously the bond length variations of some tetrahedral TiO_4 units seem to be of crucial size for the calculation of effective coordination numbers. At higher Ti contents, the effective coordination numbers reflect the distribution of conventional (local) coordination numbers. The fundamental transition from a predominant distorted fourfold coordination state at low Ti content to a broad a-TiO_2 coordination spectrum with significant contributions from distorted TiO_5 and TiO_6 as well as minor contributions from distorted under-coordinated TiO_4 units and over-coordinated TiO_7 and TiO_8 building blocks is also characteristic to the effective Ti coordination numbers. Thereby, the strong influence of atomic disorder is reflected by an increasing undervaluation of the corresponding conventional local coordination numbers. In the case of the Si ion, the SiO_4 coordination tetrahedra are clearly visible by the sharp peak close to the ideal tetrahedron coordination state of four. The heights of this peak remains almost constant over large part of the composition range and pronounced changes in the Si coordination environment do not occur until an alloy composition containing 80 mol% of Ti ions. At this composition, two distinct high coordination peaks at ∼4.7 and ∼5.8 represent distorted SiO_5 and SiO_6 coordination polyhedra. In agreement with the conventional local coordination numbers, weak indications of these high coordination states are already present from a composition parameter of $x = 0.4$ for distorted SiO_6 building blocks and throughout the entire composition range for distorted SiO_5 units. The effective coordination numbers of O ions nicely demonstrate the transition from a predominant twofold coordination in pure a-SiO_2 to a preferred threefold coordination type in pure a-TiO_2. The broader coordination number band between 2.5 and 3.0 for a-TiO_2 indicates notable disorder effects for threefold coordinated O ions. One interesting feature of the effective O ion coordination-number distributions is the occurrence of a low coordination-state tail in the ternary oxides that is not present in the pure amorphous phases of SiO_2 and TiO_2. This property agrees with the observed larger difference between conventional and effective O ion coordination numbers observed for the oxide alloys above (see figure 12). In the conventional coordination number analysis these coordination states are partially reflected by onefold coordinated O_{1c} ions in the low Ti content ternary oxides.

In order to compare further results from the local coordination-number analysis with the corresponding quantities from the effective coordination-number analysis, figure 14 illustrates the average effective coordination numbers for each conventional local coordination state in the a-$Ti_xSi_{1-x}O_2$ VASP geometries. The (average) effective coordination numbers of twofold coordinated O_{2c} ions of $\eta_{O_{2c}}[0.0] = 1.9787$ and $\eta_{O_{2c}}[1.0] = 1.9512$ in pure a-SiO_2 and a-TiO_2 indicate some degree of bond-length disorder in the binary amorphous oxides. In the amorphous alloys, the effective O_{2c} coordination numbers decrease depending on the cation ratio in the system. At composition parameters of $x = 0.2$ and $x = 0.8$, $\eta_{O_{2c}}$ reduces to ∼1.893. $\eta_{O_{2c}}$ reduces to ∼1.867 for composition parameters of $x = 0.4$ and $x = 0.6$. Similar to the O_{2c} ions, threefold coordinated O_{3c} ions show a small degree of disorder in a-SiO_2 ($\eta_{O_{3c}}[0.0] = 2.9289$), a notable degree of disorder in a-TiO_2 ($\eta_{O_{3c}}[1.0] = 2.6965$) and strong disorder influences in

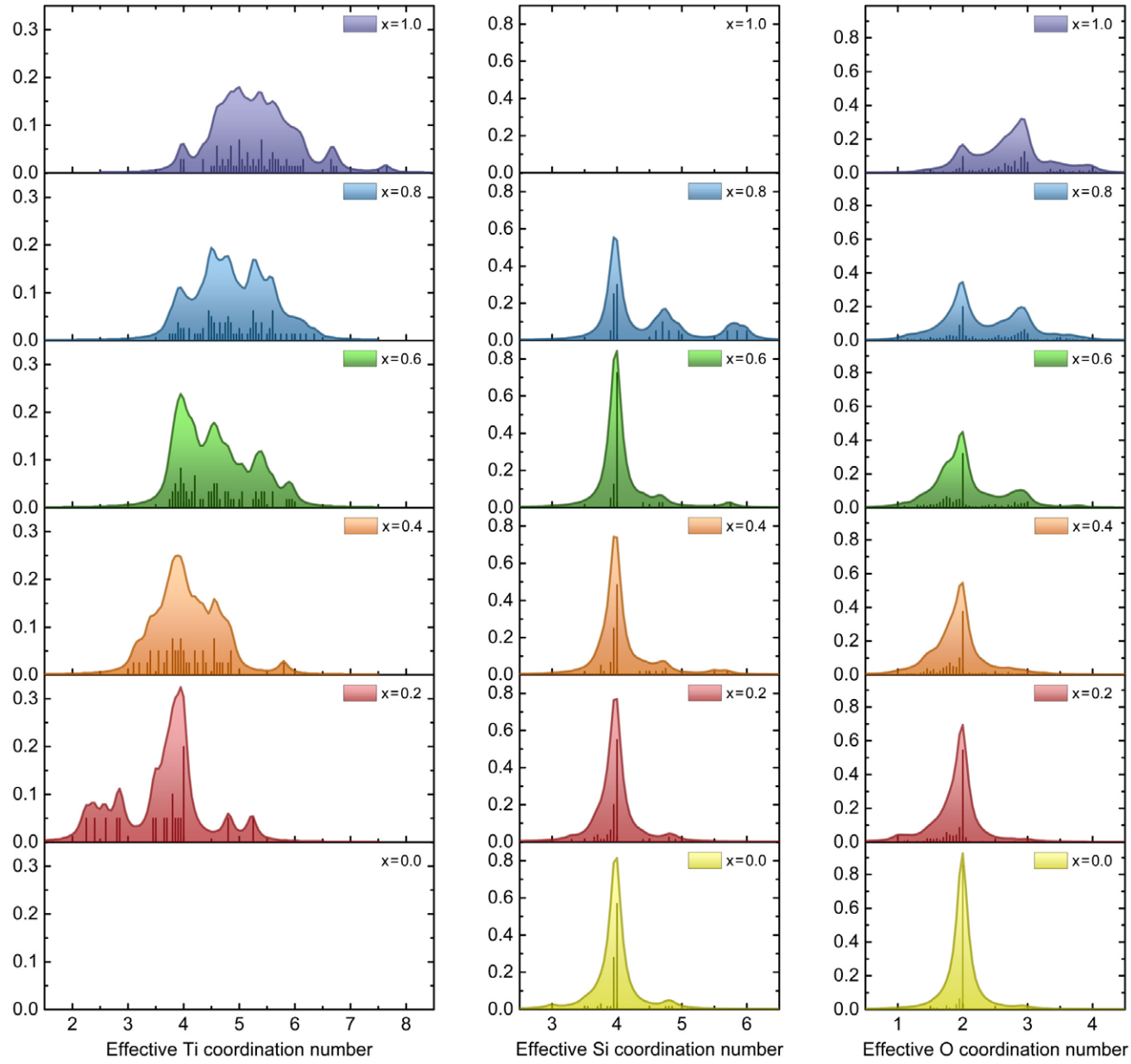

Figure 13. Effective coordination-number distributions of the various chemical components in the a-$Ti_xSi_{1-x}O_2$ VASP geometries. Illustrated are a discrete line spectrum as well as a continuos spectrum obtained by a gaussian type line broadening.

the alloys. The effective O_{3c} coordination number is reduced to its minimal value of $\eta_{O_{3c}}[0.4] = 2.1215$ at a composition parameter of $x = 0.4$. The effective O_{4c} coordination number varies between $\eta_{O_{4c}}[0.8] = 3.1671$ and $\eta_{O_{4c}}[0.6] = 3.7781$ indicating a notably distorted coordination environment. Compared to this strong variations in the coordination environment of O_{4c} ions, the average effective Si coordination numbers of ∼3.95±0.02 for the dominant fourfold coordination state indicate just minimal distortions of the SiO_4 coordination units. In contrast, fivefold coordinated Si_{5c} and sixfold coordinated Si_{6c} ions show a notable degree of disorder. The effective Si_{5c} coordination number in pure a-SiO_2 of $\eta_{Si_{5c}}[0.0] = 4.8120$ decreases with increasing Ti content to $\eta_{Si_{5c}}[0.6] = 4.5880$. However, for the highest SiO_5 coordination polyhedra fraction of 25% at a composition parameter of $x = 0.8$ the effective coordination number increases to $\eta_{Si_{5c}}[0.6] = 4.7511$. Sixfold coordinated Si_{6c} ions show a quite clear trend in the average effective coordination numbers. The ∼3% of SiO_6 coordination polyhedra are strongly distorted in the mid-composition range ($x = 0.4$) as characterized by an average effective coordination of $\eta_{Si_{6c}}[0.4] = 5.5858$. A higher alloy density allows the octahedral SiO_6 units to reduce their strain deformations by relaxing to a shape with an effective coordination number of $\eta_{Si_{6c}}[0.8] = 5.8452$ that is actually closer to an idealized octahedral symmetry than the TiO_6 building blocks of the c-TiO_2 brookite phase (see figure 3). Altogether, it seems always possible to deduce the corresponding conventional local coordination state form the effective (average) Si coordination numbers. In some exceptional cases, this actually changes for the effective coordination number analysis of the Ti coordination environment. The average effective coordination number of fivefold coordinated Ti_{5c} ions of $\eta_{Ti_{5c}}[0.2] = 3.7074$ does not necessarily imply a locally fivefold coordinated Ti ion and points

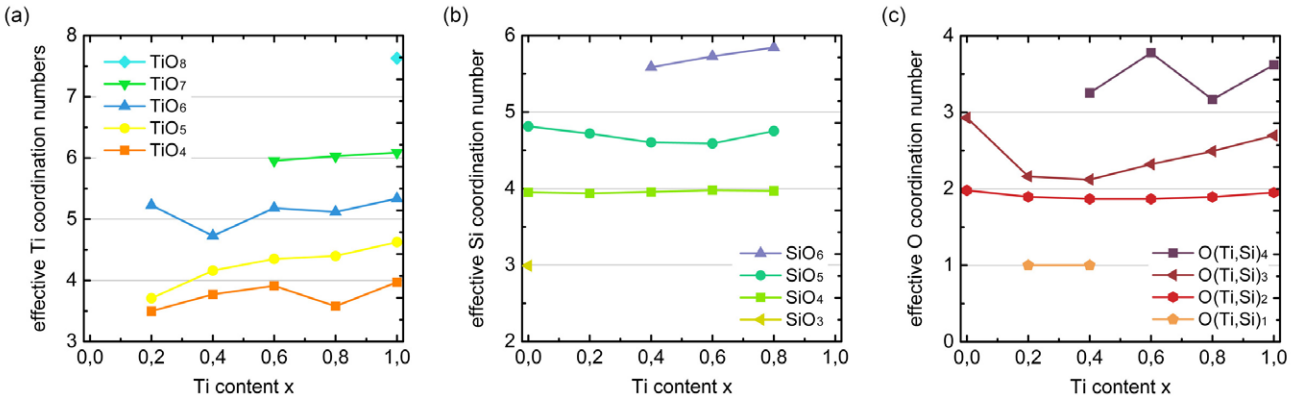

Figure 14. Average effective coordination numbers of all conventional cation and anion coordination-states (see figure 5) occurring in the a-$Ti_xSi_{1-x}O_2$ VASP geometries.

Table 5. Average effective coordination numbers of all coordination-polyhedra types (see figure 5) occurring in the a-$Ti_xSi_{1-x}O_2$ VASP geometries.

Coordination	Ion	Polyhedron	Effective coordination number					
			$x = 0.0$	$x = 0.2$	$x = 0.4$	$x = 0.6$	$x = 0.8$	$x = 1.0$
$n_c = 1$	**O**	[SB-1]-[Ti]		1.0000	1.0000			
$n_c = 2$	**O**	[HOA-2]-[Ti]		1.8006	1.8850	1.9186	1.9462	1.9512
		[HOL-2]-[Ti]				1.9290		
		[HOA-2]-[Si]	1.9784	1.9853	1.9902	1.9957	1.9886	
		[HOL-2]-[Si]	1.9936	1.9954				
		[HEA-2]		1.6830	1.6982	1.7192	1.7216	
		[HEL-2]		1.4992				
$n_c = 3$	**Si**	[TP-3]	2.9910					
	O	[TP-3]	2.9289	2.0607	2.0925	2.2821	2.5298	2.7411
		[TPY-3]		2.2033	2.1983	2.3108	2.4935	2.6791
		[TS-3]			2.0905	2.5269	2.1872	2.8283
$n_c = 4$	**Ti**	[TTBPY-4]		2.8225	3.9174			3.9771
		[T-4]		3.4564	3.8314	3.9197	3.9364	3.9619
		[SS-4]		3.8610	3.5773	3.8689	3.3990	
	Si	[TTBPY-4]	3.4981					
		[T-4]	3.9587	3.9367	3.9565	3.9781	3.9649	
		[SS-4]	3.9434				3.9869	
	O	[T-4]					3.2215	3.6834
		[SS-4]			3.2531	3.7781	3.0857	3.5339
$n_c = 5$	**Ti**	[SPY-5]		3.0361	4.3998	4.3034	4.3825	4.6701
		[TBPY-5]		4.3787	3.9806	4.3727	4.4146	4.5531
	Si	[SPY-5]	4.8071	4.6970	4.6630	4.6428	4.8344	
		[TBPY-5]	4.8144	4.7815	4.4839	4.5606	4.6956	
$n_c = 6$	**Ti**	[PPY-6]						5.0139
		[O-6]		5.2284	5.7988	5.1275	5.0390	5.3283
		[TPR-6]			4.7070	5.5266	5.3068	5.3139
		[TPBPY-6]			3.7010	5.0681	5.5476	5.4598
	Si	[O-6]			5.5858	5.7292	5.8452	
$n_c = 7$	**Ti**	[PBPY-7]					6.0286	6.0722
		[MO-7]						6.1656
		[MTPR]				5.9560		
$n_c = 8$	**Ti**	[TD-8]						7.6298

towards strongly distorted TiO_5 coordination units in the low density a-$Ti_xSi_{1-x}O_2$ hybrid oxides. For higher Ti content and, with it, a notably higher fraction of TiO_5 coordination polyhedra in the alloy, the effective TiO_5 coordination number increases to $\eta_{Ti_{5c}}[0.4] = 4.1603$, still indicating strongly distorted TiO_5 units. Further increase of the Ti content successively raises the effective coordination to $\eta_{Ti_{5c}}[1.0] = 4.6246$ in pure a-TiO_2. Less distinct trends are observed for the effective coordination numbers of fourfold coordinated Ti_{4c} ions and sixfold coordinated Ti_{6c} ions. The average effective Ti_{4c} coordination numbers show strong oscillations between $\eta_{Ti_{4c}}[0.2] = 3.4951$ and $\eta_{Ti_{4c}}[1.0] = 3.9695$. With exception of a composition parameter of $x = 0.4$, TiO_6 coordination polyhedra exhibit an average effective coordination number of ~5.23±0.11. For $x = 0.4$ a small effective coordination number of $\eta_{Ti_{6c}}[0.4] = 4.7285$ is obtained. This minimum directly correlates with the bond length maximum as well as bond angle minimum of TiO_6 units that is observed before the formation of higher coordinated TiO_n coordination polyhedra (see figures 10(*a*) and 10(*b*)). The average effective coordination number of over-coordinated Ti_{7c} ions remains close to six and shows a marginal increase from $\eta_{Ti_{7c}}[0.6] = 5.9560$ to $\eta_{Ti_{7c}}[0.6] = 6.0877$. These strong deviations from the

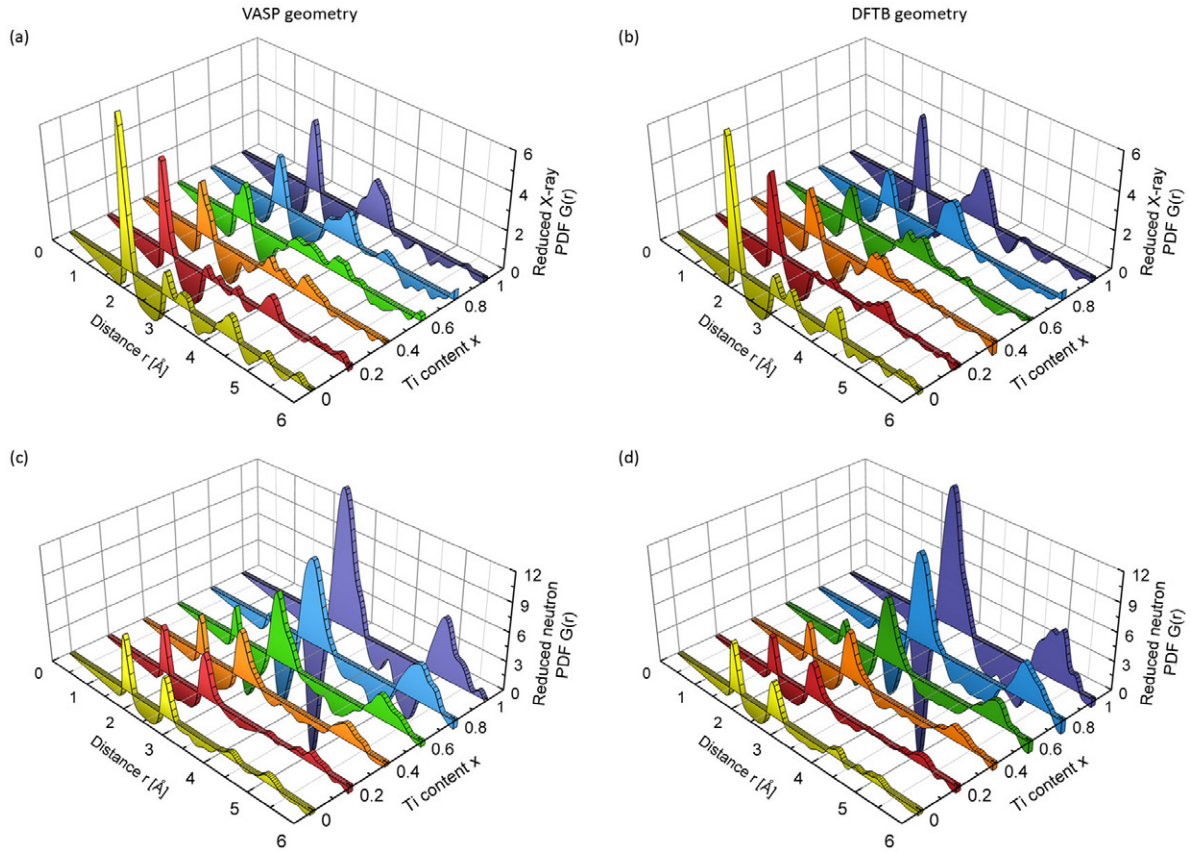

Figure 15. Reduced total x-ray (upper panels) and neutron (lower panels) pair distribution functions G(r) for the a-$Ti_xSi_{1-x}O_2$ VASP (left) and DFTB (right) geometries.

conventional local coordination state indicate a strongly disordered coordination environment in TiO_7 coordination polyhedra. In contrast, smaller differences to the conventional coordination state are found by an average effective coordination number of $\eta_{Ti_{8c}}[1.0] = 7.6298$ of eightfold coordinated Ti_{8c} ions in pure a-TiO_2.

The multi-peak structure of several peaks in the distribution of effective coordination numbers in figure 13 suggests that effective coordination numbers might also be useful to estimate the number of various coordination-polyhedra geometry types that might exist for a given coordination state. In order to identify specific coordination polyhedra solely by their effective coordination number, the average effective coordination numbers for each coordination-polyhedra type, listed in figure 5, are summarized in table 5. With a few exceptions, it does not seem possible to find a unique mapping of coordination-polyhedra geometries onto the effective coordination numbers that applies to the entire composition range. For example, there seems to be a change in the effective coordination-number ratio for planar and pyramidal $O(Ti,Si)_3$ units. In Ti rich alloys ($x \geqslant 0.8$) as well as pure a-TiO_2, the planar $O(Ti,Si)_3$ units and $O(Ti)_3$ units, respectively, exhibit larger effective coordination numbers than their pyramidal distorted counterpart. Lower Ti concentrations in the amorphous alloy result in a higher effective coordination number for [TPY-3]-type $O(Ti,Si)_3$ units. Based on the relatively small number of O_{3c} ions in the Si rich alloys, it is difficult to estimate if this behavior describes a basic trend or is the artifact of the partially small data basis for evaluation of the effective coordination numbers. Observable trends are actually limited to the lower coordination states. The effective coordination numbers of twofold coordinated O_{2c} ions are highest ($\eta_{OSi_2} \leq 1.98$) for homopolar OSi_2 units, slightly smaller for homopolar OTi_2 units ($1.80 \leq \eta_{OTi_2} \leq 1.95$), and notably smaller for heteropolar $O(Ti,Si)_2$ coordination units ($1.50 \leq \eta_{O(Ti,Si)_2} \leq 1.72$). The effective coordination numbers of [T-4]-type coordination polyhedra clearly increase with the Ti content from $\eta_{TiO4[T-4]}[0.2] = 3.4564$ in a-$Ti_{0.2}Si_{0.8}O_2$ to $\eta_{TiO4[T-4]}[1.0] = 3.9619$ in pure a-TiO_2. For higher coordination states it becomes increasingly difficult to identify trends for a specific coordination-polyhedron geometry type.

In general, it seems difficult to extract clear trends from the effective coordination numbers of individual coordination-polyhedra types. This suggests that a purely exponential weighting function, defined according to equation 11, might not be an ideal choice to characterize the atomic short-range order in an amorphous solid. Especially, the more deformable coordination environment of the Ti ions shows strong variations in the effective coordination state. This shortcoming seems to be related to the extreme sensitivity of the weighting function against bond-length variations of distorted coordination polyhedra in the amorphous oxides. In order to extract well converged trends from an effective coordination number analysis it might be necessary to increase the analyzed data basis notably by increasing the structure models and/or performing averages over a large number of equilibrium MD configurations at fixed temperature. However, due to the general

density dependence of the coordination-polyhedra shapes, a unique identification of a specific coordination-polyhedron geometry-type by a single-number quantity, as the effective coordination number, might be out of reach even with an optimally chosen weighting function.

In sum, both the conventional and the effective coordination numbers provide fundamental information to characterize the short-range order in amorphous oxides. While an in depth coordination-polyhedra analysis remains an elaborate task and the conventional coordination numbers do not provide a measure for the degree of disorder within different coordination polyhedra, the effective coordination-number approach serves both purposes. Effective coordination numbers, as used in this study, are suited to determine the local coordination state of ions in the investigated amorphous hybrid oxides and to obtain information on the degree of disorder within the first coordination shell. Indeed, the possible existence of various geometry types for a particular coordination state is clearly indicated, whereas, a unique identification of the different polyhedra types at various alloy-mass densities remains ambiguous.

4.6. Radial distribution functions

The (radial) pair distribution functions are the most common tool to investigate the atomic structure of amorphous solids. Figure 15 illustrates the total reduced x-ray as well as neutron pair distribution functions for our generated VASP and DFTB structure models of a-$Ti_xSi_{1-x}O_2$ hybrid oxides. In case of the a-$Ti_xSi_{1-x}O_2$ VASP geometries (see figure 15(*a*)), the first x-ray pair correlation peak of Ti–O pairs and Si–O pairs nicely reflect the continuos transition between the pure binary oxides. The Si rich hybrid oxides show a sharp Si–O correlation peak around ∼1.6 Å that decays linearly with the increasing Ti content. Analog, the sharp Ti–O correlation peak around ∼1.9 Å of Ti rich oxide alloys decays linearly with the decreasing Ti content. The difference in the average Si–O and Ti–O corellation length allows the differentiation of both pair correlations in the mid composition range. Both the a-$Ti_{0.4}Si_{0.6}O_2$ and a-$Ti_{0.6}Si_{0.4}O_2$ VASP geometries show indications of this double peak substructure. Our calculated Si–O as well as Ti–O pair correlation length of ∼1.6 Å and ∼1.9 Å are in excellent agreement with experimental data. Wallidge *et al* [166] reported x-ray correlation lengths, and virtually identical neutron-correlation lengths, of 1.60 Å and 1.93 Å for sol-gel formed amorphous $(TiO_2)_x(SiO_2)_{1-x}$ samples (calcined to 250 °C) at a composition parameter of $x = 0.41$. Almost identical neutron correlation lengths for sol-gel derived $(TiO_2)_x(SiO_2)_{1-x}$ glasses have been reported by Rigden *et al* [72] as well as Pickup *et al* [167]. The clearly visible correlation features in the Ti rich composition range in the bond-length region between ∼3.0 Å and ∼4.0 Å belong to homonuclear correlations between Ti–Ti pairs. The characteristic two-peak substructure of this correlation peak can be assigned to different Ti–Ti distances of Ti ions in either corner-linked or edge-linked TiO_n coordination polyhedra. It proves to be quite difficult to identify the characteristic O–O correlation features in the total a-$Ti_xSi_{1-x}O_2$ pair-correlation functions, that should be observable below ∼3.0 Å. Similaly, the homonuclear Si–Si and heteronuclear Ti-Si pair correlations can hardly be separated from the low correlation lengths Ti–Ti pair correlations in the total correlation functions.

The reduced neutron pair distribution functions in figures 15(*c*) and (*d*) look qualitatively extremely different from the x-ray pair distribution functions. These differences are most pronounced in the case of the Ti rich oxide alloys as well as pure a-TiO_2 and a direct consequence of the notably negative neutron-scattering length of Ti ions. Therefore, Ti–O and Ti–Ti pair correlations are characterized by negative features in the distribution function and, thus, easily distinguishable from purely Si and O related correlations. Overall, the neutron pair distribution functions show three characteristic positive correlation features below a correlation length of 6.0 Å. The low distance feature around ∼1.6 Å clearly arises from Si–O correlations and decays with increasng Ti content. In contrast to the total x-ray distribution functions, the homonuclear O–O pair-correlation peak appears prominently in the neutron pair distribution functions. The O–O pair-correlation peaks are located around ∼2.7 Å and become the dominant positive correlation peaks in the Ti rich alloys and pure a-TiO_2. The long distance positive feature around 5 Å represents second coordination-shell pair correlations of O ions. The dominant negative feature of the reduced neutron pair-distribution functions around ∼2.0 Å is associated to first coordination shell Ti–O pair correlations, as indicated by the strong increase with the Ti content in the amorphous alloy. Compared to the x-ray pair distribution functions, the neutron pair distribution functions strongly support the differentiation of the closely spaced Ti–O and Si–O pair correlations in the mid-composition range. The negative feature around ∼4.2 Å can be attributed to second coordination shell Ti–O pair correlations. In general, it is quite difficult to identify the various contributions of homonuclear and heteronuclear cation–cation pair correlations in the distance range between ∼3.0 Å and ∼4.0 Å in the total neutron pair distribution functions.

The direct comparison of the total x-ray pair-correlation functions for the VASP and DFTB geometries indicates quite similar ordering characteristics for both numerical approaches. Merely, the separation between Ti–O and Si–O pair correlations is less distinct in the DFTB a-$Ti_xSi_{1-x}O_2$ geometries, which is best illustrated for the a-$Ti_{0.6}Si_{0.4}O_2$ alloy. Similar to the x-ray distribution functions, the neutron pair distribution functions of the VASP and DFTB geometries show qualitatively identical ordering characteristics. Slight differences seem to be present for the higher-order pair correlations in the Ti rich alloys.

Altogether, the total pair-correlation functions do not, per se, allow the identification of structure correlations between arbitrary pairs of chemical elements. Most problematic, short-range order differences within the first correlation shell, as indicated by the local coordination number differences for different composition parameters and between the VASP and DFTB geometries (see figure 7), are not resolved, or rather hidden in the total pair correlation functions.

Nevertheless, further insights into the atomic structure are provided by the partial reduced (x-ray) pair correlation functions $G_{\alpha\beta}(r)$ illustrated in figure 16 for the a-$Ti_xSi_{1-x}O_2$

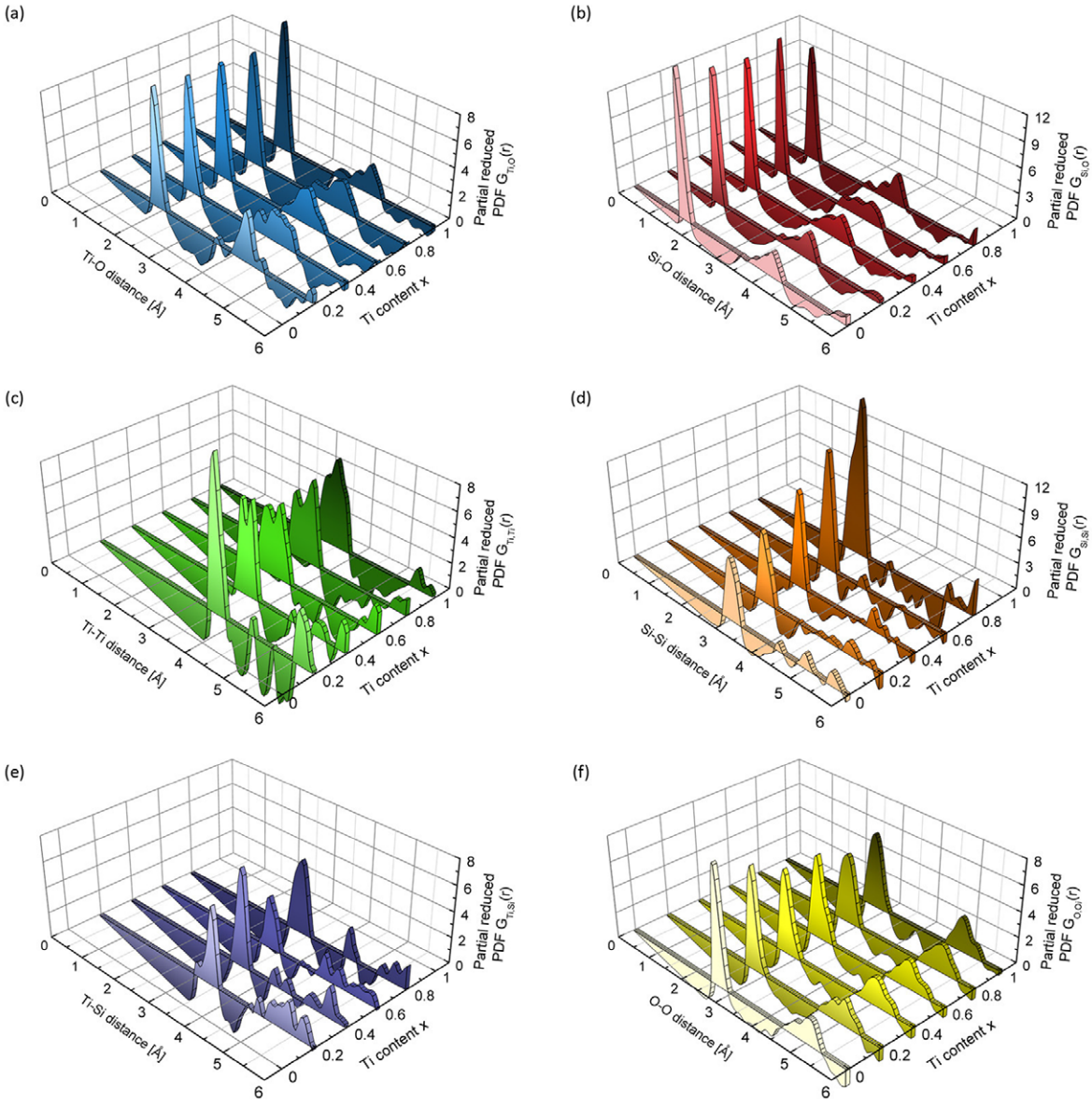

Figure 16. Reduced partial x-ray pair distribution functions $G_{\alpha\beta}(r)$ for the a-$Ti_xSi_{1-x}O_2$ VASP geometries.

VASP geometries. The first Ti–O pair-correlation peak in figure 16(*a*) shows some minor position dependence on the alloy composition. The central-peak position increases continuously from ∼1.9 Å in a-$Ti_{0.2}Si_{0.8}O_2$ to ∼2.0 Å in pure a-TiO_2. Since by trend, the individual coordination polyhedra show a decreasing average bond length with increasing alloy density (see figure 10), such an increase directly reflects the occurrence of increasingly higher coordinated TiO_n building blocks. Compared to the average Ti–O coordination-polyhedra bond length of 1.860 Å in table 3, the a-$Ti_{0.2}Si_{0.8}O_2$ Ti–O correlation peak position around ∼1.9 Å indicates a dominant fourfold Ti coordination state with minor contributions from higher coordination states. This observation nicely agrees with the 75%, 20%, and 5% of Ti_{4c}, Ti_{5c}, and Ti_{6c} ions observed in the (conventional) coordination-polyhedra analysis above (see figure 7(*a*) and table 1). Due to an average TiO_6 coordination-polyhedra bond length of 1.993 Å, the Ti–O correlation-peak position around ∼2.0 Å indicates that, at least by majority (54.2%), a-TiO_2 is built from octahedral TiO_6 building blocks. Since the average Ti–O bond length of under-coordinated TiO_4 and TiO_5 building blocks are below the value of sixfold coordinated crystal-like coordination units and above this value for over-coordinated TiO_7 and TiO_8 building blocks, coordination defects in a-TiO_2 have to be a mixture of both defect types. In fact, our a-TiO_2 VASP structure model shows 27.8% of under-coordinated Ti ions and 18.1% of over-coordinated Ti ions (see table 1). Ti–O pair correlation of the second coordination shell are observed by a correlation feature located at a pair distances around ∼4.3 Å. With increasing mass density the width of this correlation peak is increasingly broadened on the small correlation-length edge.

The first Si–O pair-correlation peak in figure 16(*b*) shows basically identical structure-correlation characteristics, just merely shifted to smaller correlation distances. The center of the first correlation-shell peak shifts from ∼1.6 Å in pure a-SiO_2 to ∼1.7 Å in a-$Ti_{0.8}Si_{0.2}O_2$. A correlation length around

~1.6 Å is an indication of predominantly fourfold coordinated Si ions in a-SiO_2 since the average bond length of SiO_4 coordination polyhedra is 1.639 ± 0.002 Å in the entire composition range (see table 2). Again, the fact that the first correlation peak shifts with increasing mass density, clearly indicates an increase in the fraction of over-coordinated SiO_m units in the Ti rich alloys since the average polyhedra-bond lengths remain only constant (SiO_4) or decrease (SiO_5 and SiO_6, see figure 10(*b*)) with increasing alloy-mass density. In contrast to the Ti–O correlation peak, the position shift does not depend linear on the Ti content. A notable peak shift is not notable until a composition parameter of $x = 0.8$ is reached. This observation is in close agreement with the observed fraction of SiO_4 coordination polyhedra which remains roughly constant at 90 ± 4% up to a composition parameter of $x = 0.6$ (see figure 7(*c*) and table 1). In the a-$Ti_{0.8}Si_{0.2}O_2$ alloy the fraction of tetrahedral coordination units is reduced to 60.0% and the remaining 40.0% are portioned into 25.0% of SiO_5 and 15.0% of SiO_6 coordination polyhedra with average Si–O coordination-bond lengths of 1.729 Å and 1.784 Å, respectively. Si–O pair correlations of the second correlation shell are observed between ~3.5 Å and ~4.5 Å over the entire composition range.

Ti–Ti pair correlations (see figure 16(*c*)) are observed as a broad feature around pair distances of 3.5 Å. The Ti–Ti pair correlation peaks show a qualitative transition from a single-peak characteristic at low Ti content ($x = 0.2$) to a double-peak characteristic in the mid-composition range and additional modifications in pure a-TiO_2. This transition reflects an important ordering characteristic of the Ti–O coordination polyhedra in the a-$Ti_xSi_{1-x}O_2$ hybride oxides. The different Ti–Ti correlation distances originate from TiO_n coordination polyhedra sharing either a common oxygen ion, a polyhedron corner/vertex respectively (e.g. see figure 2(*d*-7)), or two common oxygen atoms, two polyhedron vertices or a common polyhedron edge respectively (e.g. see figure 2(*d*-6)). In general, the Ti–Ti correlation length is longer for corner-linked coordination polyhedra than for edge-linked coordination units. For our structure models, the single-peak characteristic of the partial Ti–Ti pair correlation functions is actually limited to the low Ti content regime. The Ti–Ti pair correlation peak is located around ~3.6 Å in a-$Ti_{0.2}Si_{0.8}O_2$. At low Ti content the Ti ions are incorporated into the almost perfectly corner-linked amorphous framework of a-SiO_2 (see figure 2(*a*-2)). The extreme predominance of corner-linking is the results of the relatively small tetrahedral coordination units. Edge-linking would cause a small and thus, energetically unfavorable distance between the central cations. Therefore, low-coordinated TiO_n units are exclusively interconnected with each other via bridging Ti–O–Ti bonds, with a single shared O ion. From the coordination-polyhedra analysis above, it is further known that 75% of the Ti ions adopt the fourfold coordination state of the Si ions. Due to the sparse distribution, the Ti ions will more often connect to the network by sharing common oxygen atoms with the surrounding SiO_4 coordination polyhedra (see figure 3(*c*-5)). Similarly, also the 20% and 5% of fivefold and sixfold coordinated Ti_{5c} and Ti_{6c} ions are almost exclusively incorporated into the a-SiO_2 matrix by sharing common corners with the neighboring SiO_4 coordination polyhedra (see figures 3(*c*-4) and (*c*-2) for examples of TiO_5 and TiO_6 coordination polyhedra corner-linked to SiO_4 coordination units). All in all, the single-peak characteristic of the partial Ti–Ti pair correlation peak indicates that the amorphous network remains virtually entirely corner-linked despite the presence of Ti ions. However, in order build in the 25% of non-tetrahedrally coordinated Ti_{5c} and Ti_{6c} ions, the amorphous framework needs to adapt to the higher connectivity of these coordination units. Since the Si–O coordination environment has repeatedly proven to be rather stiff and only 5% of the Si ions increase their local coordination number to five, the amorphous network itself needs to change its mid-range order characteristics in order to incorporate the Ti_{5c} and Ti_{6c} ions as discussed below. The increase of the Ti content beyond 20 mol% inevitably leads to the splitting of the Ti–Ti pair correlations peaks into two sub-peaks. More precisely, the occurrence of an additional smaller Ti–Ti correlation-lengths feature that merges with the Ti–Ti pair-correlation peak of the corner-linked coordination polyhedra. Thereby, the central positions of the corner-linked polyhedra peaks do not change notably throughout the entire alloy-composition range indicating a qualitatively equivalent type of Ti–O–Ti bridging oxygen bonds for all corner-linked TiO_n coordination polyhedra. The additional smaller correlation-length feature is observed around ~3.4 Å in a-$Ti_{0.4}Si_{0.6}O_2$ and caused by small entities of edge-linked TiO_n coordination polyhedra. These edge-linked entities are exclusively formed by a mixture of the higher fivefold and sixfold TiO_n coordination states whose fractions in a-$Ti_{0.4}Si_{0.6}O_2$ increased to 55.0 % and 10.0 %, respectively. However, the size of the new atomic cluster-type conglomerates is initially limited to a few (typically three to four) TiO_n coordination polyhedra as exemplified in figure 3(*d*-7). Increasing the Ti content to 60 mol% on the one hand increases the number of small edge-linked atomic clusters (see figure 4(*c*-2)). On the other hand, existing highly coordinated edge-linked atomic conglomerates favor the aggregation of additional TiO_n coordination polyhedra (see figure 4(*c*-6)). In addition, the high coordination clusters can be seen as local generators of new high coordination states as indicated by the TiO_7 coordination unit in the edge-linked cluster visualized in figure 4(*c*-6). Sporadically, the edge-linked TiO_n conglomerates starts to form chain-like fragments. The peak width and position of the Ti–Ti pair correlations of edge-linked TiO_n coordination polyhedra strongly depends on the Ti content for $x \leqslant 0.6$. The central peak position shifts notably from ~3.4 Å in a-$Ti_{0.4}Si_{0.6}O_2$ to ~3.2 Å in a-$Ti_{0.6}Si_{0.4}O_2$ and remains basically constant at even higher Ti percentages. This basically indicates that the TiO_n coordination polyhedra start to form well defined a-TiO_2 phases in all Ti rich a-$Ti_xSi_{1-x}O_2$ hybrid oxides. The smallest qualitative differences in the partial Ti–Ti pair correlation functions are observed between the amorphous 60 mol% and the 80 mol% containing oxides. Thereby, the a-$Ti_{0.8}Si_{0.2}O_2$ alloy shows the most distinct separation into the two sub-peaks around ~3.2 Å and ~3.6 Å. Compared to

the characteristic Ti–Ti distances in the naturally occurring c-TiO_2 phases, these correlation features closely resemble the Ti–Ti distances in long-range ordered networks of [O-6]-type TiO_6 coordination polyhedra. In c-TiO_2 rutile the Ti–Ti distance within the formed edge-linked TiO_6 polyhedra chains is 2.97 Å. These edge-linked polyhedra chains are interconnected by shared oxygen atoms and the corresponding Ti–Ti distance between Ti ions in neighboring chains is 3.61 Å. The three dimensional edge-linked octahedral coordination network of c-TiO_2 anatase shows Ti–Ti distances of 3.09 Å between all edge-linked TiO_6 coordination polyhedra. The Ti–Ti distances between TiO_6 coordination-polyhedra sharing a common oxygen atom are 3.81 Å. Since the c-TiO_2 brookite phase shows a combination of rutile and anatase features, the Ti–Ti distances of edge-linked TiO_6 polyhedra range from 2.97 Å to 3.12 Å, thus, covering the values of the higher symmetry crystal phases. Similarly, the Ti–Ti distances between Ti ions in corner-linked TiO_6 coordination polyhedra vary between 3.56 Å and 3.83 Å. In view of the highest fraction of octahedrally coordinated Ti ions among all a-$Ti_xSi_{1-x}O_2$ hybrid oxides of 58.8%, the a-$Ti_{0.8}Si_{0.2}O_2$ alloy has the strongest characteristics of a disordered octahedral TiO_2 phase. The actual distribution of edge-linked coordination units, and TiO_n coordination polyhedra in general, in a-$Ti_{0.8}Si_{0.2}O_2$ is quite isotropic without notable tendencies to form a fine grained mixture of larger clusters. Basically, the a-$Ti_{0.8}Si_{0.2}O_2$ alloy represents a low density amorphous phase of TiO_2 including fragments of the lower coordinated SiO_2 framework inside its cavities (see figure 19). In pure a-TiO_2 the sub-peaks around crystal-like Ti–Ti correlation lengths of ∼3.2 Å and ∼3.6 Å remain clearly visible. However, the main Ti–Ti pair-correlation sub-feature is located around ∼3.5 Å and represents the typical Ti–Ti distance in corner-linked TiO_6 building-block units as visualized in figure 2(*d*-7), whereas, the ∼3.6 Å feature seems to be related to Ti–Ti distances involving over-coordinated (n>6) TiO_n coordination polyhedra. In summary, the partial Ti–Ti pair-correlation peaks give deep insides to the incorporation characteristics of TiO_n coordination polyhedra into the disordered framework of a-SiO_2. In the Ti rich and high density a-$Ti_xSi_{1-x}O_2$ hybrid oxides the stepwise formation of isotropic amorphous TiO_2 phases is indicated by the formation of a characteristic double-peak distribution for Ti–Ti pair-correlation length.

The partial Si–Si pair-correlation features (see figure 16(*d*)) contain much less information on the amorphous oxide-ordering characteristics. The Si–Si pair correlation features are centered around ∼ 3.0 Å in the entire alloy-composition range indicating the predominance of one single Si–O–Si bond type of corner-sharing SiO_m coordination polyhedra. Solely for a composition parameter of $x = 0.8$, notable pair correlations from higher-coordinated edge-linked SiO_m coordination units are weakly indicated by a small distance shoulder of the Si–Si pair correlation peak. A characteristic example of edge-linked SiO_m coordination polyhedra is visualized in figure 4(*d*-4) for a pair of SiO_5 and SiO_6 polyhedra. Nevertheless, identical pairs of edge-linked SiO_m coordination polyhedra units are likewise, but only occasionally, present in the a-$Ti_{0.4}Si_{0.6}O_2$ (see figure 3(*d*-5)) and a-$Ti_{0.6}Si_{0.4}O_2$ (see figure 4(*c*-7)) oxide alloys.

Heteronuclear Ti–Si pair correlations functions (see figure 16(*e*)) show one dominant first correlation-shell feature around correlation lengths of ∼ 3.3 Å for all mixed oxides. This value lies roughly half between the correlation lengths of homonuclear Si–Si pair correlations around ∼3.0 Å and the homonuclear Ti–Ti pair correlations of corner-linked TiO_n coordination polyhedra. Thus, the observed Ti–Si pair correlation features can, most likely, be attributed to cross-linking Ti–O–Si bonds connecting corner-sharing TiO_n and SiO_m coordination polyhedra. The stronger developed pair-correlation lengths tail around ∼ 3.0 Å at a composition parameter of $x = 0.2$ correlating with the high fraction (75.0%) of tetrahedrally coordinated Ti_{4c} ions in the a-$Ti_{0.2}Si_{0.8}O_2$ alloy and the formation of corner-linked TiO_4–SiO_4 pairs (see figure 3(*c*-5)). At higher composition parameters, the Ti–Si pair correlation functions show a broader single peak feature due to the larger number of available coordination states that allow a manifold of corner-linked TiO_n–SiO_m polyhedra pairs (e.g. see figure 4(*d*-7)). Finally, the partial O–O pair-correlation functions (see figure 16(*f*)) show a well defined first correlation-shell feature around ∼2.7 Å throughout the entire alloy-composition range as well as the two binary oxides. The mass-density dependence of the O–O pair correlations is expressed by a successive broadening of the corresponding pair-correlation peak. This broadening directly originates from the transition from the twofold (98.6%) O–$(Ti,Si)_2$ coordination environment of pure a-SiO_2 to the predominantly threefold (68.1%) O–$(Ti,Si)_3$ coordination environment of pure a-TiO_2 (see figure 7(*e*)). Thereby, the higher O ion coordination state offers more degrees of freedom in shape and arrangement of the trigonal $O(Ti,Si)_3$ coordination units. Second coordination shell pair correlations are clearly visible in the distance range between ∼4.5 Å and ∼5.5 Å and show a similar position independence on the alloy composition.

In summary, the pair-distribution function analysis primarily allows to deduce ordering characteristics of the coordination polyhedra among themselves. Hints on extended mid-range ordering features within the amorphous hybrid oxides are given semi-indirectly in the partial pair-distribution functions. Deeper insights into the mid-range order of a-$Ti_xSi_{1-x}O_2$ oxide alloys require more specialized structure-analysis techniques.

4.7. Ring statistics

While we have repeatedly seen that a-TiO_2 is a material whose structure is governed by short-range order features, it is well known that a-SiO_2 is a prototypical Zachariasen glass characterized by ring-like structural-ordering features of the disordered oxide framework [100], [102–106]. As visualized in figure 17, well defined ring-like ordering features are a also the fundamental structure characteristic of all tetrahedrally coordinated c-SiO_2 low-pressure phases. The most common α-quartz phase is constructed from 12 atom (see figure 17(*a*)) and 16 atom wide rings (see figure 17(*b*)) that are built by six

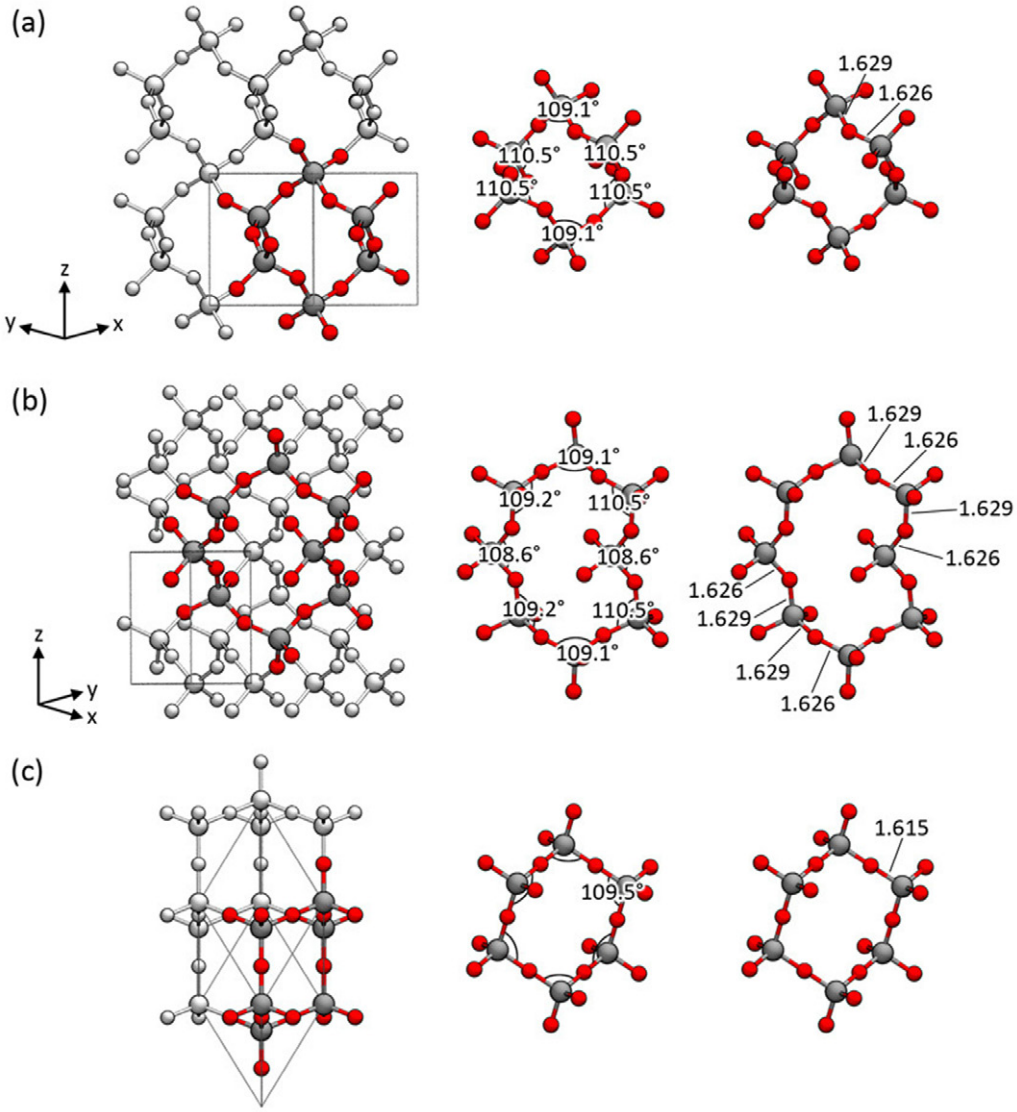

Figure 17. Illustration of ring-like structures in c-SiO_2 phases. Displayed are (*a*) the 12-atom $(SiO_4)_6$ and (*b*) the 16-atom $(SiO_4)_8$ rings of α-quartz as well as (*c*) the 12-atom $(SiO_4)_6$ rings of (Fd3m) β-cristobalite.

and eight SiO_4 coordination polyhedra, respectively. Besides, the high symmetry β-cristobalite phase of c-SiO_2 is completely composed from sixfold $(SiO_4)_6$ rings (see figure 17(*c*)). In addition, sixfold $(SiO_4)_6$ rings are, among others, found in the c-SiO_2 polymorphs cristobalite and moganite, while eightfold $(SiO_4)_8$ rings are present in keatite and coesite. Fourfold $(SiO_4)_4$ rings are found in the c-SiO_2 polymorph moganite and coesite as well as fivefold $(SiO_4)_5$ rings in the c-SiO_2 polymorph keatite and tridymite. Threefold $(TiO_2)_3$ rings are also found in the ultra-dense octahedrally coordinated c-SiO_2 polytypes seifertite and stishovite.

TiO_2 is commonly not characterized in terms of rings due to its higher connectivity and the resulting ordering characteristics. Nevertheless, ring statistics are easily applied to crystalline and amorphous TiO_2 materials. Two edge-linked TiO_n coordination polyhedra always form an four-atomic ring. Thus, twofold $(TiO_6)_2$ rings are present in all octahedral c-TiO_2 phases that contain edge-linked TiO_6 coordination polyhedra. Corner-linked TiO_6 coordination polyhedra in c-TiO_2 rutile form six-atomic $(TiO_6)_3$ rings. The regular arrangement of four TiO_6 coordination polyhedra leads to the formation of eight-atomic $(TiO_6)_4$ rings in the rutile as well as anatase phases. Again, the c-TiO_2 brookite phase unifies structural ordering features from rutile and anatase with twofold, threefold, and fourfold $(TiO_6)_n$ rings. Eight-atomic $(TiO_6)_4$ rings are also present in the columbite-type TiO_2(II) phase. In addition, c-TiO_2 phases with lower mass-densities show even more extended ring like complexes. 12-atomic $(TiO_6)_6$ rings are present in ramsdellite-type TiO_2(R) and hollandite-type TiO_2(H) even shows 16-atomic $(TiO_6)_8$ rings. Ring-like structures are also present in non-octahedrally coordinated high-pressure polymorphs of c-TiO_2. Six-atomic $(TiO_7)_3$ and eight-atomic $(TiO_7)_4$ rings are found in the sevenfold coordinated c-TiO_2 baddeleyite-type TiO_2(MI) and orthorhombic TiO_2(OI) phases.

It is a central question in the structure analysis of amorphous solids in general, and more specifically glasses, to what extent the regular mid-range order characteristics of perfectly

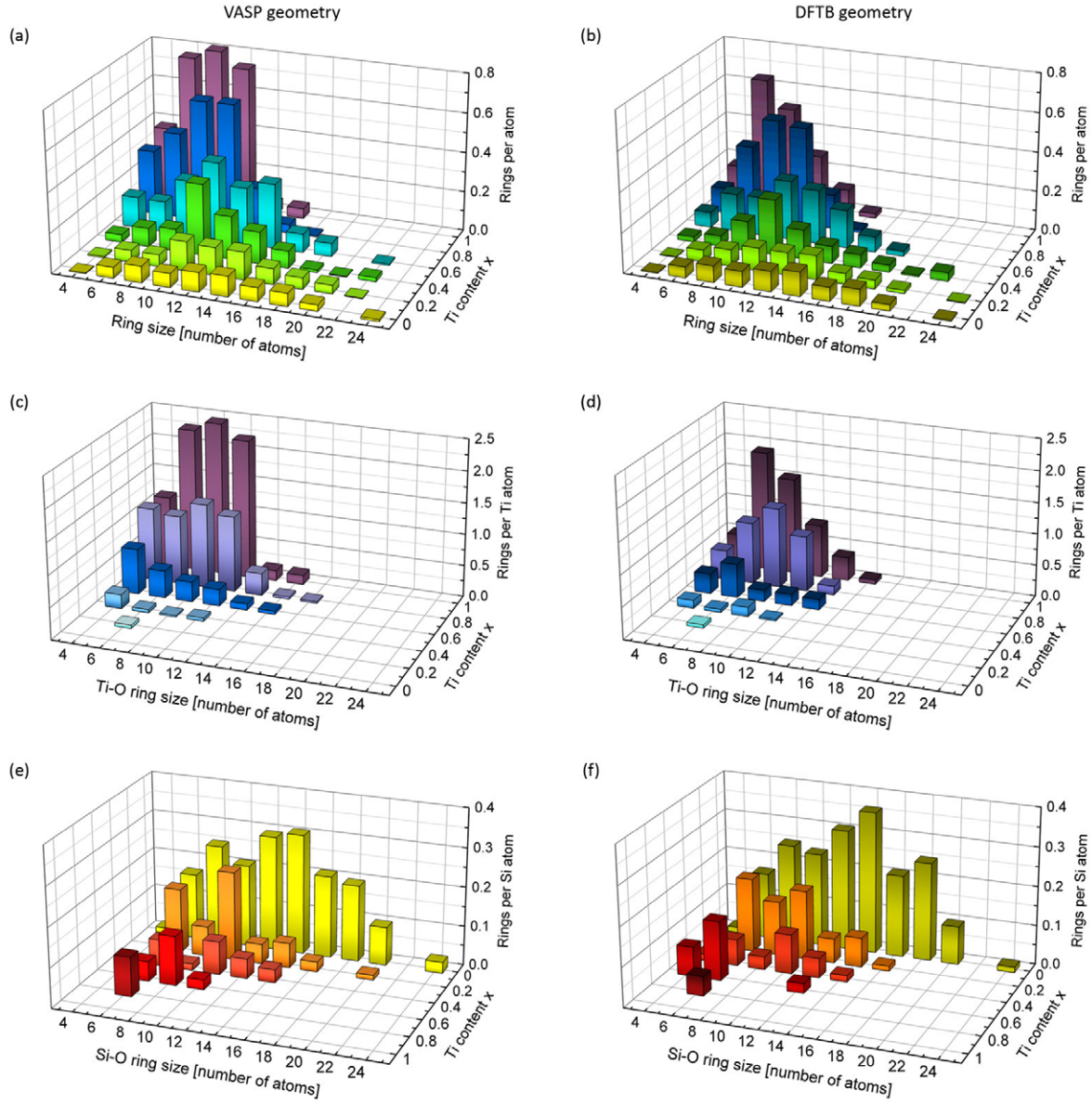

Figure 18. Total distribution of oxide type Ti/Si–O (upper panels), Ti–O (middle panels), and Si–O (lower panels) rings in the a-$Ti_xSi_{1-x}O_2$ VASP (left) and DFTB (right) geometries.

long-range ordered crystalline oxides are preserved, modified respectively, in the disordered material phases.

The total as well as TiO_2-type and SiO_2-type ring size distributions of the a-$Ti_xSi_{1-x}O_2$ VASP and DFTB geometries are visualized in figure 18. As discussed above, the generated amorphous structures virtually show a perfect oxide-like atomic structure free of homonuclear cation-cation or anion-anion bonds. Consequently, there are no relevant contributions from rings with an odd number of atoms. The binary amorphous oxides clearly illustrate the various connectivities of Ti and Si ions as well as the resulting short-range and mid-range order characteristics. The ring-size distribution of pure a-TiO_2 is centered around eight-atom rings. Almost identical contributions from six-atomic and 10-atomic rings are observed. Only very small fractions of larger 12 and 14 atom wide rings are present in the system. The sharp drop in the number of 12-atomic and larger rings seems to be quite characteristic to the short-range ordered atomic structure of a-TiO_2. Compared to the ring-like features of the crystalline TiO_2 phases rutile and columbite-type TiO_2(II), that roughly show the same mass densities of 4.2 g cm^{-3}, mainly the existence of a large number of 10-atomic rings distinguishes the crystalline and disordered TiO_2 phases. 10-atomic rings in pure a-TiO_2 might be seen as a reminiscence to larger $(TiO_6)_n$ rings in low-density c-TiO_2 phases. The relative frequency of small four-atomic rings from edge-linked TiO_n coordination polyhedra is roughly half as much as the occurrence of the three dominating ring types. According to figure 18(*c*) every Ti ion participates in the formation of approximately one four-atomic ring. In other words, every TiO_n coordination polyhedron shares statistically at least one common edge with another TiO_n coordination polyhedron. Moreover, the

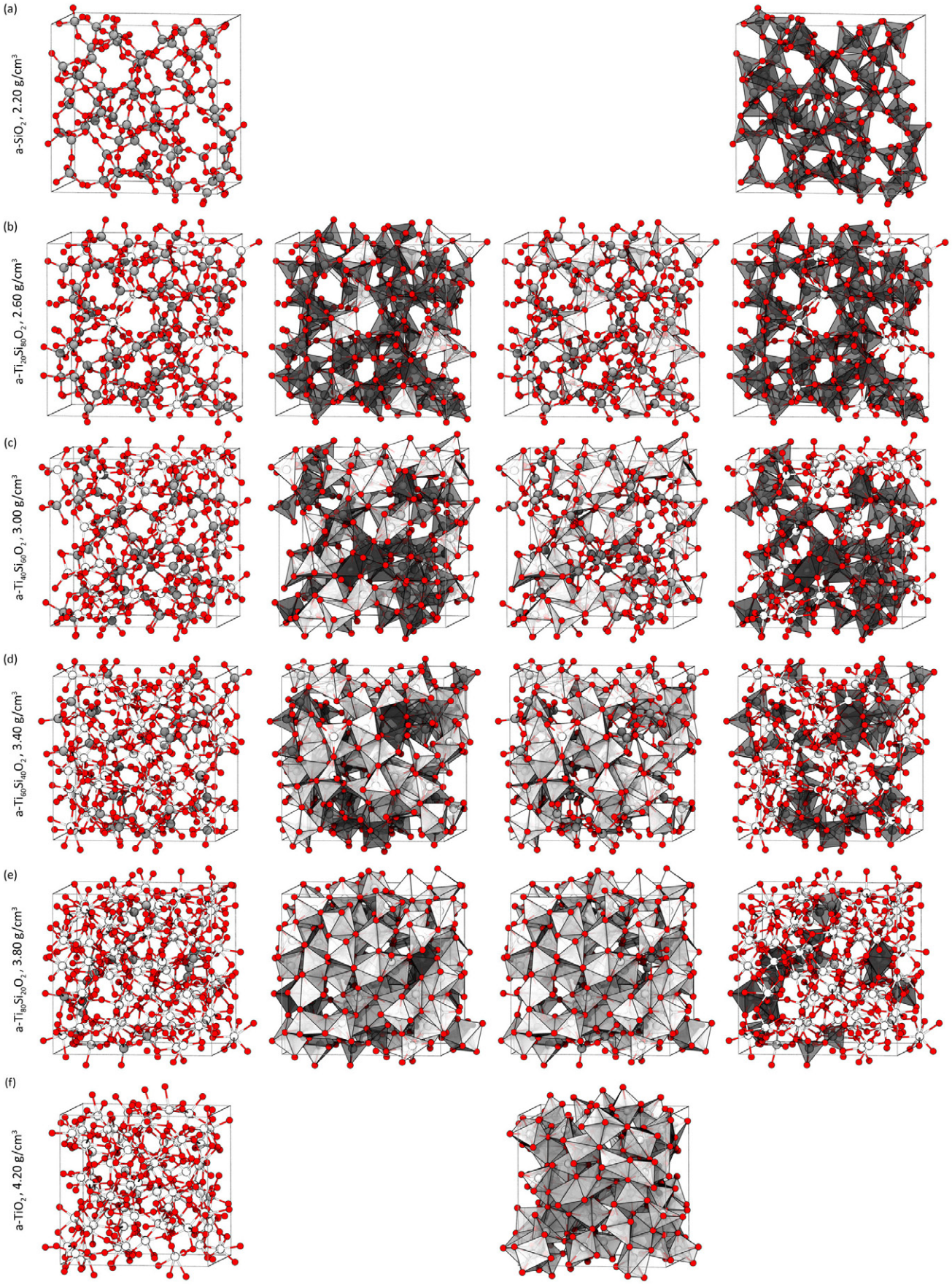

Figure 19. Ball and stick as well as coordination polyhedra representation (Ti: white, Si: dark gray and O: red) of the a-$Ti_xSi_{1-x}O_2$ VASP geometries.

statistics suggest that every Ti ion, on average, contributes equally to the formation of two six-atomic, eight-atomic, and 10-atomic TiO_2 rings.

In contrast to the ring-size distribution of pure a-TiO_2, that remains quite similar to the ring sizes observed in the crystal phases, the ring-size distribution of pure a-SiO_2 shows stronger deviations from the characteristic ring sizes in c-SiO_2 phases. While the tetrahedrally coordinated c-SiO_2 phases, including very low density phases, typically show 8, 10, 12 and 16 atom wide ring-like features, the more flexible amorphous framework of a-SiO_2 allows the formation of several new ring types. The SiO_2 rings in a-SiO_2 show a continuos distribution between four-atomic and 24-atomic rings which is located around a weakly pronounced maximum of 14 atoms wide. Thus, the absence of crystal-like long-range order allows the disordered SiO_4 coordination-polyhedra network to adopt new structural features on a mid-range order length scale as one might expect from a good glass forming material. An identical range of ring-like features has been reported recently by Kohara *et al* [106] for a DFT optimized structure model of a-SiO_2 whereas the ring-size maximum is slightly shifted to 12-atom wide rings. Slightly narrower size distributions ranging from six-atomic to 20-atomic rings as well as six to 18 atom wide rings have been published by Rino *et al* [102] from empirical potential MD as well as Pasquarello *et al* [103] and Giacomazzi *et al* [104] on the basis of DFT simulations, respectively.

The ring distributions of the a-$Ti_xSi_{1-x}O_2$ oxide alloys illustrates the continuos decay of mid-range order features upon increasing Ti content. According to the total ring distribution of a-$Ti_{0.2}Si_{0.8}O_2$ (see figure 18(*a*)), low fractions of Ti ions do not dramatically change the qualitative mid-range order characteristics of the a-SiO_2 matrix. The integration of 20 mol% Ti into the amorphous framework basically produces the same distribution width of ring sizes. Additionally the number of *medium-sized* 10, 12, and 14 atom wide rings increases notably. This increase is obviously not related to binary TiO_2 type rings (see figure 18(*b*)) since pure TiO_2 type rings remain extremely exceptional in the a-$Ti_{0.2}Si_{0.8}O_2$ alloy. Similarly, the larger numbers of rings do not originate from binary SiO_2 type rings (see figure 18(*c*)). In fact, with exception of 6-atomic and 10-atomic rings, whose fractions remain almost constant, the number of all pure SiO_2 rings breaks down. The large majority of the SiO_2 type rings is just slightly modified by the incorporation of TiO_n coordination polyhedra (e.g. see figures 3(*c*-4) and (*c*-5)). The majority of TiO_4 coordination units, despite their larger size, simply replace tetrahedral SiO_4 units within ring structures. In addition, the 25.0% of non-tetrahedrally coordinated Ti_{5c} and Ti_{6c} ions not only replace tetrahedral SiO_4 polyhedra, rather these non-tetrahedral units add new bonding sites to the existing SiO_2 rings without destroying them. The additional bonding sites of the TiO_5 and TiO_6 coordination polyhedra connect to the amorphous SiO_4 network and promote the formation of additional 14, 12, and, especially, 10 atom wide rings. Thus, low amounts of Ti ions in a-SiO_2 actually act as a network forming and a network modifying species that selectively support the additional formation of certain ring sizes, thereby, strengthening the mid-range order within the amorphous oxide alloy. Similar qualitative trends in the modification of the network-order characteristics are observed in the mid composition range at composition parameters of $x = 0.4$ and $x = 0.6$. In a-$Ti_{0.4}Si_{0.6}O_2$ the higher number of non-tetrahedrally coordinated Ti ions promotes the formation of medium-sized rings. Thereby, 10-atomic rings are more and more favored over other ring types. Due to the formation of further medium sized rings, the number of large rings (>18 atoms) starts to decay successively. In agreement with the first observation of a Ti–Ti pair-correlation double peak, that indicates the existence of edge-linked TiO_n coordination polyhedra, the first formation of four-atomic TiO_2 type rings is observed in the ring distribution of the a-$Ti_{0.4}Si_{0.6}O_2$ alloy. Binary SiO_2 type rings are observed less frequent and are restricted to ring sizes of six and 14 atoms. In a-$Ti_{0.6}Si_{0.4}O_2$ the number of four-atomic TiO_2 type rings increases notably. In general, the contributions from smaller ring sizes are enhanced by the progressively increasing number of c-TiO_2 characteristic ring sizes. Medium-sized rings of 12 and 14 atom width are also observed more frequently. Altogether, all a-$Ti_xSi_{1-x}O_2$ oxides with Ti contents $\leqslant$60 mol% show a similar width of their ring-size distribution and might be characterized as mid-range ordered oxide alloys. Looking back to the local coordination numbers, a common feature of all these mid-range ordered oxides is that a majority of 90 ± 4% of Si ions remains tetrahedrally coordinated (see figure 7(*c*)). In addition, the strong increase of medium sized rings directly correlates with TiO_5 coordination polyhedra as the main Ti coordination state (see figure 7(*a*)). The most distinct changes in the alloy-ordering characteristics are observed between composition parameters of $x = 0.6$ and $x = 0.8$. This is quite relevant, since the analysis of the partial pair-correlations, especially between homonuclear Ti pairs, did not indicate notable changes in the atomic structure. Amorphous $Ti_{0.8}Si_{0.2}O_2$ is the first alloy that shows a clear predominance of smaller rings and that, thus, might be characterized as a short range ordered material. Contributions from ring sizes above 12 atoms are notably reduced due to the high Ti content and rings larger than 16 atoms have vanished completely. The number of rings containing 10 or less atoms is roughly doubled. It is quite obvious that these changes correlate with octahedral TiO_6 coordination units becoming the dominant coordination-polyhdera type in the a-$Ti_xSi_{1-x}O_2$ alloys (see figure 7(*a*)). The complete loss of the remaining 20 mol% of Si ions weakly affects the qualitative ring-size distribution characteristics. Most notable, the amount of c-TiO_2 type rings, containing six to 10 atoms, increases significantly, while the number of edge linked TiO_n coordination polyhedra remains constant. Therefore, the notable increase of over-coordinated TiO_7 coordination polyhedra favors corner-linkages between TiO_n coordination units and the additional formation of c-TiO_2 like ring structures in the disordered framework of pure a-TiO_2. The comparison of the ring-size distribution in the VASP and DFTB geometries indicates extremely similar ring-size distributions in the Si-rich a-$Ti_xSi_{1-x}O_2$ hybrid oxides. However, the mid-range order characteristics are partially affected by the structure-simulation approach. On the one hand, four-atomic rings, edge linked TiO_n coordination polyhedra, occur

less frequently. The smaller number of edge-linked coordination units is a consequence of general preference for a fivefold Ti_{5c} ion coordination state over the octahedral Ti_{6c} coordination state at all compositions (see figure 7(*b*)). On the other hand, the number of eight-atomic and 10-atomic rings in pure a-TiO_2 is significantly reduced. Again, this underestimation is a consequence of the, in general, smaller average Ti coordination number in the DFTB geometries. However, the actual width of the total ring-size distribution is just marginally narrower for the Ti-rich oxides.

In summary, ring statistics allow for the clear identification of mid-range order features that characterize the atomic structure of a-SiO_2. Even if not commonly applied to this material class, ring statistics reveal a narrow ring-size distribution in a-TiO_2. In the a-$Ti_xSi_{1-x}O_2$ oxide alloys the ring distribution reflects the competitive nature of both structure-ordering types. The mid-to-short-range order transition between pure a-SiO_2 and pure a-TiO_2 is less continuos as might be expected, for instance, from the various pair-distribution functions. In fact, the pair distribution functions predominantly reflect short-range order features of the atomic structure. In the case of the partial cation-correlation functions, this implies some information on the bonding characteristics of coordination polyhedra to their nearest-neighbor coordination units, whereas, it is not trivially possible to relate higher-order pair correlations to distinct mid-range order features. This causes some *insensitivity* of the atomic pair-correlation functions to actual mid-range order characteristics as the atomic rings of a glassy multi-component oxide network. Doping a-SiO_2 with minor fractions of Ti seem to increase the network connectivity without destroying, shorten respectively, existing rings. Thus low concentrations of Ti in a-SiO_2 glass act as both a glass forming and a glass modifying species that partially enhance the connectivity of the amorphous framework. This observation is quite consistent with the usage of low Ti content SiO_2-TiO_2 glass as an ultra-low thermal expansion material [168–171]. In the mid-range order regime, the additional, predominantly fivefold coordinated, Ti ions enhance the formation of medium-size rings without narrowing the ring-size distribution notably. At high Ti content ($x \geqslant 0.8$) the amorphous oxide alloys lose their mid-range order characteristics which indicates the formation of a low-density a-TiO_2 phase that is weakly disturbed by the presence of small amounts of Si ions.

4.8. Nanoscale phase separation

Finally, we address the question of phase separation in amorphous a-$Ti_xSi_{1-x}O_2$ hybrid oxides. It is quite obvious that our structure models describe rather the atomically mixed amorphous oxides than a phase separated material with notable domains of pure binary amorphous, or even crystalline, oxides. The chemically decomposed polyhedra representations of the a-$Ti_xSi_{1-x}O_2$ VASP geometries in figure 19 clearly show that the generated structure models are atomically mixed and no phase separation, phase segregation of a TiO_2 rich phase respectively, occurs throughout the entire composition range. As discussed above, cluster-like TiO_2 conglomerates are restricted to the mid-composition range and the size

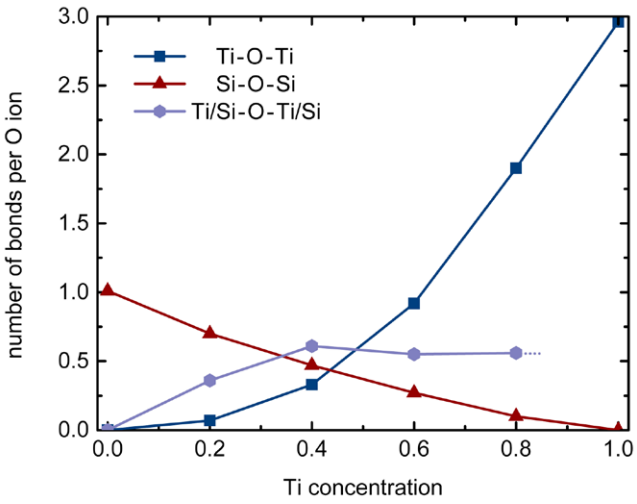

Figure 20. Number of homonuclear Ti–O–Ti and Si–O–Si as well as heteronuclear Ti/Si–O–Ti/Si cross linking bonds between various coordination polyhedra in the a-$Ti_xSi_{1-x}O_2$ VASP geometries.

of a few TiO_n coordination units (see figure 4(*c*-6)). The Ti rich a-$Ti_xSi_{1-x}O_2$ alloys systematically form mixed edge and corner-linked a-TiO_2 phases of diverse mass-density.

Some additional insights into the mixing properties are provided by the amount of homopolar Ti–O–Ti and Si–O–Si as well as heteropolar Ti/Si–O–Ti/Si bonds linking various coordination polyhedra illustrated in figure 20. Amorphous SiO_2 type network features dominate the ordering characteristics of the alloy below a composition of $x \approx 0.3$. With the beginning of edge-linking between TiO_n coordination polyhedra (see figure 18), Ti–O–Ti linkages become the dominant type of polyhedra bonds above a composition parameter of $x \approx 0.5$. In the small window between $x \approx 0.3$ and $x \approx 0.5$, mixed heteronuclear polyhedra linkages become the dominating bonding type. In pure a-SiO_2 the number of Si–O–Si bonds per O ion decrease slightly nonlinear from a value of 1.01, that is characteristic to an almost perfectly tetrahedrally coordinated SiO_4 network, to zero. Due to the higher connectivity of Ti ions, the number of Ti–O–Ti bonds increases quadratically to a value of 3.02 indicating, on average, an octahedral TiO_2 network. For both types of homopolar bonds the observed dependence on the Ti content, mass density respectively, indicates a continuos transition between the binary oxides. In contrast to homonuclear O ion linkages, the number of heteronuclear polyhedra-linking Ti/Si–O–Ti/Si bonds shows an discontinuous dependence on the Ti content. Up to 40 mol% of Ti ions, the number of Ti/Si–O–Ti/Si bonds per O ion increases to a value of 0.61 indicating that more than every second O ion in the a-$Ti_{0.4}Si_{0.6}O_2$ alloy interlinks a TiO_n coordination polyhedron with a SiO_m coordination polyhedron. Above a composition parameter of $x = 0.4$ the number of polyhedra-linking Ti/Si–O–Ti/Si bonds per O ion remains approximately constant. The constant number of Ti/Si–O–Ti/Si bonds per O ion indicates an increasing Si coordination state since the number of the Si ions decrease continuously and, thus, the connectivity of SiO_m coordination polyhedra has to increase to enhance the number of Ti/Si–O–Ti/Si bonds. This strongly suggest that the Si ions

are isotropically distributed in the Ti rich alloys and increase their coordination states in response to the surrounding higher coordination states of Ti ions. If SiO_2 would exist phase separated from TiO_2 only the coordination state of Si ions at the domain boundaries might change with variations in the alloy composition. Similarly, the formation of a separate TiO_2 phase should be reflected in the number of Ti–O–Ti linkages. Assuming the commonly reported coordination model of TiO_2 doped SiO_2 glasses, Ti ions are commonly fourfold coordinated at low Ti content and adopt a octahedral coordination state somewhere above 20 to 40 mol% of Ti ions. This would suggest that also the number of Ti–O–Ti polyhedra linkages should show indications of the tetrahedral-octahedral Ti coordination transition.

Altogether, no explicit indications of phase separation are given in our structure models indicating the general possibility of atomically mixed a-$Ti_xSi_{1-x}O_2$ hybrid oxides even at high Ti concentrations. However, it cannot be excluded that reheating beyond the crystallization temperature in successive MD runs favors the formation of a c-TiO_2 phase, most likely anatase or rutile, over an atomically mixed alloy phase.

5. Summary and conclusion

To conclude our study on the atomic structure of ternary a-$Ti_xSi_{1-x}O_2$ hybrid oxides, we briefly summarize our key results:

- Short and mid-range order in the amorphous phases of $Ti_xSi_{1-x}O_2$ hybrid oxides are comprehensively characterized by bond length and bond-angle statistics, pair distribution function analysis, coordination number and coordination polyhedra statistics, as well as ring statistics.
- The fundamental composition dependences of the cation-coordination numbers, observed in both the VASP and the DFTB geometries, mean that notable fractions of the Ti and Si ions experience a change in their local atomic coordination states with respect to their predominant coordination in crystalline binary (di)oxides.
- The average Si coordination number of $N_{C_{Si}} = 4.03$ indicates a virtually perfect tetrahedral coordination in pure a-SiO_2. The extrapolation towards a very dilute Si dispersion indicates a coordination number around ∼4.8 at very high Ti contents.
- The average Ti coordination number shows a cubic dependence on the composition parameter and an extrapolated fourfold coordination state in the limit of a very dilute distribution of Ti ions in the disordered framework of a-SiO_2. The average coordination number of pure a-TiO_2 of $N_{C_{Ti}}[1.0] = 5.89$ remains slightly below the crystal-coordination limit.
- The total coordination number of O ions changes nonlinear from an almost perfect ($N_{C_O}[0.0] = 2.01$) crystalline Si_{2c} coordination state in pure a-SiO_2 to $N_{C_O}[1.0] = 2.94$ which is close to the O coordination in crystalline TiO_2.
- An average Ti coordination number close to the sixfold crystalline coordination is by far no evidence for a disordered a-TiO_2 network that is predominantly formed by (distorted) octahedron building blocks. Just slightly more than half of all Ti ions (∼ 54%) preserve their crystalline coordination state. All other Ti coordination states arise from coordination defects that increase or decrease the local atomic coordination number by ±1 or ± 2.
- The intermediate fivefold Ti coordination state contributes notably to the a-$Ti_xSi_{1-x}O_2$ coordination characteristics. In the a-$Ti_{0.6}Si_{0.4}O_2$ oxide alloy TiO_5 building blocks even become the predominant coordination-polyhedra type.
- With progressively decreasing Ti content, the Ti ions tend to adopt the dominant fourfold coordination state of Si ions in a-SiO_2.
- The local Si coordination numbers indicate that SiO_4 coordination polyhedra are very robust with respect to changes of the chemical composition parameter in a-$Ti_xSi_{1-x}O_2$. The fraction of SiO_4 coordination polyhedra remains roughly constant at 90 ± 4% up to a composition parameter of $x = 0.6$.
- The fractions of over-coordinated Si ions increase for a notable fraction of SiO_m coordination polyhedra only in the presence of a large number of higher coordinated Ti ions ($x \geqslant 0.8$).
- The detailed analysis of the coordination-polyhedra shapes demonstrates that disorder in binary and ternary a-$Ti_xSi_{1-x}O_2$ oxides is not only related to changes in the local coordination numbers but also to variations in the basic coordination-polyhedra symmetry types. Amorphous alloys do not necessarily contain only weakly distorted versions of a single crystal-like coordination polyhedron, rather various deformed polyhedra types coexist side by side.
- Bond lengths and bond-angles distributions indicate that the SiO_m coordination polyhedra participate rather passively in the formation of the amorphous frameworks of a-$Ti_xSi_{1-x}O_2$ hybrid oxides. Individual coordination units do not absorb significant fractions of atomic short-range disorder by beeing distorted into new coordination-polyhedra geometry types.
- The formation of new high Ti coordination states in a-$Ti_xSi_{1-x}O_2$ hybrid oxides depends critically on the Ti content. The average bond lengths and bond angles indicate that the formation of new TiO_n coordination polyhedra closely resembles bifurcation-like changes in a complex system. The mass density acts as the critical system parameter for the spontaneous formation of new coordination units that itself is triggered by strong deformations in the coordination environment of existing coordination-polyhedra building blocks.
- Effective coordination numbers prove to be quite sensitive to symmetry reductions of the local cation coordination environment and thus, the particular shape and symmetry type of a coordination polyhedron. Thus, the effective coordination numbers might be used as qualitative and, if compared to the conventional coordination numbers, quantitative measures for the degree of disorder within the first coordination shell around an atom.

- The disorder of the amorphous network increases with increasing Ti content. A dominant but almost constant fraction of disorder is carried by the local Ti ion coordination environments, and to a much smaller extent by the local Si ion coordination environments. Further disorder effects are projected onto the spatial arrangement of the coordination polyhedra, a.k.a. the amorphous network itself.
- Both the conventional and the effective coordination numbers provide fundamental information on the short-range order in amorphous oxides. While an in depth analysis of coordination-polyhedra remains an elaborate task and the conventional coordination numbers do not provide a measure for the degree of disorder within different coordination polyhedra, the effective coordination-number approach serves both purposes. Effective coordination numbers, as used in this study, are suited to determine the local coordination state of ions in the investigated amorphous hybrid oxides and to obtain information on the degree of disorder within the first coordination shell.
- It seems difficult to extract clear trends from the effective coordination numbers of individual coordination-polyhedra geometry types. This observation suggests that a purely exponential weighting function, might not be an ideal choice to characterize the atomic short-range order in an amorphous solid.
- Total pair-correlation functions do not, per se, allow us to identify structure correlations between arbitrary pairs of chemical elements. In addition, short-range order differences within the first correlation shell, that are indicated in the local coordination number analysis, are not resolved, or rather hidden, in the total pair correlation functions.
- Coordination polyhedra show a decreasing average bond length with increasing alloy density, thus the observed first correlation-shell shift of Ti–O and Si–O pair correlations to higher bond lengths with increasing Ti content necessitates the occurrence of successively higher coordinated TiO_n as well as SiO_m building blocks.
- The Ti–Ti pair correlation peaks show a qualitative transition from a single-peak characteristic at low Ti content ($x = 0.2$) to a double-peak characteristic in the mid-composition range. The different Ti–Ti correlation lengths originate from TiO_n coordination units connected by sharing either a common corner or a common edge with a neighboring TiO_n coordination polyhedron.
- The analysis of the partial pair-distribution functions allows us to deduce ordering characteristics of the coordination polyhedra among themselves. Hints on extended mid-range ordering features within the amorphous oxides are given indirectly. Deeper insights into the mid-range order of a-$Ti_xSi_{1-x}O_2$ oxide alloys require more specialized structure-analysis techniques as ring statistics.
- Even if not commonly applied to this material class, ring statistics reveal a quite narrow ring-size distribution in a-TiO_2 with predominant ring sizes below 12 atoms. In the a-$Ti_xSi_{1-x}O_2$ oxide alloys the ring distribution reflects the competitive nature of both short-range and mid-range types of atomic order.
- At low concentrations, Ti in a-SiO_2 glass acts as both a glass forming and a glass modifying species that partially enhances the connectivity of the amorphous framework without destroying existing rings.
- No explicit indications of phase separation are found in our structure models indicating the general capability of a-$Ti_xSi_{1-x}O_2$ hybrid oxides to form atomically mixed alloys even at high Ti concentrations.

The present study provides a comprehensive database for the characterization and interpretation of experimental data on short-range and mid-range order characteristics for the wide class of technologically important a-TiO_2 and a-SiO_2 containing amorphous and nano-structured oxides. The potential of various structure analysis approaches to describe atomic ordering features on various atomic length scales is comprehensively demonstrated for the disordered atomic frameworks of ternary a-$Ti_xSi_{1-x}O_2$ hybrid oxides. The results of this analysis will serve the future understanding of structure related electronic and optical properties of a-$Ti_xSi_{1-x}O_2$ alloys and disordered material phases in general.

Acknowledgments

The calculations were done using grants of computer time from the Regionales Rechenzentrum of the Universität zu Köln (RRZK), the Paderborn Center for Parallel Computing (PC2) and the Höchstleistungs-Rechenzentrum Stuttgart. The Deutsche Forschungsgemeinschaft is acknowledged for financial support.

References

[1] Yu-Zhang K, Boisjolly G, Rivory J, Kilian L and Colliex C 1994 *Thin Solid Films* **253** 299
[2] Gallas B, Brunet-Bruneau A, Fisson S, Vuye G and Rivory J 2002 *J. Appl. Phys.* **92** 1922
[3] Miyashita K, Kuroda S, Tajima S, Takehira K, Tobita S and Kubota H 2003 *Chem. Phys. Lett.* **369** 225
[4] Lu J, Kosuda K M, Van Duyne R P and Stair P C 2009 *J. Phys. Chem.* C **113** 12412
[5] Liu C, Fu Q, Wang J B, Zhao W K, Fang Y L, Mihara T and Kiuchi M 2005 *J. Korean Phys. Soc.* **46** 104
[6] Yoon J-G, Oh H K and Kwag Y J 1998 *J. Korean Phys. Soc.* **33** 699
[7] Wang Z M, Fang Q, Zhang J-Y, Wu J X, Di Y, Chen W, Chen M L and Boyd I W 2004 *Thin Solid Films* **453–4** 167
[8] Larouche S, Szymanowski H, Klemberg J E, Martinu L and Gujrathi S C 2004 *J. Vac. Sci. Technol.* A **22** 1200
[9] Gracia F, Yubero F, Holgado J P, Espinos J P, Gonzalez A R and Girardeau T 2006 *Thin Solid Films* **500** 19
[10] Gracia F, Yubero F, Espinos J P, Holgado J P, Gonz A R and Girardeau T 2006 *Surf. Interface Anal.* **38** 752
[11] Busani T, Devine R A B, Yu X and Seo H-W 2006 *J. Vac. Sci. Technol.* A **24** 369
[12] Smith D Y, Black C E, Homes C C and Shiles E 2007 *Phys. Status Solidi c* **4** 838
[13] Cheng S C 2008 *J. Non-Cryst. Solids* **354** 3735
[14] Nakayama T 1994 *J. Electrochem. Soc.* **141** 237
[15] Demiryont H 1985 *Appl. Opt.* **24** 2647
[16] Chao S, Wang W-H, Hsu M-Y and Wang L-C 1999 *J. Opt. Soc. Am.* A **16** 1477

[17] Chao S, Wang W-H and Lee C-C 2001 *Appl. Opt.* **40** 2177
[18] Wang X, Masumoto H, Someno Y and Hirai T 1999 *Thin Solid Films* **338** 105
[19] Matsuda A, Matsuno Y, Katayama S and Tsuno T 1989 *J. Mater. Sci. Lett.* **8** 902
[20] Bahtat M, Mugnier J, Bovier C, Roux H and Serughetti J 1992 *J. Non-Cryst. Solids* **147–8** 123
[21] Holmes A S, Syms R R A, Li M and Green M 1993 *Appl. Opt.* **32** 4916
[22] Doolin P K, Alerasool S, Zalewski D J and Hoffman J F 1994 *Catal. Lett.* **25** 209
[23] Almeida R M, Orignac X and Barbier D 1994 *J. Sol–Gel Sci. Technol.* **2** 465
[24] Liu Z and Davis R J 1994 *J. Phys. Chem.* **98** 1253
[25] Keshavaraja A, Ramaswamy V, Soni H S, Ramaswamy A V and Ratnasamy P 1995 *J. Catal.* **157** 501
[26] Rigden J S, Newport R J, Smith M E and Dirken P J 1996 *Mater. Sci. Forum* **228–31** 519
[27] Orignac X, Barbier D, Du X M and Almeida R M 1996 . *Appl. Phys. Lett.* **69** 895
[28] Henderson G S and Fleet M E 1997 *J. Non-Cryst. Solids* **211** 214
[29] Van Grieken R, Sotelo J L, Martos C, Fierro J L G, López-Granados M and Mariscal R 2000 *Catal. Today* **61** 49
[30] Jung K Y and Bin Park S 2004 *Mater. Lett.* **58** 2897
[31] Davis R J and Liu Z 1997 *Chem. Mater.* **9** 2311
[32] Ääritalo V, Areva S, Jokinen M, Lindén M and Peltola T 2007 *J. Mater. Sci.: Mater. Med.* **18** 1863
[33] Indrea E, Peter A, Silipas D T, Dreve S, Suciu R-C, Rosu M C, Danciu V and Cosoveanu V 2009 *J. Phys.: Conf. Ser.* **182** 012066
[34] Cernuto G, Galli S, Trudu F, Colonna G M, Masciocchi N, Crevellino A and Guagliardi A 2011 *Angew. Chem.* **50** 10828
[35] Burn N, Colliex C, Rivory J and Yu-Zhang K 1996 *Microsc. Microanal. Microstruct.* **7** 161
[36] Nakamura M, Kobayashi M, Kuzuya N, Komatsu T and Mochizuka T 2006 *Thin Solid Films* **502** 121
[37] Areva S, Ääritalo V, Tuusa S, Jokinen M, Lindén M and Peltola T 2007 *J. Mater. Sci.: Mater. Med.* **18** 1633
[38] Masuda Y, Jinbo Y and Koumoto K 2009 *Sci. Adv. Mater.* **1** 138
[39] Sorek Y, Reisfeld R, Finkelstein I and Ruschin S 1993 *Appl. Phys. Lett*. **63** 3256
[40] Syms R R A and Holmes A S 1993 *IEEE Photon. Technol. Lett.* **5** 1077
[41] Bovard B G 1993 *Appl. Opt.* **32** 5427
[42] Poitras D, Larouche S and Martinu L 2002 *Appl. Opt.* **41** 5249
[43] Lorenzo E, Oton C J, Capuj N E, Ghulinyan M, Navarro-Urrios D, Gaburro Z and Pavesi L 2005 *Phys. Status Solidi c* **9** 3227
[44] Netterfield R P, Martin P J, Pacey C G, Sainty W G and McKenzie D R 1989 *J. Appl. Phys.* **66** 1805
[45] Wang X, Masumoto H, Someno Y and Hirai T 1998 *J. Vac. Sci. Technol.* A **16** 2926
[46] Gao X and Wachs I E 1999 *Catal. Today* **51** 233
[47] Dagan G, Sampath S and Lev O 1995 *Chem. Mater.* **7** 446
[48] Jung K Y and Park S B 2000 *Appl. Catal. B: Environ.* **25** 249
[49] Pitoniak E, Wu C-Y, Mazyck D W, Powers K W and Sigmund W 2005 *Environ. Sci. Technol.* **39** 1269
[50] Qi K, Chen X, Liu Y, Xin J H, Mak C L and Daouda W A 2007 *J. Mater. Chem.* **17** 3504
[51] Thangaraj A, Sivasanker S and Ratnasamy P 1991 *J. Catal.* **131** 394
[52] Pei S, Zajac W, Kaduk J A, Faber J, Boyanov B I, Duck D, Fazzini D, Morrison T I and Yang D S 1993 *Catal. Lett.* **21** 333
[53] Anderson M W, Terasaki O, Ohsuna T, Phillppou A, MacKay S P, Ferreira A, Rocha J and Lidin S 1994 *Nature* **367** 347
[54] Uguina M A, Serrano D P, Ovejero G, Van Grieken R and Camacho M 1995 *Appl. Catal. A: Gen.* **124** 391
[55] Liu Z, Crumbaugh G M and Davis R J 1996 *J. Catal.* **159** 83
[56] Roberts M A, Sankar G, Thomas J M, Jones R H, Du H, Chen J, Pang W and Xu R 1996 *Nature* **381** 401
[57] Borello E, Lambreti C, Bordiga S, Zecchina A and Are C O 1997 *Appl. Phys. Lett.* **71** 2319
[58] Ko Y S and Ahn W S 1998 *Korean J. Chem. Eng.* **15** 182
[59] Kuznicki S M, Bell V A, Nair S, Hillhouse H W, Jacubinas R M, Braunbarth C M, Toby B H and Tsapatsis M 2001 *Nature* **412** 720
[60] Méndez-Vivar J and Mendoza-Serna R 2006 *Silicon Chem.* **3** 59
[61] Cao S, Yao N and Yeung K L 2008 *J. Sol–Gel Sci. Technol.* **46** 323
[62] Gamba A, Tabacchi G and Fois E 2009 *J. Phys. Chem.* A **113** 15006
[63] Faustini M, Vayer M, Marmiroli B, Hillmyer M, Amenitsch H, Sinturel C and Grosso D 2010 *Chem. Mater.* **22** 5687
[64] Serrano D P, Uguina M A, Ovejero G, Van Grieken R and Camacho M 1996 *Microporous Mater.* **7** 309
[65] Notari B 1993 *Catal. Today* **18** 163
[66] Uguina M A, Ovejero G, Van Grieken R, Serrano D P and Camacho M 1994 *J. Chem. Soc. Chem. Commun.* **1** 27
[67] Best M F and Condrate R A Sr 1985 *J. Mat. Sci. Lett.* **4** 994
[68] Soriano L, Fuentes G G, Quirós C, Trigo J F, Sanz J M, Bressler P R and Gonz A R 2000 *Langmuir* **16** 7066
[69] Espin J P, Lassaletta G, Caballero A, Fernández A and Gonz A R 1998 *Langmuir* **14** 4908
[70] Sandstorm D R, Lytle F W, Wei P S P, Greegor R B, Wong J and Schultz P 1980 *J. Non-Cryst. Solids* **41** 201
[71] Greegor R B, Lytle F W, Sandstorm D R, Wong J and Schultz P 1983 *J. Non-Cryst. Solids* **55** 27
[72] Rigden J S, Walters J K, Dirken P J, Smith M E, Bushnell-Wye G, Howells W S and Newport R J 1997 *J. Phys.: Condens. Matter* **9** 4001
[73] Orignac X, Vasconcelos H C and Almeida R M 1997 *J. Non-Cryst. Solids* **217** 155
[74] Farges F, Brown G E Jr and Rehr J J 1996 *Geochim. Cosmochim. Acta* **60** 3023
[75] Farges F, Brown G E Jr, Navrotsky A, Gan H and Rehr J J 1996 *Geochim. Cosmochim. Acta* **60** 3039
[76] Farges F, Brown G E Jr, Navrotsky A, Gan H and Rehr J J 1996 *Geochim. Cosmochim. Acta* **60** 3055
[77] Andersson S and Wadsley A D 1961 *Acta Chem. Scand.* **15** 663
[78] Markgraf S A, Halliyal A, Bhalla A S, Newham R E and Prewitt C T 1985 *Ferroelectrics* **62** 17
[79] Nyman H, O'Keefe M and Bovin J-O 1978 *Acta Cryst.* B **34** 905
[80] Yarker C A, Johnson P A V, Wright A C, Wong J, Greegor R B, Lytle F W and Sinclair R N 1986 *J. Non-Cryst. Solids* **79** 117
[81] Dingwell D B, Paris E, Seifert F, Mottana A and Romano C 1994 *Phys. Chem. Minerals* **21** 501
[82] Farges F and Brown G E Jr 1997 *Geochim. Cosmochim. Acta* **61** 1863
[83] Osipov A A, Korinevskaya G G, Osipova L M and Muftakhov V A 2012 *Glass Phys. Chem.* **38** 357
[84] Bandyopadhyay I and Aikens C M 2011 *J. Phys. Chem.* A **115** 868
[85] Rosenthal A B and Garofalini S H 1988 *J. Non-Cryst. Solids* **107** 65
[86] Elstner M, Porezag D, Jungnickel G, Elsner J, Haugk M, Frauenheim T, Suhai S and Seifert G 1998 *Phys. Rev.* B **58** 7260

[87] Porezag D, Frauenheim T, Köhler T, Seifert G and Kaschner R 1995 *Phys. Rev.* B **51** 12947
[88] Frauenheim Th, Seifert G, Elstner M, Haynal Z, Jungnickel G, Suhai S and Scholz R 2000 *Phys. Status Solidi* B **227** 41
[89] Hohenberg P and Kohn W 1964 *Phys. Rev.* **136** B864
[90] Kohn W and Sham L J 1965 *Phys. Rev.* **140** A1133
[91] Vegard L 1921 *Z. Phys.* **5** 17
[92] Denton A R and Ashcroft N W 1991 *Phys. Rev.* A **43** 3161
[93] Dolgonos G, Aradi B, Moreira N H and Frauenheim Th 2010 *J. Chem. Theory Comput.* **6** 266
[94] Blöchl P E 1994 *Phys. Rev.* B **50** 17953
[95] Kresse G and Joubert D 1999 *Phys. Rev.* B **59** 1758
[96] Kresse G and Furthmüller J 1996 *Comput. Mater. Sci.* **6** 15
[97] Perdew J P, Burke K and Ernzerhof M 1996 *Phys. Rev. Lett.* **77** 3865
[98] Landmann M, Köhler T, Köppen S, Rauls E, Frauenheim T and Schmidt W G 2012 *Phys. Rev.* B **86** 064201
[99] Köhler T, Turowski M, Ehlers H, Landmann M, Ristau D and Frauenheim T 2013 *J. Phys. D: Appl. Phys.* **46** 325302
[100] Le Roux S and Jund P 2010 *Comput. Mat. Sci.* **49** 70
[101] Le Roux S and Petkov V 2010 *J. Appl. Cryst.* **43** 181
[102] Rino J P, Ebbsj R K, Kalia, Nakano A and Vashishta P 1993 *Phys. Rev.* B **47** 3053
[103] Pasquarello A and Car R 1998 *Phys. Rev. Lett.* **80** 5145
[104] Giacomazzi L, Umari P and Pasquarello A 2009 *Phys. Rev.* B **79** 064202
[105] Martin-Samos L, Bussi G, Ruini A, Molinari E and Caldas M J 2010 *Phys. Rev.* B **81** 081202
[106] Kohara S, Akola J, Morita H, Suzuya K, Weber J K R, Wilding M C and Benmore C J 2011 *Prog. Natl Acad. Sci.* **108** 14780
[107] Halder N C and Wagner N J 1967 *J. Chem. Phys.* **47** 4385
[108] Billinge S J L 2004 *Z. Kristallogr.* **219** 117
[109] Billinge S J L 2008 *J. Solid State Chem.* **181** 1698
[110] Kalikka J, Akola J and Jones R O 2013 *J. Phys.: Condens. Matter* **25** 115801
[111] Los J H, Kühne T D, Gabardi S and Bernasconi M 2013 *Phys. Rev.* B **87** 184201
[112] Kohara S *et al* 2006 *Appl. Phys. Lett.* **89** 201910
[113] Kalikka J, Akola J, Jones R O, Kohara S and Usuki T 2012 *J. Phys.: Condens. Matter* **24** 015802
[114] Gabardi S, Caravati S, Bernasconi M and Parrinello M 2012 *J. Phys.: Condens. Matter* **24** 385803
[115] Franzblau D S 1991 *Phys. Rev.* B **44** 4925
[116] Yuan X and Cormack A N 2002 *Comput. Mat. Sci.* **24** 343
[117] Wooten F 2002 *Acta Cryst.* A **58** 346
[118] King S V 1967 *Nature* **213** 1112
[119] Guttman L 1990 *J. Non-Cryst. Solids* **116** 145
[120] Henderson G S and Fleet M E 1995 *Can. Mineral.* **33** 399
[121] Bernard C, Chaussedent S, Monteil A and Ferrari M 2002 *Phil. Mag.* B **82** 681
[122] Werner A 1893 *Z. Anorg. Chem.* **3** 267
[123] Hartshorn R M 2007 *Pure Appl. Chem.* **79** 1779
[124] Bhandary K K and Girgis K 1977 *Acta Cryst.* A **33** 903
[125] Landmann M, Rauls E and Schmidt W G 2012 *J. Phys.: Condens. Matter* **24** 195503
[126] Johnson N W 1966 *Can. J. Math.* **18** 169
[127] Wolf G H, Durben D J and McMillan P F 1990 *J. Chem. Phys.* **93** 2280
[128] Stebbins J F 1991 *Nature* **351** 638
[129] Stebbins J F 1999 *Geophys. Res. Lett.* **26** 2521
[130] Perron H, Domain C, Roques J, Drot R, Simoni E and Catalette H 2007 *Theor. Chem. Acc.* **117** 566
[131] Lazzeri M, Vittadini A and Selloni A 2001 *Phys. Rev.* B **63** 155409
[132] Beltrán A, Gracia L and Andrés J 2006 *J. Phys. Chem.* B **110** 23417
[133] Berry R S 1960 *J. Chem. Phys.* **32** 933
[134] Ugi I, Marquarding D, Klusacek H, Gillespie P and Ramirez F 1971 *Acc. Chem. Res.* **4** 288
[135] Roessler B, Pfennig V and Seppelt K 2001 *Chem. Eur. J.* **7** 3652
[136] Ellern A and Seppelt K 1995 *Angew. Chem. Int. Edn Engl.* **34** 1586
[137] Mo S-D and Ching W Y 1995 *Phys. Rev.* B **51** 13023
[138] Hoffman R, Howell J M and Rossi A 1976 *J. Am. Chem. Soc.* **98** 2484
[139] King R B 2001 *J. Organometall. Chem.* **623** 95
[140] Alvarez S, Avnir D, Llunell M and Pinsky M 2002 *New J. Chem.* **26** 996
[141] Casanova D, Cirera J, Llunell M, Alemany P, Avnir D and Alvarez S 2004 *J. Am. Chem. Soc.* **126** 1755
[142] Ruff O and Keim R 1930 *Z. Anorg. Allg. Chem.* **193** 176
[143] Adams W J, Thompson H B and Bartell L S 1970 *J. Chem. Phys.* **53** 4040
[144] Randić M and Maksić Z 1966 *Theor. Chim. Acta* **4** 145
[145] Cotton F A, Duraj S A and Roth W W J 1984 *Inorg. Chem.* **23** 4046
[146] Das A K, Chatterjee M and Chattopadhyay S 2011 *Inorg. Chem. Commun.* **14** 1337
[147] Bar-Yam Y and Joannopoulos J D 1986 *Phys. Rev. Lett.* **56** 2203
[148] Branz H M and Schiff E A 1993 *Phys. Rev.* B **48** 8667
[149] Hoppe R 1970 *Angew. Chem Int. Edn Engl.* **9** 25
[150] Hoppe R, Voigt S, Glaum H, Kissel J, Müller H P and Bernet K 1989 *J. Less-Common Met.* **156** 105
[151] Ferraris G 2002 Mineral and inorganic crystals *Fundamentals of Crystallography* ed G Giacovazzo (New York: Oxford University Press) pp 503–84
[152] Da Silva J L F, Walsh A and Wei S-H 2009 *Phys. Rev.* B **80** 214118
[153] Piotrowski M J, Piquini P and Da Silva J L F 2010 *Phys. Rev.* B **81** 155446
[154] Da Silva J L F, Kim H G, Piotrowski M J, Prieto M J and Tremiliosi-Filho G 2010 *Phys. Rev.* B **82** 205424
[155] Da Silva J L F 2011 *J. Appl. Phys.* **109** 023502
[156] Takikawa H, Matsui T, Sakakibara T, Bendavid A and Martin P J 1999 *Thin Solid Films* **348** 145
[157] Zhao Z W, Tay B K, Lau S P and Yu G Q 1993 *J. Cryst. Growth* **268** 543
[158] Luca V, Djajanti S and Howe R F 1998 *J. Phys. Chem.* B **102** 10650
[159] Petkov V, Holzhüter G, Tröge U, Gerber Th and Himmel B 1998 *J. Non-Crystal. Solids* **231** 17
[160] Sorantin P I and Schwarz K 1992 *Inorg. Chem.* **31** 567
[161] Calatayud M, Mori-Sánchez M, Beltrán A, Pend A M, Francisco E, Andrés J and Recio J M 2001 *Phys. Rev.* B **64** 184113
[162] Demuth Th, Jeanvoine Y, Hafner J and Ángyán J G 2011 *J. Appl. Phys.* **109** 023502
[163] Van Hoang V 2007 *J. Phys.: Condens. Matter* **19** 416109
[164] Van Hoang V 2007 *Phys. Status Solidi b* **244** 1280
[165] Matsui M and Akaogi M 1991 *Mol. Simul.* **6** 239
[166] Wallidge G W, Anderson R, Mountjoy G, Pickup D M, Gunawidjaja P, Newport R J and Smith M E 2004 *J. Mater. Sci.* **39** 6743
[167] Pickup D M, Sowrey F E, Newport R J, Gunawidjaja P, Drake K O and Smith M E 2004 *J. Phys. Chem.* B **108** 10872
[168] Schulz P 1976 *J. Am. Ceram. Soc.* **59** 214
[169] Hayashi T, Yamada T and Saito H 1983 *J. Mater. Sci.* **18** 3137
[170] Kim K -D and Khalil T 1996 *J. Non-Cryst. Solids* **195** 218
[171] Beall G H and Pinckney L R 1999 *J. Am. Ceram. Soc.* **82** 5

Paper VI

GaN m-plane: Atomic structure, surface bands and optical response

M. Landmann, E. Rauls, W. G. Schmidt, M. D. Neumann, E. Speiser, and N. Esser

PHYSICAL REVIEW B **91**, 035302, 9 pp. (2015)

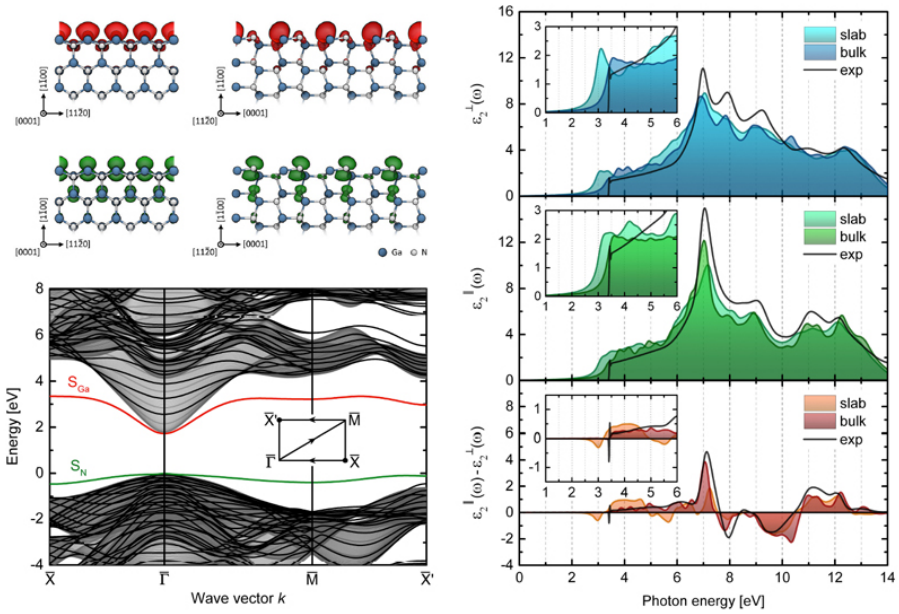

GaN *m*-plane: Atomic structure, surface bands, and optical response

M. Landmann,[1] E. Rauls,[1] W. G. Schmidt,[1] M. D. Neumann,[2] E. Speiser,[2] and N. Esser[2]
[1]*Lehrstuhl für Theoretische Physik, Universität Paderborn, 33095 Paderborn, Germany*
[2]*Leibniz-Institut für Analytische Wissenschaften-ISAS e.V., Schwarzschildstrasse 9, 12489 Berlin, Germany*
(Received 7 October 2014; published 7 January 2015)

Density-functional-theory calculations are combined with many-body perturbation theory in order to elucidate the geometry, electronic, and optical properties of the wz-GaN($1\bar{1}00$) surface, i.e., the so-called m-plane. The optical absorption and reflection anisotropy related to electronic transitions between surface states are identified by comparison with measured data covering transition energies from 2.4 up to 5.4 eV. Our results show a surface relaxation mechanism consistent with the electron counting rule that causes a moderate buckling of the GaN surface dimers and gives rise to two distinct surface states: The doubly occupied N dangling bonds form a surface band that is resonant with the GaN valence-band edge at the center of the Brillouin zone, whereas the empty Ga dangling bonds occur within the GaN band gap closely following the dispersion of the conduction-band edge. These two states contribute strongly to the formation of surface excitons that redshift the optical absorption with respect to the bulk optical response. The surface optical absorption i.e., the excitonic onset below the bulk band gap followed by a broad absorption band at higher energies related to the dispersion of the surface band structure, is calculated in agreement with the experimental data.

DOI: 10.1103/PhysRevB.91.035302 PACS number(s): 73.20.At, 68.35.B−, 78.40.Fy

I. INTRODUCTION

Gallium-nitride-based heterostructures have been routinely used since the 1990s for electronic and optoelectronic applications [1] that exploit its wide band gap of approximately 3.4 eV at room temperature. The low sensitivity of the material to ionizing radiation as well as its functionality at high temperatures and high voltages make it attractive for various electronic devices. Typically these devices are based on heterostructures grown on c-plane substrates; see Fig. 1 for the illustration of the most relevant low-index GaN crystal-surface planes. This orientation, however, gives rise to strong electric fields in the wurtzite material [2] that are often disadvantageous for the performance of devices. It has been demonstrated, however, that the epitaxial growth in a nonpolar direction allows the fabrication of structures free of electrostatic fields [3]. For this reason, in addition to the common c-plane, the nonpolar GaN surfaces, i.e., the m-plane with ($1\bar{1}00$) and the a-plane with ($11\bar{2}0$) orientation, are also of increasing interest. Both surfaces may contain an equal number of threefold-coordinated Ga and N in the top atomic layer, thus allowing charge neutrality to be obtained without changes in stoichiometry or reconstruction.

However, despite the well-defined and simple atomic structure of the m-plane surface, its electronic properties have been controversially discussed for years. Density functional calculations within the local density approximation (DFT-LDA) by Northrup and Neugebauer [4] predicted the stoichiometric surface structure, shown in Fig. 1, to be stable for almost any value of the Ga chemical potential and found a relaxation mechanism reminiscent of conventional III-V(110) surfaces: The cation changes its hybridization from a pure sp^3-type to a sp^2-like configuration, which was found to lead to a surface-layer buckling of about 7° with the N (Ga) moving out (in) by 0.02 Å (0.20 Å), as indicated in Fig. 1. The electronic structure calculations of Ref. [4] allowed the identification of two surface states. An occupied surface state is derived from surface N-2p orbitals, while the unoccupied surface state corresponds to Ga-localized dangling bonds. The moderate atomic relaxation of the surface layer increases the gap between these states by more than 1 eV such that for the fully relaxed structure, the N-derived band lies just below the valence-band maximum (VBM), while the Ga-derived band lies just above the conduction-band minimum (CBM). Thus, according to these DFT-LDA calculations, there should be no intrinsic surface states in the fundamental gap of the GaN m-plane [4].

This contrasts with DFT calculations by Segev and Van de Walle [5,6]. They used particularly modified pseudopotentials in order to cope with the DFT band-gap underestimation and predicted an unoccupied Ga-dangling-bond state at ∼0.7 eV below the CBM for the GaN m-plane. The occupied surface band, according to Refs. [5,6], is associated with dangling bonds on the N atoms and overlaps energetically with the bulk valence band, i.e., it does not create levels within the band gap. Consistent with the picture by Northrup and Neugebauer, but deviating from the results by Segev and Van de Walle, more recent DFT-LDA calculations [7] predict the doubly degenerate N-derived highest-occupied and Ga-derived lowest-unoccupied surface states to be energetically degenerate with the corresponding bulk band edges.

Interestingly, the most recent calculations on that system known to us come to a different conclusion: The LDA + U approach by Lymperakis *et al.* [8] yields a Ga-derived surface state that is in the whole Brillouin zone in the fundamental band gap of GaN and never resonant with the bulk bands. Thus, the theoretical studies on the GaN m-plane agree on the relaxation mechanism and orbital character of surface states, but differ appreciably concerning the energy position of the unoccupied surface state with respect to the bulk band edge.

Experimentally, there are also contradicting reports on the existence of empty surface states in the GaN bulk band gap. From earlier scanning tunneling microscopy and spectroscopy (STM and STS, respectively) data on the GaN m-plane surface [7,9], it was concluded that both the N and Ga dangling-bond

 ©2015 American Physical Society

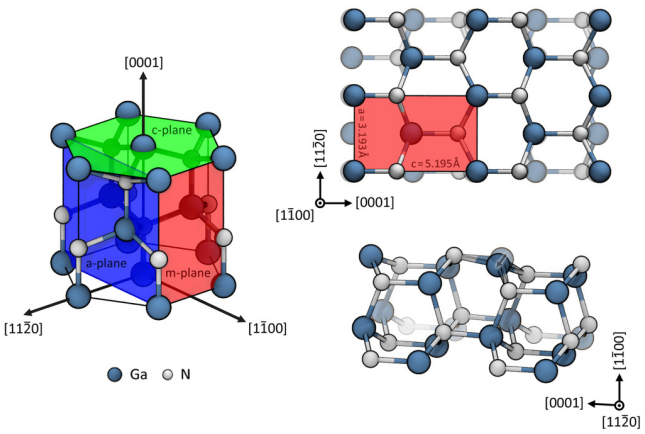

FIG. 1. (Color online) Left: Conventional unit-cell representation of wz-GaN bulk material including the definition of the most relevant low-index crystal-surface planes. The polar c-plane and the two nonpolar m- and a-planes are shown in green, red, and blue, respectively. Right: Atomic structure of the relaxed GaN m-plane surface shown as top view, including the definition of the surface unit cell (top), and side view indicating the surface relaxation mechanism (bottom). Atoms within (below) the topmost atomic double layers are shown in full (translucent) color in the top view.

states are outside of the fundamental gap, while the most recent data obtained with high resolution [8] yield a different picture. The debated empty surface state was found well below the conduction-band minimum within the fundamental band gap, but with a very low density of states due to its dispersion characteristics. According to Ref. [8], the GaN m-plane is intrinsically pinned at around 0.6 eV below the CBM. The shrinkage of the GaN bulk band gap due to the occurrence of surface states agrees with recent reflection anisotropy spectroscopy (RAS) data [10], which have shown surface optical transitions around 3.3 eV, i.e., below the GaN bulk band gap at 3.4 eV, attributed to gap states.

In the present study, we aim to clarify the electronic properties of the GaN m-plane. Thereby, we go methodologically beyond previous theoretical studies by performing hybrid functional in addition to (semi)local functional DFT calculations and include many-body effects in the surface optical response on the Bethe-Salpeter equation (BSE) level of theory. Our results show a strong sensitivity with respect to the slab size and demonstrate the existence of bound Ga-derived surface states just below the CBM. Moreover, we address the surface optical response experimentally and detect optical absorption related to surface electronic states. In particular, a surface excitonic absorption at an energy below the bulk absorption onset is found, accompanied by a broad spectral feature that extends to higher energies, which is related to the dispersion of the two surface bands.

II. METHODOLOGY AND NUMERICAL DETAILS

The present calculations are performed using density functional theory (DFT) within the generalized gradient approximation (GGA) to the electron exchange and correlation (XC) as well as using hybrid functional DFT. Specifically, the Perdew-Burke-Ernzerhof (PBE) [11] and Heyd-Scuseria-Ernzerhof (HSE) functionals [12] were used for the GGA and hybrid functional calculations, respectively. In the latter, a 32% fraction of exact exchange (EXX) from Hartree-Fock theory was used. As previously demonstrated, the increased EXX fraction accurately reproduces features of the GW quasiparticle band structure [13]. Additionally, self-energy–corrected (Ga_{3d} as well as N_{2p} states; for details see Ref. [13]) LDA-1/2 [14], and Hubbard-corrected PBE + U (corrections to Ga_{3d} and N_{2p} states) calculations were performed in order to compare various approaches to overcome the DFT band-gap problem [15]. The electron-ion interaction is described by the projector-augmented wave scheme [16], where the Ga $3d$ states are treated as valence electrons. The electronic wave functions are expanded into plane waves up to a kinetic energy of 400 eV. All calculations were performed using the Vienna *Ab initio* Simulation Package (VASP) [17].

The surface is modeled by periodically repeated symmetric slabs. Each supercell contains between 16 and 48 atomic layers as specified below, and a vacuum region equivalent to about 16 atomic layers (∼22 Å). The uppermost 4 (16) atomic layers on each side of the 16-layer (48-layer) slabs are allowed to relax until the forces on the atoms are below 0.001 meV/Å. The Brillouin-zone integration is performed using regular Γ-centered meshes with a **k**-point density of $16 \times 24 \times 1$ ($8 \times 12 \times 1$) for the 16 (48) atomic layers slab. The surface calculations were performed using the DFT-PBE equilibrium lattice constants of $a = 3.193$ Å and a c/a ratio of 1.627, which are close to the experimental values of $a = 3.189$ Å and $c/a = 1.626$ at room temperature [18]. In addition, these lattice parameters are very close to the DFT-HSE parameters $a = 3.198$ Å and $c/a = 1.627$ [19]. The deviation between calculated and measured lattice parameters changes the band-structure energies by less than 0.1 eV.

Starting from the DFT-PBE electronic structure but using the eigenvalues from the hybrid DFT, the optical response of GaN bulk and surface slabs has been calculated solving the Bethe-Salpeter equation for coupled electron-hole excitations [20–22]. It incorporates the screened electron-hole attraction as well as the unscreened electron-hole exchange. Specifically, we use the time-evolution method developed by one of the present authors [23,24] as well as an iterative diagonalization procedure [25] to obtain the polarizability. The deviations resulting from using the HSE eigenvalues rather than the GW quasiparticle energies in the BSE is found to be of the order of one tenth of an eV.

In contrast to zinc-blende or diamond-type semiconductors, GaN in the wurtzite crystal structure exhibits a pronounced bulk optical anisotropy which is superimposed onto the surface optical anisotropy. Recently, it has been demonstrated that by surface modification due to oxygen adsorption, the optical anisotropy is significantly changed, which has been interpreted in terms of quenching the surface optical response [10].

In the present study, the anisotropy of the optical response is simulated from the BSE dielectric functions in terms of a three-layer model and compared to experimental RAS data. Compared to previous experimental results [10], the RAS measurements have been extended to a broader energy window between 2.4 and 5.4 eV.

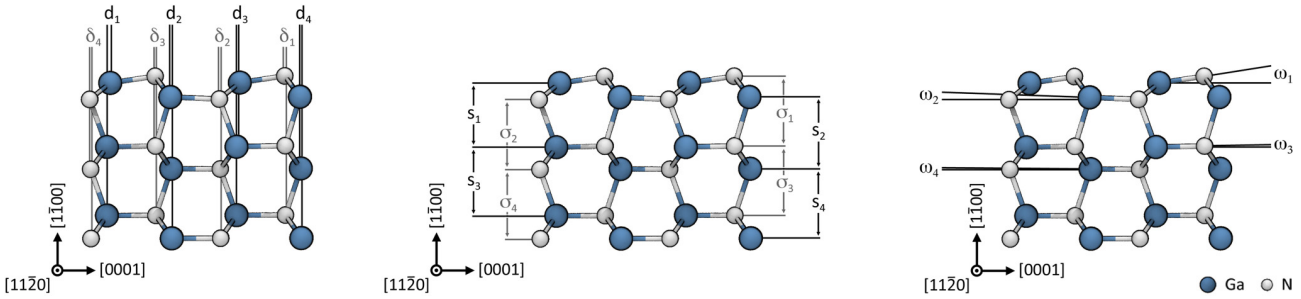

FIG. 2. (Color online) Definition of characteristic structural relaxation parameters for the GaN m-plane. Left: Lateral displacement parameters d_i and δ_i defined along the [0001] surface direction for the Ga and N sublattices. Middle: Interlayer spacing parameters s_i and σ_i defined separately for interatomic distances along the [1$\bar{1}$00] surface normal for the Ga and N sublattices. Right: Buckling parameters ω_i describing the tilting of Ga-N dimers with respect to the surface plane. The parameters are defined for the topmost four layers ($i = 1,2,3,4$) with respect to the DFT optimized atom positions.

In contrast to optically isotropic materials such as zinc-blende or diamond-type semiconductors, the often used thin-layer approximation of an anisotropic surface layer on an isotropic substrate (bulk) [26,27] is no longer valid. Instead the sample is modeled as an optically uniaxial slab with finite thickness on top of an optically uniaxial film in an isotropic ambient, using the expressions for the reflection by stratified planar structures [28]. Thereby, the calculated optical response, i.e., the dielectric functions (DFs) of slab and bulk and the slab thickness, are used as input parameters. In order to account for the influence of the two sides of the slab on the calculated DF, the imaginary part of the DF is divided by two and an effective film thickness of 11 Å is used. Since the RAS experiments are performed near normal incidence, the sensitivity to the out-of-plane component of the DF is negligible.

III. RESULTS AND DISCUSSION

A. Surface relaxation

The side view of the structurally relaxed GaN m-plane is shown in Fig. 2, with the calculated values for key structural parameters obtained within either local or hybrid DFT summarized in Table I. The relaxed geometry calculated here agrees with previous calculations, e.g., Refs. [4,5], which find a moderate buckling in the uppermost atomic layer with the surface N (Ga) atoms moving out (in) with respect to their bulk positions. The buckling angle in the uppermost layer of about 8° calculated here is similar to the value predicted in Ref. [4], where 7° is reported. Also the contraction of the Ga-N dimer length of about 7–8 % calculated here agrees with the value of 6 % determined in Ref. [4]. Interestingly, the geometry of the relaxed surface does not change considerably if hybrid functional rather than local DFT calculations are performed, with deviations even at the outermost atoms below 0.1 Å. Changes of similar magnitude are observed if the slab size is increased from 16 to 48 atomic layers. The present calculations thus suggest that the relaxation mechanism as well as the relaxation parameters are robust with respect to the treatment of the XC effects and that a 16-layer slab is sufficient to model the *structural* surface properties.

Northrup and Neugebauer [4] suggest that the structural relaxation is caused by a rehybridization of the surface N and Ga atoms towards a sp^3 and sp^2 configuration, respectively. This leads to a tilting of the GaN dimer because the sp^2 hybridized Ga prefers a planar bonding situation. This relaxation mechanism is well known from III-V(110) surfaces [29,30] and is consistent with electron counting heuristics [31]. The latter states that stable compound semiconductor surfaces are typically characterized by all the dangling bonds on the

TABLE I. Summary of structural relaxation parameters defined in Fig. 2 as well as Ga-N dimer-bond lengths b_i calculated within DFT-PBE and DFT-HSE. All lateral displacement and interlayer spacing parameters are given in Å. Buckling parameters are given in degree. Values in brackets are the percentage change with respect to the values in wz-GaN bulk.

	16 monolayers		48 monolayers
	DFT-PBE	DFT-HSE	DFT-PBE
d_1	0.145	0.150	0.129
d_2	−0.044	−0.030	−0.044
d_3	0.008	0.011	0.009
d_4	−0.017	−0.021	−0.023
δ_1	−0.015	−0.025	−0.023
δ_2	−0.040	−0.033	−0.049
δ_3	−0.002	−0.005	−0.003
δ_4	−0.011	−0.011	0.013
s_1	2.563 (−7.87)	2.514 (−9.07)	2.572 (−6.98)
s_2	2.871 (3.82)	2.839 (2.67)	2.859 (3.39)
s_3	2.741 (−0.86)	2.715 (−1.82)	2.742 (−0.83)
s_4	2.785 (0.70)	2.781 (0.58)	2.802 (1.34)
σ_1	2.789 (0.86)	2.710 (−2.00)	2.780 (0.54)
σ_2	2.800 (1.25)	2.777 (0.43)	2.798 (1.18)
σ_3	2.775 (0.51)	2.758 (−0.26)	2.787 (0.77)
σ_4	2.772 (0.24)	2.768 (0.10)	2.776 (0.38)
ω_1	8.34	7.63	8.01
ω_2	2.45	2.20	2.46
ω_3	1.12	1.28	1.35
ω_4	0.37	0.39	0.67
b_1	1.818 (−7.14)	1.800 (−8.08)	1.823 (−6.86)
b_2	1.963 (0.29)	1.956 (−0.08)	1.954 (−0.15)
b_3	1.948 (−0.48)	1.942 (−0.78)	1.946 (−0.59)
b_4	1.958 (0.31)	1.968 (0.50)	1.965 (0.37)

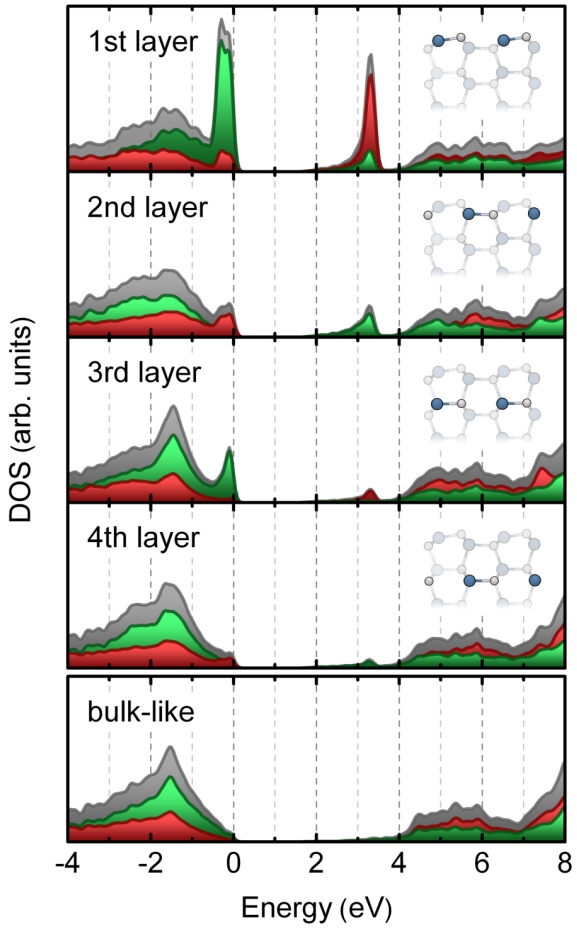

FIG. 3. (Color online) Layer-resolved total (gray shaded) as well as Ga (red) and N (green) projected contributions to the GaN 16-layer surface-slab DFT-PBE density of states. Insets: The atoms that have been considered in the projection of the density of states. The bulklike contributions in the lowermost panel originate from the average of the eight central atomic layers of the surface slab.

electronegative element occupied and all the dangling bonds on the electropositive element empty, given the number of available electrons [32,33]. In the present case, this implies a charge transfer from surface Ga to N. This charge transfer occurs indeed, as demonstrated in the layer-resolved and atomic projected electron density of states (DOS) given in Fig. 3. Obviously, the first-layer DOS deviates significantly from its bulk value in the sense that additional filled N states appear close to the VBM, while empty Ga states appear below the bulk CBM. This agrees nicely with the finding discussed above that the Ga atom assumes a more planar bonding configuration consistent with a moderate buckling of about 8°. However, as shown in Fig. 3, a similar, albeit far smaller, charge transfer from Ga to N occurs in the third layer, and gives rise to a buckling of about 1°. A slight accumulation of filled Ga states and empty N states close to the bulk VBM and CBM, however, occurs in the second and, to some extent, even in the fourth atomic layer. Accordingly, a buckling of opposite direction of about 2° and below 1° occurs in these layers. The DOS underneath the fourth atomic layer, finally, is reminiscent of the bulk characteristics in both 16- and 48-layer slabs.

B. Surface electronic band structure

In order to address the controversy on the precise position of the Ga and N surface states with respect to the GaN bulk band edges, we explore the surface band structure and compare the calculated and experimentally determined optical anisotropy. Data obtained within PBE for a 16-layer surface slab are shown in Fig. 4. Thereby, the alignment of the bulk and surface bands has been done using the average of the local electrostatic potentials [34]. Two bound surface states, i.e., one occupied and one unoccupied, occur in the GaN band gap. The filled surface state is energetically degenerate with the bulk VBM at the Γ point, but otherwise well separated from the continuum of bulk states. The empty surface states are below the bulk GaN conduction states throughout the surface Brillouin zone, and just below (PBE, 16-layer slab) or slightly underneath (see $\Delta E_{S_{\mathrm{Ga}}}$ in Table II) the bulk CBM at the Γ point. The orbital character of the respective states is shown in Fig. 5. It can be seen that the occupied surface state is mainly formed by N-2p orbitals from the uppermost surface anion, with minor contributions from the surface Ga atoms and second-layer N. The unoccupied surface state corresponds mainly to a surface Ga localized nonbonding p orbital, with minor contributions from the cations in the second, third, and fourth atomic layer. These findings corroborate the electron-counting rule driven relaxation mechanism discussed above as well as the early assignment by Northrup and Neugebauer [4]. The energy of the surface states, however, deviates somewhat from Ref. [4] where these were found to be resonant with bulk states at the bulk edges. On the other hand, the separation between the Ga-derived surface state and the bulk band edge calculated here is far smaller than predicted in Refs. [5,6,8].

In order to determine the precise position of the Ga-derived surface state, we investigate the influence of the slab size as well as of the approximation for electron XC effects. Lymperakis *et al.* [8] pointed out that slabs consisting of less than 24 layers do not contain enough bulklike material to correctly describe the onset of the bulk conduction band. Therefore, we perform additional calculations using 48-layer slabs. The corresponding results for the energy gap between the surface states as well as the position of the Ga-derived surface state are compared with the bulk band gap calculated using the same approximation in Table II. The table presents results obtained using local as well as hybrid XC functionals (PBE

TABLE II. Fundamental direct Γ-Γ band gaps of GaN($1\bar{1}00$) surface slabs as well as wz-GaN bulk material calculated on various levels of theory (see text). The parameter $\Delta E_{S_{\mathrm{Ga}}}$ quantifies the band position of the Ga dangling-bond-related state below the bulk CBM at the Γ point.

XC	Layers	$E_{\mathrm{gap}}^{\mathrm{surf}}$	$E_{\mathrm{gap}}^{\mathrm{bulk}}$	$\Delta E_{S_{\mathrm{Ga}}}$
PBE	16	1.73	1.89	0.07
	48	1.65	1.85	0.20
HSE	16	3.31	3.55	0.20
	48	3.31	3.58	0.27
LDA-1/2	16	3.03	3.53	0.09
	48	2.96	3.16	0.20
PBE + U	48	2.68	3.35	0.66

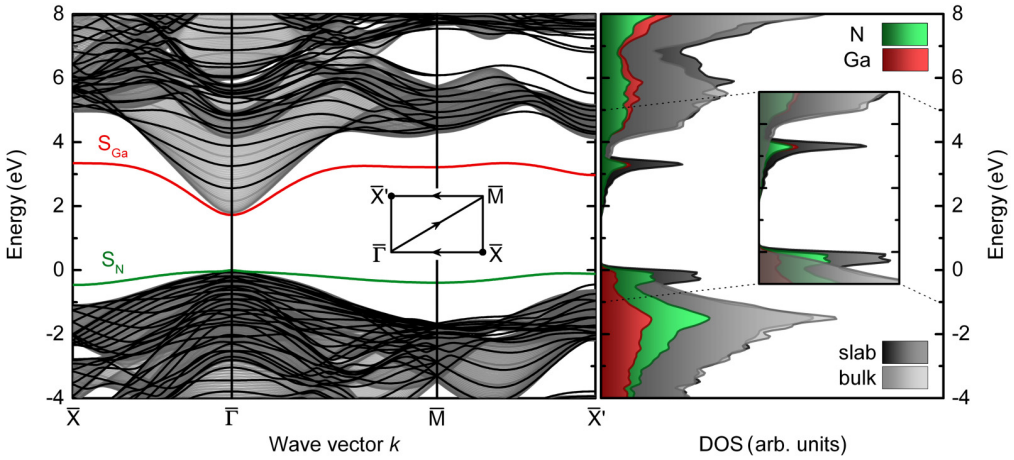

FIG. 4. (Color online) Left: DFT-PBE band structure (black lines) of the GaN m-plane 16-layer surface slab along high symmetry lines of the two-dimensional surface Brillouin zone (cf. inset). The Ga dangling-bond surface state S_{Ga} and the N dangling-bond surface-resonance state S_N derived energy bands are highlighted in red and green. The projection of the bulk electronic band structure is indicated in gray. Right: Total slab (dark-gray shaded) and wz-GaN bulk (light-gray shaded) densities of states as well as partial Ga (red) and N (green) projected surface-slab densities of states.

and HSE, respectively) in addition to LDA-1/2 and PBE + U results. The surface-state energy for the 16-layer slab has been determined from aligning the surface and bulk band structures by the microscopic average of the electrostatic potential. For 48-layer slabs, all band-energy differences, including the bulk band gap, have been extracted from the surface-slab eigenvalue spectrum. A direct comparison of the band structures and densities of states obtained for 16- and 48-layer surface slabs is shown in Fig. 6. Irrespective of the specific treatment of the XC effects, the usage of the ticker surface slab downshifts the energy of the Ga-derived surface state with respect to the bulk CBM. For the 48-layer slab, we obtain energy separations of 0.20, 0.27, and 0.20 eV within PBE, HSE, and LDA-1/2, respectively. The far-larger energy separation between the bulk conduction-band edge and the Ga surface state of 0.6 or 0.7 eV predicted on the basis of LDA + U calculations [8] or specifically designed pseudopotentials with additional repulsive contributions [5,6] are reproduced in the present work by PBE + U. The latter results in an energy separation of 0.66 eV. This value certainly marks the upper limit for the downshift of the empty surface state with respect to the bulk CBM. On the other hand, from the theoretical calculations, it appears clear that there is also a finite separation between empty bulk and surface states at Γ.

Experimentally, this separation has been doubted in early investigations [7,9]. This is easily understood from the low surface-state DOS compared to the bulk data, as can be seen in Figs. 4 and 6. Experimental hints for such a separation stem from highly resolved tunneling data [8], and in particular from measurements of the surface optical response [10].

C. Surface optical anisotropy

Based on the electronic structure above, the surface and bulk optical responses are calculated considering two-particle

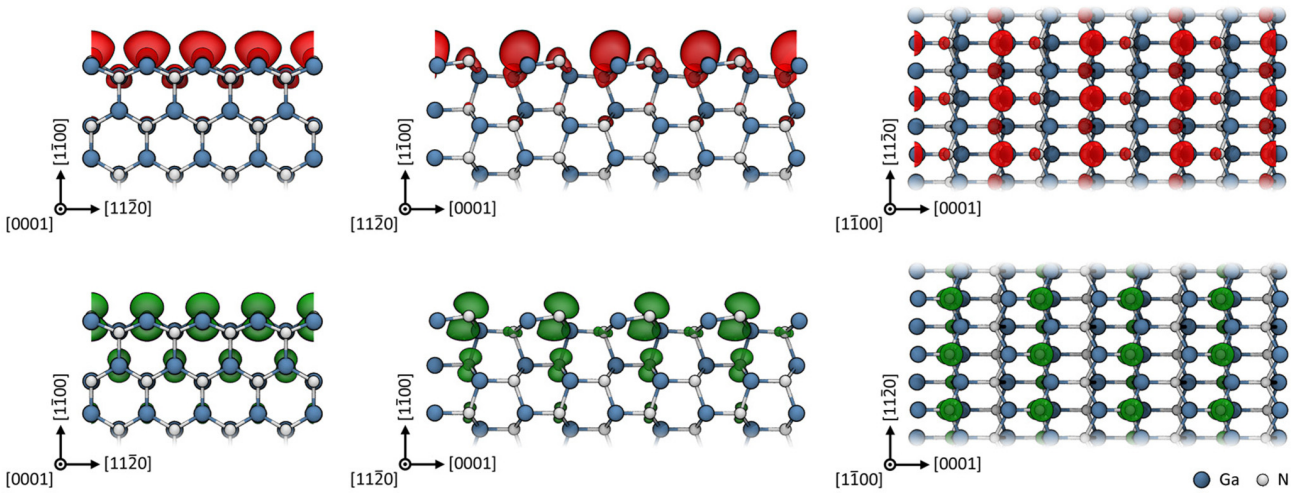

FIG. 5. (Color online) Visualization of the partial DFT-PBE charge densities (isovalue: 0.01 e/Å^3) of the surface state S_{Ga} (red) and the surface-resonance state S_N (green) (see Fig. 4) of the 16-layer surface slab along different viewing directions.

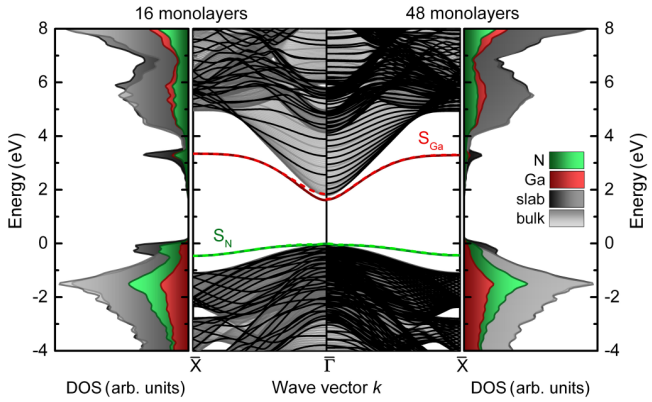

FIG. 6. (Color online) DFT-PBE band structure along the $\overline{\Gamma}$-$\overline{X}$ direction (black lines) as well as total (dark-gray shaded) and partial Ga (red) and N (green) densities of states for 16- (left) and 48-layer (right) surface slabs. The projection of the bulk electronic band structure along the $\overline{\Gamma}$-$\overline{X}$ surface direction is given in gray.

electron-hole excitations within the BSE formalism. The present calculations for the bulk optical response agree with earlier calculations [36,37] and closely resemble experimental findings obtained by spectroscopic ellipsometry of GaN($1\bar{1}00$) wurtzite-film samples at $T = 295$ K [35]; see Fig. 7. This holds in particular for the difference between the ordinary [$\varepsilon_2^{\perp}(\omega)$, light polarization perpendicular to the c direction] and extraordinary [$\varepsilon_2^{\parallel}(\omega)$, light polarization along c] dielectric function. The presence of an intrinsic surface state substantially influences the m-plane optical response. If one compares the results for GaN bulk and the 16-layer surface slab shown in Fig. 7, one sees that the onset of the optical response is redshifted with respect to the bulk data by about a few tenths of an eV. In particular, we find an enhanced optical anisotropy for low photon energies.

In order to quantify the contribution of the N and Ga surface states to the surface dielectric function, we perform additional calculations where the exciton Hamiltonian is set up from specific states only, and iteratively diagonalized. The contribution of surface-surface, surface-bulk, and bulk-bulk transitions to the total optical response of the 16-layer surface slab can thus be separately determined. The calculated data clearly show that electronic transitions between N- and Ga-derived surface states contribute to the total surface optical response at low photon energies; see top panel in Fig. 8. Thereby, the maximum of the ordinary and extraordinary dielectric function occurs at different energies, i.e., there is a clear surface-state-related contribution to the surface optical anisotropy.

However, exclusive transitions between the two surface states are not sufficient to model the onset of the surface dielectric function. The coupling to the unoccupied and occupied (cf. second and third panel in Fig. 8) bulklike bands of the slab is necessary in order to reproduce the low-energy part of the optical response. Moreover, in contrast to the low joint density of states at the Brillouin-zone center due to the particularly strong dispersion of Ga-derived surface band at $\overline{\Gamma}$, the surface optical absorption shows a pronounced peak associated with the onset of optical absorption in the ordinary

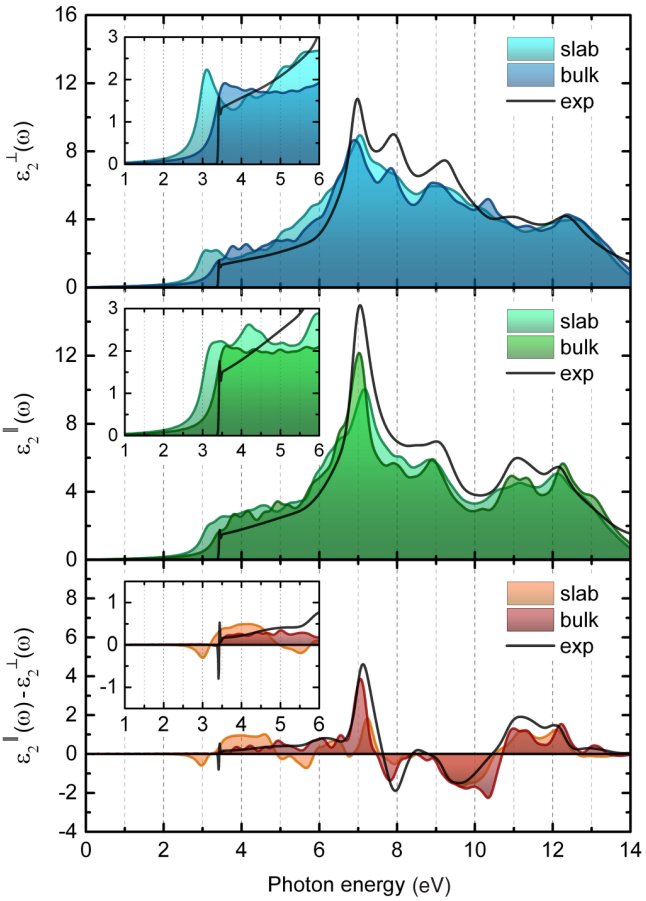

FIG. 7. (Color online) Polarization-dependent imaginary parts of the dielectric functions of the GaN m-plane surface slab and wz-GaN bulk material calculated on the BSE level of theory. The ordinary $\varepsilon_2^{\perp}(\omega)$ and extraordinary $\varepsilon_2^{\parallel}(\omega)$ imaginary components of the complex dielectric functions as well as the difference $\varepsilon_2^{\parallel}(\omega) - \varepsilon_2^{\perp}(\omega)$ are shown in the top, middle, and bottom panel, respectively. Black lines represent experimental data [35].

dielectric function. This indicates the formation of excitonic states at the GaN m-plane which extend into the subsurface layers. Consequently, N- and Ga-derived surface states as well as bulk states of the slab contribute to the surface exciton which defines the onset of the optical absorption of the m-plane.

It is also obvious from Fig. 8 that the lowest-unoccupied and highest-occupied surface bands give rise to characteristic features in the optical response: It shows a strong optical anisotropy related to very distinct absorption bands from above 3 eV, i.e., below the fundamental band gap, up to 5.5 eV. A narrow excitonic absorption in the calculated ordinary dielectric function occurs below the bulk band gap and a broad optical absorption band for higher energies in the extraordinary dielectric function. Consequently, the surface band-related optical absorption should give rise to a characteristic optical anisotropy. Indeed, this is observed experimentally. Figure9 shows RAS spectra obtained on clean GaN and after subsequent exposure to residual gas; see Ref. [10] for experimental details. There, photoelectron spectroscopy was used in conjunction with RAS to demonstrate that the change in optical anisotropy is due to the quenching of surface states.

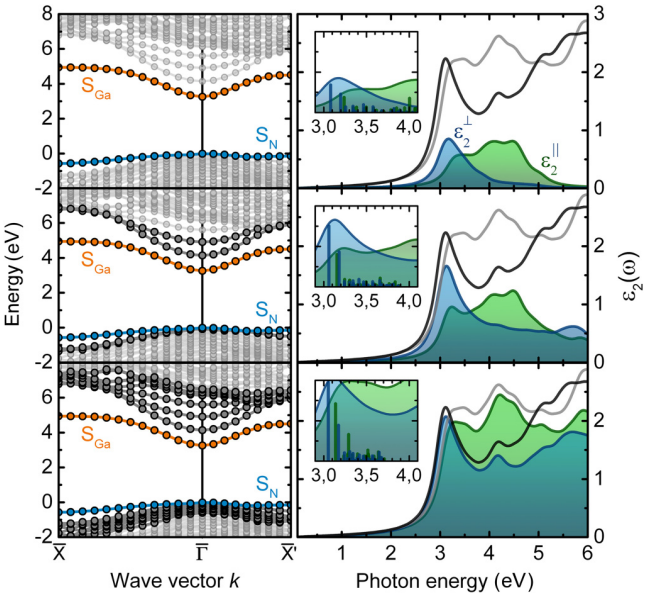

FIG. 8. (Color online) Illustration of the energy-band dependence of the GaN m-plane optical response. The panels on the right-hand side visualize the particular polarization-dependent contributions from the various surface-surface, surface-bulk, and bulk-bulk transitions to the surface optical response that stem from the bands indicated in full color on the left-hand side. Electron bands shown in translucent color where neglected in the respective calculations. Also shown on the right-hand side are the lowest eigenvalues of the BSE and their oscillator strength scaled by a factor of 10. Gray and black lines represent the total polarization-dependent dielectric functions of the GaN surface slab.

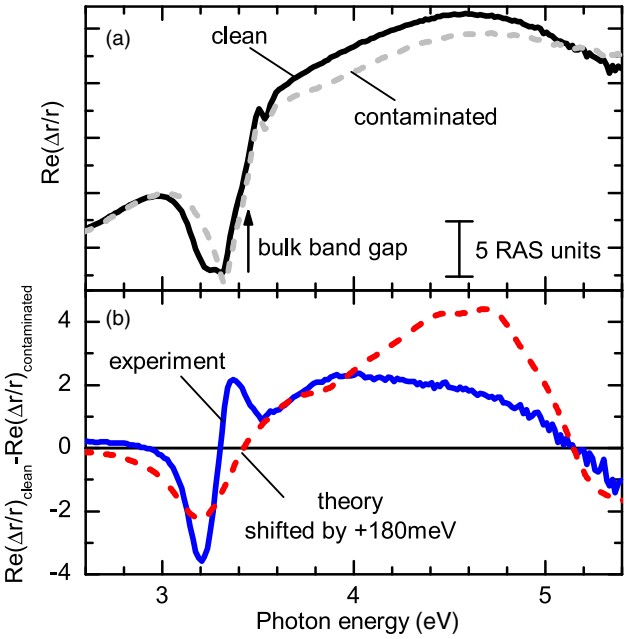

FIG. 9. (Color online) Optical anisotropy of m-plane GaN. (a) Experimental spectra of clean and contaminated GaN (see also Ref. [10]). (b) Difference of the two experimental RAS spectra obtained on the clean and contaminated surface (solid blue line) as well as the difference of the calculated RAS spectra of bulk plus surface and bulk, using the dielectric functions from Figs. 7 and 8.

In the present study, the spectral range of the RAS experiments is extended to higher energies in order to cover all interband transitions within the surface band structure. In the upper panel of Fig. 9, the optical anisotropy spectra of the clean and adsorption modified m-plane GaN surface are shown in the spectral range from 2.4 to 5.4 eV. In the lower panel, the difference between the spectra of clean and adsorption modified m-plane samples is plotted. The difference should be related to the surface optical anisotropy, assuming that the bulk anisotropy remains unaffected by surface contamination. For a more quantitative comparison between the measured data and the present calculations, we model the optical anisotropy on the basis of the calculated dielectric functions within the three-layer optical model. Thereby, we describe the system by a surface layer on top of the optically anisotropic GaN bulk material. The result, based on the respective calculated slab and bulk dielectric functions shown in Fig. 7, is given in the bottom panel of Fig. 9. The overall agreement between calculation and experiment is evident. The deviations between the measured and simulated amplitudes are not too surprising: On the one hand, the surface states might not be fully quenched by the residual gas absorption, and finite-temperature effects as well as sample inhomogeneities are not considered in the calculation. On the other hand, the three-layer model itself is an approximation and the accuracy of the calculated bulk and slab dielectric functions suffers from the limited number of electron states that can be included in the solution of the Bethe-Salpeter equation. Still, the contribution of the surface states to the optical anisotropy is very clearly visible both in experiment and simulation. It gives rise to a narrow negative feature below the band gap (due to the onset of $\varepsilon_2^{\perp}$) followed by a broad positive band above the fundamental band gap (due to $\varepsilon_2^{\parallel}$).

IV. SUMMARY AND CONCLUSION

First-principles calculations on the structural properties, electronic bands, and optical response of the GaN m-plane have been performed and compared to the surface optical anisotropy of GaN. Our results show that the surface is characterized by a charge transfer from the surface Ga to the more electronegative surface N atom. This charge transfer results in a rehybridization of the surface atoms that causes a buckling of about 8° of the surface atoms, where the Ga atoms move into the surface. The filled N-derived p-like surface state is resonant with the bulk VBM at the origin of the Brillouin zone. The empty Ga-derived p-like surface state, on the other hand, is well separated from the bulk CBM by at least 0.2 eV within the whole Brillouin zone and this gives rise to an intrinsic pinning of the Fermi level at the GaN m-plane. Both surface states contribute to the surface optical response and its anisotropy. The optical anisotropy shows strong and distinct contributions related to the N and Ga dangling-bond-derived surface bands, starting below the fundamental band gap up to approximately 5 eV. Our calculations show that the onset of the optical absorption of the GaN m-plane is defined by surface excitons which intermix contributions of the two surface states and near-band-edge electronic bands of the bulk.

ACKNOWLEDGMENTS

The numerical calculations were done using grants of computer time from the Regionales Rechenzentrum of the Universität zu Köln (RRZK), the Paderborn Center for Parallel Computing (PC^2), and the Höchstleistungs-Rechenzentrum Stuttgart (HLRS). The Deutsche Forschungsgemeinschaft (DFG) is acknowledged for financial support (Grants No. TRR142 and No. GRK1464). M. Himmerlich and S. Krischok are gratefully acknowledged for help with the experimental surface preparation.

[1] S. Nakamura, T. Mukai, and M. Senoh, Appl. Phys. Lett. **64**, 1687 (1994).
[2] F. Bernardini, V. Fiorentini, and D. Vanderbilt, Phys. Rev. B **56**, R10024 (1997).
[3] P. Waltereit, O. Brandt, A. Trampert, H. Grahn, J. Menniger, M. Ramsteiner, M. Reiche, and K. Ploog, Nature (London) **406**, 865 (2000).
[4] J. E. Northrup and J. Neugebauer, Phys. Rev. B **53**, R10477 (1996).
[5] D. Segev and C. G. Van de Walle, Europhys. Lett. **76**, 305 (2006).
[6] C. G. Van de Walle and D. Segev, J. Appl. Phys. **101**, 081704 (2007).
[7] M. Bertelli, P. Löptien, M. Wenderoth, A. Rizzi, R. G. Ulbrich, M. C. Righi, A. Ferretti, L. Martin-Samos, C. M. Bertoni, and A. Catellani, Phys. Rev. B **80**, 115324 (2009).
[8] L. Lymperakis, P. H. Weidlich, H. Eisele, M. Schnedler, J.-P. Nys, B. Grandidier, D. Stivenard, R. E. Dunin-Borkowski, J. Neugebauer, and P. Ebert, Appl. Phys. Lett. **103**, 152101 (2013).
[9] L. Ivanova, S. Borisova, H. Eisele, M. Dähne, A. Laubsch, and P. Ebert, Appl. Phys. Lett. **93**, 192110 (2008).
[10] M. Himmerlich, A. Eisenhardt, S. Shokhovets, S. Krischok, J. Räthel, E. Speiser, M. D. Neumann, A. Navarro-Quezada, and N. Esser, Appl. Phys. Lett. **104**, 171602 (2014).
[11] J. P. Perdew, K. Burke, and M. Ernzerhof, Phys. Rev. Lett. **77**, 3865 (1996).
[12] J. Heyd, G. E. Scuseria, and M. Ernzerhof, J. Chem. Phys. **118**, 8207 (2003).
[13] M. Landmann, E. Rauls, W. G. Schmidt, M. Röppischer, C. Cobet, N. Esser, T. Schupp, D. J. As, M. Feneberg, and R. Goldhahn, Phys. Rev. B **87**, 195210 (2013).
[14] L. G. Ferreira, M. Marques, and L. K. Teles, Phys. Rev. B **78**, 125116 (2008).
[15] F. Bechstedt, *Festkörperprobleme/Advances in Solid State Physics* (Vieweg, Braunschweig/Wiesbaden, 1992), Vol. 32, p. 161.
[16] G. Kresse and D. Joubert, Phys. Rev. B **59**, 1758 (1999).
[17] G. Kresse and J. Furthmüller, Comput. Mater. Sci. **6**, 15 (1996).
[18] I. Vurgaftman and J. R. Meyer, J. Appl. Phys. **94**, 3675 (2003).
[19] J. Heyd, J. E. Peralta, G. E. Scuseria, and R. L. Martin, J. Chem. Phys. **123**, 174101 (2005).
[20] S. Albrecht, L. Reining, R. DelSole, and G. Onida, Phys. Rev. Lett. **80**, 4510 (1998).
[21] L. X. Benedict, E. L. Shirley, and R. B. Bohn, Phys. Rev. Lett. **80**, 4514 (1998).
[22] M. Rohlfing and S. G. Louie, Phys. Rev. Lett. **83**, 856 (1999).
[23] W. G. Schmidt, S. Glutsch, P. H. Hahn, and F. Bechstedt, Phys. Rev. B **67**, 085307 (2003).
[24] P. H. Hahn, W. G. Schmidt, and F. Bechstedt, Phys. Rev. Lett. **88**, 016402 (2001).
[25] F. Fuchs, C. Rödl, A. Schleife, and F. Bechstedt, Phys. Rev. B **78**, 085103 (2008).
[26] N. Esser, W. G. Schmidt, C. Cobet, K. Fleischer, A. I. Shkrebtii, B. O. Fimland, and W. Richter, J. Vac. Sci. Technol. B **19**, 1756 (2001).
[27] K. Hingerl, D. E. Aspnes, I. Kamiya, and L. T. Florez, Appl. Phys. Lett. **63**, 885 (1993).
[28] R. Azzam and N. Bashara, *Ellipsometry and Polarized Light*, 3rd ed. (North-Holland, Amsterdam, 1996).
[29] José Luiz A. Alves, J. Hebenstreit, and M. Scheffler, Phys. Rev. B **44**, 6188 (1991).
[30] J. Hebenstreit, M. Heinemann, and M. Scheffler, Phys. Rev. Lett. **67**, 1031 (1991).
[31] M. D. Pashley, Phys. Rev. B **40**, 10481 (1989).
[32] W. G. Schmidt, Appl. Phys. A **65**, 581 (1997).
[33] W. G. Schmidt, Appl. Phys. A **75**, 89 (2002).
[34] W. G. Schmidt, F. Bechstedt, and G. P. Srivastava, Surf. Sci. Rep. **25**, 141 (1996).
[35] M. Feneberg, M. F. Romero, M. Röppischer, C. Cobet, N. Esser, B. Neuschl, K. Thonke, M. Bickermann, and R. Goldhahn, Phys. Rev. B **87**, 235209 (2013).
[36] R. Laskowski, N. E. Christensen, G. Santi, and C. Ambrosch-Draxl, Phys. Rev. B **72**, 035204 (2005).
[37] L. C. de Carvalho, A. Schleife, J. Furthmüller, and F. Bechstedt, Phys. Rev. B **87**, 195211 (2013).

Paper VII

Understanding band alignments in semiconductor heterostructures: Composition dependence and type-I–type-II transition of natural band offsets in nonpolar zinc-blende $Al_xGa_{1-x}N/Al_yGa_{1-y}N$ composites

M. Landmann, E. Rauls, and W. G. Schmidt

PHYSICAL REVIEW B **95**, 155310, 14 pp. (2017)

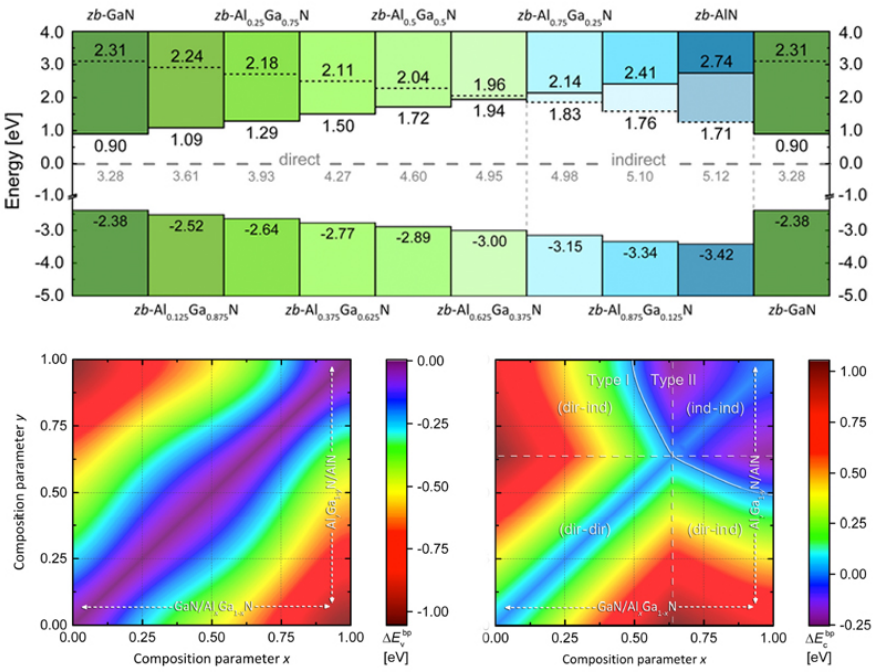

Understanding band alignments in semiconductor heterostructures: Composition dependence and type-I–type-II transition of natural band offsets in nonpolar zinc-blende $Al_xGa_{1-x}N/Al_yGa_{1-y}N$ composites

M. Landmann, E. Rauls, and W. G. Schmidt
Theoretische Physik, Universität Paderborn, Warburger Strasse 100, D-33098, Germany
(Received 24 January 2017; revised manuscript received 15 March 2017; published 12 April 2017)

The composition dependence of the natural band alignment at nonpolar $Al_xGa_{1-x}N/Al_yGa_{1-y}N$ heterojunctions is investigated via hybrid functional based density functional theory. Accurate band-gap data are provided using Heyd-Scuseria-Ernzerhof (HSE) type hybrid functionals with a composition dependent exact-exchange contribution. The unstrained band alignment between zincblende (*zb*) $Al_xGa_{1-x}N$ semiconductor alloys is studied within the entire ternary composition range utilizing the Branch-point technique to align the energy levels related to the bulklike direct $\Gamma_v \rightarrow \Gamma_c$ and indirect, *pseudodirect*, respectively, $\Gamma_v \rightarrow X_c$ type transitions in *zb*-$Al_xGa_{1-x}N$. While the *zb*-GaN/$Al_xGa_{1-x}N$ band edges consistently show a type-I alignment, the relative position of fundamental band edges changes to a type-II alignment in the Al-rich composition ranges of *zb*-$Al_xGa_{1-x}N$/AlN and *zb*-$Al_xGa_{1-x}N/Al_yGa_{1-y}N$ systems. The presence of a direct-indirect band-gap transition at $x_c = 0.63$ in *zb*-$Al_xGa_{1-x}N$ semiconductor alloys gives rise to a notably different composition dependence of band discontinuities in the direct and indirect energy-gap ranges. Below the critical direct-indirect Al/Ga-crossover concentration, the band offsets show a close to linear dependence on the alloy composition. In contrast, notable bowing characteristics of all band discontinuities are observed above the critical crossover composition.

DOI: 10.1103/PhysRevB.95.155310

I. INTRODUCTION

In the recent past substantial breakthroughs in group-III nitride (AlN, GaN, and InN) based materials science have advanced design and fabrication of optoelectronic devices as diodes [1,2], transistors [3–6], catalysts [7,8], or sensors [9,10] from fundamental research to commercial distribution. Group-III nitrides naturally crystallize as stable hexagonal (*hex*) crystals in a polar wurtzite (*wz*) structure belonging to space group $P6_3mc$ (C_{6v}^4). Artificially grown, nonpolar group-III nitrides have been synthesized in a metastable cubic (*c*) phase with $F\bar{4}3m$ (T_d^2) symmetry zincblende (*zb*) structure as well as a $Fm\bar{3}m$ (O_h^5) symmetry rocksalt (*rs*) polytype at high pressure [11–13]. In addition to these conventional three-dimensional bulk phases, the recent interest in two-dimensional materials also promoted substantial research on quasi-two-dimensional ultrathin film quantum structures of GaN [14] and led to quite recent preparation breakthroughs in the preparation of two-dimensional GaN via graphene encapsulation [15] promising the extension of group-III nitride-based optoelectronics, beyond two-dimensional BN [16], towards the regime of artificial two-dimensional van der Waals-type semiconductors. The hexagonal group-III nitrides AlN and GaN exhibit direct Brillouin-zone centered $\Gamma_v \rightarrow \Gamma_c$ band gaps of ∼3.3 eV in *wz*-GaN [17,18] and ∼6.0 eV in *wz*-AlN [19–21] at room temperature (300 K). The corresponding zero-temperature band gaps amount to ∼3.5 eV for *wz*-GaN [17,18] and ∼6.2 eV for *wz*-AlN [19]. The band gaps of the cubic analogs have been determined by room-temperature spectroscopic ellipsometry to 3.23 eV in *zb*-GaN [22] and 5.3 eV (indirect $\Gamma_v \rightarrow X_c$) [23,24] and 5.93 eV (direct $\Gamma_v \rightarrow \Gamma_c$) in *zb*-AlN [24]. A low temperature *zb*-GaN band gap of 3.293 eV was reported [22], while the low temperature *zb*-AlN band gap has been estimated to 5.997 eV assuming similar low-to-room-temperature (direct) band-gap differences in the polar and nonpolar phases [25].

The group-III nitride-based design of novel functional materials for optoelectronic devices as diodes, transistors, photodetectors, and sensors, and in particular solar cells, commonly involves the formation of small-scale multicomponent semiconductor complexes to exploit the material system's full technological potential beyond *simple* bulk-band gap engineering. Group-III nitride materials, especially, show beneficial material properties for utilization in intersubband devices working at both the near-infrared telecommunication wavelength regime as well as the far-infrared THz wavelength edge by exploiting electronic transitions between nanostructure-confined electronic states in single or multiple quantum well as well as quantum-dot heterostructures [26–29]. In any semiconductor heterostructure the alignment of electronic bands at built-in heterojunctions, by means of valence-band edge and conduction-band edge offsets, is crucial for the electron-transport dynamics and charge carrier confinement. Thereby, the large range of accessible band-gap energies in *zb*-$Al_xGa_{1-x}N$ semiconductors translates into a broad range of valence band offsets (VBOs) and conduction band offsets (CBOs) that determine how the band-gap difference between the interfacing materials is distributed among valence and conduction band states and, thus, the fundamental heterojunction type with electron and hole wave-function confinement in either a common spatial region (type I—*straddling gap*) or different spatial regions (type II—*staggered gap*). Consequentially, a transition from a type-I to a type-II alignment of electronic states substantially impacts the optoelectronic properties of heterostructure devices. Especially, the charge-carrier separation in type-II aligned heteromaterials represents an appealing characteristic for *light harvesting* in high-efficient photovoltaic devices.

The determination of band discontinuities from *ab initio* calculations inevitably necessitates the alignment of energy levels of the respective interfacing semiconductor alloys to

 ©2017 American Physical Society

a common energy reference. Common choices of *universal* alignment levels are the vacuum level following Anderson's electron-affinity rule [30], characteristic marker levels in the electronic structure (e.g., core-level energies) [31–35], microscopic and macroscopic averages of the (electrostatic) onsite potentials [36–38], or charge neutrality levels [39–41], branch-point energies, respectively [42–44]. Band offsets derived from alignment to a *universal* reference point as the vacuum level or branch-point energies, without making reference to particular strain conditions of the involved materials, are termed *natural* or unstrained. The alignment of electronic states under particular strain conditions at the interfaces of *real* semiconductor heterostructures can be incorporated *a posteriori* via volume deformation potentials [45–48], which is the common modus operandi in numerically efficient simulation approaches relying on parametrized model theories. A more direct approach to strained band offsets is provided via the heterostructure-alignment approach. Thereby, the influence of lattice deformation through interfacial strain is directly incorporated via atomistic modeling of the involved interfaces within the supercell approach [36–38]. An extended overview on different alignment techniques and case study on natural and strained band offsets between nonpolar group-III nitrides will be published elsewhere [49]. In general, the *ab initio* calculation of band offsets via heterostructure alignment is computationally rather expensive due to the involved interface modeling. On the contrary, branch-point alignment allows an efficient treatment of the composition dependence of band offsets, even by computationally demanding hybrid functional DFT, due to the restriction to bulk calculations. Hence we rely on the branch-point approach to align the energy states of different *zb*-$Al_xGa_{1-x}N$ semiconductor alloys. The natural valence and conduction band offsets ΔE_v^{bp} and ΔE_c^{bp}, derived via branch-point alignment, are intrinsically commutative and transitive, hence they satisfy $\Delta E_{v,c}^{bp}(A,B) = -\Delta E_{v,c}^{bp}(B,A)$ and $\Delta E_{v,c}^{bp}(A,C) = \Delta E_{v,c}^{bp}(A,B) + \Delta E_{v,c}^{bp}(B,C)$.

Within the present study, we will focus on the less common nonpolar zincblende phases of $Al_xGa_{1-x}N$ alloys, whose centrosymmetric crystal structure effectively prevents the technologically limiting emergence of polarization fields [6,27,50]. A key characteristic of the electronic structure and, thus, related physical properties of the nonpolar *zb*-$Al_xGa_{1-x}N$ semiconductors, is the presence of a *direct-indirect* band-gap crossing around $x \approx 0.65$ in the fundamental alloy-energy gap [51]. This transition is related to the fact that, in contrast to the direct semiconductor *zb*-GaN, *zb*-AlN exhibits an indirect $\Gamma_c \rightarrow X_c$ fundamental band gap between the Γ-point valence-band maximum and global Brillouin-zone edge X-point minimum of the conduction band, which lies roughly 1 eV below the Γ-point conduction-band valley [51]. Similar composition dependent direct-indirect band-gap crossings are known for ternary Al containing (cubic) group-III arsenides and antimonides, as well as certain Ga containing (cubic) group-III phosphides [52–55]. Considering the alignment of electronic states to a common energy scale in order to extract the band discontinuities between two materials, material compositions, respectively, one might expect a similar transition becoming manifested in the natural conduction band offsets between different *zb*-$Al_xGa_{1-x}N$ materials at sufficiently high Al concentration. This direct-indirect transition inevitably leads to an alloy-characteristic composition dependence of conduction band offsets that discriminates between the *direct*, predominantly Ga-rich, and an *indirect* Al-rich composition regimes of *zb*-$Al_xGa_{1-x}N/Al_yGa_{1-y}N$ heterostructures. Examining the extraordinary role of group-III nitride heterostructure components, integrated into current state-of-the-art optoelectronic devices, a detailed understanding of the material-intrinsic band-alignment characteristics is indispensable for the optimization and enhancement of current generation devices, as well as future design of efficient and high-capacity heterostructure devices.

While manifold experimental and theoretical data on band offsets between the binary group-III nitrides has been reported in literature (e.g., see data review and discussion in Ref. [49]), literature data on band offsets in ternary nitride compounds and a detailed characterization of composition dependence is sparse. Using modulation spectroscopy and photoluminescence combined with deep-acceptor level alignment, Hang *et al.* [56] investigated the composition dependence of band offsets between *wz*-GaN and ternary *wz*-$Al_xGa_{1-x}N$ using material samples in the composition range $0 < x < 0.22$. Band-offset dependencies of $\Delta E_v(wz\text{-GaN}/Al_xGa_{1-x}N) = -0.45x - 2.57x^2 \pm 0.05x$ (eV) and $\Delta E_c(wz\text{-GaN}/Al_xGa_{1-x}N) = 0.6x + 5.05x^2 \pm 0.03x$ (eV) were determined indicating an average conduction-to-valence band-offset ratio of 65:35. Most notable, both the valence and the conduction band offsets are characterized by a *massive* downward bowing. Therefore, straightforward extrapolation clearly leads to substantially biased band offsets in an Al-rich alloy regime. The origin of this overestimation of band-offset bowing features is traceable to the reported composition dependencies of the changes in the yellow shallow-donor–deep-acceptor level luminescence and the measured band-gap differences between *wz*-GaN and *wz*-$Al_xGa_{1-x}N$. Reddy *et al.* [57] comprehensively studied the band alignment at *c*-plane surfaces and interfaces of *wz*-AlGaN thin-film samples grown on *c*-plane sapphire and native single-crystalline *wz*-AlN substrates. The composition dependence of (natural) valence and conduction band offsets at polar *wz*-$Al_xGa_{1-x}N/Al_yGa_{1-y}N$ interfaces has been estimated within the entire composition range from the measured charge-neutrality levels and the interface-induced gap-states model as well as Anderson's electron affinity rule to $\Delta E_v(wz\text{-}Al_xGa_{1-x}N/Al_yGa_{1-y}N) \approx -|0.9(x-y)|$ (eV) and $\Delta E_c(wz\text{-}Al_xGa_{1-x}N/Al_yGa_{1-y}N) \approx |x^2 - y^2 + 0.8(x-y)|$ (eV) indicating a linear composition dependence of the valence band offset but a nonlinear dependence of the conduction band offset characterized by an assumed bowing parameter of 1.0 eV. Thereby, the band gap difference at the group-III nitride interfaces with comparable Al and Ga concentrations is split approximately two-third to one-third between the conduction and valence band offsets. In the limiting material system *wz*-$GaN/Al_xGa_{1-x}N$ the band-offset ratio is found to decrease with decreasing Al concentration reaching approximately a 50:50 ratio. Likewise, the band-offset ratio of *wz*-$Al_xGa_{1-x}N$/AlN increases with increasing Al concentration to an approximate ratio of 75:25. Wan *et al.* [58] determined a *wz*-$GaN/Al_{0.17}Ga_{0.83}N$ valence band offset of -0.13 ± 0.07 (eV) from x-ray

photoelectron spectroscopy forming a type-I band lineup together with the calculated conduction band offset of 0.22 ± 0.07 (eV). Both values roughly fall into line with the band-offset dependencies discussed above. Assuming a linear interpolation between the binary end components of $\Delta E_v(wz\text{-GaN}/\text{Al}_x\text{Ga}_{1-x}\text{N}) = -0.8x$ (eV), Litvinov *et al.* [59] calculated a (strained) conduction band offset of $\Delta E_c(wz\text{-GaN}/\text{Al}_x\text{Ga}_{1-x}\text{N}) \approx 0.603x + 0.99x^2$ (eV) for wz-$\text{Al}_x\text{Ga}_{1-x}\text{N}$ layers pseudomorphically strained to wz-GaN. These composition trends are virtually identical to the Reddy *et al.* data. Bhouri and Lazzari [60] investigated the composition dependence of band offsets at strained and unstrained binary AN/BN as well as ternary $\text{A}_x\text{B}_{1-x}\text{N}/\text{A}_y\text{B}_{1-y}\text{N}$ (A, B = Al, Ga, In) wz-group-III nitride heterojunctions from theoretical model calculations relying on parametric input. The wz-$\text{GaN}/\text{Al}_x\text{Ga}_{1-x}\text{N}$ heterojunctions were characterized as type-I heterostructures. The composition dependence of strained band offsets in wz-$\text{Al}_x\text{Ga}_{1-x}\text{N}/\text{Al}_y\text{Ga}_{1-y}\text{N}$ was found to follow the analytical expressions $\Delta E_v(wz\text{-Al}_x\text{Ga}_{1-x}\text{N}/\text{Al}_y\text{Ga}_{1-y}\text{N}) = (x-y)[(0.5073x - 0.8162) - (0.0228 + 0.0614x)(x + y)]$ (eV) and $\Delta E_c(wz\text{-Al}_x\text{Ga}_{1-x}\text{N}/\text{Al}_y\text{Ga}_{1-y}\text{N}) = (x - y)[(0.0034x + 1.116) + (0.6729 - 0.0371x)(x + y)]$ (eV). The unstrained band offsets in the binary system wz-GaN/AlN have been estimated as $\Delta E_v(wz\text{-GaN}/\text{AlN}) \approx 0.8$ eV and $\Delta E_c(wz\text{-GaN}/\text{AlN}) \approx 2.0$ eV which agrees well with the previous results. The comparison between the strained and unstrained cases indicated that the conduction band offset is less affected by interfacial strain, while the valence band offset behaves differently under tensile or compressive strain.

In summary, the reported experimental and theoretical band-offset data on the polar wz-$\text{Al}_x\text{Ga}_{1-x}\text{N}/\text{Al}_y\text{Ga}_{1-y}\text{N}$ material system strongly indicate an almost linear dependence of the untrained (natural) valence band offset on the alloy composition. Thereby, the composition dependence of the valence band offset closely follows the linear change of measured charge-neutrality levels, the branch-point energy, respectively, in wz-$\text{Al}_x\text{Ga}_{1-x}\text{N}$ samples [57]. Besides, the conduction band offset, originating from direct electronic transitions located at the Brillouin-zone centers, shows a nonlinear composition dependence with notable downward-bowing characteristics.

In addition to investigations on the band-offset dependence on chemical composition, an order driven heterostructure-type transition was reported by Dudiy and Zunger [61]. This type-I-to-type-II transition occurs between random and ordered domains of wz-$\text{Al}_x\text{Ga}_{1-x}\text{N}$ at a composition parameter of $x \simeq 0.4$. The origin of the transition was found to be the hole confinement on Ga-rich monolayers which pushes the valence-band maximum of the ordered material below the valence-band maximum of the surrounding random alloy. A type-II alignment has also been reported by Belabbes *et al.* [62] for cubic zb-AlN inclusions in hexagonal wz-AlN on the basis of hybrid-functional DFT and G_0W_0 quasiparticle theory based electronic structure simulations.

In contrast to the polar wurtzite phases, substantially less data have been reported on the composition dependence of band offsets between the nonpolar cubic polytypes. Wei *et al.* [63] used a combination of electron holography and cathodoluminescence measurements to determine the strained band offsets in a zb-$\text{GaN}/\text{Al}_{0.3}\text{Ga}_{0.7}\text{N}$ heterostructure grown on 3C-SiC substrate yielding valence and conduction band offsets of -0.13 and 0.65 eV, respectively, and a high conduction-to-valence band-offset ratio of 5:1. A smaller zb-$\text{GaN}/\text{Al}_{0.3}\text{Ga}_{0.7}\text{N}$ band-offset ratio of $0.5/0.15 \approx 3.3$ was determined by Mourad [44] using branch-point alignment of empirical tight-binding band energies to determine unstrained natural band offsets. These values are slightly different from the previously discussed band offsets between the wurtzite-type group-III nitride analogs [57,60]. Especially, a different conduction-to-valence band-offset ratio is indicated for the cubic polytypes. Differences existing in the natural band offsets of the hexagonal and cubic group-III nitride material systems, despite common tetrahedral coordination, point towards the fundamental influence of symmetry related polarization fields on the band alignment, in general. Besides the predominantly reported type-I alignment between alloys on the Ga-rich composition side, a type-II band alignment with valence and conduction band offsets of -0.39 and -0.17 eV, was reported by Buongiorno Nardelli *et al.* [64] for a strained zb-$\text{Al}_{0.5}\text{Ga}_{0.5}\text{N}/\text{AlN}$ (001) heterojunction from electronic structure theory. The possible formation of type-II aligned group-III nitride heterojunctions discriminates the hexagonal and cubic material systems, fundamentally.

The origin of infrequent experimental band-offset data is most likely related to the limited availability of high quality samples of cubic group-III nitrides in the entire composition range. However, present growth techniques allow for high quality growth of zb-$\text{Al}_x\text{Ga}_{1-x}\text{N}$ bulk semiconductors, thin films, and multiple quantum well heterostructures meeting the demands on phase purity and chemical composition which are necessary to extract fundamental alloy parameters not only for the binary but also the multicomponent nonpolar group-III nitride semiconductors [23,27,65–69]. Another complication in dealing with nonpolar group-III nitrides is the fundamentally indirect nature of the zb-AlN band gap. The zb-$\text{Al}_x\text{Ga}_{1-x}\text{N}$ alloy intrinsic indirect electronic-structure features at high Al content are difficult to detect in optical spectroscopy which is an essential component in the experimental process of band-offset determination.

Within the present study we utilize density functional theory based first-principles theory to investigate the composition dependence of natural band offsets in nonpolar zb-$\text{Al}_x\text{Ga}_{1-x}\text{N}/\text{Al}_y\text{Ga}_{1-y}\text{N}$ composites. To this purpose the present paper is organized as follows: Section II summarizes numerical and methodological details involved in the *ab initio* band-offset calculation via the branch-point alignment approach. Section III is used for presentation of numerical results and discussion of the character and the composition dependence of natural band discontinuities in nonpolar zb-$\text{Al}_x\text{Ga}_{1-x}\text{N}/\text{Al}_y\text{Ga}_{1-y}\text{N}$ materials. Finally, Sec. IV summarizes the present study and highlights essential results.

We expect that the detailed quantitative and qualitative understanding of natural band offsets in nonpolar group-III nitride systems as zb-$\text{Al}_x\text{Ga}_{1-x}\text{N}/\text{Al}_y\text{Ga}_{1-y}\text{N}$ provides a useful orientation guide to future utilization and optimization of optoelectronics devices based on this promising class of materials.

II. METHODOLOGY

The present calculations are performed using density functional theory (DFT) within the generalized gradient approximation (GGA) to the electron exchange and correlation (XC) interaction as well as using hybrid XC functionals. Specifically, the Perdew-Becke-Ernzerhof (PBE) [70] GGA functional and Heyd-Scuseria-Ernzerhof (HSE) type [71–74] hybrid functionals were used for structural relaxations and electronic structure calculations, respectively. In the latter, the fraction of exact exchange (EXX) from Hartree-Fock theory, 25% in the conventional HSE03/HSE06 functionals, was increased to match the experimentally observed band gaps as well as to reproduce features of the *GW* quasiparticle band structure [51]. EXX adjusted HSE-type hybrid functionals, henceforward referred to as *HSEmod*, provide an efficient way to approximate more rigorous band-structure calculation schemes within the framework of Greens function based quasiparticle theory, thus, effectively overcome limitations due to the so called *band-gap problem* [75–79] existing in conventional (semi)local XC-functional-based DFT. In detail, EXX fractions of 30% and 36% have been used for the limiting binary components *zb*-GaN and *zb*-AlN, respectively [80]. The EXX fractions for hybrid-functional calculations on ternary *zb*-$Al_xGa_{1-x}N$ have been interpolated linearly. The accurate description of band discontinuities via EXX adjusted HSE-type functionals has been demonstrated for several group III-V semiconductor heterostructures [81].

All calculations were performed using the Vienna *ab initio* simulation package (VASP) [82,83]. The electron-ion interaction is described by the projector-augmented wave (PAW) scheme [83,84], where the Ga_{3d} semicore electrons are treated as valence states. The electronic wave functions are expanded into plane waves up to a kinetic energy cutoff of 400 eV. The Brillouin zone integration is performed using regular Γ-centered meshes with a **k**-point density of $2 \times 2 \times 2$.

The ternary *zb*-$Al_xGa_{1-x}N$ alloys are modeled by cubic 64 atom unit cells and random distributions of Ga and Al ions in the cation sublattice. As demonstrated previously, see Ref. [51], this unit-cell setup sufficiently reduces finite-size *periodicity errors* originating from the enforced artificial alloy periodicity. The calculations are performed at the experimental lattice parameters of 4.503 Å for *zb*-GaN [85] and 4.373 Å for *zb*-AlN [68]. The lattice constants of ternary *zb*-$Al_xGa_{1-x}N$ alloys have been interpolated linearly between the binary compounds in terms of Vegard's law. The validity of Vegard's law for group-III nitride alloys has been confirmed experimentally for polar *wz*-$Al_xGa_{1-x}N$ [86] as well as theoretically for nonpolar *zb*-$Al_xGa_{1-x}N$ [66] in several studies on group-III nitride-semiconductor alloys [87–89]. All atomic positions were relaxed on the DFT-PBE level of theory until the forces on each atom were less then 0.01 meV/Å.

The band-edge positions are extracted by averaging the bulk-degenerate Γ_v valence-band and X_c conduction-band manifolds which are splitted in the ternary materials due to local fluctuations in the alloy compositions. In order to estimate the band discontinuities, the valence and conduction band edges are aligned according to the branch-point energies of the semiconducting systems which are commonly believed to represent a universal energy reference point. In detail, we rely on the Brillouin zone averaging technique over valence and conduction band states proposed by Schleife *et al.* [42] to approximate the natural band discontinuities in *zb*-$Al_xGa_{1-x}N/Al_yGa_{1-y}N$ over the entire composition range [42,90]. Following this approach, the branch-point energy E_{bp} of a semiconducting system is approximated as

$$E_{bp} \approx \frac{1}{2N_k} \sum_{\mathbf{k}} \left[\frac{1}{N_{vb}} \sum_{i}^{N_{vb}} \varepsilon_{v_i}(\mathbf{k}) + \frac{1}{N_{cb}} \sum_{j}^{N_{cb}} \varepsilon_{c_j}(\mathbf{k}) \right], \quad (1)$$

where N_k is the number of **k** points used to sample the Brillouin zone and $\varepsilon_{v_i}(\mathbf{k})$ and $\varepsilon_{c_j}(\mathbf{k})$ are the ith highest and jth lowest valence and conduction band states at wave vector **k**, respectively. Commonly, inclusion of the two highest valence bands and the lowest conduction band allows a reasonable estimation of branch point energies in case of the primitive two-atom unit cells of binary zincblende semiconductors [42,90]. Variations in the number of electronic bands, included in the branch-point evaluation, tend to shift the branch point energies uniformly while roughly preserving the alignment characteristics [91]. Here the 64 highest valence and 32 lowest conduction states are included in the evaluation of branch-point energies for the 64 atom unit cells of *zb*-$Al_xGa_{1-x}N$ [92]. The mean absolute error of branch-point aligned band offsets has been estimated by Hinuma *et al.* as ∼0.1 eV for a broad selection of zincblende semiconductors [91].

Throughout the present paper the following sign convention is used for all band offsets. All band offsets are given relative to the valence band edge of the particular small-gap material. Hence, all valence band offsets are negative while the conduction band offsets are either positive or negative, with the sign discriminating between a type-I (positive CBO) or a type-II energy-level alignment (negative CBO). The sign convention is also consistently applied to cited literature data in order to maintain consistent data throughout the entire paper. Analog to the determination of band-gap bowing characteristics, the composition dependencies of band offsets between *zb*-$Al_xGa_{1-x}N$ and the binary end compositions *zb*-GaN and *zb*-AlN are fitted to a second order polynomial via

$$\begin{aligned} \Delta E^{bp}_{v,c}(A_xB_{1-x}/A,B) &= A + B\,x + C\,x^2 \\ &\equiv \Delta E^{bp}_{v,c}(A,B)x - b^{bp}_{v,c}\,x(1-x) \\ &\quad + \Delta E^{bp}_{v,c}(A_xB_{1-x})(1-x), \end{aligned} \quad (2)$$

where A_xB_{1-x} is the composition dependent ternary alloy and A and B are the respective binary end semiconductors. The fitting parameters are related according to $A \equiv \Delta E^{bp}_{v,c}(A_xB_{1-x})$, $B \equiv [\Delta E^{bp}_{v,c}(A,B) - b^{bp}_{v,c} - \Delta E^{bp}_{v,c}(A_xB_{1-x})]$, and $C \equiv b^{bp}_{v,c}$. The parameter $b^{bp}_{v,c}$ represent chemical (dis)order induced deviations from a linear Vegard's-law-type composition dependence of physical material parameters in multicomponent solid solutions. b^{bp}_{v} and b^{bp}_{c} indicate a *so called* downward bowing in case of $b^{bp}_{v,c} > 0$ and an upward bowing in case of $b^{bp}_{v,c} < 0$.

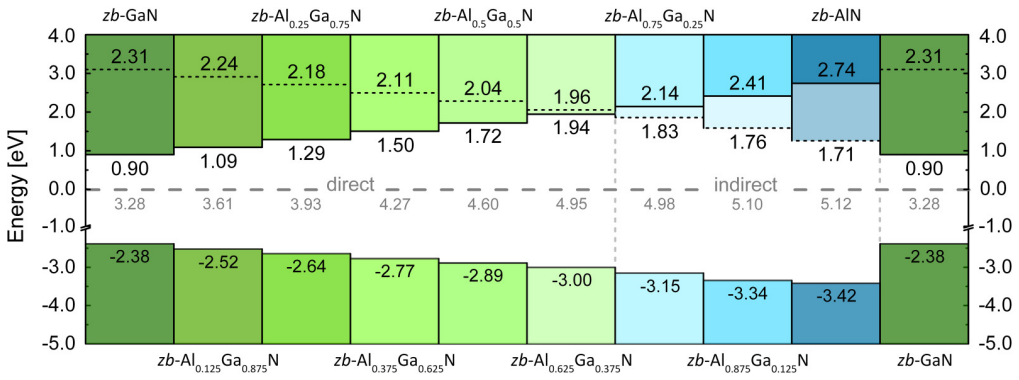

FIG. 1. DFT-HSEmod valence and conduction-edge diagram of zb-$Al_xGa_{1-x}N$. Both the conduction states related to the lowest bulklike Γ_c-type energy levels (solid lines) as well as the conduction states related to the lowest bulklike X_c-type energy levels (dashed lines) are indicated. The given numbers indicate the positions of energy levels aligned relative to their branch-point energies (zero point of energy scale) and gray numbers are the fundamental energy gaps of the alloys. Regions of direct and indirect fundamental alloy-energy gaps are indicated.

III. RESULTS AND DISCUSSION

A. A short recap on energy gaps

Before we turn to the band-offset characteristics of zb-$Al_xGa_{1-x}N/Al_yGa_{1-y}N$, we briefly recapitulate the fundamental nature of the electronic band gap in zb-$Al_xGa_{1-x}N$. Fundamental electronic band gaps of 3.28 eV (direct, $\Gamma_v \rightarrow \Gamma_c$) and 5.12 eV (indirect, $\Gamma_v \rightarrow X_c$) have been found in the binary end semiconductors zb-GaN and zb-AlN using exact exchange adjusted hybrid functionals of the HSE type. The corresponding indirect, direct, respectively, transition energies are 4.70 eV for the indirect $\Gamma_v \rightarrow X_c$ band gap of zb-GaN and 6.16 eV for the direct $\Gamma_v \rightarrow \Gamma_c$ band gap of zb-AlN. In the ternary zb-$Al_xGa_{1-x}N$ alloys the composition dependence of the direct ($\Gamma_v \rightarrow \Gamma_c$)-type energy gap is fitted according to $E_{gap}^{dir}(zb\text{-}Al_xGa_{1-x}N) = 6.16\,x - 0.50\,x(1-x) + 3.28(1-x)$ (eV). The composition dependence of the indirect ($\Gamma_v \rightarrow X_c$)-type band gap reads $E_{gap}^{ind}(zb\text{-}Al_xGa_{1-x}N) = 5.12\,x + 0.04\,x(1-x) + 4.70(1-x)$ (eV). The fundamental alloy-energy gap of nonpolar zb-$Al_xGa_{1-x}N$ exhibits a distinct transition between these direct ($\Gamma_v \rightarrow \Gamma_c$)-type and indirect ($\Gamma_v \rightarrow X_c$)-type energy gaps occurring at a critical aluminum content of $x_c = 0.63$. Hence, the fundamental energy gap of zb-$Al_xGa_{1-x}N$ increases with a moderate downward bowing of $b_\Gamma = 0.50$ eV for $0 \leqslant x < 0.63$, changes nonmonotonically at the crossover composition $x_c = 0.63$, and progresses virtually linear with $b_X = -0.04$ eV at high Al concentrations ($0.63 > x \leqslant 0.63$). The calculated band gaps, branch-point aligned band-edge energies, as well as direct and indirect energy-gap regions are illustrated in Fig. 1.

While most *ab initio* studies on multicomponent semiconductor alloys focus on details of the fundamental energy gaps, only a few studies dedicated the same level of accuracy to investigate the composition dependence of the fundamental alloy band offsets. Similar experiments profiling the entire composition dependence of an alloy's band-offset profile are rare either to limited availability of high quality samples in the entire composition ranges or technical limitations of the experimental setup. By way of example, a thorough experimental study on band offsets has, recently, been conducted by Yi *et al.* [53] on the composition dependence of ternary (AlGaAs) and quaternary (AlGaInP) semiconductor alloys.

B. Band offsets between nonpolar zb-$Al_xGa_{1-x}N$ semiconductor alloys

The intermixed unoccupied Γ_c-type and X_c-type electronic states, responsible for the fundamental band gaps of the binary composition ends, not only give rise to a direct-indirect crossover but also four possible alignment types of unoccupied bands and conduction band offsets, respectively, at zb-$Al_xGa_{1-x}N$ heterojunctions. In detail, direct-direct ($\Gamma_c \rightarrow \Gamma_c$)-type, direct-indirect ($\Gamma_c \rightarrow X_c$)-type, indirect-direct ($X_c \rightarrow \Gamma_c$)-type, and indirect-indirect ($X_c \rightarrow X_c$)-type conduction band offsets can be determined. Depending on the alloy composition (and strain conditions) a proper subset of these offsets will form the *fundamental* conduction band offset. In order to elucidate the fundamental character of the band offsets between nonpolar zb-$Al_xGa_{1-x}N$ semiconductor alloys, the composition dependence of all offset types is analyzed in detail. The natural band offsets at the binary/ternary group-III nitride heterojunctions zb-$GaN/Al_xGa_{1-x}N$ and zb-$Al_xGa_{1-x}N/AlN$ are presented in Fig. 2 while the full ternary/ternary composition dependence is considered in Figs. 3 and 4.

The composition dependence of all ternary/binary offsets has been fitted to a second order polynomial [cf. Eq. (2)] across the entire composition range of the ternary zb-$Al_xGa_{1-x}N$ component yielding the bowing parameters b. However, the obtained band offsets point to a characteristic composition dependence of all involved band offsets, which clearly discriminates the composition regimes below and above the critical direct-indirect crossing at $x_c = 0.63$. Separate fitting in the predominantly Ga-rich composition regime $0 \leqslant x \leqslant 0.63$ and the Al-rich composition regime $0.63 \leqslant x \leqslant 1$ indicate a transition from a more linear dependence on composition to a considerably nonlinear dependence in the natural valence as well as conduction band offsets of both zb-$GaN/Al_xGa_{1-x}N$ and zb-$Al_xGa_{1-x}N/AlN$. The band-offset bowing parameter b_{dir} in the direct, predominantly Ga-rich, regime does not go above an absolute value of 0.29 eV while the bowing parameter in the Al-rich regime does not fall below 1.22 eV. The degree of nonlinearity, indicated by the global bowing parameter b, falls in between b_{dir} and b_{ind} in most cases (see Table I). The natural band-offset bowing parameters b, b_{dir}, and b_{ind} are summarized in Table I for the zb-$GaN/Al_xGa_{1-x}N$

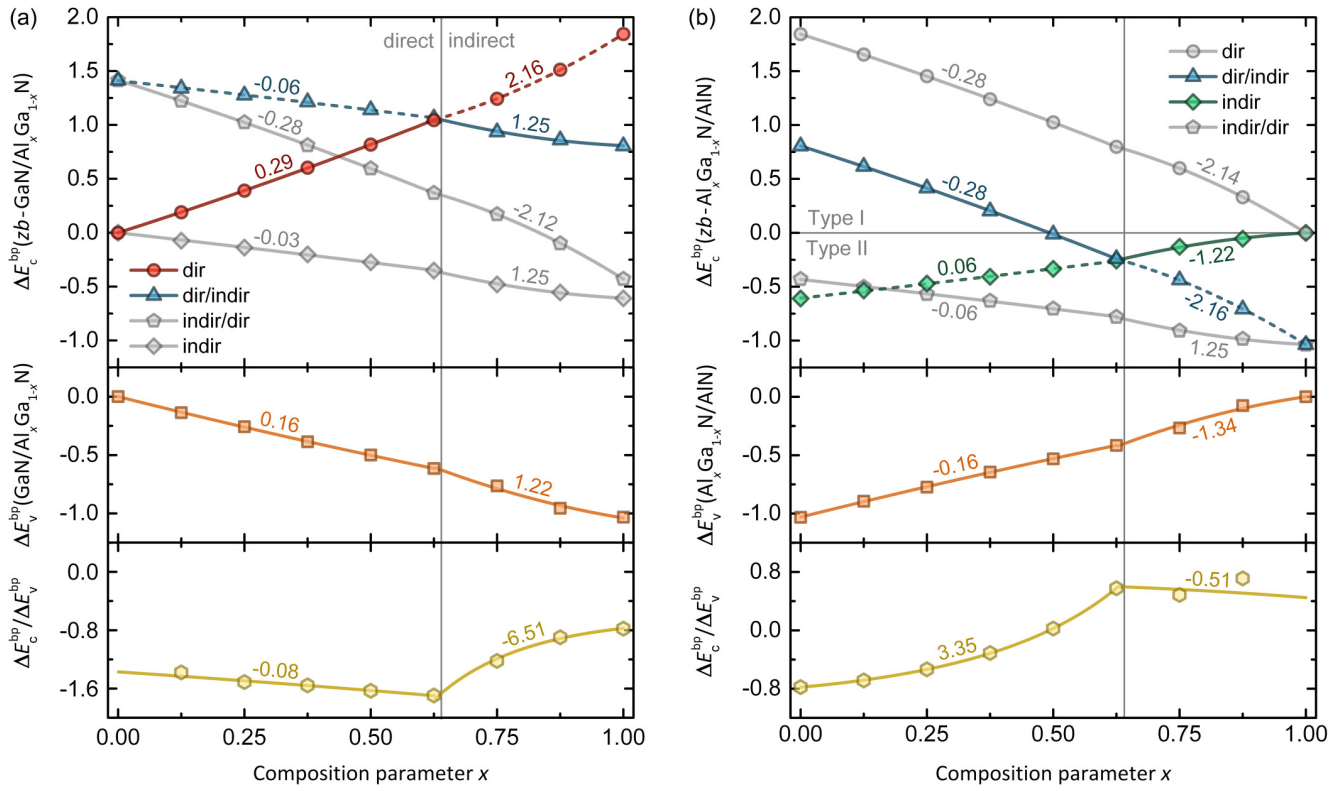

FIG. 2. Composition dependence of branch-point aligned DFT-HSEmod natural valence band offsets ΔE_v^{bp} and conduction band offsets ΔE_c^{bp} between (a) *zb*-GaN and *zb*-$Al_xGa_{1-x}N$ and (b) *zb*-$Al_xGa_{1-x}N$ and *zb*-AlN. In detail, the direct-direct ($\Gamma_c \rightarrow \Gamma_c$)-type, direct-indirect ($\Gamma_c \rightarrow X_c$)-type, indirect-direct ($X_c \rightarrow \Gamma_c$)-type, and indirect-indirect ($X_c \rightarrow X_c$)-type conduction band offsets are illustrated. The solid colored offsets represent the fundamental natural conduction band offsets in the *zb*-GaN/$Al_xGa_{1-x}N$ and *zb*-$Al_xGa_{1-x}N$/AlN systems. All band offsets are given in eV. For *zb*-GaN/$Al_xGa_{1-x}N$ the direct-indirect crossover of the conduction band offset is indicated. Sign change in the *zb*-$Al_xGa_{1-x}N$/AlN conduction band offsets indicates the transition from a type-I to a type-II energy-level alignment. The composition dependence of band offsets is fitted separately to Eq. (2) below and above the direct-indirect crossover. The particular bowing parameters are given. The lower panels show the conduction-to-valence band-offset quotient $\Delta E_c^{bp}/\Delta E_v^{bp}$ calculated from the fitted band-offset curves.

and *zb*-$Al_xGa_{1-x}N$/AlN systems. An overview of fitting parameters, used to illustrate the composition dependencies in Fig. 2, is provided in Table II. Moreover, the different bowing features in the direct and indirect alloy regimes are well reproduced by data fitting to a conventional fifth order polynomial of the form $y = A_0 + A_1\,x + A_2\,x^2 + A_3\,x^3 + A_4\,x^4 + A_5\,x^5$. The corresponding fitting parameters are provided in Table III for the binary/ternary systems. According to this, the two-dimensional composition dependencies of ternary/ternary *zb*-$Al_xGa_{1-x}N$/$Al_yGa_{1-y}N$ band offsets are fitted to a two-dimensional fifth order polynomial of the form $z = z_0 + A_1\,x + A_2\,x^2 + A_3\,x^3 + A_4\,x^4 + A_5\,x^5 + B_1\,y + B_2\,y^2 + B_3\,y^3 + B_4\,y^4 + B_5\,y^5$ (see Figs. 3 and 4 and parameter list Table IV).

Subsequently, we discuss the respective composition dependencies in detail.

1. *zb*-GaN/$Al_xGa_{1-x}N$

The natural valence band alignment of *zb*-GaN/$Al_xGa_{1-x}N$ [cf. Fig. 2(a)] increases, according to an amount, with a minor downward bowing of $b_{dir} = 0.16$ eV in the direct gap regime. The valence band offset decreases further in the Al-rich regime with an enhanced downward bowing of $b_{ind} = 1.22$ eV and reaches maximum of -1.04 eV for valence-band alignment between the binary end semiconductors *zb*-GaN and *zb*-AlN. The overall monotonic valence band-offset dependence on alloy composition can be attributed to the fact that the valence-band extrema are located at the Brillouin-zone centers in both *zb*-GaN as well as *zb*-AlN and, hence, within all ternary alloys. The fundamental conduction band offset in *zb*-GaN/$Al_xGa_{1-x}N$ is determined by the alignment of the Γ_c-type conduction band minima below $x_c = 0.63$. The Al X_c-type conduction state minima, lowering in energy with increasing alloy composition, determines the fundamental conduction band offsets in the Al-rich composition range. Hence, the fundamental conduction band offset exhibits a distinct maximum marking the direct-indirect transition. Analog to the valence band offset, the bowing characteristics of all considered conduction band offsets are substantially enhanced beyond the direct-indirect crossover composition.

In detail, the direct-direct ($\Gamma_c \rightarrow \Gamma_c$)-type conduction band offset, representing the fundamental *zb*-GaN/$Al_xGa_{1-x}N$ conduction band offset in the composition range from $0 \leqslant x \leqslant 0.63$, increases from zero to 1.05 eV with a moderate downward bowing of $b_{dir} = 0.29$ eV. Above x_c, the downward bowing is much more pronounced ($b_{ind} = 2.16$ eV) and the direct-direct conduction band offset grow to 1.84 eV across the Al-rich composition range. The direct-indirect

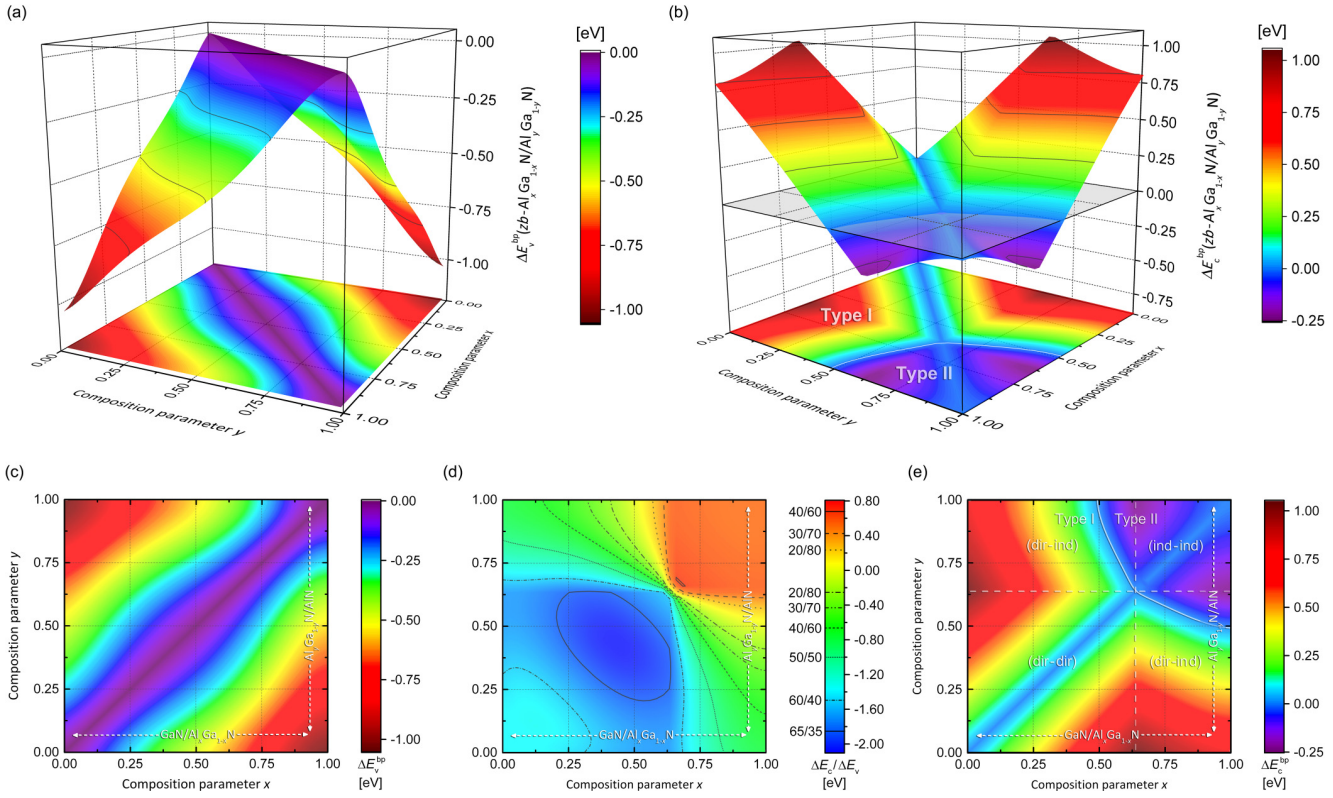

FIG. 3. (a) and (b) Three-dimensional illustrations of the two-dimensional x,y-composition dependence of branch-point aligned DFT-HSEmod natural valence band offsets ΔE_v^{bp} and conduction band offsets ΔE_c^{bp} in *zb*-$Al_xGa_{1-x}N/Al_yGa_{1-y}N$. (c)–(e) Two-dimensional contour plots of the *zb*-$Al_xGa_{1-x}N/Al_yGa_{1-y}N$ valence band offset, the conduction-to-valence band-offset quotient $\Delta E_c^{bp}/\Delta E_v^{bp}$, the $|\Delta E_c^{bp}| : |\Delta E_v^{bp}|$ ratio, respectively, and the conduction band offset. Isovalue lines of the band-offset quotient as well as boundary lines between direct and indirect composition regimes (dashed white lines) and type-I–type-II alloy composition regimes (solid white line) are highlighted.

($\Gamma_c \rightarrow X_c$)-type conduction band offset decreases continuously from 1.41 eV in *zb*-GaN to 1.06 eV at the crossover concentration. The fundamental direct-indirect conduction offset branch decreases to 0.81 eV in *zb*-AlN with an intermediate downward bowing of $b_{ind} = 1.25$ eV.

Since the fundamental band offsets do not change their sign upon alloy composition, the band-edge alignments between *zb*-GaN and *zb*-$Al_xGa_{1-x}N$ exclusively form type-I aligned heterojunctions, whose composition dependence is characterized by two distinct bowing parameters indicating downward bowing throughout the entire composition range. The conduction-to-valence band ratio of the fundamental *zb*-$GaN/Al_xGa_{1-x}N$ band offsets, illustrated in the lowest panel of Fig. 2, illustrates the changes in basic material

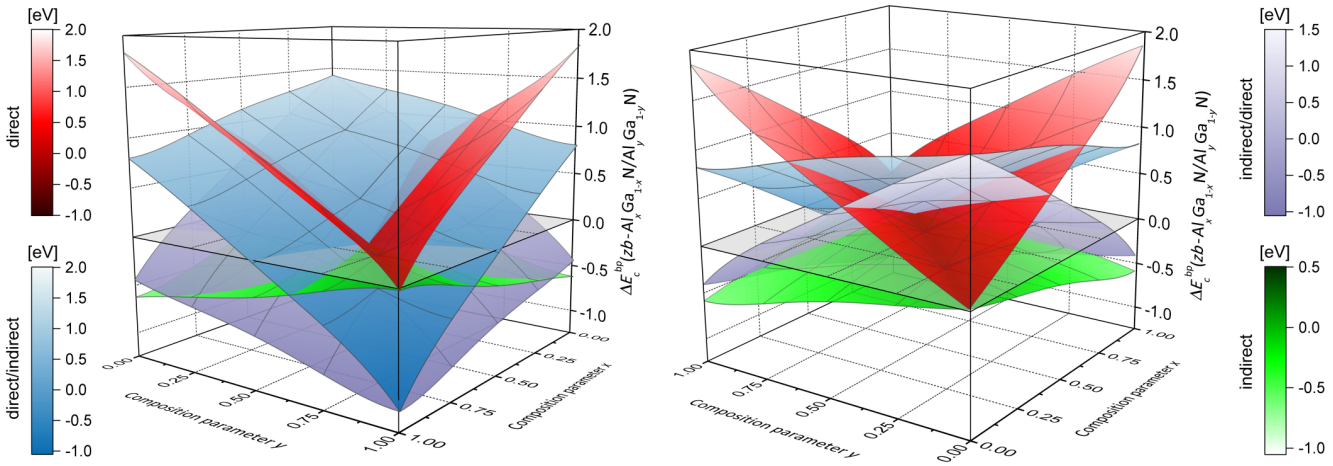

FIG. 4. Three-dimensional representations of the two-dimensional x,y-composition dependence of direct-direct ($\Gamma_c \rightarrow \Gamma_c$)-type, direct-indirect ($\Gamma_c \rightarrow X_c$)-type, indirect-direct ($X_c \rightarrow \Gamma_c$)-type, and indirect-indirect ($X_c \rightarrow X_c$)-type branch-point aligned DFT-HSEmod conduction band offsets.

TABLE I. Bowing parameters of the natural valence and conduction band offsets fitted via Eq. (2) in the predominantly Ga-rich direct (b_{dir}) and Al-rich indirect (b_{ind}) composition ranges below and above the critical direct-indirect crossover composition ($x_{\mathrm{c}} = 0.63$) as well as across the bowing parameter (b) fitted to the entire composition range (cf. Fig. 2). Also given are the bowing parameters of the conduction-to-valence band-offset quotient $\Delta E_{\mathrm{c}}^{\mathrm{bp}}/\Delta E_{\mathrm{v}}^{\mathrm{bp}}$ of the fundamental alloy band offsets.

System	Offset	Type	Bowing parameter (eV)		
			b	b_{dir}	b_{ind}
zb-GaN/$Al_xGa_{1-x}N$	$\Delta E_{\mathrm{v}}^{\mathrm{bp}}$	$(\Gamma_{\mathrm{v}} - \Gamma_{\mathrm{v}})$	− 0.09	0.16	1.22
	$\Delta E_{\mathrm{c}}^{\mathrm{bp}}$	$(\Gamma_{\mathrm{c}} - \Gamma_{\mathrm{c}})$	0.42	0.29	2.16
		$(\Gamma_{\mathrm{c}} - X_{\mathrm{c}})$	− 0.11	− 0.06	1.25
		$(X_{\mathrm{c}} - \Gamma_{\mathrm{c}})$	− 0.42	− 0.28	− 2.12
		$(X_{\mathrm{c}} - X_{\mathrm{c}})$	− 0.11	− 0.03	1.25
	$\Delta E_{\mathrm{c}}^{\mathrm{bp}}/\Delta E_{\mathrm{v}}^{\mathrm{bp}}$			− 0.08	− 6.51
zb-$Al_xGa_{1-x}N$/AlN	$\Delta E_{\mathrm{v}}^{\mathrm{bp}}$	$(\Gamma_{\mathrm{v}} - \Gamma_{\mathrm{v}})$	0.09	− 0.16	− 1.34
	$\Delta E_{\mathrm{c}}^{\mathrm{bp}}$	$(\Gamma_{\mathrm{c}} - \Gamma_{\mathrm{c}})$	− 0.42	− 0.28	− 2.14
		$(\Gamma_{\mathrm{c}} - X_{\mathrm{c}})$	− 0.42	− 0.28	− 2.16
		$(X_{\mathrm{c}} - \Gamma_{\mathrm{c}})$	− 0.11	0.06	− 1.22
		$(X_{\mathrm{c}} - X_{\mathrm{c}})$	0.11	− 0.06	1.25
	$\Delta E_{\mathrm{c}}^{\mathrm{bp}}/\Delta E_{\mathrm{v}}^{\mathrm{bp}}$			− 0.08	− 6.51

parameters originating from mixing the direct and indirect electronic-structure features, insistently. Below the direct-indirect crossover, the ratio decreases virtually linearly ($b_{\mathrm{dir}} = -0.08$ eV) from a 58:42 ration in the *dilute limit* of vanishing Al concentration to 63:37 at the crossover composition. A characteristic 60:40 ratio is estimated for the *zb*-GaN/$Al_{0.26}Ga_{0.74}N$ system. Beyond x_{c}, the *zb*-GaN/$Al_xGa_{1-x}N$ band-offset ratio increase to a 50:50 equipartition at a composition parameter of $x = 0.83$ and a 44:56 ratio for the binary end system *zb*-GaN/AlN. This substantial change in band-offset ratios is reflected in the extreme bowing characteristics ($b_{\mathrm{ind}} = -6.51$ eV) in the Al-rich composition range.

In summary, *zb*-GaN/$Al_xGa_{1-x}N$ represents a prototypical example of a type-I heterojunction forming material system, whose alloy characteristics are determined by a direct-indirect band-gap crossing. In that the nonpolar Al/Ga based nitrides exhibit electronic structure features quite similar to the archetypical group-III arsenide representative of this class, *zb*-GaAs/$Al_xGa_{1-x}As$. In $Al_xGa_{1-x}As$ the direct-indirect band-gap crossover transition occurs at a composition parameter of $x_{\mathrm{c}} \approx 0.38$ [46,55,93,94] between the direct $(\Gamma_{\mathrm{v}} \rightarrow \Gamma_{\mathrm{c}})$-type energy gap and the indirect $(\Gamma_{\mathrm{v}} \rightarrow X_{\mathrm{c}})$-type energy gap. Similar to the cubic nitride alloys, the direct energy gaps show a moderate bowing characteristic ($b_{\Gamma} = 0.03$ eV), whereas the indirect alloy gap depends virtually linearly ($b_X = 0.055$ eV) on the alloy composition [55,94]. The resulting type-I band alignment in *zb*-GaAs/$Al_xGa_{1-x}As$ heterostructures exhibits a valence band offset depending linearly on Al concentration and a conduction band offset increasing continuously as a function

TABLE II. Valence and conduction band-offset parameters fitted according to Eq. (2). The composition dependencies are fitted separately in the direct (b_{dir}) and indirect (b_{ind}) composition ranges below and above the critical direct-indirect crossover composition ($x_{\mathrm{c}} = 0.63$) (cf. Fig. 2). Also included are the fitting parameters for the conduction-to-valence band-offset quotient $\Delta E_{\mathrm{c}}^{\mathrm{bp}}/\Delta E_{\mathrm{v}}^{\mathrm{bp}}$ of the fundamental alloy band offsets.

System composition	Offset	Type	Band-offset fitting parameters (eV)					
			$0 \leqslant x \leqslant 0.63$			$0.63 \leqslant x \leqslant 1$		
			$\Delta E_{\mathrm{v,c}}^{\mathrm{bp}}(A_xB_{1-x})$	b_{dir}	$\Delta E_{\mathrm{v,c}}^{\mathrm{bp}}(A,B)$	$\Delta E_{\mathrm{v,c}}^{\mathrm{bp}}(A_xB_{1-x})$	b_{ind}	$\Delta E_{\mathrm{v,c}}^{\mathrm{bp}}(A,B)$
zb-GaN/$Al_xGa_{1-x}N$	$\Delta E_{\mathrm{v}}^{\mathrm{bp}}$	$(\Gamma_{\mathrm{v}} - \Gamma_{\mathrm{v}})$	− 0.92	0.16	0.00	− 1.04	1.22	0.88
	$\Delta E_{\mathrm{c}}^{\mathrm{bp}}$	$(\Gamma_{\mathrm{c}} - \Gamma_{\mathrm{c}})$	1.78	0.29	0.00	1.84	2.16	1.07
		$(\Gamma_{\mathrm{c}} - X_{\mathrm{c}})$	0.84	− 0.06	1.41	0.81	1.25	2.27
		$(X_{\mathrm{c}} - \Gamma_{\mathrm{c}})$	− 0.37	− 0.28	1.42	− 0.43	− 2.12	0.38
		$(X_{\mathrm{c}} - X_{\mathrm{c}})$	− 0.57	− 0.03	0.00	− 0.61	1.25	0.87
	$\Delta E_{\mathrm{c}}^{\mathrm{bp}}/\Delta E_{\mathrm{v}}^{\mathrm{bp}}$		− 1.93	− 0.08	− 1.37	− 0.80	− 6.51	− 7.30
zb-$Al_xGa_{1-x}N$/AlN	$\Delta E_{\mathrm{v}}^{\mathrm{bp}}$	$(\Gamma_{\mathrm{v}} - \Gamma_{\mathrm{v}})$	− 0.11	− 0.16	− 1.03	0.00	− 1.34	− 1.98
	$\Delta E_{\mathrm{c}}^{\mathrm{bp}}$	$(\Gamma_{\mathrm{c}} - \Gamma_{\mathrm{c}})$	0.06	− 0.28	1.84	0.00	− 2.14	0.79
		$(\Gamma_{\mathrm{c}} - X_{\mathrm{c}})$	− 0.97	− 0.28	0.81	− 1.04	− 2.16	− 0.26
		$(X_{\mathrm{c}} - \Gamma_{\mathrm{c}})$	− 0.03	0.06	− 0.61	0.00	− 1.22	− 1.45
		$(X_{\mathrm{c}} - X_{\mathrm{c}})$	− 1.01	− 0.06	− 0.43	− 1.04	1.25	0.43
	$\Delta E_{\mathrm{c}}^{\mathrm{bp}}/\Delta E_{\mathrm{v}}^{\mathrm{bp}}$		2.51	3.35	− 0.74	0.40	− 0.51	0.58

TABLE III. Valence and conduction band-offset parameters obtained from fitting a fifth order polynomial of the form $y = A_0 + A_1 x + A_2 x^2 + A_3 x^3 + A_4 x^4 + A_5 x^5$.

			Band-offset fitting parameters (eV)					
System	Offset	Type	A_0	A_1	A_2	A_3	A_4	A_5
zb-GaN/Al$_x$Ga$_{1-x}$N	ΔE_v^{bp}	$(\Gamma_v - \Gamma_v)$	0.00	− 0.71	− 3.88	13.95	− 18.68	8.29
	ΔE_c^{bp}	$(\Gamma_c - \Gamma_c)$	0.00	1.45	0.28	1.36	− 3.39	2.15
		$(\Gamma_c - X_c)$	1.42	− 0.68	0.65	− 0.20	− 1.87	1.49
		$(X_c - \Gamma_c)$	1.41	− 1.45	− 0.28	− 1.36	3.39	− 2.15
		$(X_c - X_c)$	0.00	− 0.68	0.65	− 0.20	− 1.87	1.49
zb-Al$_x$Ga$_{1-x}$N/AlN	ΔE_v^{bp}	$(\Gamma_v - \Gamma_v)$	− 1.03	0.71	3.88	− 13.95	18.68	− 8.29
	ΔE_c^{bp}	$(\Gamma_c - \Gamma_c)$	1.84	− 1.45	− 0.28	− 1.36	3.39	− 2.15
		$(\Gamma_c - X_c)$	0.81	− 1.45	− 0.28	− 1.36	3.39	− 2.15
		$(X_c - \Gamma_c)$	− 0.43	− 0.68	0.65	− 0.20	− 1.87	1.49
		$(X_c - X_c)$	− 0.61	0.68	− 0.65	0.20	1.87	− 1.49

of x with a distinct change in slope when going from the direct to the indirect energy-gap regime at the crossover composition [53,95,96]. Nonmonotonic composition dependencies have also been observed in experimental band-offset data on quaternary group-III phosphides as lattice-matched GaAs/(Al$_x$Ga$_{1-x}$)$_{0.51}$In$_{0.49}$P heterostructures [53]. In general, similar composition-dependence trends of physical properties can be expected as a common fundamental characteristic of cubic semiconductor alloys, which admix nondirect electronic features of at least one of the alloying binary semiconductors.

2. *zb-Al$_x$Ga$_{1-x}$N/AlN*

The natural band alignment of the *zb*-Al$_x$Ga$_{1-x}$N/AlN material system is visualized in Fig. 2(b). Due to the commutativity and transitivity of the branch-point aligned band offset, the natural offsets in *zb*-Al$_x$Ga$_{1-x}$N/AlN qualitatively show the same basic trends just shifted on the energy scale due to alignment with *zb*-AlN and partially changed by the used sign convention (cf. Table III). In contrast to *zb*-GaN/Al$_x$Ga$_{1-x}$N, the fundamental conduction band offset between *zb*-Al$_x$Ga$_{1-x}$N and *zb*-AlN is completely determined by indirect offset features, namely direct-indirect ($\Gamma_c \rightarrow X_c$)-type and indirect-indirect ($X_c \rightarrow X_c$)-type alignment.

In detail, the valence band offset between direct gap *zb*-Al$_x$Ga$_{1-x}$N and indirect gap *zb*-AlN is found to decrease, according to an amount almost linear ($b_{dir} = -0.16$ eV) from -1.03 to -0.42 eV. Passing the direct-indirect crossover point, the valence band offset continues to decrease further to zero with an enhanced upward bowing of $b_{ind} = -1.34$ eV. The fundamental branch of the direct-indirect energy offset between Γ_c and X_c conduction-edge states decreases from 0.81 to -0.24 eV with a characteristic upward bowing of $b_{dir} = -0.28$ eV. At higher x the upward bowing increases substantially to $b_{ind} = -2.16$ eV and the offset reaches a value of -1.04 eV for $x = 1.0$ representing the difference between the direct and indirect DFT-HSEmod band gaps of *zb*-AlN. The indirect-indirect ($X_c \rightarrow X_c$)-type conduction band offset decreases, according to an amount, from -0.61 to -0.26 eV with almost negligible downward bowing of $b_{dir} = 0.06$ eV. The fundamental branch above x_c decreases to zero with an intermediate upward bowing of $b_{dir} = -1.22$ eV. In addition to the direct-indirect crossover, the natural conduction band offset exhibits a change from type-I-to-type-II alignment at an almost

TABLE IV. *zb*-Al$_x$Ga$_{1-x}$N/Al$_y$Ga$_{1-y}$N valence and conduction band-offset parameters obtained from fitting a two-dimensional fifth order polynomial of the form $z = z_0 + A_1 x + A_2 x^2 + A_3 x^3 + A_4 x^4 + A_5 x^5 + B_1 y + B_2 y^2 + B_3 y^3 + B_4 y^4 + B_5 y^5$. The fitted graphs are visualized in Figs. 3 and 4.

			Band-offset fitting parameters (eV)									
Offset	Type	Composition	z_0	A_1	A_2	A_3	A_4	A_5	B_1	B_2	B_3	B_4	B_5
ΔE_v^{bp}	$(\Gamma_v - \Gamma_v)$	$x < y$	0.00	0.71	3.88	− 13.95	18.68	− 8.29	− 0.71	− 3.88	13.95	− 18.68	8.29
		$x > y$	0.00	− 0.71	− 3.88	13.95	− 18.68	8.29	0.71	3.88	− 13.95	18.68	− 8.29
ΔE_c^{bp}	$(\Gamma_c - \Gamma_c)$	$x < y$	0.00	− 1.45	− 0.28	− 1.36	3.39	− 2.15	1.45	0.28	1.36	− 3.39	2.15
		$x > y$	0.00	1.45	0.28	1.36	− 3.39	2.15	− 1.45	− 0.28	− 1.36	3.39	− 2.15
	$(\Gamma_c - X_c)$	$x < y$	1.41	− 1.45	− 0.28	− 1.36	3.39	− 2.15	− 0.68	0.65	− 0.20	− 1.87	1.49
		$x > y$	1.41	− 0.68	0.65	− 0.20	− 1.87	1.49	− 1.45	− 0.28	− 1.36	3.39	− 2.15
	$(X_c - \Gamma_c)$	$x < y$	1.41	− 0.68	0.65	− 0.20	− 1.87	1.49	− 1.45	− 0.28	− 1.36	3.39	− 2.15
		$x > y$	1.41	− 1.45	− 0.28	− 1.36	3.39	− 2.15	− 0.68	0.65	− 0.20	− 1.87	1.49
	$(X_c - X_c)$	$x < y$	0.00	0.68	− 0.65	0.20	1.87	− 1.49	− 0.68	0.65	− 0.20	− 1.87	1.49
		$x > y$	0.00	− 0.68	0.65	− 0.20	− 1.87	1.49	0.68	− 0.65	0.20	1.87	− 1.49

equipartitionally occupied cation sublattice as indicated by the conduction band-offset sign change in Fig. 2(b). Starting from a composition parameter of $x = 0.49$, well below the direct-indirect crossover transition, the *zb*-$Al_xGa_{1-x}N$/AlN system retains its type-II character throughout the entire Al-rich composition range. The most pronounced type-II alignment occurs at the direct-indirect transition, where the fundamental conduction band offset exhibits its extremal reversal point. In contrast to the direct-indirect crossover, the type-I-to-type-II transition represents a pure alignment feature rather than an electronic structure feature. Therefore, the alignment-type transition, occurring in both the direct and indirect alloy-gap regimes, shows no influence on the slope of the natural band offset.

Our data are in reasonable agreement with numerical data on the *zb*-$Al_{0.5}Ga_{0.5}N$/AlN (001) heterojunction reported by Buongiorno Nardelli *et al.* [64]. Utilizing plane-wave DFT at the local density approximation level, the virtual crystal approximation to model the ternary alloy, and electrostatic-potential alignment, Buongiorno Nardelli *et al.* reported a staggered type-II band alignment with strained (average in-plane lattice constant) valence and conduction band offsets of -0.39 and -0.17 eV, respectively. In addition, valence and conduction band offsets of -0.37 and -0.09 eV were reported for a fully relaxed *zb*-AlN_1GaN_1/AlN (001) superlattice. These values compare well with the corresponding natural valence and conduction band offsets of -0.53 and -0.01 eV, obtained within the present study.

The conduction-to-valence band ratio of the fundamental *zb*-GaN/$Al_xGa_{1-x}N$ band offsets increases with a large downward bowing ($b_{\mathrm{dir}} = 3.35$ eV) from the 44:56 ratio in *zb*-GaN/AlN towards a 37:63 ratio at the direct-indirect transition point. A 40:60 ratio is passed at a composition parameter of $x = 0.14$. The offset ratio approximately reaches a plateau in the indirect Al-rich composition range, where the offset ratio decreases only slightly to 31:69 in the limit of dilute Ga concentration. Hence, aligning conduction-edge states of different fundamental symmetry type, Γ_c and X_c-type, respectively, causes a substantial nonlinearity in the conduction-to-valence band-offset ratio, while the ratio shows only small and almost linear variation in case of conduction band offsets calculated from Γ_c-type or X_c-type states only.

In summary, the cubic symmetry, and the associated indirect nature of the fundamental *zb*-AlN band gap, introduce the possibility of forming staggered gap type-II heterojunctions in Al-rich *zb*-$Al_xGa_{1-x}N$/AlN or, in other words, control the heterostructure type by alloying. Such type-II alignment as well as composition dependent type-I-to-type-II transitions in multicomponent semiconductor alloys have been observed in other group-III-V semiconductor materials. Especially indium containing nitride/arsenide and antimonide/arsenide quantum well or quantum dot heterostructures show promising material characteristics, in this respect [97–104]. Very recently, Reddy *et al.* [105] conducted a x-ray photoelectron-spectroscopy study on the band alignment between silicon nitride (Si_3N_4) and *wz*-$Al_xGa_{1-x}N$. Despite the large (indirect) Si_3N_4 band gap of 5.3 eV [106], which is comparable to the indirect band gap of cubic *zb*-AlN, the relative positions of the valence and conduction-edge bands of Si_3N_4 cause all Si_3N_4/$Al_xGa_{1-x}N$(0001) interfaces to form a staggered type-II alignment, independent of the nitride-alloy composition. Type-II band alignment for technological application has also been studied in various other semiconducting material classes. Due to the recently rising interest in two-dimensional materials, various experimental and theoretical studies on the electronic structure features of single- and few-layer transition metal dichalcogenides have demonstrated the basic potential for type-II aligned lateral heterostructures [107]. In addition, transition metal dichalcogenides also show bulk-to-thin-film indirect-direct transitions [108–110]. Type-II alignment between binary materials and composition dependent type-I-to-type-II transitions have been reported for selenide and sulfide based core/shell quantum-dot heterojunctions [111–115]. Type-I-to-type-II transitions have also been observed in magnetic semiconductor-quantum wells and superlattices based on different selenide and telluride alloys as a response to external magnetic fields [116–118]. In all these materials type-II alignment is provided by a delicate combination of binary, ternary, and also quaternary semiconductor alloys. Hence, precise *tailoring* of heterostructures nanomaterials for technological application substantially benefits from profound reference data on the composition dependence of band discontinuities. In that spirit, we proceed in our study with the analysis of band alignments within the complete two-dimensional composition range of nonpolar *zb*-$Al_xGa_{1-x}N/Al_yGa_{1-y}N$ bulk nitrides.

3. *zb*-$Al_xGa_{1-x}N/Al_yGa_{1-y}N$

In contrast to strained band offsets, where one material is strained to the other at a time, the absolute values of natural band offsets do not show a symmetry breaking *forward-backward asymmetry* upon interchange of the composition parameters x and y, in general. Following the sign convention, according to agreement above, the natural band-offset data on *zb*-$Al_xGa_{1-x}N/Al_yGa_{1-y}N$ inevitably exhibit the characteristic mirror symmetry (cf. Figs. 3 and 4) with respect to the equal-composition diagonal ($x \equiv y$).

The roughly linear composition dependence of the natural valence band offsets, which originate from the alignment of Brillouin-zone center localized Γ_v-type alloy states at the top of the valence band, extends straightforward throughout the entire two-dimensional composition range of nonpolar *zb*-$Al_xGa_{1-x}N/Al_yGa_{1-y}N$ composites.

Due to the mixing of direct and indirect-type alloy states, the fundamental conduction band offset changes discontinuously at the direct-indirect transition lines [see dashed lines in Fig. 3(e)]. The composition dependencies of the four possible alignment types of Γ_c-type and X_c-type conduction-edge states are illustrated in Fig. 4. The fundamental conduction band offset of nonpolar *zb*-$Al_xGa_{1-x}N/Al_yGa_{1-y}N$ alloys represents a combination of these different alignment types. Four distinct composition ranges, each showing a characteristic alignment type, are predefined by the critical direct-indirect crossover concentrations of the two *zb*-$Al_xGa_{1-x}N$ alloys [cf. Fig. 3(e)]. In detail, distinct conduction-band alignment features can be observed in the pure direct regime (dir-dir) for $(0 \leqslant x \leqslant 0.63) \wedge (0 \leqslant y \leqslant 0.63)$, two mixed direct-indirect composition regimes (dir-ind) for $(0 \leqslant x \leqslant 0.63) \wedge (0.63 \leqslant y \leqslant 1)$

and $(0.63 \leqslant x \leqslant 1) \wedge (0 \leqslant y \leqslant 0.63)$, and the pure indirect regime (ind-ind) for $(0.63 \leqslant x \leqslant 1) \wedge (0.63 \leqslant y \leqslant 1)$.

Due to the restriction to Brillouin-zone center-type electronic states, the fundamental conduction band offset changes roughly linearly with (x, y) composition in the predominantly Ga-rich direct alloy regime. The related conduction-to-valence band-offset quotient $\Delta E_c^{bp}/\Delta E_v^{bp}$, the $|\Delta E_c^{bp}| : |\Delta E_v^{bp}|$ ratio, respectively, show only moderate changes in this regime [cf. Fig. 3(e)]. Nonpolar *zb*-$Al_xGa_{1-x}N/Al_yGa_{1-y}N$ alloys exhibit a similar band-offset ratio close to 65:35 in a wide composition range around the equimolar/equimolar composite *zb*-$Al_{0.5}Ga_{0.5}N/Al_{0.5}Ga_{0.5}N$. The ratio is slightly modified to roughly 60:40 at low Al content $[(x \lesssim 0.25) \wedge (y \lesssim 0.25)]$ heterojunctions. These band-offset ratios show strong resemblance to the experimentally determined band-offset ratios between polar *wz*-$Al_xGa_{1-x}N$ nitride alloys reported by Reddy *et al.* [57]. The overall comparable composition dependencies of conduction band offsets in the cubic and hexagonal $Al_xGa_{1-x}N/Al_yGa_{1-y}N$ material systems highlight the common nature of direct-gap states in polar as well as nonpolar tetrahedrally coordinated III-V semiconductors, in general.

The natural band-offset ratio shows substantial variations in the transition regions around the direct-indirect crossover lines. This strong variation in the ratio of natural band offsets suggests that a precise control of the band-offset profile will be more delicate close to the direct-indirect crossover composition. Clearly, composition fluctuations and small band-offset variations due to interfacial strain might be most crucial for device design in this composition range. The conduction-to-valence band ratio flattens out in the vicinity of the binary/binary heterojunctions and reaches a ratio of roughly 45:55 in *zb*-GaN/AlN.

The conduction-to-valence band ratio reaches a plateau of roughly 35:65 in the pure indirect regime, that is to say the ratio will virtually be inverted with respect to the direct-direct composition range. Due to the the weak nonlinear nature of the valence band offsets, the band-offset ratio clearly reflects the existing types of conduction band offsets in the *zb*-$Al_xGa_{1-x}N/Al_yGa_{1-y}N$ system, overall.

The type-II alignment range includes the entire indirect-indirect composition regime, but also extends towards the mixed direct-indirect regime with the equimolar-ternary/binary system *zb*-$Al_{0.5}Ga_{0.5}N$/AlN roughly marking the lowest Al content, hence smallest energy gap, type-II alignment limit. The most pronounced type-II alignment character is formed between *zb*-Al and the ternary alloys close to the crossover composition. I detail the valence and conduction band offsets between *zb*-$Al_{x_c}Ga_{1-x_c}N$ with $x_c = 0.63$ and *zb*-AlN amount to -0.41 and -0.24 eV, respectively.

IV. SUMMARY AND CONCLUSION

We have used exact-exchange adjusted hybrid functional based DFT and the branch-point alignment technique to analyze the natural band alignment at unstrained heterojunctions of nonpolar ternary $Al_xGa_{1-x}N$ alloys. The alignment of bulklike direct $\Gamma_v \rightarrow \Gamma_c$ and indirect, *pseudodirect*, respectively, $\Gamma_v \rightarrow X_c$ type energy states in *zb*-$Al_xGa_{1-x}N$ show a rather complex composition dependence of fundamental band discontinuities in the *zb*-$Al_xGa_{1-x}N/Al_yGa_{1-y}N$ material system, which is characterized by the direct-indirect band-gap crossing of *zb*-$Al_xGa_{1-x}N$ alloys and a type-I-to-type-II band-alignment type transition. The *zb*-$GaN/Al_xGa_{1-x}N$ band edges consistently show a type-I alignment. In addition, the presence of a direct-indirect band-gap transition in the investigated cubic *zb*-$Al_xGa_{1-x}N$ semiconductor alloys gives rise to a notable composition dependence of band discontinuities with weak nonlinear character in the predominantly Ga-rich direct-alloy regime below the critical direct-indirect Al/Ga-crossover concentration $x_c = 0.63$ but substantial bowing characteristics in the Al-rich alloy regime. The relative position of fundamental band edges changes to a staggered type-II alignment in the Al-rich composition ranges of *zb*-$Al_xGa_{1-x}N$/AlN and the *zb*-$Al_xGa_{1-x}N/Al_yGa_{1-y}N$ system, in general.

Our results indicate that semiconductor alloys with mixed direct-indirect band-gap characteristics, systems obeying a direct-indirect band-gap crossing, respectively, possess nontrivial fundamental band-alignment features that not only deviate from the trivial linear dependencies expressed in Vegard's law but also exhibit quite sharp derivative discontinuities that prevent straightforward fitting of composition dependencies to monotonic power laws. Likewise, there is no straightforward justification for the assumption of composition independent band-offset ratios in the band discontinuities between group-III nitrides or comparable semiconductor systems. Therefore, we emphasize the general need for detailed numerical studies on the composition dependence of multicomponent composite semiconductors using state-of-the-art first-principles approaches as a sound basis for interpretation of experimental data as well as reliable input to highly parametrized calculation approaches on the basis of more phenomenological model theories.

Despite being fundamentally unaffected by the strain conditions of a real heterostructure, the efficient calculation of natural band offsets via branch-point alignment allows the systematic study of composition dependent band-alignment trends, which are of vital interest for the design of opto-electronic devices. The natural band offsets itself can further be utilized alongside volume deformation potentials as input to effective mass theory based simulation approaches (e.g., see Refs. [29,119]) allowing effective modeling of nanometer sized semiconductor heterostructures. Albeit providing a sound data basis, remaining uncertainties, as possible accuracy limits due to the utilized branch-point alignment (see Ref. [49]) or limited availability of volume deformation potentials across the entire composition range, still leave room for future verification and refinement of the identified trends by *ab initio* studies on strained band offsets at the interfaces between cubic group-III nitride materials.

The promotion of charge separation via spatially separated localization of electrons and holes is, in general, a committed heterostructure-alignment feature in the design of photovoltaic devices in order to prevent charge-carrier recombination. Even though the band gap of Al-rich *zb*-$Al_xGa_{1-x}N$ semiconductor alloys exceeds the size desirable for utilization in visible light-emission applications and energy harvesting devices, a

limitation that can be overcome by alloying *zb*-$Al_xGa_{1-x}N$ with InN, the large accessible range of band gaps and band offset promotes fabrication of intersubband devices working in the technology eminent THz wavelength regime. Especially, the spatial separation of electron and hole wave functions within the type-II aligned heterostructures, a property rarely observed in the group-III nitride material system, allows individual tuning of charge carrier confinement potentials through variations of the layer widths.

ACKNOWLEDGMENTS

The numerical calculations were done using grants of computer time from the Regionales Rechenzentrum of the Universität zu Köln (RRZK), the Paderborn Center for Parallel Computing (PC^2), and the Höchstleistungs-Rechenzentrum Stuttgart (HLRS). The Deutsche Forschungsgemeinschaft (DFG) is acknowledged for financial support (Grants No. TRR142 and No. GRK1464).

[1] S. Nakamura, S. Pearton, and G. Fasol, *The Blue Laser Diode: The Complete Story* (Springer, Berlin, 2000).
[2] M. R. Krames, O. B. Shchekin, R. Mueller-Mach, G. O. Mueller, L. Zhou, G. Harbers, and M. G. Craford, J. Disp. Technol. **3**, 160 (2007).
[3] Y.-F. Wu, B. P. Keller, S. Keller, D. Kapolnek, P. Kozodoy, S. P. Denbaars, and U. K. Mishra, Appl. Phys. Lett. **69**, 1438 (1996).
[4] G. Steinhoff, M. Hermann, W. J. Schaff, L. F. Eastman, M. Stutzmann, and M. Eickhoff, Appl. Phys. Lett. **83**, 177 (2003).
[5] U. K. Mishra, L. Shen, T. E. Kazior, and Y. F. Wu, Proc. IEEE **96**, 287 (2008).
[6] D. Bouguenna, A. B. Stambouli, N. M. Maaza, A. Zado, and D. As, Superlattices Microstruct. **62**, 260 (2013).
[7] I. M. Huygens, K. Strubbe, and W. P. Gomes, J. Electrochem. Soc. **147**, 1797 (2000).
[8] H. S. Jung, Y. J. Hong, Y. Li, J. Cho, Y.-J. Kim, and G.-C. Yi, ACS Nano **2**, 637 (2008).
[9] J. Schalwig, G. Müller, U. Karrer, M. Eickhoff, O. Ambacher, M. Stutzmann, L. Görgens, and G. Dollinger, Appl. Phys. Lett. **80**, 1222 (2002).
[10] B. S. Kang, F. Ren, B. P. Gila, C. R. Abernathy, and S. J. Pearton, Appl. Phys. Lett. **84**, 1123 (2004).
[11] Y. Xie, Y. Qian, S. Zhang, W. Wang, X. Liu, and Y. Zhang, Appl. Phys. Lett. **69**, 334 (1996).
[12] S. Limpijumnong and W. R. L. Lambrecht, Phys. Rev. Lett. **86**, 91 (2001).
[13] M. P. Halsall, P. Harmer, P. J. Parbrook, and S. J. Henley, Phys. Rev. B **69**, 235207 (2004).
[14] X. Rong, X. Wang, S. V. Ivanov, X. Jiang, G. Chen, P. Wang, W. Wang, C. He, T. Wang, T. Schulz *et al.*, Adv. Mater. **28**, 7978 (2016).
[15] Z. Al Balushi, Y. K. Wang, R. K. Ghosh, R. A. Vilá, S. M. Eichfeld, J. D. Caldwell, X. Qin, Y.-C. Lin, P. A. DeSario, G. Stone *et al.*, Nat. Mater. **15**, 1166 (2016).
[16] G. Cassabois, P. Valvin, and B. Gil, Nat. Photon. **10**, 262 (2016).
[17] K. P. Korona, A. Wysmolek, K. Pakula, R. Stepniewski, J. M. Baranowski, I. Grzegory, B. Lucznik, M. Wróblewski, and S. Porowski, Appl. Phys. Lett. **69**, 788 (1996).
[18] E. Oh, S. K. Lee, S. S. Park, K. Y. Lee, I. J. Song, and J. Y. Han, Appl. Phys. Lett. **78**, 273 (2001).
[19] Q. Guo and A. Yoshida, Jpn. J. Appl. Phys. **33**, 2453 (1994).
[20] J. Li, K. B. Nam, M. L. Nakarmi, J. Y. Lin, H. X. Jiang, P. Carrier, and S.-H. Wei, Appl. Phys. Lett. **83**, 5163 (2003).
[21] E. Silveira, J. A. Freitas, M. Kneissl, D. W. Treat, N. M. Johnson, G. A. Slack, and L. J. Schowalter, Appl. Phys. Lett. **84**, 3501 (2004).
[22] M. Feneberg, M. Röppischer, C. Cobet, N. Esser, J. Schörmann, T. Schupp, D. J. As, F. Hörich, J. Bläsing, A. Krost *et al.*, Phys. Rev. B **85**, 155207 (2012).
[23] M. P. Thompson, G. W. Auner, T. S. Zheleva, K. A. Jones, S. J. Simko, and J. N. Hilfiker, J. Appl. Phys. **89**, 3331 (2001).
[24] M. Röppischer, R. Goldhahn, G. Rossbach, P. Schley, C. Cobet, N. Esser, T. Schupp, K. Lischka, and D. J. As, J. Appl. Phys. **106**, 076104 (2009).
[25] M. Feneberg, M. F. Romero, M. Röppischer, C. Cobet, N. Esser, B. Neuschl, K. Thonke, M. Bickermann, and R. Goldhahn, Phys. Rev. B **87**, 235209 (2013).
[26] M. Beeler, E. Trichas, and E. Monroy, Semicond. Sci. Technol. **28**, 074022 (2013).
[27] D. J. As and C. Mietze, Physica Status Solidi (a) **210**, 474 (2013).
[28] M. Beeler, C. Bougerol, E. Bellet-Amalaric, and E. Monroy, Physica Status Solidi (a) **211**, 761 (2014).
[29] T. Wecker, G. Callsen, A. Hoffmann, D. Reuter, and D. J. As, Jpn. J. Appl. Phys. **55**, 05FG01 (2016).
[30] J. Ihm and M. L. Cohen, Phys. Rev. B **21**, 3754 (1980).
[31] E. A. Kraut, R. W. Grant, J. R. Waldrop, and S. P. Kowalczyk, Phys. Rev. Lett. **44**, 1620 (1980).
[32] E. A. Kraut, R. W. Grant, J. R. Waldrop, and S. P. Kowalczyk, Phys. Rev. B **28**, 1965 (1983).
[33] E. T. Yu, E. T. Croke, D. H. Chow, D. A. Collins, M. C. Phillips, T. C. McGill, J. O. McCaldin, and R. H. Miles, J. Vac. Sci. Technol. B **8**, 908 (1990).
[34] C. Mitra, B. Lange, C. Freysoldt, and J. Neugebauer, Phys. Rev. B **84**, 193304 (2011).
[35] J. P. Bosco, D. O. Scanlon, G. W. Watson, N. S. Lewis, and H. A. Atwater, J. Appl. Phys. **113**, 203705 (2013).
[36] C. G. Van de Walle and R. M. Martin, J. Vac. Sci. Technol. B **4**, 1055 (1986).
[37] C. G. Van de Walle and R. M. Martin, Phys. Rev. B **35**, 8154 (1987).
[38] A. Baldereschi, S. Baroni, and R. Resta, Phys. Rev. Lett. **61**, 734 (1988).
[39] C. Tejedor and F. Flores, J. Phys. C **11**, L19 (1978).
[40] J. Tersoff, Phys. Rev. B **30**, 4874 (1984).
[41] J. Tersoff, Phys. Rev. Lett. **52**, 465 (1984).
[42] A. Schleife, F. Fuchs, C. Rödl, J. Furthmüller, and F. Bechstedt, Appl. Phys. Lett. **94**, 012104 (2009).
[43] W. Mönch, J. Appl. Phys. **109**, 113724 (2011).
[44] D. Mourad, J. Appl. Phys. **113**, 123705 (2013).
[45] J. Bardeen and W. Shockley, Phys. Rev. **80**, 72 (1950).
[46] S. Adachi, J. Appl. Phys. **58**, R1 (1985).
[47] C. G. Van de Walle, Phys. Rev. B **39**, 1871 (1989).
[48] R. Resta, Phys. Rev. B **44**, 11035 (1991).

[49] M. Landmann, E. Rauls, and W. G. Schmidt (to be published).
[50] S.-H. Park and S.-L. Chuang, J. Appl. Phys. **87**, 353 (2000).
[51] M. Landmann, E. Rauls, W. G. Schmidt, M. Röppischer, C. Cobet, N. Esser, T. Schupp, D. J. As, M. Feneberg, and R. Goldhahn, Phys. Rev. B **87**, 195210 (2013).
[52] I. Vurgaftman, J. R. Meyer, and L. R. Ram-Mohan, J. Appl. Phys. **89**, 5815 (2001).
[53] W. Yi, V. Narayanamurti, H. Lu, M. A. Scarpulla, A. C. Gossard, Y. Huang, J.-H. Ryou, and R. D. Dupuis, Appl. Phys. Lett. **95**, 112102 (2009).
[54] J. W. Nicklas and J. W. Wilkins, Appl. Phys. Lett. **97**, 091902 (2010).
[55] D. A. Beaton, K. Alberi, B. Fluegel, A. Mascarenhas, and J. L. Reno, Appl. Phys. Express **6**, 071201 (2013).
[56] D. R. Hang, C. H. Chen, Y. F. Chen, H. X. Jiang, and J. Y. Lin, J. Appl. Phys. **90**, 1887 (2001).
[57] P. Reddy, I. Bryan, Z. Bryan, J. Tweedie, S. Washiyama, R. Kirste, S. Mita, R. Collazo, and Z. Sitar, Appl. Phys. Lett. **107**, 091603 (2015).
[58] W. Xiao-Jia, W. Xiao-Liang, X. Hong-Ling, W. Cui-Mei, F. Chun, D. Qing-Wen, Q. Shen-Qi, Z. Jing-Wen, H. Xun, C. Shu-Jun *et al.*, Chin. Phys. Lett. **30**, 057101 (2013).
[59] V. I. Litvinov, A. Manasson, and D. Pavlidis, Appl. Phys. Lett. **85**, 600 (2004).
[60] A. Bhouri and J.-L. Lazzari, Mater. Sci. Semicond. Process. **41**, 121 (2016).
[61] S. V. Dudiy and A. Zunger, Appl. Phys. Lett. **84**, 1874 (2004).
[62] A. Belabbes, L. C. de Carvalho, A. Schleife, and F. Bechstedt, Phys. Rev. B **84**, 125108 (2011).
[63] Q. Y. Wei, T. Li, J. Y. Huang, F. A. Ponce, E. Tschumak, A. Zado, and D. J. As, Appl. Phys. Lett. **100**, 142108 (2012).
[64] M. Buongiorno Nardelli, K. Rapcewicz, and J. Bernholc, Phys. Rev. B **55**, R7323 (1997).
[65] B. Daudin, G. Feuillet, J. Hübner, Y. Samson, F. Widmann, A. Philippe, C. Bru-Chevallier, G. Guillot, E. Bustarret, G. Bentoumi *et al.*, J. Appl. Phys. **84**, 2295 (1998).
[66] T. Koizumi, H. Okumura, K. Balakrishnan, H. Harima, T. Inoue, Y. Ishida, T. Nagatomo, S. Nakashima, and S. Yoshida, J. Cryst. Growth **201-202**, 341 (1999).
[67] J. Schörmann, S. Potthast, D. J. As, and K. Lischka, Appl. Phys. Lett. **90**, 041918 (2007).
[68] T. Schupp, K. Lischka, and D. As, J. Cryst. Growth **312**, 1500 (2010).
[69] S. Novikov, C. Staddon, F. Luckert, P. Edwards, R. Martin, A. Kent, and C. Foxon, J. Cryst. Growth **350**, 80 (2012).
[70] J. P. Perdew, K. Burke, and M. Ernzerhof, Phys. Rev. Lett. **77**, 3865 (1996).
[71] J. Heyd, G. E. Scuseria, and M. Ernzerhof, J. Chem. Phys. **118**, 8207 (2003).
[72] J. Heyd and G. E. Scuseria, J. Chem. Phys. **121**, 1187 (2004).
[73] J. Heyd, J. E. Peralta, G. E. Scuseria, and R. L. Martin, J. Chem. Phys. **123**, 174101 (2005).
[74] J. Heyd, G. E. Scuseria, and M. Ernzerhof, J. Chem. Phys. **124**, 219906 (2006).
[75] C. S. Wang and W. E. Pickett, Phys. Rev. Lett. **51**, 597 (1983).
[76] L. J. Sham and M. Schlüter, Phys. Rev. Lett. **51**, 1888 (1983).
[77] M. S. Hybertsen and S. G. Louie, Phys. Rev. Lett. **55**, 1418 (1985).
[78] L. J. Sham and M. Schlüter, Phys. Rev. B **32**, 3883 (1985).
[79] F. Bechstedt, *Festkörperprobleme/Advances in Solid State Physics* (Vieweg, Braunschweig/Wiesbaden, 1992), Vol. 32, p. 161.
[80] The EXX fractions have been slightly modified compared to the 32% and 39% fractions for *zb*-GaN and *zb*-AlN in Ref. [51] to account for minor changes in the experimental lattice parameters and to provide a better balance between the description of the direct and indirect band gap of *zb*-AlN.
[81] A. Wadehra, J. W. Nicklas, and J. W. Wilkins, Appl. Phys. Lett. **97**, 092119 (2010).
[82] G. Kresse and J. Furthmüller, Comput. Mater. Sci. **6**, 15 (1996).
[83] G. Kresse and D. Joubert, Phys. Rev. B **59**, 1758 (1999).
[84] P. E. Blöchl, Phys. Rev. B **50**, 17953 (1994).
[85] T. Schupp (unpublished).
[86] Y. Koide, H. Itoh, N. Sawaki, I. Akasaki, and M. Hashimoto, J. Electrochem. Soc. **133**, 1956 (1986).
[87] L. K. Teles, J. Furthmüller, L. M. R. Scolfaro, J. R. Leite, and F. Bechstedt, Phys. Rev. B **62**, 2475 (2000).
[88] M. B. Kanoun, S. Goumri-Said, A. E. Merad, and H. Mariette, J. Appl. Phys. **98**, 063710 (2005).
[89] B.-T. Liou, Appl. Phys. A **86**, 539 (2007).
[90] B. Höffling, A. Schleife, C. Rödl, and F. Bechstedt, Phys. Rev. B **85**, 035305 (2012).
[91] Y. Hinuma, A. Grüneis, G. Kresse, and F. Oba, Phys. Rev. B **90**, 155405 (2014).
[92] Also see Ref. [49] for additional details on the evaluation of branch-point energies in group-III nitride semiconductors.
[93] G. Oelgart, R. Schwabe, M. Heider, and B. Jacobs, Semicond. Sci. Technol. **2**, 468 (1987).
[94] L. Pavesi and M. Guzzi, J. Appl. Phys. **75**, 4779 (1994).
[95] W. Wang, Solid-State Electron. **29**, 133 (1986).
[96] D. Vignaud and F. Mollot, J. Appl. Phys. **93**, 384 (2003).
[97] A. J. Williamson, A. Franceschetti, H. Fu, L. W. Wang, and A. Zunger, J. Electron. Mater. **28**, 414 (1999).
[98] S. R. Johnson, P. Dowd, W. Braun, U. Koelle, C. M. Ryu, M. Beaudoin, C.-Z. Guo, and Y.-H. Zhang, J. Vac. Sci. Technol. B **18**, 1545 (2000).
[99] Y. Chen, G. H. Li, Z. M. Zhu, H. X. Han, Z. P. Wang, W. Zhou, and Z. G. Wang, Appl. Phys. Lett. **76**, 3188 (2000).
[100] G. Li, Y. Chen, Z. Fung, K. Ding, H. Han, W. Zhou, and Z. Wang, Physica Status Solidi (b) **223**, 157 (2001).
[101] T. T. Chen, C. L. Cheng, Y. F. Chen, F. Y. Chang, H. H. Lin, C.-T. Wu, and C.-H. Chen, Phys. Rev. B **75**, 033310 (2007).
[102] R. A. Arif, H. Zhao, and N. Tansu, Appl. Phys. Lett. **92**, 011104 (2008).
[103] J. Wang, F. Xu, X. Zhang, W. An, X.-Z. Li, J. Song, W. Ge, G. Tian, J. Lu, X. Wang *et al.*, Sci. Rep. **4**, 6221 (2014).
[104] R. Neffati, I. Saïdi, S. B. Radhia, K. Boujdaria, and C. Testelin, Semicond. Sci. Technol. **30**, 085008 (2015).
[105] P. Reddy, S. Washiyama, F. Kaess, M. H. Breckenridge, L. H. Hernandez-Balderrama, B. B. Haidet, D. Alden, A. Franke, B. Sarkar, E. Kohn *et al.*, J. Appl. Phys. **119**, 145702 (2016).
[106] T. E. C. Jr., C. C. Fulton, W. J. Mecouch, R. F. Davis, G. Lucovsky, and R. J. Nemanich, J. Appl. Phys. **94**, 3949 (2003).
[107] J. Kang, S. Tongay, J. Zhou, J. Li, and J. Wu, Appl. Phys. Lett. **102**, 012111 (2013).
[108] S. Tongay, J. Zhou, C. Ataca, K. Lo, T. S. Matthews, J. Li, J. C. Grossman, and J. Wu, Nano Lett. **12**, 5576 (2012).

[109] I. G. Lezama, A. Arora, A. Ubaldini, C. Barreteau, E. Giannini, M. Potemski, and A. F. Morpurgo, Nano Lett. **15**, 2336 (2015).
[110] Y. Zhang, T.-R. Chang, B. Zhou, Y.-T. Cui, H. Yan, Z. Liu, F. Schmitt, J. Lee, R. Moore, Y. Chen *et al.*, Nat. Nanotechnol. **9**, 111 (2014).
[111] A. Nemchinov, M. Kirsanova, N. N. Hewa-Kasakarage, and M. Zamkov, J. Phys. Chem. C **112**, 9301 (2008).
[112] G. Jia, Y. Wang, L. Gong, and J. Yao, Digest J. Nanomater. Biostruct. **6**, 43 (2011).
[113] C. M. Tyrakowski, A. Shamirian, C. E. Rowland, H. Shen, A. Das, R. D. Schaller, and P. T. Snee, Chem. Mater. **27**, 7276 (2015).
[114] N. Razgoniaeva, P. Moroz, S. Lambright, and M. Zamkov, J. Phys. Chem. Lett. **6**, 4352 (2015).
[115] A. Dalui, A. Chakraborty, U. Thupakula, A. H. Khan, S. Sengupta, B. Satpati, D. D. Sarma, I. Dasgupta, and S. Acharya, J. Phys. Chem. C **120**, 10118 (2016).
[116] N. Dai, H. Luo, F. C. Zhang, N. Samarth, M. Dobrowolska, and J. K. Furdyna, Phys. Rev. Lett. **67**, 3824 (1991).
[117] A. Ribayrol, D. Coquillat, A. Kavokin, J. Lascaray, H. Zhou, C. S. Torres, and D. A. B. Lunn, J. Phys. IV **03**, 409 (1993).
[118] B. König, U. Zehnder, D. R. Yakovlev, W. Ossau, T. Gerhard, M. Keim, A. Waag, and G. Landwehr, Phys. Rev. B **60**, 2653 (1999).
[119] C. Mietze, M. Landmann, E. Rauls, H. Machhadani, S. Sakr, M. Tchernycheva, F. H. Julien, W. G. Schmidt, K. Lischka, and D. J. As, Phys. Rev. B **83**, 195301 (2011).

Paper VIII

Identification of the Nitrogen Split Interstitial $(N–N)_N$ in GaN

J. von Bardeleben, J. L. Cantin, U. Gerstmann, A. Scholle, S. Greulich-Weber, E. Rauls, M. Landmann, W. G. Schmidt, A. Gentils, J. Botsoa, and M. F. Barthe,

PHYSICAL REVIEW LETTERS **109**, 206402, 5 pp. (2012)

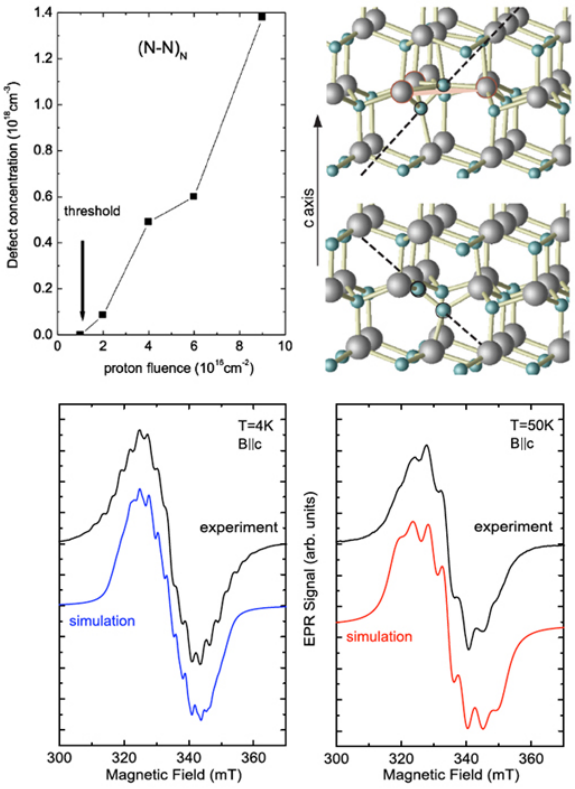

Identification of the Nitrogen Split Interstitial $(N\text{-}N)_N$ in GaN

H. J. von Bardeleben,[1,*] J. L. Cantin,[1] U. Gerstmann,[2] A. Scholle,[2] S. Greulich-Weber,[2] E. Rauls,[2] M. Landmann,[2] W. G. Schmidt,[2] A. Gentils,[3,4] J. Botsoa,[4] and M. F. Barthe[4]

[1]*INSP, Université Pierre et Marie Curie, UMR 7588 au CNRS 4 place Jussieu, 75005 Paris, France*
[2]*Department Physik, Universität Paderborn, Warburger Strasse 100, 33098 Paderborn, Germany*
[3]*CSNSM, Université Paris-Sud and CNRS-IN2P3, 91405 Orsay Campus, France*
[4]*CNRS/CEMHTI, CNRS UPR 3079/CEMHTI, 1D avenue de la Recherche Scientifique, 45071 Orléans, France*

(Received 21 August 2012; published 16 November 2012)

Combining electron paramagnetic resonance, density functional theory, and positron annihilation spectroscopy (PAS), we identify the nitrogen interstitial defect in GaN. The isolated interstitial is unstable and transforms into a split interstitial configuration $(N\text{-}N)_N$. It is generated by particle irradiation with an introduction rate of a primary defect, pins the Fermi level at $E_C - 1.0$ eV for high fluences, and anneals out at 400 °C. The associated defect, the nitrogen vacancy, is observed by PAS only in the initial stage of irradiation.

DOI: 10.1103/PhysRevLett.109.206402 PACS numbers: 71.55.Eq, 71.15.−m, 76.30.Mi, 78.70.Bj

Gallium nitride is a wideband semiconductor with a multitude of applications in micro- and optoelectronics. Its high cohesive energy imposes particular growth conditions, and as-grown epitaxial film or bulk samples contain a high number of point and extended defects, which influence their electronic and optical properties [1–3]. Contrary to the case of GaAs where most of the native intrinsic defects have been identified and characterized in detail [4], this is not the case for GaN. The nature of the intrinsic defects in GaN is not known with the exception of the Ga interstitial [5–7] and the Ga monovacancy [8]. Numerous other paramagnetic defects have been observed, mainly by optically detected magnetic resonance, but their hyperfine structure was in general not resolved rendering their identification impossible. In particular, experimental results for the defects related to the nitrogen sublattice are missing: the N vacancy has not yet been clearly detected by positron annihilation spectroscopy (PAS) or electron paramagnetic resonance (EPR) and the N interstitial has escaped any detection. As GaN is considered radiation hard as compared to other III–V compounds such as GaAs and GaP, it is of considerable interest to clarify whether low thermal annealing stages of nitrogen sublattice related defects are at the origin of this property.

In this work, we have studied in detail an irradiation-induced, intrinsic defect characterized by an introduction rate of a primary defect. We present its identification by EPR as a N interstitial in a split-interstitial configuration (cf. Fig. 2). Based on density functional theory (DFT) and molecular dynamics calculations [9–11] the model of N split-interstitial defects has been proposed before as the stable configuration of the N interstitial, but up to now no experimental evidence for this defect had been obtained. Its identification in this work is based on EPR measurements and theoretical prediction of the hyperfine structure and the g tensors of the main intrinsic defects in GaN. It should be recalled that intuitive models established in the absence of such calculations have often turned out to be erroneous [8,12,13]. We show that in GaN the situation is also complicated, making the support from detailed model calculations a necessity. We also show by PAS the concurrent formation and room temperature stability of nitrogen and gallium monovacancies.

For the controlled formation of intrinsic defects we have chosen particle irradiation. We have irradiated undoped and 2×10^{18} cm^{-3} Si doped n-type GaN bulk crystals grown by hydride vapor phase epitaxy by different types of particles: high energy (20 MeV) electrons, high-energy protons (12 MeV), and swift heavy Si ions (120 MeV). Fluences of up to $10^{18} e-/\text{cm}^2$, $8 \times 10^{16} p+/\text{cm}^2$, and $10^{14}\text{Si}+/\text{cm}^2$ have been applied. Given the sample thickness of 340 μm, a homogeneous defect formation can be expected for such $e-$ and $p+$ irradiation conditions. For example, the simulated projected range for 12 MeV protons, e.g., is 450 μm. We observe by EPR in all three cases the same dominant irradiation-induced paramagnetic defect. As the most detailed results have been obtained for proton irradiation, these results will be presented here in particular.

EPR measurements have been performed with X-band and Q-band spectrometers including *in situ* optical excitations. In addition, high frequency (345 GHz) EPR measurements, decisive for establishing the defect symmetry, have also been performed. The absolute defect concentration has been determined with the help of a spin standard sample (Al_2O_3:Cr). For the room temperature PAS experiments, a fast positron source (^{22}Na) in a conventional fast-fast coincidence spectrometer with a time resolution of 225 ps was used. After subtracting the source and background components, the lifetime spectra $L(t) = \sum_i I_i \exp(-t/\tau_i)$ were fitted using a modified version of the software POSFIT [14]. In the analysis of the PAS results on the

 © 2012 American Physical Society

2×10^{18} Si doped samples, the information obtained from the EPR measurements showing a progressive electrical compensation with a Fermi-level shift from initially $E_c - 35$ meV (Si shallow donor) to $E_c - 1.0$ eV for fluences above $1 \times 10^{16} p + /\text{cm}^2$ has been crucial.

In Fig. 1 (left), we show a typical X-band EPR spectrum observed under thermal equilibrium conditions at $T = 4$ K. It displays a rich, partially resolved HF structure which is best resolved for $B \parallel c$. When measured at Q band the EPR spectrum is unchanged (cf. Fig. 1, left) proving that its structure is due to HF interaction and belongs to one single defect. At Q-band frequencies a weak anisotropy of the center of gravity of the spectrum is observed between $g_{\parallel c} = 2.000$ and $g_{\perp c} = 1.998$, which might indicate an axial C_{3v} symmetry. However, the very high frequency (345 GHz) EPR measurements for B 20° from the c axis (cf. Fig. 1, right) show that the symmetry is lower, C_{1h} or C_1, with a clearly anisotropic g tensor with $\Delta g > 0.01$. The concentration of this defect is very high and increases linearly with dose (Fig. 2) after a threshold fluence of 1×10^{16} cm^{-2}. Calibration with the spin standard sample gives a concentration of 1.3×10^{18} cm^{-3} in the 4×10^{16} cm^{-2} irradiated sample corresponding to an introduction rate of 33 cm^{-1} for 12 MeV protons. The spectrum is photosensitive: under *in situ* photoexcitation at 4 K with a threshold energy of 1.0 eV its intensity is increased, demonstrating that this defect pins the Fermi level at $E_c - (1.0 \pm 0.1)$ eV for fluences above 2×10^{16} cm^{-2}. This observation is in agreement with transport measurements in heavily neutron, proton, or electron irradiated GaN, which showed a Fermi-level pinning close to $E_c - 0.9$ eV [15–17]. Based on its level position, this defect was tentatively attributed to a N interstitial.

In GaN, the attribution of a paramagnetic center to a specific defect model even in the case of resolved HF structure is not straightforward when more than one nucleus is involved. The coexistence of two Ga isotopes with nuclear spin $I = 3/2$ and comparable natural abundance, but different nuclear g factor, ^{69}Ga ($g_N = 1.34439$, 60.1%) and ^{71}Ga ($g_N = 1.70818$, 39.9%) as well as two nitrogen isotopes ^{15}N, ^{14}N render the analysis difficult. Most often, multiple HF interactions lead generally to broad lines without resolved HF structure. But even when the HF structure is resolved, detailed calculations are required for their assignment. For this reason we have calculated the defect structures as well as the spectroscopic signatures for the main intrinsic defects from first principles within DFT. We use supercells containing up to 324 atoms, standard norm-conserving pseudopotentials, a plane-wave basis with an energy cutoff of 90 Ryd (Ga 3d electrons in the valence [18]), and the spin-polarized Perdew-Burke-Ernzerhof (PBE) [19] functional. All defect structures have been fully relaxed using $2 \times 2 \times 2$ Monkhorst-Pack k-point samplings. The EPR parameters are calculated taking into account relativistic effects. Whereas the HF splittings are determined by the magnetisation density $m(\vec{r})$ in a very small region around the nuclei [20], the deviation of the g tensor from the free-electron value 2.002319 is driven by spin-orbit coupling as mediated by the spin currents $\vec{j}(\vec{r})$ induced by the external magnetic field [21]. To calculate these characteristic deviations $\Delta g_{\mu\nu}$, we use the gauge-including projector augmented plane wave approach [22] as implemented in the QUANTUM-ESPRESSO package [23]. Note that at least $4 \times 4 \times 4$ k-point samplings are necessary to obtain well-converged elements of the electronic g tensor.

As shown in Fig. 3, the low temperature EPR spectrum for $B \parallel c$ can be well simulated by the parameters

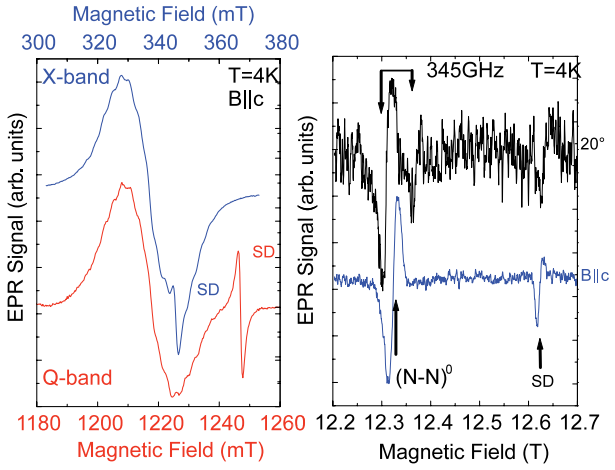

FIG. 1 (color online). Left: X-band (blue, top) and Q-band (red, bottom) EPR spectrum at $T = 4$ K of the $(\text{N-N})_\text{N}$ center and the shallow donor (SD) center for $B \parallel c$. Right: High frequency spectra (345 Ghz) for $B \parallel c$ and 20° from the hexagonal c axis, $T = 4$ K.

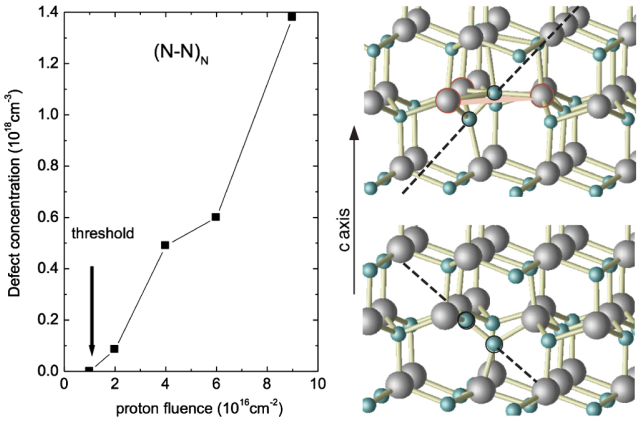

FIG. 2 (color online). Left: $(\text{N-N})_\text{N}$ defect concentration as a function of $p+$ fluence. Right: Ground state (bottom) and excited configuration (top), where one of the N-N dimer atoms has moved through the plane of the 3 Ga ligands (red). Defect axes (orientation of the N-N dimers, dashed lines) are also given.

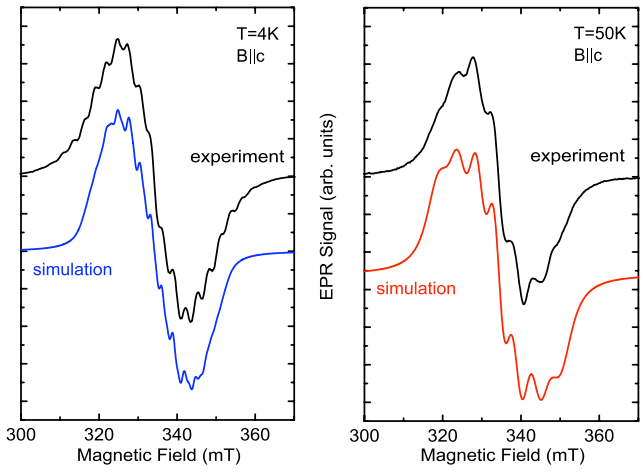

FIG. 3 (color online). X-band EPR spectrum of the $(\text{N-N})_\text{N}$ center at $B \parallel c$ measured at $T = 4$ K (left) and 50 K (right) and the spectra simulated with the values given in Table I.

calculated for the neutral N split interstitial: it is a spin $S = 1/2$ center with C_1 symmetry, a g factor of 2.0016, and a HF interaction with *two* N and *four inequivalent* Ga neighbors (cf. Table I). Its HF structure is similar (magnitude of the splittings) but distinctly different from the previously observed $L1$ center. Based on the assignment of its HF stucture to three Ga neighbors, it had been attributed to a gallium vacancy [6]. The $L1$ center is not observed in our samples, nor any spectrum related to Ga interstitials [5–7]. The calculated g values and HF interactions for the isolated V_Ga, the $V_\text{Ga}V_\text{N}$ divacancy, and also for the $V_\text{Ga}\text{O}_\text{N}$ pairs all give similar results but do not correspond to those of our measured spectrum.

In order to further confirm its *neutral* charge state, we have calculated the energy of the $(\text{N-N})_\text{N}$ charge transitions using the concept of the Slater-Janak transition state [24]. The standard PBE functional leads to values of $E_c - 1.5$ eV $(^{2+/+})$ and $E_c - 0.35$ eV $(^{0/-})$, which both do not agree with the experimental value of -1.0 eV (see Table II). The accuracy of charge transition levels calculated using local functionals like PBE, however, suffers from the well-known DFT band gap problem. To get more reasonable estimates, we performed additional total energy calculations using the nonlocal Heyd-Scuseria-Ernzerhof (HSE) hybrid functional [25] which is known to improve the energetics of defect levels [26]. A range-dependent incorporation of up to 32% Hartree-Fock exact exchange corrects the band gap from 1.89 eV (PBE) to 3.55 eV, close to the experimental value of 3.51 eV [27]. Moreover, the $(^{0/-})$ transition level is shifted considerably: a HSE value of $E_v + 2.54$ eV, 1.01 eV below the conduction band, agrees nicely with the experimental finding.

The HF structure of this defect is temperature dependent (cf. Fig. 3): for $T > 50$ K it changes and the spectrum becomes isotropic with a resolved structure for all orientations of the applied field. The EPR spectrum can be observed up to 300 K. It can again be explained by the HF interaction with *two* N and *four* Ga nuclei but with modified HF parameters. A thermally activated reorientation of a defect leading to a change in the HF parameters has often been observed in semiconductors. We have been able to model this new structure in the following way. At 4 K the structure has C_1 symmetry with the unpaired electron mainly localized in the p-like orbitals of the two central N atoms. The resulting magnetization density resembles a four-leaf clover which is tilted with respect to the crystal axes (cf. Fig. 4). For $T > 50$ K the central N atoms start to fluctuate in position, and the clover leaf oscillates with respect to the N-N axis. The resulting thermally averaged structure shows a higher symmetry, C_{1h}, whereby the distance between the two N atoms is reduced. The magnetization density is also reduced and partially transferred to two of the nearest Ga ligands. The result is a modified HF interaction and EPR line shape with a pronounced central structure. It should be noted that a similar EPR spectrum measured at 77 K has been reported very recently by Son *et al.* in electron irradiated GaN [28,29]. It has been tentatively attributed by these authors to a $V_\text{Ga}\text{O}_\text{N}$ center. However, this assignment is not supported by our modeling.

We have investigated the annealing stage by isochronal annealings (30 min) between 100 °C and 400 °C. Even though the electrical compensation changes only slightly after the 400°C treatment (the samples are still highly resistive), we observe a complete annealing of this defect in the 300 °C to 400 °C range. Figure 2 (right) also shows an excited configuration (0.35 eV higher in energy) from which one of the N-N dimer atoms can easily move

TABLE I. Calculated and experimental g tensor and hyperfine tensors $|A|$ [MHz] (^{69}Ga and ^{14}N) of the $(\text{N-N})_\text{N}^{2+}$ split interstitial for $B \parallel c$ and different EPR measuring temperatures.

		$g_\parallel$	A_N1	A_N2	A_Ga1	A_Ga2	$A_\text{Ga3,4}$
V_Ga^{2-}	C_{1h}	2.0051	52			66	70
$(V_\text{Ga}\text{O}_\text{N})^-$	C_{1h}	2.0049	52			67	71
$(V_\text{Ga}V_\text{N})^-$	C_{1h}	2.0059	52			67	71
$(\text{N-N})_\text{N}^{2+}$	C_{1h}	1.9868	15	3		12	82
$(\text{N-N})_\text{N}^0$	C_1	2.0016	25	42	116	82	45/50
Exp. 4 K		2.0000	15	42	117	92	65/75
Exp. 50 K		2.0005	10	30	110	110	<25
$(\text{N-N})_\text{N}^0$	C_{1h}	2.0009	10	18	125	125	20

TABLE II. Charge transition levels of the $(\text{N-N})_\text{N}$ split interstitial [eV] with respect to the conduction band minimum E_c

Functional	$(2+/+)$	$(+/0)$	$(0/-)$	E_gap
PBE	-1.50	-0.72	-0.35	1.89 eV
HSE	-2.56	-1.45	-1.01	3.55 eV
Exp. (this work)			-1.0	3.51 eV

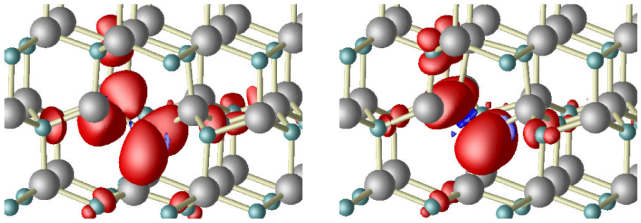

FIG. 4 (color online). Magnetization density (unpaired electron) of the neutral N split interstitial: "symmetry-free" ground state (left) and thermally averaged state with C_{1h} symmetry (right).

through the plane of the three Ga ligands. Hence, this configuration can assist in an efficient *stepwise* N diffusion along the hexagonal channels parallel to the c axis. In SiC, carbon split interstitials $(\text{C-C})_\text{C}$ anneal in the same low temperature range [11]. Their diffusion and rearrangements play an important role in the amorphization process under high fluences of particle irradiation. We expect that N split interstitials play a similar role in GaN.

In n-type and semi-isolating material, the Ga monovacancy will be in the diamagnetic V_Ga^{3-} charge state and is EPR silent. If the Fermi level is pinned at $E_c - 1.0$ eV, the same is true for the N vacancy, which is equally in the diamagnetic V_N^{+} state [3]. PAS spectroscopy is complementary to EPR in the sense that it is not restricted to paramagnetic charge states. It probes neutral and negative vacancies as the V_Ga^{3-}: The average positron lifetime τ_av in our samples increases with the proton fluence (cf. Table III), meaning that the concentration and/or the average size of the vacancy defects increases. Hence, besides an irradiation-induced modification of the electrical compensation, several lifetime compounds must be considered in a detailed analysis of the PAS results. The longest lifetime component τ_3 (235 ± 10 ps) has already been detected by Saarinen *et al.* in GaN [30,31]. It has been convincingly attributed to a V_Ga-related defect which can be either the isolated Ga vacancy or a complex involving V_Ga. Its intensity increases from 35.9% for the lowest fluence to 74.9% for the highest one, indicating that the concentration of the V_Ga-related defects increases with the proton fluence. For the lowest fluence, we observe an additional lifetime component τ_2 of 181 ± 1 ps. This lifetime is clearly shorter than the 235 ps for V_Ga and longer than the bulk value ("as-received" sample), suggesting a second type of vacancy defect; its intensity decreases rapidly with increasing proton fluence. The obvious candidate is the nitrogen vacancy: Tuomisto *et al.* [30] have observed a N-vacancy related lifetime of 180–190 ps in low energy electron irradiated GaN. With increasing fluence of particle irradiation it can be expected to switch from a negative or neutral to a positive charge state [30] becoming, thus, invisible in PAS. The best decomposition of the lifetime spectra, however, is obtained using three lifetime components, one free component and the two others fixed at 190 and 235 ps (cf. Table III). The free component gives short lifetimes between 146 and 154 ps, very close to the bulk value, suggesting that shallow traps are still detected after irradiation.

TABLE III. Experimental positron lifetimes obtained at fluences $\leq 2 \times 10^{16}$ cm^{-2} for an analysis with three lifetime components, one free and two fixed to 190 and 235 ps. In the sample irradiated at 4×10^{16} cm^{-2}, $\tau_\text{av} = 208$ ps is observed.

Fluence	τ_av	τ_1	I_3 [%]	τ_2	I_2 [%]	τ_3	I_3 [%]
As-received		155.3	100.0				
1×10^{15}	187.4	153.4	52.4	190.0	14.4	235.0	33.0
1×10^{16}	191.3	146.4	36.8	190.0	27.2	235.0	36.0
2×10^{16}	200.4	154.2	41.0	190.0	6.0	235.0	53.0

In summary, we report the EPR observation of a nitrogen sublattice defect in GaN which is generated by room temperature particle ($e-$, $p+$, ions) irradiation, the $(\text{N-N})_\text{N}$ split interstitial. It is electrically active and pins the Fermi level 1 eV below the conduction band. The N split interstitial anneals at 400 °C, the first annealing stage for room temperature irradiation. Its high introduction rate and multiple gap levels demonstrate its importance for the electrical compensation under radiation conditions. Our results modify the current understanding of the electrical compensation due to particle irradiation. Whereas previously the compensation between N vacancy donors, N interstitial acceptors, and Ga vacancy acceptors has been considered [32,33], our results show that the N interstitial is ambipolar, i.e., a deep acceptor defect with a level at $E_c - 1.0$ eV in n-type material and a deep donor in p-type material. As its introduction rate is close to the theoretical value for primary N interstitials, the transformation in the split interstitial is apparently complete in n-type and semi-insulating material.

The work was funded by DFG. The calculations have been done at PC^2 (Paderborn) and HLRS (Stuttgart). We thank the Grenoble high field laboratory for the high frequency EPR measurements.

*vonbarde@insp.jussieu.fr

[1] K. Saarinen, T. Suski, I. Grzegory, and D. C. Look, Physica (Amsterdam) B **308–310**, 77 (2001).
[2] F. Tuomisto, T. Paskova, S. Figge, D. Hommel, and B. Monemar, J. Cryst. Growth **300**, 251 (2007).
[3] C. G. van de Walle and J. Neugebauer, J. Appl. Phys. **95**, 3851 (2004).
[4] J. C. Bourgoin, H. J. von Bardeleben, and D. Stievenard, J. Appl. Phys. **64**, R65 (1988).
[5] K. H. Chow, G. D. Watkins, A. Usui, and M. Mizuta, Phys. Rev. Lett. **85**, 2761 (2000).
[6] K. H. Chow, L. Vlasenko, P. Johannesen, C. Bozdog, G. Watkins, A. Usui, H. Sunakawa, C. Sasaoka, and M. Mizuta, Phys. Rev. B **69**, 045207 (2004).

[7] H. Itoh, A. Kawasuso, T. Ohshima, M. Yoshikawa, I. Nashiyama, S. Tanigawa, S. Misawa, H. Okumura, and S. Yoshida, Phys. Status Solidi A **162**, 173 (1997).
[8] K. Saarinen, T. Suski, I. Grzegory, and D. C. Look, Phys. Rev. B **64**, 233201 (2001).
[9] F. Gao, E. J. Bylaska, and W. J. Weber, Phys. Rev. B **70**, 245208 (2004).
[10] H. Y. Xiao, F. Gao, X. T. Zu, and J. Weber, J. Appl. Phys. **103**, 123529 (2008).
[11] H. Y. Xiao, F. Gao, X. T. Zu, and J. Weber, J. Appl. Phys. **105**, 123527 (2009).
[12] B. Aradi, A. Gali, P. Deák, J. Lowther, N. Son, E. Janzén, and W. Choyke, Phys. Rev. B **63**, 245202 (2001).
[13] T. T. Petrenko, T. L. Petrenko, and V. Ya Bratus, J. Phys. Condens. Matter **14**, 12 433 (2002).
[14] P. Kirkegaard and M. Eltrup, Comput. Phys. Commun. **3**, 240 (1972).
[15] D. C. Look, Z. Q. Fang, and B. Claflin, J. Cryst. Growth **281**, 143 (2005).
[16] A. Y. Polyakov *et al.*, J. Appl. Phys. **100**, 093715 (2006).
[17] A. Y. Polyakov, I.-H. Lee, N. B. Smirnov, A. V. Govorkov, E. A. Kozhukhova, N. G. Kolin, A. V. Korulin, V. M. Boiko, and S. J. Pearton, J. Appl. Phys. **109**, 123703 (2011).
[18] U. Gerstmann, A. P. Seitsonen, and F. Mauri, Phys. Status Solidi B **245**, 924 (2008).
[19] J. P. Perdew, K. Burke, and M. Ernzerhof, Phys. Rev. Lett. **78**, 1396 (1997).
[20] P. E. Blöchl, Phys. Rev. B **62**, 6158 (2000).
[21] U. Gerstmann, M. Rohrmüller, F. Mauri, and W. G. Schmidt, Phys. Status Solidi C **7**, 157 (2010).
[22] Ch. J. Pickard and F. Mauri, Phys. Rev. Lett. **88**, 086403 (2002).
[23] P. Giannozzi *et al.*, J. Phys. Condens. Matter **21**, 395502 (2009); http://www.quantum-espresso.org.
[24] S. Sanna, Th. Frauenheim, and U. Gerstmann, Phys. Rev. B **78**, 085201 (2008).
[25] J. Heyd and G. E. Scuseria, J. Chem. Phys. **121**, 1187 (2004).
[26] A. Janotti, J. L. Lyons, and C. G. Van de Walle, Phys. Status Solidi A **209**, 65 (2012).
[27] C. Mietze, M. Landmann, E. Rauls, H. Machhadani, S. Sakr, M. Tchernycheva, F. Julien, W. Schmidt, K. Lischka, and D. As, Phys. Rev. B **83**, 195301 (2011).
[28] N. T. Son, C. Hemmingsson, T. Paskova, K. Evans, A. Usui, N. Morishita, T. Ohshima, J. Isoya, B. Monemar, and E. Janzén, Phys. Rev. B **80**, 153202 (2009).
[29] N. T. Son, C. G Hemmingsson, N. Morishita, T. Ohshima, T. Paskova, K. R. Evans, A. Usui, J. Isoya, B. Monemar, and E. Janzén, Phys. Scr. **T141**, 014015 (2010).
[30] F. Tuomisto, V. Ranki, D. Look, and G. Farlow, Phys. Rev. B **76**, 165207 (2007).
[31] K. Saarinen *et al.*, Physica (Amsterdam) B **273–274**, 33 (1999).
[32] D. C. Look, D. Reynolds, J. Hemsky, J. Sizelove, R. Jones, and R. Molnar, Phys. Rev. Lett. **79**, 2273 (1997).
[33] D. C. Look, G. C. Farlow, P. J. Drevinsky, D. F. Bliss, and J. R. Sizelove *et al.*, Appl. Phys. Lett. **83**, 3525 (2003).

Paper IX

Computational approach for structure design and prediction of optical properties in amorphous TiO_2 thin-film coatings

T. Köhler, M. Turowski, H. Ehlers, M. Landmann, D. Ristau, and T. Frauenheim

JOURNAL OF PHYSICS D: APPLIED PHYSICS **46**, 325302, 9 pp. (2013)

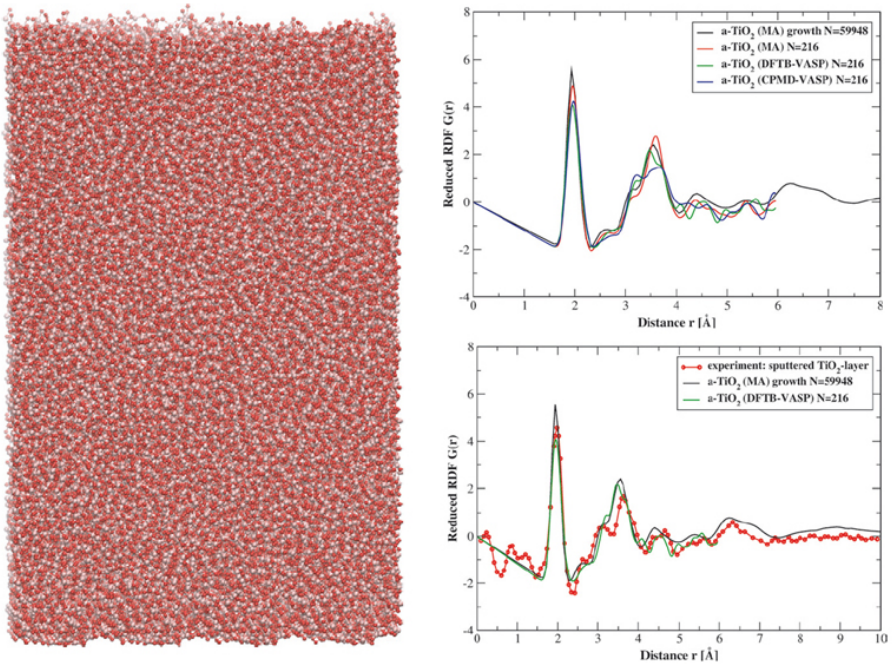

J. Phys. D: Appl. Phys. **46** (2013) 325302 (9pp) doi:10.1088/0022-3727/46/32/325302

Computational approach for structure design and prediction of optical properties in amorphous TiO_2 thin-film coatings

Thomas Köhler[1], Marcus Turowski[2], Henrik Ehlers[2], Marc Landmann[3], Detlev Ristau[2] and Thomas Frauenheim[1]

[1] Bremen Center for Computational Materials Science, University of Bremen, Am Fallturm 1, 28359 Bremen, Germany
[2] Laser Zentrum Hannover e.V., Hollerithallee 8, 30419 Hannover, Germany
[3] University of Paderborn, Physics Department, Theoretical Physics, 33095 Paderborn, Germany

Received 22 February 2013, in final form 12 June 2013
Published 17 July 2013
Online at stacks.iop.org/JPhysD/46/325302

Abstract
We have investigated the structural and electronic properties of amorphous TiO_2 using molecular dynamics (MD) simulations based on *ab initio* density functional theory, a numerically efficient density-functional-based tight-binding approach and classical many-body potentials. The lower level approximations are successively validated by the higher level ones through comparison of the calculated structural and electronic properties. The classical results reproduce all relevant structural features of a-TiO_2 as obtained by quantum-mechanical simulation and reproduce the experimentally observed reduced radial distribution function. This gives convincing justification for the use of classical MD in the simulation of ion beam sputtering synthesis of large-area amorphous thin films. Cross-correlation of electronic data with the statistics of disorder-induced under- and over-coordination is derived as a basis for evaluating the optical quality of thin-film coatings.

(Some figures may appear in colour only in the online journal)

1. Introduction

The performance of optical components and particularly, the quality of their surfaces are of critical importance for the success of optical technologies in general. Since most of the presently used optical components feature a thin-film coating, an improvement in optical layer quality is critical for best performance. Therefore, modern coating techniques represent important process tools to prepare thin films with enhanced optical properties [1]. In particular, ion coating methods (e.g. ion beam sputtering (IBS), ion assisted deposition, magnetron sputtering) tend to produce thin films which are amorphous in their atomic structure and show advanced properties such as low porosity, surface smoothness and high optical homogeneity. Experimentally, an improvement in optical layer quality is achieved empirically by comparing the properties of the optical coatings deposited under varying conditions. While such studies clearly confirm the relevance of momentum transfer mechanisms from high energetic growth species to the thin-film formation and overall quality of such superior thin-film coatings [2], they however do not allow a quantitative prediction of the deposited atomistic structures and the resulting optical parameters. One suggestion to a more comprehensive approach is to obtain a rather complete understanding of the correlation of deposition parameters (energy, incident angle of atoms, ions, molecular fragments) with the optical properties and quality of the films, based on atomistic modelling. Reliable numerical simulations of the film growth process would allow the prediction of the film structure and stoichiometry, obtained under certain deposition conditions. Based on atomic structure details, electronic, optical, and mechanical properties of thin films become accessible for further calculations.

Atomistic simulations are in most cases carried out by quantum-mechanical approaches, i.e. density functional theory (DFT), or by classical simulation techniques (classical molecular dynamics (MD), kinetic Monte Carlo (kMC) methods) [3–5]. Simulations by DFT approaches are quite accurate but are limited to short simulation times in the order of a few times 10 ps and to relatively small structure

 © 2013 IOP Publishing Ltd Printed in the UK & the USA

super-cell sizes of a few hundred atoms. Otherwise, it is known from experience that representative data of optical film properties can be obtained in analysing layers of several nm in thicknesses. Thus, simulation on longer-time and larger-length scale have to be used to investigate the growth and formation of such thin films. To consider all processes taking place during the development of dielectric thin films (i.e. deposition, thermal relaxation, surface diffusion and thermal desorption), classical MD based on many-body empirical potentials are employed in most cases. The difference of ion coating processes such as IBS compared to other common techniques is, in particular, the kinetic energy of the coating material arriving at the substrate. While an average kinetic energy of approximately 10 eV can be assumed for the IBS process, the deposition energy of common thermal coating processes is much lower, about 0.1 eV. Particularly, with regard to the energetic adatom deposition process, which is expected to be important for modelling the dependence of energy impact in the already existing and growing film, classical MD simulations have been already used [6, 7].

The most critical factor for classical MD simulations is to find a classical potential describing all interatomic interactions of the involved species at an accuracy comparable to quantum-mechanical methods. A suitable potential is of paramount importance and decides on the validity and predictive ability of the simulation results. In the literature several procedures are known to derive many-body empirical potentials for desired combinations of chemical elements. They either can be deduced by semi-empirical fitting procedures to experimental data [8] or they can be adapted to the results of *ab initio* simulations [9]. In the case of TiO_2 a reliable interatomic potential can be obtained following the suggestion of Matsui *et al* [10]. Classical modelling based on the Matsui–Akaogi (MA) potential has been successfully used to investigate the stability of different titania polymorphs [10, 11], phase transitions between liquid and amorphous TiO_2 phases [12, 13], structure factors of amorphous TiO_2 nanoparticles [14], pressure-induced transitions [15, 16], and agglomeration of differently oriented TiO_2 nanoparticles [17]. The polarizable version of this potential has been proposed to be applicable to charge transfer processes in titania [18]. There have also been successful attempts to employ variable-charge models to simulate bulk defects and surface properties of rutile [19] as well as to study the deposition process of Ti_xO_y clusters with an impact energy up to 40 eV onto the (1 1 0) rutile [20, 21], anatase and amorphous [21] surfaces. The latter studies revealed that the crystal phase tends to grow further upon the Ti_xO_y cluster bombardment onto the (1 1 0) rutile surface, whereas only amorphous structures form when the amorphous or anatase substrate is used.

In the listed literature predominantly structural properties of amorphous titania thin films have been reported. Relevant to measurable optical layer properties are, in particular, the film density and the surface roughness of the growing film. However, to characterize the modelled thin films in terms of their optical properties, an accurate determination of the electronic properties is required. To our knowledge, no work has been published yet on a direct correlation between the atomic structure and the electronic and optical properties in simulating the growth of metal oxides. This is due to the simple reason that the electronic properties are not accessible when taking into account 10 000 s of atoms in the classical MD simulations.

For treating large enough structures, including thin-film growth under realistic deposition conditions, and at the same time being predictive in calculating the electronic and optical properties at an accuracy desired by experiment, the synergetic combination of accurate quantum methods and efficient classical approaches is highly demanded. Therefore, the major goal of this paper is to demonstrate how both approaches perform in the case of modelling the structure and growth of amorphous titania thin films under a set of realistic coating conditions. If a sufficient correlation can be demonstrated, this paper forms an essential basis for further detailed investigations on the effect of varying process parameters on thin-film growth and in particular, the formation of structural and optical layer properties. Consequently, the structures obtained by classical and quantum-mechanical simulations have to be compared for validation of the approximation. This can be achieved, in particular, by evaluating the atomistic short-range order and the related electronic properties of equally sized three-dimensional super-cell models obtained after MD simulations by DFT-based and classical methods. Comparing the respective models in terms of their accuracy to represent the atomistic bonding arrangement provides a first evidence for the quality of the classical potential in modelling thin-film growth. Additionally, this gives confidence to employ this methodology on a larger scale, and to provide a link between the classical models and the optical properties based on a detailed knowledge of the electronic structure.

The paper is organized as follows. In section 2 the employed methodology and computational details will be described. In section 3 the results of atomistic super-cell simulations with quantum and classical approaches will be summarized, including a detailed comparison of structural and electronic properties. In section 4 the structures grown by classical simulation will be analysed in terms of their structural and chemical homogeneity, and compared to the quantum generated models of section 3. In conclusion, in section 5 a possible cross-correlation between optical properties and the structural details, in particular the TiO_x-polyhedra distribution, will be discussed.

2. Methodology and computational details

To model the structure formation in stoichiometric amorphous TiO_2 thin films, we performed MD simulations within the self-consistent-charge density-functional-based tight-binding scheme (DFTB) [22–24]. This method provides a good compromise between accuracy and computational efficiency in a wide range of applications. We refer the reader to earlier studies on diamond nucleation in amorphous carbon systems [25], or the discussion of the properties of exo-fluorinated carbon nanotubes [26], as examples for either extended or low-dimensional structures of interest. The recently developed 'tiorg' set of diatomic Ti–X (X = Ti,H,C,N,O,S) DFTB

Slater–Koster integral tables [27], together with the 'mio' set for light elements and their atomic pairs [22, 23], has been employed in this work, see also www.dftb.org. The former set has been shown [27] to provide an adequate description of geometrical, energetic and electronic properties of rutile and anatase bulk phases and their low-index surfaces [27]. All DFTB calculations have been carried out using the open source DFTB + software (version 1.1) [28, 29].

For the MD simulations we prepared initial structures containing 216 atoms, spatially and chemically randomly distributed, like a gas of hard spheres. The atoms are placed in a fixed-volume cubic super-cell arrangement of varying size corresponding to the microscopic mass densities to be studied and the given ideal 1 : 2 stoichiometry. We have performed MD simulated annealing (MD-SA) for model structures with densities of $3.50\,\mathrm{g\,cm^{-3}}$, $3.80\,\mathrm{g\,cm^{-3}}$, $4.00\,\mathrm{g\,cm^{-3}}$, $4.20\,\mathrm{g\,cm^{-3}}$ and $4.50\,\mathrm{g\,cm^{-3}}$, respectively. In each case the dynamical quenching path for relaxation started from a partly equilibrated liquid state of the model structures at 5000 K and followed a path of exponentially decreasing temperature towards room temperature (300 K). The total duration of the cooling procedure was 23 ps. Newton's equations of motion were solved using the Verlet algorithm. The coupling to a heat bath according to the canonical (NVT)-ensemble was realized by the Anderson thermostat.

To validate the results obtained with the DFTB method, we performed *ab initio* DFT Car-Parrinello molecular dynamics (CPMD) simulations [30] under similar conditions. The CPMD calculations were performed by using norm-conserving pseudo-potentials of the Troullier-Martins type [31, 32] and the Becke88 exchange functional [33]. Due to the computational demand, the total simulation time was shortened to 8.6 ps, being discretized in 51 000 steps with time steps of 7 atomic time units, to ensure the energy convergence. At the beginning at 5000 K and at the end of the cooling process at 300 K, we performed thermal equilibration in 4000 and 5000 steps, respectively, whereas in between we followed as well an exponential path approximated by a suitable stepwise function. Here the Nose–Hoover thermostat ensures the conditions of a canonical ensemble, while the volume was kept constant.

In addition to this, we validated the classical many-body potential proposed by Matsui and Akaogi (MA) [10] against the CPMD and DFTB derived models. In the classical MD with the MA-potential we followed again a 23 ps annealing path (identical to the DFTB simulation), also using the Anderson thermostat. For the CPMD as well as in the classical simulation with the MA-potential the same initial structure of the DFTB-calculation has been used.

The room temperature CPMD and DFTB structures in [34] have been subjected to further conjugate gradient relaxation by using the Vienna Ab Initio Simulations Progam (VASP) to obtain final zero temperature models [35]. An energy cut-off of 400 eV was used and the 3s and 3p semicore states of Ti have been treated as valence states within the PAW potentials throughout this work. The atomic positions have been relaxed using the PBE83 (Perdew–Burke–Ernzerhof) functional, a $2\times2\times2$ Monkhorst–Pack k-point sampling, and a force convergence criterion of $0.01\,\mathrm{eV\,\AA^{-1}}$. Further analysing these structures the electronic structure, band gap and defect localization, as well as frequency-dependent optical data have been calculated.

Based on the studies of structure formation in amorphous TiO_2 super-cell models, a-TiO_2 thin-film growth was simulated using classical MD by applying IBS specific process parameters. To calculate the forces, the MA-potential was applied by introducing a real space cut-off of 8 Å for all interactions. The integration time step was set to 2 fs and a velocity Verlet integrator [36] was applied. A relaxed titania structure of ideal stoichiometry, consisting of 9600 atoms, was prepared as substrate for successive adatom growth at room temperature (300 K). Having a horizontal surface of about $56\,\mathrm{nm^2}$, the substrate density was approximately $3.74\,\mathrm{g\,cm^{-3}}$. To ensure thin-film growth in the direction perpendicular to the surface (z-direction), periodic boundary conditions were implemented only in the horizontal directions (labelled as x-, y-direction).

The simulation of TiO_2 thin-film growth was carried out by the deposition of single titanium and oxygen atoms on the prepared amorphous titania substrate structure, and each deposition event was modelled by a separate individual MD simulation. For simulating the impact, the atom was placed at a random position above the substrate. The space between the atom and the surface was set to 8 Å, in accordance with the interaction cut-off. The velocity vector of the atom was adjusted to perpendicular incidence and a fixed kinetic energy of 10 eV. This corresponds approximately to the average kinetic energy of adatoms in the IBS process. To save computation time and to realize the desired large structure, the modelling of a deposition event started immediately after the end of the previous one. Each deposition process in the simulation was carried out in two steps. In the first step, the integration of the Newtonian equations was performed using NVE conditions to model the energy impact in the already existing thin film. In a second step the atom structure was coupled to a heat bath according to the NVT-ensemble in order to cool the structure down to room temperature 300 K. The total simulation time for the NVE and the subsequent NVT section in this approach was approximately 1 ps. To realize a stoichiometric titania layer the initial deposition ratio of Ti : O=1 : 2 had to be increased in favour of oxygen. This became necessary because the sticking coefficient for oxygen is smaller than 1.0 in contrast to titanium atoms. By changing the deposition ratio, titania thin films with ideal stoichiometry could be prepared for further investigation and comparison to super-cell models obtained by DFT-based simulations. The simulation cycle was repeated until 5×10^4 atoms were deposited on the substrate, which in turn corresponds to a film thickness of approximately 10 nm.

3. Results and discussion

3.1. Structural and electronic properties of amorphous TiO_2 super-cell models

3.1.1. Structural properties. As a result of the MD super-cell simulations we have obtained metastable stoichiometric amorphous titanium-dioxide structures at different mass

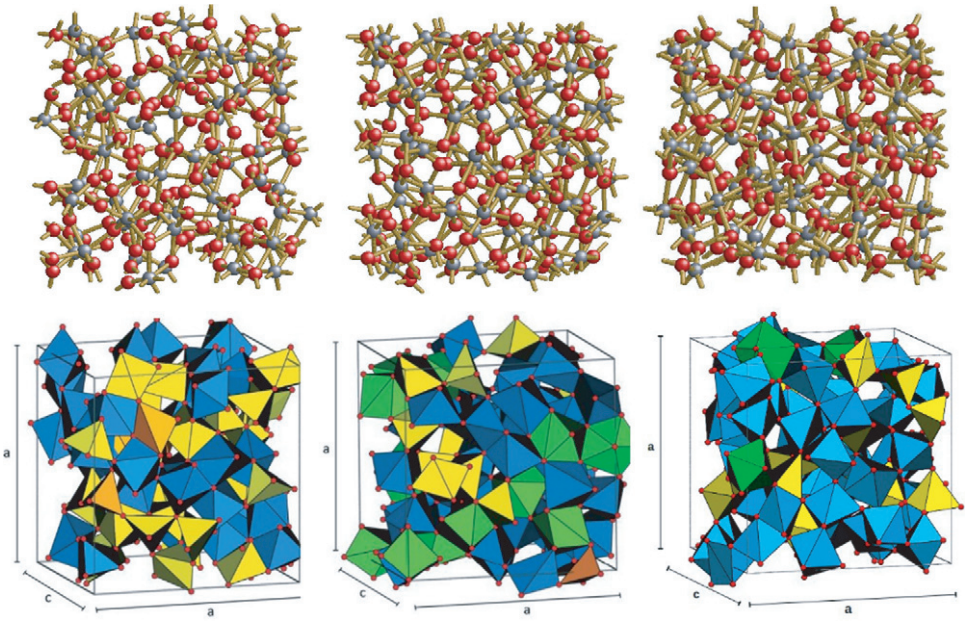

Figure 1. Structural snapshots of the amorphous TiO_2- networks at mass density 4.20 g cm^{-3} (IV, CP, MA from left to right)—upper part, and in an representation showing TiO_x-building blocks—lower part.

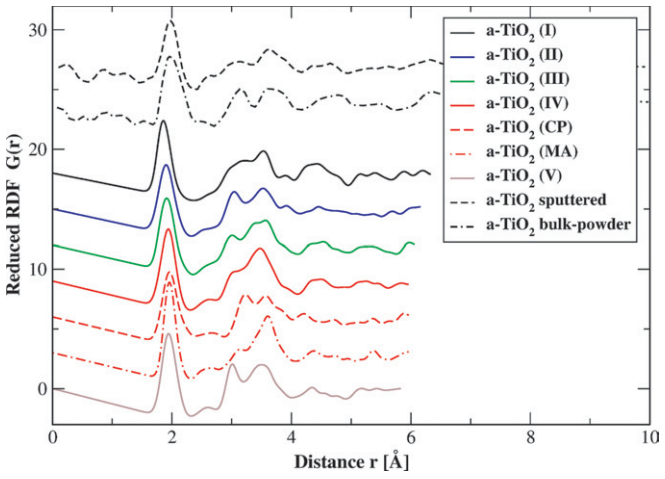

Figure 2. Reduced pair-distribution function $G(r)$ of the amorphous TiO_2 models.

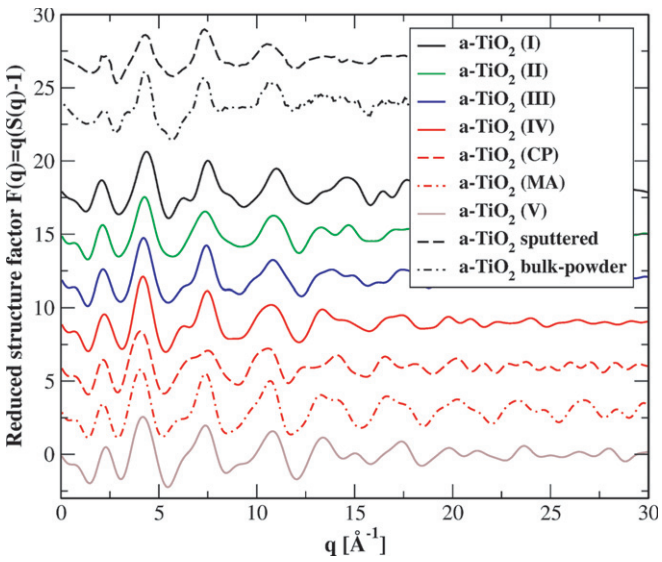

Figure 3. Reduced structure factors $F(q) = q(S(q) - 1)$ for a-TiO_2 models, comparison to experiments.

densities. In figure 1 (upper part) selected images of the amorphous bonding network at mass density of 4.2 g cm^{-3} are shown. For better identification of the characteristic TiO_x building blocks, a polyhedral representation is also given in figure 1 (lower part). The microstructure of relaxed TiO_2 models at room temperature can be characterized by the analysis of the mean interatomic distances and coordination numbers, extracted from the radial distribution functions (RDFs). RDFs and related structure factors are shown in the figures 2 and 3, compared with experimentally derived data for sputtered thin films and bulk-powder samples [37]. Important structural and electronic information is summarized in table 1. The models obtained by the DFTB method will be denoted by roman numerals (I–V), whereas the models obtained by using the CPMD method and the classical MA-potential by CP and MA, respectively.

As a fingerprint of the short-range order in the amorphous structure, we list in table 1 the coordination numbers $k_{\mathrm{Ti-Ti}}$, $k_{\mathrm{Ti-O}}$, $k_{\mathrm{O-Ti}}$, $k_{\mathrm{O-O}}$, which are the average numbers of the nearest neighbours for the corresponding elements in their first coordination shell. Those numbers can be derived from element specific lengths-statistics, as well as from the partial radial distribution functions. Additionally, the mean pair distances $R_1^{\mathrm{Ti-Ti}}$, $R_1^{\mathrm{Ti-O}}$, $R_1^{\mathrm{O-O}}$ and their deviations are given.

The atomic arrangement in the amorphous TiO_2 models consists of short staggered chains of TiO_6-octahedrons, like in the crystalline modifications anatase, rutile and brookite, and, according to the mass density, of a more-or-less large number of coordination defects (TiO_5, TiO_4-units), which can be found on titanium-dioxide surfaces [38] and in more complex magneli phases [39–42]. An increase in the number of TiO_6 octahedral units is clearly mirrored in the Ti–O, respectively, O–Ti coordination numbers $k_{\mathrm{Ti-O}}$ and $k_{\mathrm{O-Ti}}$, which tend

Table 1. Structural information and HOMO–LUMO band gaps of a-TiO_2 models.

Model	ρ (g cm^{-3})	$R_1^{Ti-Ti} \pm \Delta$ (Å)	$R_1^{Ti-O} \pm \Delta$ (Å)	$R_1^{O-O} \pm \Delta$ (Å)	k_{Ti-Ti}	k_{Ti-O}	k_{O-Ti}	k_{O-O}	E_{gap} (eV)
aTiO_2-(I)	3.50	3.38 ± 0.21	1.87 ± 0.09	2.91 ± 0.22	6.14	4.44	2.22	9.88	3.14
aTiO_2-(II)	3.80	3.37 ± 0.24	1.91 ± 0.11	2.84 ± 0.24	7.00	4.87	2.44	9.81	2.30
aTiO_2-(III)	4.00	3.38 ± 0.22	1.93 ± 0.11	2.8 ± 30.23	7.75	5.10	2.55	10.50	2.93
aTiO_2-(IV)	4.20	3.38 ± 0.22	1.94 ± 0.1	2.80 ± 0.24	8.69	5.36	2.68	10.76	2.68
aTiO_2-(CP)	4.20	3.38 ± 0.22	1.99 ± 0.13	2.78 ± 0.23	8.50	5.83	2.92	10.14	2.74
aTiO_2-(MA)	4.20	3.41 ± 0.24	1.98 ± 0.09	2.80 ± 0.25	8.97	5.81	2.90	10.80	2.70
aTiO_2-(V)	4.50	3.32 ± 0.23	1.96 ± 0.1	2.72 ± 0.23	8.53	5.79	2.90	10.42	2.12

towards the 'ideal' values of $k_{Ti-O} = 6$ and $k_{O-Ti} = 3$ of the crystalline modifications with increasing mass density. Obviously, those ideal mean values are not reached in the amorphous phase. Experimentally determined coordination numbers as well as reverse Monte Carlo simulations (RMCs) [37] show that amorphous TiO_2 systems always stay below those ideal values. For sputtered and sol–gel processed TiO_2 layers, Petkov *et al* [37] report coordination numbers of $k_{Ti-Ti} = 8.8$, $k_{Ti-O} = 5.4$, $k_{O-Ti} = 2.7$, $k_{O-O} = 10.5$ and $k_{Ti-Ti} = 6.5$, $k_{Ti-O} = 4.5$, $k_{O-Ti} = 2.25$, $k_{O-O} = 12.5$, respectively, whereas for bulk-like TiO_2-powders they obtain $k_{Ti-Ti} = 8.7$, $k_{Ti-O} = 5.6$, $k_{O-Ti} = 2.8$, and $k_{O-O} = 10.0$. Considering the mass density of 4.20 g cm^{-3}, which is close to the density of rutile, we see that the DFTB model (IV) nearly perfectly matches the numbers given for sputtered amorphous layers, while the values from CP and MA models are closer to the bulk-like powder samples, without exactly reaching the ideal coordination of crystalline modifications. In particular in the case of the classical many-body MA-potential, the slightly higher coordination numbers may be understood as the result of the fitting procedure to reproduce properties of the 6-fold coordinated crystalline modifications [12]. In contrast, the quantum mechanics based DFTB approach covers the coordination chemistry of the local bonding environment more flexibly. Thus, DFTB also describes properties of under- and over-coordinated titania, i.e. surfaces, clusters and magneli phases, at the same level of precision [27]. Considering the average values of the pair distances R_1, and their deviations as characteristic measures for the first neighbour coordination shells, the mean Ti–O bond length for all densities and methods lies approximately between 1.8 and 2.1 Å, which is also found for the crystalline modifications. Experimentally smaller values (1.79–1.93 Å) are seen for layers produced in the sol–gel process. A value of 1.96 Å is given for layers grown by a sputtering process, which was also confirmed by recent RMC-modelling [37]. Our values for densities near that of crystalline modifications (see model (IV) at 4.20 g cm^{-3}) again tend more to the numbers of sputtered amorphous titanium-dioxide materials. Here, we monitor through the super-cell percolating twinned chain of octahedral TiO_6–units, flanked by less coordinated $TiO_{4,5}$-polyhedra, as building blocks of possible under-coordination defects. The averaged bond length of 1.98–1.99 Å for the CPMD and MA models at the same density are slightly larger. This is due to their increased coordination number of ~5.8, caused by the slightly higher content of ideal octahedron-building blocks.

As shown in figures 2 and 3, all trends discussed above are qualitatively reflected in the calculated reduced structure factors $F(q) = q[S(q) - 1]$ and their Fourier-transforms, the reduced atomic pair-distribution functions $G(r)$ (see equation (2) in [34]). Comparing those to available experimental data [37] on structure factors and RDFs, the rutile-equivalent mass density of 4.20 g m^{-3} matches the reported data best and has therefore been chosen for further analysis. Choosing a density the same as for one of the crystalline phases also allows the separation of disorder effects from effects of density variations in the electronic structure data.

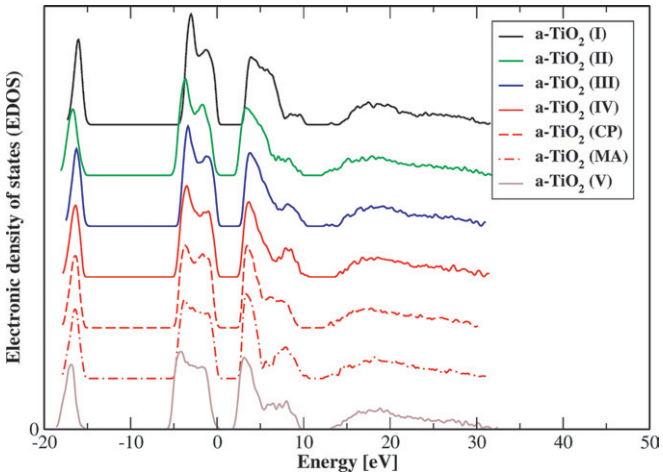

Figure 4. Electronic density of states of a- TiO_2 models. Each case Fermi energy is shifted to 0 eV.

3.1.2. Electronic properties. A characteristically pronounced feature of all stoichiometric amorphous TiO_2 models, obtained at different mass densities and using different simulation methods, is that no electronic defect levels in the band gap appear which could be caused by direct Ti–Ti or O–O bonds. All participating elements are 'bridged' by the other atom species. This leads to a well-defined electronic HOMO–LUMO gap that is comparable to the band gap of crystalline TiO_2 modifications. The width of the electronic band gaps, deduced by means of the DFTB method, is given for all model geometries in table 1. The total electronic density of states (EDOS) for each model is plotted in figure 4. As seen in figure 5, the energy gap shows an approximately linear decrease with increasing mass density. It is interesting to note that the band gap of the three models with the same density of 4.20 g m^{-3} but generated by the three different methods (IV, CP, MA), match almost perfectly.

The electronic and optical properties of the VASP post-relaxed CP and DFTB-(IV) models have been analysed in

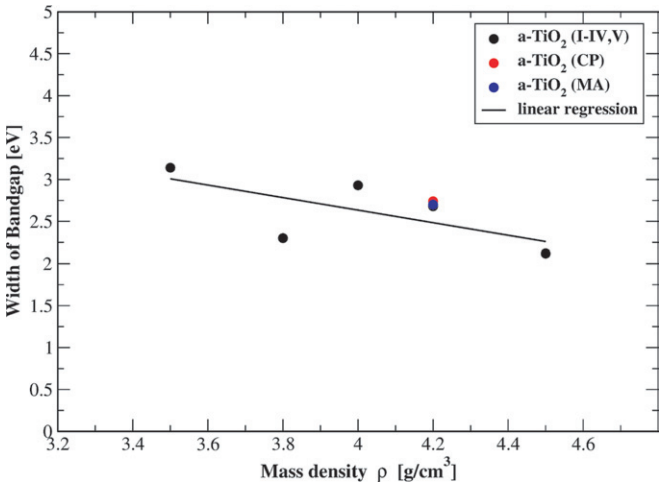

Figure 5. Electronic HOMO–LUMO gap of amorphous TiO_2 models.

detail by Landmann *et al* [34]. Here we briefly summarize the results. DFT calculations with the semi-local Perdew–Burke–Ernzerhof functional [43] resulted in the electronic energy gap of 2.21 eV and 2.25 eV for these two models, i.e. larger than the ones calculated in the crystalline TiO_2 phases rutile, brookite and anatase (1.88 eV, 1.86 eV, 1.94 eV, respectively). Direct correlations between structural data (polyhedral statistics) and the frequency-dependent optical constants, calculated from the complex dielectric function in independent particle approximation, have been derived from higher level electronic structure data obtained by the HSE06 screened hybrid functional [44]. Besides similar absorption characteristics between the most common crystalline phases and amorphous TiO_2, distinct differences in the optical spectra in the energy region between 5 eV and 8 eV were reported, in good agreement with experiments. These differences have been assigned to the loss of symmetry in the local atomic structure of the disordered material. While the crystalline phase rutile, anatase, and brookite are well described by periodic arrangements of partially distorted TiO_6 octahedral building blocks, the amorphous phase is characterized by partial loss of this octahedral coordination and the disorder-induced formation of under- and over-coordinated Ti ions. The optical characteristics of the amorphous phase were discussed as a superposition of optical transitions reflecting various local symmetries occurring in the manifold known as synthesizable crystalline TiO_2 phases. The DFTB band gap of 2.70 eV, presented here for the IV-DFTB, CP, MA models of a-TiO_2, is an underestimation with respect to the experimentally confirmed HSE06 band gap of 3.69 eV [34] but is larger than the PBE gap of 2.21 eV. While the PBE gap reflects the common local DFT underestimation, the DFTB gap is additionally affected by the use of a minimal basis.

Since the major focus of this study, is on the validation of the classical MD results rather than on demanding electronic structure calculations, we restrict further discussions of the electronic structure to the DFTB level of accuracy and base our arguments on the convincing agreement of electronic band gap values for the three (DFTB-(IV), CP, MA) model structures discussed in this article.

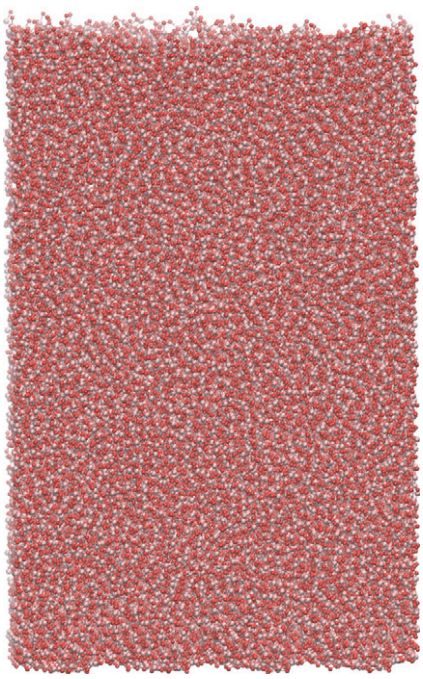

Figure 6. Structural snapshot of classical grown a-TiO_2 model.

4. Structural properties of the classical MA-grown a-TiO_2-model

The large-scale amorphous titania model, obtained by classical MD growth simulations using the empirical MA-potential, contains 59948 atoms in total, see figure 6. Again, we characterize the atomic correlations of the amorphous structure in terms of the reduced RDF $G(r)$ and the reduced structure factor $F(q)$. Figure 7 shows the reduced RDF of the amorphous TiO_2 models obtained by the classical MA-potential (216 atom super-cell and 59948 atom MD-grown) in relation to the 300 K DFTB and CPMD-models (left) and the VASP post-relaxed structures (right), which have been studied for accurate electronic structure and optical characterization in [34]. All models have an identical rutile-equivalent mass density of 4.20 g cm^{-3}.

The reduced RDFs are characterized by a sharp main peak between 1.95 and 2.0 Å, representing the first coordination shell of Ti-O pair correlations. The small second peak around 2.6 Å is due to O–O correlations within the amorphous network, whereas the broad peak structure between 2.9 and 4.0 Å is shaped by Ti–Ti distances. The latter correlation pattern is split into two sub-peaks, due to local structure characteristics of the amorphous polyhedron network. In detail, they arise from edge-linked TiO_x- and corner-sharing TiO_x-building blocks, with distances around 3.2 Å and 3.6 Å, respectively. This splitting is common for all structures, however, with differences in the relative weight of the two sub-peaks. The classically obtained models compare best with the VASP post-relaxed structure. In figure 8 we directly compare the radial correlations, expressed in the reduced RDFs, of the classical growth simulation model and the DFTB (left) as well as the VASP post-relaxed DFTB result (right) [34] to the electron diffraction data [37] for sputtered titania.

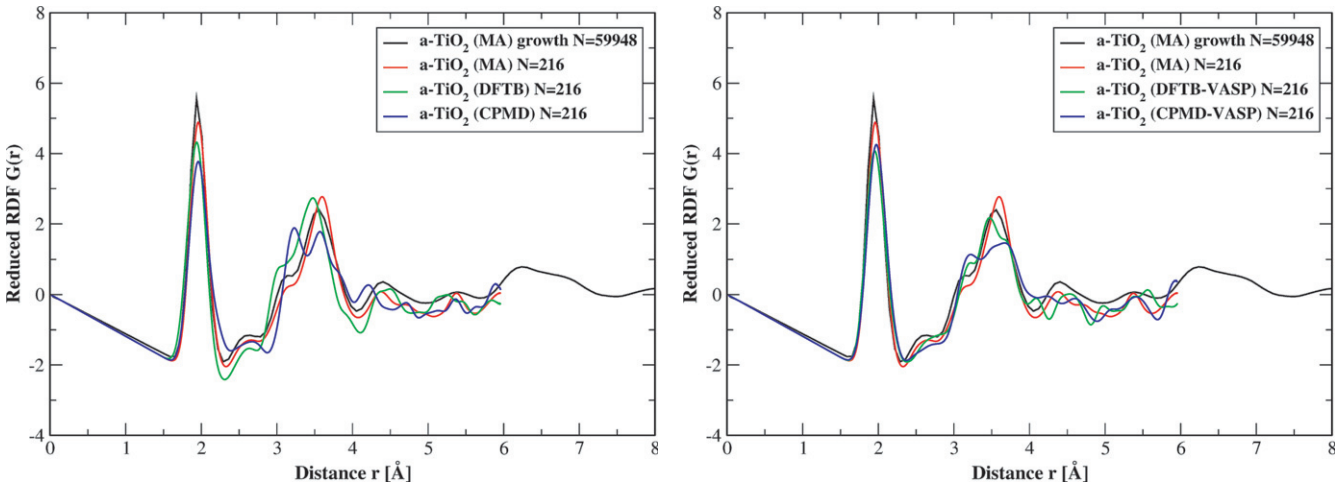

Figure 7. Reduced pair-distribution function $G(r)$ of the large classical grown a-TiO_2 model in comparison to selected super-cell simulations, left: (MA,CPMD and DFTB) 300 K structures; right: VASP post-relaxed 0 K (CPMD and DFTB) structures.

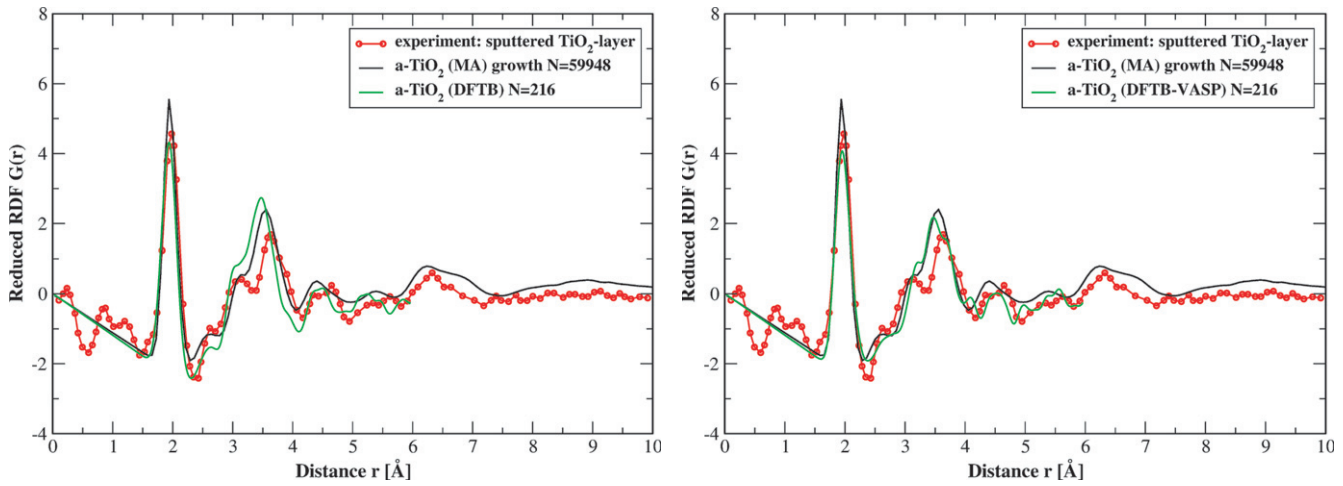

Figure 8. Reduced pair-distribution function $G(r)$ of the classical a-TiO_2 growth model in comparison to DFTB-super-cell simulation—left and VASP post-relaxed structure—right, to those determined experimentally by electron diffraction for sputtered TiO_2 layers [37].

Comparison of the curves clearly demonstrates the quality of the classical MD simulations in describing all relevant experimental features, in particular the location of maxima and minima, and the general shape of the distributions. If looking at the first two correlation shells, characterized by Ti–O and O–O nearest neighbour correlations, we see only small quantitative differences between the classical and *ab initio* based models. Since the classical MA-potential is somewhat stronger biased for the 6-fold coordination of crystalline TiO_2 polymorphs, a slightly higher mean coordination number (5.91) is observed as compared to the IBS-grown films [37]. This is also reflected in the height of the first coordination peak. The differences in the Ti–Ti correlations are more pronounced. Here the CPMD-VASP curves nicely compare with the bulk-powder short-range order, whereas the classical MD and DFTB-VASP models tend to better reflect the ordering in sputtered layers. At larger distances the limited cell volume of the smaller 216 atoms models leads to an information loss about medium and long range order. In comparison to the *ab initio* data, the curves of the classically grown models can be regarded as envelope for the further correlation spheres. In conclusion, the obtained structural data of the classically grown models compare very well with the DFTB- and VASP post-relaxed DFTB results. This gives convincing validation for the use of classical MD growth in large-scale simulations of amorphous thin films.

Finally, in figure 9, the reduced structure factor $F(q)$ for the VASP relaxed DFTB and CPMD super-cell models is compared to the classical simulation result. At first glance, a qualitatively good agreement for all simulation methods and system sizes can be found with respect to position, shape, and amplitude of oscillations. Especially for the lower q-wave (scattering) vectors, the results are very similar. For higher wave vectors the differences become larger, e.g. in the region ($12 < q < 16\,\text{Å}^{-1}$) we see a slight double peak in the classical and in the quantum mechanics based small 216-atom models. This splitting is most pronounced in the CPMD-VASP data but is completely absent in the large-scale MA-grown model. In table 2 we summarize the mean Ti–O coordination numbers and the related polyhedral statistics of the VASP post-relaxed CPMD and DFTB structures, and of the two different classical MD super-cells.

At a first look, the mean Ti–O coordination number of the models, generated by different simulation techniques,

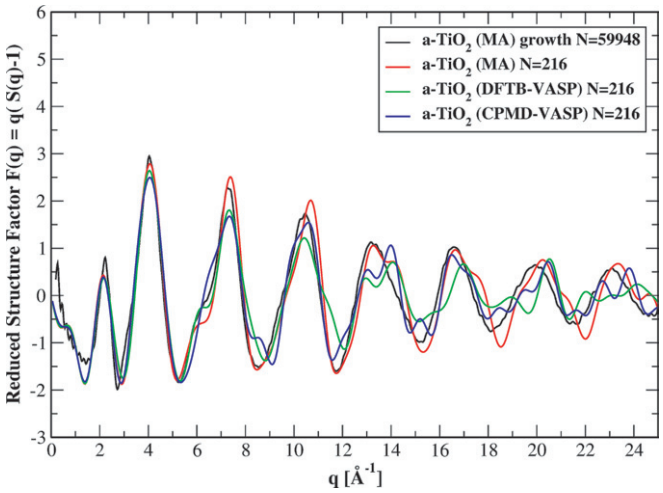

Figure 9. Reduced structure factor $F(q) = q[S(q) - 1]$ of the large classical grown a-TiO_2 model in comparison to selected DFTB super-cell models.

Table 2. Mean Ti–O coordination number, polyhedra statistics.

Model (number of atoms)	$\langle k \rangle$	4-fold	5-fold	6-fold	7-fold	8-fold
DFTB-VASP (216)	5.85	4.2%	25.0%	54.2%	15.3%	1.4%
CPMD-VASP (216)	6.00	1.4%	15.3%	65.3%	18.0%	—
a-TiO_2-(MA) (216)	5.83	1.4%	20.8%	70.8%	7.0%	—
MA Growth (59948)	5.91	0.6%	15.8%	75.5%	8.0%	0.1%

compare to each other quite well, approaching nearly the ideal 6-fold-coordination of the TiO_2 bulk polymorphs at room temperature and atmospheric pressure. The distribution of TiO_x-polyhedra building blocks however differs. The amorphous state gives rise to an averaged picture, including under-coordinated TiO_x building blocks as well as over-coordinated Ti atoms that are characteristic for high-pressure polymorphs. Under-coordinated TiO_x units with $x = 4.5$ can be found on various titania surfaces [38] and in magneli phases [39–42]. 7-fold Ti coordination is known from the monoclinic (baddeleyite type $P2_1/c$) [45–47] and the orthorhombic (Pbca) TiO_2 polymorphs [48]. The cubic (fluorite type, $Fm3m$) TiO_2 phase (c-TiO_2) [49, 50] shows an 8-fold coordination. The fraction of extraordinary 9-fold and 8-fold coordinated Ti sites is very small and approaches almost zero for all different simulation pathways and methods.

5. Summary and conclusions

To achieve a deeper understanding of the fundamental processes during film growth of high-performance optical coatings, a simulation approach for modelling the formation of TiO_2 thin films using classical MD simulations under realistic IBS coating conditions was developed. The classical many-body potentials used in energetic atom-by-atom deposition are successively validated against higher level DFT-based approaches through detailed comparison of the calculated structural and electronic properties of super-cell models. While the crystalline phase rutile, anatase, and brookite are well described by periodic arrangements of partially distorted TiO_6 octahedral building blocks, the amorphous phase is characterized by partial loss of this octahedral coordination and the disorder-induced formation of under- and over-coordinated Ti ions.

The large-scale amorphous TiO_2-model, obtained by classical MD growth simulations was characterized in terms of the reduced RDF $G(r)$ and the reduced structure factor $F(q)$. Comparison of the curves with the MA super-cell model and the quantum-mechanically generated DFTB and VASP post-relaxed structures clearly demonstrate the quality of the classical MD growth simulations in describing all relevant, experimentally observed structural features. This makes us confident in using classical MD growth simulations for investigating the influence of IBS deposition parameters on structure formation and further analysing the electronic and optical quality by cross-correlation of electronic data with the disorder-induced statistics of TiO_x polyhedra.

Acknowledgments

The authors are grateful to the BMBF, Germany, for financial support in terms of the PLuTO-grant to promote modern optical technologies. We also thank Mr Grigoriy Dolgonos for fruitful discussions and preparation of the DFTB titania parametrisation.

References

[1] Kaiser N and Pulker H K (eds) 2003 *Optical Interference Coatings (Springer Series in Optical Sciences* vol 88) (Berlin: Springer)
[2] Guenther K H 1993 Thin films for optical systems *Proc. SPIE* **1782** 344
[3] Leach A R 2001 *Molecular Modeling: Principles and Applications* (Englewood Cliffs, NJ: Prentice-Hall)
[4] Evarestov R A 2007 *Quantum Chemistry of Solids* (Berlin: Springer)
[5] Frenkel D and Smit B 2002 *Understanding Molecular Simulation: From Algorithms to Applications* (New York: Academic)
[6] Baguer N, Georgieva V, Calderin L, Todorov I T, Van Gils S and Bogaerts A 2009 *J. Cryst. Growth* **311** 4034–43
[7] Taguchi M and Hamaguchi S 2007 *Thin Solid Films* **515** 4879–82
[8] Georgieva V, Saraiva M, Jehanathan N, Lebedev O I, Depla D and Bogaerts A 2009 *J. Phys. D: Appl. Phys.* **42** 065107
[9] Carreé A, Horbach L, Ispas S and Kob W 2008 *Europhys. Lett.* **82** 17001
[10] Matsui M and Akaogi M 1991 *Mol. Simul.* **6** 239–44
[11] Akindeju M K, Pareek V K, Rohl A L, Carter D J and Tade M O 2010 *Int. J. Chem.* **2** 26–37
[12] Hoang V V 2007 *Phys. Status Solidi* b **244** 1280–7
[13] Hoang V V 2008 *Nanotechnology* **19** 105706
[14] Kaur K, Prakash S, Goyal N, Singh R and Entel P J 2011 *Non-Cryst. Solids* **357** 3399–404
[15] Hoang V V 2007 *J. Phys. D: Appl. Phys.* **40** 7454–61
[16] Hoang V V, Zung H and Trong N H B 2007 *Eur. Phys. J.* D **44** 515–24
[17] Yan W, Li S Q, Zhang Y Y, Yao Q and Tse S D 2010 *J. Phys. Chem.* C **114** 10755–60
[18] Kerisit S, Deskins N A, Rosso K M and Dupuis M 2008 *J. Phys. Chem.* C **112** 7678–88
[19] Hallil A, Tetot R, Berthier F, Braems L and Creuze J 2006 *Phys. Rev.* B **73** 235308

[20] Vernon L J, Smith R and Kenny S D 2009 *Nucl. Instrum. Methods* B **267** 3022–4
[21] Vernon L J, Kenny S D and Smith R 2010 *Nucl. Instrum. Methods* B **268** 2942–6
[22] Porezag D, Frauenheim T, Köhler T, Seifert G and Kaschner R 1995 *Phys. Rev.* B **51** 12947–57
[23] Elstner M, Porezag D, Jungnickel G, Elsner J, Haugk M, Frauenheim T, Suhai S and Seifert G 1998 *Phys. Rev.* B **58** 7260–8
[24] Elstner M, Frauenheim T and Suhai S 2003 *J. Mol. Struct. (Theochem.)* **632** 29–41
[25] Lifshitz Y, Köhler T, Frauenheim T, Guzmann I, Hoffman A, Zhang R Q, Zhou X T and Lee S T 2002 *Science* **297** 1531–3
[26] Seifert G, Köhler T and Frauenheim T 2000 *Appl. Phys. Lett.* **77** 1313–5
[27] Dolgonos G, Aradi B, Moreira N H and Frauenheim T 2010 *J. Chem. Theory Comput.* **6** 266–78
[28] Aradi B, Hourahine B and Frauenheim T 2007 *J. Phys. Chem.* A **111** 5678–84
[29] The DFTB+ program can be downloaded from www.dftb-plus.info
[30] Car R and Parrinello M 1985 *Phys. Rev. Lett.* **55** 2471–4
[31] Glassford K M, Troullier N, Martins J L and Chelikowsky J R 1990 *Solid State Commun.* **76** 635–38
[32] Langel W 2002 *Surf. Sci.* **496** 141–50
[33] Becke A D 1988 *Phys. Rev.* A **38** 3098–100
[34] Landmann M, Köhler T, Köppen S, Rauls E, Frauenheim T and Schmidt W G 2012 *Phys. Rev.* B **86** 064201
[35] Kresse G and Furthmüller J 1996 *Comput. Mater. Sci.* **6** 15
[36] Verlet L 1967 *Phys. Rev.* **159** 98–103
[37] Petkov V, Holzhüter G, Tröge U, Gerber T and Himmel B 1998 *J. Non-Cryst. Solids* **231** 17–30
[38] Diebold U 2003 *Surf. Sci. Rep.* **48** 53–229
[39] Anderson S 1960 *Acta Chem. Scand.* **14** 1161–72
[40] Liborio L and Harrison N 2008 *Phys. Rev.* B **77** 104104-1-10
[41] Liborio L, Mallia G and Harrison N 2009 *Phys. Rev.* B **79** 245133
[42] Schreiber S, Fidler M, Dulub O, Schmid M, Driebold U, Hou W, Aschauer U and Selloni A 2012 *Phys. Rev. Lett.* **109** 136103
[43] Perdew J P, Burke K and Ernzerhof M 1996 *Phys. Rev. Lett.* **77** 3865
[44] Heyd J, Scuseria G E and Ernzerhof M 2003 *J. Chem. Phys.* **118** 8207
[45] Haines J and Léger J M 1993 *Physica* B **192** 233
[46] Lagarec K and Desgreniers S 1995 *Solid State Commun.* **94** 519
[47] Sato H, Endo S, Sugiyama M, Kikegawa T, Shimomura O and Kusaba K 1991 *Science* **251** 786
[48] Dubrovinskaia N A, Dubrovinsky L S, Ahuja R, Prokopenko V B, Dmitriev V, Weber H P, Osorio-Guillen J M and Johansson B 2001 *Phys. Rev. Lett.* **87** 275501
[49] Mattesini M, de Almeida J S, Dubrovinsky L, Dubrovinskaia N, Johansson B and Ahuja R 2004 *Phys. Rev.* B **70** 212101
[50] Kim D Y, de Almeida J S, Koči L and Ahuja R 2007 *Appl. Phys. Lett.* **90** 171903

Paper X

Consistent Atomic Geometries and Electronic Structure of Five Phases of Potassium Niobate from Density-Functional Theory

F. Schmidt, M. Landmann, E. Rauls, N. Argiolas, S. Sanna, W. G. Schmidt, and A. Schindlmayr

Advances in Materials Science and Engineering, Article ID 3981317, 13 pp. (2017)

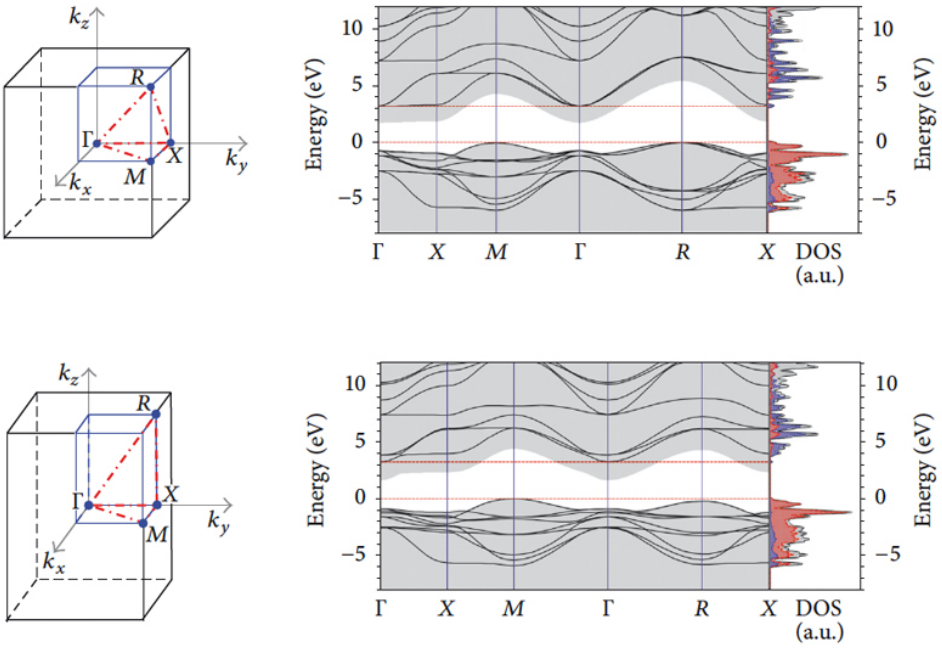

Hindawi
Advances in Materials Science and Engineering
Volume 2017, Article ID 3981317, 13 pages
https://doi.org/10.1155/2017/3981317

Research Article

Consistent Atomic Geometries and Electronic Structure of Five Phases of Potassium Niobate from Density-Functional Theory

Falko Schmidt,[1] Marc Landmann,[1] Eva Rauls,[1] Nicola Argiolas,[2] Simone Sanna,[1] W. G. Schmidt,[1] and Arno Schindlmayr[1]

[1]*Department Physik, Universität Paderborn, 33095 Paderborn, Germany*
[2]*Dipartimento di Fisica e Astronomia, Universitá di Padova, 35131 Padova, Italy*

Correspondence should be addressed to Arno Schindlmayr; arno.schindlmayr@uni-paderborn.de

Received 8 September 2016; Revised 11 November 2016; Accepted 24 November 2016; Published 30 January 2017

Academic Editor: Pascal Roussel

Copyright © 2017 Falko Schmidt et al. This is an open access article distributed under the Creative Commons Attribution License, which permits unrestricted use, distribution, and reproduction in any medium, provided the original work is properly cited.

We perform a comprehensive theoretical study of the structural and electronic properties of potassium niobate ($KNbO_3$) in the cubic, tetragonal, orthorhombic, monoclinic, and rhombohedral phase, based on density-functional theory. The influence of different parametrizations of the exchange-correlation functional on the investigated properties is analyzed in detail, and the results are compared to available experimental data. We argue that the PBEsol and AM05 generalized gradient approximations as well as the RTPSS meta-generalized gradient approximation yield consistently accurate structural data for both the external and internal degrees of freedom and are overall superior to the local-density approximation or other conventional generalized gradient approximations for the structural characterization of $KNbO_3$. Band-structure calculations using a HSE-type hybrid functional further indicate significant near degeneracies of band-edge states in all phases which are expected to be relevant for the optical response of the material.

1. Introduction

The study of perovskites, oxidic compounds with the chemical formula ABO_3 and an ideal or distorted cubic crystal structure, is of both academic and technological interest. On one hand, perovskite minerals are the most abundant components in the Earth's mantle [1]. On the other hand, they exhibit a large variety of interesting physical properties [2, 3], which can be modified by composition-induced structural modifications.

Among the human-made perovskites, potassium niobate ($KNbO_3$) belongs to the important class of perovskite-structure ferroelectrics [4]. It crystallizes at about 1325 K in a paraelectric cubic phase (space group $Pm\bar{3}m$) and, similar to $BaTiO_3$ [5], undergoes three successive ferroelectric phase transitions [6]: to a tetragonal phase (space group $P4mm$) at 691 K, from the tetragonal to an orthorhombic phase (space group $Amm2$) at 498 K, and from the orthorhombic to a rhombohedral phase (space group $R3m$) at 263 K. In addition, a new monoclinic phase (space group Pm) was very recently discovered in $KNbO_3$ nanomaterials synthesized via a hydrothermal method [7]. It has long been known that the room-temperature orthorhombic phase, in particular, is characterized by unusual dielectric properties and an exceptionally large nonlinear optical coefficient. For this reason, $KNbO_3$ is widely used in nonlinear optics and holographic applications, where it represents a viable alternative to the more diffused $LiNbO_3$.

Due to its technological importance, pure and defective $KNbO_3$ has been subject to many experimental [8–12] and theoretical [13–19] studies. The previous theoretical investigations were typically aimed at the description of the ground-state structure and the identification of defect centers relevant for the optical properties. For the most part, they used density-functional theory [20, 21] with classical local or semilocal exchange-correlation functionals or even simpler semiempirical models. While these approaches are appropriate for atomic geometries and the mechanical properties of a material if not too high accuracy is required, they are much less accurate with regard to the electronic and

optical properties, because important factors like quasiparticle renormalization of the electronic band gap, thermal effects due to the electron-phonon coupling, or excitonic effects in the linear and nonlinear optical absorption are missing. Furthermore, most of the published work so far concentrated on the structurally simple cubic and tetragonal phases, while less attention has been given to the remaining polymorphs. As a consequence, a thorough quantitative *ab initio* study of the electronic and optical properties of $KNbO_3$, especially of the more complex but technologically relevant room-temperature phase, with state-of-the-art methods that go beyond density-functional theory and take the above-mentioned effects into account, as recently carried out for its sister material $LiNbO_3$ [22–25], is still missing. The accurate theoretical description of the atomic structure of the relevant $KNbO_3$ phases remains a prerequisite for all such studies, however.

In order to pave the way for future investigations along these lines, here we perform a comprehensive study of the structural and electronic properties of all the five known phases of $KNbO_3$, including the newly discovered monoclinic phase, based on density-functional theory. The influence of different parametrizations of the exchange-correlation functional on the investigated properties is discussed in detail, and the results are compared to available experimental data. Such a systematic approach is especially important for $KNbO_3$ because the energetic separation and the structural differences between the various phases are small and therefore potentially sensitive to details of the computational procedure. Indeed, our results show that several recently introduced exchange-correlation functionals give, overall, a better description of the atomic geometries throughout the various phases than common standard functionals as used in earlier studies. Band-structure calculations are additionally performed with a nonlocal hybrid functional to correct the well-known underestimation of the fundamental band gap incurred with conventional local or semilocal functionals, which stems from the absence of a derivative discontinuity with respect to the particle number as in the exact functional [26, 27].

This paper is organized as follows. In Section 2, we give an overview of our computational method. In Section 3, we present our results for the optimized atomic geometries of the five considered phases of $KNbO_3$ and compare the performances of different exchange-correlation functionals in relation to experimental data. Furthermore, we discuss the effects of the differently broken symmetries on the electronic band structure through the successive phase transitions. We finally summarize our conclusions in Section 4.

2. Computational Method

All calculations of this study are performed with the Vienna *Ab initio* Simulation Package (VASP) [28, 29], a plane-wave implementation of density-functional theory (DFT). The electron-ion interaction is described by the projector-augmented-wave (PAW) scheme [29, 30], where the K 3*s* and the Nb 4*s* electrons are treated explicitly as valence states. For the exchange and correlation between the electrons, we test several different schemes in order to compare their performance, namely, the local-density approximation (LDA), semilocal generalized gradient approximations (GGA), a semilocal meta-GGA, and a nonlocal hybrid functional. In detail, we use the LDA as parametrized by Perdew and Zunger [31]. The conventional Perdew-Burke-Ernzerhof (PBE) parametrization [32] and the more recently introduced PBEsol [33] and AM05 [34] functionals are considered on the GGA side; the latter two are chosen because they are known to yield accurate lattice parameters comparable to hybrid-functional DFT calculations at a moderate computational cost [35]. Furthermore, the revised Tao-Perdew-Staroverov-Scuseria (RTPSS) meta-GGA [36] is employed. Band-structure calculations are additionally performed for the relaxed PBEsol geometries with the Heyd-Scuseria-Ernzerhof (HSE) screened-Coulomb-potential hybrid functional [37, 38]. The fraction of the exact exchange from Hartree-Fock theory, 25% in the conventional HSE06 functional, is increased to 30% to match the experimentally observed band gap of the cubic $KNbO_3$ phase. Nonlocal HSE-type hybrid functionals offer a reliable way to approximate more rigorous band-structure calculation schemes within the framework of quasiparticle theory and thus effectively overcome the band gap problem of conventional DFT calculations with local or semilocal exchange-correlation functionals at a lower numerical cost [39, 40].

The electronic wave functions are expanded into plane waves up to a kinetic energy of 600 eV for the lattice-parameter optimization. All structural degrees of freedom are relaxed until the forces on each atom are below 0.001 meV/Å. The cutoff energy is reduced to 400 eV in the hybrid-functional band-structure calculations. The Brillouin-zone integrations are performed using a shifted Monkhorst-Pack $6 \times 6 \times 6$ **k**-point mesh for all $KNbO_3$ phases. In calculations with the HSE hybrid functional, a regular Γ-centered $6 \times 6 \times 6$ **k**-point mesh is used instead.

3. Results and Discussion

Figure 1 illustrates the five different phases of $KNbO_3$ considered here with exaggerated deformations from the cubic configuration (Figure 1(a)). Starting from the cubic phase, the tetragonal phase is reached by elongation along a axis and compression along the other two axes (Figure 1(b)). Further distortions of the lattice parameters transform the tetragonal phase into an orthorhombic polymorph with distinct lattice parameters a', b', and c' (Figure 1(c), left). The crystal structure of orthorhombic $KNbO_3$, whose rectangular unit cell contains two formula units, that is, ten atoms, can alternatively be characterized by a smaller rhombic unit cell with lattice parameters $a \neq b = c$ and $\alpha \neq \beta = \gamma = 90^\circ$ which contains only one formula unit (Figure 1(c), right); it is this nonrectangular primitive unit cell that we employ in all structure optimizations and electronic-structure calculations. The relation between the orthorhombic and the rhombic unit cells, including the ion displacements, is further illustrated in Figure 2. The orthorhombic phase transforms into the monoclinic phase by choosing mutually distinct lattice parameters $a \neq b \neq c$ (Figure 1(d)). Alternatively,

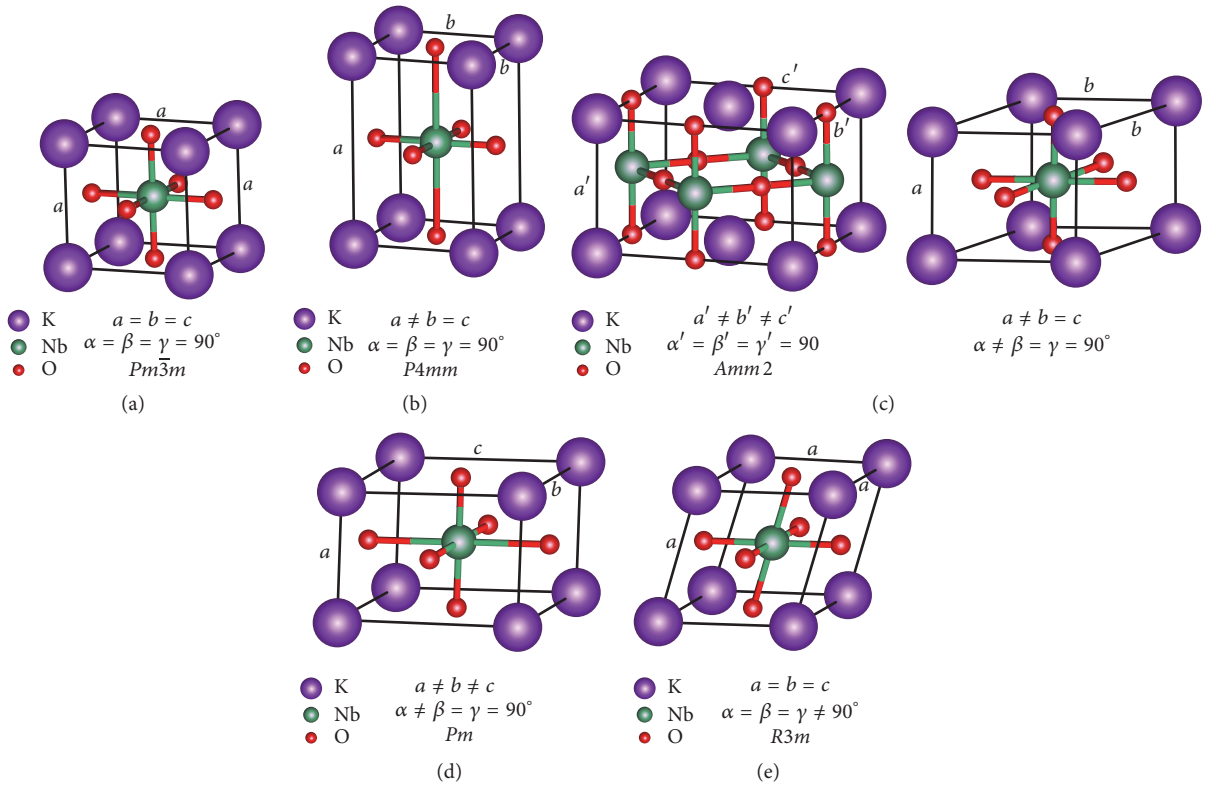

FIGURE 1: Different phases of $KNbO_3$: (a) cubic, (b) tetragonal, (c) orthorhombic (left: conventional orthorhombic unit cell, right: primitive rhombic unit cell), (d) monoclinic, and (e) rhombohedral with lattice parameters, angles, and space groups in Hermann-Mauguin notation. The deformations are actually small and are exaggerated here for clarity.

the rhombohedral phase is obtained by choosing equal lattice parameters $a = b = c$ together with equal but acute angles $\alpha = \beta = \gamma$ (Figure 1(e)).

3.1. Structure Optimization. In order to study the influence of different approximations for exchange and correlation on the DFT results for $KNbO_3$, we perform complete structure optimizations of the lattice parameters and the atomic displacements for all five phases using the LDA, PBE, PBEsol, AM05, and RTPSS functionals. We start with the high-temperature cubic phase and then follow the order in which the phases would occur for decreasing temperature.

Table 1 lists the calculated lattice parameter a and the optimized unit-cell volume V for the cubic phase obtained with the different exchange-correlation functionals as well as experimental data for comparison. Consistent with the cubic symmetry, all lattice parameters have precisely the same value, and all lattice vectors are perpendicular to each other. There are no internal degrees of freedom and hence no atomic displacements in the cubic phase. At first glance, the PBE results appear to agree best with the experimental lattice constant, but it must be borne in mind that the measurement was performed at 708 K, whereas the calculations correspond to 0 K. The good quantitative agreement is in fact fortuitous and due to an error cancellation between the neglect of thermal expansion and the well-known tendency of PBE (and other conventional GGAs) to overestimate lattice constants

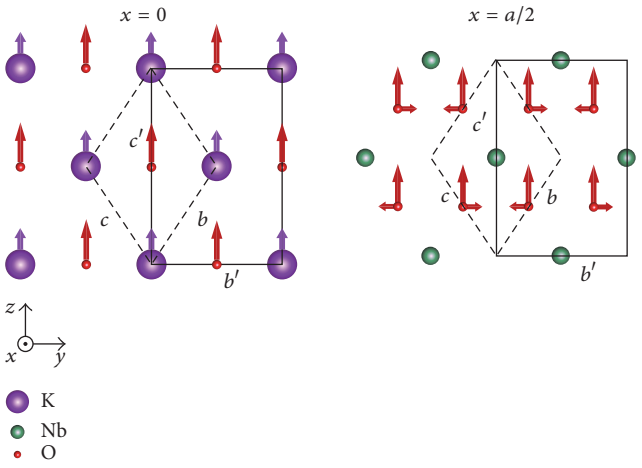

FIGURE 2: Atomic displacements in the conventional orthorhombic (solid lines) and primitive rhombic (dashed lines) unit cells of the orthorhombic $KNbO_3$ polymorph. The unit cell is split into two layers of atoms perpendicular to a axis. The deformations are exaggerated for clarity.

at zero temperature. The LDA predicts the smallest value for a, while the results from other functionals are in between; the same applies to the equilibrium unit-cell volume. In concordance with literature data on various other materials,

Table 1: Lattice parameter a and equilibrium unit-cell volume V calculated with different exchange-correlation functionals for the cubic phase of $KNbO_3$. Data in brackets represent relative deviations from the experimental values in percent.

$Pm\bar{3}m$	LDA	PBE	PBEsol	AM05	RTPSS	Expt.[a]
a (Å)	3.954 (−1.69)	4.024 (+0.05)	3.985 (−0.92)	3.989 (−0.82)	4.008 (−0.35)	4.022
V (Å^3)	61.72 (−5.13)	65.16 (+0.15)	63.28 (−2.74)	63.47 (−2.44)	64.38 (−1.05)	65.06

[a]Ref. [41]; measured at 708 K.

Table 2: Lattice parameters a and b, ratio a/b, equilibrium unit-cell volume V, atomic displacements along a axis in percent of a, and total-energy difference ΔE per formula unit with respect to cubic $KNbO_3$ calculated with different exchange-correlation functionals for the tetragonal phase of $KNbO_3$. Data in brackets represent relative deviations from the experimental values in percent.

$P4mm$	LDA	PBE	PBEsol	AM05	RTPSS	Expt.[a]
a (Å)	3.989 (−1.82)	4.193 (+3.20)	4.058 (−0.12)	4.098 (+0.86)	4.085 (+0.54)	4.063
b (Å)	3.945 (−1.30)	3.994 (−0.08)	3.969 (−0.70)	3.968 (−0.73)	3.992 (−0.13)	3.997
a/b	1.0112 (−0.52)	1.0498 (+3.28)	1.0224 (+0.58)	1.0328 (+1.60)	1.0233 (+0.67)	1.0165
V (Å^3)	62.08 (−4.36)	66.87 (+3.02)	63.93 (−1.51)	64.52 (−0.60)	65.10 (+0.29)	64.91
ΔK	1.072	1.762	1.462	1.635	1.634	1.8
ΔNb	0	0	0	0	0	0
ΔO1	2.859	6.142	4.109	4.972	4.277	4.4
ΔO2	3.026	4.962	3.850	4.352	3.934	4.0
ΔO3	3.026	4.962	3.850	4.352	3.934	4.0
ΔE (eV)	−0.0069	−0.0522	−0.0201	−0.0330	−0.0231	

[a]Ref. [41]; measured at 543 K.

we find that PBEsol, AM05, and RTPSS provide accurate and quite similar lattice parameters [36, 42–46].

For the tetragonal phase, the data listed in Table 2 is obtained with equal lattice parameters b and c and perpendicular lattice vectors. In contrast to the cubic phase, the displacements do not vanish in this case. If we keep the Nb atom fixed at its ideal position in the center of the unit cell, we observe that all other atoms shift towards positive values along a axis; displacements along the other axes are forbidden due to symmetry constraints. Since the experimental lattice parameters shown for comparison refer to 543 K and include effects of thermal expansion, the ratio a/b is also listed. The lattice parameter a is best matched by PBEsol, while the PBE value for b is closest to the experiment. The latter is fortuitous, however, as indicated by the large overestimation of a which exceeds 3% and constitutes the largest deviation among all tested functionals. The deficiency of the PBE functional is further reflected in the ratio a/b of 1.0498, which shows the strongest deviation from the experimental value of 1.0165, while LDA (1.0112) slightly underestimates the experimental value, PBEsol (1.0224) and RTPSS (1.0233) slightly overestimate it by a similar amount, and AM05 (1.0328) yields a somewhat larger ratio. Despite the reasonably accurate LDA lattice-parameter ratio, the associated equilibrium volume of the unit cell of 62.08 Å^3 shows the poorest agreement with the experimental volume of 64.91 Å^3. The equilibrium volume is excellently reproduced by the RTPSS value of 65.10 Å^3, followed by the AM05 value of 64.52 Å. As for the relative atomic displacements, all functionals except the LDA, which predicts systematically too small shifts, are in reasonable agreement with the experimental data. However, RTPSS clearly shows the best performance in the description of these internal degrees of freedom, aside from the accidentally close PBE displacement of the K atom. Overall, we thus conclude that PBEsol and RTPSS are well suited to describe the tetragonal phase of $KNbO_3$, although RTPSS provides the most balanced description of all structural degrees of freedom. This highlights the importance of incorporating all external as well as internal degrees of freedom in the evaluation of functional performance for structural properties.

Table 3 contains our results for the orthorhombic phase. We point out again that the primitive rhombic unit cell is not rectangular, as only the double unit cell exhibits the actual orthorhombic structure. The arrows in Figure 2 indicate the direction of the displacements in the plane perpendicular to a axis; there are no detectable displacements parallel to a. As can be seen, the atoms shift mainly along c' direction of the double unit cell. In the rotated basis system of the primitive single unit cell, the displacements have roughly equal components along b and c directions. As before, the LDA lattice parameters and volume substantially underestimate the experimental data. In addition, LDA tends strongly towards cubic symmetry, as indicated by the almost right angle of 89.91°, a/b ratio of 0.9922 that is close to unity, and the significantly underestimated atomic displacements. The PBE parametrization shows the smallest (for a) and largest (for b) deviations from the experimental values among all considered functionals, indicating a similar imbalance in the description of lattice parameters as observed for the tetragonal phase. In contrast, the functionals PBEsol, AM05, and RTPSS provide reasonable lattice parameters with comparably small deviations from the experimental values for both a and b. This more balanced description of lattice parameters

Table 3: Lattice parameters a and b, angle α, ratio a/b, equilibrium unit-cell volume V, atomic displacements in percent of b, and total-energy difference ΔE per formula unit with respect to cubic $KNbO_3$ calculated with different exchange-correlation functionals for the orthorhombic phase of $KNbO_3$. Data in brackets represent relative deviations from the experimental values in percent.

*Amm*2	LDA	PBE	PBEsol	AM05	RTPSS	Expt.[a]
a (Å)	3.940 (−0.83)	3.983 (+0.25)	3.961 (−0.30)	3.958 (−0.38)	3.984 (+0.28)	3.973
b (Å)	3.971 (−1.59)	4.100 (+1.61)	4.021 (−0.35)	4.043 (+0.20)	4.048 (+0.32)	4.035
α (°)	89.91 (+0.20)	89.66 (−0.08)	89.82 (+0.10)	89.76 (+0.03)	89.81 (+0.09)	89.73
a/b	0.9922 (+0.77)	0.9715 (−1.33)	0.9851 (+0.05)	0.9790 (−0.57)	0.9842 (−0.04)	0.9846
V (Å^3)	62.13 (−3.94)	66.95 (+3.51)	64.04 (−0.99)	64.70 (+0.03)	65.28 (+0.93)	64.68
ΔK	0.632	1.095	0.877	0.987	0.971	0.974
ΔNb	0	0	0	0	0	0
ΔO1	1.793	2.942	2.306	2.618	2.381	2.568
ΔO2	1.615	2.768	2.131	2.432	2.216	2.413
ΔO3	1.615	2.768	2.131	2.432	2.216	2.413
ΔE (eV)	−0.0080	−0.0617	−0.0245	−0.0401	−0.0289	

[a]Ref. [41]; measured at 295 K.

is underlined by improved a/b ratios with PBEsol (0.9851) and RTPSS (0.9842) which show virtually identical but opposing minimal deviations from the experimental value (0.9846). While all functionals predict a very similar small reduction of angle α, the experimental value of 89.73° is most accurately reproduced by AM05 (89.76°). AM05 also yields the equilibrium volume (64.70) closest to experiment (64.68). The three functionals PBEsol, AM05, and RTPSS not only yield results in reasonable quantitative agreement with the experimental data but also give a good account of the atomic displacements, although the best description of the internal degrees of freedom is provided by the AM05 parametrization. Overall, AM05 provides the best balanced description of all structural degrees of freedom in orthorhombic $KNbO_3$.

The results for the newly discovered monoclinic phase depend sensitively on the starting parameters for the atomic displacements, as the structure tends to relax to the orthorhombic phase for poorly chosen initial displacements. The only previous theoretical study of $KNbO_3$ in the monoclinic phase was reported by Zhang et al. [48]. In our simulations, we take the displacements given in [48] as the initial configuration. In this way, we eventually obtain a properly relaxed monoclinic structure, which corresponds to a local minimum of the total-energy landscape, indicating that the monoclinic phase is metastable not only for $KNbO_3$ nanomaterials but also for the bulk. The results listed in Table 4 show that the performance of the different functionals is the same as that for the related orthorhombic phase, which occurs in the same temperature range. The universal trends of underestimation and overestimation of lattice parameters by the LDA and PBE functionals are clearly reflected in equilibrium volumes of 62.13 Å^3 and 66.99 Å^3 which fall below or exceed the experimental volume of 64.86 Å^3, respectively. Surprisingly, LDA performs best for angle α as well as for the ratios a/b and a/c. A notable improvement over the LDA and PBE values is observable for the other functionals, but no clear trend emerges. PBEsol, AM05, and RTPSS provide virtually the same accuracy for the lattice parameters. The atomic displacements have again roughly equal components along b and c directions and no detectable component along a. Compared to PBEsol and RTPSS, AM05 shows a slight tendency towards larger atomic displacements. Although there are no directly comparable experimental values, the calculated displacements are compatible with those of Zhang et al. [48] based on density-functional theory in combination with the otherwise rarely used Wu-Cohen functional [49].

Finally, for the rhombohedral phase, we set the starting values for the displacements of all atoms except Nb to two percent along each lattice vector, because the structure tends to relax to the cubic phase for too small initial displacements. The resulting optimized values are listed in Table 5. The lattice parameter a and angle α obtained from PBEsol, AM05, and RTPSS are overall in good agreement with the experimental data. The performance of LDA and PBE follows that for the other phases and shows characteristic underestimation and overestimation of the lattice parameters, respectively. Our calculated atomic displacements are notably larger than those reported by Fontana et al. in 1984 [41], especially for the oxygen atoms. The reason for this discrepancy remains unclear. On one hand, the theoretical results are very consistent for all functionals considered here and thus appear robust. On the other hand, the low-temperature rhombohedral phase has received relatively little attention in the literature so far, so that there are no other, more recent experimental characterizations of this structure which could be used for further comparison. In our simulations, all displacements are predominantly along the spatial diagonal of the unit cell with roughly equal components along all three lattice vectors.

3.2. Phase Stability. For the purpose of comparison, Table 6 summarizes our results for the total-energy differences ΔE per formula unit for the various phases of $KNbO_3$, which correspond to the formation energies relative to the cubic polymorph. Although the numerical differences are generally small, we find that the rhombohedral structure is energetically favored by all exchange-correlation functionals considered in this work. As the calculations refer to 0 K, this is gratifyingly consistent with the experimental fact that the

Table 4: Lattice parameters a, b, and c, angle α, ratios a/b and a/c, equilibrium unit-cell volume V, atomic displacements in percent of b, and total-energy difference ΔE per formula unit with respect to cubic $KNbO_3$ calculated with different exchange-correlation functionals for the monoclinic phase of $KNbO_3$. Data in brackets represent relative deviations from the experimental values in percent.

Pm	LDA	PBE	PBEsol	AM05	RTPSS	Expt.[a]
a (Å)	3.940 (−1.28)	3.983 (−0.20)	3.961 (−0.75)	3.958 (−0.83)	3.984 (−0.18)	3.991
b (Å)	3.972 (−1.83)	4.104 (+1.43)	4.023 (−0.57)	4.045 (−0.02)	4.049 (+0.07)	4.046
c (Å)	3.970 (−1.17)	4.098 (+2.02)	4.020 (+0.07)	4.041 (+0.60)	4.047 (+0.75)	4.017
α (°)	89.91 (+0.02)	89.66 (−0.26)	89.82 (−0.08)	89.76 (−0.14)	89.81 (−0.09)	89.89
a/b	0.9919 (+0.56)	0.9705 (−1.61)	0.9846 (−0.18)	0.9785 (−0.80)	0.9839 (−0.25)	0.9864
a/c	0.9924 (−0.11)	0.9719 (−2.17)	0.9853 (−0.83)	0.9795 (−1.41)	0.9844 (−0.92)	0.9935
V (Å^3)	62.13 (−4.21)	66.99 (+3.28)	64.06 (−1.23)	64.70 (−0.25)	65.28 (+0.65)	64.86
ΔK	1.260	2.194	1.736	1.971	1.942	
ΔNb	0	0	0	0	0	
ΔO1	3.571	5.906	4.626	5.234	4.771	
ΔO2	3.208	5.583	4.262	4.876	4.443	
ΔO3	3.197	5.679	4.263	4.890	4.446	
ΔE (eV)	−0.0085	−0.0623	−0.0250	−0.0405	−0.0294	

[a]Ref. [47]; measured at 298 K.

Table 5: Lattice parameter a, angle α, equilibrium unit-cell volume V, atomic displacements in percent of a, and total-energy difference ΔE per formula unit with respect to cubic $KNbO_3$ calculated with different exchange-correlation functionals for the rhombohedral phase of $KNbO_3$. Data in brackets represent relative deviations from the experimental values in percent.

R3m	LDA	PBE	PBEsol	AM05	RTPSS	Expt.[a]
a (Å)	3.961 (−1.37)	4.059 (+1.07)	4.001 (−0.37)	4.014 (−0.05)	4.027 (+0.27)	4.016
α (°)	89.95 (+0.03)	89.80 (−0.13)	89.90 (−0.02)	89.86 (−0.07)	89.95 (+0.03)	89.92
V (Å^3)	62.15 (−4.05)	66.87 (+3.24)	64.05 (−1.11)	64.67 (−0.15)	65.30 (+0.82)	64.77
ΔK	1.296	2.281	1.794	2.046	2.037	1.300
ΔNb	0	0	0	0	0	0
ΔO1	3.340	5.548	4.360	4.945	4.580	0.301
ΔO2	3.340	5.548	4.360	4.945	4.580	0.333
ΔO3	3.340	5.548	4.360	4.945	4.580	0.333
ΔE (eV)	−0.0087	−0.0623	−0.0256	−0.0410	−0.0305	

[a]Ref. [41]; measured at 230 K.

Table 6: Calculated total-energy differences ΔE with respect to the cubic phase in eV per formula unit with different exchange-correlation functionals for the five phases of $KNbO_3$.

Phase	LDA	PBE	PBEsol	AM05	RTPSS
$Pm\bar{3}m$	0	0	0	0	0
P4mm	−0.0069	−0.0522	−0.0201	−0.0330	−0.0231
Amm2	−0.0080	−0.0617	−0.0245	−0.0401	−0.0289
Pm	−0.0085	−0.0623	−0.0250	−0.0405	−0.0294
R3m	−0.0087	−0.0623	−0.0256	−0.0410	−0.0305

rhombohedral phase is stable in the low-temperature limit. It is followed, in ascending order, by the monoclinic, the orthorhombic, the tetragonal, and finally the cubic structure, consistent among all functionals. The energetic ordering of the different phases thus follows the sequence in which they become stable for increasing temperature. A proper *ab initio* description of the phase transitions requires a numerical evaluation of the temperature-dependent free energies with the full incorporation of phonon contributions [54] which goes beyond the present study, however.

Figure 3 illustrates the correlation between the unit-cell volume and the relative formation energies. The remarkably narrow spread of the LDA results and the much larger spread of the PBE results for the different phases are clearly visible. This is in accordance with our earlier observation that the LDA tends to underestimate and PBE tends to overestimate symmetry-breaking deformations relative to the cubic structure. The PBEsol and AM05 results lie between the LDA and PBE values, indicating a more balanced description of the structure and energetics. The RTPSS results span a similar energy range as PBEsol and AM05 but are shifted to slightly larger volumes. In addition, Figure 3 shows an almost linear dependence of the formation energies on the unit-cell volume, suggesting a dominant volume effect on the phase stability of the $KNbO_3$ polymorphs. Similar trends in the correlation between formation energies and equilibrium volume have also been observed for other oxide materials that exhibit extended structure polymorphism [55, 56].

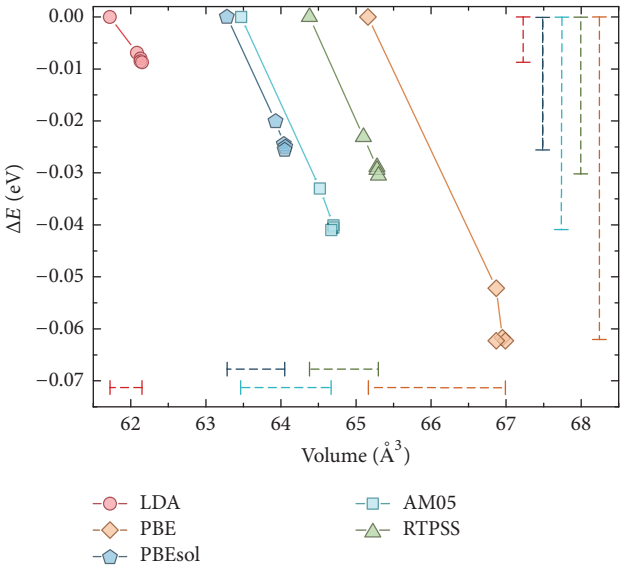

Figure 3: Correlation between the equilibrium unit-cell volume V and the total-energy difference per formula unit ΔE with respect to the cubic phase calculated with different exchange-correlation functionals. The solid lines are intended to guide the eyes. The dashed bars indicate the total volume and energy ranges encompassing all five $KNbO_3$ phases for a particular functional.

3.3. Functional Performance. The underestimation and overestimation of lattice parameters by LDA and by conventional generalized gradient approximations like PBE, respectively, observed consistently throughout this work for all investigated $KNbO_3$ polymorphs, are well known and documented for a large variety of materials [45, 57, 58]. In particular, these trends were confirmed in a DFT study of various ferroelectric perovskites by Tinte et al. [59]. Nevertheless, the reasonable overall agreement with experimental data together with the well-understood performance in numerical simulations makes these established functionals a sound reference for the benchmarking of other exchange-correlation functionals. The improved prediction of structural data by PBEsol, AM05, and RTPSS observed here for $KNbO_3$ is likewise in accordance with recent studies for simple metallic and semiconducting systems [36, 42–46, 58], but our results demonstrate that this extends to oxides with various stable and metastable polymorphs of complex symmetry, which exhibit manifold internal degrees of freedom. We note in this context that it is also possible to improve conventional semilocal functionals through restriction to specific classes of materials by introducing system-dependent parameters that modify the localization of the exchange-correlation hole [59], an idea that is not strictly *ab initio* but presently has a strong influence on the construction and use of hybrid functionals.

The energetic ordering (Table 6) of the five $KNbO_3$ polymorphs is identical for all considered functionals and, most importantly, in accordance with the observed experimental sequence. Hence, even though the LDA energy differences are close to the overall numerical accuracy of current implementations of plane-wave DFT for solid-state systems, this does not disqualify any of the considered exchange-correlation functionals from applications to $KNbO_3$. This happenstance of correct phase ordering independent of specific functionals, especially among structurally complex oxides characterized by polymorph-rich phase diagrams, is in fact rather fortuitous. In the case of TiO_2, for example, common local (LDA) and semilocal (PBE and PBEsol) as well as hybrid functionals fail to reproduce the experimentally observed energy ordering among the three main crystallographic phases rutile, anatase, and brookite, which structurally differ solely by distortions and rearrangements of the TiO_6 octahedral building blocks [60–63]. Furthermore, the choice of exchange-correlation functionals in general, as well as the fraction of exact exchange in various hybrid functionals, has been found to alter the phase stability of oxide systems [63, 64].

Table 7: Complete list of calculated PBEsol lattice parameters for the five different phases of $KNbO_3$, which are used in the HSE electronic-structure calculations.

Phase	$Pm\bar{3}m$	$P4mm$	$Amm2$	Pm	$R3m$
a (Å)	3.985	4.058	3.961	3.961	4.001
b (Å)	3.985	3.969	4.021	4.023	4.001
c (Å)	3.985	3.969	4.021	4.020	4.001
α (°)	90	90	89.82	89.82	89.90
β (°)	90	90	90	90	89.90
γ (°)	90	90	90	90	89.90

The body of data for the atomic structure and phase energetics suggests that there is no good justification to stick to the LDA or to conventional GGAs when dealing with complex oxide materials. More recent parametrizations like PBEsol or AM05, which specifically aim at an accurate description of solid-state systems, as well as meta-GGAs like RTPSS, constructed to satisfy a maximum of exact constraints for the exchange-correlation functional without empirical parameters, offer a reliable and numerically efficient way to improve the accuracy of state-of-the-art *ab initio* simulations. All three functionals provide a sound basis for subsequent calculations. In the following, we largely restrict the analysis of the electronic structure to the PBEsol geometries summarized in Table 7, as we do not expect qualitatively different trends for geometries from AM05 or RTPSS. In view of future studies, these functionals seem to be well suited as a starting point not only for hybrid-functional DFT but also for higher-level perturbative approaches within the framework of many-body perturbation theory [65]. The analysis of vibrational properties in $KNbO_3$ will equally benefit from the qualitative and quantitative reliability provided by these functionals, as recently demonstrated for the related material $LiNbO_3$ [24].

3.4. Band Structures. We now proceed to analyzing the effects of the structural deformations in the various phases on the electronic band structures. In a preliminary step, we study the influence of the structural parameters and the exchange-correlation functionals for the cubic phase, which serves as a test case. Table 8 shows results for the fundamental band

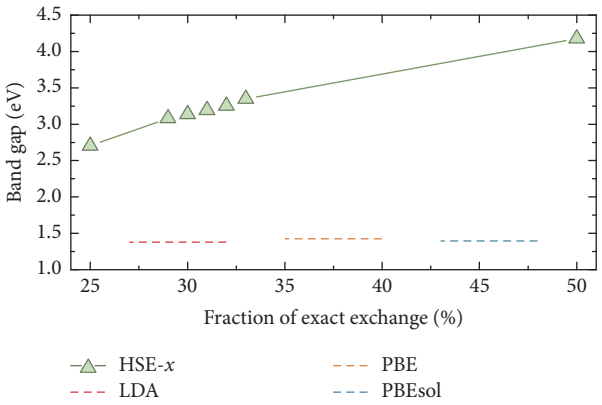

Figure 4: Fundamental $R_v \rightarrow \Gamma_c$ band gaps for the cubic phase of $KNbO_3$ calculated with different exchange-correlation functionals (see Table 8). The HSE-x band gaps are calculated for PBEsol equilibrium geometries and depend on the fraction of exact exchange x. The solid lines are intended to guide the eyes. The dashed lines mark the size of the fundamental LDA, PBE, and PBEsol band gaps.

gaps with different combinations of structural parameters (see Table 1) and functionals. In all cases, the band gap is predicted to be indirect and corresponds to a transition between the valence-band maximum at R, the corner of the cubic Brillouin zone, and the conduction-band minimum at Γ, its center. Furthermore, we find that the band gap is not very sensitive to the lattice parameter and that, as expected, all (semi)local functionals like LDA, PBE, or PBEsol systematically underestimate the reported experimental values, which lie between 3.14 eV [50] and 3.24 eV [52]. According to the preceding section, we consistently use structural parameters from PBEsol (see Table 7) from now on, and we perform a series of additional band-structure calculations with the nonlocal HSE functional. In our notation, HSE-x means that the HSE functional is used with x percent exact exchange, which we treat as a tunable parameter. Depending on x, the hybrid-functional band gap can be positioned between the lower limit of (semi)local DFT and the upper limit of Hartree-Fock theory. In Figure 4, the dependence of the fundamental band gap of cubic $KNbO_3$ on the fraction of exact exchange is illustrated for $25 \leq x \leq 50$. In the most relevant region $28 \leq x \leq 32$, close to the experimentally reported band gap, an almost linear dependence on x is observed. The LDA, PBE, and PBEsol band gaps are shown for comparison and exhibit an underestimation by a factor of one half. According to Table 8, a choice of 30% exact exchange leads to much better agreement with the experimental band gap than the standard setting of 25%, so that we use the HSE-30 variant in the following. The improved description of band gaps and the electronic structure in general with an increased fraction of exact exchange in HSE-type hybrid functionals has previously been demonstrated for oxide semiconductors [61] and nitride semiconductor alloys [66, 67], for instance. Wang et al. [68] also noted that an increased fraction of exact exchange improves the band gap of $KNbO_3$. Although adjusting the fraction of exact exchange for a single polymorph might not yield perfect agreement between experiment and theory for other phases, it represents a reasonable approach to study physical trends among the various polymorphs.

Table 8: Fundamental $R_v \rightarrow \Gamma_c$ band gaps for the cubic phase of $KNbO_3$ calculated with different lattice parameters and exchange-correlation functionals (see Figure 4).

Geometry	Functional	Band gap (eV)
Expt.	PBE	1.426
LDA	LDA	1.377
PBE	PBE	1.426
	PBEsol	1.125
PBEsol	PBE	1.540
	PBEsol	1.396
PBEsol	HSE-25	2.701
	HSE-29	3.080
	HSE-30	3.138
	HSE-31	3.194
	HSE-32	3.252
	HSE-33	3.346
	HSE-50	4.176

Table 9: Fundamental band gaps for the different phases of $KNbO_3$ with the HSE-30 functional from the band structures in Figure 5 compared to experimental values.

Phase	HSE-30		Expt.
	Transition	Band gap (eV)	Band gap (eV)
$Pm\bar{3}m$	$R_v \rightarrow \Gamma_c$	3.14	3.14[a], 3.16[b], 3.24[c]
$P4mm$	$M_v \rightarrow \Gamma_c$	3.23	3.08[c], 3.30[d]
$Amm2$	$T_v \rightarrow \Gamma_c$	3.59	3.15[c], 3.17[e], 3.25[f]
Pm	$A_v \rightarrow \Gamma_c$	3.63	3.09[e], 3.15[f]
$R3m$	$Z_v \rightarrow \Gamma_c$	3.80	

[a]Ref. [50]; optical gap from absorption spectrum.
[b]Ref. [51]; optical gap from UV-vis diffuse reflectance spectrum.
[c]Ref. [52]; optical gap from absorption spectrum.
[d]Ref. [53]; optical gap from X-ray photoelectron spectrum.
[e]Ref. [47]; optical gap from absorption spectrum.
[f]Ref. [48]; optical gap from diffuse reflectance UV-vis spectroscopy.

Figure 5 shows the calculated band structures for the five different phases of $KNbO_3$. Furthermore, in Table 9, we compare the fundamental band gaps with experimental values. The calculated HSE-30 band gaps show a broad spread of 0.66 eV between the fundamental band gaps of cubic (3.14 eV) and rhombohedral (3.80 eV) $KNbO_3$. It should be noted that our results refer to electronic band gaps, which can be measured, in principle, by photoemission spectroscopy. No such measurements have been reported for $KNbO_3$ so far, however. Instead, the experimental values listed in the table are deduced from optical spectroscopies and thus refer to optical band gaps. The difference between the two equals the exciton binding energy, whose magnitude is unknown for $KNbO_3$, but detailed investigations of the related material $LiNbO_3$ [25] suggest that it may be significant. In addition, the experimental values include thermal effects due to thermal expansion and electron-phonon coupling, particularly in the high-temperature phases, as well as size and geometry

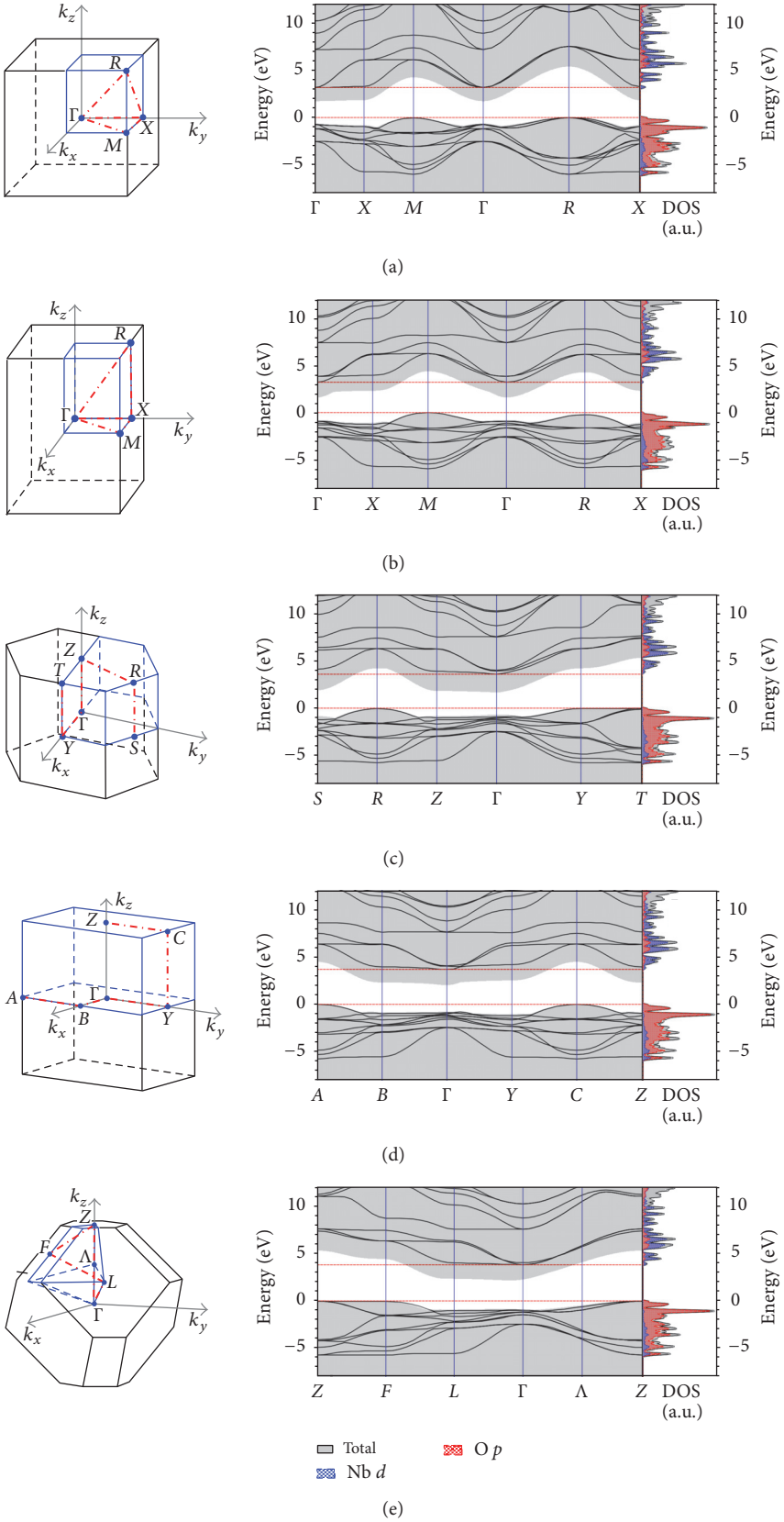

FIGURE 5: Band structures calculated with the HSE-30 functional for the cubic (a), tetragonal (b), orthorhombic (c), monoclinic (d), and rhombohedral (e) phases of $KNbO_3$ with corresponding densities of states (DOS) in arbitrary units. The grey-shaded areas indicate the PBE band structures for comparison, and the dashed horizontal lines mark the valence-band maxima and conduction-band minima. All band-structure calculations are based on structural data from PBEsol (see Table 7). On the left-hand side, the chosen paths within the first Brillouin zone are indicated by thick dash-dotted lines.

Table 10: Calculated valence-band edge $E_v(\mathbf{k})$ and conduction-band edge $E_c(\mathbf{k})$ at high-symmetry $\mathbf{k}$ points for the different phases of $KNbO_3$. Energies are given in eV relative to the position of the valence-band maximum. The valence-band maximum and the conduction-band minimum are italicized.

Cubic ($Pm\bar{3}m$)			Tetragonal ($P4mm$)			Orthorhombic ($Amm2$)			Monoclinic (Pm)			Rhombohedral ($R3m$)		
$\mathbf{k}$	$E_v(\mathbf{k})$	$E_c(\mathbf{k})$	$\mathbf{k}$	$E_v(\mathbf{k})$	$E_c(\mathbf{k})$	$\mathbf{k}$	$E_v(\mathbf{k})$	$E_c(\mathbf{k})$	$\mathbf{k}$	$E_v(\mathbf{k})$	$E_c(\mathbf{k})$	$\mathbf{k}$	$E_v(\mathbf{k})$	$E_c(\mathbf{k})$
Γ	−0.72	*3.14*	Γ	−0.90	*3.23*	S	−1.23	4.10	A	*0*	6.34	Z	*0*	7.35
X	−0.94	3.27	X	−1.24	3.96	R	−0.04	6.30	B	−0.97	3.92	F	−0.04	6.13
M	−0.04	6.11	M	*0*	6.26	Z	−1.01	3.87	Γ	−0.88	*3.63*	L	−1.04	3.98
R	*0*	7.51	R	−0.21	6.16	Γ	−0.92	*3.59*	Y	−1.19	4.14	Γ	−0.97	*3.80*
						Y	−0.04	6.30	C	−0.004	6.34	Λ	−0.60	5.71
						T	*0*	7.36	Z	−0.97	3.90			

effects, because the experiments were typically not carried out for bulk samples but for nanostructures, such as microcubes in [52] or nanowires in [48]. Nanoparticles of TiO_2, for instance, exhibit much smaller band gaps than in the bulk [69]. For all these reasons, the comparison in Table 9 can only be indicative. No experimental band gap is available for the rhombohedral phase, but our results are consistent with earlier calculations by Wang and Rappe [70] which yielded a fundamental band gap of 3.33 eV with the HSE-25 functional and LDA structural data; our own HSE-25 calculation with structural data from PBEsol for the rhombohedral phase yields 3.38 eV.

The graphical band structures in Figure 5 as well as the numerical data in Table 10, which lists energy values of the highest valence band and the lowest conduction band at selected high-symmetry $\mathbf{k}$ points, confirm that in all phases there are states elsewhere in the Brillouin zone which are nearly degenerate with the valence-band maximum or the conduction-band minimum. For example, in the orthorhombic phase that is stable at room temperature, the valence-band edge at Y lies only 0.04 eV below the valence-band maximum, which is located at T. It is expected that such near degeneracies strongly influence the optical properties close to the absorption edge due to strong mixing of electronic transitions at different $\mathbf{k}$ points in the optical response. The corresponding densities of states (DOS) in Figure 5 share many similar features, independent of the particular polymorph. The DOS contributions from the K atoms are negligible around the band edges in all phases. The topmost valence bands are consistently formed by oxygen $2p$ states and give rise to two prominent peaks close to the valence-band edge: the first peak arises from the valence-band maximum and the nearly degenerate electronic states at other high-symmetry $\mathbf{k}$ points, while the second peak originates from an almost degenerate continuum of states around Γ; its energetic distance from the conduction-band edge equals the direct band gap at Γ for all $KNbO_3$ phases. The lowest conduction bands, in contrast, are mainly formed by niobium $4d$ states.

4. Conclusions

In summary, we have performed a comprehensive analysis of the structural and electronic properties of $KNbO_3$ in its five known phases, including the only very recently discovered monoclinic phase, based on density-functional theory. As the energetic separation and the structural differences between the phases are small and thus potentially sensitive to details of the computational procedure, we have placed special emphasis on the influence of different approximations for the exchange-correlation functional. To this end, we compared the LDA with a range of GGAs, a meta-GGA, and, in the case of band structures, a HSE-type hybrid functional. As an important result, we find that all functionals predict the same energetic ordering of the phases, which, moreover, coincides with the order in which the phases become stable for increasing temperature. Our results further confirm that the monoclinic configuration, which has so far only been observed in synthesized nanostructures, is also metastable in the bulk. Among the considered functionals, PBEsol as well as AM05 and RTPSS yield structural data in consistently good quantitative agreement with experimental measurements for all phases; in contrast, LDA and PBE systematically underestimate and overestimate the lattice parameters, respectively, and are also less accurate with respect to the atomic displacements inside the unit cell. For this reason, we even-handedly recommend PBEsol, AM05, or RTPSS as reasonable starting points for *ab initio* investigations with higher-level perturbative methods that require accurate equilibrium geometries. In particular, phonons, which not only are crucial in the context of phase transitions but also play a significant role for the temperature dependence of the electronic and optical properties due to the electron-phonon coupling, are sensitive to small changes in the atomic spacing.

Our band-structure calculations performed with the HSE hybrid functional and 30% exact exchange confirm that the fundamental band gap is indirect for all phases. The variation in the size of the gap amounts to 0.66 eV through the successive phase transitions. In particular, in the room-temperature orthorhombic phase, the band gap is appreciably larger than in the tetragonal phase, which is often used as a structurally simpler substitute in theoretical simulations. For all phases, our results further indicate a range of near degeneracies of band-edge states in different parts of the Brillouin zone which are expected to be relevant for the linear and nonlinear optical properties of $KNbO_3$. More elaborate *ab initio* band-structure calculations with a proper treatment of quasiparticle and thermal effects, which go beyond the present study, are highly desirable, however.

Competing Interests

The authors declare that there are no competing interests regarding the publication of this paper.

Acknowledgments

The authors gratefully acknowledge financial support from the Deutsche Forschungsgemeinschaft (DFG) via Sonderforschungsbereich TRR 142.

References

[1] C.-M. Fang and R. Ahuja, "Structures and stability of ABO_3 orthorhombic perovskites at the Earth's mantle conditions from first-principles theory," *Physics of the Earth and Planetary Interiors*, vol. 157, no. 1-2, pp. 1–7, 2006.

[2] R. H. Mitchell, *Perovskites: Modern and Ancient*, Almaz Press, Thunder Bay, Canada, 2002.

[3] R. J. D. Tilley, *Perovskites: Structure-Property Relationships*, John Wiley & Sons, Chichester, UK, 2016.

[4] B. T. Matthias, "New ferroelectric crystals," *Physical Review*, vol. 75, no. 11, p. 1771, 1949.

[5] S. Sanna, C. Thierfelder, S. Wippermann, T. P. Sinha, and W. G. Schmidt, "Barium titanate ground- and excited-state properties from first-principles calculations," *Physical Review B*, vol. 83, no. 5, Article ID 054112, 2011.

[6] A. W. Hewat, "Cubic-tetragonal-orthorhombic-rhombohedral ferroelectric transitions in perovskite potassium niobate: neutron powder profile refinement of the structures," *Journal of Physics C: Solid State Physics*, vol. 6, no. 16, pp. 2559–2572, 1973.

[7] S. Kim, J.-H. Lee, J. Lee et al., "Synthesis of monoclinic potassium niobate nanowires that are stable at room temperature," *Journal of the American Chemical Society*, vol. 135, no. 1, pp. 6–9, 2013.

[8] S. Simsek, H. Koc, V. A. Trepakov, A. M. Mamedov, and E. Ozbay, "Electron spectroscopy and the electronic structure of $KNbO_3$: first principle calculations," *Ferroelectrics*, vol. 461, no. 1, pp. 99–105, 2014.

[9] L. Grigorjeva, D. K. Millers, V. Pankratov et al., "Experimental and theoretical studies of polaron optical properties in $KNbO_3$ perovskite," *Solid State Communications*, vol. 129, no. 11, pp. 691–696, 2004.

[10] E. A. Kotomin, R. I. Eglitis, G. Borstel, L. Grigorjeva, D. Millers, and V. Pankratov, "Theoretical and experimental study of primary radiation defects in $KNbO_3$ perovskite crystals," *Nuclear Instruments and Methods in Physics Research B*, vol. 166-167, pp. 299–304, 2000.

[11] E. E. Krasovskii, O. V. Krasovska, and W. Schattke, "Ab initio calculation of the optical and photoelectron spectra of $KNbO_3$ and $KTaO_3$," *Journal of Electron Spectroscopy and Related Phenomena*, vol. 83, no. 2-3, pp. 121–127, 1997.

[12] S. Torbrügge, M. Imlau, B. Schoke et al., "Optically generated small electron and hole polarons in nominally undoped and Fe-doped $KNbO_3$ investigated by transient absorption spectroscopy," *Physical Review B*, vol. 78, no. 12, Article ID 125112, 2008.

[13] H. Donnerberg and M. Exner, "Derivation and application of ab initio Nb^{5+}–O^{2-} short-range effective pair potentials in shell-model simulations of $KNbO_3$ and $KTaO_3$," *Physical Review B*, vol. 49, no. 6, pp. 3746–3754, 1994.

[14] T. Neumann, G. Borstel, C. Scharfschwerdt, and M. Neumann, "Electronic structure of $KNbO_3$ and $KTaO_3$," *Physical Review B*, vol. 46, no. 17, pp. 10623–10628, 1992.

[15] S. Cabuk, "Electronic structure and optical properties of $KNbO_3$: first principles study," *Optoelectronics and Advanced Materials—Rapid Communications*, vol. 1, no. 3, pp. 100–107, 2007.

[16] A. V. Postnikov, T. Neumann, G. Borstel, and M. Methfessel, "Ferroelectric structure of $KNbO_3$ and $KTaO_3$ from first-principles calculations," *Physical Review B*, vol. 48, no. 9, pp. 5910–5918, 1993.

[17] R. I. Eglitis, A. V. Postnikov, and G. Borstel, "Semiempirical Hartree-Fock calculations for $KNbO_3$," *Physical Review B*, vol. 54, no. 4, pp. 2421–2427, 1996.

[18] E. A. Kotomin, R. I. Eglitis, A. V. Postnikov, G. Borstel, and N. E. Christensen, "First-principles and semiempirical calculations for bound-hole polarons in $KNbO_3$," *Physical Review B*, vol. 60, no. 1, pp. 1–5, 1999.

[19] N. E. Christensen, E. A. Kotomin, R. I. Eglitis et al., "Quantum mechanical modelling of pure and defective $KNbO_3$ perovskites," in *Defects and Surface-Induced Effects in Advanced Perovskites*, G. Borstel, A. Krumins, and D. K. Millers, Eds., pp. 3–16, Kluwer, Dordrecht, The Netherlands, 2000.

[20] P. Hohenberg and W. Kohn, "Inhomogeneous electron gas," *Physical Review*, vol. 136, no. 3B, pp. B864–B871, 1964.

[21] W. Kohn and L. J. Sham, "Self-consistent equations including exchange and correlation effects," *Physical Review*, vol. 140, no. 4A, pp. A1133–A1138, 1965.

[22] C. Thierfelder, S. Sanna, A. Schindlmayr, and W. G. Schmidt, "Do we know the band gap of lithium niobate?" *Physica Status Solidi (C) Current Topics in Solid State Physics*, vol. 7, no. 2, pp. 362–365, 2010.

[23] A. Riefer, S. Sanna, A. Schindlmayr, and W. G. Schmidt, "Optical response of stoichiometric and congruent lithium niobate from first-principles calculations," *Physical Review B*, vol. 87, no. 19, Article ID 195208, 2013.

[24] M. Friedrich, A. Riefer, S. Sanna, W. G. Schmidt, and A. Schindlmayr, "Phonon dispersion and zero-point renormalization of $LiNbO_3$ from density-functional perturbation theory," *Journal of Physics Condensed Matter*, vol. 27, no. 38, Article ID 385402, 2015.

[25] A. Riefer, M. Friedrich, S. Sanna, U. Gerstmann, A. Schindlmayr, and W. G. Schmidt, "$LiNbO_3$ electronic structure: many-body interactions, spin-orbit coupling, and thermal effects," *Physical Review B*, vol. 93, no. 7, Article ID 075205, 2016.

[26] L. J. Sham and M. Schlüter, "Density-functional theory of the energy gap," *Physical Review Letters*, vol. 51, no. 20, pp. 1888–1891, 1983.

[27] J. P. Perdew, "Density functional theory and the band gap problem," *International Journal of Quantum Chemistry*, vol. 28, no. 19S, pp. 497–523, 1985.

[28] G. Kresse and J. Furthmüller, "Efficiency of ab-initio total energy calculations for metals and semiconductors using a plane-wave basis set," *Computational Materials Science*, vol. 6, no. 1, pp. 15–50, 1996.

[29] G. Kresse and D. Joubert, "From ultrasoft pseudopotentials to the projector augmented-wave method," *Physical Review B*, vol. 59, no. 3, pp. 1758–1775, 1999.

[30] P. E. Blöchl, "Projector augmented-wave method," *Physical Review B*, vol. 50, no. 24, pp. 17953–17979, 1994.

[31] J. P. Perdew and A. Zunger, "Self-interaction correction to density-functional approximations for many-electron systems," *Physical Review B*, vol. 23, no. 10, pp. 5048–5079, 1981.

[32] J. P. Perdew, K. Burke, and Y. Wang, "Generalized gradient approximation for the exchange-correlation hole of a many-electron system," *Physical Review B*, vol. 54, no. 23, pp. 16533–16539, 1996.

[33] J. P. Perdew, A. Ruzsinszky, G. I. Csonka et al., "Restoring the density-gradient expansion for exchange in solids and surfaces," *Physical Review Letters*, vol. 100, no. 13, Article ID 136406, 2008.

[34] R. Armiento and A. E. Mattsson, "Functional designed to include surface effects in self-consistent density functional theory," *Physical Review B*, vol. 72, no. 8, Article ID 085108, 2005.

[35] A. E. Mattsson, R. Armiento, J. Paier, G. Kresse, J. M. Wills, and T. R. Mattsson, "The AM05 density functional applied to solids," *Journal of Chemical Physics*, vol. 128, no. 8, Article ID 084714, 2008.

[36] J. Sun, M. Marsman, G. I. Csonka et al., "Self-consistent meta-generalized gradient approximation within the projector-augmented-wave method," *Physical Review B*, vol. 84, no. 3, Article ID 035117, 2011.

[37] J. Heyd, G. E. Scuseria, and M. Ernzerhof, "Hybrid functionals based on a screened Coulomb potential," *Journal of Chemical Physics*, vol. 118, no. 18, pp. 8207–8215, 2003.

[38] J. Heyd, G. E. Scuseria, and M. Ernzerhof, "Erratum: hybrid functionals based on a screened Coulomb potential [Journal of Chemical Physics 118, 8207 (2003)]," *Journal of Chemical Physics*, vol. 124, no. 21, Article ID 219906, 2006.

[39] J. Heyd and G. E. Scuseria, "Efficient hybrid density functional calculations in solids: assessment of the Heyd-Scuseria-Ernzerhof screened Coulomb hybrid functional," *Journal of Chemical Physics*, vol. 121, no. 3, pp. 1187–1192, 2004.

[40] J. Heyd, J. E. Peralta, G. E. Scuseria, and R. L. Martin, "Energy band gaps and lattice parameters evaluated with the Heyd-Scuseria-Ernzerhof screened hybrid functional," *Journal of Chemical Physics*, vol. 123, no. 17, Article ID 174101, 2005.

[41] M. D. Fontana, G. Metrat, J. L. Servoin, and F. Gervais, "Infrared spectroscopy in $KNbO_3$ through the successive ferroelectric phase transitions," *Journal of Physics C: Solid State Physics*, vol. 17, no. 3, pp. 483–514, 1984.

[42] G. I. Csonka, J. P. Perdew, A. Ruzsinszky et al., "Assessing the performance of recent density functionals for bulk solids," *Physical Review B*, vol. 79, no. 15, Article ID 155107, 2009.

[43] J. P. Perdew, A. Ruzsinszky, G. I. Csonka, L. A. Constantin, and J. Sun, "Workhorse semilocal density functional for condensed matter physics and quantum chemistry," *Physical Review Letters*, vol. 103, no. 2, Article ID 026403, 2009.

[44] R. Peverati and D. G. Truhlar, "Performance of the M11-L density functional for bandgaps and lattice constants of unary and binary semiconductors," *Journal of Chemical Physics*, vol. 136, no. 13, Article ID 134704, 2012.

[45] L. He, F. Liu, G. Hautier et al., "Accuracy of generalized gradient approximation functionals for density-functional perturbation theory calculations," *Physical Review B*, vol. 89, no. 6, Article ID 064305, 2014.

[46] C. Lin, Y. Zhao, and G. Yin, "Calculation of the lattice constant of solids with the use of valence electron structure parameters," *Computational Materials Science*, vol. 97, pp. 86–93, 2015.

[47] P. G. Kang, B. K. Yun, S. Shin et al., "Possible origin of stabilized monoclinic structure of $KNbO_3$ nanomaterials at room temperature," *Materials Science and Engineering B*, vol. 210, pp. 19–23, 2016.

[48] T. Zhang, W. Lei, P. Liu et al., "Insights into the structure-photoreactivity relationships in well-defined perovskite ferroelectric $KNbO_3$ nanowires," *Chemical Science*, vol. 6, no. 7, pp. 4118–4123, 2015.

[49] Z. Wu and R. E. Cohen, "More accurate generalized gradient approximation for solids," *Physical Review B*, vol. 73, no. 23, Article ID 235116, 2006.

[50] J. W. Liu, G. Chen, Z. H. Li, and Z. G. Zhang, "Hydrothermal synthesis and photocatalytic properties of $ATaO_3$ and $ANbO_3$ (A = Na and K)," *International Journal of Hydrogen Energy*, vol. 32, no. 13, pp. 2269–2272, 2007.

[51] T. Su, H. Jiang, H. Gong, and Y. Zhai, "An alternative approach of solid-state reaction to prepare nanocrystalline $KNbO_3$," *Journal of Materials Science*, vol. 45, no. 14, pp. 3778–3783, 2010.

[52] T. Zhang, K. Zhao, J. Yu et al., "Photocatalytic water splitting for hydrogen generation on cubic, orthorhombic, and tetragonal $KNbO_3$ microcubes," *Nanoscale*, vol. 5, no. 18, pp. 8375–8383, 2013.

[53] Y. Shiozaki, E. Nakamura, and T. Mitsui, *Ferroelectrics and Related Substances: Oxides Part 1: Perovskite-Type Oxides and $LiNbO_3$ Family*, New Series III/36A1, Landolt-Börnstein, 2001.

[54] M. Friedrich, A. Schindlmayr, W. G. Schmidt, and S. Sanna, "$LiTaO_3$ phonon dispersion and ferroelectric transition calculated from first principles," *Physica Status Solidi B*, vol. 253, no. 4, pp. 683–689, 2016.

[55] J. K. Dewhurst and J. E. Lowther, "High-pressure structural phases of titanium dioxide," *Physical Review B*, vol. 54, no. 6, pp. R3673–R3675, 1996.

[56] A. Beltrán, L. Gracia, and J. Andrés, "Density functional theory study of the brookite surfaces and phase transitions between natural titania polymorphs," *The Journal of Physical Chemistry B*, vol. 110, no. 46, pp. 23417–23423, 2006.

[57] A. van de Walle and G. Ceder, "Correcting overbinding in local-density-approximation calculations," *Physical Review B*, vol. 59, no. 23, pp. 14992–15001, 1999.

[58] P. Haas, F. Tran, and P. Blaha, "Calculation of the lattice constant of solids with semilocal functionals," *Physical Review B*, vol. 79, no. 8, Article ID 085104, 2009.

[59] S. Tinte, M. G. Stachiotti, C. O. Rodriguez, D. L. Novikov, and N. E. Christensen, "Applications of the generalized gradient approximation to ferroelectric perovskites," *Physical Review B*, vol. 58, no. 18, pp. 11959–11963, 1998.

[60] J. Muscat, V. Swamy, and N. M. Harrison, "First-principles calculations of the phase stability of TiO_2," *Physical Review B*, vol. 65, no. 22, pp. 4112–4126, 2002.

[61] M. Landmann, E. Rauls, and W. G. Schmidt, "The electronic structure and optical response of rutile, anatase and brookite TiO_2," *Journal of Physics Condensed Matter*, vol. 24, no. 19, Article ID 195503, 2012.

[62] F. Labat, P. Baranek, C. Domain, C. Minot, and C. Adamo, "Density functional theory analysis of the structural and electronic properties of TiO_2 rutile and anatase polytypes: performances of different exchange-correlation functionals," *Journal of Chemical Physics*, vol. 126, no. 15, Article ID 154703, 2007.

[63] M. Gerosa, C. E. Bottani, L. Caramella, G. Onida, C. Di Valentin, and G. Pacchioni, "Electronic structure and phase stability of oxide semiconductors: performance of dielectric-dependent hybrid functional DFT, benchmarked against *GW* band structure calculations and experiments," *Physical Review B*, vol. 91, no. 15, Article ID 155201, 2015.

[64] M. T. Curnan and J. R. Kitchin, "Investigating the energetic ordering of stable and metastable TiO_2 polymorphs using DFT+U and hybrid functionals," *Journal of Physical Chemistry C*, vol. 119, no. 36, pp. 21060–21071, 2015.

[65] A. Schindlmayr, "The *GW* approximation for the electronic self-energy," in *Many-Electron Approaches in Physics, Chemistry and Mathematics*, V. Bach and L. Delle Site, Eds., vol. 29 of *Mathematical Physics Studies*, pp. 343–357, Springer International, Cham, Switzerland, 2014.

[66] M. Landmann, M. Feneberg, M. Röppischer et al., "Transition energies and direct-indirect band gap crossing in zinc-blende $Al_xGa_{1-x}N$," *Physical Review B*, vol. 87, no. 19, Article ID 195210, 2013.

[67] C. Mietze, M. Landmann, E. Rauls et al., "Band offsets in cubic GaN/AlN superlattices," *Physical Review B*, vol. 83, no. 19, Article ID 195301, 2011.

[68] G. Wang, H. Chen, Y. Li, A. Kuang, H. Yuan, and G. Wu, "A hybrid density functional study on the visible light photocatalytic activity of (Mo,Cr)–N codoped $KNbO_3$," *Physical Chemistry Chemical Physics*, vol. 17, no. 43, pp. 28743–28753, 2015.

[69] M. M. Khan, S. A. Ansari, D. Pradhan et al., "Band gap engineered TiO_2 nanoparticles for visible light induced photoelectrochemical and photocatalytic studies," *Journal of Materials Chemistry A*, vol. 2, no. 3, pp. 637–644, 2014.

[70] F. Wang and A. M. Rappe, "First-principles calculation of the bulk photovoltaic effect in $KNbO_3$ and $(K,Ba)(Ni,Nb)O_{3-\delta}$," *Physical Review B*, vol. 91, no. 16, Article ID 165124, 2015.